ISRES Publishing

The Eurasia Proceedings of Science, Technology, Engineering & Mathematics

EPSTEM

VOLUME 21 IConTES CONFERENCE

ISSN: 2602-3199

ISBN: 978-605-72832-4-5

IConTES 2022: International Conference on Technology, Engineering and Science (IConTES)

November 16 - 19, 2022

Antalya, Turkey

Edited by: Prof.Dr. Mehmet Özaslan - Gaziantep University, Turkey

The Eurasia Proceedings of
Science, Technology, Engineering & Mathematics (EPSTEM)
ISSN: 2602-3199

IConTES 2022 NOVEMBER

Volume 21, Pages 1-540 (November 2022)

The Eurasia Proceedings of Science, Technology, Engineering & Mathematics (EPSTEM)

e-ISSN: 2602-3199

Address: Istanbul C. Cengaver S. No 2 Karatay/Konya/TURKEY

Website: www.isres.org

Contact: isrespublishing@gmail.com

Conference: IConTES 2022: International Conference on Technology, Engineering and Science (IConTES)
Conference website: https://www.2022.icontes.net
Dates: November 16 – 19, 2022
Location: Antalya, Turkey
Edited by: Prof. Dr. Mehmet Özaslan

About Editor(s)
Prof Dr. Mehmet Ozaslan
Department of Biology, Gaziantep University, Turkey
Website: http://mehmetozaslan.com/
E-mail: ozaslanmd@gantep.edu.tr

Language Editor(s)
Assoc. Prof. Dr. Kagan Buyukkarci
Department of English Language Education, Suleyman Demirel University, Turkey
E-mail: kaganbuyukkarci@sdu.edu.tr

Editorial Policies

ISRES Publishing follows the steps below in the procedings book publishing process.
In the first stage, the papers sent to the conferences organized by ISRES are subject to editorial oversight. In the second stage, the papers that pass the first step are reviewed by at least two international field experts in the conference committee in terms of suitability for the content and subject area. In the third stage, it is reviewed by at least one member of the organizing committee for the suitability of references. In the fourth step, the language editor reviews the language for clarity.

The Eurasia Proceedings of
Science, Technology, Engineering & Mathematics (EPSTEM)
ISSN: 2602-3199

Review Process

Abstracts and full-text reports uploaded to the conference system undergo a review procedure. Authors will be notified of the application results in three weeks. Submitted abstracts will be evaluated on the basis of abstracts/proposals. The conference system allows you to submit the full text if your abstract is accepted. Please upload the abstract of your article to the conference system and wait for the results of the evaluation. If your abstract is accepted, you can upload your full text. Your full text will then be sent to at least two reviewers for review. The conference has a double-blind peer-review process. Any paper submitted for the conference is reviewed by at least two international reviewers with expertise in the relevant subject area. Based on the reviewers' comments, papers are accepted, rejected or accepted with revision. If the comments are not addressed well in the improved paper, then the paper is sent back to the authors to make further revisions. The accepted papers are formatted by the conference for publication in the proceedings.

Aims & Scope

Technology and basic sciences are closely related fields. Developments and innovations in one of them affect the other. Therefore, the focus of the conference is on studies related to these two fields. Studies in the fields of technology and basic sciences are accepted to the conference even if they are not associated with other field. The conference committee thinks that a study in only one field (for example, mathematics, physics, etc.) will contribute to other field (such as technology) in future studies, even if it is not associated with the presentation at the conference. In line with this perspective, studies in the following fields are accepted to the conference: Biology, Chemistry, Physics, Mathematics and Technology.

The aim of the conference is to bring together researchers and administrators from different countries, and to discuss theoretical and practical issues in all fields of technology and basic science.

Articles: 1-67

CONTENTS

The Eurasia Proceedings of
Science, Technology, Engineering & Mathematics (EPSTEM)
ISSN: 2602-3199

The Eurasia Proceedings of
Science, Technology, Engineering & Mathematics (EPSTEM)
ISSN: 2602-3199

The Eurasia Proceedings of
Science, Technology, Engineering & Mathematics (EPSTEM)
ISSN: 2602-3199

The Eurasia Proceedings of
Science, Technology, Engineering & Mathematics (EPSTEM)
ISSN: 2602-3199

The Eurasia Proceedings of Science, Technology, Engineering & Mathematics (EPSTEM)
ISSN: 2602-3199

The Eurasia Proceedings of Science, Technology, Engineering & Mathematics (EPSTEM), 2022

Volume 21, Pages 1-10

IConTES 2022: International Conference on Technology, Engineering and Science

Modeling and Simulation of Marine Current Energy Conversion System with Six-Phase Permanent Magnet Synchronous Generator

Omokhafe James TOLA
Federal University of Technology Minna

Jacob TSADO
Federal University of Technology Minna

Edwin Albert UMOH
Federal Polytechnic Kaura Namoda

Yahaya Asizehi ENESI
Federal University of Technology Minna

Eugene Okenna AGBACHI
Federal University of Technology Minna

Abstract: This paper presents the analysis and simulation for a marine tidal current turbine system with a six-phase permanent magnet synchronous generator. The aim is to demonstrate the possibility of harnessing electricity generation for small towns along continental shorelines from strong marine tidal currents in the coastal region of the Gulf of Guinea along the Southwest region of Nigeria. Due to its advantages of being a clean form of renewable energy and much more predictable than wind and solar, marine current energy has received much attention in recent years. One of the most popular technologies for producing wind and tidal energy is the permanent magnet synchronous generator (PMSG), which is suitable for low speed tidal current and offers better power control choices for marine current turbines with a horizontal axis. However, multiphase PMSG is a machine for reaching this goal for low maintenance, high reliability systems in the tough underwater circumstances. Due to the turbine power coefficient's ability to effectively follow the ideal curve with any change in water current speed, the maximum electrical power extraction of 198 kW is made possible within the permitted range of tidal currents. The effectiveness of the proposed model was extensively investigated with MATLAB/Simulink software

Keywords: PMSG, Marine tidal current, Multi-phase, Power coefficient, Gulf of Guinea

Introduction

Discourse on global energy discussion is currently centered on the implications of energy source depletion and price variations. As a result, it is now urgently necessary to support possible abilities of generating energy through the development of low-carbon technologies, particularly those based on renewable resources. Marine tidal current energy is available on some remote islands and is a potential renewable energy source for Nigeria's coastal regions because of its great predictability (Okoli et al., 2017).

The kinetic energy in tidal currents can be transform into electricity utilizing rather advanced turbine tools, despite there being many different types of energy that may be collected from the ocean, including wave energy, thermal energy, ocean osmosis (salinity gradients), and biomass energy. With current technology, it is projected

- Selection and peer-review under responsibility of the Organizing Committee of the Conference

that there is 75 GW of marine current power that can be used globally and 11 GW in Europe. Among the European nations, the UK and France have the biggest tidal current capabilities (6 GW and 3.4 GW, respectively) (Zeyringer et al., 2018). It ought to be highlighted that the distinct benefit of energy from tidal is tied to the resource's great certainty. Gravitational interplay of the Earth, Moon, and Sun system determines the astronomical nature of tides, which makes the tidal currents greatly predictable with 98 percent accuracy for some years (Zhou et al., 2017).

The two essentially methods for utilizing marine tidal resources are: creating a tidal barrage over a bay or an estuary, or by directly capturing kinetic energy from moving tidal currents. The only disadvantage of the barrage approach is the a sizable barrage configuration might alter the hydrology and take a detrimental effect on the surrounding ecology(Zhou et al., 2017). Technologies have been created for some years that directly harness the kinetic energy of tidally-driven marine currents. The variable system scalability of tidal current turbines over tidal barrages is one benefit. Tidal barrages are more expensive and typically designed based on high GW competencies, which may be more than tiny coastal communities or isolated islands require.

The current consensus among energy stakeholders is that non-conversional energy expertise may be effectively used to close the growing breach amid energy demand, its sustainable supply, affordable, and abundant as well as to assure a less contaminated atmosphere. The best options among the renewable energies appear to be wind and hydropower (Amarante Mesquita et al., 2014; Güney & Kaygusuz, 2010; Zhou et al., 2019). The potential energy contained in reservoirs is harnessed by conventional hydropower through the use of dams and impoundments to create a hydraulic head difference, which is then turned into electrical energy by proper turbo machinery. Marine and hydrokinetic energy conversion technology, on the other hand, is a new class of hydro-to-electrical power systems that is rapidly becoming acknowledged as a distinctive and non-conventional energy solution (Ibrahim et al., 2021).

A marine current turbine (MCT) is a device that transforms the kinetic energy from the tidal fluctuation into electrical energy. Its process looks like that of wind turbines, with the exception that fluid density is substantially higher since energy is generated by the flow of water rather than air. Utilizing the kinetic energy of rivers, streams, tidal, or other artificial waterways for the purpose of producing energy is known as hydrokinetic energy conversion. It is a type of hydropower known as "zero head" that harnesses the energy of flowing water's velocity to drive a generator. It can alternatively be described as a low pressure, run-of-the-river turbine with an extremely low head requirement of less than 0.2 meters (Ladokun et al., 2013). Although they obtain energy via the hydrodynamic process as opposed to the aerodynamic lift or drag, their operating principle is identical to that of wind turbines. This innovative technique is viewed as a unique and unconventional approach to power generation that falls under the area of marine energy and in-land water resources (Güney & Kaygusuz, 2010).

Utilizing and converting ocean energy resources—derived from wind, waves, tidal currents, or marine currents— to reliable, abundant electrical power. Transformation systems can be simply incorporated into the existing utility power supply infrastructure and networks and are easily customizable. However, many nations have adopted policies in the development of renewable energy technology that are heavily dependent on the conversion of huge amounts of offshore wind energy into electrical power, with little focus being paid to other forms of renewable energy. It is important to avoid marginalizing the use of other non-conversional resources, such as marine energy sources, by focusing work and rerouting the available funds to offshore wind alone, despite the fact that this imbalance is understandable given how much more advanced wind technologies are.

However, low maintenance, high-reliability systems are strongly advised to support the progress in this area because the harsh underwater conditions hold down technological advancements. Therefore, a high-power density generation system is needed to efficiently harness marine current power and use tidal current, and a permanent magnet synchronous machine is needed to drive the rotor that has a high power-density and high efficiency. From the perspectives of efficiency, greater power factor, and higher torque density, is typically favoured over induction machines(Tola et al., 2022; Tola et al., 2021; Tola & Umoh, 2017). The high magnetic loading provided by the high residual flux density allows for a comparatively small active region of the air gap and thus a relatively compact overall machine (Tola et al., 2022).

Utilizing multiphase machines is another technique for achieving this goal, and it is made possible by the advent of power electronics converters. Less torque pulsation and little zero sequence harmonics are among its features, as well as high fault tolerance, or the capacity to continue operating even if one or two phases are defective (Wei et al., 2022) (Levi et al., 2016). Strong tidal current is necessary for tidal power, and a tidal current generator can be constructed in a region where a flow rate of at least 1.0 m/s occurs. The majority of tidal power plants that employ permanent magnet synchronous generators (PMSG) are capable of producing electricity at different

speeds (Abo-Khalil & Alghamdi, 2021). Additionally, it is recommended that low speed tidal current generators use direct drive permanent magnet synchronous generators (PMSGs), which have superior power management options for horizontal axis marine current turbines than doubly fed induction generators (DFIG) (Zhou et al., 2019).

Nigeria's hydrological setting is consecrated with a setup of waterways, tributaries, tidal, and marine currents along with non-natural water passages and other water physiques, displays substantial hydro potential both at the greater measure (megawatts) and the lesser measure (Kilowatts), which is based on the necessity to embrace and upturn renewable energy skills in Nigeria's energy network (Ladokun et al., 2013).

In order to generate electricity for remote or off-grid areas and to increase the output of already-existing non-conventional power plants, marine current energy conversion technology is being deployed in this study along with detailed modeling and analysis of six-phase PMSG. And it also emphasizes and gives a brief overview of the chances for using marine current resources in the Gulf of Guinea, which is in the southwest of Nigeria and along the Atlantic Ocean. This area is a possible site for the construction of tidal energy plants.

Methodology

A Marine Current Turbine

As with wind turbines for systems that convert wind energy, the stream turbine is utilized to capture the kinetic energy of the tidal current. In contrast to the vertical axis turbine's aerodynamic drag, marine current and wind energy systems frequently employ horizontal axis turbines, which have superior efficiency. The turbine's kinetic power output and the accompanying speed are given as (Abo-Khalil & Alghamdi, 2021).

$$P_t = \frac{1}{2}\rho C_p(\lambda,\beta)Av^3 \tag{1}$$

$$C_p(\lambda,\beta) = 0.5176\left[\left(\frac{116}{\lambda_i} - 0.4\beta - 5\right)e^{-\left(\frac{21}{\lambda_i}\right)} + 0.0068\lambda\right] \tag{2}$$

$$\lambda_i^{-1} = \left(\lambda - 0.08\beta\right)^{-1} - 0.035\left(1+\beta^3\right)^{-1} \tag{3}$$

Where $C_p(\lambda,\beta)$ is how efficient the turbine is, and depends on how efficiently the turbine operates and how the turbine blades move in relation to the fluid flow, ρ is sea water density and β is the pitch angle and the term λ is the "tip speed ratio" refers to the relative speed between the water and the turbine blades and is defined as:

$$\lambda = \frac{\omega r}{v} \tag{4}$$

Where v is the velocity of the fluid, ω the angular velocity of the turbine and r is the turbine blade radius and ρ is sea water density. For a certain tip speed ratio λ_{opt}, the power coefficient will achieve its maximum value for a precise tip speed ratio, and the turbine will afterwards provide the most power capture.

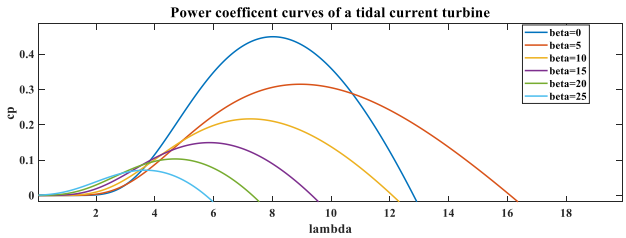

Figure 1. Power coefficient curves verse speed trip ratio

The main speed ratio at its optimum value, as shown in Figure 1, determines the output coefficient of the tidal current turbine, with varying pitch angles acting as a dependent variable. Additionally, the ideal speed ratio determines the tidal current turbine's output coefficient. It is essential to run at peak performance in order to generate the most power possible based on the flow rate.

This shows how the power coefficient of performance and tip speed ratio λ for different blade pitch angles β for a common maritime turbine relate to one another. Cp typically ranges from 0.25 to 0.5 for wind turbines. The maximum is for extremely effective machinery with minimal mechanical losses. According to Figure 1, Cp for marine turbines is thought to be between 0.35 and 0.5.

According to (Okoli et al., 2017), the tidal velocity of the Nigerian coastline region is examined using the harmonic analysis method. Tidal currents can be described as a stream of harmonics using equation (5) because they are a regular horizontal water flow that accompanies the rise and fall of the tide.

$$v(t) = \sum v_i . \sin\left(2\pi f_i t + p_i\right) \tag{5}$$

where the sinusoidal relationship between the tidal current magnitude and speed vi, tidal period f_i, and harmonic phase p_i.

The data supplied in (Okoli et al., 2017) the constituent of the tidal current in the coastal region of Nigeria are model and the tidal current simulation model are shown as illustrated in Figure 2.

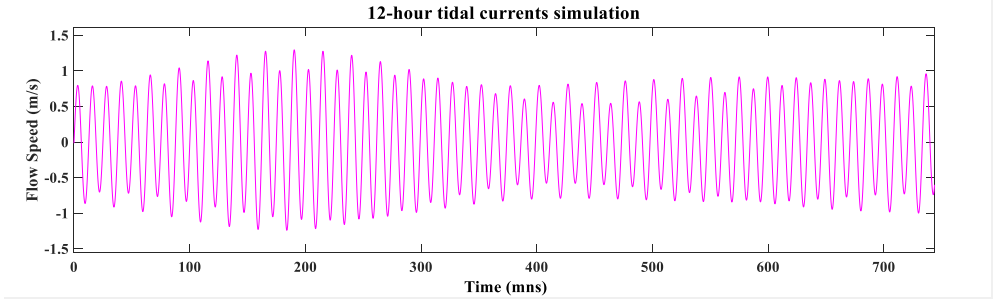

(a)

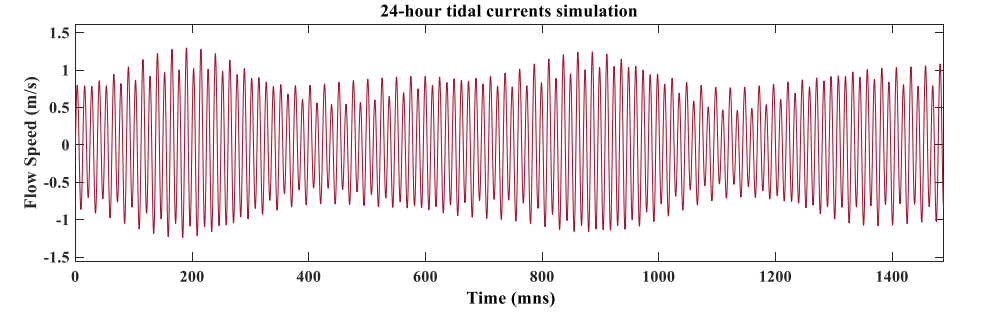

(b)

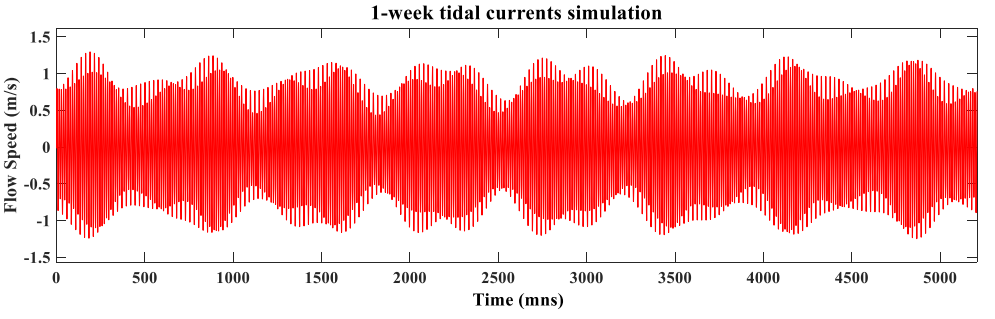

(c)

Figure 2. Tidal current simulation (a) 12-hour hour (b) 24-hour (c) 1-week

Modelling of a Six-Phase PMSG

The machine has two sets of three-phase stator windings: (abc) and (xyz). According to Figure 3, the two windings abc and xyz, whose magnetic axes are offset by 30^0, share a common magnetic structure and are located in the same stator slots (Kim et al., 2013; Karttunen et al., 2014; Tola et al., 2022). The following is the expression for the voltage equations that explain the electrical behavior of the machine in the machine variable (Tola et al., 2017):

$$\begin{cases} V_{abcs} = -R_s i_{abcs} + p\lambda_{abcs} \\ V_{xyzs} = -R_s i_{xyzs} + p\lambda_{xyzs} \end{cases} \tag{6}$$

where

$$\begin{cases} \lambda_{abcs} = L_{abc} i_{abcs} + L_{abcxyz} i_{xyzs} + \psi_{PM} \\ \lambda_{xyzs} = L^T_{abcxyz} i_{abcs} + L_{xyz} i_{xyzs} + \psi_{PM} \end{cases} \tag{7}$$

The flux linkages are functions of inductances and currents. And the flux linkage can be expressed as

$$L_{abc} = \begin{bmatrix} L_{la} + L_{aa} & L_{ab} & L_{ac} \\ L_{ba} & L_{lb} + L_{bb} & L_{bc} \\ L_{ca} & L_{cb} & L_{lc} + L_{\mathrm{cc}} \end{bmatrix} \tag{8}$$

$$L_{xyz} = \begin{bmatrix} L_{lx} + L_{xx} & L_{xy} & L_{xz} \\ L_{yx} & L_{ly} + L_{yy} & L_{yz} \\ L_{zx} & L_{zy} & L_{lz} + L_{zz} \end{bmatrix} \tag{9}$$

$$L_{abcxyz} = L_{12} + L_{l12} \tag{10}$$

$$\begin{cases} L_{12} = \begin{bmatrix} L_{ax} & L_{ay} & L_{az} \\ L_{bx} & L_{by} & L_{bz} \\ L_{cx} & L_{cy} & L_{cz} \end{bmatrix} \\ L_{l12} = \begin{bmatrix} L_{lax} & L_{lay} & L_{laz} \\ L_{lbx} & L_{lby} & L_{lbz} \\ L_{lcx} & L_{lcy} & L_{lcz} \end{bmatrix} \end{cases} \tag{11}$$

where L_{lax}, L_{lby}, L_{lcx} are inductances (mutual leakage) between the winding sets, L_{aa}, $L_{bb}, L_{cc}, L_{xx}, L_{yy}, L_{zz}$ are self –inductances, L_{ax}, L_{by}, L_{cz} are inductances (mutual) between the winding sets, ψ_{PM} is the PM flux linking the stator and considering sinusoidal distribution with ε as the displacement angle between the sets winding and λ_m is the permanent magnet amplitude is expressed as:

$$\psi_{PM} = \lambda_m \begin{bmatrix} \sin\theta \\ \sin\left(\theta - \frac{2\pi}{3}\right) \\ \sin\left(\theta + \frac{2\pi}{3}\right) \\ \sin(\theta - \varepsilon) \\ \sin\left(\theta - \frac{2\pi}{3} - \varepsilon\right) \\ \sin\left(\theta + \frac{2\pi}{3} - \varepsilon\right) \end{bmatrix} \tag{12}$$

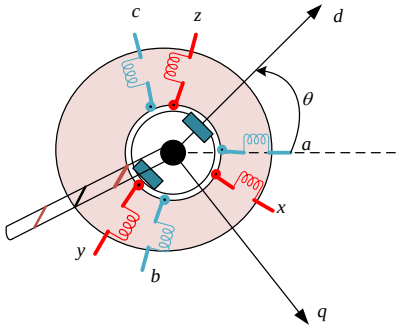

Figure 3. abc phase and xyz phase model of PMSM

The generator model's voltage and flux linkage equations in the d-q reference frame are expressed as:

$$\begin{cases} \frac{di_{d1}}{dt} = -\frac{1}{L_d} v_{d1} - \frac{R_s}{L_d} i_{d1} + \frac{L_q}{L_d} \omega_r i_{q1} \\ \frac{di_{q1}}{dt} = -\frac{1}{L_q} v_{q1} - \frac{R_s}{L_q} i_{q1} - \frac{L_d}{L_q} \omega_r i_{d1} - \frac{\lambda_m}{L_q} \omega_r \\ \frac{di_{d2}}{dt} = -\frac{1}{L_d} v_{d2} - \frac{R_s}{L_d} i_{d2} + \frac{L_q}{L_d} \omega_r i_{q2} \\ \frac{di_{q2}}{dt} = -\frac{1}{L_q} v_{q2} - \frac{R_s}{L_q} i_{q2} - \frac{L_d}{L_q} \omega_r i_{d2} - \frac{\lambda_m}{L_q} \omega_r \end{cases} \tag{13}$$

The six-phase PMSG electromagnetic torque and its dynamic are given by:

$$T_e = \frac{3n_p}{2}\left[-\lambda_m\left(i_{q1} + i_{q2}\right) + \left(L_d - L_q\right)\left(i_{d1}i_{q1} + i_{d2}i_{q2}\right)\right] \tag{14}$$

$$T_e = J\frac{d\omega_m}{dt} + f\omega_m \tag{15}$$

where n_p is the number of pole pair, J is moment of inertia, f is the viscous friction coefficient and ω_m is the generator speed.

The total electricalpower expressed in the abc variables is expressed as

$$P_{out} = v_{abc}^{T} i_{abc} + v_{xyz}^{T} i_{xyz} \tag{16}$$

$$P_{dq} = v_{dq}^{T} (k^{-1})^{T} (k^{-1}) i_{dq} \tag{17}$$

where k is the transformation constant. Therefore, the active and reactive power are expressed as:

$$\begin{cases} P = \left(v_{d1} i_{d1} + v_{q1} i_{q1}\right) + \left(v_{d2} i_{d2} + v_{q2} i_{q2}\right) \\ Q = \left(v_{d1} i_{q1} + v_{d2} i_{q2}\right) - \left(v_{q1} i_{d1} + v_{q2} i_{d2}\right) \end{cases} \tag{18}$$

And the KVA rating of the generator is given as:

$$S = \sqrt{P^2 + Q^2} \tag{19}$$

Results and Discussion

The following figures show the results of a dynamic simulation used to illustrate how well the generator performs when the region's tidal current speed fluctuations are used. When the tidal flow is at zero pitch angle and the turbine in Figure 1 is operating at tip speed ratio of 8, the power performance parameters of the turbine are within the operational range of 0.48. At a given zero, pitch angle, the stator currents are shown in Figure 4. The output power of the proposed generator, which is 198 kW and about equal to the machine's rated power, is shown in Figure 7 along with its active, reactive, and apparent power. The stator winding current is shown in Figure 4 with a clear indication of the displacement of the two-winding set. Figure 5 shows the electromagnetic torque, which is 6500 N-m and stable after 4 seconds. Figure 6 depicts the generator's rotational speed, which is 1500 rpm and synchronized after 4 seconds.

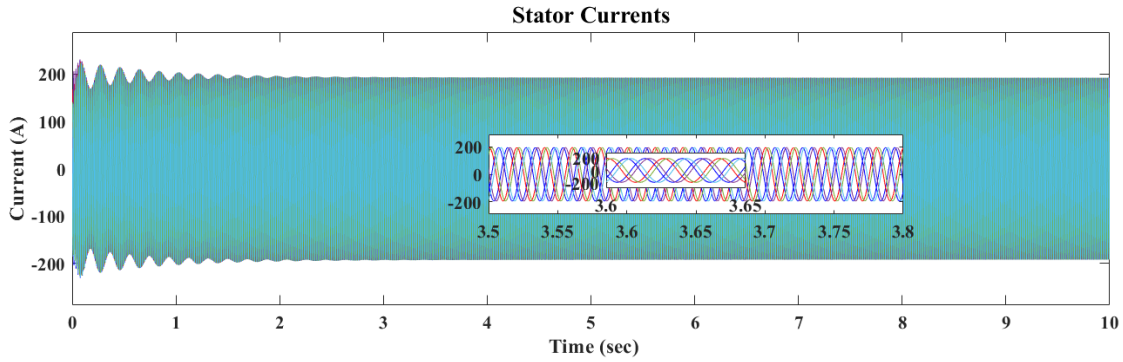

Figure 4. Stator currents

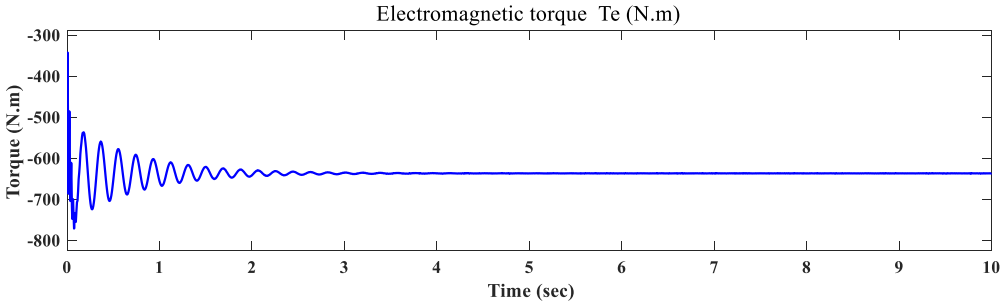

Figure 5. Electromagnetic torque

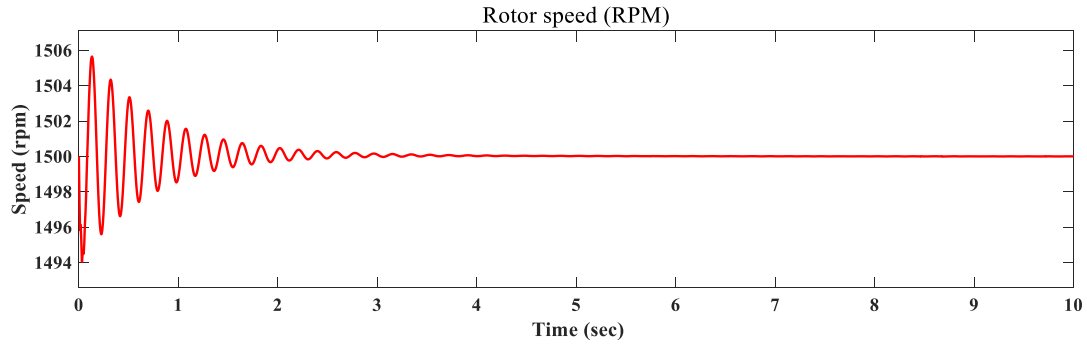

Figure 6. Rotor speed

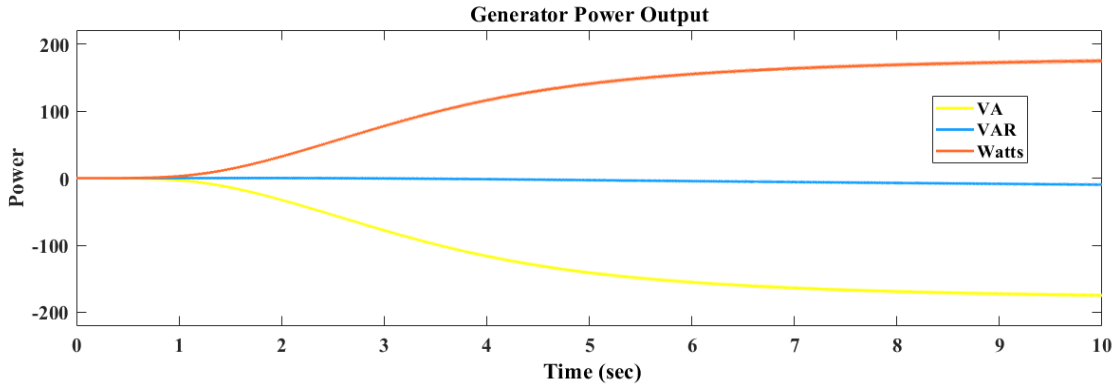

Figure 7. Generator Power

Conclusion

The fundamental need for human life is energy. Currently, oil and fossil fuels are used to meet the majority of the world's energy needs. However, these are finite resources. Therefore, harnessing renewable energy sources is urgently needed on a global scale. Since tidal energy is independent of the seasons and weather, it has some advantages over other renewable energy sources like wind and solar energy because it is more predictable over a longer time scale. Tides are a substantial potential source of clean renewable energy for generation of electricity in the coastal region of the Gulf of Guinea along the South-West region of Nigeria and small communities located near continental shorelines, or on remote islands with strong marine tidal currents. An overview of the power extraction from a marine tidal current turbine's speed profile is given. Moreover, d-q rotor reference frame has been used to model a detail PMSG model due to its advantages. Based on the speed of the tidal current in the Nigerian coastline region with a zero-pitch angle, the generator current, output power, electromagnetic torque, and rotor angular speed in a transient state are also shown. The outcomes suggest that the six-phase PMSG can be used successfully in the coastal region.

Scientific Ethics Declaration

The authors declare that the scientific ethical and legal responsibility of this article published in EPSTEM journal belongs to the authors.

Acknowledgements or Notes

* This article was presented as an oral presentation at the International Conference on Technology, Engineering and Science (www.icontes.net) held in Antalya/Turkey on November 16-19, 2022.

References

Abo-Khalil, A. G., & Alghamdi, A. S. (2021). MPPT of permanent magnet synchronous generator in tidal energy systems using support vector regression. *Sustainability*, *13*(4), 1–15. https://doi.org/10.3390/su13042223

Amarante Mesquita, A. L., Amarante Mesquita, A. L., Palheta, F. C., Pinheiro Vaz, J. R., Girão De Morais, M. V., & Gonçalves, C. (2014). A methodology for the transient behavior of horizontal axis hydrokinetic turbines. *Energy Conversion and Management*, *87*, 1261–1268. https://doi.org/10.1016/j.enconman.2014.06.018

Güney, M. S., & Kaygusuz, K. (2010). Hydrokinetic energy conversion systems: A technology status review. *Renewable and Sustainable Energy Reviews*, *14*(9), 2996–3004. https://doi.org/10.1016/j.rser.2010.06.016

Kim, H., Shin, K., Englebretson, S., Frank, N. & Arshad. W. (2013). Analytical model of multi-phase permanent magnet synchronous machines for energy and transportation applications. *IEEE, Electric Machines and Drives Conference (IEMDC), 2013*.

Ibrahim, W. I., Mohamed, M. R., Ismail, R. M. T. R., Leung, P. K., Xing, W. W., & Shah, A. A. (2021). Hydrokinetic energy harnessing technologies: A review. *Energy Reports*, *7*, 2021–2042. https://doi.org/10.1016/j.egyr.2021.04.003

Karttunen, J., Kallio, S., Peltoniemi, P., Silventoinen, P. & Pyrhonen. O. (2014). Decoupled vector control scheme for dual three-phase permanent magnet synchronous machines. *IEEE Transactions on Industrial Electronics*, *61*(4).

Ladokun, L. L., Ajao, K. R., Sule. B. F. (2013). Hydrokinetic energy conversion system Nigeria. *Nigerian Journal of Technology (NIJOTECH)*, *32*(3), 538–549.

Levi, E., Barrero, F., & Duran, M. J. (2016). Multiphase machines and drives-revisited. *IEEE Transactions on Industrial Electronics*, *63*(1), 429–432. https://doi.org/10.1109/TIE.2015.2493510

Tola, O. J., Obe, E. S., Obe, C. T., & Anih L. U. (2022). Finite element analysis of dual stator winding line start permanent magnet synchronous motor. *Przegląd Elektrotechniczny*, *4*(1), 47–52. https://doi.org/10.15199/48.2022.04.11

Okoli, C., Uhunmwangho, R., & Nwogu, H. (2017). A simulation model for tidal energy extraction in Nigeria using tidal current turbine. *Proceedings - 2017 IEEE PES-IAS PowerAfrica Conference: Harnessing Energy, Information and Communications Technology (ICT) for Affordable Electrification of Africa, PowerAfrica 2017*, 500–505. https://doi.org/10.1109/PowerAfrica.2017.7991276

Tola O. J., Ambafi, J. G.,. Umoh, E. A. & Olusegun, O. E. (2022). Performance analysis of a pmsm for traction applications in electric vehicles with hairpin winding technology. *International Conference on Disruptive Technology for Sustainable Development (NIGERCON)*, 987–1-6654-7978-3/22. https://doi.org/10.1109/NIGERCON54645.2022.9803182.

Tola O. J., Umoh, E. A., Yahaya, E. A. & Olusegun, O. E. (2022). Permanent magnet synchronous generator connected to a grid via a high speed sliding mode control. *International Journal of Robotics and Control Systems*, *2*(2), 379–395. https://doi.org/10.31763/ijrcs.v2i2.701

Tola O. J., Umoh, E. A., & Yahaya, E. A. (2021). Pulse width modulation analysis of five-level ınverter- fed permanent magnet synchronous motors for electric vehicle applications. *International Journal of Robotics and Control Systems*, *1*(4), 477–487. https://doi.org/10.31763/ijrcs.v1i4.483

Tola, O. J., Obe, E. S., & Anih, L. U. (2017). Modeling and analysis of dual stator windings permanent magnet synchronous motor. *IEEE 3rd International Conference on Electro-Technology for National Development (NIGERCON)*, 861–871. https://doi.org/10.1109/NIGERCON.2017.8281954

Tola, O. J., & Umoh, E. A. (2017). Modeling and analysis of a permanent magnet synchronous generator dedicated to wind energy conversion. *2nd International Engineering Conference (IEC 2017)*, 216–225.

Wei, Y., Qiao, M., & Zhu, P. (2022). Fault-tolerant operation of five-phase permanent magnet synchronous motor with ındependent phase driving control. *CES Transactions on Electrical Machines and Systems*, *6*(1), 105–110. https://doi.org/10.30941/cestems.2022.00014

Zeyringer, M., Fais, B., Keppo, I., & Price, J. (2018). The potential of marine energy technologies in the UK – Evaluation from a systems perspective. *Renewable Energy*, *115*, 1281–1293. https://doi.org/10.1016/j.renene.2017.07.092

Zhou, D., Chen, H., Zheng, Y., Kan, K., & Yu, A. (2019). Development and numerical performance analysis. *Energies*, *12*(22), 4264.

Zhou, Z., Ben Elghali, S., Benbouzid, M., Amirat, Y., Elbouchikhi, E., & Feld, G. (2019). Control strategies for tidal stream turbine systems - A comparative study of ADRC, PI, and High-Order sliding mode controls. *IECON Proceedings (Industrial Electronics Conference)*, *2019-Octob*, 6981–6986. https://doi.org/10.1109/IECON.2019.8927629

Zhou, Z., Benbouzid, M., Charpentier, J. F., Scuiller, F., & Tang, T. (2017). Developments in large marine current turbine technologies – A review. *Renewable and Sustainable Energy Reviews*, *71*, 852–858.

https://doi.org/10.1016/j.rser.2016.12.113

Author Information

Omokhafe James Tola
Federal University of Technology, Minna
Electrical and Electronic Department
Nigeria
omokhafe@futminna.edu.ng

Edwin Albert Umoh
Federal Polytechnic Kaura Namoda
Department of Electrical and Electronic Engineering Technology, Nigeria

Jacob Tsado
Federal University of Technology, Minna
Electrical and Electronic Department, Nigeria

Yahaya Asizehi Enesi
Federal University of Technology, Minna
Electrical and Electronic Department, Nigeria

Eugene Okenna Agbachi
Federal University of Technology, Minna
Electrical and Electronic Department,
Nigeria

To cite this article:

Tola, O. J., Umoh, E. A., Tsado, J., Enesi, Y. A., Agbachi, E. O. (2022). Modeling and simulation of marine current energy conversion system with six-phase permanent magnet synchronous generator. *The Eurasia Proceedings of Science, Technology, Engineering & Mathematics (EPSTEM), 21*, 1-10

The Eurasia Proceedings of Science, Technology, Engineering & Mathematics (EPSTEM)
ISSN: 2602-3199

The Eurasia Proceedings of Science, Technology, Engineering & Mathematics (EPSTEM), 2022

Volume 21, Pages 11-17

IConTES 2022: International Conference on Technology, Engineering and Science

Evaluation of Electricity Consumption in Turkey via Cubic Regression Analysis and One Way Anova Test

Ezgi GULER
Bilecik Seyh Edebali University

Suheyla YEREL-KANDEMIR
Bilecik Seyh Edebali University

Abstract: In the globalizing world, the importance of energy is increasing day by day. Countries can make investment plans within the analysis of production and consumption data for electrical energy. In this study, sectoral electricity consumption data (State Agency, Industrial Enterprise, Business, Residence, Agricultural Irrigation, Street Lighting) in Turkey were analyzed with statistical techniques. Using the sectoral data between 2000 and 2020, the consumption data for the next 5 years was estimated via Cubic Regression Analysis. The success of the Cubic Regression models was evaluated with the success criteria of MAPE (Mean Absolute Percent Error), RMSE (Square Root Mean Errors), and R^2 (Coefficient of Determination). In addition, the One-Way ANOVA technique was used in the study to make sector comparisons for electricity consumption data. It was investigated whether there was a significant difference between the averages of the sector groups, the suitability of variance was examined and the Tamhane T2 test, one of the Pairwise Comparison Tests (Post Hoc), was used. As a result, in this study, electricity consumption data was analyzed with different statistical techniques, and information was produced for both current and future periods.

Keywords: Cubic regression analysis, Electricity consumption, Forecasting

Introduction

Environmental degradation, global warming, and the need for energy are among the biggest challenges for societies in today's world. Given the expansion of the Internet of Things, some estimates indicate that the energy supply in 2040 will exceed the expected energy demand for 2040 (Duranton et al., 2022; Gellert et al., 2022). In this context, energy modeling has become a subject of interest for researchers interested in energy production and consumption. Modeling, analyzing, and estimating electricity consumption, which is one of the important energy resources, is also of critical importance for national and international maintenance and planning activities (Grigoryan, 2021). Electricity consumption forecasting refers to the forecast of future electricity sales by collecting and analyzing historical consumption data (Duan et al., 2019). There are many studies in the literature that include electricity consumption estimation and statistical analysis. Some of these studies are summarized:
Saranj and Zolfaghari proposed a hybrid approach to estimating electricity consumption based on wavelet transfer. Forecasting models are based on autoregressive integrated moving average with adaptive WT (AWT)-long short-term memory (LSTM) and explanatory variable (ARIMAX)-generalized autoregressive conditional variable variance (GARCH) type models (Saranj and Zolfaghari, 2022). Tyagi and Singh compared prediction models such as support vector regression (SVR), gradient boost decision tree (GBDT), artificial neural network (ANN), random forest (RF), and extreme gradient boost (XGBoost) for electricity consumption estimation. They used the extreme gradient boosting method to predict future building electricity consumption (Tyagi and Singh, 2022). Soyler and Izgi measured the annual electrical energy use of 23 public hospitals with over 100 beds in Istanbul, and after determining the monthly peak loads, they created two new forecasting models using

regression techniques for maximum demand forecasting. A positive result was obtained from the linear regression technique, which is one of the basic regression techniques, and a new design factor was determined in the light of the determined data, and the maximum power requirement of the hospital was estimated (Soyler and Izgi, 2022). Nsangou et al. evaluated the performance of electricity consumption factors using quantitative regression, decision tree, and neural network models for prediction. They used a data sample from a household electricity consumption survey in Cameroon to apply these three models through a comparative analysis (Nsangou, et al.,2022).

In this study, electricity consumption in different sectors/areas in Turkey is analyzed statistically. Consumption data for the years 2000-2020 are obtained from TURKSTAT (URL-1). 5-year estimation data are obtained by Cubic Regression Analysis. One Way ANOVA analysis is conducted to determine the consumption relations between sector groups. The difference between groups was tested with the Tamhane T2 test.

Method

In this study, the electricity consumption in Turkey data for the next 5 years was estimated via Cubic Regression Analysis. The success of the Cubic Regression models was evaluated with the success criteria of MAPE, RMSE, and R^2. In addition, the One-Way ANOVA technique was used in the study to make sector comparisons for electricity consumption data. It was investigated whether there was a significant difference between the averages of the sector groups, the suitability of variance was examined and the Tamhane T2 test, one of the Pairwise Comparison Tests (Post Hoc), was used.

Cubic Regression Analysis

Polynomial Regression Analysis is essentially a special case of multivariate linear regression (Meyers et al., 2016). Only one independent variable (x) is considered in Polynomial Regression Analysis. The variable x is “period (day, month, year, etc.)” for time series. In this study, the variable x is taken as "year". For the polynomial regression model, when the degree of the independent variable x is “3”, the related model is called the “Cubic Regression Model”. The cubic regression model is given in Eq. (1) (Guler and Kandemir, 2022).

$$y_i = \beta_0 + \beta_1 x_i + \beta_2 x_i^2 + \beta_3 x_i^3 + \mathcal{E} \quad (1)$$

where y_i is the dependent variable, β_0 is the regression constant, β_1, β_2, β_3 are the regression coefficients, x_i is the independent variable, $\mathcal{E}$ is the error term.

Model Evaluation Criteria

MAPE (Mean Absolute Percent Error)

MAPE is an error metric that represents the percent error between actual and estimated values (Ozkaya et al., 2022). The MAPE value is high when the estimated values do not reflect or overlap the actual values. When the MAPE value is below 10%, the accuracy of the prediction model is stated as very high (Gonultas et al., 2020). The MAPE formula giving the absolute error percentage is given in Eq. (2).

$$MAPE = \frac{100}{N} \sum_{j=1}^{N} \left| \frac{y_j - \hat{Y}_j}{y_j} \right| \quad (2)$$

Where, y_j and $\hat{Y}_j$ are actual and predictive values, N is sample size or the number of values.

RMSE (Square Root Mean Errors)

The formula of RMSE in comparison to regression equations is given in Eq. (3) (Tatliyer, 2020).

$$RMSE = \sqrt{\frac{1}{N} \sum_{j=1}^{N} (y_j - \hat{Y}_j)^2} \quad (3)$$

Where, y_j and $\hat{Y}_j$ are actual and predictive values, N is sample size or the number of values.

R^2 (Coefficient of Determination)

The R^2 calculated in the regression analysis measures how well the relationship between the predictive values and actual values fits a linear curve. A high R^2 value is a desirable feature for the regression model (Yerel and Ersen, 2013). The formula for R^2 is given in Eq. (4) (Piepho, 2019).

$$R^2 = 1 - \frac{\sum_{j=1}^{N}(y_j - \hat{Y}_j)^2}{\sum_{j=1}^{N}(y_j - \bar{Y}_j)^2} \quad (4)$$

Where, y_j and $\hat{Y}_j$ are actual and predictive values, $\bar{Y}_j$ is the mean value of the dataset, N is the sample size or the number of values.

One-Way ANOVA

If there are more than two independent groups and the data in these groups are quantitative data, it is decided by ANOVA of variance whether there is a statistically significant difference between the group means (URL-2). H_0 and H_1 hypotheses are established in the One-Way ANOVA test. If the H_0 hypothesis is rejected, there can be a statistically significant difference between the means of the groups. However, it cannot be determined between which averages there is a difference. For this, it is necessary to look at multiple comparison tests. If the variances are homogeneous, tests such as Tukey are used. If there is no homogeneity of variance, the Tamhane T2 test can be used.

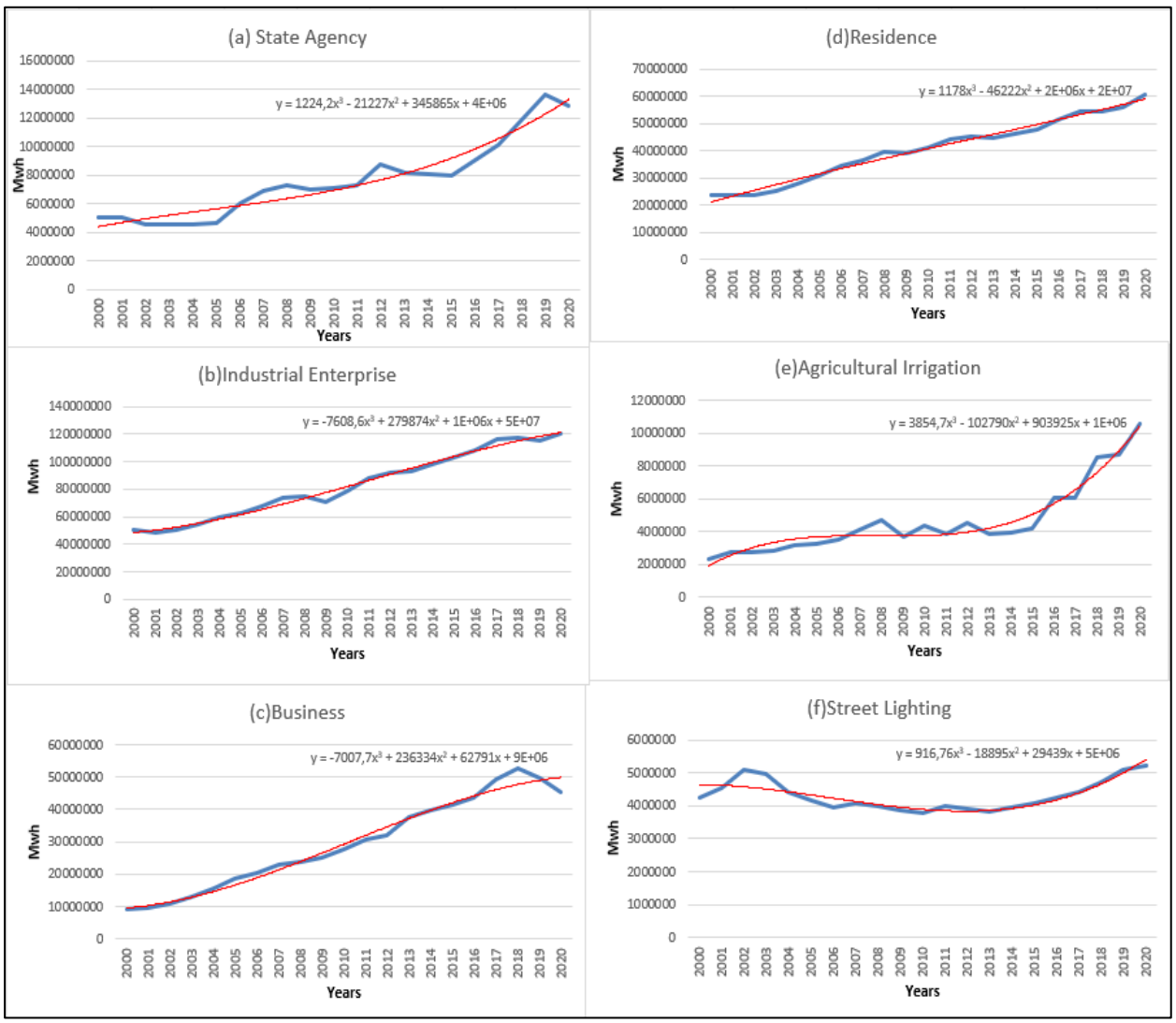

Figure 1. Forecasting model equations and graphs for sectors

Results and Discussion

In this study, Turkey's electricity consumption data between the years 2000-2020 has been analyzed. A cubic regression model was established for each sector group. Forecasting model equations and graphs obtained via cubic regression analysis are given in Figure 1. The values of the model evaluation criteria calculated as a result of the analysis of the cubic regression models are given in Table 1.

Table 1. Cubic regression models' evaluation criteria for sector groups

		Sector Groups					
		State Agency	Industrial Enterprise	Business	Residence	Agricultural Irrigation	Street Lighting
Model Evaluation Criteria	MAPE	0.09	0.04	0.05	0.08	0.10	0.09
	RMSE	722740.85	3804307.07	1993084.46	3896972.73	522048.55	420659.21
	R^2	0.93	0.99	0.98	0.98	0.94	0.80

According to Table 1, the cubic regression model accuracies for all groups are "quite good". With a MAPE value of 0.10, the regression model created for the Agricultural Irrigation group can be evaluated between "very good" and "good". The other calculated values also showed that the model accuracies can be predicted strongly. Estimated electricity consumption values for the next 5 years obtained via cubic regression models are given in Table 2.

Table 2. Estimated electricity consumption values for sector groups

		Sector Groups					
		State Agency	Industrial Enterprise	Business	Residence	Agricultural Irrigation	Street Lighting
Years	2021	14370443.60	126442643.20	50149068.40	54171896.00	12180835.60	6264138.48
	2022	15620653.40	128479509.80	50202193.10	55881288.00	14314499.90	6835860.92
	2023	16997348.80	130026137.60	49760923.20	57660800.00	16774532.80	7496306.24
	2024	18507875.00	131036875.00	48783212.50	59517500.00	19584062.50	8250975.00
	2025	20159577.20	131466070.40	47227014.80	61458456.00	22766217.20	9105367.76

In this study, One-Way ANOVA test was used as a different statistical analysis. It has been investigated whether there is a significant difference between the averages of electricity consumption data in terms of sector groups. In the analysis, firstly, homogeneity of variance was investigated. Table 3 contains the variance homogeneity table.

Table 3. Test of homogeneity of variances

Levene Statistic	df1	df2	Sig.
40.71	6	140	.00

Since the significance level (Sig.) is less than 0.05, the H_0 hypothesis, which accepts the variance of the groups as equal, is rejected. That is, group variances are not homogeneous. One-Way ANOVA test results are given in Table 4.

Table 4. Results of One-Way ANOVA

	Sum of Squares	df	Mean Square	F	Sig.
Between Groups	107235640463489696.00	6	17872606743914950.00	131.98	.000
Within Groups	18958480213475988.00	140	135417715810542.83		
Total	126194120676965696.00	146			

Since the significance level (Sig.) is less than 0.05, the H_0 hypothesis, which accepts the mean of the groups as equal, is rejected. That is, group variances are not homogeneous. That is, there is a statistically significant difference between the average of the sector groups.

In this study, the Tamhane T2 test was used to analyze the difference between the averages of which sector groups. (yazim formati farkli) Results of Tamhane T2 test are given Table 5.

Table 5. Results of Tamhane T2 test

(I) Sector Group	(J) Sector Group	Mean Difference (I-J)	Std. Error	Sig.
State Agency	Industrial Enterprise	-75462742.81*	5356512.88	.00
	Business	-21800143.57*	3155278.62	.00
	Residence	-32885684.05*	2605760.31	.00
	Agricultural Irrigation	2996483.48*	757171.95	.01
	Street Lighting	3345061.57*	597360.44	.00
Industrial Enterprise	State Agency	75462742.81*	5356512.88	.00
	Business	53662599.24*	6160755.09	.00
	Residence	42577058.76*	5898229.13	.00
	Agricultural Irrigation	78459226.29*	5345318.46	.00
	Street Lighting	78807804.38*	5325031.42	.00
Business	State Agency	21800143.57*	3155278.62	.00
	Industrial Enterprise	-53662599.24*	6160755.09	.00
	Residence	-11085540.48	4006577.07	.17
	Agricultural Irrigation	24796627.05*	3136236.98	.00
	Street Lighting	25145205.14*	3101533.90	.00
Residence	State Agency	32885684.05*	2605760.31	.00
	Industrial Enterprise	-42577058.76*	5898229.13	.00
	Business	1108554.48	4006577.07	.17
	Agricultural Irrigation	35882167.52*	2582670.32	.00
	Street Lighting	36230745.62*	2540416.53	.00
Agricultural Irrigation	State Agency	-2996483.48*	757171.95	.01
	Industrial Enterprise	-78459226.29*	5345318.46	.00
	Business	-24796627.05*	3136236.98	.00
	Residence	-35882167.52*	2582670.32	.00
	Street Lighting	348578.09	486866.23	1.00
Street Lighting	State Agency	-3345061.57*	597360.44	.00
	Industrial Enterprise	-78807804.38*	5325031.42	.00
	Business	-25145205.14*	3101533.90	.00
	Residence	-36230745.62*	2540416.53	.00
	Agricultural Irrigation	-348578.09	486866.23	1.00

*The mean difference is significant at the 0.05 level.

According to the results in Table 5, there is no significant difference between the average of Business and Residence electricity consumption. Since the sig value is greater than 0.05, there is no significant difference between the average of electricity consumption from Agricultural Irrigation and Street Lighting. The difference between the means of the other groups is statistically significant.

Conclusion

Analyzing electricity production and consumption data is the most important factor facilitating planning in this area. In this study, electricity consumption data in Turkey were analyzed statistically. Data between 2000 and 2020 were obtained and cubic regression analysis was applied for the electricity consumption values of 6 different sector groups. The success of the prediction models was analyzed and verified by calculating MAPE, RMSE and R^2 values. Consumption data for the next 5 years are estimated with the created forecast models. Different from the studies in the literature, additional analysis was made in the study and the electricity consumption averages between the groups were examined. The variance and differences of the groups were examined with the One-Way ANOVA test. Differentiating groups were evaluated using the Tamhane T2 test. It is important for researchers and decision makers that the study can create statistically different outcomes.

Recommendations

For future studies, the scope of the study can be expanded by including different dependent and independent variables in the analysis. Comparisons can be made using different regression techniques. Apart from regression analysis, different estimation techniques can be used.

Scientific Ethics Declaration

The authors declare that the scientific ethical and legal responsibility of this article published in EPSTEM journal belongs to authors.

Acknowledgements or Notes

* This article was presented as an oral presentation at the International Conference on Technology, Engineering and Science (www.icontes.net) held in Antalya/Turkey on November 16-19, 2022.

References

Duan, J., Tian, X., Ma, W., Qiu, X., Wang, P., & An, L. (2019). Electricity consumption forecasting using support vector regression with the mixture maximum correntropy criterion. *Entropy, 21(7),* 707.

Duranton, M., Bosschere, K.D., Gamrat, C., Maebe, J., Munk, H., Zendra, O. (2022, Jul 30). *The HIPEAC Vision 2017*, Retrieved from https://www.hipeac.net/vision/2017/

Gellert, A., Fiore, U., Florea, A., Chis, R., & Palmieri, F. (2022). Forecasting electricity consumption and production in smart homes through statistical methods. *Sustainable Cities and Society, 76*, 103426.

Gonultas, H., Kizilaslan, H., & N. Kizilaslan. (2020). Projections of effects of global warming on rainfall regime in some provinces; Ankara, Rize, Aydin and Hakkâri provinces example. *Turkish Journal of Agriculture-Food Science and Technology*, *8*(10), 2156-2163.

Grigoryan, H. (2021, November). Electricity consumption prediction using energy data, Socio-economic and weather indicators. A case study of Spain. In *2021 9th International Conference on Control, Mechatronics and Automation (ICCMA)* (pp. 158-164). IEEE.

Guler, E., & Kandemir, S. Y. (2022). Lineer ve kubik regresyon analizleri kullanilarak OECD ülkelerinin CO_2 emisyonlarinin tahminlemesi. *European Journal of Science and Technology, (34),* 175-180.

Meyers, L.S., Gamst, G., & Guarino, A.J. (2016). *Applied multivariate research: Design and interpretation*, 1st ed., New York, USA: SAGE Publications.

Nsangou, J. C., Kenfack, J., Nzotcha, U., Ekam, P. S. N., Voufo, J., & Tamo, T. T. (2022). Explaining household electricity consumption using quantile regression, decision tree and artificial neural network. *Energy, 250*, 123856.

Ozkaya, U., & Ozturk S. (2022). Gaussian regression models for day-level forecasting of COVID-19 in European countries. Understanding COVID-19: The role of computational ıntelligence. *Springer, Cham*, 339-356.

Piepho, H. P. (2019). A coefficient of determination (R2) for generalized linear mixed models. *Biometrical Journal*, *61*(4), 860-872.

Saranj, A., & Zolfaghari, M. (2022). The electricity consumption forecast: Adopting a hybrid approach by deep learning and ARIMAX-GARCH models. *Energy Reports*, *8*, 7657-7679.

Soyler, I., & Izgi, E. (2022). Electricity demand forecasting of hospital buildings in Istanbul. *Sustainability, 14(13),* 8187.

Tatliyer, A. (2020). Turkiye'deki tiftik uretimi degisiminin regresyon analizi ile incelenmesi. *Turkiye Tarimsal Arastirmalar Dergisi, 7(3),* 321-326.

TURKSTAT, (2022). *Energy Report*. https://www.tuik.gov.tr/

Tyagi, S., & Singh P. (2022). Short term and long-term building electricity consumption prediction using extreme gradient boosting. *Recent Advances in Computer Science and Communications, 15,* 1082-1095.

URL-1: TURKSTAT (2021) Electricity comsumption data.

URL-2: https://avys.omu.edu.tr/storage/app/public/burcinseyda.corba/122288/5.HAFTA.pdf

Yerel S. & Ersen T. (2013). Prediction of the calorific value of coal deposit using linear regression analysis. *Energy Sources, Part A: Recovery, Utilization, and Environmental Effects, 35(10),* 976-980.

Author Information

Ezgi Guler
Bilecik Seyh Edebali University
Bilecik, Turkey
Contact e-mail: *ezgi.guler@bilecik.edu.tr*

Suheyla Yerel Kandemir
Bilecik Seyh Edebali University
Bilecik, Turkey

To cite this article:

Guler, E. & Yerel Kandemir, S. (2022). Evaluation of electricity consumption in Turkey via cubic regression analysis and One-Way ANOVA test. *The Eurasia Proceedings of Science, Technology, Engineering & Mathematics (EPSTEM), 21*, 11-17.

The Eurasia Proceedings of Science, Technology, Engineering & Mathematics (EPSTEM)
ISSN: 2602-3199

The Eurasia Proceedings of Science, Technology, Engineering & Mathematics (EPSTEM), 2022

Volume 21, Pages 18-26

IConTES 2022: International Conference on Technology, Engineering and Science

Flow Pattern Analysis for Oscillatory Flow inside Resonator Tube for Thermoacoustic Refrigerator Using PIV Measurement

Siti Norsyahira MOHD ZAHARI
Universiti Malaysia Pahang

Nor Atiqah ZOLPAKAR
Universiti Malaysia Pahang

Nurrizatul Atikha RAHMAT
Universiti Malaysia Pahang

Abstract: A thermoacoustic refrigerator system is an alternative cooling system that uses air or inert gas as a cooling fluid. The environmentally friendly characteristics make this system potential as a green alternative for a cooling system. However, due to its low efficiency compared to conventional vapor compression systems, its application is limited. Since a thermoacoustic refrigerator is based on the oscillatory flow to generate a cooling effect, the understanding of a flow pattern inside the resonator tube is crucial to enhance the coefficient of performance (COP) of the system. In this study, Particle Image Velocimetry (PIV) is used to visualize the flow pattern inside the resonator tube. PIV is an optical, noninvasive technique that uses a high-speed camera, high-power multipulse laser, and synchronizer to capture the particle movement in the resonator with a length of 1 m, and the frequency applied is 100 Hz. The result shows that there is a formation of a vortex at the entrance and at the exit of the stack. The formation of the vortex at the entrance induces by the flow disturbance created by the stack. This vortex formation varied with the location of the stack and the amplitude of the wave applied. The velocity distribution of the particle inside the resonator tube is also presented and discussed in this paper. These findings indicate that the flow patterns and velocity distribution should be further analyzed to interpret the effect of these characteristics on the system. These results are expected to give a better understanding of the future development of the thermoacoustic system.

Keywords: Thermoacoustic, Flow pattern, Velocity distribution, PIV

Introduction

Thermoacoustic refrigeration (TAR) showed potential as an alternative for the cooling system. (L. Xiao et al., 2022) The environmentally friendly characteristics make this technology a desirable alternative method. The limitation of TAR to being commercialized or practically used widely is due to its low efficiency compared to conventional vapor compression systems(Chase, 1995), (Girgin & Türker, 2012),(Swift, 2017),(Biwa, 2021). Most of the researchers focus on the stack, which is the main component in TAR to improve efficiency(Alamir, 2019),(Babu & Sherjin, 2018), (Ilori et al., 2021). But, since the working principle of TAR is based on the oscillatory flow-powered sound wave, there is a minimal study that discussed the flow characteristics inside the resonator tube (Berson et al., 2008). Analyzing the acoustic flow, such as flow pattern and velocity distribution, is crucial to understand the behavior of the oscillatory flow inside the tube and then relate it with the heat transfer process. Understanding how heat is transmitted may help to boost the system's efficiency.

Recent studies by Allafi et al., 2021 found that the vortex appears where heat is transferred (Almukhtar Allafi et al., 2021). The appearance of the vortex may be influencing heat transfer. This phenomenon is owing to the

oscillatory flow's ability to facilitate heat transfer. A vortex would create a black hole in which heat transmission is impossible. Therefore, an oscillatory flow that is smooth and fluid would be more advantageous. Additionally, Zhang et al. (2013) also found the development near the end of the stack and concluded that the emergence of the vortex impacts pressure and velocity. (D. W. Zhang et al., 2013). As the formation of vortex is observed by (Almukhtar Allafi et al., 2021)and (Hireche et al., 2020), the current theoretical formulation by Rott is the linear theory of acoustic that assumes the flow is laminar may create the deviation between theoretical study with the actual system. Hence, studying the relation between oscillatory flow and the heat transfer process inside a resonator tube is crucial. Thus, the efficiency of the overall system can be improved.

There are several possible ways of obtaining reliable flow characteristic information (velocity profile, temperature distribution, and pressure) to perform detailed quantitative measurements for a thermoacoustic system. The methods that used in past researches for measuring velocity profiles are divided into two categories: simulation-based and experimental-based. The simulation-based methods involve Computational Fluid Dynamic (CFD) and Design Environment for Low Amplitude Thermoacoustic Energy Conversion (DeltaEC) methods to determine the velocity profiles. Meanwhile, for experimental-based, there are three methods that were applied by the previous researchers, which are Hot-Wire Anemometry (HWA), Laser Doppler Anemometry (LDA), and Particle Image Velocimetry (PIV). Based on the limited number of past research works done in investigating the velocity profile of thermoacoustic systems, majority of the researchers (X. Xiao et al., 2020), (Mohd Saat et al., 2019), (Abd El-Rahman et al., 2017) prefer to conduct research using simulation-based methods, especially the CFD method compared to experiment-based.Thus, the flow characteristic of thermocoustic system limited to the simulation data compared to the actual phenomenon. This may be due to the high cost of having to set up the experiment rig that involves certain components, especially for PIV and LDA setup.

For LDA systems are used by scientists and business professionals to better understand fluid dynamics. Using the measurement data, product designs may be fine-tuned to increase aerodynamic effectiveness, quality, and safety. Bailliet and co are the only groups that study the flow measurement in a resonator of TAR by using LDA. From LDA, they have taken note of the pressure and velocity of flow in the resonator. Then, validate by using an analytical method. Since the error is less than 8%, the result from the experiment is agreeable with the analytical. It showed that LDA is proved a good technique for study flow.(Bailliet et al., 2000). However, Zhang (2002) found LDA bias in the flow measurement (Z. Zhang, 2002). By using past raw data of TAR in 1D, 2D and 3D, he compared it with numerical which calculated. As result, the mean velocity was constant in all measured data. This showed that LDA is biased as turbulence influences the measurement.

Meanwhile, PIV is a technique that studies the velocity vector measurement by measuring the movement of particles between two image frames. This image was captured by the camera in between two light pulses (laser). In 2012, Blanc and his colleague investigate the effect of the vortex on heat transfer by using PIV. They used an acoustic pressure at 500Pa and 2500Pa. As result, they found out that the emergence vortex increases, and this phenomenon effecting of additional heating despite want loss of heat (Blanc-Benona et al., 2012). To evaluate acoustic and streaming in a thermoacoustic system, Debesse and his friend used undersample PIV measurement. By using different data processing tool in PIV, they found that when acoustic wave intensity increases, irregular streaming appear (Debesse et al., 2014). In 2020, Hireche and co study the generated convection flow in the thermoacoustic device by using PIV experimentally and also in simulation. They used all the thermoacoustic core with and also without a heat exchanger. As result, it was found that natural convection flow is significant that it affects the thermoacoustic effects (Hireche et al., 2020). From the past studies, it can be seen that using PIV in experiments helped researchers find multiple data that related to the flow. In TAR, even a slight change in parameters of the system allows multiple studies can be observed like Zhang et. al. Thus, this paper will study the flow pattern and velocity distribution inside the resonator in thermoacoustic system using PIV measurement.

Experimental Setup Using PIV

The standing wave thermoacoustic device contains a resonator with a length of 43 cm. The thermoacoustic device also contains a stack, a speaker for acoustics as shown in Figure 1a). The stack is designed to fit the resonance tube and is made from Acrylonitrile butadiene styrene (ABS) material using a 3D printer as shown in Figure 1b). 3D printer is chosen because it is more precise, and time saving compared to other alternative choices. The material selected for this stack should have low thermal conductivity. The thermal conductivity of the stack material has a negative impact on the performance of the thermoacoustic refrigerator. If the thermal conductivity of the stack material is high, the heat which has been pumped by the system will be conducted back to the cold side, thus reversing the cooling effect. Thus, ABS was chosen since it has low thermal conductivity. ABS was used for the stack material because of the good balance of impact, chemical, dimensional stability,

tensile strength, surface hardness and is also rigid. The designed stack has a diameter of 65 mm, and the length of the stack is 45 mm. Each plate in the stack has a thickness of 0.5 mm while the distance between each plate is precisely 1 mm. The plate is given spacing to also the movement of acoustic frequency and heat. This shape is chosen because of the as to study the acoustic particle velocity via a particle image velocimetry.

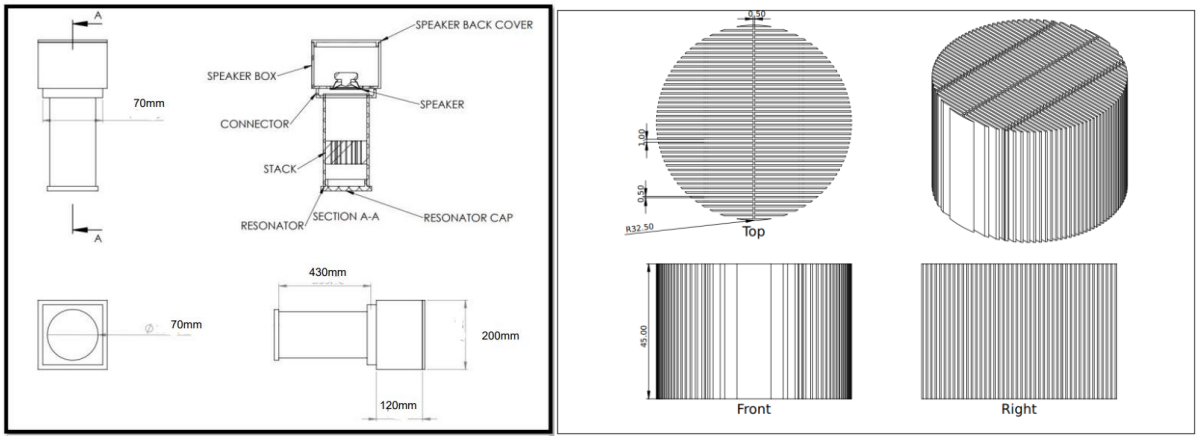

a) b)

Figure 1. a) Schematic diagram of TAR system b) Schematic diagram of stack

The components required for PIV setup is illustrated in Figure 2 for schematic and actual components. The laser beam is generated by a dual-resonator Nd: YAG laser with a wavelength of 532 nm. The laser has a repetition rate of 15 Hz. The laser energy could reach 135 mJ with an energy stability of 2 %. This is powerful enough to illuminate the seeding particles. The laser is placed on top of transparent rectangular lance to light the view window area. The light beam optical lens has 40 cm to the upper wall of the resonator. The short duration of light pulse is 5e7 ns, and the time between two laser pulses changes with the velocity which effectively freezes the particle position. The system uses a singular camera system for the PIV. The camera is a IMPERX ICL-B1620 with 1600 X 1200 pixels and 14-bit resolution CCD sensor, The camera lens is Nikon AF-S VR MICRO-NIKKOR 105 mm on the camera which is installed on a multi axis tripod with a 1:2.8 D lenses.

In PIV measurements, the velocity of the particles suspended in the flow is observed and measured by using seeding particles which serves as the "velocity indicator." The particles must be in appropriate size so that the flow can be accurately observed, and sufficient light can be scattered for the camera to detect them. The particles should be buoyant in the flow, and their density should be approximately the same as that of the fluid. Three types of particles are considered as seeding particles: the glass beads, the incense granules, and fog of silicone oil. Among them, the glass beads can be easily bonded to the plexiglass wall and the incense smoke is difficulty to control. As a result, the measurement plane is seeded with oil fog generated by a fog generator in the test.

Before the ejection of the droplet, the fog generator had a heating stage for about 20 minutes. The oil fog is then injected into the resonator before turning the loudspeaker on and is added at any time if the particle concentration is reduced. The particles are generated automatically with diameters ranging from 1 to 3 mm. The acoustic oscillation makes seeding particles homogeneous in the resonator and measurement of the velocity particles in the test bench could be performed.

In the measurement, the CCD camera has 60 frames per second at full resolution and the maximum laser frequency is 15 Hz; The laser frequency is lower than the frequency of the oscillation flow. Thus, it is not possible to shoot the images of the different phases in one cycle. To overcome this problem, a phase averaging method by phase locking technology is employed to acquire the images. First, the velocity signal near the resonator close end is transformed to square wave signal with the same frequency. Then, the converted signal is adjusted by the function generator and becomes TTL signal. In this procedure, the acoustic cycle is subdivided in 24 equally spaced phases. The adjusted signal triggers the laser and the camera to acquire the same phase of the cycles. Instantaneous velocity fields are acquired for each phase and averaged to obtain a phase-averaged velocity field. The PIV data processing software, dynamic studio v3.4 is used to determine the velocity maps. Based on past PIV research, the study area should be small enough so that no significant velocity gradient is present within the study area.

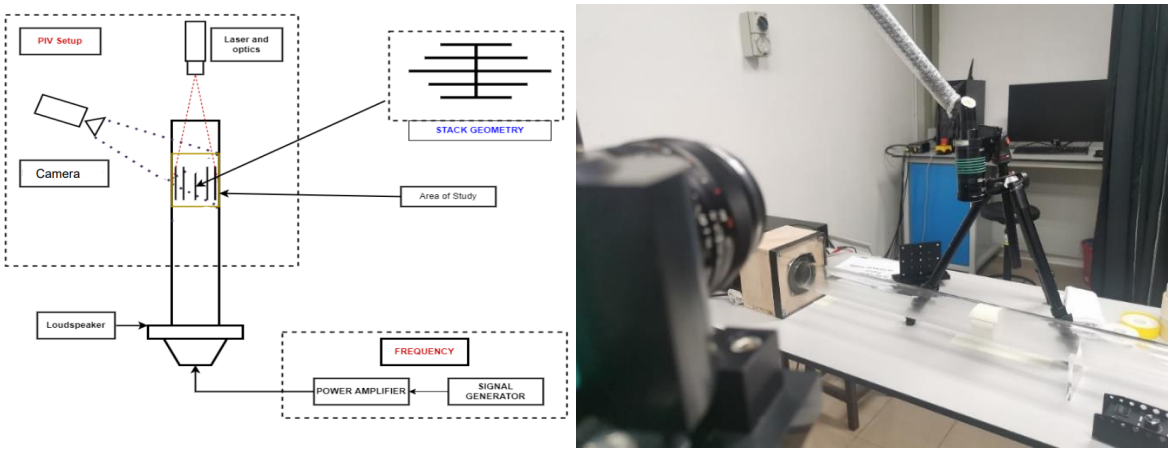

a) b)

Figure 2. a) Schematic diagram of TAR system with PIV b) Actual experiment setup with TAR system and PIV

Attachment of TAR System with PIV Measurement

To conduct the experiment, the thermoacoustic device is placed in front of the PIV measurement device. To do this a few steps need to be executed. Firstly, the camera and laser need to align exactly to the position where the stack will be placed. To do this a calibration plate is needed. A calibration plate is a series of evenly dotted lines which represents the 2-dimensional plane of the study area. The calibration area should exactly be the size of the study area, so that during the alignment process the cameras can be aligned properly. As we know the dimension of the stack is 65mm x 45mm. So, the calibration plate will be 65mm x 65 mm in size. The extra 20 mm is to see the behaviour of the airflow during the entrance and the exit from the stack.

Next is the camera and laser alignment. For this step the calibration plate is first placed in the position where the stack (study area) will be placed. For this experiment the calibration plate is placed about 30 mm deep of the stack so that all the stack fins can be measured. This position is also chosen due to the bridge in the middle of the stack which holds all the plates together. The laser is then aligned until it is in the same plane as the calibration plate. This step is important so that only particles at that plane is measured and not obstructed by the bridge in the middle of the stack. Next, the camera is then aligned to fit picture perfectly the study area which now being represented by the calibration plate. The multi axis tripod of the camera is adjusted to get the perfect position in Z-axis, Y-axis, and X-axis. The camera angle should also be adjusted to fit perfectly on the calibration plate. The measurement of the camera tripod from home position is as follows: -

X-axis – 358.00 mm
Y-axis – 0.00 mm
Z-axis – 400.00 mm

After this step, the alignment of the camera and laser is validated by using the dynamic studio v3.4 software. If the alignment is perfect, then the calibration plate position is marked and replaced with the thermoacoustic test rig. The position of the study is validated again so that no errors occur during the experiment. For this experiment, the variable that needs to fixed is the frequency of the acoustic flow. To decide this, we need to consider the past study and the capabilities of the existing thermoacoustic resonator. As stated, before the existing thermoacoustic device was designed for a 20Hz acoustic frequency. The 20Hz is selected because the whole thermoacoustic device is built in mind with that frequency.

Result and Discussion

Flow Pattern inside Thermoacoustic Resonator

Figure 3(a), (b), (c), and (d) show the flow formation inside the resonator tube from t = 0 until t = 1s. The black box is showing the location of the stack inside the resonator tube. From the flow pattern captured by PIV, there are several important observation can be made. Firstly, as the loudspekar is turn on, the velocity of the air is increasing as the effect of the acoustic sound wave inside the resonator. Then, as the sound wave entering the stack, there are increament of air velocity at the entrance and induce the vortex formation. This observation

supported by the previous study conducted by Allafi et al., 2021 that oscillatory flow past parallel plate structures creates significant vortex structures at the entrance and at the end of plates. The formation of the vortex also stronger at the end of plates as the flow changes direction after reflected at the end of the resonator. The air velocity between the parallel plate of the stack is equal with the velocity of the air before the entrance velocity. As the air leaving the stack, the air velocity increasing again as air is escaping from narrow gap between stack plate and can be observed from the figure, there are formation of the significant vortex at the exit of the stack. This finding is crucial and need to further investigation since the flow pattern will effect the heat transfer process between plate and the working fluid. This result also suggests that there maybe enough instabilities present in the flow to trigger turbulent transition.

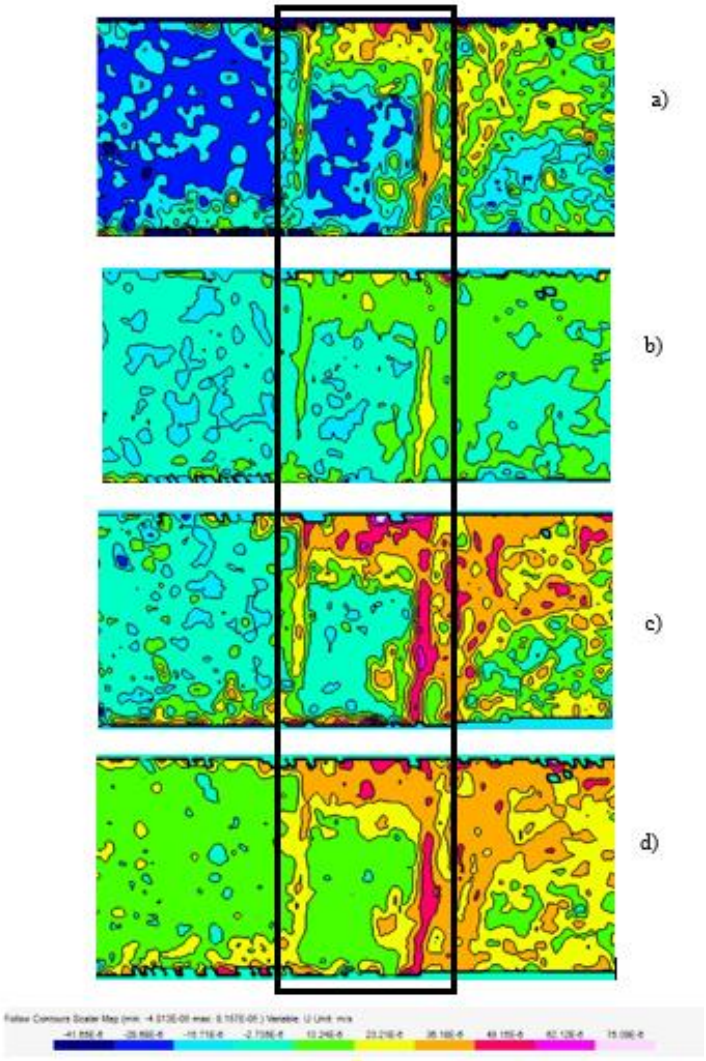

Figure 3. Flow pattern inside resonator when a) t = 0 s b) t = 0.333 s c) t = 0.667 s d) t = 1.00 s after the loudspeaker is turn on

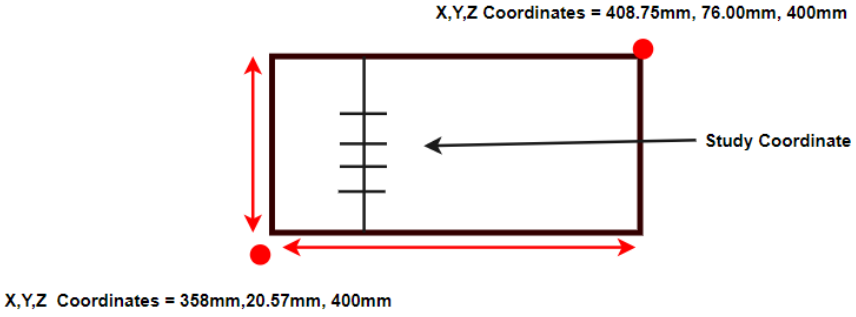

Figure 4. Study area in the resonator tube

Velocity Distribution in Thermoacoustic Resonator

To understand better about the results we need to understand the coordinates of the study area. The coordinate of the study is dependent on the home position of the camera rig. The study area coordinate starts from coordinates X= 358mm, Y= 20.57mm, and Z= 400mm. The study area is also in a rectangular shape due to the camera frame. The other end of the study area is X = 408.75mm, Y = 76.00 mm and Z = 400mm as shown in Figure 4, noted that the velocity distribution that will be discussed in this section only presenting the velocity at the entrance of the stack and the value of the velocity is an average value for particles captured by PIV measurement system.

For this analysis multiple coordinates in x coordinate over varying Y coordinate are chosen to study the difference in the flow pattern and differentiate the velocity profile. For a better understanding of the results and graphs the position of stack is quite important. The stack is at X coordinate 390 mm. The graph from Figure 5 (a) shows a harmonic flow pattern as the coordinates are in front of the stack region. The graph in figure 5(b) is bit different as it has higher Y velocity causing an unusual pattern in the resultant velocity. The formation of the flow pattern due to the disturbance of flow from large space to the narrow space, the spacing of the stack plate is 0.5mm which is narrow enough to form the vortex at the entrance of stack. In Figure 5(c) the point 4 and 2 shows the maximum velocity of 0.0595 m/s and 0.0565 m/s. This is because the flow just went past around the stack and create vortex formation at the entrance of the stack. This produces high velocity at both boundaries of stack. For Figure 5, it can be observec that only one point has a maximum velocity of 0.0439 m/s. By comparing the velocity of the flow in y direction for every x coordinate, it is observed in Figure 5(a), 5(b), and 5(c) the velocity at point 3 shows the minimum velocity which is at the middle point in y-coordinate for the stack. This may be due to the design of the stack that have structure support of the stack plate. The support of the stack completely blocks the flow thus it creates sudden velocity drop at that location.

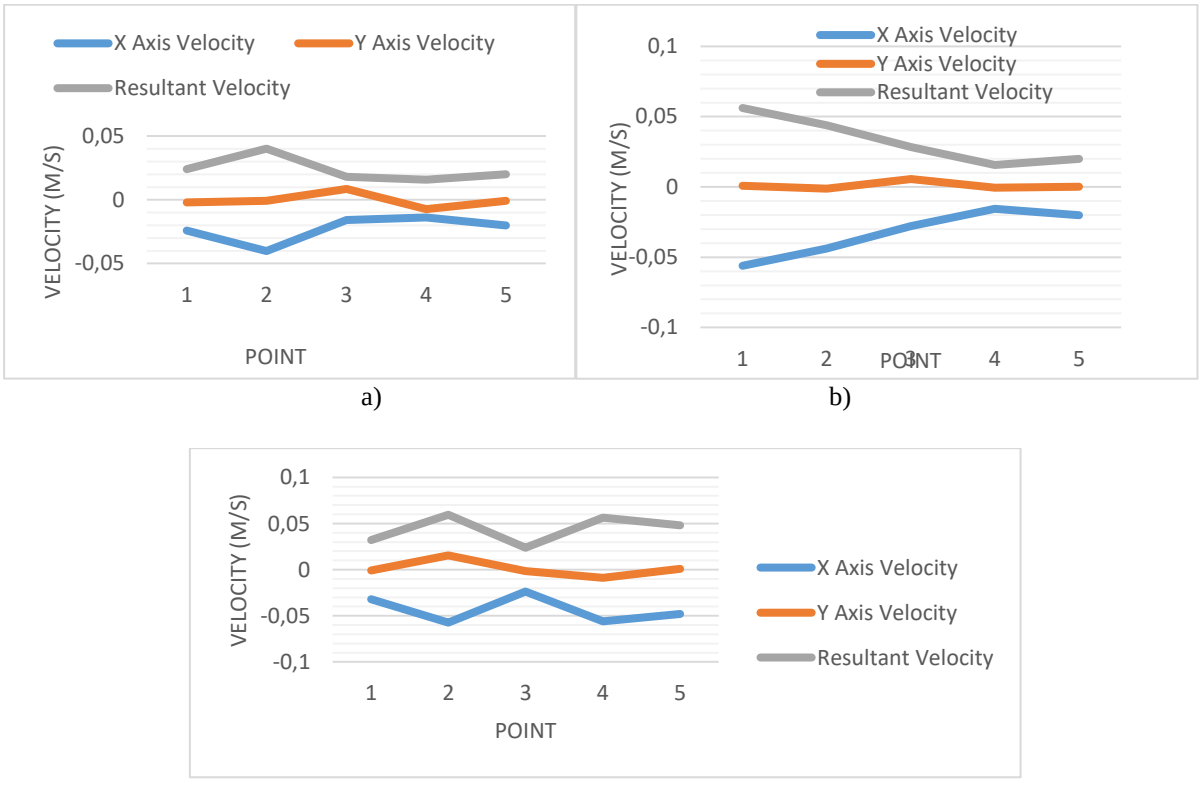

Figure 5. Velocity measurement when a) X axis is 372.43 mm b) X axis is 384.05 c) X axis is 395.68 mm

For this study multiple coordinates in Y coordinate over varying X coordinate are chosen to study the difference in the flow pattern and differentiate the velocity profile. For a better understanding of the results and graphs the position of stack is quite important. The stack is at X coordinate 390 mm. From Figure 6(a), 6(b), and 6(c) the point 1 and 2 are in a incline straight line showing a harmonic oscillatory flow because it is in front of the stack. Velocity of point 3 in Figure 6(b) which is 0.0595 m/s is quite high compared to point 3 and 4 in other figures indicating that the flow just went past around the stack and create vortex formation at the entrance of the stack. This produces high velocity at both boundaries of stack. By comparing the velocity of the flow in y direction for

every X coordinate, it is shown that the point 2 and 3 in the Figures 6(a), 6(b), and 6(c) show a higher resultant velocity of particle movement compared to point 1 and 4. This is caused by the vortex flow phenomena. Vortex flow reduces the pressure behind the stack and has a high velocity. This can be clearly seen in the graph trend. The velocity in Figure 6 is in the range of 0.018 m/s to 0.0283 m/s which is the minimum value for all three graphs. This may be due to the design of the stack that have structure support of the stack plate. The support of the stack completely blocks the flow thus it creates sudden velocity drop at that location.

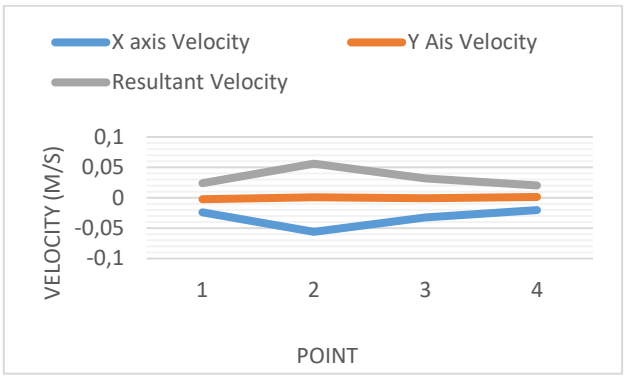

a)

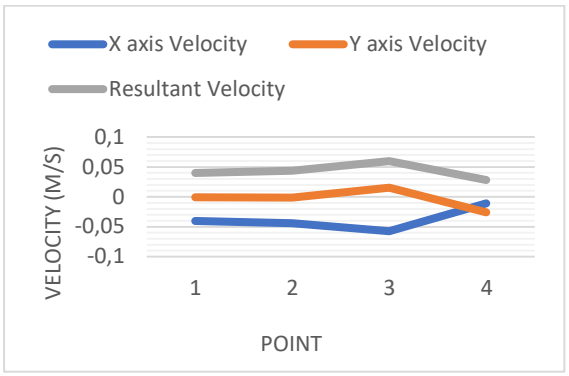

b)

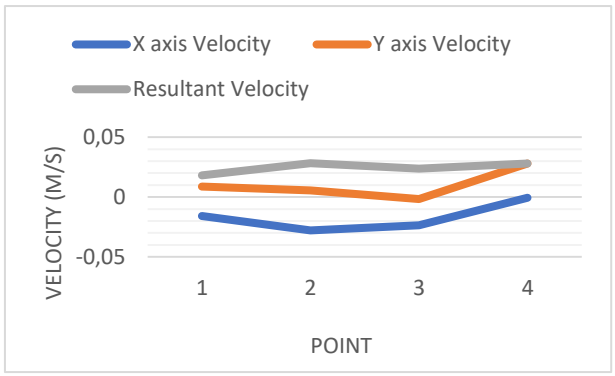

c)

Figure 6. Velocity measurement when a) Y axis is 20.57 mm b) Y axis is 35.11 mm c) Y axis is 48.19 mm

Conclusion

This experiment was done with the purpose of understanding the flow pattern of oscillatory flow and the effect of stack on the flow pattern in the thermoacoustic refrigerator. From the results of the experiment a lot has been understood regarding the flow pattern in a thermoacoustic refrigerator. From the experiment, the flow in the front of stack is known to be harmonic and linear. From the same result obtained, it can be concluded that the flow pattern of the oscillating flow forms vortex flows after the stack region. This is because it can also be clearly noticed that the acoustic flow separates from the stack on its two downstream sides, and, as the boundary layer becomes detached and curls back on itself, the fluid forms vortices. At the entrance of the stack the flow also creates vortex formation. The formation of the flow pattern might be due to the disturbance of flow from large space to the narrow space. The spacing of the stack plate is 0.5 mm which is narrow enough to form the vortex at the entrance of stack. At the middle of the stack, the velocity is minimum. This may be due to the design of the stack that have structure support of the stack plate. The support of the stack completely blocks the flow thus it creates sudden velocity drop at that location.

Scientific Ethics Declaration

The authors declare that the scientific ethical and legal responsibility of this article published in EPSTEM journal belongs to authors.

Acknowledgements or Notes

* This article was presented as an oral presentation at the International Conference on Technology, Engineering and Science (www.icontes.net) held in Antalya/Turkey on November 16-19, 2022.

*The authors acknowledge the Fundamental Research Grant Scheme (FRGS/1/2019/TK10/UMP/03/2) from the Ministry of Higher Education and grant RDU1803144 from Universiti Malaysia Pahang for providing financial support, and also for the use of the research facilities through the course of this research.

References

Abd El-Rahman, A. I., Abdelfattah, W. A., & Fouad, M. A. (2017). A 3D investigation of thermoacoustic fields in a square stack. *International Journal of Heat and Mass Transfer*, *108*, 292–300. https://doi.org/10.1016/J.IJHEATMASSTRANSFER.2016.12.015

Alamir, M. A. (2019). *Experimental study of the stack geometric parameters effect on the resonance frequency of a standing wave thermoacoustic refrigerator*. https://doi.org/10.1080/15435075.2019.1602533

Almukhtar Allafi, W., Mohd Saat, F. A. Z., & Mao, X. (2021). Fluid dynamics of oscillatory flow across parallel-plates in standing-wave thermoacoustic system with two different operation frequencies. *Engineering Science and Technology, an International Journal*, *24*(1), 41–49. https://doi.org/10.1016/J.JESTCH.2020.12.008

Babu, K. A., & Sherjin, P. (2018). Experimental investigations of the performance of a thermoacoustic refrigerator based on the Taguchi method. *Journal of Mechanical Science and Technology*, *32*(2), 929–935. https://doi.org/10.1007/s12206-018-0143-x

Bailliet, H., Lotton, P., Bruneau, M., Gusev, V., Valière, J. C., & Gazengel, B. (2000). Acoustic power flow measurement in a thermoacoustic resonator by means of laser Doppler anemometry (L.D.A.) and microphonic measurement. *Applied Acoustics*, *60*(1), 1–11. https://doi.org/10.1016/S0003-682X(99)00046-8

Berson, A., Michard, M., & Blanc-Benon, P. (2008). Measurement of acoustic velocity in the stack of a thermoacoustic refrigerator using particle image velocimetry. *Heat Mass Transfer*. https://doi.org/10.1007/s00231-007-0316-x

Biwa, T. (2021). Various thermoacoustic devices. *Introduction to Thermoacoustic Devices*, 1–21. https://doi.org/10.1142/9781944659776_0001

Blanc-Benona, P., Poignand, G., & Jondeaua, E. (2012). Investigation of the acoustic field in a standing wave thermoacoustic refrigerator using time-resolved particule image velocimetry. *AIP Conference Proceedings*, *1474*(1), 287–290. https://doi.org/10.1063/1.4749352

Chase, V. (1995). Here's a chilling thought: How to keep cool without CFCs. *Research and Development (Barrington, Illinois)*, *37*(11), 39–40.

Debesse, P., Baltean Carlès, D., Lusseyran, F., & François, M. X. (2014). Oscillating and streaming flow identification in a thermoacoustic resonator, from undersampled PIV measurements. *Measurement Science and Technology*, *25*(2). https://doi.org/10.1088/0957-0233/25/2/025005

Girgin, İ., & Türker, M. (2012). Thermoacoustic systems as an alternatives to conventional coolers. In *Journal of Naval Science and Engineering* (Vol. 8, Issue 1).

Hireche, O., Ramadan, I., Weisman, C., Bailliet, H., Fraigneau, Y., Baltean-Carlès, D., & Daru, V. (2020). Experimental and numerical investigation of natural convection flows in two horizontal thermoacoustic cavities. *International Journal of Heat and Mass Transfer*, *149*, 119195. https://doi.org/10.1016/J.IJHEATMASSTRANSFER.2019.119195

Ilori, O. M., Jaworski, A. J., Mao, X., & Ismail, O. S. (2021). Effects of edge shapes on thermal-fluid processes in oscillatory flows. *Thermal Science and Engineering Progress*, *25*. https://doi.org/10.1016/J.TSEP.2021.101004

Mohd Saat, F. A. Z., Mattokit, E., Mustaffa, S. H. A., & Ghazali, N. M. (2019). Numerical study of turbulence related to vortex shedding structures of an oscillatory flow in thermoacoustic energy system. *Energy Procedia*, *156*, 239–243. https://doi.org/10.1016/J.EGYPRO.2018.11.135

Swift, G. W. (2017). *Thermoacoustics a unifying perspective for some engines and refrigerators second edition*. https://doi.org/10.1007/978-3-319-66933

Xiao, L., Xu, J., Luo, K., Chen, G., & Luo, E. (2022). Numerical study of a heat-driven thermoacoustic refrigerator based on a time-domain lumped acoustic–electrical analogy model. *Energy Conversion and Management*, *268*, 115982. https://doi.org/10.1016/J.ENCONMAN.2022.115982

Xiao, X., Gu, X., & Zhang, X. (2020). Combination of thermoacoustic heat dissipation with oscillating convection: A novel cooling method. *International Journal of Heat and Mass Transfer*, *160*, 120177.

https://doi.org/10.1016/J.IJHEATMASSTRANSFER.2020.120177

Zhang, D. W., He, Y. L., Yang, W. W., Wang, Y., & Tao, W. Q. (2013). Particle image velocimetry measurement on the oscillatory flow at the end of the thermoacoustic parallel stacks. *Applied Thermal Engineering*, *51*(1–2), 325–333. https://doi.org/10.1016/J.APPLTHERMALENG.2012.09.011

Zhang, Z. (2002). Velocity bias in LDA measurements and its dependence on the flow turbulence. *Flow Measurement and Instrumentation*, *13*(3), 63–68. https://doi.org/10.1016/S0955-5986(02)00029-8

Author Information

Siti Norsyahira Mohd Zahari
Universiti Malaysia Pahang
26600 Pekan, Pahang
Malaysia

Nor Atiqah Zolpakar
Universiti Malaysia Pahang
26600 Pekan, Pahang
Malaysia
Contact e-mail: *noratiqahz@ump.edu.my*

Nurrizatul Atikha Rahmat
Universiti Malaysia Pahang
26600 Pekan, Pahang
Malaysia

To cite this article:

Mohd Zahari, S.N., Zolpakar, N.A., Rahmat, N.A. (2022). Flow pattern analysis for oscillatory flow inside resonator tube for thermoacoustic refrigerator using PIV measurement. *The Eurasia Proceedings of Science, Technology, Engineering & Mathematics (EPSTEM), 21*, 18-26

The Eurasia Proceedings of Science, Technology, Engineering & Mathematics (EPSTEM)
ISSN: 2602-3199

The Eurasia Proceedings of Science, Technology, Engineering & Mathematics (EPSTEM), 2022

Volume 21, Pages 27-38

IConTES 2022: International Conference on Technology, Engineering and Science

A Review of Solar-Powered Membrane Distillation System: Concept Design and Development

Mohd Amirul Hilmi Mohd HANOIN
Universiti Malaysia Pahang

Farah Najihah ZAINUDDIN
Universiti Malaysia Pahang

Nadzirah Mohd MOKHTAR
Universiti Malaysia Pahang

Abstract: Rising freshwater demands and environmental pollution lead to the increase of renewable energy utilization for seawater desalination system. One of the rapidly advancing technology for seawater desalination is the membrane distillation (MD) that has the potential to be integrated with renewable energy-driven operating systems, usually solar energy. This configuration is well known as solar-powered membrane distillation (SPMD), which can solve freshwater scarcity without increasing electricity cost. Numerous researchers have examined the integration of solar energy and MD for eco-friendly water desalination. However, there is a lack of information regarding this integrated system, although the system was invented over four centuries ago. In this review, the SPMD system was discussed in terms of its concept design and development. The significant contributions of the latest development of the SPMD system towards renewable energy and desalination technology were highlighted. In addition, the future research outlook in the area of SPMD is further discussed.

Keywords: Solar powered membrane distillation, Integrated system, Renewable energy, Solar energy, Desalination

Introduction

Water is a source of life and is needed for all social and economic endeavors. The earth has 97% of its water in saline form that has left only 3% of the freshwater that can be used by living creatures (Garud and Mane 2019). Of these, 2.5% fresh water is frozen in ice caps while the remaining 0.5%, accounting for 10 million m^3, corresponds to the available fresh water and its sustainable utilization and protection is vital for human survival (Byrne et al., 2015). Increasing population, rapid industrialization, uneven distributions of fresh water to the population, and the changing patterns of rainfall elevate the global issue of water scarcity. By 2050, water scarcity was predicted to increase further in most of the countries. About 73% of the people affected by water scarcity presently live in Asia (Boretti and Rosa, 2019). The domestic water supply for isolated communities or villages located in isolated areas typically originates from underground water, which can be classified as brackish water. The occurrence of freshwater scarcity crisis is due to the lack of water purity. This issue limits the water consumption of residents; thus, affecting the productivity of daily life and increasing the number of diseases. Therefore, to overcome this issue, researchers claimed that water is potable if it contained less than 500 parts per million (ppm) of salt. The desalination process is a possible method found capable of removing salt from seawater and brackish water. During the past 30 years, this process has been proven to be able to compensate for the freshwater scarcity in areas where a clean water source is not available. The common desalination processes are generally categorized as membrane-treatment and thermal desalination (Gude, 2016). The membrane-treatment technologies are comprised of reverse osmosis (RO), forward osmosis (FO),

electrodialysis (ED), and nanofiltration (NF). Meanwhile, the thermal desalination process incorporated phase change steps such as multi-effect evaporation distillation (MED), multi-stage flash distillation (MSF), thermal vapor compression (TVC), and mechanical vapor compression (MVC). Another desalination process is the hybrid operation, which combined both phase change and membrane-treatment, such as membrane distillation (MD) and the processes of RO cooperative with MSF or MED. Over the last decade, MD and RO are among the superior advanced desalination technologies for both brackish and seawater applications (Pangarkar et al., 2017; Swaminathan et al., 2018). However, the RO process had some problems due to the membrane fouling, lower flux, and requires a higher pressure that led to higher energy consumption (Pangarkar et al., 2017). Consequently, the MD, which is a thermal membrane process, were capable of overcoming these problems. MD system as a trans-membrane evaporation process that combines both membrane process and thermal distillation. The system also can be described as the vapor passes through the membrane by several mechanisms which can be classified into four configurations: direct contact membrane distillation (DCMD), vacuum membrane distillation (VMD), sweeping gas membrane distillation (SGMD), and air-gap membrane distillation (AGMD). Moreover, some advantages of MD over the RO process comprised higher resistance to fouling, and lower operating temperature and pressure that led to a more economical process to produce safe drinking water. Structurally, the conventional MD system makes use of full electrical supply from the grid system to power up the electrical components such as the pump, chiller, heater, sensor etc. in the system. As a result, it will increase the cost of electricity and pollution from fossil-fuel power station through the grid power supply. However, the feed solution only requires low temperature (around < 90 °C) to be heated and not necessarily heated to the boiling point. Therefore, the MD system has the potential of being coupled with renewable energies, especially solar energy, to heat the feed solution.

The solar-powered membrane distillation (SPMD) system was introduced to address the issues confronted by the MD system. The system has been invented since 1551 by Arab alchemists, and the first publication was in 1991. SPMD can be categorized as a sustainable desalination process with a green technology approach due to the integration of a secondary renewable energy source. From the desalination process, it can be proven that the utilization of renewable energy sources will lessen the environmental issues, save a non-renewable energy source for further implementations, and many other clean energy advantages (Nematollahi et al., 2013). SPMD can be explained structurally as an integration between the MD system and the solar collector. A solar collector is an energy exchanger that converts solar irradiation energy into either thermal energy through working fluid (air, water, or oil) in solar thermal collector (STC) applications, or to the electrical energy in photovoltaic (PV) applications. The solar collector has two types of design, which are the concentrating and non-concentrating collector (Wang et al., 2015; Jamar et al., 2016). The MD is capable of being integrated with both applications (STC and PV), while at the same time can be coupled with both types of solar collector. Coupling with non-concentrating collectors is commonly applied on remote arid, small-scale areas, whereas the concentrating collectors are normally utilized for large scale areas. Since the last decade, the commercialization of concentrating collectors has noticeably grown. However, a concentrating collector plant integrated with the desalination technology required higher electricity demand to drive the operation. Thus, the selection of STC types for integration with the MD system depends on different scenarios and requirement. Besides, the SPMD operation could also be used as a stand-alone or hybrid system. The stand-alone SPMD system is operated by a combination of STC and PV panels, while the hybrid system is driven by both STC and grid power supply. In the SPMD stand-alone system, the PV unit transforms the radiation into electricity aimed at controlling the electrical components, while the STC device transforms the radiation into thermal energy to manage the phase-change processes. Therefore, the system has the potential to produce freshwater in targeted areas with difficulties in obtaining freshwater due to the portability and the stand-alone feature of the grid power supply (Chafidz et al., 2016). For this reason, the SPMD acquired great attention in the past decade.

Integration of Solar Energy through Membrane Distillation

Most of the desalination systems require thermal and/or electrical input that can be provided by solar energy and much focus has been given to solar-based systems. Solar-driven desalination is categorized by potentially free energy supply and is suitable, especially in remote arid areas and for small scale production of freshwater where the availability of conventional energy supplies is limited. MD is a trans-membrane evaporation process comparable with other desalination and separation processes. Fundamentally, the conventional MD is dependent 100% on the electrical energy delivered from the electrical grid or based on a power plant which was used to control all electrically powered devices including for heating the saline solution and cooling down the permeate stream. However, the low operating temperatures, normally within the range of 50–90 °C, allow MD to be integrable with renewable energy sources like solar and geothermal energy (Zhani et al., 2016). Nematollahi et al. (2013) reported that the application of renewable energy sources in MD modules allows conventional energy

to be used for other applications; thus, minimizing the environmental issues, a choice of cheaper and low-maintenance energy source, and sustainable. All renewable energy sources can be utilized to produce useful energy in the form of electrical energy. Some renewable energy sources can also produce thermal energy for heating and cooling applications. Wind and water energies are converted to electricity, while solar, biomass, and geothermal energies can be converted to both electricity and thermal energy. Accordingly, the MD system requires thermal energy as a hot stream in the loop distillation system and electrical energy to power the electrical equipment. As reported by Blanco et al. (2009), the most suitable potential between all the renewable energies is solar energy. This claim was also supported by Mekhilef et al. (2011) that stated the utilization of solar energy became more attractive, clean with abundant of its quantity, capable to replace non-renewable energy sources, and able to meet the majority of the world's energy requirement in the future. A prelude on solar technologies, as well as the operational principle, is a requirement to investigate the current plus possible situation of solar-powered desalination. Solar energy can be utilized directly as electricity or as thermal energy, whether utilized in heating or cooling systems or impels turbines to produce electricity. Solar technologies are comprised of two general forms: solar thermal collector (STC) and solar photovoltaic (PV). STC is a device that converts solar radiation into thermal energy, while solar PV convert solar radiation into electricity. Jamar et al. (2016) have reviewed comprehensive studies on the STC device operated as solar water heater that consists of solar collector, storage tank and heat transfer fluid. Numerous efforts to integrate the solar energy with MD for seawater desalination have been recorded in the literature.

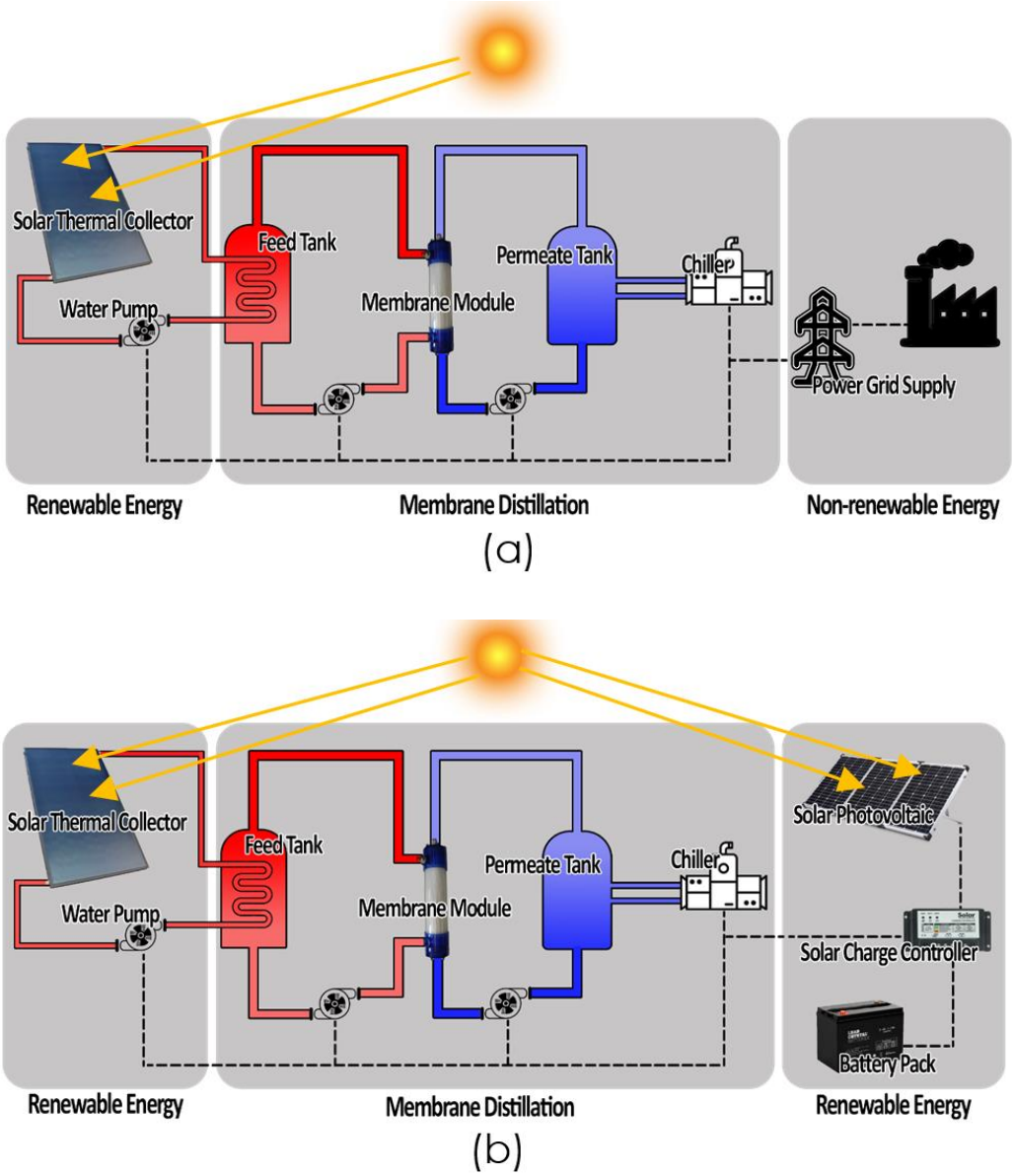

Figure 1. Two types of configurations: (a) solar assisted and (b) stand-alone SPMD system

As illustrated in Figure 1, Qtaishat and Banat (2013) stated that two different configurations of SPMD exist, which is solar-assisted and solar stand-alone membrane distillation system. The first configuration of solar assisted in MD modules is explained as a hybrid system that combines solar energy (renewable energy) and electricity grid (non-renewable energy) sources, as shown in Figure 1(a). From this configuration, solar technologies assist in heating up the feed solution only, whereas the energy needed for the rest of the processes will be generated by the electricity grid. Among the two types of solar technologies, STC is normally utilized as the thermal energy contributor for an MD system compared to solar PV because the energy transition of solar PV could lead to most heat loss issues. Over the last decade, STC has become of concern for numerous researchers and academicians around the globe due to its capability to collect heat by absorbing sunlight. In a simple definition, the STC acts as a piece of equipment that provides thermal energy through the hot water stream in the MD modules. The utilization of STC as solar thermal technology is further divided into two categories according to concentrating ratios; non-concentrating collectors and concentrating collectors. These different types of design depend on various desired applications. The STC supplied heat either directly to the feed solution or through the heat exchanger. However, there are situations when insufficient energy occurs whereby STC could not supply enough thermal energy into the MD system. This is due to the performance and efficiency of STC to absorb, convert, and transmit the energy through the MD system. Therefore, an auxiliary heater will be added to back up the insufficient thermal energy issues.

On the other hand, the second configuration known as autonomous SPMD system utilizes only energy from the sun; thus, eliminating the electricity grid from a power plant, as shown in Figure 1(b). The system is quite similar to the first configuration in all its aspects except that the solar PV panels are utilized rather than the electricity grid from a power plant to provide the required electricity. From this configuration, both electrical and thermal energy sources are produced by collecting solar energy from the sun. The thermal energy is formed through the STC system, while the electrical energy is produced by the solar PV system. Therefore, this stand-alone SPMD system can be considered as a dependable technology capable of working on zero-energy concept due to the clean source of energy. Furthermore, freshwater demand and solar energy are highly related to each other especially when located in coastal and remote arid areas, whereby both freshwater demand and the potential of solar energy increase during the summer season (Chafidz et al., 2016).

System Characterization

Based on previous research, the SPMD system can be classified into three designs, which are open-loop (direct), closed-loop (indirect), and directly integrated SPMD system. These systems can be operated by using a pump (active system) or natural thermo-siphon (passive system).

Open-Loop SPMD System

It is known as a “compact-system” with the simplest and typically the least expensive system to install. The hot water stream from the MD modules is directly heated from the STC panel without any heat exchanger, which allow efficient heat transfer directly to the water. A conventional compact system operates when the cold feed water is pumped out into the condenser of the MD modules from the inlet point to the outlet point in a counter flow while heating up, as shown in Figure 2(a). The STC that is connected right away from the condenser channel the outflow of MD, receiving the pre-heated feed water. Then, it is re-circulated to the evaporator. The temperature differences on both sides of the membrane caused partial pressure differences that lead to the driving force of the vapor passing through the membrane. As a result, the distillate is obtained from the distillate outlet. The advantages of this system are the simple design with an acceptable level of effectiveness due to fewer heat losses to the surrounding and no heat exchanger is required. Meanwhile, the shortfall of the open-loop system is that the STC system must be corrosion resistant from the feed water stream (Porrazzo et al., 2013). This is due to the configuration of the system that is directly connected from the feed (untreated) water of the MD module through the STC system. Moreover, open-loop direct systems are only appropriate for mild and moderate climates where freezing is minimal.

Koschikowski et al. (2009) reported six compact systems were established in five different countries since December 2004. Pozo Izquierdo in Gran Canaria is the earliest system installed followed by Alexandria (Egypt), Irbid (Jordan), Kelaa de Sraghna (Morocco), Freiburg (Germany), and lastly in Tenerife (Spain) since December 2007. Raluy et al. (2012) conducted the first compact system experiment in December 2004. The solar system coupled with MD compact system was established in the Instituto Tecnologico de Canarias (ITC) facilities. The result showed an average of 5–120 L per day of water production from the device, while the distillate production

of daily maximum during the winter months was achieved. The specific thermal energy consumption and conductivity of distillate water were obtained within the limits of 140–350 kWh/m^3 and 20–200 μS/cm, respectively.

Closed-Loop SPMD System

On the contrary, the design of the closed-loop SPMD system is slightly different from the open-loop system because this system aims for daily capacities of higher than 1000 L (Koschikowski et al.. 2009). Thus, this "large-system" is known as an indirect or two-loop system in terms of its design configuration. A flow diagram of the typical indirect SPMD process is shown in Figure 2(b). Structurally, the system has two loops, which is the STC loop and the MD loop. These two loops are connected by a heat exchanger that operated as the equipment to transfer thermal energy from the STC loop through the MD loop. Basically, the closed-loop SPMD system consists of a similar basic component like the open-loop SPMD, with the difference only in the additional heat storage tank and heat exchanger equipment. The closed-loop systems are generally more complicated than an open-loop system because these systems need either a tank with a heat exchanger coil or an external heat exchanger. Besides, these systems are slightly less efficient than open-loop systems as there is a potential for heat loss through the heat exchanger. However, the special benefit of the closed system is the ability to extend the time of operation up to 24 h/day due to the installation of the heat storage tank and the utilization of freeze-resistant fluid that are more suitable for frost-prone areas.

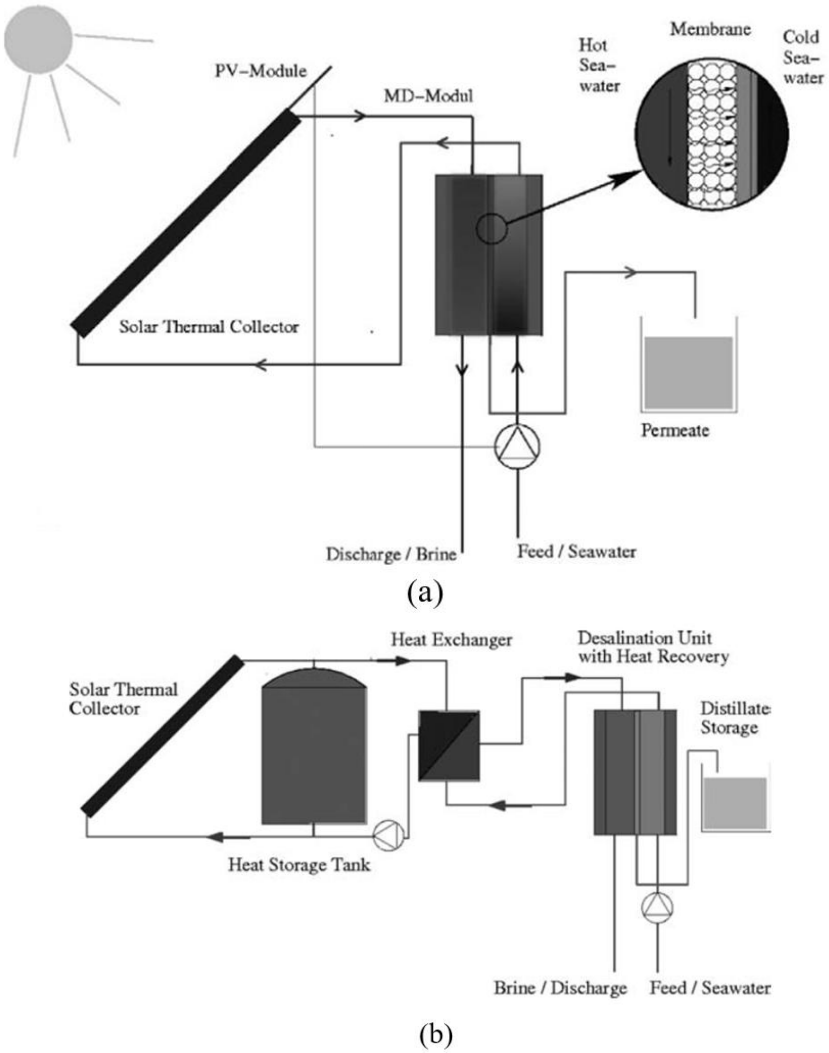

Figure 2. Conventional types of systems configuration: (a) open-loop SPMD system and (b) closed-loop SPMD system (Koschikowski et al., 2009)

Koschikowski et al. (2009) conducted the experimental investigation of closed-loop SPMD system by solar driven stand-alone MD system for remote areas. This system used collector field, MD modules, STC loop, and

components of two loop system installed at Gran Canaria, Spain. The STC type was an FPC double glass AR-coated with two loops AGMD for MD type. The result reported that the water production volume is 1200 L/day.

Directly Integrated SPMD System

The conventional SPMD system is designed with physically separated STC and MD modules. A complex system of pipes, thermal storage tank, heat exchanger, fittings, and other apparatus arrangements in these systems are needed to manage the heat and mass transfer for the STC with the MD unit. The system mainly uses thermal energy after conversion from solar radiation to heat up the feed solution. Structurally, the membrane section is located or directly integrated with the absorber section of the STC system. Due to the high price and complexity, a study of the STC design that is directly integrated into the distillation unit of several types of MD modules such as DCMD, AGMD, and VMD has been investigated (Mericq et al., 2011; Ho et al., 2016; Li et al., 2019). Figure 3 shows the differences between the conventional SPMD system and the directly integrated SPMD system design. This inventive combination of STC and MD unit exhibits an unconventional method that integrates both units into an effective, inexpensive, and more compact units with lesser heat loss throughout the energy flow from STC into the MD processes. According to the economic study, a method known as the "Lean Canvas" approach was implemented on the directly integrated SPMD system focusing at rural communities of Gujarat, India (Li et al., 2018).

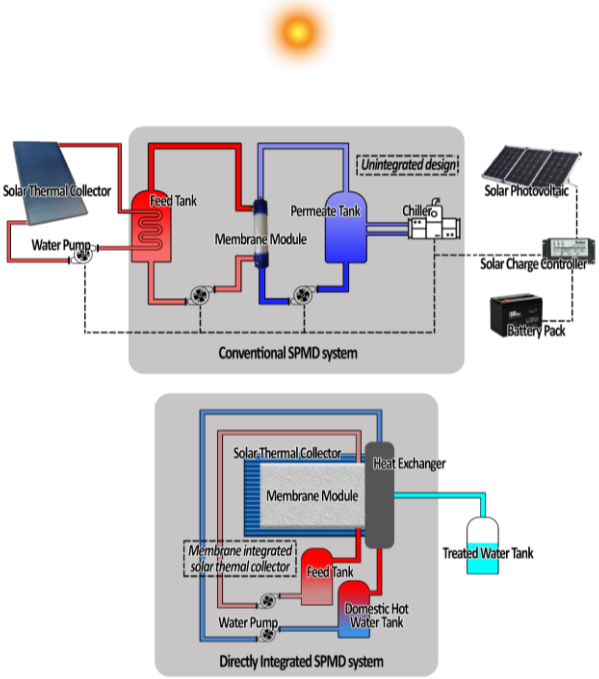

Figure 3. Comparable design between the conventional and directly integrated SPMD system

SPMD Development

The integration between STC and MD modules has gained attention from various researchers over the world. As illustrated in Figure 4, the first invention of SPMD was accomplished in 1551 by Arab alchemists and afterward by Della Porta in 1589, continued by Lavoisier in 1862, and Mauchot in 1869 (Al-Hayeka and Badran, 2004). However, Flendrig et al. (2009) stated that Wilson is the first Swedish engineer who invented the conventional solar still plant constructed on a large scale in 1872 for allocating freshwater to the neighboring folks and mine laborer at northern Chile. An insight into the "SPMD emergence phase", the first publication in 1991 was documented from the University of New South Wales, Australia by Hogan et al. (1991). After that, extensive literature was available during that era for promoting SPMD.

During the "SPMD resurrection phase", it is proven that SPMD has gained interest from influential companies specializing in MD modules focusing on MD systems integrated with solar energy. The research project's attention on SPMD has been sponsored by a multi-organization entity identified as the European Commission (EC) and reinforced by the other participating entities. The projects were funded by EC purposely to improve

the methods of environment-friendly desalination for freshwater production. In 2003, two projects were operated under the Fifth EC Framework known as the SMADES and MEMDIS. The SMADES stands for "SMAll-scale, stand-alone DESalination", was established to deliver continuous water source for folks living in specific regions far away from the grid supply. A small-scale operation by Banat et al. was first developed through the SMADES EC-funded project called "compact SMADES" to identify process parameters of design for the larger-scale namely "large SMADES" system (Banat et al., 2007b). The system is simple and easy to control that does not require a battery and thermal heat storage tanks. As a result, around 120 L per day of distillate flow rate was supplied with the distillate conductivity of below than 5 µS/cm throughout the summer period, and approximately 50 L per day within the cloudy winter days. This project development of a stand-alone SPMD unit was intentionally designed and manufactured for independent operation in arid and semi-arid remote regions with insufficient electricity supply but blessed with an abundance of solar radiation. With the same project under SMADES funded by EC, Banat et al. have sustained to advance the previous version known as the "large SMADES" system establishment located at Aqaba on the Red Sea (Banat et al., 2007a). This system was a continuous innovation from the previous "compact SMADES" unit. The system is comprised of two loops that consisted of seawater loop with the covered area of the 10 MD modules separated from the second loop of 72 solar collectors by heat exchanger made up of corrosion resistant titanium. The MD material is made of polytetrafluoroethylene (PTFE), which is the same as those used in the compact systems. In the two-loop system, the working fluid acting as the heat transfer medium must be of non-corrosive liquid. Thus, the use of anti-corrosive material is optional for the collector. There were four spiral-wound air-gap MD modules operated in parallel. Experimental results from the large system showed that the maximal distillate flux was produced around 1.5 L/ h of membrane surface area. Another EC project was known as MEMDIS that was generally referred to as "Development of stand-alone, solar thermally driven and photovoltaic-supplied desalination system based on innovative membrane distillation". This stand-alone project used to be operated when the MD system required thermal energy from STC and the electrical energy was separated provided by solar PV system to power the electrical components (Koschikowski et al., 2009). Two systems with compact and large-scale system under the MEMDIS project were manufactured at the ITC facilities at Pozo Izquierdo (Gran Canaria Island) (Subiela et al., 2009).

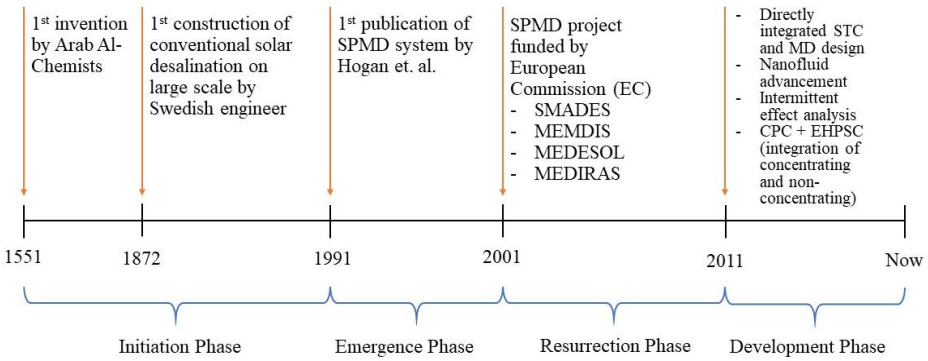

Figure 4. Timeline in the development of SPMD

As mentioned in the previous system characterization section, directly integrated SPMD system is one of the advanced technologies developed during the "SPMD development phase". Li et al. (2019) conducted an experiment and mathematic practicability review of directly integrated solar driven MD system using evacuated tube heat pipe solar collector as STC. The system operated by replacing the heat pipe with hollow fiber membranes inserted inside evacuated solar tubes (EST). Thus, the integrated collector system comprises of an evacuated tube equipped by membrane modules and heat exchanger. The experimental result showed the integrated system could provide ~3.2-4.8 L of potable water plus ~2.5-6 kWh of thermal energy. A 35,000 ppm salinity level of feed water (i.e. seawater) can be reduced into 10–200 ppm of water. Furthermore, the authors suggested steps such as suitable cleaning techniques and efficient drying process for future work to increase the durability of the product.

Another new type of research for SPMD enhancement is by the application of photothermal nanofluid that has great solar energy utilization performance because of the localized surface plasmon resonance form. Based on Figure 5, Zhang et al. conducted an experiment by incorporating the photothermal nanofluid through the feed solution as an energy collector from the STC into the MD system (Zhang et al., 2014). The experiment was carried out by a range of TiN concentrations and solar radiation powers. As a result, the TiN nanofluid indicated the best optical absorption efficiency, less sedimentation possibility, and the highest membrane distillation flux.

Moreover, it is around 57.4% of membrane distillation flux and solar energy utilization enhanced as compared to the base fluid (35 g/L NaCl aqueous solution).

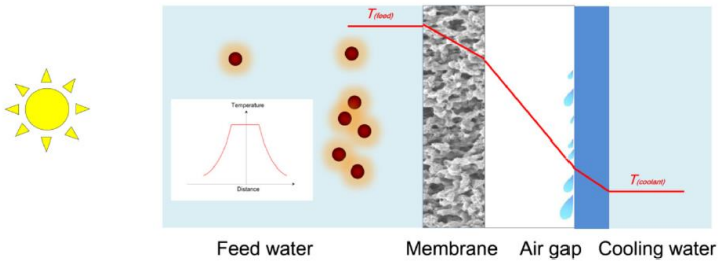

Figure 5. The utilization of photothermal nanofluids through feed solution of SPMD system (Zhang et al., 2018)

For large-scale energy power generation, the application of concentrating collector through DCMD has been studied by the previous researcher. Soomro and Kim (2018a; 2018b; 2018c) studied three types of concentrating collector integrated with DCMD, such as the solar power tower (SPT) linear Fresnel reflector (LFR), and parabolic trough plant (PT). All investigations showed that the combination of concentrating plant with DCMD system might be a sustainable and eco-friendly approach to deal with the rising demand for electricity and freshwater. The integrated SPT plant with DCMD showed higher average freshwater production compared to the LFR and PT plants, which is 40759 L/day, 31844.6 L/day, and 14330 L/day respectively. Chafidz et al. (2016) conducted an experiment by combining evacuated tube as the non-concentrating collector and compound parabolic concentrator as the concentrating collector as illustrated in Figure 6. The system operated by combining both types of solar collector and integrated with Memsys effect stages as the MD module. As a result, the amount of distillate produced was around 70 L/day. This distillate output can be categorized as a low output, but it can be simply increased to meet the water demand by rising the number of the Memsys "effect stages".

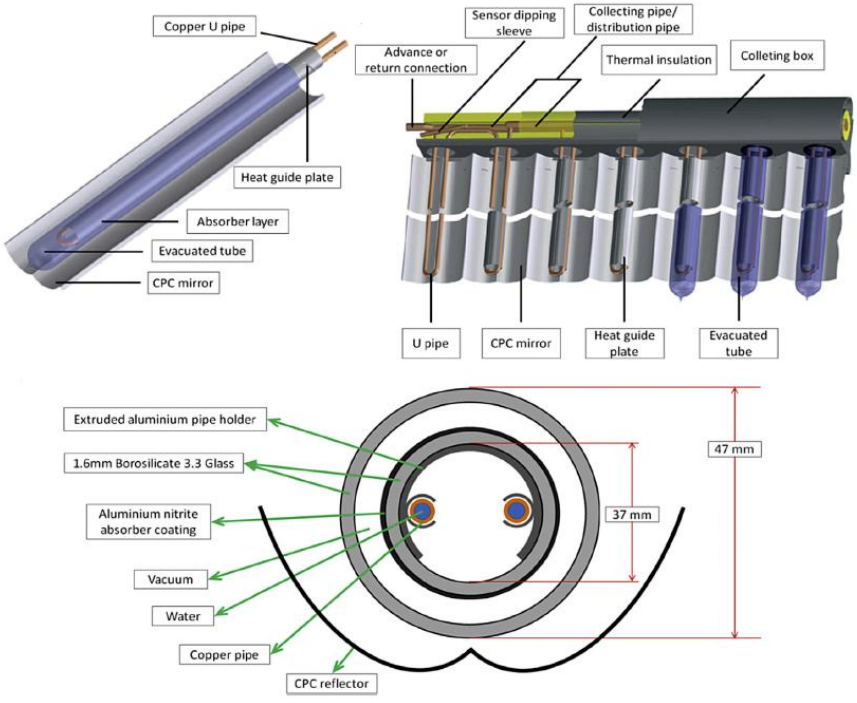

Figure 6. The integrations STC types design between evacuated tube (non-concentrating collector) and compound parabolic concentrator (concentrating collector)

Apart from the design advancement of the SPMD system, some researchers investigated the problem confronted by the SPMD system itself, such as the occurrence of intermittent effects. In all probabilities, the autonomous SPMD system will function intermittently. Hejazi et al. (2019) studied the effect of the intermittent operation on the performance of an SPMD system. As shown in Figure 7, a bench-scale MD unit was set up with programmable temperature-controller proposedly to produce a feed temperature pattern similar to the temperature output of a real pilot solar-powered system. The result revealed the permeate flux is higher with

lower specific thermal energy consumption (STEC) during the afternoon compared to the morning. Furthermore, the negative impact of the performance of MD was observed whenever the module was left to dry all night. Moreover, the ultrasonic cleaning of the used hollow fibers helped in recovering their hydrophobicity. Other details on effort to solve the intermittent effect issues can be referred to Gil et al. (2018a; 2018b). With the continuously growing interest in the SPMD process in wide applications, Saffarini et al. (2012) believed that SPMD has the potential to be established in off-grid areas with strong solar radiation.

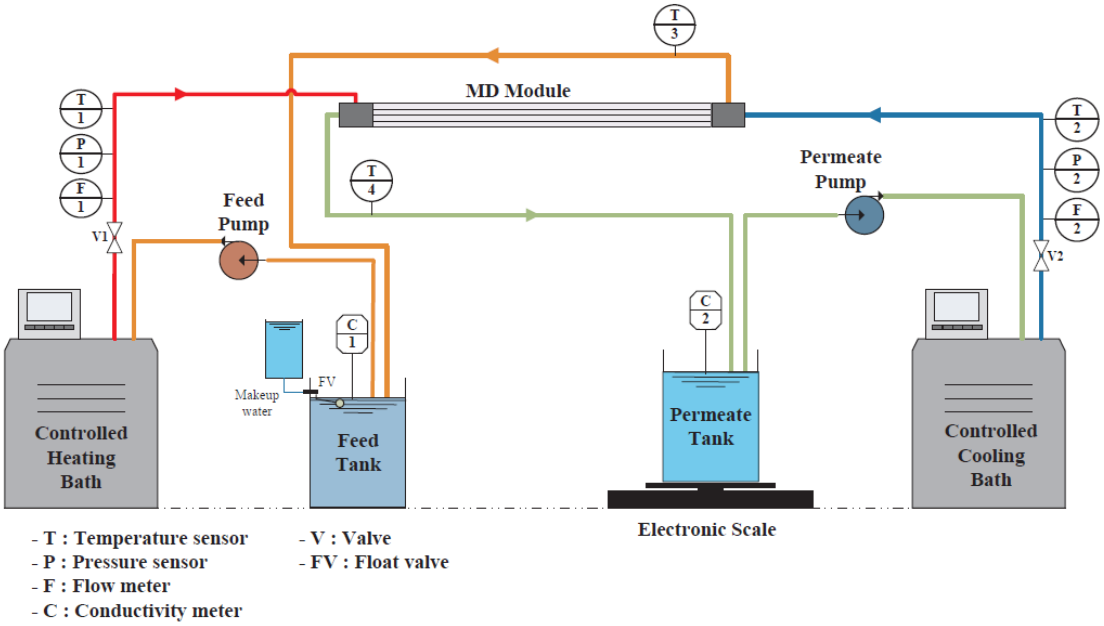

Figure 7. A schematic diagram of programmable temperature-controlled for MD unit (Hejazi et al., 2019)

Conclusion and Future Outlook

Nowadays, the sea or brackish water desalination has gained attention due to the scarcity of water. The utilization of solar energy through desalination processes indicated the capability of further growth, from the point of view of energy conservation and/or cost-cutting approaches. Numerous researchers have examined the integration of solar energy and MD for eco-friendly water desalination. Based on the literature study, these subsequent suggestions might be useful for future research:

- Identifying the ways that could make solar thermal collector produce the highest thermal efficiency into the membrane distillation module.
- Improving the membrane flux by new innovations of membrane materials such as copolymers, dual-layer membrane, and nano-fibrous membranes.
- Determining the optimal parameters such as water flow rate, temperature, etc., that will coincide with economical evaluation.
- Additional numerical and experimental data that contributed to the development of these systems to become more economical and effective in the future.

Furthermore, reviewing and categorizing the previous research on SPMD configurations with different kinds of system give us awareness into the contribution of solar energy for managing sea or brackish water issues. Moreover, the focus to the decrease of emission that matched with environmental policy and aid from the government/society proved that the utilization of renewable energy to be more reliable.

Scientific Ethics Declaration

The authors declare that the scientific ethical and legal responsibility of this article published in EPSTEM journal belongs to authors.

Acknowledgements or Notes

* This article was presented as an oral presentation at the International Conference on Technology, Engineering and Science (www.icontes.net) held in Antalya/Turkey on November 16-19, 2022.

* The authors gratefully acknowledge Universiti Malaysia Pahang (UMP) for financial support under grant number PDU213225 and RDU190395. Sincere gratitude also expressed to UMP for providing MRS scholarship.

References

Al-Hayeka, I., & Badran, O.O. (2004). The effect of using different designs of solar stills on water distillation. *Desalination, 169*, 121–127. https://doi.org/10.1016/j.desal.2004.08.013

Banat, F., Jwaied, N., Rommel, M., & Koschikowski, J. (2007a). Performance evaluation of the 'large SMADES' autonomous desalination solar-driven membrane distillation plant in Aqaba, Jordan. *Desalination, 217*, 17–28. https://doi.org/10.1016/j.desal.2006.11.027

Banat, F., Jwaied, N., Rommel, M., Koschikowski, J., & Wieghaus, M. (2007b). Desalination by a 'compact SMADES' autonomous solarpowered membrane distillation unit. *Desalination, 217*, 29–37. https://doi.org/10.1016/j.desal.2006.11.028

Blanco, J., Malato, S., Fernández-Ibañez, P., Alarcón, D., Gernjak, W., & Maldonado, M.I. (2009). Review of feasible solar energy applications to water processes. *Renewable and Sustainable Energy Reviews, 13*, 1437–1445. https://doi.org/10.1016/j.rser.2008.08.016

Boretti, A., & Rosa, L. (2019). Reassessing the projections of the World Water Development Report. *npj Clean Water, 2*, 15. https://doi.org/10.1038/s41545-019-0039-9

Byrne, P., Fournaison, L., Delahaye, A., Oumeziane, Y.A., Serres, L., Loulergue, P., Szymczyk, A., Mugnier, D., Malaval, J., Bourdais. R., Gueguen, H., Sow, O., Orfi, J., & Mare, T. (2015). A review on the coupling of cooling, desalination and solar photovoltaic systems. *Renewable and Sustainable Energy Reviews, 47*, 703–717. https://doi.org/10.1016/j.rser.2015.03.083

Chafidz, A., Kerme, E.D., Wazeer, I., Khalid, Y., Ajbar, A., & Al-Zahrani, S.M. (2016). Design and fabrication of a portable and hybrid solar-powered membrane distillation system. *Journal of Cleaner Production, 133*, 631–647. https://doi.org/10.1016/j.jclepro.2016.05.127

Flendrig, L.M., Shah, B., Subrahmaniam, N. & Ramakrishnan, V. (2009). Low cost thermoformed solar still water purifier for D&E countries. *Physics and Chemistry of the Earth, Parts A/B/C, 34*, 50–54. https://doi.org/10.1016/j.pce.2008.03.007

Garud, R.R., & Mane, P.B. (2019). Smart farming using temperature sensor, moisture sensor, flow sensor and ultrasonic sensor leading to water conservation. *International Journal of Recent Technology and Engineering, 8*, 4426–4431. https://doi.org/10.35940/ijrte.C5541.098319

Gude, V.G. (2016). Desalination and sustainability - An appraisal and current perspective. *Water Research, 89*, 87–106. https://doi.org/10.1016/j.watres.2015.11.012

Gil, J.D., Roca, L., Zaragoza, G., & Berenguel, M. (2018a). A feedback control system with reference governor for a solar membrane distillation pilot facility. *Renewable Energy, 120*, 536–549. https://doi.org/10.1016/j.renene.2017.12.107

Gil, J.D., Roca, L., Ruiz-Aguirre, A., Zaragoza, G., & Berenguel, M. (2018b). Optimal operation of a solar membrane distillation pilot plant via nonlinear model predictive control. *Computers & Chemical Engineering, 109*, 151-165. https://doi.org/10.1016/j.compchemeng.2017.11.012

Ho, C.D., Ng, C.A., Wang, P.H. & Cheng, C.H. (2016). Theoretical and experimental studies of immediate assisted solar air gap membrane distillation systems. *Desalination and Water Treatment, 57*, 3846–3860. https://doi.org/10.1080/19443994.2014.989274

Hogan P.A., Sudjito, Fane, A.G., & Morrison, G.L. (1991). Desalination by solar heated membrane distillation. *Desalination, 81*, 81–90. https://doi.org/10.1016/0011-9164(91)85047-X

Hejazi, M.A.A., Bamaga, O.A., Al-Beirutty, M.H., Gzara, L., & Abulkhair, H. (2019). Effect of intermittent operation on performance of a solar-powered membrane distillation system. *Separation and Purification Technology, 220*, 300–308. https://doi.org/10.1016/j.seppur.2019.03.055

Jamar, A., Majid, Z.A.A., Azmi, W.H., Norhafana, M., & Razak, A.A. (2016). A review of water heating system for solar energy applications. *International Communications in Heat and Mass Transfer, 76*, 178–187. https://doi.org/10.1016/j.icheatmasstransfer.2016.05.028

Koschikowski, J., Wieghaus, M., Rommel, M., Ortin, V.S., Suarez, B.P., & Betancort Rodríguez, J.R. (2009). Experimental investigations on solar driven stand-alone membrane distillation systems for remote areas. *Desalination, 248*, 125–131. https://doi.org/10.1016/j.desal.2008.05.047

Li, Q., Lian, B., Wang, Y., Taylor, R.A., Dong, M., Lloyd, T., Liu, X., Tan, J., Ashraf, M.M., Waghela, D. & Leslie, G. (2018). Development of a mobile groundwater desalination system for communities in rural India. *Water Research*, *144*, 642–655. https://doi.org/10.1016/j.watres.2018.08.001

Li, Q., Beier, L., Tan, J., Brown, C., Lian, B., Zhong, W., Wang, Y., Ji, C., Dai, P., Li, T., Clech, P.L., Tyagi, H., Liu, X., Leslie, G., & Taylor, R.A. (2019). An integrated, solar-driven membrane distillation system for water purification and energy generation. *Applied Energy*, *237*, 534–548. https://doi.org/https://doi.org/10.1016/j.apenergy.2018.12.069

Mekhilef, S., Saidur, R., & Safari, A. (2011). A review on solar energy use in industries. *Renewable and Sustainable Energy Reviews*, *15*, 1777–1790. https://doi.org/10.1016/j.rser.2010.12.018

Mericq, J.P., Laborie, S., & Cabassud, C. (2011). Evaluation of systems coupling vacuum membrane distillation and solar energy for seawater desalination. *Chemical Engineering Journal*, *166*, 596–606. https://doi.org/https://doi.org/10.1016/j.cej.2010.11.030

Nematollahi, F., Rahimi, A., & Gheinani, T.T. (2013). Experimental and theoretical energy and exergy analysis for a solar desalination system. *Desalination*, *317*, 23–31. https://doi.org/10.1016/j.desal.2013.02.021

Pangarkar, B.L., Sane, M.G., & Guddad, M. (2011). Reverse osmosis and membrane distillation for desalination of groundwater: A review. *ISRN Materials Science*, *2011*, 523124. https://doi.org/10.5402/2011/523124

Porrazzo, R., Cipollina, A., Galluzzo, M., & Micale, G. (2013). A neural network-based optimizing control system for a seawater-desalination solar-powered membrane distillation unit. *Computers & Chemical Engineering*, *54*, 79–96. https://doi.org/10.1016/j.compchmeng.2013.03.015

Qtaishat, M.R., & Banat, F. (2013). Desalination by solar powered membrane distillation systems. *Desalination*, *308*, 86–197. https://doi.org/10.1016/j.desal.2012.01.021

Raluy, R.G., Schwantes, R., Subiela, V.J., Peñate, B., Melián, G., & Betancort, J.R. (2012). Operational experience of a solar membrane distillation demonstration plant in Pozo Izquierdo-Gran Canaria Island (Spain). *Desalination*, 290, 1–13. https://doi.org/10.1016/j.desal.2012.01.003

Saffarini, R.B., Summers, E.K., Arafat, H.A. & Lienhard V, J.H. (2012). Technical evaluation of stand-alone solar powered membrane distillation systems. *Desalination*, *286*, 332–341. https://doi.org/https://doi.org/10.1016/j.desal.2011.11.044

Soomro, M.I., & Kim, W.S. (2018a). Performance and economic investigations of solar power tower plant integrated with direct contact membrane distillation system. *Energy Conversion and Management*, *174*, 626–638. https://doi.org/10.1016/j.enconman.2018.08.056

Soomro, M.I., & Kim, W.S. (2018b). Performance and economic evaluation of linear Fresnel reflector plant integrated direct contact membrane distillation system. *Renewable Energy*, *129*, 561–569. https://doi.org/10.1016/j.renene.2018.06.010

Soomro, M.I., & Kim, W.S. (2018c). Parabolic-trough plant integrated with direct-contact membrane distillation system: Concept, simulation, performance, and economic evaluation. *Solar Energy*, *173*, 348–361. https://doi.org/10.1016/j.solener.2018.07.086

Subiela, V.J., de la Fuente, J.A., Piernavieja, G., & Peñate, B. (2009). Canary Islands Institute of Technology (ITC) experiences in desalination with renewable energies (1996–2008). *Desalination and Water Treatment*, *7*, 220–235. https://doi.org/10.5004/dwt.2009.733

Swaminathan, J., Chung, H.W., Warsinger, D.M., & Lienhard V, J.H. (2018). Energy efficiency of membrane distillation up to high salinity: Evaluating critical system size and optimal membrane thickness. *Applied Energy*, 715-734. https://doi.org/10.1016/j.apenergy.2017.11.043

Wang, Z., Yang, W., Qiu, F., Zhang, X., & Zhao, X. (2015). Solar water heating: From theory, application, marketing and research. *Renewable and Sustainable Energy Reviews*, *41*, 68–84. https://doi.org/10.1016/j.rser.2014.08.026

Zhani, K., Zarzoum, K., Ben Bacha, H., Koschikowski, J., & Pfeifle, D. (2016). Autonomous solar powered membrane distillation systems: state of the art. *Desalination and Water Treatment*, *57*, 23038–23051. https://doi.org/10.1080/19443994.2015.1117821

Zhang, Y., Liu, L., Li, K., Hou, D., & Wang, J. (2018). Enhancement of energy utilization using nanofluid in solar powered membrane distillation. *Chemosphere*, *212*, 554–562. https://doi.org/10.1016/j.chemosphere.2018.08.114

Author Information

Mohd Amirul Hilmi Mohd Hanoin
Universiti Malaysia Pahang
Faculty of Civil Engineering Technology, Universiti Malaysia Pahang, Lebuhraya Persiaran Tun Khalil Yaakob, 26300 Kuantan, Pahang, Malaysia
Contact e-mail: hilmihanoin*@gmail.com*

Farah Najihah Zainuddin
Universiti Malaysia Pahang
Faculty of Civil Engineering Technology, Universiti Malaysia Pahang, Lebuhraya Persiaran Tun Khalil Yaakob, 26300 Kuantan, Pahang, Malaysia

Nadzirah Mohd Mokhtar
Universiti Malaysia Pahang
Faculty of Civil Engineering Technology, Universiti Malaysia Pahang, Lebuhraya Persiaran Tun Khalil Yaakob, 26300 Kuantan, Pahang, Malaysia

To cite this article:

Hanoin, M.A.H.M., Zainuddin, F.N., & Mokhtar, N.M. (2022). A review of solar-powered membrane distillation system: Concept design and development. *The Eurasia Proceedings of Science, Technology, Engineering & Mathematics (EPSTEM), 21*, 27-38

The Eurasia Proceedings of Science, Technology, Engineering & Mathematics (EPSTEM)
ISSN: 2602-3199

The Eurasia Proceedings of Science, Technology, Engineering & Mathematics (EPSTEM), 2022

Volume 21, Pages 39-45

IConTES 2022: International Conference on Technology, Engineering and Science

Wireless Channel Availability Forecasting with a Sparse Geolocation Spectrum Database by Penalty-Regularization Logistic Models

Vladimir II Christian OCAMPO
De La Salle University

Lawrence MATERUM
De La Salle University

Abstract: Television uses electromagnetic waves that carry audio and video. The unused frequencies or channels in broadcasting services are referred to as television white spaces. The unused spectrum can be managed to provide internet access in coordination with surrounding TV channels to avoid interference. Different ways of dynamically managing spectrum management have been conceived, and geolocation databases are considered the better option. Geolocation databases, when updated and complete, are helpful when frequencies are dynamically shared. In real life, the spectrum availability for a secondary user lacks numerous information; hence, it is sparse. This paper forecasts wireless channel availability given a sparse geolocation spectrum database. A dynamic sparse forecasting model is proposed through logistic penalized regression. Results show that forecasting accuracy is mostly above 90% on average when sparsity penalty terms are incorporated into the model. Forecasting accuracy is improved when penalty terms are integrated into the logistic regression models to account for sparsity.

Keywords: Channel availability, Forecasting, Geolocation database, Penalized logistic regression, TVWS

Introduction

Television (TV) uses electromagnetic (EM) waves that carry modulated audio and video to broadcast. The TV EM waves have long wavelengths and travel far distances. The spectrum is divided into channels, which may be occupied or not. An unused portion of the spectrum is called white space.

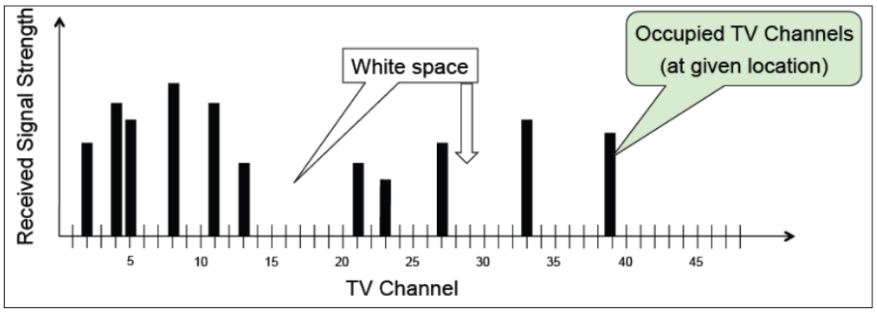

Figure 1. Concept of white space.

TV White Space (TVWS) communications involves using the white spaces in the TV spectrum for other non-broadcasting purposes such as point-to-point connectivity, Internet services, emergency communications, and the like. Studies have explored using these white space bands with an increased demand for network usage and remote areas needing communication access. Some applications on TVWS include environment monitoring,

emergency tracking, and communication that can reach far-flung and remote areas, which are hard to reach using traditional communication technologies, such as the Internet. TVWS communication is a growing technology allowing dynamic frequency spectrum usage, which can benefit rural and underserved areas of developing countries like the Philippines. According to Inquirer, a map of digital poverty in the Philippines discovered that rural areas have no access to sufficient Internet speeds. This outcome means that rural areas are left behind in terms of connectivity (Sy, 2021). TVWS can be used for a super-high-speed Wi-Fi, called Wi-Fi 2.0, that can provide access to underserved areas. This Wi-Fi can reach gigabits per second speeds (Sarkar et al., 2016). TVWS has been tried in different countries, such as Japan, India, Singapore, and even the Philippines (Mody, 2017).

There is a drawback to TVWS, at least when using existing technologies. TVWS uses dynamic sharing of frequencies across space and time. In addition, TVWS has no protection from interference, especially from primary incumbents like TV stations. So, there must be a way to coordinate the white space devices (WSD). Spectrum sensing was one way of coordinating WSDs where the device senses the unoccupied frequencies. However, design and performance were challenging, as tested by the Federal Communications Committee (FCC) (Gurney et al., 2008). Geolocation databases are better options because they contain information such as occupied frequencies at a given location and time. A WSD can query the geolocation database, and the geolocation database responds with the information needed by the WSD, such as frequency availability. However, geolocation databases are sparse, and no study has attempted to forecast using sparse TVWS geolocation databases, giving this research the aim to address this problem.

Literature Review

Previous studies explored methods of spectrum management so that dynamic sharing of the spectrum between primary and secondary devices without interference with primary users is achieved. Martin et al. (2016) developed the General Enhanced Detection Algorithm (GEDA) to enhance the detection of primary users (PU) and optimize the secondary user's Quality-of-Service (QoS). Bourdena et al. (2012) developed a real-time secondary spectrum market (RTSSM) through a spectrum broker. Zhao et al. (2015) used game theory in dynamic spectrum management.

Some studies dealt with the TVWS geolocation database. Deep learning methods were applied to make predictions using a geolocation database in the study of Shawel et al. (2019). However, there are no studies yet involving sparse geolocation data.

Hurley & Rickard (2009) compared numerous sparsity measures. Benarabi et al. (2021) used density, which is the ratio of the number of non-zero elements to the total number of elements in a vector, as a basis for its sparsity measure. Goswami et al. (2018) measured the sparsity of a network graph using measures based on the Gini index. The integration of sparsity in predictive analytics has not yet been explored.

Some studies investigated forecasting using time series models. Wu et al. (2012) derived the Adversarial Sparse Transformer (AST) from Generative Adversarial Networks (GANs). Ardia et al. (2019) employed time series aggregation using computed textual sentiment to forecast high-dimensional data. Flaxman et al. (2019) propose a generic spatio-temporal forecasting method for a challenge in predicting crimes in real time. Spatio-temporal forecasting was also performed on sparse data to predict urban traffic flow (Zheng et al., 2020). The space and time complexity of models increase if data are sparse. Model algorithms might behave in extraordinary results if sparsity is present. No studies have considered the sparsity factor in forecasting models, especially spectrum forecasting. Geolocation prediction capabilities have been developed primarily using deep learning models. However, no studies have explored using sparse forecasting capabilities for geolocation databases. This area is a potential novel contribution of this study.

Sparsity

Sparsity can be thought of as having a small amount of information or packing a large proportion of energy in a small number of coefficients (Hurley & Rickard, 2009). For instance, a matrix with many zeros is referred to as sparse. The concept of sparsity is widely used in various areas of research. Areas such as ocean engineering, antennas and propagation, and image processing employ this concept (Hurley & Rickard, 2009). In addition, sparsity was a central concept for the success of machine learning algorithms and numerous techniques such as

matrix factorization, signal processing, dictionary learning, and support vector machines. Because the concept of sparsity could be abstract, many measures of sparsity were introduced.

$$\|\mathbf{c}\|_p = \left(\sum_{j=1}^{N} |c_j|^p \right)^{\frac{1}{p}} \tag{1}$$

The majority of the studies use ℓ^p-based sparsity measures, with ℓ^0 and ℓ^1 being most common. Given a vector $\mathbf{c} \in \mathbb{R}^N$, the traditional definition of ℓ^p norm is described in (1). The ℓ^0 measure simply counts the number of non-zero elements in a vector. It is the traditional measure in a lot of mathematical settings. However, ℓ^0 is difficult to solve as the derivative of the measure has no information (Hurley & Rickard, 2009), and problems involving ℓ^0 are combinatorial in nature. Given this, the ℓ^1 measure is usually an approximation of the ℓ^0 norm and is being employed in many optimization problems. ℓ^1 can be used as a penalty. Other ℓ^p based measures use $0 < p < 1$, such as the study of Xu et al. (2010) that proposed the use of $\ell^{\frac{1}{2}}$ norm. Other sparsity measures are the Hoyer and Gini indices, as defined in (2) and (3), respectively.

$$\mathrm{HI} = \left(\sqrt{N} - \frac{\sum_j c_j}{\sqrt{\sum_j c_j^2}} \right) \left(\sqrt{N} - 1 \right)^{-1} \tag{2}$$

$$\mathrm{GI} = 1 - 2 \sum_{k=1}^{N} \frac{c_{(k)}}{\|\mathbf{c}\|_1} \left(\frac{N - k + \frac{1}{2}}{N} \right) \tag{3}$$

given ordered data: $c_{(1)} \leq c_{(2)} \leq \cdots \leq c_{(N)}$

Logistic Regression and Regularization

A logistic regression models variables whose response is categorical. A categorical variable takes on discrete values and does not use the ratio scale (Czepiel, 2002). Logistic regression derives from the generalized linear model developed by Nelder and Wedderburn. For a binary logistic model, the response variable has two possible values, and the model is defined in (4).

$$\mathrm{logit}(\pi_i) = \log\left(\frac{\pi_i}{1 - \pi_i} \right) = \sum_{\mathrm{k}=0}^{K} x_{ik} \beta_k = (\mathbf{X}\boldsymbol{\beta})_i \tag{4}$$

In (4), π_i represents the probability of success, x_{ik} represents the predictor variables and β_k is a parameter of the model. The predictor variables can also be put in a matrix $\mathbf{X} \in \mathbb{R}^{N \times (K+1)}$, and $x_{i0} = 1$ for $i = 1,2, \ldots, N$. Unlike linear models, where parameters are found by minimizing the squares of the errors—the Least Squares Estimate—logistic models use maximum likelihood. For a binary logistic model, the likelihood is the binomial probability distribution.

$$L(\boldsymbol{\beta}|\boldsymbol{y}) = \prod_{i=1}^{N} \binom{n_i}{y_i} \pi_i^{y_i} (1 - \pi_i)^{n_i - y_i} \tag{5}$$

When estimating the parameters by maximum likelihood, the log-likelihood is maximized, or equivalently, the negative of the log-likelihood is minimized, as in (6). However, Czepiel (2002) noted that estimating the maximum likelihood is computationally intractable, and numeric methods are employed instead.

$$\arg\min_{\boldsymbol{\beta}} - \ln L(\boldsymbol{\beta}|\mathbf{y}) \tag{6}$$

Binary logistic regression can be extended to form Multinomial Logistic Regression (MLR), in which the response variable can take at least two values. For an MLR model, given J discrete categories of the response where $J \geq 2$, with the Jth category as the baseline, the model is defined in (7). The probability distribution of the multinomial response variable y is defined in (8).

$$\log\left(\frac{\pi_{ij}}{\pi_{ij}}\right) = \log\left(\frac{\pi_{ij}}{1 - \sum_{j=1}^{J-1}\pi_{ij}}\right) = \sum_{k=0}^{K} x_{ik}\beta_{kj} \tag{7}$$

$$f(\boldsymbol{y}|\boldsymbol{\beta}) = \prod_{i=1}^{N}\left[\frac{n_i!}{\prod_{j=1}^{J} y_{ij}!} \cdot \prod_{j=1}^{J} \pi_{ij}^{y_{ij}}\right] \tag{8}$$

Methodology

For predicting channel availability, penalized logistic regression models have been formulated. From the whole data set, 80% are relegated training, and 20% are for testing. The training and testing data points are randomly selected, and the testing data is used to evaluate the model. Online sources include primary user information such as company name, channel, and location (longitude and latitude). Channel availability is surveyed from 00:00H (12:00 AM) to 23:59H (11:59 PM) in 30-minute intervals. For a secondary user, the channel is deemed available if the primary user broadcasting on the channel is off-air or does not interfere with a primary user. Availability is labeled with a 1 for available channels and 0 for unavailable channels. The dataset is available online (Ocampo, Vladimir, n.d.). The model input-process-output diagram is illustrated in Figure 2.

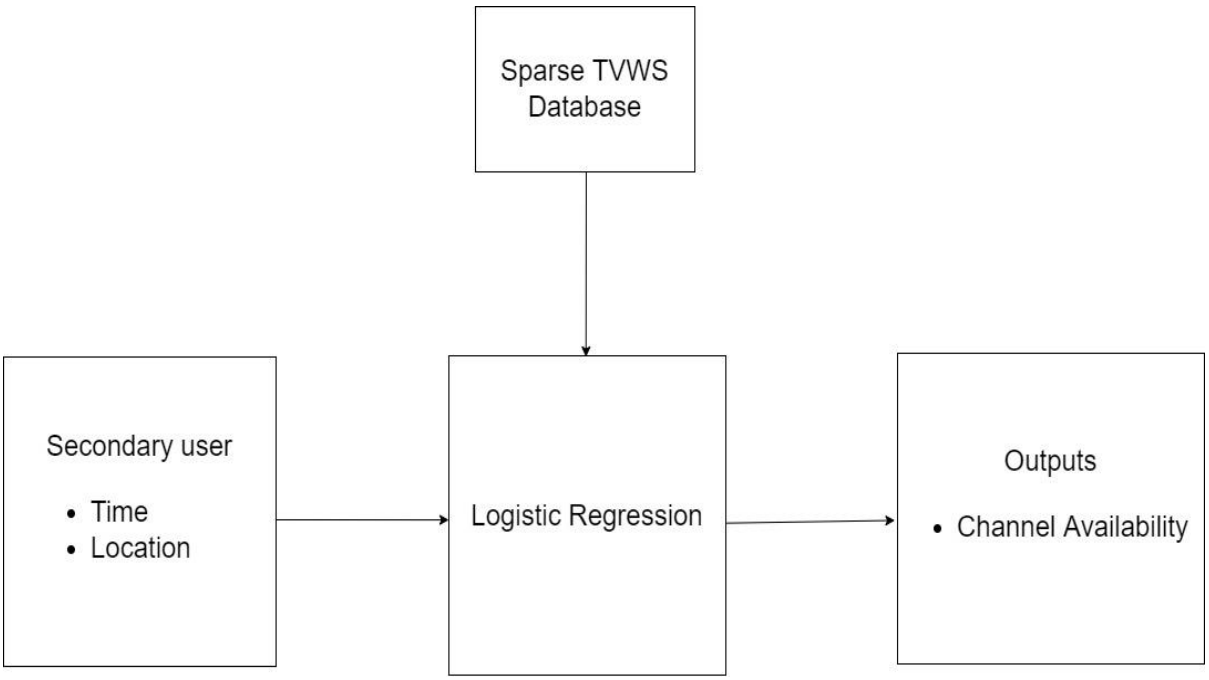

Figure 2. Input-process-output diagram

Penalized logistic models have been developed to predict channel availability. The training and test data points are randomly selected. The penalties included in the study are Lasso (ℓ^1), Ridge (ℓ^2), and Elastic net ($\ell^1 + \ell^2$). The analysis has been carried out through R with the source codes available online (Vladimir Ocampo, 2022).

For evaluating the model, accuracy is used. This metric is determined by hits, misses, false alarms, and correct rejections. A hit (true positive) is called when an available channel is predicted available. A miss (false negative) is called when an available channel is predicted as unavailable. A false alarm (false positive) is called when an unavailable channel is predicted as available. A correct rejection is called when an unavailable channel is predicted as unavailable. Table 1 summarizes the evaluation criteria of hits, misses, false alarms, and correct rejections.

Table 1. Forecast quality evaluation criteria

	Forecasted TVWS channel availability	
Observed TVWS channel availability	Available	Not Available
Available	Hit (True Positive)	Miss (False Negative)
Not Available	False Alarm (False Positive)	Correct Rejection (True Negative)

The accuracy is defined in (9).

$$\%\text{Accuracy} = \frac{\text{Hit} + \text{Miss}}{\text{Total samples in test data}} \times 100\% \qquad (9)$$

Results and Discussion

In predicting the channel availability for TVWS, logistic regression with and without regularization is developed. The inputs include day and time and whether there is an interference or not. The model has been carried out for eight channels: 4, 5, 7, 9, 11, 13, 27, and 37. Thirty trials have been conducted, where in each trial, training and test data are randomly selected from the whole data set. The model is evaluated in terms of accuracy, precision, and recall, and the averages of those values are taken from those thirty trials. Figure *3* shows a bar graph of the average accuracies of logistic regression (Logit), cross-validated lasso (Cvlasso), cross-validated ridge (Cvridge), and cross-validated elastic net (Cvelnet).

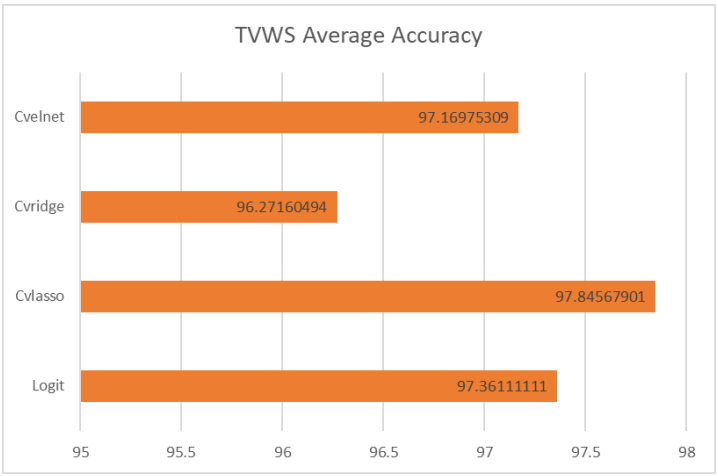

Figure 3. Average accuracies of TVWS logistic models.

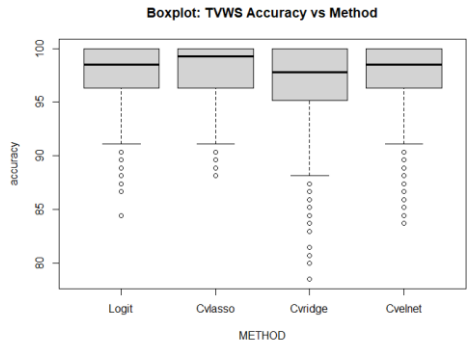

Figure 4. Boxplot of the accuracies of the model (generated with R)

In addition, a statistical analysis is carried out to determine if regularization has a significant effect. For each trial, the accuracy of the model is taken. Using the Shapiro-Wilk test, the accuracy data is not normally distributed; thus, Kruskal-Wallis was carried out to determine the significance of regularization. The boxplot is shown in Figure *4*. The Kruskal-Wallis test resulted in a significant difference among groups. However, the boxplot shows that regularized logistic regression performs just as well as unregularized logistic regression in

terms of accuracy. Post-hoc tests confirm that was the case, seeing a difference between elastic net and ridge regressions, probably due to the presence of outliers. The insignificant difference between regularized and unregularized logistic models may be because the input variables are limited when there could have been more variables in reality.

Conclusion

Due to sparse spectrum availability for a secondary user, the paper formulated logistic regression models with sparsity regularization to forecast wireless coverage and frequency availability in sparse geolocation spectrum databases. The sparsity penalty terms incorporated in the logistic regression models are Lasso (ℓ^1), Ridge (ℓ^2), and Elastic Net ($\ell^1 + \ell^2$). The average accuracies of the models range from 96.27% to 97.85%. Statistical analyses indicate that regularized logistic regression has no significant difference from unregularized logistic regression in terms of accuracy, which could be due to a limited number of variables used in the model.

Recommendations

Given that the regularized logistic regression performs just as well as the unregularized logistic regression, the number of input variables may be limited. A future direction for this research would include more input variables. In addition, other sparsity penalty terms can be explored, such $\ell^{\frac{1}{2}}$ and a function of the Fisher information matrix.

Scientific Ethics Declaration

The authors declare that the scientific ethical and legal responsibility of this article published in EPSTEM journal belong to authors.

Acknowledgements or Notes

* This article was presented as an oral presentation at the International Conference on Technology, Engineering and Science (www.icontes.net) held in Antalya/Turkey, on November 16-19, 2022.

* The researcher would like to thank DOST ERDT for the funding and support for the research.

References

Ardia, D., Bluteau, K., & Boudt, K. (2019). Questioning the news about economic growth: Sparse forecasting using thousands of news-based sentiment values. *International Journal of Forecasting*, *35*(4), 1370–1386.

Benarabi, T., Adnane, M., & Mansour, M. (2021). Energy and sparse coding coefficients as sufficient measures for VEBs classification. *Biomedical Signal Processing and Control*, *67*, 102493. https://doi.org/10.1016/j.bspc.2021.102493

Bourdena, A., Mastorakis, G., Pallis, E., Arvanitis, A., & Kormentzas, G. (2012). A dynamic spectrum management framework for efficient TVWS exploitation. *2012 IEEE 17th International Workshop on Computer Aided Modeling and Design of Communication Links and Networks (CAMAD)*, 51–55.

Czepiel, S. A. (2002). Maximum likelihood estimation of logistic regression models: Theory and implementation. *Available at Czep. Net/Stat/Mlelr. Pdf*, *83*.

Flaxman, S., Chirico, M., Pereira, P., & Loeffler, C. (2019). Scalable high-resolution forecasting of sparse spatiotemporal events with kernel methods: A winning solution to the NIJ "Real-time crime forecasting challenge." *The Annals of Applied Statistics*, *13*(4), 2564–2585.

Goswami, S., Murthy, C., & Das, A. K. (2018). Sparsity measure of a network graph: Gini index. *Information Sciences*, *462*, 16–39.

Gurney, D., Buchwald, G., Ecklund, L., Kuffner, S. L., & Grosspietsch, J. (2008). Geo-location database techniques for incumbent protection in the TV white space. *2008 3rd IEEE Symposium on New Frontiers in Dynamic Spectrum Access Networks*, 1–9.

Hurley, N., & Rickard, S. (2009). Comparing measures of sparsity. *IEEE Transactions on Information Theory*, *55*(10), 4723–4741.

Martin, J. H., Dooley, L. S., & Wong, K. C. P. (2016). New dynamic spectrum access algorithm for TV white space cognitive radio networks. *IET Communications*, *10*(18), 2591–2597.

Mody, A. (2017). Tutorial on whitespaces, technologies and standardization... Means to bridge the digital divide. *IEEE P802 22-17-0054-Rev0/Ec-17-0147-00-WCSG*, 1–81.

Ocampo, V. (n.d.). *A 2022 television white space geolocation database of the greater manila area of the Philippines*. IEEE DataPort. https://doi.org/10.21227/YZ26-E616

Sarkar, B. D., Shankar, S., Verma, S., & Singh, A. K. (2016). Utilization of television white space for high speed Wi-Fi application TVWS usage. *2016 6th International Conference-Cloud System and Big Data Engineering (Confluence)*, 240–243.

Shawel, B. S., Woldegebreal, D. H., & Pollin, S. (2019). Convolutional LSTM-based long-term spectrum prediction for dynamic spectrum access. *2019 27th European Signal Processing Conference (EUSIPCO)*, 1–5.

Sy, S., Araneta, A., Rahemtulla, H., Carrasco, B., & Balgos, S. (2021). *Mapping digital poverty in PH*. INQUIRER.Net. https://business.inquirer.net/318223/mapping-digital-poverty-in-ph

Vladimir, O.. (2022, October 27). *Wireless channel availability forecasting with a sparse geolocation spectrum database by penalty-regularization logistic models*. Code Ocean. https://codeocean.com/capsule/9352952/tree

Wu, Q., Law, R., & Xu, X. (2012). A sparse Gaussian process regression model for tourism demand forecasting in Hong Kong. *Expert Systems with Applications*, *39*(5), 4769–4774.

Xu, Z., Zhang, H., Wang, Y., Chang, X., & Liang, Y. (2010). L1/2 regularization. *Science China Information Sciences*, *53*(6), 1159–1169.

Zhao, Q., Shen, L., & Ding, C. (2015). Dynamic spectrum access with goe-location database: A utility-based distributed learning approach. *2015 IEEE China Summit and International Conference on Signal and Information Processing (ChinaSIP)*, 918–922. https://doi.org/10.1109/ChinaSIP.2015.7230538

Zheng, Z., Shi, L., Sun, L., & Du, J. (2020). Short-term traffic flow prediction based on sparse regression and spatio-temporal data fusion. *IEEE Access*, *8*, 142111–142119. https://doi.org/10.1109/ACCESS.2020.3013010

Author Information

Vladimir II Christian Ocampo
De La Salle University, Philippines
Contact e-mail: *vladimir_ii_ocampo@dlsu.edu.ph*

Lawrence Materum
De La Salle University, Philippines
Tokyo City University, Japan

To cite this article:

Ocampo, V. C. & Materum, L. (2022). Wireless channel availability forecasting with a sparse geolocation spectrum database by penalty-regularization logistic models. *The Eurasia Proceedings of Science, Technology, Engineering & Mathematics (EPSTEM)*, *21*, 39-45.

The Eurasia Proceedings of Science, Technology, Engineering & Mathematics (EPSTEM)
ISSN: 2602-3199

The Eurasia Proceedings of Science, Technology, Engineering & Mathematics (EPSTEM), 2022

Volume 21, Pages 46-54

IConTES 2022: International Conference on Technology, Engineering and Science

Improving Core Quality in Power Distribution Transformers Using Machine Learning Methods

Nihat PAMUK
Zonguldak Bulent Ecevit University

Abstract: The estimation of individual core losses of wound core power distribution transformers are particularly important since their core costs account for around 30% of their overall material cost and are one of the key determinants of their quality. In addition, accurate calculations of individual core actual losses are extremely difficult, since actual losses show a divergence of up to 20%, in relation to the theoretical individual core losses. This paper demonstrates the use of Machine Learning (ML) techniques, namely Decision Trees (DTs) and the Learning Vector Quantization (LVQ) neural network to the enhancement of each core's quality in wound core power distribution transformers. The DTs method makes use of inductive inference to automatically build decision rules and apply them to the power distribution transformers production procedure. In the LVQ neural network, any set of input vectors can be classified by using supervised training of competitive layers. Real industrial measurements were used to create the learning and test set. Information includes measurements of the production line's quality control as well as the electrical properties of grain-oriented steel. The resulting DTs present a success rate of 94%. Based on these DTs, rules comprising the most significant parameters and their threshold values can be derived. These are used to lower the actual losses of individual cores, hence raising their quality. The LVQ neural network approach achieves a total classification success rate of 95%.

Keywords: Power distribution transformer, Core quality improvement, Losses, Learning vector quantization, Decision trees

Introduction

Transformer losses in the power distribution network account for a significant portion of all losses (Pamuk, 2022). Distribution transformer iron losses in Turkey are thought to make up to 12% of all distribution network losses (Matiskova & Hrehova, 2021). Predicting iron losses of individual cores is a critical problem in an industrial setting that deals with the transformers with wound cores for distribution built since these losses have a substantial impact on both the quality and functionality of the resulting three-phase power transformers. Additionally, core expenses account for around 30% of the total power transformer material cost (Riemer et al., 2013). In fact, it would be ideal if individual core iron losses could be predicted in the early stages of core production because it would allow for potential corrective steps to be taken while the manufacturing process is still ongoing. It should be noted that the actual individual core iron losses differ from the anticipated iron losses by up to 20%. This is because precise calculations of the iron losses in each core are exceedingly challenging because each core is affected by a variety of qualitative and quantitative characteristics (Pamuk, 2020), (Alatawneh & Pillay, 2012).

The DTs approach and the LVQ neural network are employed in order to investigate the effects of some of these characteristics on unique core iron losses. The DTs approach is a non-parametric learning strategy that can create classifiers for a given problem and is a member of the inductive inference methods (Altayef et al., 2022), (Russell & Norvig, 2015), (Li & Yeh, 2008). Any collection of input vectors can be classified nonlinearly using the LVQ neural network (Melin et al., 2014), (Liu et al., 2010), (Kugler & Lopes, 2007). The information for new, unseen cases is reduced by using the classifiers developed from these two techniques. This research

- Selection and peer-review under responsibility of the Organizing Committee of the Conference

presents the use of these two artificial intelligence techniques for enhancing the quality of individual cores. The design of wound core power transformers in fundamental terms, an overview of the DTs methodology and the LVQ neural network, and the application of the two various methodologies for the quality enhancement of individual cores are all covered in the sections that follow.

Projection of Wound Core Quality in Power Distribution Transformers

In order to build the wound core power distribution transformer, the raw material is initially cut into bands of a standard width. After being cut to predetermined lengths, the sheets are coiled around a circular mandrel. The circular core is then compressed into a rectangular shape using the appropriate press. The next step is annealing, which restores the physical and electrical properties of the core (Nie et al., 2016). This is typically accomplished in a protected atmosphere at temperatures between 790 and 880 ^{0}C. (Jardini et al., 2005). Pure, dry nitrogen is the most frequently utilized protective environment because it prevents the steel from oxidizing. Up to 2% of hydrogen may be found in the environment. Four stages make up the annealing cycle used in our application: the beginning and heating up stages (which aim to prevent oxidation and typically achieve a temperature of 815°C), the soaking stage (which aims to ensure that all cores have a uniform temperature distribution), the slow cooling stage (which aims to cool the load slowly in order to prevent the development of internal stresses in the cores), and the fast cooling stage (which aims to reduce the internal stresses) (Nagpal et al., 2006).

The individual cores are divided into two tiny and two large ones that should be used while building a distribution transformer with a wrapped core in three phases. In many cases, F2's width is twice that of F1's. The theory of modest individual core single-phase iron losses, often known as W (1), is presented by:

$$W(1) = WPK_1 * CTW_1 \tag{1}$$

where CTW_1 is the hypothetical tiny core's weight as specified in and WPK_1 is hypothetical with the specified magnetic induction, iron losses particular to each individual core (Awadallah et al., 2015). In Figure 1, the typical loss spider chart is displayed. The huge individual core's hypothetical iron losses, W (2), are as follows:

$$W(2) = WPK_1 * CTW_2 \tag{2}$$

where CTW_1 is the massive core's theoretical weight (Pamuk, 2014).

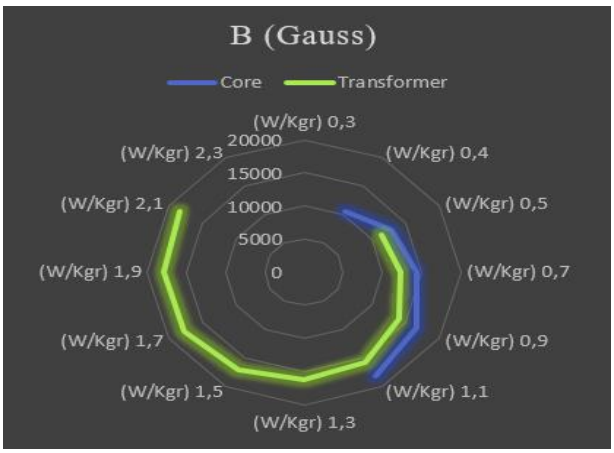

Figure 1. Typical loss spider chart

Decision Trees (DTs) Methodology

The DT is an upside-down tree with a Learning Set as its foundation (LS). The LS consists of a number of pre-classified states that are each defined by a candidate qualification list. Beginning with the entire LS of pre-classified Measurement Sets, at the root node, a DT is first created (MS). The test T that splits these MS "optimally" into the most "pure" subgroups is investigated. A definition of the test T is:

$$T = A_1 \leq t \tag{3}$$

t is the ideal threshold value, while A_1 is the qualification *i* value for a specific MS. Maximizing the additional information learned from a test determines which test is the best choice. If a node is terminal or "sufficiently" class pure, its classification entropy is compared to a minimal pre-set value $Human_{min}$. It is not further split if it is less than H_{min}, indicating that the node is class-pure enough. These nodes are known as "Limbs." If not, the best splitting rule is used to find an appropriate test to separate the node. The node is labeled a "Blind-Alley" and is not divided if no test can be identified that provides a statistically significant knowledge gain. Test sets (TS), which are collections of related, pre-classified, but separate MS, are used to evaluate DTs. Applying the tests of the various non-terminal nodes allows us to compare the classes of each of these MS to the classes that the terminal node ultimately leads to. This comparison reveals the degree of success of the DT categorization.

Learning Vector Quantization Neural Network Architecture

The input space is divided into several unique regions by the learning vector quantization process, and each zone is identified by representative vectors (Nova & Estevez, 2014). The two tiers of an LVQ network. Figure 2 depicts the LVQ's architecture, including R inputs, S1 competitive neurons, and S2 linear neurons. It shows the competitive transfer function as well as the linear transfer function using CTF and LTF, respectively. The competitive layer, which is the initial layer, uses the Kohonen rule to categorize input vectors according to the "winner-take-all" logic (Kohonen, 2012). The winning cutting-edge neuron creates a2(1) when its weight vector matches the input vector closest using the Euclidean distance measure. Up to S1 subclasses can be learned by the competitive layer because it has one neuron per class.

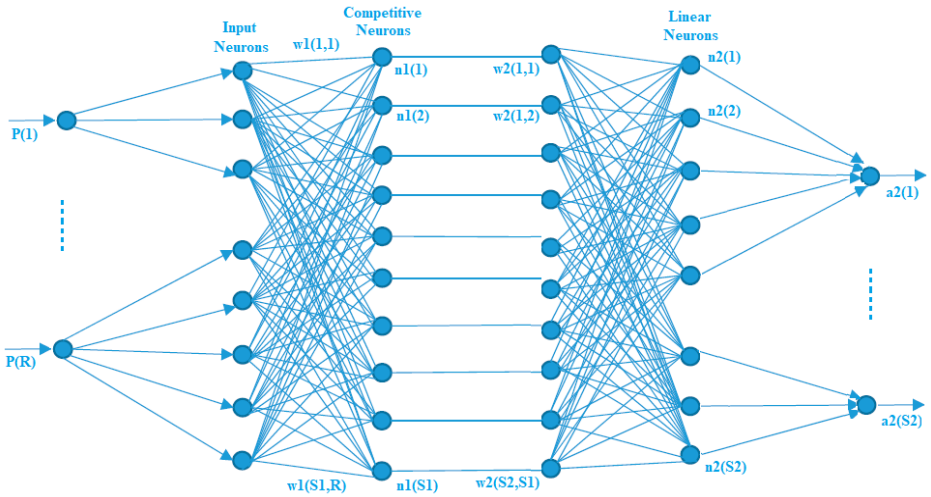

Figure 2. LVQ neural network architecture

Competition in the layer classes is transformed into user-defined S2 goal categories (vector a2) by the linear (second) layer. Using the network targets a2 and the linear layer weights w2, the aim vector a2(l) for the cutting-edge layer is calculated as follows:

$$a2(1) = w2^T * a2 \tag{4}$$

When a competitive neuron *i* wins and its target is 1, the Kohonen rule is solely applied to adjust the measurements of that neuron. As a result, a successful neuron weights only shift in favor of the input vector if it belongs to the current target class (Hammer et al., 2014):

$$\Delta w1(i, j) = I_r * a1(i) * (p(j) - w1(i, j)) \tag{5}$$

I_r in the above equation represents the process learning rate. However, the Kohonen rule is implemented with a sign change if the victorious neuron belongs to a subclass of a class different than the present target class. The weights of the successful neurons are shifted away from the input vector as a result:

$$\Delta w1(i, j) = -I_r * a1(i) * (p(j) - w1(i, j)) \quad (6)$$

So, the LVQ-NN algorithm may categorize any set of input vectors in a non-linear manner, not simply sets that can be linearly separated.

Grading of Core Certain Iron Losses

Establishing the Knowledge Base

The enhancement of individual core quality is the goal. In particular, the quality of the magnetic substance in the core and the impact of the annealing cycle are considered as input factors, as is the difference between the core weight's theoretical and real values. The identical 230 kVA distribution power transformer design and core magnetic material supplier were used throughout all testing. It was made of M3, 0.23 mm, magnetic material. Table 1 displays the design criteria for the 230-kVA distribution transformer. According to the annealing procedure, six requirements have been looked into in Table 2.

Table 1. Design parameter for the 230-kVA distribution transformer

Parameter Names	Values
Rated power	230 kVA
Voltages	20-15/0.4 kV
Connection	Dyn11
Coil material	Copper
Frequency	50 Hz
Type of low voltage coil	Foil
Type of high voltage coil	Wire
Turns of low voltage coil	31
Rated magnetic induction	15200 Gauss
Type of magnetic material	M3
Thickness of magnetic material	0.23 mm
Theoretical weight of small core	65 Kg
Theoretical weight of large core	74.5 Kg
Theoretical losses of small core	46.8 Watt
Theoretical losses of large core	53.6 Watt
Leg thickness at the core	60.2 mm
Width of the main leg	190 mm
Size of the core window	230 mm
Width of window of small core	63 mm
Width of window of large core	120 mm

Table 2. Annealing qualifications

Symbol	Description	High	Low
QUALIF1	Annealing final temperature	855 ^{0}C	825 ^{0}C
QUALIF2	Rising temperature period	4 hours	3 hours
QUALIF3	Temperature of the furnace's opening	350 ^{0}C	250 ^{0}C
QUALIF4	Length of time at a certain temperature	3 hours	2 hours
QUALIF5	Arrangement of the core in the furnace	Up	Down
QUALIF6	Protective environment	98% N_2 & 2% H_2	100% N_2

Table 3. The various annealing tests' conditions

Symbol	Annealing test number							
	1	2	3	4	5	6	7	8
QUALIF1	High	High	High	Low	High	High	High	Low
QUALIF2	Low	High	High	High	High	High	Low	Low
QUALIF3	Low	Low	Low	Low	Low	Low	High	High
QUALIF4	Low	Low	High	High	Low	Low	Low	High
QUALIF5	High	Low	High	Low	High	High	High	Low
QUALIF6	Low	High	High	High	Low	Low	Low	Low

32 experiments are needed to account for all possible combinations with two values for each of the six requirements Low and High. The SDE method can be used to reduce the number of implemented experiments because using all combinations requires a lot of time and money. By using this technique, the necessary number of experiments for my study is reduced to 8. Table 3 displays the characteristics of each of the 8 tests.

It is clear from the symmetrical feature that only four tests are done with each qualification at its lowest value while the other four are run at its highest value. According to SDE, numerous factors can be changed simultaneously and in a methodical way, ensuring the accuracy and independence of the research into the effects and interactions of all the significant components in the production process. A total of 96 cores (48 small and 48 large) were built for each of the eight tests. It should be noted that the same furnace was used to anneal all of the cores. The real-world to hypothetical core weight ratio (QUALIF7) and the particular losses of the core magnetic material are two additional considerations (QUALIF8). The core measurements for one small and one large core are shown in Table 4 as an arithmetic illustration for these requirements.

Table 4. Actual measurements for one small and one large core

Parameter Names	Small Core	Large Core
Annealing test number	4	5
Actual weight (Kg)	65.4	74
Material specific losses (Watt/Kg)	0.72	0.70
Single phase losses (Watt)	54.3	55.3

These qualifications can be assessed using equation 7 for the small core.

$$QUALIF7 = \frac{65.4Kg}{65Kg} = 1.006$$
$$QUALIF8 = 0.72\frac{Watt}{Kg} \tag{7}$$

The values of the qualifications for the two cores under consideration are shown in Table 5.

Table 5. Qualifications for the small and large cores considered

Symbol	Small Core	Large Core
QUALIF1	825 ^{0}C	825 ^{0}C
QUALIF2	4 hours	4 hours
QUALIF3	250 ^{0}C	350 ^{0}C
QUALIF4	3 hours	2 hours
QUALIF5	Down	Up
QUALIF6	98% N_2 & 2% H_2	100% N_2
QUALIF7	1.006	0.993
QUALIF8	0.72 Watt/Kg	0.70 Watt/Kg

Comparing the particular actual losses of iron to the theoretically projected particular iron losses is the basis for defining core iron losses as unacceptable, if the parameter “Ratio” is defined as in equation 8."

Ratio = (Actual Specific Iron Losses of Core) / (Theoretical Specific Iron Losses of Core) (8)

$$RATIO_1 = \frac{\frac{54.3Watt}{65.4Kg}}{\frac{46.8Watt}{65.0Kg}} = 1.153, \quad SmallCore$$
$$RATIO_2 = \frac{\frac{55.3Watt}{74.0Kg}}{\frac{53.6Watt}{74.5Kg}} = 1.039, \quad L\arg eCore \tag{9}$$

If "Ratio" exceeds "Limit," one core is unacceptable; otherwise, it is acceptable. The acceptance limit is indicated by the parameter "Limit," which primarily depends on the needs of the customer. For the core construction described in Tables 4 and Table 5, the parameter "Ratio" for the small and large core is defined as in equation 9 respectively. The little core under consideration is labeled as unacceptable if the parameter "Limit" is set to 1,15, whereas the large core is categorized as acceptable. The percentage of accepted cores per annealing test is displayed in Table 6. For the purpose of creating the learning and test sets, 768 samples were gathered. The remaining 3/4 (576) were utilized as a test set and the remaining 192 as a learning set.

Table 6. Number (%) of approved cores for each test

Percentage	Annealing test number							
	1	2	3	4	5	6	7	8
(%)	94	95	93	69	94	98	98	93

The Outcomes of the DTs Methodology

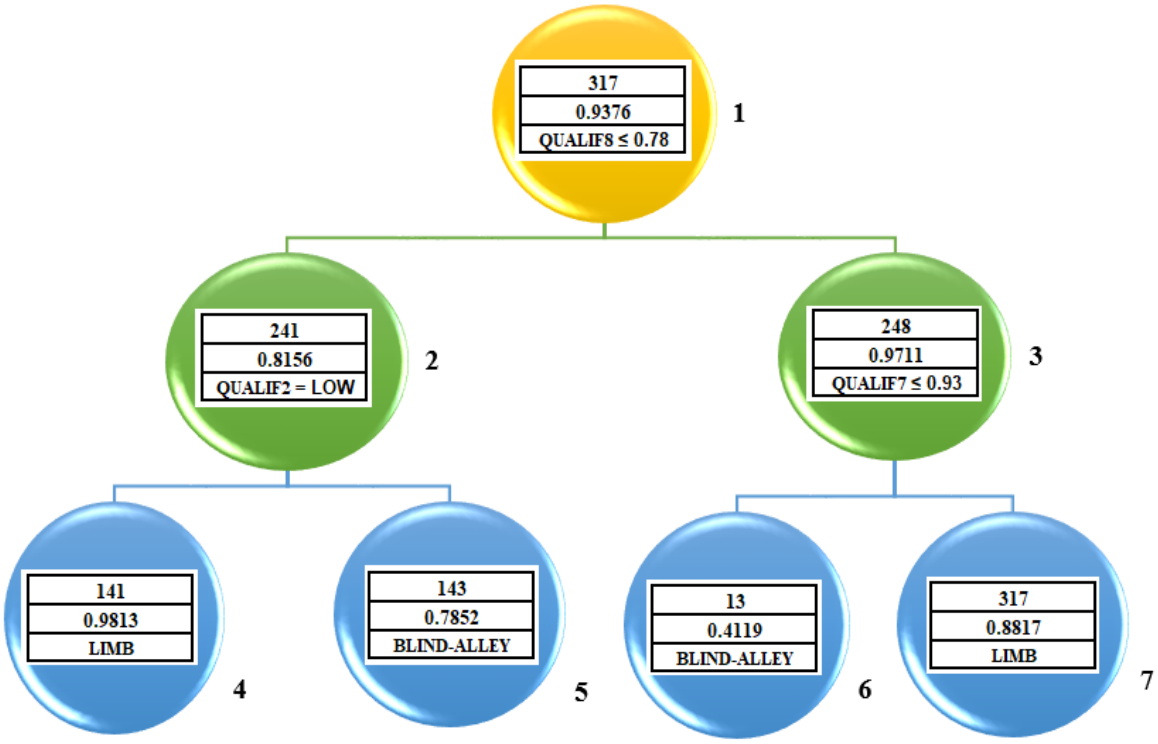

Figure 3. DT was improved using the 8-qualification level

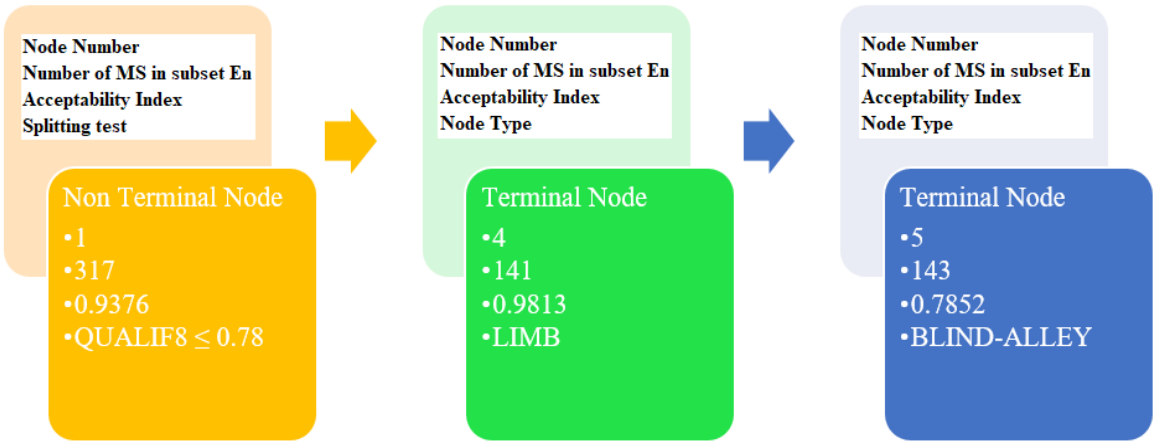

Figure 4. Notes on the nodes of the DTs

In Figure 3 characteristic DTs are shown, improved with the 8-qualification list and 0.986 assurance degree. When measured against the TS comprising 192 MS is 94%. Figure 4 explains the notation that is applied to DT nodes. A node's acceptability index is defined as the proportion of the acceptable MS in the node *n* subset E_n to the total MS in E_n. The MS "dropping" to a terminal node is classified as acceptable if its acceptability index is more than 0.5, and unacceptable otherwise.

The three qualifications that show up when the DT performed its node splitting tests in Figure 3 are QUALIF8, QUALIF2, and QUALIF7, in decreasing order of relevance. The coefficient QUALIF8 reveals the level of the substance since it is equivalent to the particular in the core magnetic material losses. The coefficient QUALIF2 denotes the time at which the temperature rises throughout the annealing cycle, whereas coefficient QUALIF7 the ratio of actual to theoretical core weight is expressed.

Given that each qualification is linked to the caliber of the individual core, their selection is logical and expected. It is noteworthy that QUALIF2 is the only variable that is pertinent to the tempering cycle and occurs in the DT's node splitting tests. This is because QUALIF4, QUALIF5, and the length of the stages of gradual and rapid cooling are all substantially connected, even though the tempering cycle's duration is thought to be constant. However, QUALIF7, which states where the core is located in the furnace, is not significant. Rules that are helpful to the production department are generated from the DTs of Figure 3. If it is technically and financially viable, nodes 4 and 7's connecting cores should be built. The acceptance indices for these nodes are higher than 93%. The measurement sets classified as unacceptable are those that follow the rules QUALIF8>0.78 and QUALIF70.88 and are led to node 6. The production division must raise QUALIF7 to prevent this. This is similar to adding more magnetic material to the core to make it heavier in real terms in order for the simulated core weight ratio (QUALIF7) to be greater than 0.88. The best annealing test can be chosen based on the magnetic material's quality (QUALIF8) as follows:

- The annealing test number 7 must be chosen if QUALIF8≤0.7. The explanation for this is that leading to node 4 in this situation is good. The QUALIF2 requirement can be deduced from the node 2 splitting rule. Additionally, it is clear from Table 6 that tests 6 and 7's annealing cycles are the best because they result in 98% acceptable cores. Only Test 7 of these two tests has a QUALIF2 that is equal to low. This outcome looks odd at first glance. However, if the entire annealing cycle is considered, this can be explained. This comprises the period of constant temperature as well as the phases of slow and rapid cooling. It also includes the time the temperature rises.
- Any one of the eight annealing tests may be chosen if QUALIF8>0.7. The explanation is that the annealing variables have no effect on the node 3 splitting rule.

Results Obtained Using the LVQ-NN Methodology

With the help of the neural network toolbox in MATLAB, the LVQ training algorithm simulator was developed. Considering the size of the LS and TS parameters as parameters that can be provided and changed interactively, "Limit" values were calculated and the number of candidate requirements was increased to 8. This includes the number, learning rate, and the number of competitive neurons in the allowed presentations and target vectors. The test set's categorization results, as determined by the LVQ neural network, are shown in table 7.

Table 7. LVQ-NN classification results

Limit Values	Competitive Neurons	Classification Success Rate
1.05	12	87.2%
1.08	12	90.8%
1.10	15	91.9%
1.12	18	93.3%
1.15	18	95.0%

When the classes are combined, a lower classification success rate is seen (for example, when "Limit" is 1.05, 61.7% of the MS are acceptable while the remaining are not). The classification success rate is equal to 95% if the "Limit" is set equal to 1.15 (the value considered for the DTs creation). It is demonstrated that the LVQ-NN technique is ideally suited for the categorization of precise iron losses to each particular core given the knowledge base employed and the candidate qualification sets chosen. The thresholds of the important features that could be exploited to enhance core quality are not, however, indicated by this method.

Conclusions

For the classification of precise iron losses to each particular core, the DT_S and the LVQ neural network are used in this study. The basic steps for applying the approach are explained, including building the knowledge base, selecting the requirements for candidates, and determining the proper DTS and neural network topologies. The resulting DT has an accuracy rate for classification of 94%, whereas the LVQ-NN structure has an accuracy rate for classification of 95%. On the basis of this DT, guidelines on the core's real weight that are helpful to the production department are derived. Additionally, the best annealing test can be chosen based on the magnet's composition and quality. By lowering their real losses, these two different artificial intelligence techniques are used to improve the quality of individual cores.

Scientific Ethics Declaration

The author declares that the scientific ethical and legal responsibility of this article published in EPSTEM journal belongs to the author.

Acknowledgements or Notes

* This article was presented as an oral presentation at the International Conference on Technology, Engineering and Science (www.icontes.net) held in Antalya/Turkey, on November 16-19, 2022.

References

Alatawneh, N., & Pillay, P. (2012). The impact of rotating field on core loss estimation in electrical machine laminations. *4th Annual IEEE Energy Conversion Congress and Exposition, (ECCE 2012)*, 15-20 September 2012, 2696-2703, https://doi.org/10.1109/ECCE.2012.6342535.

Altayef, E., Anayi, F., Packianather, M., Benmahamed, Y.,& Kherif, O. (2022). Detection and classification of lamination faults in a 15 kVA three-phase transformer core using SVM, KNN and DT algorithms. *IEEE Access*, 10, 50925-50932, https://doi.org/10.1109/ACCESS.2022.3174359.

Awadallah, M. A., Venkatesh, B., & Singh, B. N. (2015). Impact of solar panels on power quality of distribution networks and transformers. *Canadian Journal of Electrical and Computer Engineering*, *38*(1), 45-51, https://doi.org/10.1109/CJECE.2014.2359111.

Hammer, B., Hofmann, D., Schleif, F. M., & Zhu, X. (2014). Learning vector quantization for (dis-) similarities. *Neurocomputing*, *131*, 43-51, https://doi.org/10.1016/j.neucom.2013.05.054.

Jardini, J. A., Brittes, J. L. P., Magrini, L. C., Bini, M. A., Yasuoka, J. (2005). Power transformer temperature evaluation for overloading conditions. *IEEE Transactions on Power Delivery*, *20*(1), 179-184, https://doi.org/ 10.1109/TPWRD.2004.835433.

Kohonen, T. (2012). Self-organization and associative memory. *Springer Science & Business Media*, 3rd Edition, 241-268.

Kugler, M., Lopes, H. S. (2007). A configware approach for the implementation of a LVQ neural network. *International Journal of Computational Intelligence Research*, *3*(1), 21-25.

Li, D. C., Yeh, C. W. (2008). A non-parametric learning algorithm for small manufacturing data sets. *Expert System with Applications*, *34*(1), 391-398, https://doi.org/10.1016/j.eswa.2006.09.008.

Liu, J., Zuo, B., Zeng, X., Vroman, P., Rabenasolo, B. (2010). Nonwoven uniformity identification using wavelet texture analysis and LVQ neural network. *Expert System with Applications*, *37*(3), 2241-2246, https://doi.org/10.1016/j.eswa.2009.07.049.

Matiskova, D., Hrehova, S. (2021). Innovation of a control transformer design. *TEM Journal*, *10*(4), 1933-1937, https://doi.org/10.18421/TEM104-58.

Melin, P., Amezcua, J., Valdez, F., Castillo, O. (2014). A new neural network model based on the LVQ algorithm for multi-class classification of arrhythmias. *Information Sciences*, *279*, 483-497, https://doi.org/10.1016/j.ins.2014.04.003.

Nagpal, M., Martinich, T. G., Moshref, A., Morison, K., Kundur, P. (2006). Assessing and limiting impact of transformer inrush current on power quality. *IEEE Transactions on Power Delivery*, *21*(2), 890-896, https://doi.org/10.1109/TPWRD.2005.858782.

Nie, X., Zou, C., Li, Z., Meng, X., Qi, X. (2016). Numerical simulation of the electrical properties of shale gas reservoir rock based on digital core. *Journal of Geophysics and Engineering*, *13*(4), 481-490, https://doi.org/10.1088/1742-2132/13/4/481.

Nova, D., Estevez, P. A. (2014). A review of learning vector quantization classifiers. *Neural Computing and Applications*, *25*(3), 511-524, https://doi.org/10.1007/s00521-013-1535-3.

Pamuk, N. (2014). Using sweep frequency response method to identify mechanical integrity of core and winding structure in power transformers. *BEU Journal of Science*, 3(2), 117-125, https://doi.org/10.17798/beufen.87600.

Pamuk, N. (2020). Numerical method for calculations of the multi-dielectric fields based on flux density in high voltage power transformer apparatus. *Balkan Journal of Electrical and Computer Engineering*, 4(8), 342-347, https://doi.org/10.17694/bajece.768188.

Pamuk, N. (2022). Finite element analysis of thermal performance behavior in medium voltage current transformer. *TEM Journal*, 11(2), 797-801, https://doi.org/10.18421/TEM112-37.

Riemer, B., Lange, E., Hameyer, K. (2013). Calculation of the flux distribution of three phase five limb power transformers considering nonlinear material properties. *Compel: International Journal for Computation and Mathematics in Electrical and Electronic Engineering*, 32(4), 1230-1243, https://doi.org/10.1108/03321641311317059.

Russell, S. J., Norvig, P. (2015). Artificial intelligence: A modern approach. *Pearson Education Limited*, 3rd Edition, Edinburg Gate, Harlow, 757-762.

Author Information

Nihat Pamuk
Department of Electrical Electronics Engineering
Faculty of Engineering, Zonguldak Bulent Ecevit University
Zonguldak/Turkey
Contact e-mail: *nihatpamuk@beun.edu.tr*

To cite this article:

Pamuk, N. (2022). Improving core quality in power distribution transformers using machine learning methods. *The Eurasia Proceedings of Science, Technology, Engineering & Mathematics (EPSTEM), 21,* 46-54.

The Eurasia Proceedings of Science, Technology, Engineering & Mathematics (EPSTEM)
ISSN: 2602-3199

The Eurasia Proceedings of Science, Technology, Engineering & Mathematics (EPSTEM), 2022

Volume 21, Pages 55-63

IConTES 2022: International Conference on Technology, Engineering and Science

Learning-Based Algorithm for Fault Prediction Combining Different Data Mining Techniques: A Real Case Study

Laura LUCANTONI
Universita Politecnica Delle Marche

Filippo Emanuele CIARAPICA
Universita Politecnica Delle Marche

Maurizio BEVILACQUA
Universita Politecnica Delle Marche

Abstract: In recent years, new Data Mining (DM) algorithms and methodologies are increasingly used as an industrial solution for manufacturing improvements. In this context, new techniques are widely required by companies in the field of maintenance due to the need to reduce breakdowns intervention and take advantage of the increasing availability of data. This paper aims to propose a new learning-based algorithm to improve knowledge extraction by combining different DM techniques from a predictive maintenance perspective. First, the J48 algorithm and Random Forest (RF) are used as a predictive model to classify a set of failure modes according to their influence on the Overall Equipment Effectiveness (OEE). Then, the Apriori algorithm is used to identify the relationship among failure events belonging to the lowest OEE range for which, therefore, a predictive maintenance strategy should be defined. In order to describe the learning-based algorithm proposed in this paper, a real case study is presented and detailed. The experimental results showed a valuable tool for knowledge extraction and the definition of a set of predictive maintenance strategies for those failures most affecting the process. In this way, the complexity of decision-making on maintenance strategies can be reduced mainly when dealing with a large amount of information or a challenging dataset.

Keywords: Algorithms, Knowledge extraction, Failure prediction, Data mining, Case study.

Introduction and Background

In the current scenario, data-driven approaches are used by companies to support decision-makers in managing the wide amount of data in multiple contexts: energy consumption (Mugnini et al., 2021), industrial operations productivity (Antomarioni et al., 2021), efficiency (Görür et al., 2021), sustainability (Linke et al., 2019) and so on. Due to the integration of data analytics techniques and the advancement of information technologies, both efficiency and productivity areas have demonstrated the most potential improvement in manufacturing (Mansouri et al., 2020), mainly for failure detection in the field of maintenance (Görür et al., 2021).

Earlier, the term “maintenance” has referred to Breakdown or Time-based maintenance policies, thus attributing a cyclic nature to the fault occurrences and neglecting aspects such as the stochastic unavailability, due to the lack of quantity and quality data.

Since over the years a proper maintenance plan resulted in management, performance, and profit benefits (Lucantoni et al., 2019), the idea of maintenance has moved to a more scientific policy, namely Preventive maintenance, for failure occurrences prevention and proper operating condition restoration in manufacturing

(Ding & Kamaruddin, 2015). Among strategies, Predictive Maintenance (PdM) is considered one of the most interesting in the field of fault prediction, continuously growing with the technological advancement in manufacturing: due to the growing number of machines, systems, equipment, and products, DM models for data management through algorithms analytics (Frontoni et al., 2017) has demonstrated interesting prediction capabilities and decision making from a PdM perspective (Paolanti et al., 2017). In this context, the current paper aims to develop an algorithm for failure prediction. In particular, the algorithm proposed in this work is based on detecting hidden relationships within those failure events most influencing the OEE value using the integration of descriptive and predictive DM techniques.

In the literature, several contributions deal with the development of fault prediction strategies through DM techniques: some authors proposed the use of regression tree models for failure classification (Mohamed et al., 2019; Sezer et al., 2018) while, as the failure event is rarely random, Association Rules techniques are used for recognizing hidden patterns among failures (Antomarioni et al., 2022b) and Support Vector Machine for recognizing special patterns from signals (Gharoun et al., 2019; Widodo & Yang, 2007). Researchers also considered mathematical programming for predicting breakdowns in complex systems (Pisacane et al., 2021); while recently deep learning predictive models for selective maintenance optimization are proposed with successful results (Hesabi et al., 2022). An overview of the literary contributions dealing with the application of J48, RF, and Apriori algorithms for failure and fault prediction is also provided and summarized in Table 1.

Table 1. Literary contributions overview dealing with fault prediction

Algorithms	# of papers	# of relevant papers
Decision Tree J48	131	12
RF	118	35
Apriori	10	5
RF and Apriori	-	-
Decision Tree J48 and RF	89	8
Decision Tree J48 and Apriori	1	1
Decision Tree J48, RF and Apriori	-	-

Although valuable research is available in the literature, researchers usually consider the integration of one or two of those techniques to the best of the author's knowledge. However, several contributions integrated J48, RF, and Apriori algorithms in the educational and medical fields (Hussain et al., 2018; Kiu, 2018); while 31 research mainly used RF and Apriori algorithms in the technological fields, e.g., for software defects prediction (Abualghanam et al., 2022; Thapa et al., 2020). In particular, it should be highlighted that 70% of papers regarding the integration of J48 and RF algorithms, occurred only substituting “J48” with “Decision Tree”. Likewise, Among papers using the Apriori algorithm for fault prediction, only one also applied the Decision Tree model for the decision-making process in the field of telecommunications (Yang et al., 2017).

To sum up, even though all the methodologies have been successfully investigated in several contexts, there is no evidence of scientific paper dealing with fault prediction through the integration of J48, RF, and Apriori algorithms in the field of fault prediction. For this reason, the aim of the learning-based algorithm proposed in this paper is to reduce this research gap by developing and testing a new decision-making procedure that is based on the integration of three different DM techniques: J48, RF, and Apriori algorithms. In addition, the purpose of the current paper is to support maintainers in their decision-making process by providing reliable knowledge regarding the most appropriate maintenance strategy for the management of each failure mode (FM). In particular, the proposed algorithm enables OEE improvement by exploiting the strengths of different algorithms: Random Forest and J48 algorithms are used to classify failure events according to the OEE labels. Then, the Apriori rule is used to predict the hidden relationship between failure events belonging to the lowest OEE label to enhance failure prevention. The rest of the paper is as follows: this introduction is followed by the description of the learning-based algorithmic model description and implementation (Section 2). The results and discussion about theoretical and practical contributions are detailed in Section 3, while the conclusions and possible feature research topics are summarized in Section 4.

Algorithm Implementation

The algorithm developed in this paper has been applied and tested in a fully automatic assembly line within the automotive sector in order to reduce failure occurrences and improve the maintainer's decision-making process for fault prediction. The learning-based algorithm is structured and logically detailed as Figure 1 leveraging the availability of a huge amount of data. The methodology is summarized as follows:

1) *Preliminary analysis* for data gathering, pre-processing, and OEE calculation and classification. The main objective is to understand "what" kind of failure events has occurred.
2) *Data Mining* for analyzing data through DM techniques and checking the most impacting FMs relationships. The main objective is to understand "why" a failure event has occurred.
3) *Decision-making* to identify the most suitable maintenance policy and strategy for each major fault relationship. The main aim is to "predict" further occurrences by differentiating maintenance policies and actions.

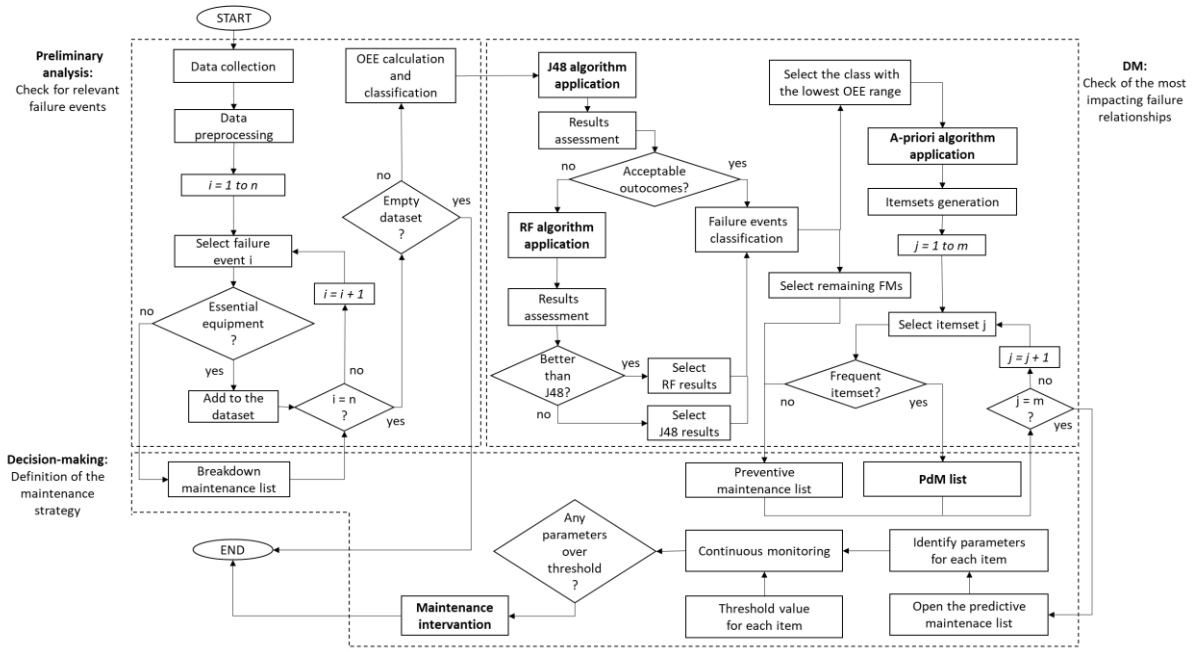

Figure 1. Learning-based algorithm for failure prevention

Preliminary Analysis

The Preliminary analysis layer is the foundation of the learning-based algorithm proposed in this paper. Its early activity involves data collection and pre-processing for failure events selection and cause identification. The real case study regards a fully automated line consisting of twelve assembly stations. In this experiment, the Computerized Maintenance Management System (CMMS) and Manufacturing Execution System (MES) are used to collect maintenance and manufacturing process information, respectively.

As a first step, data pre-processing is used for creating a single dataset with relevant information reporting: failure events, the date of the event, the shift in which the event occurred, and the production losses parameters, (availability, performance, quality). All inconsistencies were then removed thus providing a consistent dataset. Next, one-to-one failure modes selection is required for cause identification: if the equipment's or product's failures are not essential for operations or product, the failure mode is added to the *Breakdown maintenance list* (e.g., low-cost equipment repaired when needed); otherwise, it is left in the dataset as input to the second layer. The real dataset consisted of 1020 instances with 139 attributes describing the different failure modes, i.e:

- 143 instances with 32 attributes from the breakdown maintenance list;
- 877 instances with 107 attributes that need in-depth analysis and OEE calculation and classification.

OEE is a performance-measurement indicator with a range of 0 – 1 used to measure different types of production losses such as availability, performance, and quality (Muchiri & Pintelon, 2008). Data conversion and normalization have been applied to the following attributes before the evaluation of the prediction model:

- The failure modes attribute is converted to binary (0 | 1)
- 1st OEE range (f1) and 2nd OEE range (f2) are based on the assessment of attributes of the equipment effectiveness losses (Table).

Table 2. OEE classification

OEE range	Class Code	# of instances
0< 0EE <0,695	f1	436
0,695<= OEE <1	f2	441

Data Mining

The main aim of the DM layer is the processing of observations, data classification, and analytics to discover hidden relationships among the occurrences of different FMs. In particular, the objective of the learning-based algorithm is to identify correlations among the data, parameterize and recognize failure patterns for relevant knowledge extraction through the integration of multiple DM algorithms. It should be noted that the algorithm proposed in this work is designed for *off-line* operation with regular updating. The DM layer mainly consists of two main areas aiming to make the analyses easily accessible and user-friendly:

- *Decision Tree J48* and *RF* algorithm application for predicting OEE labels and values.
- *Apriori* algorithm application for the interpretable pattern recognition among the FMs most influencing OEE and the identification of the best maintenance strategy.

J48 and RF application

For data prediction among the selected failure events, supervised learning, including Classification techniques, is usually used to classify each item in a set of data into one of a predefined set of classes or groups (Kesavaraj & Sukumaran, 2013). To do that, the Weka DM tool (Waikato Environment for Knowledge Analysis) is used to perform the analysis as open-source software. Two supervised DM techniques, namely, Decision Tree J48 (the open-source Java implementation in Weka of the C4.5 algorithm), and the infrequent Random Forest techniques (Mikut & Reischl, 2011) have been selected for the major failure events analysis and classification. Hence, in the real case study, the 107 attributes that need in-depth analysis are used to predict the final OEE label. The main objective is to perform a "pruning" of the tree, removing branches incomprehensible or creating “noise” among the data. Once the J48 algorithm application, the output of Weka is as in Figure 2:

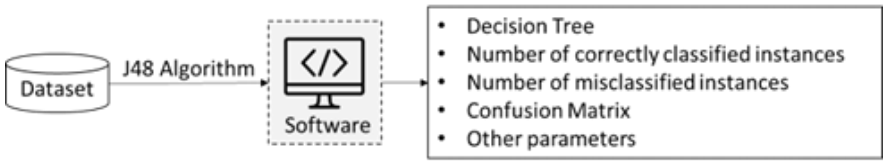

Figure 2. J-48 algorithm output

Decision Trees have a hierarchical structure of arcs and nodes:

- The *internal nodes* represent an FM.
- The *arcs* correspond to the FM’s value (i.e., binary value).
- The *root nodes* make a classification by grouping OEE into two labels.

In the current experiment, a binary Decision Tree J48 is provided, i.e., only two conditions can be evaluated in the splitting:

- Different from zero (! =0) if the fault occurs.
- Equal to zero (= 0) if the fault does not occur.

The methodology should be followed until reaching all the leaves and the final classification is thus achieved when the OEE label assignment is completed. Starting with the root node (= FM 5), the splitting is performed. If such a failure event occurs (i.e., arc value “ ! = 0 ”) the classification proceeds with the branch on the right immediately leading back to a leaf node performing the classification. Otherwise, if it does not occur (i.e., arc value “ = 0 ”) the classification proceeds with the left branch leading to a different attribute in order to perform the next splitting. This procedure is followed until the final classification. Hence, the assignment of the respective OEE label namely f1 or f2 is achieved.

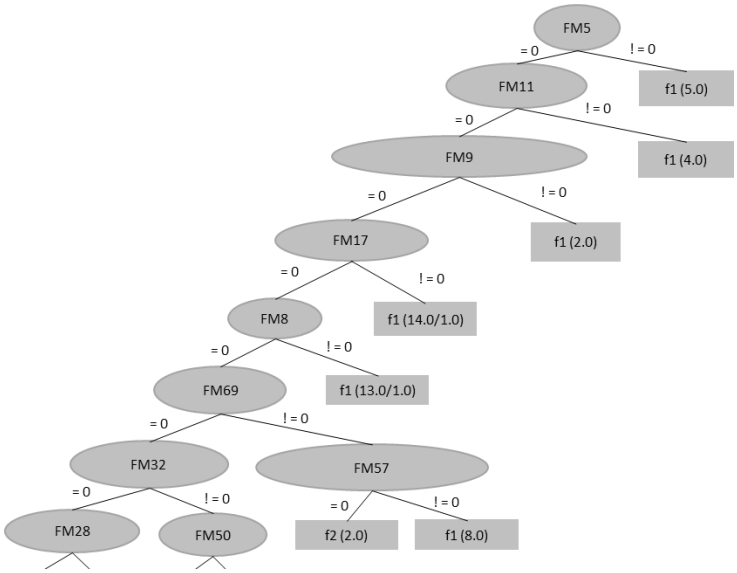

Figure 3. Extraction of the DT J48

Likewise, starting from the "FM 69" node, instead of reaching the leaf with the relevant classification immediately, two other nodes have been provided. This implicates that if a failure event related to "FM 69" occurs then a failure event related to "FM 32" also occurs; otherwise, the failure is related to "FM 57".

Once the classification is completed, it is important to take into account the misclassification error and possible inconsistencies that could be explained as the presence of a fault with limited or no impact on the performance of the production line under consideration (e.g., if band *f2* is assigned when a fault occurs). Hence, the evaluation of this classification is provided after the explanation of two more different experiments for the best results selection.

- 2nd classification: The day of the week is included among the attributes, from "1 = Monday" up to "7 = Sunday". The DT J48 has a similar classification to the previous one with the addition, in a few parts, of nodes with the day of the week attribute, which, however, does not significantly affect the whole DT structure. In fact, most of the same classification criteria present in the first tree have been observed.
- 3rd classification: RF, i.e., a multitude of trees into a single model, is provided. The tree-related graph has not been provided since generating a multitude of trees: 150 in the case under examination.

Eventually, results are assessed by the "Confusion Matrix" for the classification error quantification and accuracy evaluation (Figure 4):

CONFUSION MATRIX		CLASSIFICATION ACCURACY
a b <-- classified as 246 190 | a = f1 163 278 | b = f2	First classification	= 60 %
a b <-- classified as 218 218 | a = f1 150 291 | b = f2	Second classification	= 58 %
a b <-- classified as 222 214 | a = f1 147 294 | b = f2	Third classification	= 59 %

Figure 4. Confusion matrix and accuracy assessment

The first classification, namely, the DT J48 only considering the FMs attributes, provided 246 instances correctly classified as *f1* and 278 as *f2*. All remaining ones are considered misclassification probably due to the challenging dataset. In the second classification -2% in the accuracy value is highlighted mainly due to a decrease in *f1* correct classification. Then, the classification achieved from the RF is very similar and almost completely comparable with the J48 algorithm in terms of returned parameters.

Then, faults belonging to the lower OEE range should be selected: since the first classification appears to have the best accuracy, all the instances belonging to the f1 class have been selected as at-risk failure events to be better analyzed through the Apriori algorithm application. All the remaining FM not appearing in the lowest OEE class should be added to the preventive maintenance list.

Apriori Algorithm Application

The learning-based algorithm proposed in this paper proceeds with the identification of the most frequent itemset among failure events belonging to the lower OEE label. Association rules, i.e., "*if→then*" prepositions formed by an antecedent and consequent for pattern extraction from huge amounts of data. In particular, the current work procedure can be summarized as follows:

a) Scanning the database for frequent itemsets generation using the "*Confidence*" and the "S*upport"* values, which respectively identifies the strength and the statistical significance of the rule (Antomarioni et al., 2022a): itemsets didn't reach the minimum support value as a threshold should be added to the *preventive maintenance* list to follow the existing regular maintenance plan, i.e., every 1000 pieces assembled in the real case study.
b) From the frequent itemsets, association rules are extracted as reported in Table 3 with an average accuracy of 0,59: the hidden patterns discovered among FMs have been added to the *PdM list* to schedule maintenance based on the asset conditions.

Once all itemsets have been analyzed, the FMs typically result in an OEE reduction and relevant hidden patterns among them are detected to enhance the decision-making strategy described in the paragraph below.

Decision-Making

The Decision-making layer only concerned the frequent itemsets selected in the previous DM layer, i.e., those FMs for which PdM strategies should be generated. After identifying the critical FMs and their relationships, the most appropriate maintenance policy should be selected for each of the most frequent items. In particular, each FM which is part of the precursors of the rule should be predicted in order to avoid the occurrence of the consequent in the rule. The choice of maintenance policies derives both from the *Preliminary analysis* and *Data mining* layers of the learning-based algorithm in this work.

Table 3. PdM strategy

Failure code to predict	Faulure patterns	Parameters to be monitored
5	103, 6, 11	Workstation energy consumption
44	7, 4, 12, 55	Part positioning coordinates
47	10, 22, 30, 63	Tool vibrations
61	34, 51, 98	Workstation energy consumption
69	89, 32, 57	Tool deterioration
90	1, 15	Tool deterioration
102	48, 3, 27, 81	Workstation temperature

As previously reported, the most suitable maintenance strategy is identified among the main maintenance policies:

- Breakdown maintenance,
- Preventive maintenance,
- Predictive maintenance.

Regarding PdM, the basic idea in the current real experimentation is based on the continuous monitoring of the asset conditions and signals degradation. Hence, in order to provide some predictability to such failures

belonging to the PdM list in the real case study, seven predictive maintenance strategies have been identified as shown in Table 3 in order to avoid both the antecedent failure and its consenquents.

Results and Discussion

After implementing the learning-based algorithm, 139 FMs belonging to the source database have been classified as follows:

- The 23% is related to the corrective maintenance list due to their lack of predictability, as well as, human error without explanation.
- The 55% is assigned to the preventive maintenance list as no frequent itemset was found. This means that maintainers will continue to handle such failure events according to their experience and strategy.
- The 22% of failure modes have been associated with the predictive maintenance list due to relevant patterns among FMs most reducing OEE.

Some consistency in the number of corrective maintenance interventions has been found. Otherwise, an average reduction of 15% in preventive maintenance interventions has been observed, then replaced by PdM interventions as a result of the detection of 11 over-threshold parameter values. In addition, to deal with the last point, 7 PdM actions have been applied by monitoring the assembly line for two weeks. An average improvement in OEE of 0.5 percent is assessed due to the PdM actions taken.

Based on these results, since much research in the literature usually compared different DM techniques identifying the best one for the specific case study without founding one technique universally superior to the others, the implementation of the learning-based algorithm proposed in this work results particularly useful to exploit as many strengths as possible from multiple DM techniques.

It should be stated that the proposed algorithm is beneficial on huge datasets, as homogeneous and consistent as possible with the business reality, thus proving poor applicability to manually manufacturing contexts or challenging datasets. In conclusion, despite the moderate classification accuracy values of 60%, the challenging nature of the source dataset was highlighted thus requiring improvement.

Conclusion

DM is the process of discovering previously unknown and potentially valuable relationships, patterns, and information within huge databases. In particular, this paper demonstrated how integrating J48, RF, and Apriori algorithms can be significant for early failure prediction in a real case study, supporting the maintenance decision-making process. Hence, early fault prediction with this learning-based algorithm also supports the identification of failure occurrences relationship most influencing the Overall Equipment Effectiveness. In this way, maintainers may be able to perform better in their daily maintenance interventions.

In future development, a more accurate learning-based algorithm for predicting early failure occurrences can be provided by integrating other DM techniques, such as Network Analysis to represent the hidden relationship among failures to facilitate their comprehension. In conclusion, a regular algorithm application should be tested in the long term from a continuous improvement perspective in the field of fault prediction.

Scientific Ethics Declaration

The authors declare that the scientific ethical and legal responsibility of this article published in EPSTEM journal belongs to the authors.

Acknowledgements or Notes

* This article was presented as an oral presentation at the International Conference on Technology, Engineering and Science (www.icontes.net) held in Antalya/Turkey on November 16-19, 2022.

References

Abualghanam, O., Al-Khatib, S. N., & Hiari, M. O. (2022). Data mining model for predicting customer purchase behavior in e-commerce context. *International Journal of Advanced Computer Science and Applications*, *13*(2), 421. https://doi.org/10.14569/IJACSA.2022.0130249

Antomarioni, S., Ciarapica, F. E., & Bevilacqua, M. (2022a). Association rules and social network analysis for supporting failure mode effects and criticality analysis: Framework development and insights from an onshore platform. *Safety Science*, *150*. https://doi.org/https://doi.org/10.1016/j.ssci.2022.105711

Antomarioni, S., Ciarapica, F. E., & Bevilacqua, M. (2022b). Data-driven approach to predict the sequence of component failures: a framework and a case study on a process industry. *International Journal of Quality & Reliability Management*. https://doi.org/10.1108/IJQRM-12-2020-0413

Antomarioni, S., Lucantoni, L., Ciarapica, F. E., & Bevilacqua, M. (2021). Data-driven decision support system for managing item allocation in an ASRS: A framework development and a case study. *Expert Systems with Applications*, *185*, 115622. https://doi.org/10.1016/J.ESWA.2021.115622

Ding, S. H., & Kamaruddin, S. (2015). Maintenance policy optimization—literature review and directions. *Int J Adv Manuf Technol*, *76*, 1263–1283. https://doi.org/10.1007/s00170-014-6341-2

Frontoni, E., Pollini, R., Russo, P., Zingaretti, P., & Cerri, G. (2017). Hdomo: Smart sensor integration for an active and independent longevity of the elderly. *Sensors*, *17*(11).

Gharoun, H., Keramati, A., Nasiri, M. M., & Azadeh, A. (2019). An integrated approach for aircraft turbofan engine fault detection based on data mining techniques. *Expert Systems*, *36*(4). https://doi.org/10.1111/exsy.12370

Görür, O. C., Yu, X., & Sivrikaya, F. (2021). Integrating predictive maintenance in adaptive process scheduling for a safe and efficient industrial process. *Applied Sciences*, *11*(11), 5042.

Hesabi, H., Nourelfath, M., & Hajji, A. (2022). A deep learning predictive model for selective maintenance optimization. *Reliability Engineering & System Safety*, *219*. https://doi.org/https://doi.org/10.1016/j.ress.2021.108191

Hussain, S., Dahan, N. A., Ba-Alwib, F. M., & Ribata, N. (2018). Educational data mining and analysis of students' academic performance using WEKA. *Indonesian Journal of Electrical Engineering and Computer Science*, *9*(2), 447–459. https://doi.org/10.11591/ijeecs.v9.i2.pp447-459

Kesavaraj, G., & Sukumaran, S. (2013). A study on classification techniques in data mining. *Fourth International Conference on Computing, Communications and Networking Technologies (ICCCNT)*, 1–7. https://doi.org/10.1109/ICCCNT.2013.6726842

Kiu, C.-C. (2018). Data mining analysis on student's academic performance through exploration of student's background and social activities. *2018 Fourth International Conference on Advances in Computing, Communication & Automation (ICACCA)*, 1–5. https://doi.org/10.1109/ICACCAF.2018.8776809

Linke, B. S., Garcia, D. R., Kamath, A., & Garretson, I. C. (2019). Data-driven sustainability in manufacturing: selected examples. *Procedia Manufacturing*, *33*, 602–609. https://doi.org/https://doi.org/10.1016/j.promfg.2019.04.075

Lucantoni, L., Bevilacqua, M., & Ciarapica, F. E. (2019). An enhanced approach for implementing risk-based maintenance in a total productive maintenance perspective. *XXIV Summer School "Francesco Turco" – Industrial Systems Engineering*, 53–59. http://www.summerschool-aidi.it/edition-2019/cms/extra/papers/211.pdf

Mansouri, S., Castronovo, F., & Akhavian, R. (2020). Analysis of the synergistic effect of data analytics and technology trends in the AEC/FM ındustry. *Journal of Construction Engineering and Management*, *146*(3).

Mikut, R., & Reischl, M. (2011). Data mining tools. *Wiley Interdisciplinary Reviews: Data Mining and Knowledge Discovery*, *1*, 431–443. https://doi.org/10.1002/widm.24

Mohamed, A., Hamdi, M. S., & Tahar, S. (2019). Decision tree-based approach for defect detection and classification in oil and gas pipelines. In *Advances in Intelligent Systems and Computing* (Vol. 880, pp. 490–504). https://doi.org/https://doi.org/10.1007/978-3-030-02686-8_37

Muchiri, P., & Pintelon, L. (2008). Performance measurement using overall equipment effectiveness (OEE): literature review and practical application discussion. *International Journal of Production Research*, *46*(13). https://doi.org/https://doi.org/10.1080/00207540601142645

Mugnini, A., Polonara, F., & Arteconi, A. (2021). Energy flexibility curves to characterize the residential space cooling sector: The role of cooling technology and emission system. *Energy and Buildings*, *253*. https://doi.org/https://doi.org/10.1016/j.enbuild.2021.111335

Paolanti, M., Sturari, M., Mancini, A., Zingaretti, P., & Frontoni., E. (2017). Mobile robot for retail surveying and inventory using visual and textual analysis of monocular pictures based on deep learning. *2017 European Conference on Mobile Robots (ECMR)*. https://doi.org/10.1109/ECMR.2017.8098666

Pisacane, O., Potena, D., Antomarioni, S., Bevilacqua, M., Ciarapica, F. E., & Diamantini, C. (2021). Data-

driven predictive maintenance policy based on multi-objective optimization approaches for the component repairing problem. *Engineering Optimization*, *53*, 1–20. https://doi.org/https://doi.org/10.1080/0305215x.2020.1823381

Sezer, E., David Romero, D., Guedeal, F., Macchi, M., & Emmanouilidis, C. (2018). An Industry 4.0-enabled low cost predictive maintenance approach for SMEs: A use case applied to a cnc turning centre. *24th International ICE-Conference on Engineering, Technology and Innovation*. https://doi.org/10.1109/ICE.2018.8436307

Thapa, S., Alsadoon, A., Prasad, P. W. ., Al-Dala'in, T., & Rashid, T. A. (2020). Software defect prediction using atomic rule mining and random forest. *5th International Conference on Innovative Technologies in Intelligent Systems and Industrial Applications (CITISIA)*, 1–8. https://doi.org/10.1109/CITISIA50690.2020.9371797

Widodo, A., & Yang, B.-S. (2007). Support vector machine in machine condition monitoring and fault diagnosis. *Mechanical Systems and Signal Processing*, *21*(6), 2560–2574. https://doi.org/https://doi.org/10.1016/j.ymssp.2006.12.007

Yang, Q., Ji, G., & Zhou, W. (2017). The correlation analysis and prediction between mobile phone users complaints and telecom equipment failures under big data environments. *2nd International Conference on Advanced Robotics and Mechatronics (ICARM)*, 201–206. https://doi.org/10.1109/ICARM.2017.8273160

Author Information

Laura Lucantoni
Universita Politecnica Delle Marche
Via Brecce Bianche, 12, 60131 Ancona AN
Contact e-mail: *l.lucantoni@pm.univpm.it*

Filippo Emanuele Ciarapica
Universita Politecnica Delle Marche
Via Brecce Bianche, 12, 60131 Ancona AN

Maurizio Bevilacqua
Universita Politecnica Delle Marche
Via Brecce Bianche, 12, 60131 Ancona AN

To cite this article:

Lucantoni, L., Ciarapica, F. E., & Bevilacqua, M. (2022). Learning-based algorithm for fault prediction combining different data mining techniques: A real case study. *The Eurasia Proceedings of Science, Technology, Engineering & Mathematics (EPSTEM), 21*, 55-63.

The Eurasia Proceedings of Science, Technology, Engineering & Mathematics (EPSTEM)
ISSN: 2602-3199

The Eurasia Proceedings of Science, Technology, Engineering & Mathematics (EPSTEM), 2022

Volume 21, Pages 64-69

IConTES 2022: International Conference on Technology, Engineering and Science

Experimental Study of Yellowing Index Comparison between 430 Stainless Steel and 441 Stainless Steel Burner Plates on Domestic Gas Hobs

Berkent PARIM
Haier Europe, Research and Development Center

Mehmet KARA
Haier Europe, Research and Development Center

Ayberk Salim MAYIL
Haier Europe, Research and Development Center

Abstract: For the household appliances, one the critical design parameter is esthetic. On the surface of the domestic gas hob burner plates, yellowness problem is seen with the high temperature flame effect. When the burner plate surface is getting higher yellowness, esthetical problem is occurred. In this study, for evaluating yellowness period and comparing the yellowness ratio, 6 hobs are tested and measured yellowing index by using colorimetry method in Haier Europe Quality Reliability Laboratory. 3 of the 6 hobs have the 430SS burner plate, other 3 hobs have the 441SS burner plate. During 360 cycles of hob working, 4 times yellowness is measured in the beginning (cycle 0), then end of the 120,240 and 360. cycles. Each measurement is repeated 2 times on one area to increase accuracy of measurement. In the end of the study, results show that 441SS material has lower yellow color changing than 430SS material as a burner plate in the same conditions.

Keywords: Colorimetry, Gas hobs, Yellowness

Introduction

Color is one of the basis esthetical design parameters on domestic appliances. During usage, metal surfaces of hobs are exposed to high temperature and oxidation happens (Wang & Duh, 1995, Naylor, 1950). By thermal oxidation, yellowness and redness occur in the course of time. In the standard, there is not any specific rule to esthetical design point of view for yellowness and redness rate. To create design guide, yellowness characterization is needed. One of the good methods to measure yellowness is colorimetry method (Muduroglu et al., 2018, Maskan, 2001, Taskin, 2018).

CIE L*a*b* remarked 4 colors as a basis color which they are red, green, yellow and blue (Colorimetry, 1986). With the white and black hues, there are mainly 6 colors. Other colors are derived from these 6 main colors (Gilchrist & Nobbs, 2017).

In this study, 6 hobs are tested to measure yellowing ratio by using colorimetry method in Haier Europe Quality Reliability Laboratory. 3 of the 6 hobs have the 430SS burner plate, other 3 hobs have the 441SS burner plate. During 360 cycles of hob working, 4 times yellowness is measured in the beginning (cycle 0), then end of the 120,240 and 360. cycles. Each measurement is repeated 2 times on one area to increase accuracy of measurement.

Materials and Methods

In this experimental study, Haier Europe 60cm gas hob model is used. As a burner plate of hob, 2 different sheet metals are used. As a total 12 hobs are tested. 3 of them with 430SS sheet, other 3 with 441SS sheet for the burner plate of hob. Figure 1 shows the Haier Europe 60cm hob model to use for experimental study.

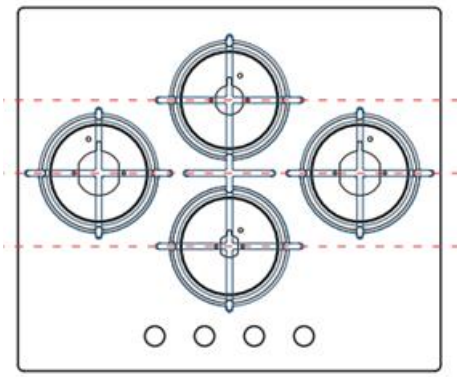

Figure 1**.** Haier Europe 60cm gas hob

Table 1. Test classification

Hob Model / Burner Plate	430 Stainless Steel Sheet	441 Stainless Steel Sheet
60cm Gas Hob	3 Samples	3 Samples

Table 1 shows the test classifications to measure Yellowness ratio above. For hob models, 8 critical areas are determined to measure yellowing ratio as shown Figure 2 below. Each measurement is repeated 2 times to increase the accuracy of values. Each measurement is indicated as a M1 and M2 as a first measurement and second measurement respectively. Apart from beginning, 3 different times (twice for each) measurement are taken at end of cycle 120, cycle 240 and cycle 360. 1 working cycle means; maximum power working for 20 minutes, minimum power working for 40 minutes and cooling (hob is off) for 30 minutes for gas hobs during QRL tests. Working cycle logic is shown Figure 3 below.

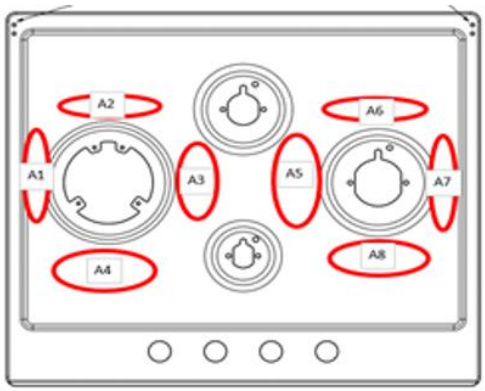

Figure 2. 60cm Hob measurement area

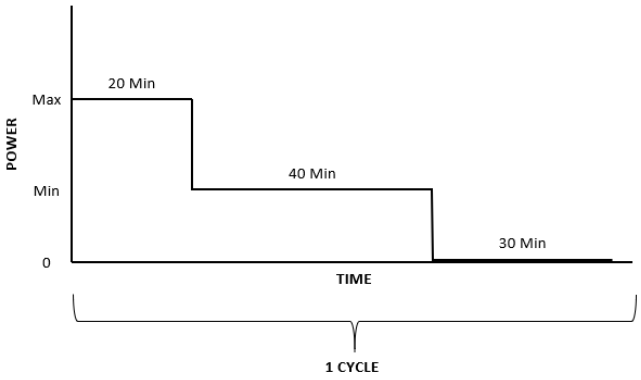

Figure 3. Hob 1 working cycle

During the measurement, Hunterlab MSEZ 4500L Colorimeter is used as shown Figure 4 below.

Figure 4. Colorimeter

Theory

Colorimetry measurement method is applied based on L*, a*, b* color space as shown Figure 5. L* represents lightness, a* represents redness and b* represents yellowness on positive side. On negative side, L* represents darkness, a* represents greenness and b* represents blueness (Onur et.al., 2017).

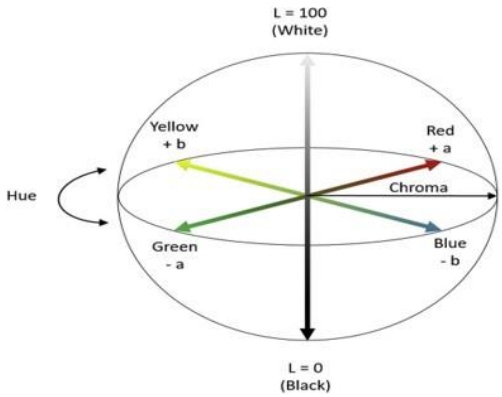

Figure 5. L* a* b* Color diagram

Color measurement is explained equation 1, 2 and 3 below. Total color change is shown in Equation 1. Chroma and Hue angle are shown are shown in Equation 3 and 4 respectively (Mask, 2001).

$$\Delta E = \sqrt{(L_0 - L)^2 + (a_0 - a) + (b_0 - b)} \quad [1]$$

$$C = (a^2 + b^2)^{1/2} \quad [2]$$

$$Hue\ Angle = tan^{-1}\left(\frac{b}{a}\right) \quad [3]$$

L, a and b values are color change, “o” index means color reading on materials (Stainless Steel Sheet).

Results

In this study, 6 hobs are tested to check yellowness measurements. 8 area are specified as a critical region as get effected by high temperatures during the working cycles. 3 hobs of test samples have 430SS burner plate, others have 441SS burner plate. Table 2, 3 and 4 shows yellowness measurements of 430SS hobs below. Table 5,6 and 7 shows yellowness measurements of 441SS hobs below.

Table 2. 430 stainless steel b* values at cycle 120

Cycle 120	Sample 1		Sample 2		Sample 3	
Area	M1	M2	M1	M2	M1	M2
A1	1,51	1,96	2,42	1,96	2,49	2,31
A2	1,26	1,74	2,21	1,47	1,95	2,11
A3	2,65	3,14	3,43	3,6	4,09	4,25
A4	1,26	1,72	1,92	1,79	2,07	2,15
A5	1,95	2,34	2,29	2,52	2,13	2,15
A6	1,56	1,64	1,39	1,82	1,7	1,61
A7	1,74	1,93	1,93	1,69	1,86	1,75
A8	1,52	1,45	1,42	1,79	1,87	1,67

Table 3. 430 stainless steel b* values at cycle 240

Cycle 240	Sample 1		Sample 2		Sample 3	
Area	M1	M2	M1	M2	M1	M2
A1	4,62	4,01	8,13	5,59	5,52	5,29
A2	2,44	2,48	3,46	6,17	3,12	3,75
A3	5,02	4,61	7,79	10,07	5,76	5,95
A4	1,43	1,43	2,74	4,28	2,21	1,88
A5	8,5	5,75	10,2	10,47	5,51	4,81
A6	3,33	2,78	10,12	4,48	1,58	1,19
A7	1,77	1,46	1,91	1,32	1,67	1,59
A8	0,86	0,95	1,36	5,6	0,89	1,13

Table 4. 430 stainless steel b* values at cycle 360

Cycle 360	Sample 1		Sample 2		Sample 3	
Area	M1	M2	M1	M2	M1	M2
A1	3,05	3,75	2,03	5,89	4,31	4,65
A2	3,18	4,04	6,66	8,75	3,77	4,8
A3	5,82	4,88	10,62	11,34	6,54	6,5
A4	1,95	2,36	5,92	2,40	3,93	3,14
A5	3,87	8,15	9,81	10,05	6,23	4,61
A6	4,21	1,88	10,70	3,81	1,9	1,72
A7	1,52	0,77	2,21	1,22	1,94	1,32
A8	1,17	1,35	1,48	7,93	1,13	1,38

Table 5. 441 stainless steel b* values at cycle 120

Cycle 120	Sample 1		Sample 2		Sample 3	
Area	M1	M2	M1	M2	M1	M2
A1	1,11	1,10	0,76	0,79	1,26	1,26
A2	1,09	1,26	0,98	0,62	1,17	0,83
A3	2,07	1,47	0,93	0,62	1,00	0,68
A4	1,68	1,17	0,92	0,71	0,98	0,71
A5	1,17	0,93	0,67	0,59	0,62	0,50
A6	1,52	1,54	0,63	0,69	0,76	0,59
A7	1,30	1,10	0,82	0,47	0,80	0,54
A8	1,29	1,02	0,90	0,52	0,67	0,48

Table 6. 441 stainless steel b* values at cycle 240

Cycle 240	Sample 1		Sample 2		Sample 3	
Area	M1	M2	M1	M2	M1	M2
A1	4,98	2,43	4,08	3,01	2,91	3,02
A2	2,27	2,47	2,15	2,58	1,88	2,15
A3	3,57	3,39	3,52	3,31	3,71	3,15
A4	2,19	1,96	2,29	2,3	1,64	1,93
A5	3,25	2,82	4,03	4,71	2,72	2,43
A6	1,49	1,39	1,87	2,3	1,75	1,54
A7	2,28	2,19	2,36	3,06	1,78	1,44
A8	1,53	1,38	2	1,87	1,04	1,31

Table7. 441 stainless steel b* values at cycle 360

Cycle 360	Sample 1		Sample 2		Sample 3	
Area	M1	M2	M1	M2	M1	M2
A1	2,33	2,43	3,11	2,58	2,41	1,99
A2	2,08	3,78	2,45	2,89	2,35	2,14
A3	3,47	3,42	3,59	3,69	3,78	3,37
A4	2,53	2,1	2,28	2,79	1,41	1,14
A5	2,7	3,55	3,82	3,65	2,5	1,79
A6	1,47	1,47	2,29	2,39	2,12	1,4
A7	1,73	1,82	2,46	2,08	1,7	1,31
A8	1,44	2,09	2,1	2,36	1,07	1,46

Each measurement repeated to times to increase the accuracy of experimental study. There are 10% - 25% variation between measurements. Results showed that, 441SS material have better behavior than 430SS under high temperature conditions from yellowness perspective.

Table 8. Measurement of b* values for each sample/material comparison table

Material / Cycle	Sample 1			Sample 2			Sample 3		
	C120	C240	C360	C120	C240	C360	C120	C240	C360
430SS	1.84	3.50	3.25	2.10	5.86	6.30	2.26	3.24	3.62
441SS	1.30	2.40	2.47	0.73	2.78	2.84	0.80	2.00	2.15

Table 8 shows overall summary of the results, indicated each sample – materials values. In the Figure 6, results show prominently 441SS material have better behavior than 430SS material under high temperature condition from yellowness perspective. There are 45% - 55% differences between two materials.

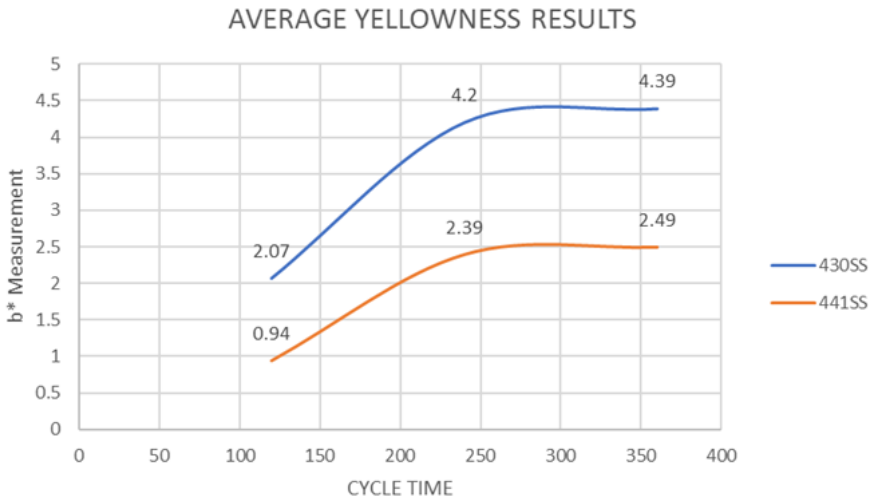

Figure 6. Average yellowness comparison

Conclusion

In this paper, yellowness measurement of materials as a hob burner plate has been investigated. As a total 6 hobs are tested for 6 months for each sample as a life test. In the end, results show that 441SS material is more qualified than 430SS material for the yellowness point of view. This is very effective on esthetical design, also for customer usage. After experimental evaluation, it is decided that 441SS will be used as a burner plate for the high segment products.

Scientific Ethics Declaration

The authors declare that the scientific ethical and legal responsibility of this article published in EPSTEM journal belong to authors.

Acknowledgements

* This article was presented as an oral presentation at the International Conference on Technology, Engineering and Science (www.icontes.net) held in Antalya/Turkey on November 16-19, 2022.

*This study is supported by Haier Europe Company. Hob models are Haier commercial models of Haier Europe and for all tests, Haier Europe Quality Reliability Laboratory is used.

References

CIE Publication 15.2 (1986). *Colorimetry*. CIE

Gilchrist, A., & Nobbs, J. (2017). *Colorimetry, theory. Encyclopedia of spectroscopy and spectrometry*. 328-333.

Maskan, M. (2001). Kinetics of colour change of kiwifruits during hot air and microwave drying. *Journal of Food Engineering, 48*(2), 169-175.

Muduroglu, R., Kivrak, T. C., & Nalcaci, A. (2018). Renk belirlenmesinde kullanilan yontem ve cihazlar. *Cumhuriyet Dental Journal, 21*(1), 61-69.

Naylor, C. E. (1950). *Electrocoloring of stainless steels in aqueous solutions*. Plates.

Taskin, O., Gokcen, I. Z. L. I., & Nazmi, I. Z. L. I. (2018). Convective drying kinetics and quality parameters of european cranberrybush. *Journal of Agricultural Sciences, 24*(3), 349-358.

Wang, J. H., & Duh, J. G. (1995). Colour tone and chromaticity in a coloured film on stainless steel by alternating current electrolysis method. *Surface and Coatings Technology, 73*(1-2), 46-51.

Author Information

Berkent Parim
Haier Europe
75. OSB ESKISEHIR 8. Str. No:1
Turkey

Mehmet Kara
Haier Europe
75. OSB ESKISEHIR 8. Str. No:1
Turkey

Ayberk Salim Mayil
Haier Europe
75. OSB ESKISEHIR 8. Str. No:1,
Turkey
Contact e-mail: *amayil@hoover.com.tr*

To cite this article:

Parim, B. , Kara, M., & Mayil, A. S., (2022). Experimental study of yellowing index comparison between 430 stainless steel and 441 stainless steel burner plates on domestic gas hobs. *The Eurasia Proceedings of Science, Technology, Engineering & Mathematics (EPSTEM), 21*, 64-69.

The Eurasia Proceedings of Science, Technology, Engineering & Mathematics (EPSTEM)
ISSN: 2602-3199

The Eurasia Proceedings of Science, Technology, Engineering & Mathematics (EPSTEM), 2022

Volume 21, Pages 70-78

IConTES 2022: International Conference on Technology, Engineering and Science

The Prospective of Particle Image Velocimetry (PIV) Measurement Velocity Profile in Thermoacoustic System

Siti Norsyahira MOHD ZAHARI
Universiti Malaysia Pahang

Nor Atiqah ZOLPAKAR
Universiti Malaysia Pahang

Mimi Muzlina MUKRI
Universiti Malaysia Pahang

Abstract: Precise measurement of fluid velocities is essential in several applications, including thermoacoustic refrigeration systems. A thermoacoustic refrigeration system uses a high-amplitude acoustic standing wave to generate a cooling effect. Understanding the fluid flow characteristic between the refrigerant and a stack is important to improve the heat transfer process and minimise thermal and viscous losses. This paper reviews the various methods employed by previous researchers in analysing the velocity profiles in the thermoacoustic refrigeration system and the prospective implementation of Particle Image Velocimetry (PIV). PIV is a non-invasive technique that estimates velocity at several points of the measuring region. This review looked at the method employed to analyse the velocity profile, error analysis, and the effectiveness of another measurement method compared to the PIV measurement. The discussions include related parameters that past researchers have considered.

Keywords: Thermoacoustic, Velocity profile, Particle image velocimetry

Introduction

The development of thermoacoustic technology is motivated by the prospect that this technology can replace and reduce reliance on the current vapour compression technology. One of the significant contributions to the current environmental and energy crisis the world faces is cooling technology. Cooling technology generates hazardous gases that are released into our environment at a high energy cost. Thermoacoustic technology is an emerging technology that aims to convert low and medium temperature waste or solar heat into cooling or electricity, domestically and in the industrial. The thermoacoustic refrigerator is an innovative alternative for clean cooling. To summarise, the benefits of the thermoacoustic system include environmental friendliness, potentially high reliability due to the simple structure and the minimum number of moving parts, and reasonable efficiency(Nazmi et al., 2021).

Efficiency is always the primary concern related to the thermoacoustic system (Zolpakar et al., 2016). Under the same design and operating conditions, the thermoacoustic refrigerator's efficiency is only half of the conventional vapour-compression refrigerator (Tartibu, 2016). The efficiency of the thermoacoustic refrigerator is affected due to the acoustic and streaming losses in the thermoacoustic mechanism. It is identified that thermal and viscous losses are considered significant losses contributing to the thermoacoustic refrigerator's reduction in performance.

Thermoacoustic refrigerators work based on a thermal interaction between an oscillatory compressible flow and the solid structures, which are the stack and heat exchanger. The function of the stack is to produce a refrigeration effect by inducing acoustic excitation. These heat transfer processes are based on the 'thermoacoustic effect' whereby appropriately phased pressure, and velocity oscillations enable the compressible fluid to undergo a thermodynamic cycle in the vicinity of the stack. Figure 1 shows the heat flux streams between the device and the surroundings and the internal heat transfer streams on the interfaces between the stack and heat exchangers. One of the main obstacles in designing a thermoacoustic system is the lack of reliable heat transfer correlations for the oscillatory flow conditions (Shi et al., 2010b). Most of the time, it is assumed that the length of the heat exchangers should simply be equal to the displacement amplitude of the fluid particle, while the heat transfer rates are predicted using correlation for steady flow conditions. This shows the need for experimental investigations on heat transfer rates in the oscillatory flows to developing relevant heat transfer correlations for the thermoacoustic device environment.

As discussed in the above paragraph, a thermoacoustic system's heat transfer depends on the resonator tube's velocity and pressure profile. Therefore, this review is driven by the need for a better understanding of the methods employed by previous researchers in determining heat transfer rates, precisely the method of velocity measurement for the thermoacoustic system. This is crucial because the characteristics of the velocity of oscillatory flow are one of the determinants of achieving higher thermodynamic efficiencies and improving the performance of the overall thermoacoustic system.

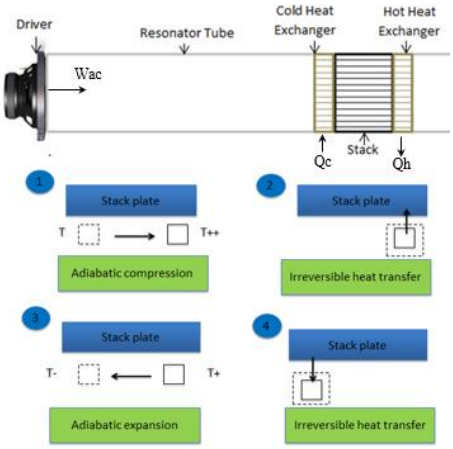

Figure 1. General schematic of the overall heat fluxes in a standing wave thermoacoustic refrigeration

General Review on Velocity Profile Measurement

There are several possible ways of obtaining reliable heat transfer information (velocity profile, temperature distribution, and pressure) to perform detailed quantitative measurements for a thermoacoustic system. This brief review paper divides the methods for measuring velocity profiles into two categories: simulation-based and experimental-based. The simulation-based methods involve Computational Fluid Dynamic (CFD) and Design Environment for Low Amplitude Thermoacoustic Energy Conversion (DeltaEC) ways to determine the velocity profiles. Meanwhile, for experimental-based, three methods were applied by the previous researchers, which are Hot-Wire Anemometry (HWA), Laser Doppler Anemometry (LDA), and Particle Image Velocimetry (PIV). Based on the limited number of past research works done in investigating the velocity profile of thermoacoustic systems, 65% of the researchers prefer to conduct research using simulation-based methods, especially the CFD method, compared to experiment-based, which only encompass 35%. This may be due to the high cost of setting up the experiment rig that involves specific components, especially for PIV and LDA setup. The details for every measurement are discussed in the following section.

Simulation Work in Measuring Velocity Profile

In the thermoacoustic system, DeltaEC (Design Environment for Low Amplitude Thermoacoustic Energy Conversion) is the only software built specifically for the use of the system and was developed by Ward et al. (Ward et al., 2017). DeltaEC has been extensively used either in the preliminary design of a thermoacoustic system or as data validation. Zoontjens et al. (Zoontjens et al., 2006) used DeltaEC as an initial design process

in designing their thermoacoustic refrigerator. This study also applied Ansys, a CFD software used to compare results from DeltaEC, experimental work was performed for verification. Based on the experiment results, even though DeltaEC is a one-dimensional analysis, the software provided adequate accuracy to enable the design of devices. Other researchers, like Tijani et al. (Tijani et al., 2002), Tasnim et al. (Tasnim et al., 2012), and Hariharan et al. (Hariharan et al., 2012), used DeltaEC as a tool to validate their experiment results. Even though DeltaEC shows excellent benefits in terms of high speed of calculation and good agreement with experimental work, it also suffers from significant drawbacks, such as the need for relatively good estimation for DeltaEC to converge. In addition, this software can only solve 1D problems with minimum ability to detect nonlinear flows, such as turbulence and streaming effects (Tomas & Tomas, 2018). Thus, for researchers who want to investigate the effect of oscillatory flow on the thermoacoustic system, it is better to consider other software, such as CFD and OpenFOAM.

The most widely used method in measuring velocity profiles for thermoacoustic systems is the Computational Fluid Dynamic (CFD) method. Most researchers prefer the CFD method due to the ability of the software to examine the physical properties of fluid flow, such as velocity, pressure, temperature, density, and viscosity. The pioneer researcher that applied CFD in the whole thermoacoustic system is Zoontjens (Zoontjens et al., 2008), who also investigated fluid behaviour during the thermoacoustic cycle with a single plate stack. Other researchers who used CFD in their works are listed in Table 1.

Table 1. List of studies using CFD

No	Author, Year	Methodology	Part of simulation	Parameter measured
1.	Zink et al., (Zink et al., 2010)	CFD	TAR/TAE	Velocity, temperature, and heat flux
2.	Zoontjens et al. (Zoontjens et al., 2008)	CFD	Resonator with single plate stack	Fluid behaviour in thermoacoustic cycle
3.	Hanschk et al. (Hantschk, C.C Vortmeyer, 1999)	CFD	Rijke tube	Pressure and velocity amplitude
4.	Entezam et al. (Entezam & Moorhem, 1997)	CFD	Rijke tube	Relationship of velocity and pressure to the heat transfer process
5.	Rahpeina & Ebrahimi (Rahpeima & Ebrahimi, 2019)	2D COSMOL	TAR	Cooling temperature, COP
6.	Mohd Saat et al.(Mohd Saat et al., 2019)	2D CFD	TAR	Velocity distribution
7.	Allafi et al.(Almukhtar Allafi et al., 2021)	ANSYS FLUENT CFD	TAR	Velocity profile
8.	Allafi and Mohd Saat, (Almukhtar et al., 2020)	ANSYS FLUENT CFD	TAR	Velocity profile in entrance and exit at the stack plate
9.	Skaria et al. (Skaria et al., 2015)	CFD and DeltaEC	SWTAPM, TWTAPM, SWTAR	Pressure, temperature, and contour,
10.	Xiao et al. (Xiao et al., 2020)	CFD	Thermoacoustic Heat Dissipation System	Temperature gradient, fluid oscillating amplitude
11.	Namdar et al. (Namdar et al., 2015)	OpenFOAM CFD	Single plate stack, heat exchanger, resonator	Temperature gradient
12.	Kuzuu & Hasegawa (Kuzuu & Hasegawa, 2017)	CFD	Thermoacoustic engine	Temperature gradient
13.	Tisovsky and Vit, (Tomas & Tomas, 2018)	OpenFOAM	TAR/TAE	Acoustic pressure and velocity
14.	Narasimmanaidu et al. (Narasimmanaidu et al., 2021)	CFD	Porous Structure of Stack	Flow behavior

A study conducted by Mohd Saat et al. (Mohd Saat et al., 2019) found that the velocity prediction starts to deviate from the linear theory with a drive ratio of 1% when using the CFD method. In this paper, the researchers also observed that the length of the plate greatly influences the velocity change within the channel even though the porosity of the structure and the flow condition are the same. This finding opposes the theoretical equation whereby it is stated that the length of the stack does not affect the velocity calculation. Hence, this study suggested that the length of the stack influencing the velocity profile within the channel should be considered in the theoretical equation. The researchers also observed the formation of a vortex-shedding phenomenon at the end of the stack plate. As the drive ratio increases, the returning vortex on the velocity within the channel becomes more significant; thus, the turbulent effect must be seriously considered in the thermoacoustic analysis. This result is supported by Allafi et al. (Almukhtar Allafi et al., 2021) which

formed two vortex layers near the surface of the solid structure as a result of the CFD method, as shown in Figure 2. The layers are named the main and the secondary vortex layers, and they move with the cyclic flow and affect the shape of the velocity profile within the channel. The latest finding follows this by Allafi et al. (Almukhtar et al., 2020), which presents the entrance and exit effects of oscillatory flow within a parallel-plate structure inside the resonator. Allafi and his team concluded that oscillatory flow across a parallel-plate structure is commonly found in the thermoacoustic system, and the effect of developing flow to the thermoacoustic performance should be seriously considered in the design.

The prior study by Kuzuu and Hasegawa (Kuzuu & Hasegawa, 2017) investigated the acoustic characteristics and temperature field of the oscillatory flow around the thermoacoustic device using the CFD method. The study found that the vortex generation near the driver causes high energy dissipation, but it is still acceptable according to the linear theory. Meanwhile, the asymmetrical temperature oscillation was measured within the heat exchangers for the temperature distribution. The authors argued that this behaviour could not be predicted using the linear theory because the non-uniform temperature gradient in the engine unit is transferred stream-wise by convection. Meanwhile, Namdar et al. (Namdar et al., 2015) studied the effect of the pressure nodes on the temperature of the heat exchanger in the thermoacoustic system using CFD software. The optimum location of the heat exchanger was determined by plotting a pressure and velocity distribution in the resonator. This result shows the importance of simulation work and how it helps in visualising the thermoacoustic effect and understanding the parameters that need to be investigated to improve the performance of the thermoacoustic system.

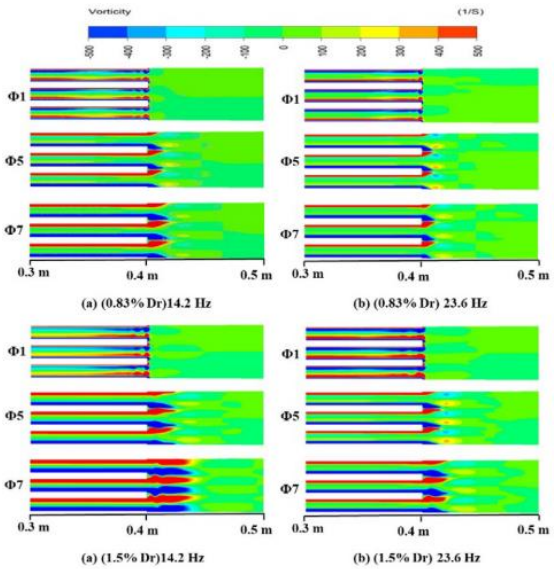

Figure 2. Vortex structure within and at the end of the plate for three different drive ratio

General Review on Velocity Profile Measurement

Acoustic velocity in a thermoacoustic system can also be measured experimentally using several methods. The experiment methods that will be discussed in this paper are Hot-Wire Anemometry (HWA), Laser Doppler Anemometry (LDA), and Particle Image Velocimetry (PIV). Prior researchers commonly used these three methods in experimentally measuring acoustic velocity in thermoacoustic systems.

The mechanism of HWA starts when an electrically heated wire is placed in a flowing gas stream, where heat is transferred from the wire to the gas, causing the wire's temperature to reduce and, due to this, the resistance of the wire also changes. The change in the resistance of the wire is used to measure the flow rate or velocity. HWA is widely used for measuring flow velocity and turbulence since it provides an accurate and compact anemometer for low velocity continuous flows, and it is also easy to install and cost-effective compared to LDA and PIV. Jerbi et al. (Jerbi et al., 2013) adopted the HWA method in measuring acoustic velocity based on acoustic pressure measurement via their relationship using a linear acoustic model. The result in this paper stated that due to the difference in the heat transfer between the oscillating fluid and the hot-wire, the velocity either increases towards the resonance or decreases beyond it. This follows the law of the acoustic velocity amplitude whereby it is not continuous when the resonance frequency is crossed. This result was supported by

Elger and Adam (Elger & Adam, 1989), who affirmed that HWA in the oscillating flows requires dynamic calibration because dynamic heat transfer differs from steady-flow heat transfer.

LDA is a measurement system consisting of two coherent laser beams that intersect to form a series of interference fringes where fluid velocity is to be measured (Yaacob & Velte, 2021). A tracer particle suspended in the fluid passes through these fringes. The intensity of the light scattered from the particle is modulated at a frequency proportional to the spatial component of particle velocity that is normal to the fringes. The movement of the tracer particle is assumed to follow the motion of the fluid. The scattered light is collected by a receiver lens and focused on a photodetector. The scattered light contains a Doppler shift, known as the Doppler frequency (fD), which is proportional to the velocity component and perpendicular to the bisector of the two laser beams. The photodetector converts the fluctuating light intensity into electrical signals, and through several processors, the velocity of the flow is provided.

Bailliet et al. (Bailliet et al., 2000) examined the acoustic power flow in the resonator tube using LDA and microphonic measurement. This measurement setup enables the plotting of the velocity profile and pressure measurement inside the resonator tube. The outcome of this setup aligns with the analytical results. In this work, the size is taken at 4 cm from the loudspeaker, the total length of the resonator is 49.7 cm, and the stack center position is located 14 cm from the loudspeaker. Thus, the results did not represent the stack component's velocity and pressure profiles at entry, inside, and exit. Meanwhile, Thompson and Atchley (Thompson et al., 2005) adapted LDA and burst spectrum analysis (BSA) to investigate the acoustic streaming generated in a cylindrical standing wave resonator filled with air. It is observed that LDA/BSA generated a significant error in the time-averaged velocity-signal component. Due to the error, Lagrangian streaming velocities are determined using the time-harmonic signal components and the arrival time of the velocity component, and the results align with Rott's theory. Again, in this study, the stack component is not considered in the experiment setup; thus, the results are only valid when using an empty resonator tube.

Particle Image Velocimetry (PIV) is an optical measurement technique whereby the velocity field of an entire region within the flow is measured simultaneously. PIV uses the displacement of the particle image in the plane as the measurement principle to determine the displacement of the particle in the flow. The most common way for measuring displacement is by dividing the image from the two-time exposures. A typical PIV setup includes a high-speed camera, a high-power multi-pulse laser, an optical arrangement to convert laser output light sheet, and a synchroniser that controls the synchronisation between the laser and the camera. Figure 3 shows the common setup of a PIV measurement.

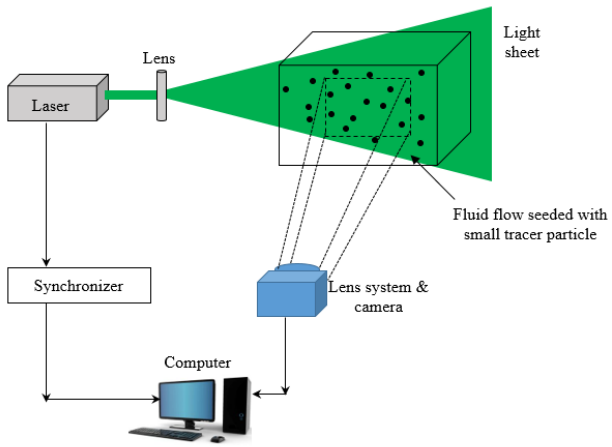

Figure 3. Schematic diagram of a PIV setup

The lack of heat transfer correlations for oscillatory flow led Shi et al. (Shi et al., 2010b) to use PIV and Planar Laser-Induced Fluorescence (PLIF) to measure time-resolved temperature and velocity fields in the thermoacoustic system. PIV alone can only measure velocity, but with the addition of PLIF, it can measure the temperature in the region. Since the test rig includes a microphone, the pressure data was recorded during the experiment. The results show that there is an overshoot in velocity and temperature distribution. The velocity overshoot is due to the viscous and inertial effect in the gas, while the overshoot of temperature is caused by the velocity overshoot and the combined effect of the viscous and thermal boundary layers. This result highlights the strong relationship between velocity and temperature fields in the thermoacoustic system, as shown in

Figure 4. In other works done by Shi et al. (Shi et al., 2010a), PIV was used to identify a range of vortex shedding flow patterns at the end of parallel-plate thermoacoustic stacks based on the effect of Reynolds number (Re), Keulegan-Carpenter number (KC), and Womersley number (Wo). It is found that Wo plays an essential role in determining the detailed classification of such transitions within each flow pattern region. Another work done by Shi and his team on oscillatory flow patterns can be found in (Shi et al., 2011).

Zhang et al. (Zhang et al., 2019) applied PIV in measuring the oscillatory flow at the end of the thermoacoustic parallel plate. In this study, Zhang and his team experimented with and without the stack using two different resonator lengths to indicate different fundamental frequencies. The results show that heat transfer enhancement is due to increased resonator length. Therefore, decreasing the fundamental frequency and increasing the velocity amplitude enlarges the ejection vortices.

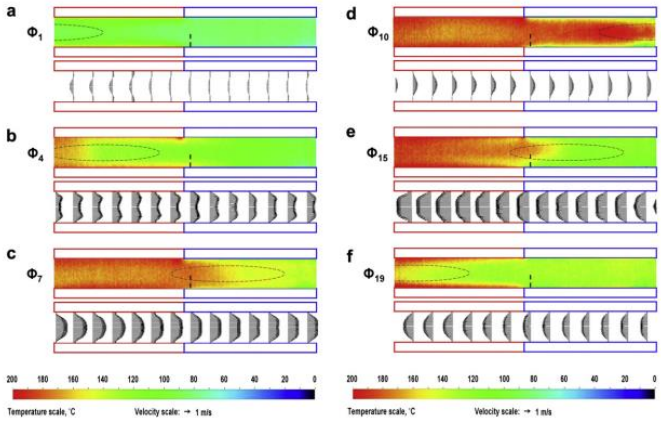

Figure 4. Temperature and velocity distributions for six selected phases in an acoustic cycle (Shi et al., 2010b)

Discussion on Velocity Measurement Methods

Since velocity and pressure distribution determine the heat transfer rate in the thermoacoustic system, researchers must investigate the characteristics of the velocity profile inside the resonator tube with the existence of the stack component. The lack of correlation that represents the oscillatory flow for thermoacoustic systems, as stated by Shi et al. (Shi et al., 2010a)' is the main issue that requires solving. For simulation-based methods, when comparing CFD and DeltaEC, DeltaEC has the advantage of solving the problem in a short time and still gives reliable results since it is consistent throughout the experiment. However, the main drawback is that the software has a minimal ability to detect turbulence and streaming flow, which is crucial in investigating oscillatory flow. Meanwhile, CFD showed its ability to illustrate the streaming effect, as reported by Mohd Saat et al. (Mohd Saat et al., 2019) and Allafi et al. (Almukhtar Allafi et al., 2021), (Almukhtar et al., 2020).

To confirm the outcome of the simulation works, an experiment must be done to evaluate the result to the real application system. HWA has the simplest setup compared to LDA and PIV. It has advantages in terms of no seeding required in the flow and provides a relatively high temporal resolution of the acquired signal. HWA can also identify velocity fluctuations related to vortex shedding at the stack's entrance and exit, as Mao et al. reported (Mao et al., 2008). However, to cover the flow region, the probe must be relocated a thousand times to collect the data for the whole system, which is troublesome considering the tight space at the stack and heat exchanger. In addition, HWA is the only invasive method, as the probe needs to be inserted into the resonator. Even though it is stated that the probe will have the minimum effect on the flow, it will also introduce another error that adds leakage while running the experiment.

Meanwhile, the LDA method can measure acoustic velocity and acoustic power flow with a good spatial resolution (Bailliet et al., 2000), but evidently, the LDA method is not suitable to be applied in the thermoacoustic system due to the difficulties of introducing a convergent laser beam in the tight space. For PIV measurement, this method enables the visualisation of the velocity distribution inside the resonator tube and can detect the streaming effect at the entrance and exit of the stack, as reported by Shi et al. (Shi et al., 2010a). The PIV method can also record temperature parameters if the PIV system adds on the PLIF component. These benefits make it the preferred experimental method compared to LDA and HWA. However, PIV requires several components in the setup; hence, this method can be costly.

Conclusion

In conclusion, every measurement method has its advantages and drawbacks. For velocity measurement for oscillatory flow in thermoacoustic systems, CFD is the preferred simulation-based method compared to DeltaEC because of its ability to detect turbulence and streaming in the flow. Thus, the reason why the majority of the researchers conducted their research using the CFD method. Meanwhile, for experimental-based methods, PIV showed significant advances compared to HWA and LDA in terms of its ability to visualise the oscillatory flow with the streaming effect in the thermoacoustic system. Even so, there are minimal studies that were conducted using this particular method. This shows the vast opportunities for researchers to investigate further the characteristics of the velocity profile in the oscillatory flow for thermoacoustic devices.

Scientific Ethics Declaration

The authors declare that the scientific ethical and legal responsibility of this article published in EPSTEM journal belongs to authors.

Acknowledgements

* This article was presented as an oral presentation at the International Conference on Technology, Engineering and Science (www.icontes.net) held in Antalya/Turkey on November 16-19, 2022.

*The authors acknowledge the Fundamental Research Grant Scheme (FRGS/1/2019/TK10/UMP/03/2) from the Ministry of Higher Education and grant RDU1803144 from Universiti Malaysia Pahang for providing financial support, and also for the use of the research facilities through the course of this research.

References

Almukhtar Allafi, W., Mohd Saat, F. A. Z., & Mao, X. (2021). Fluid dynamics of oscillatory flow across parallel-plates in standing-wave thermoacoustic system with two different operation frequencies. *Engineering Science and Technology, an International Journal*, *24*(1), 41–49. https://doi.org/10.1016/J.JESTCH.2020.12.008

Almukhtar, W., Al, F., & Mohd, Z. (2020). Entrance and exit effects on oscillatory flow within parallel-plates in standing-wave thermoacoustic system with two different operating frequencies. *Journal of King Saud University - Engineering Sciences*, *34*(5), 350-360. https://doi.org/10.1016/j.jksues.2020.12.008

Bailliet, H., Lotton, P., Bruneau, M., Gusev, V., Valière, J. C., & Gazengel, B. (2000). Acoustic power flow measurement in a thermoacoustic resonator by means of laser Doppler anemometry (L.D.A.) and microphonic measurement. *Applied Acoustics*, *60*(1), 1–11. https://doi.org/10.1016/S0003-682X(99)00046-8

Elger, D. F., & Adam, R. L. (1989). Dynamic hot-wire anemometer calibration using an oscillating flow. *J. Phys. E: Sci. Instrum*, *166*(22), 166–172.

Entezam, B., Van Moorhem, W., Majdalani, J., Entezam, B., Van Moorhem, W., & Majdalani, J. (1997). Modeling of a Rijke-tube pulse combustor using computational fluid dynamics. In *33rd Joint Propulsion Conference and Exhibi*t (p. 2718).

Hantschk, C.C., & Vortmeyer, D. (1999). Numerıcal sımulatıon of self-excıted thermoacoustıc ınstabılıtıes In A Rıjke Tube. *Journal of Sound and Vibration*, *277*, 511–522.

Hariharan, N. M., Sivashanmugam, P., & Kasthurirengan, S. (2012). Influence of stack geometry and resonator length on the performance of thermoacoustic engine. *Applied Acoustics*, *73*(10), 1052–1058. https://doi.org/10.1016/j.apacoust.2012.05.003

Jerbi, F. J., Huelsz, G., & Kouidri, S. (2013). Acoustic velocity measurements in resonators of thermoacoustic systems using hot-wire anemometry. *Flow Measurement and Instrumentation*, *32*, 41–50. https://doi.org/10.1016/j.flowmeasinst.2013.03.005

Kuzuu, K., & Hasegawa, S. (2017). Numerical investigation of heated gas flow in a thermoacoustic device. *Applied Thermal Engineering*, *110*, 1283–1293. https://doi.org/10.1016/j.applthermaleng.2016.08.093

Mao, X., Yu, Z., Jaworski, A. J., & Marx, D. (2008). PIV studies of coherent structures generated at the end of a stack of parallel plates in a standing wave acoustic field. *Experiments in Fluids*, *45*(5), 833–846. https://doi.org/10.1007/S00348-008-0503-7/FIGURES/10

Namdar, A., Kianifar, A., & Roohi, E. (2015). Numerical investigation of thermoacoustic refrigerator at weak and large amplitudes considering cooling effect. *Cryogenıcs*, *67*, 36–44. https://doi.org/10.1016/j.cryogenics.2015.01.005

Narasimmanaidu, S. R., Narasimmanaidu, S. R., Anuar, F. S., Al-zahrah, F., Sa, M., & Tokit, E. M. (2021). Numerical and experimental study of flow behaviours in porous structure of aluminium metal foam. *Evergreen Joint Journal of Novel Carbon Resource Sciences & Green Asia Strategy*, *8*(3), 658–666.

Nazmi, M., Roslan, H., Nazmi, M., Roslan, H., Zolpakar, N. A., & Mohd-ghazali, N. (2021). Analysis of 3D printed stack in thermoacoustic cooling analysis of 3D printed stack in thermoacoustic cooling. *Evergreen Joint Journal of Novel Carbon Resource Sciences & Green Asia Strategy*, *8*(1), 131–137.

Rahpeima, R., & Ebrahimi, R. (2019). Numerical investigation of the effect of stack geometrical parameters and thermo-physical properties on performance of a standing wave thermoacoustic refrigerator. *Applied Thermal Engineering*, *149*(May 2018), 1203–1214. https://doi.org/10.1016/j.applthermaleng.2018.12.093

Saat, F. A. M., Mattokit, E., Mustaffa, S. H., & Ghazali, N. M. (2019). Numerical study of turbulence related to vortex shedding structures of an oscillatory flow in thermoacoustic energy system. *Energy Procedia*, *156*, 239-243.

Shi, L., Yu, Z., & Jaworski, A. J. (2010a). Vortex shedding flow patterns and their transitions in oscillatory flows past parallel-plate thermoacoustic stacks. *Experimental Thermal and Fluid Science*, *34*(7), 954–965. https://doi.org/10.1016/j.expthermfluscı.2010.02.012

Shi, L., Yu, Z., & Jaworski, A. J. (2010b). Application of laser-based instrumentation for measurement of time-resolved temperature and velocity fields in the thermoacoustic system. *International Journal of Thermal Sciences*, *49*(9), 1688–1701. https://doi.org/10.1016/j.ıjthermalscı.2010.03.015

Shi, L., Yu, Z., & Jaworski, A. J. (2011). Investigation into the Strouhal numbers associated with vortex shedding from parallel-plate thermoacoustic stacks in oscillatory flow conditions. *European Journal of Mechanics - B/Fluids*, *30*(2), 206–217. https://doi.org/10.1016/j.euromechflu.2010.10.005

Skaria, M., Rasheed, K. K. A., Shafi, K. A., Kasthurirengan, S., & Behera, U. (2015). Simulation studies on the performance of thermoacoustic prime movers and refrigerator. *Computers and Fluıds*, *111*, 127–136. https://doi.org/10.1016/j.compfluid.2015.01.011

Tartibu, L. K. (2016). Maximum cooling and maximum efficiency of thermoacoustic refrigerators. *Heat and Mass Transfer*, *52*(1), 95–102. https://doi.org/10.1007/s00231-015-1599-y

Tasnim, S. H., Mahmud, S., & Fraser, R. A. (2012). Effects of variation in working fluids and operating conditions on the performance of a thermoacoustic refrigerator . *International Communications in Heat and Mass Transfer*, *39*(6), 762–768. https://doi.org/10.1016/j.icheatmasstransfer.2012.04.013

Thompson, M. W., Atchley, A. A., & Introduction, I. (2005). *Simultaneous measurement of acoustic and streaming velocities in a standing wave using laser Doppler Anemometry*. *117*(August 2004). https://doi.org/10.1121/1.1861233

Tijani, M. E. H., Zeegers, J. C. H., & De Waele, A. T. A. M. (2002). Design of thermoacoustic refrigerators. *Cryogenics*, *42*(1), 49–57. https://doi.org/10.1016/S0011-2275(01)00179-5

Tomas, T., & Tomas, V. (2018). Design of numerical model for thermoacoustic devices using OpenFOAM. *36th Meeting of Department of Fluid Mechanics and Thermodynamics*, *020043*(September 2017).

Ward, B., Clark, J., & Swift, G. (2017). *Design environment for low-amplitude thermoacoustic energy conversion DeltaEC version 6.4b2.7 users guide*. www.lanl.gov/thermoacoustics

Xiao, X., Gu, X., & Zhang, X. (2020). Combination of thermoacoustic heat dissipation with oscillating convection: A novel cooling method. *International Journal of Heat and Mass Transfer*, *160*, 120177. https://doi.org/10.1016/J.ijheatmasstransfer.2020.120177

Yaacob, M. R., & Velte, C. M. (2021). Mapping of energy cascade in the developing region of a turbulent round jet turbulent round jet. *Evergreen Joint Journal of Novel Carbon Resource Sciences & Green Asia Strategy*, *8*(2), 379–396.

Zhang, W., Zhang, L., Wang, S., Ren, B., & Meng, S. (2019). Optimization of machining parameters of 2.25Cr1Mo0.25V steel based on response surface method and genetic algorithm. *International Journal on Interactive Design and Manufacturing*, *13*(2), 809–819. https://doi.org/10.1007/s12008-018-00525-8

Zink, F., Vipperman, J., & Schaefer, L. (2010). CFD simulation of thermoacoustic cooling. *International Journal of Heat and Mass Transfer*, *53*(19–20), 3940–3946. https://doi.org/10.1016/j.ijheatmasstransfer.2010.05.012

Zolpakar, N. A., Mohd-Ghazali, N., & Hassan El-Fawal, M. (2016). Performance analysis of the standing wave thermoacoustic refrigerator: A review. *Renewable and Sustainable Energy Reviews*, *54*, 626–634. https://doi.org/10.1016/j.rser.2015.10.018

Zoontjens, L., Howard, C. Q., Zander, A. C., & Cazzolato, B. S. (2008). Numerical comparison of

thermoacoustic couples with modified stack plate edges. *International Journal of Heat and Mass Transfer, 51*(19-20), 4829-4840..

Zoontjens, L., Howard, C. Q., Zander, A. C., & Cazzolato, B. S. (2006). Modelling and optimisation of acoustic inertance segments for thermoacoustic devices. In *Proceedings of ACOUSTICS (*Vol. 2006).

Author Information

Siti Norsyahira Mohd Zahari
Universiti Malaysia Pahang
26600 Pekan, Pahang
Malaysia

Nor Atiqah Zolpakar
Universiti Malaysia Pahang
26600 Pekan, Pahang
Malaysia
Contact e-mail: *noratiqahz@ump.edu.my*

Mimi Muzlina Mukri
Universiti Malaysia Pahang
26600 Pekan, Pahang
Malaysia

To cite this article:

Mohd Zahari, S.N., Zolpakar, N.A., & Mukri, M.M. (2022). The prospective of particle image velocimetry (PIV) measurement velocity profile in thermoacoustic system. *The Eurasia Proceedings of Science, Technology, Engineering & Mathematics (EPSTEM), 21*, 70-78.

The Eurasia Proceedings of Science, Technology, Engineering & Mathematics (EPSTEM)
ISSN: 2602-3199

The Eurasia Proceedings of Science, Technology, Engineering & Mathematics (EPSTEM), 2022

Volume 21, Pages 79-87

IConTES 2022: International Conference on Technology, Engineering and Science

New Trends in Aluminum Die Casting Alloys for Automotive Applications

Tanya A. BASER
Coskunoz CKM R&D Center

Elif UMAY
Coskunoz CKM R&D Center

Volkan AKINCI
Coskunoz CKM R&D Center

Abstract: In order to provide ecological balance, new technologies are being developed to reduce fuel consumption. Within these new technologies, usage of light alloys such as aluminum and magnesium has gained great importance in the automotive applications. The advantages of aluminum alloys in terms of light weight, recycling, machinability and corrosion resistance led to increase application area of these alloys. Due to these characteristics of aluminum alloys, fuel-saving light-weight material selection plays an important role for automotive parts. Aluminum applications increase not only in automotive, but also in aerospace, space shuttle, marine, and defense applications. According to the production methods, aluminum alloys are generally classified as casting, sheet, forging and extrusion. Aluminum die casting alloys are generally used the production of suspension systems, engines and gears parts. However, with the developing aluminum casting technologies, the aluminum die casting method makes it possible to manufacture multiple body parts in one piece. It is predicted that number of aluminum die casting parts will increase, especially in electric vehicles. In this study, the importance of the use of aluminum die casting alloys in the automotive industry is emphasized. Research and trends so far of the development of aluminum die casting alloys are also summarized.

Keywords: Light weighting, Aluminum casting alloys, Fuel consumption.

Introduction

Recently, weight reduction through the use of light-weight materials plays an important role in improving fuel economy and reducing harmful emissions. The importance for reducing CO_2 emissions by lightweight structure design for automotive applications, lead to increase the usage of medium strength aluminum alloys (Taub et al, 2007). Replacing steel components with high strength aluminum alloys became a spot light in automotive industry for light-weighting (Baser, 2012). Aluminum can be assumed that the 2nd metal element which can be provided on earth. It is the most used material in today's industry after steel. Aluminum alloys are widely preferred due to their light-weight, low density, good formability and high corrosion resistance characteristics (Cuniberti et al, 2010).

In last decade studies on energy saving reveals that production of light and economical vehicles plays an important role for less fuel consumption. Aluminum alloys are widely preferred in passenger cars, buses, primarily in trains as well as the construction of marine applications (Zeytin, 2000). In fact, aluminum alloys have been used in the aviation and defense industry for a long time. The adaptation of aluminum to the automotive industry has started due to the advantages seen in aviation and defense applications.

Casting aluminum alloys are widely used in automotive industry (Baser et al, 2013). Aluminum casting is a variation of this that uses only aluminum and aluminum alloys as the liquid metal that is poured into the mold. Aluminum castings are used to make complex and detailed parts very efficiently (Engler et al, 2010). Casting aluminum alloys are quite widespread and find more and more applications in modern industry. According to different estimates, up to 20–30% of all aluminum products manufactured worldwide are used for aluminum die castings (Criqui et al, 2009).

Due to considerable improvements in casting technologies, now it is possible to produce high-quality aluminum die casting components with properties that are comparable to those of similar wrought products (sheet and extrusion). Moreover, this can be done not only for high-quality alloys, but also for those manufactured with substantial amounts of aluminum scrap (Brinkman et al, 2010). In the latter case the advantage, of course, is in lower production costs.

Significant improvements in the quality of aluminum die were achieved due to improved production processes. Today it is possible to employ advanced methods of molten metal handling, which result in dramatic reduction of harmful nonmetallic impurities. For instance, hot isostatic pressing is used to reduce shrinkage porosity. All these and many other innovations result in significant improvement of aluminum die casting quality as well as mechanical properties (Zolotorevsky et al, 2007). This study focuses on the importance of the use of aluminum die casting in the automotive industry. Research so far of the developments and global trends of aluminum die casting were also summarized.

Aluminum Die Casting

Aluminum Die Casting Alloys

In recent years, aluminum die casting alloys have become one of the crucial alloy groups in many industrial applications. Features of aluminum alloys such as energy and fuel saving and light weight properties were underlined since CO_2 in the automotive has become an important issue to achieve. Aluminum die casting alloys have a classification system consisting of 3 digits and decimal places (Tanwir et al, 2017). Heat treatment can be also applied to aluminum casting alloys (Kaufman et al, 2004). Master alloy additions can be made to improve the properties of aluminum casting alloys according to customer needs. Grain refinement is one of the most common process in order to obtain fine micro structure in cast aluminum alloys. Within the grain refinement process, the grain morphology of coarse grained Al-Si alloys is refined and the mechanical properties are increased (Kaufman et al, 2004). Titanium-boron, titanium and boron alloys such as $AlTi_5B_1$, Al_3B, $TiAl_3$, and AlB2 are widely used as grain refiners (Spittle et al, 2006). Among the aluminum casting alloys, 300 series is mostly preferred especially in parts such as housing and bracket in the automotive applications. 300 aluminum casting alloys especially aluminum-silicon based with an additional copper or magnesium elemental percentage (Kaufman et al, 2004).

The highest volume of aluminum components in vehicles are aluminum castings, such as engine blocks, cylinder heads and chassis parts (Graf, 2021). New aluminum die casting techniques came up with improved material properties and functional integration that enables aluminum to meet the desired requirements. This trend is driven by the needs of the automotive manufacturers to substantially reduce weight of the power train and chassis components. Additional features for achieving a better vehicle performance gain an unacceptable increase in vehicle weight (Baser, 2012). Already well-established in high class automobile engines, a significant weight reduction can be obtained by aluminum die casting usage-smaller but high volume compact-size vehicles (Kaufman et al, 2004).

Aluminum Casting Methods

Among aluminum casting methods sand mold casting, precision casting and high pressure die casting methods are most common used aluminum casting methods in the literature (Kaufman et al, 2004). However, in recent years, when the geometric difficulties in the parts, the porosity in their internal structures and the expectations in the casting cavities are revealed, it is noticed that the demands for the high pressure casting method have increased. In the automotive industry, aluminum alloys are classified according to their production methods as in Figure 1.

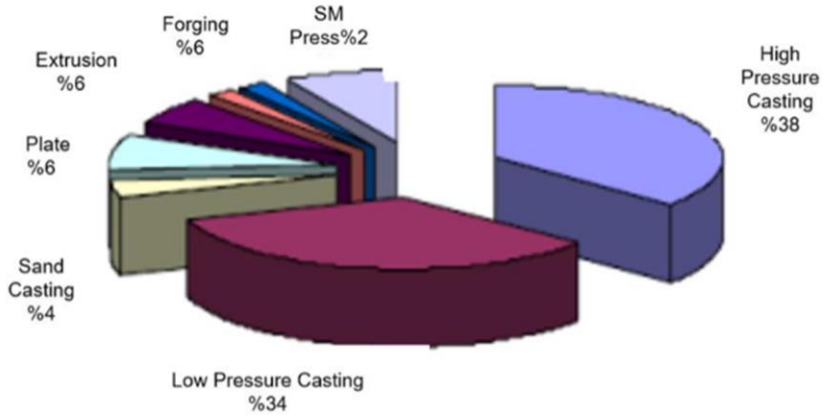

Figure 1. Classification of aluminum alloys in automotive by production method (Ozcomert, 2006).

Sand casting method is one of the most preferred production methods when not only the automotive sector is considered. (Dalquist et al, 2004). Sand mold castings are handled in two ways. It is classified as removable and perishable. While the perishable model is not very common, the removable model is widely used. There are many parameters that are important in the sand mold casting method. These can be listed as follows; molding process, pattern, sand quality, cores. The molding process is a very important parameter in the sand mold casting method. The process using molding sand creates the compacted sand model cavity. Thanks to the runner system, it is aimed to give the desired geometry by pouring the melted metal alloy into the mold cavity. After the hardened parka is removed from the mold, the final piece is obtained after the excess parts such as burrs, runners and feeders are cleaned. (Wang et al, 2010).

The precision casting method is a production method used especially in the production of parts that are very difficult to manufacture (Pattnaik et al, 2012). Prototype productions are completed faster because the final part is obtained faster. In order to meet the expectations in the final parts, it is preferred especially because of its advantage in the machining process. Allowing freedom in design selection, obtaining detailed parts in good quality with high measurement precision, providing surfaces with high quality and roughness levels specific to the application method and the mold used, production can be carried out from parts with very little weight to parts with heavy weight. It also stands out with its features such as processing on complex parts, providing dimensional accuracy, obtaining parts with high production numbers in a short time, reducing costs, reducing machine operations and the number of processes (Pattnaik et al, 2012).

Die casting is an efficient, economical process offering a broader range of geometry and components for automotive industry as well as other applications than any other manufacturing technique. Parts have long service life and may be designed to complement the visual appeal of the surrounding part. Automotive parts designers can gain a number of advantages and benefits by specifying aluminum die casting parts (Cheșa, 2019).

High-speed production – Die casting is able to manufacture automotive parts with complex geometries in minimum tolerances respect to rest of the mass production processes. Machining is not required and over thousands of automotive die casting parts can be produced before repairing the molds (Cheșa, 2019). Dimensional accuracy and stability – Die casting produces automotive parts that are durable and dimensionally stable, while maintaining close tolerances (Cheșa, 2019).

Strength and weight – Thin wall castings of aluminum die cast automotive parts includes high strength and lighter respect to other casting methods. In addition, because aluminum die castings do not consist of separate parts welded or fastened together, the strength of automotive components after die casting is that of the alloy rather than the joining process (Cheșa, 2019). Multiple finishing techniques – Aluminum die cast automotive parts with smooth or textured surfaces can be obtain by aluminum die casting. They are easily plated or finished with a minimum of surface preparation (Cheșa, 2019).

High pressure aluminum die casting (Figure 2a) is a manufacturing process in which molten metal (aluminum) is injected with a die casting machine under force using considerable pressure into a steel mold or die to form products (Kaufman et al, 2004). In addition, short cycle times are feature advantage of high pressure casting in the production of thin-walled parts with complex and difficult geometric structures (Kridli et al, 2021). High pressure die casting production is rather fast relative to other aluminum casting processes (Zolotorevsky et al, 2007). Aluminum die casting applications also allow to offer aggressive casting delivery times (Kridli et al,

2021). Because of the excellent dimensional accuracy and the smooth surfaces, most of components which are manufactured by high pressure die casting do not require machining except the removal of flash around the edge and possible drilling and tapping holes (Zolotorevsky et al, 2007). High pressure casting method has also disadvantages such as higher investment costs and process fees compared to other aluminum casting methods. Complex shape and high-cost aluminum injection molds are used (Zolotorevsky et al, 2007).

Low pressure aluminum die casting (Figure 2b) can be also preferred for the components without concern for high quality (Kridli et al, 2021). Since the low pressure casting method is longer in terms of cycle time, it is generally preferred for parts with lower annual numbers as well as the production volume. Low pressure casting is the preferred method of manufacturing components such as engine blocks, wheels and suspension parts.

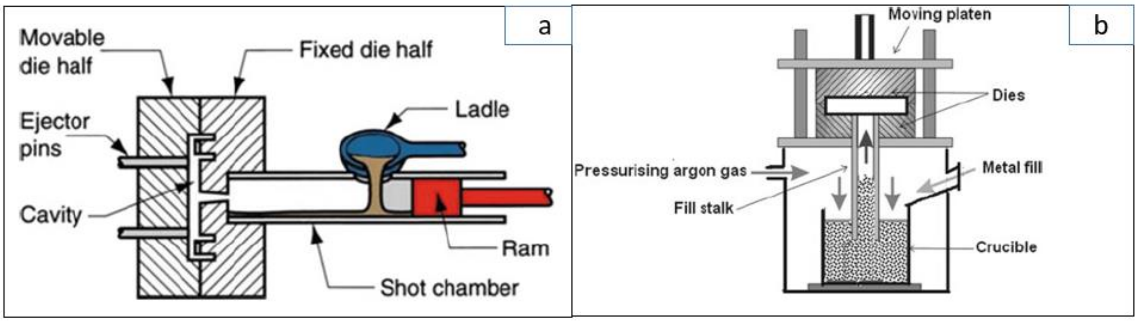

Figure 2. Illustration of; high pressure die casting (a), low pressure die casting (b) methods (Bonollo et al, 2015).

Aluminium Die Casting Applications & Trends for Automotive Industry

Automotive industry is at the forefront of this trend looking for effective alternatives to cut down on weight without sacrificing durability, which is under constant pressure to adhere to increasingly strict fuel economy standards, while addressing the efficiency in production, understanding of minimizing operating costs is dominant (Cheșa, 2019). Although the most important parameters are safety, it is also aimed to produce fuel-saving vehicles. Therefore, aluminum casting parts have entered a rapidly rising trend in the automotive industry in recent years. According to calculations in literature, 0.6 liters of fuel consumption is obtained in every 100 kg of weight reduction per 100 km. within the aluminum casting parts usage (Kelly et al, 2015).

Figure 3. Examples of aluminum die casting components (Cheșa, 2019).

Use of aluminum casting parts in a 1400 kg vehicle, approximately 300 kg of weight gain can be achieved. This corresponds 20% of weight reduction that provides the fuel saving is 1.8 liters per 100 km. (Palencia et al, 2012). According to literature, aluminum when replacing steel in today's vehicles, could save approximately 44 million tons of CO_2 emissions per year (Palencia et al, 2012). The recycling application of aluminum can be carried out without sacrificing the material quality. Nearly 90 % percent of the aluminum used in vehicles is recycled at the end of its life cycle. (Ozcomert, 2012).

Fasteners, brake systems, engine system, pistons can be examples for aluminum die casting vehicle parts in automotive applications. Figure 3 shows of engine parts produce through aluminum die casting as an example. (Cheșa, 2019). The stator is generally also made through aluminum die casting. Stators have many variations in size. This is why using die casting is such a good method, because it allows for different sized mechanical parts to be created with the highest degree of accuracy every time (Figure 3). Brackets are also manufactured through the process of aluminum die casting. Brackets are used in the electrical part of the motors. Also, stepper motors also use die casted brackets and these are generally created as per the specifications of the customers (Figure 3). Electronic covers are created in many parts of vehicles, for instance, gearbox but also the shades pole, the motor and on the stepping motor. These are but a few examples of where electronic covers are used through die casting processes (Figure 3). Heat sinks manufactured using the casting methods are primarily suitable for forced ventilation systems. This type of heat sink is usually made of cast aluminum (Smith et al, 2014).

Aluminum casting producers have been perfecting and improving their methods and techniques to streamline the production processes to increase output at a reasonable cost. Structural die casting components (Figure 4, a-c) are increasingly popular for the automotive industry (Hirsch et al, 2011, Baser, 2012, Hartlieb, 2013). Currently, they are proving their strengths above all with upper class cars such as the new Jaguar I-Pace, the BMW series 8 Coupé or the Mercedes-Benz C class (Hirsch et al, 2011, Baser, 2012). In automobile manufacturing, an increasing number of structural components such as shock towers (Figure 4, d) are being implemented. They can be used to replace multiple individual components, thereby substantially lowering the weight of a vehicle. Lightweight construction is significant for hybrid and electric vehicles coming to market: the additional weight of batteries and the electric motor for hybrids can be substantially offset by replacing steel structures with aluminum die castings. The market for structural components has already multiplied over the past five years. At the same time, manufacturing costs were decreased by approximately 20 %; however, OEMs suggest that an additional 20 to 30 % cost reduction is required to make these parts viable for high volume vehicles (Ducker Worldwide, 2017).

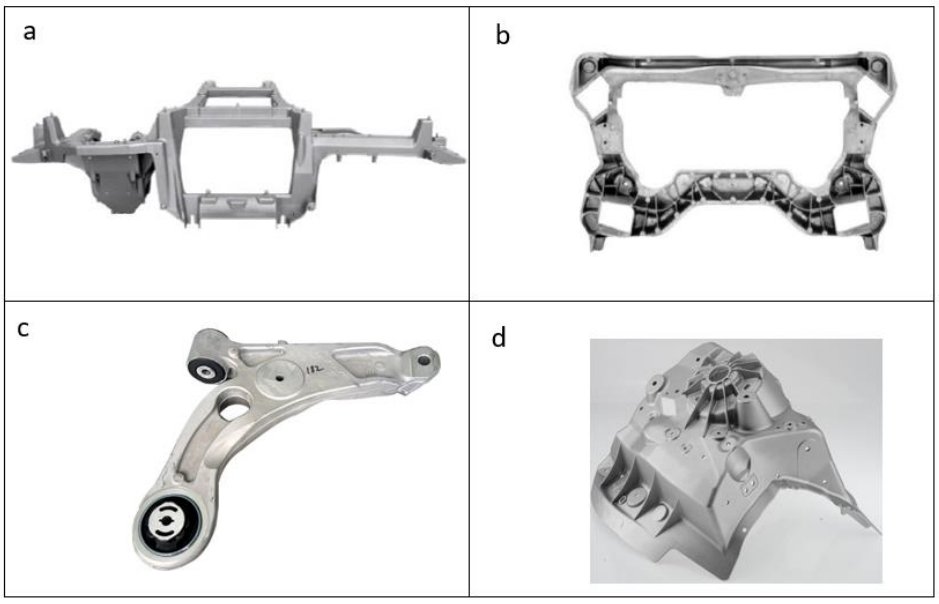

Figure 4. Examples for Al casting structural parts; cross car beam (a), engine cradle (b), control arm (c) , shock tower (d) (Hirsch et al, 2011, Baser, 2012, Hartlieb, 2013).

Aluminium has been the fastest growing material in light vehicles now for more than 50 years. The first wave of aluminum growth was mainly for casting in powertrain, chassis and wheels. Automotive aluminum content continues to steadily grow within multiple product forms and vehicle applications. Figure 5 shows the long term aluminum growth by product forms (Ducker Frontier, 2020).

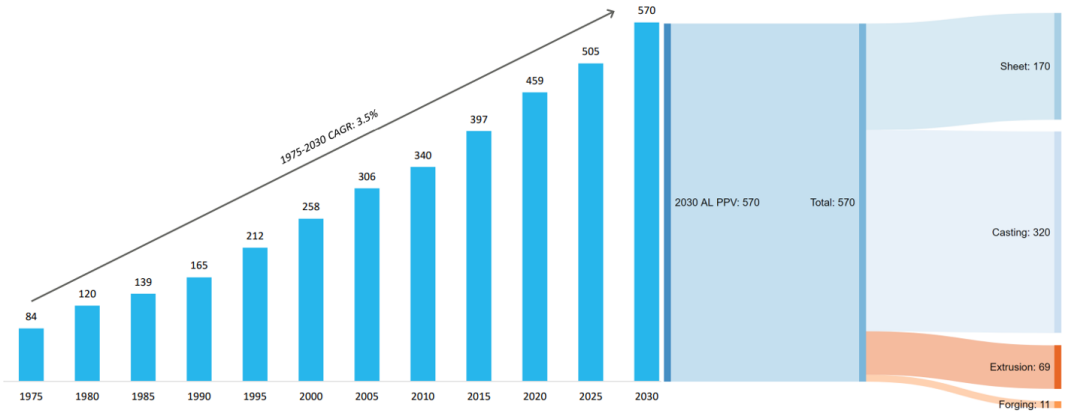

Figure 5. The long term aluminum growth by product forms (Ducker Frontier, 2020).

Average aluminum alloy content per vehicle is expected to 20 kg increase by 2025. Aluminum casting is expected to remain the predominant forming process. In 2025, the use average aluminium content per vehicle considering product forms such as cast, sheet, extrusion and forged forms will be 118 kg, 43 kg, 26 kg and 10 kg, respectively (Ducker Frontier, 2019). North American Light Vehicle Aluminum Content report currently reveals that aluminum usage has already experienced significant increases in last ten years. In 2010, the average aluminum content per vehicle was at 154 kg. At that time, the applications for aluminum were rather limited, with only small amounts of body sheet was used. Since 2010, additional aluminum usage in automotive applications was demonstrated more than 50 kg per vehicle, with 210 kg of average aluminum content per vehicle expected in 2030. According to reports (Ducker Frontier, 2020), more than 30 platforms in 2025 will have more than 230 kg of aluminum content in vehicles. Within next years, aluminum is expected to see another burst of growth, with average aluminum content to exceed 250 per vehicle, a 12% increase from the current numbers.

Advanced manufacturing technologies are needed to adapt new materials as well as production strategies. Figure 6 shows emerging manufacturing processes in the automotive applications (Center for Automotive Research, 2019). Among those emerging manufacturing processes, high-pressure thin-walled aluminum die casting was also underlined. It was expected that application of high pressure aluminium die casting will be increased towards to 2040. High-pressure die-casting (HPDC) is a technology that is proper for high production rates. Nowadays, about 50% of the world production of light metal castings is obtained through this technology.

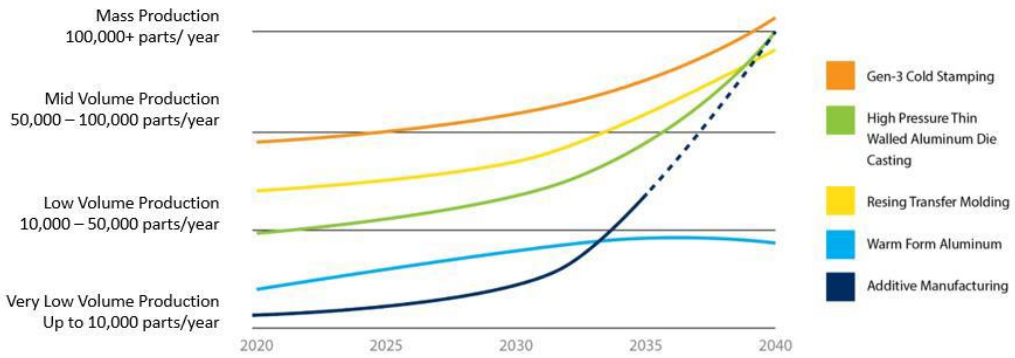

Figure 6. Emerging manufacturing processes in the automotive applications (Center for Automotive Research, 2019).

Aluminum cast parts for automobile manufacturing also include oil pumps, water pump housings, connectors, transmission parts, and a wide variety of brackets. The durability and reliability of aluminum cast parts has made them an essential part in auto design improvements and innovations (Hartlieb, 2013). Aluminum casting still account for the largest amount of aluminum content at 65% with about 135 kg per vehicle in 2025 through 2030, aluminum castings per vehicle is expected to grow to 145 kg. However, this will take up a smaller amount of the overall aluminum content at 61%. In general, the amount of aluminum powertrain castings has been decreasing, in part due to the downsizing of engine blocks and the number of cylinders. Instead, there is a new trend towards structural castings, especially for BEVs (battery electric vehicle) and plug-in hybrids. For example, Tesla is adopting a large structural casting for the rear of its electric SUV (Sports Utility Vehicle). The massive casting is said to replace over 70 extrusions and stamped sheet components, combining them into a

single piece. However, Volvo has just announced its desire to build body-in-white architectures using giant aluminum castings which is called mega-giga casting technology (Duckers, 2022). The Swedish automobile producers invests more than a billion euros for future EV's (electric vehicle). They also consider to meet several objectives with mega-casting in order to get weight reduction in vehicles. In additional it was also aimed to improve the use of interior space, and to be able to develop several vehicles capable of using the same modules based on the same body-in-white elements (mega castings). Volkswagen also revealed recently that their "Project Trinity" will likely use Tesla-like manufacturing processes in order to speed up production including potential mega-casting solutions (Duckers, 2022).

Mega-castings provides reducing assembly time, length of the assembly line. Mega-casting involves molding a section of a vehicle with as many components built into the panel as possible, reducing complexity when it comes to main assembly. Tesla introduces Giga-casted parts for the front of the future Model 3. Production of Tesla Model 3 is revealed Tesla model Y by mega-giga casting technology, which provides 2 parts instead of combined 171 parts (Figure 7). Tesla has already been producing the Model Y with a single rear body piece that replaced 70 different parts in the vehicle (Duckers, 2022).

Figure 7. Production of Tesla Model 3 is revealed Tesla model Y by mega-giga casting technology (Duckers, 2022).

Recently, Volvo and its premium EV brand Polestar are joining in, with the adoption of the Giga Press named mega-giga castings is shown in Figure 8. Volvo plans to use the technology to create a single mega-cast aluminium floor pan. The mega-cast floor pans for Volvo's next-generation EVs will have the mounting points for items like suspension arms and electric motors already built in, which negates the need for a rear subframe (Carney, 2022).

Figure 8. The megacasting replaces many stamped parts at the rear of this Volvo's chassis (Carney, 2022).

Two Chinese EV startups as Nio and Xpeng, have already followed Tesla's lead by ordering injection molding machines capable of 12,000 tons of force (Duckers, 2022). Compared to using methods such as welding multiple small parts in chassis production, the mega casting is expected to help enable the production of chassis parts in monolithic. In this way, it is aimed to eliminate many additional steps during assembling stage which provides cost reduction as well as energy efficient vehicles. The German automaker Mercedes-Benz aim to maximum cost and weight reduction (which megacasting makes possible) in order to provide management of energy consumption to increase EV range (Duckers, 2022).

Conclusion

Increasing global competition and the preservation of the ecological balance have pushed automobile manufacturers to new searches. It was aimed to produce vehicles keeping the the product costs at reasonable

levels while maintaining efficiency in production, less fuel consumption, efficient material recycling as well as improve comfort without sacrificing safety. With the increase in the use of light metals, aluminum alloys became an indispensable material with its high engineering properties for the automotive industry. In recent years, aluminum die casting alloys have become one of the crucial alloy groups in many industrial applications. There have been many challenges in aluminum die casting to establish casting processes to produce high-integrity components from aluminum alloys. Advances in new casting technology mainly have been in pressure die casting; high-pressure die-casting is the most efficient process to reduce porosity, and hence can be used to produce both thinner and thicker parts. Most of engine parts such as fasteners, brake systems, engine system, pistons can be examples for aluminum die casting vehicle parts in automotive applications. Aluminum casting producers have been perfecting and improving their methods and techniques to streamline the production processes to increase output at a reasonable cost. Structural die casting are increasingly popular for the automotive industry. Besides, advanced emerging manufacturing processes are also needed to adapt new materials as well as production strategies. Among emerging manufacturing processes, high-pressure thin-walled aluminum die casting was underlined. It was expected that application of high pressure aluminium die casting will be increased towards to 2040. High-pressure die-casting is a technology that is proper for high production rates. Nowadays, about 50% of the world production of light metal castings is obtained through this technology. In general, the amount of aluminum powertrain castings has been decreasing, in part due to the downsizing of engine blocks and the number of cylinders. Instead, there is a new trend towards structural castings, especially for BEVs and plug-in hybrids. For example, Tesla is adopting a large structural casting for the rear of its electric SUV. The massive casting is said to replace over 70 extrusions and stamped sheet components, combining them into a single piece. However, Volvo has just announced its desire to build body-in-white architectures using giant aluminum castings which is called mega-giga casting technology.

Scientific Ethics Declaration

The authors declare that the scientific ethical and legal responsibility of this article published in EPSTEM journal belongs to authors.

Acknowledgements or Notes

* This article was presented as an oral presentation at the International Conference on Technology, Engineering and Science (www.icontes.net) held in Antalya/Turkey on November 16-19, 2022.

References

Alam, T., & Ansari, A. H. (2017). Review on aluminium and its alloys for automotive applications. *Int. J. Adv. Technol. Eng. Sci*, *5*, 278-294.

Baser, T. A. (2012). Aluminum alloys and automotive applications. *Journal of Engineering and Machine, 53* (635): 51-58.

Baser, T. A., Usta M., Cetin H., Ozcan S., Celiker, T. (2013). A study of bending on AA6XXX extruded profiles, *7th International Conference and Exhibition on Design and Production of Machines and Dies/Molds*, 77.

Brinkman, CH. J., Engler, O., Hirsch J., & Schroder, D. (2010). INALCO2010. *GDA-Aluminium Congress,* Essen/Germany

Carney, D. (2022, March 14). *Design news, automotive engineering.* https://www.designnews.com/automotive-engineering/volvo-joins-tesla-giga-press-club

Center for Automotive Research (CAR). *2019 Center for Automotive Research Annual Report.* https://www.cargroup.org/2019-annual-report/

Chesa, A., & Graz, T. (2019, June). *Present and future in automotive applications* (Master's thesis). Die Casting Technology

Criqui, B. (2009). *Proc. Int. SLC Conference on innovative developments for lightweight vehicle structures*, May, 2009, Germany, p. 157

Cuniberti, A., Tolley, A., Riglos, M. C., & Giovachini, R. (2010). Influence of natural aging on the precipitation hardening of an AlMgSi alloy. *Materials Science and Engineering: A, 527*(20), 5307-5311.

Dalquist, S., & Gutowski, T. (2004, January). Life cycle analysis of conventional manufacturing techniques: sand casting. In *ASME International Mechanical Engineering Congress And Exposition* (Vol. 47136, pp. 631-641).

Ducker Frontier (2019, October 10). *Aluminum Content in European Cars, European Aluminium Public Summary*. https://www.european-aluminium.eu/media/2714/aluminum-content-in-european-cars_european-aluminium_public-summary_101019-1.pdf

Ducker Frontier (2020, April). *North America light vehicle aluminum content and outlook final report summary*.

Ducker Worlwide (2017, September 25). *Automotive lightweighting insights.* https://societyofautomotiveanalysts.wildapricot.org/resources/Documents/SAA_Ducker%20Worldwide%20Automotive%20Lightweighting%20September%2025%202017%20Distribution.pdf

Duckers (2022, May 11). *Mega-casting trends for automotive manufacturers*. https://www.linkedin.com/pulse/mega-casting-trends-automotive-manufacturers-2022-ducker worldwide/?trk=organization-update-content_share-article

Engler ,O., Brinkman, H. J. & Hirsch, J. (2010). Strategien des karosseriebaus, , Bad Neuheim, Ed. *Automotive Circle International.*

Glazoff, M. V., Zolotorevsky, V. S., & Belov, N. A. (2010). *Casting aluminum alloys*. Elsevier.

Graf, A. (2021). Aluminum alloys for lightweight automotive structures. In *Materials, Design and Manufacturing for Lightweight Vehicles* (pp. 97-123). Woodhead Publishing.

Hartlieb,M., & Rheinfelden, KG. (2013). Primary aluminium alloys for pressure die casting. *A company of the Aluminium Rheinfelden Group*, Friedrichstraße 80, Alloys GmbH & Co.

Hirsch, J. (2011). Aluminium in innovative light-weight car design. *Materials Transactions, 52*(5), 818-824.

Kaufman, J. G., & Rooy, E. L. (2004). *Aluminum alloy castings: properties, processes, and applications*. Asm International.

Kelly, J. C., Sullivan, J. L., Burnham, A., & Elgowainy, A. (2015). Impacts of vehicle weight reduction via material substitution on life-cycle greenhouse gas emissions. *Environmental Science & Technology, 49*(20), 12535-12542.

Kridli, G. T., Friedman, P. A., & Boileau, J. M. (2021). Manufacturing processes for light alloys. In *Materials, Design And Manufacturing For Lightweight Vehicles* (pp. 267-320). Woodhead Publishing.

Ozcomert, M. (2006). *Aluminum in automotive industry* (Master thesis).Istanbul Trade Center.

Palencia, J. C. G., Furubayashi, T., & Nakata, T. (2012). Energy use and CO2 emissions reduction potential in passenger car fleet using zero emission vehicles and lightweight materials. *Energy, 48*(1), 548-565.

Pattnaik, S., Karunakar, D. B., & Jha, P. K. (2012). Developments in investment casting process—a review. *Journal of Materials Processing Technology, 212*(11), 2332-2348.

Reddy, B. M., & Nallusamy, T. (2021). Degassing of aluminum metals and its alloys in non-ferrous foundry. In *Advances in Materials Research* (pp. 637-644). Springer, Singapore.

Smith, L. J. B., Corbin, S. F., Hexemer, R. L., Donaldson, I. W., & Bishop, D. P. (2014). Development and processing of novel aluminum powder metallurgy materials for heat sink applications. *Metallurgical and Materials Transactions A, 45*(2), 980-989.

Spittle, J. A. (2006). Grain refinement. In S*hape Casting Of Aluminium Alloys*.

Taub, A. I., Krajewski, P. E., Luo, A. A., & Owens, J. N. (2007). *The evolution of technology for materials processing over the last 50 years*: *the automotive example*. *Jom, 59*(2), 48-57.

Wang, W., Stoll, H. W., & Conley, J. G. (2010*). Rapid tooling guidelines for sand casting*. Springer.

Zeytin H. (2000). *Aluminum alloys and automotive applications in future*, MAM MKTAE Project Number: 50H5602.

Author Information

Tanya A. Baser
Coskunoz CKM R&D Center
Fethiye OSB, Sari cad No1 Bursa, Turkey
Contact e-mail: *tbaser@coskunoz.com.tr*

Elif Umay
Coskunoz CKM R&D Center
Fethiye OSB, Sari cad No1 Bursa, Turkey

Volkan Akinci
Coskunoz CKM R&D Center
Fethiye OSB, Sari cad No1 Bursa, Turkey

To cite this article:

Baser, T.A., Umay, E., Akinci, V. (2022). New trends in aluminum die casting alloys for automotive applications. *The Eurasia Proceedings of Science, Technology, Engineering & Mathematics (EPSTEM), 21, 79-*87.

The Eurasia Proceedings of Science, Technology, Engineering & Mathematics (EPSTEM)
ISSN: 2602-3199

The Eurasia Proceedings of Science, Technology, Engineering & Mathematics (EPSTEM), 2022

Volume 21, Pages 88-95

IConTES 2022: International Conference on Technology, Engineering and Science

Fluid-Structure Interaction: Impact of Reservoir Simulation Approach Considering Far-Field Boundary Condition in Dam Seismic Response

Reza GOLDARAN
Cyprus International University (CIU)

Abstract: Given the vitality of dams to life and the catastrophe caused by their failure, an adequate safety margin must be considered while designing for permanent and transient loads. Neglecting the transient loads in design make the dam structure vulnerable to damage; consequently, the earthquake load is crucial as a transient dynamic load. The horizontal component of an earthquake causes acoustic waves to exert hydrodynamic pressure on the dam's upstream face in addition to hydrostatic pressure. This study aims to assess the dynamic response of a dam using Lagrangian-Lagrangian and Lagrangian-Eulerian modeling approaches for a solid-liquid interaction. To this end, as a case study, time-domain analysis is carried out using ANSYS to determine the PINE FLAT dam response subjected to the horizontal component of the TAFT ground motion. The results indicate that considering the following points, the dam's dynamic responses in both approaches are almost identical. In order to absorb the scattered acoustic waves in the Eulerian reservoir, a condition involving a particular boundary element at the far field with a specific geometry must be provided. Also, the length-to-height ratio of the reservoir must not be less than a specific value in the Lagrangian fluid to minimize the effect of propagated acoustic wave reverberation.

Keywords: Fluid-structure interaction, Hydrodynamic pressure, Concrete dam, Added mass, Dam reservoir interaction

Introduction

Dams are essential for the supply of water resources, yet their failure may inflict severe consequences on a country's economy. Therefore, it seems necessary to investigate the behavior of dams in different conditions. The dynamic dam–reservoir interaction upon an earthquake has been demonstrated to be a crucial parameter in the design of such structures. Failure to incorporate the dynamic load of earthquakes into the design of a dam would lead to seismic damage to the structure. Furthermore, the overdesign of the dam would lead to an uneconomic structure.

Westergaard (Westergaard, 1933) modeled hydrodynamic pressure on a gravity dam two-dimensionally under horizontal ground motions, assuming a rigid dam body with a vertical upstream surface, horizontal bottom, and the reservoir as a continuum of infinite length. It was found that a portion of the reservoir would vibrate with the dam body, and the hydrodynamic force is distributed parabolically along the dam height, referred to as Westergaard's added mass (Feltrin, 1997). Zengar (Zangar & Haefeli, 1952) pursued Westergaard's work and demonstrated that his theory's validity was satisfactory. Chopra (Chopra & Chakrabarti, 1973) investigated the effects of water compressibility and dam flexibility on the dam-reservoir interaction. They showed that the stable response of pressure would not be damped by moving away from the reservoir when the loading frequency is higher than the first mode frequency of the reservoir, and it would be propagated. The Department of Earthquake Engineering (Council, 1991) invalidated Westergaard's added mass due to significant errors. With the development of numerical methods in the 1970s, Fin (Finn & Varoğlu, 1973) adopted the finite element method (FEM) to solve the dam–reservoir interaction equations. Some studies investigated boundary conditions

- Selection and peer-review under responsibility of the Organizing Committee of the Conference

in the dam–reservoir interaction, among which the major one is applying Sommerfeld's boundary condition for the far end of the infinite reservoir (Kucukarslan, 2005).

The influence of reservoir length on the seismic response of gravity dams subjected to ground motions from local and far faults was investigated by Bayraktar (Bayraktar et al., 2010). Using Lagrangian (Akkose & Simsek, 2010) and Eulerian (Altunisik et al., 2019) approach, an investigation was carried out to determine the nonlinear seismic performance of concrete gravity dams exposed to near and far fault motions. Sevim (Sevim et al., 2011) demonstrated the impacts of water height and length on the seismic reactivity of arch dam-reservoir-foundation configurations considering the Lagrangian viewpoint.

The nonlinear seismic assessments of concrete gravity dams performed by Wang (Wang et al., 2012) involved utilizing a 3D dam model that accounted for the hydrodynamic influences of the impounded water. The absorbing boundary conditions for vibration analysis were investigated by Samii (Samii & Lotfi, 2013). The research was conducted by Wick (Wick, 2013) regarding the coupling of arbitrary Lagrangian-Eulerian approaches and fully Eulerian for the purpose of fluid-structure interaction (FSI) simulations. In addition to dams, FSI would be of the utmost importance in pipelines, where it may, in conjunction with corrosion, lead to pipe bursting and have disastrous effects. It is possible to identify damages at an early stage by utilizing various damage detection strategies, such as those based on vibration and ultrasonic waves. (Goldaran & Kouhdaragh, 2021; Goldaran & Turer, 2020). Scholars have implemented a variety of investigations in order to evaluate the seismic responses of dams by taking into account the interactions between the various components of dam-reservoir-sediment-foundation systems (Baghban et al., 2021; Girme & Waghmare, 2021; Mandal & Maity, 2018; Moallemi et al., 2020; Srivastava & Sahoo, 2022; Yazdani & Alembagheri, 2017).

In the current work, the dynamic response of a dam was assessed using Lagrangian-Lagrangian and Lagrangian-Eulerian methods for a solid-liquid interaction. To evaluate the effect of the horizontal component of the TAFT earthquake on the PINE FLAT dam - as a case study - a time-domain analysis is performed with ANSYS. In both approaches, the dam's dynamic responses are almost equivalent. A far-field boundary element must be involved to absorb scattered acoustic waves in the Eulerian reservoir. For mitigating wave reverberation, the reservoir's length-to-height ratio must not be less than a specific value in the Lagrangian fluid.

Dam–reservoir system equations

The dam–reservoir interaction is obtained by solving two coupled quadratic differential equations. The differential equations of the structure and reservoir are written as follows:

$$[M]\{\ddot{u}\} + [C]\{\dot{u}\} + [K]\{u\} = \{f_1\} - [M]\{\ddot{u}_{gh}\} - [M]\{\ddot{u}_{gv}\} + [Q]\{P_h(t)\} \quad (1$$

$$[G]\{P_h\} + [C']\{\dot{P}_h\}[K']\{P_h\} = \{f_2\} - \rho[Q]^T\{\ddot{u}\} \quad (2$$

Where [M], [C], and [K] are the mass, damping, and stiffness matrices of the dam, while [G], [C'], and [K'] are the mass, damping, and stiffness matrices of the reservoir, respectively. Furthermore, [Q] is the coupled structure–reservoir matrix, $\{f_1\}$ denotes the vector of body and hydrostatic forces, $\{f_2\}$ represents the vector of the acceleration-induced forces on the dam–reservoir interface, {P} is the pressure vector, {u} is the displacement vector, $\{\ddot{u}_g\}$ is the gravitational acceleration vector, and ρ is the fluid density. According to Fig. 1, with the assumption of compressible, non-viscous, and irrotational fluid, the governing equations of the reservoir domain for flexible dam bodies considering the given boundary conditions are in the form of relations (3) to (7).

$$\nabla^2 P = \frac{1}{C^2}\frac{\partial^2 P}{\partial t^2} \quad \text{boundary condition } \Omega_f \quad (3$$

$$\frac{\partial P}{\partial n} = -\rho a_g^n \quad \text{boundary condition } \Gamma_1 \quad (4$$

$$\frac{\partial P}{\partial n} = 0 \quad \text{boundary condition } \Gamma_2 \quad (5$$

$$P = 0 \quad \text{boundary condition } \Gamma_3 \quad (6$$

$$\frac{\partial P}{\partial n} = -\frac{1}{C}\frac{\partial P}{\partial t} \quad \text{boundary condition } \Gamma_4 \quad (7$$

Sommerfeld's boundary condition may be employed at the end of the reservoir to absorb acoustic waves. Sommerfeld's boundary condition (Eq. (7)) is an approximate solution in which P, *t*, and *n* are pressure, time, and normal vector, respectively.

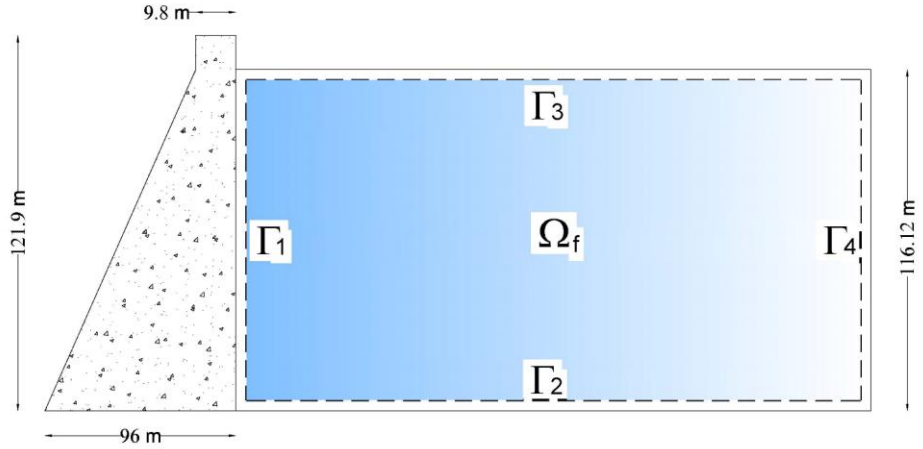

Figure 1. Pine flat dam geometry along with boundary condition

Its approximate solution is because of the ability to absorb only one-dimensional, normal waves. The Impedance boundary condition was employed to provide acoustic wave absorption at the far end of the reservoir. In applying this wave absorption condition, the reservoir is modeled in a rectangle fashion, and likely satisfies the Summerfield boundary condition. Water's dynamic viscosity (MU) must be set to 1 to meet the mentioned boundary condition.

Method

For simulating the dam-reservoir interaction and analyzing the model, ANSYS software was utilized. As mentioned earlier, the present work investigated the PINE FLAT dam under the horizontal ground motion records of the TAFT earthquake. Figure 1 and Tables 1 to 3 represent the specification of geometry and material properties of both the dam body and reservoir.

Table 1. Geometry of dam body

Height (m)	Crest width (m)	Bottom width (m)	Upstream slope	Downstream slope	Water level (m)
121.90	9.80	96	1 to 0.05	1 to 0.78	116.12

Table 2. Reservoir specification

Water Density (kg/m^3)	Acoustic wave velocity in water (m/s)	Reservoir bottom absorption factor	Viscosity (Mpa.s)	Bulk modulus (kg/cm^2)	Poison ratio	length (m)
1000	1440	0.5	1.307	2.1e8	0.49	300

Table 3. Material (concrete) properties of dam body

Density (kg/m^3)	E (kg/cm^2)	Poison ratio	Damping ratio (%)
2500	2.785e9	0.2	5

Euler–Lagrange model

The Plane182 element was exploited for the dam body. Plane182 is a four-node element with two translational degrees of freedom (U_x, U_y) in each node. The Fluid29 element was employed to model the reservoir. It is a four-node element with two translational and one pressure degree of freedom (U_x, U_y, and P) in each node. It has the ability to model acoustic waves and includes the wave absorption factor. The dam structure was modeled under two settings:

(I) keypoint(2) = 0 for elements in contact with the solid surface (dam structure)
(II) keypoint(2) = 1 for elements not in contact with the solid surface, as shown in Figure 2.

The FLUID129 acoustic wave absorption element was employed at the end of the reservoir to model the far end (semi-infinite) and satisfy Sommerfeld's boundary condition. A FLUID129 is a 2-node element and must lie on a circular boundary and entirely contain the domain meshed with FLUID29 elements, as shown in Fig. 2. For the best results, the circle's center should be placed as close to the model's center as possible.

In the present work, MU was set to 0.5 in the Fluid29 element to define the bottom absorption conditions. It varies from 0 (no absorption) to 1 (full absorption) and may even be higher than 1 in some cases.

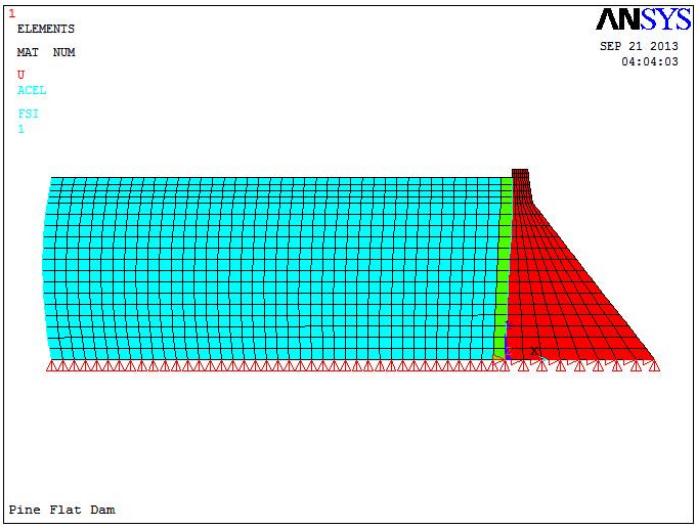

Figure 2. Eulerian-Lagrangian simulation

Dynamic Analysis of the Dam under Horizontal Ground Motions

The ANSYS Parametric Design Language (APDL) is utilized to import the ground motion time-history record. The 14-second horizontal component of the TAFT earthquake record was introduced at a 0.02-second increment in TRANSIENT analysis. Figure 3 represents the ground-motion accelerogram of the TAFT earthquake prepared by SeismoSignal.

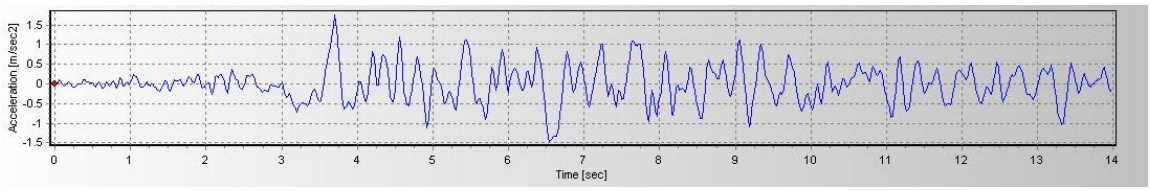

Figure 3. Ground-motion accelerogram of Taft earthquake

Coupling

Since the model consisted of both fluid and solid phases; hence, coupled field analysis was employed. To this end, it was required to couple the reservoir and dam on the interface, which could be carried out using either sequential or direct analysis.

Sequential analysis

In this procedure, numerous consecutive analyses are undertaken, each pertaining to a different field.

Direct analysis

To conduct an FSI analysis with this method, coupling participants are linked to a component system named System Coupling. A system that contributes to or receives data in a coupled analysis is called a participant

system. Here, there are two coupling participants: Fluent (the first) and ANSYS Mechanical (the second). System coupling first gathers data from the participants to synchronize the simulation's whole setup, and the information that needs to be shared is then given to the respective participant. The following phase is to organize the sequence of the exchange of information. Ultimately, at the end of each coupling iteration, the convergence of the coupling step is evaluated.

It is noteworthy that direct analysis requires coupled-field elements. The present work adopted direct analysis considering Fluid29 is a coupled-field element. Figure 4 shows the deformed shape of the dam body under direct analysis, and Fig. 5 and table 4 represent the time history and maximum displacement of the dam crest, respectively. Figure 6 plots the analysis result of the model excluding the Fluid129 element. As shown, ignoring the Fluid129 absorption element disturbed the responses.

Lagrange–Lagrange model

The Solid65 element was employed to model the dam body. In this 8-node element, each node has three transitional degrees of freedom (U_x, U_y, U_z). The reservoir was modeled with the 8-node Solid185 element in which each node has three transitional degrees of freedom (U_x, U_y, U_z). This element has the capability of large deflection without entering the nonlinear phase. The dam-reservoir interface was modeled using the Contact178 element with axial and shear stiffness of 10e10 kg/cm^2. This element's parameters are set so that it transmits compressive force but does not resist tensile loads. A friction coefficient (MU) of 0.2 was set for the Contact178 element.

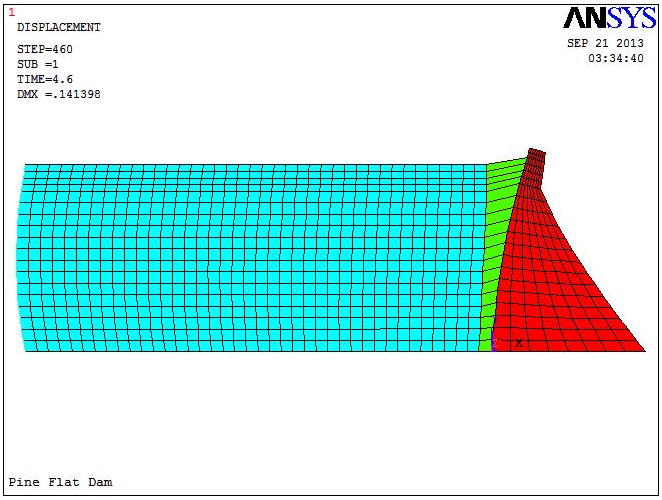

Figure 4. Deformed shape of dam body

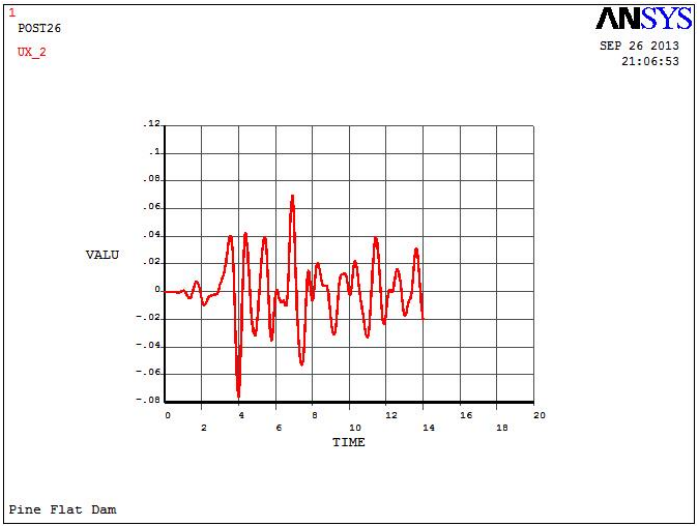

Figure 5. Displacement time history at the dam crest level

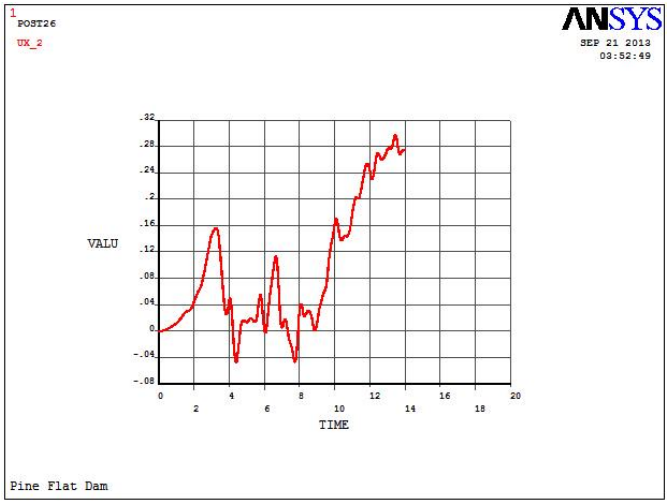

Figure 6. Displacement time history at the dam crest level in the absence of acoustic wave absorption element

The critical point is the correct application of the restrictions of the support. All dam body's nodes in contact with the ground were constrained in all directions, and the reservoir nodes in contact with the ground or semi-infinite boundary were constrained only in one direction so that, in practice, it is not also possible for the fluid to move in that direction. Figure 7a illustrates the dam model, and Fig. 7b represents the displacement time history of the dam crest applying the Lagrange–Lagrange approach. Table 4 reports the maximum displacement of the dam crest induced by both procedures. It may be seen that considering the following conditions, both methods lead to approximately the same response. In the Lagrangian-Lagrangian simulation, the length-to-height ratio of the reservoir must be large enough to mitigate the wave reflection (here, it was limited to 2.5).

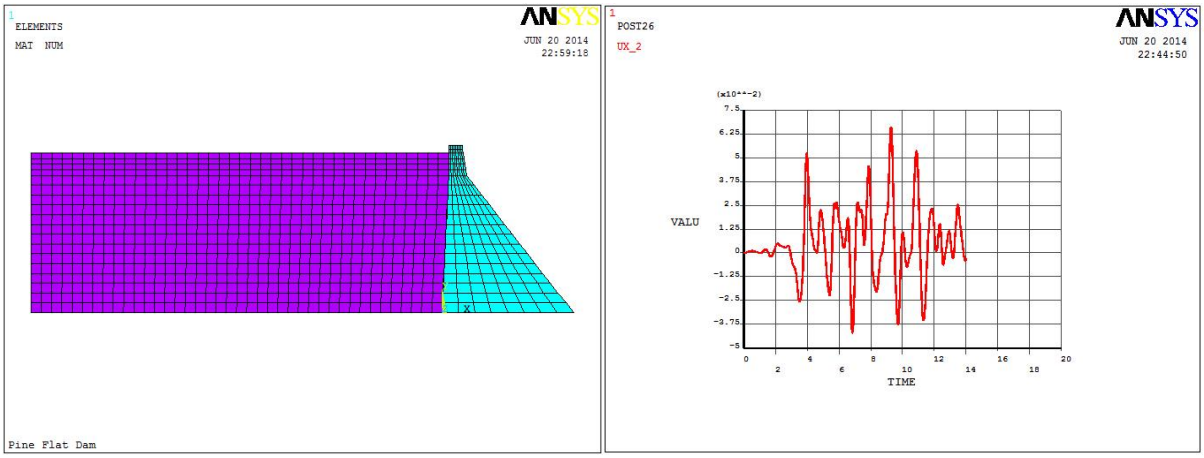

Figure 7. a) Lagrangian – Lagrangian simulation, b) Displacement time history at the dam crest level

Table 4. Maximum displacement of the dam crest

Lagrange–Lagrange method (m)	Euler–Lagrange method (m)
0.068	0.065

Conclusion

In the present work, the dynamic response of the PINE FLAT dam, as a case study, due to FSI under the TAFT earthquake was carried out using ANSYS to illustrate the results derived from two different perspectives, the Lagrangian-Lagrangian, and Lagrangian-Eulerian approaches. It is concluded that both methods are very effective, efficient, and capable of producing almost identical results (error < 5%) to any desired degree of accuracy considering the following points.

- A condition including a particular boundary element at the far field with a specific geometry is required to absorb the scattered acoustic waves in the Eulerian reservoir. To achieve this goal, the FLUID129

acoustic wave absorption element was used, which is a 2-node element and must lie on a circular boundary and totally encapsulate the domain meshed with FLUID29 elements.

- For the best results, the generated circle's center by the mentioned 2-node boundary element should be as close to the model's center as possible.
- In the Lagrangian-Lagrangian simulation, the length-to-height ratio of the reservoir, which is restricted to 2.5 in the present study, must be large enough to minimize the effect of propagated acoustic wave reflection.
- Excluding wave absorption elements at the Eulerian reservoir's far end led to unreliable results.

Scientific Ethics Declaration

The author declares that the scientific ethical and legal responsibility of this article published in EPSTEM journal belongs to author.

Acknowledgements or Notes

* This article was presented as an oral presentation at the International Conference on Technology, Engineering and Science (www.icontes.net) conference held in Antalya/Turkey on November 16-19, 2022.

References

Akkose, M., & Simsek, E. (2010). Nonlinear seismic response of concrete gravity dams to near-fault ground motions including dam-water-sediment-foundation interaction. *Applied Mathematical Modelling*, *34*(11), 3685–3700.

Altunisik, A. C., Sesli, H., Husem, M., & Akkose, M. (2019). Performance evaluation of gravity dams subjected to near-and far-fault ground motion using Euler approaches. *Iranian Journal of Science and Technology, Transactions of Civil Engineering*, *43*(2), 297–325.

Baghban, M. H., Faridmehr, I., Goldaran, R., & Amoly, R. S. (2021). Seismic analysis of concrete arch dam considering material failure criterion. *IOP Conference Series: Materials Science and Engineering*, *1117*(1), 12004.

Bayraktar, A., Turker, T., Akkose, M., & Ates, S. (2010). The effect of reservoir length on seismic performance of gravity dams to near-and far-fault ground motions. *Natural Hazards*, *52*(2), 257–275.

Chopra, A. K., & Chakrabarti, P. (1973). Dynamics of gravity dams-significance of compressibility of water and three dimensional effects. *International Journal of Earthquake Engineering and Structural Dynamics*, *2*, 103–104.

Council, N. R. (1991). *Earthquake engineering for concrete dams: design, performance, and research needs*. National Academies Press.

Feltrin, G. (1997). *Absorbing boundaries for the time-domain analysis of dam-reservoir-foundation systems* (Vol. 232). ETH Zurich.

Finn, W. D. L., & Varoğlu, E. (1973). Dynamics of gravity dam-reservoir systems. *Computers & Structures*, *3*(4), 913–924.

Girme, P. D., & Waghmare, M. V. (2021). Effect of dam reservoir interaction on response of dam subjected to dynamic load. In *Recent Trends in Civil Engineering* (pp. 945–961). Springer.

Goldaran, R., & Kouhdaragh, M. (2021). Structural health monitoring of beams with moving oscillator: theory and laboratory. *Građevinar*, *73*(07.), 693–704.

Goldaran, R., & Turer, A. (2020). Application of acoustic emission for damage classification and assessment of corrosion in pre-stressed concrete pipes. *Measurement*, *160*, 107855.

Kucukarslan, S. (2005). An exact truncation boundary condition for incompressible–unbounded infinite fluid domains. *Applied Mathematics and Computation*, *163*(1), 61–69.

Mandal, K. K., & Maity, D. (2018). Transient response of concrete gravity dam considering dam-reservoir-foundation interaction. *Journal of Earthquake Engineering*, *22*(2), 211–233.

Moallemi, R., Mahboubi, B., Bakhtiari, P., Rezaiy, R., & Manalo, O. (2020). Seismic performance of concrete reservoirs considering soil-structure-fluid interaction under near-and far-field seismic excitations. *Journal of Civil Engineering and Materials Application*, *4*(1), 55–73.

Samii, A., & Lotfi, V. (2013). A high-order based boundary condition for dynamic analysis of infinite reservoirs. *Computers & Structures*, *120*, 65–76.

Sevim, B., Altunssik, A. C., Bayraktar, A., Akkose, M., & Calayir, Y. (2011). Water length and height effects on the earthquake behavior of arch dam-reservoir-foundation systems. *KSCE Journal of Civil Engineering*, *15*(2), 295–303.

Srivastava, R. K., & Sahoo, D. R. (2022). Seismic analysis of a concrete gravity dam considering dam-water-sediment-foundation interaction. *Dams and Reservoirs*, 1–27.

Wang, H., Feng, M., & Yang, H. (2012). Seismic nonlinear analyses of a concrete gravity dam with 3D full dam model. *Bulletin of Earthquake Engineering*, *10*(6), 1959–1977.

Westergaard, H. M. (1933). Water pressures on dams during earthquakes. *Transactions of the American Society of Civil Engineers*, *98*(2), 418–433.

Wick, T. (2013). Coupling of fully Eulerian and arbitrary Lagrangian–Eulerian methods for fluid-structure interaction computations. *Computational Mechanics*, *52*(5), 1113–1124.

Yazdani, Y., & Alembagheri, M. (2017). Nonlinear seismic response of a gravity dam under near-fault ground motions and equivalent pulses. *Soil Dynamics and Earthquake Engineering*, *92*, 621–632.

Zangar, C. N., & Haefeli, R. J. (1952). Electric analog indicates effect of horizontal earthquake shock on dams. *Civil Engineering*, *22*(4), 54–55.

Author Information

Reza Goldaran
Cyprus International University (CIU)
Nicosia, Northern Cyprus
Contact e-mail: *rezagoldaran@gmail.com*

To cite this article:

Goldaran, R. (2022). Fluid-structure interaction: Impact of reservoir simulation approach considering far-field boundary condition in dam seismic response. *The Eurasia Proceedings of Science, Technology, Engineering & Mathematics (EPSTEM), 21*, 88-95.

The Eurasia Proceedings of Science, Technology, Engineering & Mathematics (EPSTEM)
ISSN: 2602-3199

The Eurasia Proceedings of Science, Technology, Engineering & Mathematics (EPSTEM), 2022

Volume 21, Pages 96-109

IConTES 2022: International Conference on Technology, Engineering, and Science

Comparison of Transparent Insulated and Non-Insulated Solar Cell

Lida EBRAHIMI-VAFAEI
Near East University

Abstract: In today's world, non-renewable sources such as coal, petroleum, and natural gas have become unreliable sources of fuel for energy production because of price volatility caused by geo-political issues and the depletion of these resources. Nonetheless, there's a rapid increase in energy consumption globally. Therefore, alternate energy sources are seriously required if the above challenges are to be resolved. These alternate energy sources are wind power, hydropower, solar energy, biomass, biofuel, and geothermal energy. In the Turkish Republic of North Cyprus (TRNC), weather conditions favor solar energy applications. However, the efficiency of solar cells is negatively affected by high temperatures. Therefore, transparent insulation materials are applied to the solar cell. Transparent or translucent insulation materials (TIM) represent a new class of materials with a high potential for increasing the efficiency of solar thermal systems. This paper investigates the advantages of applying transparent insulation materials to solar cells with respect to their efficiency by theoretical and experimental analysis. The cells are attached to a levered plane with a protractor that acted like a "see-saw" to adjust the angle of the solar cells to the Sun. Around the plane, a column of cardboard was constructed with black fabric covering the inside and bottom surfaces to prevent unwanted reflections. The time of day, temperature, voltage, and current were recorded in the experimental analysis. Using Microsoft Excel, the data (voltage, current, and calculated power) was graphed with respect to time. In the result, we compare solar cells with TIM and solar cells without (TIM). The results of the investigation show that solar cells with TIM have better efficiency compared to solar cells without TIM.

Keywords: Solar energy, Solar cell, Transparent insulation materials.

Introduction

Solar cell (photovoltaic cell or photoelectric cell) is a solid-state electrical device that converts the energy of light directly into electricity by the photovoltaic effect. The energy of light is transmitted by photons-small packets or quanta of light. Electrical energy is stored in electromagnetic fields, which in turn can make a current of electrons flow. Assemblies of solar cells are used to make solar modules which are used to capture energy from sunlight. When multiple modules are assembled together (such as prior to the installation of one pole-mounted tracker system), the resulting integrated group of modules all oriented in one plane is referred as a solar panel. The electrical energy generated from the modules is an example of solar energy. Photovoltaic is the field of technology and research related to the practical application of photovoltaic cells in producing electricity from light, though it is often used specifically to refer to the generation of electricity from sunlight. Cells are described as photovoltaic cells when the light source is not necessarily sunlight. These are used for detecting light or other electromagnetic radiation near the visible range, for example, infrared detectors, or measurement of light intensity.

History and Development of Solar Cell Technology

The development of solar cell technology began with the 1839 research of French physicist Antoine-César Becquerel. Becquerel observed the photovoltaic effect while experimenting with a solid electrode in an

electrolyte solution when he saw a voltage develop when the light fell upon the electrode. The major events are discussed briefly below, and other milestones can be accessed by clicking on the image shown below.

- Charles Frits - **First Solar Cell**: The first genuine solar cell was built around 1883 by Charles Frits, who used junctions formed by coating selenium (a semiconductor) with an extremely thin layer of gold. The device was only about 1 percent efficient.
- Albert Einstein - **Photoelectric Effect:** Albert Einstein explained the photoelectric effect in 1905 for which he received the Nobel Prize in Physics in 1921.
- Russell Oh l - **Silicon Solar Cell:** Early solar cells, however, had energy conversion efficiencies of under one percent. In 1941, the silicon solar cell was invented by Russell Oh 1.

Gerald Pearson, Calvin Fuller, and Daryl Chapin - **Efficient Solar Cells:** In 1954, three American researchers, Gerald Pearson, Calvin Fuller, and Daryl Chapin, designed a silicon solar cell capable of a six percent energy conversion efficiency with direct sunlight. They created the first solar panels. Bell Laboratories in New York announced the prototype manufacture of a new solar battery. Bell had funded the research. The first public service trial of the Bell Solar Battery began with a telephone carrier system (Americus, Georgia) on October 4, 1955 (Khoja,2013).

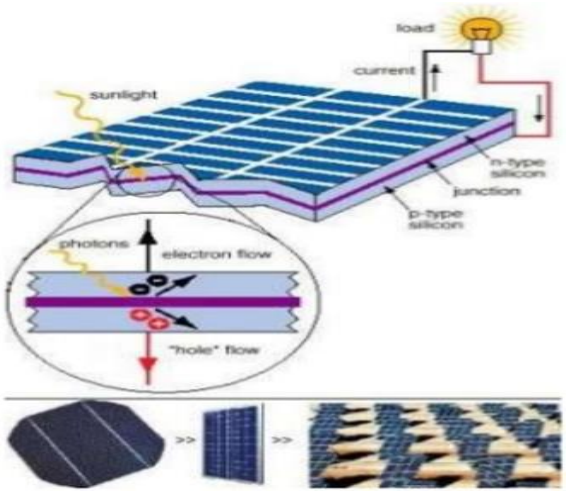

Figure 1. Photovoltaic cell or photoelectric cell (Khoja, 2013).

How Solar Cells Work - Components & Operation of Solar Cells

Since a solar cell is the only generator in a solar PV system, it is one of the most important parts of a solar PV system. In the following paragraphs, a simple introduction of a solar cell and how it operates is discussed (Miller, 2013). A solar cell is an electronic device that directly converts sunlight into electricity. Light shining on the solar cell produces both a current and a voltage to generate electric power.

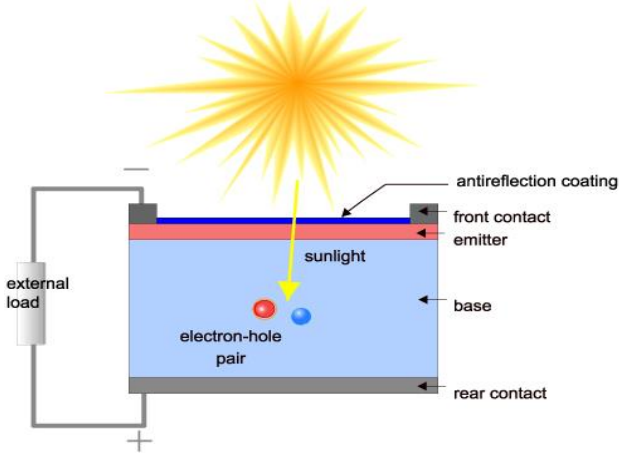

Figure 2. Solar cell structure (Miller, 2013).

This process requires firstly, a material in which the absorption of light raises an electron to a higher energy state, and secondly, the movement of this higher energy electron from the solar cell into an external circuit. The electron then dissipates its energy in the external circuit and returns to the solar cell. A variety of materials and processes can potentially satisfy the requirements for photovoltaic energy conversion, but in practice, nearly all photovoltaic energy conversion uses semiconductor materials in the form of a *p*-*n* junction (Maxwell,2011). A solar cell structure is shown in figure 2 and a solar panel configuration is in figure 3.

The basic steps in the operation of a solar cell are:

- The generation of light-generated carriers;
- The collection of the light-generated carries to generate a current;
- The generation of a large voltage across the solar cell; and
- The dissipation of power in the load and in parasitic resistances.

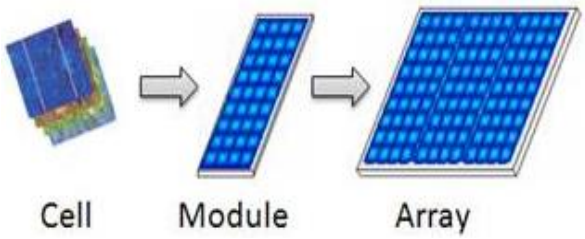

Figure 3. Solar panel configuration (Miller, 2013).

Light-Generated Current

The generation of current in a solar cell, known as the "light-generated current", involves two key processes. The first process is the absorption of incident photons to create electron-hole pairs. Electron-hole pairs will be generated in the solar cell provided that the incident photon has an energy greater than that of the band gap. However, electrons (in the *p*-type material), and holes (in the *n*-type material) are meta-stable and will only exist, on average, for a length of time equal to the minority carrier lifetime before they recombine. If the carrier recombines, then the light-generated electron-hole pair is lost and no current or power can be generated.

A second process, the collection of these carriers by the *p*-*n* junction, prevents this recombination by using a *p*-*n* junction to spatially separate the electron and the hole. The carriers are separated by the action of the electric field existing at the *p*-*n* junction. If the light-generated minority carrier reaches the *p*-*n* junction, it is swept across the junction by the electric field at the junction, where it is now a majority carrier. If the emitter and base of the solar cell are connected together (i.e., if the solar cell is short-circuited), the light-generated carriers flow through the external circuit. The ideal flow at a short circuit is shown in Figure 4(Finch, 2003). The absorption of a photon creates an electron-hole pair. Ideally, the minority carrier (in this case a hole) makes it across the junction and becomes a majority carrier. After passing through the load the electron meets up with a hole and completes the circuit.

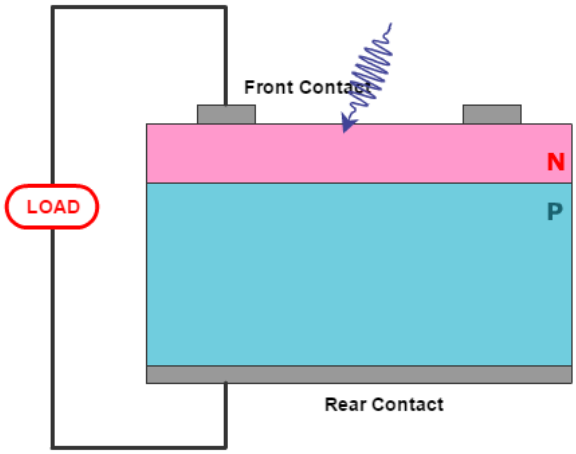

Figure 4. The ideal short circuit flow of electrons and holes at a p-n junction (Finch,2003).

Materials Used in Solar Cell

Various materials display varying efficiencies and have varying costs. Materials for efficient solar cells must have characteristics matched to the spectrum of available light. Some cells are designed to efficiently convert wavelengths of solar light that reach the Earth's surface. However, some solar cells are optimized for light absorption beyond Earth's atmosphere as well. Light-absorbing materials can often be used in multiple physical configurations to take advantage of different light absorption and charge separation mechanisms. Materials presently used for photovoltaic solar cells include monocrystalline silicon, polycrystalline silicon, amorphous silicon, cadmium telluride, and copper indium selenite/sulfide. Many currently available solar cells are made from bulk materials that are cut into wafers between 180 to 240 micrometers thick that are then processed like other semiconductors. Other materials are made as thin-films layers, organic dyes, and organic polymers that are deposited on supporting substrates. A third group is made from Nanocrystals and used as quantum dots (electron-confined nanoparticles). Silicon remains the only material that is well-researched in both bulk and thin-film forms. Examples: Crystalline silicon, Thin films, Cadmium telluride solar cells, Copper indium gallium selenite, Gallium arsenide multifunction, Silicon thin films…etc. (Khoja, 2013).

Transparent Insulation Material (TIM)

The input object "Surface Control: Movable Insulation" allows modeling Transparent Insulation Materials (TIM) that were originally designed for use in solar collector systems, where there was a need to increase the insulation in the solar collector without dramatically reducing solar energy transmittance. Transparent Insulation provides both these properties, insulation from heat loss and transmittance of solar energy. The combination of these properties is achieved because Transparent Insulation is a transmitter of short-wave radiation but a barrier to long-wave radiation. Therefore, short-wave solar radiation passes through the Transparent Insulation, and long-wave heat radiation is insulated by the transparent insulation. Incident solar energy falling on the transparent insulation is reflected and re-reflected within the material and eventually falls on the absorber. In addition, transparent insulation materials also have increased thermal resistance due to conduction in comparison to standard glass. Honeycomb transparent insulation was first developed in the 1960s to enhance the insulation value of glazing systems with minimal loss to light transmission. Over the past 25 years, transparent insulation materials (TIMs) have been applied to windows, walls, skylights, roofs, and high-performance solar collectors.

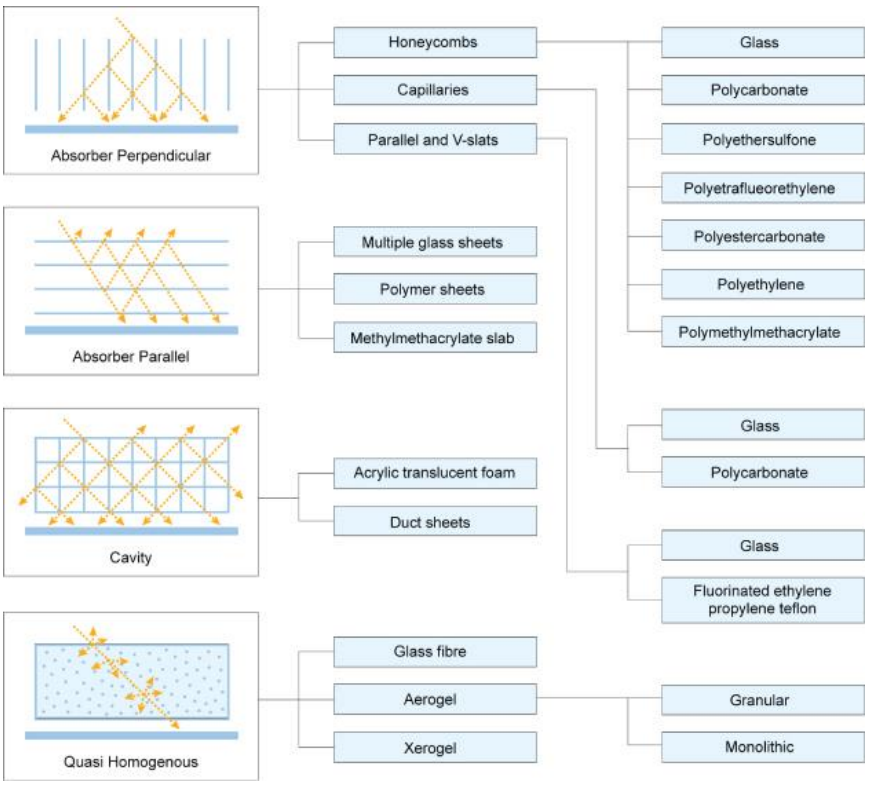

Figure 5. Types of transparent insulation (Happold, 2022).

Transparent insulation materials perform a similar function to opaque insulation, but they have the ability to transmit daylight and solar energy, reducing the need for artificial light and heating. They transmit heat, mainly through conduction and radiation, but convection is usually suppressed. The thermal and optical properties of transparent insulation materials depend on the material, its structure, thickness, quality, and uniformity. They typically consist of either glass or plastic arranged in a honeycomb, capillary or closed-cell construction. Alternatively, granular or monolithic silica aerogel can be used to achieve higher insulation values. Depending on the structure of the material, its arrangement can be classified as:

- Absorber perpendicular.
- Absorber parallel.
- Cavity.
- Quasi-homogeneous.

Figure 6 (below) compares the thermal conductivity of various transparent insulation materials and other insulation products. Okalux Glass Honeycomb is a commercially produced absorber perpendicular TIM with a thermal conductivity of 0.039W/m.K. Translucent silica aerogel, a quasi-homogenous TIM, has the lowest thermal conductance of any known solid at 0.004-0.018W/m.K. Only vacuum technology is comparable with thermal conductivities in the region of 0.005W/m.K.

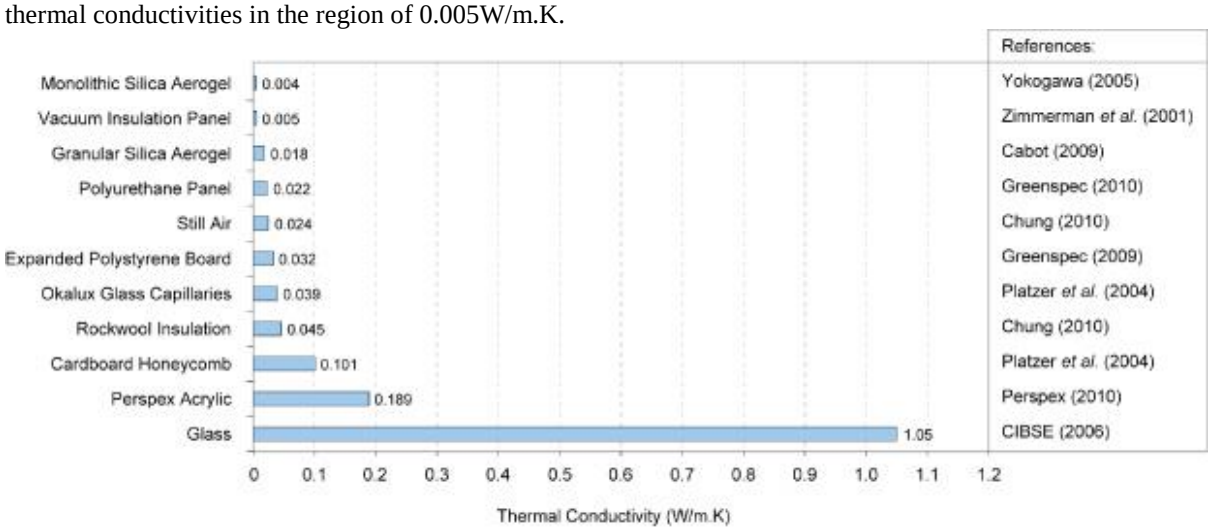

Figure 6. Thermal conductivities of insulation materials (Happold, 2022).

The Experiment of a Solar Cell

Solar cells convert light energy into electrical energy. With a few simple tools on a sunny day, you can measure how efficient a solar cell is at transforming sunlight into electricity by taking a reading from the multimeter.
Here are the few equipment required

- Solar cell
- Multimeter
- Crocodile clips
- Tapes
- Wooden or Cardboard base for the inclination of the solar cell
- Transparent layer

Calibration

The most important setting is to calibrate the measuring instrument and in this, it is a multimeter. These are the steps to calibrate a multimeter

- Set the multimeter to the highest resistance range by turning the dial to the highest "ohm" setting.
- Touch the test probes of your digital multimeter together. The digital display of the multimeter should read "0 ohms."

Press the calibration knob until the display reads "0" on the digital multimeter if you don't see "0 ohms" initially.

Investigation

Working outside, in a sunny place, set the multimeter to the DC voltage scale so it can measure a few volts. Using the clip lead, connect the positive terminal of the meter to the positive terminal of the solar cell. Then use the black clip lead to connect the common (COM) terminal of the meter to the negative terminal of the solar cell (see photos below). Measure the open circuit voltage and current across the solar cell.

Figure 7. Solar cell set up without transparent layer

Then repeat the same process for the solar cell with the transparent layer on it.

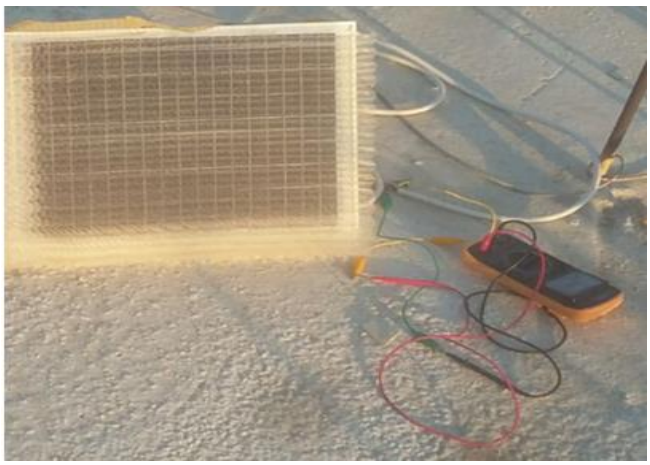

Figure 8. Solar cell set up with transparent layer.

Figure 9. Solar cell set up

The values of the voltage and current after being recorded are substituted into the formula of power which is

Power = Voltage (volts) × Current (amp)

The graph is then plotted in comparison of the values attained by solar with the transparent layer and without the transparent layer. I would like to thank Muhammad ABID KHAN and Taha BIN IMAM for their help

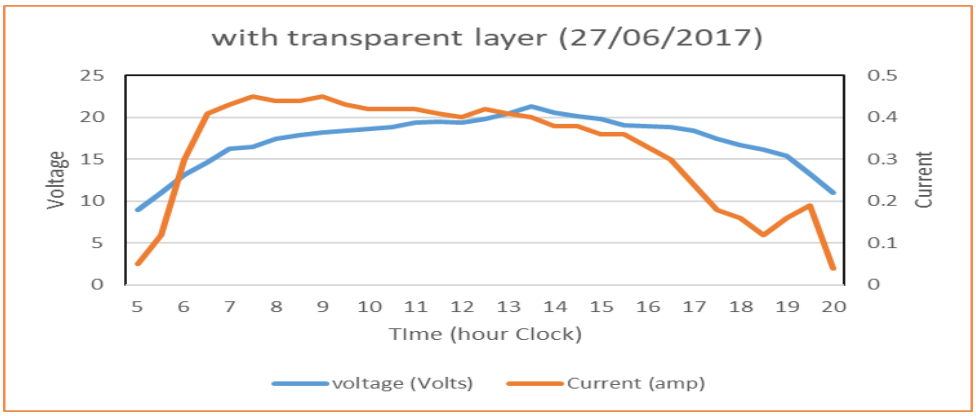

Figure 10. Trend of current and voltage with the transparent layer

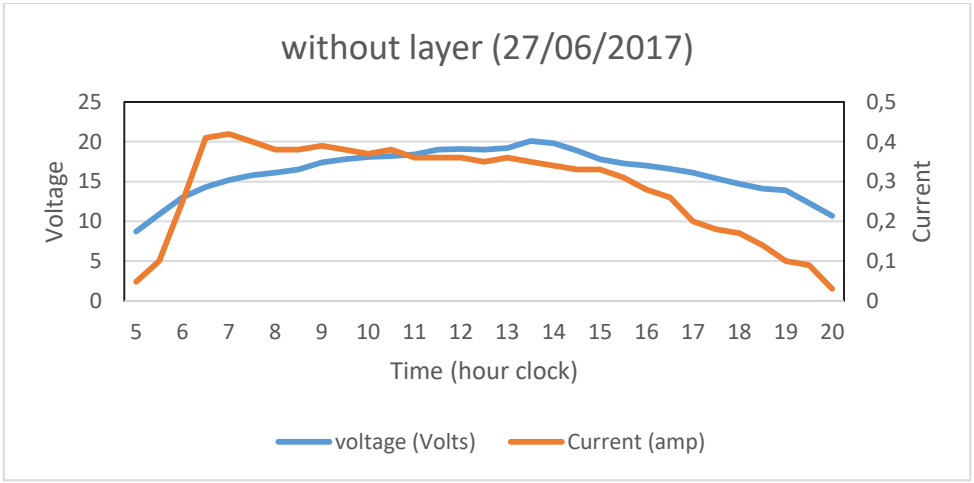

Figure 11. Trend of current and voltage without the transparent layer

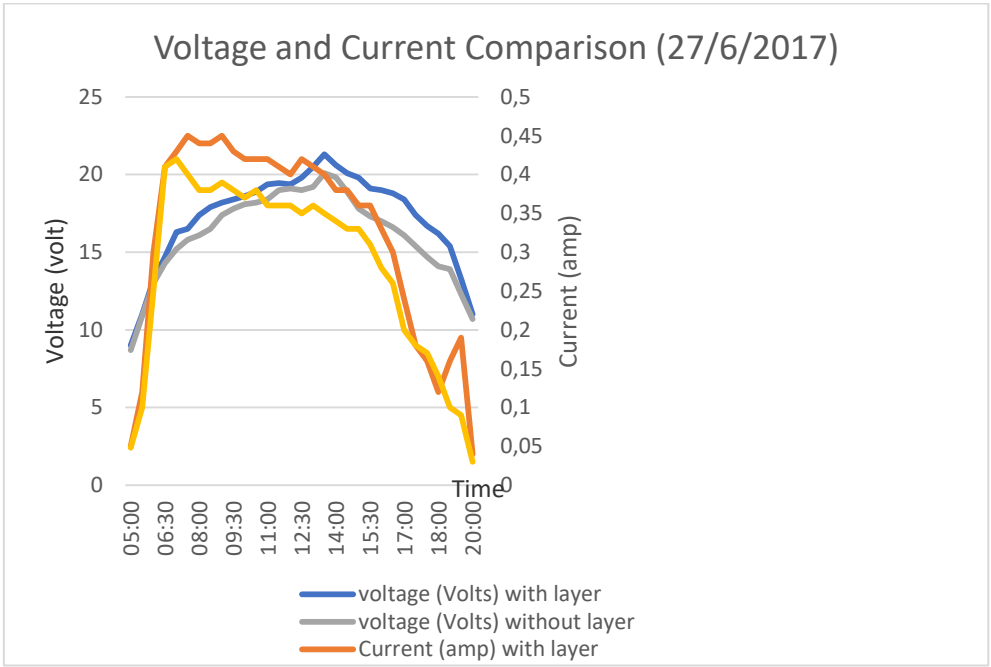

Figure 12. Graphical comparison of voltage and current

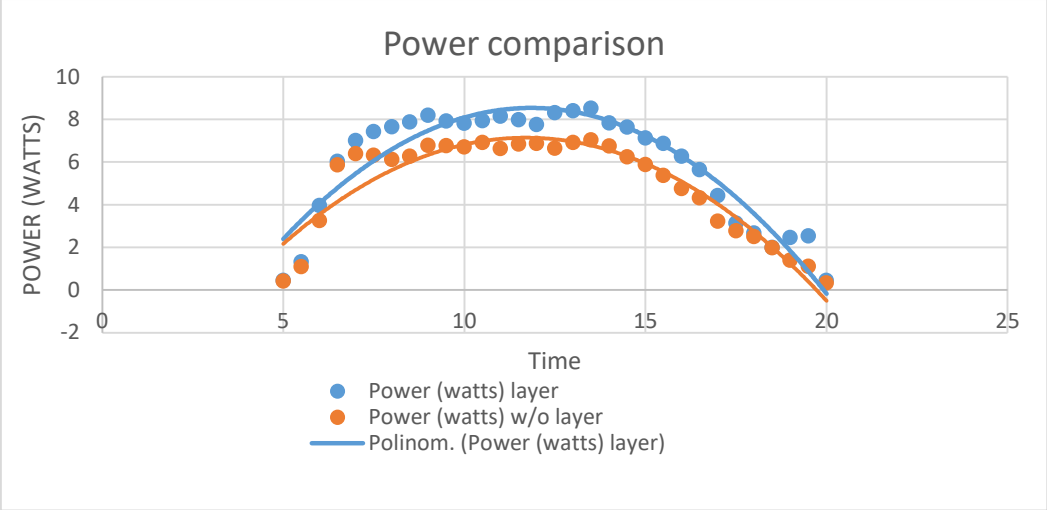

Figure 13. Graph of power for with and without layer

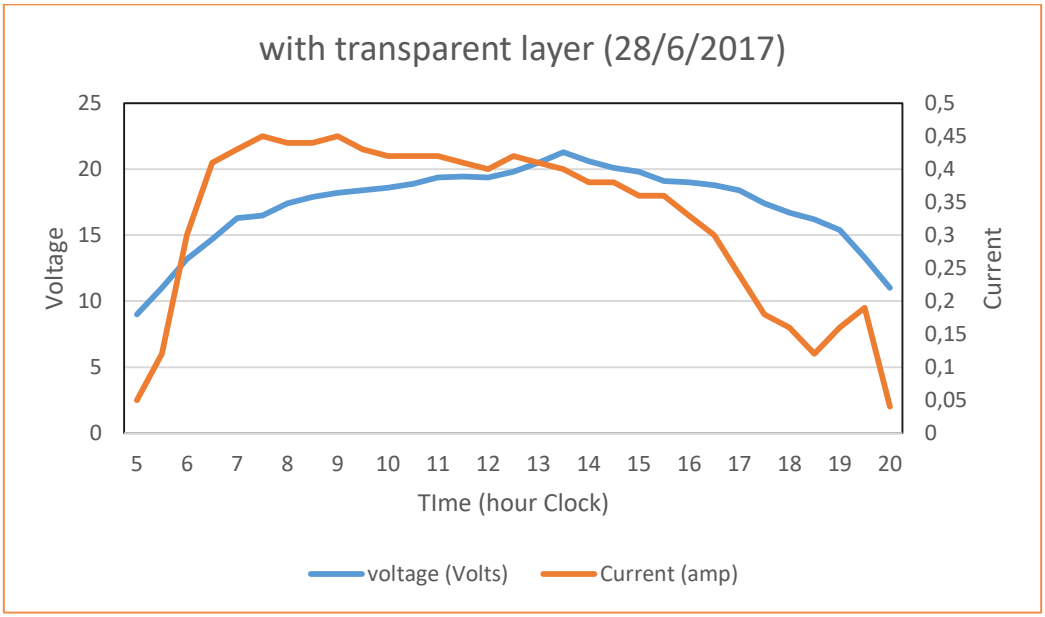

Figure 14. Graph of voltage and current with layer

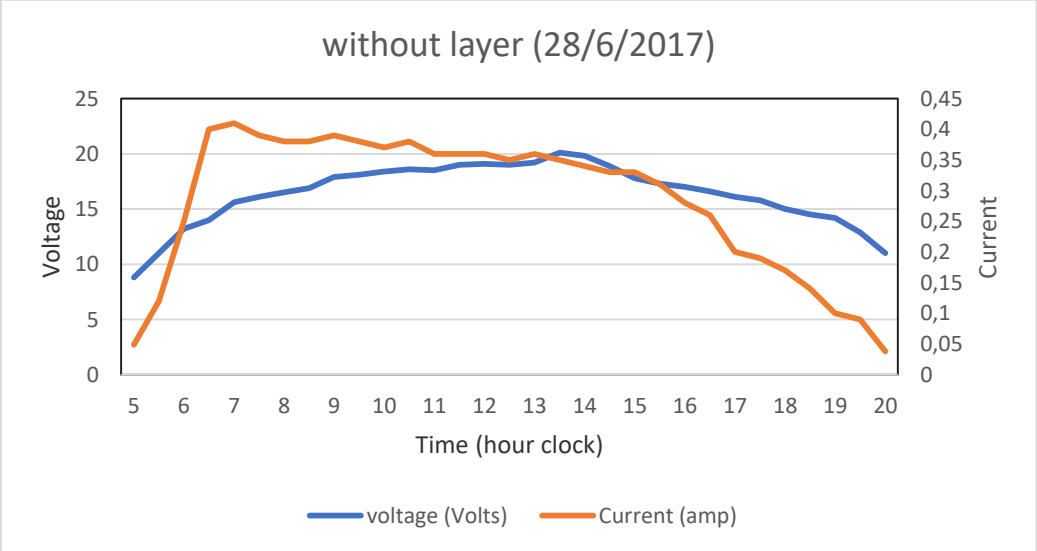

Figure 15. Graph of voltage and current without layer

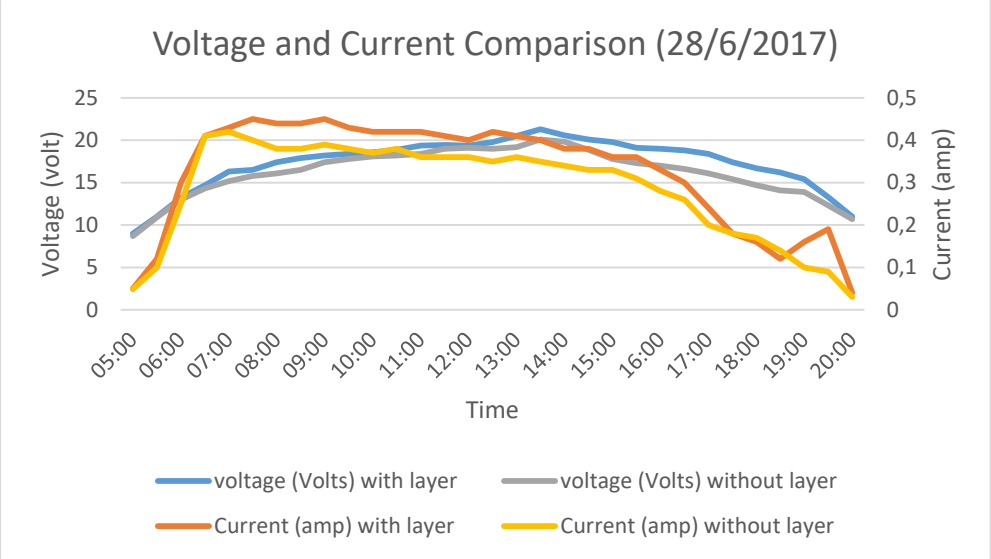

Figure 16. Graphical comparison of current and voltage with and without layer

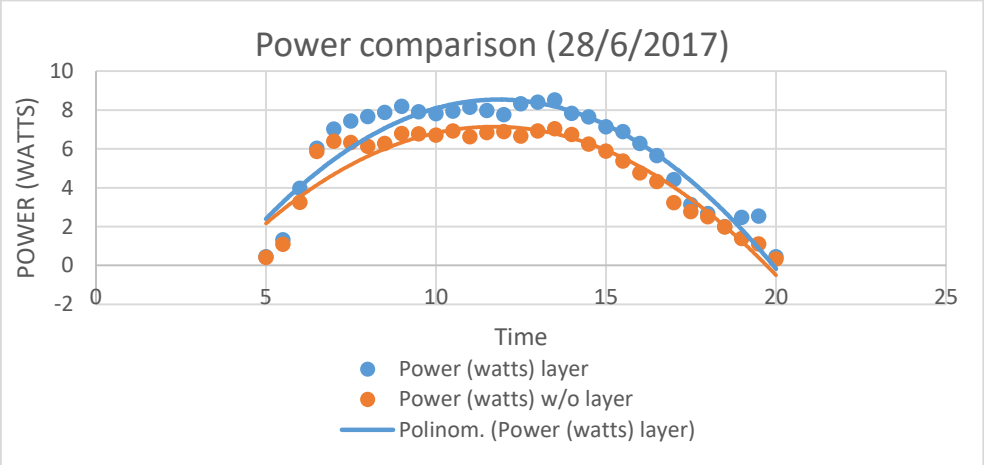

Figure 17. Graphical comparison of power

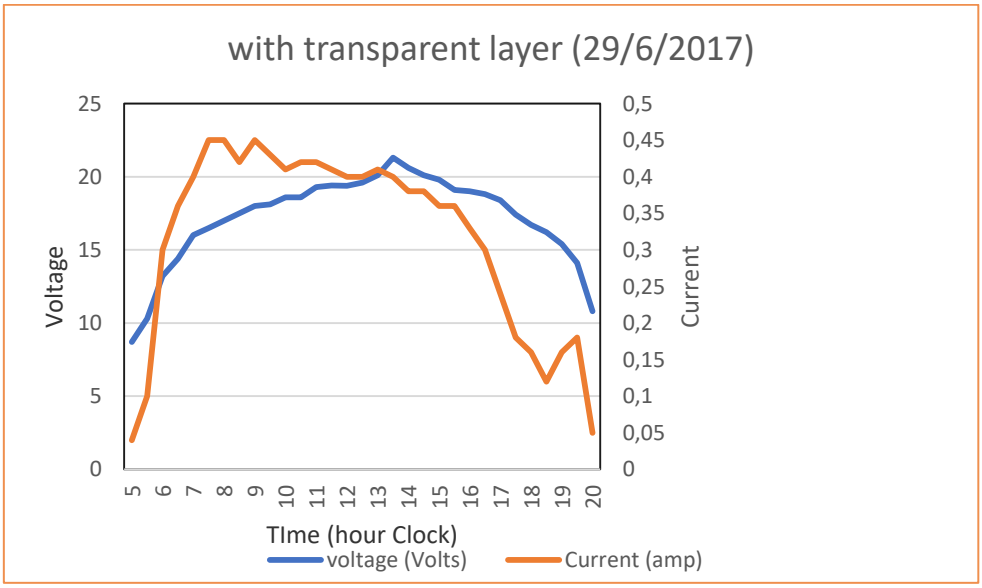

Figure 18. Graphical analysis of voltage and current with transparent layer

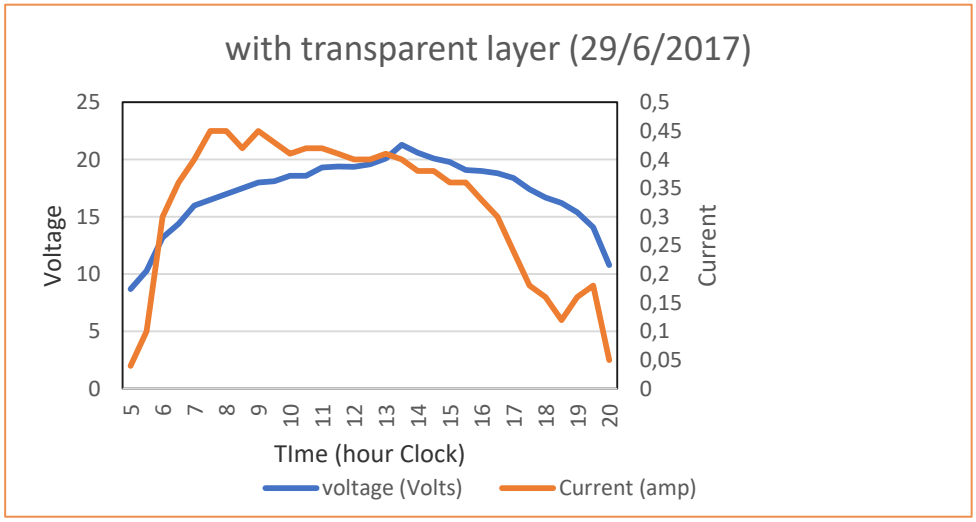

Figure 19. Graphical with transparent layer

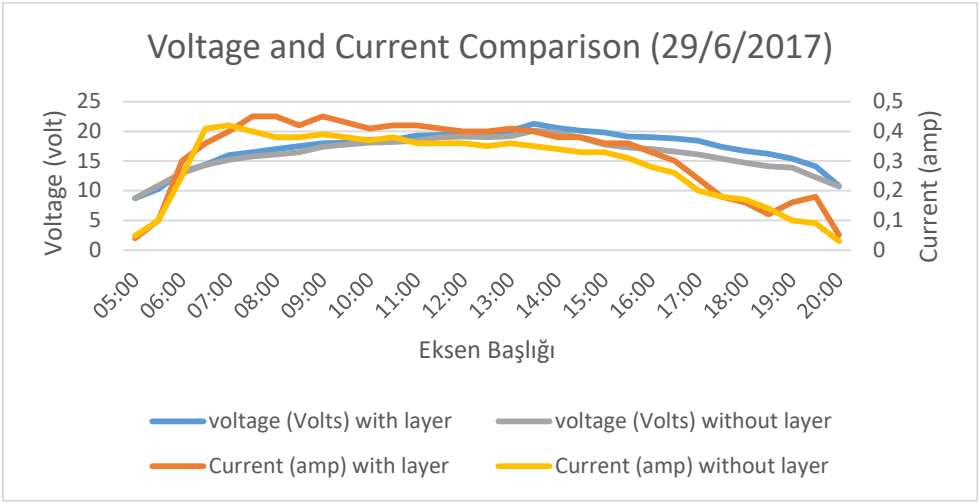

Figure 20. Graphical comparison of current and voltage with and without layer

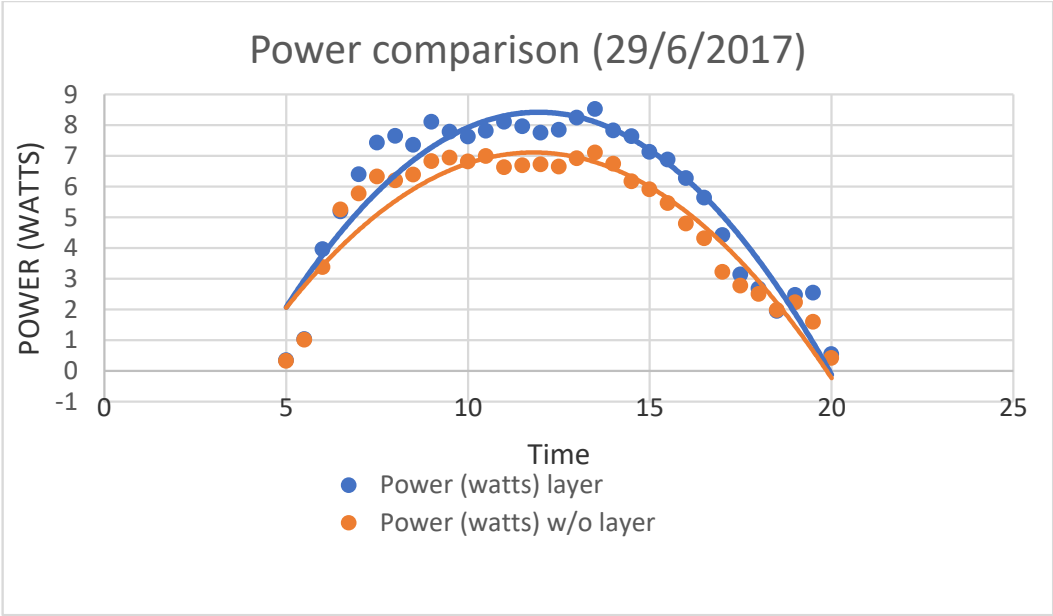

Figure 21. Graphical comparison of power with and without layer

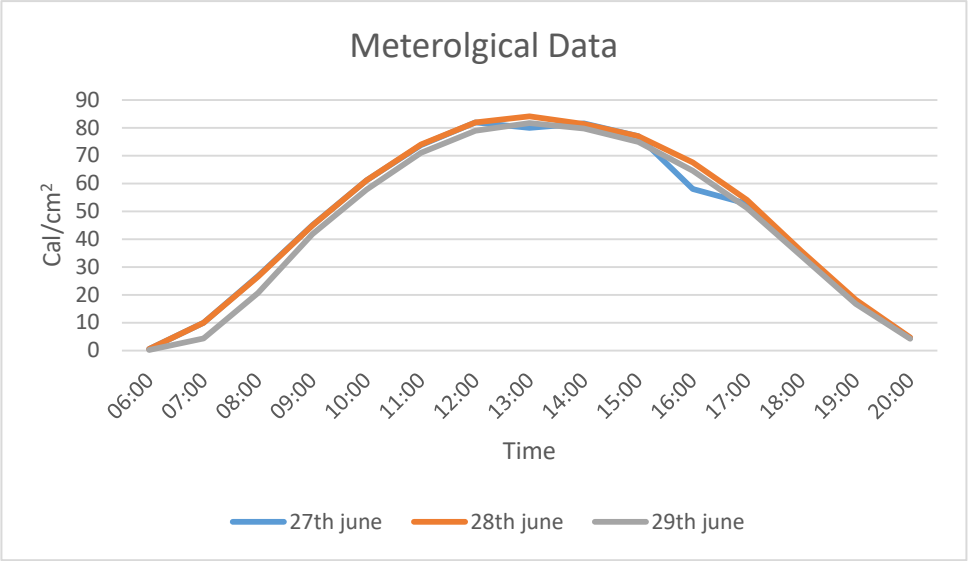

Figure 22. Graphical analysis of meteorological data

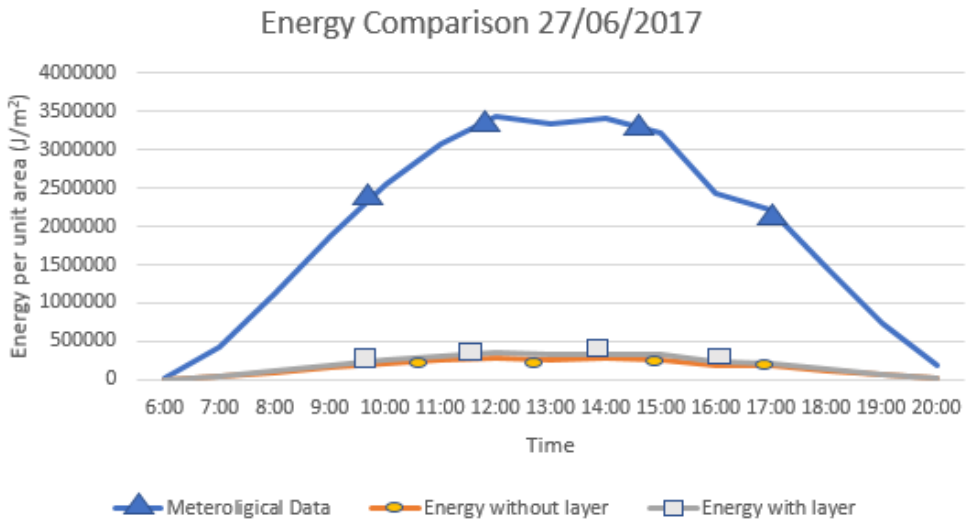

Figure 23. Graphical analysis of meteorological data and power reading

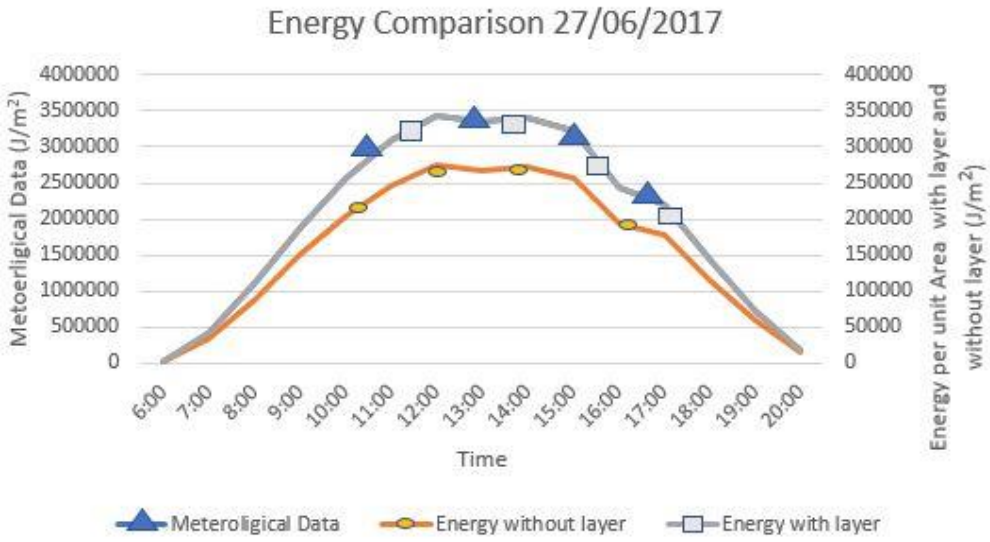

Figure 24. Graphical analysis of meteorological data and power reading

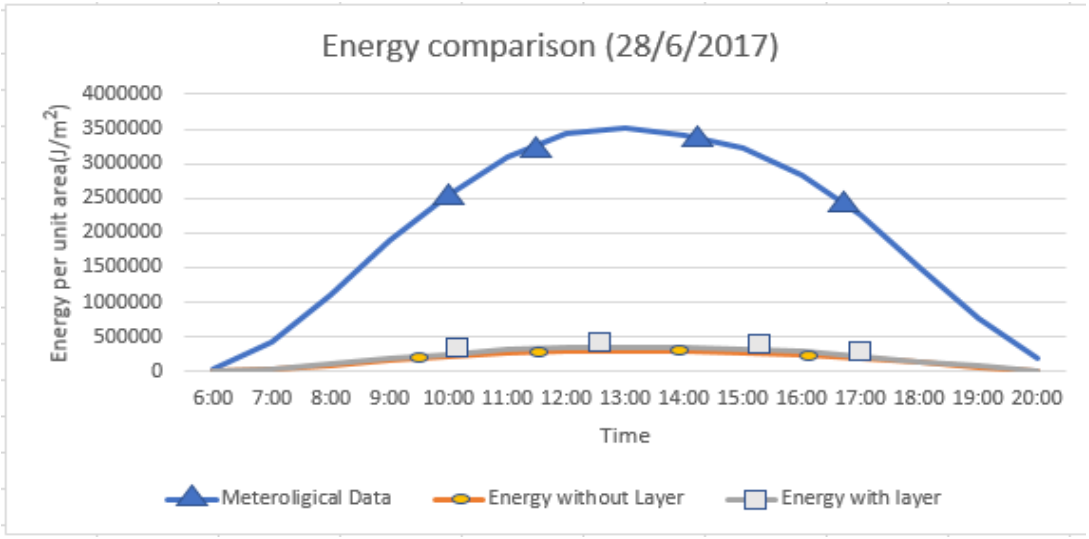

Figure 25. Graphical analysis of meteorological data and power reading

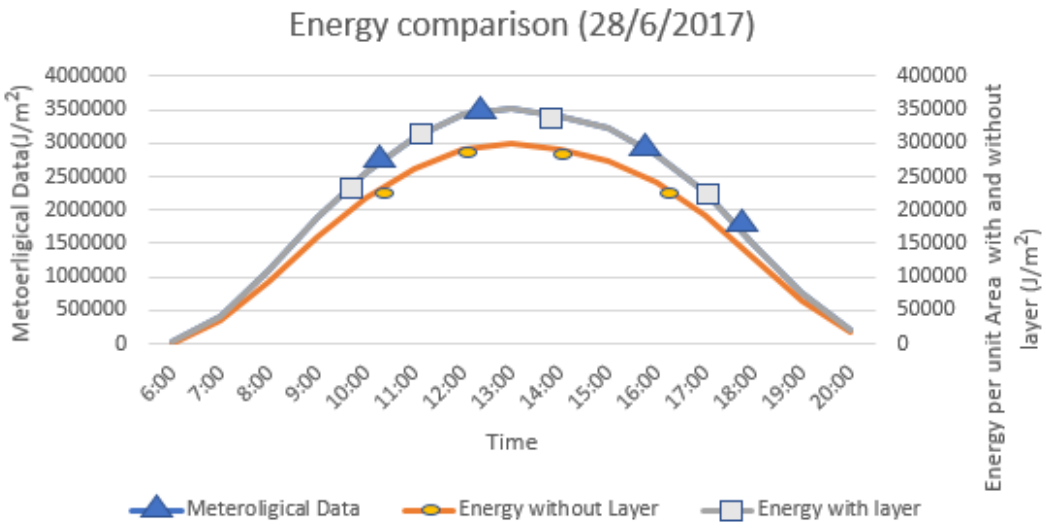

Figure 26. Graphical analysis of meteorological data and power reading

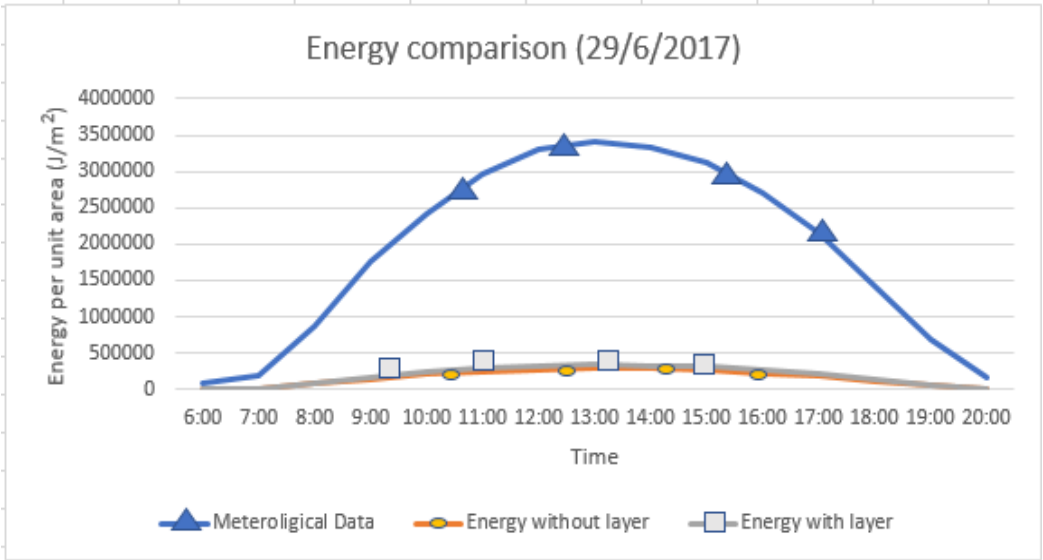

Figure 27. Graphical analysis of meteorological data and power reading

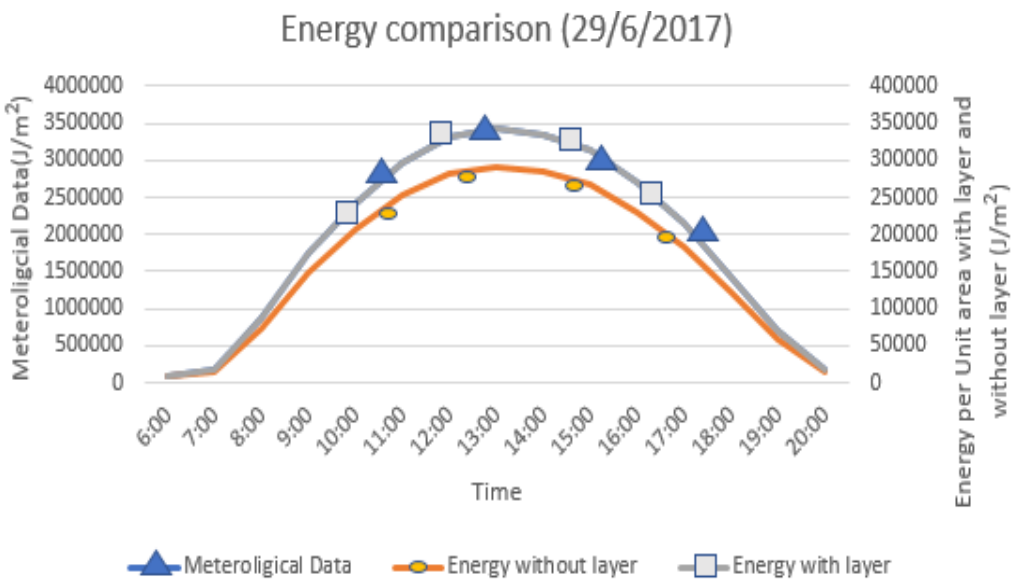

Figure 28. Graphical analysis of meteorological data and power reading

Conclusion

After the extensive investigation, we found that the performance of solar cells is affected by the transparent insulation. As the transparent insulation is put in place, the power output is observed to increase compared to non-insulated solar cell. It is observed that the difference between the metrology data and solar cell was 10 times. The world is rapidly gravitating towards renewable energy applications. Therefore, any technology such as transparent or translucent insulation materials which seeks to improve renewable energy harvesting and utilization is greatly welcomed. This reduces the use of fossil fuels and thereby minimizes the destruction of the environment. Transparent or translucent insulation materials are a new class of materials that are now in development and in some instances already on the market. They may have important applications in improving the energy balance of buildings. The definition of such a material is that it has a high transmission of solar radiation and good thermal insulation qualities. For future recommendations, the effect of temperature and the effect of resistance must take into account for taking solar readings and the insulation reading must be recorded in a controlled temperature system. As the values are recorded manually the chances of human error increases so to avoid such a scenario a continuous data logger can be used to record values on every instance.

Scientific Ethics Declaration

The authors declare that the scientific ethical and legal responsibility of this article published in EPSTEM journal belongs to authors.

Acknowledgements or Notes

This article was presented as an oral presentation at the International Conference on Technology, Engineering and Science (www.icontes.net) held in Antalya/Turkey on November 16-19, 2022.

References

Finch, A. (2003, December 5). *Light generated current*. Retrieved from http://www.pveducation.org/pvcdrom/light-generated-current

Happold, B. (2022). Transparent insulation. *Designing Building the Consturction Wiki.*

Khoja, A. (2013, April 4). *Seminar report on suratgarh super thermal power station*. Retrieved from https://www.slideshare.net/mahendrakhoja33/ashok1111

Maxwell, G. (2011, July 5). *Solar cell structure*. Retrieved from http://www.pveducation.org/pvcdrom/solar-cell-structure

Miller, D. (2013, May 13). *Solar level*. Retrieved from http://solarlove.org/how-solar-cells-work-components-operation-of-solar-cells/

Author Information

Lida Ebrahimi Vafaei
Near East University
Nicosia Mersin, Cyprus
Contact e- mail:*lida.ebrahimivefaei@neu.edu.tr*

To cite this article:

Ebrahimi-Vafaei, L. (2022). Comparison of transparent insulated and non-insulated solar cell *The Eurasia Proceedings of Science, Technology, Engineering & Mathematics (EPSTEM), 21*, 96-109.

The Eurasia Proceedings of Science, Technology, Engineering & Mathematics (EPSTEM)
ISSN: 2602-3199

The Eurasia Proceedings of Science, Technology, Engineering & Mathematics (EPSTEM), 2022

Volume 21, Pages 110-115

IConTES 2022: International Conference on Technology, Engineering and Science

Analysis of Eye Movements with 2D Images Obtained by EOG Signals

Yurdagul KARAGOZ-SAHIN
Turkcell Technology

Mehmet Recep BOZKURT
Sakarya University

Elcin KILIC
Erzincan Binali Yildirim University

Abstract: EOG signals are used for diagnosing of various eye diseases and dysfunctions and eye movement monitoring in neurological disorders. It has also been used as a source signal for various electronic systems and human-machine interfaces, especially in recent years, since the movements of the eye in the horizontal and vertical axis and blinking movements can be detected by EOG. In using EOG signals as source signals, it is necessary to analyze this signal and use various features extracted from the signal. In this study, EOG signals from one of the authors were used with the Biopac MP30 device within the scope of the Sakarya University Electrical and Electronics Engineering, Biomedical Laboratory course. EOG signs were used in four classes looking up, down, right and left. Scalogram matrices are extracted for each movement in the EOG signals with the continuous wavelet transform. As a result of the imaging of the scalogram matrices, it was seen that there were significant differences in the images of the four classes. It is predicted that the results of the analysis made on the images can improve the accuracy rates in classification systems according to one-dimensional analysis methods when used together with expert systems.

Keywords: Electro-oculography, Medical signal processing, Signal classification, Scalogram computation

Introduction

Electrooculogram (EOG) is an electrophysiological measurement method that measures the available resting electrical potential between the cornea and Bruch's membrane. The movements of the eyeball in the horizontal and vertical axes and the blinking movements can be distinguished on the EOG marks. This relationship between EOG signs and eyeball movements has been the source of many studies.

Electooculogram is a biological signal of electrical origin resulting from hyperpolarization and depolarization between eye movements and cornea-retina. Since eye movements act as dipole sources, they can be monitored and measured as vector moments. The amplitude of the raw EOG signal is 50-3500 μV, and the frequency band is between 0 -100Hz. EOG is measured with electrodes placed around the eyes. Electrodes are placed on the right and left of the eye as a horizontal channel, above and below the eye as a vertical channel, and on the forehead as a reference point. There is no potential difference between the electrodes when the eyes are at rest. Moving the eye to the right becomes more positive compared to the other electrode and more negative when moving to the left. An amplitude changes of 1 degree 14, 16μV in horizontal movement, and 14μV in vertical movement of the eye occurs. (Karagoz, Y., 2019)

In a study, they tried to detect four basic directional movements with the Neuro-Fuzzy model, an artificial intelligence technique; within this scope, a fuzzy neural controller with two inputs and one output is designed.

After the fuzzification process, the inputs are trained with artificial neural networks. Finally, they made a performance analysis and achieved 98% success (Erkaymaz et al., 2015). In another example, EOG signals are depurated of noise with the pre-threshold filtering algorithm, and horizontal and vertical movements are used as input to the classifier. In the system developed with artificial neural networks, statistical accuracy and confusion matrix analyzes were made, and a performance of 94% levels was obtained (Erkaymaz et al., 2015). In another study, a system for estimating gaze direction was designed using EOG signals. In this system, after applying a Butterworth filter and Bessel filter to the EOG signals, framing and normalization are to make the signals easier to classify. After the features were determined, they were classified with the Back Propagation Neural Network, and 96% success was achieved at the point of detection of different directions (Bei et al., 2016). Another study proposes a system to detect eye dystonia by eye movement analysis. The designed system is aimed at counting the number of blinks for a specific time interval and to determining the risk of eye dystonia. After EOG signals are acquired, blinks are classified using the combination of the Radial Fundamental Function (RBF) kernel, the Support Vector Machine (SVM) classifier, and the Feedforward Neural Network classifier, Wavelet coefficients, Autoregressive (AR) parameters, and Power Spectral Density and Hjorth parameters. A maximum average accuracy of 95.33% over all classes and participants is obtained using the RBF-SVM classifier with a feature field of AR parameters of order 5 and PSD taken together (Banerjee et al., 20). In another study, wavelet filtering and normalization are performed after EOG signals are obtained, and then the signals are separated by discrete wavelet transform. After the signals were processed, they were classified with the Support Vector Machine to detect four main directions as right, left, up, and down, and 93.8% accuracy in horizontal eye movements and 86.3% accuracy in vertical eye movements was obtained (Li et al., 2018). In another study, the max and min peaks of the signals obtained with right, left and two blinks were determined. After the peaks were detected, they were classified with the k-NN algorithm, and the highest accuracy rate has been obtained when k=3 (Vahdani-Manaf & Pournamdar, 2017). Feature extraction is an essential step of signal processing. Extraction from the EOG signals in the time domain was done, and classification performances have been tested with feature reduction methods. In one study, the number of features was reduced with f-score and, 97% accuracy of classification was achieved using selected features (Zengin et al., 2019).

In this study, using EOG signals as source signals, 2-dimensional scalogram graphics were created to be input to the deep learning system in a study that will be designed as a brain-computer interface for paralyzed patients. The EOG data on the horizontal and vertical axes were first filtered, then split into windows that would contain only one eye movement. Continuous wavelet transform scalogram matrices were obtained from these single motion data. By showing the scalogram matrices as two-dimensional graphs, distinctive differences were observed in the graphs of looking right and left on the horizontal axis and looking up and down on the vertical axis. It has been seen that scalogram graphs are suitable for use in deep learning by generating source signals for BCI from EOG signals.

Method

Data Collection

In this study, EOG signals from one of the authors were used with the Biopac MP30 device within the scope of Sakarya University Electrical and Electronics Engineering, Biomedical Laboratory course. The Biopac MP30 is an electrically isolated 4-channel data acquisition unit designed for physiological measurements. It has different presets customized for different physiological measurements and filters suitable for the sign to be measured. This data collection device is used by connecting to a computer and the data is saved to the computer. EOG marks are recorded on the horizontal and vertical axis. There are 2 classes on each axis, a total of 4 classes. Right and left gaze on the horizontal axis and up and down gaze on the vertical axis are considered separate classes. The data obtained with the Biopac MP30 device were properly recorded and the data processing steps were performed in the Matlab program.

Data Processing

All data processing steps were performed using Matlab 2021a program licensed by Sakarya University. The obtained data were first preprocessed, then continuous wavelet transform was performed and as a result scalogram matrices were obtained. Data processing is completed by displaying the scalogram matrices as two-dimensional graphics. Since the Biopac MP30 device has preset filters for the EOG mark, extensive filtering was not required. An average moving filter was used to make the sign smoother. Data files containing more than

one motion sign were divided into parts to contain a single motion. This process was performed manually as the data were not very large. With these processes, the preprocessing step was completed.

Continuous Wavelet Transform

The natural state of signals is often non-stationary. In this respect, it is important to examine non-stationary signals in many different disciplines. Wavelet analysis has found broad scope in the study of non-stationary signals (Newland, 2012). It is widely used in fields such as data compression (Vetterli & Jelena, 1998) and biomedical engineering (Akay, 1998 and Carmona et. al.,1995).

Similar to the Fourier transform, in the wavelet transform, a function called the main wavelet is the window, but this main wavelet is scaled and translated during the transform process. Scaling corresponds to the expansion and contraction of the wave, and translation corresponds to the displacement of the wave in the time axis (Ari et al., 2008). Since the width of window function, which remains constant throughout the Fourier transform, changes continuously in the wavelet transform, the resolution of both the time and frequency domains increases. In this respect, the wavelet transform is superior to the Fourier transform.

The most important parameter of the wavelet transform is the wavelet. The function of the window function in the Fourier transform is performed by the main wavelet functions in the wavelet transform. For a function to be a wavelet depends on the condition that its duration is limited and its mean value is zero. Therefore, the wavelet function should oscillate in the positive and negative directions of the amplitude axis and this oscillation should end by sitting at zero on the amplitude axis as it progresses in the time axis. A normal wavefunction such as sine and cosine oscillate along the amplitude axis but has infinite duration. Therefore, wave and wavelet are different concepts. There are many main wavelets with different properties and uses. The term wavelet is expressed in the sense of a small wave. The smallness here can be defined as the window function of a certain length. The main wavelet is a prototype, and when considered qualitatively, it should have a real-valued function that satisfies the following two conditions.

$$\int_{-\infty}^{+\infty} \psi(x)^2 dx = 1 \tag{1}$$

$$\int_{-\infty}^{+\infty} \psi(x) dx = 0 \tag{2}$$

Some main wavelet functions used in wavelet transform are given in Figure 1. As can be seen in the figure, the main wavelets oscillate in the amplitude axis and settle to zero.

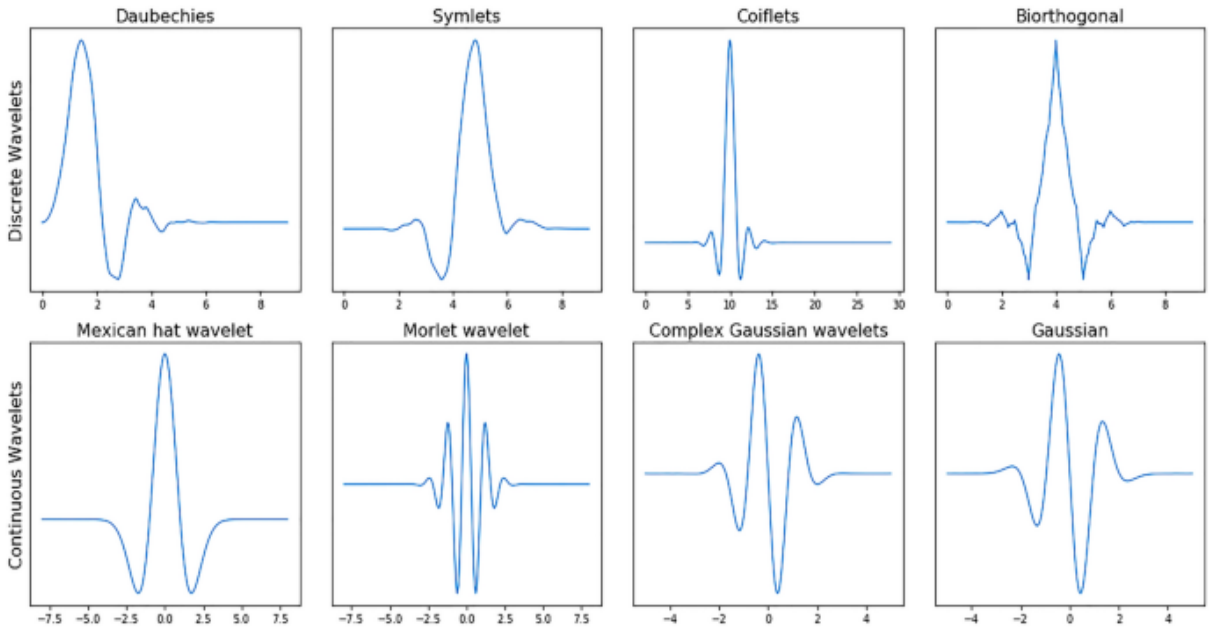

Figure 1. Sample wavelet functions.

The continuous wavelet transform (CWT) is obtained by shifting the wavelet function and multiplying it by a scale, then summing over the time domain and is calculated as follows (Ari et al., 2008).

$$SDD_{(s,\tau)} = \int_{-\infty}^{+\infty} g(t)\psi(x)^*_{(s,\tau)}(t)dt$$

*: Kompleks eslenik
$g(t)$: donusumu yapilacak fonksiyon
$\psi(x)^*_{(s,\tau)}(t)dt$: Dalgacik ya da ana dalgacik fonksiyonu
τ : Kaydirma Parametresi
τ >0: zaman ekseninde saga dogru kayma,
τ <0: zaman ekseninde sola dogru kayma
s: Olcek Parametresi
(s>1: zaman ekseninde fonksiyon genisler ve genligi duser)
(s<1: zaman ekseninde fonksiyon daralir ve genlik buyur)
(s<0: t=0 noktasina gore simetri alinir)

Wavelet analysis, which eliminates the problem of time information loss in the Fourier transform, can detect the times and the amplitudes of all frequency components in a signal. Because of these advantages, wavelet analysis is widely used. In this study, scalogram matrices obtained by continuous wavelet transform were used. Since the continuous wavelet transform has the ability to represent a signal in the time-frequency domain, a 1-dimensional signal can be represented in 2-dimensional at various scales. As a result of this process, the signal is obtained in an expanded and scaled form (Acharya et al., 2017).

With the help of continuous wavelet transform, 2-dimensional Scalogram image matrices for 4 different classes of EOG signals were obtained. These images have been resized to 128x128 pixels. In the resulting Scalogram matrices, the x-axis represents the translational shift along the time-axis and the y-axis represents the scaling factor of the wavelet. For this study, different wavelet functions were tried and when the images obtained for the "Coiflet 1" wavelet were examined, it was seen that there was a significant difference between the classes. With this study, Scalogram images obtained from EOG signs can be used to distinguish classes.

Results and Discussion

This study was carried out as a preliminary study of a deep learning-based classification design. In the study, EOG sign was recorded for a total of 4 movements from 2 movements in the horizontal and vertical axes. These signs were filtered with the Moving Average filter and windowed manually. Scalogram matrices were created and plotted by using different wavelet functions on the windowed signals. Among the different wavelet functions, the most distinctive graphs are obtained with the Coiflet-1 wavelet. In Figure.2, scalogram graphs created with Coiflet-1 wavelet are given for 4 different classes. In this way, the distinctiveness of scalogram graphs is shown by obtaining different graphs between different classes.After this stage, the classification process can be done by using the scalogram matrices obtained as input to various classification algorithms. The advanced phase of this study is planned as deep learning. In deep learning, high-performance results are obtained against two-dimensional graphics inputs.

A large number of EOG samples should be taken for classification processes and the system should be trained with a large number of inputs. The use of more professional devices in the acquisition of EOG data and the base correction and filtering of the received signals will increase the success rate. EOG signs taken from different people can be evaluated in a pool and a system that will give accurate results when applied to different people can be created. The next step after the classification is to establish a BCI that the person can manage with eye movements using these classes.

Conclusion

Within the scope of this study, EOG data were recorded in 4 different classes (class 1, class 2, class 3 and class 4) against the movements of the eyeball in the horizontal and vertical axis. These data were filtered by the Moving Average filter and windowed manually. Then, continuous wavelet transforms with different wavelet

functions is applied to these windows. As a result of these processes, scalogram matrices and related graphics were obtained. When the results of different wavelet functions were compared, it was seen that the discrimination of the scalogram matrices obtained as a result of the transformation performed with the Coiflet -1 wavelet was higher. The scalogram graphs obtained by using the Coiflet -1 wavelet are given in Figure.2. The results show that the scalogram graphs obtained from the EOG signs are distinctive for the classes. The system can be made more successful with the suggestions given in the discussion section. This system, which was designed as a preliminary study of a classifier design based on deep learning, has achieved the desired success.

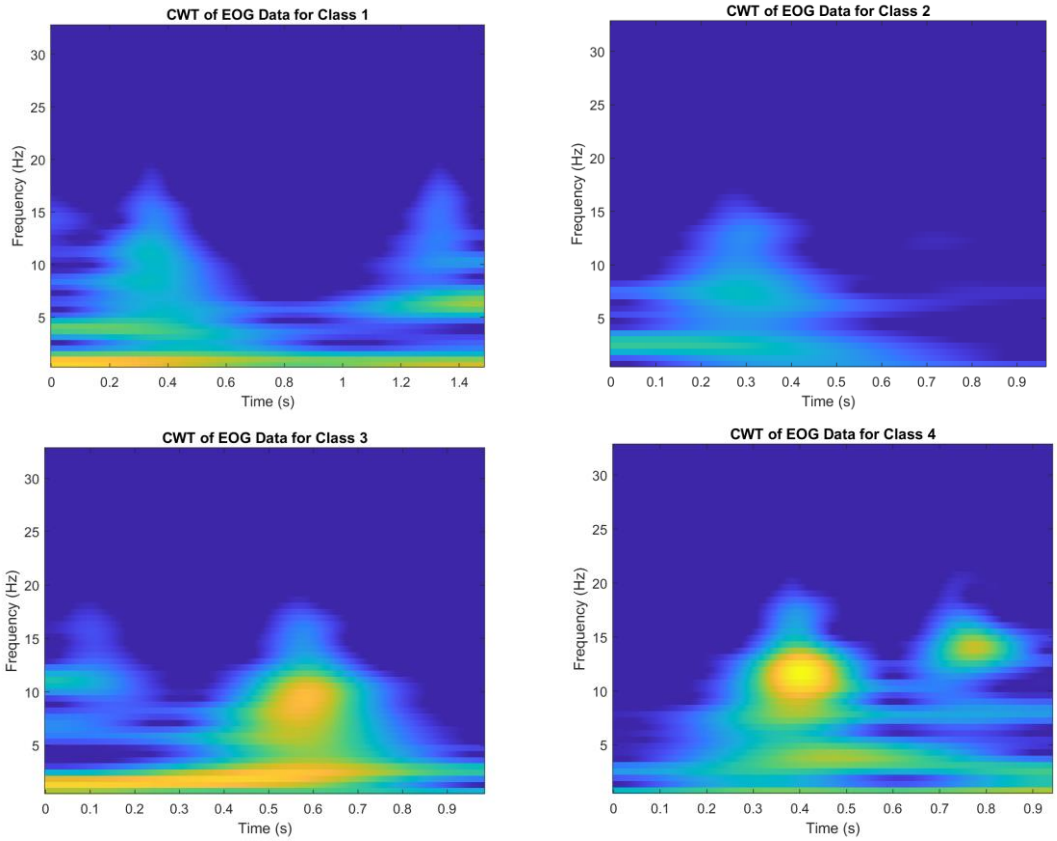

Figure. 2. The scalogram graphs obtained by using the Coiflet -1 wavelet

Scientific Ethics Declaration

The authors declare that the scientific ethical and legal responsibility of this article published in EPSTEM journal belongs to the authors.

Acknowledgements or Notes

* This article was presented as an oral presentation at the International Conference on Technology, Engineering and Science (www.icontes.net) held in Antalya/Turkey on November 16-19, 2022.

*We thank Turkcell corporation for financing the presentation of this study. We also thank Sebahattin Babur, a lecturer in Turk-Alman University, for his contributions.

References

Acharya, U. R., M., Fujita, H., Sudarshan, K. V., … Chua, C. K., (2017). Automated characterization of coronary artery disease, myocardial infarction, and congestive heart failure using contourlet and shearlet transforms of electrocardiogram signal. *Knowledge-Based Systems.* 156–166.

Akay, M. (1998). *Time frequency and wavelets in biomedical signal processing*. IEEE press series in Biomedical Engineering.

Ari, N., Ozen, S. & Colak, O. H. (2008). *Dalgacik teorisi.* Palme Yayincilik, Ankara.

Banerjee, A., Pal, M., Tibarewala, D. N., & Konar, A. (2015). Electrooculogram based blink detection to limit the risk of eye dystonia. *Eighth International Conference on Advances in Pattern Recognition*, C

Bei, Y., Sichun, Y., Mengke, L., & Xiangkun, L., (2016). Gaze estimation method based on EOG signals. *Sixth International Conference on Instrumentation & Measurement, Computer, Communication and Control*, 443-446.

Carmona, R. A., Hwang W. L. & Frostig, R. D., (1995). Wavelet analysis for brain-function imaging. *Transactions on Medical Imaging*. 556-564.

Erkaymaz, H., Ozer M., & Kaysa, C., (2015). EOG controlled direction detect system with neuro-fuzzy approach. *19th National Biomedical Engineering Meeting, 1-4*

Erkaymaz, H., Ozer M., Kaya, C., & Orak. M., (2015). EOG based intelligent direction detect system with pre-filtering algorithm. *23nd Signal Processing and Communications Applications Conference*, 1228 - 1231

Fidan, H. (2006). *Dalgacik donusumu teknigi ile motor ariza tespiti*. Diss. SDU Fen Bilimleri Enstitusu.

Hanteh, M., Rezaifar, O. & Gholhaki, M., (2021). Selecting the appropriate wavelet function in the damage detection of precast full panel building based on experimental results and wavelet analysis. *Journal of Civil Structural Health Monitoring volume*. 1013–1036. https://www.biopac.com/wp-content/uploads/MP30-35-spec.pdf Accessed: November 6, 2022

Karagoz, Y., (2019). *Electrooculogram based human-machine interface application*. Sakarya University – 591126.

Li, T., Yang, J., Bai, D. & Yang, Y. (2018). A new directional intention identification approach for intelligent wheelchair based on fusion of EOG signal and eye movement signal. *International Conference on Intelligence and Safety for Robotics*, 470-474.

Newland, D. E. (2012). *An introduction to random vibrations, spectral & wavelet analysis*. Dover Publications.

Vahdani-Manaf, N. & Pournamdar, V., (2017). Classification of eye movement signals using electrooculography in order to device controlling. *4th International Conference on Knowledge-Based Engineering and Innovation.* 0339 – 0342.

Vetterli, M. & Jelena, K. (1998). *Wavelets and subband coding.* Vol. 995. Englewood Cliffs: Prentice Hall.

Zengin, I., Bozkurt, M. R. & Ucar, M. K., (2019). Determining effective features to use the EOG sign as a source sign. *Sakarya University Journal of Computer and Information Sciences.* 134-144.

Author Information

Yurdagul Karagoz Sahin
Turkcell Technology
Maltepe, Istanbul, Turkey
Contact e-mail: *yurdagul.sahin@turkcelll.com.tr*

Mehmet Recep Bozkurt
Sakarya University
Serdivan, Sakarya, Turkey

Elcin Kilic
Erzincan Binali Yildirim University
Erzincan, Turkey

To cite this article:

Karagoz-Sahin, Y., Bozkurt, M. R., Kilic, E. (2022). Analysis of eye movements with 2D images obtained by EOG signals. *The Eurasia Proceedings of Science, Technology, Engineering & Mathematics (EPSTEM), 21,* 110-115.

The Eurasia Proceedings of Science, Technology, Engineering & Mathematics (EPSTEM)
ISSN: 2602-3199

The Eurasia Proceedings of Science, Technology, Engineering & Mathematics (EPSTEM), 2022

Volume 21, Pages 116-124

IConTES 2022: International Conference on Technology, Engineering and Science

Effect of Protan Recoloring Algorithm on Inserted Watermark in Presence of the Superimposed AWGN

Zoran MILIVOJEVIC
Academy of Applied Technical and Preschool Studies

Bojan PRLINCEVIC
Kosovo and Metohija Academy Division Zvecan

Abstract: In this paper, the effect of the protan recoloring algorithm on an image with an inserted watermark is analyzed. In addition, the effect of degradation of the quality of the recolored image due to the insertion of watermarks and superimposed AWGN was also analyzed. In the first part of the paper, the effect of color vision deficiency, as a consequence of anomalies in L cones, which is designated as protanomaly (protanopia), is described. People with protanopia do not see a wide range of colors because the colors from the L channel are missing. After that, the recoloring algorithm, which performs recoloring of the image, so that, in protan persons, the visible spectrum of colors is expanded, is described. Then, the algorithm for inserting a watermark, in order to protect copyrights, is described. In the second part of the work, the Experiment, in which the quality of the recoloring image was tested, as well as the quality of the extracted watermark, was described. The results of the experiment are shown with pictures and tables. By applying a comparative analysis of the results of the experiment, using objective (MSE, PSNR, NC and SSIM) and subjective (visual inspection) methods, the insertion factor of the watermark, α, which preserves the quality of the recoloring image as well as the quality of the extracted watermark, was determined. Visual inspection determined the SNR at which visible image degradation and watermarks occur.

Keywords: Trichromacy, Protanomaly, Image recoloring, Watermark, SVD algorithm

Introduction

Many algorithms in digital image processing are conceptually designed in accordance with the Human Visual System (HVS). The first organ in the HSV is the eye. Therefore, for quality digital image processing, it is necessary to have a good understanding structure of the human eye. It is very important to understand the distribution and functions of photoreceptors on the retina. The photoreceptors are a special type of neurons, which are sensitive to the effect of the light. The wavelength range of the light, that HSV can detect, is λ = 370 - 720 nm (Curcio et al., 1990). According to the spectral characteristics, the photoreceptors can be divided into two groups: a) sensitive to light intensity (luminance) and b) sensitive to the quality, that is, the color of the light. The photoreceptors that are sensitive to the intensity of the light, according to their physical appearance, are in the form of rods. The human eye has about 120,000,000 rods. Functionally, their role is to enable so-called black-white vision. They are extremely sensitive to light intensity and enable vision even at very low intensities (night vision). The photoreceptors that are sensitive to the color of the light have the physical shape of cones. The human eye has about 6,000,000 cones. The cones are mostly concentrated in the central parts of the retina. The cones are sensitive to the color of light, especially at higher brightness levels. From the point of view of spectral sensitivity, there are three types of the cone. The first type are the cones that are sensitive to light in the long wavelength range, $L(\lambda)$. In the L range, the red color, R, is dominant. Another type of the cones are sensitive to light in the medium wavelength range, $M(\lambda)$. In the M range, the dominant color is green, G. The third type of the cones are sensitive to light in the range of short wavelengths, $S(\lambda)$. In people who do not have

functional vision problems, rods and all three types of cones function properly. Such people have so-called normal or trichromatic vision (Blake & Sekuler, 2006).

Color is created in the consciousness of the observer, as the brain processes signals from L, M and S cones (Zhenyang et al., 2021). Statistically speaking, over 200,000,000 people around the world have problems with color perception. Color vision deficiency, CVD, occurs when one, two or all types of the cones do not function correctly. CVD can be classified as anomalous type: a) trichromacy (some types of the cones do not function in their visual range, but are shifted to one frequency side), b) dichromacy (with this anomaly there are only two types of the cones, which are capable of perceiving color. The functions of the third type of the cones are completely inactive); and c) monochromacy (none of the cones are active. Only the rods are active and enable black-and-white vision) (Milivojevic et al., 2022). In order to help CVD people see a wider range of the colors in the observed image, it is necessary to perform image pre-processing to correct the types of colors in the image (Nam et al., 2005). This process is, in the scientific literature, called Recoloring (Zhenyang et al., 2021), (Lin et al., 2019).

Intensive exchange of the images over the Internet enables unauthorized use of the images. For this reason, there was a need to protect the Recoloring (RC) image from unauthorized use. One of the ways of copyright protection is to insert watermarks into the image. The watermark can be: a) visible and b) invisible. The visible watermark clearly indicates the owner of the image. However, the visible watermark degrades the image quality. The invisible watermark is inserted into the RC image in the transformation domain, and does not perform visible degradation. On the other hand, it is possible to extract it from the RC image, and, in this way, prove the ownership of the image. The paper (Pramoun et al., 2017) describes an algorithm for inserting and extracting watermarks from RC images, which was created for protan CVD people. Protan CVD is an anomaly of the *L* cones such that their spectral sensitivity is sifted in the direction of the spectral sensitivity of the *M* cones. In order to insert the watermarks, using the Block SVD (Singular Value Decomposition) algorithm, the RC image processing is realized in the LMS color space (Pramoun et al., 2018) (Crenshaw, 2014).

In this paper, the effect of the protan RC algorithm on the inserted watermark is analyzed. First, the RC algorithm (Crenshaw, 2014) is described. After that, the modified Block SVD watermarking (Chang et al., 2007) is described. The modification was made by the authors of this paper. The second part of the paper describes an Experiment in which the performance of the Blok SVD watermark was tested on: a) protan RC algorithm, and b) superimposed AWGN. Additionally, the effect of inserted watermark and superimposed AWGN on quality of the RC image was analyzed. The algorithm, according to which the Experiment was carried out, is presented. The Test image, on which recoloring was performed, is *Flowers*. The inserted Watermark was the *Logo* of Academy of Applied Technical and Preschool Studies, Niš, Serbia. The performance of extracted watermark and RC image was tested using: a) objective measures (MSE, PSNR, NC and SSIM), and b) visual inspection. The results of the Experiment are RC image and extracted watermarks. In addition, the numerical results for are shown using graphs. Based on the results, a comparative analysis was performed and conclusions were drawn about the effects of the RC algorithm and AWGN on watermark performance.

Further organization of work is as follows. In Section II, CVD anomalous is presented. In Section III, the Recoloring algorithm for protanopia, is presented. In Section IV, the Watermarking algorithm, is described. In Section V the Experiment, is described. Section VI is the Conclusion.

CVD Anomalous

In people with normal (trichromatic) vision, color images are perceived using all of three types of cones (LMS). In people with color vision deficiency (CVD), some or even all types of cones do not function correctly. According to the type of cones that do not function correctly, CVD is classified as: a) trichromacy, b) dichromacy, or c) monochromacy. CVD trichromacy is an anomaly when one type of the cones does not function correctly. An anomaly in the CVD dichromacy is that one of the tip cones does not work. With CVD monochromacy anomaly, neither type of cones works. Therefore, people with CVD monochromacy see only with rods photoreceptors, that is, they have monochromatic vision (lumination, black-and-white vision). CVD trichromacy and dichromacy, depending on whether the abnormalities occur in *L*, *M* or *S* cones, can be classified as: a) protan, (abnormalities occur in *L* cones), b) deutan (abnormalities occur in *M* cones) or c) tritan (abnormalities occur in *S* cones) defects. Protan, deutan and tritan defects in anomalous trichromacy and dichromacy are called protanomaly (protanopia), deuteranomaly (deuteranopia) or tritanomaly (tritanopia), respectively (Milivojevic et al., 2022).

In fig. 1.a shows the normalized spectral sensitivity of human cone cells of: a) short $S(\lambda)$, b) middle $M(\lambda)$ and c) long $L(\lambda)$ wavelength types. The cones, which have these spectral characteristics of sensitivity, enable normal, that is, trichromatic vision. In the consciousness of the observer, the feeling of the presence of colors from the entire visible spectrum (fig. 1.b) is formed. Protanomaly is an abnormal trichromacy, which is a consequence of the poor functionality of the L cones (Zhenyang et al., 2021). In this case, the spectral sensitivity of the L cones is shifted by $\Delta\lambda$ in the direction of the spectral sensitivity of the M cones. In protan CVD, the spectral sensitivity is $L_a(\lambda) = L_a(\lambda + \Delta\lambda)$, where $\Delta\lambda$ = (0 - 20) nm, that is, protan is 0 - 100%. In fig. 1.c shows the spectral sensitivities of the L cones for 100% protan CVD. The color experience of 100% protan CVD people is shown in fig. 1. d.

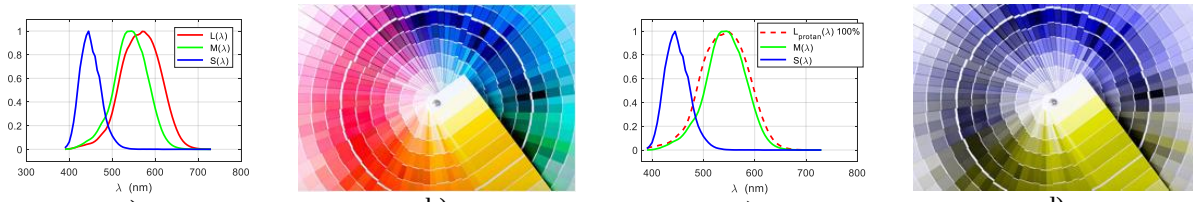

a) b) c) d)

Figure 1. a) Normalized spectral sensitivity of human cone cells of short $S(\lambda)$, middle $M(\lambda)$ and long $L(\lambda)$ wavelength types with normal vision. b) test image Spectrum, c) spectral sensitivity of the L cones at 100% protan CVD, and d) color experience of 100% protan CVD people.

CVD protan people often cannot see all the color details in the image. In order to reduce this discomfort, it is possible to perform color correction (recoloring) in the image so that people with CVD protan problem can see better. Image recoloring is the creation of a different version of the image colors that is more suitable for such people.

Recoloring Algorithm for Protan CVD

In (Crenshaw, 2014) the Recoloring (RC) algorithm for the protanopia CVD class, is described. The RC algorithm is implemented using color transformation in the LMS color space. The RC algorithm is implemented in the following steps:

Input: I - Original image in the RGB color space.
Output: I_{RC} - Recolored image in the RGB color space

Step 1: Image transformation from RGB color space (I_{RGB}) to the LMS color space (I_{LMS}):

$$\begin{bmatrix} L \\ M \\ S \end{bmatrix} = \begin{bmatrix} 17.8824 & 43.5161 & 4.11935 \\ 3.45565 & 27.1554 & 3.86714 \\ 0.0299566 & 0.184309 & 1.46709 \end{bmatrix} \times \begin{bmatrix} R \\ G \\ B \end{bmatrix}, \quad (1)$$

where R, G and B are red, green and blue color components of image I in RGB color space.

Step 2: Simulated color perception of CVD protan people:

$$\begin{bmatrix} L_p \\ M_p \\ S_p \end{bmatrix} = \begin{bmatrix} 0 & 2.02344 & -2.52581 \\ 0 & 1 & 0 \\ 0 & 0 & 1 \end{bmatrix} \times \begin{bmatrix} L \\ M \\ S \end{bmatrix}. \quad (2)$$

where L_p, M_p and S_p are the simulated components in the LMS state space.

Step 3: Error between normal and color-blind perception in LMS color space:

$$\begin{bmatrix} E_L \\ E_M \\ E_S \end{bmatrix} = \begin{bmatrix} L \\ M \\ S \end{bmatrix} - \begin{bmatrix} L_p \\ M_p \\ S_p \end{bmatrix}. \quad (3)$$

Step 4: The errors are redistributed to the other two visible color components, i.e. M and S color components by applying the below transformation.

$$\begin{bmatrix} E_{L\_MOD} \\ E_{M\_MOD} \\ E_{S\_MOD} \end{bmatrix} = \phi \begin{bmatrix} -0.2 & 0 & 0 \\ 0.1 & 1 & 0 \\ 0.1 & 0 & 1 \end{bmatrix} \times \begin{bmatrix} E_L \\ E_M \\ E_S \end{bmatrix}, \quad (4)$$

where E_{L_MOD}, E_{M_MOD}, and E_{S_MOD}, are the portion of error from colors associated with color blind to colors associated with normal perception (Chang et al., 2007), and ϕ is a scalar value between 0 to 1, and is used to vary the chrominance strength.

Step 5: The recolored image (RC image) in the LMS color space is:

$$\begin{bmatrix} L_{p,RE} \\ M_{p,RE} \\ S_{p,RE} \end{bmatrix} = \begin{bmatrix} E_{L\_MOD} \\ E_{M\_MOD} \\ E_{S\_MOD} \end{bmatrix} + \begin{bmatrix} L \\ M \\ S \end{bmatrix}. \quad (5)$$

Step 7: The RC image in the RGB color space is:

$$\begin{bmatrix} R_{re} \\ G_{re} \\ B_{re} \end{bmatrix} = \begin{bmatrix} 0.080944 & -0.130504 & 0.11672 \\ -0.01025 & 0.054019 & -0.11362 \\ -0.00037 & -0.004122 & 0.69351 \end{bmatrix} + \begin{bmatrix} L_{p,RE} \\ M_{p,RE} \\ S_{p,RE} \end{bmatrix} \quad ,(6)$$

where R_{re}, G_{re}, and B_{re} are the colored components in the RGB color space (RC image, I_{RC}).

An example of processing the Test image, which is presented in the RGB color space, using the RC algorithm. The Test image is shown in fig. 2.a. Protan CVD person perceives colors as in fig. 2.b. (BL image, *Step 2*). After color correction, the protan CVD person experiences colors as in fig. 2.c (RC image, *Step 7*). From the described example, it can be concluded that the effect of the image processing using the RC algorithm led to an increased range of color perception.

a) b) c)

Figure 2. a) Test image, b) BL image and c) RC image.

Block SVD Watermarking Algorithm

The Block SVD Watermarking Algorithm is presented in (Chang et al., 2007). It is based on the embedded of one bit of the watermark in one 4 x 4 image block. In this paper, embedding of the watermark is done in a color image. Embedding of the watermark is done in the *M* component of the image in the LMS color space.

Watermark Embedding Algorithm

Input: *I* - image in the RGB color space. *W* - watermark (Mw_m x Nw_m). Insertion factor α.
Output: *Iw* - watermarked image

Step 1: Transformation of image *I* from RGB color space (I_{RGB}) to LMS color space (I_{LMS}).
Step 2: Extracting the *M* component from the image I_{LMS}.
Step 3: The image component *M* is divided into non-overlapping blocks *B* dimension 4 x 4.
FOR $i = 1 : Mw_m$
FOR $j = 1 : Nw_m$
Step 4: Selecting (*i, j*) block, $B_{i,j}$, of the *M* image component.
Step 5: SVD transformation of the block $B_{i,j}$:

$$B_{i,j} = U_{i,j} \times S_{i,j} \times V_{i,j}^T, \qquad (7)$$

where $U_{i,j}$ and $V_{i,j}$ are orthogonal matrices, $U_{i,j} = [u_1\ u_2\ u_3\ u_4]$ and , $V_{i,j} = [v_1\ v_2\ v_3\ v_4]^T$, respectively, while $S_{i,j}$ is a diagonal matrix $S_{i,j} = \text{diag}(\sigma_1, \sigma_2, \sigma_3, \sigma_4)$.
Step 6: Assigning the value $\sigma_{3n} = \sigma_2$.
Step 7: Inserting the bit $W_{i,j}$ of the watermark *W*: $\sigma_{2n} = \sigma_2 + \alpha \cdot W_{i,j}$.
Step 8: Modification of the matrix *S* according to: **IF** $\sigma_1 < \sigma_{2n}$ **THEN** $\sigma_{1n} = \sigma_{2n}$; **ELSE** $\sigma_{1n} = \sigma_1$; **END**, after which the diagonal matrix with watermark bit is matrix $Sw_{i,j} = \text{diag}(\sigma_{1n}, \sigma_{2n}, \sigma_{3n}, \sigma_4)$.
Step 9: Reconstruction of the block with the mark $Bw_{i,j}$:
Step 10: Reconstructing the *Mw* component with the embed watermark $Mw \Leftarrow Bw_{i,j}$.
END *j*
END *i*
Step 11: The reconstructed image with the watermark (Iw_{LMS}) is translated from the LMS color space into the RGB color space (Iw_{RGB}), and the image with the embedded watermark *Iw* is finally obtained.

Watermark Extraction Algorithm

Input: *Iw* - Image with watermark. Mw_m x Nw_m - dimensions of watermark block. α - insertion factor.
Output: *We* - extracted watermark.
Step 1: Transformation of image *Iw* from RGB color space (Iw_{RGB}) to LMS color space (Iw_{LMS}).
Step 2: Extracting the *Mw* component from the image Iw_{LMS}.
Step 3: The image component *Mw* is divided into non-overlapping blocks *Bw*, dimension 4 x 4.
FOR $i = 1 : Mw_m$
FOR $j = 1 : Nw_m$
Step 4: Selecting (*i, j*) block, $Bw_{i,j}$, of the *Mw* image component.
Step 5: SVD transformation of the block $Bw_{i,j}$:

$$Bw_{i,j} = U_{i,j} \times Sw_{i,j} \times V_{i,j}^{T} . \quad (8)$$

Step 6: The values of the watermark bit, $We_{i,j}$, which is extracted from the block $Bw_{i,j}$ are determined according to **IF** $\sigma_2 < \sigma_3$; **THEN** $We_{i,j} = 1$; **ELSE** $We_{i,j} = 0$; **END**.
END *j*
END *i*

Experimental Results and Result Analysis

Experiment

An Experiment, in which the tested robustness of the Blok SVD watermark to: a) recoloring of the image for protan CVD people, and b) superimposed AWGN with some SNR values, was realized. The RC algorithm for the protanopia CVD class is used for recoloring of the Test image. After inserting the watermark into the Test image, AWGN, with SNR = {0, 10, 20, 30, 40, 50} dB, is superimposed. The performance of the extracted watermark, as well as the RC image, was tested using: a) objective measures, and b) visual inspection. Standard objective measures, which are intensively used in digital signal processing, especially in digital image processing: a) Mean Square Error, MSE, b) Peak Signal to Noise Ratio, PSNR, c) Normalized Correlation, NC and d) Structure Similarity Index, SSIM, were used. The Experiment was done in the following steps:

Input: *I* - Test image in the RGB color space. *W* - binary watermark. Insertion factor α.
Output: Objective measures MSE, PSNR, NC and SSIM.
Step 1: Inserting a watermark *W* into Test image *I* with the insertion factor α, and creating an image with a watermark I_{WM}.
Step 2: Superimpose AWGN to Test image with inserted watermak I_{WM}. and create image $I_{WM,AW}$ with specified SNR.
Step 3: Changing the colors of the image $I_{WM,AW}$ by applying the RC algorithm, RC image with changed colors, which are adapted to Protain CVD persons, are created.
Step 4: Extracting watermark *We* from RC image.
Step 5: Visual inspection of the RC image and determination of α_C at which the watermark begins to be seen in the image.
Step 6: Visual inspection of the RC image and determination of the SNR_C at which the AWGN begins to be seen in the image.
Step 7: Determining the performance of the extracted watermark *We* and RC image using MSE, PSNR, NC and SSIM measures.

The results of the objective measure are shown graphically. After that, a comparative analysis of the results is presented.

Base

For the Experiment purposes the Image database was created. The Image database is made up of: a) Test image *Flowers*, 200 x 256 pixels, (fig. 3.a), and b) an electronic watermark (*Logo* of Academy of Applied Technical and Preschool Studies, Niš, Serbia), 32 x 32 pixels. In order to distribute the watermark over the entire Test image, a new watermark (50 x 64 pixels), which was obtained from multiple repetitions of the Logo (fig. 4.a), was created.

Results

The Test image used in this experiment is shown in fig. 3.a. By applying the RC algorithm, the following were obtained: a) Color blind image (CB image), which is with colors as they are perceived by protan CVD people (fig. 3.b), and b) Recolored image (RC image) whose colors are perceived by CVD protons as a wide spectrum

(fig. 3.c). The binary watermark, which was created by spatial repetition of the Logo of Academy of Applied Technical and Preschool Studies, is shown in fig. 4. a. The RC image with inserted watermark is shown in fig. 6, for the values of the insertion factor: a) $\alpha = 0$, b) $\alpha = 0.02$, c) $\alpha = 0.05$, d) $\alpha = 0.1$, and e) $\alpha = 0.3$. RC image with superimposed AWGN, for $\alpha = 0$, is shown in fig. 7: a) SNR = 50 dB, b) SNR = 20 dB, c) SNR = 10 dB, d) SNR = 0 dB, e) SNR = -10 dB. By applying the Blok SVD watermarking algorithm, the binary watermark was inserted and extracted for the insertion factor $\alpha = 0 - 0.3$, with a step of $\Delta\alpha = 0.001$. The extracted watermarks, for SNR = 50 dB, are shown in fig. 4.b ($\alpha = 0.02$), fig. 4.c ($\alpha = 0.05$), fig. 4.d ($\alpha = 0.1$) and fig. 4.e ($\alpha = 0.3$). The extracted watermarks, for insertion factor $\alpha = 0.02$, are shown in fig. 5.b (SNR = 50 dB), fig. 5.c (SNR = 40 dB), fig. 5.d (SNR = 30 dB), and fig. 5.e (SNR = 20 dB). RC images are shown in: fig. 6.a ($\alpha = 0$), fig. 6.b ($\alpha = 0.02$), fig.6.c ($\alpha = 0.05$), fig. 6.d ($\alpha = 0.1$) and fig. 6.e ($\alpha = 0.3$). The objective measurements, determined between the original and extracted watermarks, depending on the SNR, are shown in: a) fig. 8.a (MSE), b) fig. 8.b (PSNR), c) fig. 8.c (NC), and d) fig. 8.d (SSIM). The objective measurements, determined between the Test image and Test image with inserted watermark, depending on the SNR, are shown in a) fig. 9.a (MSE), b) fig. 9.b (PSNR), c) fig. 9.c (NC) and d) fig. 9.d (SSIM). The objective measurements, determined between the RC image and RC image with inserted watermark, depending on the SNR, are shown in a) fig. 10.a (MSE), b) fig. 10.b (PSNR), c) fig. 10.c (NC) and d) fig. 10.d (SSIM).

a) b) c)

Figure 3. a) Test image *Flowers*, b) CB image and c) RC image.

a) b) c) d) e)

Figure 4. a) Watermark (*Logo*). Extracted Watermark, for SNR = 50 dB, for insertion factor: b) $\alpha = 0.02$, c) $\alpha = 0.05$, d) $\alpha = 0.1$, e) $\alpha = 0.3$

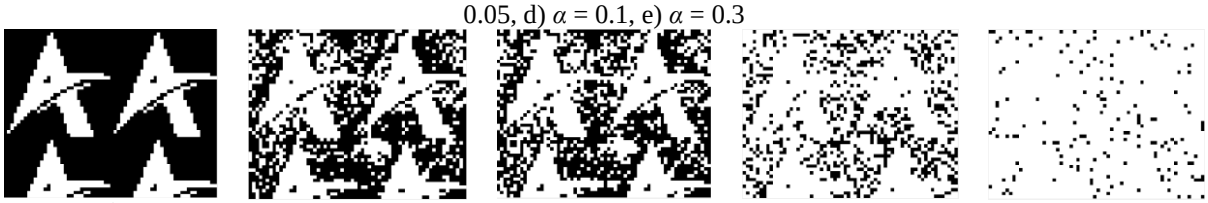

a) b) c) d) e)

Figure 5. a) Watermark (*Logo*). The extracted watermarks, for insertion factor $\alpha = 0.02$: b) SNR = 50 dB c) SNR = 40 dB, d) SNR = 30 dB, e) SNR = 20 dB.

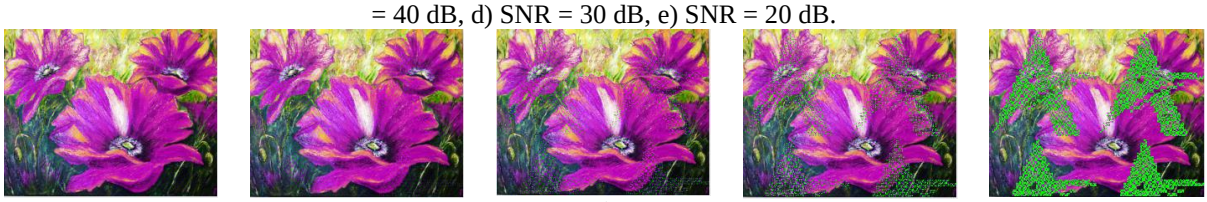

a) b) c) d) e)

Figure 6. The RC image with inserted watermark: a) $\alpha = 0$, b) $\alpha = 0.02$, c) $\alpha = 0.05$, d) $\alpha = 0.1$, e) $\alpha = 0.3$.

a) b) c) d) e)

Figure 7. RC slika sa superponiranim AWGN ($\alpha = 0$): a) SNR = 50 dB, b) SNR = 20 dB, c) SNR = 10 dB, d) SNR = 0 dB, e) SNR = -10 dB.

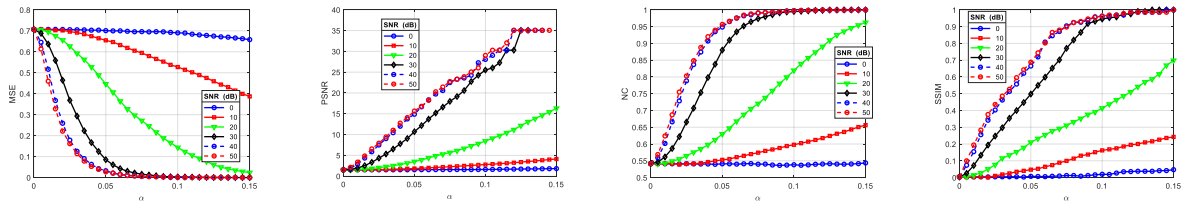

a) b) c) d)

Figure 8. The objective measurements between the original and extracted watermarks: a) MSE, b) PSNR, c) NC, and d) SSIM.

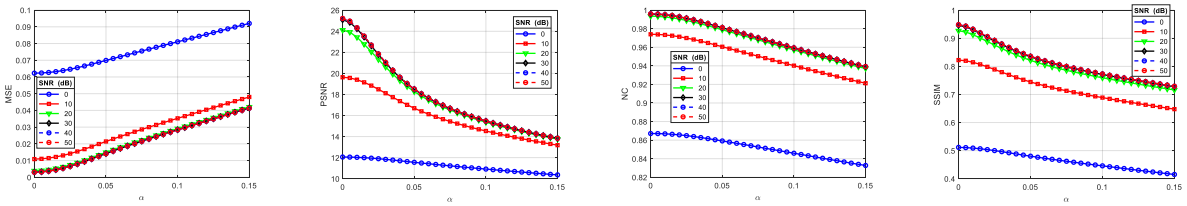

a) b) c) d)

Figure 9. Objective measurements between the Test image and Test image with inserted watermark, depending on the SNR,: a) MSE, b) PSNR, c) NC, and d) SSIM.

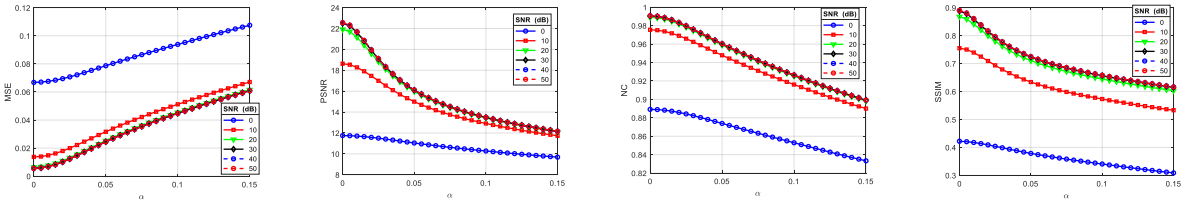

a) b) c) d)

Figure 10. Objective measurements between the RC image and RC image with inserted watermark, depending on the SNR, a) MSE, b) PSNR, c) NC, and d) SSIM.

Analysis of Results

Using the subjective method, which was realized by visual inspection of the quality of the RC image and extracted watermark, the critical value of the insertion factor $\alpha_C = 0.02$ (fig. 6.b), was determined. Increasing the insertion factor causes visible degradations in the RC image (fig. 6.c - fig. 6.e). The degradation of the RC image is such that the watermark becomes visible (fig. 6.e). However, increasing the insertion factor α causes an increase in the quality of the extracted watermark (fig. 4). The visual quality of the extracted watermark, which is inserted with the insertion factor α_C, is satisfactory, and as such it can be used to prove the ownership of the RC image (fig. 4.b). The visibility of the superimposed AWGN in the RC image was tested by visual inspection. Visibility of AWGN is beginning to occur at SNR_C. = 20 dB (fig. 7.d). RC image degradations increase with decreasing SNR (fig. 7.e). Visible degradations of the AWGN are distributed over the entire surface of the RC image. The effect of AWGN on the quality of the watermark, when the SNR is less than the SNR_C, is so degrading that the existence of the watermark in the RC image cannot be proven (fig. 5).

The objective measurements between the original and extracted watermarks, observing the graphics in fig. 8, for $\alpha_C = 0.02$, and SNR = 20 dB are: a) $MSE_{WM} = 0.6572$ (fig. 8.a), b) $PSNR_{WM} = 1.8231$ (fig. 8.b), c) $NC_{WM} = 0.5546$ (fig. 8.c) and d) $SSIM_{WM} = 0.0556$ (fig. 8.d). The objective measures of degradation of the Test image

with an inserted watermark and superimposed AWGN (fig. 7.a) compared to the Test image without a watermark and AWGN (fig. 3.a) are: a) MSE_{TI} = 0.0062 (fig. 9.a), b) $PSNR_{TI}$ = 22.0581 (fig. 9.b), c) NC_{TI} = 0.9904 (fig. 9.c) and d) $SSIM_{TI}$ = 0.8891 (fig. 9.d). The objective measures of degradation of the RC image with an inserted watermark and superimposed AWGN (fig. 7.a) compared to the RC image without a watermark and AWGN (fig. 3.c) are: a) MSE_{RC} = 0.0109 (fig. 10.a), b) $PSNR_{RC}$ = 19.6079 (fig. 10.b), c) NC_{RC} = 0.9817 (fig. 10.c), and d) $SSIM_{RC}$ = 0.8000 (fig. 10.d). An example of drastic degradation of the RC image (α = 0.3, SNR = 50 dB) is shown in fig. 6. e. The extracted watermark has excellent visual quality (fig. 4.e). Appropriate objective measures for watermarks are: a) MSE_{WM} = 0.00 (fig. 8.a), b) $PSNR_{WM} = \infty$ (fig. 8.b), c) NC_{WM} = 1.00 (fig. 8.c) and d) $SSIM_{WM}$ = 1.00 (fig. 8.d). Objective measures of the RC image are: a) MSE_{RC} = 0.0915 (fig. 10.a), b) $PSNR_{RC}$ = 10.3845 (fig. 10.b), c) NC_{RC} = 0.8555 (fig. 10.c) and d) $SSIM_{RC}$ = 0.5554 (fig. 10.d).

Objective measures, as well as subjective measures, indicate that increasing the insertion factor α affects the increase in the visual quality of the extracted watermark, as well as the decrease in the quality of the RC image. Also, objective measures, as well as subjective measures, indicate a significant degradation of the RC image due to the superimposed AWGN. The AWGN effect is particularly reflected in the quality of the extracted watermark. In order to increase the quality of the extracted watermark, the RC image should be pre-processed before extracting the watermark, which will be the following activities.

Conclusion

This paper describes an algorithm for recoloring images, which are intended for the protan CVD persons. For copyright purposes, a watermark has been inserted into the image using the Block SVD algorithm. In order to determine the quality of the watermark due to the effect of the RC algorithm, as well as the degradation of the RC image due to the effect of the watermark, an experiment was carried out. Additionally, AWGN superimposition was performed for some SNRs. The experimental results were analyzed using: a) subjective method (visual inspection), and b) objective measures (MSE, PSNR, NC and SSIM). Using a visual inspection, it was shown that, for the watermark insertion factor α_C = 0.02, there is an invisibility of the watermark in the image. In addition, it has been shown that the extracted watermark is of satisfactory quality for proving copyright. Visibility of AWGN is beginning to occur at SNR_C = 20 dB. Visible degradations of the AWGN are distributed over the entire surface of the RC image. Further reduction of the SNR leads to visible degradation of the RC image and extracted watermark.

Scientific Ethics Declaration

The authors declare that the scientific ethical and legal responsibility of this article published in EPSTEM journal belongs to the authors.

Acknowledgements or Notes

* This article was presented as an oral presentation at the International Conference on Technology, Engineering and Science (www.icontes.net) held in Antalya/Turkey on November 16-19, 2022.

References

Blake, R., & Sekuler, R. (2006). *Perception*. McGraw-Hill.

Chang, C., Hu, Y., & Lin, C. (2007). A digital watermarking scheme based on singular value decomposition. from *ESCAPE 2007 First International Symposium*, Hangzhou, 82–93.

Crenshaw, C. (2014). *Realtime color vision deficiency correction*, U.S. Patent: 20140066196 A1.

Curcio, C. A., Sloan, K. R., Kalina, R. E., & Hendrickson, A. E. (1990). Human photoreceptor topography. *J. Compar. Neurol*., *292*(4). 497–523.

Lin, H., Chen, L., &, Wang, M. (2019). Improving discrimination in color vision deficiency by image re-coloring. *Sensors*, *19*(10), 2250: 1-19.

Milivojevic, Z., Prlincevic, B., Kostic, D. (2022). Degradation recoloring cvd protan image from blok svd watermark, proceedings from erk 2022. *31th International Electrotechnical and Computer Science Conference*, Portoroz, Slovenia.

Nam, J., Yong, R., Huh, Y., &, Kim, M. (2005). Visual content adaptation according to user perception characteristics. *IEEE Transactions on Multimedia, 7*(3), 435–445.

Pramoun, T., Supasirisun, P., & Amornraksa, T. (2018). Digital watermarking on recolored images for protanopia. proceedings from *15th International Conference on Electrical Engineering/Electronics, Computer, Telecommunications and Information Technology*. 62 - 65.

Pramoun, T., Thongkor, K., & Amornraksa, T. (2017). Image watermarking against color blind image correction. proceedings from ubi-media. *10th International Conference on Ubi-media Computing and Workshops*, 1-6.

Zhenyang, Z., Toyoura, M., Go, K., Kashiwagi, K., Fujishiro, I., Wong, T., & Mao, X. (2021). Personalized image recoloring for color vision deficiency compensation. *IEEE Transactions on Multimedia*, 24, 1721 - 1734.

Author Information

Zoran Milivojevic
Academy of Applied Technical and Preschool Studies
A. Medvedeva 20, Nis, Serbia
e-mail: *zoran.milivojevic@akademijanis.edu.rs*

Bojan Prlincevic
Kosovo and Metohija Academy Division,
Zvecan, Serbia

To cite this article:

Milivojevic, Z. & Prlincevic, B. (2022). Effect of protan recoloring algorithm on inserted watermark in presence of the superimposed AWGN. *The Eurasia Proceedings of Science, Technology, Engineering & Mathematics (EPSTEM), 21*, 116-124.

The Eurasia Proceedings of Science, Technology, Engineering & Mathematics (EPSTEM)
ISSN: 2602-3199

The Eurasia Proceedings of Science, Technology, Engineering & Mathematics (EPSTEM), 2022

Volume 21, Pages 125-130

IConTES 2022: International Conference on Technology, Engineering and Science

Implementation of an Augmented Reality Application for Basic Electrical Circuits

Omer Emin CINAR
Konya Technical University

Salih GUNES
Konya Technical University

Abstract: It is noteworthy that augmented reality is a technology used for educational purposes along with a wide range of applications ranging from defense industry to construction, medicine to automotive. In this paper, a recognition-based AR application named ARKTUNApp that can be used on basic electrical circuits in the field of electrical and electronics engineering was developed under these conditions, especially when the COVID-19 pandemic necessitates distance education. A QR code was identified as the marker, a booklet was prepared and it consisted of such basic circuit examples as short circuit, open circuit, circuit with series-connected resistors, circuit with parallel-connected resistors, RLC circuit, diode and LED circuit, environmental currents method and node voltage method with QR codes. When the users scan them, they can observe 3D simulations and animations of those circuit examples thanks to the AR application developed. Using Vuforia SDK as the software development kit and Unity3D as the application development platform, it was aimed to concretize abstract concepts and enhance interactive educational experiences. In addition, C# programming language was used to develop this application for smart devices with Android operating system. 30 students participated in the user study and their feedback about the AR application developed was obtained with a questionnaire.

Keywords: Application, Augmented reality, Circuit, Education, Engineering

Introduction

An application named ARKTUNApp was developed using augmented reality technology within the scope of this study, and theoretical concepts and situations related to basic electrical circuits taught in electrical and electronics engineering modules were simulated in a 3D environment (Cinar, 2020). Many educational institutions have turned to distance education as a result of the COVID-19 pandemic that has affected the entire world since the beginning of 2020. Considering this point, the significance of the AR application developed becomes higher.

Augmented reality is the process of combination or “augmentation” of video or photographic images in computer programming by superimposing images with useful data generated on the computer (Hosch, 2020). According to another definition, it is a variation of virtual reality and AR allows the user to see the real world with virtual objects superimposed or combined on the real world and augmented reality systems have such three basic properties as combining real and virtual environment, providing real-time interaction and being 3D (Azuma, 1997). Morton Heilig, known as one of the pioneers of visual reality, produced the cinematograph named “Sensorama” in 1957 and patented this device in 1962 (Cinar, 2020). It was followed by the fact that Ivan Sutherland and Bob Sproull developed the first HMD augmented reality application named “The Sword of Damocles” in 1966 (Yuen et al., 2011). Through this HMD, 2D object images were brought together and 3D image illusion was presented to the user (Sutherland, 1968). In 1970s and 1980s, some researchers received

education on AR at NASA, US Air Force and North Carolina University (Feiner, 2022). The terms of augmented reality were first used by Thomas P. Caudell in 1990 (Caudell & Mizell, 1992). After 2000, such giant companies as Nokia, HTC, Google and Microsoft have allocated resource for this technology, made investment in this direction and developed AR glasses.

Augmented reality consists of some components and they are basically hardware and software components. Hardware components are as follows: sensors, input devices, processors, displays and integrated systems (Tunali, 2015). Software components are as follows: software directly inside an AR application, software used to create the AR application, software used to create content for the AR application, other AR-related software (Craig, 2013).

Tracking and marker are important concepts in augmented reality. The first one is the process of recognizing the reference object and calculating its 3D location and direction. A tracking system consists of two main components: targets and sensors (Ercan, 2010). The latter one is one of the elements used to enable the real world to be mapped in 3D. It is also expressed as images that applications can define (Aslan, 2015). The most known and used marker systems are circular and square markers (Ercan, 2010).

Method

Details about the platforms to be used for the AR application developed within the scope of this study were given in the first section. The AR application was expressed thoroughly in the second section.

Platforms Used for the AR Application

Unity 3D was used because it allows its users to create games and animations in 2D or 3D. Furthermore, applications developed thanks to this platform can be run on devices with Android and iOS operating system. Android SDK was used because it allows the application to run on smart devices with Android operating system. Vuforia SDK was used because a QR code was defined as marker for this AR application and this software development kit allows its users to create a single local application.3DS Max was used because 3D models of the basis electrical circuits can be created for the AR application.

Figure 1. Addition of the QR code marker to Unity (Cinar, 2020)

Implementation of the AR Application

First of all, an educational booklet including basic electrical circuits (short circuit, open circuit, circuit with series-connected resistors, circuit with parallel-connected resistors, RLC circuit, diode and LED circuit, environmental currents method and node voltage method) was prepared. After QR codes next to these circuits are scanned by smart devices, users can see 3D models and simulations of these circuits. After this process, such

circuit components as battery, resistor, switch, diode, LED, capacitor were designed on 3DS Max. 3D models of the aforementioned basic electrical circuits were designed by using the aforementioned circuit components on 3DS Max. 3D models of the circuits were converted to FBX files and transferred to Unity3D. A menu was designed for the AR application and its user can click which circuit is wanted to be seen. C# was used to create interrelations between menu and scenes. An APK file should be created to run this application on a smart device with Android (minimum 7.0 version) operating system. Therefore, it was created on Unity3D and tested on smart devices (Cinar, 2020).

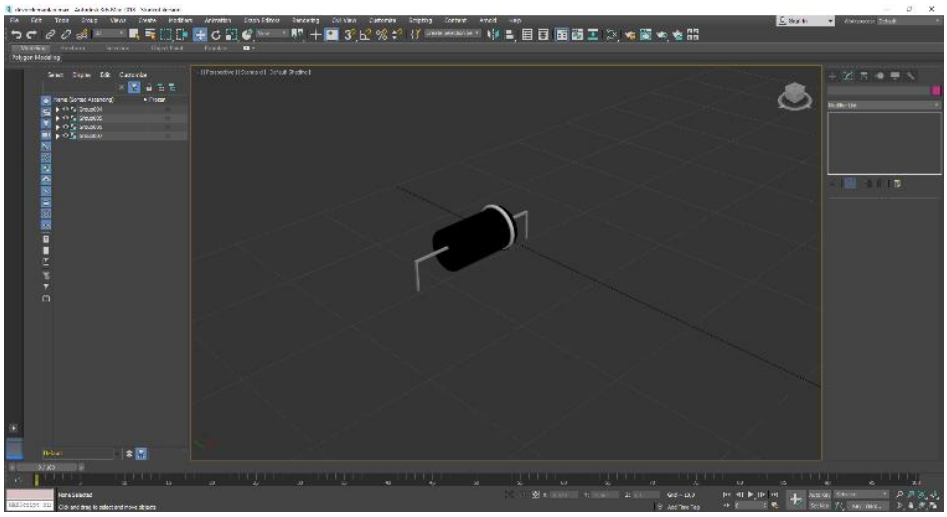

Figure 2. A 3D resistor design developed in accordance with resistor color codes for the application (Cinar, 2020)

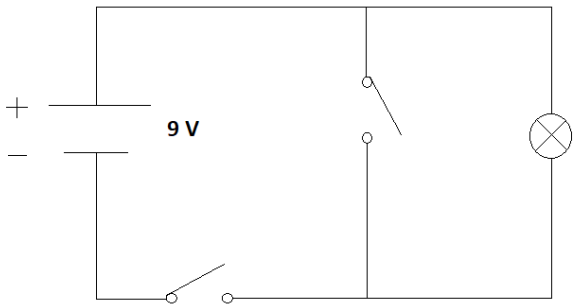

Figure 3. A 3D diode design in which the anode is shown in black and the cathode in white for the application in accordance with the original one (Cinar, 2020)

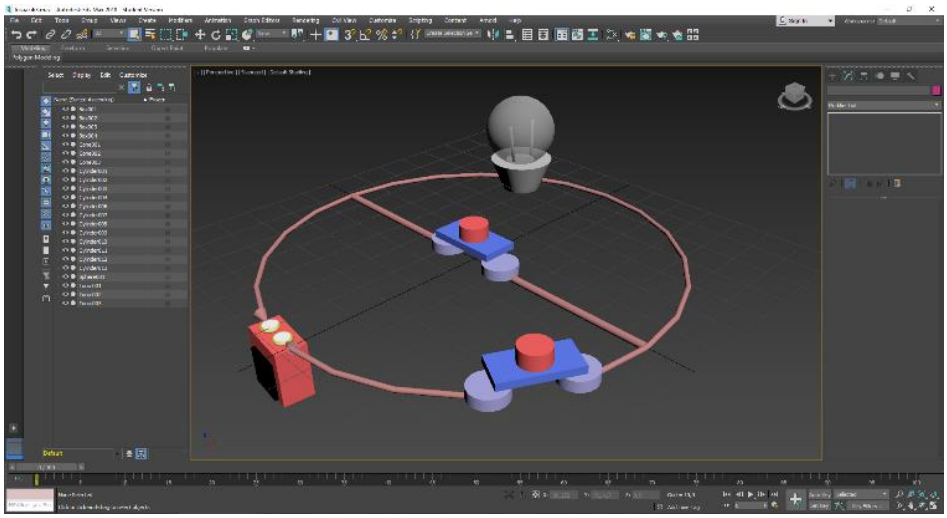

Figure 4. Example of open and short circuit found in the first place of the educational booklet (Cinar, 2020)

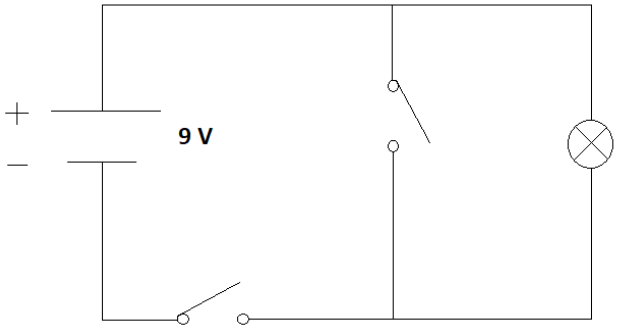

Figure 5. 3D open and short circuit design realized according to the example (Cinar, 2020)

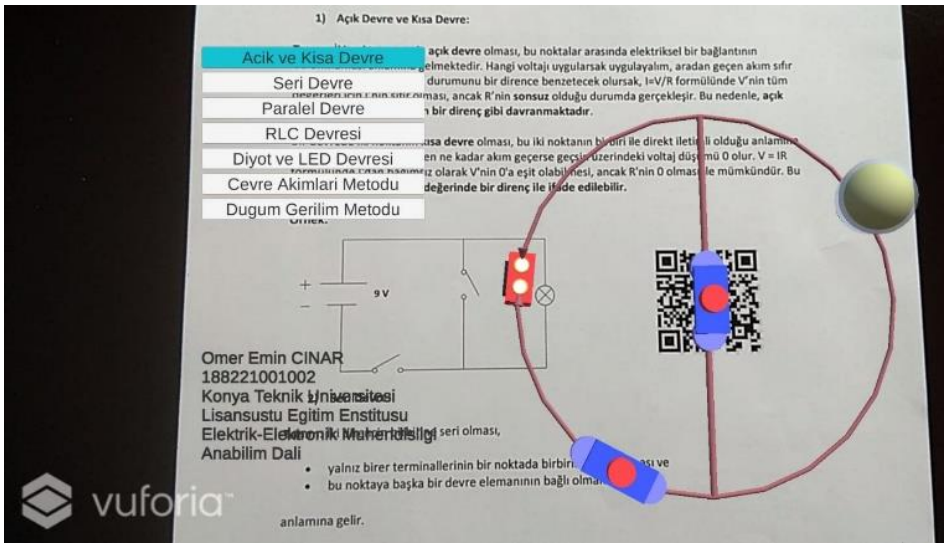

Figure 6. Menu interface and appearance of open/short circuit in the educational booklet of the AR application developed (Cinar, 2020)

Results and Discussion

Results

In order to obtain feedback on the AR application developed, totally 30 persons being undergraduate students in the Department of Electrical and Electronics Engineering or graduate students in the Department of Electrical and Electronics Engineering of Konya Technical University were informed about the purpose, content and operation of the application and they were asked to use the application. The booklet and the download link of the application file were also shared with the participants. A questionnaire was prepared so that the participants could report their ideas and experiences regarding the application. Likert scale was used in the questionnaire and 10 statements were presented. In order to indicate whether they agree with these opinions or not, 5 opinion sentences were included in the questionnaire (Cinar, 2020).

Discussion

The results of the questionnaire suggested that the AR application developed made a positive contribution to the level of understanding and comprehension of the participants about the relevant courses. 93% of the participants found the AR application useful. 97% of them thought that abstract concepts became more comprehensible. 97% of them found the menu interface of the application useful. 90% of them thought that the application contains enough circuit examples related to Electrotechnics and Circuit Analysis at the basic level. 87% of them thought that the application made learning easier. All of the participants thought that the resistance values on the circuits in the booklet match the resistor color codes in the 3D models in the application. All of them thought that the circuit components on the circuits in the booklet and the 3D models in the application are compatible with each other. They agreed that the 3D models of the circuit components and animations in the application are

realistic. 83% of them thought that the AR application increased their achievement in the related courses (Cinar, 2020). Survey results are given in more detail in Table 1.

Table 1. Survey results (Adapted from Cinar, 2020)

No	Statement	Strongly Agree	Somewhat Agree	Neutral	Somewhat Disagree	Strongly Disagree
1	I think this application is useful.	20	8	2	-	-
2	Abstract concepts became more understandable thanks to this application.	19	10	1	-	-
3	Menu interface of the application is convenient.	19	10	-	1	-
4	The application basically contains enough circuit examples related to Electrotechnics and Circuit Analysis.	16	11	-	3	-
5	This application has made learning easier.	18	8	4	-	-
6	The resistance values on the circuits in the booklet and the resistor color codes in the 3D models match each other.	26	4	-	-	-
7	The circuit elements on the circuits in the booklet and the 3D models match each other.	25	5	-	-	-
8	3D models of circuit elements are realistic.	21	9	-	-	-
9	Animations in the application are realistic.	21	9	-	-	-
10	This application has increased my achievement in related courses.	14	11	3	2	-

Conclusion

ARKTUNApp augmented reality application was developed with the aim of concretizing basic electrical circuits with 3D models and animations. 3DS Max, Android SDK, Vuforia SDK and Unity3D were used in the development of the application. It was made available for the use 30 undergraduate and graduate students, and their feedback about the application was obtained through a survey study. They found the application useful, functional, realistic and interesting (Cinar, 2020).

Recommendations

Considering the time spent on smart devices, especially mobile phones, and the recent trend towards distance education with the impact of the COVID-19 pandemic, the use of augmented reality will also increase in engineering education. Further progress can be made in this area once sufficient hardware infrastructure and know-how are provided. The approach in this paper can also be adapted to a variety of subjects and courses. The use of augmented reality technology can be very useful in lessons that may remain abstract such as Analog Electronics, Digital Electronics, Logic Circuits, as well as Electromagnetic Wave Theory. Augmented reality application can be made more useful by combining them with different technologies such as deep learning, machine learning, computer vision, image processing.

Scientific Ethics Declaration

The authors declare that the scientific ethical and legal responsibility of this article published in EPSTEM journal belongs to the authors.

Acknowledgements

* This article was presented as an oral presentation at the International Conference on Technology, Engineering and Science (www.icontes.net) held in Antalya/Turkey on November 16-19, 2022.

* The students who participated in the survey and provided feedback about the AR application developed deserve thanks.

References

Aslan, C. B. (2015). *Interior design and decision making using augmented reality*. (Master dissertation). Retrieved from Thesis Center of the Council of Higher Education

Azuma, R. T. (1997). A survey of augmented reality, *Presence: Teleoperators and Virtual Environments, 6*(4), 355-385.

Caudell, T. P., & Mizell, D. W. (1992). Augmented reality: An application of heads-up display technology to manual manufacturing processes. *Proceedings of the Twenty-Fifth* Hawaii *International Conference on System Sciences.* Hawaii, USA.

Cinar, O. E. (2020). *Application of augmented reality technology on basic electrical circuits*. (Master dissertation). Retrieved from Thesis Center of the Council of Higher Education

Craig, A. B. (2013). Understanding augmented reality: concepts and applications. *Morgan Kaufmann.* Amsterdam, 125-149.

Ercan, M. (2010). *A 3d topological tracking system for augmented reality*. (Master dissertation). Retrieved from Thesis Center of the Council of Higher Education

Feiner, S. K. (2002). Augmented reality: A new way of seeing, *Scientific American, 286*(4), 48-55.

Hosch, W. L. (2020). Augmented reality, *Encyclopedia Britannica.* Retrieved from https://www.britannica.com/technology/augmented-reality

Sutherland, I. (1968). A head-mounted three-dimensional display. *Fall Joint Computer Conf., Am. Federation of Information Processing Soc. (AFIPS), 33*, 757-764.

Tunali, U. (2015). *The augmented reality application in computer engineering education*. (Master dissertation). Retrieved from Thesis Center of the Council of Higher Education

Yuen, S., Yaoyuneyong, G., & Johnson, E. (2011). Augmented reality: An overview and five directions for AR in education. *Journal of Educational Technology Development and Exchange, 4*(1), 119-140.

Author Information

Omer Emin Cinar
Konya Technical University
Department of Electrical and Electronics Engineering,
Konya, Turkey
Contact e-mail: *omeremincinar@gmail.com*

Salih Gunes
Konya Technical University
Department of Electrical and Electronics Engineering,
Konya, Turkey

To cite this article:

Cinar, O. E. & Gunes, S. (2022). Implementation of an augmented reality application for basic electrical circuits. *The Eurasia Proceedings of Science, Technology, Engineering & Mathematics (EPSTEM), 21*, 125-130.

The Eurasia Proceedings of Science, Technology, Engineering & Mathematics (EPSTEM)
ISSN: 2602-3199

The Eurasia Proceedings of Science, Technology, Engineering & Mathematics (EPSTEM), 2022

Volume 21, Pages 131-138

IConTES 2022: International Conference on Technology, Engineering and Science

Comparing Performance of OFDM based V2V System in Rayleigh and Weibull Fading Channels

Didem Kivanc TURELI
Istanbul Okan University

Zainab QASSAB
Istanbul Okan University

Abstract: The performance of communication systems across wireless channels is limited by fading. This is particularly true for vehicular networks, which require highly reliable links. Orthogonal Frequency Division Multiplexing (OFDM) is used today in a wide range of communication systems. It may also be part of the standard for vehicular networks. This paper compares the performance of a vehicular communication system using Quadrature Phase Shift Keying (QPSK) communication over Orthogonal Frequency Division Multiplexing (OFDM) in two channel models found to fit the vehicular channel: Rayleigh and Weibull fading models by comparing the bit error rate under constant signal to noise ratio (SNR). The exact BER has been derived based on the derived of the effective noise sample distribution at the OFDM demodulator output over the Weibull Fading and the log-normal fading channel in AWGN. The Monte Carlo simulation results have verified the validity of the derived analytical BER expressions with an exact match to the simulation results.

Keywords: Fading, Multipath channels, Raleigh fading model, Weibull fading model

Introduction

In multipath channels copies of the signal arrive from different directions due to reflection and refraction off different surfaces. Frequency selective fading, the amplification of certain frequencies and the attenuation of others occurs due to the phase delay induced by the reflections. In OFDM the cyclic prefix allows the gain to remain relatively constant over the bandwidth of a given carrier, reducing the effect of frequency selective fading to multiplication by a scalar for each individual subcarrier. However, the gain of each subcarrier is not identical. This means that certain carriers are more suitable for communication than others. The effect of fading can be split into two: fast fading which changes on the time scale of a single symbol and slow fading which refers to signal changes on the order of several symbols (Bingham, 1990).

While systems can usually adapt to large scale fading through power control or adaptive modulation and coding (AMC), small scale fading changes quickly so that the process of channel estimation, feedback and adaptation of system parameters may take too long to have the desired effect. For this reason, it is important to study the effect of small scale fading on communication. In this paper we study the effects of Rayleigh and Weibull fading models, which model small scale fading. These models have been found to accurately model a vehicular communication channel scenario (Sen & Matolak, 2008).

With the advent of intelligent transportation systems, it becomes necessary to characterize the channel used for communication between vehicles. The wireless channel environment has a significant impact on the performance of wireless communication systems in these cases. Some studies have found that Rayleigh and Weibull distributions accurately model the small scale fading on vehicular links (Sen & Matolak, 2008). These links are time varying and need to be modeled accurately (Matolak & Frolik, 2011). There has been prior work

- Selection and peer-review under responsibility of the Organizing Committee of the Conference

on modeling these links at the packet scale (Wang *et al.,* 2019; Jameel *et al.,* 2017). In this paper we calculate analytically and by simulation the probability of bit error in these scenarios and compare the results.

Orthogonal Frequency Division Multiplexing (OFDM) was first introduced in the late 1960s, for military applications but the technique required may RF chains and was not practical for commercial use (Bingham, 1990). To eliminate the need for analog subcarrier oscillators, Weinstein proposed employing a Discrete Fourier Transform (DFT) to generate and receive OFDM signals. Using the Fast Fourier Transform (FFT), an efficient implementation of DFT, allowed for an easy implementation of OFDM. 4G and 5G cellular systems and WiFi also use OFDM (Prasad, 2004). This paper compares theoretically and through simulations the average bit error rate (BER) experienced under Rayleigh and Weibull fading channels.

OFDM System Model

Orthogonal Frequency Division Multiplexing (OFDM) divides the available spectrum into many narrow subcarriers (Goldsmith, 2005). The subcarrier frequencies are selected so that they are orthogonal, packing the signal into a tight spectrum. OFDM systems have high spectral efficiency and are resistant to multipath. In terrestrial environments, OFDM is better for transmitting a lot of data than single-carrier transmissions, because OFDM can handle a lot of different types of interference. This is due to the frequency diversity introduced by multiple channels. OFDM does have some drawbacks, for instance frequency and timing estimation are critical for accurate symbol estimation and the high peak to average power ratio (PAPR) of the OFDM waveform needs to be compensated for at the receiver (Ladaycia *et al.,* 2017). Figure 1 shows the architecture of the OFDM system.

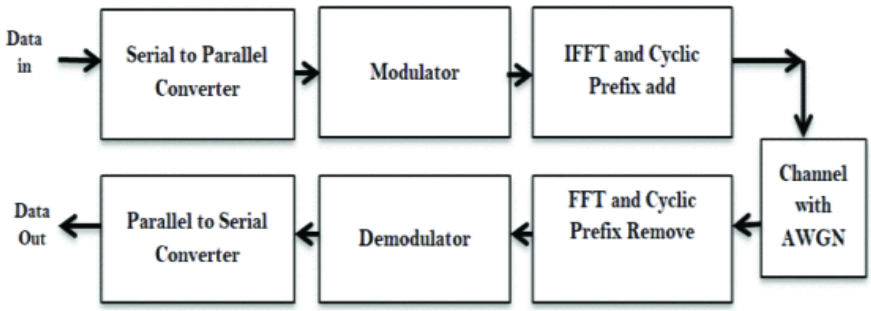

Figure 1. OFDM architecture (Ladaycia *et al.,* 2017).

Consider a system with N information symbols $x_0, x_2, \ldots, x_{N-1}$ to be transmitted. The *N*-symbol OFDM block $X = (X_k)$ where $k = 0,1,...,N-1$ is calculated as:

$$X_k = \frac{1}{\sqrt{N}} \sum_{n=0}^{N-1} x_n \, e^{j2\pi kn/N} \quad k = 0,1,...,N-1 \tag{1}$$

To make this system easier to analyze, now assume that the message symbols which are the input of the OFDM system are statistically independent and identically distributed. Considering the central limit theorem, where *N* is large, the real and imaginary parts of the OFDM signal are the linear combination of Gaussian random variables, which also makes these symbols independent and identically distributed Gaussian random variables with mean zero and variance (Mishra and Sood, 2011).

$$\sigma^2 = E\left\{\left(\mathrm{Re}\{X_k\}\right)^2 + \left(\mathrm{Im}\{X_k\}\right)^2\right\} \tag{2}$$

where $E\{\cdot\}$ denotes the expected value of the expression.

Then the probability density function (pdf) of the OFDM symbol is

$$f\left(X_k\right)=\frac{1}{\sqrt{2\pi}\sigma}e^{-X_k{}^2/2\sigma^2}\quad k=0,1,...,N-1 \tag{3}$$

Assuming the pulse shape is purely rectangular and each symbol duration is exactly T_s, the baseband representation of the transmitted analog OFDM waveform is

$$s(t)=\frac{1}{\sqrt{N}}\sum_{n=0}^{N-1}x_n\,e^{jn\Delta ft}\qquad 0\le t\le T_s,\ \Delta f=\frac{1}{T_s} \tag{4}$$

The output of the OFDM channel is:

$$r(t)=s(t)*h(t)+n(t) \tag{5}$$

where $h(t)$ is the impulse response of the channel and $n(t)$ is white Gaussian noise with $N_0/2$ power spectral density, and * is the convolution operator.

The impulse response of the multipath channel is:

$$h(t)=\sum_{i=1}^{L}h_i\delta\left(t-\tau_i\right) \tag{6}$$

In a multipath environment with time-invariant channel, we assume that the transmitted subcarrier bandwidth $\Delta f=1/T_s$ is narrow relative to the channel coherence bandwidth. In this case where inter-symbol interference (ISI) is neglected, further neglecting the pulse shape the effect of the channel is to multiply the message on each subcarrier by a constant channel gain and phase offset. In the baseband representation:

$$\begin{aligned}r(t)&=\frac{1}{\sqrt{N}}\sum_{i=1}^{L}h_i\sum_{n=0}^{N-1}x_n\,e^{jn\Delta f\left(t-\tau_i\right)}+n(t)=\frac{1}{\sqrt{N}}\sum_{n=0}^{N-1}\sum_{i=1}^{L}h_ix_n\,e^{jn\Delta f\left(t-\tau_i\right)}+n(t)\\&=\frac{1}{\sqrt{N}}\sum_{n=0}^{N-1}\sum_{i=1}^{L}h_ie^{-jk\Delta fn\tau_i}x_n\,e^{j\Delta fnt}+n(t)=\frac{1}{\sqrt{N}}\sum_{n=0}^{N-1}\underbrace{\left(\sum_{i=1}^{L}h_ie^{-jk\Delta fn\tau_i}\right)}_{H_n}x_n\,e^{j\Delta fnt}+n(t)\end{aligned} \tag{7}$$

where H_n is the complex valued baseband gain for the nth subcarrier channel. The output of the multipath channel is then:

$$r(t)=\frac{1}{\sqrt{N}}\sum_{n=0}^{N-1}H_nx_n\,e^{jn\Delta ft}+n(t)\qquad 0\le t\le T_s \tag{8}$$

The receiver will get N samples from this, making the OFDM symbol

$$r_k=r\left(kT_s\right)=\frac{1}{\sqrt{N}}\sum_{n=0}^{N-1}H_nx_n\,e^{jn\Delta f\left(kT_s\right)}+n\left(kT_s\right)=\frac{1}{\sqrt{N}}\sum_{n=0}^{N-1}H_nx_n\,e^{j\frac{nk}{N}}+n_k\qquad 0\le k\le N-1 \tag{9}$$

At the output of the OFDM receiver (FFT) we will see

$$\begin{aligned}y_m&=\frac{1}{\sqrt{N}}\sum_{k=0}^{N-1}r_k\,e^{-j\frac{km}{N}}=\frac{1}{\sqrt{N}}\sum_{k=0}^{N-1}\left(\frac{1}{\sqrt{N}}\sum_{n=0}^{N-1}H_nx_n\,e^{j\frac{nk}{N}}+n_k\right)e^{-j\frac{km}{N}}\qquad 0\le k\le N-1\\&=\frac{1}{N}\sum_{k=0}^{N-1}\sum_{n=0}^{N-1}H_nx_n\,e^{j\frac{(n-m)k}{N}}+\frac{1}{N}\sum_{k=0}^{N-1}n_k\,e^{-j\frac{km}{N}}=\frac{1}{N}\sum_{n=0}^{N-1}H_nx_n\sum_{k=0}^{N-1}e^{j\frac{(n-m)k}{N}}+\tilde{n}_k=\frac{1}{N}\sum_{n=0}^{N-1}H_nx_n\,N\delta(n-m)+\tilde{n}_k\\y_m&=H_mx_m+\tilde{n}_k\end{aligned} \tag{10}$$

where $\tilde{n}_k$ has the same probability distribution as n_k since it is the linear combination of independent Gaussian random variables, and the coefficients add to 1.

Multipath Channel

Communication in multipath channels is impaired due to their frequency selectivity. This section derives the probability of error when data is transmitted across a frequency selective channel using OFDM and QPSK modulation. The effect of phase is not considered since phase variation is considered to be slow enough for the system to adapt to. Only the effect of magnitude on the SNR is considered. An average BER is calculated for transmission across the channel. Standard Rayleigh fading is considered as well as Weibull fading in the channel. Weibull channels are interesting because they have been used to model vehicular channels.

Rayleigh Fading

It can be seen from Equation (8) that the subcarrier gain is the sum of many smaller components. When the number of multipath components *L* is large, the sum approaches a Gaussian random variable. In this assumption, the real and imaginary parts of the baseband channel gain H_n are both Gaussian distributed. Since the transmitted symbols x_n are independent and identically distributed, the sum of these terms makes two identically distributed Gaussian random variables.
In Equation (10) we see that the symbol is multiplied by the subcarrier gain H_n which is the Discrete Fourier Transform (DFT) of the channel impulse function:

$$H_n = \sum_{i=1}^{L} h_i e^{-jk\Delta f n\tau_i} \tag{11}$$

For the Rayleigh fading channel since the channel coefficients h_i are circular complex Gaussian random variables with mean 0 and standard deviation 1, the linear combination of those random variables H_n will also be a Gaussian random variable, thus the received OFDM signal power will be Rayleigh distributed with variance L.

The magnitude $r = |H_n|$ is a Rayleigh random variable with probability density function

$$f(r) = 2re^{-r^2} \tag{12}$$

For these types of channel, the probability of error for Quadrature Phase Shift Keying (QPSK) modulated signals is (Goldsmith, 2005).

$$P_b = \frac{1}{2}\left[1 - \sqrt{\frac{\gamma_0/2}{1+\gamma_0/2}}\right] \quad \text{where} \quad \gamma_0 = \frac{E_b}{\sigma_n^2} \tag{13}$$

Weibull Fading

Weibull fading is generally considered to be a worse type of fading channel than Rayleigh fading, in that the channel gains change more and cause a higher probability of error. However, similarly to Rayleigh fading, the received signal is given by Equation 10 with channel gain again given by Equation 11. The difference in this case is that the multipath coefficients h_i are Weibull distributed. Even when this is true, as long as the number of multipath components *L* is large, on the order of 10 or more, the real and imaginary parts of the subcarrier gain H_n will be well approximated with the Gaussian distribution. Then the channel experienced will also be a Rayleigh fading channel, but with a higher variance equal to:

$$\sigma^2 = L\beta^2\left[\Gamma\left(1+\frac{2}{k}\right)-\left(\Gamma\left(1+\frac{1}{k}\right)\right)^2\right] \tag{14}$$

The probability of error is then given by:

$$P_b = \frac{1}{2}\left[1-\sqrt{\frac{\beta^2\left[\Gamma\left(1+\frac{2}{k}\right)-\left(r\left(1+\frac{1}{k}\right)\right)^2\right]\frac{E_b}{2\sigma_n^2}}{1+\beta^2\left[\Gamma\left(1+\frac{2}{k}\right)-\left(\Gamma\left(1+\frac{1}{k}\right)\right)^2\right]\frac{E_b}{2{\sigma_n}^2}}}\right] \tag{15}$$

Log-normal

The log-normal distribution is recognized to statistically define fading in various propagation contexts, including ultra wide-band indoor channels, radio channels influenced by body worn devices , and the shadowing phenomenon in outdoor scenarios . The calculation of the average bit error rate or average symbol error rate is thought to be a crucial factor in determining how well digital modulation schemes perform in fading channels. The statistical expectation of error rate in an additive white gaussian noise (AWGN) over a probability density function describing a fading environment determines the average error rate for coherent detection of various digitally modulated signals (Khandelwal, 2013).

A continuous distribution in which the logarithm of a variable has a normal distribution. A log normal distribution results if the variable is the product of a large number of independent, identically-distributed variables in the same way that a normal distribution results if the variable is the sum of a large number of independent, identically distributed variables (Singh and Singh, 2013).
log-normal distribution can be expressed as:

$$p_h(h_k^r) = \frac{1}{\sqrt{2\pi\sigma^2}h_k^r}e^{\left(-(\ln h_k^r-\mu)^2/(2\sigma^2)\right)} \tag{16}$$

where $h_k^r > 0$, Real and imaginary parts of the Gaussian random variable are r = {ℜ, ℑ}, σ 2 and μ the variance and the mean of the random variable (Al-Rubaye *et al.*, 2019).

Simulation Results

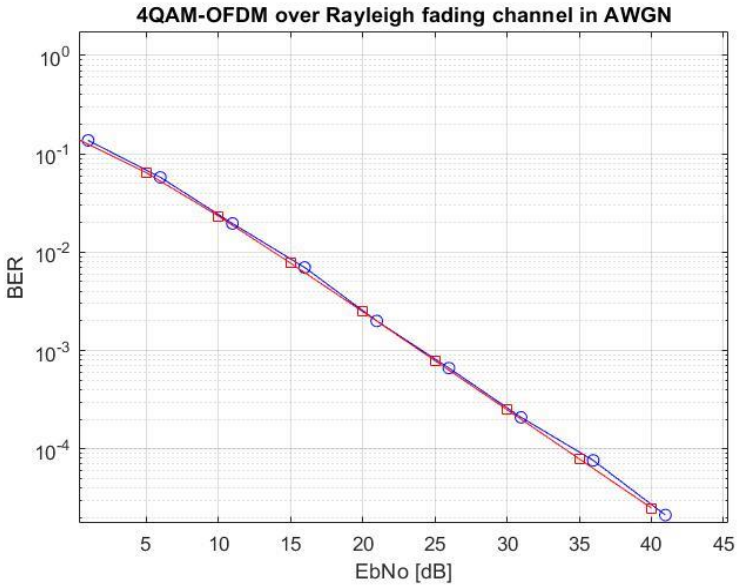

Figure 2. SNR vs BER for OFDM-QPSK over Rayleigh fading channel in AWGN.

Simulations using Matlab were performed to verify the probability of error derived in the previous section. In this work, we consider an OFDM system where the data symbols x_k are drawn from QPSK symbols $\{\pm 1 \pm 1j\}$. The performance of OFDM is presented under the Rayleigh fading channel considering Bit Error Rate and Signal to Noise Ratio. The simulation results for QPSK-OFDM in AWGN channel are shown Rayleigh fading channel in Figure 2.

As can be seen the BER of Rayleigh and the difference between Weibull. Thus, it can be concluded that using QPSK modulation in AWGN channel to see difference when we chose three values equal to Rayleigh and over, less than Rayleigh as shown in Figure 3. And for log normal channel, the BER of Rayleigh and the difference between Log-Normal. Thus, it can be concluded that using QPSK modulation in AWGN channel to see difference when we chose three values equal to Rayleigh and over, less than Rayleigh as shown in Figure 4.

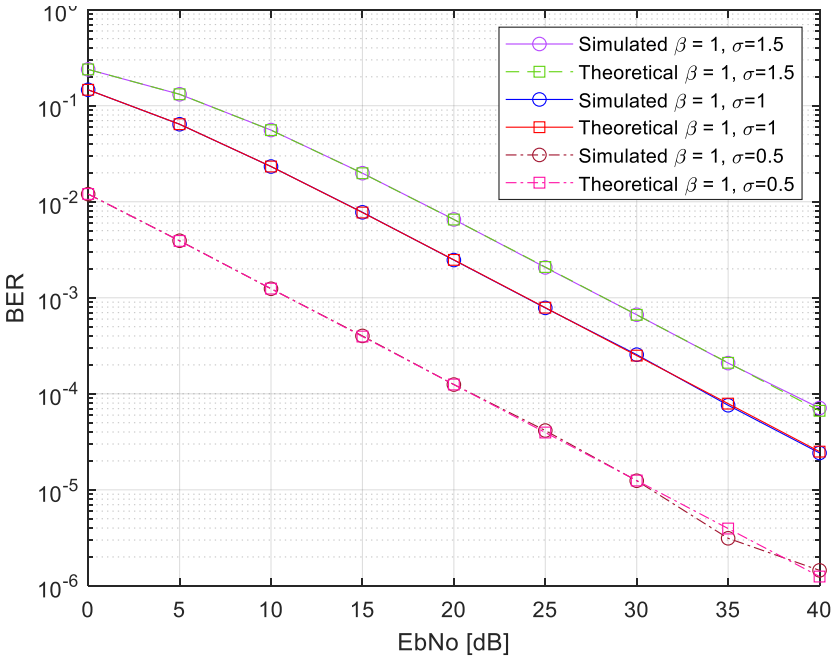

Figure 3. SNR vs BER for OFDM-QPSK over Weibull fading channel in AWGN

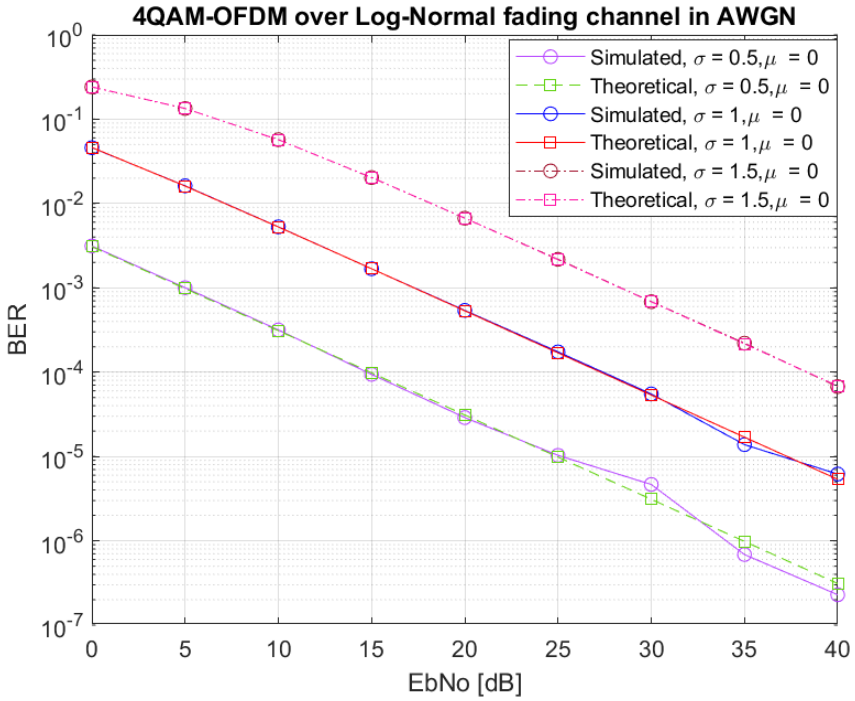

Figure 4. SNR vs BER for OFDM-QPSK over log-normal fading channel in AWGN

Conclusion

In this paper we have compared the performance of QPSK modulated OFDM systems in Rayleigh, Log-Normal and Weibull fading channels. The bit error rate results are compared using both simulations and analytical results. We find that Weibull and Log Normal fading is more challenging than Rayleigh fading.

Appendix

Derivation of BER of QPSK in Rayleigh fading in Equation 13

This section outlines the calculation of BER for QPSK-OFDM in Rayleigh fading and derives Equation 13 following Alouini and Goldsmith (1999). First it is observed that the magnitude of the subcarrier gain in Equation 11 is Rayleigh distributed. Since H_n is the sum of complex Gaussian random variables, it is also complex Gaussian random variables and its magnitude is Rayleigh distributed. In calculating the probability of error for QPSK we consider the in phase and quadrature components separately, since phase and frequency offsets are set to zero. In this case for the Rayleigh fading channel the gain of the in phase component is a Gaussian distributed random variable with mean 0 and variance $0.5\sigma_h^{\,2}$. Define $\gamma_0 = E_s \big/ N_0$. The SNR $\gamma_s = |h|^2 \gamma_0$ can be shown to be an exponential distributed random variable (Goldsmith, 2005):

$$f(\gamma) = \frac{1}{\gamma_0} e^{-\gamma/\gamma_0} u(\gamma) \tag{17}$$

The instantaneous BER for QPSK in a channel with instantaneous SNR $\gamma_s = |h|^2 \gamma_0$ is

$$P_b(h) = Q\left(\sqrt{\gamma_s}\right) = Q\left(\sqrt{|h|^2 \gamma_0}\right) \tag{18}$$

Averaging the BER over the Rayleigh distribution of the random channel gain h gives

$$P_b(\gamma_0) = E\left\{P_b(h\gamma_0)\right\} = \int_0^\infty Q\left(\sqrt{\gamma_s}\right) \frac{1}{\gamma_0} e^{-\gamma_s/\gamma_0} d\gamma \tag{19}$$

By definition the above function is the moment generating function (MGF) for the Gaussian distribution with some scalar adjustments. From this observation and the definition of the MGF leads to Equation 13.

Derivation of BER of QPSK in Weibull fading in Equation 15

The probability of error for OFDM-QPSK in Weibull fading is derived similarly to that in Rayleigh fading. The most important observation is that for larger numbers of multipath components, that is, larger values of *L*, the sum of independent identically distributed Weibull random variables with uniformly distributed phase will be a complex Gaussian random variable. Thus, the magnitude of H_n will be Rayleigh distributed. Define $\gamma_0 = E_s \big/ N_0$. The SNR $\gamma_s = |h|^2 \gamma_0$ can be shown to be an exponential distributed random variable (Goldsmith, 2005), with probability density function (pdf) as given by Equation 16. The derivation then proceeds the same as the derivation of Equation 13 but with the variance given by Equation 14.

Scientific Ethics Declaration

The authors declare that the scientific ethical and legal responsibility of this article published in EPSTEM journal belongs to the authors.

Acknowledgements

* This article was presented as an oral presentation at the International Conference on Technology, Engineering and Science (www.icontes.net) held in Antalya/Turkey on November 16-19, 2022.

References

Alouini, M. S., & Goldsmith, A. J. (1999). A unified approach for calculating error rates of linearly modulated signals over generalized fading channels. *IEEE Transactions on Communications*, *47*(9), 1324-1334.

Al-Rubaye, G. A., Tsimenidis, C. C., & Johnston, M. (2019). Performance evaluation of T-COFDM under combined noise in PLC with log-normal channel gain using exact derived noise distributions. *IET Communications*, *13*(6), 766-775.

Bingham, J. A. (1990). Multicarrier modulation for data transmission: An idea whose time has come. *IEEE Communications magazine*, *28*(5), 5-14.

Goldsmith, A. (2005). *Wireless communications*. Cambridge university press.

Jameel, F., Haider, M. A. A., & Butt, A. A. (2017, March). Performance analysis of VANETs under Rayleigh, Rician, Nakagami-m and Weibull fading. In *2017 International Conference on Communication, Computing and Digital Systems (C-CODE)* (pp. 127-132). IEEE.

Khandelwal, V. (2013). A new approximation for average symbol error probability over log-normal channels. *IEEE Wireless Communications Letters*, *3*(1), 58-61.

Ladaycia, A., Abed-Meraim, K., Bader, A., & Alouini, M. S. (2017, August). CFO and channel estimation for MISO-OFDM systems. In *2017 25th European Signal Processing Conference (EUSIPCO)* (pp. 2521-2525). IEEE.

Matolak, D. W., & Frolik, J. (2011). Worse-than-Rayleigh fading: Experimental results and theoretical models. *IEEE Communications Magazine*, *49*(4), 140-146.

Mishra, M. K., & Sood, N. (2011). SER analysis of OFDM system over rayleigh fading channel. *International Journal of Computer Applications*, *975*, 8887.

Prasad, R. (2004). *OFDM for wireless communications systems*. Artech House.

Sen, I., & Matolak, D. W. (2008). Vehicle–vehicle channel models for the 5-GHz band. *IEEE transactions on intelligent transportation systems*, *9*(2), 235-245.

Singh, N. S., & Singh, G. (2013). Performance evaluation of log-normal and negative exponential channel modeling using various modulation techniques in OFDM-FSO communication. *International Journal of Computers & Technology*, *4*(2c2), 639-647.

Wang, Y., Liu, F., & Wang, P. (2019, April). Performance analysis of V2V links in highway scenarios with weibull-lognormal composite fading. In *2019 IEEE Wireless Communications and Networking Conference (WCNC)* (pp. 1-6). IEEE.

Author Information

Zainab Qassab
Istanbul Okan University
Istanbul, Turkey
Contact e-mail: *zainabusaqi143@gmail.com*

Didem Kivanc Tureli
Istanbul Okan
University Istanbul,
Turkey

To cite this article:

Qassab, Z. & Tureli, D. (2022). Comparing performance of OFDM based V2V system in Rayleigh and Weibull fading channels. *The Eurasia Proceedings of Science, Technology, Engineering & Mathematics (EPSTEM), 21*, 131-138.

The Eurasia Proceedings of Science, Technology, Engineering & Mathematics (EPSTEM)
ISSN: 2602-3199

The Eurasia Proceedings of Science, Technology, Engineering & Mathematics (EPSTEM), 2022

Volume 21, Pages 139-143

IConTES 2022: International Conference on Technology, Engineering and Science

Determination of Setting Times of Mortar Mixtures Prepared with Cement Having Different C_3A Ratios

Kemal KARAKUZU
Bursa Uludag University

Veysel KOBYA
Bursa Uludag University

Ali MARDANI
Bursa Uludag University

Abstract: The duration of concrete transportation to the construction site, its workability and formwork removal time are significantly affected by the setting time of cement. Therefore, it is of great importance to know the initial and final setting times of concrete mixtures in construction applications. According to the literature survey, the setting time of cementitious systems is generally determined on cement paste mixture by the Vicat test. However, it was understood that a limited number of studies were carried out on the determination of the setting time using concrete mixtures. In this study, the effect of cement C_3A ratio variation on the initial and final setting times of cementitious systems was determined using mortar mixtures. For this purpose, mortar mixtures were prepared by using cement having four different C_3A content (2%, 3%, 6% and 9%). The ratios of water/cement and sand/cement as well as slump-flow values were kept constant as 0.485, 2.75 and 27±2 cm, respectively. In order to provide the desired flowability, polycarboxylate ether-based water-reducing admixture (PCE) was used. The initial and final setting times of the mortar mixtures were determined using a concrete penetrometer equipment. According to the results, PCE demand to provide the target slump-flow value increased by increasing the cement C_3A content. In addition, the setting time values reduction was observed with the increase of cement C_3A content. It was determined that the results obtained are compatible with the literature.

Keywords: Setting time, C_3A, Penetrometer, PCE requirement

Introduction

The term setting of cementitious systems is meant to transition cement-based materials from a flowable to a hardened state (Mindess et al, 2002; Hong et al, 2020; Kaya, 2022). It is of great importance to know the initial and final setting times of concrete mixtures in construction applications in terms of the duration of concrete transportation to the construction site, its workability and formwork removal time. However, the setting times of the mixtures can be obtained differently from each other due to the various methods used in practice. This situation can cause serious adverse effects on the properties of cementitious systems. situation can cause (Mindess et al, 2002; Durgun et al, 2022; Lee & Hover, 2016).

The fresh-properties of cementitious systems depend on many physical and chemical parameters. The rate of hydration and workability of the cementitious system are significantly affected by some factors such as the chemical composition of cement, especially its C_3A content and fineness as well as the gypsum type and amount added to its clinker during the manufacturing process (Zingg et al, 2009; Karakuzu et al, 2021; Kobya et al, 2022). C_3A is the most reactive component of cement (Mehta & Monteiro, 2006; Karakuzu et al, 2022). The

- Selection and peer-review under responsibility of the Organizing Committee of the Conference

formation of needle-like ettringite as a result of the C_3A reaction consumes some of the free water in the solution and adversely affects the fresh state properties of cementitious systems (Luke & Aitcin, 1990). Therefore, low C_3A content in cementitious systems is preferred in terms of fresh-state properties (Aitcin, 2004; Gawlicki et al, 2010).

The rapid hydration of C_3A seriously affects the setting time of the mixtures. In this context, the C_3A content of cement is one of the important parameters to be considered in terms of setting time and workability properties. The setting time of cement is usually measured with the Vicat test. It was understood that there is detailed information in the literature on this subject. However, it was determined that there is a lack of information in the literature about the determination of the setting time of mixtures using penetrometer apparatus. In this study, the effect of different C_3A ratios on the setting time of mortar mixtures was investigated. For this purpose, mortar mixtures were prepared using cement with 4 different C_3A ratios produced from the same raw material. A penetrometer was used to determine the initial and final setting times of the mixtures.

Materials and Method

Materials

In this study, CEMI 42.5R type cement having 4 different C_3A ratios and conforming to EN 197-1 was used. The chemical composition, as well as physical and mechanical properties of cement provided by their manufacturer is shown in Table 1. The designation of the cement was concluded according to its C_3A ratio. Some properties of the polycarboxylate based water reducing admixture (PCE) used in the preparation of the mortar mixtures are shown in Table 2. The CEN sand in accordance with EN 196-1 was used in the preparation of mortar mixtures.

Table 1. Chemical composition as well as physical and mechanical properties of cements

		Cement type			
Chemical Properties	Unit	C2	C3	C6	C9
C_3A	%	2.1	3.6	6.8	9.05
C_3S	%	58.9	47.6	52.9	48.42
C_2S	%	9.8	20.2	16.7	21.25
C_4AF	%	16.8	16.1	12.5	10.07
Physical and mechanical properties					
Specific gravity		3.21	3.20	3.17	3.1
Specific surface area	cm^2/g	3786	3754	3659	4259
28-day compressive strength	MPa	48.5	48.4	51.0	50.7

Table 2. Some properties of PCE

Type	Solid content (%)	Density (g/cm^3)	pH 25°C	Chloride content (%)	Alkali ratio, Na_2O (%)
Polycarboxylate based	40	1.070	2-5	<0.1	<10

Method

The mortar mixtures were prepared in accordance with ASTM C109. In all of the mortar mixtures, the water/cement ratio, sand/cement ratio and target slump-flow values were kept constant as 0.485, 2.75 and 270±20 mm, respectively. Hobart mixer was used to prepare the mixtures homogeneously. Slump-flow value of mortar mixtures was determined in accordance with ASTM C1437.

The initial and final setting times of the mortar mixtures were determined using a penetrometer device in accordance with ASTM C403. For each cement type, the mortar mixture in which the target slump-flow (27±2 cm) values were provided by using different ratios of PCE was prepared. The prepared mixtures were filled into 150 mm cube molds and recorded the time at which initial contact was made between cement and mixing water. When the penetration needle of the penetrometer device with a bearing-area of 16 mm^2 penetrates 25 mm into the specimen, the resistance value was determined as the first penetration resistance. From this measurement,

the penetration test was repeated at 30-minute intervals. The time during which the penetration resistance of 3.5 MPa was determined was obtained as the initial setting time, and the time during which the penetration resistance of 27.6 MPa was determined as the final setting time. The average of three specimen measurements was taken to determine the initial and final setting times. The penetrometer device and the experiment for determining the setting times are shown in Figure 1 and Figure 2, respectively.

Figure 1. Penetrometer device

Figure 2. Determination of the initial and final setting times of specimens with penetrometer

Results and Discussion

The PCE requirements and slump-flow values of the mortar mixtures are shown in Table 3. For C3, C6 and C9-cement containing mortar mixtures, the PCE requirement to provide desired slump-flow value increased by 2%, 4% and 52%, respectively, compared to the mortar mixtures prepared with C2 cement. Due to the high reactivity of C_3A, the formation of ettringite in large quantities causes the reduction of free water in the solution, thus negatively affecting the flow performance of the mixture (Mardani-Aghabaglou et al, 2017). Therefore, the increase in the C_3A ratio of cement led to an increase in the PCE requirement for the target slump-flow value of the mixtures.

Table 3. PCE requirement and slump-flow value of the mixtures

	PCE requirement (%)*	Slump-flow value (cm)
C2	0.260	26.0
C3	0.265	27.8
C6	0.270	27.9
C9	0.395	26.9

*by weight of cement

The penetration resistance values and the initial - final setting times of the mortar mixtures are shown in Figure 3. Compared to the mortar mixtures prepared with the C2 cement, the initial setting times of the C3, C6 and C9

cement-containing mixtures decreased by 6%, 8% and 9%, respectively, with the increase in the C_3A content. It was observed that there was a decrease in the final setting times of 2%, 4% and 8%, respectively. As can be seen from the results, the increase in C_3A content led to a decrease in the setting times of the mortar mixtures. In addition, the reduction in initial setting times is slightly greater than in final setting times. This is due to the fact that C_3A component is the most reactive component in cement, as stated before. Therefore, the increase in C_3A content was more effective on the initial setting time.

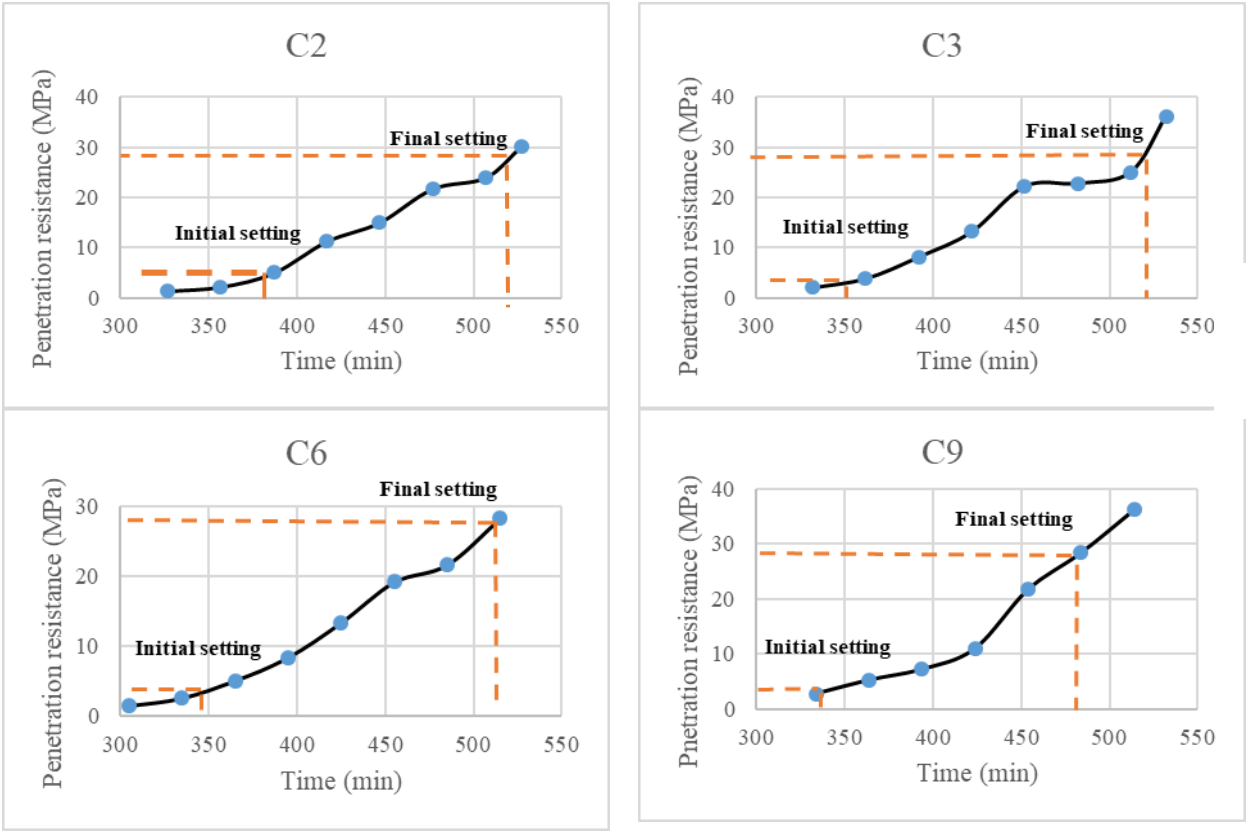

Figure 3. Penetration resistance and initial - final setting times values of the mixtures

Conclusion

The results obtained in this study, in which the initial and final setting times of mortar mixtures prepared with cements with different C_3A content were determined by penetrometer, are as follows:

• The PCE requirement to provide the desired slump-flow value in the mortar mixtures decreased by the reduction of cement C_3A content.

• The increase in C_3A content resulted in a reduction of the setting time of mortar mixtures. This effect was more pronounced for the initial setting time. It was thought that the C_3A content are more affected by elapsed time.

Scientific Ethics Declaration

The authors declare that the scientific ethical and legal responsibility of this article published in EPSTEM journal belongs to the authors.

Acknowledgements and Notes

* This article was presented as an oral presentation at the International Conference on Technology, Engineering and Science (www.icontes.net) held in Antalya/Turkey on November 16-19, 2022.

*The authors thank to the Scientific and Technological Research Council of Turkey (TUBITAK) for their contributions (Project No: 219M425). The first and second authors acknowledge the scholarship provided by Turkish Council of Higher Education (YOK 100/2000 Program) during their PhD study. The authors would also like to thank Polisan Construction Chemicals Company and Bolu Cement Company authorities for their kind assistance in providing the cement and water-reducing admixture as well as determining their properties.

References

Aitcin, P.C., (2004). *High performance concrete*. E&FN SPON.

Durgun, M. Y., Ozen, S., Karakuzu, K., Kobya, V., Bayqra, S. H., & Mardani-Aghabaglou, A. (2022). Effect of high temperature on polypropylene fiber-reinforced mortars containing colemanite wastes. *Construction and Building Materials, 316*, 125827.

Gawlicki, M., Nocuń-Wczelik, W., & Bąk, Ł. (2010). Calorimetry in the studies of cement hydration: setting and hardening of Portland cement–calcium aluminate cement mixtures. *Journal of Thermal Analysis and Calorimetry, 100*(2), 571-576.

Hong, J., Kim, R., Lee, C. H., & Choi, H. (2020). Evaluation of stiffening behavior of concrete based on contactless ultrasonic system and maturity method. *Construction and Building Materials*, *262*, 120717.

Karakuzu, K., Kobya, V., & Mardani, A. (2022). Reolojik parametreleri olculebilen farkli c3a oranina sahip hamur karisimlarinda optimum su azaltici katki dozajinin ve su muhtevasinin belirlenmesi. Avrupa *Bilim ve Teknoloji Dergisi*, *37*, 17-20.

Karakuzu, K., Kobya, V., Mardani-Aghabaglou, A., Felekoglu, B., & Ramyar, K. (2021). Adsorption properties of polycarboxylate ether-based high range water reducing admixture on cementitious systems: A review. *Construction and Building Materials*, *312*, 125366.

Kaya, Y. (2022). *The effect of utilization of different types of clinker grinding aids on the properties of cement systems* (Master's thesis). Bursa Uludag University.

Kobya, V., Kaya, Y., & Mardani-Aghabaglou, A. (2022). Effect of amine and glycol-based grinding aids utilization rate on grinding efficiency and rheological properties of cementitious systems. *Journal of Building Engineering*, *47*, 103917.

Lee, C. H., & Hover, K. C. (2016). Early-age stiffening of paste, mortar, and concrete in lab and field. *ACI Materials Journal*, *113*(1).

Luke, K., & Aitcin. P.C. (1990). Effect of superplasticiser on ettringite formation. *Ceram. Trans*., *16*, 147-166.

Mardani-Aghabaglou, A., Felekoglu, B., & Ramyar, K. (2017). Effect of cement C_3A content on properties of cementitious systems containing high-range water-reducing admixture. *Journal of Materials in Civil Engineering*, *29*(8), 04017066.

Mehta, P.K., & Monteiro, P.J.M. (2006). *Concrete*, 3rd Edn., McGraw-Hill Companies Inc.

Mindess, S., Young, J. F., & Darwin, D. (2002). *Concrete*. Pearson Eduction.

Zingg, A., Winnefeld, F., Holzer, L., Pakusch, J., Becker, S., Figi, R., & Gauckler, L. (2009). Interaction of polycarboxylate-based superplasticizers with cements containing different C3A amounts. *Cement and Concrete Composites*, *31*(3), 153-162.

Author Information

Kemal Karakuzu
Bursa Uludag University
Civil Engineering Department, Nilufer-Bursa,Turkey

Veysel Kobya
Bursa Uludag University
Civil Engineering Department, Nilufer-Bursa,Turkey

Ali Mardani
Bursa Uludag University
Civil Engineering Department,
Nilufer-Bursa, Turkey
Contact e-mail:*ali.mardani16@gmail.com*

To cite this article:

Karakuzu, K., Kobya, V. & Mardani, A. (2022). Determination of setting times of mortar mixtures prepared with cement having different C_3A ratios. *The Eurasia Proceedings of Science, Technology, Engineering & Mathematics (EPSTEM), 21*, 139-143.

The Eurasia Proceedings of Science, Technology, Engineering & Mathematics (EPSTEM)
ISSN: 2602-3199

The Eurasia Proceedings of Science, Technology, Engineering & Mathematics (EPSTEM), 2022

Volume 21, Pages 144-151

IConTES 2022: International Conference on Technology, Engineering and Science

Improving the Properties of Medium Molecular Weight Chitosan/PVA Composite Polymers via Designed ZnO Particles

Yeliz KOSE
Bilecik Seyh Edebali University

Ender SUVACI
Eskisehir Technical University

Abstract: Chitosan exhibit great potential to be a critical part of the global sustainability solution; however, its application areas are limited due to its inadequate properties for some applications. The use of chitosan is limited because of several reasons such as performance (brittleness, poor barrier properties) and processing (low thermal strength temperatures). The properties of chitosan depend on its molecular weight and there are not enough studies in the literature. The application of nanoparticles to chitosan provides new advantages both in improving the properties of chitosan and in reducing its costs. However, such nanoparticles can introduce some difficulties. Nanoparticles additives increase transparency but cause agglomerates due to the high surface/volume ratio, which reduces the local mechanical strength. Recently a novel particle technology, called as MicNo®. MicNo® particles are designed micron size hexagonal plates which are composed of primary fine particles. They only exhibit advantages of micron and nano size. For example, they exhibit superior surface coverage (up to 70% mole) with respect to spherical particles while they are transparent. Accordingly, the research goal of this study was to appraise effects of MicNo® and nano ZnO particles on structure development and hence properties of medium molecular weight Chitosan/PVA films. The results show that MicNo® particles improve UV-resistance and degree of crystallinity of the films and demonstrate great potential as new generation additive systems for biodegradable polymers to extend their application areas.

Keywords: Chitosan, Polyvinyl alcohol, Zinc oxide, UV-blocking

Introduction

The molecular weight of chitosan affects the solubility, viscosity, mechanical and antibacterial properties of the film. The solubility of chitosan depends on the pH of the solution and the molecular weight of the chitosan. Thanks to its cationic structure, chitosan can be dissolved in most dilute acids in a pH <6 environment (Knittel & Schollmeyer, 1998). As the molecular weight of chitosan increases, its solubility decreases. The high solubility of medium molecular weight chitosan appears to be attributed to reduced intermolecular interactions such as Van der Waals forces and hydrogen bonds; the lower the molecular weight, the lower the intermolecular forces of attraction (Tikhonov et al., 2006). The decrease in molecular weight causes transformation of the crystal structure, decrease in thermal stability and increase in water solubility (Qin et al., 2003). As the molecular weight increases, the viscosity of chitosan increases as the segment content in the molecular chain increases (Fox et al., 1951). As the molecular weight of chitosan decreases, the tensile strength and % elongation of the film decreases. This is due to less entanglement factor of the polymer chains. In addition, less crystallinity in the films is reported as the reason (Chen & Hwa, 1996). The molecular weight of chitosan is an effective factor in the antibacterial activity of the films. The effect of molecular weight on the antibacterial activity of chitosan is still unclear. A general conclusion could not be reached on which of the low, medium or high molecular weight chitosan exhibits the best antibacterial activity (Zheng & Zhu, 2003). Low molecular weight chitosan films show higher antibacterial activity against gram-negative bacteria species. The results of

many studies are reported that low molecular weight chitosan can be universal antimicrobial agents against all kinds of bacteria and fungi (Gerasimenko et al., 2004). High molecular weight chitosan films show higher antibacterial activity against gram positive bacteria species. Gram-positive bacteria have an intrinsically different cell wall structure. High molecular weight chitosan surrounds bacterial cells. The polymer layer formed becomes a mechanical barrier that prevents nutrient uptake and subsequently leads to the death of the vegetative form (Fernandes et al., 2009). In order to clearly determine the factors affecting the antibacterial activity and mechanical properties of chitosan, it is necessary to examine the physicochemical properties of chitosan with different molecular weights such as crystallinity and thermal stability.

It has been proven that the addition of nanoscale additives to the chitosan matrix improves its thermal and mechanical properties, reduces moisture and gas permeability (Sorrentino et al., 2007), and achieves high antibacterial and bacteriostatic activity (Chen & Wang, 2001) as well as antioxidant properties (Heras et al., 2001). Among metal oxides, ZnO is described as a functional, strategic, promising and versatile inorganic material with a wide range of applications. Recently, ZnO has been listed as a safe material by the FDA (Food and Drug Administration, SA) (Emamifar et al., 2010). ZnO has unique optical, chemical susceptibility, semiconductor, electrical conductivity, and piezoelectric properties (Fan & Lu, 2005). It is characterized by direct broad bandgap (3.3 eV) in the near UV spectrum, high excitonic binding energy (60 meV) at room temperature, and inherent n-type electrical conductivity (Wellings et al., 2008). The wide bandgap of ZnO has significant influence on its properties such as electrical conductivity and optical absorption. Although ZnO shows slightly covalent character, it has very strong ionic bond in Zn-O. It has high stability and high heat resistance against organic materials (Padmavathy & Vijayaraghavan, 2008). In addition to its unique antibacterial and antifungal properties, ZnO nanoparticles have high catalytic and high photochemical activities. ZnO nanoparticles show biocidal effects on bacteria, fungi and viral species (Adams et al., 2006). ZnO has high optical absorption in the UVA (315-400 nm) and UVB (280-315 nm) regions, making it beneficial in antibacterial response and used as a UV protector in cosmetics (Song et al., 2011).

Since it is known that ZnO properties change depending on the shape and size of the particle, the designed plate-shaped micron particle MicNo® ZnO (=Micron+naNo) was used in this study. MicNo® ZnO has the properties of both nano and micron size. Coaxial particles with a particle size of 30-35 nm coalesced to form very thin, 2-10 μm hexagonal layered structures. The specific surface area is 23.1 m^2/g, which is larger than the specific surface area of nano-sized ZnO (14.3 m^2/g). In addition to increasing the biocompatibility feature, this provides high transparency in the visible region and high barrier feature in the UV region (Genc et al., 2018).

Studies examining the effects of the use of medium molecular weight chitosan and the morphology-size relationship of ZnO on the properties are limited in the literature. Therefore, in this study, ZnO particles in the form of nano and MicNo® doped with medium molecular weight Chitosan/PVA polymer and their effects on optical, mechanical and antibacterial properties were investigated.

Experimental Procedure

Materials

Chitosan (CS) with medium molecular weight and degree of deacetylation of 75% by CDH was used. In addition, PVA with average molecular weight of 190,000–205,000 Da, glacial acetic acid and glycerol with molar weight 92.09 g/mol by Sigma-Aldrich Co.LLC were utilized. MicNo® ZnO inorganic powders with 2-10 μm sized hexagonal platelet aggregates of 30-100 nm size particles were supplied by Entekno Materials Inc. Nano ZnO inorganic powder with <100 nm individual size particles by Sigma-Aldrich Co.LLC. was used as a reference material for bench-marking.

Preparation of CS/PVA/ZnO Composites Film

CS (300 mg) was first dissolved in 30 mL of 2% aqueous acetic acid solution and PVA (1.5 g) was dissolved in 30 mL water at 80°C. Both of the clear solutions were kept overnight while they were being stirred. After that, the PVA solution (12 mL) was added to the CS solution (8 mL) while it was being magnetically stirred to get clear solution. Then, nano ZnO or MicNo® ZnO (300 mg) and glycerol (0.2 mL) were added into the Chitosan/PVA solution which was at 80°C and stirred by keeping overnight. The obtained gel-like viscous solution was poured onto a plastic substrate and the films with a thickness of 200 μm were prepared by tape

casting technique and dried in air at room temperature for 24 h. In Table 1, the designations of the samples that were studied in this project, are shown.

Table 1. Used powder systems in composite films and their names

Sample No	Sample	Sample Name
1	0 (wt.%) ZnO doped Chitosan/PVA Film	ZnO-0
2	2.5 (wt.%) nano-ZnO doped Chitosan/PVA Film	ZnO-N
3	2.5 (wt.%) MicNo® -ZnO doped Chitosan/PVA Film	ZnO-M

Materials Characterization

X-ray diffraction (XRD) analyses were performed by D2 Phaser (Bruker, Cu K_{α}=1.54Å)) for phase determination. The fourier transformed infrared (FTIR) spectra were collected by IRTracer-100 (Shimadzu, the wavelength range of 4000-600 cm^{-1}). The films were placed in the holder directly in the IR laser beam. The size and morphology of the particles were examined with scanning electron microscopy (SEM EVO 50 LP, Zeiss, operating at 10 kV). The optical measurements were conducted by UV-VIS-NIR spectrophotometer (UV-3600 Plus UV-VIS-NIR, Shimadzu) in a wavelength range of 260-750 nm. The mechanical analyses were performed in a universal testing machine (INSTRON 5581) with 5 samples in each case with a dimension of 100 x 20 mm. Antibacterial activities of films were determined by using ISO 22196:2011 standart (Perelshtein et al., 2013). Antibacterial activity was calculated according to the ISO 22196:2011 standard, the antibacterial activity value of a surface should be R≥2.

Result and Discussion

XRD Analyses

Figure 1 shows the XRD patterns of the films evaluated in this study. There are three characteristic peak formations in Chitosan/PVA films. These are the peak at 2θ=11.3° representing the crystalline phase, the 2θ=19.4° and 2θ=22.8° peaks representing the amorphous phase. While the peaks representing the amorphous phase were obtained, the peak representing the crystal phase was not obtained. This indicates that the time elapsed during the casting process after the chitosan has dissolved in acetic acid is shorter than the time required for the crystallization of the chitosan (Azizi et al., 2014). In addition to the characteristic peaks of Chitosan/PVA chitosan films, sharp characteristic peaks of hexagonal wurtize type crystal structure ZnO 2θ=32.04°- 34.71°- 36.54°- 47.85°- 56.94°- 63.20°- 68.32° was seen (JCPDS card no: 36-1451). These peaks belong to (100), (002), (101), (102), (110), (103) and (112) planes, respectively. This behavior indicates that the original structure of ZnO inorganic powders remains unchanged in the Chitosan/PVA matrix. The high hydroxyl group content of PVA prevents inorganic ZnO additives from agglomerating and ensures homogeneous dispersion in the Chitosan/PVA matrix (Rashmi et al., 2014) Since the specific surface area of MicNo® ZnO is greater than that of nano ZnO inorganic powders, it leads to an increase in the crystallinity of composite films. XRD peak intensities in MicNo® ZnO doped films are expected to be higher than nano ZnO doped films. However, XRD peak intensities were found to be low due to the homogeneity problem.

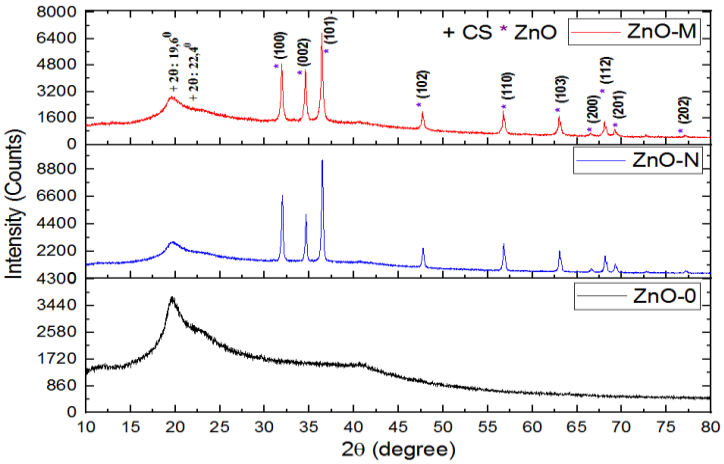

Figure 1. XRD patterns of the studied films

FTIR Analyses

The characteristic functional groups were investigated through FTIR spectra of the studied films as shown in Figure 2. The strong band between 3550-3200 cm^{-1} corresponds to the N-H and O-H stretches with hydrogen bonds. Absorption bands between 3000-2840 cm^{-1} can be attributed to C-H symmetrical and asymmetrical stresses (Biazar et al., 2015). The peak at 1543 cm^{-1}, belonging to the primary amine N-H bending, was obtained (Fernandes Queiroz et al., 2014). The reason that the intensity of the peak at 1543 cm^{-1} increases with the amount of ZnO is due to the increase in the intermolecular hydrogen bonds between -NH groups of chitosan and ZnO (Vicentini et al., 2010). The $-CH_2$ bending and $-CH_3$ symmetrical stretching are clearly visible with bands of 1458 cm^{-1} and 1371 cm^{-1}, respectively. The peak band at 1236 cm^{-1} represents the C-N stretch mode. It is seen that the absorption bands between 1155-1050 cm^{-1} belong to the C-O stretch (Lim & Hudson, 2004). Absorption bands between 995-875 cm-1 can be attributed to the C=C symmetrical stretch (Vino et al., 2012). With the addition of inorganic ZnO powders to the films, characteristic bands shifted to lower wavelengths and their intensity increased. The reason for this is the formation of intermolecular hydrogen bonds between PVA, Chitosan and ZnO.

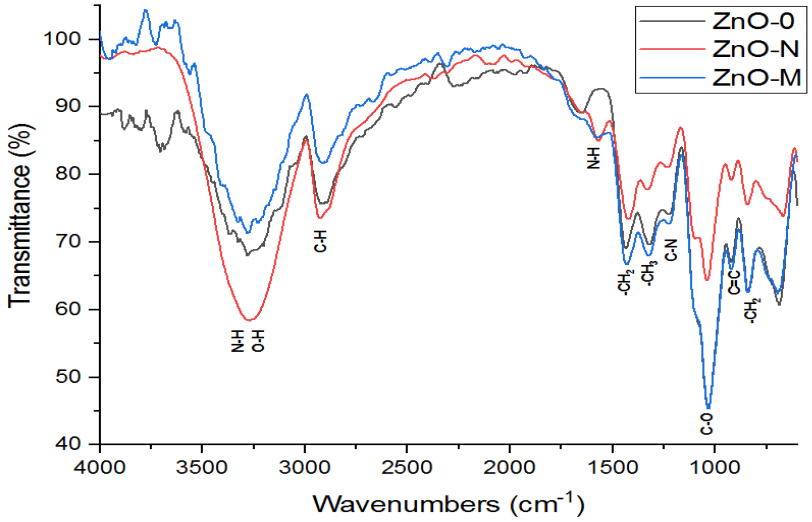

Figure 2. FTIR spectra of the studied films

SEM Analyses

Figure 3 shows SEM micrographs of the films studied in this work. Agglomerate formation is higher in MicNo® ZnO containing films with respect to nano ZnO containing films.

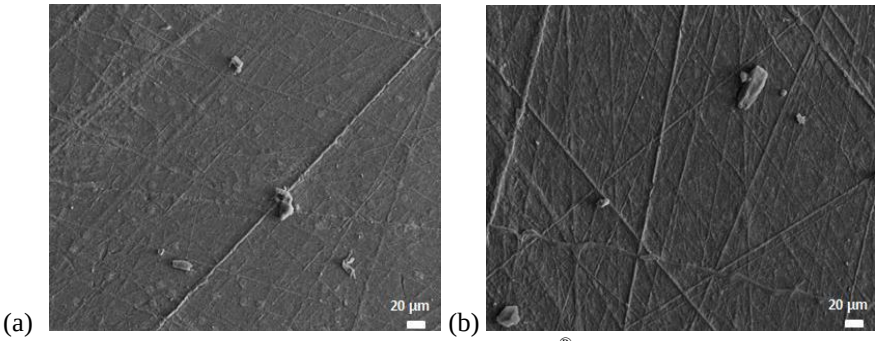

Figure 3. SEM micrographs of (a) nano ZnO and (b) MicNo® ZnO doped Chitosan/PVA film

UV-Visible Analyses

It was observed that the amount of absorption increased when ZnO was added in the UV region. The increase in UV absorption intensity between 355-375 nm indicates the presence of chromophore groups in composite films (Chouhan et al., 2015). In addition, the absorption bands shifted to higher wavelengths when ZnO was added.

The reason for this is the hydrogen bonds formed between PVA –OH groups, –OH and –NH of Chitosan and Zn ions (Kumar et al., 2014). In the UVA (315-400nm) and UVB (280-315 nm) regions, higher absorption is expected in MicNo® ZnO doping due to the higher surface area of MicNo® ZnO compared to nano ZnO doping. However, as seen in the XRD analysis, less absorption was found in the films with MicNo® ZnO doped due to the agglomeration problem in the films. The reason why the transparency in the visible region decreases with the addition of ZnO is that ZnO does not disperse homogeneously and forms agglomerates.

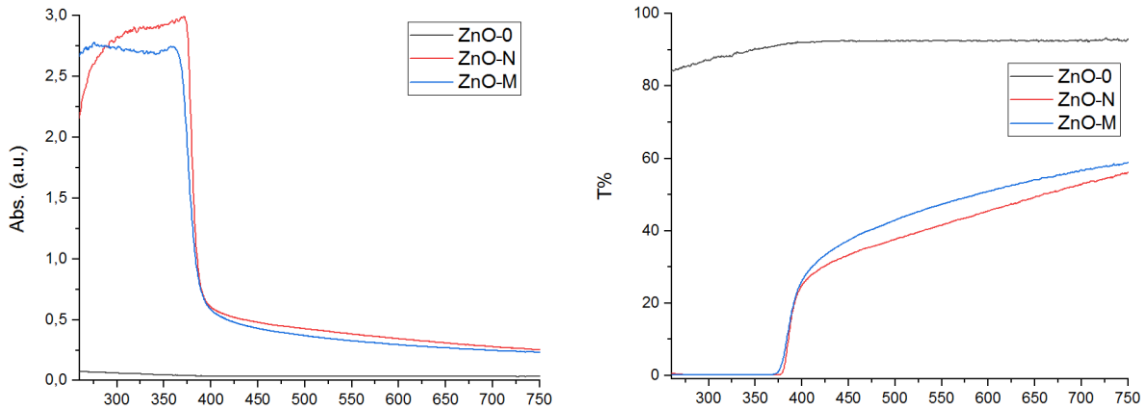

(a) (b)

Figure 4. (a) UV-vis absorbance, (b) UV-vis transparence spectra of the studied films

Mechanical Analyses

Table 2 shows average tensile strength (MPa) and % elongation values of the studied films in this work. The average tensile strength value of ZnO-0 was 0.58 MPa and the average % elongation amount was 16.42 %. An increase in tensile strength and a decrease in % elongation were observed with the addition of inorganic ZnO particles into the film. Whereas the tensile strength and the elongation values were 0.90 MPa and 10.20 %, respectively, for the nano ZnO containing system, they were 1.52 MPa and 13.33 %, respectively, for the MicNo® ZnO containing system. The reason for this change in mechanical strength is probably due to hydrogen bonds formed between PVA, Chitosan and Zn^{+2} ions. In addition, this interaction restricts the movement of molecular chain segments, which causes a decrease in elongation (Yin et al., 2018).

Table 2 Average tensile strength (MPa) and % elongation values of the studied films

Sample Name	Average Tensile Strength (MPa)	Average Elongation (%)
ZnO-0	0.58	16.42
ZnO-N	0.90	10.20
ZnO-M	1.52	13.33

Antibacterial Analyses

In Table 3, the antibacterial activity (R) values against S.Aureus and E.Coli of the studied films are shown. ZnO-0 and ZnO-N films do not exhibit adequate antibacterial effect. With the addition of MicNo® ZnO particles with high antibacterial activity into the films, the R values became compatible with the ISO 22196:2011 standard (R≥2). As the specific surface area of ZnO increases, the contact surface area/volume between microorganisms and the particles increases as in the MicNo® case and this interaction makes the adsorption of ZnO particles onto the microbial cell walls mechanism dominant (Demirel et al., 2018). Therefore, the R values of the MicNo® ZnO doped films were higher than the nano ZnO doped films.

Table 3 The antibacterial activity (R) values against S.Aureus and E.Coli of the studied films

Sample Name	S.Aureus (R)	E.Coli (R)
ZnO-0	0.08	0.30
ZnO-N	1.38	1.70
ZnO-M	2.47	2.57

Inhibition experiment (Figure 5) was applied with agar diffusion method. The occurrence of the inhibition zone indicates that the tested ZnO powder systems have different levels of antibacterial activities on bacteria (Demirel et al., 2018). ZnO-M films appear to inhibit S.Aureus (1-2 mm).

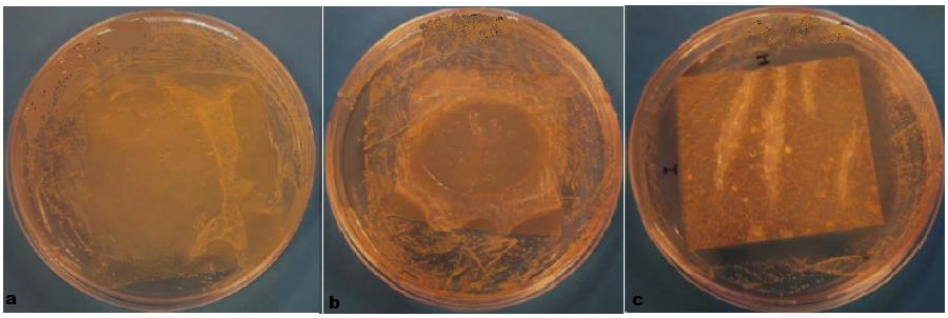

Figure 5. Inhibition zone thicknesses (mm) against S.Aureus of (a) ZnO-0, (b) ZnO-N, (c) ZnO-M

Conclusion

The changes in the film properties were investigated with ZnO doping with different size & morphology (nano-MicNo®) to the medium molecular weight Chitosan/PVA matrix. With ZnO doping, the degree of crystallinity and UV-blocking capacity of the films increase. Since the specific surface area of MicNo® sized ZnO doped films is higher than nano sized ZnO, this increase is expected to be more effective. However, due to the use of 2% (v/v) glycerol, a tendency to agglomerate was observed in the films, as supported by SEM analysis, and the homogeneous distribution of inorganic powders along the film surface was not realized. According to the mechanical strength analysis, it was observed that there was an increase in tensile strength and a decrease in % elongation with inorganic ZnO doping of the medium molecular weight Chitosan/PVA films. According to the antibacterial analysis, no bacterial growth was observed in the ZnO-M films, and a bacteriocidal effect was found.

Scientific Ethics Declaration

The authors declare that the scientific ethical and legal responsibility of this article published in EPSTEM journal belongs to the authors.

Acknowledgements or Notes

* This article was presented as a poster presentation at the International Conference on Technology, Engineering and Science (www.icontes.net) conference held in Antalya/Turkey on November 16-19, 2022.

*This research was supported financially by the Eskisehir Technical University Scientific Research Projects Commission (Project number: 20DRP036). The authors would like to thank Prof. Dr. Rasime Demirel for her contributions for the antibacterial tests.

References

Adams, L. K., Lyon, D. Y. & Alvarez, P. J. J. (2006). Comparative ecotoxicity of nanoscale TiO_2, SiO_2, and ZnO water suspensions. *Water Research, 40, 3527- 3532.*

Azizi, S., Ahmad, M. B., Ibrahim, N. A., Hussein, M. Z. & Namvar, F. (2014). Cellulose nanocrystals/ZnO as a bifunctional reinforcing nanocomposite for poly(vinyl alcohol)/chitosan blend films: Fabrication, characterization and properties. *International Journal of Molecular Sciences, 15, 11040-11053.*

Biazar, E., Zaeifi, D., Keshel, S. H., Ojani, S., Hajiaghaee, A., Safarpour, R. & Sadeghpour, S. (2015). Design of electrospun poly vinyl alcohol/chitosan scaffoldand its cellular study. *Journal of Paramedical Sciences, 6(3), 46-51.*

Chen, R. H. & Hwa, H.-D. (1996). Effect of molecular weight of chitosan with the same degree of deacetylation on the thermal, mechanical, and permeability properties of the prepared membrane. *Carbohydrate Polymers 29, 353-358.*

Chen, S. & Wang, Y. (2001). Study on b-cyclodextrin grafting with chitosan and slow release of its inclusion complex with radioactive iodine. *Journal of Applied Polymer Science 82, 2414.*

Chouhan, S., Bhatt, R., Bajpai, A. K., Bajpai, J. & Katare, R. D. (2015). Investigation of UV Absorption and Antibacterial Behavior of Zinc Oxide Containing Poly (vinyl alcohol-g-acrylonitrile) (PVA-g-PAN) Nanocomposites Films. *Fibers and Polymers, Vol.16, No.6, 1243-1254.*

Demirel, R., Suvaci, E., Sahin, I., Dag, S. & Kilic, V. (2018). Antimicrobial activity of designed undoped and doped MicNo-ZnO particles. *Journal of Drug Delivery Science and Technology 47, 309–321.*

Emamifar, A., Kadivar, M., Shahedi, M. & Zad, S. S. (2010). Evaluation of nanocomposite packaging containing Ag and ZnO on shelf life of fresh orange juice. *Innovative Food Science & Emerging Technologies 11, Issue 4 742-748.*

Fan, Z. & Lu, J.G. (2005). Zinc oxide nanostructures: synthesis and properties. *Journal of Nanoscience Nanotechnology 5(10), 1561-1573.*

Fernandes Queiroz, M., Melo, K.R.T., Sabry, D.A., Sassaki, G.L. & Rocha, H.A.O. (2014). Does the use of chitosan contribute to oxalate kidney stone formation?. *Marine Drugs, 13(1),* 141-158.

Fernandes, J. C., Eaton, P., Gomes, A. M., Pintado, M. E. & Malcata, F. X. (2009). Study of the antibacterial effects of chitosans on Bacillus cereus (and ist spores) by atomic force microscopy imaging and nanoindentation. *Ultramicroscopy, 109, 854-860.*

Fox, T. G., Fox, J. C. & Flory, P. J. (1951). The effect of rate of shear on the viscosity of dilute solutions of polyisobutylene. *Journal of the American Chemical Society 73 (5), 1901-1904.*

Genc, H., Barutca, B., Koparal, A. T., Ozogut, U., Sahin, Y. & Suvaci, E. (2018). Biocompatibility of designed Micno-ZnO particles: Cytotoxicity, genotoxicity and phototoxicity in human skin keratinocyte cells. *Toxicology in Vitro, 47, 238-248.*

Gerasimenko, D. V., Avdienko, I. D., Bannikova, G. E., Zueva, O. & Varlamov, V. P. (2004). Antibacterial effects of water-soluble low-molecular-weight chitosans on different microorganisms. *Applied Biochemistry and Microbiology, 40, 253- 257.*

Heras, A., Rodriguez, N. M. & Ramos, V. M. (2001). N-methylene. phosphonic chitosan: a novel soluble derivative. *Carbohydrate Polymer 44* (1), 1-8.

Hezma, A. M., Rajeh, A. & Mannaa, M. A. (2019). An insight into the effect of zinc oxide nanoparticles on the structural, thermal, mechanical properties and antimicrobial activity of Cs/PVA composite. *Colloids Surface A 581, 123821.*

Knittel, D. & Schollmeyer, E. (1998). Chitosan und seine derivate fur die textilveredlung teil 1: Ausgansposition. *Textilveredlung, 33,* Nr. 3/4.

Kumar, N. B. R., Crasta, V. & Praveen, B. M. (2014). Advancement in microstructural, optical, and mechanical properties of PVA (Mowiol 10-98) doped by ZnO nanoparticles. *Hindawi Publishing Corporation Physics Research International Volume 2014, Article ID 742378, 9 pages.*

Lim, S. H. & Hudson, S. M. (2004). Synthesis and antimicrobial activity of a water-soluble chitosan derivative with a fiber-reactive group. *Carbohydrate Research, 339(2), 313-319.*

Padmavathy, N. & Vijayaraghavan, R. (2008). Enhanced bioactivity of ZnO nanoparticles-an antimicrobial study. *Science and Technology of Advanced Materials 9(3), 035004.*

Perelshtein, I., Ruderman, E., Perkas, N., Tzanov, T., Beddow, J., Joyce, E., Timothy J. M., Blanes, M., Mollá, K., Patlolla, A., Frenkel, A. I. & Gedanken, A. (2013). Chitosan and chitosan-ZnO-based complex nanoparticles: formation, characterization, and antibacterial activity. *Journal of Materials Chemistry B 14, 1968–1976.*

Qin, C., Du, Y., Zong, L., Zeng, F., Liu, Y. & Zhou, B. (2003). Effect of hemicellulase on the molecular weight and structure of chitosan. *Polymer Degradation and Stability 80, 435-441*

Rashmi, S. H., Raizada, A., Madhu, G. M., Kittur, A. A., Suresh, R. & Sudhina, H. K. (2014). Influence of zinc oxide nanoparticles on structural and electrical properties of polyvinyl alcohol films. *Plastics, Rubber and Composites, Vol.44,* No.1.

Song, Z., Kelf, T. A., Sanchez, W. H., Roberts, M. S., Rička, J., Frenz, M. & Zvyagin, A. V. (2011). Characterization of optical properties of ZnO nanoparticles for quantitative imaging of transdermal transport. *Biomedical Optics Express 2* (12), *3321-3333.*

Sorrentino, A., Gorrasi, G. & Vittoria, V. (2007). Potential perspectives of bio-nanocomposites for food packaging applications. *Trends Food Science Technology 18:* 84-95.

Tikhonov, V. E., Stepnova, E. A., Babak, V. G., Yamskov, I. A., Palma-Guerrero, J., Lopez-Llorca, L. V., Salinas, J., Gerasimenko, D. V., Avdienko, I. D. & Varlamov, V. P. (2006). Bactericidal and antifungal activities of a low molecular weight chitosan and its N-/2(3)-(dodec-2-enyl)succinoyl/- derivatives. *Carbohydrate Polymers 64,* 66-72.

Vicentini, D. S., Jr, A. S., Laranjeira & Mauro C.M. (2010). Chitosan/poly (vinyl alcohol) films containing ZnO nanoparticles and plasticizers. *Material Science Engineering C 30,* 503–508.

Vino, A. B., Ramasamy, P., Shanmugam, V. & Shanmugam, A. (2012). Extraction, characterization and in vitro antioxidative potential of chitosan and sulfated chitosan from cuttlebone of sepia aculeata orbigny, 1848. *Asian Pacific Journal of Tropical Biomedicine, 2(*1), 334-341.

Wellings, J., Chaure, N., Heavens, S. & Dharmadasa, I. (2008). Growth and characterisation of electrodeposited ZnO thin films. *Thin Solid Films 516*(12), 3893-3898.

Yin, M., Lin, X., Ren, T., Li, Z., Ren, X. & Huang, T.-S. (2018). Cytocompatible quaternized carboxymethyl chitosan/poly(vinyl alcohol) blend film loaded copper for antibacterial application. *International Journal of Biological Macromolecules 120,* 992–998.

Zheng, L. Y. & Zhu, J. F. (2003). Study on antimicrobial activity of chitosan with different molecular weights. *Carbohydrate Polymers, 54*, 527-530.

Author Information

Yeliz Kose
Bilecik Seyh Edebali University
Bilecik/TURKEY
e-mail: *yeliz.kose@bilecik.edu.tr*

Ender Suvaci
Eskisehir Technical University
Eskisehir/TURKEY

To cite this article:

Kose, Y., & Suvaci, E., (2022). Improving the properties of medium molecular weight chitosan/pva composite polymers via designed ZnO particles. *The Eurasia Proceedings of Science, Technology, Engineering & Mathematics (EPSTEM), 21,* 144-151.

The Eurasia Proceedings of Science, Technology, Engineering & Mathematics (EPSTEM)
ISSN: 2602-3199

The Eurasia Proceedings of Science, Technology, Engineering & Mathematics (EPSTEM), 2022

Volume 21, Pages 152-159

IConTES 2022: International Conference on Technology, Engineering and Science

The Effect of the Arrangement of a Reinforcement on the Mechanical Behavior of a Composite VER Composite Material

Habib ACHACHE
University of Oran Mohamed Ben Ahmed

Ghezail ABDI
University of Oran Mohamed Ben Ahmed

Rachid BOUGHEDAOUI
Yahia Fares University Medea

Bel Abbes BACHIR BOUIADJRA
Djilali Liabes University

Abstract: Composites, like any material, can degrade under the action of the loading applied to them by causing mechanical degradation of the composite parts (cracking). The study of existing damage and its behavior is of great importance. In fact, the cracking resulting from the propagation of a defect can lead to the failure of a component that would promote the total ruin of the structure. Fracture mechanics is the right tool to analyze this kind of situation based on the material's fracture characteristics which are the critical stress intensity factor (K_C) or the critical energy restitution rate (G_C) also called toughness. This degradation of the composite has been studied by many authors. The objective of our work is to analyze by the finite element method the evolution of the parameter K_I stress intensity factor of two representative elementary volumes (REV) made of the same epoxy matrix and with different reinforcing fibers (Alfa and Glass) as a function of the displacement of the two fibers (a) and (b). The numerical study showed that the position of the fibers has a significant role on the composite material as well as the alfa/epoxy REV behaves better than the glass/epoxy REV due to the good mechanical characteristics of the alfa/epoxy REV.

Keywords: Representative elementary volumes (REV), Stress intensity factor, Finite element method and Crack

Introduction

The fibers used for the reinforcement of the polymer matrix are generally continuous and discontinuous fibers, the first ones (boron, glass, Kevlar ...) of which the costs of raw materials, the methods of implementation and the low production capacities, make that these composites have higher cost prices being limited to high performance applications such as aeronautics and aerospace, the gap between the properties of these fibers as well as the unreinforced polymers is filled by the staple fibers. For a REV long time, the properties of polymers have been modified using reinforcements to optimize the mechanical properties. Polymer materials reinforced with synthetic fibers, such as aramid fibers, carbon fibers or glass fibers are widely used in various fields of application. The behaviour of such a material can be predicted by studying the effect of its individual constituents on a microscopic scale. The arrangement of fibers in the matrix plays an essential role in the development of a pattern.

Finite element micromechanical analysis, using the concepts of representative elementary volume (RVE) (Gusev,1997; Segurado, 2002) or repeated unit cell (RUC), (Li,1999; Li, 2015) can be performed to assess the

heterogeneous stress field of composites, thereby more accurately predicting the effective properties and characterizing the microscopic yield and the behaviour to the damage compared to the analytical methods. The assumptions made for a typical micromechanical analysis can be seen in the work of Hori (1999). A square arrangement of fibers and matrices is a model commonly used to represent the micro-scale model of continuous fiber composites. Due to the symmetry and periodic arrangement of fibers, a single rectangular grating can be used to analyze material on a microscopic scale, called a Representative Volume Element (RVE).

The behaviour of plant fibers has recently been studied in the literature. Ameri (2016) used a new type of unidirectional linen / paper reinforcement. The linen-paper / epoxy composite is superior, both in specific resistance and in modulus, to any other linen / epoxy composite (without the paper layer). It also surpasses the specific stiffness of a unidirectional E-glass / epoxy composite. Baley (2002) studied the mechanical properties of flax fibers using micromechanical expressions, it was shown that the longitudinal Young's modulus is of the order of 59 GPa and that its transverse modulus is l 'order of 8 GPa. (Maligno, 2008) investigated (studied) using a three-dimensional micromechanical representative volume element (RVE) model with hexagonal packing the geometry and finite element method the effect of the residual stress due to the process of hardening on the evolution of damage in polymer-matrix composites reinforced with unidirectional fibers (UD) under longitudinal and transverse loading. The study is based on different failure criteria and a stiffness degradation technique was used for the damage analysis of RVE subjected to mechanical loading after hardening for a range of fiber volume fractions. The initiation and progression of predicted damage is clearly influenced by the presence of residual stresses.

Cichocki (2002) used a semi-empirical micromechanical model to estimate the anisotropy of jute fiber. Based on their simulation results, the Jute fiber-reinforced composite has a longitudinal stiffness of 39.4 GPa and a Young's transverse modulus of 5.5 GPa. Chen (2019) explored, by the finite element method with different fiber volume fractions (Vf) and RVE sizes, the mean response and isotropy of 3D representative solid elements (RVE) for elastomer composites reinforced with short fibers random (SFEC). The results found by Chen, lili et al show that the anisotropy of the RVEs decreases with the increase in the size of the RVEs and is higher for the RVEs with a higher Vf. Fiber anisotropy decreases with increasing Vf. A method of averaging the responses of each (RVE) over all loading directions greatly reduces the response variation on different RVEs, which can be used to improve the accuracy of the prediction more effectively than increasing the size of the (RVE). Bourmaud (2009) used tensile and nanoindentation tests to characterize the anisotropic behaviour of composites reinforced with hemp and sisal fibers. The tests showed that the longitudinal and transverse moduli are respectively 5, GPa and 3.9 GPa.

Our work aims to analyze by the finite element method, the evolution of the damage of a REV (Representative Elementary Volume) hybrid composite made up of the same epoxy matrix and with different reinforcing fibers (Alfa and glass), the mechanical characteristics of the materials that are presented in table 1 using the Abaqus 6.14 calculation code. Several factors were highlighted such as the length of the crack, the arrangement of the fibers in relation to the crack tip, and the distance between the two different fibers. In the first case, the first fiber placed is the Alfa fiber and the glass fiber in the second.

The objective of our work is to analyze by the finite element method the evolution of the parameter K_I stress intensity factor of two representative elementary volumes (REV) consisting of the same matrix Epoxide and with different reinforcing fibers (Alfa and Glass), whose mechanical characteristics of composite materials are shown in Table 1 (Zeddour, 2018). Our study shows the variation of the equivalent Von Mises stress of both as well as the variation of the stress intensity factor under the effect of the fiber displacement (a) (longitudinal displacement) and the fiber displacement (b) (vertical displacement). Note that the K_I factor is taken at two positions, from edge 1 and edge 2.

Geometric Model

The chosen geometrical model is a representative elementary volume of parallelogram shape of dimension 0.010*0.010*0.010 mm3 (undamaged model and damaged model), this one is subjected to an applied stress of 10 MPa along the Y-axis perpendicular to the reinforcements, the other face being fixed (see figure 1).

The fiber (a) moves along the X axis.
The fiber (b) moves along the Y axis.
We fix the fiber (a) and we move the fiber (b) and so on.

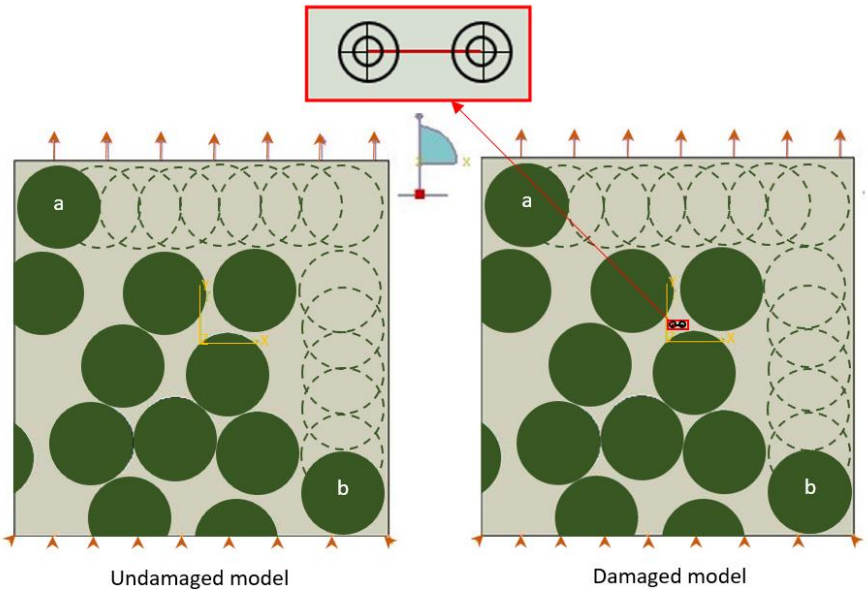

Figure 1. Geometric model and boundary conditions

Table 1. Mechanical characteristics of materials

	Density [g/m3]	Young's modulus [GPa]	Poisson's ratio
Alfa	1.4	12	0.3
Glass	2.6	27	0.3
Epoxy		5	0.33

Mesh

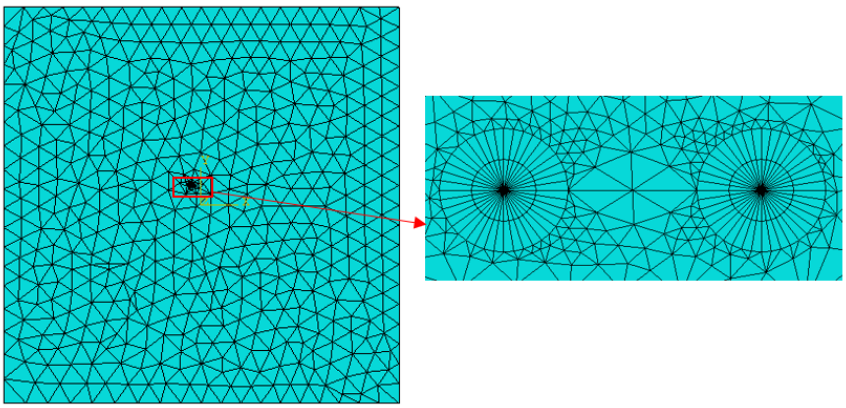

Figure 2. Model mesh

To simulate the linear behavior in tension and the influence of the longitudinal and vertical displacement of the fiber (a), (b), displacement, we used a calculation code "Abaqus" version 6.14 for the analysis of composite structures by the finite element method. This code presents a complete system, integrating not only the calculation functions themselves, but also functions of model construction (pre-processor) and processing of results (post-processor) (108).

Results and Discussions

Influence of Fiber Displacement (a) and (b) on the Von Mises Equivalent Stress for the Undamaged and Damaged Models.

To see the effect of the position of the fibers relative to each other on the equivalent Von Mises stress and on the stress intensity factor, we took a random arrangement of the fibers in our representative elementary volume (REV) so as to have one fiber (a) moving along the X-axis and another (b) moving along the Y-axis. This work is performed on an undamaged and a damaged REV using the finite element method.

Case of the REV Alfa/Epoxy

Figure 3 shows the variation of the equivalent Von Mises stress as a function of fiber displacement for the damaged (n) and undamaged (m) models and for both cases of fiber displacement (a=fixed; b=variable and b=fixed; a=variable). It is found that the displacement of the fiber (a) and the fiber (b) relative has a significant influence on the equivalent Von Mises stress. The curves are not symmetrical, this is probably due to the random arrangement of the reinforcements in our VER.

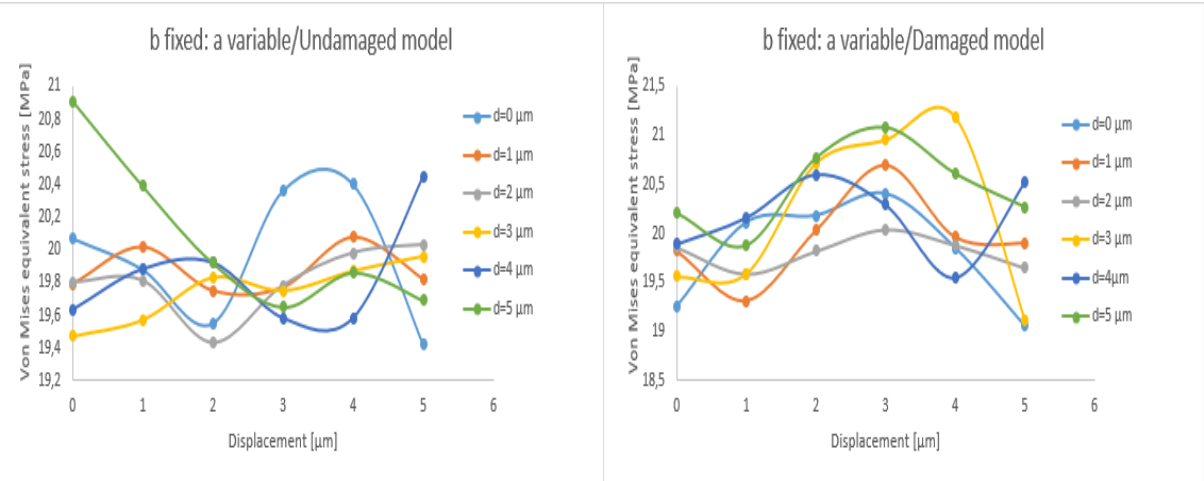

m) Model without cracks

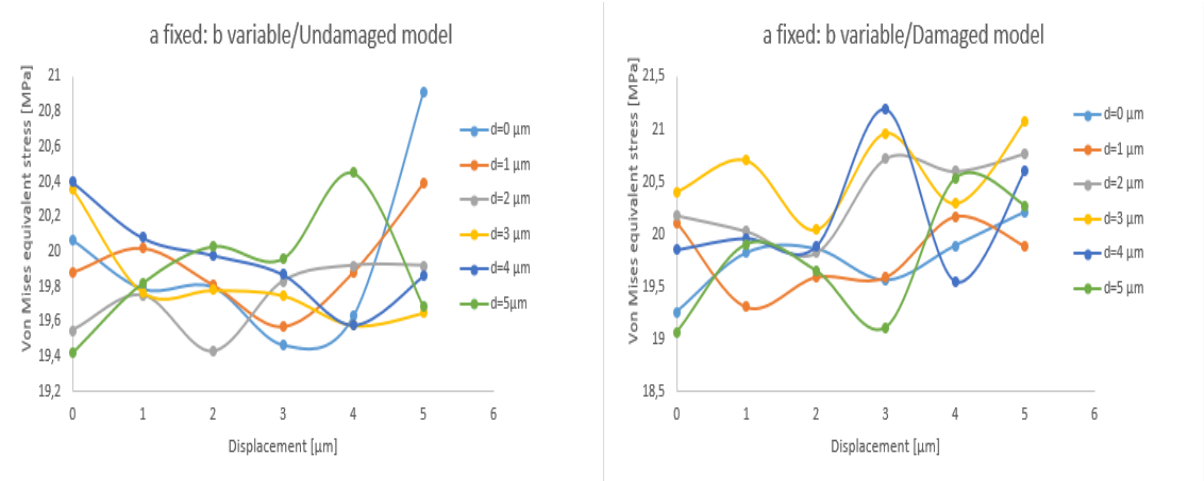

n) Model with crack

Figure 3. Variation of Von Mises equivalent stress as a function of fiber displacement for both damaged and undamaged models and for both cases of fiber displacements (fixed a; variable b and fixed b; variable a)

Comparison between Fiber a=Fixed; b=Variable and b=Fixed; a=Variable.

Figure 4 shows the variation of the equivalent Von Mises stress as a function of fiber displacement for the undamaged model and for each fiber displacement case (a fixed; b variable and b fixed; a variable). Note that the fiber displacement curve (a fixed; b variable) does not resemble the fiber displacement curve (b fixed; a variable) and this is likely due to the non-symmetrical arrangement of reinforcements in our REV.

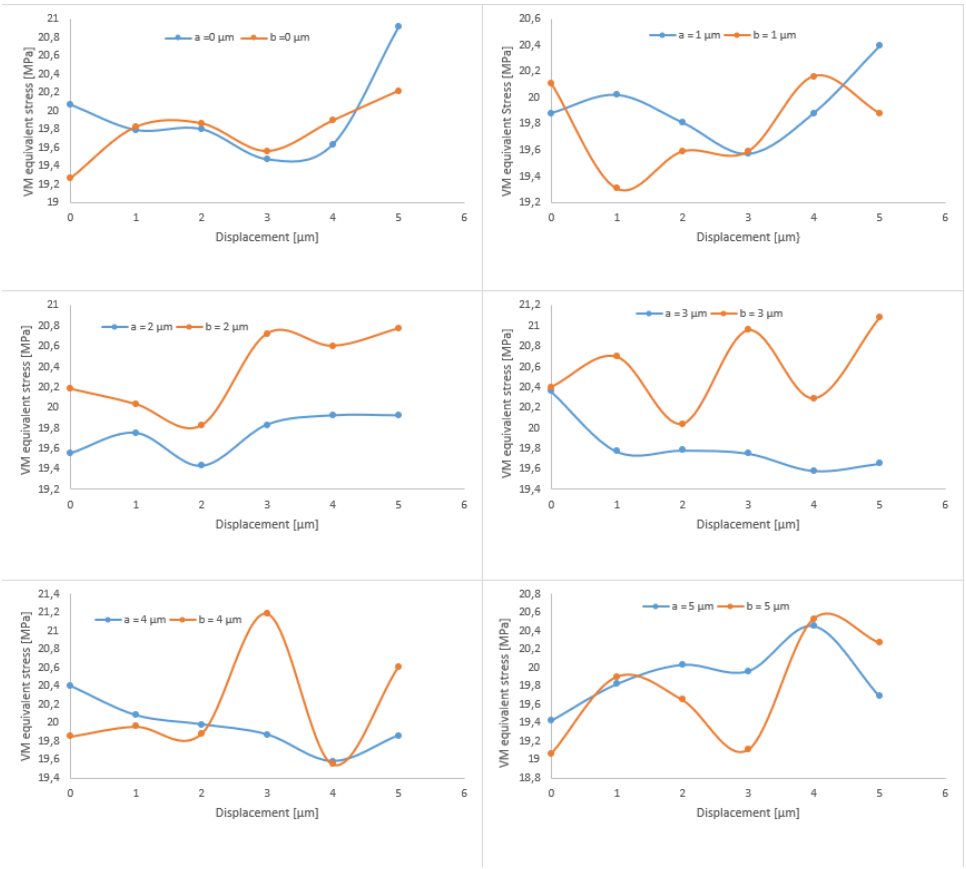

Figure 4. Variation of Von Mises equivalent stress as a function of fiber displacement for the undamaged model and for each case of fiber displacements (fixed a; variable b and fixed b; variable a)

Influence of the Width of Representative Elementary Volume on Stress Intensity Factors

Figure 5 shows the variation of the stress intensity factors K_I, K_{II} and K_{III} as a function of the width of the representative alpha/epoxy elemental volume (REV). It can be seen that the opening of composite VER occurs in pure I-mode. The stress intensity factor K_I is much higher than the other two opening modes which are negligible.

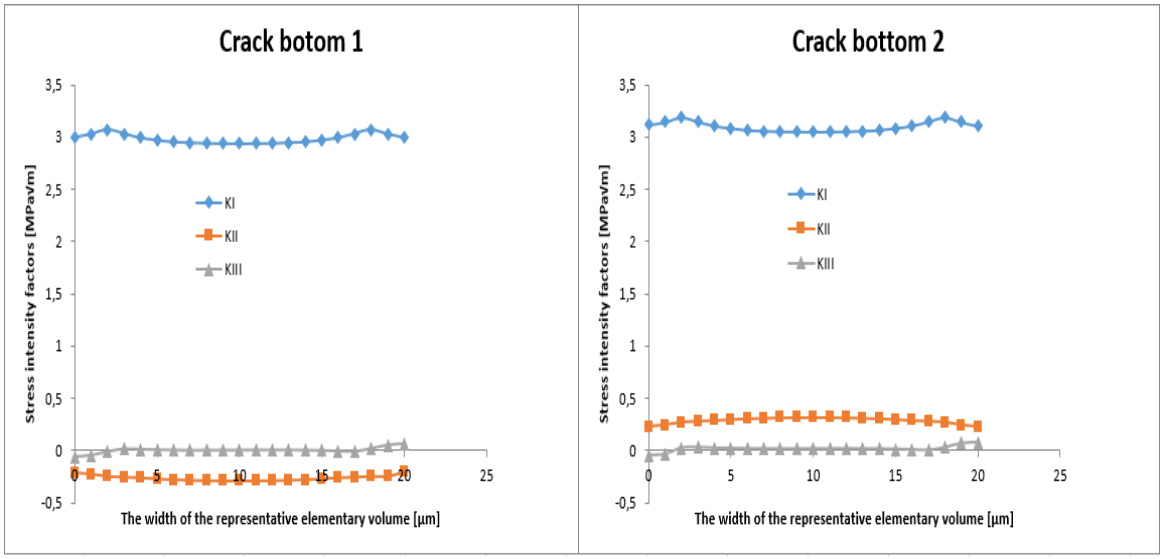

Figure 5. Variation of the stress intensity factors K_I, K_{II} and K_{III} as a function of the width of the representative elementary volume alfa/epoxy for the two crack bottoms and for d_a=0µm and d_b=0 µm

Influence of Fiber Displacement (a) and (b) on the Stress Intensity Factor for the REV alfa/epoxy

Figure 6 shows the variation of the stress intensity factor K_I as a function of the width of the alfa/epoxy REV and for the different fiber positions (a) and (b). The graphs in Figure 7 are determined for the positions of fiber (a) dep. (0) and dep. (5) and for the two crack bottoms respectively. It can be seen that whatever the position of fibers (a) and (b) of the REV alfa/epoxy composite the FIC K_I curve presents a symmetry with respect to the middle of the REV width and consequently the analysis is the same as that of the REV glass/epoxy. It is noted that the arrangement of the fibers relative to each other has a significant influence on the K_I factor.

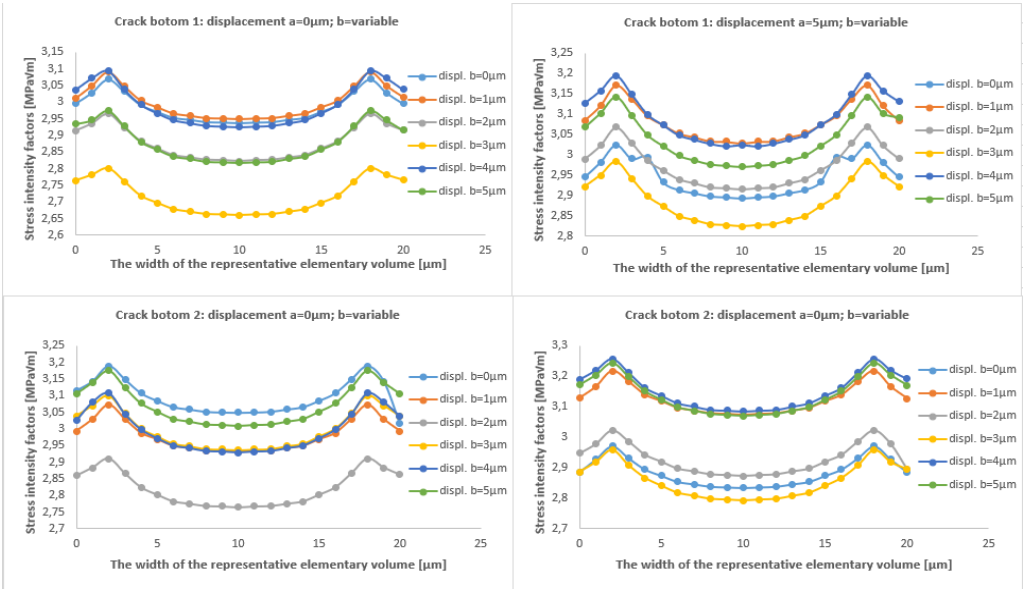

Figure 6. Variation of the stress intensity factors K_I, as a function of the width of the representative elementary volume alfa/epoxy for the two crack bottoms and for d_a=0µm and d_b=variable and d_a=5µm and d_b=variable

Influence of the Mechanical Properties of the Composite VER on the K_I Parameter

Figure 7 show the variation of SIF K_I of the two composite materials alfa/epoxy and glass/epoxy for the different fiber displacements (a) and (b) and for the two edges of the crack. It can be seen that the alfa/epoxy composite material has higher SIF K_I values than the glass/epoxy composite material. It is noted that the alfa fiber performs better than the glass fiber and this is due to the good mechanical properties.

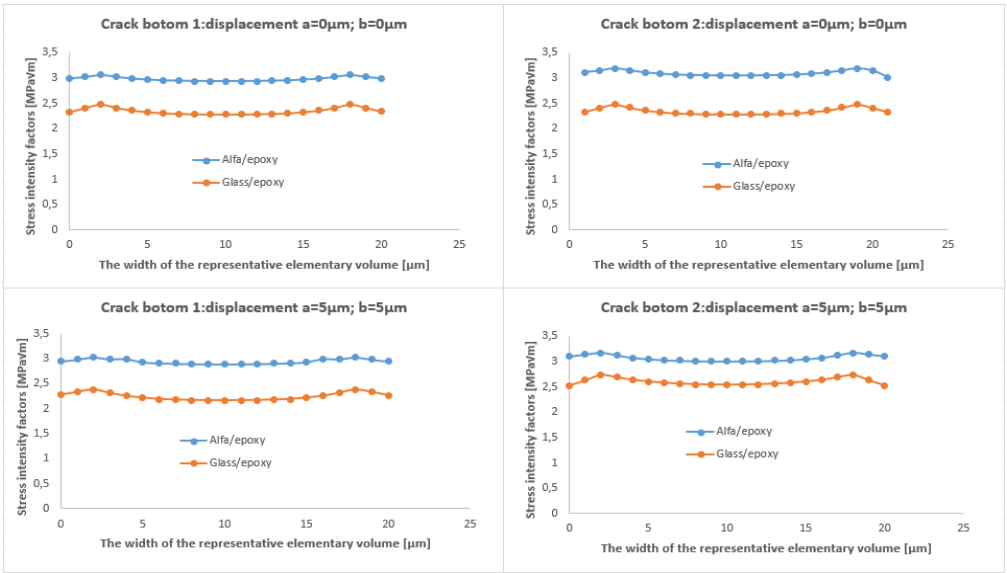

Figure 7. Variation of the stress intensity factor KI as a function of the width of the representative elementary volume alfa/epoxy and glass/epoxy for the two crack tips and for da=0µm and db=0µm and da=5µm and db=5µm.

Conclusion

From this numerical analysis using the finite element method, we can draw the following conclusions:

- The displacement of the fiber (a) and the fiber (b) relative has a significant influence on the equivalent Von Mises stress. The curves are not symmetrical, this is probably due to the random arrangement of the reinforcements in our VER.
- The fiber displacement curve (a fixed; b variable) does not resemble the fiber displacement curve (b fixed; a variable) and this is probably due to the non-symmetrical arrangement of reinforcements in our REV.
- The crack opening of the damaged composite REV occurs in pure mode I and the other two opening modes which are negligible.
- Regardless of the position of the fibers (a) and (b) of the REV alfa/epoxy composite the FIC K_I curve shows symmetry with respect to the middle of the REV width and therefore the analysis is the same as that of the REV glass/epoxy. It should be noted that the arrangement of the fibers relative to each other has a significant influence on the K_I factor.
- The alfa/epoxy composite VER performs better than glass/epoxy composite VER, this is due to its good mechanical properties following the results found numerically.

Scientific Ethics Declaration

The authors declare that the scientific ethical and legal responsibility of this article published in EPSTEM journal belongs to the authors.

Acknowledgements or Notes

* This article was presented as a poster presentation at the International Conference on Technology, Engineering and Science (www.icontes.net) held in Antalya/Turkey on November 16-19, 2022.

* I am very grateful to the organizing committee of the International Conference on Technology, Engineering and Science for allowing me to present my work, which I find interesting to exchange with other authors.

References

ABAQUS, (2014). *ABAQUS/Sandard 6.14.1*. Hibbit, Karlsson and Sorensen, Inc. Pawtuket, USA.

Ameri, E., Laperriere, L. and Lebrun, G. (2016). Mechanical characterization and optimization of a new unidirectional flax/paper/epoxy composite. *Compos. Part B Eng., 97*, 282–291. https://doi.org/10.1016/j.compo-sitesb. 2016. 04. 056

Baley, C. (2002). Analysis of the flax fiber's tensile behaviour and analysis of the tensile stiffness increase. *Composites Part A, 33*, 939–948.

Bourmaud, A., Baley. C. (2009). Rigidity analysis of olypropylene/vegetal fiber composites after recycling. *Polymer Degradation and Stability 94*, 297–305

Chen, L., Gu, B., Tao, J., & Zhou, J. (2019). The average response and isotropy of 3D representative volume elements for random distributed short fibers reinforced elastomer. *Composite Structures, 216*, 279-289. https://doi.org/10.1016/j.compstruct.2019.02.049

Cichocki, F. R. Jr., & Thomason. J. L. (2002). Thermoelastic anisotropy of a natural fiber. *Composites Science and Technology 62*, 669–678.

Gusev, A. A. (1997). Representative volume element size for elastic composites: A numerical study. *J Mech Phys Solids, 45*(9), 1449-1459. https://doi.org/10.1016/S0022-5096(97)00016-1.

Maligno A. R, Warrior, N. A. & Long, A. C. (2008). Finite element investigations on the microstructure of fibre-reinforced composites. *Express Polymer Letters, 2*(9), 665–676. https://doi.org/ 10.3144/expresspolymlett.2008.79

Hori, M., & Nemat-Nasser, S. (1999). On two micromechanics theories for determining micro–macro relations in heterogeneous solids. *Mechanics of Materials, 31*(10), 667-682. https://doi.org/10.1016/S0167-6636(99)00020-4

Li, S., Jeanmeure, L.F.C., & Pan Q. (2015). A composite material characterisation tool : UnitCells. *J Eng Math, 95*(1), 279-293. https://doi.org/10.1007/s10665- 014-9776-4

Li, S. (1999). On the unit cell for micromechanical anal-ysis of fibers-reinforced composites. *Proc R Soc London A Math Phys Eng Sci, 455,* 815-838. https://doi.org/10.1098/rspa.1999.0336

Segurado, J. & J. Llorca. (2002). A numerical approximation to the elastic properties of sphere-reinforced composites. *J Mech Phys Solids, 50*(10), 2107-2121. https://doi.org/10.1016/S0022-5096(02)00021-2

Zeddour Mohamed, B.Z. (2018) *Prediction Des Mecanismes D'endommagement Dans Un Matériau Composite* (Thèse de Doctorat), USTO-MB.

Author Information

Habib ACHACHE
Institute of maintenance and industrial safety,
Laboratory of Physical Mechanics of Materials Sidi Bel Abbes.
University of Oran2 Mohamed Ben Ahmed, Oran, Algeria
B.P 1015 El M'naouer 31000 Oran , Algéria
Contact e-mail : *habibachache@gmail.com*

Ghezail ABDI
Institute of maintenance and industrial safety,
University of Oran2 Mohamed Ben Ahmed, Oran, Algeria
B.P 1015 El M'naouer 31000 Oran, Algéria

Rachid BOUGHEDAOUI
Department of materials engineering, Faculty of Technology,Yahia FARES University Medea, Algeria
National road N°18, Urban pole 26000 Medea Algeria

Bel Abbes BACHIR BOUIADJRA
Department of Mechanical Engineering,
Laboratory of Physical Mechanics of Materials
Djilali LIABES University, Sidi Bel Abbes, Algeria
BP 89 Sidi Bel Abbes 22000-Algérie

To cite this article:

Achache, H., Abdi, G., Boughedaoui, R. & Bachir Bouiadjra, B.A. (2022). The effect of the arrangement of a reinforcement on the mechanical behavior of a composite VER composite material. *The Eurasia Proceedings of Science, Technology, Engineering & Mathematics (EPSTEM), 21,* 152-159.

The Eurasia Proceedings of Science, Technology, Engineering & Mathematics (EPSTEM)
ISSN: 2602-3199

The Eurasia Proceedings of Science, Technology, Engineering & Mathematics (EPSTEM), 2022

Volume 21, Pages 160-166

IConTES 2022: International Conference on Technology, Engineering and Science

Obtaining Nonlinear Optical Transmittance Parameters of CS_2 Using Z-Scan Experimental Setup

Ferit ARTKIN
Kocaeli University

Abstract: In a linear medium, the index of refraction and the absorption coefficient are independent of the intensity of light, the frequency of the light does not change in the medium, the frequency depends only on the source, the principle of overlap applies, Light and light cannot be controlled (photon-photon interaction does not occur). In the non-linear environment; The refractive index depends on the intensity of the light, the frequency changes, the overlap principle does not apply, the light can be controlled by light. Non-linear optics has many applications and these applications are becoming more common every day. Some of these applications are optical switching, hologram, laser physics, optical communication. The differences can be explained by the shape of the laser pulse and its deviation from the theoretical form, which is often difficult to determine. Another factor affecting the accuracy of measurements of nonlinear parameters of materials is the uncertainty of laser power measurements and the waist size of the focused beam, deviations from the Gaussian distribution, inhomogeneity of the studied material, etc. Linearity is a property of the medium, not the light. It cannot be observed in the absence of nonlinear optical matter (empty space). By changing the properties of the medium, the light causes the properties of the light passing through this medium to change, even its own properties. A high-power light source may have different energy (frequency) values as it passes through the material it passes through. If the value of the applied external electric field (E) is large enough (high energy intensity light is used), the polarization vector will also include non-linear effects. CS_2 is accepted standard test material for non-linear measurements by scientists interested in nonlinear optics. Some applications of CS_2 is fumigation, insecticide, solvent, manufacturing, health effects.

Keywords: Optics, Laser, Nonlinear optics, Measurement techniques, Z-Scan, Mechanical engineering.

Introduction

Improvement of nanotechnology and creation of new nano-materials with specific properties lead to a growing need to study the nonlinearity of the optical characteristics of the newly created materials. Nonlinear refraction and nonlinear absorption of optical materials, including the organic materials, are essential for the operation of the optical elements in systems using powerful laser sources. That, as well as the development and improvement of laser technology, requires increasing the accuracy and automation of the processes of a study of the optical nonlinearity of the materials.

There are some methods used in practice for investigation of one or another nonlinear effect. One of these methods Z-scan methods is particularly suitable for the simultaneous study of two of nonlinear effects nonlinear absorption and nonlinear refraction which are related with the dielectric permeability of matertials. Two modifications of this method are in use: open aperture Z-scan method for study of optical nonlinear absorption and closed Z-scan for study of nonlinear refraction of materials.

The field of organic nonlinear optics offers many exciting opportunities for both fundamental research and technological application. As in other high-tech areas, such as microelectronics and genetic engineering, science and technology can be expected to share a vital interplay where advances on one front enable advances and

present new challenges on the other. For example, optical devices based on nonlinear optical effects are becoming more and more widely used in practice.

The process of optimizing materials for third-order nonlinear optical applications is a complex one and no single approach is likely to emerge as dominant, due to the range of potential applications in photonics technologies and their particular requirements. Optical devices, for example, based on nonlinear optical effects are becoming more and more widely used in practice.

Non-Linear Optics Measurements

The first nonlinear optics experiment of the laser era was performed in 1961 by a team whose leader was Peter Franken (Franken et al., 1961). As shown in Figure 1., a ruby laser was focused into a slab of crystalline quartz to discover as the nonlinear reaction of the medium to the intense optical frequency radiation at 694.3 nm was strong enough to create a detectable second harmonic component at a wavelength of 347.15 nm. (The vacuum wavelength of the second harmonic component is of course half that of the fundamental).

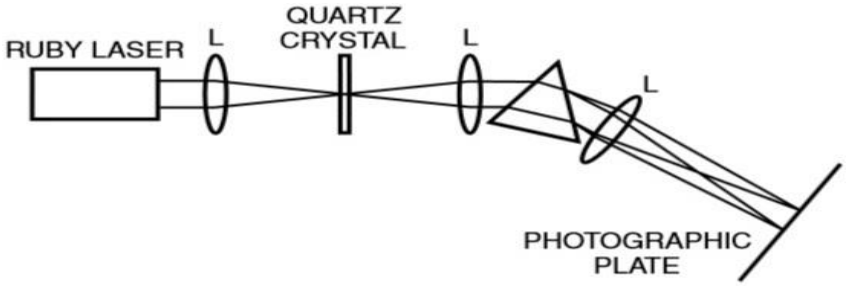

Figure 1. Schematic diagram of the first second harmonic generation experiment by Peter Franken's group at the Michigan University in 1961.

The way to think about this experiment is diagrammed in Figure 1. Consider the electrons response in the quartz to the stimulus of the optical frequency electric field of the laser beam formula becomes $E = A.cosw\omega_t$. The displacement of the electrons generates a dipole moment p per atom, or $P = N_p$ per unit volume where 'N' is accepted as the atomic number density.

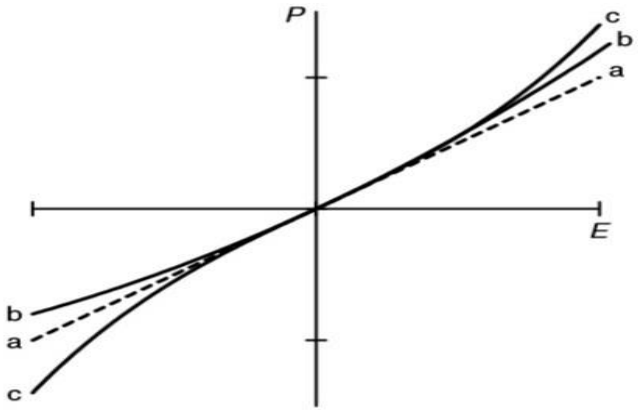

Figure 2. Linear and nonlinear response of polarization P to applied electric field E: (a) linear case (dotted), (b) quadratic nonlinearity, (c) cubic nonlinearity.

It is permitted to write the possibility of a nonlinear response

$$P = \varepsilon_0 (\chi^{(1)} E + \chi^{(2)} E^2 + \dots) \quad (1)$$

For , $\chi^{(2)} > 0$, the dependence of 'P' on 'E' is represented while in the void of the nonlinear term, Equation (1) reverts to Equation (2), and the linear relationship between E and P represented by the dotted straight line (a) in the figure is recovered.

If $E = A\cos\omega_t$ is substituted into equation, the polarization now reads

$$P = \varepsilon_0 \underbrace{(\chi^{(1)} A \cos \omega t}_{\text{Linear Term}} + \underbrace{\frac{1}{2}\chi^{(2)} A^2 (1 + \cos 2\omega t))}_{\text{Nonlinear Term}} \quad (2)$$

Nonlinear optics (NLO) is the understudy of optics that defines the actions of light in nonlinear media where the dielectric polarization **P** corresponding nonlinearly to the electric field **E** of the light which is possible to be seen in commonly at very high light densities (values of the electric field can be compared to interatomic electric fields, typically 10^8 V/m) like those provided by pulsed lasers. In the field of nonlinear optics, the superposition principle is not held any longer. Nonlinear optics kept unexplored till the discovery of Second harmonic generation right after demonstration of the first laser (P.A. Franken et al., 1961).

In the early 1980s nonlinear optical materials was extended with a new production of semiconductor materials. For example, multi-quantum well is produced by the amplification of two different semiconductor layers (GaAs and AlGaAs). That let the formation of consecutive hills and valleys of variable potential, for electrons and holes. It is regarded that the carriers are within these potential walls. Hence, they display a semi two-dimensional behavior and large optical nonlinearity.

It can be an useful instrument for network communication for Photonic information and communication systems. It has developed very fast in last years. However, using only fiber optical systems has not ability to meet the necessity on carrying the information flow in future of communication systems. Fast optical switches which can verify (process) large scale of data should be developed so as to remove the gateways caused by optoelectronic return throughout the network. Large and fast nonlinear optical (NLO) materials are appropriate tool for photo-dynamic therapy to treat serious diseases like cancer, and other biomedical applications in the near future soon (L. W. Tutt et al., 1993), (B. G. Maiya et al., 1989) for optical switches, optical correction and optical power limiting applications (T. D. Mody and J. L.Sessler, 2001).

Methods for Studying of Optical Nonlinearity of Materials Applications

There is considerable interest in finding materials having large yet fast nonlinearities. Thus, there is a need to expand this database. Methods to determine nonlinear coefficients are discussed throughout many publications.. This interest, that is driven primarily by the search for materials for all-optical switching and sensor protection applications, concerns both nonlinear absorption (NLA) and nonlinear refraction (NLR). The database for nonlinear optical properties of materials, particularly organic, is in many cases inadequate for determining trends to guide synthesis efforts.

Degenerate Four Wave Mixing, DFWM: Used for measuring third order nonlinear reaction and magnitude of this reaction. Third Harmonic Generation: Used only for measuring third order nonlinearity. Z-Scan: Used for measuring magnitude of third order nonlinearity and its sign. Electro-absorption technique: Third order nonlinearity dispersion studies are carried out with this technique. Time-Resolved Optical Kerr Effect and Transient Absorption Techniques: Used for presenting photophysical processes that determine nonlinearity (Paras N. Prasad, David J. Williams, 1991).

Z Scan Technique

In this experimental setup an aperture is placed to prevent some of the light from reaching the detector. The equipment is arranged as can be seen in the diagram. A lens focuses a laser to a certain point, and after this point the beam naturally defocuses. After a further distance an aperture is placed with a detector behind it. The aperture causes only the central region of the cone of light to reach the detector. Typically values of the normalized transmittance are between

$$0{,}1 < S < 0{,}5 \quad (3)$$

The detector is now sensitive to any focusing or defocusing that a sample may induce. The sample is typically placed at the focus point of the lens, and then moved along the z axis a distance of which is given by the Rayleigh length z_0:

$$z_0 = \frac{\pi W_0^2}{\lambda} \tag{4}$$

The thin sample approximation states that the thickness of the sample L must be less than the Rayleigh length $L < z_0$. The z-scan measurement technique (M. Sheik-Bahae et al., 1990), (M. Sheik-Bahae et al., 1989), is often used for measuring the strength of the Kerr nonlinearity (i.e. the magnitude of the nonlinear index n_2) of an optical material. Essentially, a sample of the material under investigation is moved through the focus of a laser beam, and the beam radius (or the on-axis intensity) is measured at some point behind the focus as a function of the sample position.

These quantities are affected by the self-focusing effect. If the nonlinear index is positive, and the sample is placed behind the focus, self-focusing reduces the beam divergence and thus increases the detector signal. If the sample is moved to the left-hand side of the focus, the focus is moved to the left, and the stronger divergence after the focus decreases the detector signal. From the measured dependence of the detector signal on the sample position, it is possible to calculate the magnitude of the nonlinear index.

The Z-scan technique is a method which can rapidly measure both NLA and NLR in solids, liquids and liquid solutions. The Z-scan method has gained rapid acceptance by the nonlinear optics community as a standard technique for separately determining the nonlinear changes in index and changes in absorption. However, it must always be recognized that this method is sensitive to all nonlinear optical mechanisms that give rise to a change of the refractive index and/or absorption coefficient (Paras N. Prasad, David J. Williams, 1991).

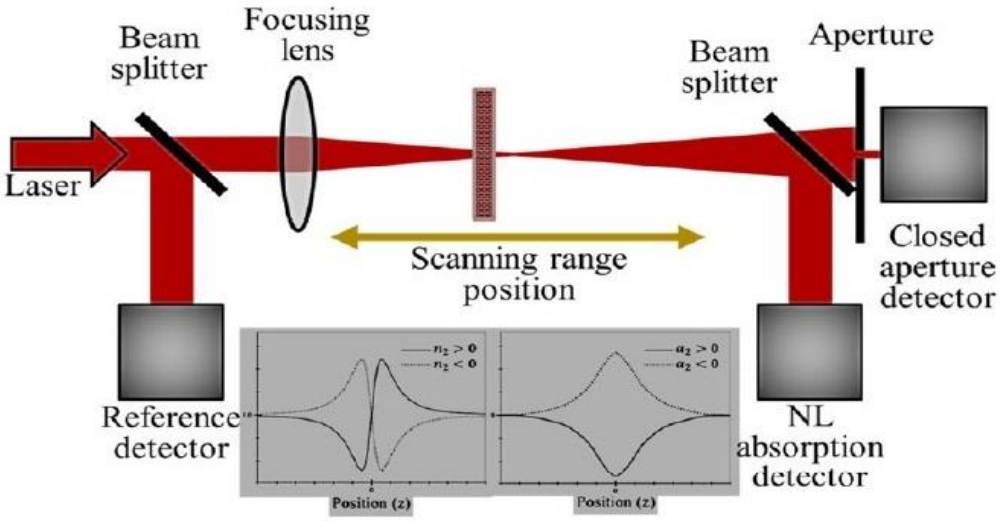

Figure 3. Typical single beam Z-Scan setup. The inset shows the characterictic Z-Scan curves for open and closed apertures (Cid B de Araujo et al., 2016).

Result and Conclusion

CS_2 is accepted standard test material for non-linear measurements by scientists interested in nonlinear optics. We used a quartz cell of 1 mm thickness with CS_2 in the experimental measurements. This information is about the chemical substance CS_2. It is accepted standart test material for non-linear measurements by scientists interesting optics. We used thickness of 1 mm quartz cell with CS_2 in the experimental measurements (Holleman &Wiberg, 2001). CS_2 polymerizes upon photolysis or under high pressure to give an insoluble material called "Bridgman's black", named after the discoverer of the polymer, P. W. Bridgman. Trithiocarbonate (-S-C(S)-S-) linkages comprise, in part, the backbone of the polymer, which is a semiconductor (Ochiai, Bungo, 2005).

Table 1. Nonlinear parameters of CS_2 (Carbon disulfide) (Breitzer, 1999).

Nonlinear Parameters	
n_2^I (Third-order nonlinear refractive index)	$3.0 \pm 0.1 \times 10^{-18}$ m^2 W^{-1}
$\chi_R^{(3)}$ (Third-order refractive nonlinear electric susceptibility)	370×10^{-33} C m V^{-3}
γ_R (Nonlinear refractive index)	0.0065×10^{-57} C m^4 V^{-3}
α_2 (Third-order absorption coefficient)	0.8×10^{-12} m W^{-1}
$\chi_I^{(3)}$ (Third-order nonlinear electric susceptibility)	84×10^{-33} C m V^{-3}
γ_I (Intensity of nonlinear refractive index)	0.0015×10^{-57} C m V^{-3}

Some applications of CS_2 are fumigation; used for fumigation in airtight storage warehouses, airtight flat storages, bins, grain elevators, railroad box cars, shipholds, barges and cereal mills (Greenwood, 1997). Insecticide: Carbon disulfide is used as an insecticide for the fumigation of grains, nursery stock, in fresh fruit conservation and as a soil disinfectant against insects and nematodes (Worthing,1991). Solvent**:** Carbon disulfide is a solvent for phosphorus, sulfur, selenium, bromine, iodine, fats, resins, rubber, and asphalt. It has been used in the purification of single-walled carbon nanotubes (Park, 2006). Manufacturing: The principal industrial uses of carbon disulfide are the manufacture of viscose rayon, cellophane film, carbon tetrachloride and xanthogenates and electronic vacuum tubes, health effects; at high levels, carbon disulfide may be life-threatening because it affects the nervous system. Significant safety data comes from the viscose rayon industry, where both carbon disulfide as well as small amounts of H_2S may be present (Artkin, 2018, 2021).

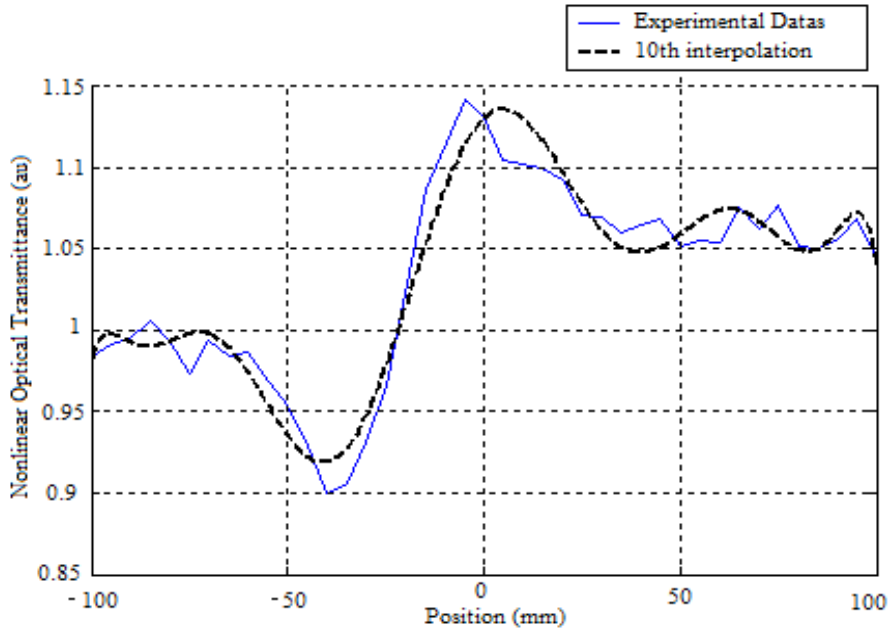

Figure 4. Position-nonlinear optical transmittance changes of CS_2 as a result of Z scan measurement.

The experimental and theoretical results obtained as a result of the movement of the CS_2 from -z (-100 mm) to +z (+100 mm) at 3 mm intervals are shown in Figure 4. In this study, the intensity of the light at the focal point was calculated as 1.3 GW/cm^2.

In the permeability change we have obtained, the minimum trough is seen before the focal point and the maximum peak after the focal point. In order to find the nonlinear refractive index, the difference between the maximum was calculated experimentally as Tp = 1.09986, Tv = 0.89986, from the graph (Fig. 4). As we mentioned before, the thickness is a very important parameter in the Z-scan technique. The graph shows the nonlinear transmittance parameters from the graphs we have drawn with the measurements we have obtained (Figure 4). The graph obtained in Matlab R 2020 b environment was drawn using the interpolation (Curve fitting) technique (10th order) (Artkin, 2005, 2014).

This study establishes the basis of my Phd studies at Sofia Technical University. My Phd studies are developed version of this study. Some of the information and data used in this article were used in the PhD study of Computer-aided Z-Scan Testing Apparatus Integrated Apparatus Integrated into Servo Motor and PLC for Investigation of Non-linear Materials' Permeability. I would like to thank Prof. Dr. Fevzi Necati Ecevit from Gebze Technical University and Associate Professor Dr. Ivanka Kalimanova from Technical University of Sofia.

Scientific Ethics Declaration

The author declares that the scientific ethical and legal responsibility of this article published in EPSTEM journal belongs to the author.

Acknowledgements or Notes

* This article was presented as an oral presentation at the International Conference on Technology, Engineering and Science (www.icontes.net) held in Antalya/Turkey on November 16-19, 2022.

References

Artkin F. (2014). *Computer aided Z-Scan testing apparatus integrated into servo motor and PLC for investigation of non-linear materials permeability*.[Doctoral Dissertation].Technical University Of Sofia. Sofia, Bulgaria.

Artkin, F. (2005). *Conversion of Z- scan experiement set up to computer aided automatic control system in nonlinear optics.* [Master dissertation] Gebze Technical University. Gebze, Turkey.

Artkin, F. (2018). Integration with opto-mechanical system design and servo-motor for computer aided z-scan experimental setup. *The Eurasia Proceedings of Science, Technology, Engineering & Mathematics (EPSTEM),4*, 113-119.

Artkin, F. (2021). The new designed mechanical systems and protypes for Z-scan and nonlinear measurements. *The Eurasia Proceedings of Science, Technology, Engineering & Mathematics (EPSTEM), 16*, 240-247.

Breitzer, J. G., Dlott, D. D., Iwaki, K. L., Kirkpatrick, S. M., & Rauchfuss, T. B. (1999). Third-order nonlinear optical properties of sulfur-rich compounds, *The Journal of Physical Chemistry A, 103*, 6930-6937.

de Araujo,C.B., Gomes, A. S., & Boudebs, G. (2016) Techniques for nonlinear optical characterization of materials: A review. Reports on progress in physics. *Physical Society (Great Britain),79*(3), 036401.

Franken, P. A., Hill, A. E., Peters, C. W., & Weinreich, G. (1961). Generation of optical harmonics. *Physical Review Letters, 7*,118- 119.

Greenwood, N. N., & Earnshaw, A. (1997). *Chemistry of the elements* .(2nd ed.).Jordan Hill, Oford: Butterworth-Heinemann.

Holleman, A. F., & Wiberg, E. (2001), *Inorganic chemistry*, San Diego: Academic Press.

Maiya, B. G., Harriman, A., Sessler, J. L., Hemmi, G., Murai, T., & Mallouk, T. E. (1989). Ground-and excited-state spectral and redox properties of cadmium (II) texaphyrin. *The Journal of Physical Chemistry, 93*(24), 8111-8115.

Mody, T. D., & Sessler, J. L. (2001). Texaphyrins: A new approach to drug development. *Journal of Porphyrins and Phthalocyanines, 5*(02), 134-142.

Ochiai, B., & Endo, T. (2005). Carbon dioxide and carbon disulfide as resources for functional polymers. *Progress in Polymer Science, 30*(2), 183-215.

Prasad, P. N., & Williams, D. J. (1991). *Introduction to nonlinear optical effects in molecules and polymers* (Vol. 1). New York: Wiley.

Park, T.J., Banerjee, S., Hemraj Benny, T., & Wong, S. S. (2006). Purification strategies and purity visualization techniques for single-walled carbon nanotubes. *Journal of Materials Chemistry 16*(2), 141–154.

Sheik Bahae, M., Said, A. A., & Van Stryland, E.W. (1989). High-sensitivity, single-beam n_2 measurements. *Optic Letters. 14* (17), 955.

Sheik Bahae, M., Said, A. A., Van Stryland, E.W., Hagan, D. J., & Wei, T. H. (1990). Sensitive measurement of optical nonlinearities using a single beam. *IEEE J. Quantum Electron, 26*(4), 760.

Tutt, L. W., & Boggess, T. F. (1993). A review of optical limiting mechanism and devices using organics, fullerenes, semiconductors and other matherials. *Progress in Quantum Electronics, 17*(4), 299-338

Worthing, C. R., & Hance. R. J. (1991). *The pesticide manual: A world compendium* (9th ed.). Farnham, UK: British Crop Protection Council

Author Information

Ferit ARTKIN
Kocaeli University,
Kocaeli, Turkey
Contact e-mail: *artkinf@kocaeli.edu.tr*

To cite this article:

Artkın,F. (2022). Obtaining nonlinear optical transmittance parameters of CS_2 using Z scan experimental setup. *The Eurasia Proceedings of Science, Technology, Engineering & Mathematics (EPSTEM), 21,* 160-166.

The Eurasia Proceedings of Science, Technology, Engineering & Mathematics (EPSTEM)
ISSN: 2602-3199

The Eurasia Proceedings of Science, Technology, Engineering & Mathematics (EPSTEM), 2022

Volume 21, Pages 167-172

IConTES 2022: International Conference on Technology, Engineering and Science

Effect of Sisal Fibers on Flexural Behavior of Cement Mortar

Taouche-Kheloui FATMA
University Mouloud Mammeri of Tizi Ouzou

Djadoun TOUFIK
University Mouloud Mammeri of Tizi Ouzou

Fedaoui-Akmousi OURDIA
University Mouloud Mammeri of Tizi Ouzou

Ben Chabane TARIK
University Mouloud Mammeri of Tizi Ouzou

Abstract: The development of techniques, manufacturing processes and the production of new materials in construction are topical. Algeria is one of the countries that have extraordinary resources in plant fibers (Palm, Alfa, Cotton, Sisal, etc.), unfortunately, their valorization in building materials is still little exploited. The aim of this research is to highlight, through an experimental investigation, the mechanical behavior of cement mortar matrix lightened by Sisal fiber under three-point bending loading. Our approach consists in taking into account the influence of the Sisal fibers slenderness, hence the use of two different lengths (7 cm and 10 cm). Several fiber percentages were used: 0%; 0.25%; 0.5%; 0.75%; 1%; 1.25% and 1.5%. After 28 days of curing, we evaluated the mechanical performance by three-point bending tests on specimens (4×4×16) cm^3.The best variant will be used in the manufacture of the multi-layer panels. The results showed that the fiber-reinforced mortars presented higher resistances compared to the control mortar. For the two slenderness studied, the best variant is given by the mortar from 1% fibers.

Keywords: Sisal fiber, Mortar, Valorization, Mechanical tests, Analyzes.

Introduction

For a long time, attempts have been made to reinforce fragile construction materials using fibers of different natures, for example: clay bricks reinforced with straw, lime mortar reinforced with animal hair, plaster reinforced with fillasse, etc. Fibers of all kinds have been tested in the reinforcement materials. The most answered are: glass, steel, plastic, carbon, and vegetable fibers.

Currently, within framework of sustainable development, considerable efforts are being made by researchers to develop building materials that respect the 'eco-friendly' environment. Among these ecological materials, plant fibres from the forestry or agricultural sector are considered today as an interesting alternative to conventional fibres (glass, carbon and aramide). The use of vegetable fibres continues to increase due to their advantages: low density compared to glass fibres, renewable, low cost, satisfactory mechanical properties. In addition, the availability of fibre plants in underdeveloped countries allows it to produce plant fibres with little technology and a small amount of grey energy.

Plant fibers have a porous structure, which leads to good thermal and acoustic insulation. On the other hand, because of their flexibility, the handling of plant fibers is very easy, especially if the percentage of fibers mixed with the matrix is high, unlike other types of fibers such as steel fibers. Natural fibers are therefore part of the new generation of reinforcements that respect the environment and can be incorporated into various matrixes to make them ecological, light and low-cost materials.

The proposed design, which has both a reduced self-weight and an acceptable resistance threshold, is intended for applications of insulation between the walls, thus making it possible to improve the thermal and acoustic properties of the structure for acceptable mechanical stresses. First of all, we will look at the influence of the slenderness of the Sisal fibers, hence the use of two different lengths (7 cm and 10 cm). Note that this fiber is very easy to grow with a short renewal time, grows wild in a hot climate in arid regions. These sisal fibers come from the leaves extracted manually and treated with mechanical means according to a protocol. The production rate of a sisal plant is around 200 to 250 leaves per plant and each leaf contains 1000 to 1200 fibers.

Several fiber percentages were used: 0%; 0.25%; 0.5%; 0.75%; 1%; 1.25% and 1.5%. After 28 days of curing, we evaluated the mechanical performance by three-point bending tests on specimens (4×4×16) cm3. The best variant will be used in the manufacture of the multi-layer panels. The results showed that the fiber-reinforced mortars presented higher resistances compared to the control mortar. For the two slenderness studied, the best variant is given by the mortar from 1% fibers.

Experimental Procedure

Materials

A single type of mortar mix was used for the confection of the different specimens. The formulation was determined using the Dreux-Gorisse method.

Cement

The cement used is a Portland cement class CEM I 42.5R. The chemical composition and physical properties of cement are shown in Tables 1 and 2.

Table 1. Chemical composition of cement

Chemical composition	%
SiO2	22
Al2 O3	5.5
Fe2O3	3
CaO	64.5
MgO	1.7
SO3	1.9
Na2O et K2O	0.2-1.3
Cl-	0.02
PAF	< 1.5

Table 2. Physical properties of cement

Physical characteristic	Value
Apparent density (kg/m^3)	1130
Absolute density (kg/m^3)	3100
Specific surface (cm^2/g)	3917
Normal consistency(%)	27.48

The Sand

Granular class 0/3 sand from a sand pit in the Tizi-Ouzou region, drinking tap water will serve as mixing water. To identify our sand we carried out characterization tests, all the results are shown in Table 3

Table 3. Characteristics of sand

Gravel	Apparent density(g/cm^3) NF P 18-554	Absolute density (g/cm^3) NF P 18-555	Fineness module MF NF P 18-101	Sand equivalent (%) NFP18-598
Sand 0/3	1,485	2,63	2,87	79.25

Sisal Fiber

The mortar matrix is reinforced with natural fibers (Sisal fiber) whose characteristics and quantities used are shown in tables 4 and 5.

Table 4. Property of sisal fiber

Property	
Width or diameter	50-300
Density (kgm^{-3})	1450
Cellulose / lignin content (%)	67/12
Module E (GNm^{-2})	9.4-22
Tensile strength (MNm^{-2})	530-640
Élongation (%)	3-7

Figure 1. a) Sisal fiber, b) length sisal fiber 7cm, c) length sisal fiber 10cm.

Mix Proportions

According to Dreux-Gorisse method, our specimens were prepared. After 24 h, the samples are demolded, and kept immersed in a water basin. The proportions of the different constituents are presented in Table 5 and table 6.

Table 5. Mortar composition (1m3).

Components	Quantity (Kg)
Cement	450
Sand	1350
Water (L)	225
W/C	0.5

Table 6. Sisal fiber quantities (length 7 and 10 cm)

Percentage (%)	Sisal fibers (g)
0.25	0.96
0.5	1.92
0.75	2.88
1	3.84
1.25	4.8
1.5	5.76

Figure 2. Experimental procedure.

Behavior in Three-Point Bending

Bending tests are carried out on specimens of dimensions (4×4×16) cm^3 according to standard NF T 54-606.

Figure 3. Bending test

The following table illustrates the mechanical flexural strengths of the fiber-reinforced mortars and the control mortar obtained for the two configurations of fiber dimensions.

Table 7. Flexural strength of the mortars studied**.**

	Flexural strength (MPa)						
% / Mortar	0	0.25	0.5	0.75	1	1.25	1.5
MFS7	8,84	7.53	7.37	7.34	8.11	7.99	7.92
MFS10	8,84	8.12	7.534	9.09	8.44	9.00	9.49

MFS7: Sisal fiber mortar with a fiber length of 7 cm.
MFS10: Sisal fiber mortar with a fiber length of 10 cm.

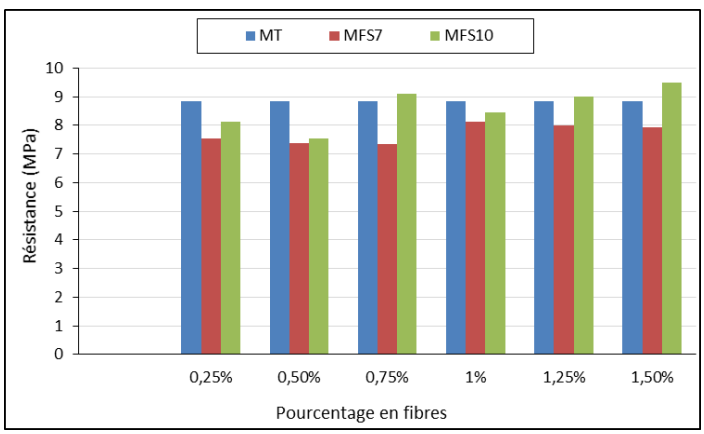

Figure 4. Three-point bending strength of the mortars studied

Figure 4 shows the evolution of the flexural strengths of unreinforced and sisal fiber reinforced mortars using two fiber lengths (MFS7) and (MFS10). The figure shows us that the mortars reinforced with sisal fibers 7 cm showed a drop in strength compared to the control mortar. While mortars reinforced with fibers 10 cm showed an increase in strength for fiber percentages greater than 0.75%.

Influence of Fiber Length

In this section, the influence of the length of Sisal fibers in the different mortars is presented and analyzed (see figure 5).

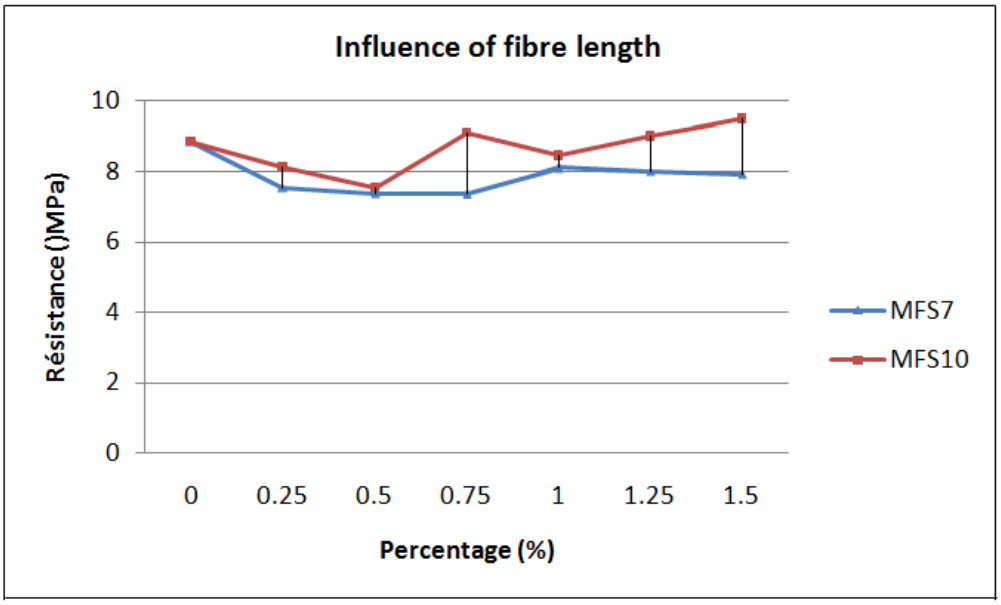

Figure 5. Influence of fiber length

The mortar (MFS10) presented a better post-peak behavior compared to the other percentages of the mortar (MFS7). It can be seen that the bending strength is closely linked to the length of the fiber incorporated into the mortar matrix. Indeed, the MFS10 mortar records a maximum resistance of 9.49MPa against a maximum resistance of 8.11MPa for the mortar (MFS7) i.e. a gain of 17%. The control mortar records a resistance of 8.84MPa. The length of the fiber of 10cm increases the resistance better, which limits the propagation and progression of cracks by a stitching effect.

Conclusion

The results obtained after these tests on the various specimens enabled us to draw the following conclusions:

- The length parameter of the Sisal fibers influences the resistance of these mortars.
- The maximum tensile strength by bending is higher for mortars with 10 cm long fibers than for the reference mortar (without fibres).
- The mortars with fibers 10 cm in length presented better performances, in tractions by bending, compared to the mortar of fibers of 7 cm. There is a difference of 17%.
- The best resistances for the 7 cm fiber are recorded for a dosage of 1%, on the other hand for the 10 cm fiber the best performance is recorded for a dosage of 1.5%..

Scientific Ethics Declaration

The authors declare that the scientific ethical and legal responsibility of this article published in EPSTEM journal belongs to the authors.

Acknowledgements or Notes

* This article was presented as a poster presentation at the International Conference on Technology, Engineering and Science (www.icontes.net) held in Antalya/Turkey on November 16-19, 2022.

References

Achour, A. (2017). *Étude des performances des mortiers renforcés de fibres naturelles: valorisation des plantes locales*, Thèse de Doctorat, Université Aboubakr Belkaïd– Tlemcen.

Agoudjil, B., Benchabane, A., Boudenne, A., Ibos, L., & Fois, M. (2011). Renewable materials to reduce building heat loss: Characterization of date palm wood. *Energy and Buildings*, *43*, 491-497.

Chamoin, J. (2013). *Optimisation des propriétés (physiques, hydriques et mécaniques) de bétons de chanvre par la maîtrise de la formulation*. Thèse de Doctorat, Université de Rennes.

Hejazi, S.M., Sheikhzadeh M., Abtahi, S.M., & Zadhoush, A. (2012), A simple review of soil reinforcement by using natural and synthetic fibers. *Construction and Building Materials*, *30*, 100-116.

Kriker, A., Debicki, G., Bali A., Khenfer ,M.M., & Chabannet, M. (2005), Mechanical properties of date palm fibres and concrete reinforced with date palm fibres in hot-dry climate. *Cement and Concrete Composites*, *27*, 554-564.

Kriker, A., Bali, A., & Debicki, G. (2006), Caractérisations physiques et mécaniques des fibres végétales de palmier dattier entrant dans le renforcement des bétons. *Séminaire International sur la Normalisation et Qualité dans la Construction,* Tlemcen.

Author Information

Taouche-Kheloui Fatma
Mouloud Mammeri University
Route de Hasnaoua BP 47, Algeria
Contact e-mail: *fatma.kheloui@ummto.dz*

Djadoun Toufik
Mouloud Mammeri University
Route de Hasnaoua BP 47, Algeria

Fadaoui-Akmoussi Ourdia
Mouloud Mammeri University
Route de Hasnaoua BP 47, Algeria

Ben Chabane Tarik
Mouloud Mammeri University
Route de Hasnaoua BP 47, Algeria

To cite this article:

Fatma, T. K, Toufik, D., Ourdia, F. A., & Tarik, B. C. (2022). Effect of sisal fibers on flexural behavior of cement mortar. *The Eurasia Proceedings of Science, Technology, Engineering & Mathematics (EPSTEM), 21,* 167-172.

The Eurasia Proceedings of Science, Technology, Engineering & Mathematics (EPSTEM)
ISSN: 2602-3199

The Eurasia Proceedings of Science, Technology, Engineering & Mathematics (EPSTEM), 2022

Volume 21, Pages 173-181

IConTES 2022: International Conference on Technology, Engineering and Science

Three States QRLE (Quantized Run Length Encoding) Based JPEG Image Compression Method

Sid Ahmed CHOUAKRI
University of Sidi Bel Abbes

Fatiha MESKINE
University of Sidi Bel Abbes

Abstract: We present in this work, an improved JPEG-based image compression method. The proposed method appeals a so-called QRLE (Quantized Run Length Encoding) technique where the couple of values ('zero' followed by its run number) is replaced just by one value. In this work, we substitute the Huffman encoding process by the QRLE method. The key idea of the QRLE method is to guarantee that the MSB bit of the binary representation of the non-null values is '0' while that of the 'zero' run number is '1'; this is done by adding the value 2^{N-1} to that number where N is its binary representation length. However, given that the zero run numbers could exceed (2^7-1≡127) value, provided that the RGB colored images are 8 bits long, the MSB is, necessarily, '1'. Even worse, the zero run number can be greater than 255 which implies occupying more than one octet. To solve that; the basic idea is to treat the zero run numbers of the AC zig-zag coefficients, according to 3 pre-defined ranges as follows: [1..127], [128..255], and [256..maximum. For the first range, '128' value is added to the zero run numbers; while for the second one, the zero run numbers are unchanged but preceded by '0' value. Finally, for the third range, the zero run numbers are kept unchanged while preceded by the number of octets of their binary representation. In terms of obtained results, comparing the proposed method with the classical JPEG, the reconstitution values remain the same for both technics. On the other hands, the compression ratio is considerably improved rising from 1:16.35 to 1:22.62 being provided an RGB image with 3 times a typical quantization matrix (for a quality of 50% as specified in the original JPEG Standard) while the PSNR is around 26.215both algorithms.

Keywords: JPEG, Run length encoding, Quantized, Compression ratio.

Introduction

Digital image compression is an important operation to save memory space when storing digital images or videos. Compression is used to reduce redundant data while maintaining the image's quality. There are two basic types of compression techniques: lossless, which allows the original image to be recovered without any loss, and lossy, which only allows for an approximate reconstruction of the original image. JPEG (Joint Photographic Experts Group) is the most widely used image compression standard since its introduction in 1992 (Wallace, 1992). It is a lossy compression method, and is widely used in digital cameras and mobile phones. The algorithm is designed to specifically discard the information that human eye cannot see easily. This can be done because slight change in the color are not perceived well by the human eye, while slight changes in the intensity (light and dark) can be easily detected. JPEG compression standard was evolved for compressing the color or gray scale still images like photographs, graphics and video stills (Firat & Fatih, 2018).

Through the years, many efforts have been made to further improve its quality and performance. Jin et al., (2008) have used a detection algorithm for zero quantized DCT coefficients. The experimental results show that the proposed algorithm can significantly reduce the redundant computations and speed up of the image encoding

without causing any performance degradation. Bheshaj et al., (2012) introduced the performance evaluation of JPEG image compression using symbol reduction technique. A new technique has been proposed by combining the JPEG algorithm and Symbol Reduction Huffman technique for achieving more compression ratio. The result shows that the performance of standard JPEG method can be improved by the proposed method by achieving about 20% more compression ratio than the Standard JPEG. Sandhya & Vijay (2017) proposed a hybrid technique that combines DCT and fractal quad tree decomposition with Huffman encoding for color images. Candra et al., (2017) adopted a Zigzag Scan with Mapping method implemented in electronic circuit. It is able to accelerate the sorting process of DCT quantized coefficients period because the input data can be immediately located in sequence position which has been determined without any value comparison and repetition process. The efforts were invested also in creation of a quantization matrix that is more suited to the human visual system (Lamia et al., 2017) optimizing for a subjective quality improvement. Attempts were also made to adapt the quantization matrix to the content of the image block; both in the spatial and transformation domain (Poth et al., 2020).

JPEG Algorithm Steps

The basic block diagram for the JPEG image compression is shown in figure 1. There are four main steps in the process of JPEG compression (Firat et al., 2018).

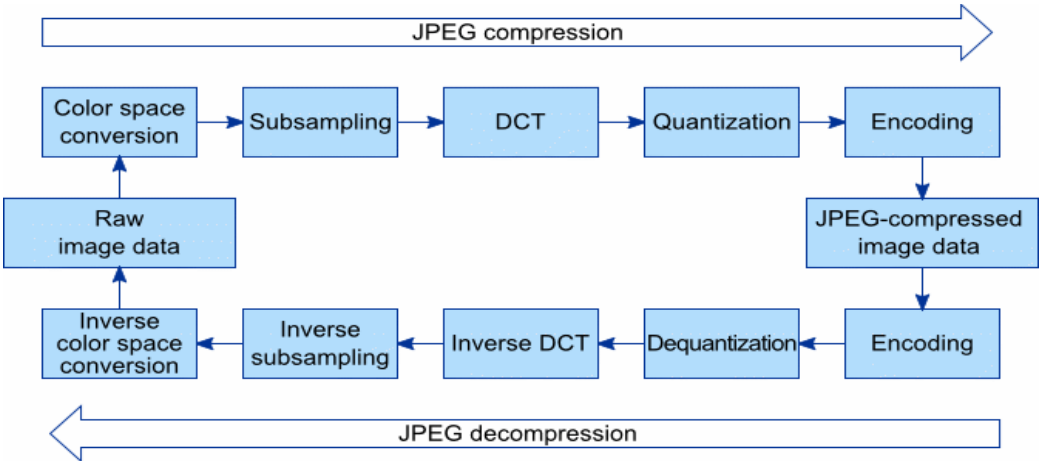

Figure 1. JPEG compression steps.

Color Transformation

RGB color format is used for easy for human to select colors form the color spaces. On the other side, YCrCb color format is useful for processing images. This operation converts the RGB image to YCbCr color space. Y is luminance commonly known as “luma” component and Cb and Cr are the blue-difference and red-difference respectively. These Y Cb Cr components can be calculated from RGB color components as given in following equations.

$$Y=0.299(R)+0.587(G)+0.114(B)$$
$$Cr=0.713(R-Y)=0.500(R)-0.419(G)-0.081(B)$$
$$Cb=0.564(B-Y)=-0.169(R)-0.331(G)+0.500(B)$$

Sub-Sampling

The human eye is less sensitive to brightness than to color. Therefore, reducing the Cr and Cb values by a certain amount will not change the image much for the human eye. Different formats used for sub-sampling are shown in the following figure.

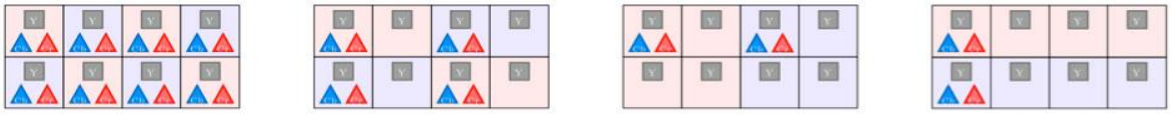

Figure 2. Formats of subsampling Y, Cb and Cr.

DCT Transform

The basic idea of data compression is to reduce the data correlation. By applying Discrete Cosine Transform (DCT), the data in time (spatial) domain can be transformed into frequency domain. Because of the less sensitivity of human vision in higher frequency, we can compress the image or video data by suppressing its high frequency components but do no change to our eye. The image data is divided up into 8x8 blocks of pixels and a DCT is applied to each block.

Forward DCT:

$$F(u,v) = \frac{1}{4}C(u)C(v)\sum_{x=0}^{7}\sum_{y=0}^{7} f(x,y)\cos\left[\frac{\pi(2x+1)u}{16}\right]\cos\left[\frac{\pi(2y+1)v}{16}\right]$$

$$\text{for } u = 0,\ldots,7 \text{ and } v = 0,\ldots,7$$

$$\text{where } C(k) = \begin{cases} 1/\sqrt{2} & \text{for } k = 0 \\ 1 & \text{otherwise} \end{cases}$$

Where u and v reprsents the horizontal and vertical spatial frequency respectively. $f(x,y)$ is the pixel value at coordinates (x,y) and $f(u,v)$ is the DCT coefficient at coordinates (u,v).

Quantization

Quantization is the step where most of the compression takes place. DCT really does not compress the image because it is almost lossless. Quantization makes use of the fact that higher frequency components are less important than low frequency components. It allows varying levels of image compression and quality through selection of specific quantization matrices. Thus quality levels ranging from 1 to 100 can be selected, where 1 gives the poorest image quality and highest compression, while 100 gives the best quality and lowest compression. As a result quality to compression ratio can be selected to meet different needs. A quantization matrix is used in combination with a DCT coefficient matrix to carry out transformation. Quantization is achieved by dividing transformed image matrix by the quantization matrix used as depicted in this equation.

$$F_q(u,v) = round\left(\frac{f(u,v)}{Q(u,v)}\right)$$

Huffman and RLE Encoding

The quantization step performs the major and lossy part of the compression in the pEG algorithm. Here, the number of different coefficient values is reduced and the number of zero value coefficients is increased. After quantization, the quantized coefficient for the zero frequency in both dimensions (so-called DC coefficient) is encoded as the difference from the DC term of the previous block. Finally, all coefficients are ordered into a "zig-zag" sequence (see Fig.3). This ordering makes entropy coding easier by placing the low-frequency coefficients before the high-frequency coefffcients (Jussi & Tapani, 1995).

As final step entropy encoding is performed and the image is compressed. There are many entropy coding algorithms available where the most known are Huffman Coding, Arithmetic Coding, Run Length Coding (RLE).

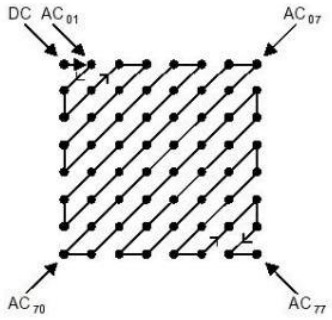

Figure 3. Zig-Zag reordering

Proposed Encoding Method

We present in this work, an improved JPEG-based image compression method. This is done by substituting, in the classical JPEG image compression algorithm, the Huffman encoding process by the QRLE method as illustrated by the following scheme:

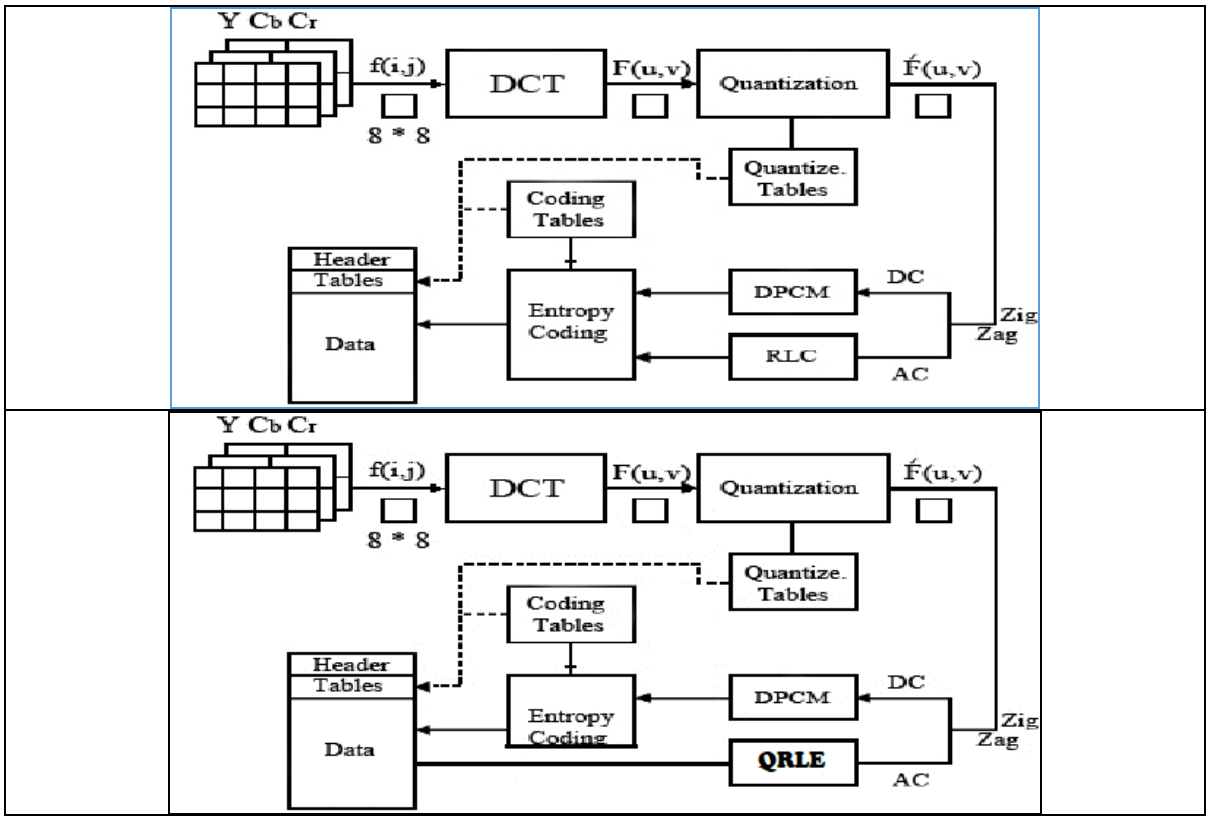

Figure 4. The classical jpeg-based huffman (shahbahrami et al., 2011) –at top- and the proposed modified jpeg-based 3 states qrle –at bottom- image compression synoptic scheme

It is necessary to mention that the original images are resized to [1536/R 1536/R] for computational reasons and will be recovered to their original sizes at the final step of the decompression process and where R is an integer value permitting better approaching to the original size of input images.
The proposed method appeals a so-called QRLE (Quantized Run Length Encoding) technique, that we have developed previously (Chouakri et al. 2018), where the couple of values (zero followed by its run number) is replaced just by one value.

The key idea of the QRLE method is to make sure that the MSB (the most significant bit) of the binary representation of the non-null values is '0' while that (the MSB) of the value indicating the 'zero' run number of

zero is '1'. This is done by adding the value 2^{N-1} to that number where N is its binary representation length as illustrated by the following figure:

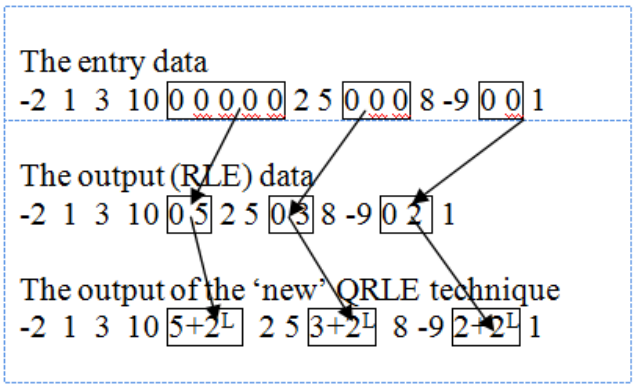

Figure 5. Quantized run-length encoding qrle example (Chouakri et al., 2018).

The first step in our QRLE method is to guarantee that the non-null values be less than 127, provided the RGB colored images are 8 bits long, that the MSB (the most significant bit) of the binary representation of these non-null values is '0'. This is done by accomplishing the following pseudocode:

Compute the minimum of non-null values ***min_non_null***;
Elevate the non-null values ***min_non_null*** to suppress the negative part ***Elev_non_null***;
Compute the maximum value of the elevated non-null values ***Max_Elev_non_null***;

$$\frac{Elev\_non\_null*((2^B-1)-5)}{Max\_Elev\_non\_null}$$

Limit the elevated non-null values ***Limit_Elev_non_null*** given by:
Add a DC offset value of ***5*** to ***Limit_Elev_non_null*** to obtain ***Final_non_null***;

Adding a DC offset value of ***'('***, to the limited elevated non-null values ***Limit_Elev_non_null*** is to avoid any interference with the byte-length of the huge zero run numbers; this value is sufficient to cover the highest possible amount of zero run number which is '16777216' that is $2^{24} \equiv 2^{(8*3)}$. It is worthy to mention that to make sure that the final obtained non-null values ***Final_non_null*** will not exceed 127 ($\equiv 2^7$ -1), the DC offset value of ***'5'***, has been first subtracted from 127 in the 4th line of the pseudocode.

Coming back to the zero run number, the proposed algorithm is faced to the following problem situation: given that the zero run numbers exceeds, at least for once, (2^7 -1≡127) value, the MSB is, necessarily, '1'. Even worse, the zero run number can be greater than 255 which implies occupying more than one octet. To solve that; the basic idea is to treat the zero run numbers of the AC zig-zag coefficients, according to 3 pre-defined ranges as follows:

[1..127], [128..255] , and [256..maximum value of zero run numbers]; where it comes the "3 states" expression. In the case of the first range, '128' value is added to the zero run numbers, to force the MSB equals '1', as given by the classical QRLE proposed previously (Chouakri et al., 2018) as well as figure 5. Fundamentally, as the size of the zero run numbers binary coded, in the second rage, i.e. [128..255], occupy strictly one byte with the MSB equals '1', the zero run numbers are unchanged but preceded by '0' value, to distinguish them from the former case.

Finally, for the third range, i. e. [256...maximum value of zero run numbers], and the zero run numbers are kept unchanged while preceded by the number of octets of their binary representation. Calculating the number of octets of the huge zero run numbers binary representation is carried out by applying the following Matlab macro command:

ceil(log10(zero_run_num+1)/log10(256))

The pseudocode of the Figure of the Three States QRLE (Quantized Run Length Encoding)-based JPEG image compression method is summarize as follows:

```
while not the end of RLE array

        while RLE coefficient ≠ 0
        Peek the RLE coefficient;
        Enqueue the RLE coefficient in QRLE array;
        Increment pointer values of RLE and QRLE arrays;
        end

        while RLE coefficient = 0
        Increment pointer value of RLE array;

        if RLE coefficient <128

        RLE coefficient ⟵ RLE coefficient +128;
        Increment pointer values of RLE and QRLE arrays;

        elseif    RLE coefficient ∈ [128,255]

        QRLE coefficient ⟵ 0;
        Increment pointer values of QRLE array;
        Peek the RLE coefficient;
        Enqueue the RLE coefficient in QRLE array;
        Increment pointer values of RLE and QRLE arrays;

        else

        QRLE coefficient ⟵ ceil(log10(zero_run_num+1)/log10(256));
        Increment pointer values of QRLE array;
        Peek the RLE coefficient;
        Enqueue the RLE coefficient in QRLE array;
        Increment pointer values of RLE and QRLE arrays;
        end

        end

end
```

Results and Discussion

This section presents and discusses the comparative analysis of our proposed algorithm performance versus the classical Huffman-based JPEG image compression. Two numerical criteria as well as visual inspection of the differential imge are employed for different algorithm's performance assessment. The numerical performance measurement criteria are the compression ratio (CR) and the Peak Signal to Noise Ratio (PSNR); they are given, respectively, by:

$$CR = \frac{numbre\ of\ samples\ of\ the\ original\ image}{number\ of\ samples\ of\ the\ compressed\ image}$$

and

$$PSNR = 10log_{10}(\frac{(255)^2}{MSE})$$

where

$$MSE = \frac{\sum_{i=1}^{N}\sum_{j=1}^{M}\left[I_{org}(i,j) - I_{rec}(i,j)\right]^2}{\text{NxM}}$$

and I_{org} and I_{rec} are, respectively, the original and reconstructed images while N and M are the number of rows and columns of the image. Obviously, a large value of PSNR indicates the good quality of reconstruction of the compressed image. It is worthy to mention that the obtained results (in terms of CR and PSNR) are given being provided an RGB image with 3 times a typical quantization matrix (for a quality of 50% as specified in the original JPEG Standard).

The following table summarizes the comparative analysis of applying our QRLE vs. Huffman based JPEG image compression algorithms. The table lists, preliminary, the name as well as the type of the original images,

their original size as well as resizing value. In terms of obtained results, the table depicts the compression ratio for our proposed algorithm vs; classical JPEG and the common value of PSNR.

Table 1. The assessment numerical values of our propose qrle vs. Huffman based-jpeg algorithm in terms of psnr and cr.

Name	Type	Original size	Resize value	PSNR	CR (our propose QRLE based-JPEG algorithm)	CR (classical JPEG algorithm)
ngc6543a	jpg	650 x 600	1536/2	38.7500	49.8780	14.0588
two	tif	3208x2672	1536	35.4824	82.2051	59.4265
peppers	png	384 512	1536/2	35.9946	17.2687	6.6498

The obtained results shows, obviously, the higher performance of our proposed JPEG-based QRLE algorithm compared to the classical one in terms of compression ratio (CR) that can reach in favorable cases till more than **82:1**. Conjointly, the restitution quality of the compressed image, which is the same for both algorithms, remains, in most of cases, good as demonstrated by the obtained numerical values. Moreover, the following figure illustrates the original images as well as their differential with their restituted versions. The visual inspection shows clearly the good restitution quality.

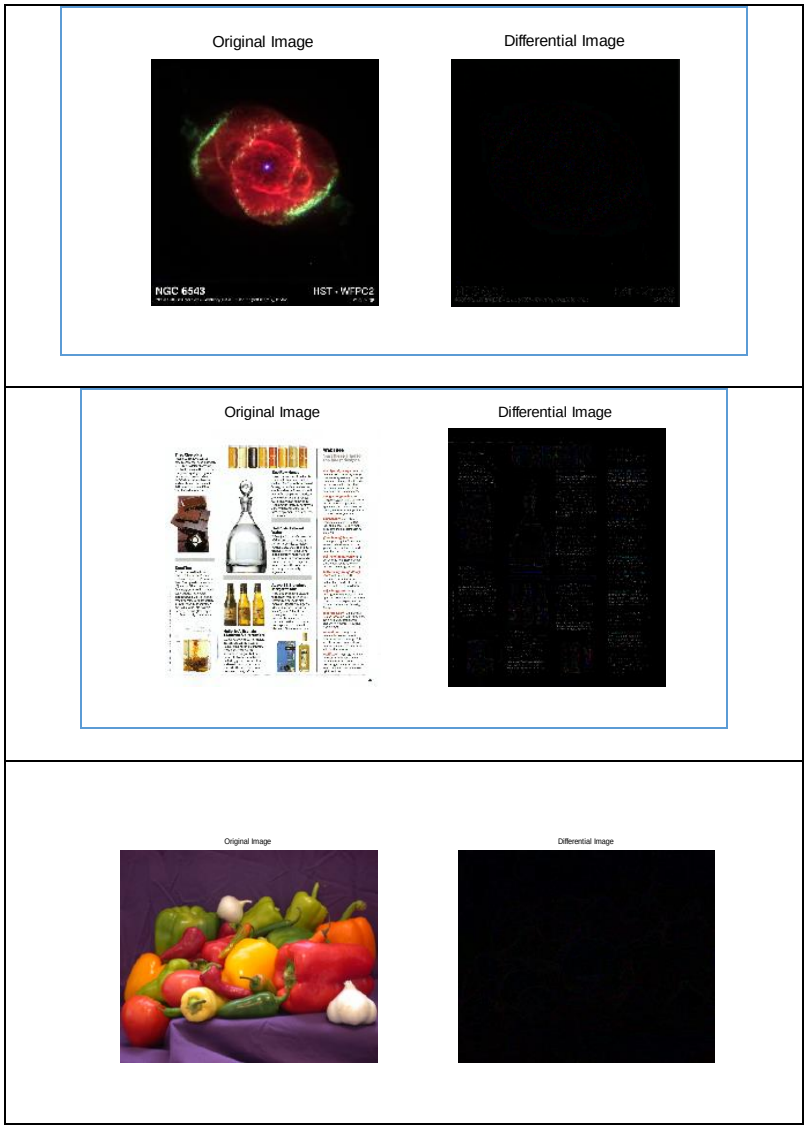

Figure 6. The visual inspection of the jpeg compression (psnr is similar for both algorithms: proposed jpeg-based qrle and huffman) in terms of original (at left) vs. differential image (at right) of images: ngc6543a.jpg, two.tif, and peppers.png (from top bottom).

Conclusion

We have presented in this work an new modified JPEG image compresssion algorithm based upon extending our anterior developed data compression method called QRLE (Quantized Run Length Encoding), firstly devloped uni-dimentional data, to the classical Huffman based-JPEG algorithm. The final work treated the processed pre-compressed image in 3 different ranges that comes the expression "Three states QRLE -based JPEG compression algorithm". This was done done by substituting the entropy Huffman coding by the QRLE technique. To assess the developed image compression algorithm performance, this latter has been applied to, mainly, 3 different types of coloured RGB images with distint sizes. Though the good and satisfactory compression results, in terms of compression ratio CR and Peak Signal to Noise Ratio PSNR as well as the visual inspection, provided by the classical JPEG-based Huffman coding, the developed JPEG-based QRLE image compression algorithm provides further performance as it was depicted along this paper. This considerably high image compression performance efficiency leads us to envisage to introduce the developed QRLE algorithm to video compression such as MPEG as future work.

Scientific Ethics Declaration

The authors declare that the scientific ethical and legal responsibility of this article published in EPSTEM journal belongs to the authors.

Acknowledgements or Notes

* This article was presented as an oral presentation at the International Conference on Technology, Engineering and Science (www.icontes.net) held in Antalya/Turkey on November 16-19, 2022.

* This work was supported by Directorate General for Scientific Research and Technological development (DGRSDT)

References

Alam, L., Dhar, P. K., Hasan, M. A. R., Bhuyan, M. G. S., & Daiyan, G. M. (2017). An improved JPEG image compression algorithm by modifying luminance quantization table. *International Journal of Computer Science and Network Security (IJCSNS)*, *17*(1), 200.

Artuger, F., & Ozkaynak, F. (2018). Performance comparison for lossy image compression algorithm. *International Journal of Advances in Electronics and Computer Science*, *5*(10), 57-61.

Candra, R., Madenda, S., Sudiro, S. A., & Subali, M. (2017). The Implementation of an efficient zigzag scan. *Journal of Telecommunication, Electronic and Computer Engineering (JTEC)*, *9*(2), 95–98.

Chouakri S. A., & Taleb-Ahmed, (2018). Quantized run length encoding QRLE -new compression method-: Application to ECG transmission via IEEE802.11b WLAN Channel. *International Conference on Innovation and Intelligence for Informatics, Computing, and Technologies* (3ICT), (pp. 1-8).

Kadam, S., & Rathod, V. J. (2017). DCT with Quad tree and Huffman coding for color ımages. *International Journal of Computer Applications*, *173*(9),33-37.

Kumar, B., Thakur, K., & Sinha, G. R. (2012). *Performance evaluation of JPEG image compression using symbol reduction technique.* Natarajan Meghanathan, et al. (Eds): ITCS, SIP, JSE-2012, CS & IT 04, 217–227.

Lammi, J., & Sarjakoski, T. (1995). lmage compression by the JPEG algorithm. *Photogrammetric Engineering & Remote Sensing*, (pp. 1261.-1266). October 1995

Li., Takala, J., Chen, M., Gabbouj, J., & Hexin. (2009). Detection algorithm for zero quantized DCT coefficients in jpeg. *IEEE International Conference on Acoustics, Speech and Signal Processing*, 31 March-4th April 2008, USA.

Miklós, P., Trpovski, Z., & Lončar-Turukalo, T. (2020). Analysis and improvement of JPEG compression performance using custom quantization and block boundary classifications. *Acta Polytechnica Hungarica*, *17*(6),171-191.

Shahbahrami, A., Bahrampour, R., Rostami, M. S., & Mobarhan, M. A. (2011). Evaluation of Huffman and arithmetic algorithms for multimedia compression standards. arXiv preprint arXiv:1109.0216.

Wallace, G. K. (1992). The JPEG still picture compression standard. *In IEEE Transactions on Consumer Electronics, 38(1).*

Author Information

Sid Ahmed CHOUAKRI
Telecommunications and Digital Signal Processing Laboratory (LTTNS), Electrical engineering Faculty
Djillali Liabes University of Sidi Bel Abbes,
22000, Algeria
Contact e-mail: *sa_chouakri@hotmail.com*

Fatiha MESKINE
Communication Networks, Architecture and Multimedia (RCAM) Laboratory, Electrical engineering Faculty
Djillali Liabes University of Sidi Bel Abbes,
22000, Algeria

To cite this article:

Chouakri, S.A. & Meskine, F. (2022). Three states qrle (quantized run length encoding) based jpeg image compression method. *The Eurasia Proceedings of Science, Technology, Engineering & Mathematics (EPSTEM), 21*, 173-181.

The Eurasia Proceedings of Science, Technology, Engineering & Mathematics (EPSTEM)
ISSN: 2602-3199

The Eurasia Proceedings of Science, Technology, Engineering & Mathematics (EPSTEM), 2022

Volume 21, Pages 182-187

IConTES 2022: International Conference on Technology, Engineering and Science

Experimental Modeling of the Compressive Behavior and Capillary Absorption of Mortars Based on Tuff of MEKLA

Ourdia FEDAOUI-AKMOUSSI
University Mouloud Mammeri of Tizi Ouzou

Tarik BENCHABANE
University Mouloud Mammeri of Tizi Ouzou

Fatma TAOUCHE-KHELOU
University Mouloud Mammeri of Tizi Ouzou

Malik HALICHE
University Mouloud Mammeri of Tizi Ouzou

Fouzia DEHBI
University Mouloud Mammeri of Tizi Ouzou

Abstract: Mineral additions are currently part of the most recent developments in the field of Civil Engineering, as their use improves the mechanical properties and durability of cementitious materials. On the other hand, their uses aim to reduce the consumption of cement (reduction of CO2), contributing in a simple and economical way to solving problems related to the environment. This study aims to study the mechanical behavior of mortars based on tuff of MEKLA as a substitute for cement, using the following percentages: 5, 10, 15, 20, 25 and 30%. All the compositions were manufactured with a water to cement W/C= 0.5 ratio. The compressive strengths were determined at different ages: 7, 14, 28 and 90 days. We also carried out capillary absorption tests on the different samples studied. The results showed that all 28-day-old tuff samples had strengths greater than 30 MPa and those 90 days-old presented strengths greater than 40 MPa. Regarding the capillary absorption tests, mortars with 5% and 10% tuff aged 28 days showed lower capillary absorption coefficients than the control mortar.

Keywords: Mortar, Tuff of MEKLA, Compressive strength, Capillary absorption.

Introduction

In the field of construction, the search for new materials with low environmental impact is developed for energy saving and CO2 reduction. Indeed, some studies have shown that the manufacture of Portland cement generates a lot of CO2 and consumes a lot of energy (Kerbouche et al., 2009).

The use of hydraulic binders to replace cement is necessary to limit CO2 emissions and reduce energy consumption in order to ensure sustainable development in the cement industry. However, the partial substitution of a certain quantity of cement by one or more mineral additions when available can be very advantageous, not only from an economic point of view, but also from a strength and durability point of view (Mebrouki, 2003).

Mineral additions affect the kinetics of the hydration reaction, improve the physical characteristics of mortars and concretes in the fresh state and contribute positively to the mechanical resistance of mortars and concretes in the hardened state, due to their chemical composition, their reactivity and their particle size (Bessa et al., 2003; Turkmenoglu et al., 2002). The valorization of Tuff in Algeria in the field of civil engineering has been studied by several researchers (Colombier, 1988). This work consists in studying the mechanical behavior and durability of mortars based on Tuff of MEKLA as a substitute for cement. Four maturations were used for the compression tests and two for the capillary absorption tests.

Experimental Method

Materials

In this study, we used a CPJ CEM II/B 42.5 type cement from LAFARGE in Algiers, its specific surface area is 3555 cm^2/g. A sand with a grain size between 0 and 3mm. A quarry tuff from MEKLA, its absolute density is 2.53 g/cm3. The chemical composition of cement and tuff are shown in Table 1.

Table 1. Chemical composition of cement and tuff

Constituents (%)	SiO_2	Al_2O_3	Fe_2O_3	CaO	MgO	SO_3	K_2O	Na_2O	P_2O_5	TiO_2	PAF
Cement	20,71	5,45	3,63	60,4	2,15	2,37	0,65	0,23	0,10	0,23	4,28
Tuff	70,78	13,50	3,83	0,84	0,27	-	5,49	2,58	0,28	0,12	1,60

After the mess, the test pieces were made and kept in the water. We made two series of test tubes, a series is intended for compression tests at 7, 14, 28 and 90 days of maturation and the other series For the hair absorption test. Each series, was studied for seven values of adding tuf (0, 5, 10, 15, 20, 25, 30) % in substitution of the cement. The compression trials were carried out on cubes (4 × 4 × 4) cm^3 with the standard (NF P 18 - 406). Regarding, the hair absorption tests, they are carried out on cubic (5 × 5 × 5) cm^3. For this test, we measure the capillary absorption coefficient as a function of time on the following deadlines: 15 min, 30 min, 1h, 2 h, 4 h., 8 h and 24 hours. The test must be completed after 24 hours. The capillary absorption coefficient is defined by the following relation :

$$C_a = \frac{M_x - M_0}{A} \ (kg/m^2)$$

With :
M_x : The mass of the test tube has a given deadline (kg);
M_0 : The initial mass of the test tube (kg);
A : The sectors section (m^2).

Results

Compressive Strength

Table (2) presents the results of the compressive strength of the various mortars studied by calculating the average of three trials.

Table 2. Compressive strength of mortars studied at different ages.

	Compressive strength (MPa)			
	7 Days	14 Days	28 Days	90 Days
M0T	32,4	46,1	45,7	59,1
M5T	29,2	38,4	46,4	54,0
M10T	30,1	32,7	43,4	51,4
M15T	30,1	32,1	39,3	44,7
M20T	26,4	26,8	35,1	43,9
M25T	23,2	28,7	37,7	42,2
M30T	22,4	28,1	31,3	41,0

The compressive strength of the different mortars studied are presented in the form of a histogram and shown in figures (1), (2), (3), (4) and (5).

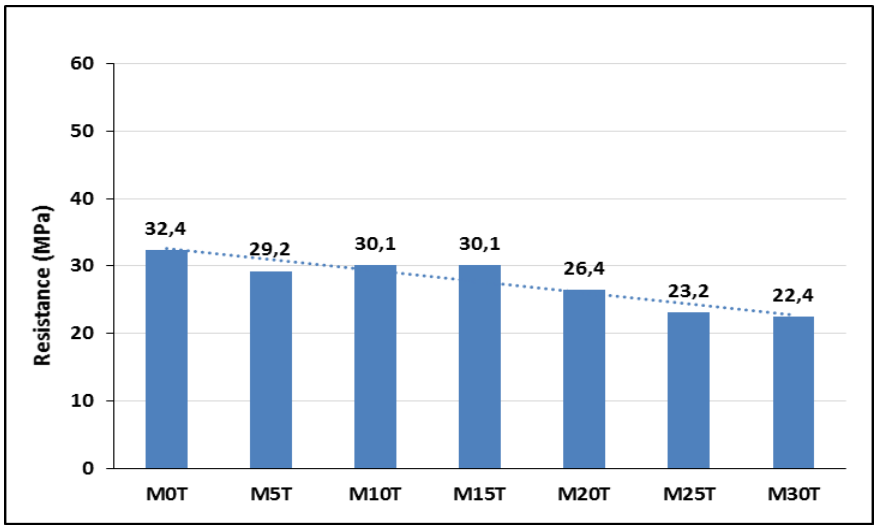

Figure 1. Compressive strength of mortars at 7 days of age.

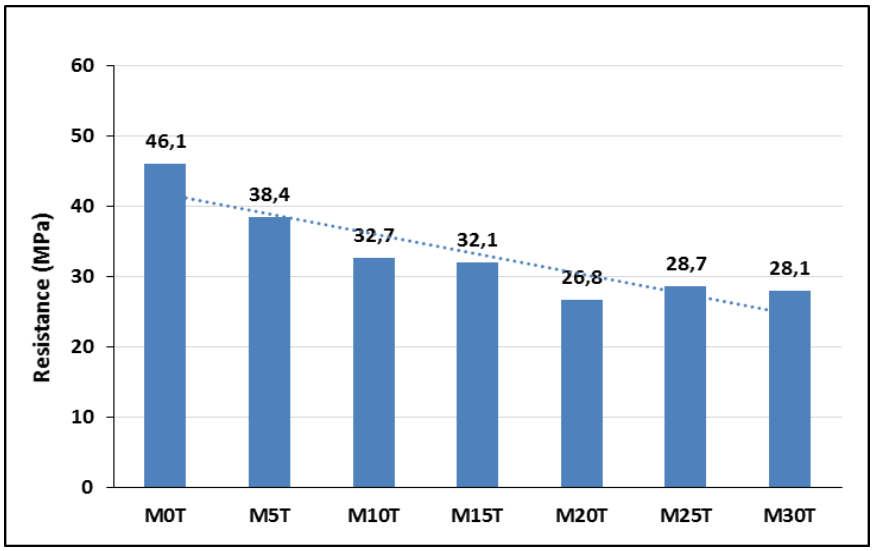

Figure 2. Compressive strength of mortars at 14 days of age.

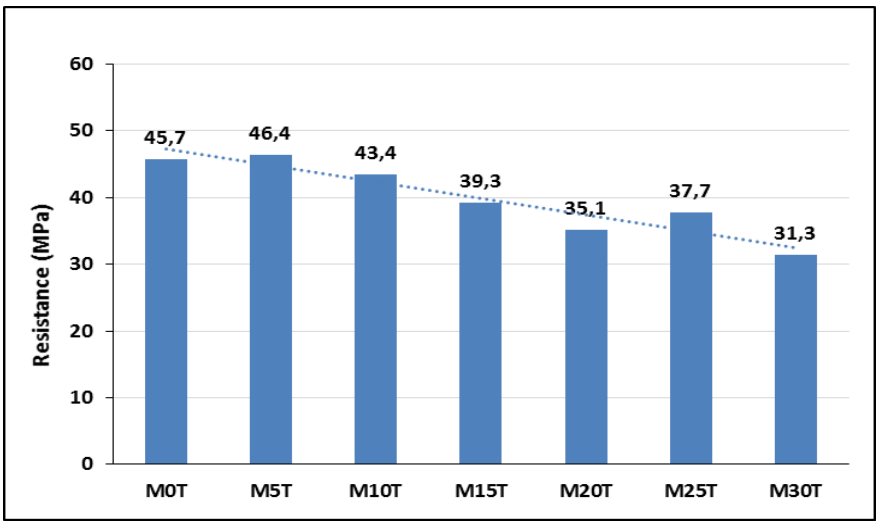

Figure 3. Compressive strength of mortars at 28 days of age.

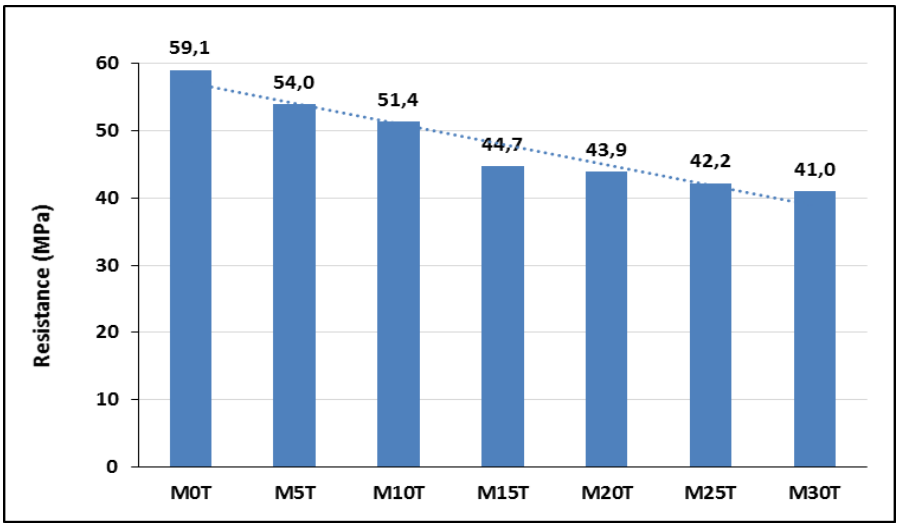

Figure 4. Compressive strength of mortars at 90 days of age.

For all ages studied, mortars with 30% of tuff presented a reduction in compressive strength of 31% compared to the control mortar. While mortars with 5% of tuff presented a decrease in resistance from 1% at 28 days and 8% at 90 days.

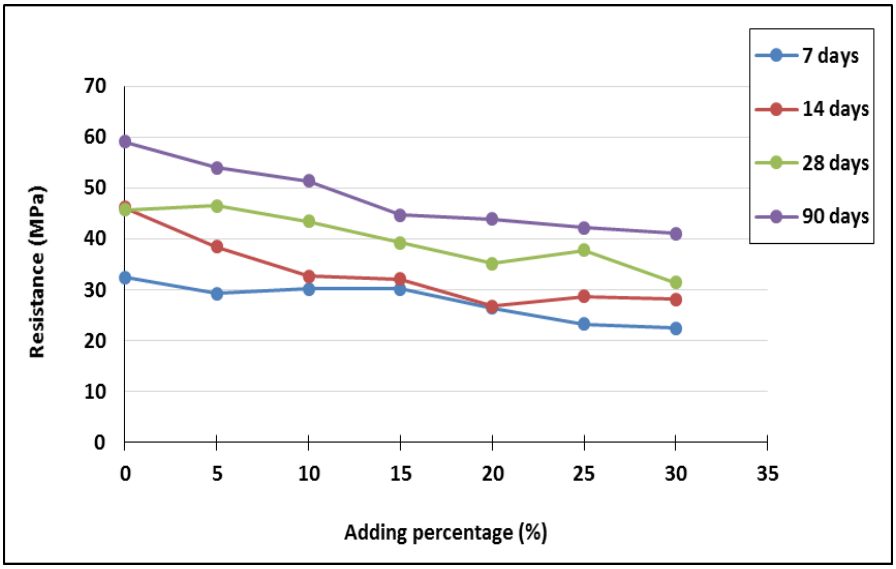

Figure 5. The compressive strength evolution as a function of the adding percentage.

At 28 days, the compressive strength of all mortars studied exceed 31.3 MPa. For 90 days, the compressive strength of all mortars exceed 41 MPa. For a substitution of 5 to 15% of tuff, the mortars presented a good compressive strength.

3.2 Capillary Absorption

The capillary absorption tests were carried out on the test tubes after 14 and 28 days of hardening. We have represented the evolution of the capillary absorption coefficient as a function of time in the figures (6) and (7).

We note that at 14 days of age, the mortars based on tuff, presented a capillary absorption coefficient greater than that of the control mortar (M0T). On the other hand at 28 days of age, the mortars with 5% (M5T) and 10% (M10T) based on tuff presented a capillary absorption coefficient lower than that of the control mortar which explains that the mortars had a less porous structure So a less important connectivity of pores. For the other tuff percentages, there is an increase in the capillary absorption coefficient, therefore a more porous structure.

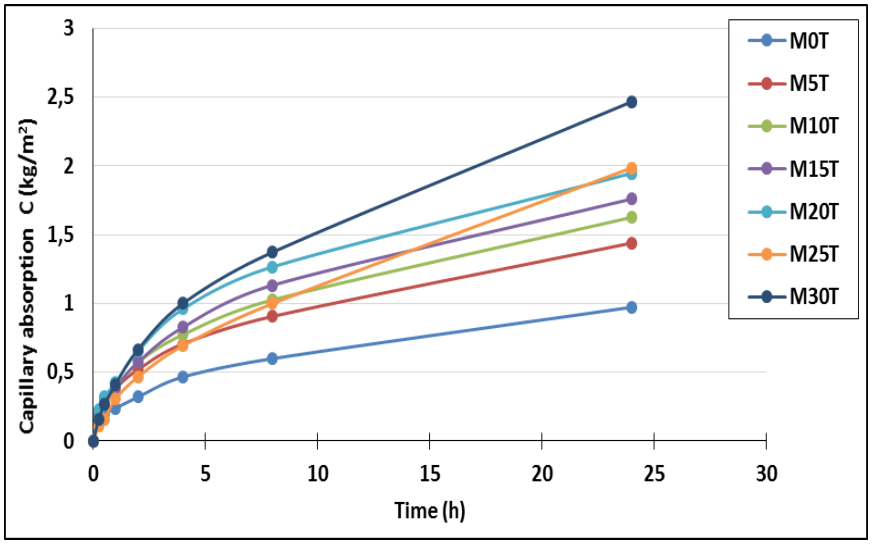

Figure 6. Evolution of the capillary absorption coefficient at 14 days of age.

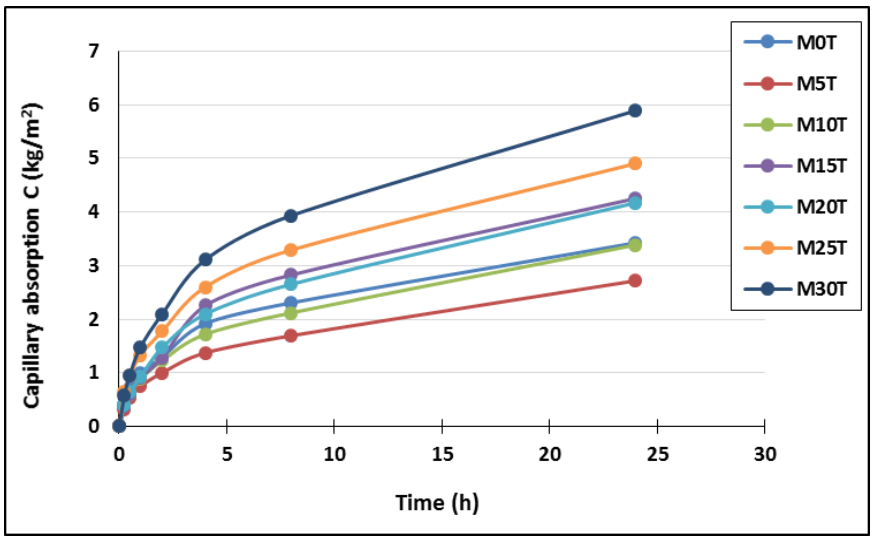

Figure 7. Evolution of the capillary absorption coefficient at 28 days of age.

Conclusion

The results obtained in this study allowed us to achieve the following conclusions:

- The mortars with 30% of tuff presented a decrease in compressive strength of 31% compared to the control mortar. While mortars with 5% tuff presented a decrease in resistance from 1% to 28 days and 8% to 90 days. At 28 days, the resistance of all the mortars studied exceeds 31.3 MPa. For 90 days, the resistances of all mortars exceed 41 MPa.

- At 28 days old, mortars with 5% (M5T) and 10% (M10T) of tuff presented a capillary absorption coefficient lower than that of the control mortar which explains that the mortars had a less porous structure therefore a connection less important pores. For the other tuff percentages, there is an increase in the capillary absorption coefficient, therefore a more porous structure.

Scientific Ethics Declaration

The authors declare that the scientific ethical and legal responsibility of this article published in EPSTEM journal belongs to the authors.

Acknowledgements or Notes

* This article was presented as a poster presentation at the International Conference on Technology, Engineering and Science (www.icontes.net) held in Antalya/Turkey on November 16-19, 2022.

References

Bessa A., Bigas J.P., & Gallias J.L., (2003). *Influence des additions minérales naturelles et industrielles sur les principaux paramètres de formulation de mortiers*, XXI èmes Rencontres Universitaires de Génie Civil.

Colombier, G., (1988). *Tufs et encroûtements calcaires dans la construction routière*, Synthèse. ISTED.

Duhahi, M., (2007). *Contribution à la valorisation des tufs et encroûtements calcaires en techniques routière saharienne*, École polytechnique d'Alger.

Kerbouche, A., Mouli, A.M., Laoufi, L., Senhadji, Y., & Benosmane, S., (2009). Influence desajouts mineraux sur les resistancesmecaniques des mortiers,SBEIDCO *-1st International Conference on sustainableBuiltEnvironment Infrastructures in Developing Countries ENSET Oran (Algeria)* – October 12-14.

Mebrouki A., (2003). *Influence de la pouzzolane de Beni-Saf sur les caractéristiques mécaniques des mortiers*. (Thèse de Magister) Université Mostaganem.

Türkmenoğlu, A. G., & Tankut, A., (2002). Use of tuffs from central Turkey as admixture in pozzolanic cements : Assessment of their petrographical properties, *Cement and Concrete Research, 32(*4), 629-637.

Author Information

Ourdia Fedaoui-Akmoussi
Mouloud Mammeri University
Route de Hasnaoua BP 47, Algeria
Contact e-mail : *fedaouio@yahoo.fr*

Tarik Benchabane
Mouloud Mammeri University
Route de HASNAOUA BP 47
Algeria

Fatma Taouche-Kheloui
Mouloud Mammeri University
Route de HASNAOUA BP 47
Algeria

Malek Haliche
Mouloud Mammeri University
Route de Hasnaoua BP 47
Algeria

Fouzia Dehbi
Mouloud Mammeri University
Route de HASNAOUA BP 47
Algeria

To cite this article:

Fedaoui-Akmoussi, Q., Tarik, B., Taouche-Kheloui, F., Haliche, M. & Dehbi , F. (2022). Experimental modeling of the compressive behavior and capillary absorption of mortars based on tuff of MEKLA. *The Eurasia Proceedings of Science, Technology, Engineering & Mathematics (EPSTEM), 21,* 182-187.

The Eurasia Proceedings of Science, Technology, Engineering & Mathematics (EPSTEM)
ISSN: 2602-3199

The Eurasia Proceedings of Science, Technology, Engineering & Mathematics (EPSTEM), 2022

Volume 21, Pages 188-195

IConTES 2022: International Conference on Technology, Engineering and Science

TVWS Geolocation Database for Secondary-User TVWS Devices for Spectrum Forecasting

Armie PAKZAD
De La Salle University

Raine Mattheus MANUEL
De La Salle University

Lawrence MATERUM
De La Salle University
Tokyo City University

Abstract: This paper suggests a MATLAB-based television white space (TVWS) database with forecasting capabilities. The availability of multiple TV frequencies for a secondary user, depending on the day and time of the inquiry, location, and device, was forecasted using reinforcement learning (RL) software. A MATLAB live script RL application was created and tested. After passing numerous tests, the algorithm was integrated into a MATLAB App Designer application so that an SU could request projections for spectrum availability. Three categories might be used to categorize the forecast—medium-term (MT), long-term (LT), and short-term (LT). The forecast for that day is referred to as ST, the following day as MT, and the days after that as LT. Based on the SU's device, the program was designed to predict the spectrum availability in relation to the SU's query time, location, and transmission details. The SU device is a fixed white space device with an EIRP power cap of 4 watts. The database and AI are both necessary for accurate predictions. The forecast's results indicated 100% accuracy, assuming the database is frequently updated. Both the forecasting and reinforcement learning programs were created using MATLAB's App Designer.

Keywords: Reinforcement learning, Television white space database, TVWS spectrum forecasting, Artificial intelligence

Introduction

TVWS communications is a developing technique and technology that introduces new opportunities and challenges in maximizing frequency spectrum utilization. The opportunity for developing countries with an abundantly available spectrum in the TV band is enormous. According to Ismail, Kissaka, and Mafole's research, despite the widespread availability of TVWS in developing countries, the average internet penetration is 30%. This observation means that a large portion of the population is still not connected to digital networks (Ismail, et al., 2019). TVWS implementation for communications can benefit developing countries in rural and other underserved areas.

TVWS communications allow for dynamic frequency spectrum utilization. Alonso, Plets, Deruyck, Martens, Nieto, and Joseph discovered that using TVWS networks in suburban and rural scenarios saves 9 to 12 times more energy than LTE networks. This finding indicates that TVWS is viable in underserved areas (Alonso et al., 2017).

When it comes to connectivity, rural areas in the Philippines lag. Inquirer Philippines reported that they collaborated with ADB and Thinking Machines on Artificial Intelligence, Big Data, and Machine Learning for Development to map digital poverty in the Philippines. They discovered that access to adequate Internet speeds deteriorates in rural areas (Araneta et al., 2021). This decline in access in rural areas leaves people without access to digital space.

Super high-speed Wi-Fi (Wi-Fi 2.0) is a way to bring Internet service to underserved areas using the TVWS band. Gigabit-per-second high-speed rates are possible with this Wi-Fi (Sarkar et al., 2016). Particularly in impoverished areas, the TV spectrum is full of white spaces. Secondary users (SUs) can quickly discover which frequency bands are available given a time and location for secondary use using a TVWS database (TVWSDB). Asking SUs for a list of available channels, the TVWSDB must be able to do so. The spectrum is dynamically changing due to primary user (PU) off-airs or various PUs in various locations. Therefore SUs that contact the TWSDB must be kept informed at the appropriate intervals and change bands as necessary to avoid interfering with the PUs.

Since spectrum usage is constantly changing, manually querying the database or continuously sensing band availability might be unreliable and inconvenient. Given a trustworthy and regularly updating TVWSDB, the application of machine learning would aid in automating the inquiry and update process for SUs.

Related Studies

TVWS offers a substitute for establishing wireless connections. The difficulty here is to avoid interfering with the primary users (PU). In their work, Makgamatha, Zuva, and Masonta used a geolocation database that employs a protocol to access the available white space while adhering to quality of service (QoS) standards (Makgamatha et al., 2018).

The study by Aji, Wibisono, and Gunawan illustrates how TVWS technology is used in Indonesia to provide rural telecommunications solutions. They claim that, especially in developing countries, there is a substantial infrastructure gap in telecommunications between urban and rural areas. They asserted that TVWS was an acceptable alternative for unplanned usage (Aji et al., 2017). The FCC and ECC standards currently in use are available to other countries.

There is a growing need for wireless spectrum resources as 5G technology matures. Because of this, a solution to the issue of dynamic spectrum access is needed. Using the TVWS frequency band, Chen and Zhang's research led to the development of a spectrum detection node with an embedded system. Their test demonstrated the potential for precise detection and system adaptability when using a distributed electromagnetic spectrum information service platform based on signal characteristics (Chen & Zhang, 2019).

As wireless communication technology advances, more applications that depend on bandwidth are starting to appear. It is, therefore, ideal to fully utilize the wireless frequency range. The use of white spaces for secondary applications is anticipated to increase due to recent improvements in TVWS technology. Mustapha, Bakura, D. Mustapha, and Abbagana evaluate TV white space strategies and a few TVWS technology implementations in Africa (Mustapha, 2019). They discovered that TVWS is trustworthy and reasonably priced, which is practical for secondary use.

Additionally, especially in developing nations, it can boost the economics of setting up wireless connections in underserved rural areas. Additionally, because of the dynamically changing spectrum in various locations and at various times, TVWS devices must adjust their operational frequency spectrum dynamically. Having hardware that is configurable and having well-designed software for the job will enable this method—having it also aids in avoiding interference when PU frequencies are used outside of business hours.

A paper published by Ma, Gao, Fu, Rong, Xiong, and Cui explored how to use TVWS to make the most use of the spectrum for various applications. They looked at how the spectrum was used in London at various fixed and mobile locations. In order to study how the spectrum is used in various channels, locations, and time instances and to exploit the white space for various purposes, they employed machine learning to analyze the dynamic usage of the spectrum based on their observations (Ma et al., 2019).

Researchers Rempe, Synder, Pracht, Schwarz, Nguyen, Vostrez, Zhao, and Vuran have created a prototype configuration that uses numerous cognitive radios, a TVWS database, and the TVWS spectrum. After using a

free frequency, an SU modifies the spectrum database, which is visible to other SUs. The cognitive radio must recognize when a frequency is unavailable due to PU use and switch to another available frequency, updating the spectrum database. Through periodic database searches, this operation is carried out (Rempe et al., 2017).

A mathematical framework was developed by Hussien, Katzis, Mfupe, and Bekele to determine the ideal separations for co-channel and adjacent channel use of digital TV (DTV) frequencies. They used HAAT values and the propagation models ITU-R P.1546-5 and P.1411-9 for the calculations in Ethiopia. Ethiopian WSD networks also established the necessary neighboring protection ratio of 27 dB (Hussien et al., 2019).

To protect PUs, the use of TVWS requires rules and regulations. White space devices (WSD) need sensing capabilities to solve this issue. However, this capability can be challenging to control and does not produce precise or organized results. Dynamic spectrum access can be tracked using a TVWSDB that is consistently updated and contains all necessary information. Alejandrino, Concepcion II, Laugico, Trinidad, and Dadios looked at the various WSD technologies on the market and any gaps that might exist in TVWS implementation. They discovered that one of the gaps is the devices' adaptability to work in various topologies. Different laws in many nations could be problematic (Alejandrino et al., 2019).

TVWS availability in the Greater Metro Manila Area was examined in a study by Morico, Porras, Judan, De Guzman, and Hilario conducted in the Philippines (GMMA). Results from propagation simulations using the Okumura-Hata and Hata-9999 models, along with measurements of the spectrum along a single path made using a portable spectrum analyzer, reveal that many white spaces outside the GMMA can be put to use for secondary purposes (Morico et al., 2020).

The paucity of TVWS geolocation datasets with SU forecasting capabilities is highlighted in the literature, a problem that this work aims to solve. The methodology section covers the forecasting process, and the findings are presented in the Results and Discussion section. The study's findings are summarized in the final section.

Methodology

A MATLAB live script reinforcement learning (RL) application was created and tested (Pakzad et al., 2022). After passing numerous tests, the algorithm was integrated into a MATLAB App Designer application so that an SU could request projections for spectrum availability. Three categories might be used to categorize the forecast—medium-term (MT), long-term (LT), and short-term (LT). The forecast for that day is referred to as ST, the following day as MT, and the days after that as LT. Based on the SU's device, the program was designed to predict the spectrum availability in relation to the SU's query time, location, and transmission details. It is believed that SU's device is a fixed white space device with an EIRP power cap of 4 watts. The FCC's fact sheet for unlicensed white space device activities (FCC Fact Sheet, 2020) served as the basis for this value. The application used MATLAB's site viewer for propagation mapping and the forecast findings. The Longley-Rice model, pre-built in MATLAB's Antenna Toolbox, was used in the PUs' propagation map. In contrast, SUs used the free-space model because of its limited coverage.

The database was generated in Microsoft Excel (Pakzad et al., 2022), imported into MATLAB, and utilized via data reading features to improve the written program's interaction with the database for training. Program schedules for PUs were gathered from various websites, including the channel networks' websites. During training, the learning data is contrasted with the PUs and SU interference calculations, as well as the program schedule of PUs, to test the forecasts' results. For making sure that the RL process resulted in accurate decision-making for the SU, this step was taken.

Results and Discussion

The App Designer application is displayed in Figure 1. Time, location, device type (fixed 4W EIRP), and distances (in km) dependent on operating frequency are all included in the SU inputs on the left and are determined using the FM and TV Propagation Curve Calculator provided by the FCC.

The spectrum information is displayed on the program's right side. The GUI displays a legend based on the user's preferences. The hue of the lamp indicates whether a channel frequency is available, while the number next to the bulb indicates how many hours a specific channel's PU is off-air. The SU that enquired is far enough

away from the PU that there will be no interference if the SU decides to use the frequency if the lamp indicates that the channel is available but indicates that the PU is on-air (0 hours result).

The type of forecasting used is displayed at the bottom of the selected day, also on the right. The day chosen before pressing the training button is considered the ST forecast or the day of inquiry; in the case of the figure, that day is Sunday. The MT forecast is the forecast day that follows the forecast inquiry. As seen in Figure 2, Monday is considered in this situation as the MT. A sample of the LT prediction, which runs from Tuesday to Saturday and is shown in Figure 3, is for the Saturday after the day of the inquiry.

Depending on the SU requests for a channel prediction, the ST forecast is provided on that day, the MT forecast is provided one day later, and the LT forecast is provided in the days following the first day following the request. If an SU were to query, for instance, on Sunday, ST would be forecast on Sunday, MT would be forecast on Monday, and LT would be forecast from Tuesday until Saturday. The programming schedule needs to be revised regularly for the forecast to be precise.

Prior to a forecast, the user must hit the train button. The button launches the reinforcement learning training program in the background to obtain the available channels for each weekend day. As illustrated in Figure 4, a pop-up window notifies the user that the training is over. Following the training, the forecast status changes from its initial red state to green. After the training, one can press the forecast button after choosing a day from the drop-down menu.

Figure 1. TVWS forecast program (ST)

Figure 2. TVWS Forecast Program (MT)

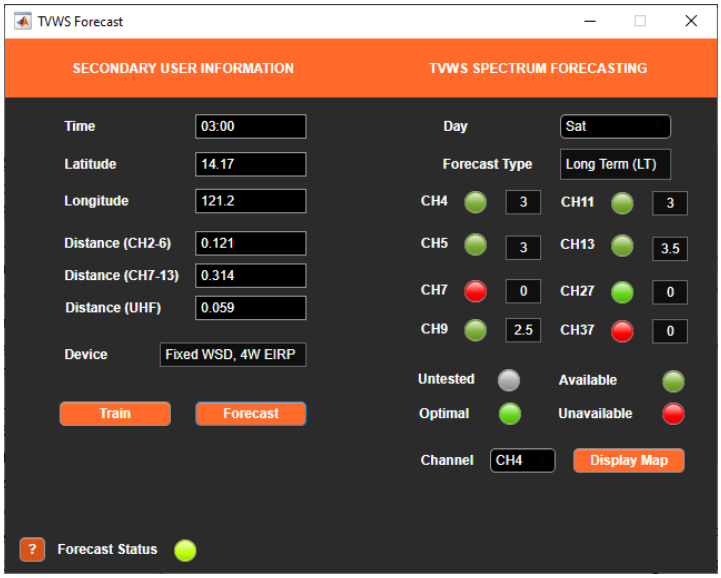

Figure 3. TVWS forecast program (LT)

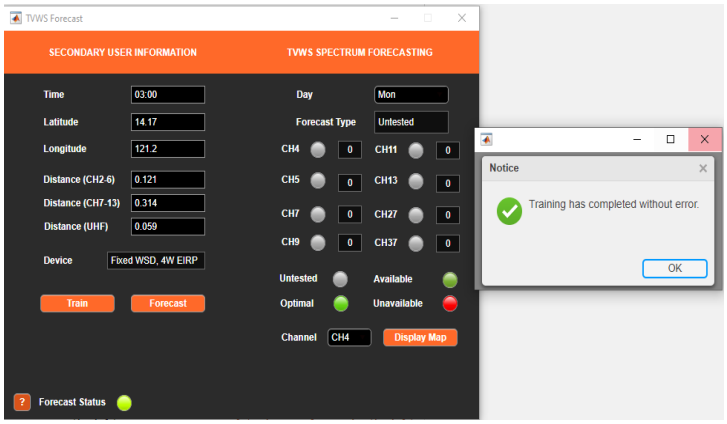

Figure 4. Training finished

The window that displays when the user hits the program's "Display Map" button is depicted in Figures 5 and 6. The contour map is zoomed in in Figure 5 to highlight how sparse the SU coverage is. The coverage of the PU can be viewed by zooming out from Figure 6. The SU uses the free-space model because of its limited coverage area, but the PU's contour map is based on MATLAB's built-in Longley-Rice model.

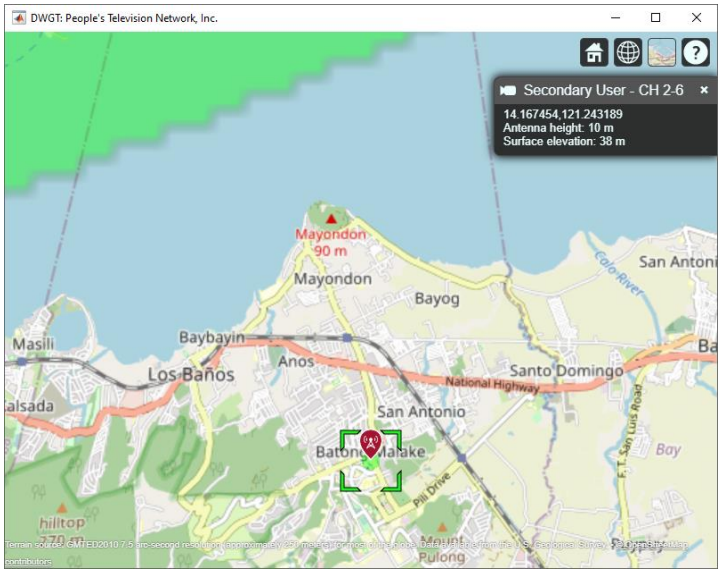

Figure 5. Secondary user location and coverage

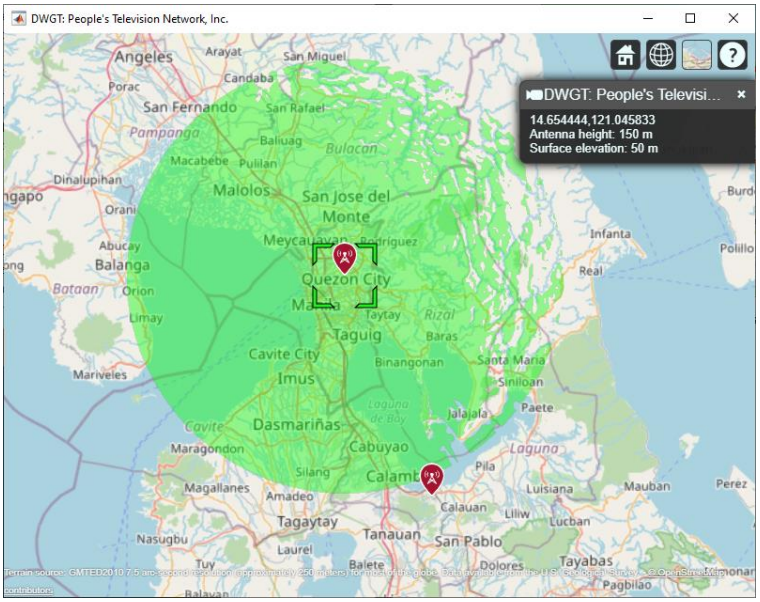

Figure 6. Primary user location and coverage

An algorithm was added after the primary learning algorithm to verify the training data's accuracy based on the SU's conditions to test the training outcomes or the Q-tables generated from the training. The testing algorithm examines the Q-table, contrasts the acceptability and deniability values for a specific channel, and compares these values to the case of the SU. The number of hours a channel is open and whether the SU would interfere with the PU is determined based on the SU's parameters, and the findings of the Q-table are compared.

The most advantageous channel is determined based on the channel's length of availability (PU off-air period) and whether the SU would interfere with the PU. The PU's frequency is selected as the best channel if it is not already in use and the SU is sufficiently far away not to interfere. The most advantageous channel is determined by which PU's frequency gives the most extended available period for secondary use of their frequency if the SU is within range of all the PUs.

Table 1 displays the accuracy results from 100 different SU cases using 100 Q-Tables on various days of the week. A 100% accuracy rate indicates that the machine learning algorithm could produce accurate forecasts of the available channels for the 100 SU scenarios provided.

Table 1. Accuracy of training results

Day	Accuracy
Monday	100 %
Tuesday	100 %
Wednesday	100 %
Thursday	100 %
Friday	100 %
Saturday	100 %
Sunday	100 %

Conclusion

TVWS implementation makes the most of the TV spectrum, especially in underdeveloped areas. SUs can ask multiple questions regarding the forecast for spectrum availability by using a TVWSDB in conjunction with RL. The authors developed a TVWSDB and RL-implemented MATLAB software that simulates an SU requesting spectrum predictions. The forecasting can be divided into three categories: ST, MT, and LT, where ST refers to the day of the inquiry, MT to the day after, and LT to the days that follow the week of the inquiry. Based on the conditions, the RL method produced a forecast that was 100 percent accurate. However, updating the database in actual implementation practice is advised because PU program schedules change over time.

Scientific Ethics Declaration

The authors declare that the scientific ethical and legal responsibility of this article published in EPSTEM journal belongs to the authors.

Acknowledgements or Notes

* This article was presented as a poster presentation at the International Conference on Technology, Engineering and Science (www.icontes.net) held in Antalya/Turkey on November 16-19, 2022.

*The authors wish to thank De La Salle University for its support.

References

Aji, L. S., Wibisono, G., & Gunawan, D. (2017, July). The adoption of TV white space technology as a rural telecommunication solution in Indonesia. In *2017 15th International Conference on Quality in Research (QiR): International Symposium on Electrical and Computer Engineering* (pp. 479-484). IEEE.

Alejandrino, J. D., Concepcion, R. S., Laugico, S. C., Trinidad, E. T., & Dadios, E. P. (2019, November). Feasibility of television white space spectrum technologies for wide range wireless sensor network: A survey. In 2019 *IEEE 11th International Conference on Humanoid, Nanotechnology, Information Technology, Communication and Control, Environment, and Management (HNICEM*) (pp. 1-6). IEEE.

Alonso, R. M., Plets, D., Deruyck, M., Martens, L., Nieto, G. G., & Joseph, W. (2017). TV white space and LTE network optimization toward energy efficiency in suburban and rural scenarios. *IEEE Transactions on Broadcasting*, *64*(1), 164-171.

Araneta, A., Carrasco, B., Rahemtulla, H., Balgos, S., & Sy, S. (2021). *Mapping digital poverty in PH*. INQUIRER .NET.

Chen, Z., & Zhang, Y. (2019). Providing spectrum information service using TV white space via distributed detection system. *IEEE Transactions on Vehicular Technology*, *68*(8), 7655-7667.

Hussien, H. M., Katzis, K., Mfupe, L. P., & Bekele, E. T. (2019, September). Coexistence of TV white space devices and DTV services in Ethiopian geolocation white space spectrum database. In 2019 *IEEE 24th International Workshop on Computer Aided Modeling and Design of Communication Links and Networks* (CAMAD) (pp. 1-5). IEEE.

Ismail, M., Kissaka, M., & Mafole, P. (2019, May). Television white space opportunities and challenges: What next for the developing countries?. In *2019 IST-Africa Week Conference (IST-Africa)* (pp. 1-9). IEEE.

Ma, Y., Gao, Y., Fu, C., Rong, W., Xiong, Z., & Cui, S. (2019). TV white space spectrum analysis based on machine learning. *Journal of Communications and Information Networks*, *4*(2), 68-80.

Makgamatha, A. S., Zuva, T., & Masonta, M. T. (2018, August). Channel selection technique to satisfy secondary users quality of service (QoS) requirements in TV white space. In 2018 *International Conference on Advances in Big Data, Computing and Data Communication Systems* 1-8.

Morico, K. E. R., Porras, K. J. G., Judan, J. M., De Guzman, M. F. D., & Hilario, C. A. G. (2021, January). Assessment of television white space in the greater metro manila area through geospatial and empirical approaches. In 2020 *International Symposium on Antennas and Propagation (ISAP)* (pp. 149-150). IEEE.

Mustapha, I., Bakura, M. U., Mustapha, D., & Abbagana, M. (2019). A review of TV white space technology and its deployments in Africa. *Arid Zone Journal of Engineering, Technology and Environment*, *15*(3), 573-585.

Pakzad, A., Asuncion, X. F., Ligayo, J. V., Manuel, R. M., Uy, J. S.,& Materum L. (2022). *TVWS geolocation database for greater manila area, Philippines as of 2020.* Retrieved from https://ieee-dataport.org/documents/tvws-geolocation-database-greater-manila-area-philippines-2020.

Pakzad, A. Manuel, R. M., & Materum L. (2022). *Reinforcement learning program for television white space database*. Retrieved from https://codeocean.com/capsule/3252664/tree.

Rempe, D., Snyder, M., Pracht, A., Schwarz, A., Nguyen, T., Vostrez, M., ... & Vuran, M. C. (2017, March). A cognitive radio TV prototype for effective TV spectrum sharing. In 2017 *International Symposium on Dynamic Spectrum Access Networks*, 1-2.

Sarkar, B. D., Shankar, S., Verma, S., & Singh, A. K. (2016, January). Utilization of television white space for high speed Wi-Fi application TVWS usage. In 2016 *6th International Conference-Cloud System and Big Data Engineering (Confluence)*, 240-243. IEEE.

Author Information

Armie Pakzad
De La Salle University
2401 Taft Avenue, Manila, Philippines
Contact e-mail: *armie.pakzad@dlsu.edu.ph*

Raine Mattheus Manuel
De La Salle University
2401 Taft Avenue, Manila, Philippines

Lawrence Materum
De La Salle University
2401 Taft Avenue, Manila, 1004 Philippines
Tokyo City University
1-28-1 Tamazutsumi, Setagaya, Tokyo, 158-8557, Japan

To cite this article:

Pakzad, A.E., Manuel, R.M. & Materum, L. (2022). Spectrum forecasting TVWS geolocation database for secondary-user TVWS devices. *The Eurasia Proceedings of Science, Technology, Engineering & Mathematics (EPSTEM), 21*, 188-195.

The Eurasia Proceedings of Science, Technology, Engineering & Mathematics (EPSTEM)
ISSN: 2602-3199

The Eurasia Proceedings of Science, Technology, Engineering & Mathematics (EPSTEM), 2022

Volume 21, Pages 196-201

IConTES 2022: International Conference on Technology, Engineering and Science

Design of Dual-Stage Ku- Band Low Noise Amplifier for Satellite Downlink Application

Naman Chetan RAJDEV
Pes University

Lasya V
Pes University

Rashmi SEETHUR
Pes University

Abstract: This paper presents the design methodology of a Low-Noise Amplifier (LNA) with a dual-stage structure. It is implemented using ultra-low-noise Pseudomorphic High Electron Mobility Transistor (PHEMT) (ATF-36077). The LNA is biased at a Vds of 3.3V with an Id of 0.029A for which 0.095W of power is consumed. A common source mode design is employed and a matching circuit is implemented using microstrip lines. The circuit adopts a single-ended dual-stage solution connected by a coupling capacitor. The amplifier provides an average forward gain (S21) of 19.944dB. It has an input and output return loss of -11.167dB and -13.099dB respectively. The Noise Figure variation at the operational frequency is 1.507dB. Ku-Band satellite applications have experienced a sharp rise in the past few years in the communication domain and a low noise amplifier is an essential element in satellite front-end applications. The designed LNA is suggested for applications in satellite downlink communications as it has an operational frequency of 11.5 GHz.

Keywords: KU-band, Low noise amplifier, Satellite dowlink application, Gallium arsenide

Introduction

With the evolution of mankind, the terrain of exploration has expanded beyond the earth into space as well. Over recent years, immense advancements in technology have resulted in a large number of satellites being launched into space. These satellites however have to be in contact with the earth. Downlink satellite communication is essential for the transmission of information from these satellites to the earth.

LNA finds applications in satellite communication systems where it is used in ground station's receiving antennas. A communication satellite is used for the purpose of receiving and retransmitting signals from the earth. Signals received from the satellites are weak as a consequence of the limited power of the satellites and their distance from the earth. LNAs are used to amplify these weak RF signals at the receiver with minimal distortion. The employment of LNA here helps to overcome feed line losses between the antenna and receiver.

A low noise amplifier (LNA) is an amplifier specifically used to amplify very low-power signals without loss of information. A typical amplifier would amplify both the signal and the noise in the input while introducing some additional noise as well. LNAs are designed to prevent degradation of the signal-to-noise ratio thus resulting in reduced additional noise. This is achieved by adopting appropriate circuit topologies and using low-noise components. Typically, an LNA configuration includes an input-matching network, a transistor amplifier, and an output-matching network as shown in Figure 1.

- Selection and peer-review under responsibility of the Organizing Committee of the Conference

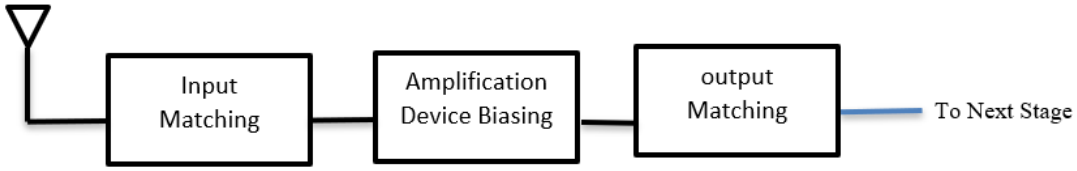

Figure 1. LNA configuration

The performance of the LNA is evaluated based on several crucial parameters. These parameters include input and output impedance matching, noise Figure (NF), gain, etc. These parameters will also influence power consumption and signal bandwidth.

This paper presents the design of a Ku-band low-noise amplifier (LNA), with an operational frequency of 11.5GHz, with its application in the Ku-Band satellite communication channel. The LNA is implemented using pHEMT (pseudomorphic high-electron-mobility transistor) technology. The transistor chosen is ATF-36077 which is acknowledged for its ultra-low noise capabilities. A 2-stage amplifier structure is chosen for this purpose(Bishoyi,2015). Keysight's ADVANCED DIGITAL SYSTEM (ADS) is used to simulate the LNA and parameters such as gain(S21), input return loss(S21), output return loss(S22), and noise Figure(nf2) are calculated. According to the results, the LNA has noise Figure(nf2) of 1.507dB and a forward gain of 19.944dB. Microstrip lines are used to implement the low noise amplifier (LNA) as they help in providing a low return loss(Venkatesh Murthy, 2020). Resistors and inductors are used in the design to provide stability. A dual-stage design is adopted to improve the forward gain.

Method

Design Implementation

The 95mW Ku-band low noise amplifier (LNA) has been designed using ATF-36077 pHEMT transistor from Hewlett Packard's. On analysis of the basic parameters for the transistor from the vendor's datasheet, it is observed that the operating frequency is from 2GHz-18GHz. Therefore, an operating frequency of 11.5GHz is chosen thus comfortably placing it in Ku-Band and satisfying the satellite downlink applications. The selected device offers a low noise figure of 0.5 dB at 12GHz. The operating voltages for gate and drain bias are fixed at 0V and 3.3V respectively resulting in an operating current Id of 0.029A.

Then the basic biasing circuit is constructed and simulated. The simulation results are shown in Figure 2. Parameters like gain, noise figure, stability, input reflection coefficient, and output reflection coefficient are plotted. It can be observed from Figure 2 that the device is unstable because its mu factor is less than 1. The transistors are conditionally stabilized using a resistor of suitable value on the output side. Input and output impedances are matched using transmission lines aiding in better noise figure. The stage one low noise amplifier is given in Figure 3. Its outputs are presented in Figure 4. Although the parameters obtained are satisfactory, the forward gain is too low for any practical application, hence we opt for a dual-stage structure. In order to ensure stability, source degeneration is used in the dual-stage LNA with 1.6nH inductors at the source. The biasing circuit is extended to a dual-stage using a capacitor of 0.5pF to increase forward gain while maintaining conditional stability. The stability is further ensured with the usage of a 47 Ohm resistor at the output. The gate and drain bias consist of a 2.2 Ohm resistor and 1.8nH inductor respectively. A 3-stage T circuit consisting of transmission lines is used at the input to act as a DC block and serves for input impedance matching. The output of the device is a T circuit consisting of transmission lines that acts as the DC Block and serves for output impedance matching. The stage two low noise amplifier is given in Figure 5.

Results and Discussion

The input impedance for the dual-stage is 62.733-j23.095ohm at 11.5GHz. Similarly, the output impedance is 7.319-j4.721ohm at 11.5GHz. The input and output impedances are matched using transmission lines. The source impedance of 62.733-j23.095ohm is matched to 50 ohms and the resulting transmission lines are converted to microstrip lines. Similarly, 50 ohms is matched to output impedance 7.319-j4.721ohm. The input and output impedances obtained after matching are shown in Figure 6. We then proceed to convert the transmission lines to microstrip lines and replace all the ideal components such as resistors, capacitors, and inductors to vendor-provided components. The input and output impedance matchings are given in Figure 7 and

Figure 8 respectively. The outputs for the dual-stage LNA after the previously mentioned conversions are given in Figure 9. We now come to the last stage of the design process which is making a layout. A layout is generated for microstrip lines and an adequate gap is left in between them to accommodate the other components such as a transistor and resistors. This layout of the microstrip lines is run for EM simulation and it is replaced into the actual schematic for which we run the co-simulation. This schematic for co-simulation is given in Figure 10. Results for the co-simulation are given in Figure 11.

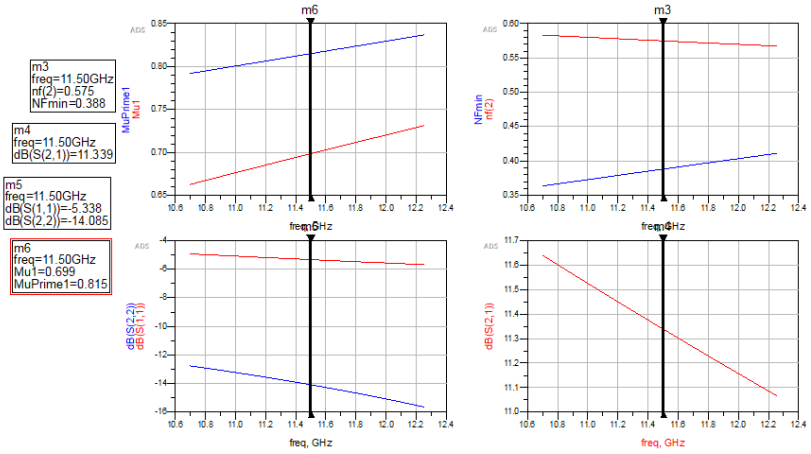

Figure 2. Outputs of biasing circuit

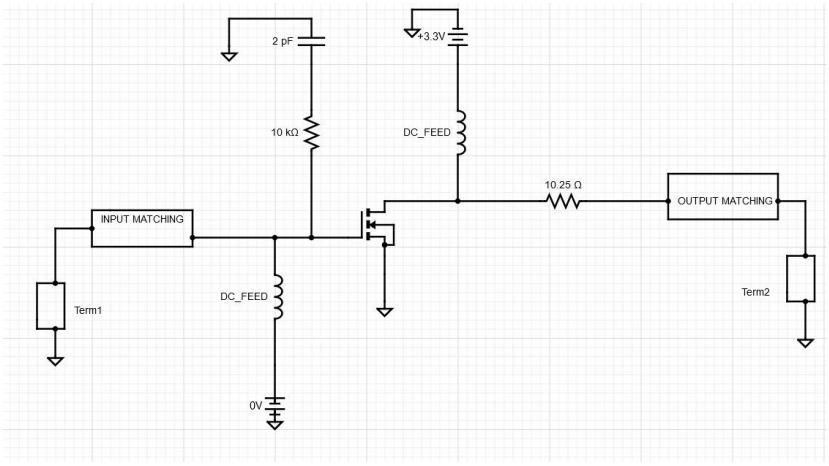

Figure 3. Single-stage LNA schematic

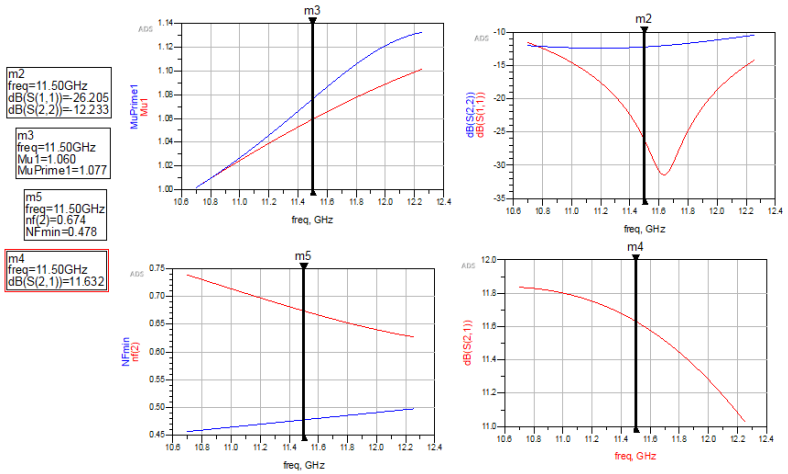

Figure 4. Outputs of single-stage LNA

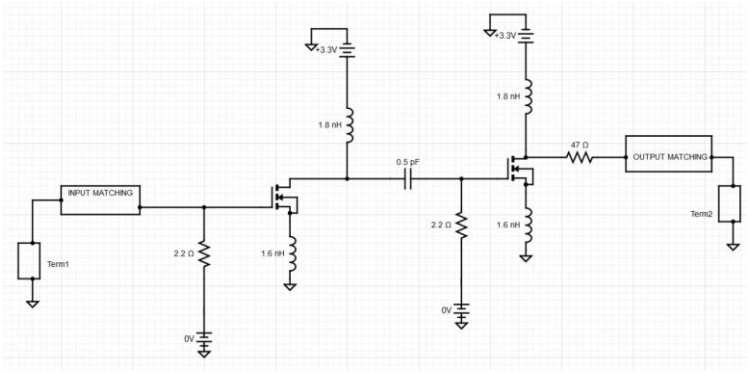

Figure 5. Dual-stage LNA schematic

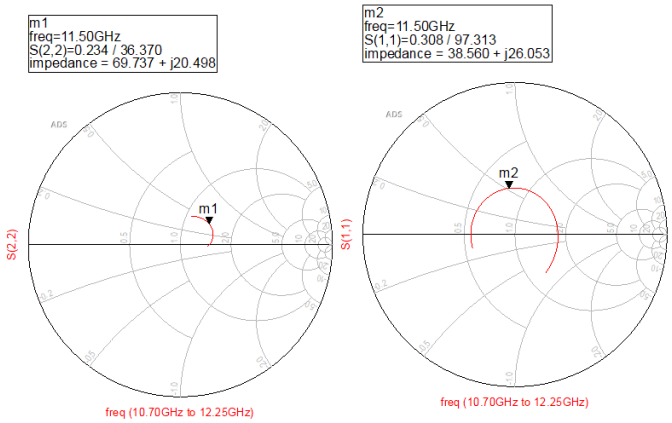

Figure 6. Input and output impedances after matching

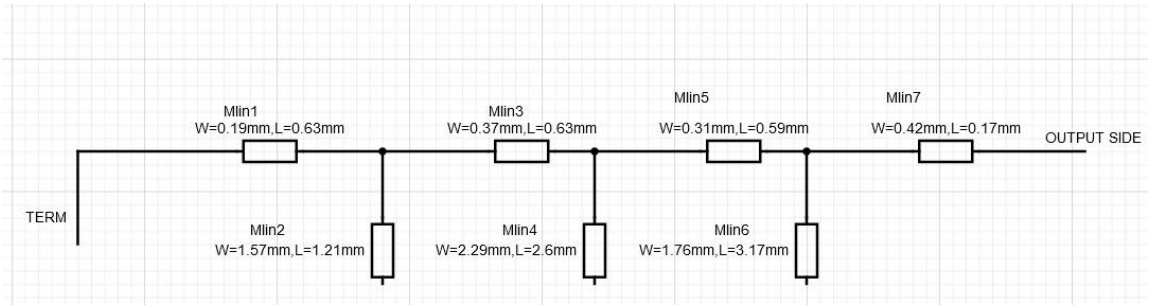

Figure 7. Input impedance matching

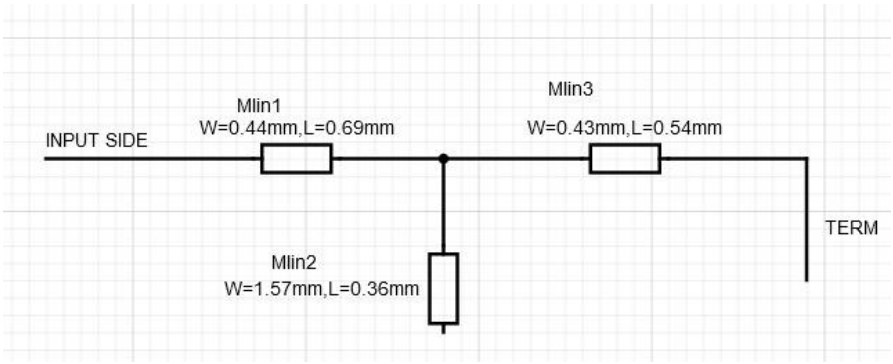

Figure 8. Output impedance matching

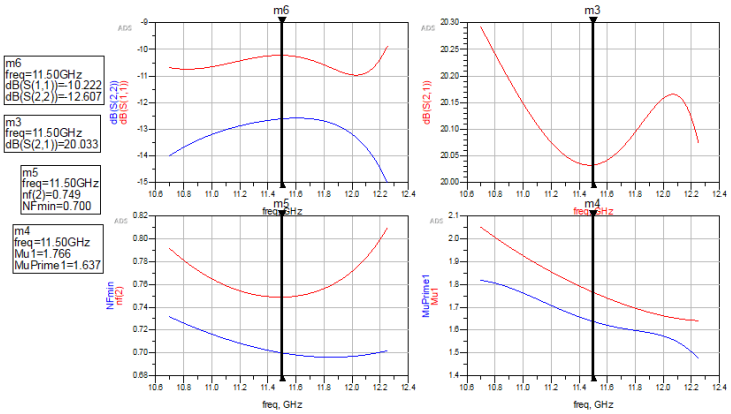

Figure 9. Outputs of dual-stage LNA with vendor components and microstrip lines

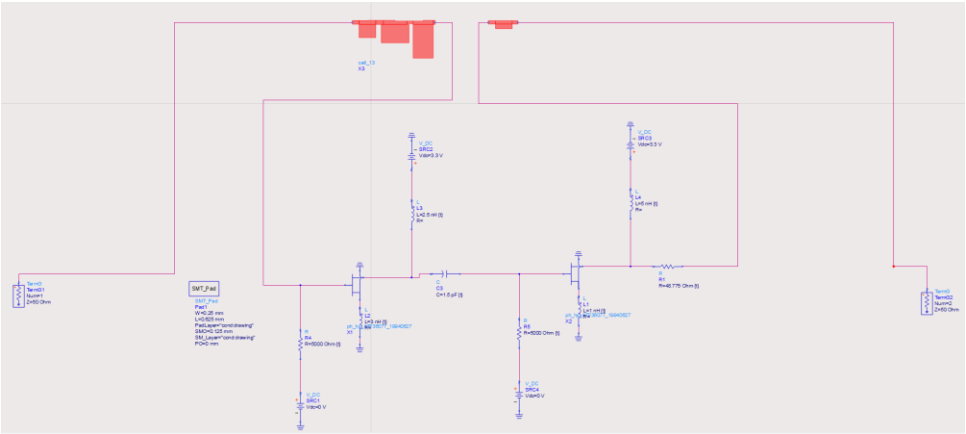

Figure 10. Co-simulation schematic

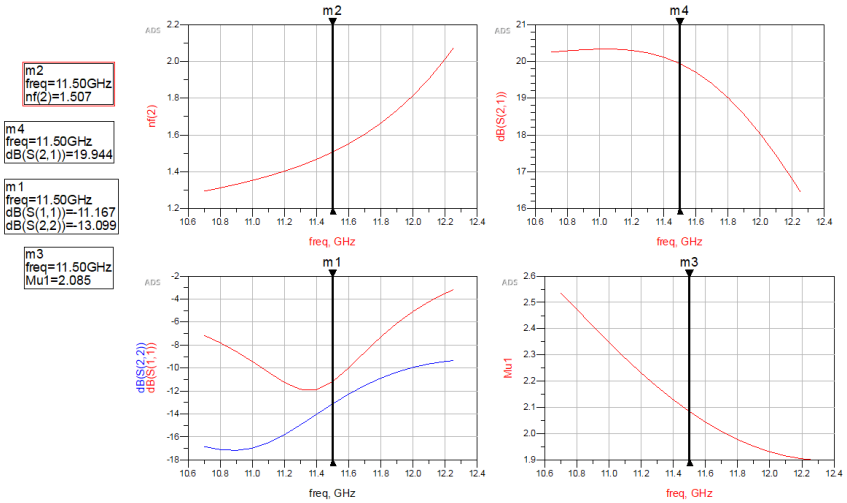

Figure 11. Outputs of co-simulation

Conclusion

Single and dual-stage low-noise amplifiers have been implemented. Also, the results of the co-simulation have been plotted. The designed LNA operates at 11.5 GHz and provides a high gain with a low noise figure which is ideal for downlink satellite communication applications. All the crucial LNA properties are attained with minimal trade-offs. A comparative analysis of the above-designed LNA is done with the other existing Ku-Band LNAs and the results are tabulated in Table 1.

Table 1. Comparative analysis of Ku band LNA results

Ref	Frequency (in GHz)	Noise figure (in dB)	Gain (in dB)	Number of stages
(Rudolph,2009)	8-10	<2.8	>18	2
(Suijker Rodenburg, 2009)	14	1.9-2.4	>19.8	3
(Resca,2013)	12.8-14.8	<1.8	>20	3
This work	11.5	1.507	19.944	2

Scientific Ethics Declaration

The authors declare that the scientific ethical and legal responsibility of this article published in EPSTEM journal belongs to the authors.

Acknowledgements or Notes

* This article was presented as an oral presentation at the International Conference on Technology, Engineering and Science (www.icontes.net) held in Antalya/Turkey on November 16-19, 2022.

References

Bishoyi, P.K., & Karthikeyan, S.S. (2015). Design of a two stage Ku band low noise amplifier for satellite applications. *2015 International Conference on Communications and Signal Processing (ICCSP)*,0270-0273.

Murthy, B. V., Singh, N. K., Jha, R., Kumar, N., & Kumar, R. (2020, June). Ultra Low Noise Figure, Low Power Consumption Ku-Band LNA with High Gain for Space Application. In *2020 5th International Conference on Communication and Electronics Systems (ICCES)* (pp. 80-83). IEEE.

Resca, D., Scappaviva, F C., Florian, S., Rochette, J.L., Muraro, V., DiGiacomo Brunel, C., & Chang, D. B. (2013). A robust Ku-band low noise amplifier using an industrial 0.25-µm AlGaN/GaN on SiC process. *Eurpean Microwave Integrated Circuit Conference*,496-499.

Rudolph, M., Dewitz, M., Liero, A., Khalil, I., Chaturvedi, N., Wipf, C., Bertenburg, R.M., Miller, J., Würfl, J., Heinrich, W., & Trankle, G. (2009). High robust x-band LNA with extremely short recovery time. *IEEE MTT-S International Microwave Symposium Digest*, 781-784.

Suijker, E. M., Rodenburg, M., Hoogland, J. A., Van Heijningen, M., Seelmann-Eggebert, M., Quay, R., ... & van Vliet, F. E. (2009, October). Robust AlGaN/GaN low noise amplifier MMICs for C-, Ku-and Ka-band space applications. In *2009 Annual IEEE Compound Semiconductor Integrated Circuit Symposium* (pp. 1-4). IEEE.

Author Information

Naman Chetan Rajdev
PES University
Bengaluru, India.
Contact e-mail: *namanrjdv@gmail.com*

Lasya V
PES University
Bengaluru, India

Rashmi Seethur
PES University
Bengaluru, India.

To cite this article:

Rajdev, N. C.. & V.L., & Seethur, R.. (2022). Design of dual-stage Ku- band low noise amplifier for satellite downlink application. *The Eurasia Proceedings of Science, Technology, Engineering & Mathematics (EPSTEM), 21,* 196-201.

The Eurasia Proceedings of Science, Technology, Engineering & Mathematics (EPSTEM)
ISSN: 2602-3199

The Eurasia Proceedings of Science, Technology, Engineering & Mathematics (EPSTEM), 2022

Volume 21, Pages 202-213

IConTES 2022: International Conference on Technology, Engineering and Science

CFD Investigation on Three Turbulence Models for Centrifugal Pump Application

Abdessalam OTMANI
Badji Mokhtar University

Slimane NIOU
Badji Mokhtar University

Sahrane SARA
Badji Mokhtar University

Azzeddine DEKHANE
Badji Mokhtar University

Salaheddine AZZOUZ
Badji Mokhtar University

Abstract: This paper highlight the influence of three numerical turbulence models on the convergence and the performance of flow simulation. The computational comparative study was realized using the COMSOL Multiphysics 5.5 code. Turbulence was generated numerically in a centrifugal water pump using the k−ϵ, k−ω and k−ω SST models. However, the geometry was performed on SolidWorks due to its complexity. The flow modelling was mainly based on the resolution of the stationary Navier—Stokes equations. The effects of the tested models on CFD numerical simulation were examined. It was found that the best calculation precision was obtained using the K−ω model, while the lowest was provided by the K−ω SST model. However, a very low calculation cost was obtained by the latter. As well as better pumping performance were recorded.

Keywords: Turbulence models, Fluid flow simulation, Centrifugal pump

Introduction

During the past years, researchers devoted a great deal of effort to formulation and testing of turbulence models (Wilcox, 1991). In fact, computational fluid dynamics tools are becoming standard in many fields of engineering involving flow of gases and liquids; numerical simulations are used both in the design phase to select between different concepts and in the production phase to analyze performance (Samy M & Mofreh H, 2011). Turbulence modeling is one of three key elements in Computational Fluid Dynamics (CFD). Very precise mathematical theories have evolved for the other two key elements, viz., grid generation and algorithm development. By its nature, far less precision has been achieved in turbulence modeling. Since the objective is to approximate an extremely complicated phenomenon (Wilcox, 1993).

The most popular turbulence models are the standard k–e model, low-Re k–e model, RNG k–e model, standard k–w model, and SST k–w model (Samy & Mofreh, 2011). In fact, it has been confirmed that the calculation results are quite different with different turbulence models, and the result under K epsilon EARSM model is better than four other models : K-Epsilon, SSG Reynolds Stress, RNG K-Epsilon, K-Omega) (Liu et al., 2012). While the k-ω model gave more realistic velocity profiles, consistently produced values that were too high for

- Selection and peer-review under responsibility of the Organizing Committee of the Conference

the turbulent shear stress (Menter, 1994). However, testing has shown that the k-e Realizable and transition SST turbulence models give the best results in the calculation of supersonic flows, typical for advanced jet engines (Pavlovich & Victorovich, 2013). Furthermore, comparison shows that the realizable k-ε predicts the flow within centrifugal pump with acceptable accuracy (Selim et al., 2016). Regarding the mean flow field of the pump, the SAS model does not show an advantage over the SST model (Markus et al., 2020).

Pump Characteristics

The centrifugal pump considered in this study contains one suction and a single discharge canal as well as a circular spiral shaped volute/casing (Figure 1). The overall plan of the pump is shown in figure 1 and the main characteristics are resumed in table 1. The geometry was realized on SolidWorks using: (Brozoski, 2018).

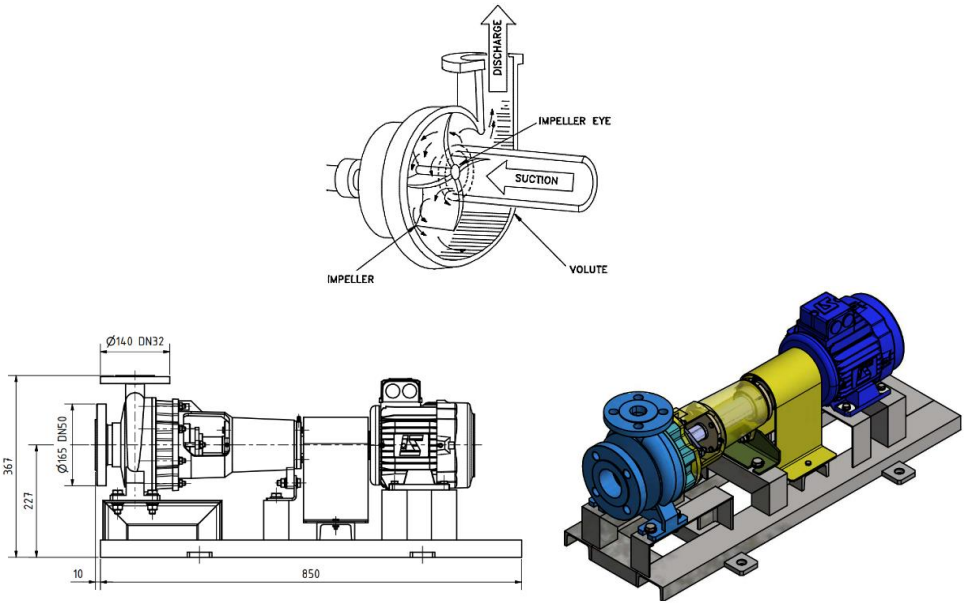

Figure 1. Centrifugal pump general view (Paul et al., n.d) and overall plan of the studied centrifugal pump (Brozoski, 2018)

Table 1. Main characteristics of the studied centrifugal pump

Suction diameter	Discharge diameter	Inlet pressure	Outlet pressure	rpm
60 mm	55 mm	0.5 (bar)	2 (bar)	720 (tr/min)

Numerical Model

Impeller Design

A centrifugal pump converts rotational energy, often from a motor, to energy in a moving fluid. The two main parts that are responsible for the conversion of energy are the impeller and the casing. While passing through the impeller, the fluid is gaining both velocity and pressure (Srivastava, 2020). Consequently, the impeller is one of the essential parts of a centrifugal pump, since it is the source of kinetic energy. The characteristics of the studied impeller are summarized in the Table 2.

Table 2. Impeller main characteristics

Outer diameter	Inner diameter	Number of blades	Tilt angle
154 mm	60 mm	8	60

Impellers can be open, semi-open, or enclosed (Figure 2). Another point is that Impellers can be either single-suction or double-suction. A single-suction impeller allows liquid to enter the center of the blades from only one direction. A double-suction impeller allows liquid to enter the center of the impeller blades from both sides simultaneously. (Paul et al., n.d). In fact, an enclosed impeller with a single-suction is considered in this study. The design (Figure 4) was carried out on SolidWorks using real dimensions shown in Figure 3.

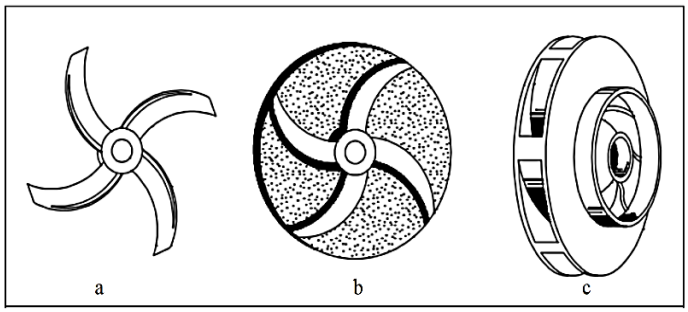

Figure 2. (a) Open, (b) Semi-Open, and (c) Enclosed Impellers

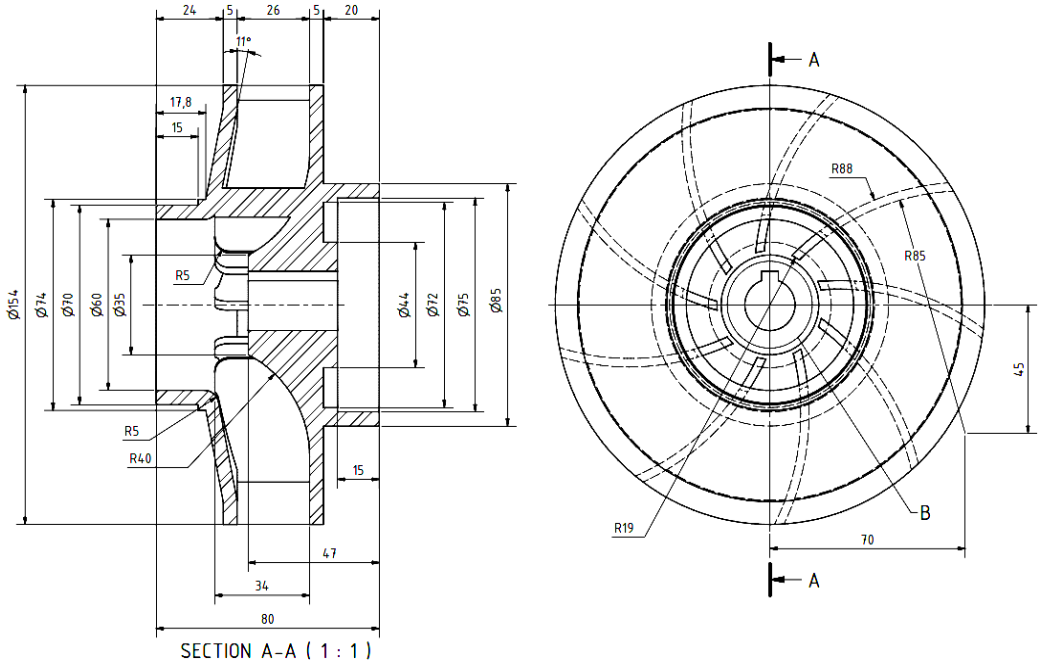

Figure 3. Studied impeller detailed plan (Brozoski, 2018)

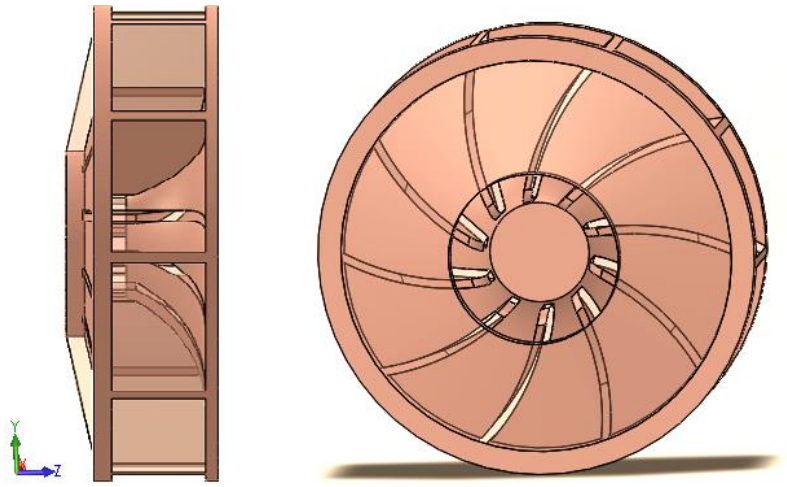

Figure 4. 3d view of the designed Impeller

Casing Design

The pump casing provides a pressure boundary for the pump and contains channels to properly direct the suction and discharge flow (Paul et al., n.d). Furthermore, it slows the flow of the liquid. Therefore, according to Bernoulli's principle, the volute converts kinetic energy into pressure by reducing speed while increasing pressure. The volute/casing considered in this study was designed based on reel dimensions shown in figure 5.

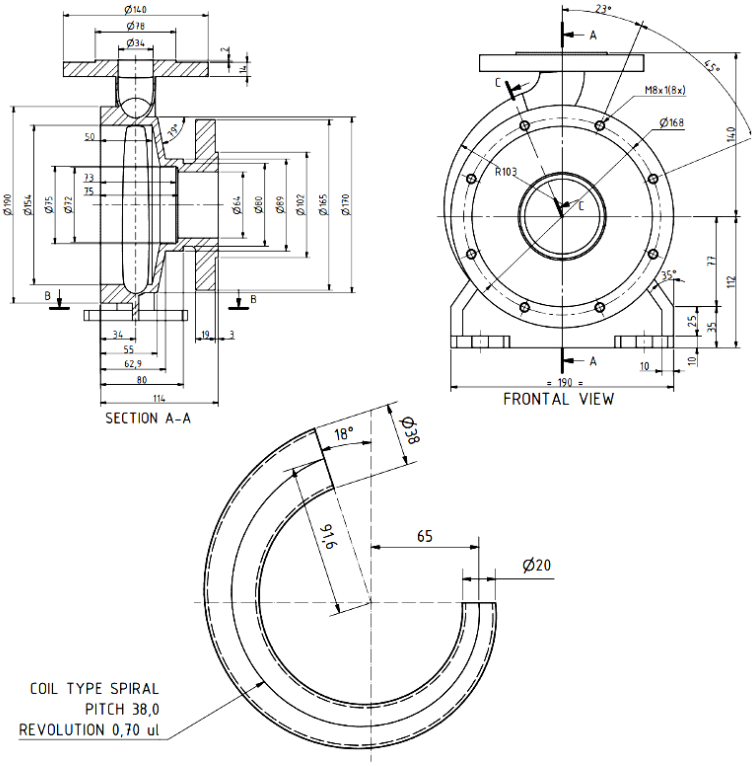

Figure 5. Casing detailed plan (Brozoski, 2018)

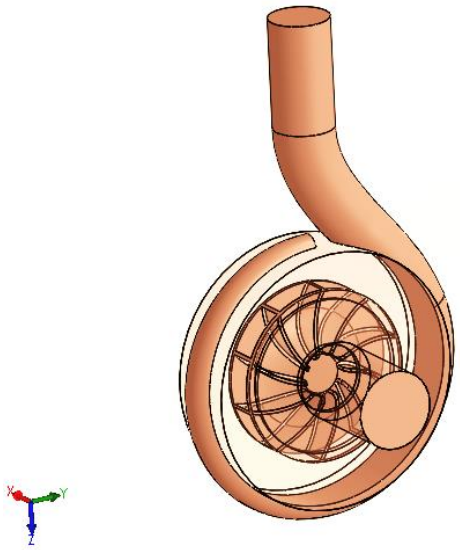

Figure 6. 3D view of the global final geometry

Mesh Structure

A free tetrahedral mesh was applied for the global final geometry. Mesh characteristics are summarized in table 3 and the final mesh structure is shown in Figures 7.

Table 3. Impeller main characteristics

Nodes number	Max element size	Min element size
88528	0.0251	0.00183

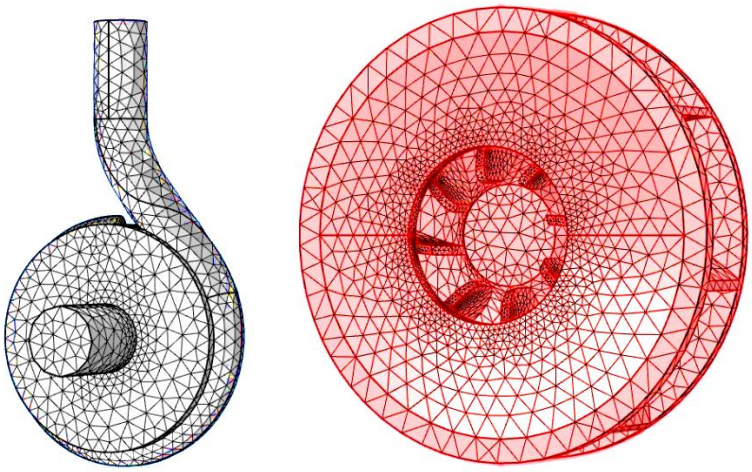

Figure 7. Final geometry as a free tetrahedral Mesh structure

Frozen Rotor Study

The Frozen Rotor study was used to compute the velocity, pressure and turbulence in Comsol-Multiphysics. The frozen rotor approach assumes that the flow in the rotating domain, expressed in the rotating coordinate system, is fully developed. Therefore, it's generally used in rotating machinery and is a special case of a Stationary study. The rotating parts are kept frozen in position, and the rotation is accounted for by the inclusion of centrifugal and Coriolis forces. This study is especially suited for flow in rotating machinery where the topology of the geometry does not change with rotation. It is also used to compute the initial conditions for time-dependent simulations of flow in rotating machinery (multiphysics).

Governing Equations

The k-ε Turbulence Model

The k-ε model is one of the most used turbulence models for industrial applications. This module includes the standard k-ε model. The model introduces two additional transport equations and two dependent variables: the turbulent kinetic energy, k, and the turbulent dissipation rate, ε. The turbulent viscosity is modeled as (multiphysics) :

$$\mu_T = \rho C_\mu \frac{k^2}{\varepsilon} \tag{1}$$

where Cμ is a model constant.

The transport equation for k reads:

$$\rho \frac{\partial k}{\partial t} + \rho u.\, \nabla k = \nabla.((\mu + \frac{\mu_T}{\sigma_k})\nabla k) + p_k - \rho\varepsilon \tag{2}$$

where the production term is :

$$p_k = \mu_T\,(\nabla u:(\nabla u+(\nabla u)^T) - \frac{2}{3}(\nabla.u)^2) - \frac{2}{3}\rho k \nabla.\, u \tag{3}$$

The transport equation for ε reads :

$$\rho \frac{\partial \varepsilon}{\partial t} + \rho u.\, \nabla\varepsilon = \nabla.((\mu + \frac{\mu_T}{\sigma_\varepsilon})\nabla\varepsilon) + C_{\varepsilon 1}\frac{\varepsilon}{k} p_k - C_{\varepsilon 2}\rho\frac{\varepsilon^2}{k} \tag{4}$$

The model constants in Equation 1, Equation 2, and Equation 4 are determined from experimental data (Wilcox,1998) and the values are listed in Table 4 (Comsol-multiphysics, 2020).

Table 4. model constants

Constant	Value
c_{μ}	0.09
$c_{\varepsilon 1}$	1.44
$c_{\varepsilon 2}$	1.92
σ_k	1.0
σ_{ε}	1.3

The k-ω Turbulence Model

The k-ω model solves for the turbulent kinetic energy, k, and for the dissipation per unit turbulent kinetic energy, ω. The CFD Module has the Wilcox (1998) revised k-ω model (Comsol-multiphysics, 2020).

$$\rho\frac{\partial k}{\partial t} + \rho u.\nabla k = p_k - \rho\beta^* k\omega + \nabla.((\mu + \sigma^*\mu_T)\nabla k) \tag{5}$$

$$\rho\frac{\partial \omega}{\partial t} + \rho u.\nabla\omega = \alpha\frac{\omega}{k}p_k - \rho\beta^*\omega^2 + \nabla.((\mu + \sigma\mu_T)\nabla\omega)$$

Where

$$\mu_T = \rho\frac{k}{\omega} \tag{6}$$

and

$$\alpha = \frac{13}{25}\ ;\beta = \beta_0 f_\beta\ ;\ \beta^* = \beta_0^* f_\beta\ ;\sigma = \frac{1}{2}; \sigma^* = \frac{1}{2}$$

$$\beta_0 = \frac{13}{125};\ f_\beta = \frac{1+70\chi_\omega}{1+80\chi_\omega}\ ;\chi_\omega = \left|\frac{\Omega_{ij}\Omega_{jk}\Omega_{ki}}{(\beta_0^*\omega)^3}\right|;\ \beta_0^* = \frac{9}{100}$$

$$f_\beta = \begin{cases} 1 & \chi_k \le 0 \\ \dfrac{1+680\chi_k^2}{1+400\chi_k^2} & \chi_k > 0 \end{cases} \qquad \chi_k = \frac{1}{\omega^3}(\nabla k.\nabla\omega) \tag{7}$$

where in turn Ω_{ij} is the mean rotation-rate tensor

$$\Omega_{ij} = \frac{1}{2}\left(\frac{\partial \bar{u}_i}{\partial \chi_j} - \frac{\partial \bar{u}_j}{\partial \chi_i}\right) \tag{8}$$

and S_{ij} is the mean strain-rate tensor

$$S_{ij} = \frac{1}{2}\left(\frac{\partial \bar{u}_i}{\partial \chi_j} + \frac{\partial \bar{u}_j}{\partial \chi_i}\right) \tag{9}$$

P_k is given by Equation 3. The following auxiliary relations for the dissipation, ε, and the turbulent mixing length, l_*, are also used:

$$\varepsilon = \beta^*\omega k\ ;\quad l_{mix} = \frac{\sqrt{k}}{\omega} \tag{10}$$

The SST Turbulence Model

To combine the superior behavior of the k-ω model in the near-wall region with the robustness of the k-ε model, Menter (1994) introduced the SST (Shear Stress Transport) model which interpolates between the two models. The version of the SST model in the CFD Module includes a few well-tested (Menter et al., 2003) modifications, such as production limiters for both k and ω, the use of S instead of Ω in the limiter for μT and a sharper cut-off for the cross-diffusion term. It is also a low Reynolds number model, that is, it does not apply

wall functions. “Low Reynolds number” refers to the region close to the wall where viscous effects dominate. The model equations are formulated in terms k and ω, (Comsol-multiphysics, 2020).

$$\rho\frac{\partial k}{\partial t}+\rho_{\boldsymbol{u}}\nabla k=P-\rho\beta_0^*k\omega+\nabla\cdot((\mu+\sigma_k\mu_T)\nabla k)$$
$$\rho\frac{\partial \omega}{\partial t}+\rho_{\mathbf{u}}\nabla\omega=\frac{\rho\gamma}{\mu_T}P-\rho\beta\omega^2+\nabla\cdot((\mu+\sigma_\omega\mu_T)\nabla\omega)+2(1-f_{v1})\frac{\rho\sigma_{\omega2}}{\omega}\nabla\omega\cdot\nabla k \quad \textbf{(11)}$$

Where,

$$P=min\,P_k,10\rho\beta_0^*k\omega \quad (12)$$

And P_k is given in Equation 3. The turbulent viscosity is given by,

$$\mu_T=\frac{\rho a_1 k}{\max(a_1\omega,Sf_{v2})}$$

Where S is the characteristic magnitude of the mean velocity gradients,

$$S=\sqrt{2S_{ij}S_{ij}}$$

The model constants are defined through interpolation of appropriate inner and outer values,

$$\phi=f_{v1}\phi_1+(1-f_{v1})\phi_2 \quad \text{for} \quad \phi=\beta,\gamma,\sigma_k,\sigma_\omega$$

The interpolation functions f_{v1} and f_{v2} are defined as,

$$f_{v1}=\tanh(\theta_1^4)$$
$$\theta_1=\min\left[\max\left(\frac{\sqrt{k}}{\beta_0^*\omega\, l_w},\frac{500\mu}{\rho\omega\, l_w^2}\right),\frac{4\rho\mu\sigma_{\omega2}k}{CD_{k\omega}l_w^2}\right]$$

$$CD_{k\omega}=\max\left(\frac{2\rho\sigma_{\omega2}}{\omega}\nabla\omega\cdot\nabla k,\,10^{-10}\right)$$

where l_w is the distance to the closest wall.

Results and Discussion

Simulation Convergence

Convergence plays a key role in the accuracy of the obtained results using numerical techniques such as finite element analysis. This is the reason why convergence needs to be highlighted. Therefore, the convergence of the studied turbulence models must be analyzed, in order to determine the optimal model in terms of precision and computational cost. On The one hand, the best calculation precision and the lowest error ,$5x10^{-7}$, was achieved using the k-ω model. While the k-ε model provided an error of $2.6x10^{-6}$ and the k-ω SST model could only achieve $2x10^{-5}$ (Figure 8). On the other hand the latter's convergence was accomplished in just 25min8s. While the k-ω model required 43min40s. Even more, the k-ω model exceeded 50 minutes (results was obtained using an intel® core (TM) i5 3470 cpu 3.20ghz processor). A more significant comparison is shown in the table below :

Table 5. Convergence parameters of the studied turbulence models

Model	Calculation time	Iteration number	Error
K-*w*	50 min, 36 s	361	5x10-7
K-*w* SST	25 min 8 s	325	2x10-5
K-*w*	43 min, 40 s	355	2.6x10-6

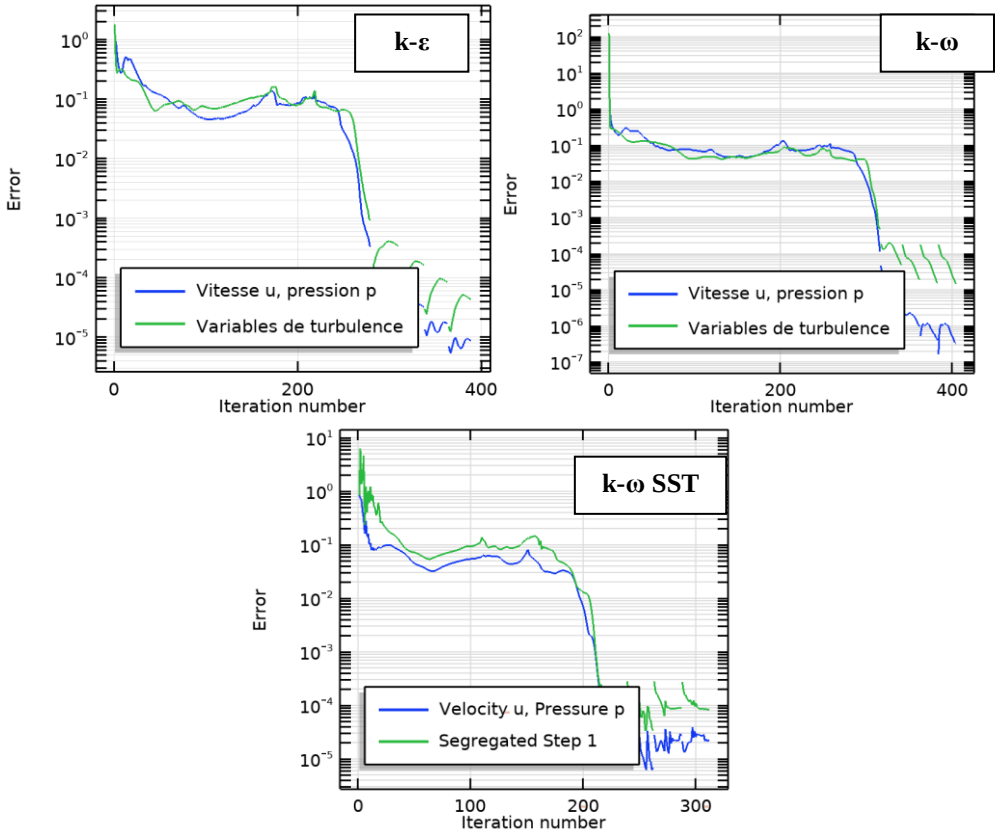

Figure 8. Convergence evolution of the three studied turbulence models.

Velocity Distribution

Water velocity evolution as a function of inlet pressure is shown in figure 9. The effect of increasing inlet pressure on the velocity is not visibly clear due to the large difference between the speed distributions of the three models; also because of the small increase in pressure.

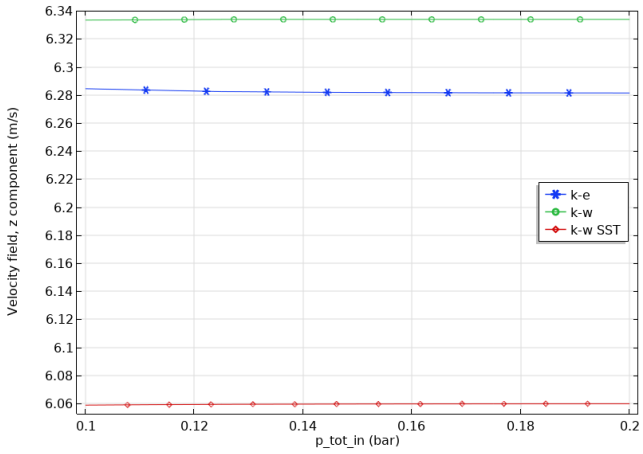

Figure 9. Maximum water velocity evolution as a function of inlet pressure

It can be seen from figure 10 that the three studied models have a certain similarity. However, on the one hand, the maximum velocity was generated by the k-ω sst model, which exceeded 9.5 m/s. On the other hand, this same model obtained the lowest outlet velocity 9. Since, according to Bernoulli's principle, the volute converts kinetic energy into pressure by reducing velocity while increasing pressure. For this reason, the maximum average water velocity was generated by the k-ω SST model. As discussed above by Figure 9, the k-ω model provided the highest discharge speed compared to the other two models. This behavior explains the increase of the Reynolds number at the discharge section for this turbulence model (Figure 11).

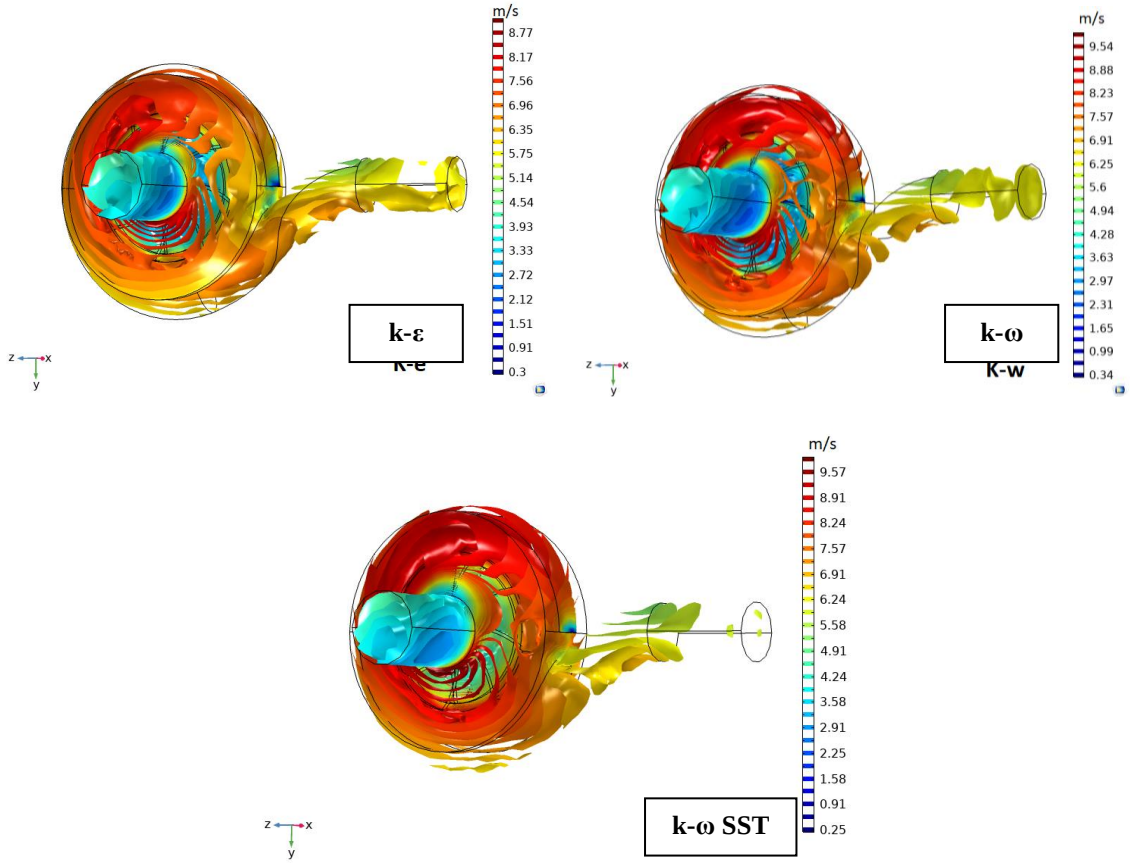

Figure 10. Average water velocity distribution in the volute for the three studied models

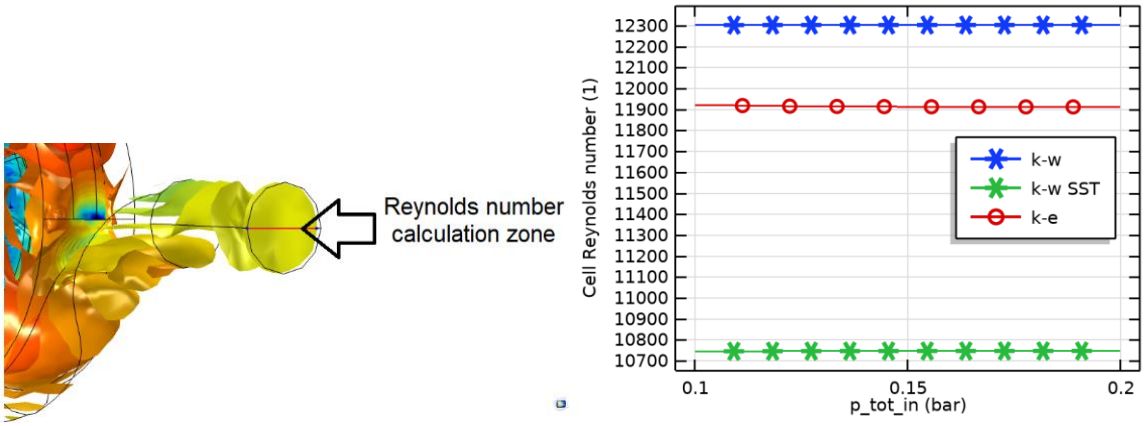

Figure 11. Reynolds number evolution in the discharge section for the three studied models

Pressure Distribution

Figure 12 shows a close-up of the water pressure profiles in the rotational zone, for the three considered models. The highest-pressure contour was obtained by the k−ω SST model. Indeed, a maximum pressure of 1.8 bar was reached with an average pressure of 1.16 bar. Which makes perfect sense, since this model provided the highest water velocity distribution in the volute. As a matter of fact, this speed has been converted into dynamic pressure. Consequently, the highest outlet pressure was recorded for this model (figure 13). Regarding the influence of increasing inlet pressure on the outlet pressure, as mentioned earlier, it is not visibly clear due to the large difference between the pressure distributions of the three models.

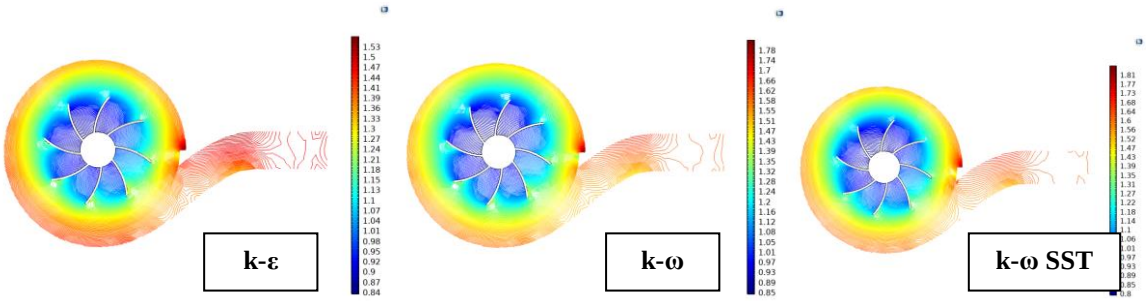

Figure 12. Water pressure [bar] contours in the volute for the three considered models

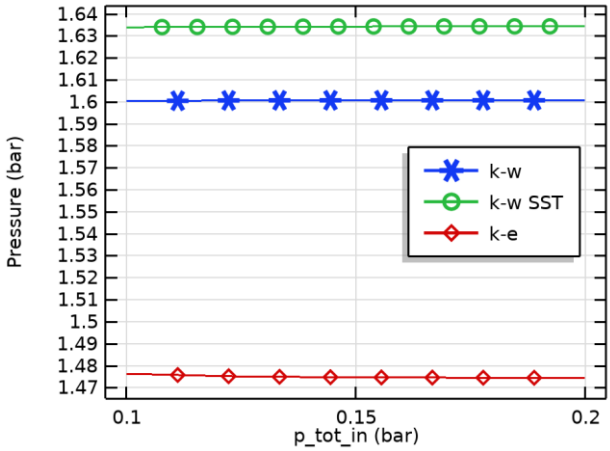

Figure 13. Maximum outlet pressure as a function of inlet pressure

Figure 14 show the static pressure profiles in the impeller domain. Obviously, the highest static pressure was generated by the k-w SST model (1.36 bar). Since he provided the maximum water pressure and velocity in the volute (Figure 12-10).

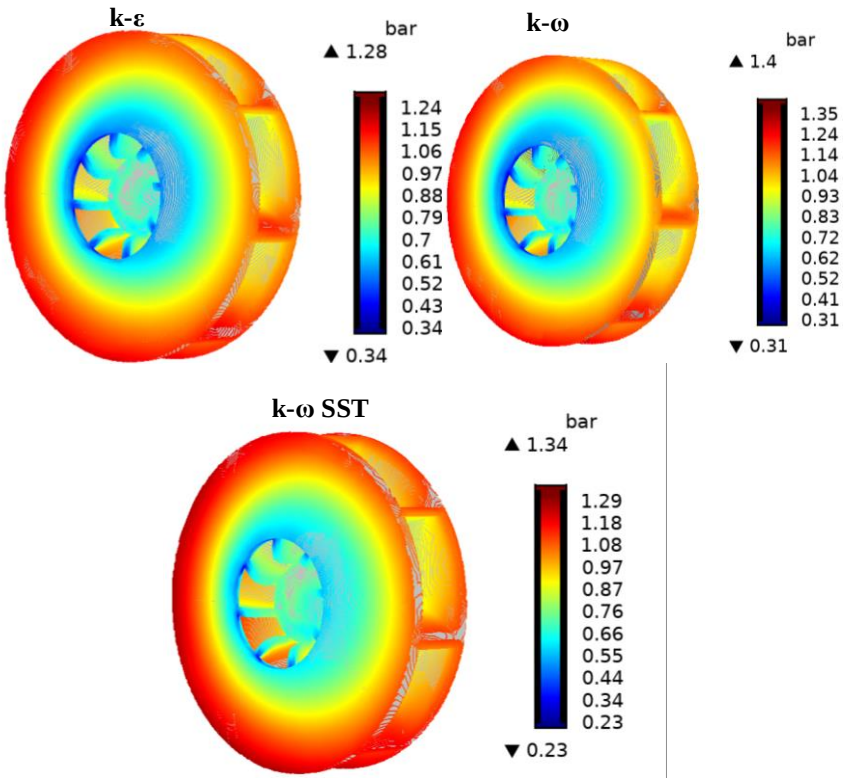

Figure 14. Static pressure contour in the impeller domain

Pump Performance

Figure 15 shows the pump performance curve. The total pressure at the inlet is expressed in terms of the pressure head, H, which is equal to (Comsol-multiphysics, 2020) :

$$H = \frac{\Delta p_{tot}}{\rho . g} \tag{13}$$

The highest head (10.85 m) was achieved by the k-w SST model. Considering that, he generated the greatest outlet pressure, As a result, the better water height was recorded

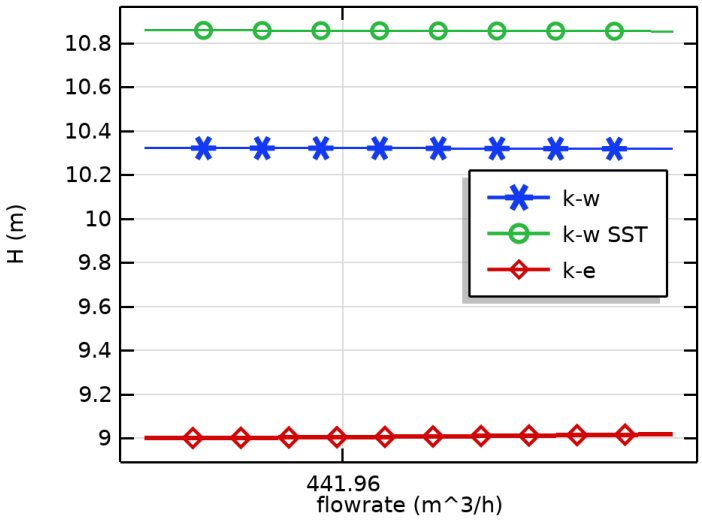

Figure 15. Pump performance curve for the three studied cases

Conclusion

The computational efficiency and performance parameters of three turbulence models were compared. First of all, their influence on the simulation convergence was highlighted. According to the results comparison, the calculation under k-ω SST was able to reach convergence after only 325 iterations. However, the other two models required more than 350 iterations. indeed, it turns out that the calculation results under k-ω SST generated the most optimal values. On the one hand, a low computational cost was recorded and on the other hand a better outlet pressure as well as a better discharge head were achieved. However, the k-ω and the k-ε model provided more precision at the expense of computational cost and the exploited memory.

Scientific Ethics Declaration

The authors declare that the scientific ethical and legal responsibility of this article published in EPSTEM journal belongs to the authors.

Acknowledgements or Notes

* This article was presented as an oral presentation at the International Conference on Technology, Engineering and Science (www.icontes.net) held in Antalya/Turkey on November 16-19, 2022.

References

Bonnet,A., & Luneu, J. (1989). *Aerodynamics theories of fluid dynamics*. Tolouse, France :Cépadués Edition.

Brozoski, A. (2018, October 10). *Solidedge centrifugal pump 01 - 09.* Retrived from https://www.youtube.com/watch?

El Behery, S. M., & Hamed, M. H.(2011). A comparative study of turbulence models performance for separating flow in a planar asymmetric diffuser. *Computers & Fluids , 44*, 248–257.

Liu, H. L., Liu, M. M., Dong, L., Ren, Y., & Du, H. (2012, November). Effects of computational grids and turbulence models on numerical simulation of centrifugal pump with CFD. In *IOP Conference Series: Earth and Environmental Science (Vol. 15*, No. 6, p. 062005). IOP Publishing.

Markus, H., Nicolas, C., Andreas, P., Sherwin, F., & Romuald, S. (2020). Assessment of scale-adaptive turbulence models for volute-type centrifugal pumps at part load operation. *International Journal of Heat and Fluid Flow, 85*, 1.

Menter, F. (1994). Two-equation Eddy-Viscosity turbulence models for engineering applications. *AIAA Journal, 32*(8), 1598-1605.

Menter, F.R.(1992). Performance of popular turbulence models for attached and separated adverse pressure gradient flows. *AIAA JOURNAL, 30* (8), 2072.

Menter, F.R., Kuntz,M., & Langtry, R. (2003). Ten years of industrial experience with the SST turbulence model. *Turbulence Heat and Mass Transfer, 4*. 625-632

Mikhail Pavlovich, B., & Pavel Victorovich, B. (2013). Comparison of turbulence models in the calculation of supersonic separated flows. *World Applied Sciences Journal , 27*(10), 1265.

Paul A, M., Dan, M., & Michael, G. (n.d.). *Fundamentals of Pumps.*Retrived from ez-pdh.com.

Selim, S. M., Hosien M. A., El-Behery, S. M., & Elsherbiny, M. (2016). Numerical analysis of turbulent flow in centrifigual pump. *Proceedings of the 17th Int. AMME Conference.* Cairo, Egypt.

Srivastava, S. (2020, Jun 14). *Centrifugal pump design and analysis using solidworks* . Retrived from skill-lync.com.

Wilcox, D. C. (1991). A half century historical review of the k-w model. *29th Aerospace Sciences Meeting*.

Wilcox, D. C. (1998). *Turbulence modeling for CFD* (2 nd ed.). La Canada, CA *:* DCW Industries.

Author Information

Abdessalam Otmani
Badji Mokhtar University
Annaba, Algeria
Contact e mail:*otmani@esti-annaba.dz*

Slimen Niou
Badji Mokhtar University
Annaba, Algeria

Azzeddine Dekhane
Badji Mokhtar University
Annaba, Algeria

Sahrane Sara
Badji Mokhtar University
Annaba, Algeria

Salahaddine Azzouz
Badji Mokhtar University
Annaba, Algeria

To cite this article:

Otmani, A., Niou, S., Dekhane, A., Sara, S., & Azzouz, S. (2022). CFD investigation on three turbulence models for centrifugal pump application. *The Eurasia Proceedings of Science, Technology, Engineering & Mathematics (EPSTEM), 21*, 202-213.

The Eurasia Proceedings of Science, Technology, Engineering & Mathematics (EPSTEM)
ISSN: 2602-3199

The Eurasia Proceedings of Science, Technology, Engineering & Mathematics (EPSTEM), 2022

Volume 21, Pages 214-217

IConTES 2022: International Conference on Technology, Engineering and Science

Electrochemical Performance of Tin-Based Solder Alloys for Secondary Lithium Batteries

Ersu LOKCU
Eskisehir Osmangazi University

Resat Can OZDEN
Eskisehir Osmangazi University

Mustafa ANIK
Eskisehir Osmangazi University

Abstract: Exploring new anode materials for large-scale lithium-ion batteries with a higher energy density, longer lifespan, and improved safety is crucial. Metal foil electrodes are suitable for high-energy batteries because they are easy to fabricate and have a high active material loading. Since the 1990s, promising studies have been carried out for the use of tin-based materials as anode materials in lithium-ion batteries. In this study, we investigated industrial-grade Tin (Sn) based solder alloys by performing the cold rolling process to obtain foil-based anodes, which are of different thicknesses and subjected to different plastic deformation amounts. The coin-type (CR2016) half-cells were used to evaluate the electrochemical performances of foil anodes. The cells were tested galvanostatically at 50 μA cm^{-2} current density. by a Neware battery testing system. When compared to pure Sn, industrial-grade Tin (Sn) based solder alloys exhibit satisfactory performances in both cycle life and Coulombic efficiency.

Keywords: Foil anode, Lithium-ion battery, Solder alloy

Introduction

The main impetus for developing lithium-ion batteries is to provide even higher energy and power densities. The anode materials in lithium-ion batteries have a better potential for achieving these values compared to cathode materials because of their diversity and high theoretical capacity. These anode materials are divided into three groups intercalation, conversion and alloying type anodes according to their reactions in the battery (Bresser et al., 2016; Ma et al., 2018). Alloying type anodes are distinct from intercalation and conversion type anodes. They react with Li ions to form alloys, which have drawn a lot of interest from LIBs due to their higher theoretical capacities, better molar ratios, safer potentials, and lower costs (Li et al., 2002)

The Sn element has interested increasing attention because of its relatively high specific capacity (for $Li_{22}Sn_5$ alloy, 994 mAh g^{-1}, 2094 Ah L^{-1}). However, the quick capacity fade is caused by Sn particle fracture and electrode delamination from the current collector due to the significant volume change (260%) during the lithiation/delithiation processes (Dong et al., 2021). Although significant achievements have been made in the performances of Sn-based anodes with the use of nanostructuring Sn and developing Sn-based composite anodes, there are still various problems to be solved (Dong et al., 2021). On the other hand, the use of metallic Sn as a foil anode in lithium-ion batteries may be more interesting due to their formability and conductivity properties (Heligman et al., 2019; Xu et al., 2019).

Using an in-situ X-ray diffraction technique, Rhodes et al. investigated the phase transformation behavior of Sn thin films during the lithiation and delithiation processes (Rhodes et al., 2012). They reported the formation of the Li_2Sn_5, β-LiSn, and $Li_{22}Sn_5$ phases. In another study, the electrochemical performances of the bulk Sn foil electrode were investigated by Yang et al. They concluded that the non-reversibility of the reactions that occur as a result of the lithiation/delithiation process causes a short cycle life (Yang et al., 2003).

In this work, we studied industrial-grade Tin (Sn) based solder alloys by performing the simple cold rolling process to obtain foil-based anodes, which are of different thicknesses and subjected to different plastic deformation amounts. The coin-type (CR 2016) half-cells were used to evaluate the electrochemical performances of foil anodes. The cells were tested within a voltage range of 0.01-2.0 V (vs. Li/Li^+) in 1.0 M $LiClO_4$:TEGDME electrolyte by a Neware battery testing system.

Method

The foils were made by the rolling process of the SnCu (wt%, 99.3/0.7) solder bar ingots of 10 mm (thickness) with a manual rolling mill equipped with 120 mm diameter rollers. The rolling was performed such that the thicknesses of the SnCu solder alloy was reduced to ~0.025 mm.

Coin cells (CR 2016) were used to test the electrochemical performances of the as-made foils. The obtained foil was punched into disks with a diameter of 16 mm for coin cell assembling. The coin cells were assembled in an argon-filled glove box with H_2O and O_2 levels less than 0.1 ppm. Lithium metal was used as the counter and reference electrodes and the glass microfiber filter (Whatman, GF/A) as a separator. 1.0 M $LiClO_4$/TEGDME was used as the electrolyte. The charge−discharge tests were performed galvanostatically at 50 μA cm^{-2} current density.

Results and Discussion

The optical photography of the obtained anodes in foil form is given in Figure 1. As can be seen from the figure, the as-made foils with poor surface quality and various residues. Therefore, as-made foils were polished with a sandpaper (2500 grit) to remove the native oxide layer and then cleaned with acetone for several times in the ultrasonic bath.

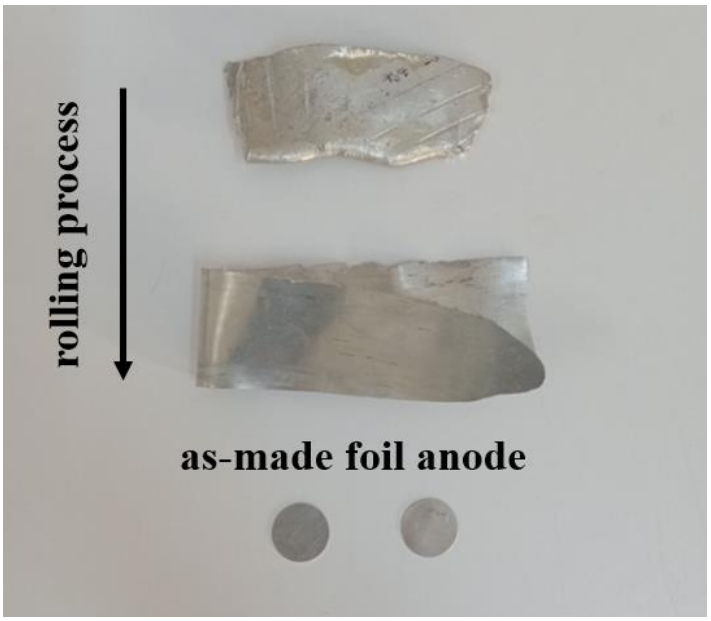

Figure 1. The optical photography of the as-made foil anodes.

Figure 2 shows the galvanostatic initial discharge (lithiation) voltage profiles of the foil anodes at a current density of 50 μA cm^{-2}. As shown in Figure 2, the discharge plateaus of Sn and SnCu solder alloy foil anodes are around 0.4671 V and 0.5419 V, respectively. The discharge process was terminated at around ~7 mAh capacity due to fluctuations in the current-voltage curve. These fluctuations correspond to the activation process of the

foil anodes. Also, as can be seen in Figure 2, foil anodes have more than one discharge plateau. As it is known from the literature, this is the result of the formation of Li-Sn based alloys, which are various discharge products in the lithiation process (Heligman et al., 2019; Xu et al., 2019). To elucidate these processes and discharge products, more detailed electrochemical and structural characterization studies are needed. However, industrial-grade solder alloy performs similarly to bulk pure Sn foil anode.

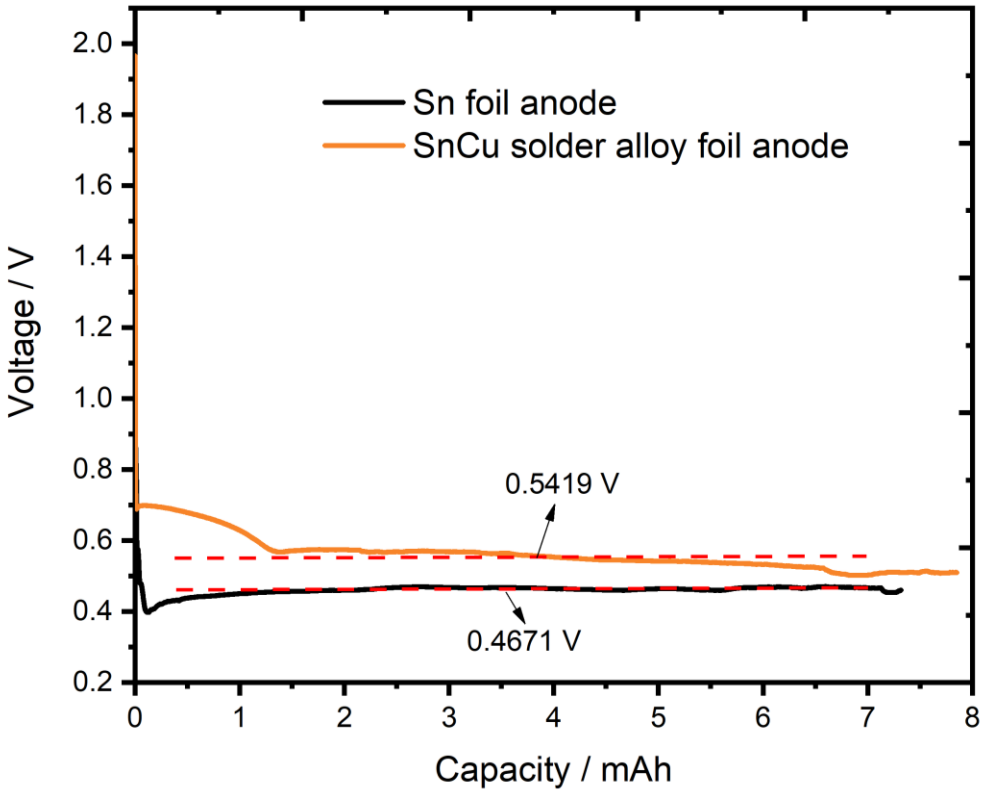

Figure 2**.** The initial discharge profiles of foil anodes at a current density of 50 μA cm^{-2} current density.

Conclusion

In this work, Sn and SnCu solder alloy foil anodes were obtained by a simple cold-rolling process and their electrochemical behaviors were observed in the Sn/Li and SnCu/Li half-cells. The electrochemical performance of the SnCu solder alloy foil anode is very satisfactory compared to the pure Sn foil anode. This work provides a concept and potential to further study the Sn-based alloy foil anodes for lithium-ion batteries.

Scientific Ethics Declaration

The authors declare that the scientific ethical and legal responsibility of this article published in EPSTEM journal belongs to the authors.

Acknowledgements or Notes

* This article was presented as an oral presentation at the International Conference on Technology, Engineering and Science (www.icontes.net) held in Antalya/Turkey on November 16-19, 2022.

References

Bresser, D., Passerini, S., & Scrosati, B. (2016). Leveraging valuable synergies bycombining alloying and conversion for lithium-ion anodes. In *Energy and Environmental Science*, *9*(11), 3348–3367. Royal Society of Chemistry. https://doi.org/10.1039/c6ee02346k

Dong, Z., Du, W., Yan, C., Zhang, C., Chen, G., Chen, J., Sun, W., Jiang, Y., Liu, Y., Gao, M., Gan, J., Yang, Y., & Pan, H. (2021). A Novel Tin-Bonded Silicon Anode for Lithium-Ion Batteries. *ACS Applied Materials and Interfaces*, *13*(38), 45578–45588. https://doi.org/10.1021/acsami.1c13547

Heligman, B. T., Kreder, K. J., & Manthiram, A. (2019). Zn-Sn ınterdigitated eutectic alloy anodes with high volumetric capacity for lithium-ıon batteries. *Joule*, *3*(4), 1051–1063. https://doi.org/10.1016/j.joule.2019.01.005

Li, G., Guo, S., Xiang, B., Mei, S., Zheng, Y., Zhang, X., Gao, B., Chu, P. K., & Huo, K. (2022). Recent advances and perspectives of microsized alloying-type porous anode materials in high-performance Li- and Na-ion batteries. *Energy Materials*, *2*(3), 200020. https://doi.org/10.20517/energymater.2022.24

Ma, Y., Ma, Y., Giuli, G., Diemant, T., Behm, R. J., Geiger, D., Kaiser, U., Ulissi, U., Passerini, S., & Bresser, D. (2018). Conversion/alloying lithium-ion anodes-enhancing the energy density by transition metal doping. *Sustainable Energy and Fuels*, *2*(12), 2601–2608. https://doi.org/10.1039/c8se00424b

Rhodes, K. J., Meisner, R., Kirkham, M., Dudney, N., & Daniel, C. (2012). In Situ XRD of Thin Film Tin Electrodes for Lithium Ion Batteries. *Journal of The Electrochemical Society*, *159*(3), A294–A299. https://doi.org/10.1149/2.077203jes

Xu, H., Li, S., Zhang, C., Chen, X., Liu, W., Zheng, Y., Xie, Y., Huang, Y., & Li, J. (2019). Roll-to-roll prelithiation of Sn foil anode suppresses gassing and enables stable full-cell cycling of lithium ion batteries. *Energy and Environmental Science*, *12*(10), 2991–3000. https://doi.org/10.1039/c9ee01404g

Yang, S., Zavalij, P. Y., & Whittingham, M. S. (2003). Anodes for lithium batteries: Tin revisited. *Electrochemistry Communications*, *5*(7), 587–590. https://doi.org/10.1016/S1388-2481(03)00135-8

Author Information

Ersu Lökçü
Eskisehir Osmangazi University
Department of Metallurgical and Materials Engineering, 26040,
Eskisehir, Turkey
Contact e-mail: *elokcu@ogu.edu.tr*

Resat Can Ozden
Eskisehir Osmangazi University
Department of Metallurgical and Materials Engineering, 26040,
Eskisehir, Turkey

Mustafa Anik
Eskisehir Osmangazi University
Department of Metallurgical and Materials Engineering, 26040,
Eskisehir, Turkey

To cite this article:

Lokcu, E., Ozden, R.C., & Anik, M. (2022). Electrochemical performance of tin-based solder alloys for secondary lithium batteries. *The Eurasia Proceedings of Science, Technology, Engineering & Mathematics (EPSTEM), 21*, 214-217.

The Eurasia Proceedings of Science, Technology, Engineering & Mathematics (EPSTEM)
ISSN: 2602-3199

The Eurasia Proceedings of Science, Technology, Engineering & Mathematics (EPSTEM), 2022

Volume 21, Pages 218-227

IConTES 2022: International Conference on Technology, Engineering and Science

R&D Project Portfolio Selection with Fuzzy Data Envelopment Analysis

Umutcan BOLUK
Gazi University

Murat ARIKAN
Gazi University

Abstract: R&D investments are becoming increasingly important in the developing world. Companies with limited resources should make the most favorable investments for their own strategies. It is crucial that these investments are transferred to the right projects. It is difficult to make decisions in an environment where there are technical difficulties as well as uncertainties. At this point, it is necessary to decide which projects should be done and which projects should not be done. In this study, project portfolio selection that seeks a systematic solution to this decision, is covered. To solve this problem, data envelopment analysis that can evaluate the parameters without the need to build precedence relationship, is used. Parameters were set after a detailed research. Vagueness that is associated with difficulty of making precise judgment, was included in the model by introducing linguistic variables. Ambiguity that characterizes the situation where there are two or more alternatives, is defined with triangular fuzzy sets and α cut method. Different models are constructed for different extreme cases to solve the ambiguity. The models provide the optimal value regardless of the α value. A sample dataset of 30 projects is created to test the models and observe the results. Optimal parameters weights are found in the models. Full pairwise comparisons are considered while examining the interdependencies. These parameters weights are recalculated according to interdependencies. Using these weights, the efficiency score of each project is calculated for each model. Projects are prioritized for different strategies by using decision making under uncertainty.

Keywords: Project portfolio selection, Data envelopment analysis, Fuzzy sets

Introduction

Technologies are becoming more sophisticated and expanding quickly, causing businesses to depend on research and development (R&D) as a survival strategy to maintain a strong competitive position in the future (Abbassi et al., 2014). The amount of money invested in research and development (R&D) worldwide is astounding. R&D expenditures worldwide were $2.3 trillion in 2019, with around half of that amount coming from business and the remaining amounts from governments and academic institutions. This amount is comparable to roughly 2% of global GDP. Furthermore, during the previous ten years, that yearly investment has increased at a rate of almost 4% (Brennan et al., 2020).

Companies will primarily undertake projects that are chosen based on how well they match with the objectives of the company in order to consolidate R&D investments. However, the risks involved in carrying out R&D projects have shown to have a strong effect since choosing the wrong projects might lead to a loss of resources, both financial and human. When choosing R&D projects in this situation, business strategy's influence is typically appropriately understood. For improved resource use, it is essential to align all projects with the organization's strategic goal (de Souza et al., 2021). A big reason why project selection is such an important topic is that these companies and organizations have a lot of projects to choose from, but they can't choose all of them because of limited resources, staff, time, and other things. As a consequence, a number of projects are

chosen from among the proposed projects in accordance with the project selection issue that will not only meet the constraint but also provide the firms the most profit (RezaHoseini et al., 2020)

The problem is to choose the optimal project portfolio from a variety of options while taking into account the enterprise's elemental financial, resource, and other external limits. The project portfolio selection (PPS) problem may take into account a variety of goals, but in financial transactions, maximizing profit is always seen as a key goal (Tofighian & Naderi, 2015).

There are several challenges associated with identifying the project portfolio. There can be varied and often conflicting objectives and some of the objectives are qualitative rather than quantitative. There is uncertainty associated with project parameters such as risk and cost. Some projects are heavily interdependent. Constraints such as money, workforce and equipment should be considered in the decision-making process. A portfolio must be balanced for certain factors important to decision makers, such as risk and completion time and the amount of viable portfolios is often very large (Ghasemzadeh et al., 1999)

Uncertainty

It was acknowledged that there are certain traits associated with R&D projects that make the portfolio selection issue more difficult and must be considered throughout the decision-making process. Common evaluation criteria for R&D projects cannot be accurately specified beforehand. There are uncertainties in the areas like capability of the research team, how well the research idea is carried out, and what kind of results it has (Mavrotas & Makryvelios, 2021).

Various studies explore and categorize sources of uncertainty. Uncertainty can be identified into three types: technical, market, and organizational. Technical uncertainty occurs due to lack of know-how knowledge, unreliability of the production process and other factors. Market uncertainty arise due to misunderstanding the customers' needs, types of sales/distribution and the project team's understanding of the relationship between their own products and those of their competitors. The difficulty of understanding customers' needs and translating them into functional features of the product creates market uncertainty. Organizational uncertainties are associated with the dynamics of the organization. Such uncertainties can occur due to as organizational resistance, lack of continuity or persistence, inconsistencies in expectations and measures, changes in strategies, or changes in internal or external partners (Zheng & Carvalho, 2016).

Interdependency

Choosing the optimal portfolio necessitates not just analyzing each project separately, but also how they relate to one another, or how one project affects the others. There is a difference between the overall cost and benefit derived from a portfolio of the projects and the sum of the individual costs and benefits when interdependencies arise and the parameters connected with a given project depend on which other projects have been chosen (Bhattacharyya et al., 2011). Projects often compete with one another for both monetary and non-monetary inputs, but economies of scale may result in savings via collaborative execution. Positive synergies between projects may happen when the sale of one item stimulates an extra demand for another good. On the other hand, negative synergies may occur when there is some degree of rivalry among the projects (Alvarez-García & Fernández-Castro, 2018).

The existing literature has provided a number of different definitions of interdependencies. Interdependencies may be broken down into the following categories; resources, knowledge and market. There are resource interdependencies as a result of the resources that are shared and needs for resource allocation across various projects, including technology. There is knowledge interdependence between projects when one project benefits from the knowledge and skills generated by another project in the portfolio. Market interdependencies arise whenever an existing market is introduced by a new product or if an existing market's expertise is used to the creation of a product that is still in the planning stages (Al Zaabi & Bashir, 2020).

Literature Review

Portfolio decisions are typically arduous by various reasons. First, these choices are intended to help in the realization of a number of different decision goals. Businesses could have a hard time determining how separate

projects contribute to shareholder value, so instead, they might rely on a number of proxy characteristics that are simpler to quantify. Second, it is difficult to make an informed judgment about which projects to prioritize since the worth of a given project is often unknown until after it has already begun. For example, a funding organization that provides research funds is required to make decisions about project applications before knowing what the final outcomes of these studies would be. In addition, the recognition of external variables may have a significant impact on the value provided by a product portfolio, which cannot be anticipated at the time product development choices are taken. Third, there is potential for the projects to interact with one another. The combined implementation costs of two R&D projects that share a common research base may be lower than those of the projects taken on individually. Finally, there are a lot of alternate portfolios available and the number of potential portfolios grows exponentially with the number of projects involved (Liesiö et al., 2021).

Zanakis et al. (1995) divided project evaluation and selection methods into descriptive methods, scoring models, Delphi method, pairwise comparison, utility theory, fuzzy set theory, decision analysis, risk analysis, linear regression, correlation analysis, and data envelopment analysis. Chu et al. (1996) divided project selection methods into two main categories as compensatory and non-compensatory methods. Compensatory methods include models such as cost-benefit analysis and the analytical hierarchy process, while non-compensatory methods are divided into multi-criteria decision-making methods and ranking models. Archer and Ghasemzadeh (1999) classified the approaches into five main groups consisting of ad-hoc methods, comparative methods, scoring methods, portfolio matrices and optimization models. Iamratanakul et al. (2008) grouped portfolio selection problems into benefit measurement methods, mathematical programming approaches, cognitive emulation approaches, simulation and heuristics models, real options, and ad-hoc methods.

Mavrotas et al. (2003) applied a two-stage method. The first step consists of multi-criteria decision making that ranks projects according to various criteria. At the end of this step, each alternative was given a score, which was used to eliminate the lowest performing alternatives. In the second step, these scores were used as the coefficients of the objective function to be maximized for a mixed integer linear programming model. Bhattacharyya et al. (2011) presented a fuzzy, three-objective R&D project portfolio selection problem that maximizes the outcome and minimizes the cost and risk involved in the problem, under constraints on resources, budget, interdependencies, output. Tavana et al. (2019) proposed a two-stage approach that combines fuzzy analytic hierarchy process and 0-1 integer programming model. In the first stage, the weights of the criteria were calculated with the fuzzy analytic hierarchy method and the evaluation score of each project was determined. In the second stage, three goals mathematical model was built. This hybrid approach provided the ability to consider both quantitative and qualitative criteria, taking into account monetary constraints and project risks.

Uncertainty

One of the factors that increases the complexity of any real world PPS process is the uncertainty that is an integral part of the process. Lack of expertise and insufficient knowledge are almost always common in investment decision making processes. Using stochastic methods to remove uncertainty is a common and popular approach in many decision-making environments. Stochastic theory applies historical data to handle uncertainty. However, it is not very common to use stochastic theory in a project portfolio selection process, as projects are unique and do not have sufficient historical data. Different techniques have been used to solve uncertainty in project portfolio selection problem. Mavrotas and Pechak (2013) used Monte Carlo simulation with stochastic parameters. Tofighian et al. (2018) considered income as stochastic. Panadero et al. (2018) defined money flows as stochastic.

Because there is a shortage of historical data, it has been common practice to consult with specialists. These specialists, drawing on their own personal experience, offer model values and the variation range that should be anticipated for unknown parameters. This motivates referring to all of these estimates as fuzzy numbers, where the membership function provides insight into the accuracy with which the parameter is being estimated (Perez & Gomez, 2016).

Zadeh (1965) introduced fuzzy sets to eliminate uncertainty. The lack of precise information and insufficient data in the projects are some of the factors that require the application of expert judgments. This is done using fuzzy sets. Fuzzy PPS has been the subject of many studies. Carlsson et al. (2007) developed a fuzzy mixed integer programming model using trapezoidal fuzzy numbers. Riddell and Wallace (2007) used a fuzzy-based approach. Bas (2012) developed a fuzzy 0-1 knapsack model. Perez and Gomez (2016) employed fuzzy

constraints in mathematical modeling. Over the years, the need for improvement of fuzzy set theory has emerged as it is applied more and more to real world problems.

Interdependency

Generally, project interdependencies occur when one project's progress is largely or entirely impacted by another project or projects, or, more precisely, when the success of a project relies upon other project or projects. Project-to-project dependencies may arise at a variety of scales, from individual tasks and goals to a group's work or even an entire project. For example, sharing resources among multiple projects will likely result in overall cost savings, while increasing opportunities for generating new knowledge. Increasing connectivity between projects can bring more benefits, however it will be more challenging to select a portfolio (Bathallath et al., 2016).

Ignoring interdependencies results in inefficient solutions and inefficient use of resources. Resource interdependency occurs when the overall cost of a portfolio is not equal to the sum of the costs of the separate projects. Technical interdependencies mainly relate to how one project affects the likelihood that another will succeed. The degree to which the success of one project is contingent upon the completion of another is an example of a technical interdependency. Market interdependencies affect total return of a portfolio. Market interdependencies may either increase or decrease the portfolio's value beyond the sum of its component projects (Schmidt, 1993).

Method

Data Envelopment Analysis (DEA) was developed by Charnes et al. (1978). DEA is a mathematical model that is used to measure the performance of decision making units (DMUs) evaluated by multiple and common inputs and outputs.

$$\max h_0 = \frac{\sum_{r=1}^{s} u_r y_{r0}}{\sum_{i=1}^{m} v_i x_{i0}}$$
$$\frac{\sum_{r=1}^{s} u_r y_{rj}}{\sum_{i=1}^{m} v_i x_{ij}} \le 1, \qquad \forall j$$
$$u_r, v_i \ge 0, \qquad \forall r, i$$

Assuming that the values of inputs and outputs of DMUs are based on the subjective opinion of d decision makers (k=1, 2, …, d), every decision maker estimates that each DMU consumes m inputs x_{ijk} ($i = 1, 2, \dots, m;\ k = 1, 2, \dots, d$) to produce s outputs y_{rjk} ($r = 1, 2, \dots, s;\ k = 1, 2, \dots, d$). The geometric mean will be used to combine the d different opinions generated for each criterion. As a result, the CCR model turns into the following model.

$$\max E_0 = \frac{\sum_{r=1}^{s} u_r \left(\prod_{k=1}^{d} y_{r0k}\right)^{1/d}}{\sum_{i=1}^{m} v_i \left(\prod_{k=1}^{d} x_{i0k}\right)^{1/d}}$$

$$\frac{\sum_{r=1}^{s} u_r \left(\prod_{k=1}^{d} y_{rjk}\right)^{1/d}}{\sum_{i=1}^{m} v_i \left(\prod_{k=1}^{d} x_{ijk}\right)^{1/d}} \le 1, \qquad \forall j$$
$$u_r, v_i \ge \varepsilon, \qquad \forall r, i$$

Tavana et al. (2013) developed a data envelopment analysis model that solved uncertainty for project portfolio selection problem. After solving vagueness and ambiguity, four extreme cases aroused. In our model, we have adopted all fuzzy parameters as triangular fuzzy numbers. Let's assume that each DMU (j=1, 2, …, n) consumes m fuzzy inputs $\tilde{x}_{ij} = (x_{ij}^1, x_{ij}^2, x_{ij}^3)$ to produce s fuzzy outputs $\tilde{y}_{rj} = (y_{rj}^1, y_{rj}^2, y_{rj}^3)$. Using a random α-cut for each triangular fuzzy number, the lower and upper bounds of the membership functions for the inputs and outputs are calculated as follows (Ali et al., 2016):

$$\left(x_{ij}^L\right)_{\alpha_i} = x_{ij}^1 + \alpha_i\left(x_{ij}^2 - x_{ij}^1\right), \qquad \alpha_i \in [0,1];\ \ i = 1, 2, \dots, m;\ \ j = 1, 2, \dots, n$$
$$\left(x_{ij}^U\right)_{\alpha_i} = x_{ij}^3 - \alpha_i\left(x_{ij}^3 - x_{ij}^2\right), \qquad \alpha_i \in [0,1];\ \ i = 1, 2, \dots, m;\ \ j = 1, 2, \dots, n$$

$$\left(y_{rj}^{L}\right)_{\alpha_r} = y_{rj}^{1} + \alpha_r\left(y_{rj}^{2} - y_{rj}^{1}\right), \qquad \alpha_r \in [0,1];\ \ r = 1,2,\dots,s;\ \ j = 1,2,\dots,n$$
$$\left(y_{rj}^{U}\right)_{\alpha_r} = y_{rj}^{3} - \alpha_r\left(y_{rj}^{3} - y_{rj}^{2}\right), \qquad \alpha_r \in [0,1];\ \ r = 1,2,\dots,s;\ \ j = 1,2,\dots,n$$

In the first case, inputs and outputs take the upper bound:

$$\max \lambda$$
$$\sum_{r=1}^{s} u_r\left(y_{rj}^{3} - \alpha_r\left(y_{rj}^{3} - y_{rj}^{2}\right)\right) - \lambda\left(\sum_{i=1}^{m} v_i\left(x_{ij}^{3} - \alpha_i\left(x_{ij}^{3} - x_{ij}^{2}\right)\right)\right) \geq 0,\ \ \forall j$$
$$\sum_{r=1}^{s} u_r\left(y_{rj}^{3} - \alpha_r\left(y_{rj}^{3} - y_{rj}^{2}\right)\right) - \sum_{i=1}^{m} v_i\left(x_{ij}^{3} - \alpha_i\left(x_{ij}^{3} - x_{ij}^{2}\right)\right) \leq 0,\ \ \forall j$$
$$u_r, v_i \geq \varepsilon,\ \ \forall r, i$$
$$\alpha_i \in [0,1],\ \ \forall i$$
$$\alpha_r \in [0,1],\ \ \forall r$$
$$0 \leq \lambda \leq 1$$

In the second case, inputs take the lower bound and outputs take the upper bound:

$$\max \lambda$$
$$\sum_{r=1}^{s} u_r\left(y_{rj}^{3} - \alpha_r\left(y_{rj}^{3} - y_{rj}^{2}\right)\right) - \lambda\left(\sum_{i=1}^{m} v_i\left(x_{ij}^{1} - \alpha_i\left(x_{ij}^{2} - x_{ij}^{1}\right)\right)\right) \geq 0,\ \ \forall j$$
$$\sum_{r=1}^{s} u_r\left(y_{rj}^{3} - \alpha_r\left(y_{rj}^{3} - y_{rj}^{2}\right)\right) - \sum_{i=1}^{m} v_i\left(x_{ij}^{1} - \alpha_i\left(x_{ij}^{2} - x_{ij}^{1}\right)\right) \leq 0,\ \ \forall j$$
$$u_r, v_i \geq \varepsilon,\ \ \forall r, i$$
$$\alpha_i \in [0,1],\ \ \forall i$$
$$\alpha_r \in [0,1],\ \ \forall r$$
$$0 \leq \lambda \leq 1$$

In the third case, inputs take the upper bound and outputs take the lower bound:

$$\max \lambda$$
$$\sum_{r=1}^{s} u_r\left(y_{rj}^{1} - \alpha_r\left(y_{rj}^{2} - y_{rj}^{1}\right)\right) - \lambda\left(\sum_{i=1}^{m} v_i\left(x_{ij}^{3} - \alpha_i\left(x_{ij}^{3} - x_{ij}^{2}\right)\right)\right) \geq 0,\ \ \forall j$$
$$\sum_{r=1}^{s} u_r\left(y_{rj}^{1} - \alpha_r\left(y_{rj}^{2} - y_{rj}^{1}\right)\right) - \sum_{i=1}^{m} v_i\left(x_{ij}^{3} - \alpha_i\left(x_{ij}^{3} - x_{ij}^{2}\right)\right) \leq 0,\ \ \forall j$$
$$u_r, v_i \geq \varepsilon,\ \ \forall r, i$$
$$\alpha_i \in [0,1],\ \ \forall i$$
$$\alpha_r \in [0,1],\ \ \forall r$$
$$0 \leq \lambda \leq 1$$

In the fourth case, inputs and outputs take the lower bound:

$$\max \lambda$$
$$\sum_{r=1}^{s} u_r\left(y_{rj}^{1} - \alpha_r\left(y_{rj}^{2} - y_{rj}^{1}\right)\right) - \lambda\left(\sum_{i=1}^{m} v_i\left(x_{ij}^{1} - \alpha_i\left(x_{ij}^{2} - x_{ij}^{1}\right)\right)\right) \geq 0,\ \ \forall j$$
$$\sum_{r=1}^{s} u_r\left(y_{rj}^{1} - \alpha_r\left(y_{rj}^{2} - y_{rj}^{1}\right)\right) - \sum_{i=1}^{m} v_i\left(x_{ij}^{1} - \alpha_i\left(x_{ij}^{2} - x_{ij}^{1}\right)\right) \leq 0,\ \ \forall j$$
$$u_r, v_i \geq \varepsilon,\ \ \forall r, i$$
$$\alpha_i \in [0,1],\ \ \forall i$$
$$\alpha_r \in [0,1],\ \ \forall r$$
$$0 \leq \lambda \leq 1$$

Conflicting rankings may arise for a given decision-making unit due to different α-cutoff levels. Because α levels were not predefined. Finally, the models are non-linear and it will be difficult to find the global optimal value. Due to these problems mentioned, the model proposed by Tavana et al. (2013) were used. To linearize the models, $\beta_r = \alpha_r u_r$ and $\gamma_i = \alpha_i v_i$ equations are modified. After the conversions, the models were still not linear that's why $\delta_i = \gamma_i \lambda$ and $\zeta_i = v_i \lambda$ added to remove the nonlinearity. So, four extreme cases were revised. In the first case, inputs and outputs take the upper bound:

$$\max \lambda$$
$$\sum_{r=1}^{s} u_r y_{rj}^{3} - \beta_r\left(y_{rj}^{3} - y_{rj}^{2}\right) - \sum_{i=1}^{m} \zeta_i x_{ij}^{3} - \delta_i\left(x_{ij}^{3} - x_{ij}^{2}\right) \geq 0,\ \ \forall j$$
$$\sum_{r=1}^{s} u_r y_{rj}^{3} - \beta_r\left(y_{rj}^{3} - y_{rj}^{2}\right) - \sum_{i=1}^{m} v_i x_{ij}^{3} - \gamma_i\left(x_{ij}^{3} - x_{ij}^{2}\right) \leq 0,\ \ \forall j$$
$$u_r, v_i \geq \varepsilon,\ \ \forall r, i$$
$$0 \leq \beta_r \leq u_r,\ \ \forall r$$
$$0 \leq \gamma_i \leq v_i,\ \ \forall i$$
$$0 \leq \zeta_i \leq v_i,\ \ \forall i$$
$$0 \leq \delta_i \leq v_i,\ \ \forall i$$
$$0 \leq \lambda \leq 1$$

In the second case, inputs take the lower bound and outputs take the upper bound:

$$\max \lambda$$
$$\sum_{r=1}^{s} u_r y_{rj}^3 - \beta_r\left(y_{rj}^3 - y_{rj}^2\right) - \sum_{i=1}^{m} \zeta_i x_{ij}^1 - \delta_i\left(x_{ij}^2 - x_{ij}^1\right) \geq 0, \ \forall j$$
$$\sum_{r=1}^{s} u_r y_{rj}^3 - \beta_r\left(y_{rj}^3 - y_{rj}^2\right) - \sum_{i=1}^{m} v_i x_{ij}^1 - \gamma_i\left(x_{ij}^2 - x_{ij}^1\right) \leq 0, \ \forall j$$
$$u_r, v_i \geq \varepsilon, \ \forall r, i$$
$$0 \leq \beta_r \leq u_r, \ \forall r$$
$$0 \leq \gamma_i \leq v_i, \ \forall i$$
$$0 \leq \zeta_i \leq v_i, \ \forall i$$
$$0 \leq \delta_i \leq v_i, \ \forall i$$
$$0 \leq \lambda \leq 1$$

In the third case, inputs take the upper bound and outputs take the lower bound:

$$\max \lambda$$
$$\sum_{r=1}^{s} u_r y_{rj}^1 - \beta_r\left(y_{rj}^2 - y_{rj}^1\right) - \sum_{i=1}^{m} \zeta_i x_{ij}^3 - \delta_i\left(x_{ij}^3 - x_{ij}^2\right) \geq 0, \ \forall j$$
$$\sum_{r=1}^{s} u_r y_{rj}^1 - \beta_r\left(y_{rj}^2 - y_{rj}^1\right) - \sum_{i=1}^{m} v_i x_{ij}^3 - \gamma_i\left(x_{ij}^3 - x_{ij}^2\right) \leq 0, \ \forall j$$
$$u_r, v_i \geq \varepsilon, \ \forall r, i$$
$$0 \leq \beta_r \leq u_r, \ \forall r$$
$$0 \leq \gamma_i \leq v_i, \ \forall i$$
$$0 \leq \zeta_i \leq v_i, \ \forall i$$
$$0 \leq \delta_i \leq v_i, \ \forall i$$
$$0 \leq \lambda \leq 1$$

In the fourth case, inputs and outputs take the lower bound:

$$\max \lambda$$
$$\sum_{r=1}^{s} u_r y_{rj}^1 - \beta_r\left(y_{rj}^2 - y_{rj}^1\right) - \sum_{i=1}^{m} \zeta_i x_{ij}^1 - \delta_i\left(x_{ij}^2 - x_{ij}^1\right) \geq 0, \ \forall j$$
$$\sum_{r=1}^{s} u_r y_{rj}^1 - \beta_r\left(y_{rj}^2 - y_{rj}^1\right) - \sum_{i=1}^{m} v_i x_{ij}^1 - \gamma_i\left(x_{ij}^2 - x_{ij}^1\right) \leq 0, \ \forall j$$
$$u_r, v_i \geq \varepsilon, \ \forall r, i$$
$$0 \leq \beta_r \leq u_r, \ \forall r$$
$$0 \leq \gamma_i \leq v_i, \ \forall i$$
$$0 \leq \zeta_i \leq v_i, \ \forall i$$
$$0 \leq \delta_i \leq v_i, \ \forall i$$
$$0 \leq \lambda \leq 1$$

Implementation

After a detailed literature research, it was decided to evaluate the models on a total of 9 criteria; cost, return on investment, project plan, research group, technical tasks, strategic objectives, feasibility, subsequent projects and environment. From the parameters selected for evaluation, cost and return on investment are preferred to be kept low in research and development projects. Therefore, these parameters were set as input parameters. For the remaining parameters, it is desired to be kept high. That's why remaining parameters were set as output parameters.

For the evaluation of the determined parameters, the 5-scale evaluation scale was used (Jafarzadeh et al., 2018). This scale consists of very low, low, medium, high and very high values. The parameters were evaluated using these linguistic expressions. It was decided to use triangular fuzzy numbers to describe linguistic expressions. Symmetrical triangular fuzzy numbers are chosen for membership function that are given in Table 1.

Table 1. Membership function

Linguistic variable	Triangular fuzzy variable		
Very low	0	0.17	0.33
Low	0.17	0.33	0.5
Medium	0.33	0.5	0.67
High	0.5	0.67	0.83
Very high	0.67	0.83	1

Results and Discussion

Within the framework of the established model, 9 different parameter values were generated to rank 30 different projects. The models were solved on GAMS. Optimal input and output coefficient values were obtained. For each model, the efficiency score was calculated separately for each decision-making unit by using the optimal parameter weight values:

$$E_j^k = \frac{\sum_{r=1}^{s} u_r^k \tilde{y}_{rj}}{\sum_{i=1}^{m} v_i^k \tilde{x}_{ij}},\ j = 1, 2, \dots, n;\ k = 1, 2, 3, 4$$

Adjoining the Interdependencies

The interdependencies that exist in the project portfolio selection problem, have not yet been considered. Within the scope of this study, 9 parameters characterizing the projects were determined. The cost parameter is used to solve resource interdependencies. The technical tasks parameter is used to analyze technical interdependencies. At the point of evaluation of technical dependencies, it is necessary to include the know-how of the companies. Because, the technical knowledge gained from previous projects will also have a positive impact. Know-how is also included when defining technical interdependencies. In problem definition, the only parameter that characterizes the outcome was chosen as the return on investment parameter. Since the return on investment parameter chosen on the problem does not fully cover the market interdependencies, the market interdependencies were excluded in our model. New methodology that was developed, enables to include all pairwise relation for the interdependencies. At this point, it is foreseen that the decision makers will establish relations and assignments have been made for these data. Evaluation scale for interdependencies is given at Table 2.

Table 2. Scale of interdependencies

Qualitative	Quantitative
0	Non synergy
1	Very low synergy
2	Low synergy
3	Medium synergy
4	High synergy
5	Very high synergy

The values of the cost parameter consumed by each decision-making unit were recalculated including interdependencies as shown below.

$$x_{1j}^{k'} = (x_{1j})(1 - \tau_{1j}),\ \forall j$$

The value defined by τ_{1j} in the equation can be called the total cost interdependence of that project. At this point, this parameter has been calculated as shown below.

$$\tau_{1j} = \sum_{j=1}^{30} (\mathfrak{f}_{ij}/\varphi)/5,\ \forall i$$

The value of $\mathfrak{f}_{ij}$ given in the above equation corresponds to the amount of synergy between project i and j. The value of φ shows that how many projects are interdependent. Calculated cost synergies are included in the model using equation below.

$$E_j^{k'} = \frac{\sum_{r=1}^{s} u_r^k \tilde{y}_{rj}}{v_1^k \tilde{x}_{1j}^{k'} + v_2^k \tilde{x}_{2j}},\ j = 1, 2, \dots, n;\ k = 1, 2, 3, 4$$

For the technical tasks' parameter, the weight of the defined criteria was calculated individually and multiplied by the total amount of synergy and its contribution to the total effectiveness score was calculated. The contribution of technical tasks synergy is shown in the equation below.

$$\mathfrak{o}_j = \frac{u_3^k \tilde{y}_{3j}}{\sum_{i=1}^{m} v_i^k \tilde{x}_{ij}} (\tau_{2j}),\ \forall j$$

The value defined by τ_{2j} can be called the total synergy of technical tasks for that project. At this point, this parameter has been calculated as shown below.

$$\tau_{2j} = \sum_{j=1}^{30} (\mathfrak{f}_{ij}/\varphi)/5\,,\ \forall i$$

The value of $\mathfrak{f}_{ij}$ given in the above equation corresponds to the amount of synergy between project i and j. The value of φ shows that how many projects are interdependent. The final efficiency score was calculated by including the contribution of the synergy of technical tasks. Efficiency scores, including the interdependencies of each decision-making unit, were calculated by the equation shown below.

$$E_j^{k''} = E_j^{k'} + \mathfrak{o}_j,\ \forall j$$

By using decision making methods under uncertainty, priority orders were determined by using optimistic, pessimistic, neutral and robust strategies (Tavana et al., 2013).

Conclusion

With the methodology adopted in this study, data envelopment analysis was used, which includes multiple inputs and outputs and allows them to be solved without defining antecedent weights. Uncertain information arises due to lack of expertise or lack of data. Main characteristics of project portfolio selection that are vagueness and ambiguity were included in the method. Vagueness was included in the model with the help of linguistic expressions. These linguistic expressions used were translated into qualitative expressions with the help of fuzzy triangular numbers. Ambiguity was solved through built different models for extreme cases. After defining the uncertainty and calculating the efficiency scores, interdependencies were also defined. Technical and resource interdependencies were included in the model. The firm's know-how is added into the identification of technical interdependencies. Efficiency scores that were calculated by including interdependencies were ranked for four different types of decision makers using decision making methods under uncertainty.

Recommendations

With this study, a model including uncertainty and interdependencies, which are the main characteristics of the project portfolio selection problem, developed. However, market interdependency is excluded due to the selected parameter values. Therefore, researchers who want to include market dependencies for future studies can choose a different parameter. By including market interdependencies, negative synergies can be defined also. The method developed for the evaluation of negative synergies can be used by updating the interdependency's scale. While defining interdependencies, crisp values were used. In future studies, these definitions can be developed and solved in accordance with fuzzy logic.

Scientific Ethics Declaration

The authors declare that the scientific ethical and legal responsibility of this article published in EPSTEM journal belongs to the authors.

Acknowledgements

* This article was presented as an oral presentation at the International Conference on Technology, Engineering and Science (www.icontes.net) conference held in Antalya/Turkey on November 16-19, 2022.

References

Abbassi, M., Ashrafi, M., & Tashnizi, E. S. (2014). Selecting balanced portfolios of R&D projects with interdependencies: A cross-entropy based methodology. *Technovation*, *34*(1), 54–56

Ali, M. Y., Sultan, A., & Khan, A. F. M. K. (2016). Comparison of fuzzy multiplication operation on triangular fuzzy number. *IOSR Journal of Mathematics*, *12*(04), 35–41

Alvarez-García, B., & Fernández-Castro, A. S. (2018). A comprehensive approach for the selection of a portfolio of interdependent projects. An application to subsidized projects in Spain. *Computers & Industrial Engineering*, *118*, 153-159.

Al Zaabi, H., & Bashir, H. (2020). Modeling and analyzing project interdependencies in project portfolios using an integrated social network analysis-Fuzzy TOPSIS MICMAC Approach. *International Journal of System Assurance Engineering and Management*, *11*(6), 1083–1106.

Bas, E. (2012). Surrogate relaxation of a fuzzy multidimensional 0–1 knapsack model by surrogate constraint normalization rules and a methodology for multi-attribute project portfolio selection. *Engineering Applications of Artificial Intelligence*, *25*(5), 958–970.

Bathallath, S., Smedberg, A., & Kjellin, H. (2016). Managing project interdependencies in IT/IS project portfolios: A review of managerial issues. *International Journal of Information Systems and Project Management*, *4*(1), 67–82.

Bhattacharyya, R., Kumar, P., & Kar, S. (2011). Fuzzy R&D portfolio selection of interdependent projects. *Computers & Mathematics with Applications*, *62*(10), 3857–3870.

Carlsson, C., Fullér, R., Heikkilä, M., & Majlender, P. (2007). A fuzzy approach to R&D project portfolio selection. *International Journal of Approximate Reasoning*, *44*(2), 93–105.

Charnes, A., Cooper, W., & Rhodes, E. (1978). Measuring the efficiency of decision making units. *European Journal of Operational Research*, *2*(6), 429–444.

Chu, P. Y. V., Hsu, Y. L., & Fehling, M. (1996). A decision support system for project portfolio selection. *Computers in Industry*, *32*(2), 141–149.

Ghasemzadeh, F., Archer, N. P., & Iyogun, P. (1999). A Zero-One model for project portfolio selection and scheduling. *Journal of Operational Research Society*, *50*(7),745–755.

Iamratanakul, S., Patanakul, P., & Milosevic, D. (2008). Project portfolio selection: From past to present. Paper presented at the 2008 *4th IEEE International Conference on Management of Innovation and Technology*, 287–292.

Jafarzadeh, H., Akbari, P., & Abedin, B. (2018). A methodology for project portfolio selection under criteria prioritisation, Uncertainty and projects interdependency – combination of fuzzy QFD and DEA. *Expert Systems with Applications*, *110*, 237–249.

Liesiö, J., Salo, A., Keisler, J. M., & Morton, A. (2021). Portfolio decision analysis: Recent developments and future prospects. *European Journal of Operational Research*, *293*(3), 811–825.

Mavrotas, G., Diakoulaki, D., & Capros, P. (2003). Combined MCDA–IP approach for project selection in the electricity market. *Annals of Operations Research*, *120*, 159-170.

Mavrotas, G., & Pechak, O. (2013). Combining mathematical programming and Monte Carlo simulation to deal with uncertainty in energy project portfolio selection. *Assessment and Simulation Tools for Sustainable Energy Systems*, *129*, 333–356.

Mavrotas, G., & Makryvelios, E. (2021). Combining multiple criteria analysis, mathematical programming and Monte Carlo simulation to tackle uncertainty in research and development project portfolio selection: A case study from Greece. *European Journal of Operational Research*, *291*(2), 794-806.

Panadero, J., Doering, J., Kizys, R., Juan, A. A., & Fito, A. (2018). A variable neighborhood search simheuristic for project portfolio selection under uncertainty. *Journal of Heuristics*, *26*(3), 353–375.

Perez, F., & Gomez, T. (2016). Multiobjective project portfolio selection with fuzzy constraints. *Annals of Operations Research*, *245*(1–2), 7–29.

Riddell, S., & Wallace, W. A. (2007). The use of fuzzy logic and expert judgment in the R&D project portfolio selection process. Paper presented at the *PICMET '07 - 2007 Portland International Conference on Management of Engineering & Technology*, 1228–1238.

Schmidt, R. L. (1993). A model for R&D project selection with combined benefit, outcome and resource interactions. *IEEE Transactions on Engineering Management*, *40*(4), 403–410.

Tavana, M., Khalili-Damghani, K., & Sadi-Nezhad, S. (2013). A fuzzy group data envelopment analysis model for high-technology project selection: A case study at NASA. *Computers & Industrial Engineering*, *66*(1), 10–23.

Tavana, M., Khosrojerdi, G., Mina, H., & Rahman, A. (2019). A hybrid mathematical programming model for optimal project portfolio selection using fuzzy inference system and analytic hierarchy process. *Evaluation and Program Planning*, *77*, 101703.

Tofighian, A. A., Moezzi, H., Khakzar Barfuei, M., & Shafiee, M. (2018). Multi-period project portfolio selection under risk considerations and stochastic income. *Journal of Industrial Engineering International*, *14*(3), 571–584.

Tofighian, A. A., & Naderi, B. (2015). Modeling and solving the project selection and scheduling. *Computers & Industrial Engineering*, *83*, 30–38.

Zadeh, L. (1965). Fuzzy sets. *Information and Control*, *8*(3), 338–353.

Zanakis, S. H., Mandakovic, T., Gupta, S. K., Sahay, S., & Hong, S. (1995). A review of program evaluation and fund allocation methods with in the service and government sectors. *Socio-Economic Planning Sciences*, *29*(1), 59–79.

Zheng, E. Z. H., & Carvalho, M. M. D. (2016). Managing uncertainty in projects: A review, trends and gaps. *Revista de Gestão e Projetos*, *07*(02), 95–109.

Author Information

Umutcan Boluk
Gazi University
Bandirma Street no:6/1, Yenimahalle/Ankara
Turkey
Contact e-mail: *umutboluk@gmail.com*

Murat Arikan
Gazi University
Bandirma Street no:6/1, Yenimahalle/Ankara
Turkey

To cite this article:

Boluk, U. & Arikan, M. (2022). R&D project portfolio selection with fuzzy data envelopment analysis. *The Eurasia Proceedings of Science, Technology, Engineering & Mathematics (EPSTEM), 21*, 218-227.

The Eurasia Proceedings of Science, Technology, Engineering & Mathematics (EPSTEM)
ISSN: 2602-3199

The Eurasia Proceedings of Science, Technology, Engineering & Mathematics (EPSTEM), 2022

Volume 21, Pages 228-236

IConTES 2022: International Conference on Technology, Engineering and Science

Comparative Study of Analysis and Cost of Flat Slab and Conventional Slab Structures in Somalia-Mogadishu

Shafie IBRAHIM
Near East University

Shaghayegh OSTOVAR RAVARI
Near East University

Rifat RESATOGLU
Near East University

Abstract: All Somalian cities favor vertical growth over lateral growth due to a combination of rapid population growth, fast urbanization, lack of urban infrastructures, and rising land prices. The use of conventional slabs has been common in Somalia, but nowadays flat slabs are widely used due to their advantages such as reduced story height, ease of formwork installation, and shorter construction period, all of which affect the cost of construction projects. However, accurate analysis and design are required for flat slabs since they are susceptible to punching shear. This study aims to investigate the performance and behavior of flat slab and conventional slab floor systems subjected to gravity loads and to compare the total cost of flat slab floor systems and conventional slab floor systems for formwork, required concrete, and steel reinforcement in Somalia. 8-story residential buildings with flat slab and conventional slab floor systems have been analyzed using ETABS software as per ACI 318-14 and ASCE 7-16. The results show that flat slab structures have obvious architectural and structural advantages and in addition, the cost of a conventional slab floor system is 18.3% to 19.9% higher compared to a flat slab floor system. Based on the cost analysis results obtained from this case study, it could be concluded that the flat slab floor system is economical compared to the conventional slab floor system in Somalia.

Keywords: Conventional slab, Cost, ETABS, Flat slab, Somalia

Introduction

The idea and desire to build multi-story buildings have changed throughout history, and today the growth of cities has increased the construction of mid-rise and high-rise buildings. In fact, factors such as high population density, lack of land, and the increase in land prices are among the factors that have led to the preference for vertical structures over horizontally expanded structures. In emerging countries such as Somalia, the urbanization process began with the industrial revolution and is still ongoing, with people moving to urban areas where more work opportunities are available as a result of industrialization. In Somalia, the construction of 5-story to 12-story buildings is widespread. These buildings are often residential or commercial or in some cases a combination of the two.

The slab system commonly used in Somalia is conventional slab structures. On the other hand, flat slab systems have been widely used in Somalia in recent years. This reinforced concrete floor system has many advantages which accelerate construction, architectural flexibility, easier formwork, and use of space. However, flat slab structures need further attention.

The estimated cost of an engineering project can be determined using a scientific method before actually starting. Although the actual cost of the project upon completion differs from the estimated cost, it should not fluctuate significantly from the estimated cost, assuming there are no unexpected or unforeseen circumstances. Cost estimation requires talent, expertise, foresight, and good judgment in addition to a thorough understanding of building procedures and material and labor costs. Estimating the approximate cost of the project helps to assess its affordability and ensure financial resources (Peurifoy & Oberlender, 2014, Serbanoiu et al., 2020)

Problem Statement

- Population growth has put pressure on the limited land area in Somalia.
- Lack of prior information, lack of a database that includes housing prices, lack of proper resources, and lack of project management affected Somalia.
- A comparative study of the analysis and cost of flat slabs and conventional slabs in Somalia has not been studied yet.

Research Objective

The main objectives of this study are listed below:

- Investigating the performance of flat slab and conventional slab structures subjected to gravity loads.
- Evaluation of the behavior of flat slab and conventional slab structures for parameters such as bending moment, shearing force, etc.
- Comparison of the analysis results of the flat slab and conventional slab structures.
- Comparison of the required amount of concrete, steel, and formwork material.
- Comparison of the total cost of the structure with flat slab and conventional slab structures for concrete, steel, and formwork.

Literature Review

There are several previous studies and academic research mainly on the comparative study of analysis and cost of the flat slab and conventional slab structures. These articles and works have been reviewed as part of this study. Sawwalakhe, et al., (2021) investigated that modern architecture often supports the normal slab with a deep beam and a thin slab, which transfers the load to the column, due to its popularity, affordability, and ability to reduce weight and speed up growth. It also offers advantages including greater stiffness and weight-carrying capacity. Grid slabs are able to carry heavier loads over longer spans and reduce void-related dead load. The goal of this experiment was to determine the most affordable slab type among grid slab, flat slab with a drop, and standard slab. Story drift, shearing force, and story displacement were some of the measurements that were made. 18 distinct constructions were examined and the dead load, live load, and seismic load have been determined. A flat slab performs better than a standard slab or grid slab when the shearing force, bending moment, displacement, and drift are taken into account (Sawwalakhe & Pachpor, 2021).

Borkar, et al., (2021) examined that selecting an appropriate type of building for a specific purpose is essential for architectural engineers since multistory structures are becoming more and more required as the need for space in living arrangements increases. This research aimed to investigate the response of flat slab structures for a variety of heights and designs using ETABS, in terms of story shear, base shear, and story drift, in seismic loads for several zones (Borkar, et al., 2021). Sayli, et al., (2020) studied that classic slab systems, including flat slabs and grid slabs, have been evaluated using ETABS and STAAD.Pro. This study aimed to examine the impacts of vertical and horizontal force, displacement, shearing force, bending moment, flexibility, and slab behavior for conventional slabs, flat slabs, and grid slabs in various earthquake zones (Sayli & Madavi, 2020).

Sathawane, et al., (2012) have presented a comparison of Grid Slab, Flat Slab with Drop, and Flat Slab without Drop researchers found that Grid Slab is the most cost-effective option. The analyses of flat slabs, flat slabs without drops, and grid slabs were conducted manually, and also by using STAAD PRO V8i, IS 456-2000 programs. This study found that compared to other slabs considered, a flat slab with a drop is more reasonably priced. More concrete is needed for a grid slab and the amount of steel needed for a flat slab with a drop is also greater than for a flat slab without a drop (Sathawane & Deotale, 2012).

Methodology

A total of 6 models were modeled, 3 of which were developed with a flat slab floor system, and the other 3 models were developed with a conventional slab floor system. The difference between the models with the same type of slab is the grid spacing, which varies between 5, 6, and 7 meters. The height of each story is typically 3.2 meters and the selected buildings are assumed to be used as residential buildings. The location of the buildings is assumed to be in Mogadishu city which is the capital and the most populous city of Somalia. In the capital region, Mogadishu, the earthquake risk is classified as very low.

Buildings were modeled using ETABS and linear analysis was conducted. ACI 318-14 (Building Code Requirements for Structural Concrete) and ASCE (Minimum design loads for buildings and other structures) were adopted. The properties of materials are shown in Table 1.

Table 1. Properties of materials

Parameter	Value
Weight per unit volume of concrete, γ_c	25 kN/m^3
Weight per unit volume of steel, γ_s	78.5 kN/m^3
Modulus of Elasticity of steel, E_s	200,000MPa
Modulus of Elasticity of concrete, E_c	24870 MPa
Compressive strength of concrete, f_c	28 MPa
Yield strength of steel, f_y	420 MPa

Design Procedure

Preliminary measurements were taken to analyze building elements (beams, slabs, and columns). The initial slab and beam sizes were calculated, and the estimated sizes of the columns were determined according to the axial loads transmitted by the slab and beams as a result of live loads and dead loads. The appropriate member sizes and minimum thickness for different slab systems were calculated as per ACI 318-14.

Loads

Load Patterns

In this study, the considered loads are dead load and live load. The dead load is the structure self-weight, which is automatically calculated by ETABS software. Super dead load is the additional load on the structures; it represents the weight of the finishing materials and partition walls of a building which is considered 2.11 kN/m^2 in this study. The live load for residential buildings is considered 2 kN/m^2 and is assumed for all floors. The minimum design dead loads and live loads were taken from ASCE/SEI 7-10.

Load Combination

Commonly, a load combination is composed of various loads, such as dead loads and live loads, which are then combined to form a strength design. The load combination was developed in accordance with ASCE 7-10 as follows, where DL is dead load and LL is live load.

$$W_u = 1{,}2DL + 1{,}6\,LL$$

Modeling by ETABS

The building parameter details for types A, B, and C, and their plans are shown below in detail. The factors considered in this work were slab type, length of span in X and Y directions, story height, slab thickness, and the size of the columns.

Table 2. Building parameters (Type A)

Parameter	Slab Systems	
	Conventional Slab	Flat Slab
Dimension of the building (Length and width)	25m×25m	25m×25m
Length of each span (X-direction)	5m	5m
Length of each span (Y-direction)	5m	5m
Number of spans	5 Rows & 5 Columns	5 Rows & 5 Columns
Story height	3.2m	3.2m
Number of stories	8	8
Slab thickness	160mm	180mm
Beam size	200mm×310mm	--------
Column size (corner)	460mm×460mm	400mm×400mm
Column size (exterior)	500mm×500mm	440mm×440mm
Column size (interior)	570mm×570mm	520mm×520mm

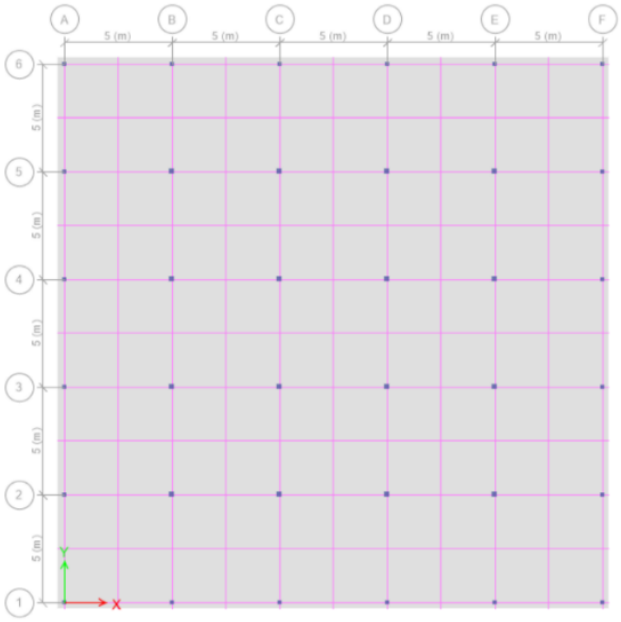

Figure 1. Plan of 8-story building (Flat slab/ Type A)

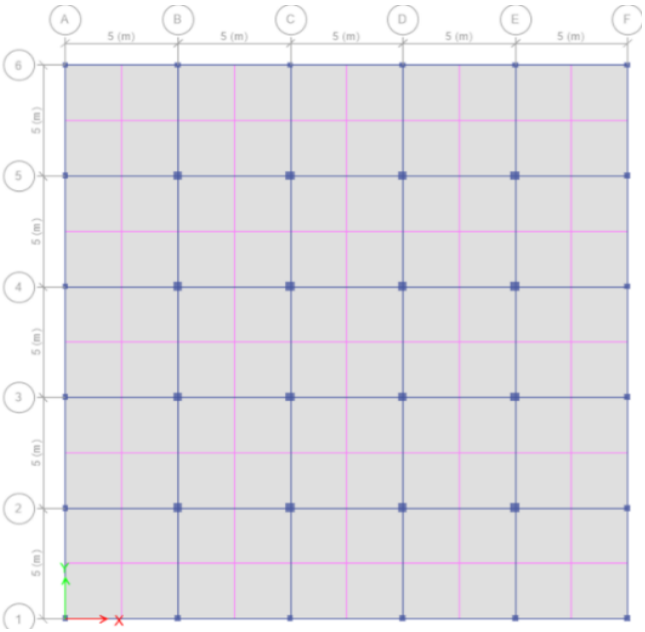

Figure 2. Plan of 8-story building (Conventional slab/ Type A)

Table 3. Building parameters (Type B)

Parameter	Slab Systems Conventional Slab	Flat Slab
Dimension of the building (Length and width)	30m×30m	30m×30m
Length of each span (X-direction)	6m	6m
Length of each span (Y-direction)	6m	6m
Number of spans	5 Row & 5 Column	5 Row & 5 Column
Story height	3.2m	3.2m
Number of stories	8	8
Slab thickness	180mm	210mm
Beam size	350mm×450mm	--------
Column size (corner)	470mm×470mm	410mm×410mm
Column size (exterior)	510mm×510mm	450mm×450mm
Column size (interior)	590mm×590mm	530mm×530mm

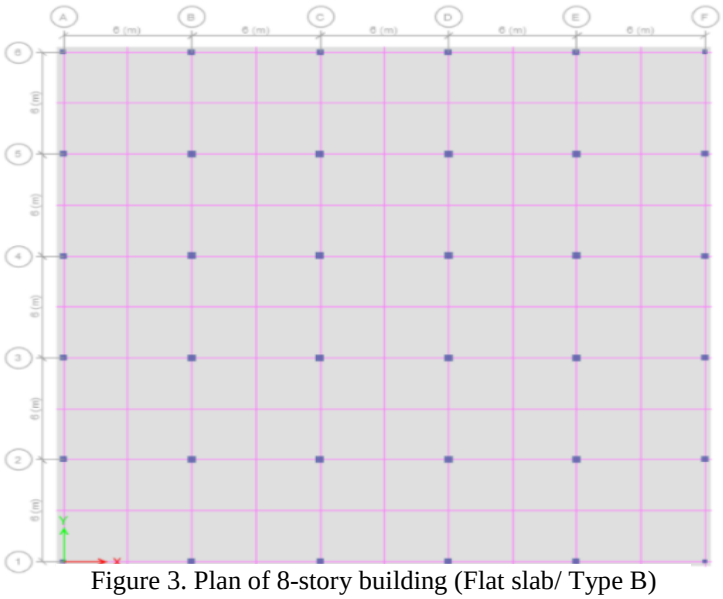

Figure 3. Plan of 8-story building (Flat slab/ Type B)

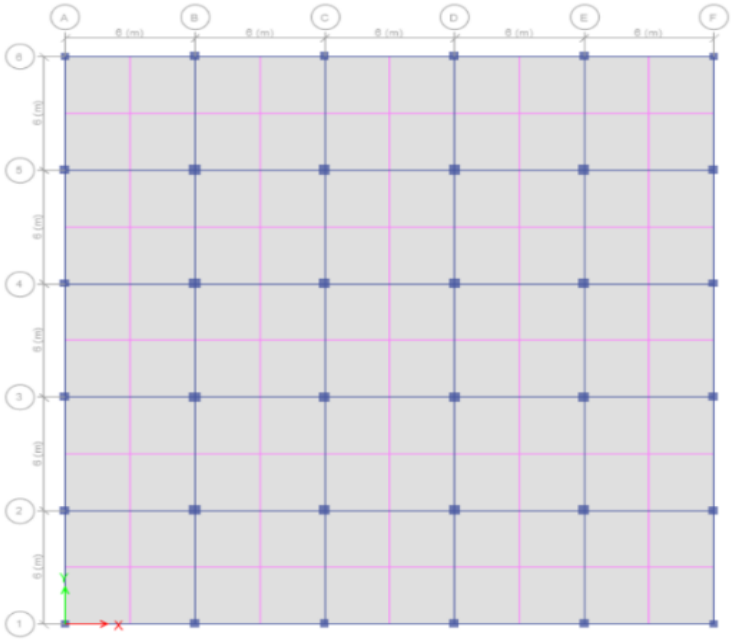

Figure 4. Plan of 8-story building (Convectional slab/ Type B)

Table 4. Building parameters (Type C)

Parameter	Slab Systems	
	Conventional Slab	Flat Slab
Dimension of the building (Length and width)	35m×35m	35m×35m
Length of each span (X-direction)	7m	7m
Length of each span (Y-direction)	7m	7m
Number of spans	5 Rows & 5 Columns	5 Rows & 5 Columns
Story height	3.2m	3.2m
Number of stories	8	8
Slab thickness	210mm	240mm
Beam size	390mm×490mm	--------
Column size (corner)	500mm×500mm	440mm×440mm
Column size (exterior)	540mm×540mm	480mm×480mm
Column size (interior)	620mm×620mm	560mm×560mm

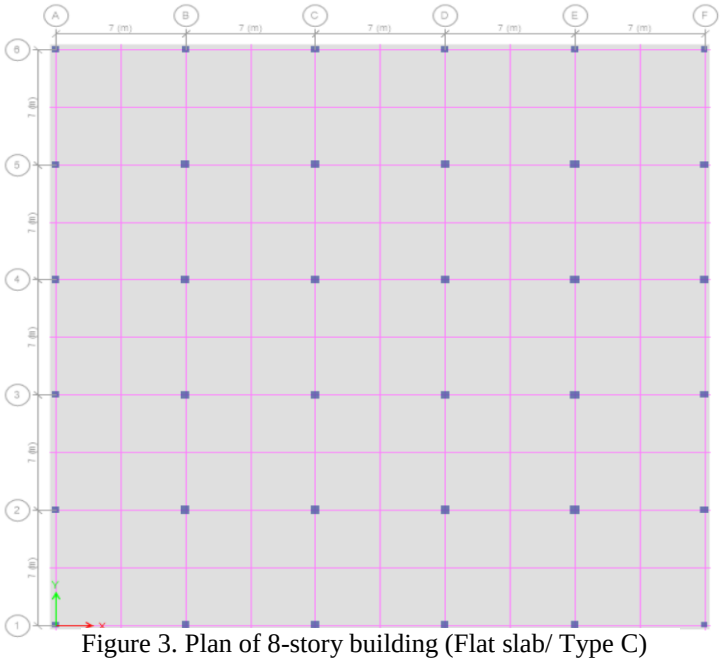

Figure 3. Plan of 8-story building (Flat slab/ Type C)

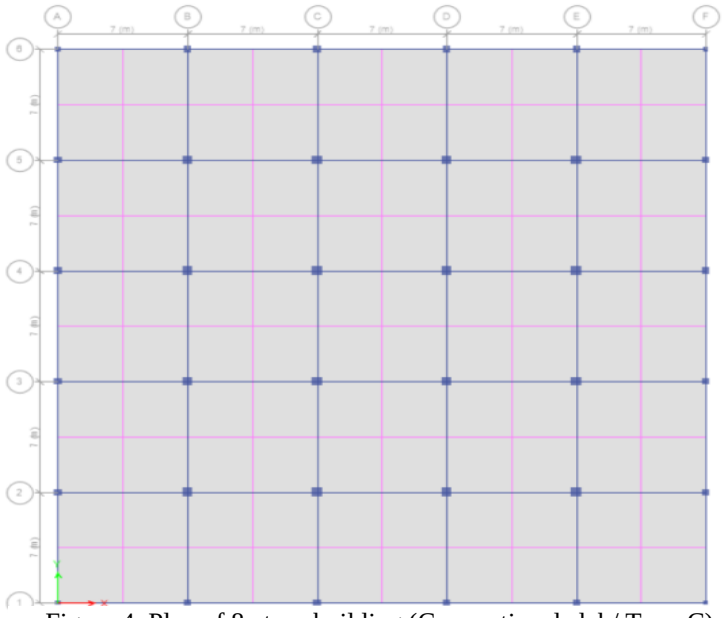

Figure 4. Plan of 8-story building (Conventional slab/ Type C)

Results and Discussion

The results include bending moment, shearing force, punching shear force, and deflection of different models shown in Table 5. As shown in Table 5, all plot sizes of the flat slab structures have greater bending moment, shearing force, and deflection with respect to conventional slab structures. Increasing the span length/plot size increases the punching shear in flat slab structures. It should be noted that the punching shear value is within the permissible limit for all plot size models in this study. The required weight of steel reinforcement, the required volume of concrete, and the required area of the formwork have been evaluated for all cases. The results are shown in the following figures.

Table 5. Analysis of results for all cases

Parameter `	Slab Systems					
	Conventional Slab			Flat Slab		
Plot Size	25m×25m	30m×30m	35m×35m	25m×25m	30m×30m	35m×35m
Span Length (m)	5	6	7	5	6	7
Slab Thickness (mm)	160	180	210	180	210	240
Bending Moment (kN.m)	38.1	66.8	92	52.6	94.3	149.7
Shearing Force (kN)	41.6	90.4	93.3	96.8	156.2	160.5
Punching Shear (kN)	-------	------	------	0.74	0.84	0.99
Deflection (mm)	1.927	2.230	3.427	3.874	5.045	5.719

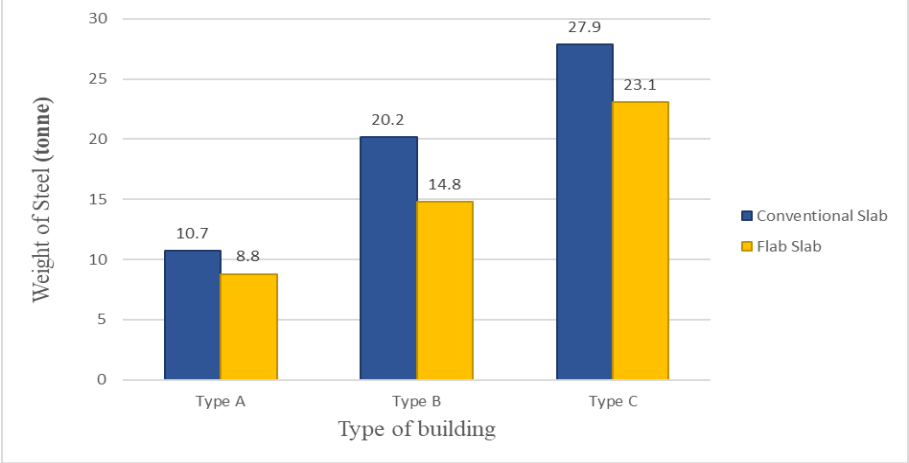

Figure 7. Weight of required steel for all cases

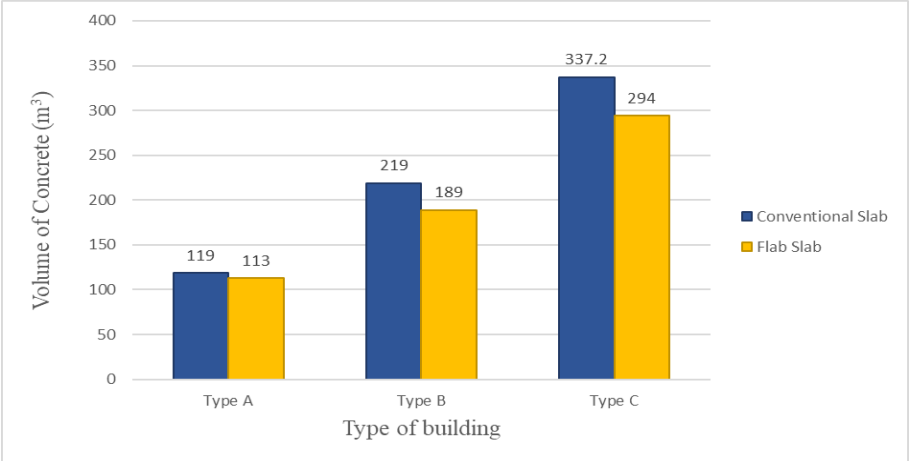

Figure 8. The volume of required concrete for all cases

As shown in the figures, the volume of concrete for a flat slab is 5% to 14% less than that of a conventional slab structure, and the required weight of steel reinforcement for a flat slab is 18% to 27% less than that of a conventional slab structure, and the required area of formwork for a flat slab is 22% to 25% less than that of a conventional slab structure. Market rates are used to calculate the total cost of steel, concrete, and formwork

used in flat slab and conventional slab systems. The price of steel and concrete in the Somali market is 950 $/ton and 135 $/m^3 respectively and the formwork rate is 25 $/m^2. Figure 10 shows the total cost of the conventional slab and flat slab structures for all cases.

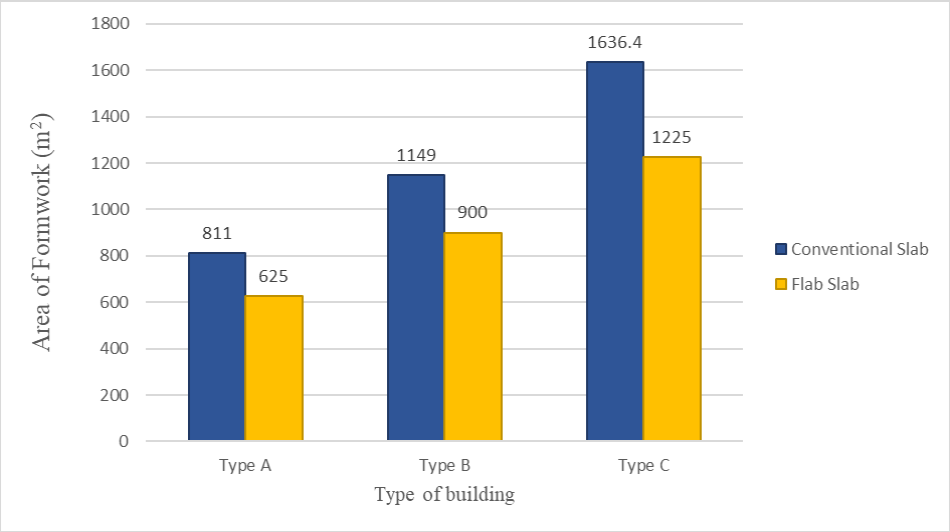

Figure 9. Area of required formwork for all cases

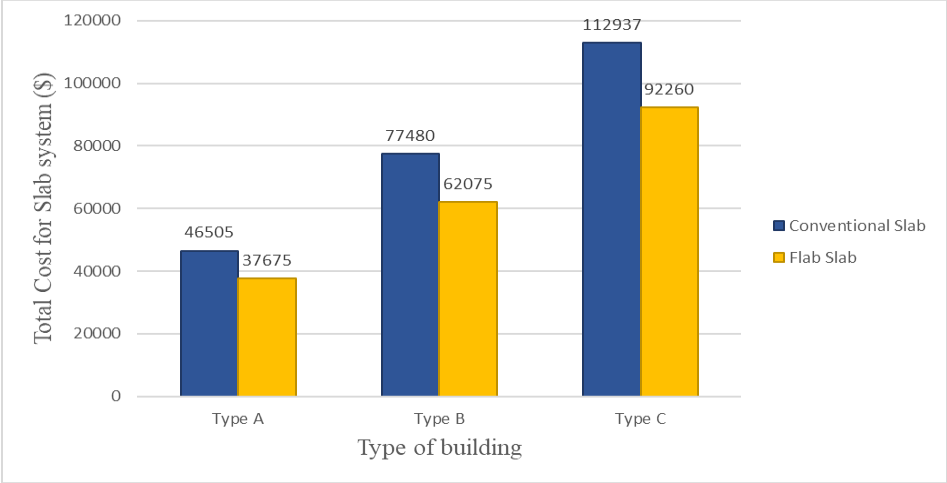

Figure 10. The total cost of the slab system for all cases

As shown in Figure 10, the total cost of flat slab structures is about 18.3% to 19.9% lower compared to conventional slab structures. Therefore, flat slab structures are more economical in terms of the cost of materials compared to conventional slab structures.

Conclusions

The results of the analysis lead to the following conclusions:

- Compared to conventional slab structures, flat slab structures are subjected to higher bending moment, shearing force, and deflection.
- The punching shear value is within the permissible limit. Therefore, the depth of the slab is sufficient for flat slab systems.
- The punching shear failure in flat slab structures is not critical in this study, but if punching shear becomes critical, drop panels, shear reinforcement, and increasing the sections of slab and column are required.
- As the span length increases, bending moment, shearing force, and deflection increase.

- A flat slab structure is more economical than a conventional slab structure. The cost of a flat slab system is 18.3% to 19.9% less than a conventional slab.
- For high-rise buildings, flat slab structures are preferable over conventional slab structures in the architectural aspect. In addition, flat slab structures provide formwork flexibility, flexural reinforcement insertion ease, concrete casting simplicity, and open space for water, air, and other piping, and enhance visual appeal.

Scientific Ethics Declaration

The authors declare that the scientific ethical and legal responsibility of this article published in EPSTEM journal belongs to the authors.

Acknowledgements

* This article was presented as an oral presentation at the International Conference on Technology, Engineering and Science (www.icontes.net) held in Antalya/Turkey on November 16-19, 2022.

References

ACI (2015). *An ACI Standard: Commentary on Building Code Requirements for Structural Concrete (ACI 318R-14), (Building Code Requirements for Structural Concrete (ACI 318–14) an ACI Report*. American Concrete Institute.

American Society of Civil Engineers (2017). *Minimum design loads for building and other structures ASCE/SEI 7-16*. Reston, VA: American Society of Civil Engineers.

Borkar, S., Dabhekar, K., Khedikar, I., & Jaju, S. (2021). Analysis of flat slab structures in comparison with conventional slab structures. *IOP Conference Series: Earth and Environmental Science, 822*(1), 012049. https://doi.org/10.1088/1755-1315/822/1/012049

Madavi, S. D., & Gajbhiye, S. M. (2020). Comparative analysis of flat slab and grid slab. *International Journal of Creative Research Thoughts (IJCRT),8*(7). 5401-5417.

Peurifoy, R.L., & Oberlender, G.D. (2014). *Estimating construction costs*. Boston: McGraw-Hill Higher Education.

Sathawane, A. A., & Deotale, R. S. (2011). Analysis and design of flat slab and grid slab and their cost comparison. *International Journal of Engineering Research and Applications*, *1*(3), 837-848.

Sawwalakhe, A. K., & Pachpor, P. D. (2021). Comparative study of conventional slab, flat slab, and grid slab using ETABS. *IOP Conference Series: Materials Science and Engineering, 1197*(1), 012020. https://doi.org/10.1088/1757-899x/1197/1/012020

Serbanoiu, A. A., & Grădinaru, C. M. (2020). *Construction cost estimate: Practical work guide*. Napoca: Cluj.

Author Information

Shafie IBRAHIM
Near East University
Near East University, Near East Boulevard, Nicosia, TRNC, Mersin 10 – Turkey, ZIP: 99138

Shaghayegh OSTOVAR RAVARI
Near East University
Near East University, Near East Boulevard, Nicosia, TRNC, Mersin 10 – Turkey, ZIP: 99138
Contact e-mail: *sh.ostovar987@gmail.com*

Rifat RESATOGLU
Near East University
Near East University, Near East Boulevard, Nicosia, TRNC, Mersin 10 – Turkey, ZIP: 99138

To cite this article:

Ibrahim, S., Ostovar-Ravari, S., & Resatoglu, R. (2022). Comparative study of analysis and cost of flat slab and conventional slab structures in Somalia-Mogadishu. *The Eurasia Proceedings of Science, Technology, Engineering & Mathematics (EPSTEM), 21*, 228-236.

The Eurasia Proceedings of Science, Technology, Engineering & Mathematics (EPSTEM)
ISSN: 2602-3199

The Eurasia Proceedings of Science, Technology, Engineering & Mathematics (EPSTEM), 2022

Volume 21, Pages 237-240

IConTES 2022: International Conference on Technology, Engineering and Science

Improved Energy Efficiency of Lithium-Air Batteries by using Alloy Based Anode and Photocatalyst Loading Cathode

Ersu LOKCU
Eskisehir Osmangazi University

Resat Can OZDEN
Eskisehir Osmangazi University

Mustafa ANIK
Eskisehir Osmangazi University

Abstract: The development of high energy density batteries has been rapidly advanced by the increasing energy demand of the modern world. The lithium-air batteries have great interest due to their having the highest energy density compared to the other battery technologies. However, the large implementation of lithium-air batteries is hindered using metallic Li anode, leading to low coulombic efficiency, low energy efficiency and safety problems. In this study, to improve the performances of these batteries, we designed the lithium-air battery by integrating the Li-Si based alloy anode and photo-catalyst loading porous carbon cathode. The results show that the designed lithium-air battery has low over potential through the extended cycling stability. The working voltage of the cell is below 2.5 V. This study indicates that the developed the lithium-air battery with higher coulombic efficiency and lower polarization values is the alternatives to the conventional lithium-air batteries, which comprise metallic Li anode and carbon-based cathode.

Keywords: Alloy anode, Photoassisted charging, Lithium-air battery

Introduction

Li-air batteries have attracted great research attention because of their theoretically promising energy density in addressing the expanding energy storage demand (Imanishi & Yamamoto, 2019). However, there are numerous technical obstacles to developing an efficient lithium-air battery. Mainly, the Li-air cells have a low practical specific energy due to their poor rate capabilities (Wang et al., 2019). The high overpotentials that occur during the charge-discharge process in Li-air batteries cause low energy efficiency (Wang et al., 2019; Imanishi & Yamamoto, 2019). Due to the considerable electrode and electrolyte decomposition brought on by these high overpotentials, the Li-air cell life is quite short. On the other hand, using very reactive metallic lithium as an anode involves various problems such as dendritic growth, O_2 crossover and low coulombic efficiency (CE) in Li-air cells. In the literature, many studies have been carried out on anode, cathode and electrolyte in order to solve to these problems (Wang et al., 2019).

Among the developed strategies related to the anode side, the use of alloy anodes is considered as very promising in elimination of many handicaps arise from the use of metallic Li anode without sacrificing the theoretical specific capacity (Li et al., 2020). Another strategy developed in Li-air batteries is to both reduce the charging voltages (<4.2 V) and extend the cycle life by using bifunctional cathodes which is quite an interesting approach. These bifunctional cathodes are formed by integrating photocatalytic (semiconductor) materials into the carbon matrix. The use of these bifunctional cathodes also introduced the concept of photo-assisted charging of Li-air batteries. During the photo-assisted charging process, electrons and holes are produced as a result of

light's excitation of the semiconductor. Due to the greater potential of the semiconductor's valence band (VB), the holes have the ability to convert the reduction state cathode into an oxidation state cathode. On the other hand, with the help of external electrical bias, the photo-generated electrons can convert M^+ to metallic M at the anode (Yan & Gao; 2022).

Herein, we developed the metal-air cell by integrating the Li-Si based alloy anode and photo-catalyst loading porous carbon cathode (g-C_3N_4/rGO) to improve the performances of Li-air batteries. The usage of a bifunctional cathode with Li-Si based alloy anode in the Li-air battery resulted in a considerable reduction in the charge potential and improved the battery cyclic performance.

Method

$Li_{22}Si_5$ alloy was synthesized by mechanical alloying. Silicon powders and Li granules were weighted in Ar atmosphere in the stoichiometric ratios. The mixtures of the powders were then put into a stainless steel vial together with the stainless steel balls in the ball to powder ratio of 100:1. The mechanical alloying was carried out by using planetary ball mill (Fritsch Pulverisette 7 Premium Line) at 500 rpm for 2 h. To prepare g-C_3N_4/rGO bifunctional cathode, melamine and rGO were mixed in methanol. After complete mixing and drying step, melamine and rGO were put in a crucible with a cover and heated up to 550 °C at a rate of 3 °C min^{-1} under Ar atmosphere and then kept at this temperature for 3 h. The more detailed active material syntheses are reported in our previous works (Lökçü et al., 2021;2022).

The alloy anode was prepared by mixing the as-synthesized alloy with Cu powders (40:60 vol%) by using the planetary ball mill and then they were pressed into a pellet with a diameter of 15 mm in the glove box. The cathodes were prepared by mixing g-C_3N_4/rGO and poly (vinylidene fluoride) (PVDF) (80:20 wt%) in the 1-methyl-2-pyrrolidone (NMP).
The discharge and charge tests were performed in 0.5 M $LiClO_4$:TEGDME:0.05 M LiI electrolyte galvanostatically, and the discharge cutoff potential was 2.0 V Li^+/Li. The charge cutoff potentials were 3.6 and 4.2 V Li^+/Li for the photoassisted and dark charging, respectively.

Results and Discussion

The developed metal-air cells were discharged and charged at 200 mA g^{-1} for 50 cycles to investigate their cyclic stability and energy efficiency. Figure 1 shows the electrochemical performance of the cell under dark charging conditions. Compared to metallic lithium in Li-air batteries, the discharge potential of the battery has decreased from 2.8 V Li/Li^+ - 2.7 V Li/Li^+ () band to 2.6 V Li/Li^+ - 2.5 V Li/Li^+ band when the $Li_{22}Si_5$ alloy anode is used (In Figure1). However, the decrease in capacity value in this cell started at the end of 16 cycles. Moreover, the overpotential value of the cell, which was initially 0.7 V, increased to 1.7 V with the increasing number of cycles.

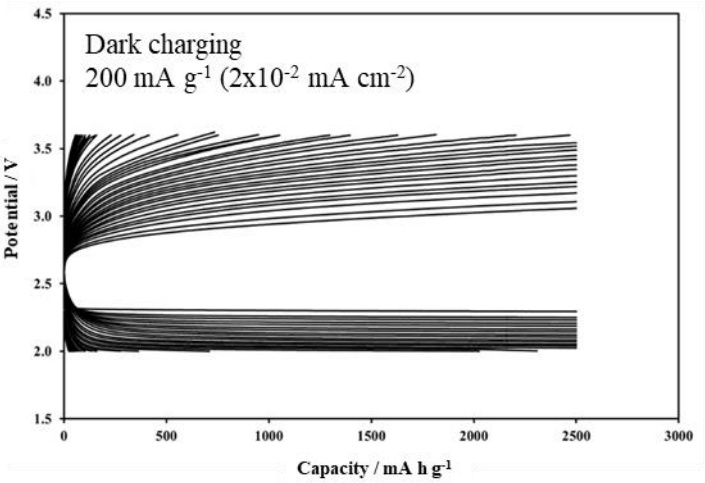

Figure 1. Discharge and charge curves gathered at 2500 mA h g^{-1} (0.25 mA h cm^{-2}) fixed capacity and 200 mA g^{-1} ($2x10^{-2}$ mA cm^{-2}) current density under dark charging conditions for 50 cycles.

Figure 2 shows the electrochemical performance of the cell under photoassisted charging conditions. While the charge potential decreases with the aid of visible light in the photoassisted charging process, it can also increase the discharge potential by the same mechanism. Obviously, photoassisted charging opens a new pathway to overcome the high overpotential problem in the Li-air batteries (Lökçü et al., 2022; Yu et al., 2014). Furthermore, the cell maintains its 2500 mA h g^{-1} capacity for 50 cycles. Hence, the electrochemical performance of the developed metal-air cell with $Li_{22}Si_5$ alloy anode and bifunctional cathode improves considerably under photoassisted charging conditions.

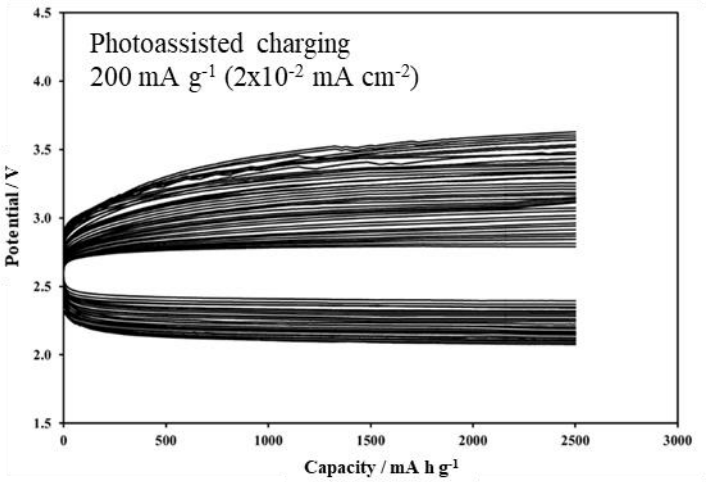

Figure 2. Discharge and charge curves gathered at 2500 mA h g^{-1} (0.25 mA h cm^{-2}) fixed capacity and 200 mA g^{-1} ($2x10^{-2}$ mA cm^{-2}) current density under photoassisted charging conditions for 50 cycles.

Conclusion

The developed metal-air cell with lower polarization values is the alternative to the lithium-air batteries configuration, which comprise a metallic Li anode and carbon-based cathode. This work demonstrated that the photoassisted charging with the efficient bifunctional cathode may open an essential path for the researchers to conduct extensive studies to approach the ultimate goal of commercializing Li-air batteries.

Scientific Ethics Declaration

The authors declare that the scientific ethical and legal responsibility of this article published in EPSTEM journal belongs to the authors.

Acknowledgements

* This article was presented as an oral presentation at the International Conference on Technology, Engineering and Science (www.icontes.net) held in Antalya/Turkey on November 16-19, 2022.

References

Imanishi, N., & Yamamoto, O. (2019). Perspectives and challenges of rechargeable lithium–air batteries. *Materials Today Advances*, *4*, 100031. https://doi.org/10.1016/j.mtadv.2019.100031

Lökçü, E., & Anik, M. (2021). Synthesis and electrochemical performance of lithium silicide based alloy anodes for Li–ion oxygen batteries. *International Journal of Hydrogen Energy*, *46*(18), 10624–10631. https://doi.org/10.1016/j.ijhydene.2020.12.179

Lökçü, E., Kaçar, N., Çayirli, M., Özden, R. C., & Anik, M. (2022). Photoassisted charging of li-ıon oxygen batteries using g-c3n4/rgo nanocomposite photocatalysts. *ACS Applied Materials and Interfaces*, *14*(30), 34583–34592. https://doi.org/10.1021/acsami.2c05607

Li, H., Yamaguchi, T., Matsumoto, S., Hoshikawa, H., Kumagai, T., Okamoto, N. L., & Ichitsubo, T. (2020). Circumventing huge volume strain in alloy anodes of lithium batteries. *Nature Communications*, *11*(1), 1–8. https://doi.org/10.1038/s41467-020-15452-0

Wang, C., Xie, Z., & Zhou, Z. (2019). Lithium-air batteries: Challenges coexist with opportunities. *APL Materials*, *7*(4). https://doi.org/10.1063/1.5091444

Yan, N., & Gao, X. (2022). Photo-assisted rechargeable metal batteries for energy conversion and storage. *Energy and Environmental Materials*, *5*(2), 439–451. https://doi.org/10.1002/eem2.12182

Yu, M., Ren, X., Ma, L., & Wu, Y. (2014). Integrating a redox-coupled dye-sensitized photoelectrode into a lithium-oxygen battery for photoassisted charging. *Nature Communications*, *5*(May), 1–6. https://doi.org/10.1038/ncomms6111

Author Information

Ersu Lökçü
Eskisehir Osmangazi University
Department of Metallurgical and Materials Engineering, 26040,
Eskisehir, Turkey
Contact e-mail: *elokcu@ogu.edu.tr*

Resat Can Ozden
Eskisehir Osmangazi University
Department of Metallurgical and Materials Engineering, 26040,
Eskisehir, Turkey

Mustafa Anik
Eskisehir Osmangazi University
Department of Metallurgical and Materials Engineering, 26040,
Eskisehir, Turkey

To cite this article:

Lokcu, E., Ozden, R.C., & Anik, M. (2022). Improved energy efficiency of lithium-air batteries by using alloy based anode and photocatalyst loading cathode. *The Eurasia Proceedings of Science, Technology, Engineering & Mathematics (EPSTEM), 21*, 237-240.

The Eurasia Proceedings of Science, Technology, Engineering & Mathematics (EPSTEM)
ISSN: 2602-3199

The Eurasia Proceedings of Science, Technology, Engineering & Mathematics (EPSTEM), 2022

Volume 21, Pages 241-247

IConTES 2022: International Conference on Technology, Engineering and Science

Threat and Vulnerability Modelling of Malicious Human Interface Devices

Mathew NICHO
Zayed University

Ibrahim SABRY
Zayed University

Abstract: The threats posed by malicious Human Interface Devices (HID) have greater potential for harm owing to the inherent trust given to them by the respective Operating Systems (OS). While HIDs vary in terms of hardware and software, the OS detects them as genuine, providing access to the malicious HID to perform and execute privileged actions as if it came from a genuine user. Since the threat can bypass normal security controls, it poses a significant challenge to security managers. While the insider (both unintentional and malicious) threat level posed by the malicious HIDs is high, research in the domain of mapping HIDs to HID attack vectors and the exploited vulnerabilities is scarce, which is evident from the paucity of research outputs in a Google Scholar search. Accordingly, the objective of this research is to create a model that maps HIDs to vulnerability categories aligned to attacks. In this connection, the paper proposes an HID Threat Vulnerability model (HidTV) that identifies the malicious HID types and evaluates the nature of HID related threats and the corresponding vulnerabilities that are exploited. The resulting model can provide security managers with a visibility of critical vulnerabilities, map specific HIDs to threats and vulnerabilities and formulate security policies to defend and mitigate against these threats. From an academic perspective, the paper provides a foundation for researchers to evaluate and propose detective and mitigation strategies for specific attack paths. While there are genuine uses for HIDs, this paper focuses on the ways they can be intentionally exploited for malicious purposes.

Keywords: Human interface device (HID), Malicious HID, HID threats, HID vulnerabilities.

Introduction

The flexibility of the USB protocol and the inherent trust given by Windows, Mac and Linux operating systems to Human Interface Devices (HIDs), mainly keyboards and mice, can be maliciously leveraged to create multiple threat vectors that can directly perform malicious activities on a system as though it were performed by a logged-in user (OPSWAT, 2014). Similarly, wired HIDs as well as Bluetooth enabled devices could stealthily switch from a legitimate profile to the HID profile, emulating the behaviour of a Bluetooth keyboard and a Bluetooth mouse by injecting keystrokes, mouse movements and click events (Xu et al.,2019).

The malicious nature of HIDs can be attributed to the development of a technology based on the Universal Serial Bus (USB) HID protocol that attacks computer systems (Zhao & Wang, 2019). Since the USB-based attacks often abuse the trust-by-default nature of the ecosystem and transcend different layers within a software stack, none of the existing defences provide a complete solution (Tian et al., 2018). Of the global population of 7.11 billion, 5.07 are connected to the Internet, representing 63.5% of the population as of October 2022 (Datareportal, 2022). From a Windows Operating Systems (OS) perspective, there are 1.4 billion active devices running Windows 10 or Windows 11 monthly (Microsoft Inc, 2022), thus presenting an enormous opportunity for hackers to penetrate computer systems and smartphones using malicious HIDs.

HID, is a form of computer device used by humans to take in input and generate the required output. The primary function of an HID is to act as an electronic information system involved in the activities of data input and data output. HIDs use the USB protocol that has a default polling rate of 125 Hz with high responsiveness and lower latency, thus giving an edge for manipulation. Forming the larger part of the hardware and peripheral system of a computer setup, HIDs include headsets, USBs, webcams, speakers and mice (Karystinos et al., 2019). The fact that HIDs have the ability to provide a relational interface between computer systems and users makes them vulnerable to attack exploitation. This occurs because these devices are commonly used to access sensitive operations that require high authorisation (ibid). Thus, cyber hackers have been able to integrate malicious and anomalous HIDs whose main function is to imitate how users control their computer systems. Malicious HIDs have presented considerable challenges in the field of information security, as multiple ranges of systems have been able to neglect the security risks they pose.

Attacks using HIDs are not easily performed by external entities due to the lack of physical access to organisational networked assets, but they can be deployed as insider threat vectors (malicious), or a hacker can leverage an unsuspecting user to connect the HID to the system. In this respect, USB devices have been leveraged as a delivery mechanism for host-side exploits, where the attackers target the USB stack by embedding malicious code in device firmware to covertly request additional USB interfaces, providing unacknowledged and malicious functionality that lies outside the apparent purpose of the device (D. J. Tian, Bates, & Butler, 2015). Functionality also plays a role where the success and widespread use of the USB protocol that connects keyboards, mouse devices, printers, webcams and several other computer peripherals can be attributed to the bus characteristics, such as simplicity, ‘plug & play’ features, ‘hot plug’ support and, particularly, the possibility of supplying power to the devices (Depari et al., 2008). In this respect, current detection and prevention solutions related to HID largely tend to concentrate on specific attacks or fail to provide a comprehensive and effective solution (Nissim et al., 2017).

Academic research on the threats, vulnerabilities and attacks specifically attributed to HIDs is scarce, as is evident from the search results on Google Scholar (since 2005). Using the phrases (without quotes) ‘Human Interface Device attacks’, ‘HID attacks’, ‘HID vulnerabilities’ and ‘Human Interface Device vulnerabilities’ presented 13, 3, 2 and 6 outputs, respectively (October 2022). Hence, while multiple studies have focused on USB hardware attacks and vulnerabilities, comprehensive research on aligning the HIDs with the associated vulnerabilities that can be exploited to execute the attack is lacking in both the academic and professional fora. Accordingly, the objective of this research is to create a model that maps HIDs to vulnerability categories aligned to attacks.

Review of Malicious HIDs

Malicious HIDs are categorised into three types in relation to their primal technique. They are wireless communication malicious HIDs, HID interface composite devices and pure HIDs. Wireless communication malicious HIDs work under the functionality that the corrupted HIDs operate through wireless communication signals (Zhao & Wang, 2019). Normally, the wireless signals are transmitted through a short-range radio using medium waves. Some of the wireless communications include Wi-Fi and Bluetooth communication. The devices that will use the wireless communication include Bluetooth and Wi-Fi mice and Bluetooth and Wi-Fi keyboards. On the other hand, composite interface malicious HIDs are devices that have been partially corrupted. In essence, they refer to original HIDs that are corrupted with manipulative files, such as malicious payloads. Finally, pure HIDs are common everyday devices that are used to interact with systems, such as mice, keyboards and audio headsets (Zhao & Wang, 2019).

Leveraging Malicious HIDs

Maliciously crafted HIDs include the Programmable HID USB Keystroke Dongle (PHUKD), USB ninja, Wi-Fi HID injector (WHID), the rubber ducky, the BadUSB and the skimmers. The PHUKD, a small hardware device that uses the Teensy microcontroller development board, allows the device to mimic keystrokes and mouse macros, thus bypassing security controls. The device can execute itself when the device is plugged into the target system or can be programmed to execute after a set time or when certain environmental conditions are met. Since the PHUKD acts like mice and keyboards, it does not require administrative privileges to be installed and function, thereby enabling the hacker to leverage it for malicious activities (Crenshaw, 2011). However, the USB ninja, a penetration and information security tool that is used for vulnerability analysis and penetration testing (VAPT), can also be leveraged for malicious methods. It works like a regular USB cable for the pairing

functions of data and power but alters its normal functionality whenever the choice of an attack payload is triggered by a wireless remote controller to the victim's computer system (Pescatore, 2019). The attack pattern involved with the deployment of the USB ninja is triggered by a concealed Bluetooth device within the cable. Whenever the device receives the command, the cable transitions from a normal USB cable to a malicious attacker by emulating a USB mouse or keyboard. The payload with the use of USB ninja devices is customisable, where Arduino IDEs can be employed in payload creation (ibid). The need for affordable and dedicated hardware gave rise to the WHID, after which it could be remotely controlled to perform its primal attacks as a malicious HID attacker. The core of the device constitutes an ESP-12s that is capable of offering Wi-Fi access (Hong, Kim, & Kim, 2019). The attack pattern involved with the deployment of the WHID is based on the creation of new payloads that could be stored locally on mobile devices, thus eliminating the need for memory injection through uploading onto the WHID. In addition, this technique of storing the payload locally makes it more strategic for the attacker, as it becomes harder for forensic analysis to trace the attack (Golushko & Zhukov, 2020).

The rubber ducky is an HID that physically imitates a USB flash drive. When plugged into a computer's serial interface, the computer configures it as a USB keyboard and accepts the input of electronic signals as keystroke commands as with the functions of a normal keyboard (Arora et al., 2021). The rubber ducky has been used by attackers in cyber adversary activities, such as webserver attacks and user login credential harvesting. The method of attack a rubber ducky uses is to incorporate keystroke technology through various injection methods so that anomalous and malicious code is executed seamlessly and rapidly on a device (Arora et al., 2021). The rubber ducky uses the ducky script as its default programming language for the execution of its payload, which is usually stored on the SD card. The BadUSB exploit that was first demonstrated at the 2014 Black Hat conference (Nohl et al., 2014) exploits USB firmware vulnerability by re-programming the USB device to imitate an HID. BadUSBs are a cyber-security threat that involves the use of malicious USB devices that are corrupted with an anomalous software. The attacker re-programs the microprocessor (Ex. Intel 8051 microcontroller) and alters its main function of a data storage device to a malicious manipulative tool (Zhao & Wang, 2019). Using Internet of Things (IoT) devices such as Raspberry Pi Pico and Intel 8051, the micro controller's logic circuit programming is altered, and the primal functioning as a simple IoT device is transformed to be used in cyber-attacks. Furthermore, HID methodology is also used for card skimming, a process where the data and information found in magnetic stripes on debit or credit cards are copied and duplicated using skimmer devices (Scaife et al., 2018). The method of attack of skimmer devices is to duplicate the data and information stored in the magnetic stripe at the Point of Sales (POS) terminals. In this respect, Proxmark3 (PM3) is a standard RFID diagnostic, testing and programming tool that allows users to read, emulate, fuzz and brute force the majority of RFID protocols. The PM3 has a USB interface to the computer where it uses the default HID USB protocol (Lorenzo et al.,2019). Skimming has allowed attackers to acquire sensitive digital information of card users, especially related to their bank and financial credentials.

Vulnerabilities Exploited by HIDs

Attacks by malicious HIDs have created various weaknesses on systems, such as on operating systems and software applications, where the attacker can find weaknesses that can be exploited to satisfy their cyber needs, such as data collection. The use of malicious HIDs has exposed the field of security, where gaps in a network system such as an OS are uncovered (Zhao & Wang, 2019). Critical vulnerabilities that can be exploited include poor encryption, data misplacement, system misconfiguration, unpatched and outdated software and weak authorisation credentials. Since HIDs are not inherently malicious devices, most USB device firmware is not typically scanned by computer systems. In addition, most common antivirus software is not able to detect or defend against these types of attacks. As such, we can infer that HIDs are more susceptible to manipulation because they gain easier access to the host machine. Once connected, they can pose as a peripheral, such as a mouse or keyboard, or even simply perform the action of injecting the malicious payload or of executing a code on the host machine that would further weaken the system.

The use of malicious HIDs has revealed the existence of poor data encryption within computers, which allows attackers to intercept the communications flowing within the computers operating system. For example, using a computer for tele-communication purposes on application software systems may lead to information security breaches. This happens if end-to-end encryption is not correctly configured. Hence, when a malicious HID is plugged in (e.g. a rubber ducky), it will tap into the duplex communication pathway and steal sensitive information (Acar et al., 2019). This vulnerability is portrayed by system assets such as operating systems where their internal settings may be at risk. In addition, the application or operating system settings may differ in terms of security. For example, skimmers are deployed by cybercriminals on account of the vulnerability of system

misconfigurations. This happens because the magnetic stripes on the ATM cards have not been equipped with enough security configurations that will enable them to evade the threat of credit card skimming (Scaife et al., 2018). Operating systems that are not updated regularly are highly vulnerable to the use of malicious HIDs. This is because the unpatched software is out of date and thus security configurations within the system application software will not be supported by the Vendor OS. As such, cybercriminals tend to track users with unpatched or outdated system software, as it will be easy to compromise, access and retrieve sensitive information and data (Zhao & Wang, 2019). Cybercriminals can also brute force themselves into a network, bypassing firewalls by guessing passwords and user credentials. The fact that credentials are weak and can be guessed provides a seamless entry to penetrate organisational systems. Figure 1 summarises the vulnerabilities and associated attack vectors.

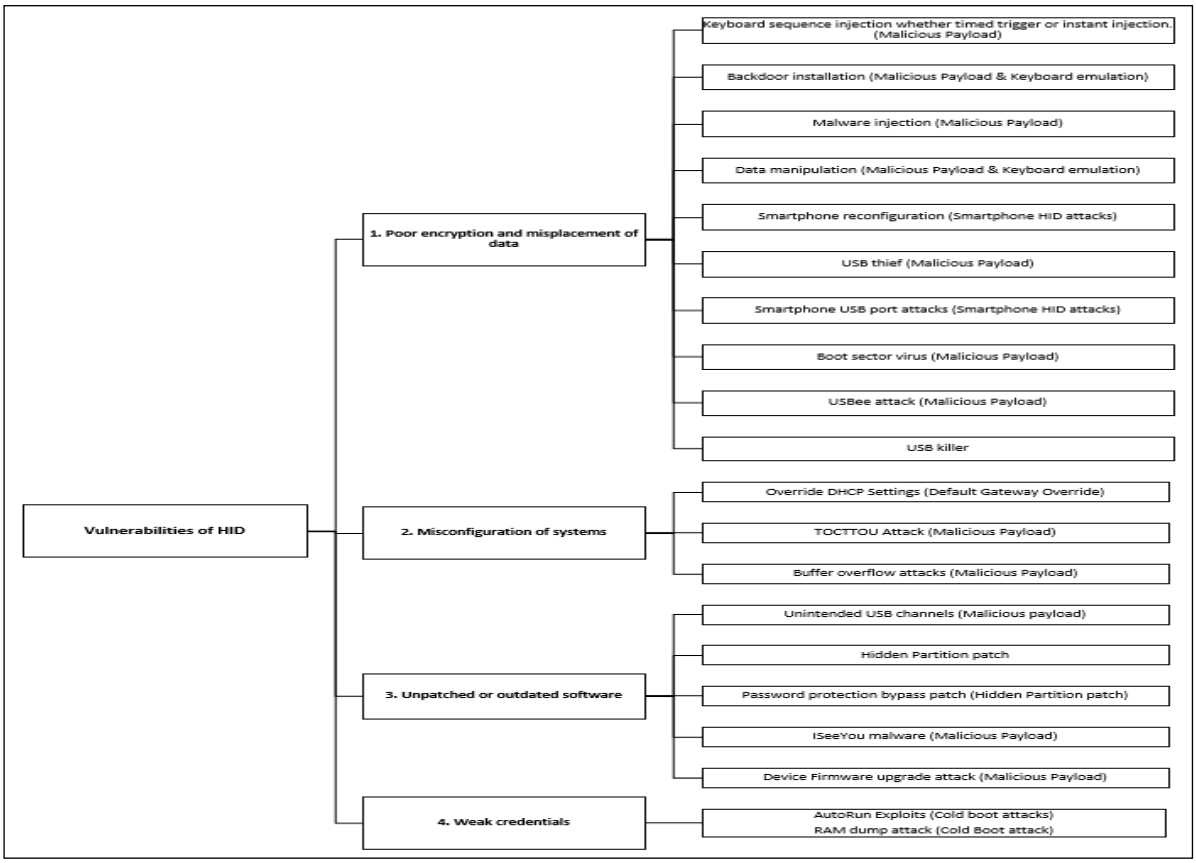

Figure 1. A classification of HID attacks attributed to system vulnerabilities

Threats from Malicious HIDs

Threats from malicious HIDs include system infections, keyboard emulations, smartphone-based attacks, cold boot attacks, default gateway overrides and hidden partition patches. Malicious HIDs have been able to spread malicious payloads into computer systems and software. Examples of such malicious HIDs are BadUSBs and rubber ducky USBs. The payload is stored as a program within the logic memory of the drives and gets injected into the computer once the drives are plugged in. Thereafter, malicious commands are sent to the computer, leading to the spread of different payloads, such as viruses, worms or Trojans (Nissim et al., 2017). Keyboard emulation is a form of attack executed through the use of a rubber ducky, where keystroke injections are spoofed and imitated using a normal USB device. In smartphone-based HID attacks, the smartphone can be used as a rubber ducky against Android or Windows, where the attacker's smartphone serves as a connected keyboard (Wang & Stavrou, 2010). For this form of attack, Android drivers that interact with Android related devices are overwritten and their interaction with Android devices is altered. The drivers are configured to interact with devices such as keyboards and mice, so that they can be used as gateways for cyber adversary practices (Nissim et al., 2017; Bojovic et al., 2019). In the cold boot attack, also known as the RAM dump attack, a USB drive plugged into a computer is used to retrieve dynamic data from secondary memory. This is achieved by incorporating a memory dumper that extracts data that has been left over from secondary memory. This mostly happens when booting is done through a USB device (Anderson & Anderson, 2010). The Default

Gateway Override attack is performed through programmable logic circuits or microcontrollers, which are programmed to act as a USB flash drive that will be identified by the computer as a normal USB. Once the USB is plugged into the USB port, the microcontroller emulates a USB Ethernet adapter, which hijacks local traffic by overriding DHCP configuration (Rodríguez Ocasio, 2019). However, in the hidden partition patch attack, the objective is to determine how a covert and concealed storage partition located within a USB could be achieved through reprogramming. This covert partition allows the USB to store ex-filtered data from the connected computer (Anderson & Anderson, 2010). Table 1 links the multiple HID attack vectors with the corresponding HIDs used to carry out the attacks. Numerical values are assigned to each malicious HID below.

USB ninja – USB cable with Bluetooth capability that can receive transmissions from other Bluetooth enabled devices in order to implement malicious payloads or scripts.

1. *Wi-Fi HID WHID injector* – wireless peripheral that can be reprogrammed to deliver malicious payloads wirelessly.
2. *Rubber ducky* – USB enabled HID that can imitate a peripheral such as keyboard or mouse in order to take control of the host machine.
3. *BadUSB* – reprogrammed microcontroller that can deliver malicious payloads or run malicious scripts.
4. *Skimmers* – devices used to mimic the appearance of HIDs and are used to scan magnetic strips in order to extract the information stored on them.

Table 1. Mapping HID attack vectors with the HIDs

Attacks	HIDs	Reference
Malicious payload	1,2,3,4	(Nissim et al., 2017; Zhao & Wang, 2019)
Keyboard emulation	3,5	(Nissim et al., 2017; Bojovic et al., 2019))
Smartphone-based HID attacks	1,2	(Wang & Stavrou, 2010; Potocky & Štulrajter, 2022)
Cold boot attacks	1,4	(Anderson & Anderson, 2010; Pham et al., 2011)
Default gateway override	3,4	(Nissim et al., 2017)
Hidden partition patch	1,4	(Anderson & Anderson, 2010; Pham et al., 2011)

The HID Threat and Vulnerability Model (HidTV)

This section discusses the HidTV model (Figure 1) that aligns the three constructs – the malicious HIDs, the corresponding multiple exploitable vulnerabilities and the attacks that are targeted at the systems based on the exploitable vulnerabilities – in an effort to demonstrate the link between them. We performed a comprehensive study of five HIDs that can be leveraged to perform malicious actions, followed by four major vulnerability categories leading to six major attacks (figure xx). In this respect, a combination of these three constructs leads to 55 different attack vectors. For instance, the USB ninja HID can be leveraged to exploit three vulnerabilities, namely poor encryption, misconfiguration and malicious payload execution, leading to 10 attack vectors.

The WHID injection can be used as a potent tool to exploit three vulnerability categories, leading to 13 attack vectors. Similarly, the rubber ducky can be deployed to target three vulnerability categories, resulting in 13 attack vectors. Not far behind is the BadUSB that exploits three vulnerability categories that can initiate 11 attack vectors. However, due to its lightweight feature, the skimmer exploits just two vulnerability categories, leading to eight attack vectors. Altogether, the 55 attack vectors highlight the potential of a hacker who can leverage HIDs to bypass security controls and perform malicious operations.

An HID is a very usable and common tool endorsed by organisations and adopted by the internetworked user to interface with the computer systems. With billions of HIDs being used by internetworked users for input and output processes, they provide a seamless avenue of opportunity for hackers to leverage them as a tool for bypassing IT controls to perform and execute malicious actions. At the same time, they present a formidable challenge for IT security managers to detect, prevent and mitigate threats and attacks owing to the inherent accessibility provided by the respective operating systems, which allow the HIDs to interface with the system. As such, mapping the HID vulnerabilities and HID-leveraged attacks to specific HIDs provides valuable information for IT security administrators/managers who deal with security concerns and HID manufacturers. The model thus provides not only a detailed map and attack vector path for the HID but also illustrates the impact of these attacks on the system.

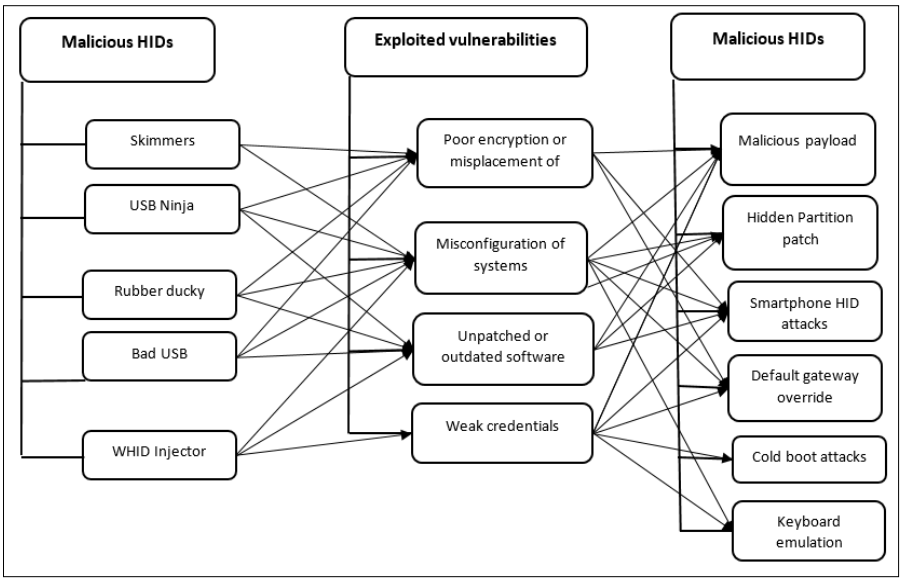

Figure 2. The HID threat and vulnerability model

Conclusion

In this paper, we conducted an extensive study on how HIDs can be leveraged to perform malicious activities, the vulnerabilities that are exploited by malicious HIDs and the attacks that can be performed. In this regard, we listed 55 attack vectors attributable to malicious HIDs. Furthermore, we aligned the HIDs to the respective system vulnerabilities that can be exploited and the corresponding attacks that can be performed. Despite their high threat potency and successful penetration of systems, malicious HIDs and their deployment are a scantily researched topic. As such, the model provides IT security managers and device manufacturers with detailed guidelines on specific areas of concern, including device misuse, the specific vulnerabilities associated with each misuse and the attacks that can be performed through the exploit. The main limitation of this research is the evolving and potential overlapping of HID categories, vulnerabilities and attacks owing to the dynamic nature of cyber-threats. One or more vulnerabilities can overlap, leading to a novel vulnerability that can be exploited that is not in this research domain. Furthermore, due to the evolving nature of HIDs, it was not feasible to incorporate the entire scope of HIDs that are available and globally used in specific industry sectors. However, future researchers could expand this model by adding and categorising HIDs from different sectors as well as adding countermeasures to the model. This would not only add considerable value to the model but also provide valuable control measures for IT managers and HID manufacturing sectors, including the IT security industry, enabling them to devise feasible solutions for countering this threat from a device perspective.

Scientific Ethics Declaration

The authors declare that the scientific ethical and legal responsibility of this article published in EPSTEM journal belongs to the authors.

Acknowledgements or Notes

* This article was presented as an oral presentation at the International Conference on Technology, Engineering and Science (www.icontes.net) held in Antalya/Turkey on November 16-19, 2022.

References

Acar, A., Lu, L., Uluagac, A. S., & Kirda, E. (2019). An analysis of malware trends in enterprise networks. *International Conference on Information Security*, 360-380.

Anderson, B., & Anderson, B. (2010). *Seven deadliest USB attacks* (1th ed.).Oxford, UK:Syngress

Arora, L., Thakur, N., & Yadav, S. K. (2021). USB rubber ducky detection by using heuristic rules. 2*021 International Conference on Computing, Communication, and Intelligent Systems (ICCCIS).*

Bojovic, P. D., Basicevic, I., Pilipovic, M., Bojovic, Z., & Bojovic, M. (2019). The rising threat of hardware attacks: USB keyboard attack case study. *7 th International Conference on Electrical, Electronic and Computing Engineering.*

Crenshaw, A. (2011). Plug and prey: Malicious USB devices. Proceedings from *ShmooCon Security Conference.*

Datareportal. (2022). *Digital around the world*. Retrieved from https://datareportal.com/global-digital-overview

Depari, A., Flammini, A., Marioli, D., & Taroni, A. (2008). USB sensor network for industrial applications. *IEEE Transactions on Instrumentation and Measurement, 57*(7), 1344-1349.

Figueroa Lorenzo, S., Añorga Benito, J., García Cardarelli, P., Alberdi Garaia, J., & Arrizabalaga Juaristi, S. (2019). A comprehensive review of RFID and bluetooth security: Practical analysis. *Technologies, 7*(1), 15.

Golushko, A. P., & Zhukov, V. G. (2020). Application of advanced persistent threat actors techniques aor evaluating defensive countermeasures. *2020 IEEE Conference of Russian Young Researchers in Electrical and Electronic Engineering (EIConRus)*,312-317.

Hong, S., Kim, K., & Kim, T. (2019). The design and implementation of simulated threat generator based on MITRE ATT&CK for cyber warfare training. *Journal of the Korea Institute of Military Science and Technology, 22*(6), 797-805.

Karystinos, E., Andreatos, A., & Douligeris, C. (2019). *S*pyduino: Arduino as a HID exploiting the BadUSB vulnerability. *15th International Conference on Distributed Computing in Sensor Systems (DCOSS 2019).*

Microsoft Inc. (2022). *Windows 10 - Microsoft by the numbers*. Retrieved from https://news.microsoft.com/bythenumbers/en/windowsdevices

Nissim, N., Yahalom, R., & Elovici, Y. (2017). USB-based attacks. *Computers & Security, 70*, 675-688.

Nohl, K., Krißler, S., & Lell, J. (2014). On accessories that turn evil. *Black Hat USA, 1*(9), 1-22.

OPSWAT. (2014, August 26). *Detecting and mitigating USB-based threats.* Retrieved from https://www.opswat.com/blog/detecting-and-mitigating-usb-based-threats

Pescatore, J. (2019). *Sans top new attacks and threat report*. SANS Institute.

Pham, D. V., Syed, A., & Halgamuge, M. N. (2011). Universal serial bus based software attacks and protection solutions. *Digital Investigation, 7*(3-4), 172-184.

Potocky, S., & Štulrajter, J. (2022). The human interface device (HID) attack on Andorid lock screen non-biometric protections and its computational complexity. *Science & Military Journal, 17*(1), 29-36.

Rodríguez Ocasio, A. (2019). *Implementing USB attacks with microcontrollers.* (MSc). Retrieved from http://hdl.handle.net/20.500.12475/140

Scaife, N., Peeters, C., & Traynor, P. (2018). Fear the reaper: Characterization and fast detection of card skimmers. Proceedings from : *The 27th USENIX Security Symposium (USENIX Security 18).*

Tian, D. J., Bates, A., & Butler, K. (2015). Defending against malicious USB firmware with GoodUSB. Proceedings from : *The 31st Annual Computer Security Applications Conference*, 261-270.

Tian, J., Scaife, N., Kumar, D., Bailey, M., Bates, A., & Butler, K. (2018). SoK:Plug & pray today–understanding USB insecurity in versions 1 through C. 2*018 IEEE Symposium on Security and Privacy, SP*,1032-1047.

Wang, Z., & Stavrou, A. (2010). Exploiting smart-phone usb connectivity for fun and profit. Proceedings from: *The 26th Annual Computer Security Applications Conference*, 357-366.

Xu, F., Diao, W., Li, Z., Chen, J., & Zhang, K. (2019). *BadBluetooth: Breaking android security mechanisms via malicious Bluetooth peripherals.* In NDSS.

Zhao, S., & Wang, X. A. (2019). A survey of malicious HID devices. *International Conference on Broadband and Wireless Computing, Communication and Applications.*

Author Information

Mathew Nicho
Zayed University
Dubai, United Arab Emirates
Contact e-mail: *Mathew. Nicho@zu.ac.ae*

Ibrahim Sabry
Zayed University
Dubai, United Arab Emirates

To cite this article:

Nicho, M., & Sabry, I. (2022). Threat and vulnerability modelling of malicious human interface devices. *The Eurasia Proceedings of Science, Technology, Engineering & Mathematics (EPSTEM), 21*, 241-247.

The Eurasia Proceedings of Science, Technology, Engineering & Mathematics (EPSTEM)
ISSN: 2602-3199

The Eurasia Proceedings of Science, Technology, Engineering & Mathematics (EPSTEM), 2022

Volume 21, Pages 248-257

IConTES 2022: International Conference on Technology, Engineering and Science

Comparison of the Effects of Vegetable Oils such as Castor and Canola Oil and Polyol Esters on the Metalworking Performance of AL 6061 and Al 7075 Metal Alloys by Tapping Torque Method

Kubra KAVUT
Gebze Technical University

Hanife GULEN-TOM
Belgin Oil R&D Center

Tugce OZPERCIN
Belgin Oil R&D Center

Abstract: Machinability of aluminum alloys still represents a challenge due to its tendency to staining and there is a great need for the development of sustainable solutions for lubrication and cooling. Therefore, researchers are performing intensively to obtain an effective way of machining such alloys. Growth of aerospace and automotive industries have increased utilization of these alloys day by day. Working for the development of more economical and environmentally friendly production technologies has gained increased interest to reduce the environmental and health risks and cost factor caused by the widely used flood lubrication. Vegetable oil and polyol esters are biodegradable synthetic base fluids that can be used as a sustainable alternative to petroleum-derived oils in many lubricant applications. In this study, the effects of castor and canola oils and trimethylolpropane trioleate (TMPTO) and trimethylolpropane trioleate complex (TMPCX), neopentyl glycol (NPG) and pentaerythritol tetra-oleate (PE-TO) type polyol esters on the machining performance of Al 6061 and Al 7075 alloys were investigated using the Tapping Torque test method. As a result, in the studies performed with neat fluids, it was determined that PE-TO showed the best performance in Al 6061, while TMP-TO showed the best performance in Al 7075. In addition, it was found that both vegetable oil types showed lower metal working performance than polyol esters in both alloys. Since similar results were obtained in the machining of both alloys, 68% emulsions were formulated with these vegetable oils and polyol esters to compare the machining performance. In contrast to neat machining, On Al 6061, PE-TO showed the most dramatic performance, while canola oil showed the highest performance. Since Al 7075 has harder machining conditions than Al 6061, the emulsion machining performance of Al 7075 alloy improved with the cooling effect of water and gave better results than neat machining.

Keywords: Sustainability, Metalworking fluids, Tapping torque, Vegetable oils, Polyol ester

Introduction

Aluminum alloys are of special interest due to their low density and special mechanical properties in engineering applications in a wide variety of industries such as aerospace, automotive and medicine. Thanks to these properties they also contribute to the reduction of harmful gas emissions into the atmosphere by reducing the weight of the vehicles, thus enabling lower fuel consumption (Carou & Davim, 2021). Aluminum is the most machinable metal on the market since its material properties make it easy to mill, drill, cut and punch. In addition, aluminum machined parts can be strong and durable (Soren et al., 2019). Along with the advantages of aluminum alloys, they also have a major disadvantage, such as a tendency to staining. The tendency of aluminum for easily stain limits the use of conventional metalworking fluids in the processing of these alloys,

and therefore special metalworking fluids are developed for the processing of these alloys (Canter, 2020). Another disadvantage of aluminum is that it is a ductile material. This feature of aluminum materials results in a large chip-tool contact area during machining, resulting in chips with a high thickness ratio. The formation of the chip-tool contact area and the increase in the chip thickness ratio cause an increase in cutting forces, machining power and heat generation (Ononiwu et al., 2021). In this regard, utilization of metal working fluids is crucial for effective machining of them. Heat generated can be reduced in the cutting zone and excessive friction can be prevented by helping of metal working fluids. As a result, life of mechanical systems can be extended (Çakır et al., 2015). The most common operation using metalworking fluids for machining light alloys is flood lubrication. However, conventional metalworking fluid formulations used in flood lubrication consist of toxic, non-biodegradable, unsustainable and environmentally harmful petroleum-derived products based on mineral oil as base oil (Santhosh et al., 2021). In line with the increasing demand for the use of light alloys in the aerospace, automotive and medical sectors, the environmental and health risks caused by flood lubrication, which is widely used in the processing of these alloys, and the demand for reducing the cost factor have increased the interest in research on the development of more economical and environmentally friendly production technologies. Another reason for the need to develop new products and technologies in the machining of light alloys is the need to produce alternative lubricants that can ensure sustainability due to the depletion of petroleum reserves (Panchal et al., 2021). There are various sustainable feedstocks to produce bio-lubricants. Highly unsaturated or high oleic vegetable oils (HOVOs), low viscosity polyalphaolefins (PAOs), polyalkylene glycols (PAGs), dibasic acid esters (DEs) and polyol esters (PEs) are categories of biodegradable base oils (Nagendramma & Kaul, 2012).

Vegetable oils which have large market share for biolubricants, are abundant and non-toxic feedstocks. They exhibit higher lubricity, higher flash point, lower volatility, and higher viscosity index than mineral oils. Presence of long chain fatty acid and polar groups in the structure of vegetable oil make them suitable for both boundary and hydrodynamic lubrications. Besides their advantages, they have low oxidation stability and their low temperature properties are poor. Thus, they can easily polymerize in the harsh working condition. This situation limits their industrial application (Wickramasinghe et al., 2021). Low viscosity biodegradable polyalphaolefins (PAOs) are another alternative for environmentally friendly lubricants and can be defined as low molecular dimers to tetramers. While low molecular weight causes undesirable high volatility for these fluids, it becomes an advantage at low temperatures where PAOs perform excellently. The absence of polarity of PAOs cause to problems of additive acceptability, but this result in excellent hydrolytic stability. Since PAOs have no double bonds or other reactive functional groups in their structure, oxidative stability of PAO with antioxidant additive is competitive to petroleum-based products.

PAOs are finding increasing use as hydraulic and engine oils, especially in cold climate applications and where hydraulic pressures increase, as they are an attractive option for converting biodegradable lubricants to water in low temperature applications. PAOs are also used as gear lubricants because of their ability to provide lower operating temperatures and lower coefficients of friction, which helps reduce wear. On the contrary of PAOs, polyalkylene glycols (PAGs) have high polarity as they have alternating ether linkages rather than essentially having a hydrocarbon backbone. However, they can be easily contaminated with moisture, resulting in increased solubility in water, which is detrimental for many lubricant applications. The solubility problem of organic additives in PAGs and the incompatibility of PAGs with conventional petroleum-based lubricants are often problematic for this species. For biodegradable PAGs usage, fire resistant fluids are often the best option. The high molecular weight of diesters makes volatility problems negligible and ester bonds provide high solubility power. Branching in alcohol fragments results in very good low temperature performance, but diesters score poorly in final biodegradability tests. For this species, ester linkages are not sterically hindered to restrict hydrolytic decomposition.

Diesters find use in biodegradable hydraulic fluids with long drain intervals, compressor oils turbine oils, and are mixed with PAOs in some synthetic lubricants. Diester fluids have outstanding solubility and cleaning ability. Because of these properties, it can have a negative effect on certain varnish or paint surfaces. This limits the use of dibasic acid esters. The most main area where dibasic acid esters find use is paint and coating applications. At last, but not least, PEs are effective feedstocks. They consist of fatty acids attached to an alcohol and hydrogen atom on the β-carbon atom does not exist in their backbone. PEs are used as environmentally acceptable base fluids in high performance lubricants. PEs have found application in many lubricants due to its very good low temperature behavior, high thermo-oxidative stability of some types, very high viscosity index, good anti-wear and low evaporation properties. The physico-chemical characteristics of PEs indicate that the properties are matching with the conventional base stocks. The development of new synthetic-based base fluids to meet the needs of high-performance lubricants is increasing day by day. As a result, the use of synthetic esters as base fluids has gained great importance in various industrial and military

applications. Examples of lubricant types using PEs are engine oils, gear oils, hydraulic oils, compressor oils, pump and turbine oils. Also, PEs are being evaluated for lubricity performance with a view for their application as metal working fluids (Nagendramma & Kaul, 2012). In the literature, these biodegradable base stocks are studied with many parameters as metal working fluids but there is limited study about their comparison of metal working behavior. When abundancy of vegetable oils and advantages of PEs are considered, comparison these two fluids can provide a valuable insight to the literature.

An important parameter in the processing of aluminum is the removal of heat from the friction between the tool and the material. Cooling performance is as important as the lubrication effect, and the cooling/lubrication balance must be maintained when machining these alloys. Heat can be removed by balancing cooling and lubricity. Water can be a good cooling agent due to its high specific heat capacity. However, achievement of homogenized solution is a challenging process due to the dispersion resistance of the oil droplets in the water. In order to formulate the base oil with water in a stable solution, surfactants are used. Surfactants consists of an amphi-hydrophilic group at the water-loving head and an oil-loving lipophilic chain at the hydrophobic tail. The hydrophilic group and the lipophilic chain have a strong attraction to the water and oil, respectively (Wickramasinghe et al., 2020).

There are various performance tests for metal working fluids. Lubricity behavior of metal working fluids can be investigated with Tapping Torque test method. It is a favorable method as bench scale test and combines qualitative and quantitative techniques. Tapping is a metal machining process to cut or form threads in a pre-drilled hole in a metal specimen which can be made of various metals while lubricating the contact zone between tap and hole wall by a metalworking fluid. Finally, a torque value to cut or form a thread is obtained. Smaller torque values indicate better metal working performance (Demmerling, & Söffker, 2020). In this study, metal working performance of vegetable oils and PEs were evaluated with Tapping Torque test method. Al 6061 and Al 7075 series were selected as the metal sample to be machined.

In this study, machining performance of the castor and canola oils and trimethylolpropane trioleate (TMPTO) and trimethylolpropane trioleate complex (TMPCX), neopentyl glycol (NPG) and pentaerythritol tetra-oleate (PE-TO) type PEs on the Al 6061 and Al 7075 alloys were investigated using the Tapping Torque test method. In addition, to investigate the effects of water input on cooling performance in these fluids, emulsions with 30% water content were formulated with these vegetable oils and PEs using alkyl polyglycol ether (C16:18 ethoxylated/propoxylated fatty alcohols) emulsifier.

Method

Materials

In the present study castor and canola oils and trimethylolpropane trioleate (TMPTO) and trimethylolpropane trioleate complex (TMPCX), neopentyl glycol (NPG) and pentaerythritol tetra-oleate (PE-TO) type polyol esters were used and their physicochemical properties were given in Table 1. Also, alkyl polyglycol ether (C16:18 ethoxylated/propoxylated fatty alcohols) emulsifier was used in the emulsions formulated with these vegetable oils and polyol esters. Castor oil and canola oil were supplied from Kim-paş A.Ş and Oleo Kimya, respectively. Trimethylolpropane trioleate (TMPTO) supplied by Oleon. TMP Complex ester (TMPCX) was supplied from Temix Oleo. Neopentyl glycol dioleate (NPGDO) was supplied from Oleon. Neopentyl glycol dioleate (NPGDO) was supplied from Oleon. Pentaerythritol tetra-oleate (PE-TO) was supplied from Oleon. Alkyl polyglycol ether (C16:18 ethoxylated/propoxylated fatty alcohols) emulsifier was supplied from Solvay.

Table 1. Physicochemical properties of used compounds in the study.

Test Parameter	Test Method	Castor Oil	Canola Oil	TMPTO	TMPCX	NPGDO	PE-TO
Kinematic Viscosity (40°C, cSt)	ASTM D 445	160	46	46	70	23	65
Kinematic Viscosity (100°C, cSt)	ASTM D 445	15	10	9,2	12.5	6	14
Viscosity Index	ASTM D 2270	93	212	187	180	228	225
Flash Point (°C)	ASTM D 92	172	≥ 190	≥ 270	300	≥ 250	≥ 280
Pour Point (°C)	ASTM D 97	≤-21	≤-18	≤-42	-33	≤-18	≤-25

Molecular structure of compounds

Molecular structure of used compounds in the study was shown in Table 2.

Table 2. Molecular structure of used compounds in the study.

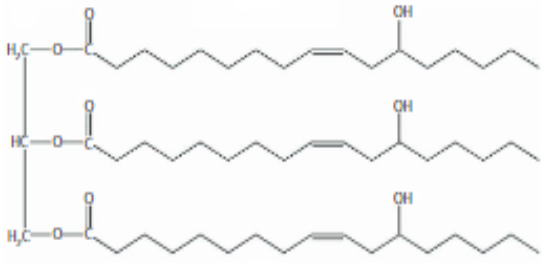 CASTOR OIL	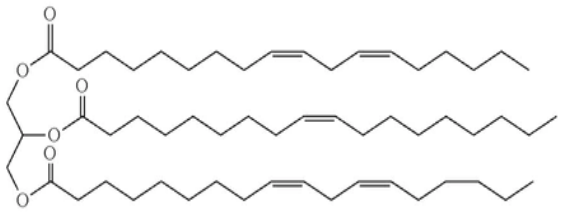 CANOLA OIL
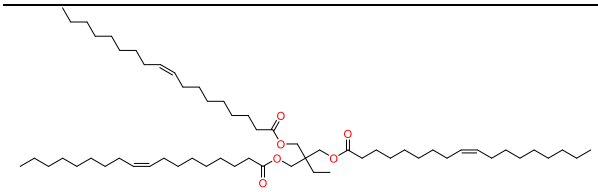 TMPTO	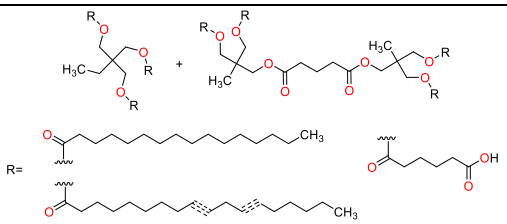 TMPCX
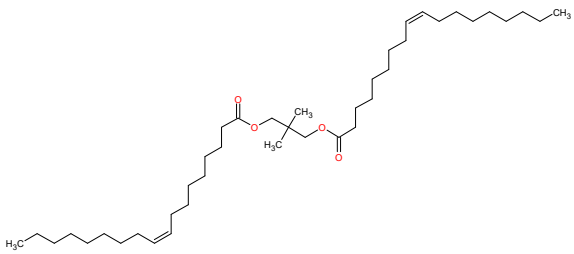 NPG- DO	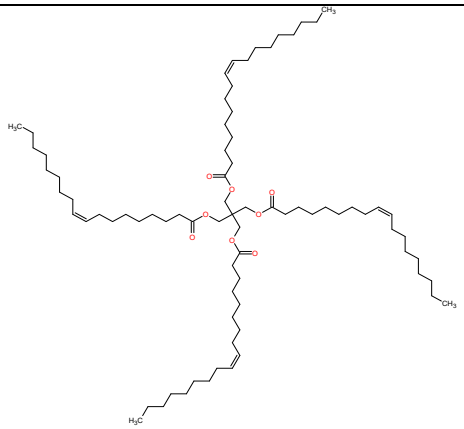 PE-TO
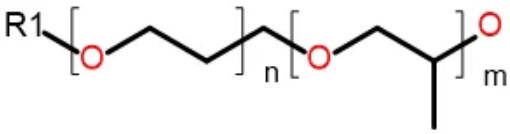 Alcohols, C16-18, ethoxylated propoxylated	

Machining performance of castor and canola oils and trimethylolpropane trioleate (TMPTO) and trimethylolpropane trioleate complex (TMPCX), neopentyl glycol (NPG) and pentaerythritol tetra-oleate (PE-TO) type polyol esters and their emulsion forms were investigated by Tapping Torque Test. Composition of samples was given in Table 3. In Tapping Torque Test, Al 6061 and Al 7075 series were used and test was carried out with 14.4 nm depth and 800 rpm.

To understand of the machining performance of the neat fluids and their emulsion forms, a tapping torque test was conducted in Labtap G8 (Microtap, Munich, Germany). The material used for the machining was a Al 6061 and Al 7075 with pre-drilled holes as shown in Figure 1. A TTT-Al 6061-M6F and TTT-Al 7075-M6F tools, size M6 with 69 helical channels per test plate was used for each fluid. The cutting fluid was poured in the holes to lubricate them during the tapping process at 800 rpm, with a 14.4 mm length of thread and each tapping process was repeated 3 times.

Table 3. Composition of samples by mass percentage, numbers in parentheses represent mass percent

Sample No	Sample Composition	Sample No	Sample Composition
1	Castor Oil (100:0)	7	Castor Oil+Water+Em (68:30:2)
2	Canola Oil (100:0)	8	Canola Oil+Water+Em (68:30:2)
3	TMPTO (100:0)	9	TMPTO+Water+Em (68:30:2)
4	TMPCX (100:0)	10	TMPCX+Water+Em (68:30:2)
5	NPG (100:0)	11	NPG+Water+Em (68:30:2)
6	PE-TO (100:0)	12	PE-TO +Water+Em (68:30:2)

Tapping Torque Test

Figure 1. Tapping torque test system

Figure 2 shows the tapping process graphically where: (a) shows the beginning of the forming; (b) indicates the torque increasing and the tool penetrating the workpiece as a result of increasing contact surface between the workpiece and the tool; (c) implies the tool forming with all its chamber teeth until the length's thread is achieved and (d) indicates the beginning of the reversal of the forming tap to bring the tool to the initial position. Consequently, the forming performance results of the fluids were determined averaging the tapping torque values (N·cm) in the 0 to 14,4 mm range of form.

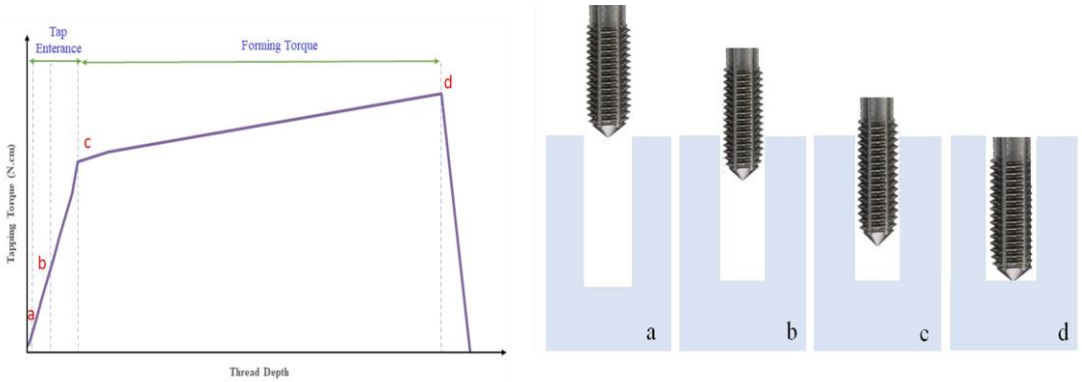

Figure 2. Graphical illustration of the tapping process and different positions of the tap during working. (a) beginning of the forming, (b) tool penetrating on workpiece, (c) teeth entering the chamber completely and (d) beginning of the reversal of the forming tap.

Results and Discussion

Tapping torque test results of samples on Al 6061 series were shown in Table 4. In addition, as shown in Figure 3 torque applied versus depth of cut graphs of each sample were obtained. It was determined that Pentaerytritol Tetraoleate (PE-TO) exhibited the best processing performance on the Al 6061 alloy, the processing performances of other polyol esters (NPG-DO, TMP-TO, TMP-CX) and canola oil were close to each other and they performed better than castor oil.

Table 4. Tapping torque test results of neat fluids for Al 6061 series.

Test plate	Test method	1	2	3	4	5	6
Al 6061 (800 rpm, d 14,4mm) (Nm)	BLN 105	161.1	142.5	140.2	141.2	144.3	136.1

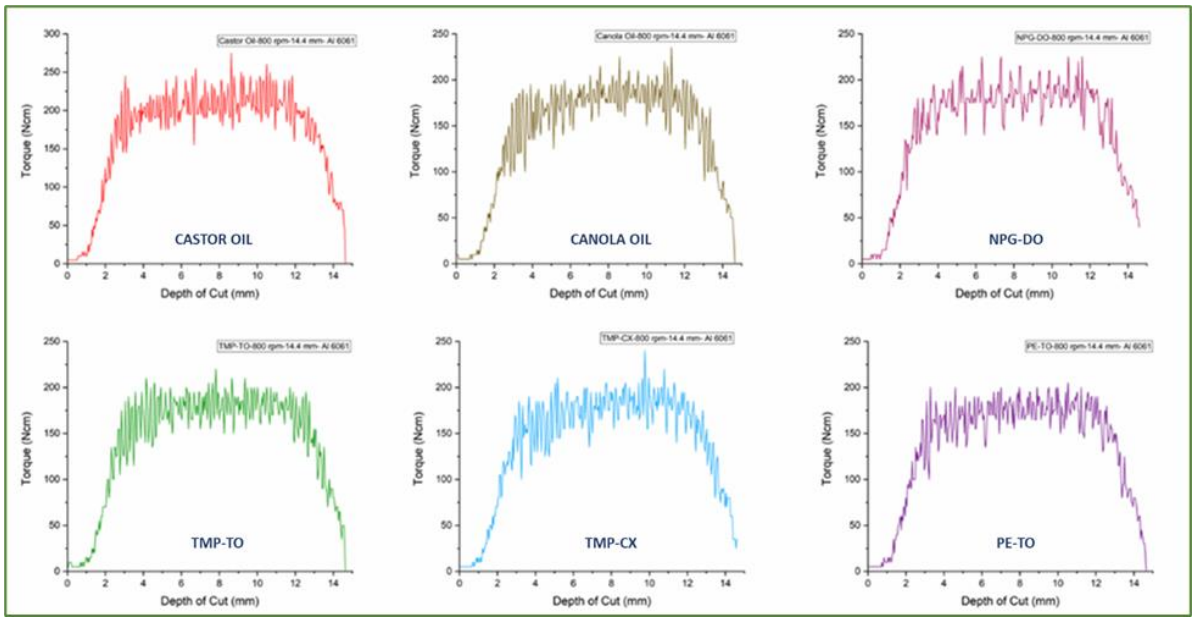

Figure 3. Tapping performance graphs of vegetable oils and esters on Al 6061.

Tapping torque test results of samples on Al 7075 series were shown in Table 5. In addition, as shown in Figure 4 torque applied versus depth of cut graphs of each sample were obtained. In the tests performed on Al 7075, it was determined that all fluids showed the same processing performance results as the tests on Al 6061, that is, PE-TO showed the best processing performance, the processing performances of other polyol esters (NPG-DO, TMP-TO, TMP-CX) and canola oil were close to each other and all these fluids performed better than castor oil.

Table 5. Tapping torque test results of neat fluids for Al 7075 series.

Test plate	Test method	1	2	3	4	5	6
Al 7075 (800 rpm, d 14,4mm) (Nm)	BLN 105	252.4	232.2	226.8	231.3	239.4	225.9

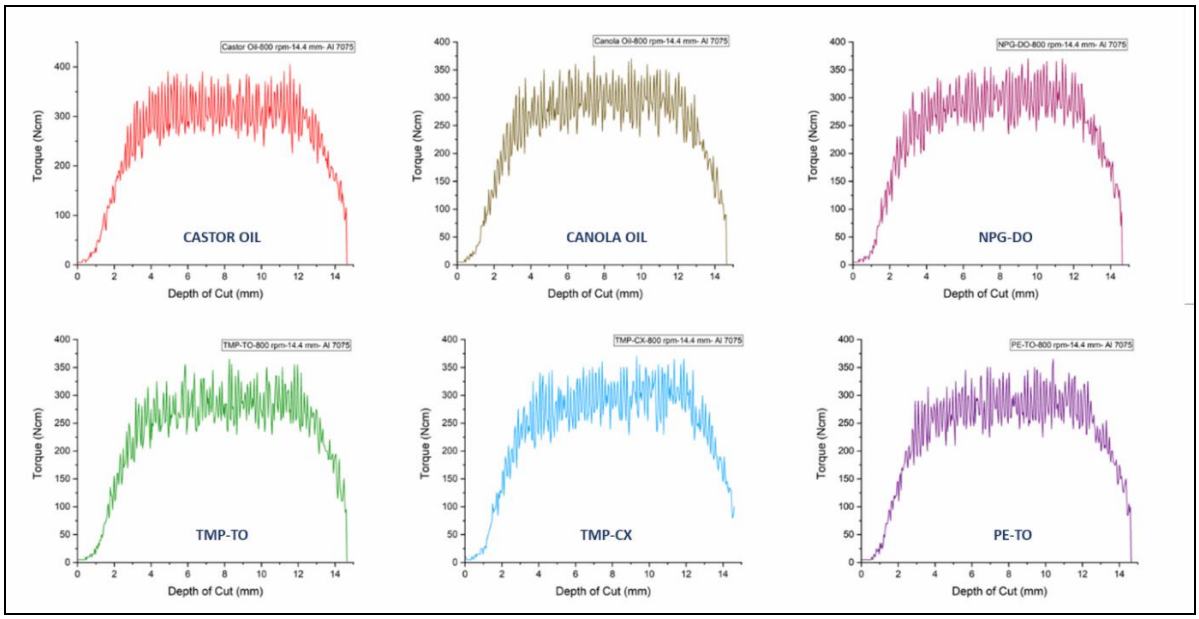

Figure 4. Tapping performance graphs of vegetable oils and esters on Al 7075.

Table 6. Tapping torque test results of emulsions for Al 6061 series

Test plate/Test condition	Test method	7	8	9	10	11	12
Al 6061 (800 rpm, d 14,4mm) (Nm)	BLN 105	143.7	115.3	144.6	153.5	165.3	182.2

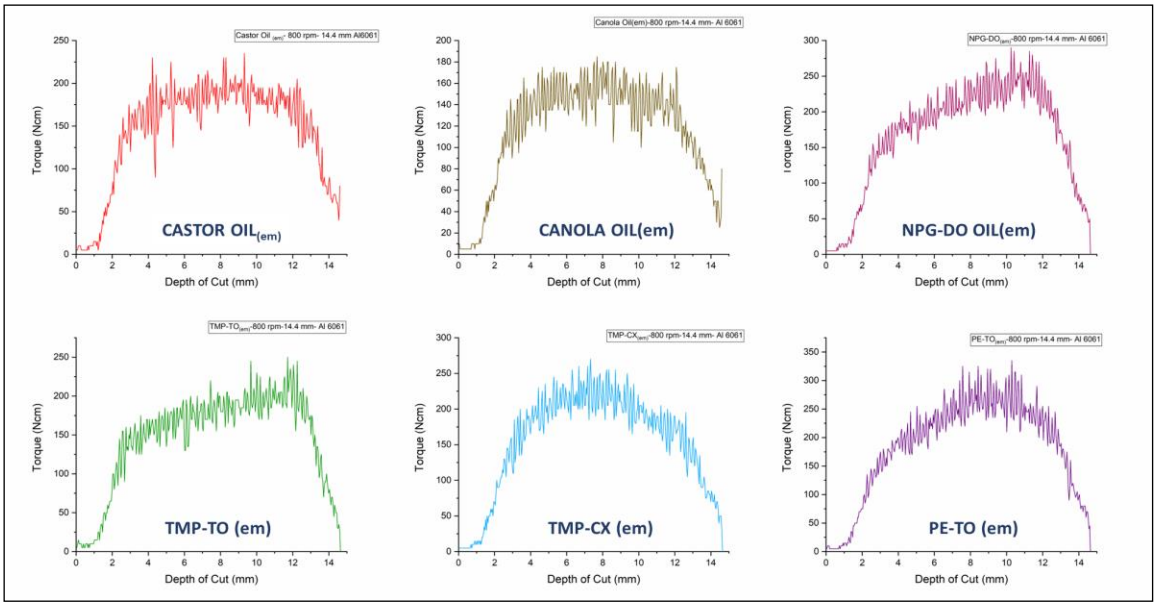

Figure 5. Tapping performance graphs of emulsion forms of vegetable oils and esters on Al 6061.

Table 7. Tapping torque test results of emulsions for Al 7075 series

Test plate/Test condition	Test Method	7	8	9	10	11	12
Al 7075 (800 rpm, d 14,4mm) (Nm)	BLN 105	225.3	207.4	218.3	221.6	215.8	209.9

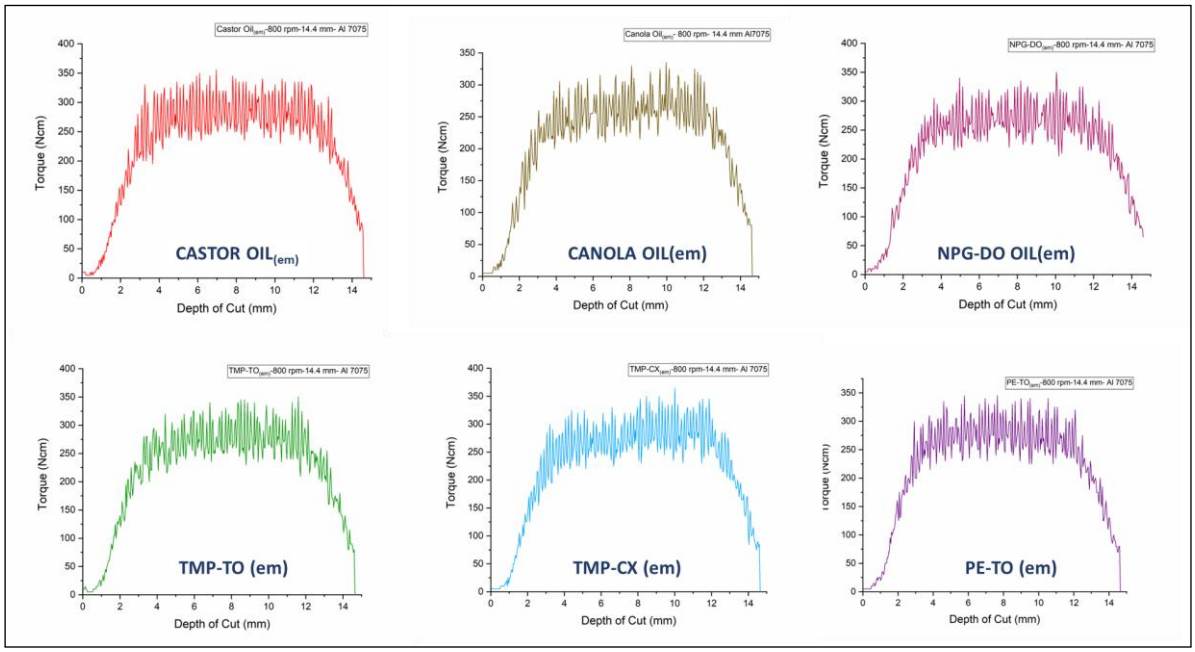

Figure 6. Tapping performance graphs of emulsion forms of vegetable oils and esters on Al 7075.

As a consequence of similar results in aluminum processing performances, 68% emulsions of vegetable oils and esters with water with a constant emulsifier ratio were prepared and tested on aluminum alloys to determine the difference in processing performances and to measure the effect of water input on cooling performance. In the emulsion tapping tests performed on Al 6061, PE-TO emulsion exhibited the worst and very low performance, contrary to the test result applied to the pure liquid. Similarly, Neopentyl glycol emulsion also showed low

tapping performance. The tapping performance of TMP-TO, on the other hand, remained unchanged and stable. Canola oil showed the highest performance. Tapping torque test results of emulsions on Al 6061 series were shown in Table 6. Also torque applied versus depth of cut graphs of each sample were shown in Figure 5.

Since Al 7075 has harder machining conditions than Al 6061, the emulsion machining performance of Al 7075 alloy improved with the cooling effect of water and gave better results than neat machining. Furthermore, torque applied versus depth of cut graphs of each sample were obtained. Test results of 68% emulsions of vegetable oils and esters were given for 7075 series in Table 7 and performance graphs were shown in Figure 6.

Conclusion

Machining performance of castor and canola oils and trimethylolpropane trioleate (TMPTO) and trimethylolpropane trioleate complex (TMPCX), neopentyl glycol (NPG) and pentaerythritol tetra-oleate (PE-TO) type polyol esters and their emulsion forms were investigated by Tapping Torque Test. It was determined that Pentaerytritol Tetraoleate (PE-TO) exhibited the best processing performance on the Al 6061 alloy and machining performance of samples was found as follows from best to worst: PE-TO > TMP-TO > TMP-CX > NPG-DO > Canola oil > Castor oil. Tapping torque test result graphs for neat liquids performed on the Al 6061 series are shown in Figure 7.

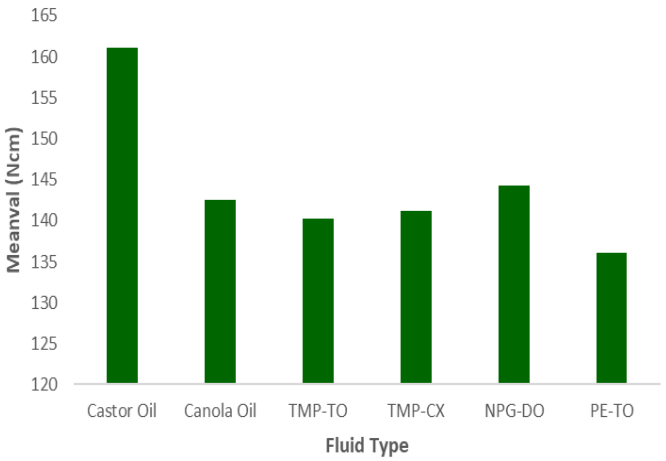

Figure 7. Tapping performance graphs of vegetable oils and esters on Al 6061.

In tests performed on Al 7075, similar machining performance results were obtained with Al 6061. Tapping torque test result graphs for neat liquids performed on the Al 7075 series are shown in Figure 8.

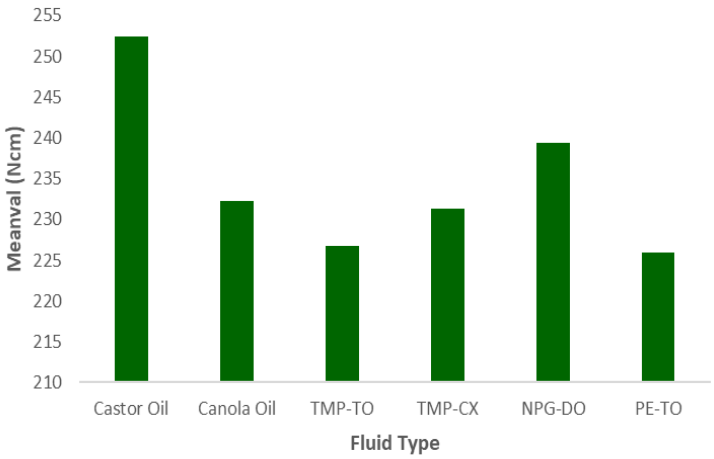

Figure 8. Tapping performance graphs of vegetable oils and esters on Al 7075.

In the tapping tests of emulsions performed on Al 6061, the PE-TO emulsion showed the worst and very poor performance, contrary to the result of the test for pure liquid. Machining performance of samples was found as

follows Canola oil > Castor oil > TMP-TO > TMP-CX > NPG-DO > PE-TO. Comparison graphs of tapping performance of neat and emulsion forms of vegetable oils and esters on Al 6061 are shown in Figure 9.

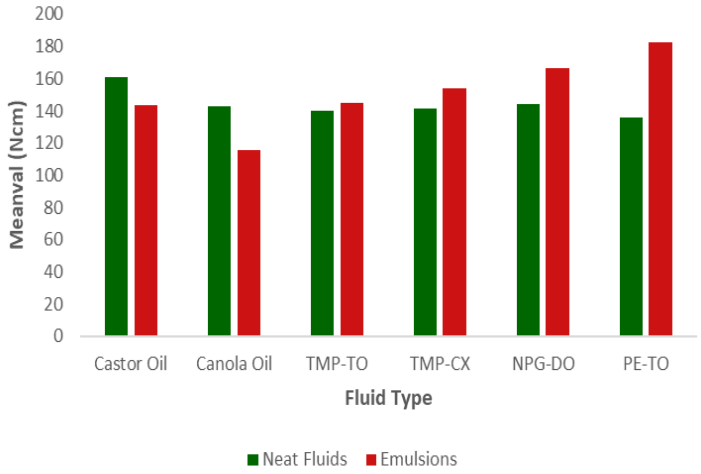

Figure 9. Tapping performance of emulsion forms of vegetable oils and esters on Al 6061.

Since Al 7075 has harder machining conditions than Al 6061, the emulsion machining performance of Al 7075 alloy improved with the cooling effect of water and gave better results than neat machining. Comparison graphs of tapping performance of neat and emulsion forms of vegetable oils and esters on Al 7075 are shown in Figure 10.

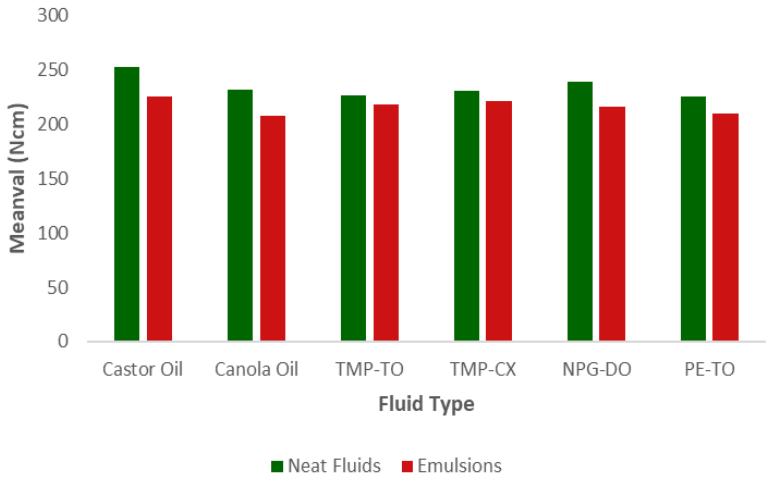

Figure 10. Tapping performance of emulsion forms of vegetable oils and esters on Al 7075.

The present study was carried out to investigate the effects of vegetable oils such as canola and castor oil and polyol esters on the machining performance of Al 6061 and Al 7075 type aluminum alloys, and based on the above results, the following inferences can be made:

1. In the tests carried out using vegetable oils on Al 6061, it was observed that the test results of emulsions with water input were better, on the contrary, using polyol esters on Al 6061, the test results of emulsions with water input were worst. The reason for this is that the heat generated at the tool-workpiece interface during neat machining with vegetable oils is quite high compared to polyol esters and the cooling effect is provided by the water input. The reason for the negative effect of water input on metalworking performance in polyol esters used in the tests performed on Al 6061 is that neat machining is sufficient to remove the heat occurring at the tool-workpiece interface and lubrication performance is required, not cooling.
2. Since Al 7075 has harsher machining conditions than Al 6061, the emulsion machining performance of the Al 7075 alloy has improved due to the cooling effect of the water, giving better results than neat machining. For this reason, the performances of neat machining of vegetable oils and esters on Al 7075 were found to be poor, unlike emulsions, and cooling performance was needed. In contrast, machining performance has improved due to the cooling effect of the water content in emulsions.

Scientific Ethics Declaration

The authors declare that the scientific ethical and legal responsibility of this article published in EPSTEM journal belongs to the authors.

Acknowledgements or Notes

* This article was presented as an oral presentation at the International Conference on Technology, Engineering and Science (www.icontes.net) held in Antalya/Turkey on November 16-19, 2022.

References

Carou, D., Davim J. P. (2021). *Machining of light alloys: Aluminum, titanium, and magnesium* (1st ed.). Boca Raton, Florida: CRC Press.

Canter, N. (2020). Metalworking fluids: Minimizing aluminum staining. *Feature*, 38-44.

Çakır, A., Yağmur, S., Kavak, N., Küçüktürk, G., & Şeker, U. (2015). The effect of minimum quantity lubrication under different parameters in the turning of AA7075 and AA2024 aluminium alloys. *The International Journal of Advanced Manufacturing Technology, 84*(9-12), 2515-2521.

Demmerling, A., & Söffker, D. (2020). Improved examination and test procedure of tapping torque tests according to ASTM D5619 using coated forming taps and water-mixed metalworking fluids. *Tribology International, 145*, 106151.

Nagendramma, P., & Kaul, S. (2012). Development of ecofriendly/biodegradable lubricants: An overview. *Renewable and Sustainable Energy Reviews, 16*(1), 764-774.

Ononiwu, N. H., Akinlabi, E., & Ozoegwu, C. (2021). Optimization techniques applied to machinability studies for turning aluminium metal matrix composites: A literature review. *Materials Today: Proceedings, 44*, 1124-1129.

Panchal, T., Patel, A., Chauhan, D., Thomas, M.,& Patel, J. (2017). A methodological review on bio-lubricants from vegetable oil-based resources. *Renewable and Sustainable Energy Reviews, 70*, 65-70.

Santhosh Kumar, S., & Ramesh Kumar, S. (2021). Ionic liquids as environmentally friendly cutting fluids - a review. *Materials Today: Proceedings, 37*, 2121-2125.

Soren, R., Kumar, R. T., Panigrahi, I., Kumar Sahoo, A., Panda, A., & Kumar Das, R. (2019). Machinability behavior of aluminium alloys: A brief study. *Materials Today: Proceedings, 18*, 5069-5075.

Wickramasinghe, K., Sasahara, H., Rahim, E., & Perera, G. (2021). Recent advances on high performance machining of aerospace materials and composites using vegetable oil-based metal working fluids. *Journal of Cleaner Production, 310*, 127459.

Wickramasinghe, K., Sasahara, H., Rahim, E., & Perera, G. (2020). Green metalworking fluids for sustainable machining applications: A review. *Journal of Cleaner Production, 257*, 120552.

Author Information

Kübra Kavut
Gebze Technical University, Belgin Oil R&D Center
Gebze-Kocaeli, Turkey
Contact e-mail: *kubra.kavut@belginoil.com*

Hanife Gülen Tom
Belgin Oil R&D Center
Gebze -Kocaeli, Turkey

Tuğçe Özperçin
Belgin Oil R&D Center
Gebze-Kocaeli, Turkey

To cite this article:

Kavut, K., Gülen-Tom, H. & Ozperçin, T., (2022). Comparison of the effects of. vegetable oils such as castor and canola oil and polyol- esters on the metalworking performance of AL 6061 and Al 7075 metal alloys by tapping torque method.*The Eurasia Proceedings of Science, Technology, Engineering & Mathematics (EPSTEM), 21*, 248-257.

The Eurasia Proceedings of Science, Technology, Engineering & Mathematics (EPSTEM)
ISSN: 2602-3199

The Eurasia Proceedings of Science, Technology, Engineering & Mathematics (EPSTEM), 2022

Volume 21, Pages 258-265

IConTES 2022: International Conference on Technology, Engineering and Science

Cyber Attacks on Unmanned Aerial Vehicles and Cyber Security Measures

Mustafa COSAR
Hitit University

Abstract: Unmanned Aerial Vehicles (UAVs) are air vehicles that can be controlled by themselves or via a ground station, can operate with mission-route definition, and can stay in the air in a limited range and time. Today, UAVs are used for various missions in line with military and civilian purposes such as reconnaissance, observation, research, search, control and transportation. In the models used for military purposes, the gun can be mounted and turned into an armed UAV. Attacks on hardware and software systems of UAVs, which are increasingly used in line with developing life conditions and technologies, are also increasing. Especially attacks on communication systems and coordinate information come to the fore. Cyber attacks on UAV systems in general include Data transmission link attacks, GPS (Global Positioning System) Scam attack, authentication attacks such as Brute Force, attacks against source code vulnerabilities, and hardware port and protocol attacks. It is known that attacks on UAV systems cause loss of life and property. It also results in other damages such as task delay, data breach, task failure, and loss of prestige. In this study, after the components, features and introduction of UAV systems, security threats to UAV systems and cyber attacks are defined. Then, the precautions to be taken against threats and attacks are listed. Some of these, importance are subjecting UAV software, hardware and transmission systems to vulnerability and risk scanning, ensuring the security of transmission with data encryption methods, controlling data traffic with a firewall application and making access control secure.

Keywords: UAV, Cyber threat and attack, Risk analysis, Cyber security

Introduction

One of the most important purposes of technology is to remove barriers and support human life. Unmanned Aerial Vehicle (UAV) is a technology developed in this direction. UAVs, which are widely used today; It is used for various missions in line with military and civilian purposes such as reconnaissance, observation, research, search, control, transportation and logistics. It comes to the fore especially in tasks that threaten human health and life safety. Another usage purpose is to be able to perform operations that exceed manpower, incorrectly and difficult to access, with the help of UAVs. It is possible to see many academic studies for these purposes in the literature. For example; Ariansyah, Dewi, and Susanto (2018) provide control and security of critical infrastructures; Falorca, Miraldes and Lanzinha (2021) in visual inspection of buildings and structures; Mademlis et al. (2019) discussed the use of UAVs in the film and advertising industry.

Every new technology has advantages as well as disadvantages. Among the advantages that can be counted; environmental awareness, high mission performance, removing obstacles and helping to provide monitoring-supervision-control-security. On the other hand, its disadvantages include energy needs, range constraints, command-control difficulties, hardware and software constraints, and low resistance to environmental conditions.

The use of UAVs in recent years, from logistics to research and development activities, from military operations to meteorological purposes, has made it a center of attraction. Therefore, it is seen that it also serves malicious purposes despite its beneficial purposes. It is also known to be used for malicious purposes such as unauthorized

and unallowed information gathering, intelligence studies, attack and destruction. In addition to these, cyber attacks against the components, systems and missions of the UAV also contain malicious purposes.

UAVs are aircraft that can be operated remotely or autonomously. The physical elements on a drone use a network of sensors and actuators that communicate with the ground control system via a wireless link (Altawy and Youssef, 2016). By their nature, UAVs consist of mechanical and electronic equipment, software codes, peripherals and payloads. The structures, working patterns, communication architectures and protocols of these units can be designed in a way that is open to threats and attacks. Attackers can even cause the UAV to crash when they catch the slightest gap.

Perhaps the most important components of UAVs exposed to cyber attacks are software systems and data transmission technologies. Among the software systems used by UAVs; autonomous driving software, image recording and processing software, map software, control center software and security software. Among communication systems, it is classified as UAV-ground control center (Ground Control Station-GCS), UAV-satellite system, UAV-UAV communication. Different signals, protocols and technologies are used between each of these communication centers.

In this study, after the components, features and introduction of UAV systems, security threats to UAV systems and cyber attacks are defined. Then, the precautions to be taken against threats and attacks are listed. Some of these measures are; Subjecting UAV software, hardware and transmission systems to vulnerability and risk scanning, ensuring the security of transmission with data encryption methods, controlling data traffic with a firewall application and providing access control.

The work has the following architecture. In the first part, the structure and technologies of UAVs are introduced. In the second part, the types of threats and attacks against the security of UAVs are explained. In the third chapter, precautions and solutions that can be taken against threats and attacks are presented. In the last part, there are the Conclusion and Evaluation stages. It is thought that the study will enable engineers, researchers and enthusiasts, who are involved in the design and use of UAV systems, to look at the cyber security window and have knowledge in this field.

2. Structure and Technologies of UAVs

2.1. General Structure of the UAV

Although nearly a century has passed since its development and first use, the UAV has become especially popular in recent years. These devices, which are popularly known as drones and their armed models are called armed UAVs (Unmanned combat aerial vehicle-UCAV), contain structures such as mechanical, electronics, and computer software and data transmission technologies. It should be assumed that these systems, whose general view is given in Figure 1, are similar, but may show changes based on the task.

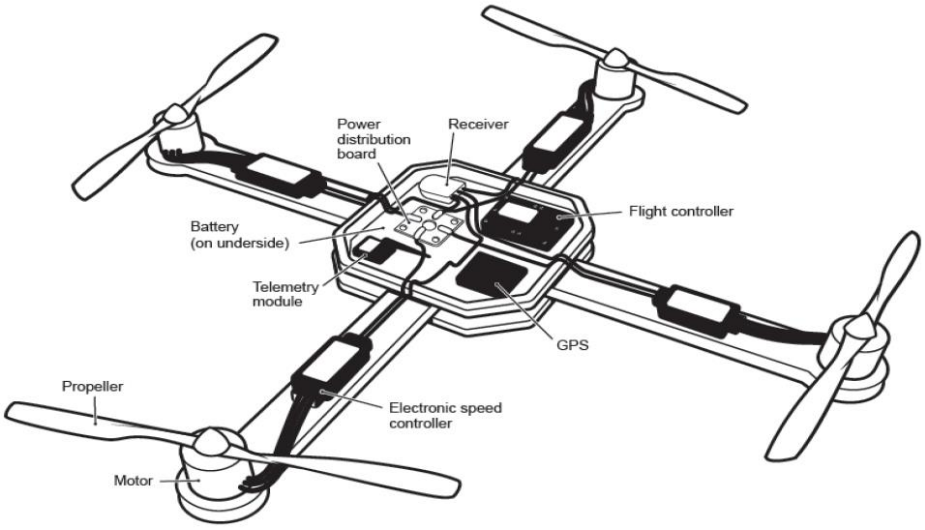

Figure 1. A standard uav structure (Karunakar et al. (2017))

As seen in Figure 1, the structure of an UAV consists of the body, electronic circuits, two or more propellers, speed and flight control devices, remote access module, GPS (Global Positioning System), energy source (battery). In addition, various sensors, transceiver antennas, data storage units, camera and weapon systems can also be found. Other mobile devices such as computers, tablets and smartphones can also be added to these components. A general view of the components of a UAV is given in Figure 2.

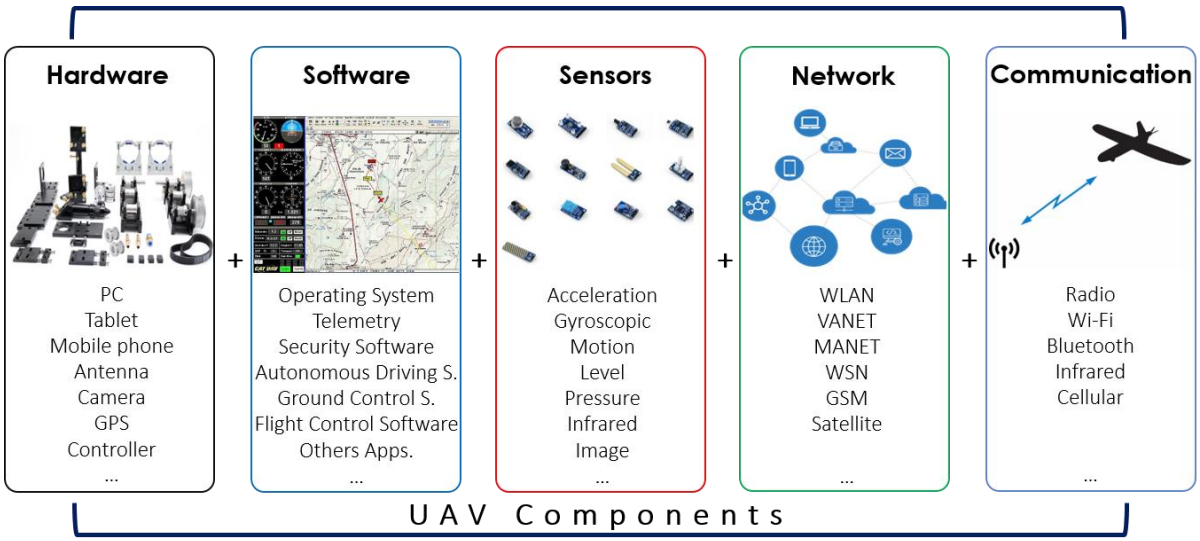

Figure 2. Basic components that make up the UAV

In addition to these components, the fuselage, wings and payload components that will not be subject to a cyber attack can be added. In addition, electronic and mechanical parts, cables and motors should be included in this system. UAV systems established with wireless network architecture adopt the rules developed by the International Institute of Electrical and Electronics Engineers (IEEE) IEEE 802.11 standards group. Private Dynamic Networks (Ad-Hoc) are networks based on collaboration of mobile nodes communicating without a general and fixed architecture. In this network architecture, as the nodes move independently, randomly and alternately, uncertain route and uncertain topology changes are experienced (Yalçın & Boyacı, 2020). Different network architectures can be established under the Ad-Hoc architecture for UAV systems. The first of these is the Mobile Ad-hoc Network (MANET) architecture. In this architecture, there are mobile devices using wireless infrastructure that can follow a random or predetermined route. In these networks, each device is considered a node, while each node has the freedom to roam freely by using its own routing protocol and its own mobility model. For this reason, losses in routing data packets, security vulnerabilities in network communications and access control vulnerabilities are seen.

The other is the Vehicle Ad hoc Network (VANET) architecture. In this network architecture, which is a subcategory of MANET networks, independent mobile devices and connection devices are connected wirelessly with sensors. Another Ad-Hoc network architecture is Wireless Sensor Networks (WSN). It is an Ad-Hoc network type created by more than one sensor. In this network architecture, the sensor nodes communicate with each other and with a base station. The most negative situation in this architecture is the intensity of energy use. Therefore, cyber attacks on the communication of the sensors in the network may cause extra energy consumption.

2.2. UAV Operation Procedures

UAVs are aerial vehicles that can be operated with remote control or autonomously. A UAV records various stages during takeoff and return from a ground point. These are respectively;

Start: Before takeoff, a system is created containing the ID of all UAVs and GCS and key pairs that allow cooperation with other UAVs. One UAV is selected as the backbone; the others are registered as group members. A control signal is sent from the GCS to the backbone UAV, which then acts as a gateway to communicate with other UAVs.

Operation: UAVs cooperate with each other to expand their mission scope, exchange information and avoid collisions. Mission information is published by the GCS and by the backbone UAV. It is then transferred from one UAV to the others.

Join: When a new UAV arrives in UAV swarms and the network, an authorization request is sent to the backbone UAV. After the backbone UAV authorizes the new UAV with ID and key pairs, it initiates communication using encrypted channels.

Flight: UAVs can move at a speed of approximately 45-285 km/h. At these speeds, itinerary planning, mission execution, flying and communicating can be difficult. For this, Static, Random, Time and Route based, Mission based, Swarm based and Topology based flight plans are prepared.

Critical Decisions: UAVs may be out of mission, leave the swarm, or even crash due to low battery levels, changes in environmental factors, time of attack, or disconnections. In such a case, the GCS and the backbone UAV may have to make new decisions. They may need to report this decision to other UAVs in the swarm. The information of a UAV in a difficult situation should also be reported to the backbone UAV or GCS. In this way, the backbone UAV can de-authenticate the UAV that has left the swarm correctly on the network. Some of these management decisions are; flight management, swarm management, service recovery management, communications management, energy management and network management decisions. Brief information about them can be given as follows.

- Service recovery management: Occurs because of network outage mainly caused by radio signal interference and communication failures. In this case, the UAV has to continue with its autonomous driving feature.
- Energy management process: With the help of this process, the UAV controls battery consumption by balancing data transmission and flight parameters and focuses on completing the mission.
- Network management process: It is the management of WLAN and WSN networks formed by the participation of two or more nodes between GCS, UAV, swarm and satellite. For example, in this process, it is possible to regulate conflicts that occur when data exchange at the same time and to ensure network security.

3. Cyber Threats and Attacks against UAVs

Cyber attacks against UAV systems; each of the hardware, software, network, sensor and communication components of the UAV given in Figure 2 are discussed separately. Since the development, production and assembly phases of each component require a separate architecture, security vulnerabilities may occur in each. It should not be forgotten that vulnerabilities related to the components of the UAV that help make critical decisions might include threats and attacks.

Cyber attacks are threats and attacks against the confidentiality, integrity and accessibility of information (Coşar, 2022). The diagram given below gives a general classification of attacks that can occur on UAV wireless networks. The types of attacks given in Figure 3 can be made separately for each of the components or against all components. For this reason, it is necessary to take the measures that can be taken against the attack by considering the whole system.

When Figure 3 is carefully examined, it is seen that the most common type of attack is network attacks. These attacks, which are sub grouped as active and passive attacks, are aimed at the network topology, network communication system, network protocols and data created by the GCS, UAV and UAV swarm. Therefore, Communication attacks, the last component given in the figure, can be included in this group. Transmission layers and routing protocols, which are an important structure of the network architecture, constitute the system that functions from the beginning to the end of the transmission. For this reason, cyber attacks against this structure include both active and passive attacks.

Routing protocols are a set of rules that ensure the appropriate and secure transmission of data packets created during transmission. Attacks against a network or a node are classified as active and passive attacks as summarized in Figure 3 (Ünal and Akçayol, 2008). Active attacks are attacks that violate the principles of confidentiality, integrity and availability to prevent the normal operation of a UAV. Passive attacks, on the other hand, are attacks on the confidentiality of information without harming the operation of the UAV. These two types of network attacks are listed in the Table 1 below.

Table 1. Types of cyber attacks against the network component of the UAV

Attack Type	Name	Definition
Active Attacks	MITM (Man in The Middle)	It is an attack in which the attacker sneaks in between two-way communication and causes the transmission to be made over himself. The attacker, who begins to listen to the transmission, begins to seize personal data, passwords, bank information, change the data or impersonate one of the parties.
	Worm Hole	Collaborating malicious nodes establish a channel with high communication quality between each other. They then announce this channel for routing and collect data packets from the surrounding nodes. Packets passing over this channel are not forwarded to their real destination or they are forwarded by changing.
	Black Hole	When the attacking node positions itself between two nodes that are communicating without encryption, it can make all kinds of changes to the packets. In a black hole attack, the malicious node responds incorrectly to routing requests on the network, presents itself to its neighbors as the shortest route, and takes all incoming packets. The malicious node can perform a denial of service attack by deleting all the packets it receives, or it can listen and redirect the packets to its true path so that the attack is not detected.
	Fabrication	The attacker attacks other nodes with false routing messages that will cause confusion in the network in order to consume resources or disrupt the functioning of the network. Example attacks: Route salvaging, sleep deprivation, and replay.
	Interrupt	It is done to prevent the transmission of packets between the source node and the destination node. When an attacker wants to break the reach of the target node, they can modify the content of the routing messages to destroy all paths to the target node.
	DoS	A denial of service attack is to prevent the network and node from working by exceeding the communication limit that the network and nodes can handle. It is generally done to consume resources such as consuming bandwidth by creating unnecessary traffic, forcing memory, CPU and disk space to process.
	SYN Flood	It is a denial of service attack. It is done by sending SYS requests to the node and the network to communicate over the limit of the data traffic that the system can handle.
	Brute Force	It is an attack of multiple login attempts to guess a user name and password on an access-controlled system. The username and password guessing process varies according to the difficulty and complexity of the information.
	Birthday Attack	It is an attack against hashing algorithms used to verify the integrity of a message, software, or digital signature. A fixed-length representative summary message of the message used for communication is created. With this attack, the probability of randomly generating the same digest message on the network is calculated. If the attacker calculates the same digest, he can replace the user's message with his own, and the recipient will not be able to detect the replacement even if they compare the digests.
Passive Attacks	Eavesdropping	The attacker listens by passing through the network traffic and analyzes by obtaining unauthorized information.
	Modification	The attacking node will redirect the packets to the wrong destination, causing the packets to circulate unnecessarily on the network and drop the packets from the network at the end of their lifetime. While packets circulating in the network cause congestion across the network, the source node that cannot deliver the packets to their original destination will unnecessarily consume its limited energy and bandwidth as it will constantly generate packets again. Example attack Misrouting.

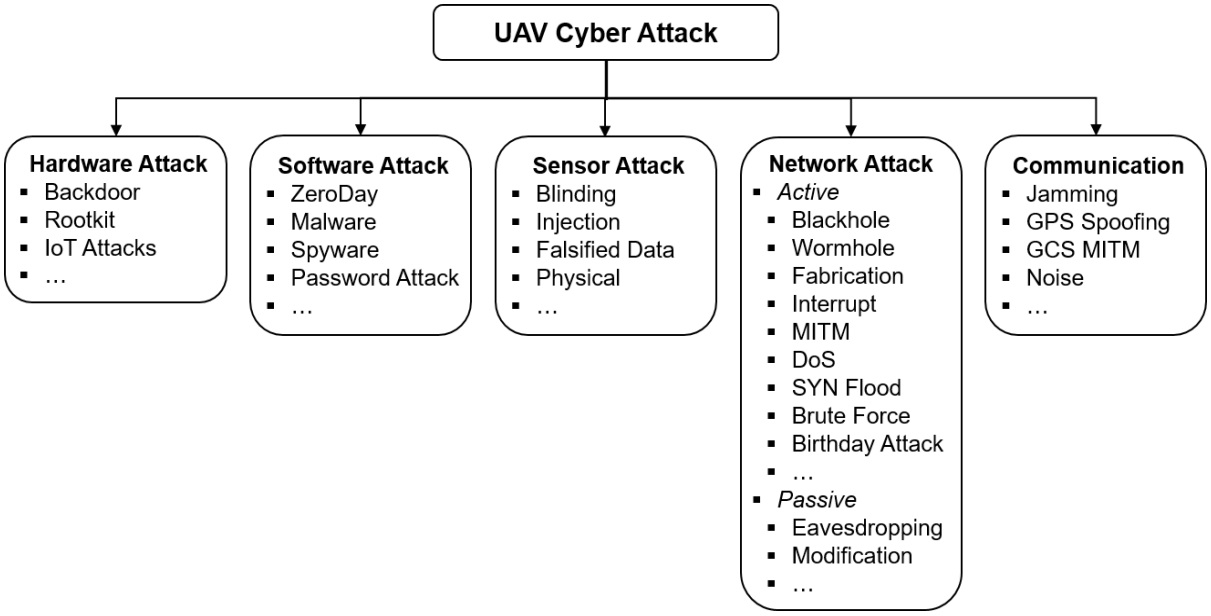

Figure 3. Cyber attack scheme for UAV components

The rapid development of information technologies and the development of new techniques help the development of both attack and defence methods in the cyber field. It should not be forgotten that it will be difficult to ensure the security of a system with such uncertainty and different communication structure.

4. Cyber Security Measures

It is known that controlling, managing and defending a remotely controlled, autonomous driving and decision-making system involves some difficulties. Some control units control and regulate the system operation on an autonomous vehicle. Information from these control units is transferred to a central ECU (Electronic Control Unit) with the help of the Controller Area Network (CAN). Xu et al. (2018), a gateway bridge can route selected data between these two layers. Therefore, there is a possibility that malicious data packets may enter the low-speed CAN layer of the AV without any detection or suspicion before being transmitted to the high-speed CAN layer via the gateway bridge, leading to consequences that are more serious. It is recommended to have message authentication code (MAC) algorithms to protect and verify the integrity of the data. To ensure that AV controllers are trustworthy, it is recommended to use certificates, firewall and cryptographic analysis to support the authentication process.

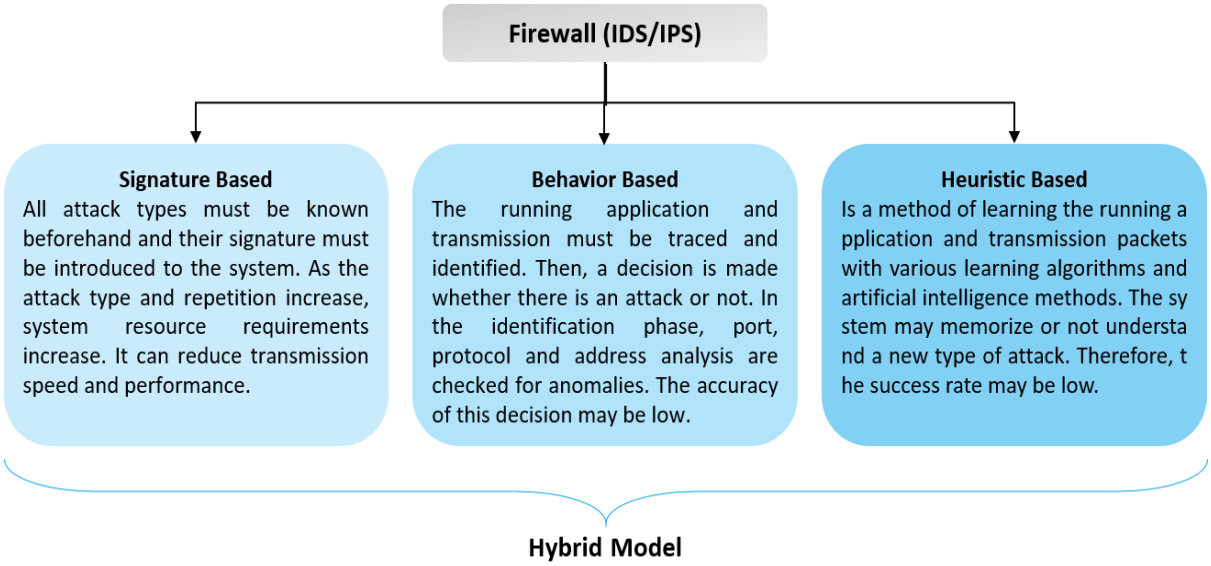

Figure 4. Firewall model for UAV communication

Routing protocols that prioritize security and use node resources efficiently should be used in Ad-Hoc network architecture. Examples of these protocols are; Destination Sequence Distance Vector (DSDV), Wireless Routing Protocol (WRP), ZHLS (Zone-based Hierarchical Link State Routing Protocol), Optimized Link State Routing (OLSR), Secure Efficient Ad Hoc Distance Vector (SEAD), A Secure On-Demand Routing Protocol for Ad-Hoc Networks (ARIADNE), Secure Routing Protocol (SRP) (Tekerek, Vural & Aydos, 2016).

As another solution suggestion, it is suggested to use a firewall with advanced features. This firewall should incorporate Intrusion Detection System (IDS) and Intrusion Prevention System (IPS) features together. In addition, port, protocol, address and application are expected to overcome abnormal situations by doing some checking. In this context, it is proposed to create a hybrid system for IDS and IPS, which is given in Figure 4. As can be seen in Figure 4, the features that a new generation firewall should have are given. These three types of IDS/IPS models have advantages and disadvantages. Especially when measuring performance, resource utilization rates and success rates in detection and prevention stages are decisive. For this reason, it is thought that a combined model will be more advantageous and the success rate will be higher. This hybrid model must be applied in accordance with the structure, intended use and other characteristics of the UAV.

Conclusion

In this study, a cyber attack and security analysis was made by separating the UAVs into their components. It has been demonstrated that a UAV system has hardware, software, sensors, network and communication components. It has been emphasized that each of these components can be exposed to cyber attacks separately. Since these components contain information technology elements, it is seen that the cyber threats and attacks encountered today may also threaten them. For this reason, it has emerged that a security model should be operated by looking at the whole of the UAV from a holistic perspective and its components from a discrete perspective due to the nature of information technologies. In the study of Mejri et al. (2014), it is recommended to create a PKI (Public Key Infrastructure) associated with VANETs and to use digital certificates as a fast authentication method in a vehicle network. To increase the security of autonomous vehicles with ultrasonic sensors, two defense strategies have been proposed, namely single sensor-based authentication (PSA) and multi-sensor consistency check (MSCC), which authenticate signals. Coşar and Kıran (2021), in their study, proposed blockchain technology to protect against cyber attacks against drone swarms. In their study, they determined that blockchain technology provides network communication security and location accuracy of GCS and drone-drone communication packages. In addition, firewalls against cyber threats and attacks, data encryption algorithms and multi-layered access control mechanisms should be applied during secure data transmission and access to hardware and software systems. In addition, multiple modulation techniques, noise canceling and reducing mechanisms should be used for the signals used in the transmission and management system. Finally, vulnerabilities and risks need to be determined beforehand by penetration testing of all components. It is then recommended to use it after the vulnerabilities are closed.

Scientific Ethics Declaration

The author declares that the scientific ethical and legal responsibility of this article published in EPSTEM journal belongs to the author.

Acknowledgements or Notes

* This article was presented as an oral presentation at the International Conference on Technology, Engineering and Science (www.icontes.net) held in Antalya/Turkey on November 16-19, 2022.

References

Altawy R. & Youssef. A.M. (2016). Security, privacy, and safety aspects of civilian drones: A survey. *ACM Transactions on Cyber-Physical Systems,1*(2), 1-25, Article 7 (November 2016), http://dx.doi.org/10.1145/3001836.

Ariansyah M.R., Dewi A.A. Susanto C.D., & Rahayu Y. (2018). Resheniye drone, the answer of digital oil spill recovery, *Conference: Oil & Gas Seminar and Competition 2*018.

Coşar, M. (2022). Privacy and security on blockchain, In book: *Blockchain innovative business processes and long-term sustainability*, Publisher: Nobel, Editors: Mert Gözde, Zeren Karagöz Seda, Yılmaz Osman, (pp.245 -270), ISBN: 978-625-433-841-0.

Cosar, M., & Kiran, H. E. (2021). Verification of localization via blockchain technology on unmanned aerial vehicle swarm. *Computing and Informatics, 40*(2), 428–445. https://doi.org/10.31577/cai_2021_2_428

Falorca, J. F., Miraldes, J. P., & Lanzinha, J. C. G. (2021). New trends in visual inspection of buildings and structures: Study for the use of drones. *Open Engineering, 11*(1), 734-743. https://doi.org/10.1515/eng-2021-0071

Karunakar, P., Jariso, M. & Kale, P. (2017). A review on geo mapping with unmanned aerial vehicles. *International Journal of Innovative Research in Computer and Communication Engineering*, 5(1), 1170-1177.

Mademlis, I., Torres-González, A., Capitán, J., Cunha, R., Guerreiro, B.J., Messina, A., Negro, F., Barz, C.L., Gonçalves, T.R., Tefas, A., Nikolaidis, N., & Pitas, I. (2019). A multiple-UAV software architecture for autonomous media production. *EURASIP European Signal Processing Conference (EUSI*PCO) 2019.

Mejri, M.N., Jalel, B. & Hamdi, M. (2014). Survey on VANET security challenges and possible cryptographic solutions, *Vehicular Communications 1*(2), https://doi.org/10.1016/j.vehcom.2014.05.001.

Tekerek, M., Vural, Y. & Aydos, M. (2016). Tasarsız ağlarda yönlendirme güvenliği üzerine kapsamlı bir araştırma. *Bilişim Teknolojileri Dergisi*, *9*(2), 171-180, https://doi.org/10.17671/btd.64124.

Ünal, M. & Akcayol, M. A. (2008). Kablosuz ağlarda güvenli yönlendirme protokolleri. *Bilişim Teknolojileri Dergisi*, *1*(3), 7-13.

Xu, W., Yan, Chen, J., Jia, W., Ji, X., Liu, J. (2018). Analyzing and enhancing the security of ultrasonic sensors for autonomous vehicles. *IEEE Internet of Things Journal*, *5*(6), 1-14. https://doi.org/10.1109/JIOT.2019.2867917

Yalçın, N. O. & Boyacı, A. (2020). İnsansız hava araçlarının hareket ve yönlendirme protokollerine göre performans ölçümü. *İstanbul Ticaret Üniversitesi Teknoloji ve Uygulamalı Bilimler Dergisi*, *3* (1), 27-40.

Author Information

Mustafa Coşar
Computer Engineering, Hitit University
Turkey
Email: *mustafacosar@gmail.com*

To cite this article:

Cosar, M. (2022). Cyber attacks on unmanned aerial vehicles and cyber security measures. *The Eurasia Proceedings of Science, Technology, Engineering & Mathematics (EPSTEM), 21*, 258-265.

The Eurasia Proceedings of Science, Technology, Engineering & Mathematics (EPSTEM)
ISSN: 2602-3199

The Eurasia Proceedings of Science, Technology, Engineering & Mathematics (EPSTEM), 2022

Volume 21, Pages 266-273

IConTES 2022: International Conference on Technology, Engineering and Science

Detection of the Mineral Presence and Its Effects on Different Tree Species Using Drone Photogrammetry and Remote Sensing Methods

Oyku ALKAN
Graduated Istanbul Technical University

Muntaha Kassım Hayder AL-ZUBADE
University of Technology

Mehmet Nurullah ALKAN
Hitit University

Abstract: It is expected that the vegetation, especially the tree roots, will be affected by the underground mines that may be discovered and have different spectral characteristics. In particular, it is possible for forest areas to be more frequent and stronger by being fed from metallic mines that are mineralized in a long process underground. For this purpose, the study was carried out in a mining area with a licensed gold and copper mineralization located in the west of Amasya province borders. Drone Photogrammetry has been studied to clearly classify the trees in the forest with dense and steep geography in the region. The spectral anomaly of tree species was investigated by using the ASTER satellite image with high spectral resolution of the region. With remote sensing methods such as SAVI, NDVI and supervised classification, satellite images were enriched to reach potential ore-intensive areas. The slope analysis was performed by creating a digital terrain model for the region, which geography is very rough and steep, and it was examined by considering tree height values from different angles. Tree species classified by the Spectral Correlation Mapping method were also evaluated together with their spectral signatures.

Keywords: Remote sensing, Drone photogrammetry, GIS

Introduction

Remote Sensing(RS) technology has become the indispensable methodology of multidisciplinary platforms and the dissemination of research in this direction is considered as an important innovation. With this method, whose importance is increasing day by day in the investigation of mineral deposits, powerful spectral analyzes can be made with the analyzes made with infrared and thermal bands of high spectral resolution satellite images. Little ore resources are used in the world and there are countless potentials waiting to be discovered (Alkan, 2019). Research with remote sensing methods is now considered indispensable in the world literature.

Analyzing systems that provide high-resolution images of mining areas are UVA tools. Drone-based mining exploration gains value when combined with remote sensing methods. Drones have quickly become one of the most cost-effective and efficient tools for collecting high-resolution data, aligning between larger-scale, lower-resolution satellite data collection and much more limited traditional terrestrial survey approaches (Hill, 2022).

A study conducted in Yankari Park in Nigeria used ASTER and Hyperion satellite data to identify alteration minerals. The algorithms used are based on Linear spectral separation and spectral angle mapping (Abubakar et al., 2017). Instead of the spectral angle mapper used in this study, the spectral correlation mapper, which is the corrected version of these methods, was preferred.

In another study conducted in the Sittampundi Anorthositic complex in South India; For thermal waters, VNIR and SWIR data from nine band high spectral resolution ASTER satellite data were examined. The usability of different multispectral satellite data and mineral ratio images for lithological differentiation has been investigated (Arivazhagan et al., 2017). A similar study was conducted in Oman to investigate the mineral mapping performance of ASTER satellite data in arid regions. ASTER bands for mineral mapping, band ratio literature was reviewed (Rajendran & Nasir, 2018).

In another study to determine the band ratio of hydrothermal alteration minerals, principal component analysis, Crosta technique and spectral angle mapper techniques were applied using ASTER satellite data. Spectroradiometry was used to extract the spectral signatures of the stone samples. (Yalçın et al., 2017). Different RS methods of ASTER bands were investigated to analyze potential mining fields in Çorum province. (Alkan et al., 2017).

Data obtained from satellites or Unmanned Aerial Vehicles (UAVs) makes these hard work equipped in a short time. Unmanned Aerial Vehicles (UAVs) or drones is a proven technology for some of these activities (Wyard, 2022). The diversity of remote sensing methods and high spatial resolution of drone data in the exploration of metallic minerals makes a great contribution to the studies. This study was carried out by combining effective methods to contribute to mineral exploration. For this purpose RS, UVA Drone and GIS processes were jointly used.

Method

Drone Photogrammetry and Remote Sensing

Drone photogrammetry and different remote sensing methods were used to investigate the metallic mines in this area. The digital elevation model of the region was prepared by taking drone images from different heights in difficult geographical conditions. Using the high spectral resolution of the ASTER, different remote sensing methods were used and the mineral presence in the region was examined. Ore-dense areas were determined using merged data from drone and ASTER images. The samples obtained from the ground control points and the drilling for field-validated.

Drone photogrammetry and different remote sensing methods were used to investigate the metallic mines in this area. UAV-based study applied to clearly classify the trees in the forest with dense and steep geography in the region. The spectral anomaly of tree species was investigated by using the ASTER satellite image with high spectral resolution of the region. With remote sensing methods such as SAVI, NDVI and supervised classification, satellite images were enriched to reach potential ore-intensive areas.The slope analysis was performed by creating a digital terrain model for the region, which geography is very rough and steep, and it was examined by considering tree height values from different angles.Tree species classified by the Spectral Correlation Mapping method were also evaluated together with their spectral signatures.

Findings

Study Area

The study area was carried out in the Taşova district of Amasya, in the eastern part of the Central Black Sea Region. Projection is UTM, Datum WGS 84 and Zone 36 (Figure 1). A continuation of the significant parts of Central Anatolia Region in the Central Black Sea Region; the most part springs in the Yeşilırmak Basin (Gulersoy, 2013). Parallel to the tectonic development of Anatolia, Amasya province is located on a large area covered by metamorphic masses, conglomerates, limestones, and sandstones. In this geological formation, the probability of high temperature harboring of metamorphic belts is considered important in terms of investigating potential geothermal areas (Ongur, 2005). Classical local drilling activities were carried out in mining studies in the research area. No study has yet to be related Remote Sensing (RS) and Drone Photogrammetry (DP) adds high- value effects to this work. One of the lateral branches of the North Anatolian Fault (NAF) line extends to the study area. The vectorial density in the fault lines updated by the General Directorate of Mineral Research and Exploration (MTA) has been evaluated to indicate potential ore-dense areas in the region. The geography of the field is a rugged area where reaches up from 460 meters to 1130 meters in the forest many kinds of trees, the study which was applied in a license area where the tough geographical conditions.

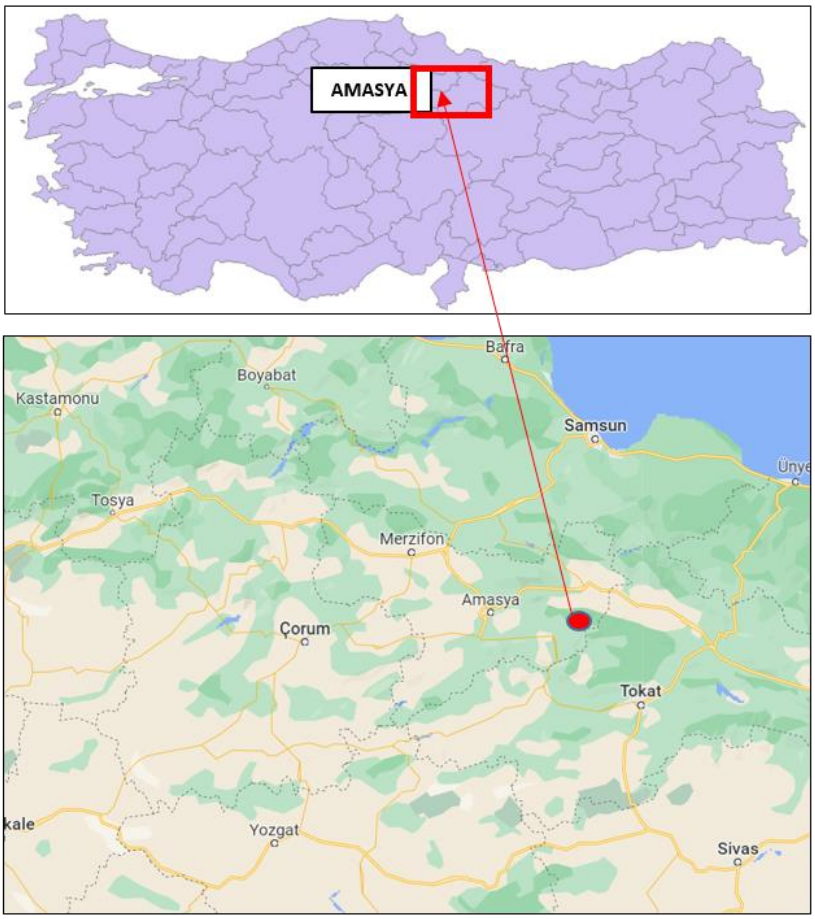

Figure 1. Study area

Drone photogrammetry and different remote sensing methods were used to investigate the metallic mines in this area. In the first stage of the study, the digital elevation model of the region was prepared by taking drone images from different heights in difficult geographical conditions. In the second stage, using the high spectral resolution of the ASTER satellite data, different remote sensing methods were used and the mineral presence in the region was examined. Ore-dense areas were determined with terrain maps created using data from drone and ASTER satellite images. For this purpose, unsupervised classification methods and band ratio techniques were used to extract the potential mineral distribution. The samples obtained from the ground control points taken as field-validated were evaluated.

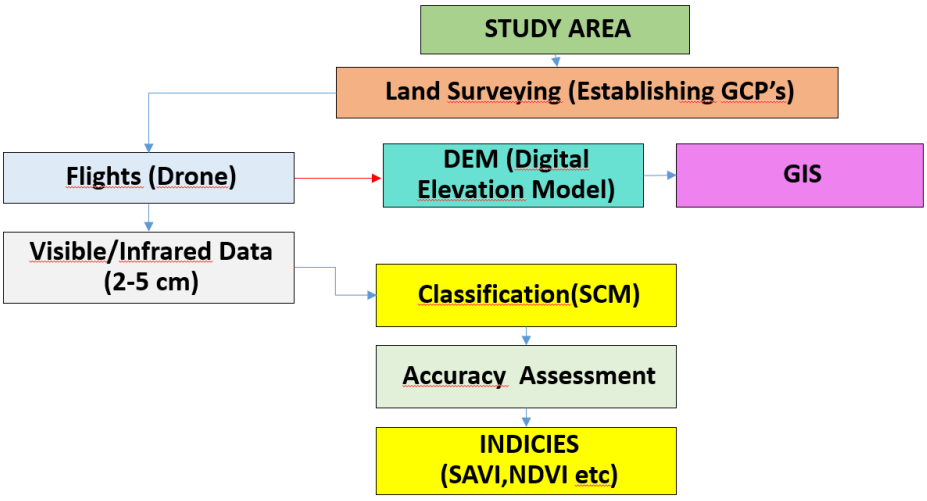

Figure 2. Flow chart

Ground sampling points were selected by using multi-spectral satellite data to be used in determining potential mineral areas in pre-classification. ASTER satellite multispectral bands are widely used in geological surveys. Separate field studies GPS measurements were carried out to determine the locations of soil classes in 4 different regions in the study area. By evaluating the spectral signatures of the samples by classification analysis, appropriate spectral ranges were determined and new test areas were created for the field study. The new samples analysis were completed by determining their positions with GPS were added to the spectral library inventory. Geometric and radiometric corrections have been applied to satellite data. Atmospheric corrections have been applied to visible, visible-infrared bands of ASTER satellite. The flow chart showing the working steps is shown in Figure 2.

Drone studies were carried out with a three planned flight by determining the ground control points. Due to the difficult geography, the flight altitude was realized as 75 m. The mosaic and DSM images obtained were combined using the data fusion method. In the first stage of the study, mosaic image and DSM image of the region was prepared by processing Pix4d software (Figure 3).

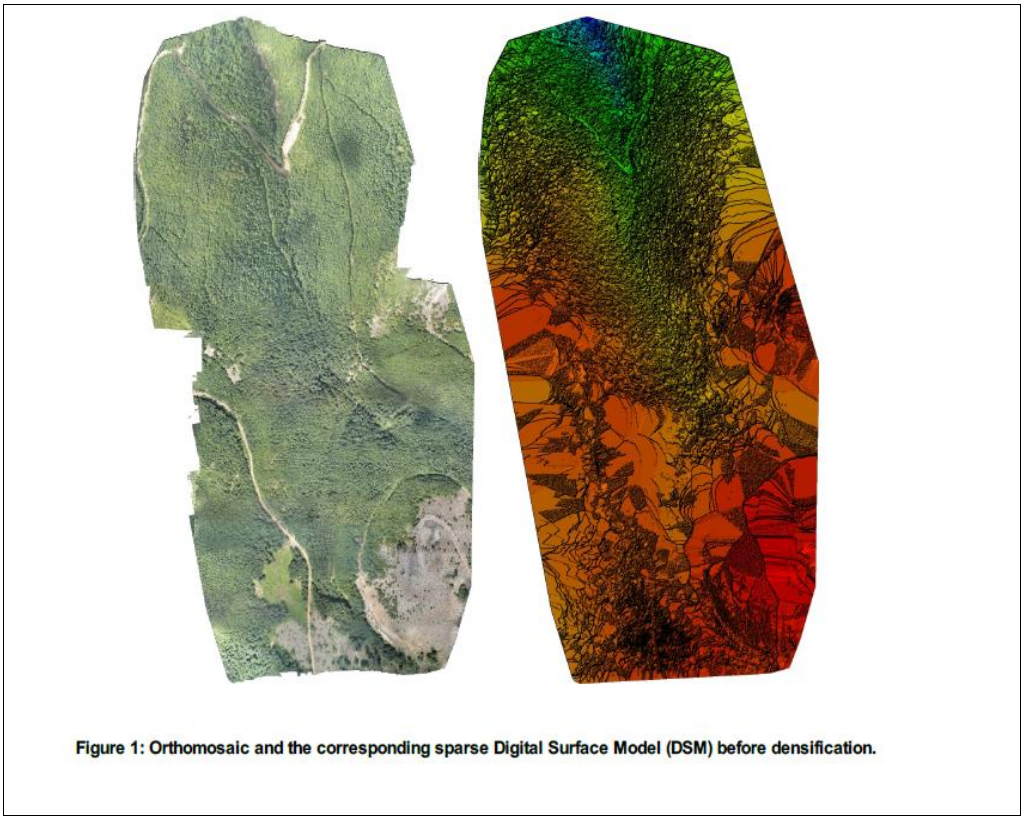

Figure 3. Ortomosaic and DSM images designed by UAV

The projection system is described in UTM and northern 36 segments. The location data of these points, Turkey national fixed satellite stations (TUSAGA-ACTIVE), is taken and converted into the national network based on the GPS coordinate system. One of the reasons for working with GPS was to test the positional accuracy of the sampling points on Google Earth, City Surf Globe and Orthophoto maps. Another was to compare the spatial accuracy of the ASTER satellite image with high spatial resolution images. It is aimed to increase the accuracy of image classification due to the ground accuracy of the samples by means of land measurements for sampling purposes (Alkan, 2019).

Drone photogrammetry and different remote sensing methods were used to investigate the metallic mines in this area.The digital elevation model of the region was generated by processing of the drone images from different heights in difficult geographical conditions. Using the high spectral resolution of the ASTER, different remote sensing methods were used and the mineral presence in the region was examined. Ore-dense areas were determined using merged data from drone and ASTER images. The samples obtained from the ground control points and the drilling for field-validated.

For the research, the measurement of ground control points with GPS was provided and sampling points were created for the classification process.. For this purpose, different algorithms were investigated for the selection

of classification methods to be used and SCM (Spectral Correlation Mapper) algorithm was preferred because it is powerful in spectral analysis (Alkan 2019), (Figure 4).It has been tested in four different class classification processes and areas showing mineral density have been evaluated by taking into account previous drilling studies.

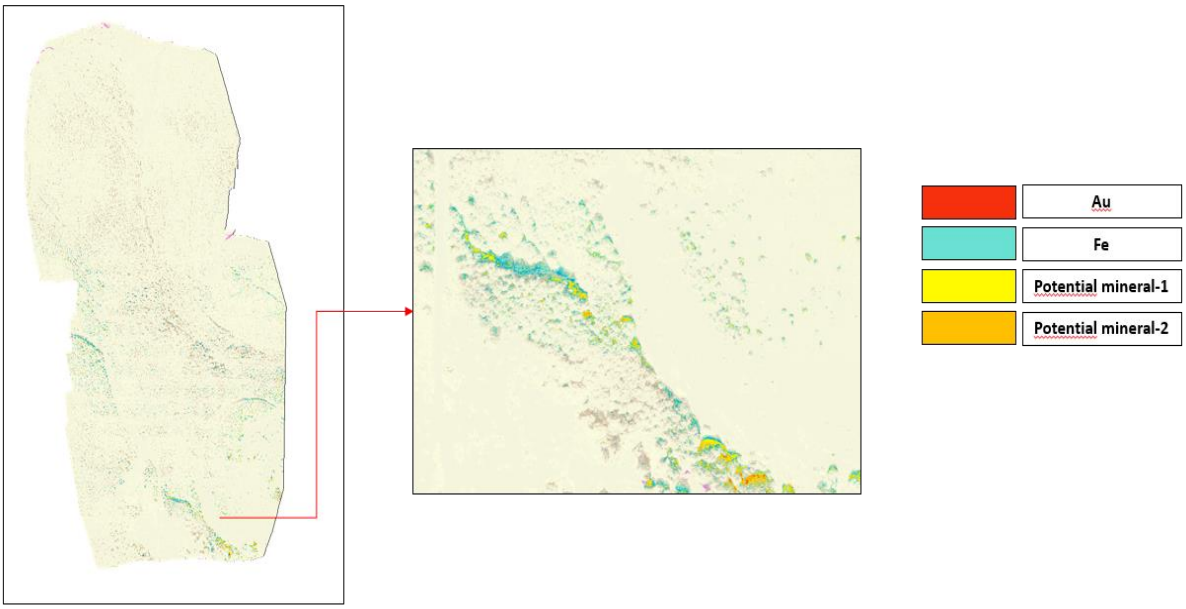

Figure 4. SCM image and sample classes

Considering the tree structure in the study area, three different ratios/indexes were studied in order to better perceive the symptoms that may occur on the surface (Figue 5). Iron-oxide ratio was studied in order to investigate the presence of gold composition in iron-intensive areas analyzed by previous drilling studies in the region. The NDVI index was studied to suppress vegetation and to better observe the spectral features in the region. NDVI and MSAVI indices were studied to suppress vegetation and to better observe the spectral features in the region.

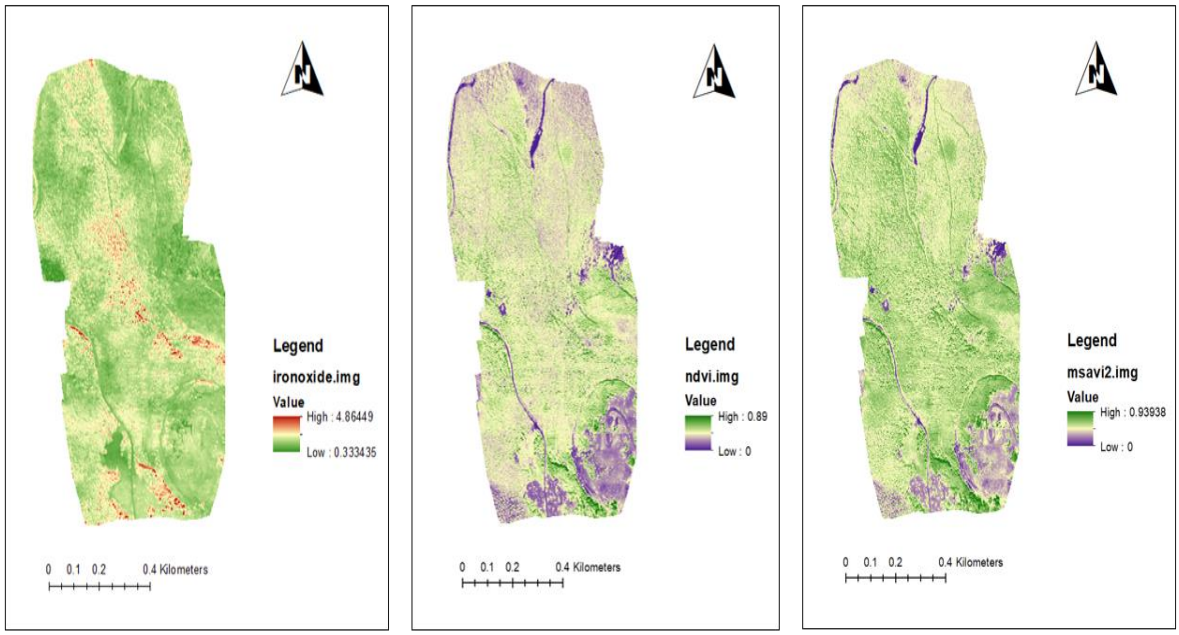

Figure 5 . Iron-Oxide, NDVI and MSAVI indexes applied the image.

DEM was generated by processing DSM image to achieve different elevations of the potential minerals for the study area (Figure 6).

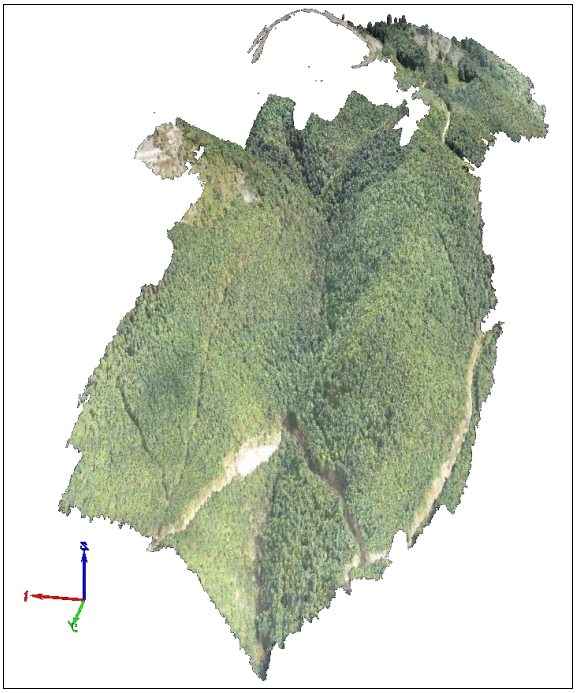

Figure 6 . DEM (Digital elevation model) generated by Pix4d

DEM study was performed with GIS to determine at which heights the potential mineral presence is located. With this study, it was aimed to contribute to the studies to be carried out in the steep and challenging conditions of the land geography (Figure 7).

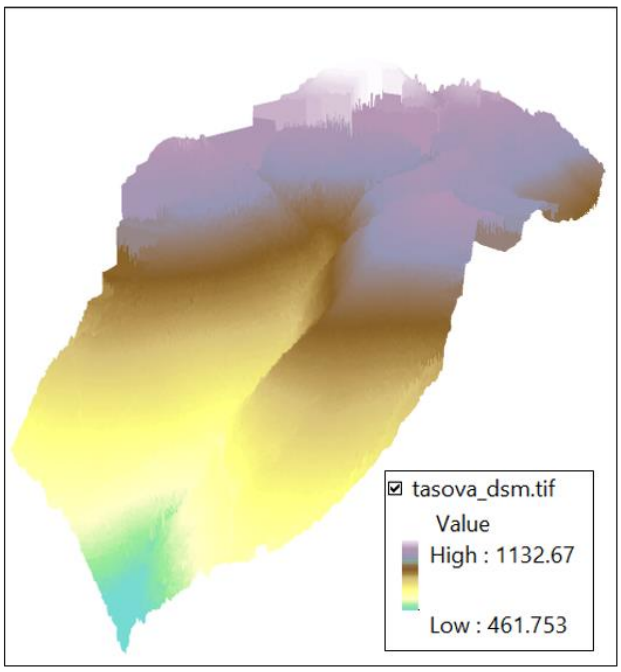

Figure 7. Distribution of the elevations of the study area generated by GIS

Accuracy analysis results were compared by using SCM classification methods for the investigation of potential mineral areas. Accuracy analysis result for SCM 0,94. The overall Kappa statistical values obtained for the 4 main classes in the SCM classifications results over 90%. Kappa, which mainly calculates the image classification accuracy, was obtained with the following formula.

In the formula, r = number of classes, xii = diagonal elements of error matrix, xi + = sum of rows; x+ i = column total, N = total number of pixels in error matrix.

$$\kappa = \frac{N \sum_{i=1}^{r} x_{ii} - \sum_{i=1}^{r} x_{i+} * x_{+i}}{N^2 - \sum_{i=1}^{r} x_{i+} * x_{+i}}$$

Discussion

The aim of this study, which was carried out using RS and Drone photogrammetry methods, was to determine the presence of minerals.. For this purpose, the SCM performances of the classification method studied to evaluate and an accuracy of 94% was obtained. In the regression analysis for the estimated potential areas, 20 test points selected from ground-tested analysied by drilling activities were used in the classification procedures. The regression analysis and the relation of mineral elements expected to exist in the predicted potential mineral areas were investigated particularly focused on Copper (Cu) and the Gold (Au) surroundings.

In the regression analysis for estimated potential mine areas, 20 points selected from the drilling-tested points were used in the classification procedures for the histograms of mineral groups respectively. Drone photogrammetry and remote sensing methods can be used for the mine areas efficiently. High spatial resolution(UAV:2-5 cm) and high spectral resolution ASTER images effectivly used in data fusion method to explorate minerals.

Conclusion

The use of RS and drone-based photogrammetry methods in the preliminary studies of mining research is great importance in terms of the cost of drilling activities. RS methods which integrate topographic, geological and geomorphological features with the help of satellite images can be used in researches, surface symptoms can be examined and statistics and potential mineral fields can be reached. Determination of mine area with computer-aided of RS Satellite data which was carried out at every stage of the study using research-planning, application-analysis, evaluation-interpretation and accuracy analysis.

- Remotely sensed satellite data can be necessary to demonstrate the usability of different methods in mineral researchs
- Related potential mineral researchers and scientists can benefit from these data
- These data can be used in the development of ground-validation studies by using a combination of UAV-based data and satellite imagery.
- Spectral library can be obtained by field work will be an important data source in the future research

Scientific Ethics Declaration

The authors declare that the scientific ethical and legal responsibility of this article published in EPSTEM journal belongs to the authors.

Acknowledgements or Notes

* This article was presented as an oral presentation at the International Conference on Technology, Engineering and Science (www.icontes.net) held in Antalya/Turkey on November 16-19, 2022.

References

Abubakar, A, J., Hashim, M. & Pour, A. B. (2017). Spectral mineral mapping for characterization of subtle geothermal prospects using ASTER data, *Journal of Physics: Conference Series, 852* (1), 012024

Alkan , Ö. (2018, December 17). *Statistical accuracy analysis of remote sensing methods used for mineral deposits and geothermal research in middle-north Anatolia region*, Doctorate Thesis, Istanbul Technical University, İstanbul.

Alkan, Ö., Coşkun, H. G., Çelik, H., Alkan, M. N., Kandil, S., Okur, Y. & Eraydın, E. (2018). Uzaktan algılama yöntemleri ile potansiyel jeotermal alanların belirlenmesi, *Afyon Kocatepe Üniversitesi Fen ve Mühendislik Bilimleri Dergisi, 17* (2017), 171-182.

Ayoobi, I. & Tangestani, M., H. (2018). Evaluation of subpixel unmixing algorithms in mapping the porphyry copper alterations using EO-1 Hyperion data, a case study from SE Iran, *Remote Sensing Applications: Society and Environment, 10* (2018), 120-127.

Guha, A. & Kumar, V. (2016). New ASTER derived thermal indices to delineate mineralogy of different granitoids of an Archaean Craton and analysis of their potentials with reference to Ninomiya's indices for delineating quartz and mafic minerals of granitoids—An analysis in Dharwar Craton, India, *Ore Geology Reviews, 74*, 76-87.

Jackisch,R., H., B.H., Zimmermann, R., Sørensen, E.V., Pirttijärvi,M.,Kirsch,M., Salmirinne,H., Lode,S., Kuronen, P., & Gloaguen, R., (2022, February). Drone-based magnetic and multispectral surveys to develop a 3D model for mineral exploration at Qullissat, Disko Island, Greenland, *Solid Earth, 13*, 793–825.

Karimpour, M. H., Stern, C. R., & Mazaheri, S. A. (2009). Hydrothermal alteration mapping in SW Birjand, Iran, using the advanced spaceborne thermal emission and reflection radiometer (ASTER) image processing. *Journal of Applied Sciences, 9*(5), 829-842.

Meer., F., Hecker, C., & Ruitenbeek, F. V. (2014). Geologic remote sensing for geothermal exploration: A review, *International Journal of Applied Earth Observation and Geoinformation, 33* (1), 255-269.

Pour, A. B., & Hashim, M. (2012). The application of ASTER remote sensing data to porphyry copper and epithermal gold deposits, *Ore Geology Reviews, 44*, 1-9.

Rajendran, S. & Nasir, S. (2017). Characterization of ASTER spectral bands for mapping of alteration zones of volcanogenic massive sulphide deposits, *Ore Geology Reviews, 88*, 317-335.

Shafaroudi, M., Karimpour, M. H., Stern, C. R. & Mazaheri, S. A. (2009). Hydrothermal alteration mapping in SW Birjand, Iran using the advanced spaceborne thermal emission and reflection radiometer (ASTER) image processing, *Journal of Applied Sciences, 9* (5), 829-842.

Shirazi ,A., Hezarkhani , A., Pour, A. B., Shirazy, A.& Hashim, M., (2022, November.). Neuro-Fuzzy-AHP (NFAHP) technique for copper explorationusing advanced spaceborne thermal emission and reflectionradiometer (ASTER) and geological datasets in the sahlabad mining area, east Iran the eclipse of listening. *The New Criterion, 15*(30), 5-13.

Srivastava,S., Seng,K.P.,Ang,L.M,, Pachas, N. A. & Lewis, T. (Eds.). (2022). Drone-based environmental monitoring and image processing, *Sensors, 22,*7872, 2-14

Author Information

Muntaha Kassım Hayder AL-ZUBADE
University of Technology,Baghdad,
Baghdad, Iraq
Contact e-mail: *muntahaalzubade@gmail.com*

Öykü ALKAN
Graduated Istanbul Technical University,
İstanbul, Turkey

Mehmet Nurullah ALKAN
Hitit University
Turkey

To cite this article:

Alzubade, M.K.H., Alkan, O & Alkan, M.N.. (2022). The role of drone photogrammetry, remote sensing and GIS methods in the detection of ore areas and their surroundings. *The Eurasia Proceedings of Science, Technology, Engineering & Mathematics (EPSTEM), 21,* 266-273.

The Eurasia Proceedings of Science, Technology, Engineering & Mathematics (EPSTEM)
ISSN: 2602-3199

The Eurasia Proceedings of Science, Technology, Engineering & Mathematics (EPSTEM), 2022

Volume 21, Pages 274-282

IConTES 2022: International Conference on Technology, Engineering and Science

Seismic Risk Prioritization of Masonry Buildings Using the First-Level Approaches for Vulnerability Assessment

Isıl SANRI-KARAPINAR
Maltepe University

Ayşe Elif OZSOY-OZBAY
Maltepe University

Abstract: This paper aims to determine the seismic risk distribution of old masonry buildings located in Galata, the historical region of İstanbul. In order to obtain seismic risk prioritization of the built environment, the seismic vulnerability assessment of 40 old masonry buildings was carried out according to both the Vulnerability Index Method (VIM) based on the European Macroseismic Scale (EMS-98) and the procedure in the Specifications for Determination of Seismically Vulnerable Buildings (SDSVB 2019). In the first part of the study, using the building data gathered by the screening process on site, the vulnerability scores (VS) comprising the structural and non-structural parameters were obtained and the performance score (PS) of each building was calculated according to SDSVB 2019. Depending on the results, in order to determine the seismic priority levels, the buildings were ranked from the lowest to the highest performance score and classified in terms of their structural vulnerability. Then, in the second part of the study, the vulnerability index (VI) for each building was determined depending on the building parameters affecting the structural vulnerabilities. On the basis of vulnerability indexes, damage grades of the buildings were estimated, and accordingly, the damage distribution was acquired for the building stock. Additionally, the seismic risk distribution maps were compiled for the building inventory according to the findings achieved from both methodologies. As a result of this study, the differences between the two first-level procedures were outlined with a comparative assessment, thereby demonstrating the importance of seismic risk prioritization of the historic built environment for city-scale risk management strategies.

Keywords: Masonry buildings, Seismic vulnerability assessment, Seismic prioritization, Damage distribution

Introduction

Historical buildings around the world have been threatened by devastating earthquakes and even subjected to severe damage leading to irreversible losses in cultural assets over centuries. Thus, especially for countries highly exposed to seismic hazards, protection of the historical built environment against the impacts of destructive earthquakes has become a major concern for disaster management authorities. In this context, in order to obtain the potential damage distribution of the building stocks in historical regions, prioritization of the masonry buildings through the use of seismic vulnerability assessment methods has gained great importance within the earthquake mitigation strategies implemented in seismic-prone countries.

The seismic vulnerability assessment methodologies are mainly based on different scoring strategies that take into account the seismicity level and the structural parameters of the assessed building to determine the seismic risk distribution of large numbers of buildings. Among these, the rapid visual screening (RVS) procedure proposed by FEMA P-154 (2015) is one of the most widely-used methods for the assessment of different building typologies that aims to identify the most vulnerable buildings using the building data obtained by standardized scoring forms filled out during the screening process. Also, in the RVS procedure proposed by The

National Research Council of Canada (NRC/IRC, 1992). The seismic vulnerability is represented by the Seismic Priority Index calculated using the structural and non-structural parameters, along with the site-specific characteristics that affect the seismic performance of the assessed building. Moreover, the method given in The New Zealand code (NZSEE, 2006) involves two levels of assessment approach through rapid visual screening and detailed seismic evaluation of the building. With the implementation of the Specifications for Determination of Seismically Vulnerable Buildings (SDSVB, 2019). The Turkish Ministry of Environments and Urbanization also set a walk-down evaluation method to be applied for the seismic vulnerability assessment of existing buildings in a regional scale. Similar to the procedures adopted in other countries, the method is based on the calculation of a building performance score taking into account the structural parameters such as the number of stories, construction quality, pounding effect and structural irregularities as well as the site topography, soil conditions and seismicity of the survey region.

Furthermore, an overview of the past research on seismic vulnerability analysis reveals that vulnerability index-based procedures also referred to as Vulnerability Index Methods (VIM) in literature, have been adopted for the large-scale seismic risk assessment of historical structures in heritage sites. As formerly proposed, VIM depends on the calculation of a vulnerability index of each building using the vulnerability parameters that represent a series of building-specific characteristics concerning the typology, construction quality, building adjacency and the structural system as well as the topography and the site conditions of the inspected area (Benedetti & Petrini, 1984). As the basis for determining the vulnerability index, the method employs the predefined vulnerability classes given in European Macroseismic Scale (EMS-98) (Grünthal, 1998).

Vulnerability index-based methodologies in the literature mainly depend on the statistical analysis of the building data regarding the typical damage observed from post-earthquake evaluation. The theory behind these methods is to represent the essential sources of building vulnerabilities that affect the structural behavior under a given seismic action and to determine the vulnerability index as a function of several parameters estimated for each assessed building (Lagomarsino & Giovinazzi, 2006; Ferreira et al. 2013). In recent index-based methodologies enhanced for seismic vulnerability assessment, additional parameters were adopted to account for the pounding effects due to the structural interactions between the adjacent buildings (Formisano et al., 2017; Chieffo et al., 2021). To investigate the physical vulnerability of the masonry buildings in Italian historic regions, Rapone et al. (2018) introduced a predictive model, directly implementing it as a case study in Scanno, Abruzzo. The proposed model was calibrated on the basis of the observed damage data from the 2009 L'Aquila Earthquake. Furthermore, Brando et al. (2021) proposed an empirical model for the buildings located in Cusco, Peru through an extensive field investigation of the historic region. Therefore, the well-documented post-earthquake building inventories have been utilized to improve and modify the existing procedures based on a vulnerability index-based approach. As can be seen from the previous studies, all the proposed methodologies have an attempt of determining the safety levels of existing buildings for the pre- and post-earthquake actions. Especially, the seismic prioritization decision is considered as a critical issue in terms of predicting and mitigating the seismic risks of heritage structures with local identity and cultural values. With this motivation, in this study, to evaluate the seismic vulnerability of the existing old masonry buildings located in the historical region of Galata, a case study was performed consisting of 40 representative buildings having similar structural characteristics that influence seismic performance. For the seismic risk prioritization of the built environment, two first-level procedures were carried out on the basis of SDSVB and VIM. As a result of this study, the seismic risk distribution maps were generated for the building inventory with respect to the findings obtained from both methodologies. Also, the importance of seismic risk prioritization of the historical built environment for city-scale risk management was revealed and emphasized with a comparative evaluation.

Methodology

The methodologies followed in this study are summarized separately in two sections. In the first section, the rapid vulnerability assessment method presented in SDSVB for masonry buildings is outlined whereas in the second section, the VIM, another rapid seismic assessment procedure introduced for masonry building stocks developed by the Italian National Group for Defense from Earthquakes (GNDT), is described.

Rapid Seismic Vulnerability Assessment according to SDSVB

In this study, the vulnerability assessment procedure introduced in SDSVB for the large existing masonry building stocks was followed. The aim of the proposed procedure is to identify, itemize, and classify the existing buildings having high-risk priorities during a forthcoming earthquake in a particular region. During the rapid

visual screenings, the vulnerability parameters for each building are detected, and performance scores (PSs) depending on both the vulnerability scores (VSs) that represent each parameter and the base score (BS) that changes according to the seismic hazard zone and the number of stories are calculated. For the calculation of BS, the seismic hazard zone concerning the seismicity of the studied district is specified with the use of an online tool supported by the National Disaster and Emergency Management Authority (AFAD). Also, for the identification of VSs, different vulnerability parameters are taken into account during on-site evaluation, namely, building typology, the number of stories, apparent quality, pounding effect, irregularity in the plan, insufficient wall amount, irregular wall openings, soft story, topographic effect and insufficient structural lintels. Under the condition of vulnerability parameter existence, a vulnerability score modifier (VSM) is determined as 0 or 1 detailed with the corresponding VSs. Among the vulnerability parameters, only for the apparent quality, VSM is decided as 0.1 or 2 pointing out the good, moderate, and bad conditions, respectively. The variation of BSs concerning the different hazard zones and VSs corresponding to each vulnerability parameter according to the number of stories are listed in Table 1.

Table 1. Base scores (BSs) and vulnerability scores (VSs) for masonry buildings

	Base Scores (BS)			Vulnerability Scores (VS)										
	Seismic hazard zones			Apparent quality		Pounding effect								
No. of stories	I ($S_{DS}\geq$ 1.0)	II-III ($0.5\leq S_{DS}$ <1.0)	IV (S_{DS} <0.5)	Material quality	Work manship quality	Damage	Soft story	Irregular wall openings	Insufficient wall amount	aligned Mid/Edge	not aligned Mid/Edge	Irregularity in Plan	Insufficient structural	Topog. Effects
1	110	120	130	-10	-5	-5	0	0	-5	0 /-5	-5 /-10	-5	-5	-5
2	100	110	120	-10	-5	-5	-5	-5	-5	0 /-5	-5 /-10	-10	-5	-5
3	90	100	110	-10	-5	-5	-5	-5	-10	0 /-5	-5 /-10	-10	-5	-5
4	80	90	100	-10	-5	-5	-10	-10	-10	0 /-5	-5 /-10	-15	-5	-5
5	70	80	90	-10	-5	-5	-10	-10	-15	0 /-5	-5 /-10	-20	-5	-5

After the determination of the BS, VS and VSM, PSs for each building are calculated by Eq. (1) to provide vulnerability judgment and identify the intervention priorities.

$$PS = BS + \sum[(VSM)\times(VS)] \tag{1}$$

With the completion of the calculation of PSs, the method assigns a class of seismic vulnerability for the entire building stock changing from low to high priority. At this point, the low PSs put forward the buildings having high priority which require a detailed assessment and retrofitting. As a result, in accordance with the risk levels obtained by this methodology, PSs are interpreted with caution and the outcomes are used to develop prioritization strategies in specific regions for seismic risk mitigation.

Vulnerability Index-Based Seismic Assessment Method

Among the methodologies introduced for the regional assessment of seismic vulnerability for prioritization of large numbers of buildings, in the second stage of the evaluation procedure implemented in this study, the seismic assessment of the old masonry building stock in the region was also performed using the vulnerability index-based methodology improved based on the approach proposed by the Italian National Group for the Defense against Earthquakes (GNDT, 1993). The method involves the evaluation of 15 parameters characterizing the structural vulnerabilities of the assessed building and the calculation of the vulnerability index in relation to the parameters considered in the implemented procedure (Formisano et al., 2015). Application of the method used in this study requires the completion of the vulnerability assessment form formerly introduced by Benedetti and Petrini (1984) as a rapid evaluation procedure aiming to investigate the seismic vulnerability of masonry buildings. The original assessment form includes 10 parameters to evaluate the performance of the building in relation with the construction quality and the structural and non-structural deficiencies. In addition to these parameters, the method used in this study includes 5 additional parameters accounting for the interaction effects between the structural units constructed adjacently. Therefore, with the use of the proposed assessment

form based on 15 parameters described in Table 2, the information related to the structural and typological characteristics is acquired from each building in the study region.

Table 2. Vulnerability assessment form with parameters

#	Parameters	Class Score (s_i)				Weight (w_i)
		A	B	C	D	
1	Organization of vertical structures	0	5	20	45	1
2	Nature of vertical structures	0	5	25	45	0.25
3	Distribution of plan-resisting elements	0	5	25	45	0.75
4	Location of the building and type of foundation	0	5	25	45	1.5
5	Type of floor	0	5	25	45	0.5
6	In-plane regularity	0	5	25	45	0.5
7	Vertical regularity	0	5	15	45	0.8
8	Roofing	0	15	25	45	0.75
9	Details	0	0	25	45	0.25
10	Physical conditions	0	5	25	45	1
11	Presence of adjacent building with different height	-20	0	15	45	1
12	Position of the building in the aggregate	-45	-25	-15	0	1.5
13	Number of staggered floors	0	15	25	45	0.5
14	Structural or typological heterogeneity among adjacent structural units	-15	-10	0	45	1.2
15	% difference of opening areas among adjacent facades	-20	0	25	45	1

As given in Table 2, a specific vulnerability score (s) is assigned to each vulnerability parameter, according to the estimated vulnerability class ranging between Class A and D, representing the worst and the best state of the related parameter. The weight (w) ranges between 0.25 and 1.5 depending on the significance of the inspected parameter on the structural vulnerability. Finally, the vulnerability index (I_v) of each structural unit is determined as the weighted sum of the score (s_i) of the estimated vulnerability class multiplied by the weight (w_i) corresponding to each parameter, using Eq. (2).

$$I_v = \sum_{i=1}^{15} s_i \,.\, w_i \tag{2}$$

The normalized vulnerability index (V_I) is also determined as

$$V_I = \left[\frac{I_v - \left(\sum_{i=1}^{15} s_{min}.w_i\right)}{\sum_{i=1}^{15}[(s_{max}.w_i) - (s_{min}.w_i)]}\right] \tag{3}$$

According to the vulnerability index-based approach used in this study, the potential damage state of each structural unit within the study region is predicted using the EMS-98 macroseismic intensity (I) obtained by the attenuation relationship given as

$$I = 1.45M_w - 2.46\ln(D) + 8.166 \tag{4}$$

where M_w and D represent the moment magnitude and source-to-site distance of the seismic action, respectively (Jaimes et al., 2015). Subsequently, determining the macroseismic intensity (I) for the specified seismic action of the study region, the mean damage grade (μ_D) of each building is calculated using Eq. (5) (Giovinazzi et al., 2006). As seen in Eq. (5), in addition to the macroseismic intensity (I), the normalized vulnerability index (V_I) and the ductility index (Q) are also used to predict the mean damage grade (μ_D) in the seismic vulnerability analysis. In order to derive the predicted damage distribution of the region, using the mean damage grade (μ_D) calculated for each structural unit, the studied buildings are classified into five discrete damage grades as no damage, slight damage, moderate damage, significant damage, severe damage and collapse denoted by D0, D1, D2, D3, D4 and D5, respectively.

$$\mu_D = 2.5\left[1 + tanh\left(\frac{I + 6.25V_I - 13.1}{Q}\right)\right] \tag{5}$$

Results and Discussion

In order to investigate the seismic vulnerability of the old masonry building stock located in Galata, 40 buildings having story numbers up to 5 were assessed as a case study and the results of the analyses conducted by two first-level methodologies (SDSVB and VIM) are presented.

In the initial stage of vulnerability analysis, for the implementation of the SDSVB method, the building data was collected through the walk-down survey. According to the VSs obtained on-site, PS for each building was calculated to classify the priority risk level. Herein, for the prioritization strategy of the surveyed buildings, PS ranges were classified as PS≤25, 25<PS≤55, 55<PS≤85 and PS>85 for high, moderate, low, and no risk levels, respectively. According to the given priority risk level categorization, the lowest scores show the group of buildings having high risk needing immediate intervention for further seismic evaluation.

Table 3 demonstrates a clear classification of the number of buildings according to the PS ranges. As detailed in the table, most of the entire building stock was graded as moderate (37.5%) and low (47.5%) priority risk levels. On the other hand, 5% of the entire building dataset was classified as high-risk priority while 10% was found to have no risk priority. It is noticeable from the table that the group of buildings within the high-priority risk range was composed of the ones with the higher number of stories. In the calculation of the PS according to the method implemented here, the BSs and VSs vary as the number of stories changes. Therefore, the number of stories appeared to be the main influential parameter affecting the seismic risk level of the assessed building.

Table 3. Distribution of the number of stories in the building dataset with respect to PS ranges

No. of stories	PS≤25	25<PS≤55	55<PS≤85	PS>85
	High	*moderate*	*low*	*no risk*
1	-	-	-	-
2	-	-	2	3
3	-	-	3	1
4	-	4	8	-
5	2	11	6	-
Σ No. of buildings	2	15	19	4
% of buildings	%5	%37.5	%47.5	%10

For determining the critical deficiencies in the studied region and investigating the effect of vulnerability parameters on the seismic risk priority, the distribution of each parameter with respect to PSs is presented in Table 4. Since all inspected buildings in the study area were constructed adjacently, the pounding effect was extensive as expected. Furthermore, for the high-risk priority building group, as can be seen, the existence of the other four parameters (insufficient wall amount, irregular wall amounts, irregularity in plan and topographic effect) caused a drastic change in the seismic risk level.

Table 4. Distribution of vulnerability parameters with respect to PS ranges.

PS Ranges	Soft story	Insufficient wall amount	Apparent quality	Irreg. wall openings	Topographic effect	Irreg.in plan
0<PS≤25	0.0	50.0	0.0	100.0	50.0	50.0
25<PS≤55	40.0	73.3	6.7	20.0	13.3	6.7
55<PS≤85	26.3	10.5	0.0	0.0	5.3	5.3
PS>85	50.0	0.0	0.0	0.0	0.0	0.0

With the completion of the steps of the SDSVB assessment, vulnerability analysis was also carried out by the VIM based on EMS-98. According to the procedure, V_I was calculated considering 15 vulnerability parameters representative of both the structural and non-structural characteristics of the assessed building. The distribution of the VIs estimated for the building stock was illustrated in Figure 1. The results of the distribution revealed that VIs ranged in between 0.16 and 0.42 having a mean value calculated as 0.25.

In order to reveal the effect of each vulnerability parameter on the seismic risk evaluation, the distribution of the estimated vulnerability classes (A, B, C and D) within the entire building stock was determined as shown in Figure 2. Considering the classes C and D, it is apparent from the figure that P1 and P6 representing the parameters related to the organization of vertical structures and in-plane irregularity, respectively, significantly penalized the seismic vulnerability performance of the buildings.

Moreover, since the masonry building stock was entirely composed of adjacent units, the percent distribution of vulnerability classes for the parameters regarding the pounding effects (P11 to P15) had a remarkable impact on the vulnerability analysis. Also, Figure 2 justifies that the adjacent buildings with the same heights, having the same opening ratio on the facades (P11 and P15) had a positive effect on the seismic performance.

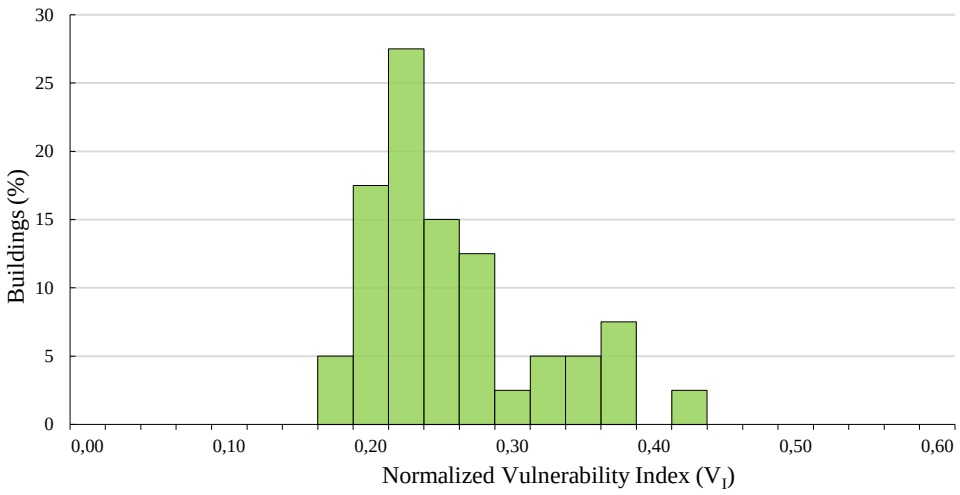

Figure 1. Distribution of the buildings with respect to normalized vulnerability index (V_I)

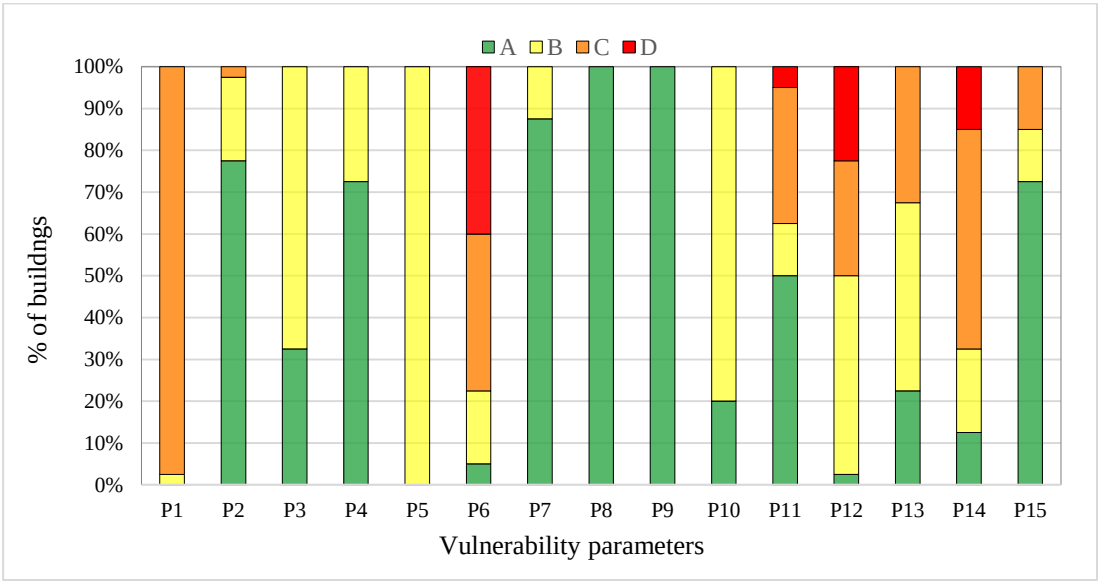

Figure 2. Distribution of vulnerability classes with respect to vulnerability parameters

The damage distribution related to the mean damage grades (μ_D) and the PSs of the building aggregate are represented in Figure 3. Following the procedures of VIM, μ_D mainly depends on EMS-98 based macroseismic intensity (I) and the normalized vulnerability index (V_I). Hence, the macroseismic intensity level concerning the seismicity of the assessed region was obtained as XI for the moment magnitude, Mw=7 and source-to-site distance of D = 20 km. The mean damage grade distribution given in Figure 3(a) implies that the entire building stock was clustered within the ranges of D1, D2 and D3 corresponding to the slight, moderate and significant damage grades, respectively. The results revealed that the majority of the surveyed buildings (77.5%) was found to sustain moderate damage (D2). On the other hand, it is forecasted from the findings that 10% of the buildings experienced slight damage (D1), whereas 12.5% suffered significant damage (D3). In Figure 3(b), PS distribution obtained by SDSVB confirmed that the majority of the surveyed buildings were graded as having moderate and low priority risk levels, as also detailed in Table 3 previously.

When the results were compared in Figure 3, moderate damage grade (D2) was correlated to the PS ranges comprising both the moderate and low priority levels. From the correlation between the degree of damage and PS, the results based on SDSVB appeared to be on the safer side. It is an expected result that this procedure, which also allows the compensation of potential errors that might be encountered during the evaluation of large numbers of buildings through visual screening in a limited time, would remain on the safer side.

In order to discuss the results obtained by the two first-level procedures, the spatial distributions showing the seismic performance of the buildings in terms of μ_D and PSs were illustrated in Figure 4.

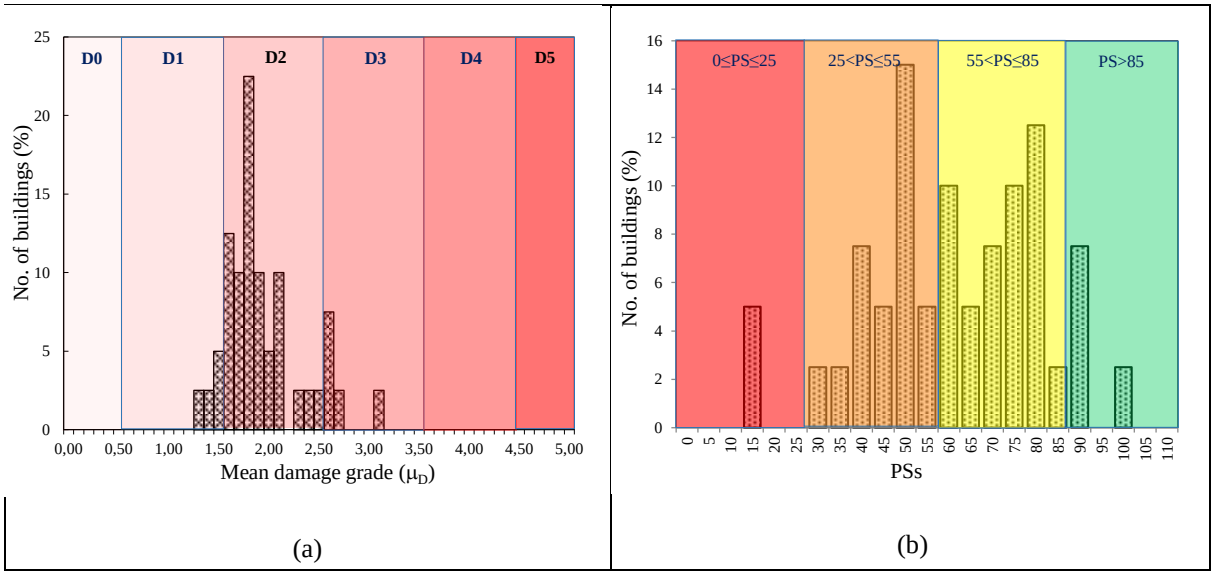

(a) (b)

Figure 3. The damage distribution related to (a) the mean damage grades (μ_D) and (b) PSs of the masonry buildings

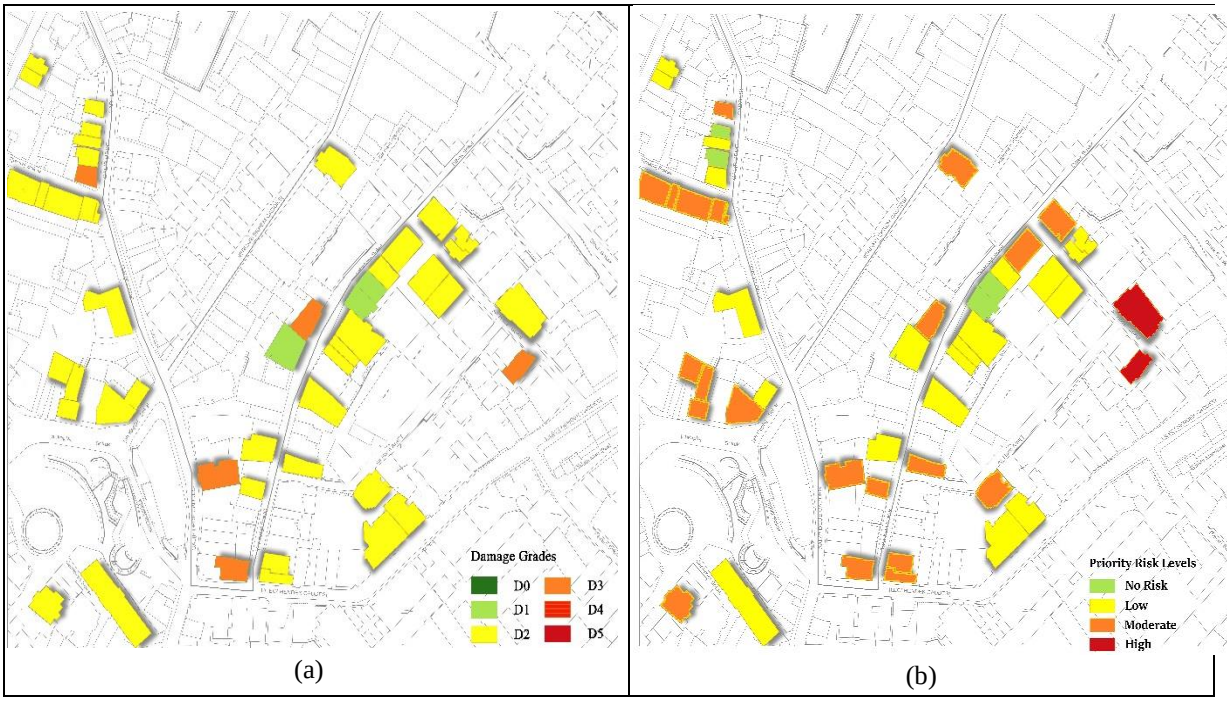

(a) (b)

Figure 4. Spatial distribution of the seismic performance of the buildings with respect to (a) mean damage grades and (b) PSs.

To sum up the results, the spatial distribution of the seismic performance of the buildings is demonstrated in Figure 4. In the analysis conducted by VIM, the damage grades were ranked in between the damage classes of D1 and D3. On the other hand, the PSs calculated with respect to SDSVB were found to be ranked in all priority categories varying from no risk to high risk level for the entire building stock. Considering the location of the buildings, the results of both first-level assessment methods on the building basis was also observed to be consistent. Taken as a whole, when Figure 4 is examined comparatively, the most critical buildings having the highest priority level in the region were also expected to suffer moderate and significant damage grade. Additionally, the buildings predicted as having slightly and moderate damage levels were classified in low and moderate seismic priority risk categories. Besides, closer inspection on the findings of SDSVB revealed that, buildings having high-risk priority were affected by the existence of more than one vulnerability parameter in a single structural unit. Particularly, the most vulnerable buildings were the ones located at the corners having insufficient wall amount and irregularity in plan.

Conclusion

This study aimed to reveal the seismic vulnerability of the masonry buildings located in Galata, a historic district of Istanbul, by carrying out two first-level procedures based on SDSVB and VIM. By the review and discussion of both methods within a case study composed of 40 masonry buildings, the differences between the interpretations of the findings about the seismic prioritization of the buildings were set out.

With the given two conceptually different methods, the expected damage grade and seismic prioritization levels, indicating the seismic performance of the buildings, were obtained for the same masonry building aggregate. First, the results obtained were examined in terms of their statistical distribution and then, their spatial distributions were derived for the surveyed region. As a result, a significant correlation was attempted to be achieved between the expected damage grades under possible earthquake effects determined by VIM and seismic risk prioritization levels obtained by SDSVB.

Contributing to literature as a component of the seismic risk mitigation approaches, this study emphasized the importance of outcomes of the structural vulnerability assessment of existing buildings for the pre-earthquake preparation and management strategies and underlined that the resiliency of cities is improved through seismic risk prioritization.

Recommendations

This article will serve for future studies on the seismic vulnerability assessment to make decisions for the prioritization of strengthening activities of the built environment. Also, this study will contribute to the strategic planning and decision-making procedure governed by local authorities, especially for the historical regions.

Scientific Ethics Declaration

The authors declare that the scientific ethical and legal responsibility of this article published in EPSTEM journal belongs to the authors.

Acknowledgements or Notes

* This article was presented as an oral presentation at the International Conference on Technology, Engineering and Science (www.icontes.net) held in Antalya/Turkey on November 16-19, 2022.

References

AFAD (2018). *Türkiye deprem haritaları interaktif web uygulaması*. Retrieved from https://tdth.afad.gov.tr/

Benedetti, D. & Petrini, V. (1984). On the seismic vulnerability of masonry buildings: an evaluation method. *L'industria delle Costruzioni*, *149*, 66-74.

Brando, G., Cocco, G., Mazzanti, C., Peruch, M., Spacone, E., Alfaro, C., Sovero K., & Tarque, N. (2021). Structural survey and empirical seismic vulnerability assessment of dwellings in the historical centre of Cusco, Peru. *International Journal of Architectural Heritage*, *15*(10), 1395-1423.

Chieffo, N., Formisano, A., & Ferreira, T. M. (2021). Damage scenario-based approach and retrofitting strategies for seismic risk mitigation: An application to the historical Centre of Sant'Antimo (Italy). *European Journal of Environmental and Civil Engineering*, *25*(11), 1929-1948.

FEMA P-154 (2015). *Rapid visual screening of buildings for potential seismic hazard: A handbook.* https://ascelibrary.org/doi/abs/10.1061/9780784479728.064

Ferreira, T. M., R., Vicente, J. A. R., Mendes da Silva, H., Varum, & Costa, A. (2013). Seismic vulnerability assessment of historical urban centres: Case study of the old city centre in Seixal, Portugal. *Bulletin of Earthquake Engineering*, *11*(5), 1753–1773.

Formisano, A., Florio, G., Landolfo, R., & Mazzolani, F.M. (2015). Numerical calibration of an easy method for seismic behaviour assessment on large scale of masonry building aggregates. *Advances in Engineering Software*, *80*, 116–138.

Formisano, A., Chieffo, N., & Mosoarca, M. (2017). Seismic vulnerability and damage speedy estimation of an urban sector within the municipality of San Potito Sannitico (Caserta, Italy). *The Open Civil Engineering Journal*, *11*, 1106–1121.

Giovinazzi, S., Lagomarsino, S., & Pampanin, S. (2006). Vulnerability methods and damage scenario for seismic risk analysis as support to retrofit strategies: An European perspective. *Proceedings of the NZSEE Conference.* Napier, New Zealand.

GNDT (1993). *National group for protection against earthquakes*. National group for protection from earthquake. manuale per il rilevamento de lla vulnerabilità sismica degli edifici, Istruzioni per la Compilazione Della Scheda di 2◦ Livello; Roma, Italy.

Grünthal, G. (1998). *European macroseismic scale EMS-98*. European Center for Geodynamics and Seismology, Luxembourg.

Jaimes, M. A, Reinoso, E, & Esteva, L. (2015). Risk analysis for structures exposed to several multi-hazard sources. *Journal of Earthquake Engineering*, *19*, 297–312.

Lagomarsino, S., & Giovinazzi, S. (2006). Macroseismic and mechanical models for the vulnerability assessment of current buildings. *Bulletin of Earthquake Engineering*, *4*(4), 415–433.

NZSEE. (2006). *Assessment and improvement of the structural performance of buildings in earthquake. New Zealand Society for Earthquake Engineering*. Retrieved from https://www.nzsee.org.nz/db/).pdf

Rapone, D., Brando, G., Spacone, E., & De Matteis, G. (2018). Seismic vulnerability assessment of historic centers: description of a predictive method and application to the case study of scanno (Abruzzi, Italy). *International Journal of Architectural Heritage*, *12*(7–8), 1171–1195

Author Information

Işıl Sanrı Karapınar
Maltepe University
İstanbul, Turkey
Contact e-mail: *isilkarapinar@maltepe.edu.tr*

Ayşe Elif Özsoy Özbay
Maltepe University
İstanbul, Turkey

To cite this article:

Sanri-Karapinar, I. & Ozsoy-Ozbay, A.E. (2022). Seismic risk prioritization of masonry buildings using the first-level approaches for vulnerability assessment. *The Eurasia Proceedings of Science, Technology, Engineering & Mathematics (EPSTEM), 21,* 274-282.

The Eurasia Proceedings of Science, Technology, Engineering & Mathematics (EPSTEM)
ISSN: 2602-3199

The Eurasia Proceedings of Science, Technology, Engineering & Mathematics (EPSTEM), 2022

Volume 21, Pages 283-287

IConTES 2022: International Conference on Technology, Engineering and Science

Improvement of Photo-Catalytic Properties of Graphene by N-Doping

Resat Can OZDEN
Eskişehir Osmangazi University

Ersu LOKCU
Eskişehir Osmangazi University

Mustafa ANIK
Eskişehir Osmangazi University

Abstract: Graphene is a two-dimensional, honeycomb-structured material consisting of a uniform monolayer of carbon atoms. Most scientists believe that graphene has revolutionary properties and research on graphene is increasing exponentially. It is considered as an alternative material that can replace silicon according to its properties, and graphene is called the supermaterial of the next century. On the other hand, some applications of graphene require the rearrangement of electronic properties. The chemical doping method is one of the most frequently used methods for this arrangement. In this study, nitrogen-doped graphene was synthesized by chemical vapor deposition (CVD) method. Urea was used as a nitrogen-doping source. Different amounts of urea were used to optimize the chemical nitrogen doping process. Raman spectroscopy was used for the characterization of the synthesized nitrogen-doped graphene. During the experiments, light (400-700 nm wavelength) was sent to the nitrogen-doped graphene surface with a solar simulator (A-type 150W, 1-3 SUN, Xenon lamp, 1.5 AM Filter). The photo-catalytic properties of the samples were measured by the potentiostatic technique.

Keywords: Energy, Graphene, Lithium, Battery

Introduction

Since its first fabrication by mechanical exfoliation in 2004, graphene, a single-atom-thick sheet of carbon, has drawn significant interest from the scientific and technical community (Novoselov et al., 2004). Graphene's distinctive 2D honeycomb lattice structure gives it several exceptional chemical and physical capabilities in addition to making it the thinnest and strongest material in the universe (Geim & Novoselov, 2007).

Heteroatom doping can be used to successfully alter the structures and characteristics of carbonaceous materials. In accordance with this theory, doping graphene with nitrogen (N) can drastically alter the characteristics and functionality of graphene-based materials. By adding more heteroatoms, it is possible to alter the band gap of graphene, causing it to exhibit semiconducting qualities. The catalytic activity of doped graphene toward electro-catalytic or photo-catalytic processes can be considerably increased by the development of active areas by asymmetric spin and charge distributions during heteroatom doping in the graphene network (Wang et al., 2012).

In the study, it was aimed to optimize the photo-catalyst properties of nitrogen-doped graphene synthesized by chemical vapor deposition (CVD) method and then to use n-doped graphene as a photo-electrode in a Li-ion oxygen battery.

Method

N-doped graphene was produced by evaporation of urea (CH_4N_2O) powder in the chemical vapor deposition method. Methane (CH_4) was used as a carbon source in the formation of graphene. The production flow chart of n-doped graphene is given in Figure 1.

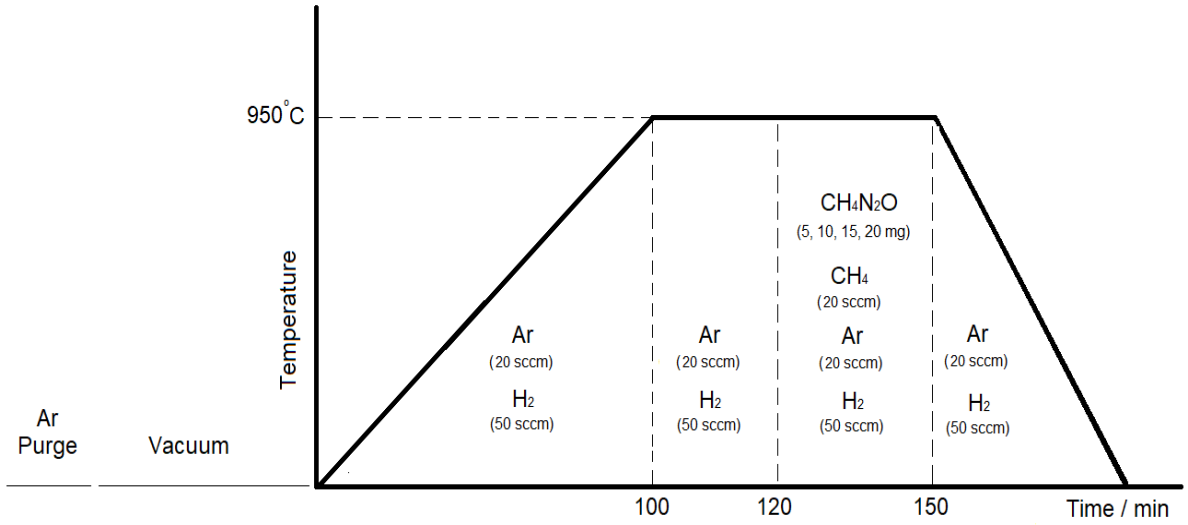

Figure 1. Production flow chart of n-doped graphene

Urea powder was evaporated by drawing it from the cold region of the quartz cell in the chemical vapor deposition furnace during the graphene growth stage to the region where the temperature varies between 60°C and 70°C, thus providing a highly controlled production. In studies conducted for this purpose, the most appropriate urea amounts were determined as 5 mg (U5), 10 mg (U10), 15 mg (U15) and 20 mg (U20) per cm^2, and comparisons were made on these 4 different compositions. Graphene is produced on copper substrates. Afterward, copper was dissolved in 50% HCl solution containing 0.5 M FeCl3. Finally, graphene was cleaned with acetone/ethanol combinations.

During the experiments, light (400-700 nm wavelength) was sent to the nitrogen-doped graphene surface with a solar simulator (A-type 150W, 1-3 SUN, Xenon lamp, 1.5 AM Filter). The photo-catalytic properties of the samples were measured by the potentiostatic technique. Samples were examined with RENISHAW RAMAN inVia Microscope brand Raman Spectroscopy. Raman measurements were made using a laser at a wavelength of 532 nm.

Results and Discussion

Raman Spectroscopy

A highly helpful technique for describing N-doped graphene is Raman spectroscopy. The main characteristics of the spectrum of N- graphene are the D, G, and 2D bands. The two main peaks of graphene, 2D (~2700 cm-1) and G (~1580 cm-1), show sp2 hybridization at carbon atoms (Ferrari et al., 2006). The D peak (~1350 cm-1) observed in addition to these two peaks indicates the presence of sp3 carbons in the structure, in other words, the defects in the structure (Ferrari et al., 2006). Observation of the 2D peak without the D peak indicates a highly crystalline surface. Small shifts in peak positions are due to differences in synthesis temperature. The ratio of the 2D peak to the G peak intensity gives information about the number of graphene layers. If this ratio is above 2, it is accepted that the graphene is in a single layer, and the number of layers increases as the ratio decreases.

Raman spectra of nitrogen-doped graphene produced with 5 mg, 10 mg, 15 mg and 20 mg urea powder are presented in Figure 2. As a result of the analysis, D (~1350 cm-1) peak was also detected. The presence of this peak, which belongs to the defects in the structure, indicates that nitrogen doping has taken place. It was also observed that as the amount of urea increased, the relative ratio of the D peak to the 2D and G peaks also increased.

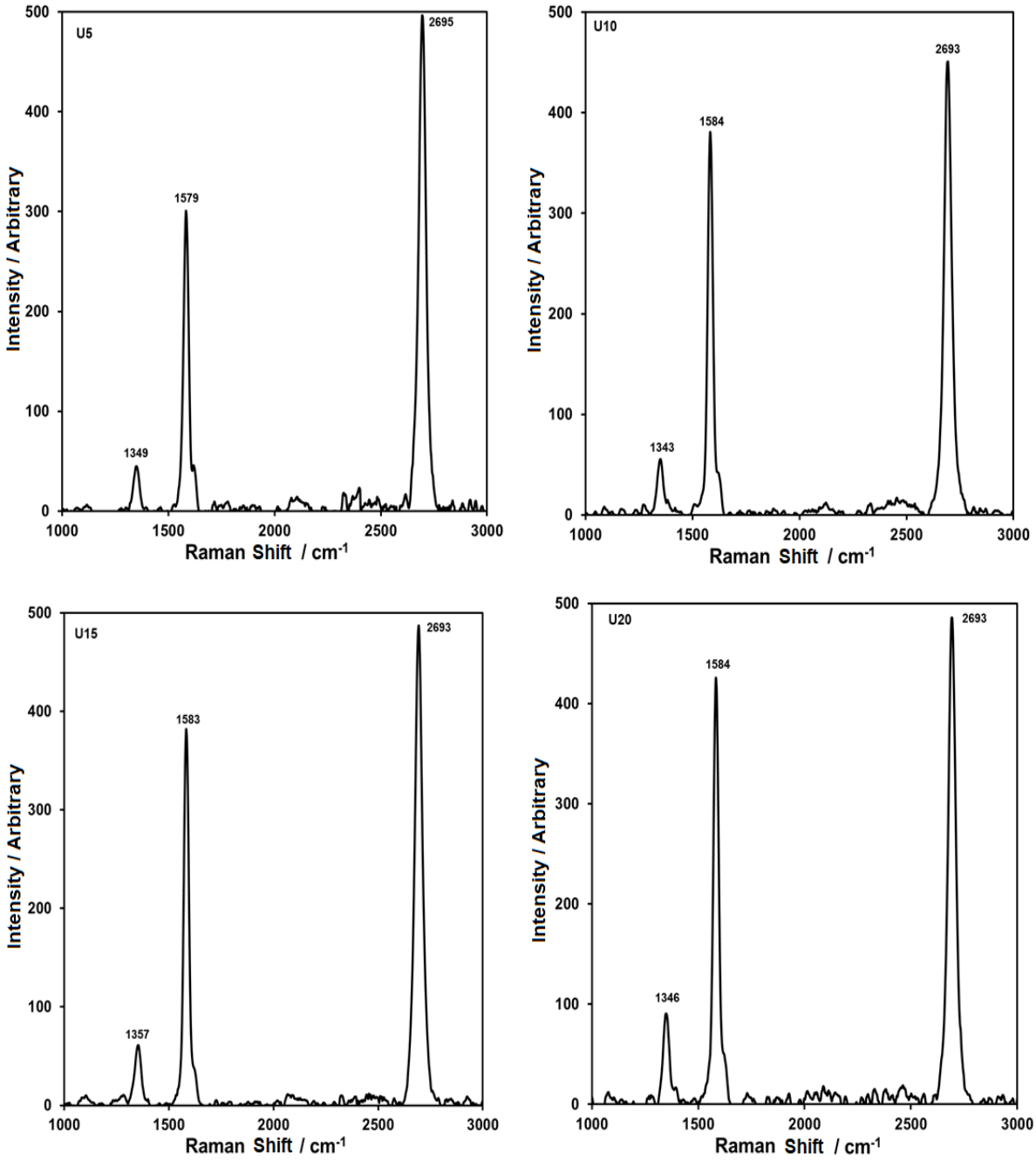

Figure 2. Raman spectra of n-doped graphene produced with 5 mg, 10 mg, 15 mg and 20 mg urea powder

Optical Properties

The optimum amount of urea for nitrogen-filled graphene to be used as photo-electrode was tried to be determined by using photo-currents. The optimum amount of urea was determined by reference to such data for both characterization and performance experiments. The photo-anodic current measurements were obtained at a very low value of 50 mV anodic overpotential. Despite this, the obtained photo-anodic current values are at a remarkable level. This exceptional-electrode performance has been achieved by depositing the semiconductor homogenously on the electrode surface.

When evaluated depending on the amount of urea powder used in the nitrogen-filled graphene synthesis process, the highest photo-anodic currents were obtained with 10 mg of urea powder (U10). Photo-current values of the U10 sample are presented in Figure 3.

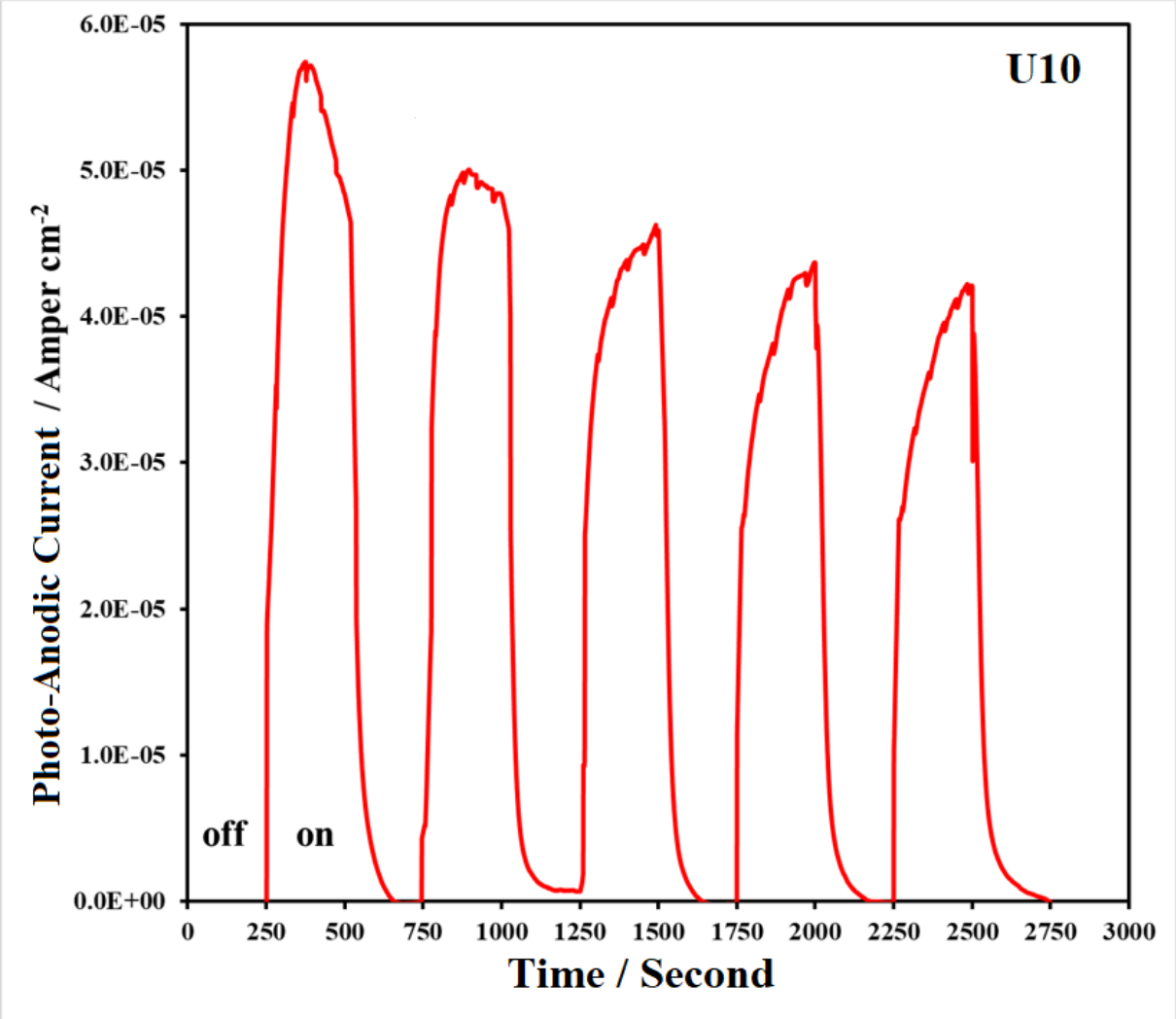

Figure 3. Photo-current values of the U10 sample are presented

Conclusion

In the study, it was determined that the n-doped graphene obtained by evaporation of 10 mg of urea powder during the graphene growth process per 1 cm2 copper substrate produced the highest photo-current. It has been observed that nitrogen doping contributes more to the photo-catalytic properties in the pyridinic, pyrrolic form compared to the graphitic form, provided that the structural integrity of graphene is preserved.

Scientific Ethics Declaration

The authors declare that the scientific ethical and legal responsibility of this article published in EPSTEM journal belongs to the authors.

Acknowledgements

*This article was presented as the poster presentation at the International Conference on Technology, Engineering and Science (www.icontes.net) held in Antalya/Turkey on November 16-19, 2022.

*This article was supported by the Scientific and Technological Research Council of Turkey under the project number 219M269.

References

Ferrari, A. C., Meyer, J. C., Scardaci, V., Casiraghi, C., Lazzeri, M., Mauri, F., Piscanec, S., Jiang, D., Novoselov, K. S., Roth, S., & Geim, A. K. (2006). Raman spectrum of graphene and graphene layers. *Physical Review Letters*, *97*(18), 1–4.

Geim, A. K., & Novoselov, K. S. (2007). The rise of graphene. *Nature Materials*, *6*(3), 183–191.

Novoselov, K. S., Geim, A. K., Morozov, S. V., Jiang, D. E., Zhang, Y., Dubonos, S. V., ... & Firsov, A. A. (2004). Electric field effect in atomically thin carbon films. *Science. 306*(5696), 666–669.

Wang, H., Maiyalagan, T., & Wang, X. (2012). Review on recent progress in nitrogen-doped graphene: Synthesis, characterization, and its potential applications. *ACS Catalysis*, *2*(5), 781–794.

Author Information

Reşat Can ÖZDEN
Eskişehir Osmangazi University
Eskişehir, Turkey
Contact e- mail:rcanozden @ogu.edu.tr

Ersu LÖKÇÜ
Eskişehir Osmangazi University
Eskişehir, Turkey

Mustafa ANIK
Eskişehir Osmangazi University
Eskişehir, Turkey

To cite this article:

Ozden R.C., Lokcu, E., & Anik, M. (2022). Improvement of photo-catalytic properties of graphene by N-doping. *The Eurasia Proceedings of Science, Technology, Engineering & Mathematics (EPSTEM), 21,* 283-287.

The Eurasia Proceedings of Science, Technology, Engineering & Mathematics (EPSTEM)
ISSN: 2602-3199

The Eurasia Proceedings of Science, Technology, Engineering & Mathematics (EPSTEM), 2022

Volume 21, Pages 288-294

IConTES 2022: International Conference on Technology, Engineering and Science

Modeling the Nonlinear Behavior of Predamaged Reinforced Concrete Beams Retrofitted with Bonded and Jacketed FRP Sheets

Souad AIT TALEB
University Mouloud Mammeri of Tizi Ouzou

Sara MEDJMADJ
University of Bejaia

Abdelmadjid SI SALEM
University Mouloud Mammeri of Tizi Ouzou

Abstract: This paper consists on the numerical simulation based-finite element modeling carried out on reinforced concrete (RC) beams predamaged and strengthened with carbon fiber sheet (CFRP) and a fiberglass (GFRP) jacket under monotonic bending loads. The retrofitted RC beams were modeled using ABAQUS to estimate the effect of concrete and steel damage rate. After the experimental validation of the proposed model, four configurations of damage rate were considered according the initial compression resistance of undamaged concrete. Indeed, the geometrical model and the choice of the finite element models were generated in a full three-dimensional (3D) space. Moreover, the real behavior of each used material has been simulated using the experimental laws of each one, namely: concrete damaged plasticity, elastoplastic steel model with isotropic hardening and orthotropic elastic one for FRP composites. The discussion of the numerical outcomes in terms of bearing capacity curves and the tensile damages maps provides the full interest of the FRP repair technology on the overall and local flexural response of predamaged RC beams.

Keywords: Predamaged beams; Repair; CFRP sheets; GFRP Jacket; Nonlinear FE simulation.

Introduction

Materials and structures damage has been almost considered as unwanted behavior state, which may cause catastrophic consequences (Ali Ahmed el al., 2022). Although the causes of a mechanical failure can be analyzed, the prediction and prevention of failures remain difficult (Djenad et al., 2022a; 2022b). Accordingly, the macroscopic mechanical behavior was generally resulting from the average effects of the microstructure (Jirawattanasomkul et al., 2020). Moreover, damages result from the combination of loading peaks, localization effect and microstructure defects (Lee el al., 2012).

In this connection, the repair and rehabilitation of damaged structures are primordial to lifetime and service usage (Malek et al, 1998; Huang et al, 2018; Rashid et al, 2019). Certainly, the most mentioned approach for the retrofitting of exciting RC beams for recovery the bearing capacity degradation was the external bonding of FRP on the critical zones susceptible to collapse (Al-Sulaimani et al, 1994; Raouf et al., 2000; Hussain et al., 1995; Daouadji, 2013; Si Salem et al., 2020). Recently, the use of FRP fibers with high corrosion and strength characteristic was widely highlighted to improve the mechanical performances of damaged existing members (Raouf et al., 2000). Furthermore, FRPs oppose to the deformations on longitudinal and transverse direction caused by dead and dynamic loads, which improve the ultimate flexural stress of pre-damaged concrete (Ait Taleb et al., 2016). In addition, numerous studies have been conducted to study the behavior and the capacities of retrofitted RC beam fully or partially wrapped with FRP. One can cite, the works of (Huang et al., 2018) on

the strengthening of RC beams with bonded GFRP and CFRP in the critical zone. The authors have shown the effectiveness of FRP to improve the flexural and the shear performances of RC beams.

Regarding the cited researches above, the present work consists to advocate a finite element base according to the initial pre-damage in the rehabilitation of the critical zones of RC beams under four-point bending. Indeed, the repair was smeared in flexion with externally bonded CFRP plates and in shear by applying and GFRP jacket. The structural analysis was established under (ABAQUS, 2014) to estimate the variation of concrete and steel damages. In this respect the bearing capacity curves are provided to assess the effective repair layout in function of bearing capacity ratio.

Finite Element Simulation Procedure

The key objective of the suggested FEM procedure is to highlight the consequence of concrete and steel damage on the characteristics which may increase the resistance ratio of pre-damaged RC beams. Accordingly, a simulated model which allows to estimate the resistance of pre-damaged and repaired RC beam submitted to monotonic loads was provided and valeted using experimental literature results.

Simulated Specimens

The real scale RC beams and FRP strengthened RC ones designed and tested by (Huang et al., 2018) were considered in the current research to validate the proposed modeling. The modeled beam's geometrical and reinforcement characteristics are illustrated in Figure 1 and Table 1. Indeed, bending/shear reinforcement was applied with CFRP sheet and GFRP Jacket respectively.

Table 1. Steel and FRP design reinforcement of simulated beams tested by (Huang et al., 2018)

Beam dimension (mm)	Steel reinforcement	FRP reinforcement
Span: 800	Repartition rebar: 2A8	Flexural: CFRP sheet
Width: 100	Flexural bars: 2C12	Shear: GFRP Jacket
Height: 160	Stirrups: 15Ø8	Combined: Carbon and glass fibers

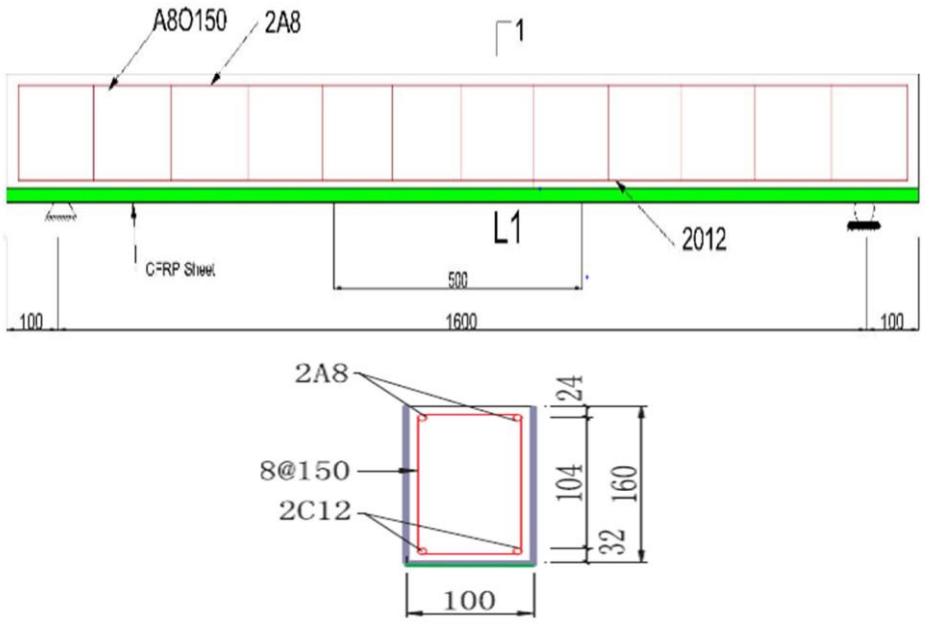

Figure 1. Longitudinal and traversal views of simulated beams tested by (Huang et al, 2018)

Used Materials Laws

All the mechanical characteristics of the materials which constitute the models, namely: concrete, steel and FRP were carefully and separately introduced for each element of our model, to take into a consideration the study's

parameters and to validate the established finite element model. In this context, three materials models integrated in (ABAQUS, 2014) were used, namely: Concrete damaged plasticity (CDP); elastoplastic behavior with kinematic and isotropic strain hardening for steel and orthotropic elastic behavior for composites.

CFRP and GFRP were modelled by quadratic finite elements model (2D), with an eight nodes solid element, with 1 cm dimension in the mains directions. The quadratic finite elements models are coupled with the hexahedral linear finite element models of concrete ones with no additional slip conditions i.e. no friction between the various components of the flexural beam. However, elastic-plastic model with isotropic strain hardening assuming bilinear behavior was used for steel reinforcement. Indeed, Table 2, recapitulates the parameters of used FRP and steel.

Table 2. Used steel and FRP parameters.

Materials	Young Modulus (GPA)	Density (kg/m^3)	Poison's ration	Thickness (mm)
GFRP	79.7	2.3E-06	0.31	0.60
CFRP	221.7	2.8E-06	0.31	0.24
Steel bars	210	7.4E-06	0.30	8 - 12

The mechanical response of concrete under a uniaxial loading, and the changes of the variables of the damage according to the stiffness recovery respectively in compression and tension are presented in the numerical concrete model. Cracking is considered to be the significant aspect of the material response. The elastic-plastic damage model involves values for material failure ratios and for tension stiffening parameters. Table 3 and 4 summary the multiaxial loading parameters of the used concrete and damaged concrete models.

Pre-damaged Modelling

To estimate the parameters influencing the materials reinforcement of RC specimens, the variation of the rate of concrete damage is focused. Indeed, the characteristics governing the values of the variables of concrete damage are summarized on Table 4. Four configuration of damage rate were considered according the initial compression resistance of undamaged concrete, as used by (Si Salem et al., 2015; Ait Taleb et al., 2015; Si Salem et al., 2017). It is important to notice that this later was experimentally measured by (Huang et al., 2018). The compressive resistance of used concrete was 41.3 MPa.

Table 3. Parameters of Concretes models.

Proprieties	Values
Dilatation Angle (°)	32
Compressive stress (Mpa)	41.3
Yield stress on compression (Mpa)	12.39
Yield stress on tension (Mpa)	3.08
Poisson's ratio	0.2
Ratio of biaxial to uniaxial compressive strength	1.16
Parameter of the flow potential	0.1

Table 4. Concrete parameters according to damage rate.

Damage rate (%)	Dilatation angle (°)	Parameter controlling the cracking energy (b_f)	fc_{28} (MPa)
10	30	30	37.17
20	28	35	33.04
30	23	40	28.91
50	15	45	20.65

Numerical Outcomes and Analyzes

Orderly to confirm the consistency of the simulation procedure, a comparison of the outcomes found with those of the tests taken on the basis of the literature review already established by different authors. Figure 4 shows the evolution of applied load versus deflection curves of the various bending-loaded RC beam. The curves obtained below are extracted from some experimental research carried out by (Huang et al., 2018) on FRP strengthened RC beams, also the results of our proposed numerical model.

Validation of Proposed FEM

Since our advocated FEM and the experimental model issued on the basis of the literature review present the same geometry and materials with the same physical properties, a comparison study was performed numerical vs. test outcomes. To verify the efficacy of the modeling, qualitative and quantitative predictions on the response of the studied structures with the test observations of Liang Huang et al [5] were established. With regard to the quantitative feature of the confrontation, the variation of the parameters identified experimentally i.e. vertical displacement and bearing capacities was emphasized. Figure 2 and 3 show the applied load versus the imposed monotonic mid-span displacement for both RC and FRP strengthened beams.

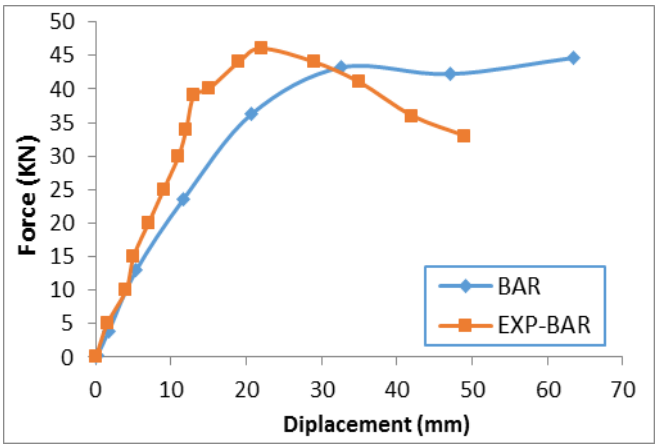

Figure 2. Confrontation of load capacity curves for RC beam: NLFEM vs. experiments

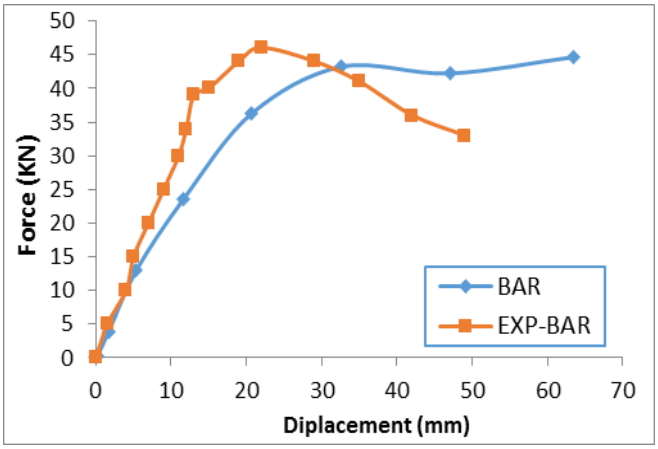

Figure 3. Confrontation of load capacity curves for FRP strengthened RC beam: NLFEM vs. experiments

The numerical outcomes present a good correspondence with experimental analysis ones of (Huang et al,2018). The values of the bearing capacity are significantly different. For the RC beam, the maximum load given by the simulation is 33.04 KN, however the average bearing capacity obtained by the tests was around of 33.81 KN. For the reinforced RC beam, the maximum load given by the simulation is 44.76 kN, however the average bearing capacity obtained by the tests is around of 47.09 KN. Indeed, a good correlation is observed, knowing that the difference between the FEM model and the experimental analysis is less than (<2.5%), which is much less than the normal experimental dispersion.

Pre-damaged Concrete Effect

Figure 4 shows the load bearing capacities of the various studied beams as function of concrete damage rate. The analysis of the outcomes, namely the of force-displacement curve clearly shows the improvement of the beam strength reinforced with FRP sheets in comparison to the reference RC beam, which represents a strength of 33.04 kN. The 10% pre-damaged reinforced beam has a maximum strength of 33.46 KN with a resistance increase of 53.14%. Also, the 20% of damage model reaches a resistance of 46.06 KN with a contribution of 48.19 %. The pre-damaged reinforced beam with 50% damage rate has a minimum resistance value to the variables of 10% and 20% respectively, which is 38.78 KN and a ratio of 69.75%.

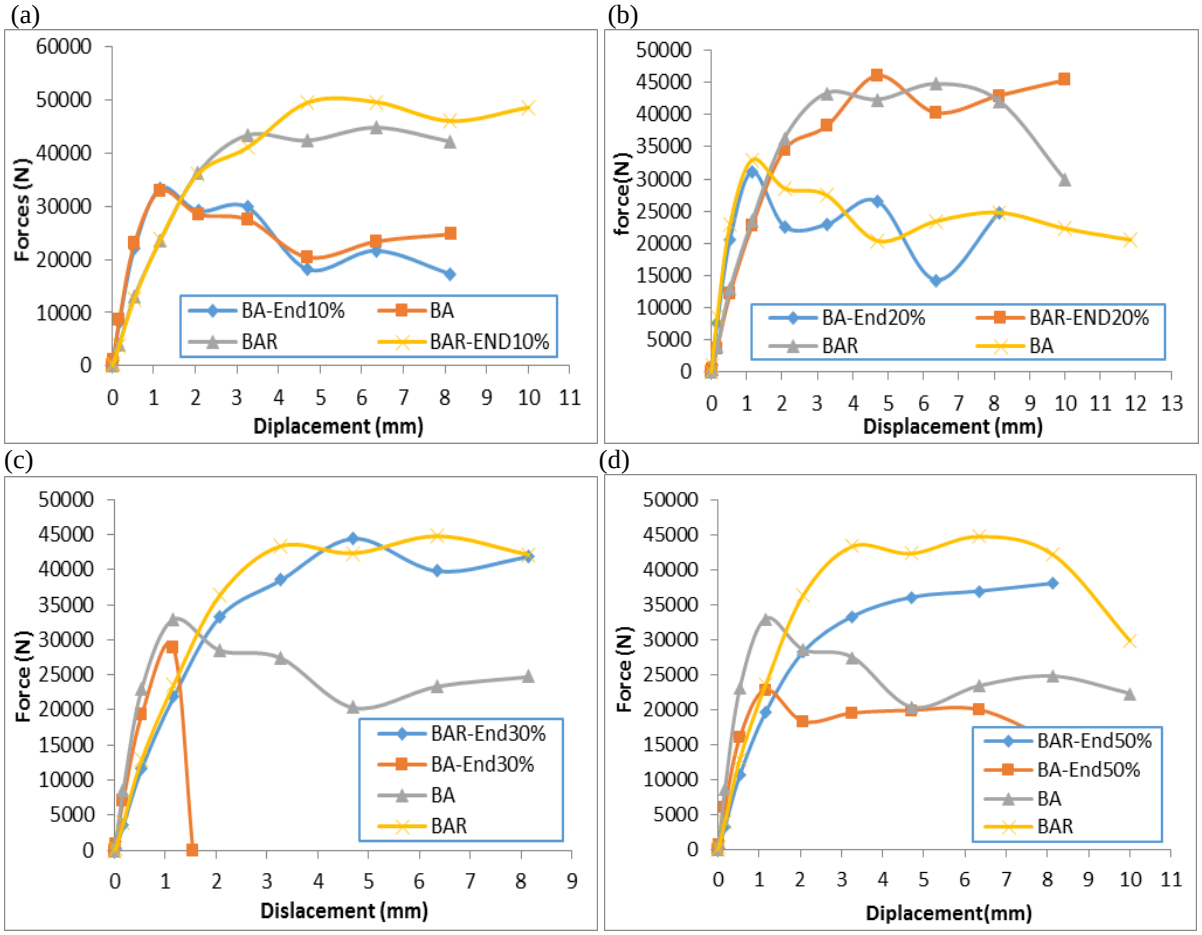

Figure 4. Load-displacement curves a) 10% damage rate; b) 20% damage rate; c) 30% damage rate; d) 50% damage rate.

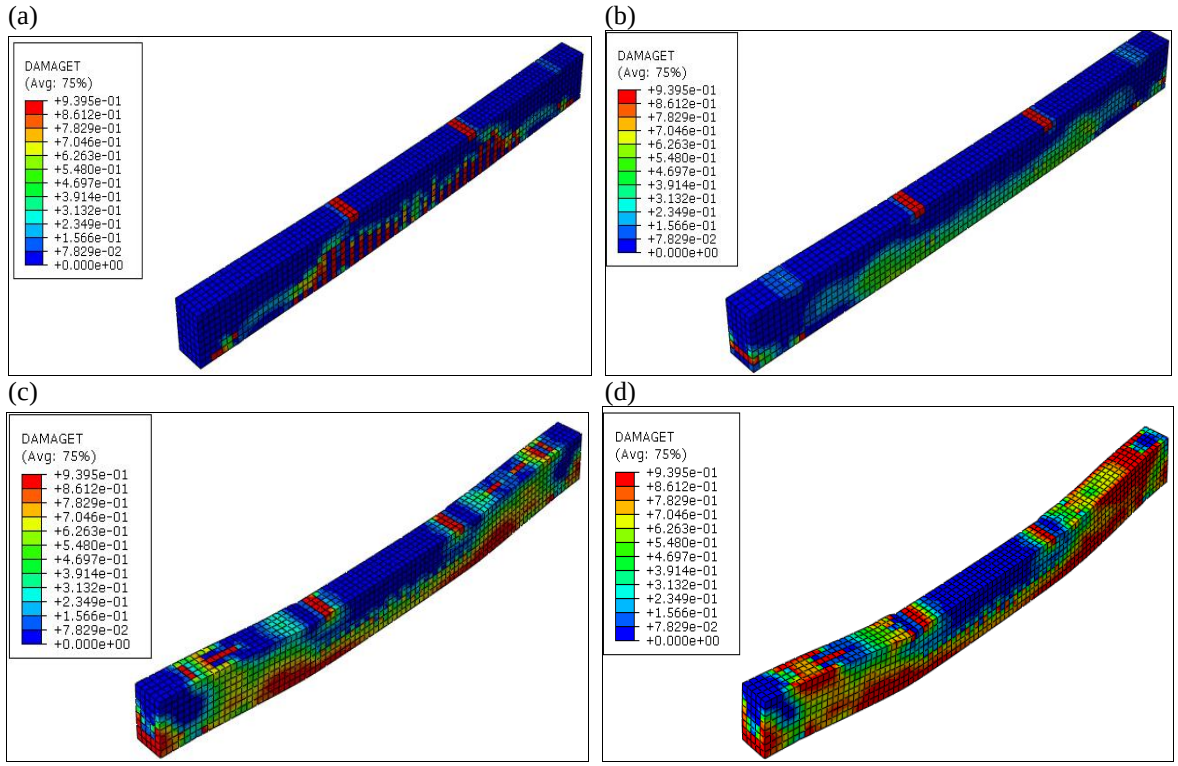

Figure 5. Tensile damages mapping a) RC beam; b) 10% damage rate; c) 30% damage rate; d) 50% damage rate.

Table 5 represents the bearing capacities of the pre-damaged beams. Indeed, the resistance contribution increases proportionally with the damage rate. Conferring to the comparison between the bearing capacity of the RC beam which is 33.04 kN and that of the FRP reinforced beam pre-damaged to 10% which is 50.30 kN one can confirm that contribution in terms resistance increases up to 52.70%. The 20% pre-damaged specimen represents a resistance of 46.10kN with a 50.70% gain; the 30% pre-damaged specimen with a strength of 28.52kN and a contribution of 22.68%. The minimum resistance is obtained on the specimen pre-damaged at 50% which is 36.72 kN. The confrontation of the outcomes of this series confirms that the damage rate has a considerable impact on the resistance of repaired RC beams.

Table 5: Numerical outcomes according to concrete damage rate

Concrete damage rate	Pre damaged RC beams strength (kN)	FRP repaired pre-damaged RC beams strength (kN)	Strength gain (%)
10%	33.46	51.24	53.14
20%	31.08	46.06	48.19
30%	28.95	44.44	53.5
50%	22.81	38.72	69.75

Conclusion

This research advocates a nonlinear models able to calculate the full bending response of repaired pre-damaged RC beams designed and already tested. Indeed, the analysis of obtained outcomes i.e. global response of the various reinforcement configurations considered, allows us to list the following conclusions:

• Reinforcement and repair using bonded FRP sheet and jacket considerably improves the bearing capacity of RC beams designed using undamaged or pre-damaged materials;

• The influence of the FRP strengthening on beam's resistance increases proportionally with the rate of damage. Indeed, damaged concrete allows the conjugation of the used composite materials characteristics;

• The growth in the damage of both concrete and steel leads to a significant reduction in the resistance gain. Indeed, steel yielding leads to brittle failure of damaged beams;

• RC beams retrofitted with GPRF and CPRF bands and pre-damaged are considered by a decrease in damage, this explains the increase in the resistance ratio of reinforced beams at a high level of damage.

Recommendations

Despite the satisfactory obtained results, which suggests the interest of the use of RFP composites to retrofit RC members, nevertheless it is necessary to supplement this study with other numerical analyses to take into account the FRP damage model as well as the interaction between all the beams components.

Scientific Ethics Declaration

The authors declare that the scientific ethical and legal responsibility of this article published in EPSTEM journal belongs to the authors.

Acknowledgements

* This article was presented as an oral presentation at the International Conference on Technology, Engineering and Science (www.icontes.net) held in Antalya/Turkey on November 16-19, 2022.

References

Abaqus (2014). *Abaqus. simulia version 6.14*, HKS Inc Providence, Sorensen Inc.

Ait Taleb, S., Si Salem, A. & Ait Tahar, K. (2015). Bending and shear behavior of a composite beam strengthened and double-confined with FRP-jacket. *Procedia Engineering*, *114*, 165-172.

Ait Taleb, S., Si Salem, A., & Ait tahar, K. (2017). Behaviour of a new graded beam reinforced with externally bonded composite sheets: theoretical and experimental studies. *European Journal of Environmental and Civil Engineering*, *21*(9), 1171-1185.

Ali Ahmed, C., Si Salem, A., Ait Taleb, S., & Ait Tahar, K. (2022). Experimental behavior and reliability of predamaged concrete columns externally repaired with FRP spiral strips under axial compression. *World Journal of Engineering*, (ahead-of-print).

Al-Sulaimani, G. J., Sharif, A., Basunbul, I. A., Baluch, M. H., & Ghaleb, B. N. (1994). Shear repair for reinforced concrete by fiberglass plate bonding. *Structural Journal*, *91*(4), 458-464.

Daouadji, T. H. (2013). Analytical analysis of the interfacial stress in damaged reinforced concrete beams strengthened by bonded composite plates. *Strength of Materials*, *45*(5), 587-597.

Djenad, S., Ait Taleb, S., Si Salem, A., & Bouzidi, M. A. (2022). NLFEA based design optimization of GFRP strips in partially confined concrete. *Procedia Structural Integrity*, *37*, 321-329.

Djenad, S., Si Salem, A., & Bouzidi, M. A. (2022). Performance and compressive axial behavior of new design partially confined concrete columns with encased-FRP/Grid strips. *Asian Journal of Civil Engineering*, 1-15.

Huang, L., Zhang, C., Yan, L., & Kasal, B. (2018). Flexural behavior of U-shape FRP profile-RC composite beams with inner GFRP tube confinement at concrete compression zone. *Composite Structures*, *184*, 674-687.

Hussain, M., Sharif, A., Baluch, I. B. M., & Al-Sulaimani, G. J. (1995). Flexural behavior of precracked reinforced concrete beams strengthened externally by steel plates. *Structural Journal*, *92*(1), 14-23.

Jirawattanasomkul, T., Likitlersuang, S., Wuttiwannasak, N., Ueda, T., Zhang, D., & Shono, M. (2020). Structural behaviour of pre-damaged reinforced concrete beams strengthened with natural fibre reinforced polymer composites. *Composite Structures*, *244*, 112309.

Lee, J. Y., Hwang, H. B., & Doh, J. H. (2012). Effective strain of RC beams strengthened in shear with FRP. *Composites Part B: Engineering*, *43*(2), 754-765.

Malek, A. M., Saadatmanesh, H., & Ehsani, M. R. (1998). Prediction of failure load of R/C beams strengthened with FRP plate due to stress concentration at the plate end. *ACI structural Journal*, *95*, 142-152.

Raoof, M., El-Rimawi, J. A., & Hassanen, M. A. (2000). Theoretical and experimental study on externally plated RC beams. *Engineering Structures*, *22*(1), 85-101.

Rashid, K., Li, X., Deng, J., Xie, Y., Wang, Y., & Chen, S. (2019). Experimental and analytical study on the flexural performance of CFRP-strengthened RC beams at various pre-stressing levels. *Composite Structures*, *227*, 111323.

Si Salem, A., Ait Taleb, S. & Ait tahar, K.(2015). Static and dynamic behavior of composite concrete-based beams with embedded Polymer/FRP Components. *Procedia Engineering*, *114*, 173-180.

Si Salem, A., Ait Taleb, S., & Ait tahar, K. (2017). A Finite Element Approach for Predicting the Flexural Response of Light Weight FRP-Concrete Beams Under Cyclic Loading. In *Applied Mechanics, Behavior of Materials, and Engineering Systems* (pp. 355-363). Springer, Cham.

Si Salem, A., Taouche-Kkheloui, F., & Ait tahar, K. (2020). Experimental investigation on the bending and buckling behavior of bio-based core innovative sandwich panels. *International Journal of Structural Integrity*, *12*(2), 226-240.

Author Information

Souad AIT TALEB
University Mouloud Mammeri of Tizi Ouzou
Tizi Ouzou, 15000, Algeria
Contact e-mail: souad.ait-taleb@ummto.dz

Sara MEDJMADJ
Laboratory LGCA, University of Bejaia
Bejaia, 06000, Algeria

Abdelmadjid SI SALEM
University Mouloud Mammeri of Tizi Ouzou
Tizi Ouzou, 15000, Algeria

To cite this article:

Ait Taleb, S. Medjmadj, S & Si Salem, A. (2022). Modeling the nonlinear behavior of predamaged reinforced concrete beams retrofitted with bonded and jacketed FRP sheets. *The Eurasia Proceedings of Science, Technology, Engineering & Mathematics (EPSTEM), 21,* 288-294.

The Eurasia Proceedings of Science, Technology, Engineering & Mathematics (EPSTEM)
ISSN: 2602-3199

The Eurasia Proceedings of Science, Technology, Engineering & Mathematics (EPSTEM), 2022

Volume 21, Pages 295-301

IConTES 2022: International Conference on Technology, Engineering and Science

Experimental Analysis of the Influence of Inter-Electrode Distance in Juice Extraction Processes Using Pulsed Electric Fields

Mohammed Hamza BERMAKI
Djillali Liabès University

Houcine MILOUDI
Djillali Liabès University

Yacine BELLEBNA
Djillali Liabès University

Amar TILMATINE
Djillali Liabès University

Abstract: Nowadays, the pulsed electric field (PEF) is widely used in the food industry. The PEF treatment of different fruits and vegetables before the extraction process has already been used, and its efficiency has already been proven concerning the increase of the quantity of juice extracted, while keeping the aroma and the nutritional quality of the product. The basic concept is to place food in a treatment chamber with two electrodes and use high electric fields to increase the permeability of these cells, a process known as electroporation. An experimental study of beet juice extraction process by pulse electric field has been presented. For this purpose, three static treatment chambers of cylindrical shape with different inter-electrode distances were used. The aim was to determine the influence of the inter-electrode distance in the PEF extraction processes. The methodology of experimental designs was used in this work by developing a fractional factorial design where the inter-electrode distance d was considered as a factor. The results obtained are satisfactory, since it leads us to validated mathematical models. For the same experimental conditions, the treatment chamber with the largest inter-electrode distance gave the best performance in terms of quantity of juice extracted. While the one with the smallest inter-electrode distance is mainly a considerable energy saving but with a low yield in terms of juice mass.

Keywords: Pulse electric field (PEF), Juice extraction, Treatment chambers, Electrodes, Experimental designs.

Introduction

Pulsed electric field (PEF) technology is widely used in the food industry (Šalaševičius et al., 2021; Mohamed et al., 2021; Leone et al., 2022), especially in juice extraction processes for different fruits and vegetables. The PEF extraction process is a multifactorial process (Parniakov et al., 2022). This implies that the development of this technology requires the analysis of the influence of each factor. Preliminary results have already shown the usefulness of having a strong electric field that allows the electroporation of the biological tissues of the food to be treated (Mitchell & Sundararajan, 2005). Also, it is important that the pulse duration is sufficient for a good treatment but should not be too long in order to avoid any heating of the product. In addition, the number of pulses must be optimized in order not to consume too much energy. The distribution of the electric field in the treatment chamber is another parameter to be taken into account in order to improve the efficiency of the PEC extraction processes (Knoerzer et al., 2012; Shorstkii et al., 2019; Arshad et al., 2020). Thus, in this paper, we will focus on another factor that can also have an influence on the yield, namely the inter-electrode distance in

the process chamber. Using the design of experiments methodology, a comparative experimental study of three cylindrical chambers has been done. The objective was to analyze the effect of the inter-electrode distance on the yield of the PEF pretreatment on the extraction of beet juice.

Materials and Methods

Pulse Generator

The experimental device used is a capacitor discharge generator. Indeed, the principle is to charge one or a set of capacitors with a high voltage delivered by a DC power supply. This voltage will then be discharged through a spark gap to the treatment chamber where the electrical impulses are produced. A simplified diagram and photography of the experimental bench used are respectively presented in Figure 1.

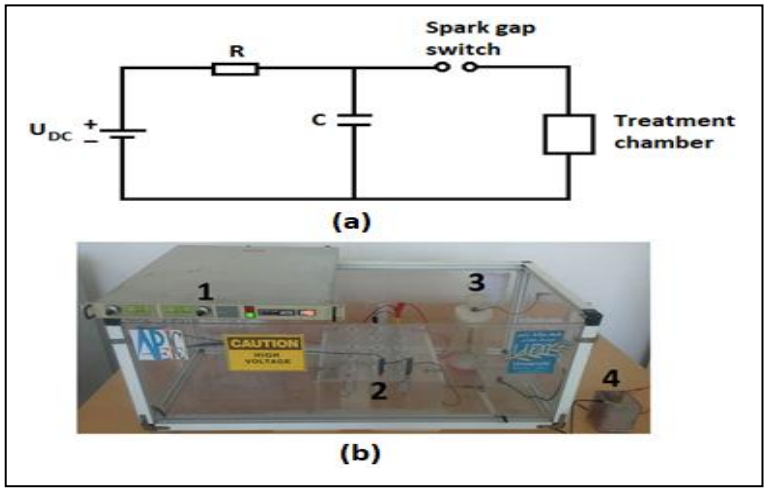

Figure 1. Experimental device (a: Descreptive schematic, b: photography)
1- HV DC power supply, 2-Set of capacitors, 3- Spark gap switch, 4-Treatment chamber

The experimental bench includes three capacitor blocks, each consisting of five 2µF capacitors connected in series. Various connections can be made between the three blocks, which allows a wide choice in terms of pulse duration. As the experimental bench used is based on the principle of charge and discharge of capacitors, the pulse generated is of decreasing exponential form.

Treatment Chambers

Three coaxial cylindrical treatment chambers were used in this work. Each chamber consists of two cylindrical electrodes, one connected to high voltage and the other to ground, and between which the food to be treated is placed. During all the experiments carried out, regardless of the treatment chamber, the applied field was kept constant and equal to 2 kV/cm. For this purpose, the voltage was varied according to the distance D, which gives: V = 2 kV for D = 1 cm, V = 4 kV for D = 2 cm and V = 6 kV for D = 3 cm, as shown in Figure 2.

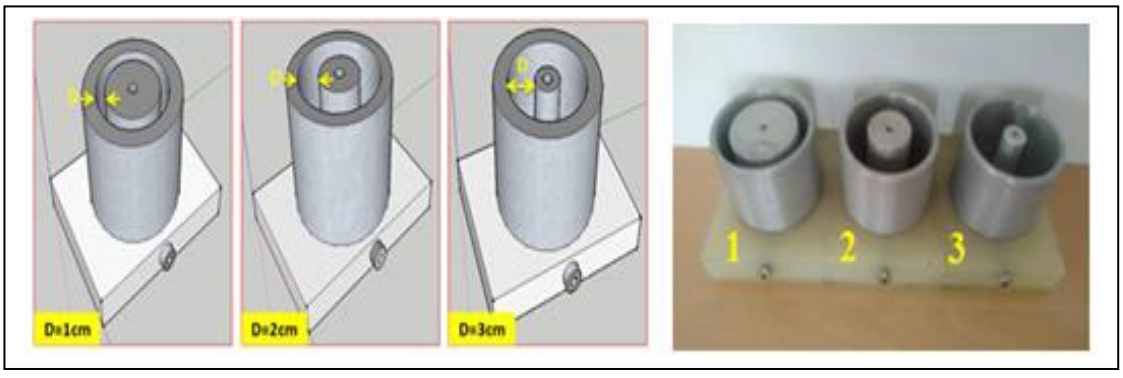

Figure 2. Coaxial cylindrical treatment chambers

Beet Juice Extraction Process by PEF

The beet juice extraction process was used to evaluate the performance of the three cylindrical processing chambers. The experimental design methodology was used and the first step is the parametric study which consists of preliminary experiments to delineate the study intervals of the different factors. All experiments were performed keeping certain factors constant throughout the study, such as:

- Mass of the grated beet sample 120g
- Constant extraction pressure P = 50 kg/cm2
- Total duration of the mechanical pressure Δt = 300 s
- Pulse repetition frequency f = 1 Hz
- Electric field E = 2 kV/cm

The variable factors are :

- Number of pulses n
- Pulse duration T (µs)
- Inter-electrode distance D (cm)

The responses are:

- Extracted juice mass (g)
- Absorbance of betanin
- PEF treatment energy (Joule)

In order to define the study interval of these three factors, a series of experiments as well as preliminary tests were performed while varying one factor at a time. Thus, the study intervals of the three factors were defined as follows:

- Number of pulses n; n min= 40 and n max= 80
- Pulse duration T (µs); T min= 20 µs and T max= 60 µs
- Inter-electrode distance D (cm); D min= 1 cm and D max= 3 cm.

Results and Discussion

Mathematical Models

A central composite face-centered design (CCF) was performed with 17 experiments carried out and the results are presented in the table.

Table 1. Results of the CCF design experiment

	Variable factors			Responses		
Exp N°	n	T (µs)	D (cm)	m (g)	Abs	W(J)
1	40	20	1	34,30	1,03	32
2	80	20	1	37,40	1,28	64
3	40	60	1	41,16	1,21	96
4	80	60	1	42,70	0,71	192
5	40	20	3	46,70	0,48	288
6	80	20	3	53,50	0,57	576
7	40	60	3	49,80	1,21	864
8	80	60	3	54,30	0,52	1728
9	40	40	2	41,70	0,99	256
10	80	40	2	43,10	0,71	512
11	60	20	2	48,50	0,63	192
12	60	60	2	48,10	0,62	576
13	60	40	1	42,00	1,34	96
14	60	40	3	52,80	0,76	864
15	60	40	2	48,20	0,70	384
16	60	40	2	48,20	0,70	384
17	60	40	2	48,20	0,70	384

The predictive quality of the juice mass, absorbance and energy models is satisfactory since the Q2 and R2 coefficient values presented in Figure 3 are close to the unit. Therefore, the models are validated and can be used for analysis and prediction.

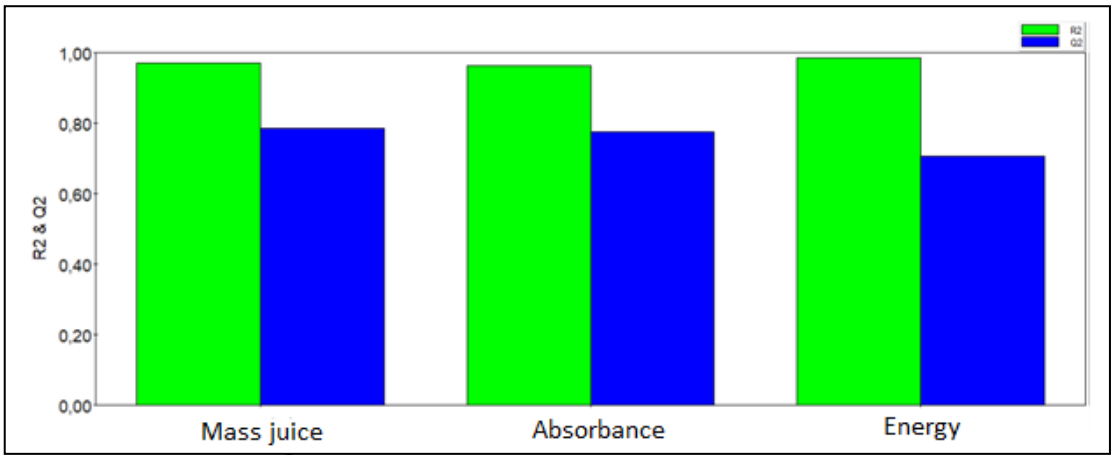

The respective mathematical models of extracted juice mass, absorbance and energy as a function of the factors studied are given by MODDE 5.0 as:

$$m=47{,}46+1{,}73\ n+1{,}56\ T+5{,}95\ d-4{,}50\ n^2$$
$$Abs=0{,}7-0{,}11\ n-0{,}2\ d-0{,}17\ T^2+0{,}25\ d^2-0{,}19\ n*T+0{,}13\ T*d$$
$$W=384+153{,}6\ n+230{,}4\ T+384\ d+80\ n*T+128\ n*d+192\ T*d$$

Effects of Variable Factors on Responses

From the mathematical models, the plots of the effects of each factor on the response are obtained (Figures 4, 5 and 6). It can be seen that for the mass of juice extracted (Figure 4), the inter-electrode distance is by far the most influential factor on the response. Therefore, it is deduced that for the same value of the electric field, higher values of the inter-electrode distance allow a better yield in terms of juice quantity. This can be explained by the fact that the food that is placed in a chamber with a wide inter-electrode space. This will allow it to be better exposed to the PEF and therefore benefit from a better treatment. The number and duration of pulses also positively affect the amount of juice extracted, but to a lesser degree compared to the inter-electrode distance.

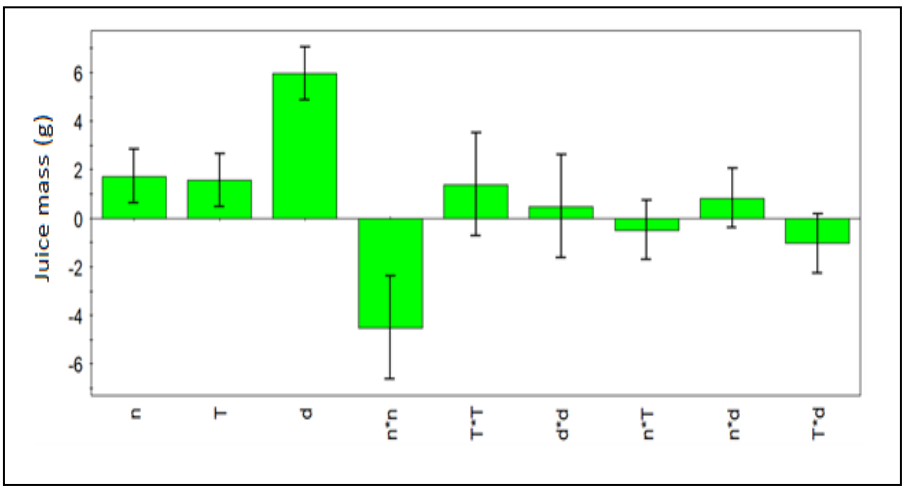

Figure 4. Effects factors plot on mass juice

For the absorbance (Figure 5), the plot shows that the inter-electrode distance is also the most significant factor but in a negative way. Indeed, the absorbance in betanin of the extracted juice decreases for high distances. Since the latter have already shown us that they allow an increase in the quantities of extracted juice. This can lead to an increase of the water content in the beet juice, as the latter is very rich in water (more than 70%), which reduces the betanin absorbance of extracted juice.

The effect of the number of pulses is less important but still negative on this response. The effect of the duration of the pulses is insignificant, one can even say null. However, the interactions of the pulse duration with the

number of pulses and the inter-electrode distance are significant and have respectively a negative and positive effect on the response.

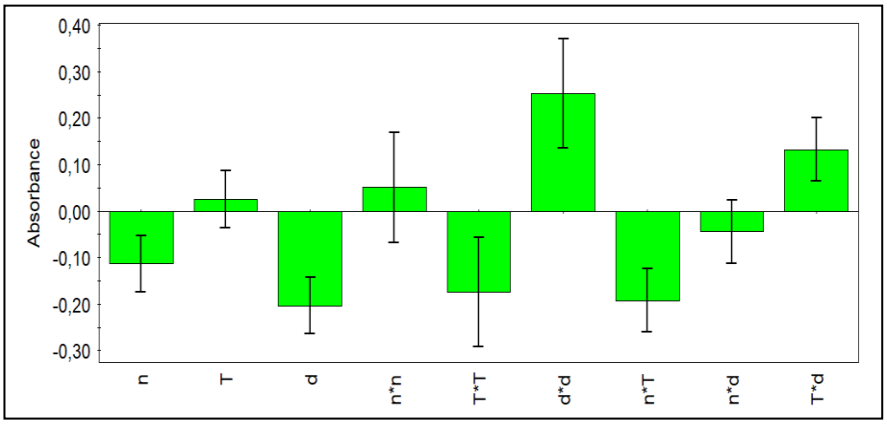

Figure 5. Effects factors plot on absorbance

The energy consumed is proportional to the three factors since it is given by the following formula :

$$W = \frac{1}{2}\, n\, C\, V^2$$

The inter-electrode distance is the most influential factor on energy consumption (Figure 6), which is logical. Because, to keep the electric field constant (2 kV/cm), it was necessary to increase the voltage each time large distances were used.

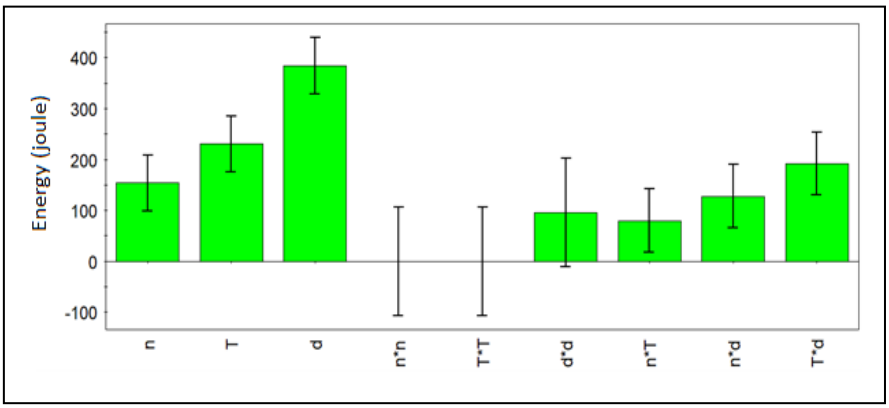

Figure 6. Effects factors plot on energy

Optimization of the Juice Extraction Process by PEF

According to this model, the optimum of the process proposed by MODDE 5.0 which gives the optimal values of the factors to obtain a maximum yield of the extraction process is presented by the Figure 7. Thus, the maximum process yield given by MODDE 5.0 software with a juice mass of 53.06 g and a betanin absorbance of 1.01 was obtained for 48 pulses, pulse duration of 60 µs, and an inter-electrode distance of 3 cm. The energy consumed in this case was 1074.43 joules.

	Factor	Role	Value	Low Limit	High Limit
1	nombre d'impulsions	Free		40	80
2	Durée d'impulsion	Free		20	60
3	Distance inter-électrodes	Free		1	3

	Response	Criteria	Weight	Min	Target	Max
1	masse de jus	Maximize	1	52,9587	54,8589	
2	Absorbance	Maximize	1	1,28245	1,3654	
3	Enérgie	Exclude				

Iteration: 5002 Iteration slider:

	1 nombre d'impulsions	2 Durée d'impulsion	3 Distance inter-électrodes	4 masse de jus	5 Absorbance	6 Enérgie	7 iter	8 log(D)
1	42,0121	53,0308	1	40,1132	1,2896	51,1155	5001	1,4847
2	48,3156	59,9765	3	53,0773	1,0159	1074,71	5001	0,9693
3	75,6281	25,4816	1	39,0764	1,289	42,7501	5000	1,543
4	48,2977	59,972	3	53,0699	1,0162	1074,3	5002	0,9686
5	48,2771	59,999	3	53,0671	1,0166	1074,43	5000	0,9679
6	75,6281	25,4816	1	39,0764	1,289	42,7501	5000	1,543
7	48,2854	59,9949	3	53,0695	1,0164	1074,51	5000	0,9682
8	48,2767	59,9999	3	53,0672	1,0166	1074,44	5000	0,9679

Conclusion

An experimental study of the beet juice extraction process using PEF has been presented in this paper. For this purpose, three static treatment chambers of cylindrical shape with different inter-electrode distances were used. The aim was to determine the influence of the inter-electrode distance in the PEF extraction processes. The design of experiments methodology was used in this work by developing a fractional factorial design where the inter-electrode distance d was considered as a factor.

The results of the realized FEC design are satisfactory, since it leads us to validated mathematical models. For the same experimental conditions, the treatment chamber with the largest inter-electrode distance gave the best performance in terms of quantity of juice extracted. While the one with the smallest inter-electrode distance allows above all a considerable energy saving but with a low yield in terms of juice mass. Because in an extraction process, the amount of juice extracted is the most important response, and the PEF technology is essentially used to increase the amount of juice extracted. It can be said that the results obtained can confirm that the use of processing chambers with high inter-electrode distances improves the performance of PEF treatment.

Scientific Ethics Declaration

The authors declare that the scientific ethical and legal responsibility of this article published in EPSTEM journal belongs to the authors.

Acknowledgements or Notes

This article was presented as the poster presentation at the International Conference on Technology, Engineering and Science (www.icontes.net) held in Antalya/Turkey on November 16-19, 2022.

References

Arshad, R. N. Abdul Malek, Z., Ahmad, M. H., Buntat, Z., Pavan Kumara, C. L .G., & Abdulameer, Z. A (2020). Coaxial treatment chamber for liquid food treatment through pulsed electric field. *Indonesian Journal of Electrical Engineering and Computer Science*, *19*(3): 1169-1176.

Knoerzer, K., Baumann, P., & Buckow,R. (2012). An iterative modelling approach for improving the performance of a pulsed electric field (PEF) treatment chamber. *International Journal of Computer Applications in Chemical Engineering*, *37*, 48-63.

Leone, A.,Tamborrino, A., Esposto, S., Berardi, A., & Servili, M. (2022). Investigation on the effects of a pulsed electric field (PEF) continuous system implemented in an industrial olive oil plant. *International Journal of Foods (MDPI), 11*(18), 2758.

Mitchell, W., & Sundararajan, R. (2005). Electric field distribution in biological tissues for various electrode configurations-a FEMLAB study. *Excerpt from the Proceedings of the COMSOL Multiphysics User's Conference.* Boston.

Mohamed, R., Lemrabout, A., Taleb, R., Kerbouac, A., & Mahmoud, A. (2021). Effect of treatment with electric field pulse on the extraction of Polyphenols. *iKSP Journal of Emerging Trends in Basic and Applied Sciences, 1*(1), 22-29.

Parniakov,O., Lebovka,N., Wiktor, A., Comiotto Alles, M., Hill, K., & Toepfl, S. (2022). Applications of pulsed electric fields for processing potatoes: Examples and equipment design. *International Journal of Research in Agricultural Engineering*, *68*(2), 47–62.

Šalaševičius, A.,Uždavinyté, D.,Visockis, M., Ruzgys, P., & Šatkauskas, S. (2021). Effect of pulsed electric field (PEF) on bacterial viability and whey protein in the processing of raw milk. *International Journal of applied sciences (MDPI), 11*(23), 11281.

Shorstkii, I., Sosnin, M., & Khudyakov, D. A. (2019). Continuously pulsed electric field treatment chamber modelling and design. *IOP Conference Series Materials Science and Engineering*, *564*(1), p. 012032). IOP Publishing.

Author Information

Mohammed Hamza Bermaki
Djillali Liabès University
Sidi Bel-Abbès, Algeria
Contact e- mail : *bermaki.hamza@gmail.com*

Yacine Bellebna
Djillali Liabès University
Sidi Bel-Abbès, Algeria

Houcine Miloudi
Djillali Liabès University
Sidi Bel-Abbès, Algeria

Amar Tilmatine
Djillali Liabès University
Sidi Bel-Abbès, Algeria

To cite this article:

Bermaki, M. H., Bellebna, Y., Miloudi, H., & Tilmatine, A. (2022). Experimental analysis of the influence of inter-electrode distance in juice extraction processes using pulsed electric fields *The Eurasia Proceedings of Science, Technology, Engineering & Mathematics (EPSTEM), 21*, 295-301.

The Eurasia Proceedings of Science, Technology, Engineering & Mathematics (EPSTEM)
ISSN: 2602-3199

The Eurasia Proceedings of Science, Technology, Engineering & Mathematics (EPSTEM), 2022

Volume 21, Pages 302-310

IConTES 2022: International Conference on Technology, Engineering and Science

Numerical Analysis of the Mechanical Behavior on the Effect of the Geometric Interface of the Aluminum/Aluminum Plate Assembly

Sidi Mohamed MEDJDOUB
University of Sidi Bel Abbes

Kouider MADANI
University of Sidi Bel Abbes

Yacine MESSID
University of Sidi Bel Abbes

Abstract: Adhesive joints are therefore often favored in the aerospace and automotive industries due to their advantages such as the formation of uniform stress distributions, the ability to join dissimilar materials, high fatigue resistance and impermeability. In this work, the use of texture manufacturing technology (Geometric shapes) to the assembly areas of Aluminum / Aluminum plates is explored. In order to improve the shear strength values of the single joint adhesive layer, it is necessary to model structural reinforcements at the interface of the bonded assembly. Through the Abaqus software; models will be developed to simulate the stress distribution along the region of interaction between the plates and the single joint adhesive layer. by an economic choice. The analysis of the dimensions of the lap length and the thickness of the adhesives are the main parameters to be modified to optimize the geometry of the assembly, because an increase in the resistance of the joint is accompanied.

Keywords: Adhesive, Single joint, Stress.

Introduction

Configurations of a single-lap joint have been studied for about more than sixty years and many analytical and numerical models have been developed. Volkersen (1938) proposed the first approach to analyze this type of structure. He considered only shear strain in the adhesive and axial deformations in the adherends. Demarkles (1955) improved the model including shear deformation of the adherends. These analyzes do not include the bending moment produced by the eccentric path of the load. The effect of the bending moment results in efforts normal to the plane of the adhesive, called peel stresses, which are important at the edges of the joint. Goland and Reissner (1944) were the first to analyze the effect of the eccentric path of the load by applying moments to the joint edges.

The most practical configuration is single-lap, which has been extensively studied, and several ideas have been proposed to improve their performance. The eccentricity of the load applied to the ends causes a significant stress concentration at the overlap ends, but minimal stresses at the core of the adhesive are noted. Several authors have tried to reduce these stress levels by using several methods. In general, there are two types of methods for reducing stress concentrations, namely changes in the material or the geometry of the adherend and adhesive. For example, introduction of notch, folding of the bonded surface or the use of corrugations at the covering ends of the adherends can reduce peel stresses at the overlap end.

Different shapes of the adhesive edges have been studied to reduce the various stresses and ensure a better distribution in adhesive joints. Harris and Adams (1984) proposed the creation of adhesive fillet, however, Giovanni et al. (2002) modified the edges of the adherends by the presence of a chamfer. On the other hand, it is difficult to manufacture these adherends and to control their shape. Therefore, these methods are rarely relied upon in practice. McLaren and MacInnes (1958) studied a different method; they varied the bending moment factor by simply deforming the adherend at the end of the overlap length. The material modifications mainly optimize the properties of the adhesive and the adherends. Pires et al. (2003) have shown that the use of a bi-adhesive system is advantageous at the joint: when the adhesive is more flexible, the stress distribution is more uniform in the single-lap joint and the concentration is minimal.

Fitton and Broughton (2005) studied the effect of varying the modulus of adhesive as a method to optimize the performance of the joint. The results from the study of Sancaktar et al. (2000) showed that the use of a rigid adherend has made the stress distribution more uniform. The geometric modifications mainly include the corrugation, pre-folding of the adherend, chamfer and notch. Other authors (Lang & Mallick 1998) have used geometric modifications in the adherends at the level of the covering part and have concluded that if the size of the modified zone increases, then the stress concentration at the edges decreases. Avila and Bueno (2004) have shown that the use of corrugated sheets allows for a uniform stress distribution. Sancaktar and Nirantar (2003) have shown that if the angle of beveling of the adherends at the overlapping ends is important, the stresses on the joint are minimal and this is well demonstrated by Oterkus et a.l (2006).

The present work aims to study the Geometric shapes influence mechanical behavior at the interface of the adhesive joint used for the assembly of two aluminum adherends (2024-T3 alloy) and thus determine the stress distributions in the adhesive layer.

Geometric Model and Mechanical Properties

In this study, the geometric model for the single lap joint of the bonded adhesive used in joining two thin aluminum plates. In order to model the geometry presented in figure 1, we need their mechanical properties, for this purpose tensile tests were carried out on Aluminum 2024-T3; in the form of a plate; and on Adekit A-140 adhesive; in the form of standardized specimens; and which allowed to have the characteristics curves shown in Figure 2. From these two curves, one can determine the mechanical properties of the two materials shown in Table 1.

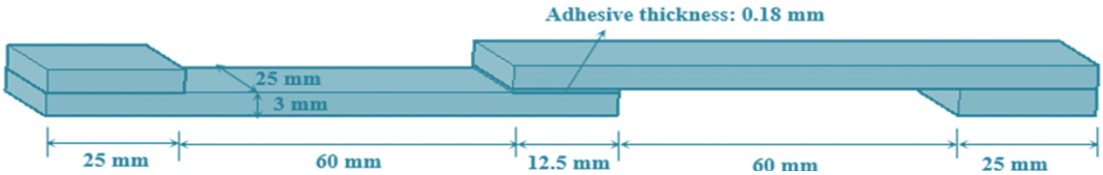

Figure 1. Geometric model of single lap joint bonded adhesive.

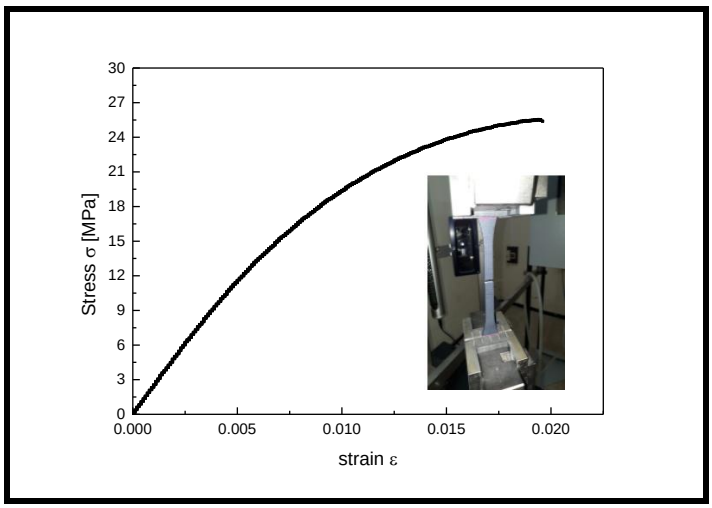

-a-

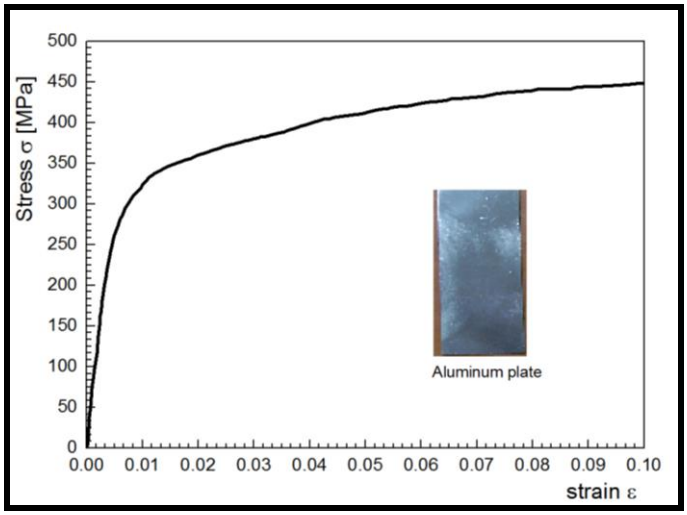

-b-

Figure 2. Tensile stress–strain curve for: a)-Aluminum plate, b) - Adhesive Adekit A140 (Madani et al. 2010).

Table 1. Mechanical properties of the joint materials (Madani et al. 2010).

Property	Materials		Description
	Aluminum	Adhesive	
E (MPa)	69000	2690	Young's modulus
G (MPa)	26500	1120	Shear modulus
ν	0.3	0.3	Poisson's Ratio
σ (MPa)	220	14.9	Yield tensile strength
ρ	2,77	1,38	Density

Mesh Description

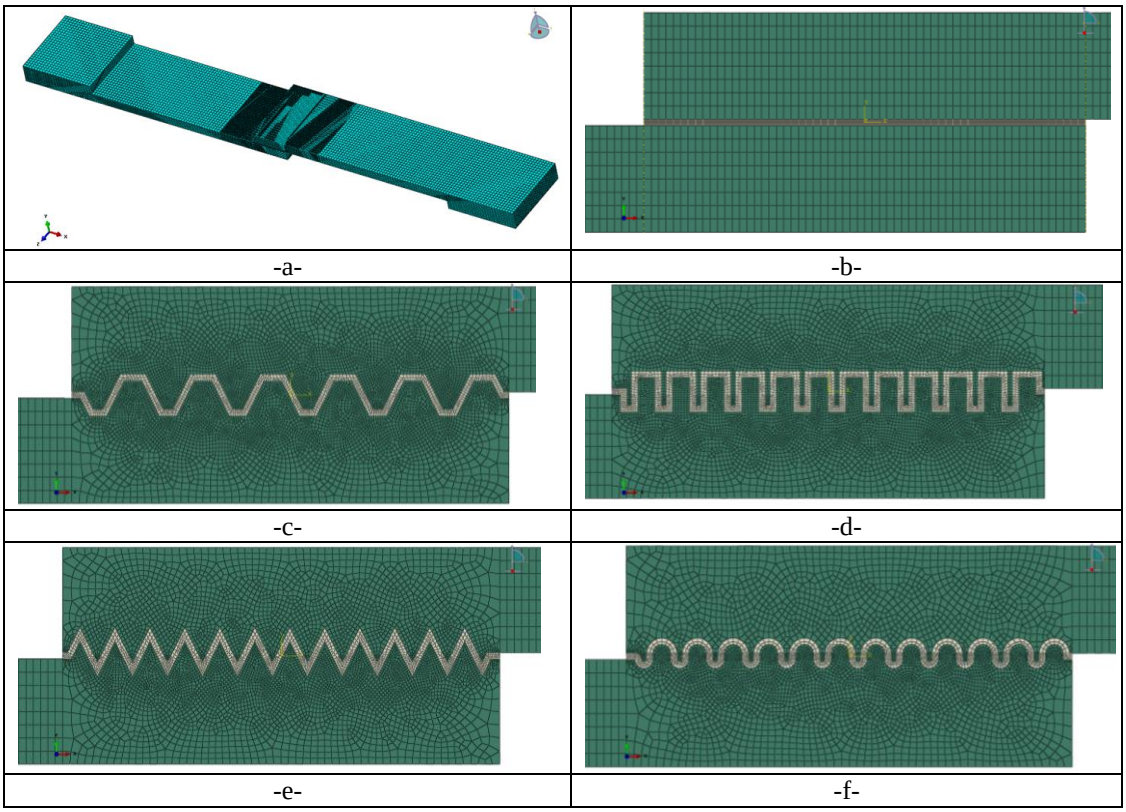

-a- -b-

-c- -d-

-e- -f-

Figure 3. Mesh of the assembled structure; a) Assembly model, b) Simple single-lap joint, c) Trapezoidal shape, d) Rectangular shape, e) Triangular shape, f) Circular shape.

The numerical analysis was performed by using the Abaqus calculation software using a non-linear static analysis, the Green-Lagrange strain formulation and three-dimensional modeling. The adhesive layer was modeled in the form of a third layer in order to introduce its real mechanical properties through its traction curve. This three-layer modeling technique has been used by several authors (Elhannani et al., 2015, Kaddouri et al., 2019, Medjdoub et al.,2022).

In our study, the single joint model is the basic model that allows us to compare it with other assembly models from the mechanical resistance point of view. We have represented five 5 different geometric models are used in the adhesive / plate interface: the simple shape, the trapezoidal shape, the rectangular shape, the triangular shape and the circular shape (Figure 3). The structure was meshed with linear hexahedral C3D8R elements (bricks), The total number of elements generated for the model was 224750. The adhesive layer is homogeneous, elastoplastic, isotropic and deforms under shear and peel stress. In the finite element model, the nodes are common between the aluminum plate and the adhesive layer so that there is continuity of deformation and stress.

Loading and Boundary Conditions

One of the joint edges is clamped, while the other extremity of the second plate is subjected to an applied normal stress of σ=10 MPa. The faces at each extremity of the two plates at the level of the heels are blocked. At the level of the embedded extremity the two faces are blocked in U1=U2= UR1=UR3=0 (Figure 4. a). On the other hand, on the level of the faces at the loaded extremity the two faces are blocked in U2= UR1=UR3=0 (Figure 4. b).

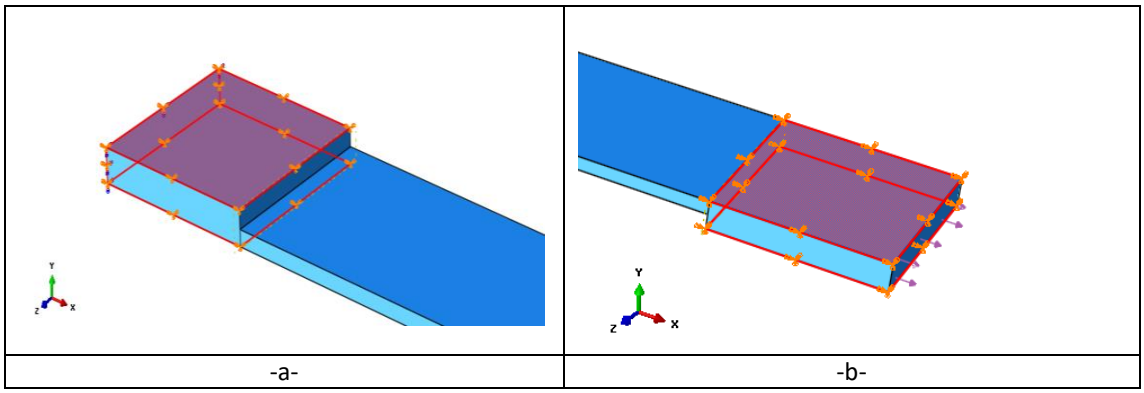

Figure 4. Boundary conditions; a) at clamped side, b) at loaded side.

Results and Discussion

The results represent the distribution of von Mises, shear and peel stresses in the five different single lap joint models used in our study: the simple shape (Basic), the trapezoidal shape, the rectangular shape, the triangular shape and the circular shape.The von Mises stress level in assembly for the simple single lap joint is shown in figure 5.a. Where it is clearly seen there is a stress concentration near the assembly zone. In figure 5.b, we show that the high stress area increases in the adhesive surface, thus relieving the high stresses at the edges. On the other hand, the core of the adhesive becomes more and more active. According to this figure we note that there is a high stress concentration at the extremity of the adhesive and it decreases in the center of this layer. The comparison of the maximum von Mises stresses between the different models (Figure 5.b.c.d.e.f) shows that the circular shape has the lowest level of stress.

Figure 6 represents the effect of adhesive layer shape on the distrubtion of von Mises stress. We note that all the modifications of the shape assembly reduce the von Mises stress in the center of the layer adhesive compared to the simple shape. But, the level of the von Mises stress for different geometries at the extremities exceeds that of the simple shape. Which, it is bad for the assembly. By comparing the different configurations assembly, the lowest von Mises values were recorded in the center and both ends of layer adhesive in the circular shape. In the circular case the reduction ratio of the maximum von Mises stress compared to the simple form is 25%; which it is beneficial.

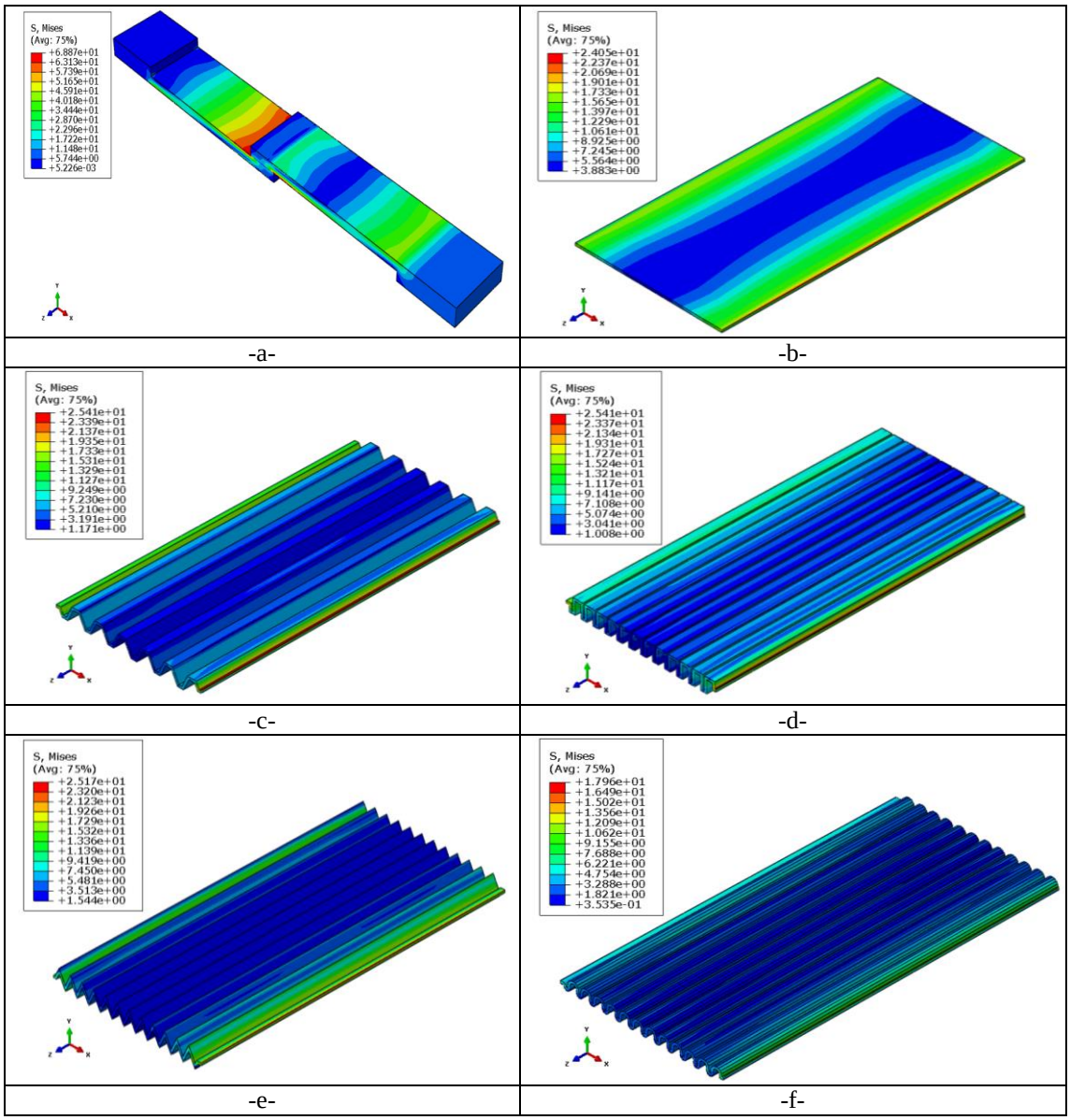

Figure 5. von Mises stress level in the adhesive joint a) The assembly b) Simple single-lap joint, c) Trapezoidal shape, d) Rectangular shape, e) Triangular shape, f) Circular shape.

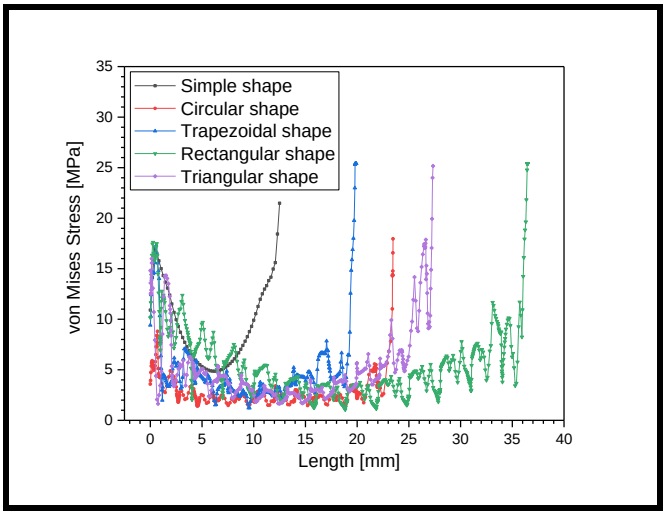

Figure 6. Distribution of von mises stress in the length of the cover joint for different shape.

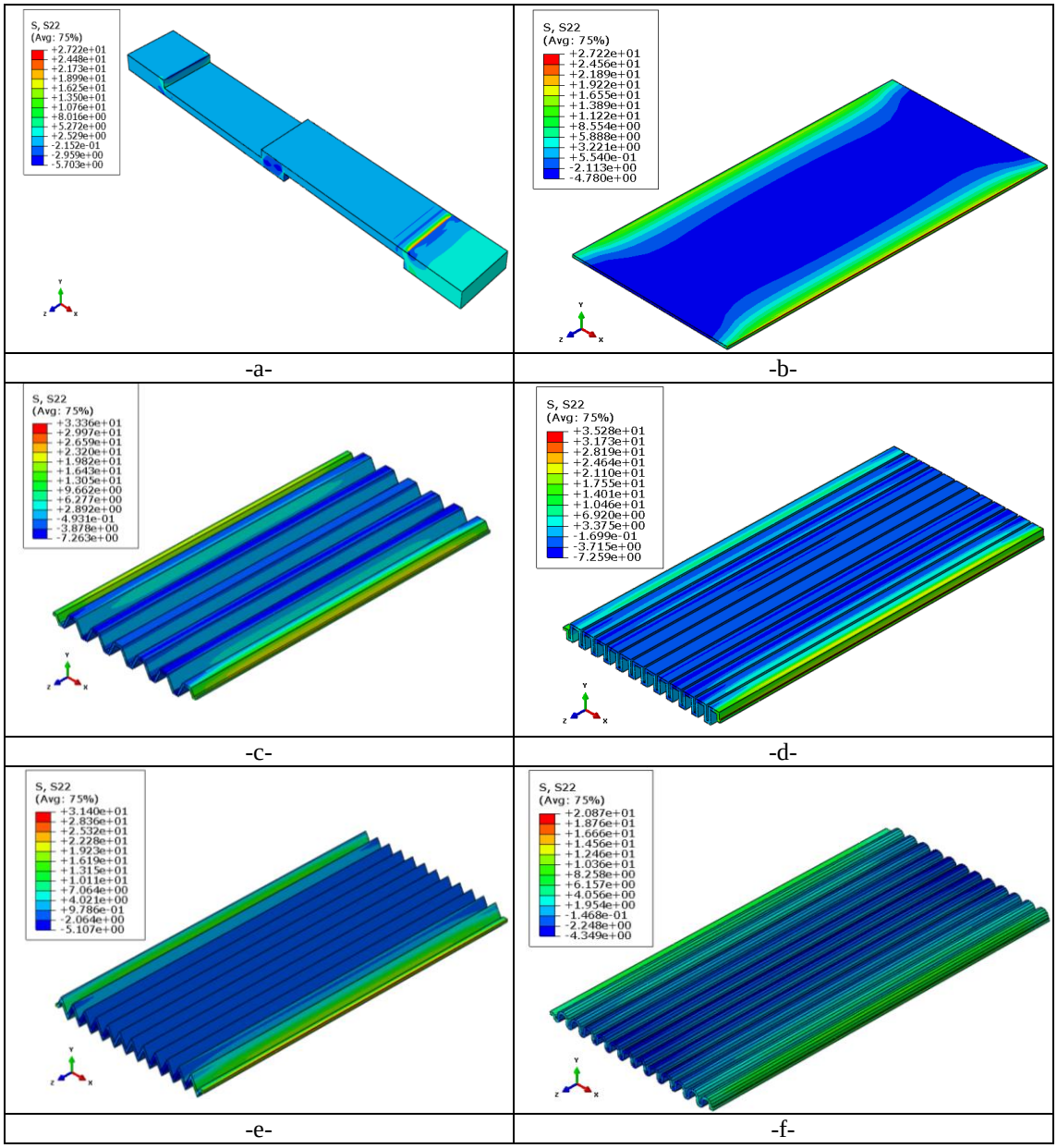

Figure 7. Peel stress level in the adhesive joint a) The assembly b) Simple single-lap joint, c) Trapezoidal shape, d) Rectangular shape, e) Triangular shape, f) Circular shape.

The figure 7 show the level of peel stress distribution at the assembly and the different shapes of the plate/adhesive interface. It is noted that is a low value of the peel stress in the center of adhesive layer for all the shape configurations. In this figure its shown a strong increase at the extremity of the adhesive layer. Also, the circular shape provides the lowest level of peel stress compared to the different geometries.

The figure 8 represent the variation of the peel stress for the different models. This figure show clearly that the circular shape significantly reduces the peel stress at the center and the ends of the adhesive layer compared to the simple shape by a rate of 23%. which is very advantageous in terms of performance and efficiency. It's very interesting to see that the geometry modification of the interface increases the surface contact between the plate and the adhesive by 65% for the same length of 12.5mm in the simple case. This promotes increasing the distribution of peel stresses over a larger surface and decreasing the concentration of these stress in the center of the adhesive layer. The effect of changing the interface geometry between the plates and the adhesive on the shear stress distribution is shown in figure 9. It can be seen that the distribution of shear stress represent a maximum at the ends of the different shapes of the adhesive layer (Figure 9.b.c.d.e). Then it starts to decrease from the extremities to have the minimum of the stresses in the center. In the same figure we record the minimum value of the shear stresses in the circular model, which confirms the effectiveness of the circular geometry.

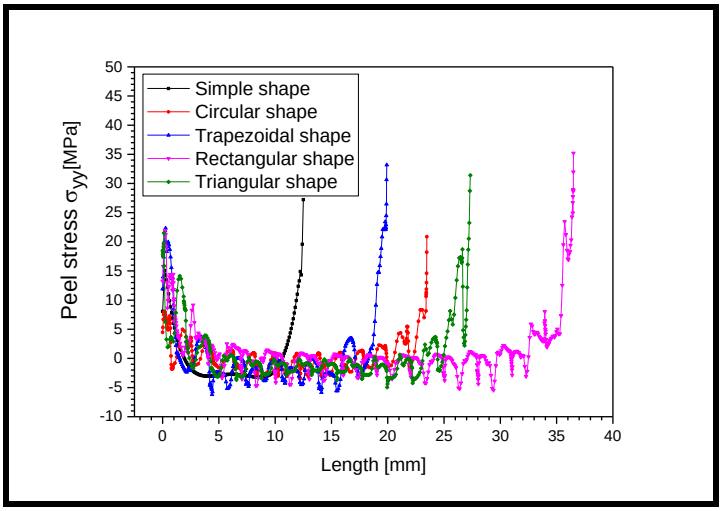

Figure 8. Distribution of peel stress in the length of the cover joint for different shape.

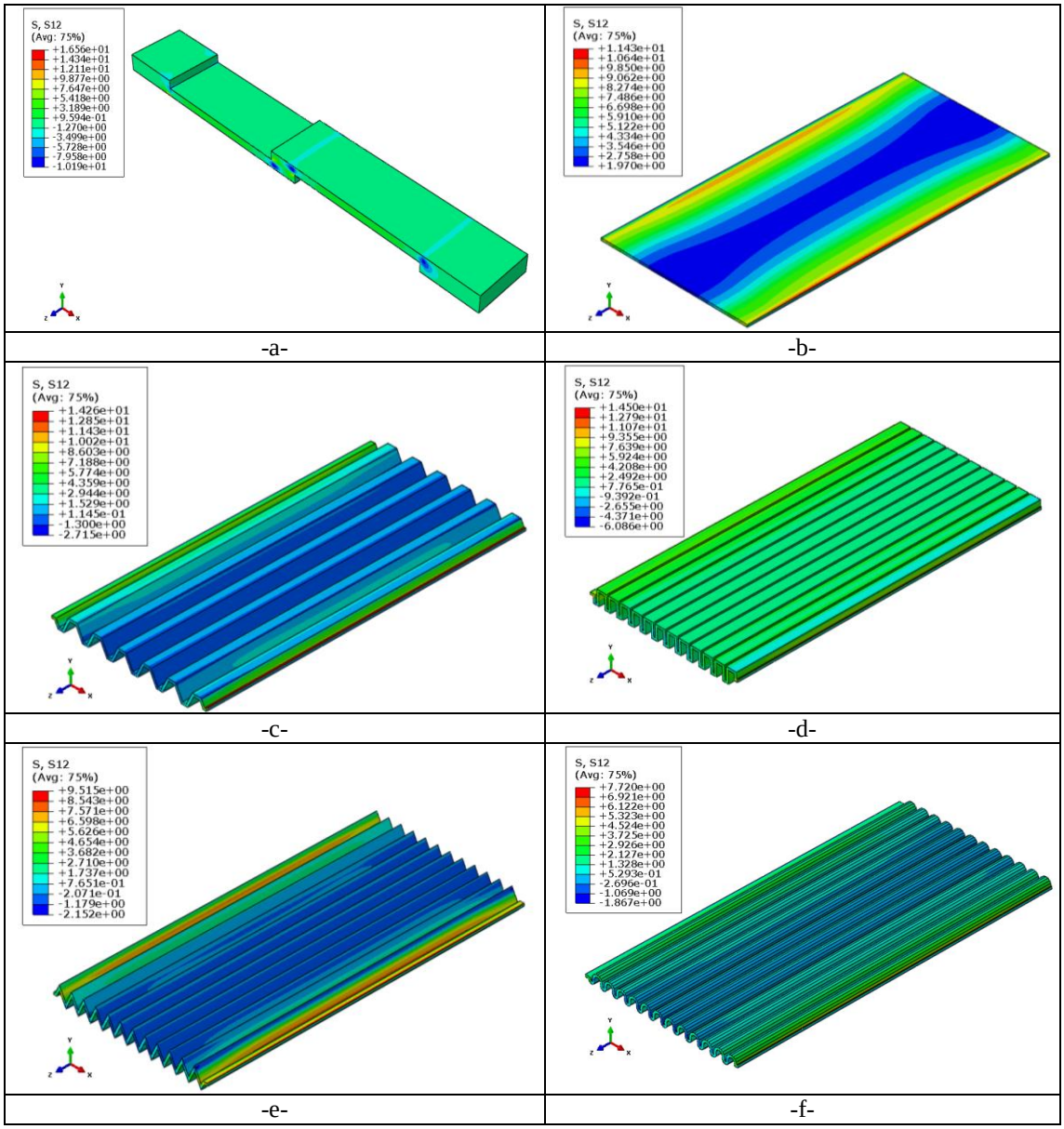

Figure 9. Shear stress level in the adhesive joint a) The assembly b) Simple single-lap joint, c) Trapezoidal shape, d) Rectangular shape, e) Triangular shape, f) Circular shape.

The evolution of shear stress along the length of the adhesive layer is illustrated in Figure 10. It is noted that the level of the shear stress of the various shapes are low at the center of the adhesive compared to the simple case. Because the length of geometric shapes (Trapezoidal, Rectangular, Triangular and Circular) promotes the distribution of shear stresses. Finally the minimum shear stress value is recorded in the circular form and this is validates the results obtained previously by reducing the shear stresses by 32%.

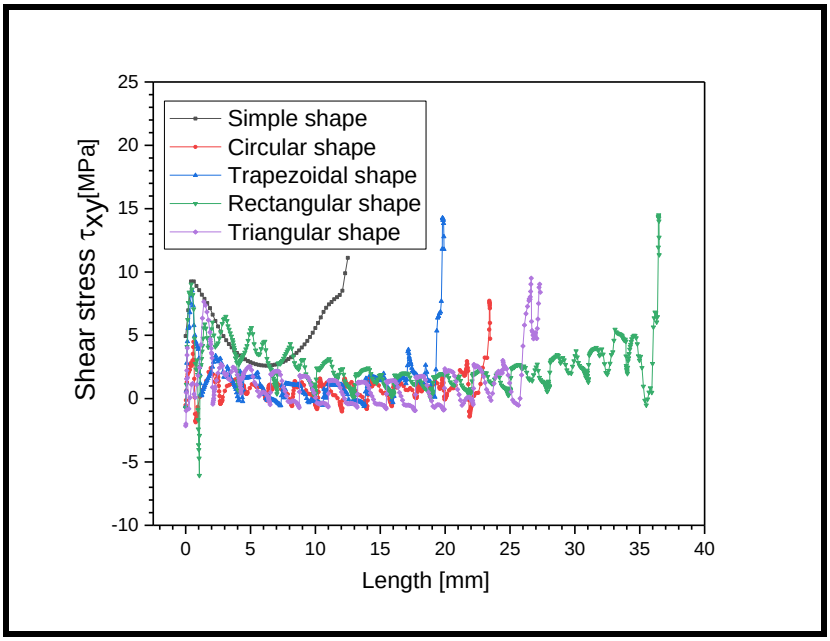

Figure 10. Distribution of shear stress in the length of the cover joint for different shape.

Conclusion

From the numerical analysis of the stress distribution in bonded assemblies, based on tensile tests carried out on different shape of adhesive layer, the following conclusions can be drawn: A geometrical modification in the interface reduce considerably the stress intensity in the center of adhesive layer.The distribution of von Mise, peel and shear stress represent a maximum at the ends of the different shapes of the adhesive layer. The circular shape assembly has the lowest stress values (von Mises, peel and shear stress), which is advantageous for the life of the structure in service.

Scientific Ethics Declaration

The authors declare that the scientific ethical and legal responsibility of this article published in EPSTEM journal belongs to the authors.

Acknowledgements or Notes

This article was presented as the poster presentation at the International Conference on Technology, Engineering and Science (www.icontes.net) held in Antalya/Turkey on November 16-19, 2022.

References

ABAQUS/CAE 6.9 (2005). *User's manual*, Hibbitt, Karlsson.

Avila, A. F., & Bueno, P. O. (2004). Stress analysis on a wavy-lap bonded joint for composites. *International Journal of Adhesion and Adhesives, 24*(5), 407-414.

Demarkles, L. R. (1955). *Investigation of the use of a rubber analog in the study of stress distribution in riveted and cemented joints.* Technical Note No. 3413, National Advisory Committee Aeronautics. Massachusetts Institute of Technology.

Elhannani, M., Madani, K., Legrand, E., Touzain, S., & Feaugas, X. (2017). Numerical analysis of the effect of the presence, number and shape of bonding defect on the shear stresses distribution in an adhesive layer for the single-lap bonded joint; Part 1. *Aerospace Science and Technology, 62*, 122-135.

Elhannani, M., Madani, K., Chama, Z., Legrand, E., Touzain, S., & Feaugas, X. (2017). Influence of the presence of defects on the adhesive layer for the single-lap bonded joint; Part 2: Probabilistic assessment of the critical state. *Aerospace Science and Technology, 63*, 372-386.

Fitton, M. D., & Broughton, J. G. (2005). Variable modulus adhesives: an approach to optimized joint performance. *International Journal of Adhesion and Adhesives, 25*(4), 329-336.

Giovanni, B., Goglio, B., & Tarditi, A. (2002). Investigating the effect of spew and chamfer size on the stresses in metal/plastics adhesive joints. *International Journal of Adhesion and Adhesives, 22*(4), 273–282.

Goland, M., & Reissner, E. (1944). The stresses in cemented joints. *Journal of Applied Mechanics, 66*, A17-A27.

Harris, J. A., & Adams, R. D. (1984). Strength prediction of bonded single lap joints by non-linear finite element methods. *International Journal of Adhesion and Adhesives, 4* (2), 65-78.

Kaddouri, N., Madani, K., Bellali, M.A., & Feaugas, X. (2019). Analysis of the presence of bonding defects on the fracture behavior of a damaged plate repaired by composite patch. *Frattura ed Integrità Strutturale, 13*(49), 331-340.

Lang, T. P., & Mallick, P. K. (1998). Effect of spew geometry on stresses in single lap adhesive joints. *International Journal of Adhesion and Adhesives, 18*(3), 167-177.

McLaren, A. S., & Maclnnes, I. (1958). The influence on the stress distribution in an adhesive lap joint of bending of the adhering sheets. *British Journal of Applied Physics, 9*, 72-77.

Medjdoub, S. M., Madani, K., Rezgani, L., Mallarino, S., Touzain, S., & Campilho, R. D. S. G. (2022). Numerical analysis of the combined aging and fillet effect of the adhesive on the mechanical behavior of a single lap joint of type Aluminum/Aluminum. *Structural Engineering and Mechanics, An International Journal, 83*(5), 693-707.

Oterkus, E., Barut, A., Madenci, E., SmeltzerIII, S. S., & Ambur, D. R. (2006). Bonded lap joints of composite laminates with tapered edges. *International Journal of Solids Structures, 43*(6), 1459-1489.

Pires, I., Quintino, L., Durodola, J. F. and Beevers, A. (2003). Performance of bi-adhesive bonded aluminum lap joints. *International Journal of Adhesion and Adhesives, 23*(3), 215-223.

Sancaktar, E., & Nirantar, P. (2003). Increasing strength of single lap joints of metal adherends by taper minimization. *Journal of Adhesion Science and Technology, 17*(5), 55-67.

Sancaktar, E., & Simmons, S. (2000). Optimization of adhesively bonded single lap joints by adherend notching. *Journal of Adhesion Science and Technology, 14*(11), 1363-1404.

Volkersen, O. (1938). Die Nietkraftverteilung in Zugbeanspruchten mit Konstanten Laschenquerschnitten. *Luftfahrtsforschung, 15*, 41-47.

Author Information

Sidi Mohamed Medjdoub
Djillali Liabes University
Department of Mechanical Engineering
Sidi Bel Abbes, Algeria
Contact e-mail: *medjdoubsm@gmail.com*

Kouider Madani
Djillali Liabes University
Department of Mechanical Engineering
Sidi Bel Abbes, Algeria

Yacine Messid
Djillali Liabes University
Department of Mechanical Engineering
Sidi Bel Abbes, Algeria

To cite this article:

Medjdoub, S.M., Madani, K., & Messid, Y. (2022). Numerical analysis of the mechanical behavior on the effect of the geometric interface of the aluminum/aluminum plate assembly. *The Eurasia Proceedings of Science, Technology, Engineering & Mathematics (EPSTEM), 21*, 302-310.

The Eurasia Proceedings of Science, Technology, Engineering & Mathematics (EPSTEM)
ISSN: 2602-3199

The Eurasia Proceedings of Science, Technology, Engineering & Mathematics (EPSTEM), 2022

Volume 21, Pages 311-315

IConTES 2022: International Conference on Technology, Engineering and Science

In-Situ Observation of Biofouling Growth in a Submerged Membrane Bioreactor using CLSM

Aida Isma MOHAMAD IDRIS
Segi University

Munira MOHAMMAD
Segi University

Putri Razreena ABDUL RAZAK
Sirim Berhad

Hazmin MANSOR
Universiti Selangor

Abstract: Biofouling is one of the primary hurdles unavoidable in the operation of membrane bioreactors. The distribution and roles of cake layers in biofouling have been extensively investigated. Transparent exopolymer particles perform a variety of biological functions, which has a substantial impact on particle distribution as it is present ubiquitously in wastewater. Fouling was seen in this investigation to be the result of the deposition of particulate, colloidal or soluble material within the pores or on the membrane surface. The distribution of biofouling on the membrane surface and in the cake layer was investigated using a membrane bioreactor operating at a membrane flux of 10 L/m^2h, with the initial concentration of mixed liquor suspended solids of 10g/L treating actual sewage. Confocal laser scanning microscope and field emission scanning electron microscope were employed to divulge the mechanism of fouling in the membrane bioreactor. The trans-membrane pressure and membrane flux were observed throughout the membrane operation. As the fouling progressed, a membrane sample was taken and examined. During the membrane bioreactor operation process, the outcome of the fluorescent staining of the foulant was depicted. In the initial stage, humic-like substances contribute to membrane fouling. Highly concentrated protein-like compounds dominated the fouling behavior. Over time, a protein-controlling cake layer was formed. It can be concluded that in the long-term stage, protein was significantly linked with irreversible fouling.

Keywords: Biofouling, CLSM, FESEM, Sewage

Introduction

In 2021, the market for membrane bioreactors had a value of USD 3.3 billion (Matin et al., 2021). Global demand for water treatment solutions is the main factor driving the market. Apart from this, expanding environmentally friendly water and wastewater management technologies in various sectors, including chemical, pharmaceutical, power, food and beverage, and textile industries, is also boosting market expansion (Xiao et al., 2019). Membrane fouling, particularly biofouling, has grown to be a significant problem with MBR operation because it impairs membrane permeability and necessitates frequent chemical cleaning, reducing membrane lifetime (Aslam et al., 2018).

The emergence of a colony of microorganisms immersed in an organic polymer matrix on membrane surfaces is known as biofouling. There has been a significant amount of research done on the development and growth of

the biofouling layer, including mitigating membrane biofouling. Maintaining the MBR operating condition at optimal MLSS level (<10 g/L), SRT (20-40 d) and, temperature (15-30^{o}C) are just a few methods to control biofouling (L.Deng et al., 2016). Other methods include introducing a spontaneous electric field in MBR, which had delayed the deposition of EPS on the membrane surface (Yin et al., 2020b), and introducing more affordable enzyme extraction methods for enzymatic membrane biofouling control (Cui et al., 2021). Therefore, to comprehensively explore the fundamental growth processes of the biofouling layer on the membrane surface, CLSM and FESEM could be employed as techniques to validate the in-situ visualization of the dynamic behavior of EPS that greatly disturbs the MBR performance.

Method

Experimental Setup

The 100 L aerobic tank makes up the submerged membrane system initially containing MLSS at a concentration of approximately 10g/L as shown in Figure 1. The MBR system had been treating raw domestic wastewater for about 6 months. 10m^2 of a hollow fiber PVDF membrane was operated at a hydraulic retention time of 8 hours with a membrane flux of 10 L/m^2.h, and the dissolved oxygen concentration was maintained above 2 mg/L. while the conditions were fully hydrated, the membrane and fouling layer was carefully removed from the bioreactor to perform additional investigation. The operation of the MBR was examined weekly, and it was shut off as soon as the TMP was above 500 mmHg.

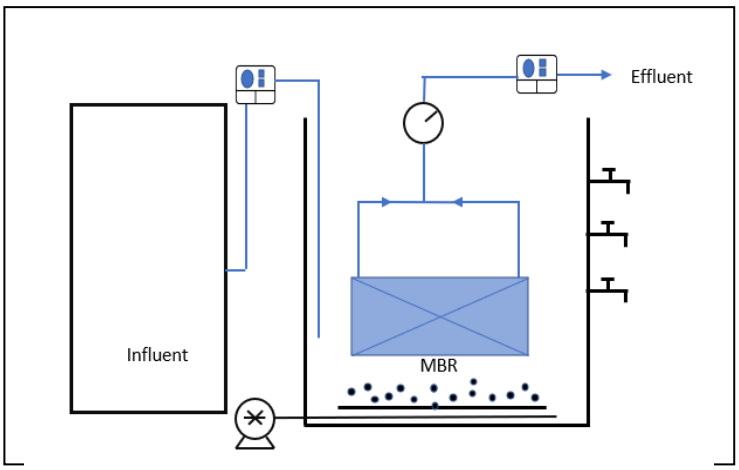

Figure 1. MBR setup in this study

FESEM Characterization

At various points during MBR operation, fouled membranes were taken out of the membrane bioreactor. All samples were dried for 24 hours at 105^{o}C and then coated with a gold sputter prior to FESEM analysis. The morphology was studied at a magnification of 100 um using a Hitachi SU8220.

CLSM Staining and Imaging

The foulants were stained with the following reagents: FITC, Con A conjugated with tetramethylrhodamine, SYTO 63 (Sigma Aldrich), Nile red, and calcofluor white. These reagents were produced following the method outlined by (Yang et al., 2007). Confocal laser scanning microscopy was used to examine the foulant structure (CLSM; Leica TCS SP8 Confocal Spectral Microscope Imaging System, Germany). Leica confocal software was used to analysed objective images at a 10x magnification. At 633 nm and 650–760 nm SYTO 63 fluorescence was observed (red). Con A conjugates were found between 550 to 590 nm (light blue). Wavelengths of Nile Red emission ranged from 630 to 700 nm (yellow). With 488 nm excitation and 500-540 nm emission, FITC was found (green). At 458 nm excitation and 460-500 nm emission, SYTOX Blue fluorescence intensity was determined (purple). Excitation at 405 nm and emission widths of 410-480 nm was used to measure the fluorescence of calcofluor white (blue). All images were scanned at a resolution of 100 µm x 100 µm, above the membrane surface.

Results and Discussion

The distribution of biofouling on the membrane surface and in the cake layer was investigated using a membrane bioreactor operating at a membrane flux of 10 L/m^{2}h, with the initial concentration of mixed liquor-suspended solids of 10g/L treating actual sewage. Figure 2 shows the depletion of membrane flux over time recorded in this study.

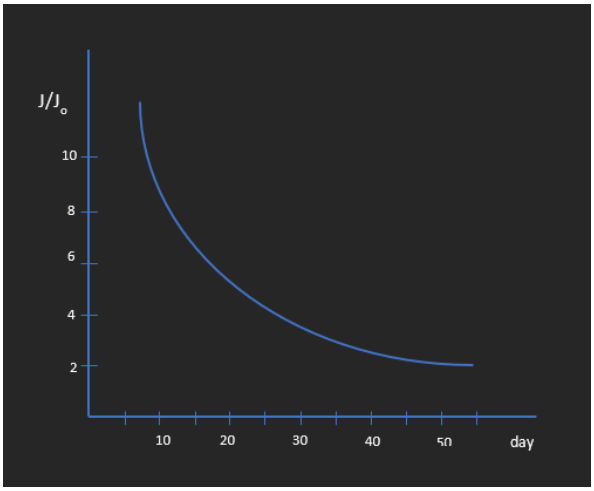

Figure 2. Membrane flux depletion in this study

CLSM images

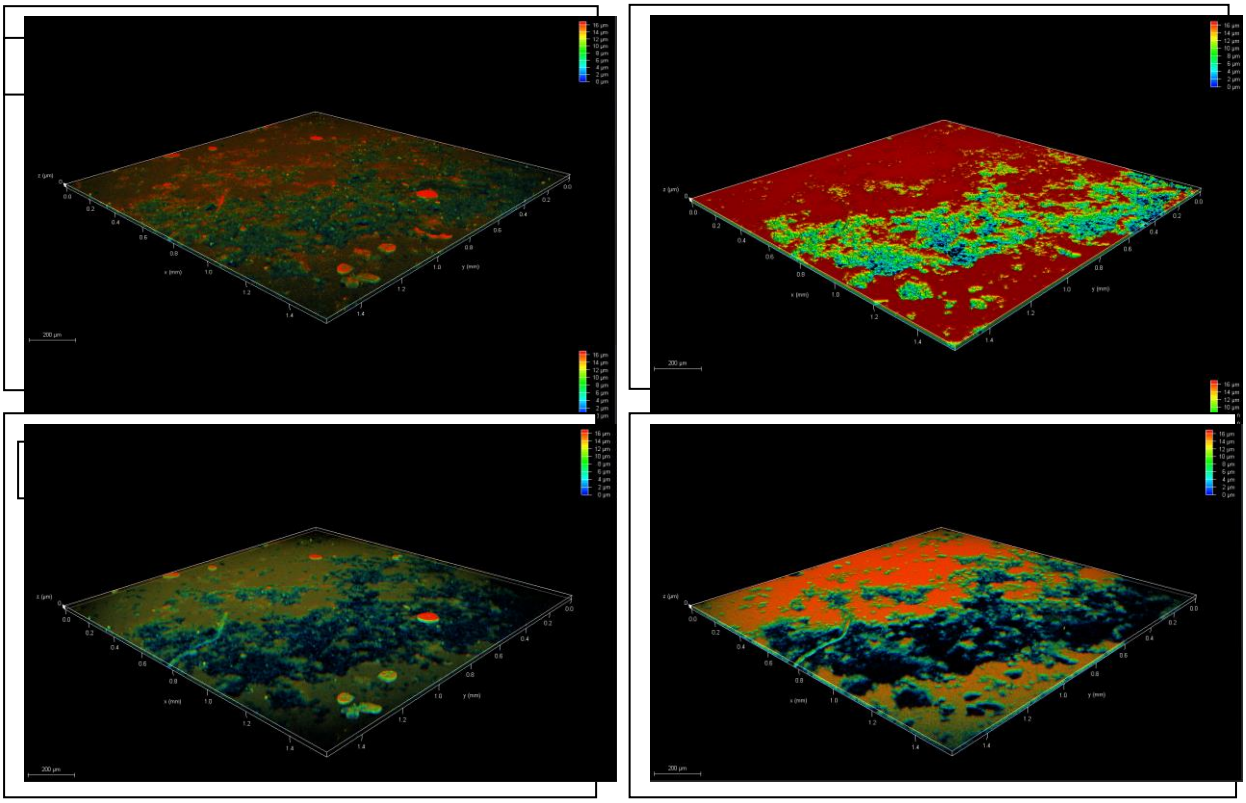

Figure 3. The biofouling 3D CLSM image is further split to denote 3D images of the constituents;(i) Polysaccharides, (ii) Protein, (iii) Lipids, (iv) Total cells.

The findings revealed that the developed biofouling layer was primarily composed of protein and polysaccharides, which are abundant in sewage. Other biological components discovered include lipids and total

cells. The protein accumulates primarily throughout the membrane structure, with a maximum depth of 16 um highlighted in red (Fig.3i), followed by polysaccharides (Fig. 3ii), lipids (Fig. 3iii), and total cells (Fig. 3iv). Protein and polysaccharides accumulation at the feed surface indicate severe membrane fouling observed and is consistent with the severe flux decline in the system.

Biofouling layers developed on the membrane surface pose a significant threat to the operation of MBR as the formation is influenced by the concentration of MLSS, the operating condition of MBR, and the concentration of pollutants. Reducing the fouling rate can be done by regulating membrane operational parameters, including cross-flow velocity and set-point flux. The growth of microorganisms on membranes should have spatial and temporal characteristics, therefore typical solutions to minimise biofouling such periodic backwashing or intermittent filtering cycles may not be sufficient to handle complicated biofouling processes.

In MBRs, EPS has typically been identified as the primary fouling component of the fouling layer, which reduces membrane flux and increases TMP (Sun et al., 2019). According to Chu and Li (2006), the EPS is made up of polysaccharides (PS), proteins (PN), extracellular DNA (eDNA) and metal ions, all of which aid in biofouling. It has also been claimed that the eDNA serves as a scaffold that provides structural integrity to the EPS matrix.

FESEM Images

The performance of MBR in terms of fouling control needs substantial improvements in order to make MBR competitive with the mature wastewater technologies. Figure 4 shows the deposited layer found on the membrane surface when fouling took place. It should be noted that there are many contributors to the development of biofouling, including bacterial cells adhere, grow and multiple (Fig 4i), and other slime layer and foulants (Fig 4ii).

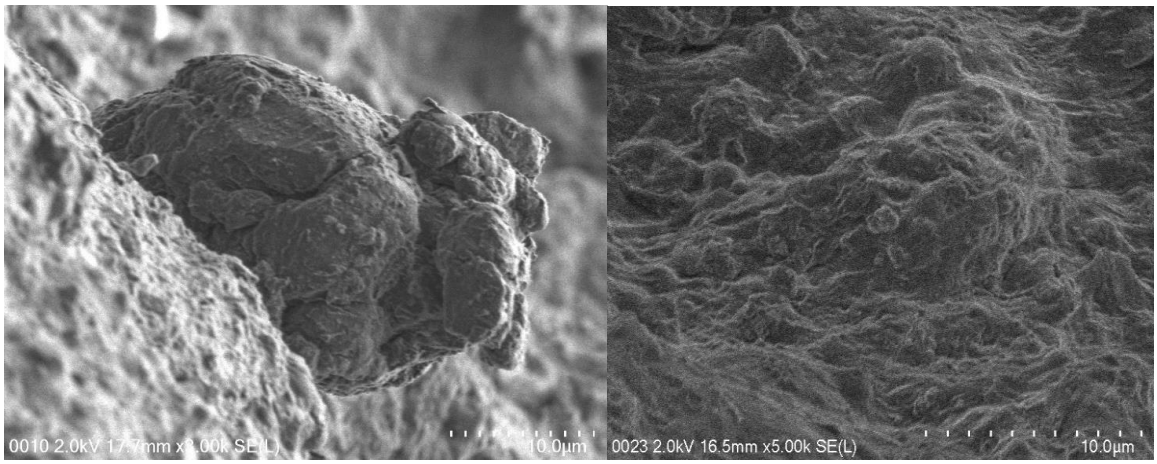

Figure 4. FESEM images; (i) bacterial cells, (ii) slime layer.

Conclusion

A membrane bioreactor treating actual sewage at a membrane flux of 10 L/m^{2}h was used in this study to investigate the distribution of biofouling on the membrane surface and in the cake layer. The CLSM results revealed that highly concentrated protein-like compounds dominated the fouling behavior. In the initial stage, humic-like substances contribute to membrane fouling, and with time, a protein-governing cake layer emerged.

Recommendations

This article will guide the scientist in comprehensively explore the fundamental growth processes of the biofouling layer on the membrane surface using CLSM and FESEM techniques to validate the in-situ visualization of the dynamic behavior that greatly disturbs the MBR performance.

Scientific Ethics Declaration

The authors declare that the scientific ethical and legal responsibility of this article published in EPSTEM journal belongs to the authors.

Acknowledgements or Notes

* This article was presented as an oral presentation at the International Conference on Technology, Engineering and Science (www.icontes.net) held in Antalya/Turkey on November 16-19, 2022.

* The authors gratefully acknowledge the support of SEGi University and Indah Water Konsortium (IWK) for the pilot plant study area, which was funded by the Fundamental Research Grant Scheme (FRGS/1/2019/TK02/SEGi/02/1) under the Ministry of Higher Education Malaysia (MOHE).

References

Asif, M., Tahar, L., Wail, F., & Mohammed, F. (2021). Fouling control in reverse osmosis for water desalination & reuse: Current practices & emerging environment-friendly technologies. *Journal of Science of the Total Environment, 765*. 142721.

Aslam, M. Ahmad, R., & Kim, J. (2018). Recent developments in biofouling control in membrane bioreactors for domestic wastewater treatment. *Separation and Purification Technology, 206*, 297 – 315.

Chu, L., & Li, S. (2006). Filtration capability and operational characteristics of dynamic membrane bioreactor for municipal wastewater treatment. *Journal of Separation and Purification Technology, 51(2)*, 173–179.

Lijuan, D., Wenshan, G., Huu, H. N., Hongwei, Z., Jie, W., Jianxin, L., Siqing, X., & Yun, W. (2016). Biofouling and control approaches in membrane bioreactors. *Journal of Bioresources Technology, 221*, 656-665.

Sun, M., Yan, L., Zhang, L., Song, L., Guo, J., & Zhang, H. (2019). New insights into the rapid formation of initial membrane fouling after in-situ cleaning in a membrane bioreactor. *Journal of Process Biochemistry, 78*, 108–113.

Xiao, K., Liang, S., Wang, X., Chen, C., & Huang, X. (2019). Current state and challenges of full-scale membrane bioreactor applications: a critical review. *Journal of Bioresource Technology, 271*, 473–481.

Yang, Z., Peng, X. F., Chen, M. Y., Lee, D. J., & Lai, J. Y. (2007). Intra-layer flow in fouling layer on membranes. *Journal of Membrane Science, 287*(2), 280–286.

Yin, C., Huan, G., Ran, Y., Lei, G., & Manjun, Z. (2021). Biological-based control strategies for MBR membrane biofouling: A review. *Journal of Water Science Technology, 83*(11), 2597 – 2614.

Yin, X., Li, X., Hua, Z. & Ren, Y. (2020b). The growth process of the cake layer and membrane fouling alleviation mechanism in a MBR assisted with the self-generated electric field. *Journal of Water Research, 171*, 115452.

Author Information

Aida Isma MOHAMAD IDRIS
Centre for Water Research, Segi University
Kota Damansara, Selangor Darul Ehsan, Malaysia
Contact e-mail: aidaisma@segi.edu.my

Munira Mohammad
Centre for Water Research, Segi University
47810 Kota Damansara, Selangor Darul Ehsan, Malaysia

Putri Razreena ABDUL RAZAK
SIRIM Berhad, Persiaran Dato' Menteri
Shah Alam, 40700 Selangor Darul Ehsan, Malaysia

Hazmin Mansor
Universiti Selangor, Bestari Jaya Campus,
45600 Selangor Darul Ehsan, Malaysia

To cite this article:

Mohamad-Idris, A.I., Mohammad, M., Abdul-Razak, P.R., & Mansor, H. (2022). In-situ observation of biofouling growth in submerged membrane bioreactor using CLSM. *The Eurasia Proceedings of Science, Technology, Engineering & Mathematics (EPSTEM), 21*, 311-315.

The Eurasia Proceedings of Science, Technology, Engineering & Mathematics (EPSTEM)
ISSN: 2602-3199

The Eurasia Proceedings of Science, Technology, Engineering & Mathematics (EPSTEM), 2022

Volume 21, Pages 316-320

IConTES 2022: International Conference on Technology, Engineering and Science

Synthesis of Nanocomposite Photo-Catalysts for Photo-Assisted Charging of Li-Ion Oxygen Batteries

Ersu LOKCU
Eskişehir Osmangazi University

Resat Can OZDEN
Eskişehir Osmangazi University

Mustafa ANIK
Eskişehir Osmangazi University

Abstract: In this work, g-C_3N_4 / 3 % rGO nanocomposite was synthesized as a photo-catalyst in order to use in the Li-ion oxygen battery. The aim was to reduce the high charging potential of the battery by the photo-assistance. The synthesis of nanocomposite was carried out by thermal decomposition of melamine which was initially mixed with the required amount reduced graphene oxide (rGO). The rGO had dual competing actions in the nanocomposite. The first action was to reduce the optical band gap of the semiconductor nanocomposite that the photo-catalyst properties of the nanocomposite were improved. Secondly, rGO degradated the visible light utilization of the nanocomposite since it favorably absorbed incident light instead of g-C_3N_4. The photo-assisted charging tests indicated that the synthesized nanocomposite reduced the charging potential and improved the cyclic discharge-charge performance of the Li-ion oxygen battery.

Keywords: Nanocomposites, Photo-charging, Li-Ion oxygen batteries

Introduction

Li-ion oxygen batteries have one important drawback in the long way to the commercialization that they have unacceptably high charging potential (4.5 $V_{Li+/Li}$) due to the sluggish oxidation kinetics of the low conducting discharge product (Li_2O_2) (Lu, 2011). It is proposed that a photo-assisted charging of the Li-ion oxygen batteries by integrating a photo-electrode with the aid of triiodide/iodide (I_3^-/I^-) redox shuttling reduce the charging potential down to the discharging potential levels (2.8 $V_{Li+/Li}$) (Yu, 2014).

g-C_3N_4, a non-metallic semiconductor, was reported as effective visible light active photo-catalyst since it has small band gap, thermal and chemical stabilities (Masih, 2017; Ragupathi, 2020). The synthesis of g-C_3N_4 based nanocomposites especially with graphene improves the poor conductivity of the g-C_3N_4 (Zhang, 2011; Li, 2013). It is reported that the band gap, conduction band (CB) edge potential and thus the valance band (VB) edge potential of g-C_3N_4 can be tuned effectively by intercalation of various amounts of the rGO (Zhang, 2011; Li, 2013).

In this work, g-C_3N_4 / 3% rGO nanocomposite is synthesized in order to use it as the photo-electrode in the Li-ion oxygen battery. The aim of our work was to get improvement in the discharge-charge performance of the Li-ion oxygen battery by the photo-assistance.

Method

Graphene oxide (GO) was synthesized by the method reported in our previous work (Çelikbilek, 2022). The nanocomposite was synthesized by mixing the melamine and rGO in ethanol at 50°C until all the methanol evaporates. After drying, the mixture was put into a crucible and heated up to 550°C at a rate of 3°C min^{-1} and then kept at this temperature for another 3 h under continues Ar flow, subsequently cooled to room temperature.

Photo-current measurements were made by linear sweep voltammetry technique in a conventional three-electrode cell with a platinum wire as the auxiliary electrode and Ag/AgCl (saturated KCl) as the reference electrode on a Gamry Reference 3000 workstation. A solar simulator (A-type 150 W, 1-3 SUN, Xenon lamb, AMO filters; 400 - 700 nm wavelength) was used as the light source. Measurements were conducted in a spectral cell contains 0.1 M KCl buffered by 0.1 M K_2HPO_4 to pH 7. For the photo-assisted charge-discharge tests the cell was assembled in an Ar-filled glove box with H_2O and O_2 levels less than 0.1 ppm. Lithium metal was used as both counter and reference electrodes and the glass microfiber filter (Whatman) was used as a separator. rGO/Super P carbon black/PVDF were mixed (80:10:10 wt%) in NMP and the slurry was coated onto one side of 16 mm - diameter GDL (TGP-H-060) with a loading rate of 0.1 mg cm^{-2} as a cathode.

X-ray diffraction (XRD) analyses were performed on a PANalytical Empyrean diffractometer with Cu K-alpha radiation at a scanning rate of 2° min^{-1}. The morphologies were examined with a ZEISS Ultraplus scanning electron microscope (SEM). UV/vis spectra were gathered by Cary 5000 UV/Vis/NIR spectrometer with diffuse reflectance accessory between 200 nm and 800 nm.

Results and Discussion

Structure and Morphology

The morphology of the synthesized nanocomposite is shown in Figure 1. The nanocomposite has slate-like stacked lamellar microstructure. Figure 2 shows the XRD patterns of the pure g-C_3N_4, pure rGO and the synthesized nanocomposite. The broad peak located at around 26° in the rGO pattern is ascribed to the presence of the loosely stacked sheets. A strong characteristic (002) peak at 27.6° in the pure g-C_3N_4 pattern is also indication of the layered structure. Another characteristic peak (100) at around 13.2° in the pure g-C_3N_4 pattern in Figure 2 corresponds to the in-plane ordering of tri-s-triazine units. The nanocomposite has almost the same characteristic peaks with the pure g-C_3N_4 in Figure 2.

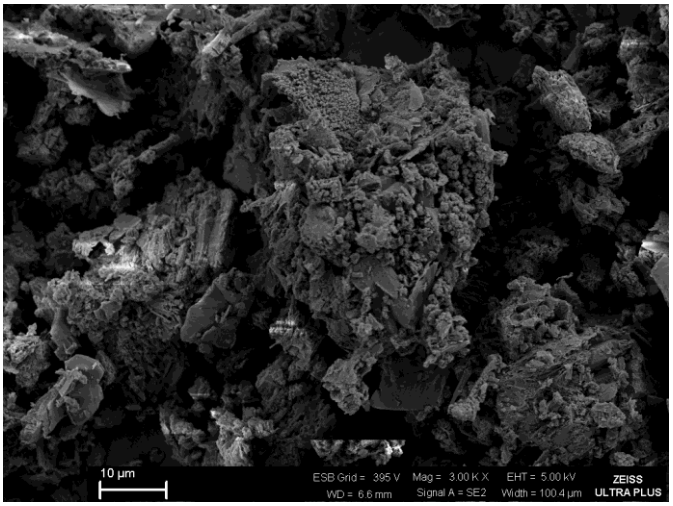

Figure 1. Morphology of the synthesized nanocomposite.

Optical Properties

The photo-anodic currents of pure g-C_3N_4, g-C_3N_4 / 3% rGO nanocomposite and g-C_3N_4 / 5% rGO nanocomposite are provided in Figure 3. The g-C_3N_4 / 3% rGO nanocomposite has improved photo-catalytic efficiency. The enhancement in the photo-currents with the presence of rGO can be attributed to the efficient visible light utilization. The further increase in the rGO content (g-C_3N_4 / 5% rGO), however, degrades this utilization and the photo-currents decline due to the more incident light absorption by rGO instead of g-C_3N_4 in Figure 3.

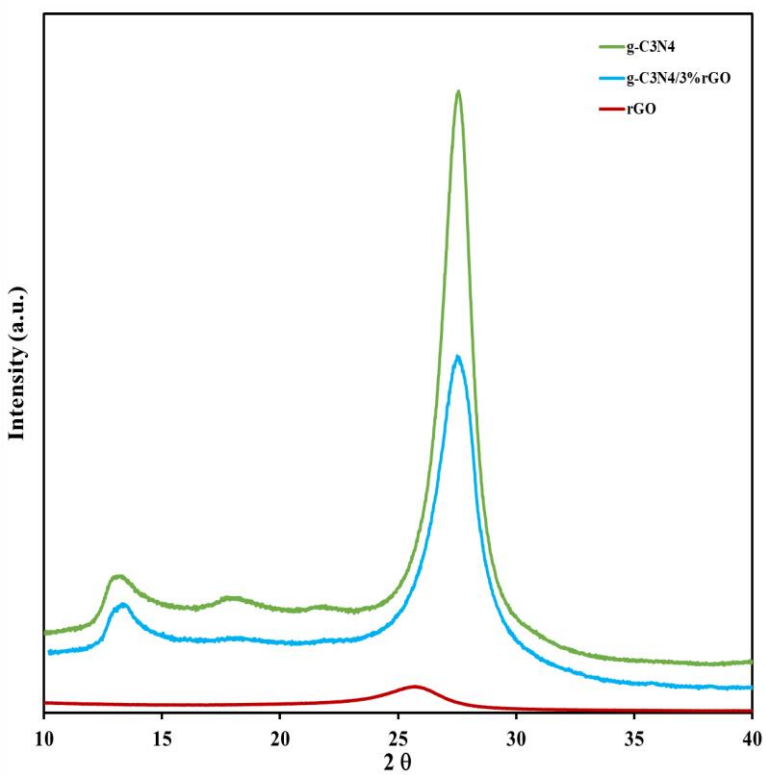

Figure 2. The XRD patterns the pure g-C_3N_4, pure rGO and synthesized nanocomposite.

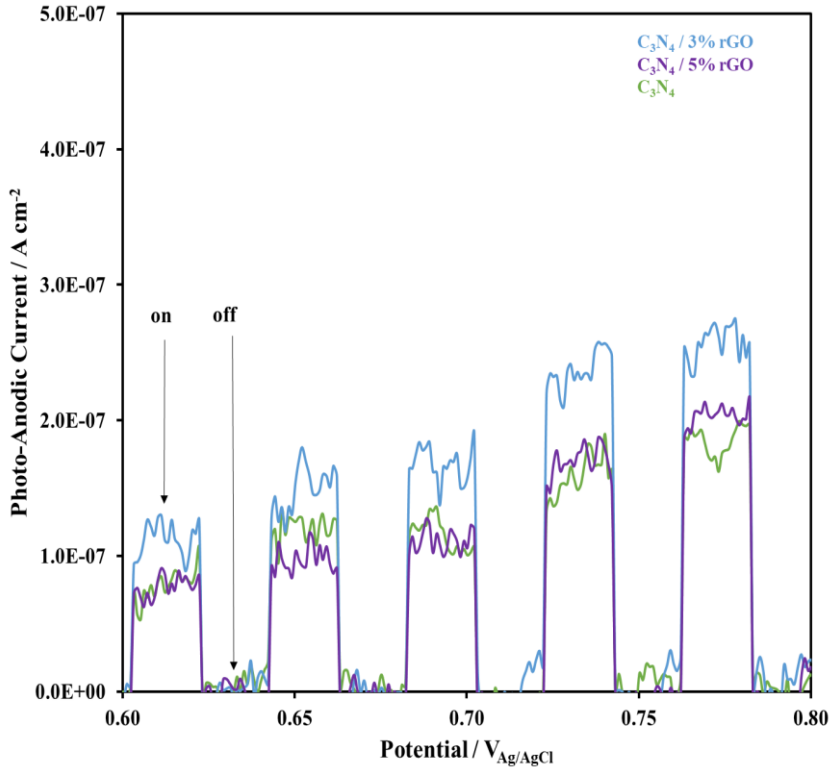

Figure 3. The photo-anodic currents of pure g-C_3N_4, g-C_3N_4 / 3% rGO and g-C_3N_4 / 5% rGO nanocomposites.

The optical band gaps (Eg) obtained from the UV-Vis diffuse reflectance spectra for the pure g-C_3N_4 and nanocomposites are given in Figure 4 that they are 2.7 eV, 2.5 eV and 2.25 eV for g-C_3N_4, g-C_3N_4 / 3% rGO and g-C_3N_4 / 5% rGO, respectively. The narrowing in the optical band gaps depend on the increase in the rGO content of the nanocomposites is attributed to a red shift in the absorption band edge (Li, 2013).

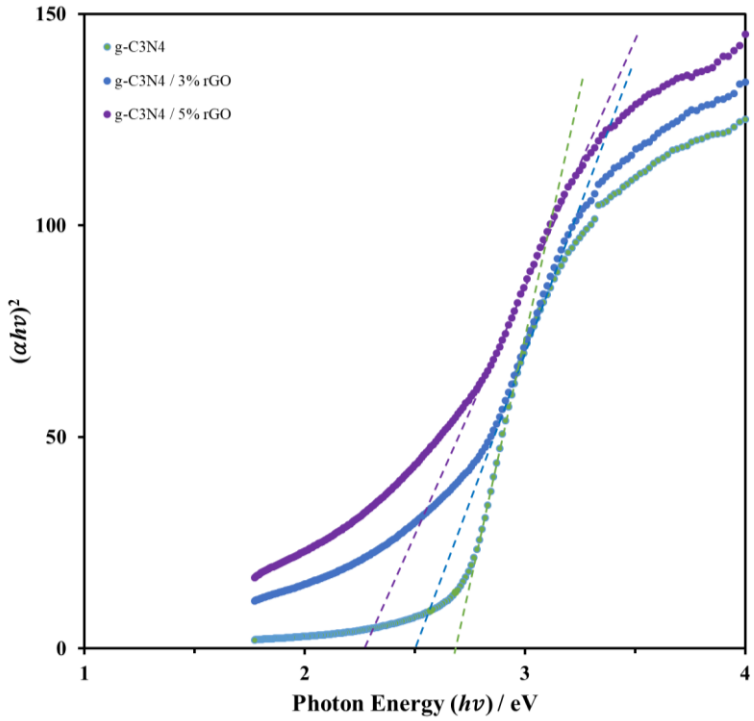

Figure 4. The optical band gaps of g-C_3N_4, g-C_3N_4 / 3% rGO and g-C_3N_4 / 5% rGO nanocomposites.

Photo-Assisted Charging of Li-Ion Oxygen Battery

The photo-assisted discharge-charge performance of the Li-ion oxygen battery for a 0.25 mA h cm^{-2} constant capacity at 0.02 mA cm^{-2} current density is shown by providing 1st, 10th and 50th cycle curves in Figure 5. Obviously, the charge potentials remain under 3.5 $V_{Li+/Li}$ with the photo-assistance for 50 cycles that the Li-ion oxygen battery performance seems improved significantly.

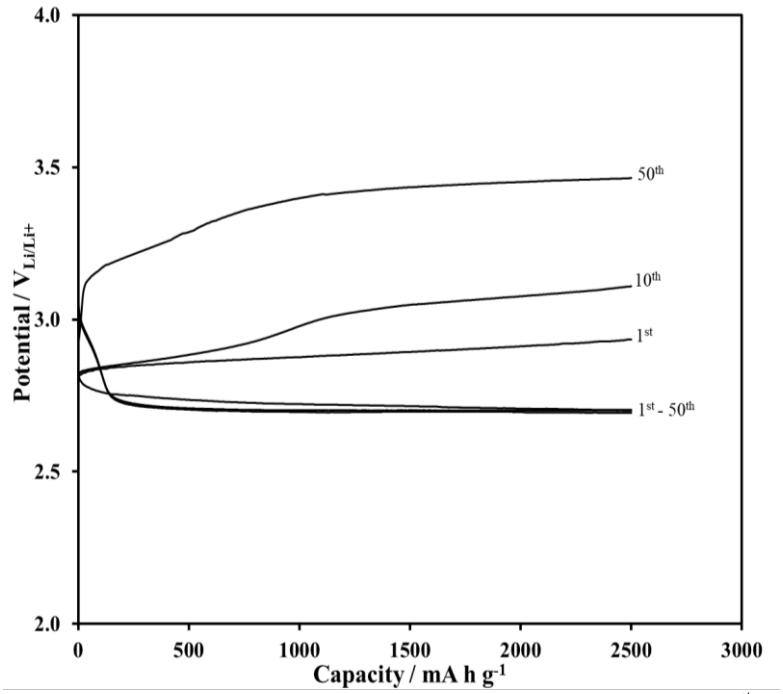

Figure 5. The photo-assisted discharge-charge curves of the Li-ion oxygen battery for 1st, 10th and 50th cycles.

Conclusion

g-C_3N_4 / 3% rGO nanocomposite was synthesized as the photo-catalyst for the photo-assisted charging of the Li-ion oxygen battery. Optical characterizations showed that there was a reduction in the optical band gap of the nanocomposite as a result of the red shift. The usage of this nanocomposite as the photo-electrode in the Li-ion oxygen battery resulted in a considerable reduction in the charge potential and improved the battery cyclic performance.

Scientific Ethics Declaration

The authors declare that the scientific ethical and legal responsibility of this article published in EPSTEM journal belongs to the authors.

Acknowledgements or Notes

* This article was presented as an oral presentation at the International Conference on Technology, Engineering and Science (www.icontes.net) held in Antalya/Turkey on November 16-19, 2022.

*This research was supported by the Scientific and Technological Research Council of Turkey under the project number 219M269.

References

Çelikbilek, Z., Can, S., Lökçü, E., & Anik, M. (2022). Effect of rGO loading on the electrochemical performance of Li22Si5/rGO composite anodes for lithium-ıon batteries. *International Journal of Energy Research*, *46*(2), 1137–1145.

Li, Y., Zhang, H., Liu, P., Wang, D., Li, Y., & Zhao, H. (2013). Cross-linked g-C3N4/rGO nanocomposites with tunable band structure and enhanced visible light photocatalytic activity. *Nano Micro Small*, *9*(19), 3336–3344.

Lu, Y. C., Kwabi, D. G., Yao, K. P. C., Harding, J. R., Zhou, J., Zuin, L., & Shao-Horn, Y. (2011). The discharge rate capability of rechargeable li-o2 batteries. *Energy & Environmental Science*, *4*(8), 2999–3007.

Masih, D., Ma, Y., & Rohani, S. (2017). Graphitic C3N4 based noble-metal-free photocatalyst Systems. *Applied Catalysis B: Environmental*, *206*, 556–588.

Ragupathi, V., Raja, M. A., Panigrahi, P., & Ganapathi Subramaniam, N. (2020). CuO/g-C3N4 nanocomposite as promising photocatalyst for photoelectrochemical water splitting. *Optik*, *208*, 164569.

Yu, M., Ren, X., Ma, L., & Wu, Y. (2014). Integrating a redox-coupled dye-sensitized photoelectrode into a lithium-oxygen battery for photoassisted charging. *Nature Communications*, *5*, 1–6.

Zhang, Y., Mori, T., Niu, L., & Ye, J. (2011). Non-covalent doping of graphitic carbon nitride polymer with graphene: Controlled electronic structure and enhanced optoelectronic conversion. *Energy & Environmental Science*, *4*(1), 4517–4521.

Author Information

Ersu LÖKÇÜ
Eskişehir Osmangazi University
Eskişehir, Turkey
Contact e-mail:elokcu@ogu.edu.tr

Reşat Can ÖZDEN
Eskişehir Osmangazi University
Eskişehir, Turkey

Mustafa ANIK
Eskişehir Osmangazi University
Eskişehir, Turkey

To cite this article:

Lokcu, E., Ozden R.C. & Anik, M. (2022). Synthesis of nanocomposite photo-catalysts for photo-assisted charging of li-ion oxygen batteries. *The Eurasia Proceedings of Science, Technology, Engineering & Mathematics (EPSTEM), 21*, 316-320.

The Eurasia Proceedings of Science, Technology, Engineering & Mathematics (EPSTEM)
ISSN: 2602-3199

The Eurasia Proceedings of Science, Technology, Engineering & Mathematics (EPSTEM), 2022

Volume 21, Pages 321-327

IConTES 2022: International Conference on Technology, Engineering and Science

Statistical Analysis of 30 Year Rainfall Data: A Case Study for Langat River Basin

Nor Faiza ABD RAHMAN
SEGi University,

Noramira HISHAM
SEGi University,

Munira MOHAMMAD
SEGi University,

Vin Cent TAI
SEGi University,

Khairi KHALID
University Teknologi Mara Cawangan Pahang

Mohamad Shakri MOHMAD SHARIF
Inti International University

Abstract: Rainfall is an important factor in civil engineering as it affects the design of hydraulic structures, bridges and culverts, canals, storm water sewers, road drainage systems, etc. This paper presents the statistical analysis of 30-year rainfall data collected at eight rainfall stations within the Langat River Basin. Ten plotting position methods were utilised to evaluate the return period of annual rainfall. The yearly rainfall was computed to assess the variability of rainfall based on the determined results; the pattern of rainfall is irregular. Weibull Distribution from Plotting Position methods is found to best fit the annual rainfall data. The findings provide the insights for determining the correct commencement and cessation of monsoon results, which have the effect on land utilisation, flood forecasting and emergency planning. This analysis contributes to water management, water resource planners, farmers, and urban engineers to evaluate the availability of water and develop the storage accordingly.

Keywords: Weibull distribution, Rainfall, Precipitation, Langat river basin, Plotting position.

Introduction

Water is essential to all life. Water is also used for transportation, as energy source, and for a number of additional domestic, agricultural, and industrial purposes. Rainfall is the most important source of water in any location, and it has a huge effect on agriculture (Rosegrant et al., 2009; Abdullah & Rahman,2015). Malaysia has distinct rainfall patterns and features compared to the rest of the globe. It has two distinct monsoon seasons, the South-East Monsoon (SEM) from May to September and the North-West Monsoon (NWM) from November to February. In recent years, the rapid change in climate has increased the number of severe floods in Malaysia. In the floods of December 2021, the calamity has taken almost 50 lives and displaced more than 40000 people, while the economic losses caused by the particular event was around USD1.46 billion (Rahman, 2022). Consitent with the rising of atmospheric temperatures and water vapour, the frequency of extreme rainfall

- Selection and peer-review under responsibility of the Organizing Committee of the Conference

occurences have increased in most land areas around the globe (Amirabadizadeh et al., 2015; Solomon, 2007). The study of rainfall mechanisms such as rainfall distribution estimation and characterization of rainfall types, rainy or dry conditions on a given day,is important for use in water resources planning and flood management. For agriculture sector, itis essential to assess the probability of rainfall occurrence using historical hydrological data sets, as agricultural output is dependent on the rainfall pattern, particularly in rain-fed areas (Maraun et al., 2010).

Suchit Kumar Rai et al. (2014) examined the change, variability, and likelihood of rainfall for crop planning in a few areas in Central India. *Student's t* was used to construct the probability distribution of rainfall, while Mann-Kendall rand statistic, Spearman rank statistic, and Gaussion low-pass were employed to examine the rainfall trend. The study concluded that the rainfall probability projections are consistent with the historical records. Nyatuame et al. (2014) conducted a study on rainfall trend for Volta Region in Ghana. Analysis of Variance (ANOVA) and Least Significant Difference (LSD) were used to analyse the rainfall data recorded over the period of 1981 to 2011. The study concluded that climate change does not affect the monthly and annual rainfall trends in the region. However, other rainfall characteristics such as extreme rainfall, rain days, and other climate change paramenters were not investigated. Rajendran et al. (2016) conducted a frequency analysis of rainy days and a rainfall fluctuation study for crop planning in Dharmapuri district in India. Markov Chain model was used to analyse the daily rainfall data from 1982 to 2013 for identifying the appropriate cropping systems in the region, while Weibull distribution was employed to compute the probability of occurence of each event. Linear regression was employed to study the relationship between the rainfall amount and rainy days. The authors concluded that the weekly, monthly, seasonal, and annual rainfall patterns and frequencies can be used as a rough guide for irrigation planning and management, as well as contingent crop planning during drought periods. Tan et al. (2019) studied rainfall trends and temperature extremes of Muda River Basin in Malaysia using historical daily climate data from 1985 to 2015. Homogeneity tests were employed to compute the Expert Team on Climate Change Detection and Indices (ETCCDI), while Non-parametric Mann-Kendall, modified Mann-Kendall, and Sen's slope tests were used to detect the trend and magnitude changes of the climate extremes. The work reveals that monthly rainfall tended to decrease in the SWM season, but increase in the NEM season, with increasing number of warmer days and nights in the basin.

This study presents the statistical analysis of 30-year rainfall data collected at eight rainfall stations within the Langat River Basin. Frequency or probability distribution is used to link the intensity of extreme occurrences, such as floods, droughts, and severe storms, to their frequency of occurrence, so that their probability of happening over time can be predicted. By fitting a frequency distribution to a set of hydrological data, the probability of occurrences may be computed. The hydrological data are evaluated in order to fit the distribution, and statistical parameters are utilised to analyse the data's variability.

Study Area

Figure 1. Langat river basin

This study focuses on the Langat river basin in Selangor, Malaysia, which has a total catchment area of 2,271 km^2. Located in the southern portion of Klang Valley, the Langat River Basin (Figure 1) is the most urbanised river basin in Malaysia. This basin is drained by the Langat River, the Semenyih River, and the Labu River.

Langat River runs roughly 182 kilometres west to the Straits of Malacca from Titiwangsa Range (Banjaran Titiwangsa) northeast of Hulu Langat (Soo et al., 2020). This study region includes two reservoirs, namely Langat dam and Semenyih dam. There are now eight water treatment facilities functioning in Langat Basin. Up till the Kajang observation station, the rainfall station analysis is located in the Upper Part of Langat River Basin (UPLRB) (Ali et al., 2014; Khalid et al., 2016; Faiza et al., 2022).

Method

The main focus of this paper is to identify the most suitable plotting position method for rainfall data in UPLRB. The rainfall data from 8 stations within the UPLRB catchment was provided by the Department of Irrigation and Drainage (DID) in Ampang within and outside the Langat River Basin. The daily rainfall at each station was then aggregated to calculate the total seasonal and the total annual data series. The analysis has been carried out for 30 years return period only. Mean rainfall for the annual and th seasonal rainfall has been determined. The plotting position methods to fit the rainfall data (Khalid et al., 2016) and details of the plotting methods are presented in Tables 1 and 2, respectively.

Table 1. Plotting position methods

No	Plotting Position	Equation
1	Adamowski	(m-1/4)/(N+1/2)
2	Beard	(m0.31)/(N+0.38)
3	Blom	(m-3/8)(N+1/4)
4	California	m/N
5	Chegodayev	(m-0.3)/(N+0.4)
6	Cunnane	(m-0.4)/(N+0.2)
7	Gringorten	(m0.44)/(N+0.12)
8	Hazen	(m-0.5)/N
9	Tukey	(3m-1)/(3N+1)
10	Weibull	m/(N+1)

Where, m is rank of the data and N = length of the sample (number of years).

Result and Discussion

Using statistical criteria, the yearly rainfall data is evaluated and the variance in distribution over the area is studied. The monthly and seasonal trends of the rainfall distribution are also investigated.. The rainfall data is arranged in decreasing order, and several plotting positions are used to establish the return period. Using the rainfall-return period equation derived from the graph for all plotting positions, the rainfall magnitudes for different return periods were determined as shown in Table 2 and Figure 2.

Table 2. Maximum Annual Rainfall based on Plotting Position Methods

Method/Return period	5	10	15	20	25	30
Adamowski	1311.759	1406.633	1510.259	1561.15484	1606.800612	1652.446
Beard	1297.716	1369.564	1467.65	1527.603278	1553.894763	1580.186
Blom	1311.759	1406.633	1510.259	1561.15484	1606.800612	1652.446
California	1311.759	1406.633	1510.259	1561.15484	1606.800612	1652.446
Chegodayev	1297.923	1370.341	1468.623	1528.275348	1555.088605	1581.902
Cunnane	1295.876	1362.743	1459.224	1522.250598	1544.02012	1565.790
Gringorten	1295.069	1359.811	1455.668	1520.277351	1540.138542	1560.00
Hazen	1293.871	1355.529	1450.554	1511.894921	1534.908522	1552.026
Tukey	1297.236	1367.766	1465.41	1526.095003	1551.183991	1576.273
Weibull	1304.306	1395.36	1501.058	1555.449119	1599.66846	1643.888
Average Max Rainfall	1301.727	1380.101	1479.896	1537.531014	1569.930484	1601.74

According to the preliminary investigation and analysis, the difference in maximum annual rainfall for different plotting positions is insignificant. For UPLRB, the Adamwoski plotting approach produces the highest value for rainfall for varied return periods, while the Hazen method produces the lowest value and is therefore deemed inapplicable for use in rainfall analysis. In contrast to other plotting positions, Weibull method yields a

maximum rainfall that is around 95% of the average maximum rainfall, and is thus the most suitable distribution for describing the yearly rainfall data for UPLRB. It can be observed from the tabulated result for 5, 10,15, 20,25 and 30 years (see Table 2), Weibull method provides the most consistent result in comparison to the average maximum rainfall given. It is also observed that the amount of rainfall increases with return period, consistent with the findings reported by Amırabadızadeh (2015) and Loo et al. (2015).

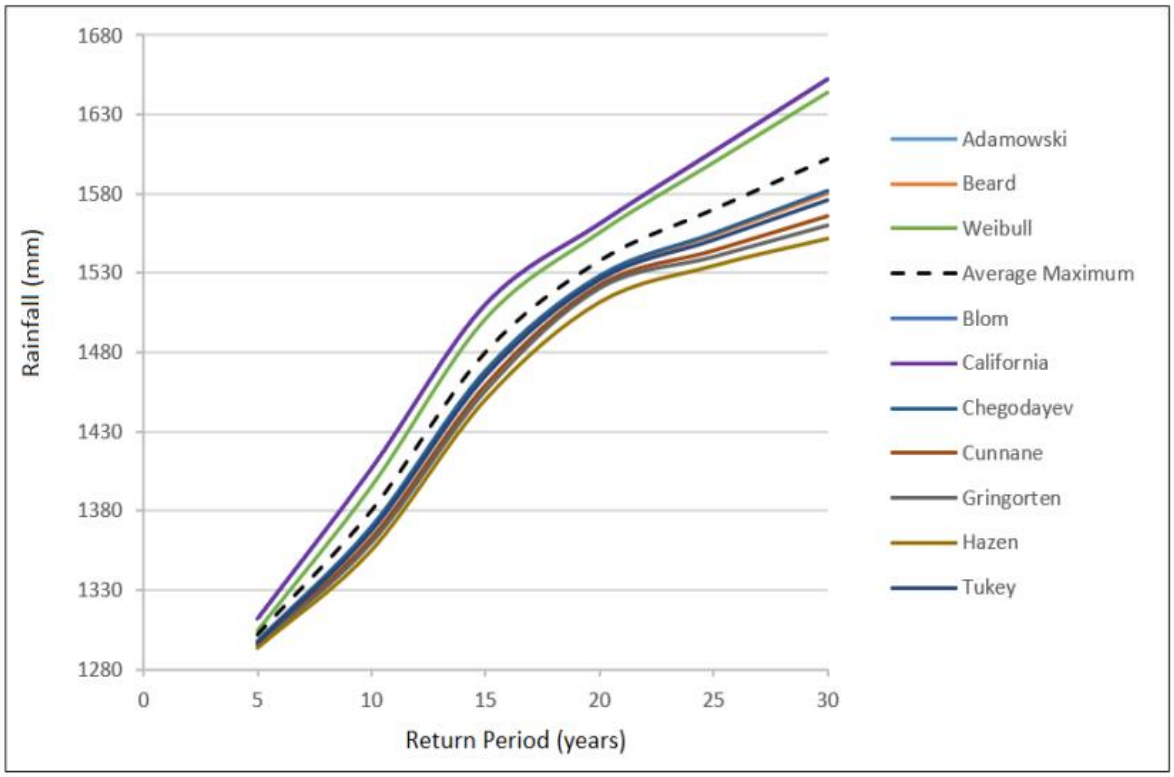

Figure 2. Plotting position

The transition between the NEM and SWM (and vice versa) in April and October is known as the inter monsoon season, which lasts between four and seven weeks (Arvind et al., 2017; Toh et al., 2013). Table 3 tabulated the average monthly rainfall and illustrated in Figure 3. The highest rainfall recorded was in November with 315.17 mm and the least amount of rainfall recorded is 113.39 mm. The mean average rainfall recorded for 12 months is a round 202.24 mm. It can be observed that January, June and July are the driest months in a year.The record shows that NEM has 9.3% higher rainfall compared to SWM. The inter-monsoon seasons have higher amount of rainfall, about 258.69 mm in April and 251.85 mm in October, respectively. Figure 4 shows the average seasonal rainfall in UPLRB.

Table 3. Average monthly rainfall in UPLRB (DID, 2014e)

Month	Average Rainfall, mm
January	113.39
February	159.88
March	225.77
April	258.69
May	208.53
June	143.89
July	150.07
August	180.35
September	228.86
October	251.85
November	315.17
December	190.47
Grand Average	202.24

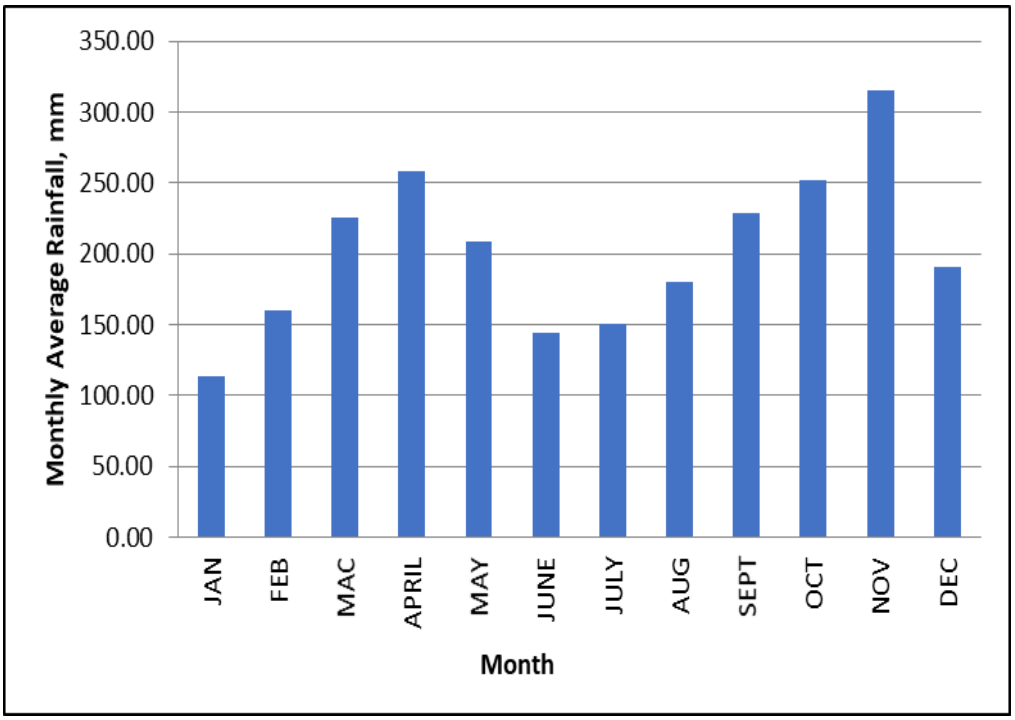

Figure 3. Bar chart of average monthly rainfall in UPLRB (DID, 2014e)

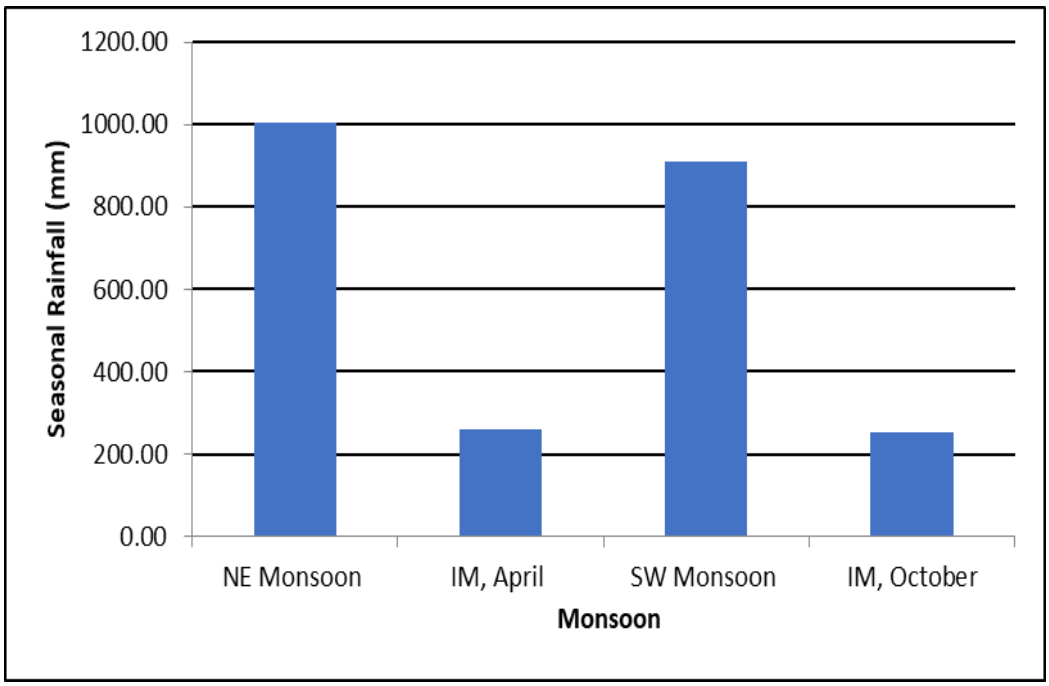

Figure 4. Average seasonal rainfall in UPLRB (DID, 2014e)

Conclusion and Recommendations

This is a preliminary data analysis for rainfall data distribution before comprehensive data analysis to be conducted. This analysis helps in understanding the rainfall pattern within the Langat River Basin. Weibull Distribution is found to best fit the annual rainfall data. It can be observed that the rainfall amount increases with return period. According to the preliminary investigation and analysis, the variance of different plotting position is insignificant. All the data are independent, stationary and homogenous. The analysis can be used to aid the policy maker to understand the conjunctive use of surface water, available rainfall, and ground water is for improved agricultural and irrigation management.

Scientific Ethics Declaration

The authors declare that the scientific ethical and legal responsibility of this article published in EPSTEM journal belongs to the authors.

Acknowledgements

* This article was presented as an oral presentation at the International Conference on Technology, Engineering and Science (www.icontes.net) held in Antalya/Turkey on November 16-19, 2022.

References

Abdullah, H. M., & Rahman, M. M. (2015). Initiating rain water harvest technology for climate change induced drought resilient agriculture: scopes and challenges in Bangladesh. *Journal of Agriculture and Environment for International Development (JAEID), 109*(2), 189-208.

Ali, M. F., Saadon, A., Abd Rahman, N. F., & Khalid, K. (2014). An assessment of water demand in malaysia using water evaluation and planning system. In *InCIEC 2013* (pp. 743-755). Springer, Singapore.

Amirabadizadeh, M., Huang, Y. F., & Lee, T. S. (2015). Recent trends in temperature and precipitation in the Langat River Basin, Malaysia. *Advances in Meteorology*, Article ID 579437 https://doi.org/10.1155/2015/579437

Arvind, G., Kumar, P. A., Karthi, S. G., & Suribabu, C. R. (2017). Statistical analysis of 30 years rainfall data: a case study. *IOP Conference Series: Earth and Environmental Science, 80*(1), p. 012067.

Faiza, N., Tai, V. C., & Mohammad, M. (2022). Trend analysis of river flow in Langat River Basin using SWAT model. *Journal of Engineering & Technological Advances, 7*(1), 13-22.

Khalid, K., Ali, M. F., Abd Rahman, N. F., Mispan, M. R., Haron, S. H., Othman, Z., & Bachok, M. F. (2016). Sensitivity analysis in watershed model using SUFI-2 algorithm. *Procedia engineering, 162*, 441-447.

Loo, Y. Y., Billa, L., & Singh, A. (2015). Effect of climate change on seasonal monsoon in Asia and its impact on the variability of monsoon rainfall in Southeast Asia. *Geoscience Frontiers, 6*(6), 817-823.

Maraun, D., Wetterhall, F., Ireson, A. M., Chandler, R. E., Kendon, E. J., Widmann, M., ... & Thiele-Eich, I. (2010). Precipitation downscaling under climate change: Recent developments to bridge the gap between dynamical models and the end user. *Reviews of Geophysics, 48*(3), 2009RG000314.

Nyatuame, M., Owusu-Gyimah, V., & Ampiaw, F. (2014). Statistical analysis of rainfall trend for Volta Region in Ghana. *Int. J. Atmos. Sci., 67*(2), 1-11.

Rahman, S. (2022). Malaysia's floods of December 2021: can future disaster be avoided? *ISEAS Perspective, 2022*(26), 1-15.

Rai, S. K., Kumar, S., Rai, A. K., Satyapriya, & Palsaniya, D. R. (2014). Climate change variability and rainfall probability for crop planning in few districts of Central India. *Atmos. Climate Sci., 4*, 394-403.

Rajendran, V., Venkatasubramani, R., & Vijayakumar, G. (2016). Rainfall variation and frequency analysis study in Dharmapuri district (India). *Indian J. Geo. Mar. Sci., 45*(11), 1560-1565.

Rosegrant, M. W., Ringler, C., & Zhu, T. (2009). Water for agriculture: maintaining food security under growing scarcity. *Annual Review of Environment and Resources, 34*(1), 205-222.

Solomon S. (2007). Climate change 2007-*The Physical Science Basis: Working Group I Contribution to the Fourth Assessment Report of the IPCC* (vol. 4), Cambridge: Cambridge University Press.

Soo, E. Z. X., Wan Jaafar, W. Z., Lai, S. H., Othman, F., Elshafie, A., Islam, T., ... & Othman Hadi, H. S. (2020). Precision of raw and bias-adjusted satellite precipitation estimations (TRMM, IMERG, CMORPH, and PERSIANN) over extreme flood events: case study in Langat river basin, Malaysia. *Journal of Water and Climate Change, 11*(S1), 322-342.

Tan, M.L., Samat, N., Chan, N.W., Lee, A.J., & Li, C. (2019). Analysis of precipitation and temperature extremes over the Muda River Basin, Malaysia. *Water, 11*(2), 283.

Toh, Y. Y., Lim, S. F., & Von Glasow, R. (2013). The influence of meteorological factors and biomass burning on surface ozone concentrations at Tanah Rata, Malaysia. *Atmospheric Environment, 70*, 435-446.

Author Information

Nor Faiza ABD RAHMAN
Centre for Modelling and Simulation, Faculty of Engineering, Built Environment, and IT, SEGi University, 47810 Petaling Jaya, Selangor, Malaysia
faizaabdrahman@segi.edu.my

Noramira HISHAM
Centre for Modelling and Simulation, Faculty of Engineering, Built Environment, and IT, SEGi University, 47810 Petaling Jaya, Selangor, Malaysia

Munira MOHAMMAD
Centre for Modelling and Simulation, Faculty of Engineering, Built Environment, and IT, SEGi University, 47810 Petaling Jaya, Selangor, Malaysia

Vin Cent TAI
Centre for Modelling and Simulation, Faculty of Engineering, Built Environment, and IT, SEGi University, 47810 Petaling Jaya, Selangor, Malaysia

Khairi KHALID
School of Civil Engineering, College of Engineering, University Teknologi Mara Cawangan Pahang, Kampus Jengka, Pahang, Malaysia

Mohamad Shakri MOHMAD SHARIFF
Faculty of Engineering and Quantity Surveying, Inti International University, Nilai Negeri Sembilan

To cite this article:

Abd Rahman, N. F., Hisham, N., Mohammad, M., Tai, V.C., Khalid, K., & Mohmad Shariff**,** M.S. (2022). Statistical analysis of 30 year rainfall data: A case study for Langat River Basin. *The Eurasia Proceedings of Science, Technology, Engineering & Mathematics (EPSTEM), 21*, 321-327.

The Eurasia Proceedings of Science, Technology, Engineering & Mathematics (EPSTEM)
ISSN: 2602-3199

The Eurasia Proceedings of Science, Technology, Engineering & Mathematics (EPSTEM), 2022

Volume 21, Pages 328-334

IConTES 2022: International Conference on Technology, Engineering and Science

Vehicle Plate Recognition System Using Image Processing

Nihat PAMUK
Zonguldak Bulent Ecevit University

Abstract: In this study, the license plate reading system, which is needed in security applications, automatic door systems, or parking lot entrance and exit processes, is designed. The main reasons for choosing this system are that it greatly reduces the workload and contributes to the acceleration of operation in areas with heavy traffic. This work has been programmed with image processing methods on MATLAB and will take an image input with an internal or external camera system and give an output to the user. When we look at all the countries of the world, it is observed that there are different shapes and sizes on the license plates. In this study, simple but effective morphological operations and Sobel edge detection method were used so that these differences do not cause the system to make any mistakes. With this approach, the letters and numbers on the plate were divided by using the bounding box method, and an effective study was carried out. After this study, the template matching approach is used to identify the characters.

Keywords: Image processing, Sobel filtering, License plate recognition system

Introduction

Nowadays, the increase in the population has led to an increase in the number of vehicles, and the increase in the number of vehicles has brought with it an increase in the problems in traffic, making it difficult to follow and control the vehicles (Yigit & Celik, 2014). For this reason, the need for traffic control has increased and the License Plate Recognition System is needed. Plates are like unique identification numbers of vehicles (Ozalp & Dugenci, 2011). All information about the vehicle to be detected can be accessed when the license plates of the relevant vehicles are found. This makes the License Plate Recognition System useful and practical.

The main usage areas of the License Plate Recognition System are applications such as places where entrances and exits must be controlled, toll collection systems and toll highways, tracking and identification of vehicles in traffic, and automatic passage systems (Bingol & Kuscu, 2008). The fact that each of these processes is done by humans increases the processing time. Today, the number of vehicles used in traffic is increasing due to the increase in vehicle brands and models, the rapid production of vehicle manufacturing factories with the industry 4.0 revolution, and the increase in the world population. This increase causes the problems of difficulty in vehicle tracking due to the density in places such as parking lots and shopping centers that can be entered by vehicle, as well as traffic density.

License Plate Recognition System is used in many areas such as automatic passage and parking systems, vehicle tracking and detection, traffic control (Yalim & Dogan, 2008). For this reason, there are many studies in the literature on license plate location and license plate recognition. Plate recognition is commonly performed by detecting the license plate region. In the old methods, image processing was frequently used to make license plate recognition. However, features such as the image being dirty and having low contrast have made this method very difficult to use and therefore a lot of preprocessing is required.

In addition to being technological devices that have entered our lives with the advancement of technology, this technology is also used in vehicles. Previously manual vehicles are now automatic, and almost every new model

vehicle is now equipped with rear view cameras (Cavuslu et al., 2008). Thanks to these cameras in the equipment of the vehicles, vehicle and license plate recognition can be done easily through the cameras in the vehicles without the need for any additional equipment. In addition to the problems mentioned, vehicle and license plate recognition is becoming increasingly important in order to understand whether the people in the vehicles are followed in any way (Eldem et al., 2017). In the study, there is primarily the license plate area in the instant vehicle images taken from the camera. The license plate characters in the resulting image are separated from the image. Finally, the characters extracted from the license plate region are given to the optimization algorithms determined for the recognition process and the license plate recognition process is completed.

Determining the Plate Area on the Vehicle

The first step we will take in this study is to find the location of the license plate region (Er, 2004), (Martinsky, 2007). It is important that the license plate area in the vehicle photo is determined correctly and without errors. If a mistake is made at this stage of the process, the data entered and received in the rest of the system will have no meaning, and the plate will not be readable. The original photo of the license plate is shown in Figure 1.

Figure 1. Original photo of the license plate

First, the original photo of the license plate is uploaded to the system. Three color values define pixels on the photograph. These colors are red, green and blue (RGB-Red, Green, Blue). These pixel components take values in the range of 0-255 (Vishali et al., 2007). After the arithmetic average of the R, G and B values of the color photograph taken as input to the system is found, the arithmetic average of the average values of these three colors is found. This value will help us determine our threshold value. After these calculations are made, some pre-processes will be applied to the photo in order to remove unnecessary areas from the photo.

The first step of these processes is to convert the image to gray level. This will prevent unnecessary details in the photo from blocking the system. Photos may have different gray brightness/contrast values as they may have been taken at different times of the day. Photos taken in cloudy or low-light conditions have darker tones, while photos taken under sunlight or bright environments have higher brightness. In order to overcome the problems that may occur due to this imbalance in brightness levels, it is necessary to transform the picture to gray level homogeneously (Arth et al., 2007). The original plate image taken in gray level is shown in Figure 2.

Figure 2. Original plate image taken in gray level

A median filter was applied to the image to remove noise and pollution in this study. The median filter looks at neighboring pixels to calculate the value of each pixel and after sorting the neighboring pixels it takes the value in the middle of the row. If the region has an even number of pixels, the median filter uses the average of these two pixels as the median value (Johan & Prabuwono, 2011). The median filtered plate definition image is shown in Figure 3.

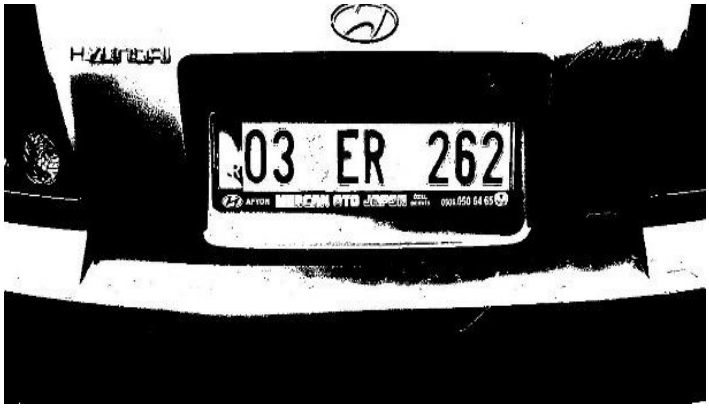

Figure 3. Median filtered plate definition image

The image has an average threshold value. After taking the initial threshold value as any value, the color intensity of the photo is checked. Accordingly, the actual threshold value of the photograph is recalculated. In order to convert the image to binary level, the gray level pixels under the new value are converted to black and the remaining pixels to white. In the binary system created, the numbers with zero represent the black colors and the numbers with one represent the white colors (Beibut et al., 2014). After the binary image created here is transferred to a two-dimensional matrix, all operations are performed on this binary matrix. The binary level image is shown in Figure 4. After the figure 4 is brought to the gray level and binary level, the edges are revealed with the Sobel edge detection algorithm. The Sobel filter reveals a real high-frequency region (sharp edges) that correspond to the edges of an image (Sarfraz et al., 2003). The Sobel filtered image is shown in Figure 5.

Figure 4. Binary level image

Figure 5. Sobel filtered image

The edge information obtained when using the Sobel filter, one of the edge detection algorithms, can be greatly affected by noise (Shapiro et al., 2004). For this reason, it is very important to perform the operations applied in the previous steps correctly. In this regard, MATLAB software has made it easier for us to analyze the image. After applying the Sobel filter, the next step is to highlight the edges. When a Sobel filter is applied to the image, it is observed that there are gaps between the lines representing the edges. This linear space is lost if the Sobel image is expanded using linear structural elements (Martin et al., 2002). Extension; It is performed by stretching the white pixels observed in the image horizontally and vertically after applying the Sobel filter. The image of the plate with its edges highlighted is shown in Figure 6.

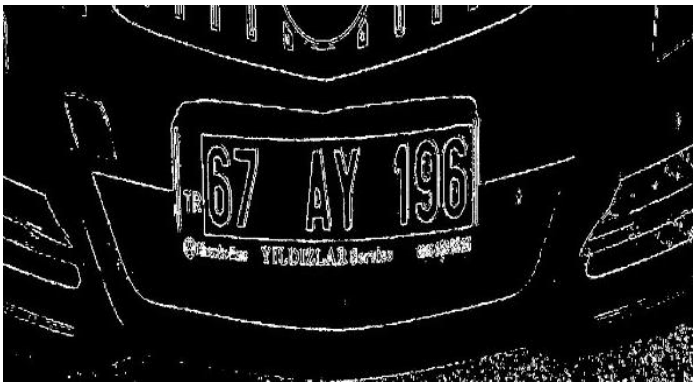

Figure 6. Image of the plate with its edges highlighted

At this stage the outline of the cell looks quite nice, but there are still holes in the cell. These holes are filled with the advantages of MATLAB software. The region of interest has been successfully partitioned, but this is not the only object found. Objects attached to the outer edges of the image can be eliminated using MATLAB functions. This helps to remove the license plate area of the vehicle. The image of filling the blank spaces in the rectangle is shown in Figure 7.

Figure 7. Image of filling the blank spaces in the rectangle

Discharge Character from the Plate Zone

The image with plate location detected is shown in Figure 8. The plate region, which was removed from the image due to the operations performed in the previous stages, was determined. After the plate area is determined in the photograph taken, the next step is to recognize the characters consisting of letters and numbers on the plate. At this stage, what is desired is to purify the characters from foreign objects and reduce the visual pollution as little as possible. Thus, the system can easily detect the characters on the plate and compare with the letters and numbers in the character library. This is the most important part for the results to be error-free. The character purification process consists of three stages: removing foreign objects, calculating the width and height values of the characters, and separating the image into characters (Yousef et al., 2020).

In the purification process, the height values of the characters are calculated by scanning the plate region. In this way, the black areas under the character size limit determined by the system were deleted and foreign objects on the image were cleaned. After the characters on the plate are cleaned of contamination, it is time to recognize these characters and convert them into text information. In this study, template matching method was used. For this method, the characters separated from the plate must be of equal size. Therefore, equalizing the sizes of the characters is essential for the correct operation of the system. After the length of the characters is equalized, their horizontal and vertical projections are extracted.

Figure 8. Image with the plate location detected

This projection is the number of pixels in rows and columns of characters (Srikanth & Kumar, 2022). In this study, the characters are synchronized at 24x42 pixels. Since the matching method is used in this study, the characters on the plate in the image must have the same appearance as the characters in the created library. For this reason, on the final image, blacks are converted to white and whites to black. This converted image is shown in Figure 9.

Figure 9. Converted image

Reading the Characters on the Plate

In the previous stages, the license plate area of the vehicle was determined from the vehicle photo and the characters consisting of numbers and letters on the plate were made clearly visible. Finally, a match for these characters to be made into a text scaling logic has been applied. With this logic, the characters on the plate will match their equivalents in the previously prepared character library and will turn into text with this reference. The identified license plate character library is shown in Figure 10.

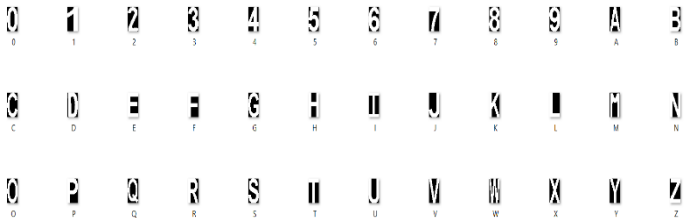

Figure 10. Identified license plate character library

User Interface

An interface has been designed with MATLAB GUIs so that the application can be run easily and this work can be presented to the user in a practical way. The process steps and flow chart of the designed program are shown in Figure 11.

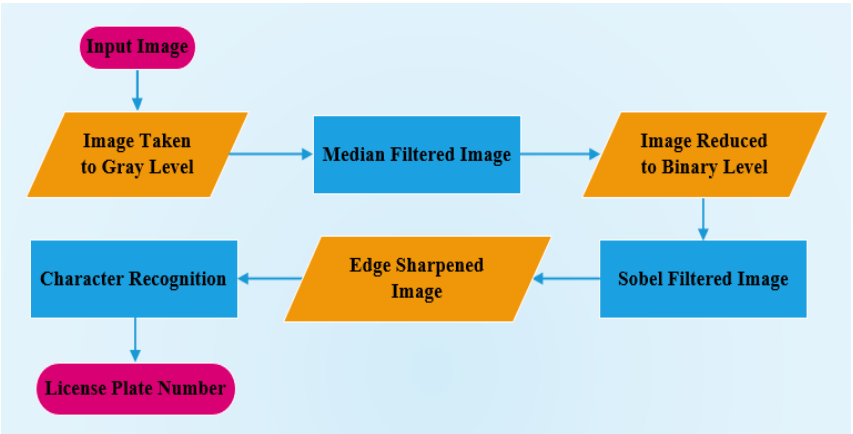

Figure 11. Process steps and flow chart

The designed interface plate recognition program is shown in Figure 12. When the select plate button is clicked on this interface, the system will direct you to the location where the images are located and wait for you to select an image from there. It will appear in the selected visual interface. Then, when the detect license plate button is clicked, the text of the plate will be printed on the output section at the bottom right.

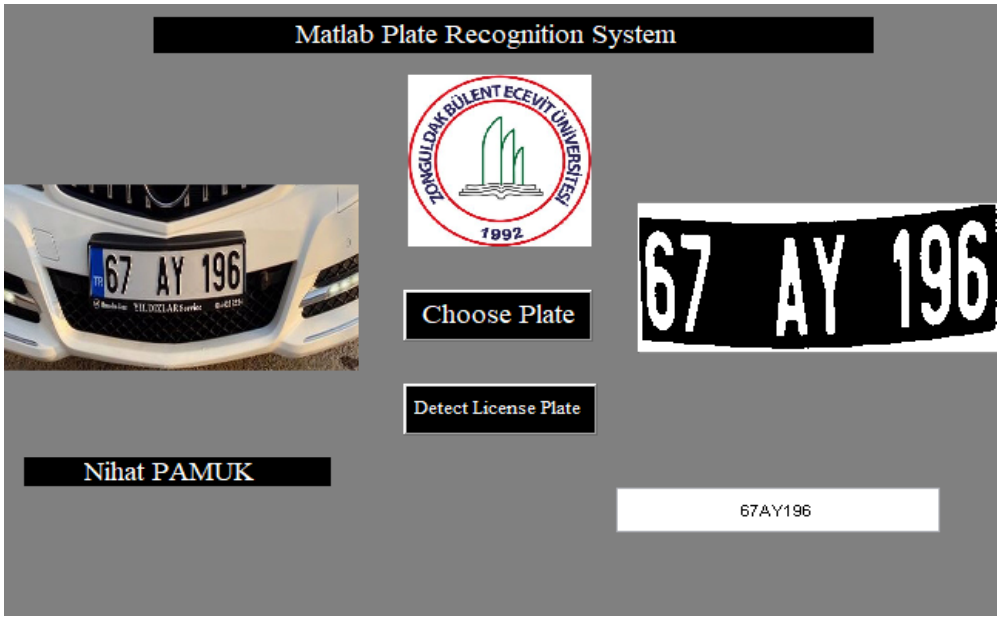

Figure 12. Designed interface program

Conclusions

This study aimed to read the license plate by processing the photograph of the vehicle taken, and high success was achieved in reading the license plate in the tests. While the written program is running, the photograph taken is suitable for the MATLAB software program using a filter. Then comes the process of determining the plate location. The method used for this process determines the rectangular part of the photo. The determined rectangular part is made suitable for reading with the filtering processes used in the MATLAB program. The output is obtained by comparing the characters in the image with the previously created library. Some undesirable situations may occur in the operation of the program. The quality of the photo containing the license plate to be read, the shooting angle, and other objects that may be included in the photo will reduce the program's success rate. For this reason, the license plate photo that is expected to be processed must be taken correctly.

Scientific Ethics Declaration

The author declares that the scientific ethical and legal responsibility of this article published in EPSTEM journal belongs to the authors.

Acknowledgements

* This article was presented as an oral presentation at the International Conference on Technology, Engineering and Science (www.icontes.net) held in Antalya/Turkey on November 16-19, 2022.

References

Arth, C., Limberger, F., & Bischof, H. (2007). Real-time license plate recognition on an embedded DSP-platform. *2007 IEEE Conference on Computer Vision and Pattern Recognition*, Minneapolis, MN, USA, 17-22 June 2007, 1-8, doi: 10.1109/CVPR.2007.383412.

Beibut, A., Magzhan, K., & Chingiz, K. (2014). Effective algorithms and methods for automatic number plate recognition. *2014 IEEE 8th International Conference on Application of Information and Communication Technologies (AICT)*, Astana, Kazakhstan, 15-17 October 2014, 1-4, doi: 10.1109/ICAICT.2014.7035951.

Bingol, O., & Kuscu, O. (2008). Bilgisayar tabanli arac plaka tanima sistemi. *Bilisim Teknolojileri Dergisi*, *1*(3), 1-5.

Cavuslu, M. A., Karakaya, F., & Altun, H. (2008). CKA tipi yapay sinir agi kullanilarak plaka yeri tespitinin FPGA'da donanimsal gerceklenmesi. *Akilli sistemlerde yenilikler ve uygulamalari sempozyumu (ASYU 2008)*, Suleyman Demirel Universitesi, Isparta, 7-9 Ekim 2008, 1-4.

Eldem, A., Eldem, H., & Palali, A. (2017). Goruntu isleme teknikleriyle yuz algilama sistemi gelistirme. *Bitlis Eren Universitesi Fen Bilimleri Dergisi*, *6*(2), 44-48, doi: 10.17798/bitlisfen.333984.

Er, O. (2004). *Insan yuzu bulma ve tanima*. Sakarya Universitesi, Fen Bilimleri Enstitusu, Yuksek Lisans Tezi, Sakarya, Turkiye.

Johan, T. M., & Prabuwono, A. S. (2011). Recognition of bolt and nut using artificial neural network. *2011 International Conference on Pattern Analysis and Intelligence Robotics*, Kuala Lumpur, Malaysia, 28-29 June 2011, 165-170, doi: 10.1109/ICPAIR.2011.5976889.

Martin, F., Garcia, M., & Alba, J. L. (2002). New methods for automatic reading of VLP's. *In Proceedings IASTED International Conference of the SPPRA*, 126-131.

Martinsky, O. (2007). *Algorithmic and mathematical principles of automatic number plate recognition systems*. Brno University of Technology, Faculty of Information Technology, Department of Intelligent Systems, B.SC. Thesis, Brno, Czech Republic.

Ozalp, A. N., & Dugenci, M. (2011). Plaka tanima sistemlerine yeni yaklasimlar. *13. Akademik Bilisim Konferansi (Akademik Bilisim'11)*, Inonu Universitesi, Malatya, 2-4 Subat 2011, 747-751.

Sarfraz, M., Ahmed, M. J., & Ghazi, S. A. (2003). Saudi Arabian license plate recognition system. *2003 International Conference on Geometric Modeling and Graphics*, London, UK, 16-18 July 2003, 36-41, doi: 10.1109/GMAG.2003.1219663.

Shapiro, V., Dimov, D. T., Bonchev, S., Velichkov, V., & Gluhchev, G. (2004). Adaptive license plate image extraction. *CompSysTech'04: Proceedings of the 5th International Conference on Computer Systems and Technologies*, Rousse, Bulgaria, 17-18 June 2004, 1-7, https://doi.org/10.1145/1050330.1050364.

Srikanth, P.,& Kumar, A. (2022). *Automatic vehicle number plate detection and recognition systems: Survey and implementation*. Autonomous and Connected Heavy Vehicle Technology, Chapter 6, Academic Press, 125-139, https://doi.org/10.1016/B978-0-323-90592-3.00007-0.

Vishali, G., Meghana, H., Kumar, M. A., & Rajesha, N. (2019). An investigation on image conversions and edge detection patterns in image processing. *2019 International Conference on Emerging Trends in Science and Engineering (ICESE)*, Hyderabad, India, 18-19 September 2019, 1-8, https://doi.org/10.1109/ICESE46178.2019.9194692.

Yalim, B., & Dogan, N. (2008). Turk tasit plaka standartlari icin plaka tanima sistemi. *Bilisim Teknolojileri Dergisi*, *1*(1), 47-50.

Yigit, T., & Celik, H. (2014). Otomatik plaka tanima ozelligine sahip akilli bariyer sistemi. *5. Ulusal Mekatronik Muhendisligi Ogrenci Kongresi (MeMOK 2014)*, Atilim Universitesi, Ankara, 24 Mayis 2014, 209-219.

Yousef, K. M. A., Mohd, B. J., Al-Khalaileh, Y. A., Al-Hmeadat, A. H., & El-Zig, B. I. (2020). Automatic license plate detection and recognition for Jordanian vehicles. *Advances in Science, Technology and Engineering Systems Journal*, *5*(6), 699-709, https://doi.org/10.25046/aj050684.

Author Information

Nihat Pamuk
Department of Electrical Electronics Engineering
Faculty of Engineering, Zonguldak Bulent Ecevit University
Zonguldak/Turkey
Contact e-mail: *nihatpamuk@beun.edu.tr*

To cite this article:

Pamuk, N. (2022). Vehicle plate recognition system using image processing. *The Eurasia Proceedings of Science, Technology, Engineering & Mathematics (EPSTEM), 21*, 328-334.

The Eurasia Proceedings of Science, Technology, Engineering & Mathematics (EPSTEM)
ISSN: 2602-3199

The Eurasia Proceedings of Science, Technology, Engineering & Mathematics (EPSTEM), 2022

Volume 21, Pages 335-348

IConTES 2022: International Conference on Technology, Engineering and Science

Study of the Correlation between the Process Parameters and the Mechanical Characteristics of the Aluminum Sheets Welded by the FSW Process

Mohamed MERZOUG
Liabes University of Sidi-Bel-Abbes

Abdelatif MIMMI
Djillali Liabes University of Sidi-Bel-Abbes

Abdelkader GHAZI
Mustapha Stambouli University of Mascara

Abstract: In recent years, friction stir welding (FSW) methods have been used to obtain good joint mechanical and process properties. The development of FSW for lap joint manufacturing will expand the number of applications that can benefit from this technology. The objective of the present work is to the modeling of parameters influencing the temperature during friction stir lap welding joints. The area of physical understanding is the influence of the tool pin geometry and material on the temperature field, microstructural refinement, resulting material flow, and the influence of flow variations on the subsequent mechanical properties of FSW butt lap joints in aluminum 3003 Alloy. The results obtained allowed us to propose a mathematical model to study the interactions between different factors. Thus, it was shown that the most influential parameters are respectively the rotation speed and weld speed. The study also presents the influence of different parameters welding on the structure of lap joints. The hardness in the welded region is significantly lower with respect to the base material. The fracture shows the characteristics of ductile-brittle mixed fracture.

Keywords: Friction stir welding, Lap joint, Aluminum 3003, Temperature, Tensile shear test, Predicting

Introduction

Friction stir welding (FSW) is a relatively new welding process that may have significant advantages compared to the fusion processes as follow: joining of conventionally non-fusion weldable alloys, reduced distortion and improved mechanical properties of weldable alloys joints due to the pure solid-state joining of metals (Chen et al., 2003). In this process, the heat is originally derived from the friction between the welding tool (including the shoulder and the probe) and the welded material, which causes the welded material to soften at a temperature less than its melting point (Threadgill et al., 2009; Mishra et al., 2005; Xue et al., 2011; Barekatain et al., 2014; Wiedenhoft et al., 2018; Naik et al., 2013). FSW can also assemble different joint configurations, such as lap, butt, and T-joints, of which the lap joints are widely applied in vehicle and aircraft design and manufacturing. Of importance for friction stir lap welding (FSLW), how- ever, is the greater diligence necessary in developing and optimizing tool designs and process parameters to break the surface oxide layer on two planar surfaces and mitigate the three main defects, i.e., kissing bonds, hooking, and top workpiece thinning (Naik et al., 2013).

Aydin et al., (2017), studied the effect of welding parameters (rotation speed and welding speed) on the mechanical properties of 3003-H12 aluminum alloy joints produced by friction stir welding where the weld

strength increased with increasing the welding speed or decreasing the rotation speed. To produce the best weld quality these parameters have to be determined for each component and alloy.

The effectiveness of these parameters on the properties of friction stir welds as well as the realization of their influence on the properties of the weld are the subject of studies carried out by several researchers (Aydin, 2010; Balasubramanian, 2014; Elangovan & Balasubramanian, 2007; Buffa et al., 2006). A great number of studies have been focused on the determine the microstructural and mechanical properties of the joints of heat treatable 3XXX aluminum alloys (Birol & Kasman, 2013a; Birol & Kasman, 2013b; Tutar et al., 2014). This last is the alloy which has been widely used purpose alloys for moderate-strength applications requiring good workability, such as stampings, spun and drawn parts and products, chemical equipment, storage tanks, fan blades, walk ways, flooring, and truck and trailer components (Tutar et al., 2014).

The object of this paper is to develop and high mechanical properties for AA3003 during friction stirs lap welding. The Design of Experiments technique was applied for the modeling and prediction of the behavior of the friction stir-welded joint. Response surface method (RSM) has been used to develop the model. In addition, this optimization allows the development of experimental results and may help to better understand the complexity of the phenomena resulting from contact parts/tool during the stirring process.

Materials and Method

The materials used were AA 3003 alloys of 2 mm thickness. Samples were cut according to the shape shown in the figure 1. The external sheets were welded parallel to the rolling direction while the central sheet was put in the long transverse direction for FSW process in order to limit potential effect of rolling texture. The chemical composition of the aluminum 3003 sheet is presented in Table1 and the mechanical properties of the sheets are presented in Table 2.

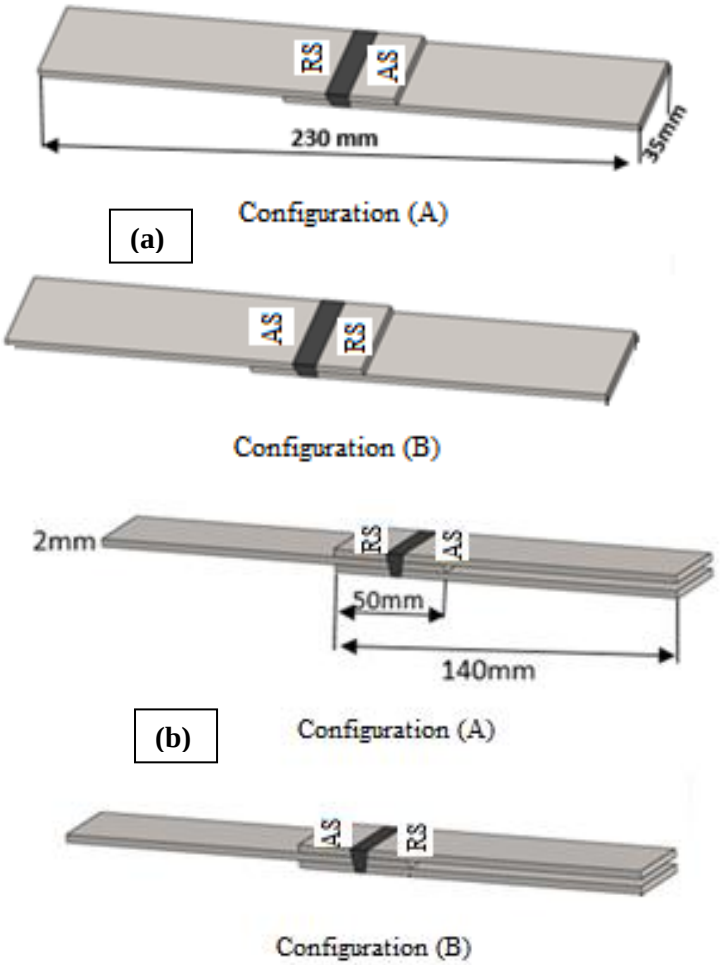

Figure1. Lap shear specimens, a) single lap, b) double lap

Table 1. Chemical composition of 3003 aluminum alloy

Element	Al	Mn	Si	Fe	Cu	Ti	Zn
%	96.7	1.3	0.9	0.9	0.13	0.1	0.3

Table 2. Mechanical properties of 3003 aluminum alloy

Rs (MPa)	UTS (MPa)	A (%)	Micro hardness (HV)	Ys (MPa)	Ym (GPa)
127	160	5.6	51	110	60

Two welding tools used for the single and double overlap joint is made of steel type 42CrMo4 (figure 2), it has the mechanical properties (Rm = 750/1300 MPa, A= 10-14 %, Re = 500/900 MPa and E = 210000 MPa). FSLW was conducted at selected rotation speeds of 1000, 1400 and 2000 rpm and selected travel speeds of 160, 200 and 250 mm/min.

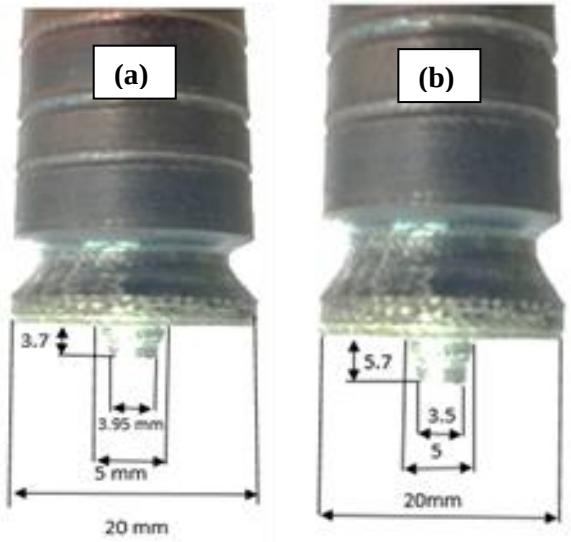

Figure 2. Geometry of the tools used, (a) single lap, (b) double lap.

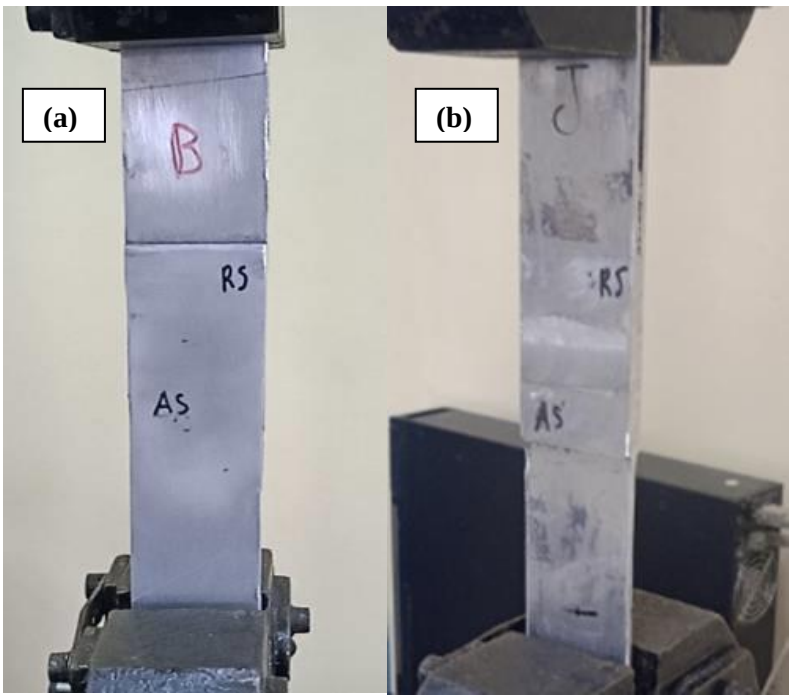

Figure 3. Overlap shear fracture testing configurations, a) single lap, b) double lap.

In this study, we conducted experiments on both formalities configuration (A) and (B) in both type's single lap and double lap on an INSTRON tensile machine at a transverse speed of 2 mm / min. The test continued until rupture will allow us to measure the ultimate elongation as shown in figure 3. The hardness on the weld cross-section was measured point wise at speeds (1400 rpm and 200 mm/min) in both forms single and double lap by shimadzu HMV-2000 micro durometer with a load 1000g and a dwell time of 10 s.

Response Surface Methodology

Analysis of variance (ANOVA) test was performed to identify the process parameters that are statistically significant. The purpose of the ANOVA test is to investigate the significance of the process parameters, which affect the temperature of FSLW joints. In addition, the rotational speeds used have a significant effect on temperature.

In order to predict the temperature during the welding operation , the response surface methodology (RSM) is used to develop the non-linear model of the FSW joints of aluminum alloys AA 3003.The response control factors for the analysis were rotation speed and welding speed. These factors and parameters were used to build up the mathematical model that could be used for prediction of the optimum factor.

Developing a Mathematical Model

Response surface methodology is a collection of mathematical and statistical techniques useful for analyzing problems in which several independent variables influence a dependent variable or response and the goal is to optimize the response. For these experimental conditions, the model used has form given below:

$$Y = \emptyset\,(x_1, x_2, \ldots\ldots\ldots\ldots\ldots, x_k) \pm e_r \qquad (1)$$

The design of experiments approach was applied to 12 tests, two replicates are considered for each combination of the input variables, which made it possible to define the coefficients summarized in Table 3.

Table 3. Results of the design of experiments

Test	Rotation speed (tr/min)	Welding speed (mm/min)	T1 Conf (A) (single lap) (°C)	T2 Conf (B) (single lap) (°C)	T1 Conf (A) (double lap) (°C)	T2 Conf (B) (doublelap) (°C)
1	1000	160	230	276	221	206
2	1400	160	225	283	241	249
3	2000	160	270	313	229	351
4	1000	200	191	295	217	198
5	1400	200	239	329	278	212
6	2000	200	274	331	283	366
7	1000	250	229	267	184	174
8	1400	250	225	327	216	184
9	2000	250	268	320	259	222
10	1400	200	239	329	278	212
11	1400	200	239	329	278	212
12	1400	200	239	329	278	212

The temperature of FSLW is a function of the welding parameters such as tool rotational speed (N) and welding speed (Sw) it can be expressed as,

Temperature = f (N, Sw).

The polynomials help optimize the temperature parameters in order to reach the desired responses. To calculate the coefficients of the models, a regression method based on the least squares criterion is used. The mathematical models suggested by MODDE 5.0 are:

$$(T_1) = 238 + 18{,}75 * rot - 0.499978 * wel + 21.25 * rot^2 - 11 * wel^2 - 0.25001 * rot * wel \quad (2)$$

$$(T_2) = 328.13 + 15{,}5798 * rot + 5.19328 * wel - 7.69192 * rot^2 - 11.3592 * wel^2 + 2.19171 * rot * wel \quad (3)$$

$$(T_3) = 273.209 + 21{,}1205 * rot - 6.49861 * wel - 8.45218 * rot^2 - 18.5031 * wel^2 + 6.50707 * rot * wel \quad (4)$$

$$(T_4) = 220.042 + 60{,}1667 * rot - 37.6667 * wel + 45.875 * rot^2 - 19.625 * wel^2 - 24.25 * rot * wel \quad (5)$$

Results and Discussion

The result of RSM design of experiment is displayed in Table 4. The residuals in figure 4 are falls on a straight line, which depicts that the errors are normally distributed (Kadaganchi et al, 2014), which reveals that there is very good correlation between the experimental value and predicted value of the responses.

Table 4. Design matrix with responses (Temperature)

Test	Rotation speed (tr/min)	Welding speed (mm/min)	T1 Conf (A) (single lap) (°C)	T2 Conf (B) (single lap) (°C)	T1 Conf (A) (double lap) (°C)	T2 Conf (B) (doublelap) (°C)
1	-1	-1	230	276	221	206
2	0	-1	225	283	241	249
3	1	-1	270	313	229	351
4	-1	0	191	295	217	198
5	0	0	239	329	278	212
6	1	0	274	331	283	366
7	-1	1	229	267	184	174
8	0	1	225	327	216	184
9	1	1	268	320	259	222
10	0	0	239	329	278	212
11	0	0	239	329	278	212
12	0	0	239	329	278	212

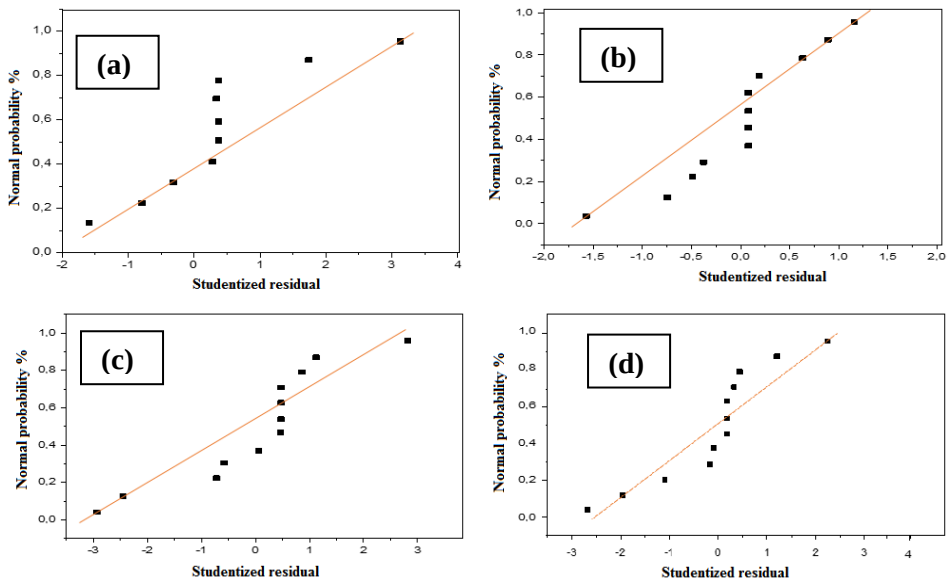

Figure 4. Normal probability plot of regression, a) configuration A (lap joint), b) configuration B (lap joint), c) configuration A (Double lap joint), d) configuration B (Double lap joint)

All the above considerations indicate an excellent adequacy of the regression models. Figure 5 shows the effect of the rotational speed and welding speed on the temperature. Experimental treatments that were conducted at different tool rotational speeds: 1000 rpm and 2000 rpm were chosen to study the effect of variation in tool rotational speed on the transient temperature distribution within the welding zone. It is noted that the

temperature decreases gradually with the increasing welding speed and this is attributed by the high rotational speed results in the metallurgical transformation (figures. 5.b, 5.d, 5.f and 5.h).

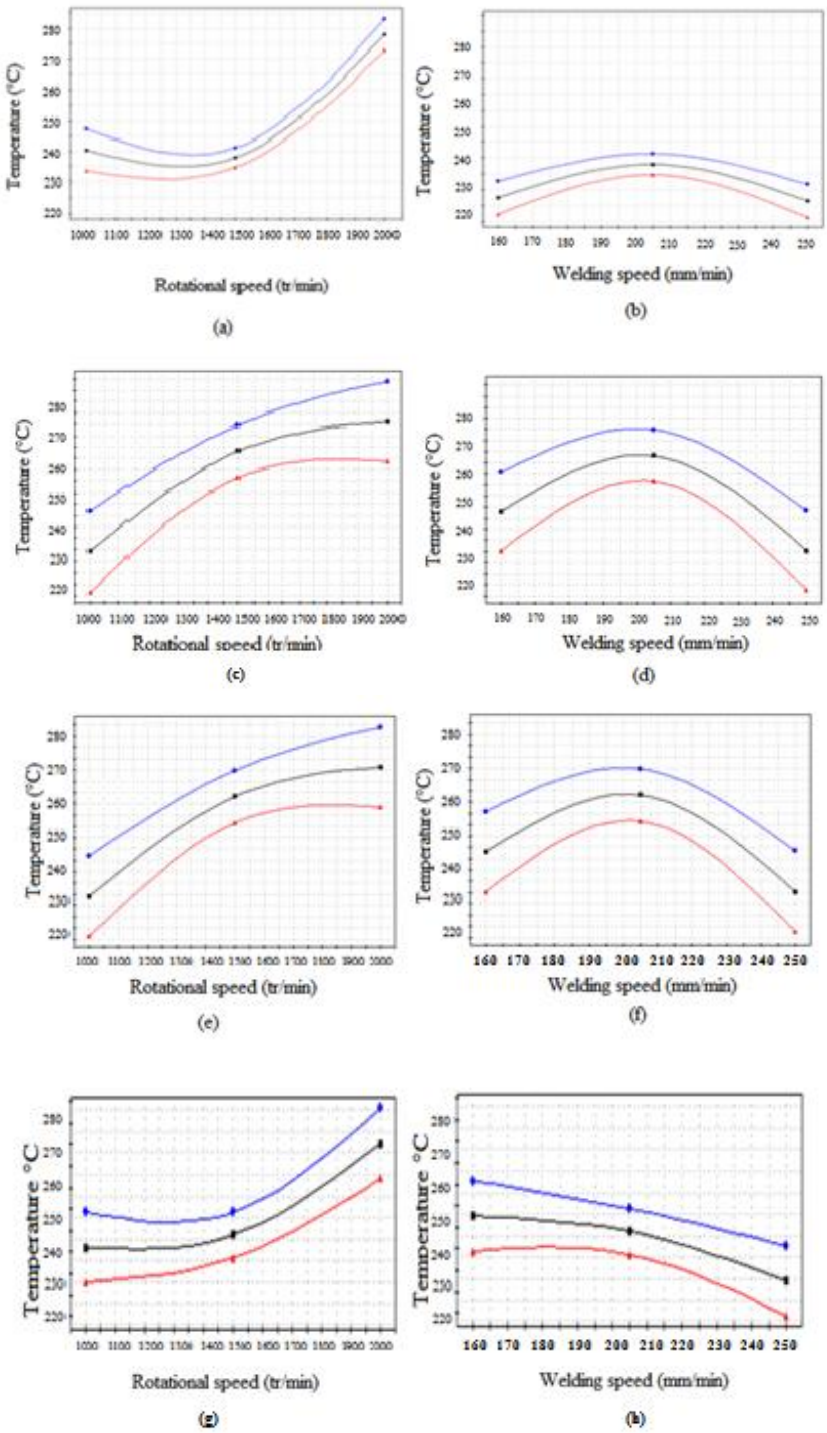

Figure 5. Analysis of thermal profile measured at the welding, a) and b) configuration A (lap joint), c) and d) configuration B (lap joint), e) and f) configuration A (Double lap joint), g) and h) configuration B (Double lap joint)

In figure (5a) maximum temperature of the experimental test that it was detected for a rotational speed of 2000 rpm was approximately 366 °C for the sample with tool speed of 200 mm/min and the minimal is detected with 1000 rpm at 184 °C. The temperature profiles have a uniform plot during the welding process which is trending symmetrically toward the peak of thermal cycles, and dropping axisymmetrically after passing through the maximum temperature.

In this analysis step, it was decided to broaden the scope of our study by taking into account the interaction between two factors. This allows viewing the output parameters on a three dimensional (3D) graph (figure 6); this graph depicts the variation of the temperature as a function of the two factors (Rotation speed and welding speed). In figure 7, it is observed that the value of the temperature was 337, 1°C at the rotational speed was 1900 rpm and the welding speed was 210 mm\min (figure 7.b), whereas the value of the temperature decreases to (272.9 °C) at the rotational speed was (2000 rpm) and the welding speed was 210 mm\min (figure.7.a). It is also observed that for the double lap joint the highest value of the temperature was 360 ° C at a rotation speed of 2000 rpm (figure.7.c) and a welding speed of 160 mm / min and decreases at 270 ° C for a rotation of 1600 rpm and a welding speed of 220 mm \ min (figure.7.d).

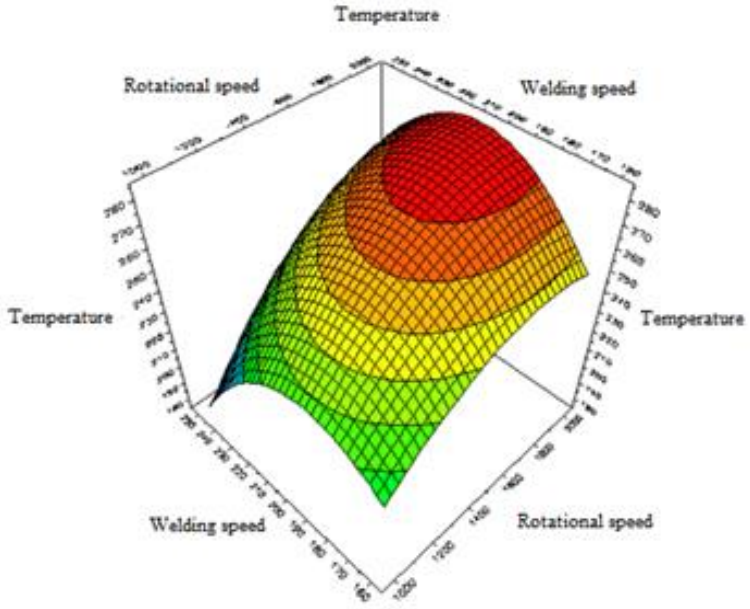

Figure 6. Three-dimensional (3D) variation of temperature as a function of rotation speed and welding speed

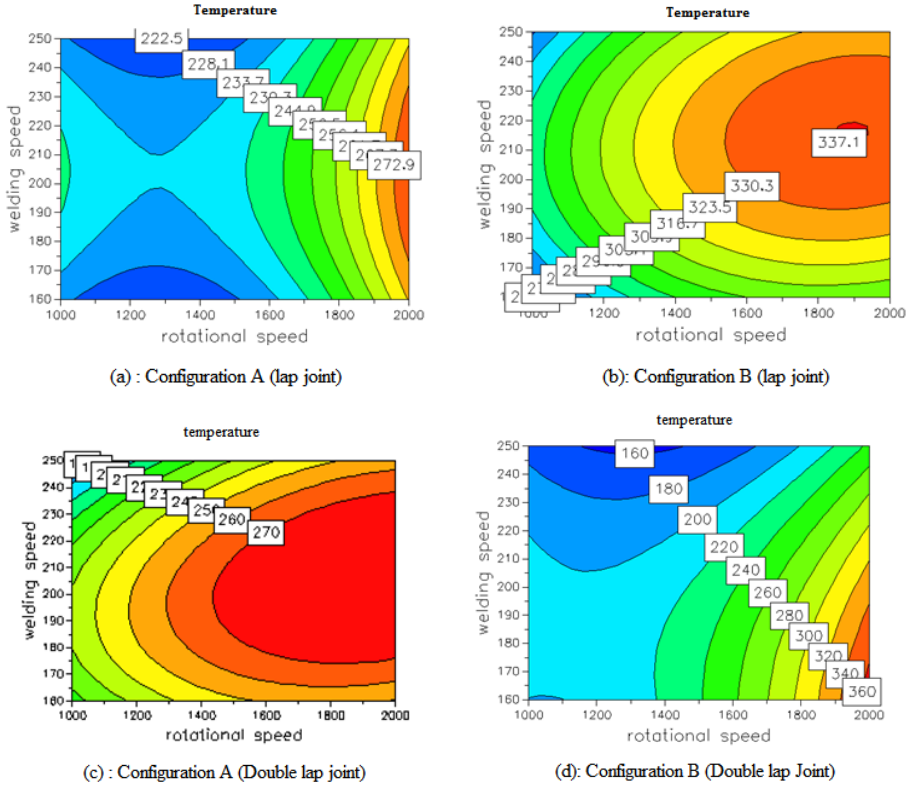

Figure 7. Variation of temperature as a function of the two factors

Figure 8 shows the most influential parameters on temperature. The effects of the factors are shown using a bar graph. This diagram gives the effects in decreasing order of their importance in absolute value. This figure clearly shows the sensitivity of the rotational speed and the welding speed respectively to temperature. A small change in rotational speed causes large temperature changes as the welding speed increases. The results obtained by this study show that the temperature is more sensitive to the speed of rotation than to the speed of welding. After a thorough analysis, these figures show that the classification of the dominant factors on the maximum temperature is as follows: (rot) and (rot * rot). (figure.7a). On the other hand, for (figure.8b), the order of dominant factors are as following: (rot) and (wel*wel).

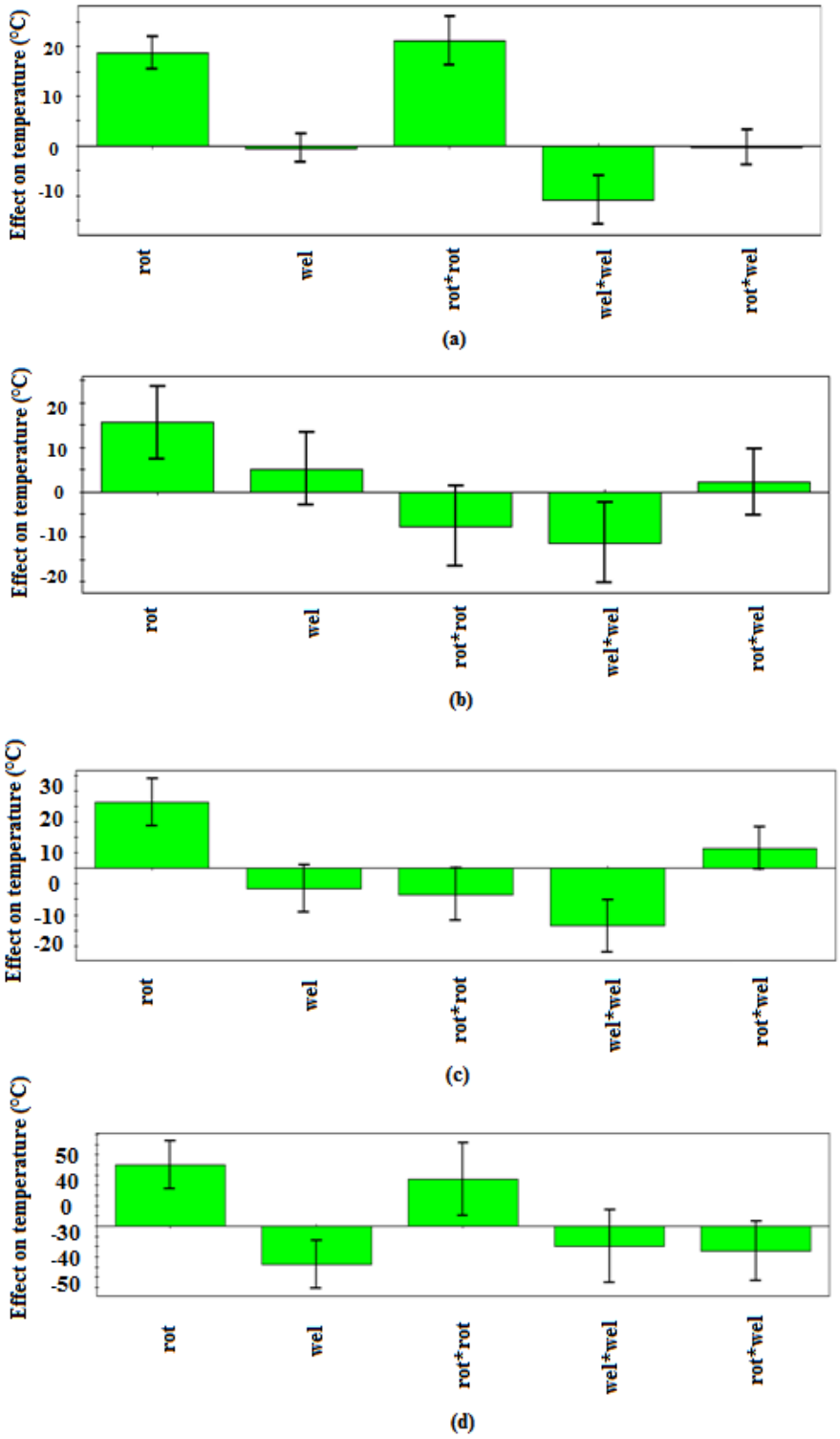

Figure 8. Effects of factors on temperature and their interaction, a) configuration A (lap joint), b) configuration B (lap joint), c) configuration A (Double lap joint), d) configuration B (Double lap joint

Sensitivity analysis, a method to identify critical parameters and rank them by their order of importance, is paramount in model validation where attempts are made to compare the calculated output with the measured data (Rajakumar et al, 2009).

Microhardness Measurements

The figure 9 shows the evolution of the hardness by defeating the speed of advance (160,200,250) mm/min and even the speed of rotation (1400 rpm), in both forms (single lap and double lap) on a SHIMADZU HMV-2000. In the hardness measurement, we used a load 1000g for 10 seconds per point and distance between the two points was 2mm along 28mm in hardness Vickers (HV).

The value of the stiffness in areas HAZ, TMAZ and NZ decreases from the value in BM due to the decrease in the displacement density resulting from FSW. We notice from the figure 9 that the value of the hardness decreases from the area HAZ in a direction TMAZ in various measurements until it reaches a minimum value and then rises in a direction NZ and this is due to the recrystallization of the grains because of the welding process (Abdulrehman et al, 2020). We also note a slight decrease in hardness value in the area NZ with an increase in welding speed (Merzoug et al, 2018). The hardness in the welded region is significantly lower with respect to the base material (50 µHV for single lap, 48 µHV for double lap). The high temperature achieved during the FSW process can be considered as the major cause of this softening effect. Even just a few microhardness values are reported for reasons of synthesis, it is possible to assert that the width of the softened region and the microhardness values recorded in the same region are influenced by the welding process parameters (D'Urso et al,, 2017).

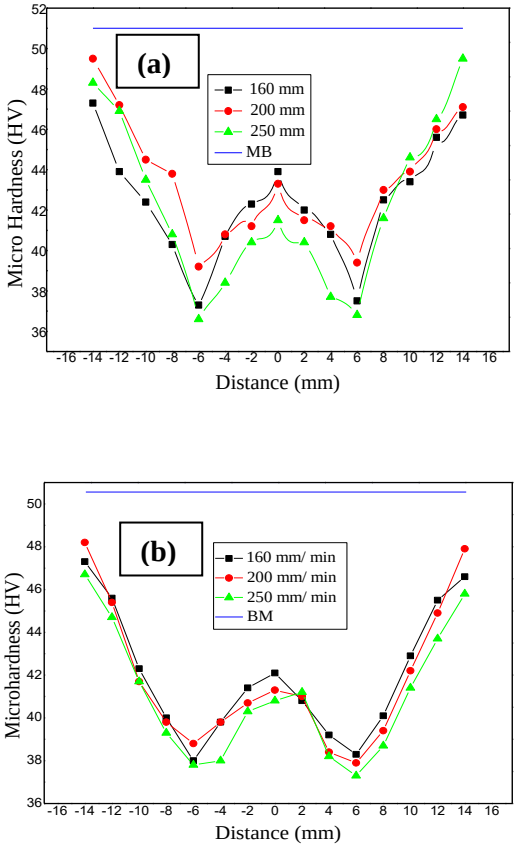

Figure 9. Hardness distribution profiles, a) Single lap, b) Double lap

Tensile Strength Test

We measured the tensile properties on the single and double lap in both configuration (A and B) are presented in figure 10 and figure 11, using constant tool rotation speeds of 1000 rpm (figure a), 1400 rpm (figure b), 2000

rpm (figure c), and tool displacement speeds of 160, 200 and 250 mm/min. To analyze the evolution of the mechanical with the welding parameters, averaged over several trials is calculated.

The results were presented according to the same parameter's to highlight the differences mechanical resistance of the two configurations (A and B). Figure 10 shows some representative curves, this figure shows that the load is maximum when the welding speed is equal to 160 mm/min (configuration B) Where the advancing side (AS) of the joint bore the main load, they reach a low value for a welding speed equal to 250 mm/min and rotation 1400 rpm (figure 10-b).

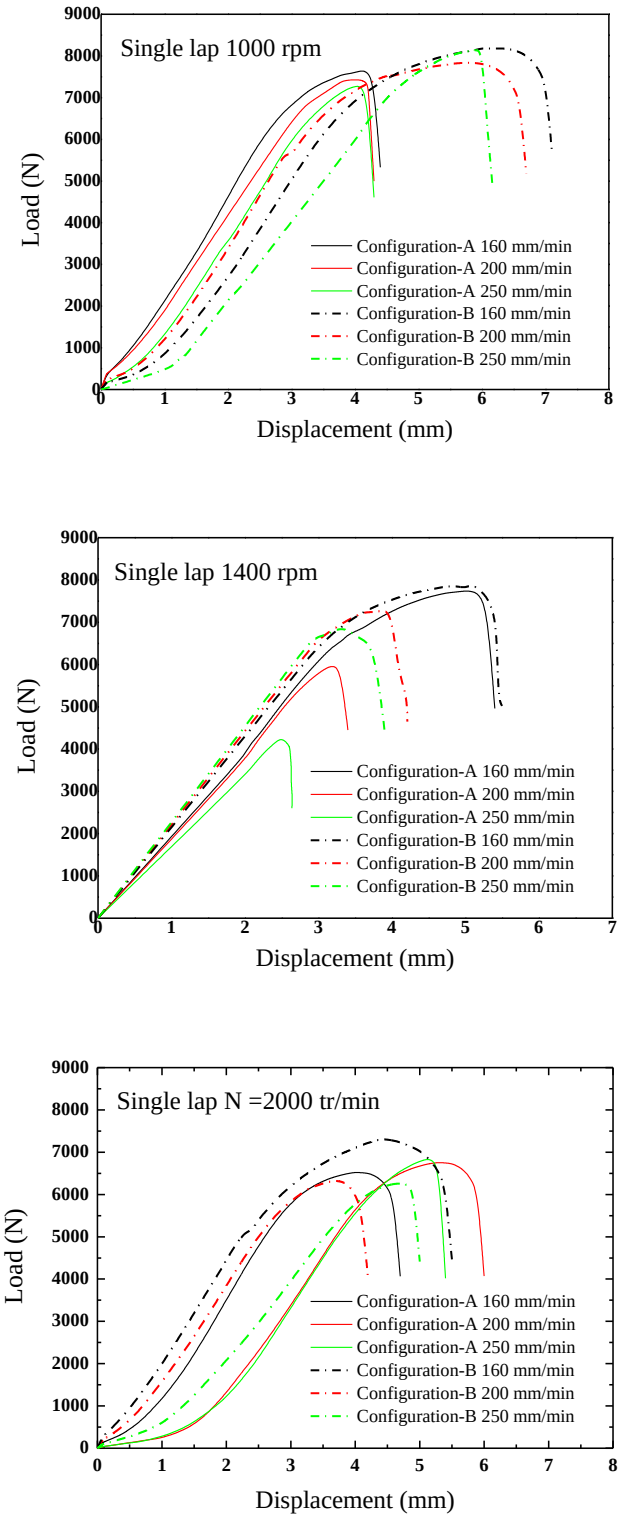

Figure 10. Load curve – displacement (single lap)

The load-displacement curve showed that the joint made at 1000 rpm possessed bigger displacement. Overall, for the configuration (B) the joint tensile shear performance was excellent. The same combination of parameters is shown in figure 11 for the double lap joint. It clearly indicates that with increasing travel speed for a constant rpm, failure load decreases for both the three cases (figures 11a, 11b and 11c). It is interesting to note that failure load of the joint can reach as high as 9000N. Through the plots the two figures, it can be seen that the double lap welds are having better tensile properties single lap welds.

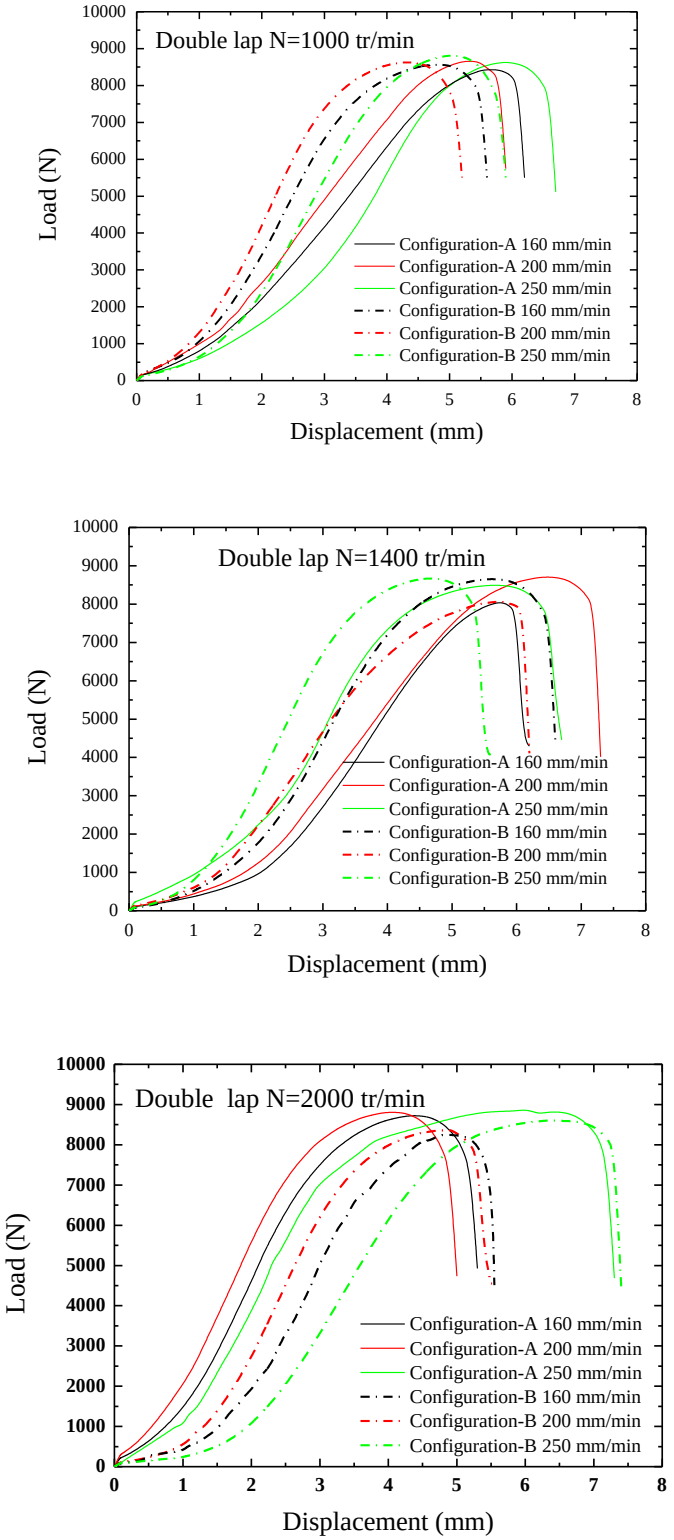

Figure 11. Load curve – displacement (double lap)

(a)

(b)

Figure 12. Specimens after tension test, a) single lap, b) double lap

Figure 12 groups the specimens after the tension test. It can be observed that final fracture is perpendicular to the loading direction in the center of the welded joint. On the test fractures of sheared samples one can see that for the lower linear welding speed a destruction (cracking) occurs along the plane passing through the weld and result in disruption of the joined elements. The fracture surfaces broken in this way, two characteristic zones can be seen in the weld area, i.e. a bright zone, which occurs on the advancing side of weld, and the darker area,

which is visible in the retreating side of weld. The presence of such an area on the retreating side of joint is due to insufficient dispersion of oxides from the surfaces, which are only rubbed into weld area and form strongly adherent layer, thus reduces the mechanical properties of the joint (Krasnowski, 2014).

Conclusion

The present work was designed to identify the most influential and optimal friction stir welding process parameters on joint strength during FSLW welding of aluminium alloy AA3003. This study focuses on the influence of three factors (speed, feed rate, welding time). In particular the changes in microstructure, micro-hardness, and tensile properties of were investigated. It was found that the welding process treatment induces higher microhardness values and lower longitudinal residual stress in the weld zone surface. The flow material is facilitated around the tool pin while the surface hardness is improved at the same time.
The important conclusions are derived from this study are:

• For aluminium 3003 alloy welds, fracture strength was found to be very sensitive to pin positioning during FSLW.
• A maximum failure load of 9000 N was exhibited by the FSLW joints (double lap) fabricated with the optimized parameters of 1000 tr/min rotational speed, 250 mm/min welding speed. Also, this value (fractured at SZ) for the pin penetrated welds is itself higher than the maximum value (fractured at the SZ or interface) reported in literature when pin penetrating condition used.
• Beyond the HAZ, it can be seen that the stresses gradually tend towards zero when passing through the HAZ zone.

Scientific Ethics Declaration

The authors declare that the scientific ethical and legal responsibility of this article published in EPSTEM journal belongs to the authors.

Acknowledgements

* This article was presented as an oral presentation at the International Conference on Technology, Engineering and Science (www.icontes.net) held in Antalya/Turkey on November 16-19, 2022.

References

Abdulrehman, M. A., Challoob, S. H., & Marhoon, I. I. (2020). Investigation of mechanical and numerical properties of friction stir welding (FSW) for 3003-H14 aluminum alloys, In *Defect and diffusion forum. Trans. Tech. Publications Ltd*, *398*, 106-116.

Aydin, H., Tutar, M., Yigit, K., & Bayram, A. (2017). Mechanical properties of friction stir welded 3003 aluminum alloy in different welding conditions. *International Journal of Mechanical and Production Engineering*, *5*, 92-96.

Aydin, H. (2010). Quality and properties of the friction stir welded AA2024-T4 aluminum alloy at different welding conditions. *Materials Testing-Materials and Components Technology*, *52*, 640-650.

Balasubramanian, V. (2014). Relationship between base metal properties and friction stir welding process parameters, *Materials Science and Engineering*. *A.*, *480* (1–2), 293–299.

Barekatain, H., Kazeminezhad, M., & Kokabi, A. H. (2014). Microstructure and mechanical properties in dissimilar butt friction stir welding of severely plastic deformed aluminum AA 1050 and commercially pure copper sheets. *Journal of Materials Science and Technology*, *30*, 826–834.

Birol, Y., & Kasman, S. (2013a). Effect of welding parameters on the microstructure and strength of friction stir weld joints in twin roll cast en AW Al-Mn1Cu plates. *Journal of Materials Engineering and Performance*, *22*(10), 3024-3033.

Birol, Y., & Kasman, S. (2013b). Friction stir welding of twin-roll cast en AW 3003 plates. *Metals and Materials International*, *19*(6), 1259–1266.

Buffa, G., Fratini, L., & Palmeri, D. (2006). On microstructural phenomena occurring in friction stir welding of aluminium alloys. *Journal of Materials Processing Technology*, *177* (1–3), 340–343.

Chen, C. M., & Kovacevic, R. (2003). Finite element modeling of friction stir welding—thermal and thermomechanical analysis. *International Journal of Machine Tools and Manufacture*, *43*(13), 1319-1326.

D'Urso, G.A., Giardini, C.A., Lorenzi, S.B., Cabrini, M.B., & Pastore, T.B. (2017). The Effects of process parameters on mechanical properties and corrosion behavior in friction stir welding of aluminum alloys. *17th International Conference on Sheet Metal, 2017, SHEMET17, Procedia Engineering*, *183*, 270 –276.

Elangovan, K., & Balasubramanian, V. (2007). Influences of pin profile and rotational speed of the tool on the formation of friction stir processing zone in AA2219 aluminium alloy. *Materials Science and Engineering A*., *459* (1–2), 7–18.

Kadaganchi, R., Gankidi, M. R., & Gokhale, H. (2014). Optimization of process parameters of aluminum alloyAA 2014-T6 friction stir welds by response surface methodology. *Defence Technology*, *11*, 209-219.

Krasnowski, K. (2014). Fatigue and static properties of friction stir welded aluminium alloy 6082 lap joints using triflute-type and smooth. *Archives of Metallurgy and Materials, 59*(1), 157-162. doi:10.2478/amm-2014-0025.

Merzoug, M.; Boulenouar, A.; Bouchouicha, B.; Serrier, M.; & Mazari, M.. (2018). Effects of welding parameters on fssw: experimental and numerical study, *Archives of Metallurgy and Materials*, *63*(1), 247-256. doi: 10.24425/118935.

Mishra, R. S., & Ma, Z. Y. (2005). Friction stir welding and processing. *Materials Science and Engineering*, *50* (2), 1-78.

Naik, B. S., Chen, D. L., Cao, X., & Wanjara, P. (2013). Microstructure and fatigue properties of a friction stir lap welded magnesium alloy. *Metallurgical and Materials Transactions A*, *44*(8), 3732-3746. doi: 10.1007/s11661-013-1728-5.

Rajakumar, S., Muralidharan, C., & Balasubramanian, V. (2010). Optimization of the friction-stir-welding process and tool parameters to attain a maximum tensile strength of AA7075–T6 aluminium alloy. *Proceedings of the Institution of Mechanical Engineers, Part B: Journal of Engineering Manufacture*, *224*(8), 1175-1191. doi:10.1243/ 0954405054JEM1802.2009.

Threadgill, P. L., Leonard, A. J., Shercliff, H. R., & Withers, P. J. (2009). Friction stir welding of aluminium alloys. *International. Materials. Reviews*, *54* (2), 49-93.

Tutar, M., Aydin, H., Yuce, C.,Yavuz, N., & Bayram, A. (2014). The optimisation of process parameters for friction stir spot- welded AA3003-H12 aluminium alloy using a Taguchi orthogonal array. *Material and Design*. *63*, 789-797.

Wiedenhoft, A. G., Amorim, H. J. D., Rosendo, T. D. S., Tier, M. A. D., & Reguly, A. (2018). Effect of heat input on the mechanical behaviour of Al-Cu FSW lap joints. *Materials Research*, *21*(4): e20170983

Xue, P., Ni, D. R., Wang, D., Xiao, B. L., & Ma, Z.Y. (2011). Effect of friction stir welding parameters on the microstructure and mechanical properties of the dissimilar Al–Cu joints. *Materials Science and Engineering A.*,*528*, 4683-4689.

Author Information

Mohamed MERZOUG
Materials and Reactive Systems Laboratory,
Mechanical Engineering Department,
Djillali Liabes University of Sidi-Bel-Abbes (22000),
BP. 89, City Larbi Ben Mhidi, Algeria
Email: m_merzoug01@yahoo.fr

Abdelatif MIMMI
Materials and Reactive Systems Laboratory,
Mechanical Engineering Department,
Djillali Liabes University of Sidi-Bel-Abbes (22000),
BP. 89, City Larbi Ben Mhidi, Algeria

Abdelkader GHAZI
Materials and Reactive Systems Laboratory,
Mechanical Engineering Department,
Mustapha Stambouli University of Mascara (29000),
Algeria.

To cite this article:

Merzoug, M., Mimmi, A., & Ghazi. A. (2022). Study of the correlation between the process parameters and the mechanical characteristics of the aluminum sheets welded by the FSW process. *The Eurasia Proceedings of Science, Technology, Engineering & Mathematics (EPSTEM), 21*, 335-348.

The Eurasia Proceedings of Science, Technology, Engineering & Mathematics (EPSTEM)
ISSN: 2602-3199

The Eurasia Proceedings of Science, Technology, Engineering & Mathematics (EPSTEM), 2022

Volume 21, Pages 349-355

IConTES 2022: International Conference on Technology, Engineering and Science

Hydrological Safety of Vaturu Dam by Evaluating Spillway Adequacy

Munira MOHAMMAD
SEGi University

Patrick Jione PAGKALE
SEGi University

Nor Faiza ABD RAHMAN
SEGi University

Mohamad Shakri MOHMAD SHARIFF
Inti International University

Abstract: Probable Maximum Flood is considered as one of the most adopted inflow design floods in assessing the adequacy of dam structure in current practices. It is the largest flood that could conceivably occur at a particular location and frequently estimated from Probable Maximum Precipitation (PMP). This study incorporates hydrological modelling using HEC-HMS to simulate the outflow providing the results used in the catchment procedure of translation of PMP to PMFs for a 24 to 168-hour duration. The adequacy of Vaturu Water Supply Dams (CA= 40 km2) which is located in Fiji will be assessed in the context of extreme meteorological events of the PMP/PMF magnitude. The flood rise during these events should not exceed or overtop the dam crest level. Vaturu dam is a domestic water supply embankment dam built in the 1980s to cater for the water supply needs of the Nadi and Lautoka supply zones. A conventional reservoir routing procedure using the Goodrich method is then carried out for all PMP/PMF durations, i.e., 24 to 168 hours. During this period, flood rise levels were noted to be restricted to the Dam Crest level of +532 m ASL. The results and its analysis validated the safety of the Vaturu Dam and the ability of the dam to discharge the onslaught of PMP/PMF safely.

Keywords: Rainfall-runoff, HEC-HMS, Vaturu Dam, PMP/PMF routing

Introduction

Failures of dam structures due overtopping raise the importance of undertaking an accurate assessment of the dams' safety features in terms of their emergency action and implementation plan in the event of probable catastrophic events (Sidek et. al., 2013; Tingsanchali et al., 2012). One of these measures is the hydrological inspection and evaluation that plays a part in the overall inspection program in terms of assessing the overtopping probability of the dam/reservoir considering an extreme meteorological event, i.e., during a probable maximum precipitation (PMP) scenario. The PMP as defined by the World Meteorological Organization is “the greatest depth precipitation for a given duration meteorologically possible for a given size storm area at a particular location at a particular time of year” (WMO, 2009). The PMF derived from PMP is the largest flood that could conceivably occur at a particular location (Graham, 2009). The PMF values are useful in dam design by reviewing the adequacy of the current spillway capacities of the existing dams (Hwee, 2013).

Over the past decade, Vaturu dam have been operating and discharge the floodwater over its spillway. However, its spillway had never been evaluated in terms of its ability to discharge extreme storm events safely. Where it is

- Selection and peer-review under responsibility of the Organizing Committee of the Conference

crucial to highlight essential outcomes such as the dams' water level and the discharge over the spillway during critical storm events, which will be compared against the safe dam operating level (Dam crest level) and the design discharge capacity of the spillway (Nathan, 2001). Thus, the objective of this paper is to simulate the rainfall-runoff relationship of Vaturu dam for the period from January 2007 to December 2019 by HEC-HMS software and to evaluate the spillway capacity adequacy of Vaturu Dam using Probable Maximum Precipitation (PMP) and Probable Maximum Flood (PMF) using the Goodrich method.

Study Area

The Fiji Islands are an archipelago of volcanic islands comprising of 2 major islands, namely Viti Levu and Vanua Levu, and 300 islands spread over 1.3 million square kilometers in the Pacific Ocean. The two large mountainous islands of Viti Levu (10,400km2) and Vanua Levu (5,540km2) comprise 87% of the total land area. On the world map, as shown in Figure 1, Fiji is located in the Southern Hemisphere at latitude 15-22 degrees south and 177 degrees west to 175 degrees east. Surrounded by the South Pacific Ocean, the Fiji group lies 5,100 km southwest of Hawaii and 3150 km northeast of Sydney, Australia, and has the 180th-degree meridian line over it.

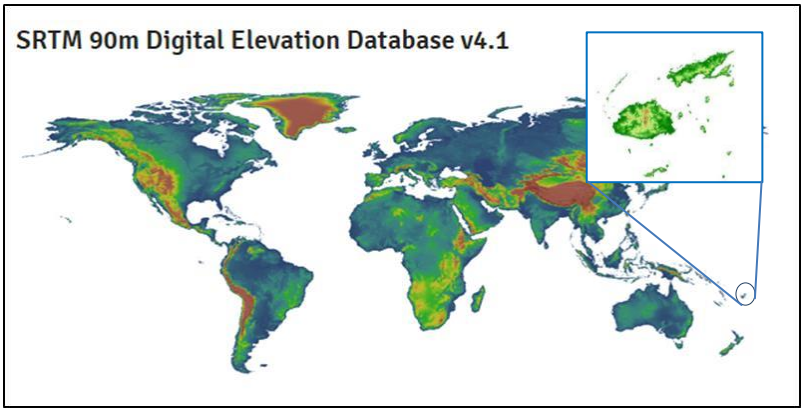

Figure 1. Location of Fiji islands

Vaturu dam is located on the western part of Viti Levu at 16^{o} 35' 23" S Latitude and 179^{o} 24' 22" E Longitude, 30 km upstream of Nadi town and is at an elevation of 528m above sea level (ASL). It is the primary water supply source for residents of the Nadi and Lautoka regional water supply systems, meeting the demand of 180,000 residents. The main inflow into Vaturu Dam are Nadi River and Viti River. It has a storage capacity of 70MCM and is the main water supply for Nadi Irrigation Scheme. The main characteristic of the dam is as shown in Table 1 and Figure 2 presents the Level, Area ,Volume Curve for Vaturu Dam (2020).

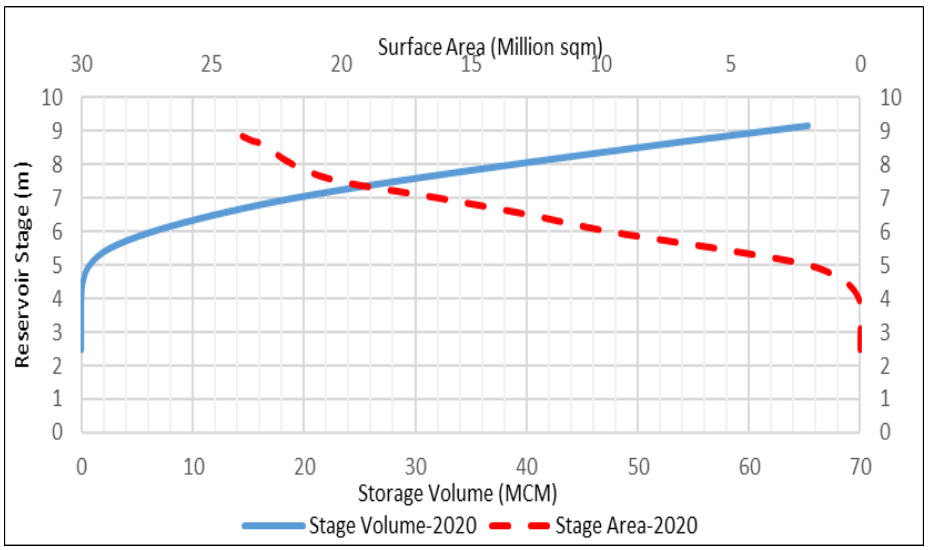

Figure 2. Level, area, volume curve for Vaturu Dam (2020)

Table 1. Properties and description of Vaturu Dam

Properties	Description
Dam Type	Clay core with earth and rockfill shoulders with spillway excavated through saddle.
Dam Crest Level	RL 532 m
Full Supply Level	RL 527 m
Minimum Operating Level	RL 502 m
Maximum Flood Level	RL 528.8 m
Critical Level	RL 510 m
Dam height	54 m
Maximum Depth	37 m
Crest width	10 m
Crest Length	297m
Surface Area	200 ha
Catchment Area	40 km^2

The rainfall data obtained for the Vaturu dam study was obtained from the Water Authority of Fiji, Water Resource Management Department (WRMD) from January 2007 to December 2019. The relationship between rainfall and the outflow of Vaturu Dam was analysed based on ten years of daily observation data. HEC HMS were used to simulate the outflow and the goodness of the outflow data was then tested using Nash Sutcliffe Coefficient, correlation, and the mean average error (Faiza et al., 2022; Güntner et al., 2004; Kaatz, 2014). The collected data was processed and screened accordingly. All missing and unreliable input data was replaced and corrected based on the neighbouring stations (Khalifeloo, 2015). The digital elevation maps of the watershed were obtained and downloaded from The Consortium for Spatial Information (CSI) for Constative Group for International Agricultural Research (CGIR) website, which provides the Shutter Radar Topography Mission (SRTM) data.

Methodology

The HEC-HMS model is a physically based and conceptually semi-distributed model designed to simulate rainfall-runoff processes such as precipitation, evapotranspiration, infiltration, interflow, overland flow, percolation, baseflow, recharge of aquifers, and streamflow. However, some of the processes were simplified. In this study, the catchment was divided into seven subbasins, as shown in Figure 3. The HEC-HMS model provide option for manual input of watershed characteristics data such as SCS curve number, lag time, and precipitation in the basin model category. The model is calibrated and validated for the extreme historical events used for calibration are considered in order to obtain the appropriate values for the parameters.

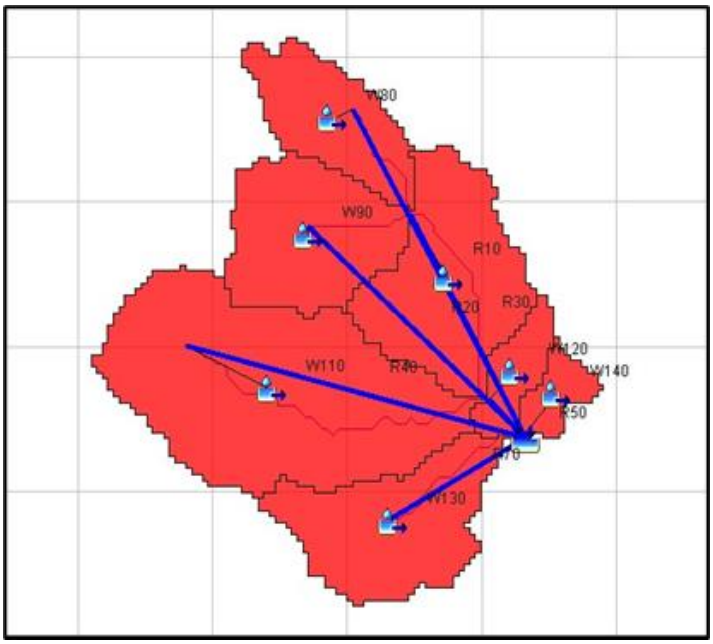

Figure 3. Vaturu Dam catchment – HEC HMS setup

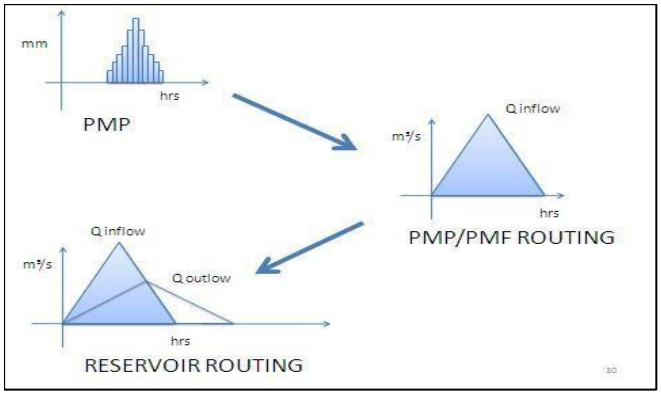

Figure 4. Reservoir routing flowchart

Figure 4 shows the reservoir routing chart where the primary function of reservoir routing is to determine the outflow of the PMP/PMF developed by Hershfield (1961,1965) as they pass through the particular location and reservoir. The freeboard or flood rise height is also estimated using the Reservoir level and change in Storage + Flow relationship.

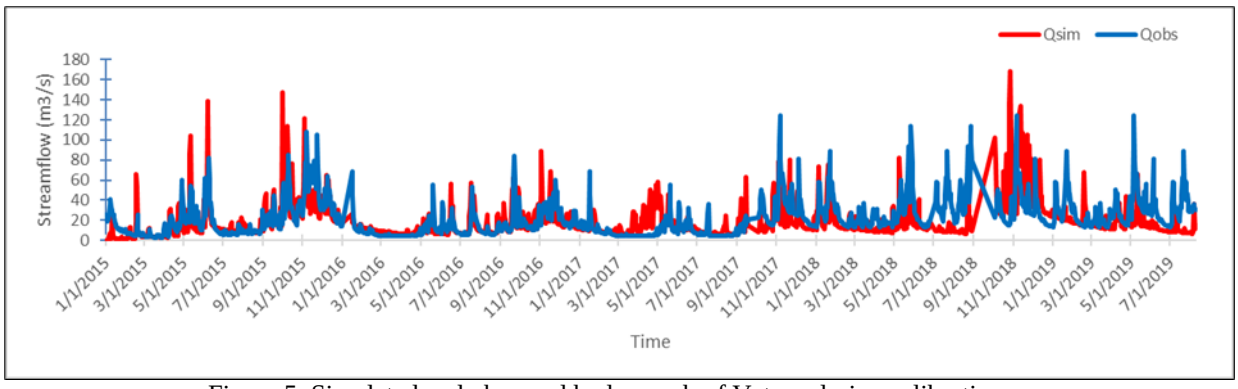

Figure 5. Simulated and observed hydrograph of Vaturu during calibration

As shown in Figure 5, the model shows a reasonable fit between the simulated and observed with Nash Sutcliff coefficient of 0.5 and correlation value of 0.57 confirm an agreeable linear relationship. Table 2 summarized the goodness of fit between the observed flow and the simulated flow for the Vaturu dam.

Table 2. Goodness of fit of the calibrated HEC-HMS

Objective Functions	Values
Nash Sutcliff Coefficient	0.51
Correlation	0.57
MAE	1.24
RMSE	1.54

Reservoir Routing (Goodrich Method)

The main function of reservoir routing is to determine the outflow of the PMP/PMF as they pass through any reservoir. The height of the freeboard or flood rise is also estimated using the reservoir level and change in storage and flow relationship. Rainfall-runoff data from 2007 to 2019 was assembled to study the weather pattern on a daily basis to study the significant trend. It can be noted that there are periods of high rainfall during the wet seasons, mainly November to April, while there were few days in the dry season where moderate precipitation occurred in the years 2011 and 2013. As observed in Figure 5, the most notable critical storm events were the floods that happened in 2013 and 2019, and this study aimed to evaluate the dam by overtopping during the 2016 floods caused by Cyclone Winston.

Figure 6 shows the PMP/PMF translation graph for the period January 2007 to December 2016, it is clear that maximum precipitation and flooding occurred from the 20th to the 25th of February 2015. The maximum

rainfall recorded on the 21st of February was 628mm. This event coincided with the arrival of a category five cyclone (Cyclone Winston) that made landfall in Fiji and claimed 44 lives. This storm event was analyzed for various durations, from 24 to 168 hours.

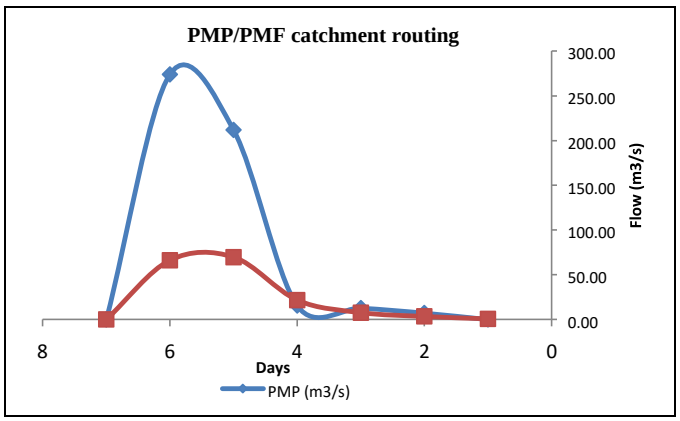

Figure 6. Flood hydrographs obtained from HEC-HMS models using the 16 h 100-year, PMP

Time (daily), precipitation discharge (m3/s), water surface elevation (m), flood discharge (m3/s), and the change in volume storage (m3) are calculated. These fields are necessary to calculate twice the difference in storage with respect to time added to the discharge at the outlet. The tabulated calculations by the formula 2S/t + Q are summarized in Table 3.

Table 3. Catchment routing using goodrich routing method

Time,t (hrs.)	Discharge,l (m^3/ sec)	Water Surface Elevation EL	Outflow Discharge, Q (m^3/ sec)	Storage,S x 10^6 (m^3)	2S/Δt + Q
0	0.00	521.15	0	19.78	916
24	274.12	528.18	66.2	19.84	985
48	211.84	528.06	69.7	25.74	1261
72	15.62	527.96	21.7	25.65	1209
96	12.81	527.86	7.7	25.42	1185
120	7.21	527.76	3.4	25.19	1170
168	0.00	527.66	0.7	24.97	1157

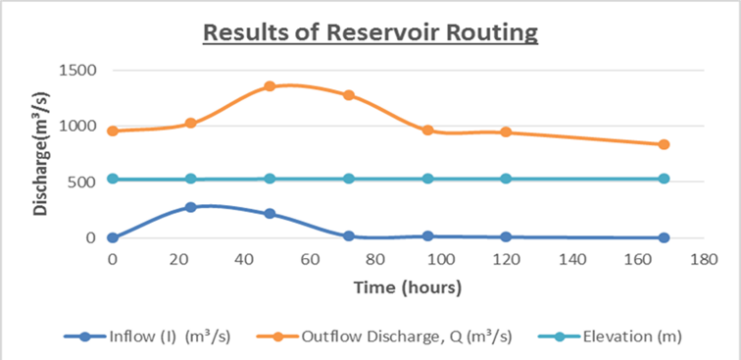

Figure 7. Goodrich method storage routing

Analysis from the flood routing table is then represented on the Goodrich Method Storage routing graph to determine the freeboard height and its corresponding flow over the spillway. As shown in Figure 7, nodes on the 2S/t + Q graph represent each day of study duration. When projected vertically to the axis above, its flow over the spillway is determined. And the value of the water level in the dam can be calculated by projecting it horizontally to the left of the axis. Finally, these values are compared to the design limitations, such as dam level should not exceed 532m (dam crest level) and the maximum spillway discharge of 1800m^3/s. The results from the graphical representation are highlighted in Table 4 below.

Table 4. Results from Goodrich method graph

Time (h)	Inflow (l) (m/sec)	Elevation (m)	Outflow Discharge Q (m^3/sec)
0	0.00	521.15	955.00
24	274.12	528.18	1025.00
48	211.84	528.06	1350.00
72	15.62	527.96	1275.00
96	12.81	527.86	963.00
120	7.21	527.76	941.00
168	0	527.66	836.00

Spillway Adequacy Analysis

Figure 8, denoting the relationship between inflow, outflow and the dam level is plotted to validate the observations made. It shows the reservoir routing procedure for the peak outflows and corresponding flood rises for a 24–168-hour duration. It can be observed that as the rainfall intensifies, the flood level rises. An almost constant water level at the dam is maintained and at its peak flood observation, the dam level rose to 528. 18m.It shows the dam with its free overspill concrete-lined crump weir is able to successfully allow safe discharge of flood events of PMP/PMF magnitude for the research period. At the highest measured flood, the dam rises to a level of 528.06m ASL, which is less than the elevation of the Dam Crest level of 532m ASL. As a result, the water level over the spillway rose by 1.06m. During this time, the flow over the spillway was 1350m3/sec. The flood rise is confined to the dam crest level; therefore, the Vaturu Dam is safe from overtopping from the onslaught of a PMP/PMF event.

Conclusion

A general approach to the determination of the spillway adequacy of the Vaturu Dam indicated that the existing spillway has the ability to discharge the probable maximum flood period safely. These observations were made over the period of one week during the storm event of Cyclone Winston. This category five cyclone caused widespread flooding over the Fiji Group, claiming 44 victims. The highest inflow discharge rate derived from the maximum daily precipitation was 274.12 m3/s, and the observed maximum reservoir level during this period was 528.06m. Discharge over the spillway yielded a flow of 1350m3/s. It is vital to compare these parameters to ensure that they are confined to the limit state per Dam Design. The Dam crest level of 532m ASL and maximum spillway discharge capacity of 1800m3/s threshold were confirmed to have not been exceeded for the storm event of Cyclone Winston.

Scientific Ethics Declaration

The authors declare that the scientific ethical and legal responsibility of this article published in EPSTEM journal belongs to the authors.

Acknowledgements

* This article was presented as an oral presentation at the International Conference on Technology, Engineering and Science (www.icontes.net) held in Antalya/Turkey on November 16-19, 2022.

References

Faiza, N., Tai, V. C., & Mohammad, M. (2022). Trend analysis of river flow in Langat River Basin using Swat model. *Journal of Engineering & Technological Advances, 7*(1), 13-22.

Graham, W. J. (2009). Major US dam failures: their cause, resultant losses, and impact on dam safety programs and engineering practice. In *Great Rivers History: Proceedings and Invited Papers for the EWRI Congress and History Symposium* (pp. 52-60).

Güntner, A., Krol, M. S., Araújo, J. C. D., & Bronstert, A. (2004). Simple water balance modelling of surface reservoir systems in a large data-scarce semiarid region, *Hydrological Sciences Journal, 49*(5). https://doi.org/ 10.1623/hysj.49.5.901.55139.

Hershfield, D. M. (1961). Estimating the probable maximum precipitation. *Journal of the Hydraulics Division*, *87*(5), 99-116.

Hershfield, D. M. (1965). Method for estimating probable maximum rainfall. *Journal-American Water Works Association*, *57*(8), 965-972.

Hwee, H.H., & Poon, H.C. (2013). Risk assessment scenario of Machap Dam overtopping using new PMP Malaysian series. *Jordan J. Civil Eng. 159*(701), 1–10

Kaatz, J. A. (2014). *Development of a HEC-HMS model to inform river gauge placement for a flood early warning system in Uganda* (Doctoral dissertation), Massachusetts Institute of Technology.

Khalifeloo, M. H., Mohammad, M., & Heydari, M. (2015). Multiple imputation for hydrological missing data by using a regression method (Klang river basin). *International Journal of Research Engineering and Technology*, *4*(6), 519-524.

Mohammad, M., Faiza, N., Low, Y.K.., & Shariff, M.S. (2020), Rainfall runoff modelling of sungai pahang by using hydrologic modeling system (HEC-HMS). *Journal of Mechanics of Continua and Mathematical Sciences*, *9*, 171-180. https://doi.org/10.26782/jmcms.spl.9/2020.05.00017

Nathan, R., & Merz, S. K. (2001). Estimation of extreme hydrologic events in Australia: Current practice and research needs. In *Proceedings of a Workshop on Hydrologic Research Needs for Dam Safety* (pp. 69-77).

Sidek, L. M., Nor, M. M., Rakhecha, P. R., Basri, H., Jayothisa, W., Muda, R. S., ... & Razad, A. A. (2013, June). Probable maximum precipitation (PMP) over mountainous region of cameron highlands-batang Padang catchment of Malaysia. In *IOP Conference Series: Earth and Environmental Science 16*(1): 012049. https://doi.org/10.1088/1755-1315/16/1/012049

Tingsanchali, T., & Tanmanee, S. (2012). Assessment of hydrological safety of Mae Sruai Dam, Thailand. *Procedia Engineering*, *32*, 1198-1204.

WMO (World Meteorological Organization). (2009). *Manual on estimation of probable maximum precipitation (PMP*), WMO-No.1045, Geneva, Switzerland.

Author Information

Munira MOHAMMAD
Centre for Water Research, Faculty of Engineering, Built Environment and Information Technology, SEGi University, 47810, Kota Damansara, Selangor, Malaysia
Contact e-mail: *muniramohammad@segi.edu.my*

Patrick Jione PAGKALE
Centre for Water Research, Faculty of Engineering, Built Environment and Information Technology, SEGi University, 47810, Kota Damansara, Selangor, Malaysia

Nor Faiza ABD RAHMAN
Centre for Water Research, Faculty of Engineering, Built Environment and Information Technology, SEGi University, 47810, Kota Damansara, Selangor, Malaysia

Mohamad Shakri MOHMAD SHARIFF
Faculty of Engineering and Quantity Surveying, Inti International University,
71800, Nilai, Negeri Sembilan, Malaysia

To cite this article:

Mohammad, M., Pagkale, P.J., Abd Rahman, N.F., & Mohmad Shariff, M.S. (2022). Hydrological safety of Vaturu Dam by evaluating spillway adequacy. *The Eurasia Proceedings of Science, Technology, Engineering & Mathematics (EPSTEM), 21,* 349-355.

The Eurasia Proceedings of Science, Technology, Engineering & Mathematics (EPSTEM)
ISSN: 2602-3199

The Eurasia Proceedings of Science, Technology, Engineering & Mathematics (EPSTEM), 2022

Volume 21, Pages 356-362

IConTES 2022: International Conference on Technology, Engineering and Science

Experimental Axial Compressive Behavior of Partially Confined Concrete Columns with Combined External and Internal FRP Strips

Abdelmadjid SI SALEM
University Mouloud Mammeri of Tizi Ouzou

Sonia DJENAD
University of Bejaia

Souad AIT TALEB
University Mouloud Mammeri of Tizi Ouzou

Abstract: Current researches have demonstrated that the partial confining design by discrete strips is a promising and economic alternative to the full strengthening technique. In this connection, this study consists to evolve a new sustainable technique for confining concrete columns under axial compression. The proposed design technique consists to embed discontinuously hexagonal fibers reinforced polymer (FRP) strips and wrapped the outer concrete partially using external circular FRP strips. A detailed experimental program was realized on standard dimension composite-encased concrete cylinders under compressive loading until failure to evaluate the axial compressive strength and the corresponding failure mode of the reinforced concrete. In addition, mechanical characterization tests were performed to provide the behavior laws of used raw materials. The emphasized experimental results namely: stress versus hoop and axial strain curves and the rupture patterns of all tested samples indicate clearly an improvement on the stiffness, axial stress and strain of the reinforced concrete columns compared to conventional unconfined ones.

Keywords: Axial behavior; Experimental; Hexagonal FRP strips; Partially confined-concrete.

Introduction

Over the last years, a considerable number of research have been conducted on the use of composite materials in concrete structures, and have shown a significant improvement in the axial compressive resistance and ductility of concrete columns due to the lateral confinement of FRP (Hadi et al., 2015; Liang et al., 2019; Wu et al., 2006). In the first experimental studies based on retrofitting columns with composite FRP, the columns were generally fully enveloped ensuring continuous confinement along their longitudinal axes. The previous investigations have revealed that fully FRP confinement can materials increased the strength and ductility of concrete columns compared to unreinforced control specimens (Guo et al., 2016; Hadi et al., 2013; Rahman et al., 2018).

Furthermore, many experimental approaches have been carried out on the behavior of partially confined specimens with different types of FRP composites (Campione et al., 2015; Totonchi et al., 2019; Zeng et al., 2020, Zeng et al 2021). Partially FRP-wrapped columns were also demonstrated to exhibit improvement in resistance and ductility, confronted with unreinforced control columns. (Djenad el al., 2022) have introduced a new confined concrete columns design with encased-FRP/Grid components with partial hexagonal FRP and steel wire grid discontinuously embedded as strips in the concrete matrix. In addition, (Ali Ahmed et al., 2022) have investigated the experimental behavior and the reliability of concrete columns repaired by externally bonded double- FRP spiral strips under axial compression loading.

In this respect, the new technique considered in this experimental program consist on the embedded of hexagonal FRP strips inside the columns to provide high mechanical proprieties of reinforced concrete by partial-embedding of FRP composite. The design of FRP strips shaped to be hexagonal is motivated by their lightness, high rigidity and form-stability combined to high compression resistance compared to conventional circular shape. This article intended to examined the behavior in axial compression of partially confined columns with a GFRP strips. A total of 12 columns were cast and tested in this article. The different results of the tests in terms of failure mechanism, stress-strain behavior, ultimate axial stress-axial strain response have been presented in detail.

Experimental Investigation

The new confinement technique suggested in the present article consists of partially confining cylinders with hexagonal and circulars FRP strips. A total of 12 concrete cylinders with dimensions Ø160 mm x 320 mm was cast and tested under axial compression. Three cylinders, considered a reference named "P", were tested to failure to measure the characteristic compressive strength of concrete at 28 days. The other cylinders were confined by partial integration of hexagonal FRP strips "FC-1", other wrapped with circular FRP strips "FC-2", and else double confined concrete with an inner and outer confinement with GFRP strips "FCC". The main objective of this work is to introduced the different results of this experimental program, understand the real observed and overall mechanical behavior to obtain preliminary conclusions about the importance of the proposed technique in terms of resistance and deformation enhancement.

Materials Preparations

The concrete used in the experimental tests for the preparation of the different cylinders is an ordinary concrete with Portland cement. The concrete mix proportion is determined from the Dreux-Gorisse method founded on the particle size analysis of different solid components. Table 1 summaries the mix proportion of the ordinary concrete defined for this experimental protocol. The cylinders were prepared according to Eurocode 2, using a conventional rotary drum concrete mix, followed by a slump test, as indicted the Figure.1 (a). The concrete was casted in standardized molds, as presented in Figure.1 (b), then demouled after 24 hours, the specimens were kept humid at a moderate and constant temperature for 28 days according to NF EN 12390-2 standard. After 28 days the specimens were dried on the surface and to avoid the eccentricity of the axial compressive force during the tests, specimens must undergo surfacing. The compressive strength of the used concrete at 28-day which was obtained to be 27.3 MPa.

Table 1. Mix proportions of used concrete

Component	Amount
Cement CPJ 42.5 (kg/ m^3)	370
Sand (kg/ m^3)	635,98
Fine aggregate (kg/ m^3)	201,5
Coarse aggregate (kg/ m^3)	424,94
Water (ml/ m^3)	200
Super plasticizer (l/m^3)	5 L
Slump test	8 cm

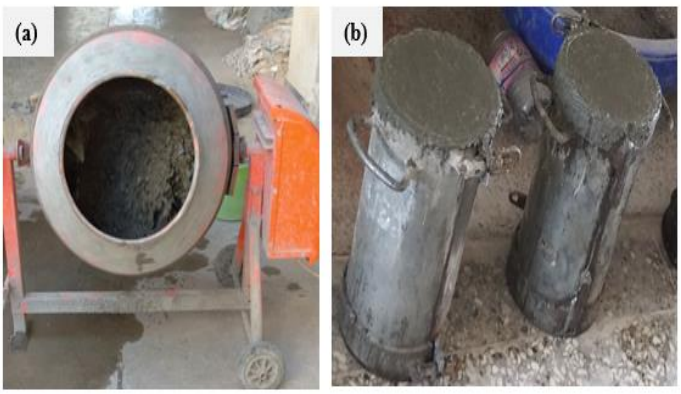

Figure 1. (a) Concrete preparation; (b) Concrete casting

For the composite strips embedded in the concrete, the used fabric is bidirectional fiberglass mat (GFRP) formed from a set of surface filaments of warps and wefts, as represented in the Figure 2 (a). The thickness of GFRP fabric is 0.35 mm. For partially concrete encased FRP strips columns, hexagonal GFRP strips of 30 mm width and 140 mm diameter have been used as inner concrete confinement. Table 2 recapitulate the different characteristics of used fabric, which have been determined by (Si Salem et al, 2015; Si Salem et al, 2020; Ait Taleb et al, 2016, Djenad et al, 2022b, Ait Taleb el al, 2020) on GFRP coupons according to ASTM D3039 standard tensile test. The specimen confinement with GFRP is ensuring by welded mesh bars of 3mm diameter, with 2 hexagonal straps of 140 mm overall diameter, as exposed in Figure.2 (b). 24 FRP strips of 45 cm length and 30 mm width were measured and catted, 4 strips then were placed around the bars using the epoxy resin STR, with net spacing of 30 mm.

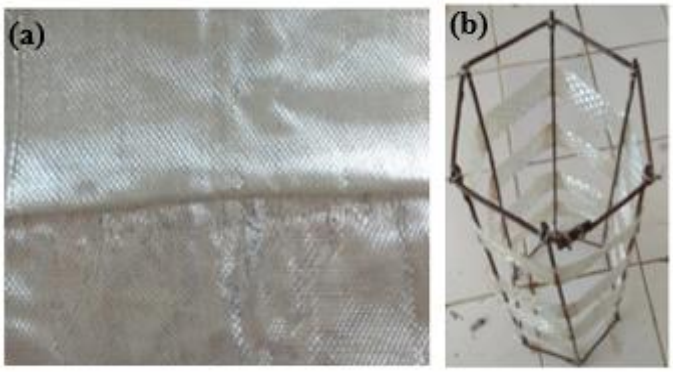

Figure 2. (a) Fiber glass fabric; Conception with GFRP strips

Table 2. Average properties of used FRP and grid

Used materials	Thickness (mm)	Young modulus (Gpa)	Tensile stress (Mpa)	Ultimate tensile strain (‰)
GFRP fabric	0.35	82	1400	5.61

A total of 12 FRP strips of 55 cm length and 6 cm width was measured using the same GFRP fabric and placed partially around the specimens to reinforced the outer concrete, figure .3 (a). After cutting, the GFRP strips were placed around the hardened specimen using an adhesive resin, as indicated in Figure.3 (b). The used epoxy resin STR was mixed with a hardener during five minutes to avoid the inclusion of air bubbles, as presented in Figure.3 (c). Finally, specimens were left to dry at room temperature during 7 days.

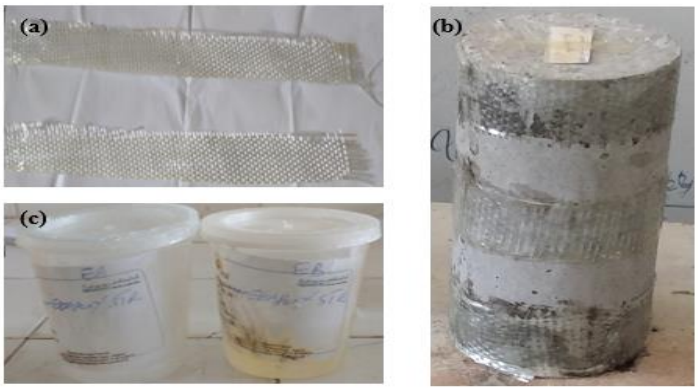

Figure 3. (a) Fiber glass strips; (b)The components of the adhesive; (c) The specimen confined with GFRP strips

Test Setup and Instrumentation

The test machine is a universal ELE (IBERTEST) type of 3000 KN capacity with a loading rate of 0.5 KN/s, equipped with a data acquisition system and a digital software control, is used for testing all the columns. The testing machine indicates the applied load as a function of longitudinal displacement, allowing thus the axial stress- axial strain curves. The loading rate is kept constant during the test procedure and the columns were instrumented to record axial stress-stain measurements, Figure.4. The test allows also to observe the failure

mechanisms of the confined concrete columns and to evaluate the contribution of the embedded metallic grid in resistance, ductility and confinement level.

Figure 4. Axial compression loading set-up

Experimental Results and Analyzes

In this session, the confrontation of the overall response of the different reinforced concrete cylinders with the unconfined concrete was performed. The failure mechanisms corresponding to the different specimens regarded in this research are performed and analysed, in order to deduce the parameters influencing the structural ductility, as well as the passage from a brittle failure mode to a ductile failure mechanism.

Stress-Strain Behavior

Figure 5 shows the axial behaviour of unconfined columns “P” and partially confined columns with GFRP strips ("FC-1”, "FC-2" and "FCC"). The test results of the three identical columns were find to be approximatively similar to each other; consequently, the average of the three columns of each confinement configuration was presented. Detailed results of all tested columns are summarized in Table 4. It can be seen from the figure that all the columns showed similar behaviour at the initial stage, a slope which follows that of the unconfined concrete, i.e., the stress increases with increasing strain. After the ultimate resistance achievement, the stress of the unreinforced columns “P” decreased considerably conducting to a total failure. The strength of the confined specimens ("FC-1”, "FC-2" and "FCC"), was significantly increased with a considerable increasing of deformation, this is due to activation of confinement effect provided by the hexagonal FRP strips. Integrating GFRP strips and the wrapped the outer concrete with GFRP strips provides high tensile strength during transversal expansion of the concrete core, which allows to prevent the cracks propagation.

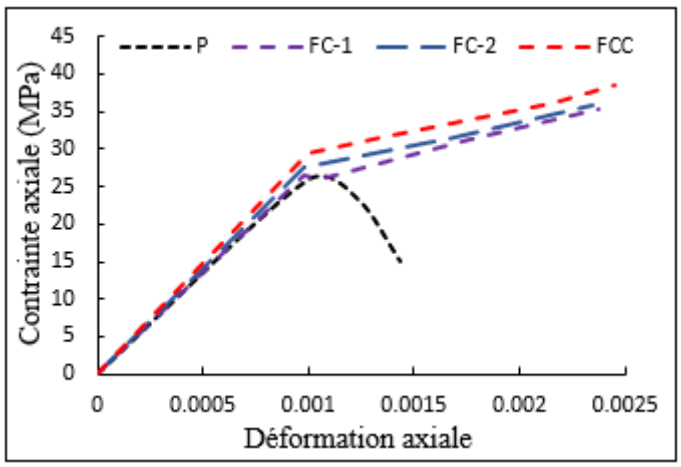

Figure 5. Axial stress-axial strain curve of the different columns

The confrontation of the different stress-strain curves illustrated in figure 6 shows a positive improvement of compressive resistance and ductility. Indeed, the ultimate concrete strengths obtained for "FC-1", "FC-2" and "FCC"), columns are respectively 35.2 MPa, 35.7 MPa and 37.5 MPa, compared to 27.3 MPa for the unreinforced column. the confined columns with encased hexagonal GFRP strip and outer confinement presents a gain in resistance of the order of 37.36 % and a more extensive deformation before rupture therefore a greater ductility effect which represents a significant contribution.

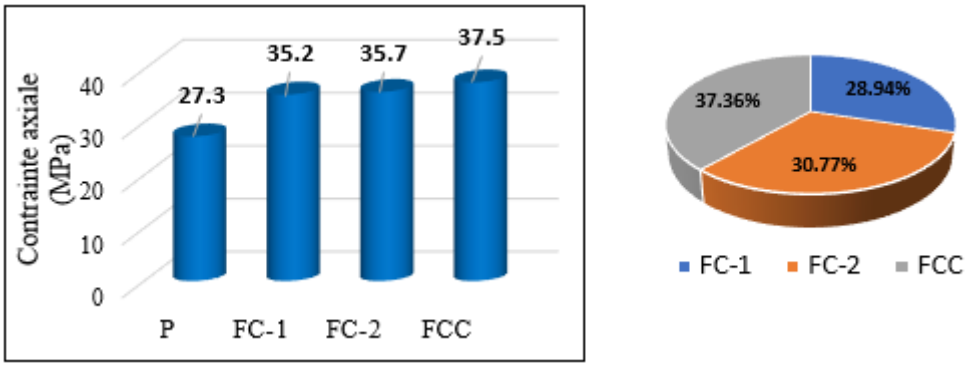

Figure 6. Confrontation of the different stress-strain curves

Failure Modes

The failure mechanisms corresponding to the different specimen subject to a uniaxial compressive load are illustrated in Figure 7. For the specimens reinforced by integrating of GFRP strips, the concrete cover collapsed because no confinement was provided to the outer concrete. For columns wrapped with GFRP strips, the concrete cover cracking is observed when the compressive resistance of the control column was approached, however, the columns still remain with higher deformation after the crushing of the concrete cover. The crushing of the outer concrete was effectively controlled owing to the confinement ensured by the GFRP. Incorporating GFRP strips in concrete induce a high tensile strength during transversal expansion of the concrete core, which helps to prevent the cracks propagation. The external GFRP composite allows the passage from a brittle failure mechanism to a ductile failure mode this ductility contribution confers on the composite column interesting deformation capacity.

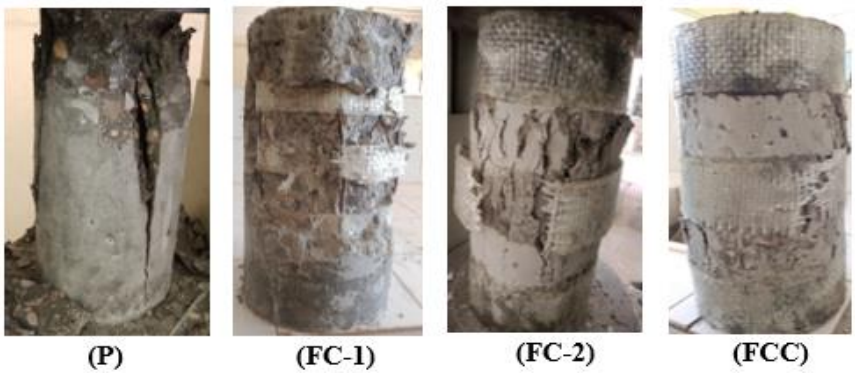

Figure 7. The modes of failure in the concrete column

Conclusion

This work consists in investigating experimentally the behaviour of confined concrete cylinder with GFRP strips. This new technique aims to increase the stiffness and strength of the member, to allow ductile failure and to prevent sudden collapse under axial compression loading. The proposed technique ensures the continuity of the concrete within the structure, avoids the problem of interface failure and facilitates the production process.

All the reinforced concrete columns achieve a considerable improvement in resistance and ductility. The hexagonal GFRP strips ensures the confinement of the inner concrete, while the GFRP jacket provides a

complement to the outer concrete but it remains insufficient because of the level of confinement is very low. The ultimate resistance and deformation of the confined columns can be significantly increased by increasing the GFRP fiber amount and decreasing the GFRP strips spacing. This study tells us that with a reasonable confinement level, the average stress of the concrete is improved by nearly 36% for the confined columns with embedded and wrapped GFRP strips.

Recommendations

The framework of this research reveals only a small part of the mechanical aspects of concrete reinforcement by GFRP strips. An important number of experiments and tests are necessary to draw complete conclusions about the interest of this technology.

Scientific Ethics Declaration

The authors declare that the scientific ethical and legal responsibility of this article published in EPSTEM journal belongs to the authors.

Acknowledgements

* This article was presented as an oral presentation at the International Conference on Technology, Engineering and Science (www.icontes.net) held in Antalya/Turkey on November 16-19, 2022.

References

Ait Taleb, S.,& Si Salem, A. (2015). Bending and shear behavior of a composite beam strengthened and double-confined with FRP-jacket. *Procedia Engineering*, *114*, 165-172.

Ait Taleb, S., Si Salem, A., & Ait Tahar, K. (2017). Behaviour of a new graded beam reinforced with externally bonded composite sheets: theoretical and experimental studies. *European Journal of Environmental and Civil Engineering*, *21*(9), 1171-1185.

Ait Taleb, S., Si Salem, A., & Ait Tahar, K. (2020). Experimental and theoretical modeling coupled to a reliability approach for flexural failure prediction in hybrid composite beams. *Asian Journal of Civil Engineering*, *21*(3), 495-504.

Ali Ahmed, C., Salem, A. S., Ait Taleb, S., & Ait Tahar, K. (2022). Experimental behavior and reliability of predamaged concrete columns externally repaired with FRP spiral strips under axial compression. *World Journal of Engineering*, (ahead-of-print).

ASTM D3039/D3039M-08 (2014). *Standard test method for tensile properties of polymer matrix composite materials*. West Conshohocken: ASTM International.

Campione, G., La Mendola, L., Monaco, A., Valenza, A., & Fiore, V. (2015). Behavior in compression of concrete cylinders externally wrapped with basalt fibers. *Composites Part B: Engineering*, *69*, 576-586.

Djenad, S., Ait Taleb, S., Si Salem, A., & Bouzidi, M. A. (2022). NLFEA based design optimization of GFRP strips in partially confined concrete. *Procedia Structural Integrity*, *37*, 321-329.

Djenad, S., Si Salem, A., & Bouzidi, M. A. (2022). Performance and compressive axial behavior of new design partially confined concrete columns with encased-FRP/Grid strips. *Asian Journal of Civil Engineering*, 1-15.

Guo, Y., Xie, J., Xie, Z., & Zhong, J. (2016). Experimental study on compressive behavior of damaged normal- and high-strength concrete confined with CFRP laminates. *Construction and Building Materials*, *107*, 411-425.

Hadi, M. N., Wang, W., & Sheikh, M. N. (2015). Axial compressive behaviour of GFRP tube reinforced concrete columns. *Construction and Building Materials*, *81*, 198-207.

Hadi, M. N., Pham, T. M., & Lei, X. (2013). New method of strengthening reinforced concrete square columns by circularizing and wrapping with fiber-reinforced polymer or steel straps. *Journal of Composites for Construction*, *17*(2), 229-238.

Liang, J. F., Zou, W. J., Wang, Z. L., & Liu, D. W. (2019). Compressive behavior of CFRP-confined partially encased concrete columns under axial loading. *Composite Structures*, *229*, 111479.

NF EN 12390-2 (2019) "Testing hardened concrete - Part 2: making and curing specimens for strength tests" AFNOR 91.100.30 *Concrete and Concrete Products*, p15.

Rahman, A., Mallick, M., & Ghosh, S. (2018). Experimental behavior of FRP confined concrete cylinder wrapped by two different FRPs. *J Mater Sci Res*, *7*(2), 18-25.

Si Salem, A., Taouche-Kkheloui, F., & Ait Tahar, K. (2020). Experimental investigation on the bending and buckling behavior of bio-based core innovative sandwich panels. *International Journal of Structural Integrity*, *12*(2), 226-240.

Totonchi, A., Ansaripour, A., & Shivaei, S. (2020). Effect of different arrangements of CFRP wraps on the axial stress–strain behaviour of confined concrete cylinders: Experimental study and numerical modelling. *Iranian Journal of Science and Technology, Transactions of Civil Engineering*, *44*(4), 1087-1100.

Wu, G., Lü, Z. T., & Wu, Z. S. (2006). Strength and ductility of concrete cylinders confined with FRP composites. *Construction and Building Materials*, *20*(3), 134-148.

Zeng, J. J., Chen, S. P., Zhuge, Y., Gao, W. Y., Duan, Z. J., & Guo, Y. C. (2021). Three-dimensional finite element modeling and theoretical analysis of concrete confined with FRP rings. *Engineering Structures*, *234*, 111966.

Zeng, J. J., Duan, Z. J., Guo, Y. C., Xie, Z. H., & Li, L. J. (2020). Novel fiber-reinforced polymer cross wrapping strengthening technique: A comparative study. *Advances in Structural Engineering*, *23*(5), 979-996.

Author Information

Abdelmadjid SI SALEM
University Mouloud Mammeri of Tizi Ouzou
Tizi Ouzou, 15000, Algeria
Contact e-mail: *abdelmadjid.sisalem@ummto.dz*

Sonia DJENAD
Laboratory LGCA, University of Bejaia
Bejaia, 06000, Algeria

Souad AIT TALEB
University Mouloud Mammeri of Tizi Ouzou
Tizi Ouzou, 15000, Algeria

To cite this article:

Si Salem, A, Djenad, S., & Ait Taleb, S. (2022). Experimental axial compressive behavior of partially confined concrete columns with combined external and internal FRP strips. *The Eurasia Proceedings of Science, Technology, Engineering & Mathematics (EPSTEM), 21*, 356-362.

The Eurasia Proceedings of Science, Technology, Engineering & Mathematics (EPSTEM)
ISSN: 2602-3199

The Eurasia Proceedings of Science, Technology, Engineering & Mathematics (EPSTEM), 2022

Volume 21, Pages 363-370

IConTES 2022: International Conference on Technology, Engineering and Science

Effect of Additive on the Structure and Performance of PVDF Hollow Fibre Membrane on Phosphorus Removal

Hazmin MANSOR
Universiti Selangor

Nur Hidayah MOHD SOBRAN
Universiti Selangor

Abstract: Similar to plants, algae are tiny creatures that inhabit watery settings and use photosynthesis to harness the energy of the sun. Depending on the kind of algae, the excessive growth, or algal bloom, can be green, blue-green, red, or brown and becomes apparent to the human eye. The phenomena are caused by excessive phosphorus in the water body. There are many methods including chemical removal, advanced biological treatment, or a combination of the two methods can remove phosphorus from wastewater. Calcium, iron, and aluminum salts are added as part of the chemical removal of phosphorus in order to achieve phosphorus precipitation by a variety of methods that are explained. However, despite the efficient chemical phosphorus removal systems, it is important to note that they may increase sludge production rates and need additional storage requirements. Using hollow fibre ultrafiltration membrane has great potential to be the alternative in treating. This study observes the effect of TiO2 as additive on the structure and performance of PVDF hollow fiber membrane for phosphorus removal. A comparative study between 0 wt% and 0.5 wt% of TiO2 with a 16 wt% and 84 wt% of polymer and solvent respectively are used in designing and fabricating the hollow fibre membrane. The morphology, water contact angle and pure water flux were being observed. The presence of nanoparticles as additive in membrane enhance the structure and performance of the hollow fiber membrane by forming more porous structure, nano pore size for nanofiltration, increase the permeability and hydrophilicity nature, increase pure water flux and increase fouling resistance that capable to remove phosphorus in wastewater treatment.

Keywords: Hollow fiber membrane, Hydrophilic, Nanofiltration, Phosphorus

Introduction

Hollow fiber membranes are thin and porous semi-permeable layer of material in hollow shape that able to separate contaminants from water when a driving force is applied. In a membrane process, fluid is passed through a barrier (Xu et al., 2016). Hydrophobic is a characteristic of membrane's layer that does not allow water molecules to pass through the membrane which make the water molecules attached on the outside layer of the membrane and caused fouling. While, hydrophilic is a characteristic of membrane's layer that allow water molecules to diffuse easily through the membrane (Gao, Thong, Yu Wang, & Chung, 2017). Nowadays, government is very concern and aware of the phenomena of the eutrophication or algae blooms cause by excessive phosphorus in wastewater (dos Santos, Ribeiro, & Ribau Teixeira, 2015).

Phosphorus is a nutrient, usually in the form of phosphates with ionic radius of 1-10 nanometers (nm) (Zeng, 2012). It is not only produced in agricultural activities, but it is also present in industrial and domestic wastewater. Excessive phosphorus in wastewater causes eutrophication and further induces to negative environmental effects. For treating phosphorus, nanofiltration (NF) provide high separation efficiency as it has a porous membrane filtration process, made from thin film layer composite of polymer that uses nanometer sized

through pores that pass through the membrane. Nanofiltration membranes have pore sizes from 0.1 until 10 nanometers, nm (Wang, Zhao, Li, Li, & Wang, 2015). In order to overcome this issues, hollow fiber membrane nanofiltration which is a portable wastewater treatment is being studied by designing and fabricating the membrane with polymer, solvent and additive to observe the characteristic and also the performance of hollow fiber membrane in treating phosphorus in wastewater.

Materials and Method

This study is conducted through experimental work. The main idea is to produce hollow fibre membrane and to observe the effect of different concentration of additive on the characterization and performance of membrane. There are two parts in membrane fabrication which are designing parameters for making dope solution and fabrication parameters during spinning process.

Materials

The chemicals used in fabrication the membrane includes the 16 % of PVDF polymer, 84 wt % of N,N-dimethylformamide as the solvent, and different variation of Titanium Dioxide (TiO2) at 0 wt% and 0.5 wt% has been used in the preparation of the dope solution. The polymer and the solvent were mixed in glass bottle to get 500 ml of dope solution. The dope solution was stirred at 300 rpm to 400 rpm with the temperature of 60^{o}C to 65^{o}C on the heated plate for 24 hours until the polymer is dissolved. The dope solution is then allowed to be cooled and homogenized at room temperature for another 24 hours.

Methods

The dopes prepared were used in the spinning process. Hollow fibre spinning machine was used to produce the hollow fibre membrane. The water bath (bore fluid) and 500 ml of dope solution were then extruded from the spinneret to form hollow fibre membrane. All the fabrication parameters were adjusted using the controller of the hollow fibre spinning machine. During the process, the hollow fibre membrane were immersed into water bath to solidify the membrane. This process takes about 1 hour to complete the production of hollow fibre membrane for 500 ml of dope solution. Then, the hollow fibre membranes were immersed in the water bath for 1 day for more solidification process. The hollow fibre membranes were then immersed with glycerol for 30 minutes to avoid the membranes from stick to each other. Finally, the hollow fibre membranes were dried in the drying oven for 1 day to remove residual solvent on the membrane before membrane characterization for analysis.

Table 1. Characterization of hollow fibre membrane.

Spinneret outer/inner diameter	1.0 mm/ 0.5 mm
Air gap distance	1.5 cm
Velocity of gear pump inverter/spinning drum	14 rpm/
Inverter (casting speed)	5 rpm
Room temperature	27.6^{o}C
Room humidity	71.7 g/m^{3}

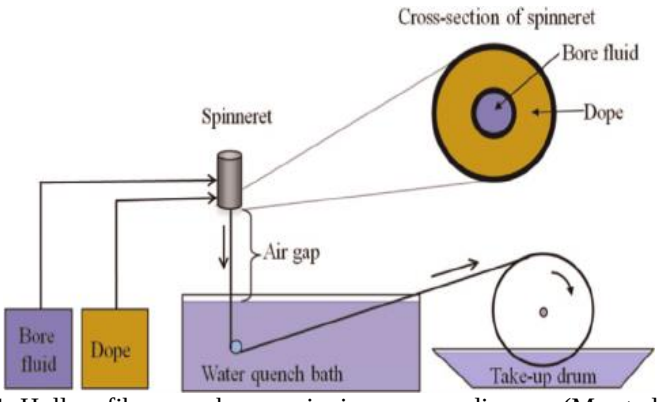

Figure 1. Hollow fibre membrane spinning process diagram (Ma et al., 2015)

Membrane Morphology

Scanning electron microscopy (SEM) was used to observe the structure and cross-section, pore size of surface and thickness of membrane. For cross-section analysis, each membrane were prepared two samples and need to dipped in the liquid nitrogen for 10 seconds so that the membrane will be hard and easy to fractured them by using knife for getting proper hollow shape of membrane. For surface analysis, no need to dipped in the liquid nitrogen and only need one sample for each membrane. Then, the samples were mounted on the brass plate and coated with platinum to increase the conductivity in the scanning electron microscopy when SEM cross-section analysis was carried out.

Water Contact Angle

Water contact angle measurement was carried out to identify the characteristic of hydrophilicity of the membrane. For water contact angle measurement, five samples of membrane were selected to measure the water contact angle accurately using the water contact angle instruments. A water drop was lowered onto the surface of the membrane from a needle tip. A magnified image of the droplet was recorded by a digital camera. Static contact angles were determined from these images with SCA20 software. The water contact angle measurement was taken as the mean value of ten different points from each membrane.

Pure Water Flux Performance

Filtration experiment was conducted using cross-flow equipment in laboratory to measure the pure water flux. This experiment is carried out to characterize the permeation performance of the prepared membranes. For membrane preparation of pure water flux test, five samples of each membrane with length of 15 cm were glued together with cotton using epoxy inside the screw adapter which was called a module after it was done. All the modules were left in room temperature for 1 day to dry. Then, the modules were soaked in the water for 30 minutes while setting up the apparatus for cross-flow filtration test. The modules were fixed into the apparatus and the water (retentate) with pressure of 30 psi was flowed through the modules for 30 minutes to get the steady static flow. After that, the reading of water flux (permeate) will be collected every two minutes for 20 minutes. The steady pure water flux (J_w) was calculated as follows:

$$J = \frac{V}{A \times \Delta t}$$

Where V is the volume of permeated pure water (L), A represents the effective area of membrane, (m2), Δt denotes the permeation time (h). The unit for the pure water flux was L/m^2.hr. (Vatsha, Ngila, & Moutloali, 2014)

Results and Discussion

Membrane Morphology

Scanning electron microscope (SEM) was used to observe the morphology of the membrane which are pore and porosity of the membrane surface, cross-sectional of hollow fibre membrane and structure of hollow fibre membrane. Based on the Figure 2, From the observation, surface membrane with TiO_2 is more porous than the surface membrane without TiO_2. The addition of TiO_2 increases the porous structure of the hollow fibre membrane which will create better performance for the water permeation and pure water flux. This will increase the ability of the hollow fibre membrane to filter the phosphorus in wastewater. By comparing with previous research, (Abdullah et al., 2018), the addition of the TiO_2 increases the porous structure of the membrane same with this result.

For the pore sizes of the surface membrane, IMAGEJ software was used to measure the size of nano pores. The mean value for the nano pore sizes of PVDF/DMF/TiO_2 membrane is 0.32 nm which is smaller than the nano pore sizes of PVDF/DMF membrane which is 1.418 nm. The combination of smaller pore size and higher porosity was required in order to obtain porous structure membrane (A.L. Ahmad et al., 2014). PVDF and DMF are good combination in forming nanofiltration membrane which can be tested for the application for phosphorus removal in wastewater treatment. By referring to the previous journal by (Ekambaram &

Doraisamy, 2016), the combination of PVDF as polymer and DMF as solvent showed that this formula can produced nano pore sizes as the nano pore sizes that has been achieved by the previous researcher is 2.619 nm. This experiment has the same result with the previous researcher as both of the membrane produced nano pore size which is 1.418 nm for the membrane without TiO_2 and 0.32 nm for the membrane with TiO_2.

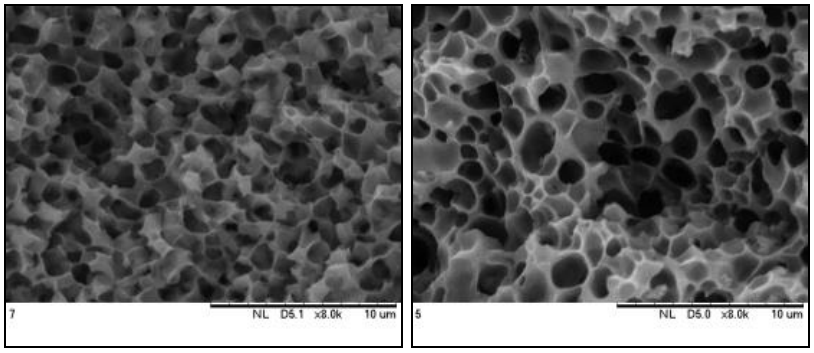

(a) (b)

Figure 2. Pores structure of the surface membrane of (a) PVDF/DMF and (b) PVDF/DMF/TiO_2

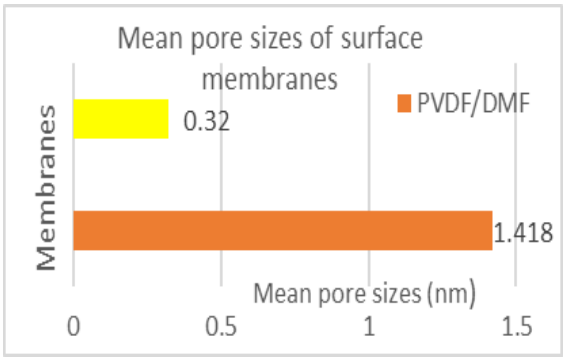

Figure 3. The horizontal bar chart graph of mean pore sizes of both membranes.

Figure 4 shows that the cross-sectional area of PVDF/DMF/TiO_2 membrane exhibit thinner wall of membrane which is 144 μm length compared to membrane without TiO_2 which is 93.1 μm. The structure of membrane with TiO_2 also forming more porous structure compared to membrane without TiO_2. The length of finger-like of membrane without TiO_2 is longer than the hollow fibre membrane with TiO_2.

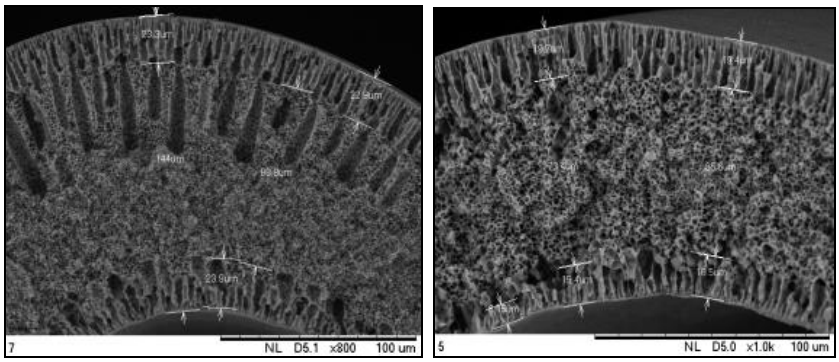

(a) (b)

Figure 4. Cross-sectional area of (a) PVDF/DMF and (b) PVDF/DMF/TiO_2.

Based on Figure 5, both of the hollow fibre membrane's structure are in irregular hollow shape. This is due to the low usage of PVDF percentage which lead to soft and improper hollow fibre membrane structure. The percentage of PVDF polymer must be increases in order to produce proper and rigid hollow structure of hollow fibre membrane. This hollow shape failure is also due to the human error when handling the sample of hollow fibre membrane such as the use of knives and hand touch during membrane preparation process.

In Figure 5 (b), there is a macrovoid defect in the structure of membrane with TiO_2 which is due to the present of voids inside the tubes of dope solution that connected to the spinneret during the hollow fibre membrane

spinning process. The SEM image shows that both hollow fibre membranes with and without TiO_2 formed porous structure, have finger-like structure at outer layer and sponge-like structure at inner layer, formed nano pore sizes and also have asymmetric structure (Yuliwati & Ismail, 2011). The sponge-like structure at the inner layer is due to the water bath as bore fluid during hollow fibre spinning process which can filter phosphorus. The formation of finger-like structure occurred because of the instantaneous demixing cause by high mutual affinity of solvent and non-solvent.

The addition of TiO_2 nanoparticles as an additive increases the porosity of the structure of membrane which acts like pore former agent, decrease the thickness of the membrane's wall and forming smaller nano pore sizes compared to membrane without additive for nanofiltration process to remove phosphorus in wastewater treatment. The number of pores of membrane increase due to the enhancement of water affinity of TiO_2. to water. (Abdullah et al., 2018)

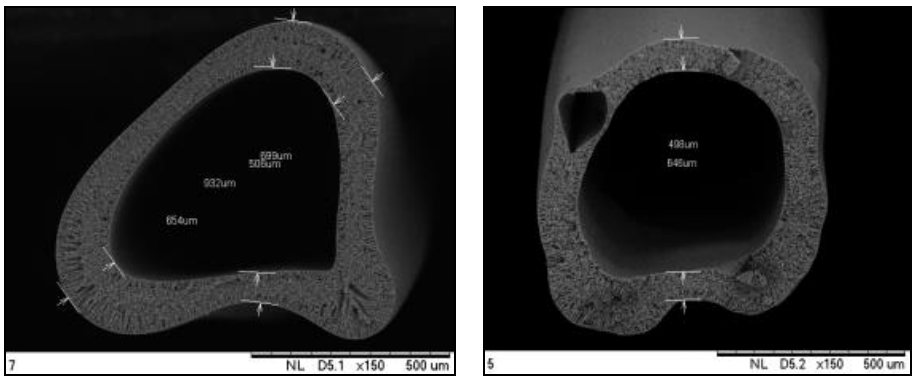

(a) (b)

Figure 5. Structure of (a) PVDF/DMF and (b) PVDF/DMF/TiO_2.

Water Contact Angle Measurement

The characteristic of hydrophilicity and wet permeability of the membrane can be identified by carrying out the water contact angle measurement.

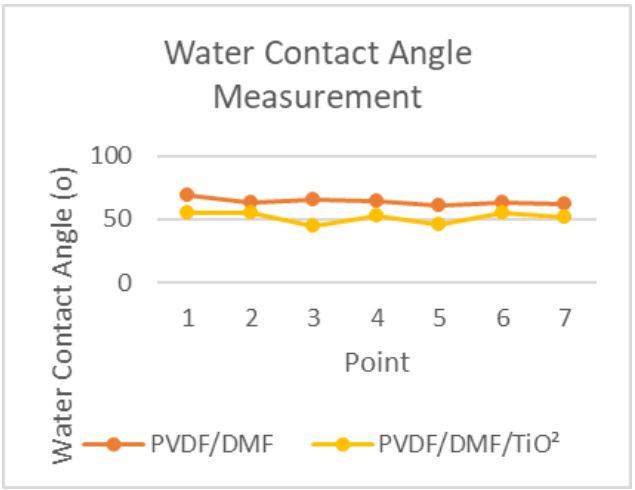

Figure 6. The line graph of water contact angle measurement of PVDF/DMF and PVDF/DMF/TiO_2.

Based on the line graph in Figure 6, the water contact angle of both hollow fibre membranes are non-uniformly pattern and fluctuated as they are increasing and decreasing but still in the same average of number of contact angle. The measurement of water contact angle of PVDF/DMF/TiO_2 are from 54.89^o to 44.70^o while the measurement of water contact angle of PVDF/DMF are from 68.73^o to 60.29$^{o.}$ This result shows that the water contact angle measurement for membrane with additive are lower than the membrane without additive. By comparing to the previous study (Shahruddin et al., 2018), combination of 15 wt% PES polymer, 84.5 wt% DMAc solvent and 0.5 wt% TiO_2 increased the hydrophilicity of the membrane as the mean water contact angle

measurement was 50.1°. This result gives slightly same contact angle measurement with the previous study as the result gained is 51.18°.

From the observation, the addition of TiO_2 nanoparticles as an additive increase the number of pores of the surface membrane, yet increase the hydrophilicity of the membrane as the water contact angle is lower than the membrane without TiO_2 which enhance the performance of water permeation rate of the membrane and give positive effect on the water diffusion across the membrane surface. Even though the PVDF has hydrophobic characteristic, the tendency of the PVDF to have hydrophilic nature is increasing due to the addition of the TiO_2 as an additive which increase the fouling resistance of the membrane.

Pure Water Flux Performance

Pure water flux experiment was conducted by using cross-flow filtration equipment to observe the performance of the permeation of water with pressure of 30 psi through the hollow fibre membrane modules. Based on the Figure 7, the pure water flux performance of PVDF/DMF/TiO_2 decreases from 8.089 L/m².hr to 6.534 L/m².hr while pure water flux performance of PVDF/DMF decreases from 2.616 L/m².hr to 2.165 L/m².hr for every 2 minutes until 20 minutes. The bar chart graph shows the pure water flux performance of PVDF/DMF/TiO_2 is higher than the water flux performance of PVDF/DMF. The pure water flux performance of both hollow fibre membrane are decreasing for 20 minutes as the water molecules started to attach in the surface of the membrane which decrease the flux of the water during the filtration test. These results show that membrane with additive has higher pure water flux than the membrane without additive.

TiO_2 nanoparticles has low tendency for aggregation and do not clogged the pores of the membrane which lead to high pure water flux. The wall of the membrane also thinner with the present of TiO_2 which make the water molecules easier to diffuse through the pores of the membrane. By comparing to the previous study by (Shahruddin et al., 2018), the membrane fabricated with 15 wt% PES polymer, 84.5 wt% Dmac solvent and 0.5 wt% TiO_2 additive gave 7.58 L/m2.hr for the mean value of pure water flux from 20 minutes to 120 minutes. This result also has slightly different mean value for the pure water flux which is 7. 14L/m^2.hr. This is due to the nano pore sizes of the hollow fibre membrane which decreases the rate of the water molecules diffusion movement through the membrane surface. The addition of TiO_2 nanoparticles as an additive increases the porosity of membrane, the permeability of the membrane's surface and the hydrophilicity nature of the membrane which enhanced high water diffusion through the membrane and high pure water flux performance due to high affinity of TiO_2 to water molecules.

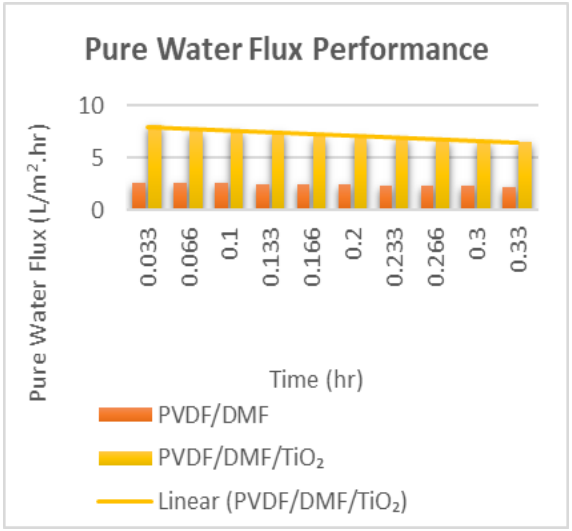

Figure 7. The bar chart graph of pure water flux performance of both modules.

Table 2. The summary of the analysis and characterization of both hollow fibre membrane.

Membranes	Mean Pore Size (nm)	Mean Water Contact Angle (°)	Mean Pure Water Flux (L/m².hr)
PVDF/DMF	1.418	63.75	2.40
PVDF/DMF/TiO_2	0.32	51.18	7.14

Conclusion

PVDF hollow fibre membrane with DMF as the solvent and TiO_2 as an additive and also another PVDF hollow fibre membrane without additive were successfully designed and fabricated. The effect of TiO_2 as additive on the structure and performance of the hollow fibre membranes such as the membrane morphology, the water contact angle measurement and the pure water flux performance have been studied and evaluated. The present of TiO_2 nanoparticles as an additive effect the structure and morphology of the hollow fibre membrane as the wall of the membrane became thinner, the porosity of the membrane's surface increased and formed nano pore size for nanofiltration process to remove phosphorus in wastewater treatment. Finger-like structure were formed at the outer layer and sponge-like structure were formed at the inner layer of the membrane and have asymmetric structure. The effect of additive increased the hydrophilicity of the membrane as hollow fibre membrane with TiO_2 has lower measurement of water contact angle as the permeability of membrane's surface increased. The addition of additive improved the hydrophilicity of the PVDF membrane and increase the fouling resistance on the membrane's surface.

PVDF hollow fibre membrane with TiO_2 showed higher pure water flux performance. TiO_2 nanoparticles is the best additive to produce nanofiltration for PVDF hollow fibre membrane which can enhanced the structure and performance to treat phosphorus. TiO_2 could serve as a basis for further work to demonstrate the capabilities of photocatalytic membrane to degrade organic pollutant such as phosphorus from industrial effluent. From this study, the present of nanoparticles as an additive in membrane formation enhanced the structure and performance of the hollow fibre membrane by forming more porous structure, nano pore size, increase the permeability and hydrophilicity nature, increase pure water flux and increase fouling resistance of the membrane that capable to remove phosphorus in waste water treatment.

Scientific Ethics Declaration

The authors declare that the scientific ethical and legal responsibility of this article published in EPSTEM journal belongs to the authors.

Acknowledgements

* This article was presented as an oral presentation at the International Conference on Technology, Engineering and Science (www.icontes.net) held in Antalya/Turkey on November 16-19, 2022.

References

Abdullah, N., Ayodele, B. V., Mansor, W. N. W., & Abdullah, S. (2018). Effect of incorporating TiO_2 photocatalyst in PVDF hollow fibre membrane for photo-assisted degradation of methylene blue. *Bulletin of Chemical Reaction Engineering & Catalysis*, *13*(3), 588–591.

Ahmad, A.L., Ideris, N., Ooi, B. S., Low, S. C., & Ismail, A. (2014). Influence of polymer concentration on pvdf membrane fabrication for immunoassay analysis. *Journal of Applied Sciences*, *14*(12), 1299–1303.

dos Santos, C., Ribeiro, A., & Ribau Teixeira, M. (2015). Phosphorus recovery from waters using nanofiltration. *Desalination and Water Treatment*, *55*(5), 1308–1315.

Ekambaram, K., & Doraisamy, M. (2016). Study on the fabrication, characterization and performance of PVDF/calcium stearate composite nanofiltration membranes. *Desalination*, *385*, 24–38.

Gao, J., Thong, Z., Yu Wang, K., & Chung, T. S. (2017). Fabrication of loose inner-selective polyethersulfone (PES) hollow fibers by one-step spinning process for nanofiltration (NF) of textile dyes. *Journal of Membrane Science*, *541*, 413–424.

Shahruddin, M. Z., Zakaria, N., Diana Junaidi, N. F., Alias, N. H., & Othman, N. H. (2018). Study of the effectiveness of Titanium Dioxide (TiO2) nanoparticle in Polyethersulfone (PES) composite membrane for removal of oil in oily wastewater. *Journal of Applied Membrane Science & Technology*, *19*(1), 33-42.

Vatsha, B., Ngila, J. C., & Moutloali, R. M. (2014). Preparation of antifouling polyvinylpyrrolidone (PVP 40K) modified polyethersulfone (PES) ultrafiltration (UF) membrane for water purification. *Physics and Chemistry of the Earth, Parts A/B/C*, *67*, 125-131.

Wang, T., Zhao, C., Li, P., Li, Y., & Wang, J. (2015). Effect of non-solvent additives on the morphology and separation performance of poly(m-phenylene isophthalamide) (PMIA) hollow fiber nanofiltration membrane. *Desalination, 365*, 293–307.

Xu, Z., Wu, T., Shi, J., Teng, K., Wang, W., Ma, M., & Fan, J. (2016). Photocatalytic antifouling PVDF ultrafiltration membranes based on synergy of graphene oxide and TiO2 for water treatment. *Journal of Membrane Science, 520*, 281–293.

Yuliwati, E., & Ismail, A. F. (2011). Effect of additives concentration on the surface properties and performance of PVDF ultrafiltration membranes for refinery produced wastewater treatment. *Desalination, 273*(1), 226–234.

Zeng, Z. (2012). *Phosphorus removal by ceramic tight ultra-filtration (CTUF) membranes for RO pre-treatment* (master thesis), Delft University of Technology, Delf.

Author Information

Hazmin MANSOR
Universiti Selangor (UNISEL)
Department of Engineering, Faculty Engineering and Life Sciences, Universiti Selangor, Jalan Timur Tambahan, 45600 Bestari Jaya, Selangor, Malaysia.
Contact e-mail: *hazmin@unisel.edu.my*

Nur Hidayah MOHD SOBRAN
Universiti Selangor (UNISEL)
Department of Engineering, Faculty Engineering and Life Sciences, Universiti Selangor, Jalan Timur Tambahan, 45600 Bestari Jaya, Selangor, Malaysia.

To cite this article:

Mansor, H. & Mohd Sobran, N.H. (2022). Effect of additive on the structure and performance of PVDF hollow fiber membrane on phosphorus removal. *The Eurasia Proceedings of Science, Technology, Engineering & Mathematics (EPSTEM), 21,* 363-370.

The Eurasia Proceedings of Science, Technology, Engineering & Mathematics (EPSTEM)
ISSN: 2602-3199

The Eurasia Proceedings of Science, Technology, Engineering & Mathematics (EPSTEM), 2022

Volume 21, Pages 371-379

IConTES 2022: International Conference on Technology, Engineering and Science

Effect of the Addition of a Fin on the Thermal Behavior of the Shell of a Rotary Cement Kiln

Mohammed BOUHAFS
University of Oran 2 Mohamed Ben Ahmed

Abed MEGHDIR
University of Oran 2 Mohamed Ben Ahmed

Abstract: This work consists of a numerical study of a thermally stressed rotary kiln shell part in a cement plant. The numerical simulations are performed by using the finite volume method for the discretization and the simple algorithm for resolution. The velocity air injection and its temperature are the main parameters under investigation. In the second step of this study, fins are inserted on the shell to examine their effect on cooling. The results analysis shows that the insertion of fins to the shell has a significant influence on the decrease in temperature of the shell's external surface. The study shows that this decrease in temperature depends significantly on the air injection rate, not on its temperature. To avoid overloading our equipment, only four fins distributed around the kiln are added to explore their effect. The results obtained give a reduction of 35% in the temperature distribution for the case of a shell with fin compared to that without fin. What makes the proposal interesting and thus lead to the preservation of shell of our rotary kiln.

Keywords: Rotary kiln, Shell, Natural convection, Nusselt number, Finite volumes.

Introduction

The rotary kiln is the main equipment of a cement plant, as it is used for firing basic materials for the production of clinker. It consists of a steel tube coated with refractory brick. The tube is slightly inclined (1 to 4 degrees) and rotates between 0.5 and 5 rpm. The rotary kiln is of great importance in the field of cement production. It represents the most thermally stressed component, and the resolution of problems associated with this phenomenon leads to a better performance of the kiln. To address these issues, we began with the study of the thermal behavior of the rotary kiln shell. To improve the evacuation of heat flow and to reduce the temperature of the shell, we worked on various system parameters, such as the rate of air injection and temperature of environment.

Due to the temperature difference between the inner surface of the rotary kiln and that of the surrounding air, there will be a large heat transfer between these two media. Many works have studied these thermal transfers. We shall mention those of (Mirhosseini et al., 2018), who studied the effect of an absorber placed around the rotary kiln to allow the recovery of part of this heat quantity for other applications. (Shahin et al.,2016) analyzed the thermal energy of a cement plant rotating kiln. They found that an increase of 10 minutes residence time of the materials inside the rotary kiln can reduce fuel consumption. (Acharya et al., 2017) studied the heat transfer by natural convection on a short and long, solid and hollow horizontal cylinder, suspended in the air and placed on the ground. By using different CFD models, (Kumar et al., 2016) discussed the effects of varying input parameters on the temperature profile of the rotary kiln. The obtained results agreed with those of the operation. (Liu et al., 2016) gave a two-fluid approach, and various heat transfer models were applied to a two-dimensional cross-section of a rotary kiln. The results found were compared with the available experimental

data. They found that the significant factors affecting fluid temperature distribution are the initial temperature of the gas and the kiln rotational velocitie. (Li et al., 2015) deduced a three-dimensional digital model of the rotary kiln configured according to the finite element method. They observed that the temperature of the outer wall of the rotary kiln had an approximately linear relationship with the crusting thickness of the kiln. (Sak et al.,2007) studied the effect of turbulence intensity and convection rate on a heated cylinder, with a Reynolds number of 27,700, for the transversal airflow and a cylinder diameter between 0.50 and 1.47 m. (Sanitjai et al., 2004) brought separate empirical correlations of Nusselt number for the region of the laminar boundary layer, re-adhesion of the shear layer region, and the periodic vortex flow region. For the mean Nusselt, an empirical correlation was suggested and compared to previous correlations considering all regimes. (Nakamura et al., 2004) studied experimentally the heat transfer from a cylinder, for *Re* values included between 70 and 30,000, and between 3000 and 15000. (Scholten et al., 1998) reported the experimental results of a heat transfer on a cylinder for a low turbulence range. Then, they studied a higher turbulence range of the free flow. (Sarma and al., 1977) performed measurements of thermal transfer on a horizontal circular cylinder undergoing a transversal airflow by considering two separate cases, i.e., forced convection and mixed convection. The study assumed the following conditions: a constant flux density, Reynolds numbers varying from 500 to 4700, the Grashof numbers ranging from 0.8×10^7 to 3.3×10^7, and the variation of the incidental turbulence intensity between 0.5 and 20 %. (Jain et al., 1976) studied the unstable forced laminar convection of a circular cylinder by solving the Navier-Stokes equations and energy for a flow of an incompressible and unsteady fluid. Using the finite difference method and varying the Reynolds number of 100 to 200, they determined a temperature field around the cylinder and the variation in Nusselt and Strouhal numbers. (Schmidt et al., 1943) produced work dealing with heat transfer to a cylinder. Numerous experimental results investigating heat transfer and the characteristics of hydrodynamics cylinders were presented.

Calculation Domain

The study was done on a 3.6 m diameter rotary kiln. Regarding the length, only the kiln section was taken, as it is the most thermally loaded. The kiln temperature (*T*), reached in these positions is 500 °C (773 K), which could damage the kiln shell. The outside temperature T_∞ is taken equal to 5 °C (278 K). The rotation velocity of the kiln is 5 rpm; the rate of injection of air blowing on the kiln is 5.85 m/s. Figure 1 present the computational domain of the studied model, and the boundary conditions used for our simulation. In our case study, which is a rotary cement kiln, where it operates at high temperatures exceeding 1400°C (internal temperature of the kiln) and around 500°C (external temperature of the shell).

Thus, to allow a combination between the different heat transfer modes at high Reynolds and Rayleigh numbers, the flow is considered to be mainly turbulent. The center of the kiln is placed 20 D upstream and 40 D downstream with respect to the X axis, while with respect to the Y axis, a range of 40 D has been taken, divided into two equal parts upstream and downstream. This computational domain will allow us to avoid the effect of a boundary condition on the characteristics of fluid flow and heat transfer. At the entrance to the domain, Air is considered as the working fluid, with velocity U∞ and a temperature T∞ are imposed. These initial conditions and computational domain are those of the paper of our validation case (Mirhosseini et al, 2018).

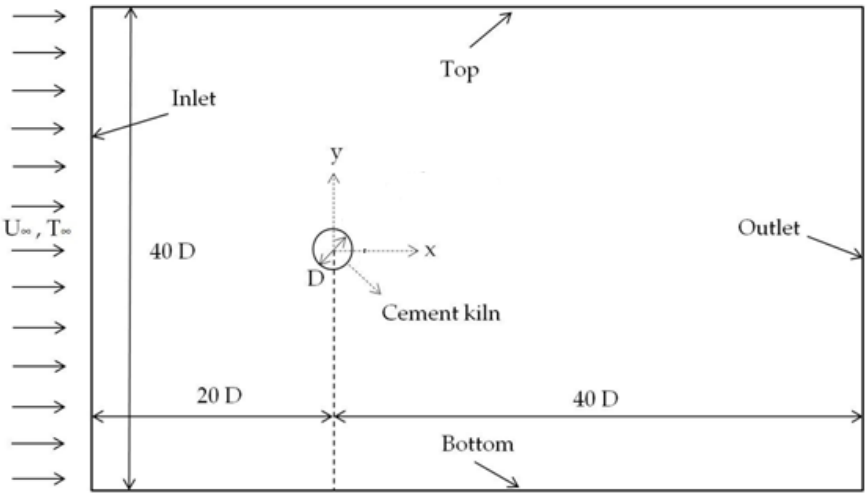

Figure 1. Rotary kiln calculation domain (Mirhosseini et al, 2018)

Modeling of Convective Transfer

Our study consists of an approach of a flow around a horizontal cylinder with a wall at high temperature. For this, it is necessary to quote the adequate formulation for this case. The resolution of the equations governing this flow is done by the K-ω-SST model of the ANSYS-CFX code, the comparison of the results of which constitutes the essential objective of this work. By adopting the SST model simulates the heat transfer of this flow. The Navier Stocks equations considered for this incompressible fluid are Patankar (1980) and Menter (1993):

Continuity equation

$$\frac{\partial U_j}{\partial x_j} = 0 \tag{1}$$

Momentum transport equations

$$\rho U_j \frac{\partial}{\partial x_j}(U_i) = -\frac{\partial P}{\partial x_j} + \mu \frac{\partial^2 u_i}{\partial x_j^2} + \underbrace{\frac{\partial}{\partial x_j}\left(-\rho \overline{u_i' u_j'}\right)}_{\text{Contraintes de Reynolds}} + \rho g_i \tag{2}$$

Energy equation

$$\frac{\partial}{\partial x_j}\left(\rho U_j T\right) = \frac{\lambda}{c_p}\frac{\partial^2 T}{\partial x_j^2} + \frac{\partial}{\partial x_j}\left(-\overline{\rho\, u_j' t_p'}\right) \tag{3}$$

All these equations can be written in the following general form:

$$\underbrace{\frac{\partial(\rho U_j \phi)}{\partial x_j}}_{1} = \underbrace{\frac{\partial}{\partial x_j}\left(\Gamma_\phi \frac{\partial \phi}{\partial x}\right)}_{2} + \underbrace{S_\phi}_{3} \tag{4}$$

Term 1 : transport of ϕ by convection.
Term 2 : transport of ϕ by diffusion.
Term 3 : local production of ϕ.

The SST model has a form similar to the standard k−ω model (Menter, 1993)

$$\frac{\delta}{\delta x_i}(\rho k\, u_i) = \frac{\delta}{\delta x_j}\left[\Gamma_k \frac{\delta k}{\delta x_j}\right] + G_k - y_k + S_k \tag{5}$$

$$\frac{\delta}{\delta x_i}(\rho \omega\, u_i) = \frac{\delta}{\delta x_j}\left[\Gamma_\omega \frac{\delta \omega}{\delta x_j}\right] + G_\omega - y_\omega + D_\omega + S_\omega \tag{6}$$

with $G_k = -\rho \overline{u_i' u_j'} \frac{\partial u_i}{\partial x_i}$, $G_\omega = \alpha \frac{\omega}{k} G_k$: the production term of k, ω respectively.

The effective diffusivities for the SST model are given by:

$$\Gamma_k = \mu + \frac{\pi_t}{\sigma_k} \tag{7}$$

$$\Gamma_\omega = \mu + \frac{\pi_t}{\sigma_\omega} \tag{8}$$

The empirical constants of the SST model are presented in Table 1:

Table 1. Value of the constants of the SST model

α_∞^*	α_∞	β_∞^*	R_β	Mt_0	α_1	$\beta_{i,1}$	$\beta_{i,2}$	$\sigma_{k,1}$	$\sigma_{k,2}$	$\sigma_{\omega,1}$	$\sigma_{\omega,2}$
1	0.52	0.09	8	0.25	0.31	0.075	0.0828	1.176	1	2	1.168

This study deals with heat transfer through the laminar regime convection between the steel shell and its external environment. It describes the movement of a fluid due to changes in density as a function of temperature. Thus, there is a coupling between the dynamic and the thermal. For all convection problems, the wall heat exchanges are measured by highlighting the value of the Nu number.

Since our study has an orientation towards heat transfer with the existence of a rectangular fin with a finite end, we give the equation that governs this phenomenon (Incropera and al, 2007):

$$\frac{d}{dx}\left(\lambda A \frac{dT}{dx}\right) - hp(T - T_{\infty}) = 0 \tag{9}$$

For heat transfer by natural convection, The Nusselt number correlation for the horizontal cylinder with plate fins (Nu) is given by [20]:

$$Nu = \left(1 - 0.117N + 0.353\left(\frac{l}{D_e}\right)\right)\left(0.6 + \frac{0.387\,Ra^{1/6}}{\left(1+(0.559/Pr)^{9/16}\right)^{8/27}}\right)^2 \tag{10}$$

The fin efficiency η, which is written as follows (Hyun et al, 2013):

$$\eta = \frac{(hp\lambda A_c)^{0.5}}{hA_f}\frac{tanh\left(\sqrt{\frac{hp}{\lambda A_c}}l\right)+\left(h/\sqrt{\frac{hp}{\lambda A_c}}\lambda\right)}{1+\left(h/\sqrt{\frac{hp}{\lambda A_c}}\lambda\right)tanh\left(\sqrt{\frac{hp}{\lambda A_c}}l\right)} \tag{11}$$

Optimizing the Grid

The quality of our simulation results is closely linked to the model used. The choice of model is contingent on the type of information we want to obtain from the simulation. We carried out three simulations to optimize the grid for reasons of result precisions and computation time. Table 2 shows the three tested grids. We have opted for a refined uniform grid near the wall of the rotary kiln. According to the results, the second grid gives a good optimization compared to the two others.

Table 2. Grid optimization

Nusselt number	Number of elements	Number of nodes
3942	578,185	557,286
4299	843,932	825,648
4300	1,254,234	1,227,695

Results and Discussion

A thermal study was performed to derive the various parameters that influence the temperature of the rotary kiln and the evolution of the Nusselt number. For this purpose, we have taken different velocities values, air injection, and kiln rotation. To illustrate our results, a tangential line to the top kiln wall parallel to the *x*-axis was designated as a reference for extracting the results. The results of the simulation were obtained using the algorithm SIMPLE as a solution method.

Validation

Table 3 shows the values of the average number of Nusselt calculated in our case study and those published by (Mirhosseini et al, 2018), as well as the percentage difference. The analysis of the results shows that the calculations of our research are very satisfactory. We note that the error in our case of study is evaluated at 3.87 % compared to the analytical solution.

Table 3. The average Nusselt number

	Nusselt number	Difference
Analytical solution (Mirhosseini and al, 2018)	4473.2572	----
Numerical solution (Mirhosseini and al, 2018)	3628.71	18.88%
Numerical solution (our study)	4299.95	3.87%

1st Case "Smooth Cylinder"

Variation of the Injection Air Velocity

The rotary kiln is industrial equipment with an outdoor installation. Thus, it is stressed by air currents which can influence the behavior of the temperature parameter. For this reason, we have taken this factor as a calculation parameter. We varied the air injection velocity from 5.86 m/s to 27.77 m/s. This velocity variation range is taken with respect to the actual conditions of an outdoor environment. The aim of this case study is to determine the effect of the air injection velocity on the thermal behavior of the shell. Four tests were carried out to deduce there from the maximum temperature value of the shell, as well as the Nusselt number.

Table 4. Nusselt number and Shell temperature as a function of air injection velocity

Air velocity (m/s)	5.86	11.11	16.66	22.22	27.77
Number of Nusselt	4375	5503	6210	7360	8845
Shell temperature (°C)	401	330	298	274	255

Table 4 shows the evolution of the Nusselt number and shell temperature as a function of the air injection velocity. Note that the Nusselt number increases proportionally with the air injection velocity; it reaches the value of 8845 for an air injection velocity of 27.77 m/s. This is justified because the increase in velocity directly induces an increase in the Reynolds number, which results in an increase in the Nusselt number. This step consists in deducing the effect of this same parameter, namely the air injection velocity, on the maximum temperature of the shell. Also in Table 4 shows the evolution of the temperature of the shell. Note that the temperature decreases relatively as the air injection velocity increases.

We notice in this part that as the air injection velocity increases, the Nusselt number increases, with a decrease in the temperature of the shell, and thus favoring the cooling of the rotary kiln shell. Figure 2 shows the variation in the temperature of the shell as a function of different values of the air injection velocity. We note that the shape of the curves corresponds well to the laminar regime characterized by the Poiseulle profile. The temperature increases to its maximum value near the shell, then it decreases to ambient temperature (5 °C) beyond the shell. For a high air injection velocity (27.77 m/s), cooling of the shell is observed, given that the temperature decreases from 401 °C to 255 °C, which corresponds to a 36 % rate of decline in temperature.

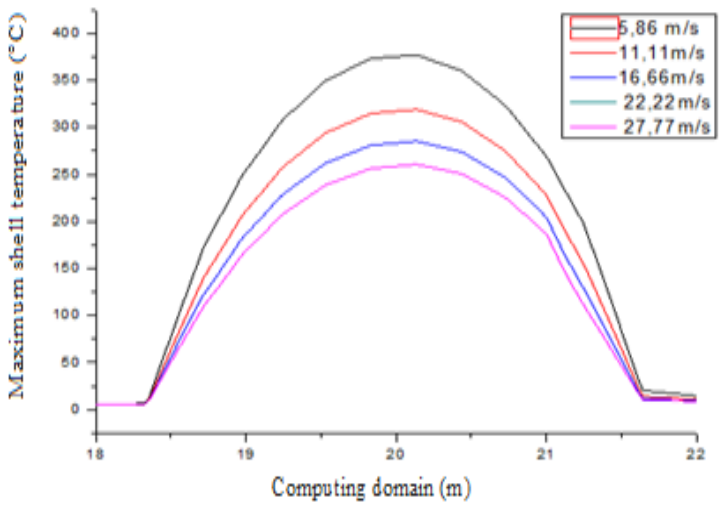

Figure 2. Temperature of the shell as a function of the air injection velocity

Variation of the Injection Air Temperature

In this section, we wanted to know the effect of the variation in ambient air temperature T_{∞}. For this purpose, we used the temperatures 5°C, 18 °C, 25 °C, and 40 °C. Figure 3 presents the variation in the temperature of the shell as a function of the temperature of the air. A rate of increase of 13 % or 276 °C to 289 °C of the shell temperature is observed when the air temperature increases from 5 °C to 40 °C.

We note that this parameter, which is the temperature of the air injected into our kiln, does not have a great effect, because our equipment operates with very high temperatures compared to those of the air injected. The choice of air temperatures is dictated by the environment surrounding the kiln.

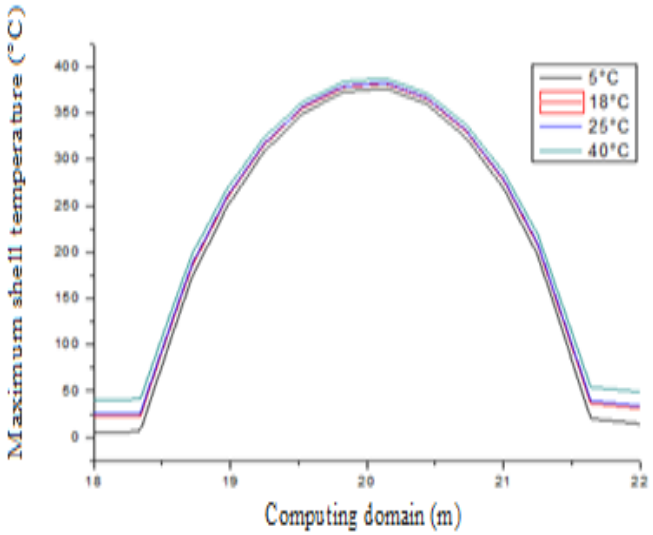

Figure 3. Temperature of the ferrule as a function of the air temperature

2nd Case "Finned Cylinder"

The first section of our study showed us the presence of a very high-temperature gradient between the outer surface of the shell and its environment. The latter indicates the presence of a heat flow that must be released to allow the preservation in good condition of the rotary kiln shell. To this end, in this second part of our study, we wanted to install fins on the shell. This way, it is possible to increase the exchange surface and thus attempt to solve the problem of the heat flow release. The geometric model has been reproduced, wherein the shell has four fins with l = 50 mm long and e = 50 mm wide. The boundary conditions are those used previously, namely that used by (Mirhosseini and al, 2018) in his work, to deduce the effect of these fins on the shell temperature behavior.

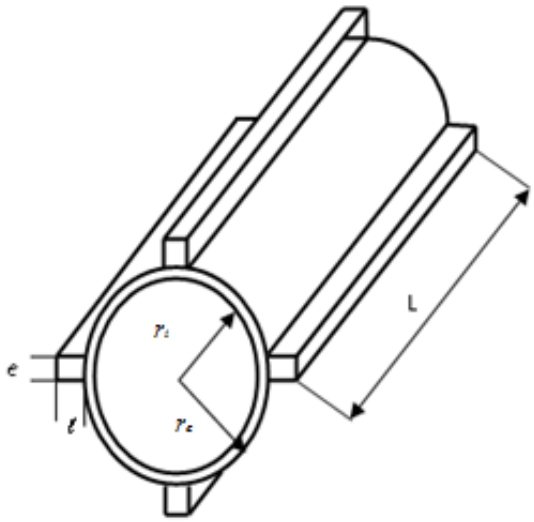

Figure 4 . Rotary kiln with four fins

Variation of the Air Injection Velocity

Under the same conditions as the case of the smooth shell, four tests were carried out to deduce the maximum value of the wall temperature, as well as the Nusselt number corresponding to each air injection velocity (Table 5). The results are shown in Table 5. The increase in the air injection velocity causes a slight decrease in the temperature of the finned shell, unlike the case of the smooth shell, where the temperature decreases considerably.

Table 5. Nusselt number and temperature according to the air injection velocity

Air velocity (m/s)	5.86	11.11	16..66	22.22	27.77
Nusselt number	4375	5503	6210	7360	8845
Shell temperature (°C)	167.7	163.4	158.8	159	158

Figure 5 shows the variation in temperature of the finned shell as a function of different air injection velocities. The temperature profiles have the same tendency due to the position of the results extraction line. The temperature gradient when increasing the air injection velocity is not very significant (6 °C). Compared to the case without fins, we notice the presence at the top of the curve of a stable temperature with light fluctuations due to the presence of the fins. We note the presence of a flat at the level of the extremum of the curve, which is caused by the fin, creating a disturbance and also favoring an increase in temperature. The flats present at the level of the structure are essentially due to the disturbances created by the fins.

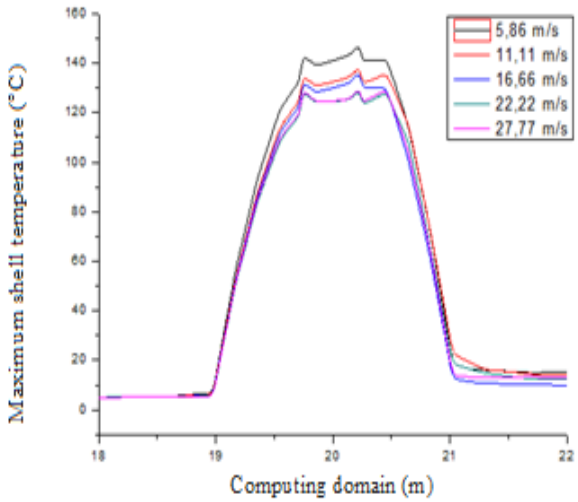

Figure 5. Evolution of the temperature as a function of the air injection velocity

Comparison between the Smooth Shell and the Finned Shell

To show the fins effect on the temperature of the kiln shell, a comparison was made between the two case studies (smooth and finned). Figure 6 shows the evolution of the temperature for the two cases. It is noted that the insertion of the fins causes a decrease in the maximum temperature for the finned shell. This decrease is about 36 %, a decrease of the maximum temperature of 401 °C for the smooth shell to 164°C for the finned shell. It is also noted that the increased temperature can only occur from 1 meter in length from the beginning of the shell, for the smooth case. While for the finned case, this only happens at 1.8 meters. This increase in distance is yielded by the decrease in temperature.

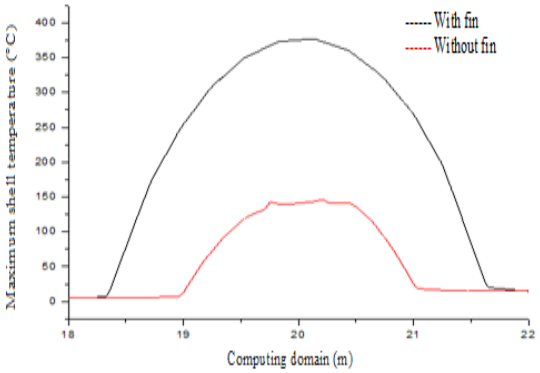

Figure 6. The temperature evolution of the smooth and finned shells

Table 6. Comparison of Nusselt number

Shells	Smooth	Finned
Nusselt Number	4299	4375

Table 7. Comparison of shell temperature as a function air velocity

	Air velocity (m/s)	5.86	11.11	16.66	22.22	27.77
case “smooth cylinder”	Shell temperature (°C)	401	330	298	274	255
case “finned cylinder”	Shell temperature (°C)	167.7	163.4	158.8	159	158

Table 6 shows the Nusselt number values in the case of smooth and finned shells for a value of the rotary velocity of the kiln of 5 rpm. From the results, it can be said that the insertion of the fins causes an increasein the Nusselt number. This increase in the Nusselt number results in asignificant exchange of the heat flow with the shell. Similarly, Table 7 summarize the drop in the external temperature of the shell. This decrease is clearly visible for this parameter, namely the air injection velocity on the kiln.

Conclusion

In this study, a numerical modeling was conducted by combining an unstructured mesh with the finite volume method. The solution was obtained by using the SIMPLE algorithm (pressure-velocity coupling). The aim was to study the thermal behavior of a rotary kiln shell. Two cases of numerical simulations were carried out. The first one consisted of simulating the rotary kiln section with the most significant thermal stress, namely the shell part where the external wall temperature was 500 °C. This shell was taken in this case as being smooth. In the second case, the same simulations were reproduced with the same boundary conditions, with additional fins inserted to the outer surface of the shell.

The results showed that the increase in Nusselt number and the decrease in temperature were a function of the air injection velocity for both cases. For a smooth shell, the rate of decrease was 36 % by increasing the air injection velocity. While for a finned shell, the decrease was 41.82 %. Overall, the predominant parameter for the shell cooling is the air injection velocity for both geometric configurations. More significant cooling may be obtained when the shell is equipped with fins.

Scientific Ethics Declaration

The authors declare that the scientific ethical and legal responsibility of this article published in EPSTEM journal belongs to the authors.

Acknowledgements

* This article was presented as an oral presentation at the International Conference on Technology, Engineering and Science (www.icontes.net) held in Antalya/Turkey on November 16-19, 2022.

References

Acharya, S., & Dash, S. K. (2017). Natural convection heat transfer from a short or long, solid or hollow horizontal cylinder suspended in air or placed on ground. *Journal of Heat Transfer*, *139*(7): 072501

Gaurav, G. K., & Khanam, S. (2016). Analysis of temperature profile and% metallization in rotary kiln of sponge iron process through CFD. *Journal of the Taiwan Institute of Chemical Engineers*, *63*, 473-481.

Incropera, F. P., DeWitt, D. P., Bergman, T. L., & Lavine, A. S. (1996). *Fundamentals of heat and mass transfer*. New York: Wiley.

Jain, P. C., & Goel, B. S. (1976). A numerical study of unsteady laminar forced convection from a circular cylinder. *J. Heat Transf*, *98*, 303-307.

Kim, H. J., An, B. H., Park, J., & Kim, D. K. (2013). Experimental study on natural convection heat transfer from horizontal cylinders with longitudinal plate fins. *Journal of Mechanical Science and Technology*, *27*(2), 593-599.

Liu, H., Yin, H., Zhang, M., Xie, M., & Xi, X. (2016). Numerical simulation of particle motion and heat transfer in a rotary kiln. *Powder Technology*, *287*, 239-247.

Li, G., Liu, Z., Jiang, G., Liu, H., & Xiong, H. (2015). Numerical simulation of the influence factors for rotary kiln in temperature field and stress field and the structure optimization. *Advances in Mechanical Engineering*, *7*(6), 1687814015589667.

Menter, F. (1993, July). Zonal two equation kw turbulence models for aerodynamic flows. In *23rd fluid dynamics, plasmadynamics, and lasers conference* (p. 2906).

Mirhosseini, M., Rezaniakolaei, A., & Rosendahl, L. (2018). Numerical study on heat transfer to an arc absorber designed for a waste heat recovery system around a cement kiln. *Energies*, *11*(3), 671.

Nakamura, H., & Igarashi, T. (2004). Variation of Nusselt number with flow regimes behind a circular cylinder for Reynolds numbers from 70 to 30 000. *International Journal of Heat and Mass Transfer*, *47*(23), 5169-5173.

Patankar, S. V. (1980). *Numerical heat transfer and fluid folw*. New York: McGraw Hill.

Sak, C., Liu, R., Ting, D. K., & Rankin, G. W. (2007). The role of turbulence length scale and turbulence intensity on forced convection from a heated horizontal circular cylinder. *Experimental Thermal and Fluid Science*, *31*(4), 279-289.

Sanitjai, S., & Goldstein, R. J. (2004). Forced convection heat transfer from a circular cylinder in crossflow to air and liquids. *International Journal of Heat and Mass Transfer*, *47*(22), 4795-4805.

Sarma, T. S., & Sukhatme, S. P. (1977). Local heat transfer from a horizontal cylinder to air in cross flow: influence of free convection and free stream turbulence. *International Journal of Heat and Mass Transfer*, *20*(1), 51-56.

Schmidt, E., & Wenner, K. (1943). Heat transfer over the circumference of a heated cylinder in transverse flow. *Forschung auf dem Gebiete des Ingenieurwesens*, *12*(NACA-TM-1050).

Scholten, J. W., & Murray, D. B. (1998). Unsteady heat transfer and velocity of a cylinder in cross flow-I. Low freestream turbulence. *International Journal of Heat and Mass Transfer*, *41*(10), 1139-1148.

Shahin, H., Hassanpour, S., & Saboonchi, A. (2016). Thermal energy analysis of a lime production process: Rotary kiln, preheater and cooler. *Energy Conversion and Management*, *114*, 110-121.

Zdravkovich, M. M. (1997). *Flow around circular cylinder*. New York, NY: Oxford University Press.

Author Information

Mohammed Bouhafs
Institute of Maintenance and Industrial Safety, Department of electromecanic, University of Oran 2 Mohamed Ben Ahmed, Algeria.
Contact e-mail:*mohamedbouhafs@yahoo.fr*

Abed Meghrir
Institute of Maintenance and Industrial Safety, Department of electromecanic, University of Oran 2 Mohamed Ben Ahmed, Algeria.

To cite this article:

Bouhafs, M. & Meghrir, A. (2022). Effect of the addition of a fin on the thermal behavior of the shell of a rotary cement kiln. *The Eurasia Proceedings of Science, Technology, Engineering & Mathematics (EPSTEM), 21*, 371-379.

The Eurasia Proceedings of Science, Technology, Engineering & Mathematics (EPSTEM)
ISSN: 2602-3199

The Eurasia Proceedings of Science, Technology, Engineering & Mathematics (EPSTEM), 2022

Volume 21, Pages 380-387

IConTES 2022: International Conference on Technology, Engineering and Science

The Role of Drone Photogrammetry, Remote Sensing and GIS Methods in the Detection of Ore Areas and Their Surroundings

Muntaha Kassım Hayder AL-ZUBADE
University of Technology,Baghdad

Oyku ALKAN
Graduated Istanbul Technical University

Abstract: Mining works take place in a laborious and long process. The terrestrial methods used include classical activities that are economically very expensive and do not lead directly to results. The geography studied in mining areas brings with it many difficulties. It requires different methods in order to ensure the sustainability of mining operations and to use time efficiently. This study was carried out in order to contribute to mining research by using the most effective methods of the study conducted for this purpose. The study area was carried out in the Bayat District of Corum, in the western part of the Central Black Sea Region. Drone photogrammetry and different remote sensing methods were used to investigate the metallic mines in this area. The study which was applied in a license area where the height difference is high in difficult geographical conditions. In the first stage of the study, the digital elevation model of the region was prepared by taking drone images from different heights in difficult geographical conditions. In the second stage, using the high spectral resolution of the ASTER satellite data, different remote sensing methods were used and the mineral presence in the region was examined. Ore-dense areas were determined with terrain maps created using data from drone and ASTER satellite images. For this purpose, unsupervised classification methods and band ratio techniques were used to extract the potential mineral distribution. The samples obtained from the ground control points taken as field-validated and the results of the regression analysis were evaluated together.

Keywords: Remote sensing, Drone photogrammetry, GIS

Introduction

With the rapid development of technology, the widespread use of Remote Sensing (RS) methods and research is considered an important innovation. Analyzes with infrared and thermal bands of high spectral resolution satellite images play an important role in the investigation of potential mining fields. A small amount of ore resources are used in the world and there are countless potentials waiting to be discovered. RS technology has taken its place in the spectrum of scientific research as a multidisciplinary. Studies with remote sensing methods have begun to leave their mark on the world literature.

Analyzing systems that provide high-resolution images of mining areas are UVA tools. Drone-based mining exploration gains value when combined with remote sensing methods. Drones have quickly become one of the most cost-effective and efficient tools for collecting high-resolution data, aligning between larger-scale, lower-resolution satellite data collection and much more limited traditional terrestrial survey approaches (Hill,2022).

A study conducted in Yankari Park in Nigeria used ASTER and Hyperion satellite data to identify alteration minerals. The algorithms used are based on Linear spectral separation and spectral angle mapping (Abubakar et al., 2017). Instead of the spectral angle mapper used in this study, the spectral correlation mapper, which is the corrected version of these methods, was preferred.

In another study conducted in the Sittampundi Anorthositic complex in South India; For thermal waters, VNIR and SWIR data from nine band high spectral resolution ASTER satellite data were examined. The usability of different multispectral satellite data and mineral ratio images for lithological differentiation has been investigated (Arivazhagan et al., 2017). A similar study was conducted in Oman to investigate the mineral mapping performance of ASTER satellite data in arid regions. ASTER bands for mineral mapping, band ratio literature was reviewed (Rajendran & Nasir, 2018).

In another study to determine the band ratio of hydrothermal alteration minerals, principal component analysis, Crosta technique and spectral angle mapper techniques were applied using ASTER satellite data. Spectroradiometry was used to extract the spectral signatures of the stone samples. (Yalçın et al., 2017). Different RS methods of ASTER bands were investigated to analyze potential mining fields in Çorum province. (Alkan et al., 2017).

Data obtained from satellites or Unmanned Aerial Vehicles (UAVs) makes these hard work equipped in a short time. Unmanned Aerial Vehicles (UAVs) or drones is a proven technology for some of these activities (Wyard, 2022). The diversity of remote sensing methods and high spatial resolution of drone data in the exploration of metallic minerals makes a great contribution to the studies. This study was carried out by combining effective methods to contribute to mineral exploration. For this purpose RS, UVA Drone and GIS processes were jointly used.

Method

Drone Photogrammetry and Remote Sensing

Drone photogrammetry and different remote sensing methods were used to investigate the metallic mines in this area. The digital elevation model of the region was prepared by taking drone images from different heights in difficult geographical conditions. Using the high spectral resolution of the ASTER, different remote sensing methods were used and the mineral presence in the region was examined. Ore-dense areas were determined using merged data from drone and ASTER images. The samples obtained from the ground control points and the drilling for field-validated.

Study Area

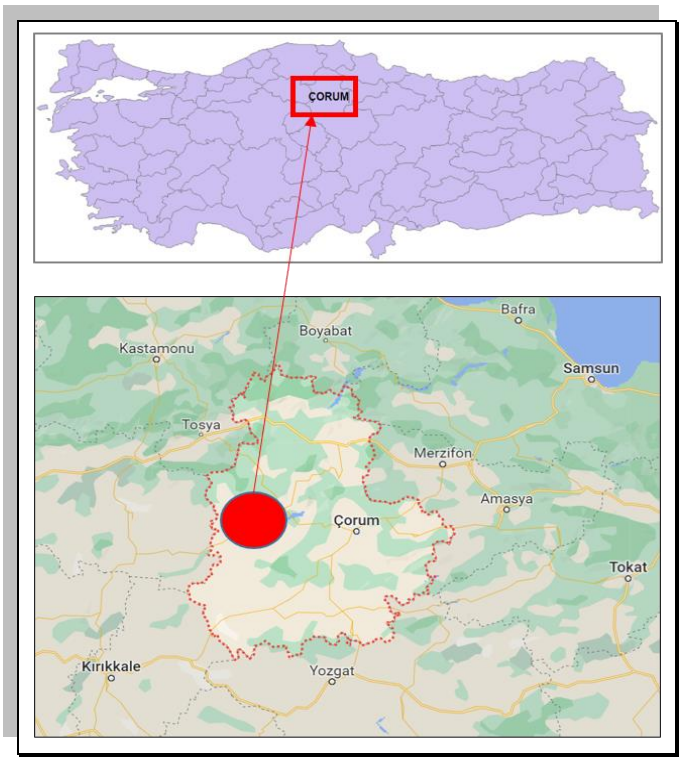

Figure 1. Study area

The study area was carried out in the Bayat district of Corum, in the western part of the Central Black Sea Region. Projection is UTM, Datum WGS 84 and Zone 36 (Figure 1). A continuation of the significant parts of Central Anatolia Region in the Central Black Sea Region; the most part springs in the Yeşilırmak Basin (Gulersoy, 2013). Parallel to the tectonic development of Anatolia, Corum province is located on a large area covered by metamorphic masses, conglomerates, limestones, and sandstones. In this geological formation, the probability of high temperature harboring of metamorphic belts is considered important in terms of investigating potential ore areas (Ongur, 2005). Classical local drilling activities were carried out in geothermal studies in the research area. No study has yet to be related Remote Sensing (RS) and Drone Photogrammetry (DP) adds high-value effects to this work.The study which was applied in a license area where the height difference is high in difficult geographical conditions. GCP, Drilling Check Points (DCP).

Experimental Design and Methods

Drone photogrammetry and different remote sensing methods were used to investigate the metallic mines in this area. In the first stage of the study, the digital elevation model of the region was prepared by taking drone images from different heights in difficult geographical conditions. In the second stage, using the high spectral resolution of the ASTER satellite data, different remote sensing methods were used and the mineral presence in the region was examined. Ore-dense areas were determined with terrain maps created using data from drone and ASTER satellite images. For this purpose, unsupervised classification methods and band ratio techniques were used to extract the potential mineral distribution. The samples obtained from the ground control points taken as field-validated and the results of the regression analysis were evaluated together.

Ground sampling points were selected by using multi-spectral satellite data to be used in determining potential mineral areas in pre-classification. ASTER satellite multispectral bands are widely used in geological surveys. Separate field studies GPS measurements were carried out to determine the locations of soil classes in 4 different regions in the study area. By evaluating the spectral signatures of the samples by classification analysis, appropriate spectral ranges were determined and new test areas were created for the field study. The new samples analysis were completed by determining their positions with GPS were added to the spectral library inventory. Geometric and radiometric corrections have been applied to satellite data. Atmospheric corrections have been applied to visible, visible-infrared bands of ASTER satellite. The flow chart showing the working steps is shown in Figure 2.

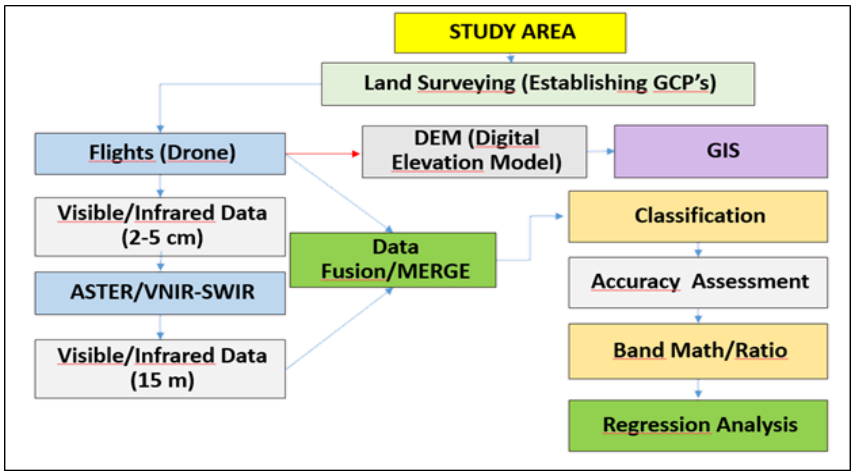

Figure 2. Flow chart

Drone studies were carried out with a two planned flight by determining the ground control points. Due to the difficult geography, the flight altitude was realized as 90 m. The mosaic and DSM images obtained were combined using the data fusion method. In the first stage of the study, mosaic image and DSM image of the region was prepared by processing Pix4d software (Figure 3).

The projection system is described in UTM and northern 36 segments. The location data of these points, Turkey national fixed satellite stations (TUSAGA-ACTIVE), is taken and converted into the national network based on the GPS coordinate system. One of the reasons for working with GPS was to test the positional accuracy of the sampling points on Google Earth, City Surf Globe and Orthophoto maps. Another was to compare the spatial accuracy of the ASTER satellite image with high spatial resolution images. It is aimed to increase the accuracy

of image classification due to the ground accuracy of the samples by means of land measurements for sampling purposes (Alkan, 2019).

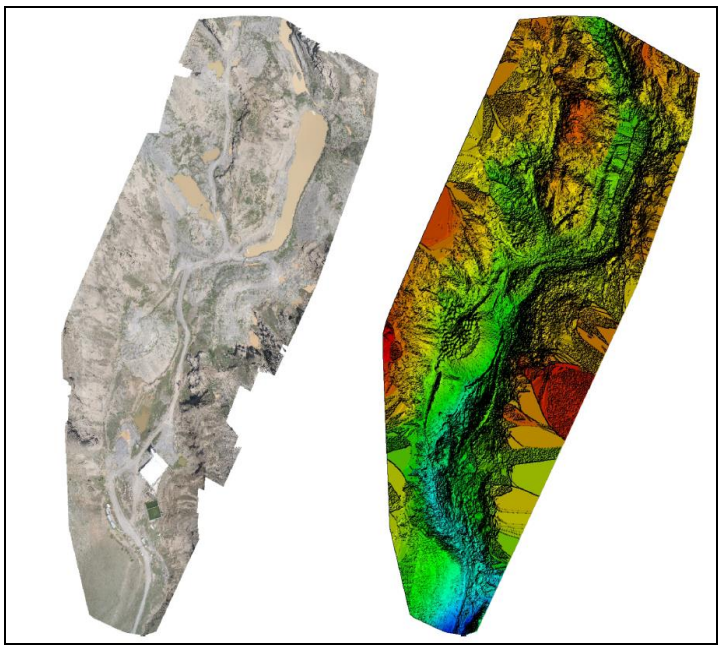

Figure 3. Ortomosaic and DSM images designed by UAV

Drone photogrammetry and different remote sensing methods were used to investigate the metallic mines in this area.The digital elevation model of the region was generated by processing of the drone images from different heights in difficult geographical conditions. Using the high spectral resolution of the ASTER, different remote sensing methods were used and the mineral presence in the region was examined. Ore-dense areas were determined using merged data from drone and ASTER images. The samples obtained from the ground control points and the drilling for field-validated.

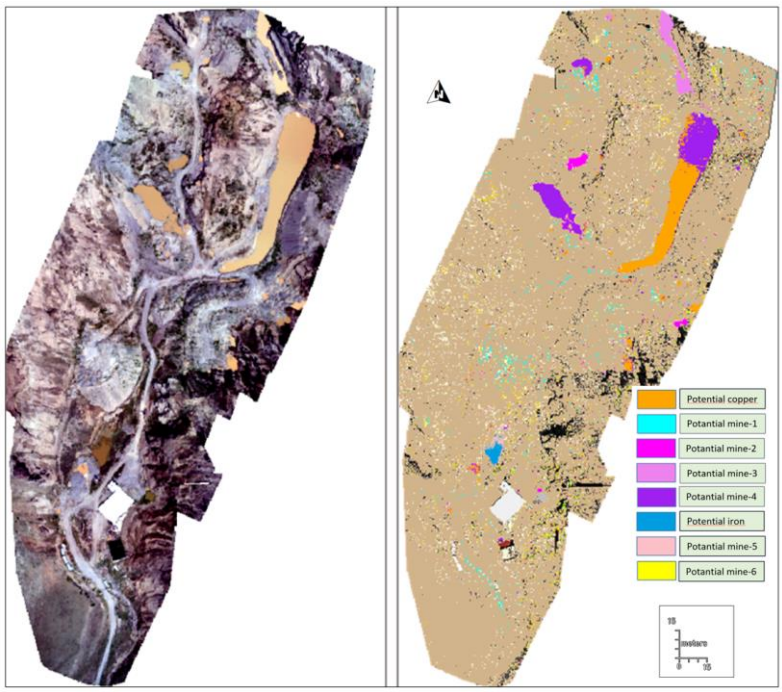

Figure 4. MLC Image

As for the exploration of ore- potential estimated in the study area, obtained by field studies; 55 points measured by GPS formed the sampling points for the classification process. It will be used for this purpose have investigated different algorithms for the selection of classification methods MLC (Maksimum Likelihood) and

SCM (Spectral Correlation Mapper) algorithms.Spectral Correlation Mapping algorithm which are defined as the modified version of SAM (Spectral Angle Mapper) (Figure 4 &5). Via pre-classification process, GPS measurements performed in the field where the mine drilling points with the coordinates of the samples assigned to eight different classes ASTER data in the same projection.

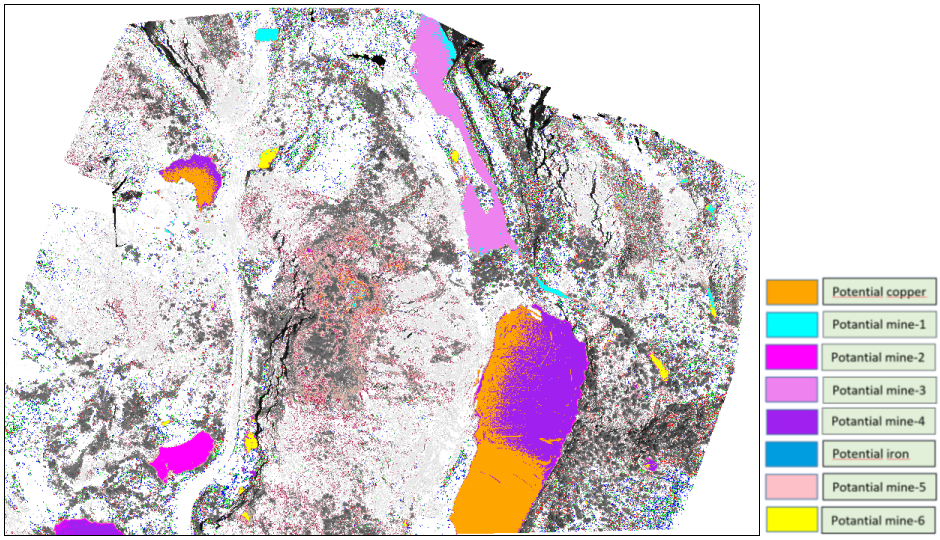

Figure 5 . SCM Image

DEM was generated by processing DSM image to achieve different elevations of the potential minerals for the study area (Figure 6).

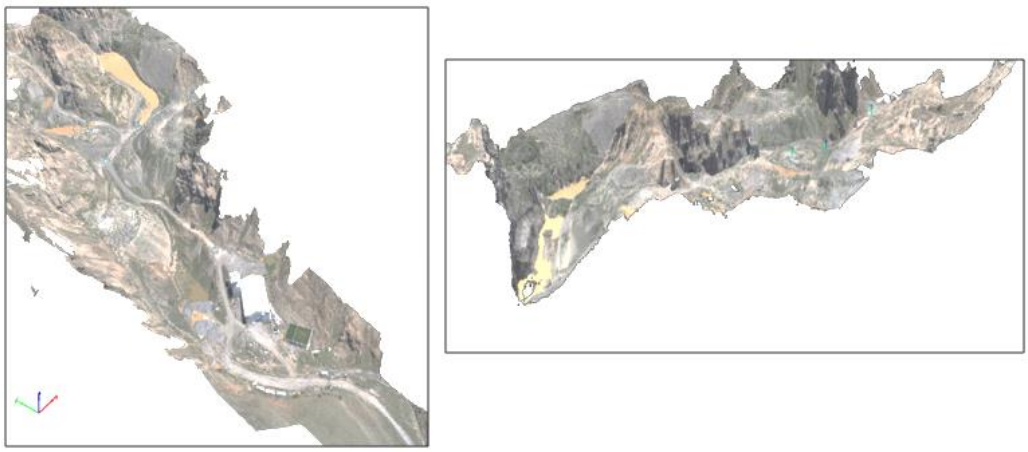

Figure 6 . DEM (Digital elevation model)

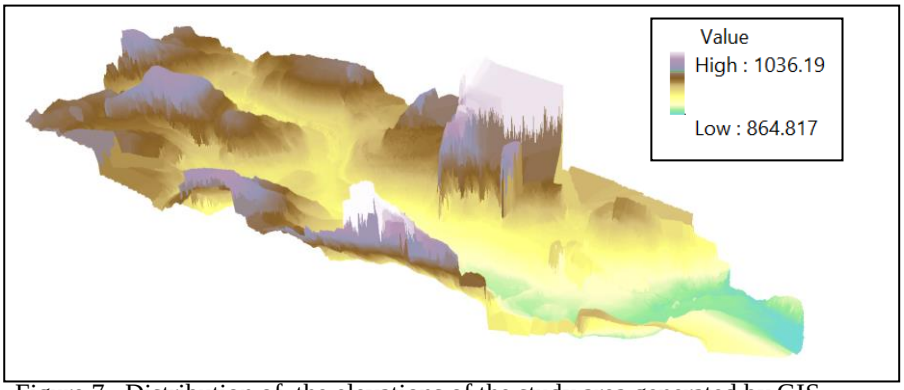

Figure 7 . Distribution of the elevations of the study area generated by GIS

Accuracy analysis results were compared by using two different classification methods (MLC and SCM) for the investigation of potential mineral areas. Accuracy analysis result for MLC 0.91 and SCM 0,94. The overall Kappa statistical values obtained for the eight main classes in the MLC and SCM classifications are shown in

Table 1. Kappa, which mainly calculates the image classification accuracy, was obtained with the following formula.

$$\kappa = \frac{N \sum_{i=1}^{r} x_{ii} - \sum_{i=1}^{r} x_{i+} * x_{+i}}{N^2 - \sum_{i=1}^{r} x_{i+} * x_{+i}}$$

In the formula, r = number of classes, xii = diagonal elements of error matrix, xi + = sum of rows; x+ i = column total, N = total number of pixels in error matrix.

Table 1. Kappa statistics of the MLC and SCM classifications

Class	Kappa	Class	Kappa
Copper	0.9412	Copper	0.9742
Iron	0.9754	Iron	0.9621
Mine-1	0.8821	Mine-1	0.9158
Mine-2	0.9087	Mine-2	0.8923
Mine-3	0.9147	Mine-3	0.9355
Mine-4	0.8941	Mine-4	0.9290
Mine-5	0.9214	Mine-5	0.8934
Mine-6	0.8946	Mine-6	0.9271

Another analysis that has been studied is on the ASTER thermal 14 band, it was aimed to reveal the mineral areas with high thermal energy in the region. Band 14 of the ASTER satellite which has 5 strong thermal bands, was tested for this study. Ore-dense areas are shown in Figure 8.

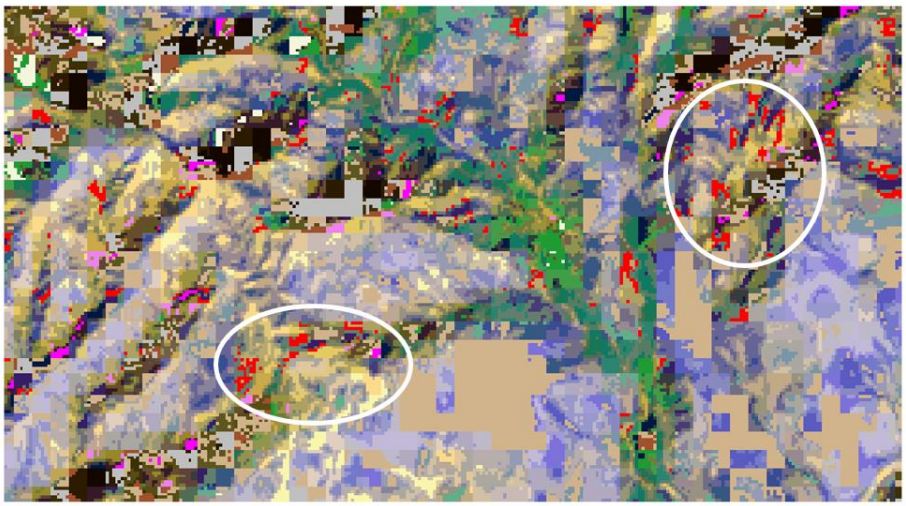

Figure 8 . Mineral presence created by ASTER 14 band performance

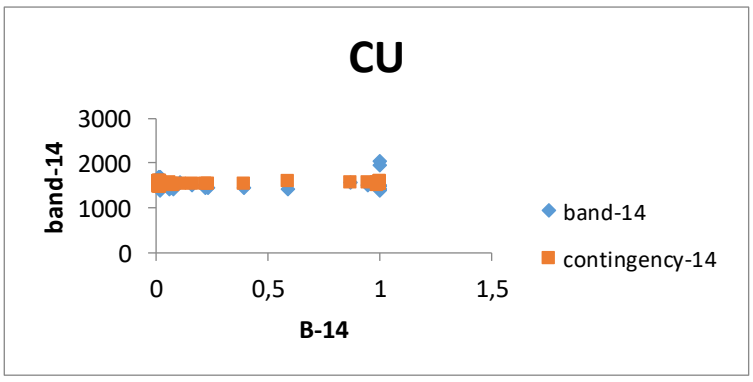

Figure 9 . Performance of the ASTER 14 band for Cu Minerals

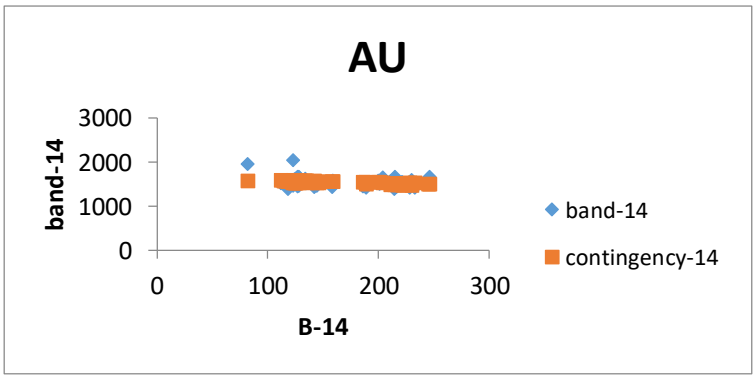

Figure10 . Performance of the ASTER 14 band for Au Minerals

The regression graph of Cu nad Au potential areas is shown in figure 9 and 10.

Results and Discussion

The aim of this study, which was carried out using RS and Drone photogrammetry methods, was to determine the presence of minerals.. For this purpose, the MLC and SCM performances of the classification methods studied were evaluated together and an accuracy of over 90% was obtained. In the regression analysis for the estimated potential areas, 55 points selected from ground-tested test points were used in the classification procedures. The regression analysis and the relation of mineral elements expected to exist in the predicted potential mineral areas were investigated particularly focused on Copper (Cu) and the Gold (Au) surroundings.

In the regression analysis for estimated potential geothermal areas, 24 points selected from the drilling-tested points were used in the classification procedures for the histograms of mineral groups respectively. Drone photogrammetry and remote sensing methods can be used for the mine areas efficiently.-High spatial resolution (UAV:2-5 cm) and high spectral resolution ASTER images effectivly used in data fusion method to explorate minerals.

Conclusion

The use of RS and drone-based photogrammetry methods in the preliminary studies of mining research is great importance in terms of the cost of drilling activities. RS methods which integrate topographic, geological and geomorphological features with the help of satellite images can be used in researches, surface symptoms can be examined and statistics and potential mineral fields can be reached.

Scientific Ethics Declaration

The authors declare that the scientific ethical and legal responsibility of this article published in EPSTEM journal belongs to the authors.

Acknowledgements or Notes

* This article was presented as an oral presentation at the International Conference on Technology, Engineering and Science (www.icontes.net) held in Antalya/Turkey on November 16-19, 2022.

References

Abubakar, A, J., Hashim, M. & Pour, A. B. (2017). Spectral mineral mapping for characterization of subtle geothermal prospects using ASTER data, *Journal of Physics: Conference Series, 852* (1), 012024Plath, S. (2000). *The unabridged journals.* K. V. Kukil (Ed.). New York, NY: Anchor.

Alkan , Ö. (2018, December 17). *Statistical accuracy analysis of remote sensing methods used for mineral deposits and geothermal research in middle-north Anatolia region*, Doctorate Thesis, Istanbul Technical University, İstanbul.

Alkan, Ö., Coşkun, H. G., Çelik, H., Alkan, M. N., Kandil, S., Okur, Y. & Eraydın, E. (2018). Uzaktan algılama yöntemleri ile potansiyel jeotermal alanların belirlenmesi, *Afyon Kocatepe Üniversitesi Fen ve Mühendislik Bilimleri Dergisi, 17*, 171-182.

Ayoobi, I. & Tangestani, M., H. (2018). Evaluation of subpixel unmixing algorithms in mapping the porphyry copper alterations using EO-1 Hyperion data, a case study from SE Iran, *Remote Sensing Applications: Society and Environment, 10* (2018), 120-127.

Guha, A. & Kumar, V. (2016). New ASTER derived thermal indices to delineate mineralogy of different granitoids of an Archaean Craton and analysis of their potentials with reference to Ninomiya's indices for delineating quartz and mafic minerals of granitoids—An analysis in Dharwar Craton, India, *Ore Geology Reviews, 74*, 76-87.

Jackisch,R., H., B.H., Zimmermann, R., Sørensen, E.V., Pirttijärvi,M.,Kirsch,M., Salmirinne,H., Lode,S., Kuronen, P., & Gloaguen, R., (Feb,2022). Drone-based magnetic and multispectral surveys to develop a 3D model for mineral exploration at Qullissat, Disko Island, Greenland, *Solid Earth, 13*, 793–825, 2022.

Karimpour, M. H., Stern, C. R., & Mazaheri, S. A. (2009). Hydrothermal alteration mapping in SW Birjand, Iran, using the advanced spaceborne thermal emission and reflection radiometer (ASTER) image processing. *Journal of Applied Sciences, 9*(5), 829-842.

Meer., F., Hecker, C., & Ruitenbeek, F. V. (2014). Geologic remote sensing for geothermal exploration: A review, *International Journal of Applied Earth Observation and Geoinformation, 33*(1):255-269.

Pour, A. B., & Hashim, M. (2012). The application of ASTER remote sensing data to porphyry copper and epithermal gold deposits, *Ore Geology Reviews, 44*, 1-9.

Rajendran, S. & Nasir, S. (2017). Characterization of ASTER spectral bands for mapping of alteration zones of volcanogenic massive sulphide deposits, *Ore Geology Reviews, 88*, 317-335.

Shafaroudi, M., Karimpour, M. H., Stern, C. R. & Mazaheri, S. A. (2009). Hydrothermal alteration mapping in SW Birjand, Iran using the advanced spaceborne thermal emission and reflection radiometer (ASTER) image processing, *Journal of Applied Sciences, 9*(5), 829-842.

Shirazi ,A., Hezarkhani , A., Pour, A. B., Shirazy, A.& Hashim, M., (2022, November.). Neuro-Fuzzy-AHP (NFAHP) technique for copper explorationusing advanced spaceborne thermal emission and reflectionradiometer (ASTER) and geological datasets in the sahlabad mining area, east Iran the eclipse of listening. *The New Criterion, 15*(30), 5-13.

Srivastava,S., Seng,K.P.,Ang,L.M,, Pachas, N. A. & Lewis, T. (Eds.). (2022). Drone-based environmental monitoring and image processing, *Sensors, 22,*7872, 2-14

Author Information

Muntaha Kassım Hayder Al-Zubade
University of Technology,Baghdad, Iraq
Contact e-mail: *muntahaalzubade@gmail.com*

Oyku Alkan
Graduated Istanbul Technical University, Turkey

To cite this article:

Alzubade, M.K.H. & Alkan, O. (2022). The role of drone photogrammetry, remote sensing and GIS methods in the detection of ore areas and their surroundings. *The Eurasia Proceedings of Science, Technology, Engineering & Mathematics (EPSTEM), 21*, 380-387.

The Eurasia Proceedings of Science, Technology, Engineering & Mathematics (EPSTEM)
ISSN: 2602-3199

The Eurasia Proceedings of Science, Technology, Engineering & Mathematics (EPSTEM), 2022

Volume 21, Pages 388-395

IConTES 2022: International Conference on Technology, Engineering and Science

Investigation of High Range Water-Reducing Admixture Requirement in Cementitious Systems Containing Fly Ash with Different Utilization Ratio and Fineness

Hatice Gizem SAHIN
Bursa Uludag University

Oznur BIRICIK
Bursa Uludag University

Ali MARDANI
Bursa Uludag University

Abstract: Mineral additives are widely used in cementitious systems to reduce CO_2 emissions. In this context, it was understood that fly ash, an industrial by-product, is the most widely used mineral additive. It is necessary to examine the binder-water reducing admixture compatibility in cementitious systems containing mineral additives. The fineness and utilization ratio of mineral additives seriously affect the compatibility in question. In this study, the effect of the use of fly ash in different utilization ratios and fineness on the flow value and consistency retention performance of mortar mixtures containing water-reducing admixture in different ratios was investigated. For this purpose, 4 different usage dosages of water-reducing admixtures (0%, 1%, 1.5% and 2%), 2 different utilization ratios (0, 15% and 30%) and fine fly ash (4000 and 6000 cm^2/g) were used. A total of 20 mortar mixtures were prepared. The flow performance of the prepared mixtures for 60 minutes was examined. As expected, the initial and 60th-minute flow values of all mixtures increased with the increase in the use of water-reducing admixture. It was understood that the change of fly ash fineness did not have a significant effect on the initial and 60th-minute flow values of the mixtures. Similarly, it was observed that the change in the utilization ratio of fly ash did not have a great effect on the initial and 60th-minute flow performance in the mixtures with no admixtures, 1% and 2% admixture usage dosages. However, it was determined that the increase in fly ash utilization ratio in mixtures with an admixture usage dosage of 1.5% increased the initial and 60th-minute flow values of the mortar mixtures. Also, it was observed that mortar mixtures containing 2% water-reducing admixture generally have the highest consistency retention capacity (95-100%), regardless of fly ash fineness and utilization ratio.

Keywords: Admixture usage dosage, Fly ash fineness and utilization ratio, Flow value, Consistency retention capacity

Introduction

During cement production, 8% of the total CO_2 emitted in the world is formed. In addition to reducing the carbon footprint, the use of mineral additives in cementitious systems has become inevitable in order to expand sustainability (Mardani-Aghabaglou, 2016; Al-Kutti et al., 2018; Ozen et al., 2022a; Sahin & Mardani, 2022a). In this context, mineral additives such as blast furnace slag, silica fume, metakaolin, rice husk ash, trass and fly ash are used in cementitious systems (Biricik et al., 2022a; Mardani-Aghabaglou et al., 2019; Sezer et al., 2016; Yuksel et al., 2016; Bayqra et al., 2022). It was understood that the fineness values of mineral additives resulting from industrial production can vary in a wide range (Win et al., 2022). In this context, it was reported

by various researchers that the effect of mineral admixture fineness on the fresh and hardened properties of cementitious systems should be investigated (Aytekin et al., 2022; Biricik et al., 2022b). Some studies on the subject are summarized. It was reported that the compressive strength and carbonation resistance of the concrete mixture increase with the increase in the fineness of the blast furnace slag (Rivera et al., 2021). However, it was reported that with the increase of the fineness of the fly ash, the heat of hydration increased (Han et al., 2019), interfacial transition zone (ITZ) (Fanghui et al., 2015), compressive strength (Arel and Shaikh, 2018), porosity (Hsu et al., 2019) and sulfate resistance (Chindaprasirt et al., 2004) improved in concrete mixtures. It was stated that this is due to the increase in the physical filling effect and the pozzolanic reaction with the increase in fineness (Han et al., 2019). However, in another study by Hsu et al (2018), it was stated that the pozzolanic reactivity is limited due to the increase in the risk of flocculation with the increase of fly ash fineness. It was stated that the heat of hydration decreases with the increase of fly ash content, and its fluidity increases due to the ball-bearing effect and smooth surface texture (Sahin & Mardani, 2022b; Moghaddam et al., 2019; Biricik and Mardani, 2022c). However, it was determined that fly ash substitution negatively affects the fluidity of the mixtures (Nguyen et al., 2019).

In addition, the presence of these fines in the system directly affects the adsorption properties of the water-reducing admixture (Mardani et al., 2017). It was declared by various researchers that the need for water-reducing admixtures will increase depending on the increase in the total surface area with the increase in the amount of fine material in the system (Faltin, 2022). However, Mardani et al. (2017) and Karakuzu et al. (2021) reported that the water-reducing admixture can adsorb more strongly to fine particles. In addition, Burgos et al. (2012) stated that the substitution of mineral additive with a higher specific surface area compared to cement causes extra surface formation leading to competition with cement for adsorption of PCE. Palacios et al. (2009) stated that the need for admixtures decreased with the substitution of blast furnace slag in the paste mixture. Yingliang et al. (2020), on the other hand, emphasized that ultrafine blast furnace slag negatively affected the fluidity of mortar mixes, but this negative effect decreased with the use of PCE. It was declared that the amount of water-reducing admixture adsorbed on cement paste containing fly ash depends on the utilization ratio of fly ash, its chemical properties, fineness and density. It was emphasized that the PCE requirement decreased with the use of fly ash (Ng & Justnes, 2016). Similar results were found by Altun et al. (2021) for mixtures containing up to 30% fly ash.

It was understood from the literature that various studies were conducted on the effect of fly ash usage rate and fineness on adsorption properties, fluidity and time-dependent behavior. However, contradictory results were found due to the large number of active parameters and the increase in fineness and the existence of 2 different mechanisms. In this study, the effect of the use of water-reducing admixture on the time-dependent flowability of mortar mixtures containing fly ash at different utilization ratios and fineness was investigated.

Material and Method

Material

Within the scope of the study, CEM I 42.5R type portland cement (PC) produced by OYAK Cement and fly ash supplied from Orhaneli Thermal Power Plant were used as binders. The chemical component, physical and mechanical properties of cement and fly ash supplied by the manufacturer are given in Tables 1 and 2, respectively.

Table 1. Chemical composition, physical and mechanical properties of cement

Chemical Properties		Physical Properties		
Oxide	(%)	Spesific gravity		3.15
SiO_2	18.74	Blaine specific surface area	cm^2/g	3600
Al_2O_3	5.37	Fineness	45 μ %	7.4
Fe_2O_3	3.04		90 μ %	0.4
CaO	64.11	Setting time	min	180
MgO	1.21	Volume expansion	mm	1
SO_3	2.68	Mechanical Properties		
Na_2O	0.34	Compressive strength	1-Day (MPa)	28.8
K_2O	0.62		28-Day (MPa)	56
Cl^-	0.038			
F.CaO	2.12			
LOI	3.6			

Table 2. Chemical and physical composition of fly ash

Chemical properties Oxide	%	Physical properties		
SiO_2	59.22	Spesific gravity	2.31	
Al_2O_3	22.86	Residual on 0.045 mm sieve (%)	10	
Fe_2O_3	6.31	Blaine Fineness (cm^2/g)	4000	
CaO	3.09	Mechanical Properties		
MgO	1.31		7-Day	85.9
SO_3	0.17	Pozzolanic Activity Index (%)	28-Day	100.7
$Na_2O+0.658\ K_2O$	1.4		90-Day	110.2
Cl^-	0.001			
IR	0.32			
LOI	3.2			
Free CaO	0.00			
Class	F			

In order to examine the effect of fly ash fineness on the performance of mortar mixtures, fly ash with a Blaine fineness of 4000 cm^2/g was ground to 6000 cm^2/g fineness by means of a laboratory ball mill. Crushed limestone sand with 0-2 mm grain size, water absorption capacity and specific gravity of 0.40 and 2.6%, respectively, was used in the production of mortar mixes. Some properties of the polycarboxylate ether based high water reducing admixture (HRWRA) used in the study are given in Table 3.

Tablo 3. Some properties of HRWRA

Type	Density (g/cm^3)	Solid Content (%)	pH	Chloride content (%)	Alkaline content, Na_2O (%)
Polycarboxylate ether-based	1.060	32	2-5	<0.1	<10

Preparation of Mixtures and Experiments

The mortar mixtures prepared within the scope of the study were produced according to ASTM C109 (2013) Standard. The ratio of water/binder and sand/binder in all mixtures was kept constant as 0.485 and 2.75, respectively.

Table 4. Material proportions of mixtures

Mixture	Cement (g)	Fly ash (g)	Water (g)	Water/binder	Sand (g)	HRWRA (weight of binder %)
FA0_0%	500	0	242.5	0.485	1375	0
FA0_1%						1
FA0_1.5%						1.5
FA0_2%						2
FA4K_15_0%	425	75	242.5	0.485	1375	0
FA4K_15_1%						1
FA4K_15_1.5%						1.5
FA4K_15_2%						2
FA4K_30_0%	350	150	242.5	0.485	1375	0
FA4K_30_1%						1
FA4K_30_1.5%						1.5
FA4K_30_2%						2
FA6K_15_0%	425	75	242.5	0.485	1375	0
FA6K_15_1%						1
FA6K_15_1.5%						1.5
FA6K_15_2%						2
FA6K_30_0%	350	150	242.5	0.485	1375	0
FA6K_30_1%						1
FA6K_30_1.5%						1.5
FA6K_30_2%						2

HRWRA: High range water-reducing admixture

In addition to the control mixture that does not contain fly ash, a total of 5 series of mortar mixtures were prepared by replacing the fly ash with two different Blaine fineness values, 4000 and 6000 cm2/g, with cement at the rates of 15% and 30% by weight. A total of 20 mixtures were obtained by adding HRWRA at 3 different usage dosages rates, 1%, 1.5% and 2%. The amount of material used in the production of mortar mixtures is shown in Table 4. The denotation of the mixtures was made according to fly ash fineness, utilization ratio and HRWRA dosage. For example, the mixture containing 15% fly ash with 4000 cm^2/g Blaine fineness and adding 1% HRWRA admixture was named FA4K_15_1%. Flow values of mortar mixtures were determined in accordance with ASTM C1437 Standard. In addition, the flow test was repeated in the mixture, which was kept for 60 minutes, in order to examine the time-dependent behavior of the mixtures.

Results and Discussion

The time-dependent flow values of the mortar mixtures are shown in Table 5. Not surprisingly, the flow values of the mixtures increased as the HRWRA usage dosage increased, regardless of the fly ash fineness and utilization ratio. This situation was caused by the electrostatic effect and the steric hindrance mechanism of the HRWRA. It was reported by Altun et al. (2020) that the structure of HRWRA consists of carboxylate functional groups and polyethylene side chains. The electrostatic effect occurs when the carboxylate groups of the HRWRA adhere to the cement surface. (Karakuzu et al., 2021; Ozen et al., 2020a; Yigit et al., 2020; Sahin et al., 2022c; Kalipcilar et al., 2016; Latifi et al., 2022; Sahin et al., 2020). At the same time, polyethylene oxide side chains provide steric hindrance (Altun et al., 2021; Ozen et al., 2021; Sahin & Mardani., 2022d; Mardani-Aghabaglou, 2021a; Ozen et al., 2020b; Ozen et al., 2022b; Mardani-Aghabaglou, 2021b).

It was understood that the change in fly ash fineness did not have a significant effect on the flow value and consistency retention capacity of the mortar mixtures. However, according to the literature, it is understood that the workability of the mixtures generally increases with the increase of fly ash fineness (Snellings et al., 2019). It was stated by Chindaprasirt et al. (2004) that this may be due to the fact that fine fly ash has a smoother surface compared to coarse fly ash. However, it was emphasized by Hsu et al. (2018) that the use of fly ash with high fineness (6300 cm^2/g) in the cement mortar mixture negatively affects the workability of the mixture. However, in this study, it was determined that the mixture with the highest flow value was FA6K_15_2% containing fly ash with higher fineness value. It was thought that this situation is due to the decrease in the water requirement of the mixture as a result of the increase in sphericity due to the increase in the fineness of the fly ash (De Maeijer et al., 2020).

Table 5. Time-dependent flow values of mortar mixtures

Mixtures	Time-dependent flow values (mm)	
	0 min.	60 min.
FA0_0%	80	75
FA0_1%	175	150
FA0_1.5%	240	185
FA0_2%	300	300
FA4K_15_0%	70	70
FA4K_15_1%	175	160
FA4K_15_1.5%	280	185
FA4K_15_2%	280	280
FA4K_30_0%	75	75
FA4K_30_1%	175	160
FA4K_30_1.5%	280	197.5
FA4K_30_2%	300	290
FA6K_15_0%	80	70
FA6K_15_1%	170	155
FA6K_15_1.5%	250	187.5
FA6K_15_2%	305	290
FA6K_30_0%	70	70
FA6K_30_1%	180	167.5
FA6K_30_1.5%	270	195
FA6K_30_2%	300	300

Regardless of the fly ash fineness, it was determined that the flow value and the consistency retention capacity were not significantly affected by the increase in the fly ash utilization ratio in all the other mixtures, except for the mixture containing 1.5% HRWRA. However, it was found that the flow value increased with the increase of the fly ash content in the mortar mixtures containing 1.5% HRWRA. It was stated by Park et al. (2021) that this situation resulted from the decrease in the reaction degree of cement with the increase in fly ash utilization ratio. Similarly, in another study by Altun, (2021), it was emphasized that the flow value of the mixtures increased with the increase in the fly ash utilization ratio. At the end of 60 minutes, it was determined that the mixtures containing 2% HRWRA had the highest consistency retention capacity, regardless of fly ash fineness and utilization ratio. It was stated by the researchers that the adsorption of the negatively charged carboxylate molecules on the surface of the fly ash particles is quite low since the fly ash surface is negatively charged (Altun, 2021; Wang et al., 2021; Cangialosi et al., 2009). Thus, the cement surface is covered with more water-reducing admixture molecules and the consistency retention capacity of the mixtures increases (Wang et al., 2021).

Conclusion

Within the scope of the study, the results obtained in line with the materials used and the tests applied are listed below:

- Regardless of fly ash fineness and utilization ratio;
  - It was observed that the flow values of the mixtures increased with the increase of the high range water-reducing admixture usage dosage.
  - It was determined that the highest consistency retention performance is in the mixtures containing 2% high range water-reducing admixture.
- The change in fly ash fineness had no significant effect on the flow value and consistency retention performance of the mortar mixtures.
- It was understood that the flow value of the mortar mixtures containing 1.5% high range water-reducing admixture increased with the increase of the fly ash utilization ratio.
- In terms of flow performance, it was determined that FA6K_15_2% mixture having 2% high range water-reducing admixture and 15% fly ash with 6000 cm^2/g fineness was the best mixture.

Scientific Ethics Declaration

The authors declare that the scientific ethical and legal responsibility of this article published in EPSTEM journal belongs to the authors.

Acknowledgements

* This article was presented as an oral presentation at the International Conference on Technology, Engineering and Science (www.icontes.net) held in Antalya/Turkey on November 16-19, 2022.

*The first author would like to acknowledge the scholarship provided by the Bursa Uludag University Science and Technology Centre (BAP) under grant number FAY-2021-579 Besides, the first author would like to acknowledge the scholarship provided by the Scientific and Technological Research Council of Turkey (TUBITAK) under grant number 219M425 and 2211-A program during her Ph.D. study. In addition, the authors would like to acknowledge Polisan Construction Chemicals Company, Oyak Factory-Bolu Quality Control Laboratory and Orhaneli Technical Power Plant for their kind assistance in providing the high range water reducing admixture, cement and fly ash as well as determining the technical properties of these products, respectively.

References

Al-Kutti, W., Nasir, M., Johari, M. A. M., Islam, A. S., Manda, A. A., & Blaisi, N. I. (2018). An overview and experimental study on hybrid binders containing date palm ash, fly ash, OPC and activator composites. *Construction and Building Materials*, *159*, 567-577.

Altun, M. G. (2021). *Effect of chemical structure of high range water reducing admixture on properties of cementitious systems containing fly ash* (Doctoral dissertation). Bursa Uludag University.

Altun, M. G., Ozen, S., & Mardani-Aghabaglou, A. (2020). Effect of side chain length change of polycarboxylate-ether based high range water reducing admixture on properties of self-compacting concrete. *Construction and Building Materials*, *246*, 118427.

Altun, M., Ozen, S., & Mardani Aghabaglou, A. (2021). Effect of side chain length change of polycarboxylate-ether-based high-range water-reducing admixture on properties of cementitious systems containing fly ash. *Journal of Materials in Civil Engineering*, *33*(4). https://doi.org/10.1061/(asce)mt.1943-5533.0003603

Arel, H. S., & Shaikh, F. U. (2018). Effects of fly ash fineness, nano silica, and curing types on mechanical and durability properties of fly ash mortars. *Structural Concrete*, *19*(2), 597-607.

ASTM C 1437 – 01. (2013). *Flow of hydraulic cement mortar*. Annual Book of ASTM Standards, American Society for Testing and Materials, Philadelphia, PA, USA.

ASTM-C109. C109/C109M-13 *Standard test method for compressive strength of hydraulic cement mortars* (Using 2-in. or [50-mm] Cube Specimens).

Aytekin B., Biricik O. & Mardani A. (2022). Effect of limestone powder fineness and substitution ratio on the rheological properties of cementitious systems. *Vi-International European Conference on Interdisciplinary Scientific Research*, 26-27 August, Bukres, Romanya Online.

Bayqra, S. H., Mardani-Aghabaglou, A., & Ramyar, K. (2022). Physical and mechanical properties of high-volume fly ash roller compacted concrete pavement (A laboratory and case study). *Construction and Building Materials*, *314*, 125664.

Biricik O., Aytekin B., & Mardani A. (2022a) Utilization of waste powder in cementitious systems, *8 th International Black Sea Coastline Countries Scientific Research Conference* 29-30 August, Sofya, Bulgaristan.

Biricik O., Aytekin B., & Mardani A. (2022b). Effect of using different types of waste powder materials on setting time and flow properties of cement systems. *14th International Scientific Research Congress*, 20-21 August, Ankara, Turkey.

Biricik, O., & Mardani, A. (2022c). Parameters affecting thixotropic behavior of self-compacting concrete and 3D printable concrete; a state-of-the-art review. *Construction and Building Materials*, *339*, 127688.

Burgos-Montes, O., Palacios, M., Rivilla, P., & Puertas, F. (2012). Compatibility between superplasticizer admixtures and cements with mineral additions. *Construction and Building Materials*, *31*, 300-309.

Cangialosi, F., Notarnicola, M., Liberti, L., & Stencel, J. (2009). The role of weathering on fly ash charge distribution during triboelectrostatic beneficiation. *Journal of Hazardous Materials*, *164*(2-3), 683-688.

Chindaprasirt, P., Homwuttiwong, S., & Sirivivatnanon, V. (2004). Influence of fly ash fineness on strength, drying shrinkage and sulfate resistance of blended cement mortar. *Cement and Concrete Research*, *34*(7), 1087-1092.

De Maeijer, P. K., Craeye, B., Snellings, R., Kazemi-Kamyab, H., Loots, M., Janssens, K., & Nuyts, G. (2020). Effect of ultra-fine fly ash on concrete performance and durability. *Construction and Building Materials*, *263*, 120493.

Faltin, B. (2022). *Performance of concrete with different cement finenesses and nano-activators*, Master Thesis, University of Nebraska.

Fanghui, H., Qiang, W., & Jingjing, F. (2015). The differences among the roles of ground fly ash in the paste, mortar and concrete. *Construction and Building Materials*, *93*, 172-179.

Han, X., Yang, J., Feng, J., Zhou, C., & Wang, X. (2019). Research on hydration mechanism of ultrafine fly ash and cement composite. *Construction and Building Materials*, *227*, 116697.

Hsu, S., Chi, M., & Huang, R. (2018). Effect of fineness and replacement ratio of ground fly ash on properties of blended cement mortar. *Construction and Building Materials*, *176*, 250-258.

Hsu, S., Chi, M., & Huang, R. (2019). Influence of fly ash fineness and high replacement ratios on concrete properties. *Journal of Marine Science and Technology*, *27*(2), 9.

Kalipcilar, I., Mardani-Aghabaglou, A., Sezer, G. I., Altun, S., & Sezer, A. (2016). Assessment of the effect of sulfate attack on cement stabilized montmorillonite. *Geomechanics and Engineering*, *10*(6), 807-826.

Karakuzu, K., Kobya, V., Mardani-Aghabaglou, A., Felekoglu, B., & Ramyar, K. (2021). Adsorption properties of polycarboxylate ether-based high range water reducing admixture on cementitious systems: A review. *Construction and Building Materials*, *312*, 125366.

Latifi, M. R., Biricik, O., & Mardani Aghabaglou, A. (2022). Effect of the addition of polypropylene fiber on concrete properties. *Journal of Adhesion Science and Technology*, *36*(4), 345-369.

Mardani-Aghabaglou, A. (2016). *Investigation of cement-superplasticizer admixture compatibility* (Doctoral dissertation, PhD Thesis. Turkey, Izmir, Ege University, Engineering Faculty, Civil Engineering Department).

Mardani-Aghabaglou, A., Felekoglu, B., & Ramyar, K. (2021b). Effect of false set related anomalies on rheological properties of cement paste mixtures in the presence of high range water reducing admixture. *Structural Concrete*, 22, E619-E633.

Mardani-Aghabaglou, A., Ilhan, M., & Ozen, S. (2019). The effect of shrinkage reducing admixture and polypropylene fibers on drying shrinkage behaviour of concrete. *Cement, Wapno, Beton. 3*. 227-237. 10.32047/CWB.2019.24.3.227.

Mardani-Aghabaglou, A., Ozturk, H. T., Kankal, M., & Ramyar, K. (2021a). Assessment and prediction of cement paste flow behavior; Marsh-funnel flow time and mini-slump values. *Construction and Building Materials*, *301*, 124072.

Mardani-Aghabaglou, A., Son, A. E., Felekoglu, B., & Ramyar, K. (2017). Effect of cement fineness on properties of cementitious materials containing high range water reducing admixture. *Journal of Green Building*, *12*(1), 142-167.

Moghaddam, F., Sirivivatnanon, V., & Vessalas, K. (2019). The effect of fly ash fineness on heat of hydration, microstructure, flow and compressive strength of blended cement pastes. *Case Studies in Construction Materials*, *10*, 218.

Ng, S., & Justnes, H. (2016). Influence of plasticizers on the rheology and early heat of hydration of blended cements with high content of fly ash. *Cement and Concrete Composites*, *65*, 41-54.

Nguyen, T. B. T., Chatchawan, R., Saengsoy, W., Tangtermsirikul, S., & Sugiyama, T. (2019). Influences of different types of fly ash and confinement on performances of expansive mortars and concretes. *Construction and Building Materials*, *209*, 176-186.

Ozen, S., Altun, M. G., & Mardani-Aghabaglou, A. (2020a). Effect of the polycarboxylate based water reducing admixture structure on self-compacting concrete properties: Main chain length. *Construction and Building Materials*, *255*, 119360.

Ozen, S., Altun, M. G., Mardani-Aghabaglou, A., & Ramyar, K. (2020b). Effect of nonionic side chain length of polycarboxylate-ether-based high-range water-reducing admixture on properties of cementitious systems. *Frontiers of Structural and Civil Engineering*, *14*(6), 1573-1582.

Ozen, S., Altun, M. G., Mardani-Aghabaglou, A., & Ramyar, K. (2022a). Multi-effect of superplasticisers main and side-chain length on cementitious systems with fly ash. *Magazine of Concrete Research*, 1-13.

Ozen, S., Altun, M. G., Mardani-Aghabaglou, A., & Ramyar, K. (2021). Effect of main and side chain length change of polycarboxylate-ether-based water-reducing admixtures on the fresh state and mechanical properties of cementitious systems. *Structural Concrete*, *22*, 607-618.

Ozen, S., Durgun, M. Y., Kobya, V., Karakuzu, K., & Mardani-Aghabaglou, A. (2022b). Effect of Colemanite Ore Wastes Utilization on Fresh Properties and Compressive Strength of Cementitious Systems. *Arabian Journal for Science and Engineering*, 1-15.

Palacios, M., Puertas, F., Bowen, P., & Houst, Y. F. (2009). Effect of PCs superplasticizers on the rheological properties and hydration process of slag-blended cement pastes. *Journal of Materials Science*, *44*(10), 2714-2723.

Park, B., & Choi, Y. C. (2021). Hydration and pore-structure characteristics of high-volume fly ash cement pastes. *Construction and Building Materials*, *278*, 122390.

Rivera, R. A., Sanjuán, M. Á., Martín, D. A., & Costafreda, J. L. (2021). Performance of ground granulated blast-furnace slag and coal fly ash ternary portland cements exposed to natural carbonation. *Materials*, *14*(12), 3239.

Sahin, H. G., & Mardani, A. (2022d) Effect of cement C3A content on some fresh state properties and compressive strength of 3D printing concrete mixtures. *Journal of Uludag University Faculty of Engineering*, *27*(2), 831-846. https://doi.org/10.17482/uumfd.1142197

Sahin, H. G., & Mardani-Aghabaglou, A. (2022b). Assessment of materials, design parameters and some properties of 3D printing concrete mixtures; a state-of-the-art review. *Construction and Building Materials*, *316*, 125865.

Sahin, H. G., Biricik, O., & Mardani-Aghabaglou, A. (2022c). Polycarboxylate-based water reducing admixture–clay compatibility; literature review. *Journal of Polymer Research*, *29*(1), 1-19.

Sahin, H., & Mardani Aghabaglou, A. L. I. (2022a). Sustainable 3d printing concrete mixtures, literature review. *Journal of Modern Technology and Engineering*, *7*. 20-29.

Sahin, H., Biricik, O, & Mardani Aghabaglou, A. (2020). The enhancement methods of polycarboxylate-based water reducing admixture performance in systems containing high amount of clay literature review. *6th International Conference on Engineering and Natural Science (ICENS*), Belgrade.

Sezer, A., Mardani-Aghabaglou, A., Boz, A., & Tanrinian, N. (2016). An investigation into strength and permittivity of compacted sand-clay mixtures by partial replacement of water with lignosulfonate. *Acta Phys Pol A*, *130*(1), 23-27.

Snellings, R., Kamyab, H., Joseph, S., Nielsen, P., Loots, M., & Van den Abeele, L. (2019). Pozzolanic reactivity of size-classified siliceous fly ashes. *Proceedings Icsbm 2*, 227.

Wang, C., Kong, F., & Pan, L. (2021). Effects of polycarboxylate superplasticizers with different side-chain lengths on the resistance of concrete to chloride penetration and sulfate attack. *Journal of Building Engineering*, *43*, 102817.

Win, T. T., Wattanapornprom, R., Prasittisopin, L., Pansuk, W., & Pheinsusom, P. (2022). Investigation of fineness and calcium-oxide content in fly ash from ASEAN region on properties and durability of cement–fly ash system. *Engineering Journal*, *26*(5), 77-90.

Yigit, B., Salihoglu, G., Mardani-Aghabaglou, A., Salihoglu, N. K., & Ozen, S. (2020). Recycling of sewage sludge incineration ashes as construction material. *Journal of the Faculty of Engineering and Architecture of Gazi University*, *35*(3), 1647-1664.

Yingliang, Z., Jingping, Q., Zhengyu, M. A., Zhenbang, G., & Hui, L. (2020). Effect of superfine blast furnace slags on the binary cement containing high-volume fly ash. *Powder Technology*, *375*, 539-548.

Yuksel, C., Mardani-Aghabaglou, A., Beglarigale, A., Ramyar, K., & Andic-Cakir, O. (2016). Influence of water/powder ratio and powder type on alkali–silica reactivity and transport properties of self-consolidating concrete. *Materials and Structures*, *49*(1), 289-299.

Author Information

Hatice Gizem Sahin
Bursa Uludag University
Civil Engineering Department, Nilufer-Bursa
Turkey
haticegizemsahin@gmail.com

Oznur Biricik
Bursa Uludag University
Civil Engineering Department, Nilufer-Bursa
Turkey

Ali Mardani
Bursa Uludag University
Civil Engineering Department, Nilufer-Bursa
Turkey

To cite this article:

Sahin, H.G., Biricik, O., & Mardani, A. (2022). Investigation of high range water-reducing admixture requirement in cementitious systems containing fly ash with different utilization ratio and fineness. *The Eurasia Proceedings of Science, Technology, Engineering & Mathematics (EPSTEM), 21*, 388-395.

The Eurasia Proceedings of Science, Technology, Engineering & Mathematics (EPSTEM)
ISSN: 2602-3199

The Eurasia Proceedings of Science, Technology, Engineering & Mathematics (EPSTEM), 2022

Volume 21, Pages 396-403

IConTES 2022: International Conference on Technology, Engineering and Science

Performance and Analysis of Thermal Energy on Solar Reflector Cooker - Application of an Alternative Source of Energy in Cyprus

Lida EBRAHIMI VAFAEI
Near East University

Samuel Nii TACKIE
Near East University

Serah BENSTEAD
Near East University

McDominic Chimaobi EZE
Near East University

Abstract: This paper proposes a solar cooking device made of a flat array of concentric mirrors tilted to focus on a small area. The mobile array of mirrors is mounted on a stand to be movable around a ball joint and with a carrier for a cooking vessel held by a double crank at the focal area of the mirrors. Current solar cooker inventions comprise a reflector that is constructed from a plurality of reflective concentric rings arranged in a planar configuration. The term planar configuration, as used herein, is defined as a configuration in which flat rings are arranged with some part of each ring lying in a plane that includes some part of each other ring although each ring has a different tilt. This configuration is to be distinguished from a parabolic configuration. The tilt of the flat concentric rings of the cooker permits sunlight to be focused at an area, about 5 inches in diameter, obviating the need for the more expensive and difficult-to-manufacturer parabolic reflector, and is more conducive to heating a cooking vessel.

Keywords: Solar cooker, Tilt angle, Thermal radiation

Introduction

Since firewood used for cooking leads to deforestation and marketable fuels are not readily accessible to the ordinary man, the need for solar cookers becomes necessary, although waste from agriculture and dried dung from cows used for cooking is a good stimulant, and the resources used for collecting fuel can be diverted to other useful purposes. With the development of so cookers and alternative energy sources for cooking, still they are yet to be utilized as expected because they are incompatible with the normal conventional cooking practice. With the situation of things, it is only appropriate for of majority of people around the world afraid of fuel and the finance to pay for cooking with fuel. Aside from the many advantages on the health, time, and income of the users and on the environment, solar cookers can be used for boiling drinkable water, this provides access to safe water to millions of people thus preventing waterborne illnesses.

Concentration of Solar cooker, or solar oven, the use up energy through sun rays (which is the heat from the sun) to cook, fry, heat or pasteurize drinks or food. The vast majority of solar cookers presently in use are, low-technology and relatively cheap devices (Althouse et al., 1979). Because they make use of no fuel and cost nothing to operate, many nonprofit organizations are promoting their use worldwide in order to help reduce fuel costs (for low-income people) and air pollution and to slow down the deforestation and desertification caused by

gathering firewood for cooking. Solar cooking as a form of cooking and deployed in a situation where marginal fuel uses up is important (Yazaki, 2010), or the threat of unintended fires is becoming great. They are similar to a solar oven, which uses heat from sunlight to cook food. It eliminates the need for fuel or electricity for the purpose of cooking. Solar cookers are available in several sizes and configurations, all of which have their pros and cons. Over time solar cookers have been exposed to numerous types of assessments to rate their performance. A set of solar cooker tests, measures, and equations was presented in other to assess the performance of the solar cookers especially box-type type cookers (Mullick et al., 1987). They presented an assessment and endorsement which was later embraced the d by the Bureau of Indian Standards (BIS). And in the, past the energy aspect has been totally concentrated on (Richard, 2005).

Figure 1. Solar panel cooker

Nevertheless, it was Funk in who 2000 discovered the necessity to change a Universal method for evaluating all solar cookers, and later his approvals were soon embraced by United States Agricultural Engineers as ASAE S580. However, subtests tests have been conducted on solar cookers, and their results convert that solar performance is related to percentage efficiency Mukaro and Tinarwo (2008) and Nandwani et al. (1997). Several experiments was conducted and assessments following ASAE S580 for box and sheet kind of solar cookers has all been tested (McMillan & Jones 2001; FSEC, 2002; El Sebaii & İbrahim, 2005)

Figure 2. 3D advance modelling and simulation of cylindrical panel solar cooker

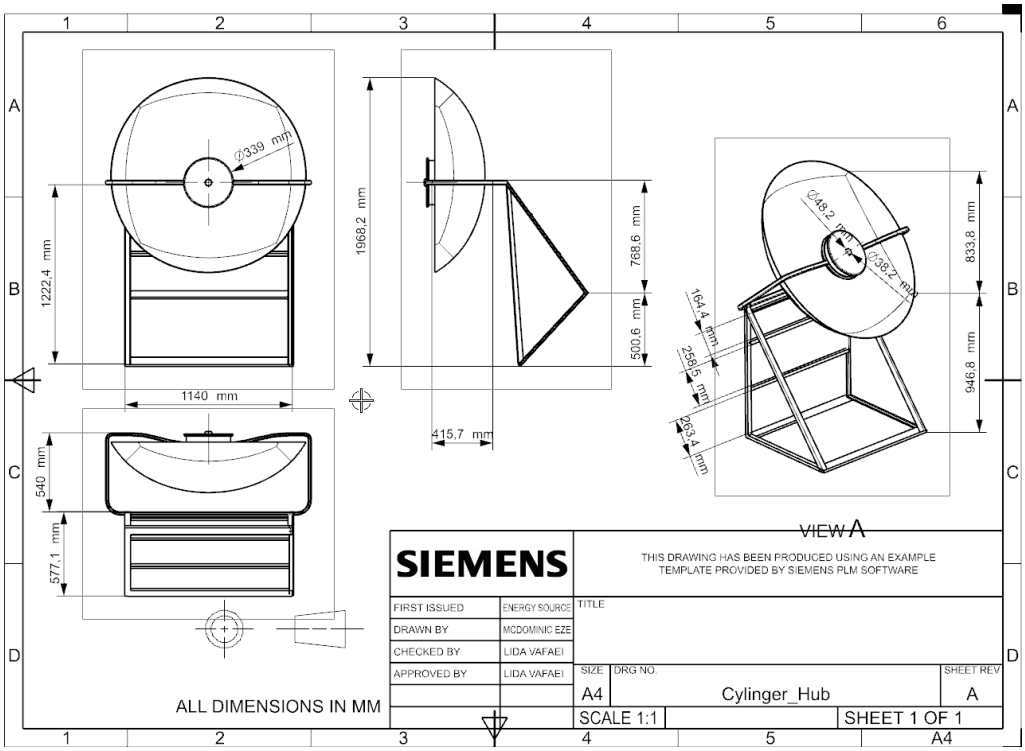

Figure 3. Geometricalional drafting of cylindrical model solar cooker

Background of the Project

European Commissioning body classified Cyprus as part of the utmost susceptible countries in the EU when it comes to reliance of energy, with regards to security of energy sources, but intensive changes are being implemented to deliver a continual swing to a supplementary energy autonomous economy, while focusing on a viable renewable means. Cyprus today has one of great prospective for solar energy of many European Union countries, but still they import record number of their electricity supplies. They presently have percentage rounding to 10 in terms of alternative energy portion, there is still an objective of increased percentage to 16 by 2020. Giving that Cyprus alternative power Roadmap, which is intended to produce within 25 - 40 percentage of required energy supply through RES in the year 2030.

The history of the solar cooker project has been a result of co-operation with one Cyprus NGO. Together the organizations, the Green Cyprus Community Project in Cyprus, and Technology for Life formed a base for the future solar cooker dissemination in Northern Cyprus. The 'Green Cyprus Community Project'(referred to later as the Green Cyprus) was originally a tree nursery in Cyprus. The Green Cyprus is a - development co-operation - program, which is a citizen's organization. The purpose of the project is to prevent complete desertification in Northern Cyprus by founding tree nurseries, planting trees and organizing environmental counselling through the approach of using solar cookers. Spearheading the drive to meet this target is an increase in using battery systems, to store excess energy and create a ‘power bank’ for the nation and sing the sun power for domestic purpose that include cooking through the use of solar cookers. Despite having massive potential in terms of both solar and wind energy, one of the problems in utilizing these energy sources, is being able to deliver them close to the point of consumption, where they are actually needed.

The 2019 budget for this sector is set at 64.96 million euros, with 58.61 million euros committed to subsidies, of which 29.81 million euros are directly related to utilizing power from renewables. The 29.81 million euros’ figure includes 25 million euros for a new subsidies plan design, to encourage the use of renewable energy sources for houses (net metering, domestic cores and roof insulation), and promoting ‘green’ transport – such as plug-in electric or hybrid vehicles. The project brought together a wide range of specialties, from sustainable architecture, carbon accounting, energy mapping and sustainable technology. “In the case of Cyprus, one thing we have to look at is the huge climate potential of the empty rooftops which provides us the concept of initiating solar cooker in Cyprus, so we know what we can do with the abundant sun. It is not about rebuilding Nicosia, but to see what can be done with existing technology.” A look at the average solar radiation per year this tells the story better.

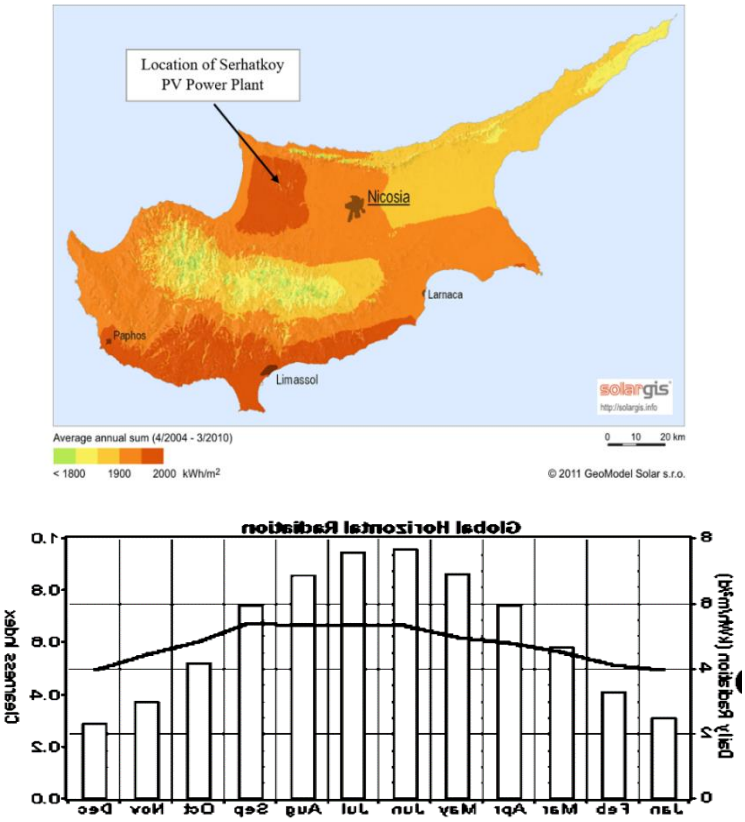

Figure 4. Daily radiation – clearness index average solar radiation in Cyprus throughout the year

Table 1. Cooking efficiency

When it is not ok	When it is ok
The sun low in the sky	The sun high in the sky
Partly cloudy	No clouds
Much wind	No wind
White or shiny—no lid	Black pots with lid
Large, heavy pot	Max 5 liter, light weight pot
Too much water	Little or no water added
Large quantity— big pieces of food	Small quantity— small pieces of food

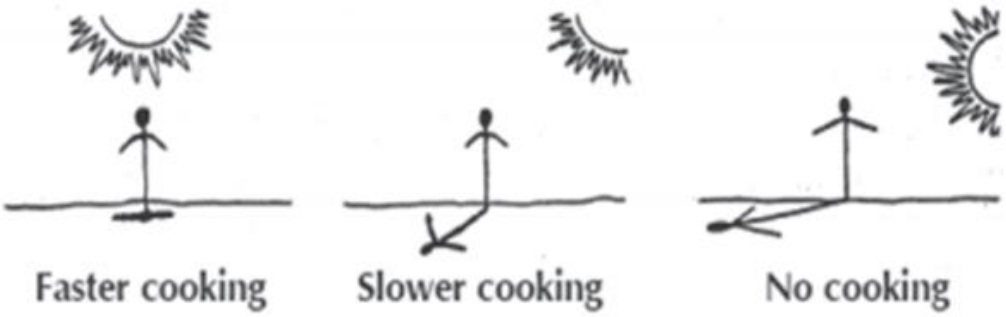

Figure 5. Cooking type with respect the position of the sun

Solar Performance Procedures Testing with the Use of New Standard

The challenges of testing several designs of solar stove devices led to the establishment of several testing criteria for assessing thermal cookers all over the world. American Society of Agricultural Engineering (ASAE) Standard S580, the standard developed by the European Committee on Solar Cooking Research (ECSCR) Bureau of Indian Standards, based on work by Mirdha and Dhariwal (2008).

Be that as it may, the three criteria have insufficiencies, India guidelines give testing standards dependent on warm test methodology for box-type sun-powered cookers. The exhibition of the reflector-based sun-based cooker executed right now is done dependent on this adhering to guidelines, IS 13429. The standard featured two techniques for testing: a stagnation (test without load) and a heap test. Test on the cooker was done in the Month of March when the sunlight-based illumination was greatest (Mukaro &Tinarwo, 2008). The test was completed between 11.00 am and 4.00 pm for ten sequential days so as to decide the most extreme plate and water temperature in the cooker during this period.

Various tests without load were directed on the cooker to decide its temperature of stagnation and furthermore to check the increased cooker inner temperature. water was placed in a cylinder pot and covered and the absorber temperature was measured, water and ambient, as well as wind speed, were measured. The temperature of stagnation, encompassing temperature (ambient) (Ta), and safeguard plate temperature (Tp) were estimated for various times between 11:00 am and 4.00 pm during the activity of the cooker utilizing Type K, mineral protected grounded intersection, 1.6mm width thermocouple with Elix advanced thermometer (LX-6500) capable of reading temperature between -50°C and 750°C. Thermo-Anemometer (PROVA Instrument, AVM 01) was utilized to gauge wind speed (v) and sun-oriented radiation was estimated utilizing a worldwide radiation meter (GRM 100).

Measurement of Performance Analysis

Solar Cooker Performance Factor

$$F_p = \frac{\text{Energy reflected by the reflectors fall on the glass cover}}{\text{Energy falling on the cover due to direct radiation}} \qquad (1)$$

The concentration of the cooker will be (F_p +1).

Rate of Heating Q/min = SPH x Mass x ΔTemperature/min (units = Joules/min)

Solar Cooker Efficiency

$$F_p = \frac{T_{wf,\max} - \overline{T}}{\overline{G}} \qquad (2)$$

$T_{wf,\max}$ is the maximum absorber surface temperature, $\overline{T}$ is the average ambient temperature, and $\overline{G}$ is the average solar intensity in the equation above. F_1 Was calculated to be 0.08 m^2K/W. A value of 0.10 m^2K/W is frequently used. The following is the thermal efficiency of solar cylindrical cookers (η):

$$\eta = \frac{\text{Energy output}}{\text{Energy input}} = \frac{\left| m_c c_{pw} (T_{wf} - T_{wi} \right| / \Delta t}{I_t A_{sc}} \qquad (3)$$

Where E_o is the energy output of the solar cooker in W; m_w is the mass of the water in kg; c_{pw} is the specific heat of the water in J/kg K; T_{wi} and T_{wf} are initial and final temperatures of the water in K; and t is the time in s.

$$\eta = \frac{mc_{pw} \Delta T / t}{GA} x100 \qquad (4)$$

From the Equation, thee water in the cooking pot is designated by m. The specific heat capacity of water is Cpw, the temperature differential of water is T, the time interval is t, the incoming solar intensity is G, and the area of aperture glazing is A. As shown in the diagram, the efficiency of a solar egg shape cooker ranges from 6.89 to 5.02 percent. The efficiency values may be considered lower when compared to similar designs without heat storage in the literature. Although the effectiveness of a propolis-based latent heat storage media is reduced slightly, the thermal energy content of oven air is preserved until late hours.

Then, if you calculate the weight of mass lost over a specific time period (e.g. 10 mins). But the beaker must be boiling first. i.e. initial mass (@100^{o}C)= 200g; and final mass (10 mins later after continuous boiling) = 175g
ThereforeΔm = 25g ($mass_{final}$ –$mass_{initial}$)
$Q_{to\ boil}$ = Q/min x time
Eg. Let's say that Q= 2516 and the time that we boiled was for 10mins, therefore:
= 2516 x10
= 25160 Joules of energy in 10 mins
Latent heat = Q_{used} / Δmass = J/g

This test was directed after the estimation of Standard Cooking Power and Standard Sensible Heating Time and is expected to quantify to what extent the cooker can keep up a high temperature without being effectively followed to follow the sun. The cooker is left stationary and the temperature of the pot substance (water) estimated, as with earlier tests. This proceeds until the pot substance had diminished in temperature by 20^{0}C from beginning temperatures (for example the last temperature toward the finish of the Standard Cooking Power test). By and by, this time estimation is standardized to 700 W/m^2

Result and Discussion

This research brings about deciding the best cooking time when using the solar cooking method, it shows the morning and night hours when the sun points are low, have low sun based radiation force and henceforth, unsatisfactory for sun based cooking. Between about 11.00 a.m. to 4.00 p.m., the sun powered force is high, running from around 650 to W/m^2, speaking to a reasonable range for sun powered cooking.

As the sun oriented radiation shifts all around and with the season, the best cooking time may go amiss in view of the impact of overcast spread. The maximum insulation resting at 480W/m^2 at exactly 2:30 pm and the minimum falls through at 50 W/m^2 at 11:00 am was noted. The ambient temperature and average solar radiation are respectively 45°C and 400 W/m^2. Usually food is fully cooked at a comparative range of 60-70 °C , water reached an amazing amount of about 59- 68°C upon testing at an insulation value of 320 – 485 W/m^2

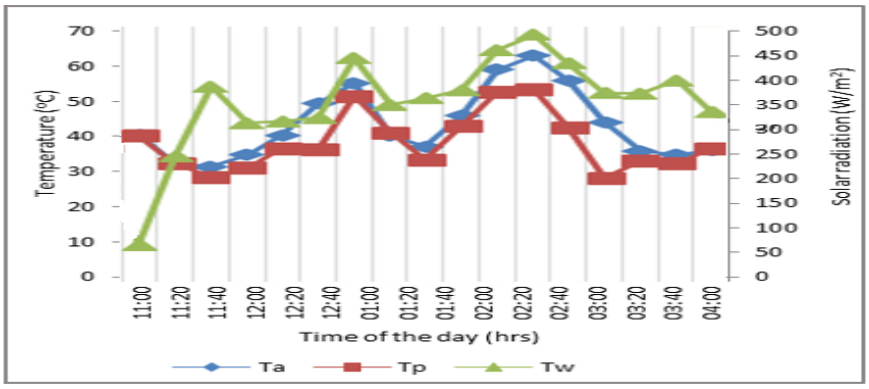

Figure 6. Solar cooker performance curve during heat test of water

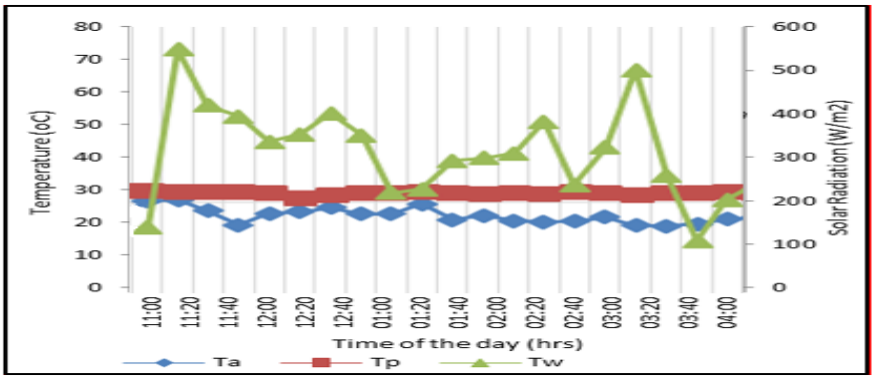

Figure 7. Solar cooker performance curve during heat test of water

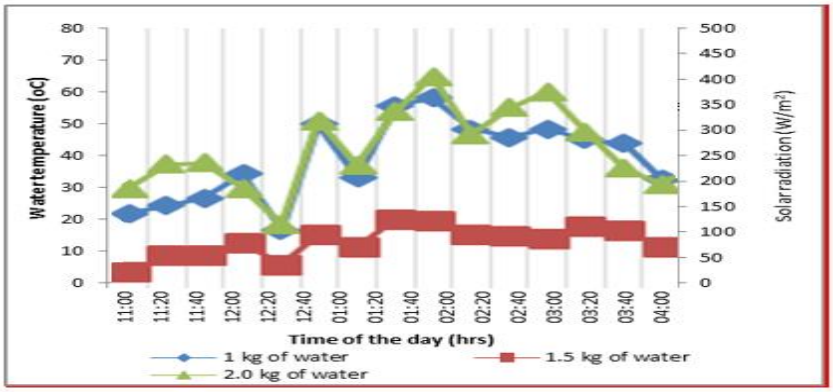

Figure 8. Temperature variation of water with time for dissimilar load

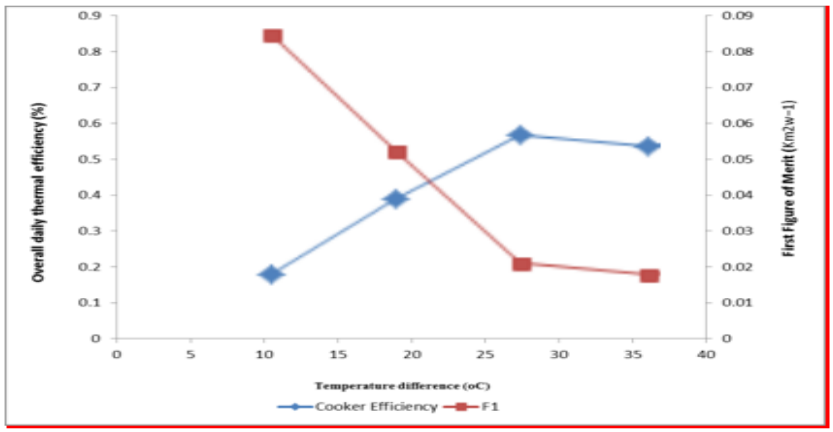

Figure 9. Overall thermal efficiency vs the varied difference in temperature

As Shown in Fig, 3, 4, 5, and 6, the connection between first figure of legitimacy and the general cooker warm effectiveness show that as the estimation of first figure of legitimacy expands, by and large warm proficiency of the cooker increments. At higher estimation of figure of value of 0.075, cooker warm productivity is 0.7 and this happen at temperature distinction of 20°C. Over this temperature, generally warm effectiveness of the cooker diminishes.

Conclusion

The paper introduced the test system and the warm presentation of allegorical sun based cooker actualized in Cyprus, an occasional cloud of climate was seen all through the trial and it caused vacillation in sun-powered radiation. The most extreme segregation of 520 W/m^2 at 2.00 pm and the least of 246W/m^2 at 11.00 am were watched. The normal sun-based radiation and surrounding temperature seen during the time of the test were 403 W/m^2 and 40^{0}C separately. The water temperature esteems somewhere in the range of 60 and 67^{0}C were seen at insolation esteems somewhere in the range of 398 and 520 W/m^2. These happen between the hour of 1:20 pm and 4:00 pm with the most noteworthy water temperature of 67oC at 3:00 pm. The presentation of the cooker as far as the first figure of legitimacy, the second figure of legitimacy, and warm effectiveness show that the cooker contrasts well and worldwide standard. The cooker has a better maintenance limit; this exhibited its appropriateness for cooking even in changing weather. From the presentation assessment of the explanatory sun-based cooker, the qualities standardized cooking power, stagnation temperature; standard reasonable warming time, unattended cooking time, and cooking power at a temperature of 40^{0}C.

Scientific Ethics Declaration

The authors declare that the scientific ethical and legal responsibility of this article published in EPSTEM journal belongs to the authors.

Acknowledgements or Notes

This article was presented as an oral presentation at the International Conference on Technology, Engineering and Science (www.icontes.net) held in Antalya/Turkey on November 16-19, 2022.

References

Althouse, A. D., Turnquist, C. H., & Bracciano, A. F. (1979). *Modern refrigeration and air conditioning.* South Holland, IL: Goodheart-Willcox.

El Sebaii, A.A., & Ibrahim, A. (2005). Experimental testing of box type solar cooker using the standard procedure of cooker power. *Renewable Energy*, *9*(32), 241-260

FSEC. (2002). *Thermal performance testing of parabolic solar cooker 333*. Retrieved from http://www.fesc.ucf.edu/solar/.

McMillan, C., & Jones, S. (2001). *Tests of the solar funnel and bowl cookers in*. Retrieved from http://www.solarcooker.org/funneltest01.htm)

Mirdha, U.S., & Dhariwal, S.R. (2008). Design optimization of solar cooker. *Renewable Energy*, *33*(3), 530 – 544.

Mukaro, R., & Tinarwo, D. (2008). Performance evaluation of a hot box reflector solar cooker using a microcontroller based measurement system. *International Journal of Energy Research*, *32*(14), 1339-1348.

Mullick, S.C., Kandpal, T.C., & Saxena, A.K. (1987). Thermal test procedure for box-type solar cooker. *Solar Energy*,*39*(4), 353-360.

Nandwani, S.S., Steinhart, J., Henning, H.M., Rommel, M., & Wittwer, V. (1997). Experimental study of multipurpose solar hot box at Freiburg, Germany. *Renewable Energy*, *12*(1), 1-20.

Richard, P. (2005). Energy analysis of solar cylindrical parabolic cooker. *Solar Energy*, *79*(3), 221-233

Yazaki. (2010, October 30). *Absorbation chillers*. Retrieved from http://www.yazakiairconditioning.com

Author Information

Lida EBRAHIMI VAFAEI
Near East University
Nicosia Mersin, Cyprus
Contact e- mail:*lida.ebrahimivefaei@neu.edu.tr*

Samuel Nii Tackie
Near East University
Nicosia Mersin, Cyprus

Serah BENSTEAD
Near East University
Nicosia Mersin, Cyprus

McDominic Chimaobi EZE
Near East University
Nicosia Mersin, Cyprus

To cite this article:

Vafaei Ebrahimi,L., Tackie, S. N., Benstead, S.,& Eze, M. D. C. (2022). Performance and analysis of thermal energy on solar reflector cooker- application of an alternative source of energy in Cyprus.. *The Eurasia Proceedings of Science, Technology, Engineering & Mathematics (EPSTEM), 21*, 396-403.

The Eurasia Proceedings of Science, Technology, Engineering & Mathematics (EPSTEM)
ISSN: 2602-3199

The Eurasia Proceedings of Science, Technology, Engineering & Mathematics (EPSTEM), 2022

Volume 21, Pages 404-411

IConTES 2022: International Conference on Technology, Engineering and Science

Performance Evaluation of Solar Assisted Membrane Distillation for Seawater Desalination Using Solar Simulator

Mohd Amirul Hilmi Mohd HANOIN
Universiti Malaysia Pahang

Nadzirah Mohd MOKHTAR
Universiti Malaysia Pahang

Abstract: The increase in freshwater demand and environmental pollution is leading to an increase in the use of renewable energy for the seawater desalination system. The emerging potential in seawater desalination technology is a solar assisted membrane distillation (SAMD) where thermal energy is supplied from the solar thermal collector to the membrane module. The objective of this study is to evaluate the performance of in-house made SAMD system for seawater application in terms of the permeate flux and salt rejection using solar simulator. In this work, Flat Plate Solar Thermal Collector (FPSC) system was designed to preheat the simulated and actual seawater as the feed solution for indoor assessment. 2.5 wt.% of sodium chloride (NaCl) was used represents the standard seawater. The heat radiation intensity remained constant during the experiment by using the tungsten lamps which are widely used as a solar simulator. During simulated seawater testing, the initial permeate flux of 3.86 kg/h.m² was obtained, then increased up to 5.39 kg/h.m², with almost 39.4% increment. This shows a similar trend with seawater MD processes. Nonetheless, the flux slightly decreased until 4.06 kg/h.m², showing about 24.7% flux reduction. Then, the flux remains decreased at a slower rate down to 3.90 kg/h.m². The declining trend in permeate flux can be attributed to the low evaporation area affected by the NaCl crystallization due to the partial membrane pore blockage. Nevertheless, the membrane still obtained 99% salt rejection in all experiments.

Keywords: Solar powered membrane distillation, Integrated system, Renewable Energy, Solar energy, Desalination

Introduction

Desalination plants usually separate the sea water into two separate streams which are retentate and permeate. The retentate is a stream with a high salt concentration (brine or concentrate) while the permeate consists of a freshwater stream with almost free of salt content (Tyszer et al., 2021). The fresh water normally called as permeate in reverse osmosis (RO) and condensate in membrane distillation (MD). Every desalination technology requires energy for the separation process, which is supplied to the system by thermal or mechanical means (generally as electrical power). The thermal desalination process technologies are based on evaporation and the subsequent condensation of the steam. Concerning pressure-driven desalination, RO is powered by electricity, thus, energy supplied from power grid is required. The RO system typically needs a high osmotic pressure (maximum operating pressure for RO is typically around 80 bar) to separate the seawater (Davenport et al., 2018). This system is not practical in rural regions because of the high energy needs to be provided to overcome osmotic pressure. In addition, severe fouling was observed during the RO desalination process. The system has high operation and maintenance costs and is difficult to integrate into the solar energy system.

Over the last decade, it is proven that MD has gained interest from the researchers and academicians to be involved in this area mainly for the water desalination process. The main advantages of the MD process over

other desalination processes are its simplicity, less sensitivity to feed salinity, a small tendency of fouling, the capacity to utilize low-grade thermal energy, needs only a small temperature difference to run, and high quality of freshwater (Muhamad et al., 2019). However, the existing MD modules operate the system by using fully electrical energy generated from power generation station through the grid power supply (Hanoin et al., 2019). Most of the power generation in Malaysia significantly depends on three major fossil fuel sources, namely coal, natural gas, and fuel oil to generate electricity. These fossil fuel-based power generations cause negative environmental consequences and depletion of fuel reserves. Thus, the challenge is to create sustainable solutions for freshwater providing using clean, affordable energy and eliminating or decreasing the cost of electricity. Solar powered membrane distillation (SPMD) is one potential solution to meet this challenge by utilizing available solar energy sources efficiently, thus enabling increased energy independence and reducing global warming as well.

As researchers believe, the SPMD system is capable of working on a stand-alone system with a zero-energy concept that does not require external energy and only utilizes solar energy for its operation. Other than the zero-energy concept, there is also possibility to hybrid solar energy with the common grid power supply energy. There is a technology that uses the solar energy in solar thermal collector (STC) to becomes external heater to the MD system. The system is namely as solar assisted membrane distillation (SAMD). To operate under SAMD, the MD system firstly must be operated at a similar range of temperatures obtained from low-temperature STC to produce continuous freshwater production. Thus, efforts to enhance the heat transfer efficiency on flat plate solar collector (FPSC) as an STC device through the MD module are required. Previously, the FPSC system is the common STC device used in the SPMD system other than Evacuated Tube Collector (ETC) and Compound Parabolic Concentrator (CPC) (Ma et al., 2020). Several parameters have practical relation to the thermal efficiency of a solar collector such as collector plate position, coating of collector plate, coating material, glazing material property, spacing between riser tubes concerning diameter, flow rate, the intensity of incident radiation, and bottom and side insulation thickness (Majumdar et al., 2020; Yassen et al., 2019). Among these, pipe diameter, pipe spacing, water flow rate, and radiation intensity are the major contributors affecting the collector efficiency (Hajabdollahi et al., 2022; Wang et al., 2019). Design modification is a facile way were tweaking the parameters can help improve compatibility in a solar energy harvesting device. Based on the study by Wang et al. (2019), they found that the larger the pipe diameter, the better the collector efficiency. Similar performance was observed for the smallest pipe spacing. Verma et al. (2020) conducted the experiment with variation of mass flow rate (0.01 - 0.05 kg/s) and radiation intensity (650 – 1150 W/m²). The result shows that the mass flow rate reaches optimum efficiency at approximately 0.025 kg/s, whiles thermal efficiency increases with enhanced intensity of radiation.

From our own analysis, we found that a pipe collector with a tube diameter of 3/4-inch achieved 3.5% and 9.4% higher thermal performance and collector efficiency respectively, compared to a tube diameter of 3/8-inch due to a larger contact area with the surface. With the same tube diameter (3/4 inch), pipe spacing of 18.5 cm tends to attain higher thermal performance and collector efficiency by 4.3% and 12.6%, compared to pipe spacing of 27 cm. An optimal working condition can be achieved at 0.03 kg/s of mass water flow rate and 1050 W/m² of heat radiation intensity for the highest average temperature in the water tank (Hanoin et al., 2021). In this study, no experimental work was conducted to investigate the effectiveness of the in-house made FPSC in supporting the MD system. Therefore, the objective of this study is to evaluate the performance of the integrated FPSC and MD system in producing freshwater from saline water and seawater. In this work, a solar simulator was used to control the radiation intensity at 1050 W/m². The SAMD system was evaluated based on feed water temperature, permeate flux and salt rejection.

Methodology

As shown in Figure 1, a schematic layout of the SAMD system involves an integration of serpentine-shaped FPSC system to DCMD modules was presented. There are three loops in the system; solar, feed and permeate loops. In view of the solar loop, the FPSC plays a vital role to gain solar radiation and convert it into thermal energy. In this area, a solar simulator was used to supply the heat radiation intensity to the serpertine-shaped FPSC system as shown in Figure 2. The detailed methodology can be found in our previous work (Hanoin et al., 2021). The FPSC system was operated early until the water temperature of the outlet collector achieved 75±1˚C. In this work, the same water inside the FPSC was circulated using coiled in the feed tank of the MD system. The FPSC turns into heat exchanger device to heat the feed solution. This is where the solar energy being used to substitute the non-renewable energy sources. However, it must be pointed out that the power supply box and battery supply are still needed to drive the electrical equipment (ex: two hydrostatic pumps, chiller, and weight balance) in the MD system. The FPSC just covered the thermal energy required of the feed solution. In terms of

MD system, two different loops are required for the process; namely as feed (hot solution) loop and permeate (cold solution) loop. The feed loop transmitted the thermal energy of the feed solution into the membrane module for the MD process while the permeate loop is used to acts as the condensing medium inside the membrane module. As MD is operated based on the vapor pressure difference between both solutions, the two loops will serve their role in order to obtain the freshwater from seawater.

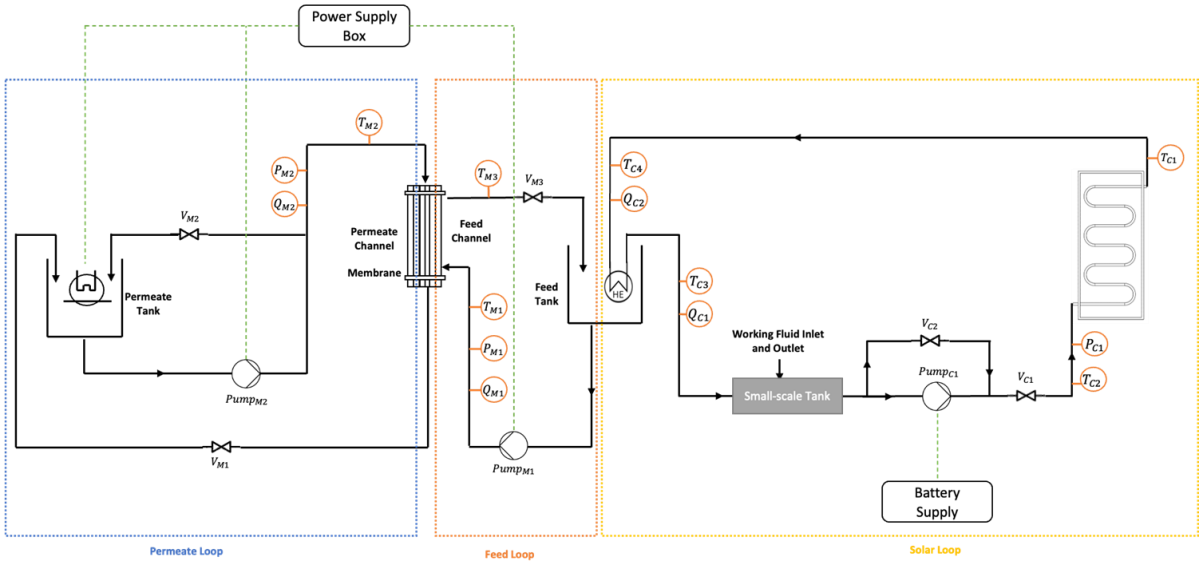

Figure 1. Schematic flow diagram of the SAMD system

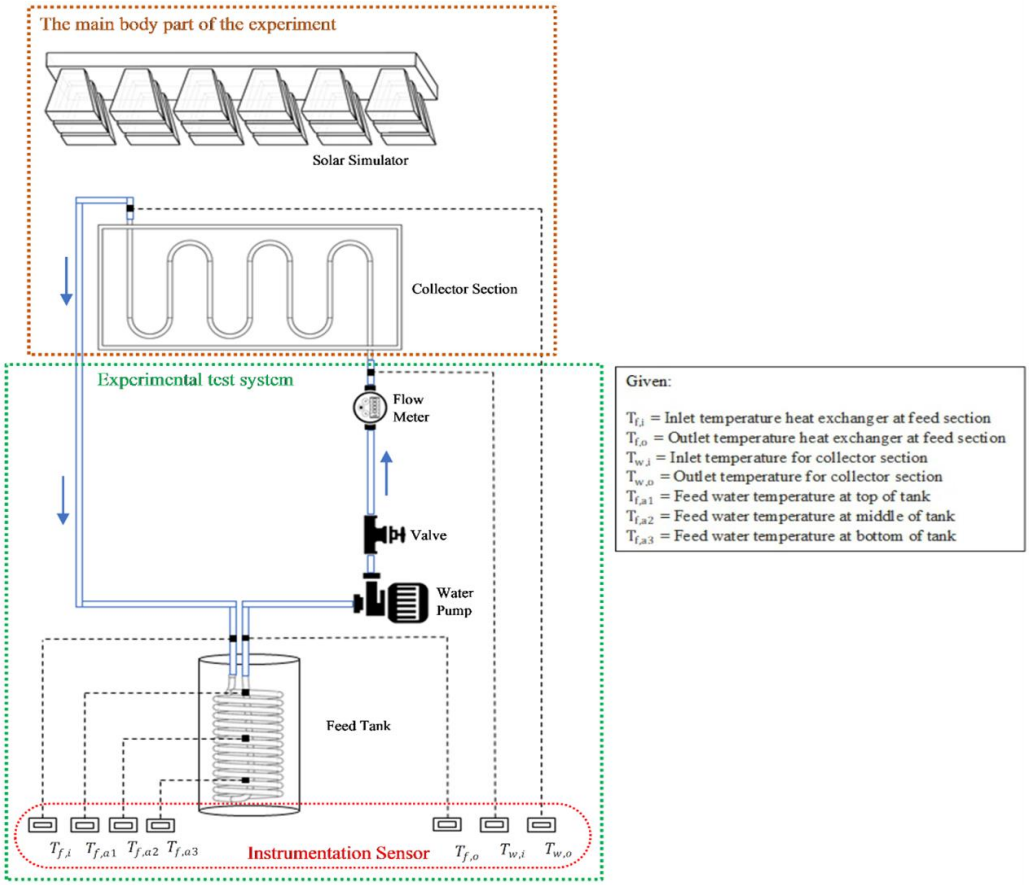

Figure 2. Schematic diagram of the FPSC system

In this study, the DCMD module was integrated with the FPSC system to investigate the overall SPMD system performance. A stainless-steel module containing 20 strands of hollow fiber membrane was prepared and used

to determine the performance of the membranes during the process. Polyvinylidene fluoride (PVDF)-bentonite hollow fiber membrane as a previous research product was used for the study. The membrane consisted of 12 wt.% of PVDF with the addition of 0.5 wt.% of bentonite powder. The membrane has a contact angle of 90.63±0.67˚ with a membrane porosity of 69.23%. The DCMD system is designed to have two circulating streams, i.e., the hot stream also known as feed stream (circulated through the membrane shell-side) and cold stream (fed through the lumen side of the hollow fiber membrane). In order to maintain the bulk feed temperature inside the feed tank at 75±1˚C, an electric heater (830, PROTECH) was used to support the system. Meanwhile, a recirculating chiller (RT2, VIVO) was used to cool down the water temperature in the permeate tank. The system was maintained at feed and permeate temperatures of 60±1˚C and 20±1˚C, respectively. It must be pointed out that the feed temperature is measure based on the inlet temperature of the membrane module. The pressures for feed and permeate were fixed at 8 psi and 2 psi. Meanwhile, the feed and permeate flow rates were controlled at 2.2 LPM and 0.5 LPM, respectively.

The feed tank and permeate tank will be filled with 1000 mL of simulated or real seawater. A 35 g of sodium chloride (NaCl) mixed with 1000 mL of deionized water will be prepared as the simulated seawater. For the permeate tank, 1000 mL of deionized water will be used. The weight of the permeate tank will be measured every 15 minutes using a digital balance. The samples of water inside the permeate tank will be taken out every 15 minutes for further analysis of the salt rejection rate. The parameter that can be used to compare proportionally the performance of the DCMD unit is the permeate flux. The MD flux, J, during the test (kg/h.m²) is characterized by:

$$J = \Delta W/(A.\Delta t) \quad (1)$$

where ΔW (kg) is the weight of permeate collected over a predetermined time t (h) of process and A (m²) is the effective membrane area. To identify the rejection, R (%) of the membrane, the following equation was employed:

$$R\ (\%) = (1 - C_p/C_f) \times 100 \quad (2)$$

where C_p and C_f are for permeate and feed concentration (mg/L), respectively.

Results and Discussion

Figure 3 presents the data of the hybrid system between FPSC and MD in terms of feed water temperature and permeate flux. In this study, the feed water temperature is the temperature detected in the feed tank. Initially, the hybrid system is started alone with the FPSC operation. For first 60 minutes, the fabricated solar collector was exposed to the solar simulator under radiation intensity of 1050 W/m² until the outlet collector temperature reached 75±1˚C. After that, MD system will take next action in purying the feed solution for 2 hours continuously. Figure 3(a) shows the permeate flux of the SAMD system when tested with distilled water as feed solution. The purpose of this test is to determine the vapor permeate flux of the SAMD system without foreign elements in the feed solution. Normally, this testing is required to set the benchmark for other types of feed solutions. As shown in Figure 3 (a), the initial permeate flux is 8.12 kg/h.m². Nonetheless, the fluxes decreased rapidly, with approximately 36.9%, until 5.12 kg/h.m² at 120th minutes. The decreasing permeates fluxes because of temperature polarization, then decreases the temperature difference between the feed and permeate side. This happens due to higher temperature difference between hot and cold solution, as the feed temperature has a strong influence on permeate flux (Mokhtar et al., 2015). The higher permeate flux was achieved at higher feed temperature as described by the Antoine equation that reflects the liquid temperature relationship with the related vapor pressure equilibrium which is the major MD process driving force (Qtaishat et al., 2008). Moreover, the difference of partial pressure occurs across the membrane and both water vapor and volatile species start to permeate through the membrane pores.

The simulated seawater through the MD process was presented in Figure 3(b). The initial permeates flux of 3.86 kg/h.m² was obtained, then increased up to 5.39 kg/h.m², with almost 39.4% increment. This shows a similar trend with seawater MD processes. Nonetheless, the flux slightly decreased until 4.06 kg/h.m², showing about 24.7% flux reduction. Then, the flux remains decreased at a slower rate down to 3.90 kg/h.m². The evaporation of the hot feed could contribute to the NaCl crystallization on the membrane surface if the experiment is continued for a long time and this can decrease the water flux due to the partial membrane pores blockage. Furthermore, membrane hydrophobicity will be reduced due to the NaCl crystals deposition on the surface of the membrane which reduces the salt rejection rate (Hubadillah et al., 2018).

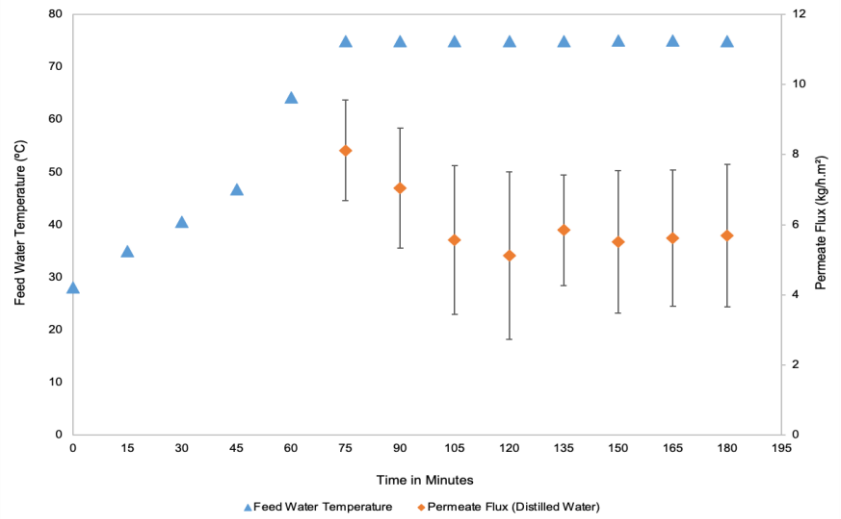

(a)

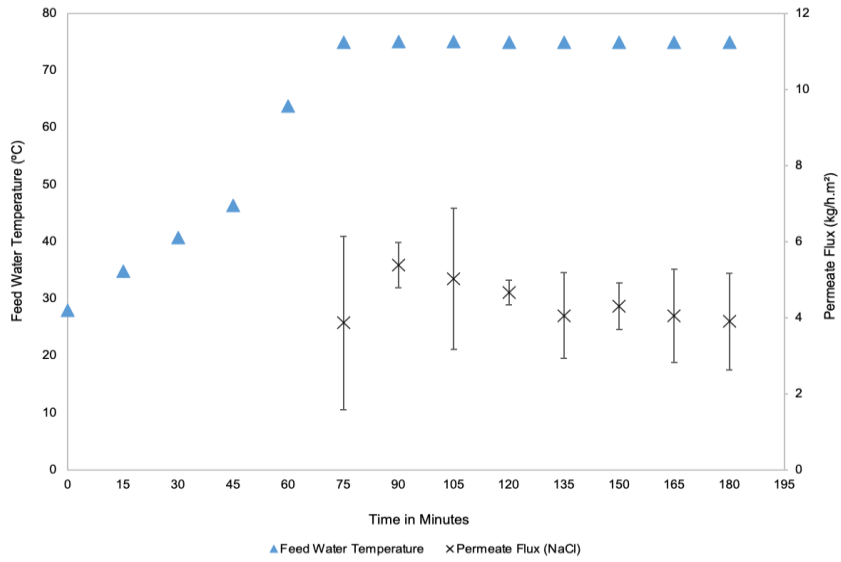

(b)

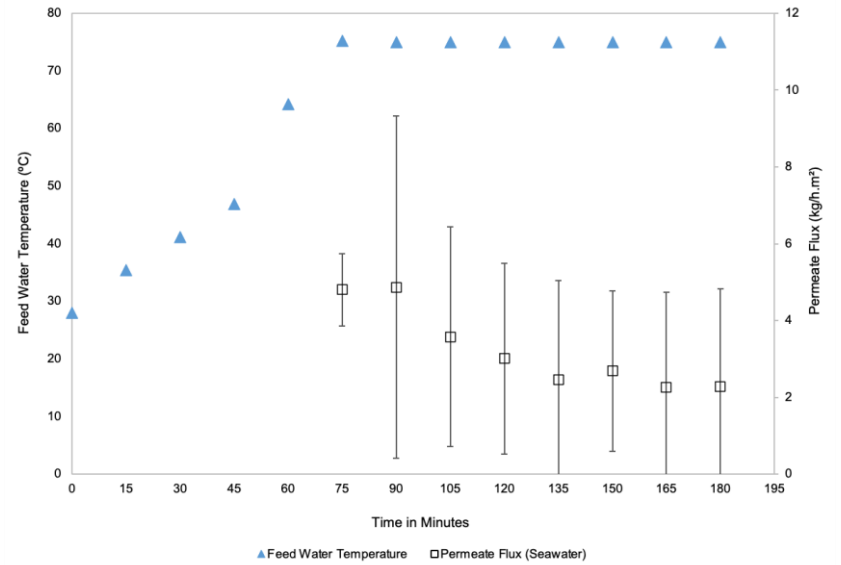

(c)

Figure 3. Permeate flux and average temperature of different feed water: (a) distilled water, (b) Simulated seawater (35g of NaCl mixed with 1000mL of deionized water), and (c) seawater

Figure 3(c) used seawater as feed water during the MD process. Result shows that the initial permeate flux of MD which recorded at around 4.80 kg/h.m² tended to increase until the highest average permeate flux achieved at 4.87 kg/h.m². However, the flux decreased rapidly until 2.45 kg/h.m², showing approximately 49.5% flux reduction. From 150th to 180th minutes, the flux of the membrane continued to drop, but at a moderate rate. Although the feed water temperature is constant due to continuously generated electricity from the electrical heater, the cold solution tended losses to the surrounding. Therefore, the temperature difference is decreasing rapidly. The decreasing trend is also caused by the severe deposition of solutes on the outer surface of membrane at the beginning of the separation process, leading to surface pore blocking and increased water vapor transport resistance. The reduction in the flux could be due to an increase in salt concentration as a result of declining vapor pressure, which is commonly observed in MD processes because the coefficient activity of water tends to be lower at higher solute concentration (Liu & Wang, 2013).

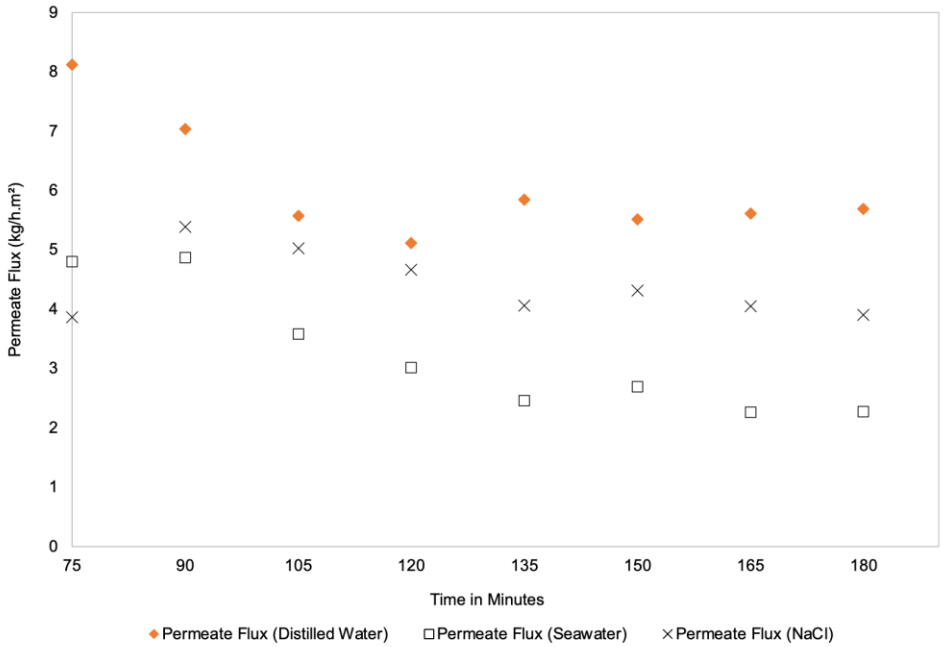

Figure 4. Comparatives permeate flux of feed solution between distilled water, simulated seawater (NaCl) and seawater

Figure 4 shows the comparative permeate flux between distilled water, simulated seawater (NaCl), and seawater. As can be seen from this figure, the permeate fluxes of distilled water were always higher than simulated seawater (NaCl) and seawater. The feed salinity affects the permeate flux and can be attributed to a decrease in the transmembrane driving force resulted from the decrease of the vapor pressure of water with increasing salt concentration. At elevated temperature, the vapor pressure of a solute will be lower than that of the distilled water at the same temperature because the polar interaction between water molecules and solute ions is stronger than the hydrogen bonding between the water molecules (Sharqawy and Zubair, 2010). Also, the increase in solute concentration increases the temperature and concentration polarization effects. In terms of salt rejection, it was observed that almost 100% rejection was achieved in experimental works with simulated seawater and seawater. The findings proved that NaCl in the feed solution has very little impact on the performance of membrane with respect to separation characteristics. The analysis is in agreement with the previous studies that using the stand alone SPMD system or hybrid SAMD system.

Conclusion and Future Outlook

Nowadays, the sea or brackish water desalination has gained attention due to the scarcity of water. The utilization of solar energy through desalination processes indicated the capability of further growth, from the point of view of energy conservation and/or cost-cutting approaches. Numerous researchers have examined the integration of solar energy and MD for eco-friendly water desalination. In this study, the self-fabricated FPSC was examined using simulated seawater and real seawater. From the analysis, almost 100% salt rejection was obtained in all experiments indicating the potential of using SAMD as the water purifier. In terms of thermal energy supply from the FPSC, the system managed to store solar energy and transfer to the feed solution and

supported the MD system. Meanwhile, the MD system shows different performance evaluation between seawater and NaCl solution. The lower permeate flux achieved by the seawater solution is presumed due to the high concentration of inorganic salts in the seawater. The variation of inorganic matters and other pollutants in the seawater may affect the overall performance.

Scientific Ethics Declaration

The authors declare that the scientific ethical and legal responsibility of this article published in EPSTEM journal belongs to authors.

Acknowledgements

* This article was presented as an oral presentation at the International Conference on Technology, Engineering and Science (www.icontes.net) held in Antalya/Turkey on November 16-19, 2022.

*The authors gratefully acknowledge Universiti Malaysia Pahang (UMP) for financial support under grant number PDU213225 and RDU190395. Sincere gratitude also expressed to UMP for providing MRS scholarship.

References

Davenport, D.M., Deshmukh, A., Werber, J.R., & Elimelech, M. (2018). High-pressure reverse osmosis for energy-efficient hypersaline brine desalination: Current status, design considerations, and research needs. *Environmental Science & Technology Letters*, *5*, 467−475. https://doi.org/10.1021/acs.estlett.8b00274

Hajabdollahi, H., Khosravian, M., & Dehaj, M.S. (2022). Thermo-economic modelling and optimization of a solar network using flat plate collectors. *Energy*, *244*, 123070. https://doi.org/10.1016/j.energy.2021.123070

Hanoin, M.A.H.M, Muhamad, N.A.S., Mokhtar, N.M., Razak, A.A., & Hadi, M.S. (2021). Effect of design parameters of serpentine-shaped flat plate solar collector under Malaysia climate conditions. *Journal of Advanced Research in Fluid Mechanics and Thermal Sciences*, *88*, 71–80. https://doi.org/10.37934/arfmts.88.1.7180

Hanoin, M.A.H.M., Mohammed, N.S., Arris, M.A.I.Z., Bakar, A.I.A., Mokhtar, N.M., & Razak, A.A. (2019). Abrication and performance evaluation of ıntegrated solar-driven membrane distillation system with serpentine-shape of flat plate solar collector for seawater desalination. *Journal of Applied Membrane Science & Technology*, *23*, 49–63. https://doi.org/10.11113/amst.v23n3.163

Hubadillah, S.K., Othman, M.H.D., Matsuura, T., Rahman, M.A., Jaafar, J., Ismail, A.F., & Amin, S.Z.M. (2018). Green silica-based ceramic hollow fiber membrane for seawater desalination via direct contact membrane distillation. *Separation and Purification Technology*, *205*, 22–31. https://doi.org/https://doi.org/10.1016/j.seppur.2018.04.089

Liu, H., & Wang, J. (2013). Treatment of radioactive wastewater using direct contact membrane distillation. *Journal of Hazardous Materials*, *261*, 307–315. https://doi.org/10.1016/j.jhazmat.2013.07.045

Ma, Q., Ahmadi, A., & Cabassud, C. (2020). Optimization and design of a novel small-scale integrated vacuum membrane distillation – solar flat-plate collector module with heat recovery strategy through heat pumps. *Desalination*, *478*, 114285. https://doi.org/10.1016/j.desal.2019.114285

Majumdar, R., Saha, S.K., & Patki, A. (2020). Novel dimension scaling for optimal mass flow rate estimation in low temperature flat plate solar collector based on thermal performance parameters. *Thermal Science and Engineering Progress*, *19*, 100569. https://doi.org/10.1016/j.tsep.2020.100569

Mokhtar, N.M., Lau, W.J., & Ismail, A.F. (2015). Effect of feed temperature on the DCMD performances in treating synthetic textile wastewater. *Advanced Materials Research*, *1113*, 776-781. https://doi.org/10.4028/www.scientific.net/amr.1113.776

Muhamad, N.A.S, Mokhtar, N.M., Naim, R., Lau, W.J., & Ismail, A.F. (2019). A review of membrane distillation process: - Before, during and after testing. *International Journal of Engineering Technology and Sciences*, *6*, 62–81. http://dx.doi.org/10.15282/ijets.6.1.2019.1006

Qtaishat, M., Matsuura, T., Kruczek, B., & Khayet, M. (2008). Heat and mass transfer analysis in direct contact membrane distillation. *Desalination*, *219*, 272–292. https://doi.org/10.1016/j.desal.2007.05.019

Sharqawy, M., & Zubair, S. (2010). Thermophysical properties of seawater: A review of existing correlations

and data. *Desalination and Water Treatment*, *16*, 354–380. https://doi.org/10.5004/dwt.2010.1079

Tyszer, M., Tomaszewska, B., & Kabay, N. (2021). Desalination of geothermal wastewaters by membrane processes: Strategies for environmentally friendly use of retentate streams. *Desalination*, *520*, 115330. https://doi.org/10.1016/j.desal.2021.115330

Verma, S.K., Sharma, K., Gupta, N.K., Soni, P., & Upadhyay, N. (2020). Performance comparison of innovative spiral shaped solar collector design with conventional flat plate solar collector. *Energy*, *194*, 116853. https://doi.org/10.1016/j.energy.2019.116853

Wang, D., Wang, X., Chen, Y., Kang, W., & Liu, Y. (2019). Experimental study on performance test of serpentine flat plate collector with different pipe parameters and a new phase change collector. *Energy Procedia*, *158*, 738-743. https://doi.org/10.1016/j.egypro.2019.01.197

Yassen, T.A., Mokhlif, N.D., & Eleiwi, M.A. (2019). Performance investigation of an integrated solar water heater with corrugated absorber surface for domestic use. *Renewable Energy*, *138*, 852-860. https://doi.org/10.1016/j.renene.2019.01.114

Author Information

Mohd Amirul Hilmi Mohd Hanoin
Universiti Malaysia Pahang
Faculty of Civil Engineering Technology, Universiti Malaysia Pahang, Lebuhraya Persiaran Tun Khalil Yaakob, 26300 Kuantan, Pahang, Malaysia
Contact e-mail: hilmihanoin@*gmail.com*

Nadzirah Mohd Mokhtar
Universiti Malaysia Pahang
Faculty of Civil Engineering Technology, Universiti Malaysia Pahang, Lebuhraya Persiaran Tun Khalil Yaakob, 26300 Kuantan, Pahang, Malaysia

To cite this article:

Hanoin, M.A.H.M. & Mokhtar, N.M. (2022). Performance evaluation of solar assisted membrane distillation for seawater desalination using solar simulator. *The Eurasia Proceedings of Science, Technology, Engineering & Mathematics (EPSTEM)*, *21*, 404-411.

The Eurasia Proceedings of Science, Technology, Engineering & Mathematics (EPSTEM)
ISSN: 2602-3199

The Eurasia Proceedings of Science, Technology, Engineering & Mathematics (EPSTEM), 2022

Volume 21, Pages 412-417

IConTES 2022: International Conference on Technology, Engineering and Science

Investigation of Wood Biomass Ash on the Thermal Behaviour of Compressed Earth Bricks

Fatma KHELOUI
University Mouloud Mammeri of Tizi Ouzou

Nadia BOUSSAA
University Mouloud Mammeri of Tizi Ouzou
University of Bejaia

Nasser CHELOUAH
University of Bejaia

Abstract – The aim of this work is to study the effect of the incorporation of wood ash from the combustion of biomass waste on the thermal properties of compressed earth bricks (BWA). These bricks were obtained as a partial substitution of the soil with different contents (0, 5, 10, 15 and 20% wt). The specimens manufactured were compacted with a compaction stress at 10 MPa, conserved in the laboratory at a temperature of 20 ± 2 °C, then allowed to harden for 7 and 28 days. The results showed that the partial substitution of the soil leads to a decrease in thermal properties.Thermal conductivity values were decreased to different soil substitution proportions and with curing time. Minimum values were achieved for specimens containing 20% by weight of WA, with better thermal insulation, at thermal conductivity values ranging from 0.78 W/mK in BWA at 28 days and 1 W/mK in BWA at 7 days. This decrease was attributed firstly to the quantity of water consumed during the pozzolanic reaction that occurs between the soil components and the lime of the WA, secondly to the microstructure of this soil used.

Keywords Wood ash, Thermal properties, Compressed earth bricks, Thermal insulation.

Introduction

Since its existence, soil has been utilized in construction as a raw material, it has many advantages namely ecological, economic and environmental that allow it to be an important and main material in the construction of buildings (Rivera et al., 2021; Mansour et al., 2016). The performance of this earth depends mainly on its hygrothermal behavior, which is directly related to thermal and hydric properties and can be characterized by thermal conductivity (Mansour et al., 2016; Balasubramaniam et al., 2021; Omar Sore et al., 2018), but its disadvantage is that they suffer from a lack of mechanical strength, cracking due to shrinkage and sensitivity to water. To remedy these problems, the researchers used different stabilizers namely cement, lime, natural materials, biomass waste and industrial by-products (Felipe –Sesé et al., 2020; Eliche – Quesada et al., 2021).It hasseveralecological,economicandenvironmentalbenefits.

The current challenge in the champ of building materials is oriented towards the recovery of wood ashresulting of combustion of biomass waste to ensure on the one hand an improvement in thermal properties and on the other hand, an energy saving (Mansour et al., 2016; Felipe –Sesé et al., 2020; Çiçek et al., 2015). The main objective of this study is to develop new, cost-effective and environmentally friendly building materials based on wood ash from the calcination of biomass waste. In this context, BWA were carried out by partially replacing the soil with WA with different percentages (0, 5, 10, 15 and 20% wt) and then compacted at a compaction stress of

10 MPa. Before the thermal behaviour test, the bricks were left to cure for 7 and 28 days, then conserved in the laboratory at a temperature of 20 ± 2 °C.

Experimental Investigations

Characterizations of Materials Used

The materials utilized in this search are a silty clay soil collected from a local quarry in the Bejaia region (Algeria), wood ashmainly from biomass waste denoted WA. These materials are shown in Figure 1.

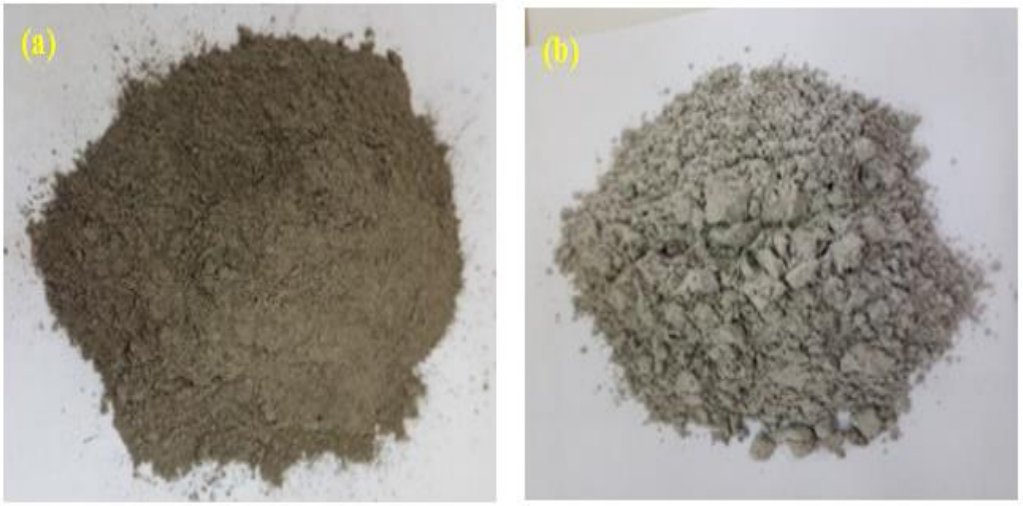

Figure 1. (a) Soil, (b) WA.

The chemical composition illustrated in Table 1 was determined by the X-ray fluorescence spectrometry (XRFS) technique. Elemental analysis of the soil yielded a high content of silica (SiO_2), alumina (Al_2O_3), iron oxide (Fe_2O_3) and calcium oxide (CaO). WA utilized as a source of lime in raw earth bricks contain a high CaO content.

Table 1. Chemical compositions of the materials used.

	Soil	WA
SiO_2	49.44	11.73
Al_2O_3	11.37	0.40
Fe_2O_3	5.31	0.02
CaO	14.63	43.74
MgO	1.70	1.58
K_2O	1.44	6.94
Na_2O	0.01	0.01
SO_3	0.70	0.82
LOI	15.38	34.55
Total	99.98	99.79

The mineralogical composition by X-ray diffraction (XRD) summarized in Figure 2 indicates that the principal phases existing in the earth are calcite, quartz and kaolinite. A laser particle size distribution (Figure 3) was performed on these materials indicates that the soil consists mainly of 87% silt and 12% clay. The clay content is low compared to the lower limits of the granular specifications proposed by the AFNOR NF XP 13-901 standard for a soil destined for the manufacture of compressed earth bricks.

The particle size of the WA revealed the presence of a high fine content of less than 20µm, of the order of 96%. The physical properties of the soil are thus evaluated (Table 2) i.e., the Atterberg limits determined according to standard NF P 94-051 and the methylene blue test was carried out according to standard NF-P18-592.

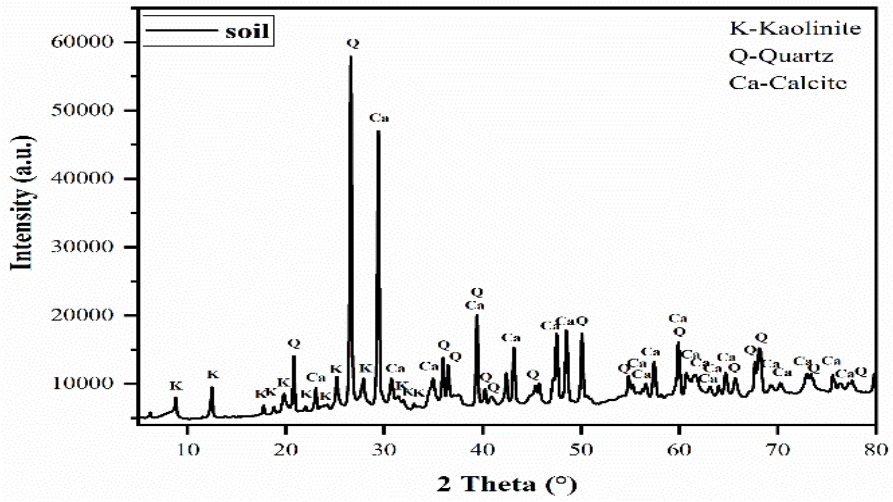

Figure 2. XRD of soil.

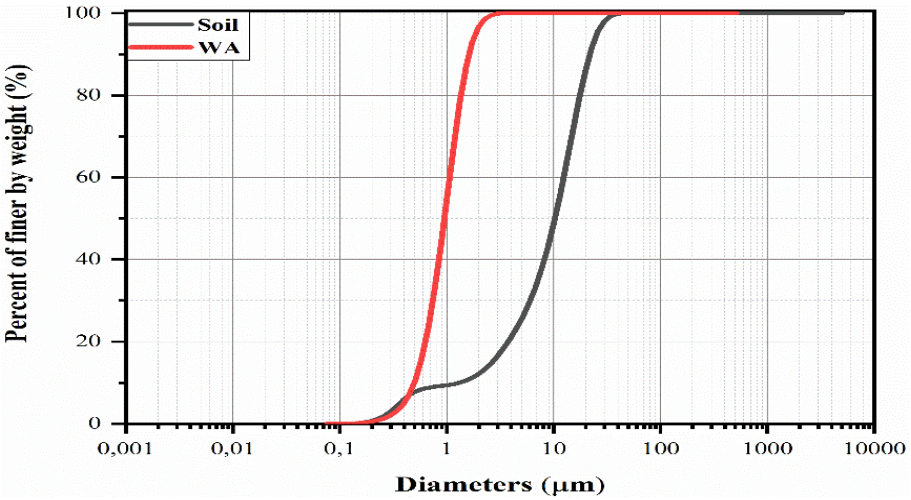

Figure 3. Particle size analyses of raw materials.

Table 2. Physical properties of the materials used.

Physical properties	Soil
Methylene Blue Value	2.77
Limits of Atterberg	
Plasticity limit Wp (%)	19
Liquidity limit WL (%)	39
Plasticity index Ip (%)	20

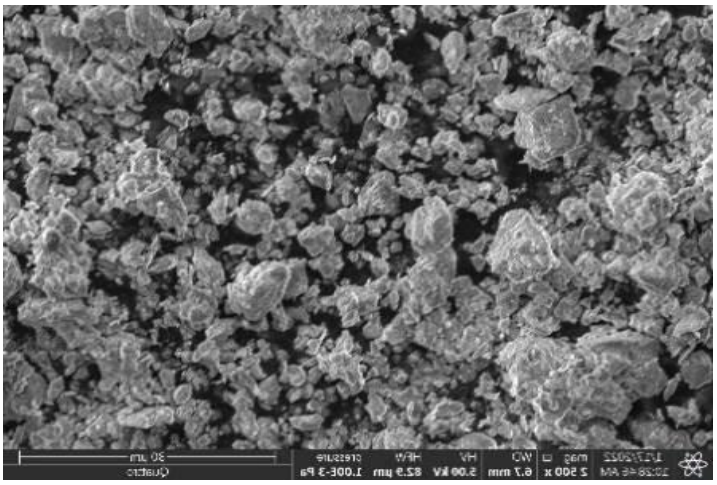

Figure 4. SEM image of soil used

The microstructure of these materials was characterized by scanning electron microscopy and SEM/EDX energy dispersion X-ray spectrometry using the high-resolution transmission electron microscope (Thermo Scientific™ Quattro ESEM). The microstructure of this soil is shown in Figure 4, has a dispersed particle size distribution with a concentration of small particles in the middle.

Preparation of BricksBWA(0-20%)

Four sets of BWA specimens were made for the different laboratory tests according to the fraction of WA added (0, 5, 10, 15 and 20% by weight). For each series three specimens were prepared. BWA(X%) are bricks mixed with WA with a partial substitution percentage X. The 0% WA reference specimens is denoted as BWA(0%). Before starting the preparation of the bricks, it is necessary to ensure that the materials are completely dry, for this, the soil and the WA have been dried in the oven at 105 °C for 24 h. The WA was first incorporated into the soil in a mixer, then the whole was mixed dry for 3 min to obtain a homogeneous mixture and that the grains of the soil were tightly mixed with those of the WA. The optimal water measured for each percentage of soil substituted by WAwas gradually added to the dry mixture and then the whole was mixed again in the mixer for 2 minutes. The assembly was then poured into steel molds of dimensions (16x5x2) cm^3, then compacted to 10 MPa utilizing a hydraulic press with a uni-axial load. After demoulding, the specimens were stored under standard laboratory conditions at a temperature of 20 ± 2°C for 7 and 28 days.

Results and Discussions

Thermal Conductivity

After curing, the thermal conductivities of manufactured specimens were evaluated in accordance with standard NF EN 993-15, measured using an CT-meter, with the hot wire method determined according to ISO 8894-1:1987. The results illustrated in Figure 5 show the decrease in the thermal conductivity of compacted earth bricks as a function of the increase in wood ash content and time cure. Thermal insulation was better in bricks stabilized with 20% of WA at 28 days, of the order of 0.78 W/mK, and 1 W/mK in BWA(20%) at 7 days compared to BWA(0%), which is in the order of 1.32W/mK. This decrease was attributed firstly to the quantity of water consumed during the pozzolanic reaction that occurs between the soil components and the lime of the wood ash, as well as the water evaporated during curing time from 7 to 28 days. Secondly to the microstructure of this soil used (Figure 4), which has a high porosity in their microstructure.

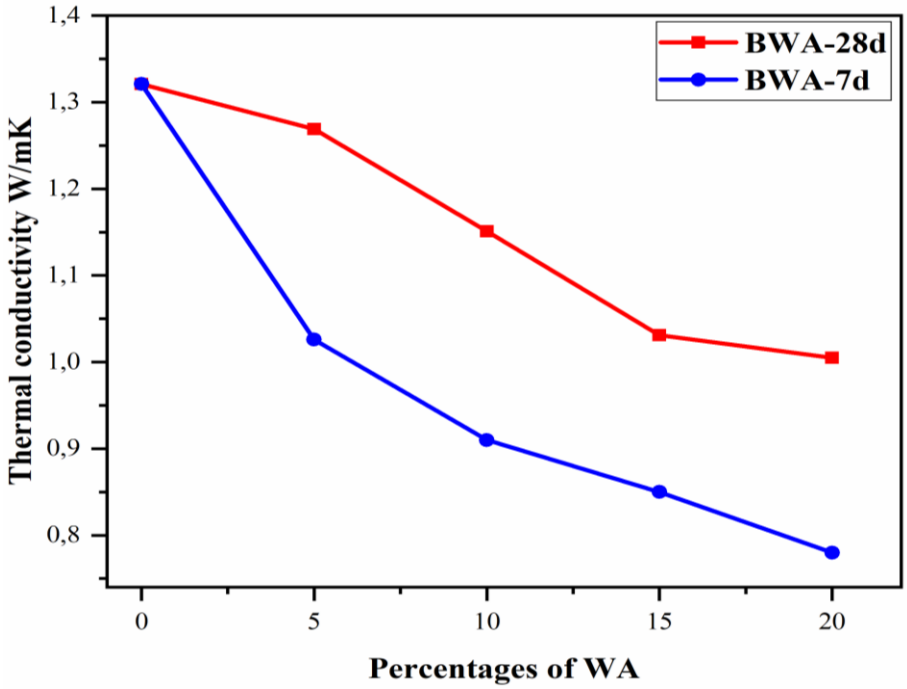

Figure 5.Thermal conductivity of raw bricks as a function of wood ash content.

This granular distribution (low clay percentages) causes pores connected to each other, forming thus a system and allowing the passage of flow between the pores of the brick. Similar results have been observed by other authors, the decrease in thermal conductivity related on the nature and amount of ash added to the mixture (Eliche – Quesadaet al., 2021; Çiçek et al., 2015; Minhaj Kazmia et al., 2018; Carrasco et al., 2014; Eliche – Quesada et al., 2018; Siddiqua et al., 2018; Rivera et al., 2021; Rivera et al., 2020; Leitão et al., 2017). The thermal conductivity values of BWA(0-20%) were below the minimum required by ASTM E2392M-10 it is of the order of 1.2W/mK.

Conclusion

Based on the results of this experimental study, it can be concluded that the recovery of wood ash as a partial substitution for silty earth was promising to produce compressed earth bricks. It's represented a sustainable solution with a good compromise between thermal, economic and environmental performance. WA are good chemical stabilizers for compacted earth bricks, they allow to achieve better thermal resistances (thermal conductivities) at 20% dosages. This experimental investigation gate on the advantage of recovering of wood ash from biomass waste to a high CaO content on the thermal properties of compressed earth bricks.

Scientific Ethics Declaration

The authors declare that the scientific ethical and legal responsibility of this article published in EPSTEM journal belongs to authors.

Acknowledgements

* This article was presented as an oral presentation at the International Conference on Technology, Engineering and Science (www.icontes.net) held in Antalya/Turkey on November 16-19, 2022.

References

AFNOR XP P13-901. (2001). *Compressed earth blocks for walls and partitions: Definitions - Specifications - Test methods - Acceptance conditions*. Saint-Denis La Plaine Cedex: AFNOR.

ASTM E2392M-10. (2016). *Standard guide for the design of earthen wall construction systems*. https://webstore.ansi.org/standards/astm/astme2392e2392m10?gclid=EAIaIQobChMIzICQyNSa_AIVApBoCR2OjAtCEAAYASAAEgIqJPD_BwE

Balasubramaniam T, Sharan Karthik P.M, Sureshkumar S, Bharath M, & Arun M. (2021). Effectiveness of industrial waste materials used as ingredients in fly ash brick manufacturing. *Materials Today: Proceedings, 45,* 7850-7858.

Carrasco, B., Cruz, N., Terrados, .J, Corpas, F.A., & Pérez, L. (2014). An evaluation of bottom ash from plant biomass as a replacement for cement in building blocks. *Fuel, 118*, 272-280.

Çiçek, T., & Çinçin, Y. (2015). Use of fly ash in production of light - weight building bricks. *Construction and Building Materials. 94*, 521-527

Eliche – Quesada, D., Sandalio – Pérez, J. A., Martínez – Martínez, S., Pérez – Villarejo, L., & Sánchez – Soto, P. J. (2018), Investigation of use of coal fly ash in eco - friendly construction materials: fired clay bricks and silica - calcareous non fired bricks. *Ceramics International, 44*, 4400-4412.

Eliche – Quesada, D., Felipe – Sesé, M. A., & Fuentes – Sánchez, M. J., (2021). Biomass bottom ash waste and by - products of the acetylene industry as raw materials for unfired bricks. *Journal of Building Engineering. 38,* 102191.

Felipe – Sesé, M. A., Pérez – Villarejo, L., Castro, E., & Eliche – Quesada, D. (2020). Wood bottom ash and GeoSilex: a by - product of the acetylene industry as alternative raw materials in calcium silicate units. Materials. *13,* 489.

ISO 8894-1. (1987). *Refractory materials-determination of thermal conductivity-Part 1: Hot wire method (Crosspiece)*. https://www.iso.org/standard/16420.html

Leitão, D., Barbosa, J., Soares, E., Miranda, T., Cristelo, N., & Briga-Sá, A. (2017). Thermal performance assessment of masonry made of ICEB's stabilised with alkali-activated fly ash. *Energy and Buildings, 139,* 44-52.

Mansour M.B, Jelidi A, Cherif A.S, & Jabrallah S.B. (2016). Optimizing thermal and mechanical performance of compressed earth blocks (CEB). *Construction and Building Materials, 104,* 44-51.

Minhaj Kazmia, S., Munir, M. J., Patnaikuni, I., Wu, Y., & Fawad, U., (2018). Thermal performance enhancement of eco-friendly bricks incorporating agro-wastes. *Energy and Buildings,158,* 1117-1129.

Omar Sore S, Messan A, Prud'homme E, Escadeillas G, Tsobnang F. (2018). Stabilization of compressed earth blocks (CEBs) by geopolymer binder based on local materials from Burkina Faso. *Construction and Building Materials. 165,* 333-345.

NF P 18-592. (1990). *Aggregates - Methylene blue test - Stain method. Association francaise de normalisation (AFNOR), Paris*. http://www.afnor.fr

NF P94-051 (1993) *Soils: Investigation and testing—Determination of atterberg limits—Liquid limit test using casagrande apparatus—Plastic limit test on rolled thread. Association Francaise de Normalisation (AFNOR), Paris.* http://www.afnor.fr

NF EN 993-15. (2006). *Test methods for dense shaped refractory products - Part 15: Determination of thermal conductivity by the hot wire (parallel) method. Association Francaise de Normalisation (AFNOR), Paris*. http://www.afnor.fr

Rivera, J., Gutiérrez, R. M., Ramirez-Benavides, S., & Orobio A. (2020). Compressed and stabilized soil blocks with fly ash-based alkali-activated cements. *Construction and Building Materials, 264,* 120285.

Rivera J, Coelho J, Silva R, Miranda T, Castro, & Cristelo N. (2021). Compressed earth blocks stabilized with glass waste and fly ash activated with a recycled alkaline cleaning solution. *Journal of Cleaner Production, 284,* 124783.

Rivera, J., Coelho, J., Silva, R., Miranda, T., Castro, F., & Cristelo N. (2021). Compressed earth blocks stabilized with glass waste and fly ash activated with a recycled alkaline cleaning solution. *Journal of Cleaner Production, 284,* 124783.

Siddiqua, S., & Barreto, P.N.M. (2018). Chemical stabilization of rammed earth using calcium carbide residue and fly ash. *Construction and Building Materials, 169,* 364-371.

Author Information

Fatma KHELOUI
Civil Engineering Department, University Mouloud Mammeri of Tizi Ouzou, 15000, Algeria
Contact e-mail:fatma.kheloui@ummto.dz

Nadia BOUSSAA
Civil Engineering Department, University Mouloud Mammeri of Tizi Ouzou, 15000, Algeria
Laboratory LGCA, Faculty of Technology, University of Bejaia, 06000 Bejaia, Algeria

Nasser CHELOUAH
Laboratory LGCA, Faculty of Technology, University of Bejaia, 06000 Bejaia, Algeria

To cite this article:

Kheloui, F., Boussaa, N., & Chelouah, N.. (2022). Investigation of wood biomass ash on the thermal behavior of compressed earth bricks. *The Eurasia Proceedings of Science, Technology, Engineering & Mathematics (EPSTEM), 21,* 412-417.

The Eurasia Proceedings of Science, Technology, Engineering & Mathematics (EPSTEM)
ISSN: 2602-3199

The Eurasia Proceedings of Science, Technology, Engineering & Mathematics (EPSTEM), 2022

Volume 21, Pages 418-422

IConTES 2022: International Conference on Technology, Engineering and Science

Correlation between Tetragonality and the Residual Stress in Cryotreated Spring Steels

Resat Can OZDEN
Eskişehir Osmangazi University

Abstract: In the conventional heat treatment process (CHT), a significant amount of compressive stress occurs in the material as a result of the quenching process. After the tempering process, it is seen that the materials lose those compressive stress. This loss can be explained by the formation of carbide structures and the loss of tetragonality of the supersaturated martensite structure. The cryogenic treatment is a complementary process that it has been given to a miscellany of materials to improve their mechanical and physical attributes. It was first commercially recognized as an effective method in achieving complete martensitic transformation in the alloyed steels. In this study, microstructural investigations were carried out in order to relate the microstructural properties to the mechanical properties following the cryogenic treatment. For this purpose, the conventional heat treatment (CHT) and the deep cryogenic treatment (DCT: -196°C) procedures were applied to various medium carbon spring steels. The martensite lattice parameters and the amount of retained austenite were measured by using high-resolution X-ray diffractometer. Rietveld analysis was used to deconvolute the overlapping peaks of martensites.

Keywords: Steel, Cryogenic, Residual stress, Rietveld

Introduction

The notion of chilling below zero degrees was proposed in the mid-1920s and subjected to extensive research in the 1940s, which created the groundwork for the complementing Cryogenic process (Villa et al., 2017). In particular, the Deep Cryogenic Treatment (DCT) procedure, which is carried out below -190°C, is frequently used to enhance the mechanical characteristics of steels (Preciado & Pellizzari, 2014). The conversion of retained austenite to martensite, a rise in carbide deposits, and enhanced homogeneity in the matrix are microstructural factors that account for this improvement in mechanical characteristics (Özden & Anik, 2020).

The quenching procedure in the conventional heat treatment method (CHT) causes the material to experience a sizable amount of compressive stress. It is observed that the samples substantially lose these compressive stresses during the tempering process. (Bensely et al., 2008). The precipitation of nano-fine carbides in the structure and the elimination of tetragonal supersaturated martensite are the causes of this reduction (Preciado & Pellizzari, 2014). Molybdenum and other carbide-forming elements are crucial in preventing grain development in the primary carbide structure. Additionally, they promote the precipitation of secondary carbide structures, which preserve compressive stresses in the structure (Michaud et al., 2007). Since spring steels operate under a variety of loads, it is extremely desirable to keep these compression stresses in the structure (Myeong & Yamabayashi, 1997).

In this work, three medium carbon spring steels (55Cr3, 51CrV4, and 52CrMoV4) with various alloying components were subjected to a cryogenic procedure. In order to quantify the tetragonality (c/a ratio) of martensite and the impact of alloying elements on residual stress, the effect of the cryogenic process was examined using X-Ray Diffraction (Rietveld Refinement and Residual Stress) technique.

Method

Medium carbon spring steels with compositions of 55Cr3, 51CrV4, and 52CrMoV4 were used in the investigation. ÇEMTAŞ (Bursa) produced the steels in a 55 mm diameter using the continuous casting method. After the casting, they were hot rolled to a diameter of 19 mm and then cut into 20 cm lengths. Table 1 displays the results of optical emission spectrometry analysis in weight %.

Table 1. Optical emission spectrometry analysis results (Weight %)

Steel	C	Si	Mn	Cr	Mo	V	P	S
55Cr3	0,57	0,30	0,85	0,91	-	-	0,010	0,005
51CrV4	0,52	0,28	0,84	0,93	-	0,13	0,008	0,004
52CrMoV4	0,54	0,26	0,87	1,12	0,19	0,11	0,009	0,003

XRD experiments were carried out with a Panalytical Empyrean diffractometer at a speed of 0.25° min^{-1} between the 2θ range of 20° - 120°. The PDF 4+ program containing the ICDD database was used for the CIF files required for Rietveld analysis. Rietveld analyzes were carried out with MAUD (materials analysis using diffraction) 2.92v program. The program was capable to refine the material structure and the microstructure simultaneously with the Marquardt least-squares method (Gasan & Erturk, 2013). The refinement was continued with new steps until the goodness of fit (GOF) coefficient stopped converging to 1.

XStress 3000 diffractometer was used to determine the residual stresses of the samples. Cr-Kα X-ray source was used throughout the experiment. 156.4° diffraction angle, 0.3 Poisson ratio, and 211 GPa Young's Modulus were selected as the experimental parameters. Average Diffraction data were measured in seven tilt angles between -40° and +40° with 20 second exposure time. These seven tilt angles were averaged to determine the residual stress and FWHM values of the sample.

Results and Discussion

X-Ray Diffaction and Rietveld Analysis

Phase evaluations of conventionally hardened and cryogenically treated spring steels used in the study were carried out using XRD technique. XRD patterns of all samples are presented in Figure 1. In the XRD examination, all the structures were characterized as tempered martensite. Steels have a very high hardenability with the effect of their carbon ratios and alloying elements. Therefore, the low amount of residual austenite in the samples could not be detected in the XRD analysis. This indicates that the amount of austenite phase is below the minimum XRD phase detection percentage of 3%. The 2θ° angles of the detected peaks are presented in Table 2.

Table 2. 2θ° angles of the detected peak

Sample	2θ° - α'(110)	2θ° - α'(200)	2θ° - α'(211)	2θ° - α'(220)
CHT-52CrMoV4	44,159	64,432	81,791	98,453
CHT-51CrV4	44,214	64,422	81,806	98,442
CHT-55Cr3	44.255	64,462	81,741	98,386
DCT-52CrMoV4	44,574	64,769	82,080	98,715
DCT-51CrV4	44,619	64,839	82,237	98,807
DCT-55Cr3	44.606	64,830	82,184	98,821

After the cryogenic treatment, the samples have a shift of about 0.4 degrees compared to the conventionally treated samples. This shift can be associated with a change in the lattice parameters. Although it cannot be determined due to the % amount, the plastic deformation effect of the new martensite structure formed by the transformation of the retained austenite structure can be shown as the reason for this shift.

Looking closely at the XRD patterns, it can be seen that there is a noticeable expansion effect at the peaks of the cryogenically treated samples as a secondary effect of cryogenic treatment. This expansion effect has been reported in the literature as an extension of the increasing strain in the structure (Warren & Averbach, 1950). It is also possible to think that this strain indicates an increase in the dislocation density. These stresses created by the dislocation density are directly related to heterogeneous stress distributions that can act as a driving force for carbide formation during the cryogenic process.

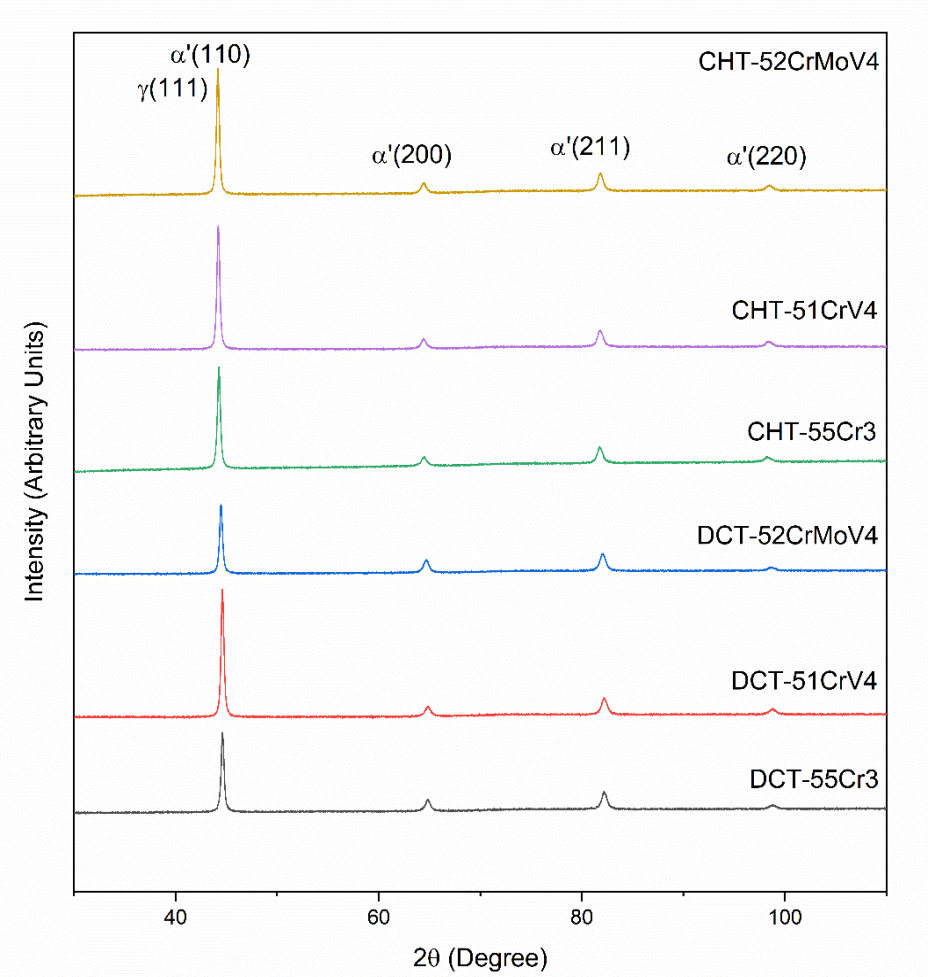

Figure 2. XRD patterns of the samples

In order to quantitatively investigate the effect of cryogenic treatment on the lattice structure of tempered martensite, Rietveld analysis was performed on the samples. The lattice parameters (a, c) and tetragonality (c/a) obtained as a result of the analysis are presented in Table 3.

Table 3. Rietveld (Space Group P42 n:1 a_M: 2.8665 Å) PDF Card - 04-003-1451

Procedure	Sample	a (Å)	c (Å)	c/a
Q	52CrMoV4	2.865949	2.921633	1.019429
	51CrV4	2.865861	2.923466	1.020100
	55Cr3	2.865536	2.918508	1.018485
CHT	52CrMoV4	2.866171	2.894268	1.009803
	51CrV4	2.865433	2.894786	1.010244
	55Cr3	2.866215	2.892435	1.009148
DCT	52CrMoV4	2.865857	2.898057	1.011236
	51CrV4	2.866244	2.899036	1.011441
	55Cr3	2.866919	2.895714	1.010044

Considering Table 3, it can be said that the deep cryogenic process causes plastic deformation in the cage, as in the XRD results, and plays an active role in preserving the tetragonality of the martensite. The deformation caused by the transformation-induced fresh martensite and carbide formation and the effect of locking the slip planes increased the tetragonality of the martensite structure.

Residual Stress Analysis

Residual stress measurement was applied to all heat treated samples to measure the effect of the deformation created by the cryogenic process on the microstructure, which can be directly related to the mechanical

properties. Tests were also applied to the quenched samples without tempering (Q) as the base sample, aiming to determine the compression stresses created by the transformation itself. Residual stress results are presented in Table 4.

Table 4. Residual stress results of samples

Sample	55Cr3		51CrV4		52CrMoV4	
	MPa	FWHM	MPa	FWHM	MPa	FWHM
Q	-102,9 (± 9,3)	3,23 (± 0,05)	-147,3 (± 5,4)	3,36 (± 0,07)	-154,46 (± 6,80)	3,23 (± 0,08)
CHT	42,3 (± 10,9)	2,22 (± 0,06)	43,1 (± 10,6)	2,12 (± 0,06)	32,47 (± 4,75)	2,70 (± 0,05)
DCT	-51,7 (± 7,3)	2,47 (± 0,07)	-67,0 (± 10,0)	2,76 (± 0,07)	-108,10 (± 6,56)	3,43 (± 0,07)

When the table is examined, it is seen that a significant amount of residual compression stress occurs as a result of the quenching (H) process, as expected. After the tempering process, it is seen that the specimens lose their compressive stress to a great extent. This reduction can be attributed to the precipitation of nanofine carbides in the structure and the removal of tetragonal supersaturated martensite (Bensely vd., 2008; Preciado ve Pellizzari, 2014). Conversion of retained austenite to martensite in cryogenic samples creates compression stresses in the internal structure and causes crystal defects in the form of dislocations and twinnings. During the martensitic transformation at cryogenic temperatures, plastic deformation is accompanied by the volume effect created by the martensitic transformation. This resulting dislocation and/or twinning slides in the plane and engulfs the inert carbon atoms and causes carbon clusters to form. During tempering, these carbon clusters serve as nucleation sites for the precipitation of fine carbides. The increase in the density of both crystal defects and nanocluster carbides caused greater locking of the already dense dislocations and therefore kept the residual stress in the system, limiting the level of relaxation in cryogenically treated samples. In particular, 52CrMoV4 steel, which contains the most intense carbide-forming element, is the steel group that loses the least compressive stress in the sample (DCT-52CrMoV4) structure.

Conclusion

In the study, the effects of cryogenic treatment on the residual stress and tetragonality of different medium carbon spring steels were investigated. Accordingly, it was observed that the efficiency of deep cryogenic processing (DCT) increased in the presence of carbide-forming alloying elements, and the desired compressive stress could be maintained in the samples. It is possible that the plastic deformation and dislocation density created by increasing tetragonality values can be associated with the persistence of these stresses in the structure.

Scientific Ethics Declaration

The authors declare that the scientific ethical and legal responsibility of this article published in EPSTEM journal belongs to the authors.

Acknowledgements

*This article was presented as the poster presentation at the International Conference on Technology, Engineering and Science (www.icontes.net) held in Antalya/Turkey on November 16-19, 2022.

*Financial assistance from Eskisehir Osmangazi University Research Fund is gratefully acknowledged (Project No: 201615A230). The author wishes to thank MMD Mechanical and Materials Technologies R&D Consulting Engineering Services Industry and Trade Limited Company for the deep cryogenic treatments.

References

Bensely, A., Venkatesh, S., Mohan Lal, D., Nagarajan, G., Rajadurai, A., & Junik, K. (2008). Effect of

cryogenic treatment on distribution of residual stress in case carburized En 353 steel. *Materials Science and Engineering A*, *479*(1–2), 229–235.

Gasan, H., & Erturk, F. (2013). Effects of a destabilization heat treatment on the microstructure and abrasive wear behavior of high-chromium white cast iron investigated using different characterization techniques. *Metallurgical and Materials Transactions A: Physical Metallurgy and Materials Science*, *44*(11), 4993–5005.

Michaud, P., Delagnes, D., Lamesle, P., Mathon, M. H., & Levaillant, C. (2007). The effect of the addition of alloying elements on carbide precipitation and mechanical properties in 5% chromium martensitic steels. *Acta Materialia*, *55*(14), 4877–4889.

Myeong, T., & Yamabayashi, Y. (1997). A new life extension method for high cycle fatigue using micro-martensitic transformation in an austenitic stainless steel. *Journal of Fatigue*, *19*(1), 69–73.

Özden, R., & Anik, M. (2020). Enhancement of the mechanical properties of EN52CrMoV4 spring steel by deep cryogenic treatment. *Materials Science & Engineering Technology*, *51*(4), 422–431.

Preciado, M., & Pellizzari, M. (2014). Influence of deep cryogenic treatment on the thermal decomposition of Fe-C martensite. *Journal of Materials Science*, *49*(23), 8183–8191.

Villa, M., Hansen, M. F., & Somers, M. A. J. (2017). Martensite formation in Fe-C alloys at cryogenic temperatures. *Scripta Materialia*, *141*, 129–132.

Warren, B. E., & Averbach, B. L. (1950). The effect of cold-work distortion on x-ray patterns. *Journal of Applied Physics*, *21*(6), 595–599.

Author Information

Reşat Can OZDEN
Eskişehir Osmangazi University
Eskişehir, Turkey
Contact e mail: *rcanozden@ogu.edu.tr*

To cite this article:

Ozden, R.C. (2022). Correlation between tetragonality and the residual stress in cryotreated sprıng steels. *The Eurasia Proceedings of Science, Technology, Engineering & Mathematics (EPSTEM), 21,* 418-422.

The Eurasia Proceedings of Science, Technology, Engineering & Mathematics (EPSTEM)
ISSN: 2602-3199

The Eurasia Proceedings of Science, Technology, Engineering & Mathematics (EPSTEM), 2022

Volume 21, Pages 423-429

IConTES 2022: International Conference on Technology, Engineering and Science

Prediction of Microhardness Profil of Friction Stir Welded Joints of AA3003 Aluminum Alloy

Chekalil ISMAIL
University of Djillali Liabes

Abdelkader MILOUDI
University of Djillali Liabes

Ghazi ABDELKADER
University of Mascara

Planche MARIE-PIERRE
University of Belfort Montbeliard

Abstract: Friction stir welding is a recommended green process that can replace other assembly techniques. FSW process reveals good mechanical properties, good corrosion resistance and good economic value. For the purpose to evaluate combinations of operating parameters and estimating the welded joint quality, mathematical relationships were carried out using a design of experiment on three levels of rotational speed, feed rate and tool tilt angle. The models allow micro-hardness prediction in the different FSW joint zones of AA3003 aluminum alloy. The interaction of the factors shows that a decrease in rotational speed, angle of inclination and an increase in feed rate leads to a decrease in temperature and good microhardness. A 'W' shape profile of microhardness was shown cross the section, indicating an efficiency equal to 88% and 79% in the nugget and the heat-affected zone successively, compared to the base metal. Contrary any deviation of welding interval may cause various defect such as tunnel voids, 'kissing-bond' defects and crack-like root flaws.

Keywords: Friction stir welding, Mathematical relationships, Microhardness, Aluminum alloy

Introduction

Friction stir welding is an environmentally friendly process and it worths replace other assembly techniques (Fahimpour et al., 2012; Humberto et al., 2016), due to that researchers have carried out several studies in order to understand the combination of the thermomechanical phenomenon exerted by the tool and the metallurgy of the part to be welded during friction stir welding and their influences on the mechanical behavior (Ji et al., 2020; Kimura et al., 2015; Wang et al., 2015).

As a part of a study, a symmetrical 'W' shape profile of hardness was observed on the FSW joints of AA6061-T6 using a stationary shoulder, where the HAZ has the lowest value, and by getting closer to the weld center this value increase sharply up to reaching the TMAZ zone (Sun et al., 2016). Xu et al. (2009) examined the microhardness of FSW joints in different plate thicknesses of AA2219-O, they indicated that the maximum hardness was on the advanced side of the nugget, they also reported that the up of the weld joint was harder than the bottom in the nugget due to the high temperature and the intense mechanical agitation. In addition, the results show clearly that the temperature increases by increasing the speed and/or decreasing the welding speed as for Abdulstaar et al., (2017). They reported that applying shot peening on the FSW joint of AA6061 generally leads to a hardness enhancement in the string zone, especially in the top surface.

The present paper aims to study the interacting of welding parameters to achieve a good quality of AA3003 FSW joint. As well as developing mathematical models to predict microhardness on the different zone of the FSW joints, the results are done by interacting the following welding parameters; rotation speed, feed rate and tool tilt angle.

Method

Butt friction stir welding were released on a vertical milling machine using an adequate tool geometry. The FSW was performef on AA3003 aluminium plates with the following dimension: 400*110*2 mm. the specimens were cut by a waterjet machine. The microhardness test were carried out on SHIMADZU HMV-2000.

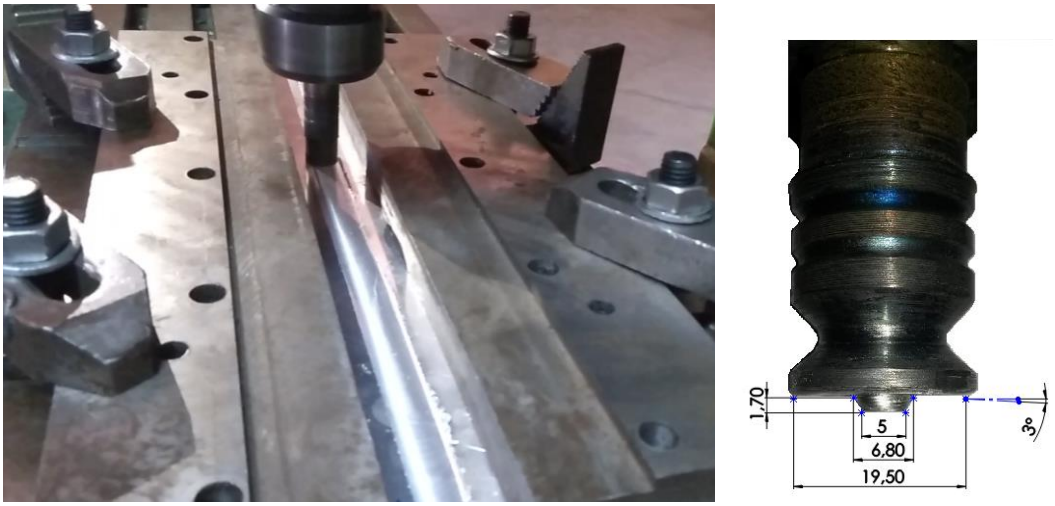

Figure 1. FSW process and the tool geometry

Figure 2. Cutting of specimens

The chemical composition and mechanical properties of the base material before welding are reported in Tabs. 1 and 2. Thechemical composition was obtained by SEM-EDX (Scanning Electron Microscopy - Energy Dispersive X-ray Analysis).

Table 1. Mechanical properties of the material before welding

Microhardness (HV)	YS (MPa)	UTS (MPa)	RS (MPa)	EL %	YM (GPa)	T Fusion (°C)
51	110	160	127	5.6	60	650

Table 2. Chemical composition of the material before welding

Element	Al	Mn	Si	Fe	Cu	Ti	Zn	Mg	Cr
%	96.7	1.3	0.9	0.9	0.13	0.1	0.03	0	0

Experimental Approach

Figure 3 presents a typical example of the profile obtained during the microhardness test; the important factors of this profil of friction stir welding (FSW) joint profile (Output experimental results) are summarized in Tab. 3.

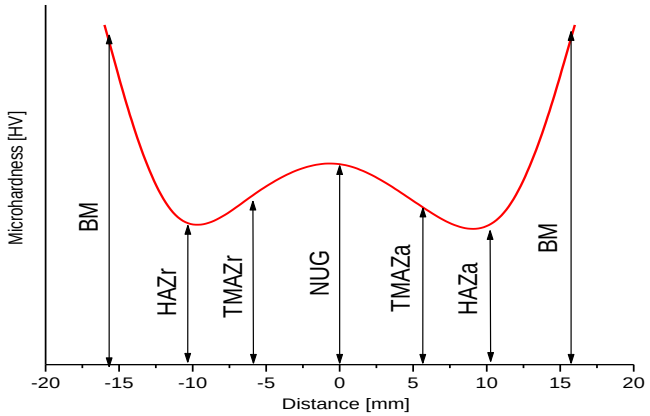

Figure 3. Typical microhardness profil of friction stir welding (FSW) joint

Table 1. Results

	Facteurs	résultats
1	HAZr	Heat affected zone retreating side
2	TMAZr	Themomechanicly affected zone retreating side
3	NUG	nugget
4	TMAZr	Themomechanicly affected zone advancing side
5	HAZa	Heat affected zone advancing side

Table 2. Parameter values for each level

Parameter	Low level -1	Central level 0	High level +1
Rotation speed (rot/min)	1000	1500	2000
Welding speed (mm/min)	200	300	400
Tilt angle (°)	0.5	1.5	2.5

The software MODDE 5.0 (Modeling and Design) [20] is used for the model elaboration and the statistical analysis of the experimental design. If there is curvature in the system, then a polynomial of higher degree must be used, such as the second-order model. The model used has the quadratic form given below:

$$y = a_0 + \sum_{i=1}^{3} a_i x_i + \sum_{1 \le j \le 3} a_{ij} x_j + \sum_{i=1}^{3} a_{ii} x_i^2 + e \qquad (1)$$

$$\boldsymbol{HAZr} = 32{,}67 - 3{,}45.10^{-3}.N + 7{,}15.10^{-2}.S - 1{,}95.T + 4{,}16.10^{-6}.N.S - 5{,}71.10^{-4}.N.T - 4{,}27.10^{-3}.S.T - 2{,}44.10^{-7}.N^2 - 1{,}11.10^{-4}.S^2 + 1{,}37.T^2 \qquad (2)$$

$$\boldsymbol{TMAZr} = 67{,}13 - 2{,}69.10^{-2}.N - 3{,}97.10^{-2}.S - 3{,}8.T + 3{,}87.10^{-6}.N.S + 2{,}33.10^{-3}.N.T - 1{,}97.10^{-3}.S.T + 7{,}04.10^{-6}.N^2 + 6{,}11.10^{-5}.S^2 - 0{,}15.T^2 \qquad (3)$$

$$\boldsymbol{NUG} = 60{,}75 - 1{,}92.10^{-2}.N - 1{,}03.10^{-2}.S - 6{,}39.T + 1{,}11.10^{-5}.N.S + 1{,}06.10^{-3}.N.T - 5{,}95.10^{-3}.S.T + 3{,}86.10^{-6}.N^2 + 6{,}66.10^{-6}.S^2 + 1{,}81.T^2 \qquad (4)$$

$$\boldsymbol{TMAZa} = 53{,}66 - 1{,}27.10^{-2}.N - 2{,}57.10^{-3}.S - 5{,}7.T + 1{,}34.10^{-5}.N.S + 1{,}15.10^{-3}.N.T - 3{,}08.10^{-3}.S.T + 1{,}63.10^{-6}.N^2 - 2{,}33.10^{-5}.S^2 + 1{,}29.T^2 \qquad (5)$$

$$HAZa = 60{,}89 - 2{,}71.10^{-2}.N - 3{,}54.10^{-2}.S - 2{,}36.-3{,}74.10^{-6}.N.+1{,}450766.10^{-3}.N.T - 4{,}56.10^{-3}.S.T + 8{,}23.10^{-6}.N^2 + 8{,}58.10^{-5}.S^2 + 0{,}19.T^2 \quad (6)$$

Table3. Results of the design of experiments tool applied to 30 samples.

Exp	Des	N [tr/min]	S [mm/min]	T [°]	HAZr [HV]	TMAZr [HV]	NUG [HV]	TMAZa [HV]	HAZa [HV]
1	a	1000	200	0.5	40.45	44.16	44.66	42.34	37.85
2	b	1500	200	0.5	34.65	37.76	38.72	41.1	32.6
3	c	2000	200	0.5	34.65	36.44	38	36.5	34.5
4	d	1000	300	0.5	41.4	45.06	49.02	45.46	40.1
5	e	1500	300	0.5	41.4	40.04	42.84	42.14	33.4
6	f	2000	300	0.5	35.3	38.8	44.62	37.42	37.3
7	g	1000	400	0.5	39.05	42.26	43.62	40.66	43.1
8	h	1500	400	0.5	38.7	38.24	42.02	39.6	37.1
9	i	2000	400	0.5	37.7	40.32	44.04	40.08	37.3
10	j	1000	200	1.5	35.7	41.86	42.56	39.32	39.55
11	k	1500	200	1.5	34.75	36.86	36.18	37.34	35.5
12	l	2000	200	1.5	34.5	41.62	36.58	33.88	35.4
13	m	1000	300	1.5	37.75	41.24	37.9	39	33.95
14	n	1500	300	1.5	35.35	35.62	36.26	35.84	30.2
15	o	2000	300	1.5	33.2	37.76	34.76	36.84	36.05
16	p	1000	400	1.5	39.95	37.68	42.06	37.66	37.35
17	q	1500	400	1.5	35.55	39.46	40.66	38.54	35.85
18	r	2000	400	1.5	34.35	40.28	38.5	37.96	35.05
19	s	1000	200	2.5	41.5	36.52	42.72	40.02	33.2
20	t	1500	200	2.5	36.2	35.7	37.14	37.18	32.8
21	u	2000	200	2.5	33.85	41	42.2	39.22	37.5
22	v	1000	300	2.5	43.6	36.08	40.72	38.36	35.8
23	w	1500	300	2.5	41.5	34.78	41.12	38.7	32.65
24	x	2000	300	2.5	37.8	36.06	38.42	37.58	32.95
25	y	1000	400	2.5	39.15	38.7	38.06	37.64	35.85
26	z	1500	400	2.5	37	34.1	37.28	35.7	31.15
27	aa	2000	400	2.5	34.75	39.58	37.96	37.4	36.25
28	bb	1500	300	1.5	37.75	38.18	37.82	36	34.1
29	cc	1500	300	1.5	37.85	34.48	38.44	37.54	30.05
30	dd	1500	300	1.5	37.6	34.1	37.06	35.38	33.1

Results and Discussion

Generally good quality of the FSW joint has been released at low rotation speed on HAZr. Contrary the low microhardness value was found tilting angle of 1.5° (Figure). In this type of interaction, Hv is large while the two factors S and N take minimal values. Therefore, in order to increase HAZr, it is necessary to decrease S and N. Finally, Figure 4 illustrates the variation of HAZr as a function of the factors T and N. In this case, Hv has high values for two intervals: the first interval corresponds to a rotational speed equal to 1000 rpm and to an angle of inclination Θ comprised between 2.2° and 2.4°, and the second interval corresponds to S comprised between 260 and 400 mm/min and to Θ equal to 0.5° and 2.48°

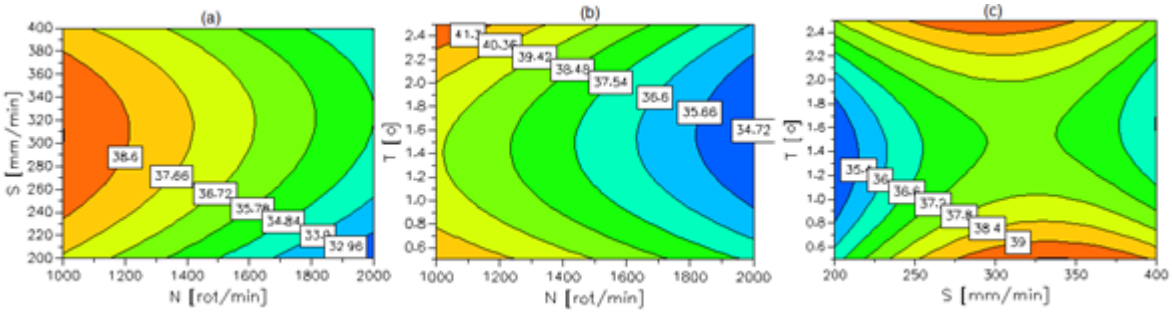

Figure 4. Variation of HAZr as a function of the three factors

Figure 5 presents the effect of the three factors S, T and N acting simultaneously TMAZr The analysis of the graph of this figure suggests that the more N decreases, the more TMAZr also increases until reaching the maximum value of 44 Hv, while S is between [200 and 240 mm/min] and [360 - 400 mm/min]. In addition, it should also be noted that σ_U can reach values closer to the maximum values for a maximum Va equal to 400 mm/min and for a Vr between 1300 and 2000 rpm. In this type of interactions, TMAZr is large while the two factors S and T take minimum and maximum values.

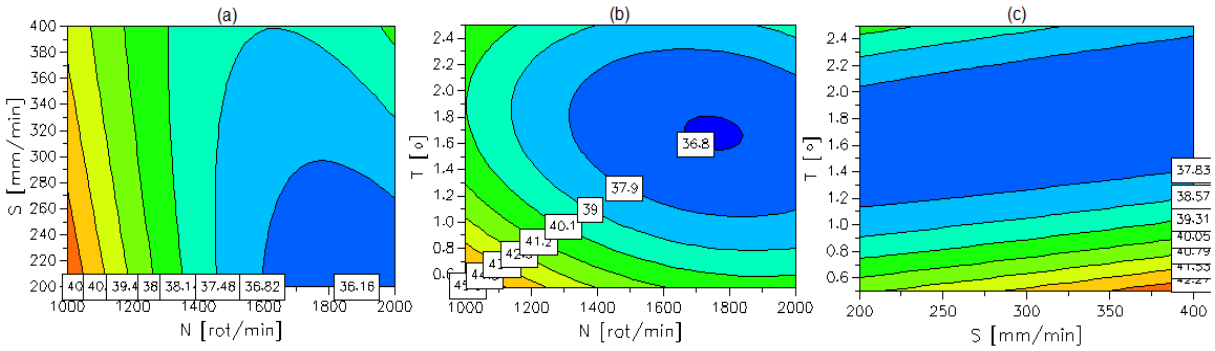

Figure 5 - Variation of nu as a function of the three factors

This new section aims to present the response surface obtained from NU, while varying S and T and N. It can be seen that NU takes maximum values while the two factors S, T and N take minimum values.

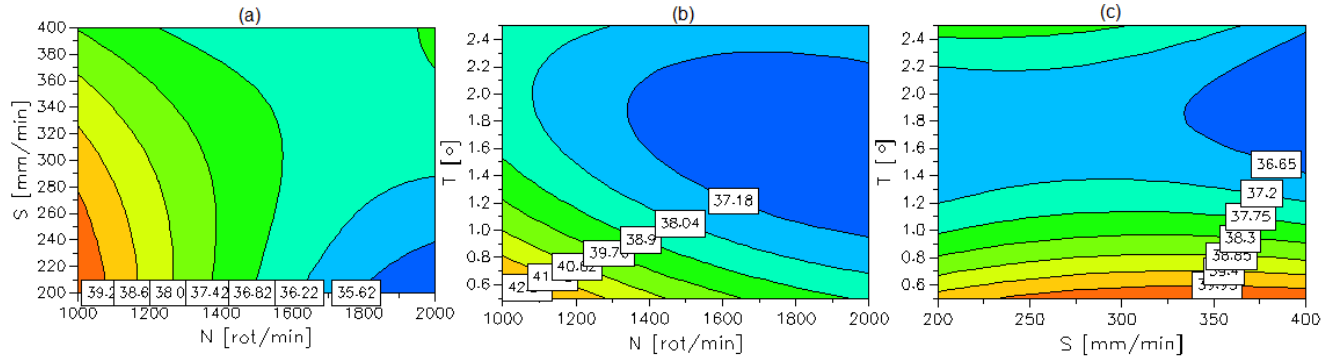

Figure 6 - Variation of tmaza as a function of the three factors

On the other hand, figure 6 illustrates the variation of TMAZa as a function of S, N and T. It can be seen that the simultaneous decrease in S and N leads to an increase in TMAZa; however, increasing S and decreasing T leads to a decrease in TMAZa amplitude. This effect is more pronounced when S is between 250 and 400 mm/min.

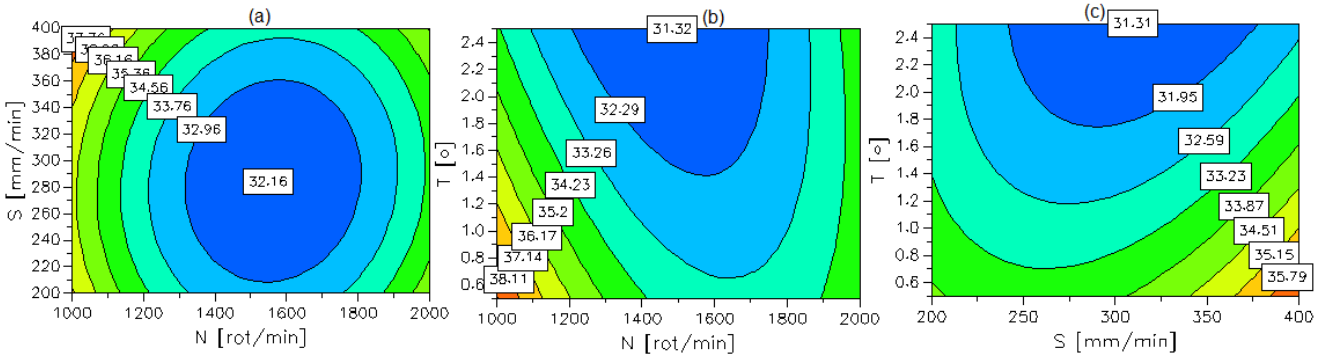

Figure 7.Variation of haza as a function of the three factors

Figure 7 presents the predicted HAZa response as a function of the three factors (S, N and T). Analysis of the curve in this figure shows that a minimum value of HAZa is obtained when the value of Θ is between 1.6 and 2.4°, that of N is in the range of 1300 to 1650 rpm, while S is maintained at 400 mm/min. From these results it is possible to derive the optimum values for the speeds of rotation and the welding speeds. The green curve corresponds to the welding speed 100 mm/min gives optimal results because there is stability on the curve.

From the obtained result (Tab 4) and the previous results we conclude that the decrease in the rotation speed (high temperature)leads to a good quality of the hardness, this result are in agreement with the founding research of (Tan et al., 2017) , where they prove that increasing in the ambient temperature cause a gradually increase in the recrystallized grains size in the nugget.

Table 4. Optimal values for the mechanical properties of the welded joint

N [rot/min]	S [mm/min]	T [°]	HAZr [HV]	TMAZr [HV]	NUG [HV]	TMAZa [HV]	HAZa [HV]
1000	234.272	2.5	41.7774	36.8592	42.3316	39.7706	34.9224
2000	399.993	0.5	37.177	39.6955	42.8259	39.8729	37.3414
1000	387.525	0.5	40.7006	43.945	46.129	42.3613	41.5184
2000	400	2.5	34.9685	39.385	39.6615	38.1189	35.7396
1000	374.061	0.5	40.965	43.7331	46.0729	42.539	41.0163
1000	227.73	0.5	39.6441	43.7325	45.7138	43.5942	38.7915
1000	315.286	0.5	41.3575	43.2261	45.8735	43.1556	39.4113
1000	387.525	0.5	40.7006	43.945	46.129	42.3613	41.5184

Conclusion

This research focusses on friction stir welding quality in term of microhardness. Microhardness measurement displays W shape profile. Cold welding shows good quality than hot welding. Whatever the welding conditions, there is a decrease in hardness in the HAZ which comes from the restoration. This phenomenon is characterized by the recombination and rearrangement of dislocations leading to a slight decrease in their density. At the limit of the HAZ and TMAZ zones, the granular structure is completely recrystallized and the grains are all equiaxed. At the same time, recrystallization takes place near the TMAZ, resulting in a significant reduction in hardness. In this zone which breaks down into two parts, we find on the HAZ zone side equiaxed grains therefore a recrystallization which is likely to be dynamic and on the core zone side a geometric dynamic recrystallization due to a hot torsion caused by the threading of the rotating pawn. The choice of the operating parameters and the welding mode must therefore be the subject of an in-depth study. It is therefore necessary to define the quality requirements of an FSW weld. The ISO/DIS 25239-3 standard defines the characteristics that the weld beads must comply with in order to validate the choice of operating parameters and the entire welding procedure.

Scientific Ethics Declaration

The authors declare that the scientific ethical and legal responsibility of this article published in EPSTEM journal belongs to authors.

Acknowledgements

* This article was presented as an oral presentation at the International Conference on Technology, Engineering and Science (www.icontes.net) held in Antalya/Turkey on November 16-19, 2022.

References

Abdulstaar, M. A., Al-Fadhalah, K. J., & Wagner, L. (2017). Microstructural variation through weld thickness and mechanical properties of peened friction stir welded 6061 aluminum alloy joints. *Materials Characterization, 126,* 64-73.

Fahimpour, V., Sadrnezhaad, S. K., & Karimzadeh, F. (2012). Corrosion behavior of aluminum 6061 alloy joined by friction stir welding and gas tungsten arc welding methods. Materials & Design, 39, 329-333.

Humberto Mota de Siqueira, R., Capella de Oliveira, A., Riva, R., Jorge Abdalla, A., & Sérgio Fernandes de Lima, M. J. W. i. (2016). Comparing mechanical behaviour of aluminium welds produced by laser beam welding (LBW), friction stir welding (FSW), and riveting for aeronautical structures. *Welding International 30*(7), 497-503.

Ji, H., Deng, Y., Xu, H., Lin, S., Wang, W., & Dong, H. (2020). The mechanism of rotational and non-rotational shoulder affecting the microstructure and mechanical properties of Al-Mg-Si alloy friction stir welded joint. Materials & Design, 192, 108729.

Kimura, M., Fuji, A., & Shibata, S. (2015). Joint properties of friction welded joint between pure magnesium and pure aluminium with post-weld heat treatment. Materials & Design, 85, 169-179.

Sun, Z., Yang, X., Li, D., & Cui, L. (2016). The local strength and toughness for stationary shoulder friction stir weld on AA6061-T6 alloy. *Materials Characterization, 111*, 114-121.

Tan, Y. B., Wang, X. M., Ma, M., Zhang, J. X., Liu, W. C., Fu, R. D., & Xiang, S. (2017). A study on microstructure and mechanical properties of AA 3003 aluminum alloy joints by underwater friction stir welding. *Materials Characterization, 127*, 41-52.

Wang, F. F., Li, W. Y., Shen, J., Hu, S. Y., & Dos Santos, J. F. (2015). Effect of tool rotational speed on the microstructure and mechanical properties of bobbin tool friction stir welding of Al–Li alloy. Materials & Design, 86, 933-940.

Xu, W., Liu, J., Luan, G., & Dong, C. (2009). Temperature evolution, microstructure and mechanical properties of friction stir welded thick 2219-O aluminum alloy joints. *Materials & Design, 30*(6), 1886-1893.

Author Information

Abdelkader Miloudi
University of Djillali Liabes, Sidi Bel Abbès, Algeria
BP 89,Sidi Bel Abbès 22000 ,
Algeria
Email: miloudidz@yahoo.fr

Ismail Chekalil
University of Djillali Liabes, Sidi Bel Abbès, Algeria
BP 89,Sidi Bel Abbès 22000 ,
Algeria

Abdelkader Ghazi
University of Mascara
Bp 305 Route de Mamounia, 29000 Mascara
Algeria

Planche Marie-Pierre
University of Belfort Montbeliard
BP 47870, 21078 Dijon Cedex
France

To cite this article:

Miloudi, A., Chekalil, I., Ghazi A., & Marie-Pierre, P. (2022). Prediction of microhardness profil of friction stir welded joints of AA3003 aluminum alloy.*The Eurasia Proceedings of Science, Technology, Engineering & Mathematics (EPSTEM), 21*, 423-429.

The Eurasia Proceedings of Science, Technology, Engineering & Mathematics (EPSTEM)
ISSN: 2602-3199

The Eurasia Proceedings of Science, Technology, Engineering & Mathematics (EPSTEM), 2022

Volume 21, Pages 430-434

IConTES 2022: International Conference on Technology, Engineering and Science

Dual Band Branch-Line Coupler Using Stub-Loaded Lines

Heba EL- HALABI
Beirut Arab University

Manal K. FATTOUM
Beirut Arab University

Abstract: This paper describes the design of a center-tapped stub loaded branch line coupler for dual band operation. In this design, the quarter wavelength transmission lines of the conventional branch line coupler are replaced with an equivalent T-shaped transmission lines. Design equations for evaluating the characteristic impedances and the electrical lengths of the coupler arms are derived based on ABCD-matrix. The proposed coupler operates at 2 and 4 GHz corresponding to S-band applications like weather radar and satellite communications. Simulations are done using Agilent ADS software on Roger RO4003 substrate with dielectric constant of 3.38. The simulated results of the S-parameters show that the return loss and isolation loss are well below -20 dB at the designed frequencies. The amplitude imbalance between the two output ports S_{21} and S_{31} does not exceed 0.3 dB. The phase difference between the output ports of the designed coupler is -89.5^o at 2 GHz and -270^o at 4 GHz. Efforts are done on reducing the size of the coupler by folding the stub towards the inner area of the coupler to be ready for fabrication.

Keywords: Branch line coupler, Dual-band, Stub loaded transmission lines

Introduction

Branch-line coupler is a passive microwave component used in various wireless communication systems. It is a four port device constructed from four quarter-wavelength ($\lambda/4$) transmission lines and is used to split/combine microwave signals and provide 90^o phase shift between the output ports (Pozar, 2012). Recently developing a dual-band branch line coupler is drawing a lot of attention. Stub loaded transmission lines is among the popular techniques for obtaining dual-band operation of a branch line coupler. Stubs can be placed at the center of the arms of the branch line coupler (Feng et al., 2020; Zhang et al., 2007), or at their input (Kim, Lee & Park, 2008). A combination of stub loading and unequal arm lengths is also proposed in Kim, et al. (2008) and Park (2009). Other techniques reported to attain dual-band operation of a coupler include: Stepped-impedance stubs (Chin et al., 2010), orthogonal coupled branches (Zhan et al.,2018) and coupled lines (Feng et al.,2018). In this paper, the design of a dual-band center-tapped stub loaded branch line coupler is presented based on the T-network in Zhang & Chen (2007). In Section II, the methodology used for calculating the impedances and electrical lengths values is investigated and verified by the S-parameters simulations conducted in section III. Finally, the paper is concluded in section IV.

Theoretical Analysis of the Stub Loaded Coupler

The structure of the proposed dual-band coupler is shown in Figure 1. To each quarter wavelength arm of the conventional coupler, a stub is attached to the arm center thus transforming the ordinary quarter wavelength

transmission line into a T-shaped line. Figure 2 shows the conventional quarter wavelength transmission line and its equivalent T-shaped line, where Z_o, θ_o correspond to the characteristic impedance and electrical length of the conventional ($\lambda/4$) coupler arm and Z_1, Z_2, θ_1 and θ_2 correspond to the T-shaped equivalent line. To obtain design equations ABCD-matrix analysis for cascaded network is used.

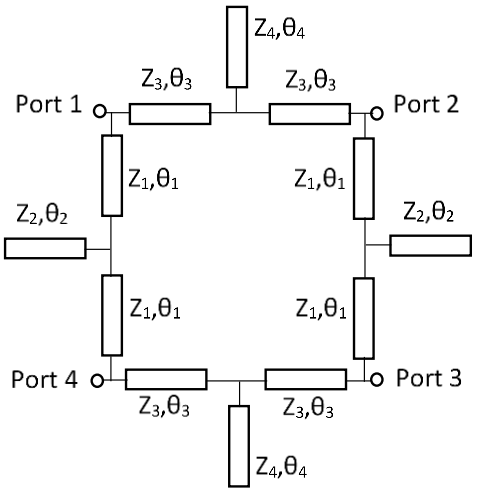

Figure 1. Proposed planar dual-band branch line coupler

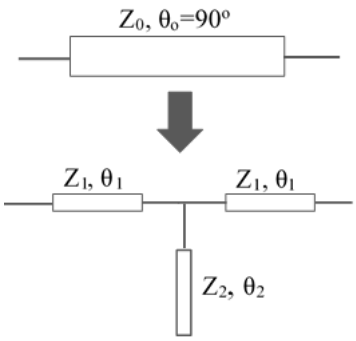

Figure 2. Conventional quarter wavelength line and its T-shaped line Equivalent

The ABCD-matrix of a conventional quarter-wavelength ($\lambda/4$) transmission line with characteristic impedance Z_o is:

$$\begin{bmatrix} A & B \\ C & D \end{bmatrix}_{\lambda/4} = \begin{bmatrix} 0 & jZ_o \\ \frac{j}{Z_o} & 0 \end{bmatrix} \quad (1)$$

The ABCD-matrix of a T-shaped line consisting of cascaded sections is:

$$\begin{bmatrix} A_T & B_T \\ C_T & D_T \end{bmatrix}_{T-shaped} = \begin{bmatrix} cos\theta_1 & jZ_1 sin\theta_1 \\ j\frac{sin\theta_1}{Z_1} & cos\theta_1 \end{bmatrix} \begin{bmatrix} 1 & 0 \\ j\frac{tan\theta_2}{Z_2} & 1 \end{bmatrix} \begin{bmatrix} cos\theta_1 & jZ_1 sin\theta_1 \\ j\frac{sin\theta_1}{Z_1} & cos\theta_1 \end{bmatrix} \quad (2)$$

In order to match the suggested T-shaped line to the conventional $\lambda/4$ line, the parameters of the $[ABCD]_{\lambda/4}$ are equated to the parameters of $[ABCD]_{T\text{-shaped}}$ to get:

$$Z_1 = \frac{Z_o}{tan\theta_1} \quad (3)$$

$$Z_2 = \frac{Z_1}{2} \tan(2\theta_1) tan\theta_2 \quad (4)$$

Since the electrical length θ_1 is function of frequency, θ_1 is defined as $\pi/2$ at f_c , and θ_2 is defined as $2\theta_1$, where f_c is the center frequency of the two pass band frequencies f_1 and f_2 defined as $f_c = (f_1 + f_2)/2$. Then θ_1 equals to $\pi/2$ x f_1 / f_c at the lower designed frequency f_1 and $\pi/2$ x f_2 / f_c at the upper designed frequency f_2 .

The design steps for the dual band branch line coupler are:

i. Start by evaluating θ_1, θ_2, θ_3 and θ_4 at the designed frequencies
ii. Evaluate Z_1, Z_2, Z_3 and Z_4 where the realizable widths of high impedance transmission lines should be taken into consideration.

Simulation Results and Discussions

Based on the previous discussion, a dual-band coupler is designed and simulated. The coupler is built over Rogers RO4003 substrate having h = 0.813mm, ε_r = 3.38 and tan(δ) = 0.0027. The calculated coupler impedances are Z_1= 28.8 Ω, Z_2= 43.2 Ω, Z_3= 21 Ω and Z_4= 30.6 Ω. The physical dimensions of the designed coupler arms are presented in Table 1.

The simulated S-parameters of the proposed dual-band branch line coupler are shown in Figure 3 and Figure 4 respectively. The center frequencies of the two pass bands are 2 and 4 GHz. Insertion losses S_{21}/S_{31} are -3.3/-3.2 dB and -3.3/-3.6 dB at 2 and 4 GHz respectively. The amplitude imbalance between the two output ports S_{21} and S_{31} does not exceed 0.3 dB. The return loss S_{11} and isolation loss S_{41} are well below –20 dB at the center frequencies.

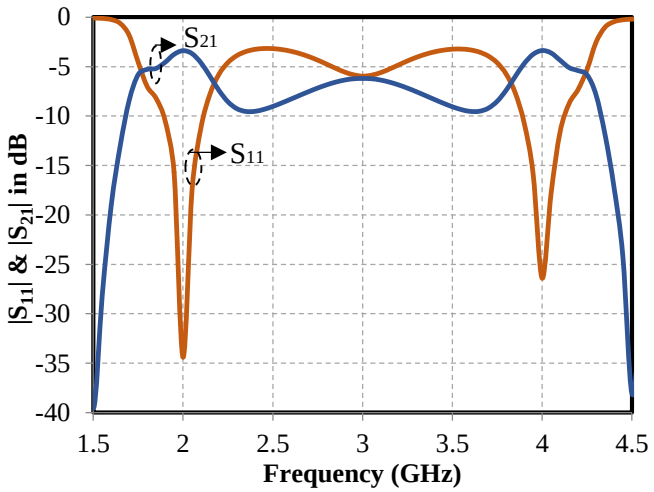

Figure 3. Simulated $|S_{11}|$ and $|S_{21}|$

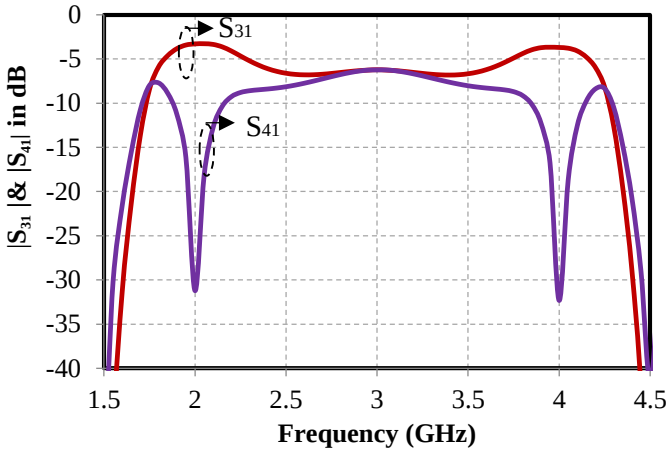

Figure 4. Simulated $|S_{31}|$ and $|S_{41}|$

The phase difference between the output ports of the designed coupler is shown in Figure 5. The phase difference between S_{31} and S_{21} is -89.5^o at 2 GHz and -270^o at 4 GHz.

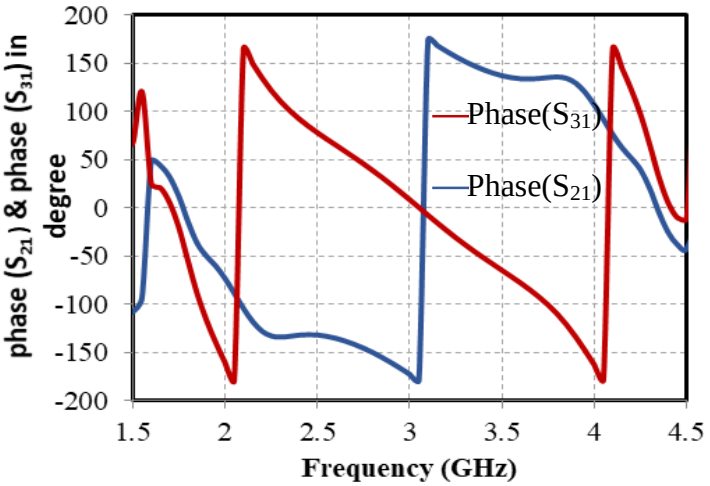

Figure 5. Phase response at the output ports

An ongoing research for obtaining a compact version of the proposed dual-band coupler is in progress. The work includes folding and bending the stubs toward the inner empty area of the coupler to reduce its overall occupied surface area.

Table 1. Dimensions of the dual-band branch line coupler

	$Z_{\lambda/4}$ = 50 Ω		$Z_{\lambda/4}$ = 35.35 Ω	
T-shaped Line	Z_1	Z_2	Z_3	Z_4
	28.8 Ω	43.3 Ω	21 Ω	30.6 Ω
	L_1	L_2	L_3	L_4
	14.8 mm	30.2 mm	14.4 mm	29.5 mm
	W_1	W_2	W_3	W_4
	4.1 mm	2.3 mm	6.2 mm	3.6 mm

Conclusion

A dual-band branch-line coupler based on stub loaded microstrip lines was presented. Design equations are obtained using ABCD-matrix analysis. The simulated results show that the designed coupler has high matching and isolation levels at the two center frequencies. Efforts are done on reducing the size of the coupler by folding the stub towards the inner area of the coupler to be ready for fabrication.

Scientific Ethics Declaration

The authors declare that the scientific ethical and legal responsibility of this article published in EPSTEM journal belongs to authors.

Acknowledgements or Notes

* This article was presented as an online presentation at the International Conference on Technology, Engineering and Science (www.icontes.net) held in Antalya/Turkey on November 16-19, 2022.

References

Chin, K., Lin, K., Wei, Y., Tseng, T., & Yang, Y. (2010). Compact dual-band branch-line and rat-race couplers with stepped-impedance-stub lines. *IEEE Transactions on Microwave Theory and Techniques*, *58*, 1213-1221.

Feng, W., Duan, X., Shi, Y., Zhou, X.Y., & Che, W. (2020). Dual-band branch-line couplers with short/open-ended stubs. *IEEE Transactions on Circuits and Systems II: Express Briefs, 67*, 2497-2501.

Feng, W., Zhao, Y., Che, W., Chen, H., & Yang, W. (2018). Dual-/tri-band branch line couplers with high power division isolation using coupled Lines. *IEEE Transactions on Circuits and Systems II: Express Briefs, 65*, 461-465.

Kim, H., Lee, B., & Park, M. (2010). Dual-band branch-line coupler with port Extensions. *IEEE Transactions on Microwave Theory and Techniques, 58*, 651-655.

Kim, T., Lee, B., & Park, M. J. (2008). Dual-band branch-line coupler with two center-tapped stubs. *Microwave and Optical Technology Letters, 50*(12), 3136-3139.

Park, M. (2009). Dual-band, unequal length branch-line coupler with center-tapped stubs. *IEEE Microwave and Wireless Components Letters, 19*, 617-619.

Pozar, D. M. (2012). *Microwave engineering*. Hoboken. Wiley.

Zhan, L., Li, Z., Wu, G., & Roblin, P. (2018). Dual-band branch-line coupler with orthogonal coupled branches. *2018 IEEE 19th Wireless and Microwave Technology Conference (WAMICON)*, 1-4.

Zhang, H., & Chen, K. (2007). A stub tapped branch-line coupler for dual-band operations. *IEEE Microwave and Wireless Components Letters, 17*, 106-108.

Author Information

Heba EL-HALABI
Beirut Arab University
Beirut, Lebanon
h.alhalabi@bau.edu.lb

Manal K. FATTOUM
Beirut Arab University
Beirut, Lebanon

To cite this article:

El-Halabi, H. & Fattoum, M.K. (2022). Dual band branch-line coupler using stub-loaded lines. *The Eurasia Proceedings of Science, Technology, Engineering & Mathematics (EPSTEM), 21*, 430-434.

The Eurasia Proceedings of Science, Technology, Engineering & Mathematics (EPSTEM)
ISSN: 2602-3199

The Eurasia Proceedings of Science, Technology, Engineering & Mathematics (EPSTEM), 2022

Volume 21, Pages 435-440

IConTES 2022: International Conference on Technology, Engineering and Science

Toxicology of Nano-Scale Materials Used in Water Treatment

Arzu OZTURK
Aksaray University

Abstract: In the last two decades, the use of nanomaterials has increased in food ingredient and packaging, water treatment, pesticides, cosmetics and many other industries. Old habits have begun to change in this process and silver nanoparticles instead of pesticides, carbon nanotubes absorbing pollutants in water treatment, titanium dioxide in smart drugs and cosmetics have become widespread. These nanoparticles, which permeate our lives in all areas, can hang in the air for kilometers and can cause DNA damage by penetrating people, animals and plant cells. Although the magnitude of the risks and the toxic effects are estimated, there are very few studies on this subject yet. Therefore, it is required to reveal the risks and toxic effects of nanomaterials, which are described as excellent technology. In this study, the toxicity of nano-scale materials, which are widely used in water treatment, and their effects on human and environmental health were investigated. Thus, the mechanism of action of the investigated nanomaterials was revealed.

Keywords: Water treatment, Nanotechnology, Toxicology

Introduction

As a result of population growth, serious problems such as rapid depletion of existing resources, hunger, inability to access water and health services have emerged worldwide. Producing fast solutions to these problems has become a priority all over the world. The introduction of nano materials, which are seen as one of these solutions, has opened the door to many innovations in the fields of medicine, science and technology, and nano materials have been included in every area of our lives. Its use has become widespread in fields such as sports and sports equipment, cosmetics, biomedical applications, electronic devices, water treatment, new generation drugs, mRNA vaccines, textiles and food (Hurt et al., 2006; Akbarzadeh et al, 2016). In addition to the convenience that nanomaterials bring to life, the magnitude of the risks involved has led to the emergence of the science of nanotoxicology. Nanotoxicology is the study of the toxic effects of nanomaterials by inhalation, contact and ingestion. One of the important factors affecting the toxicity of nanomaterials is the size of nanomaterials. These materials, which have a size of less than 100 nm, can accumulate in the body and easily reach more distant areas such as the brain and blood from the areas where they accumulate (Akbarzadeh et al, 2016; Rai et al, 2018).

The fast change and transformation of technology has also caused change and transformation in industries. Therefore, high polluting, toxic, radioactive pollutants, dyestuffs, pharmaceutical chemicals, heavy metals and organic pollutants have changed the pollution profile of wastewater (Madenli et al., 2021). Conventional treatment methods are insufficient in the treatment of such wastewater. For this reason, the use of nanomaterials in water and wastewater treatment has become widespread in recent years. These nanomaterials have been frequently used in treatment methods such as adsorption, filtration, photocatalytic, remediation and disinfection (web 1). Cu, Cr, Cd, Hg, Pb and Ni can be removed from wastewater by using carbon nanotubes in the adsorption process. Organic pollutants can be removed with the use of iron oxide nanomaterials in photocatalysis. In addition, while silver nanoparticles are used in the disinfection of drinking water and wastewater, various organic pollutants such as pesticides, polymers can be treated by photocatalysis using nano TiO2 (Jangid et al., 2021; Madenli et al., 2021; Sadegh & Ali, 2021; Xu et al., 2012). After treatment, the used

- Selection and peer-review under responsibility of the Organizing Committee of the Conference

nano silver, nano TiO_2, nano metaloxides and carbon nanotubes are released to the environment through water and are not considered as a hazardous waste (Rai et al., 2018). However, the negative effects of these materials should be investigated starting from the cellular level and covering the entire ecosystem. The widespread use of nanomaterials facilitates their entry into the living body through skin contact, inhalation, ingestion and injection. The release of significant amounts of carbon nanomaterials into the environment can adversely affect all living things, especially humans (Hurt et al., 2006).

The very small size of nanomaterials and the dangerous mechanism of action caused them to be named "Trojan horse" (Hsiao at al.,2015; Martín-de-Lucía et al., 2017; Park et al., 2010). This nomenclature is proof that scientists are seriously concerned about what they are up against. Before nanomaterials become widespread, proving their reliability should be a priority for scientists. In this study, the ways in which nanomaterials enter the human body through the water and food chain and their mechanism of action were investigated.

Nano Materials Used in Wastewater Treatment

Carbon Nanomaterials and Mechanism of Action

Carbon nano materials, which have many different forms (fullerene, CNT, graphene, etc.), are one of the most popular products used by nanotechnology. It is especially preferred in wastewater treatment to reduce environmental problems. Hazardous substances such as 1,2-dichlorobenzene and dioxin in wastewater are highly carcinogenic and cannot be degraded. These substances accumulate in the living body cause damage. Carbon nanomaterials are preferred as a highly effective absorbent in the removal of these pollutants. This is because carbon nanomaterials have a much higher absorption capacity compared to activated carbon. Because the high surface area of carbon nanomaterials causes a strong interaction with dioxins (Mubarek et al., 2014; Ong et al., 2010; Jangid & Inbaraj 2021).

Different carbon nanomaterials can be used according to the characteristics of the pollutants in wastewater. Multi-walled carbon nanotubes (MWCNT) or single-walled carbon nanotubes (SWCNT) are the most preferred nanomaterials with their cylindrical properties (Lu et al., 2016) in Figure 1.

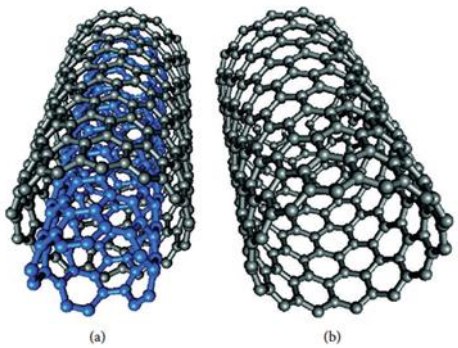

Figure 1. (Super) structure representations of (a) MWCNTs and (b) SWCNTs.

CNTs form aggregated pores due to the entanglement of thousands of individual tubes sticking together as a result of Van der Waals gravitational forces (Upadhyayula et al., 2009). CNTs are synthesized from graphite using arc discharge, chemical vapor deposition from gas, or laser ablation. In addition to many known pollutants, CNTs exhibit good mechanical strength, high sorption capacity, hydrophilic properties in the removal of some pharmaceutical compounds such as Diclofenac sodium, carbamazepine, which have caused problems in wastewater in recent years (Jangid & Inbaraj 2021). The widespread use of carbon nanomaterials due to these unique properties has accelerated the increase in treated water and its release to the environment. Nanomaterials can be easily dispersed, transported or transformed into water, soil or air environment from the environment in which they are formed. The lack of awareness of the effects of these substances on the environment and living things causes concern among scientists and environmentalists (Werkneh & Rene 2019). Due to their nature and structure, they can easily penetrate living things in the biological environment. Due to these properties, nanomaterials can cause oxidative stress, membrane irregularity, cell wall damage, formation of organic radicals and DNA damage in the absence of light. In addition, functionalized CNTs can be used in medicine as nanoplatforms in cancer therapy and nanocarriers to cross the blood-brain barrier (BBB) for

therapeutic agents to reach the brain. However, negative effects of CNTs on the vascular system are also seen, but their toxicity has not been fully resolved yet (Cao & Luo, 2019).

It is known that carbon nanomaterials penetrate into the cell in two different ways. These are the endocytic pathway and/or passive diffusion (Facciolà et al., 2019) in Figure 2. SWCNTs penetrate the cytoplasm pass through the phospholipid bilayer by passive diffusion. MWCNTs enter the cell using the endocytic pathway and accumulate in the mitochondria (Costa et al., 2016). They can easily cross the blood brain barrier and blood spinal cord barrier, which are selective permeable barriers that protect the central nervous system in the body. This situation may endanger the protective role of the blood-brain barrier, which prevents the entry of pollutants and toxins entering the body through diseases and can expose the person to serious diseases (Facciolà et al., 2019).

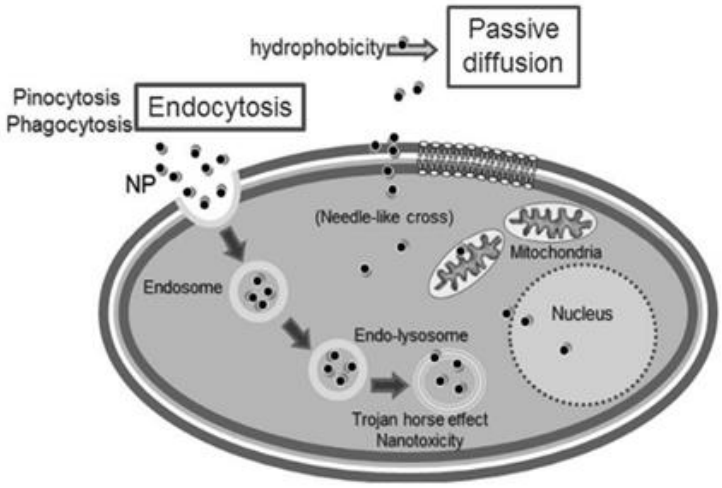

Figure 2. Mechanisms of CNTs cellular uptake

Due to the increasing use of masks in recent years, many people have been exposed to CNTs in masks by inhalation. The emerging mask wastes have left to nature in an uncontrolled manner. In the early stages of toxicological research, researchers focused on the effects of CNTs on the respiratory tract because of their similarity to asbestos. They revealed that after inhalation it triggers epithelial cells and macrophages of the respiratory system. As a result of these studies, it has been determined that CNTs cause, genotoxicity, fibrosis, tumor formation, inflammation and apoptosis in the lungs (Facciolà et al., 2019). Exposure to nanomaterials together with air pollution contributes to the progression of autism spectrum disorders, low IQ in children, Parkinson's, Alzheimer's and chronic encephalitis (Costa et al., 2016; Kafa et al., 2016).

Silver Nanomaterials and Mechanism of Action

Silver nanomaterials are zero-valent (Ag^0) silver clusters with a size of 1-100 nm. Owing to its many important features, it is used in the fields of science and technology. With its antimicrobial feature, it appears in the field of medicine, health care products, underwear and shoes, and wet wipes. Thanks to this feature it also serves as a new generation antimicrobial material in water disinfection applications (Zhang et al., 2016). Due to this antimicrobial feature, it has started to be preferred instead of chlorine in water treatment systems and filtration units in hospitals, pools and spas (Esakkimuthu et al., 2014).

Silver nanomaterials reach wastewater and natural water resources as a result of the application and consumption process. In addition, it plays an active role in the removal of E.coli and other pathogens in the treatment processes of wastewater and is released into nature with water at the outlet (Esakkimuthu et al., 2014; Jangid & Inbaraj 2021). Silver nanomaterials cause physical degradation by oxidative stress by disrupting the cellular component (Figure 3). The toxic effects of exposure to silver nanomaterials occur when they act on DNA, rendering phosphorus and sulfur elements unusable. Studies with silver ions and stabilized silver nanoparticles have shown that the toxic effect of silver occurs in bacteria and human mesenchymal stem cells in a certain concentration range (Akbarzadeh et al., 2016). Studies have shown that the toxicity of silver nanoparticles is almost the same in bacteria and humans (Greulich et al., 2012). Again, in studies on mice, it has been observed that silver nanoparticles reduce the viability of macrophage cells, which have a very important place in the immune system (Park et al., 2010).

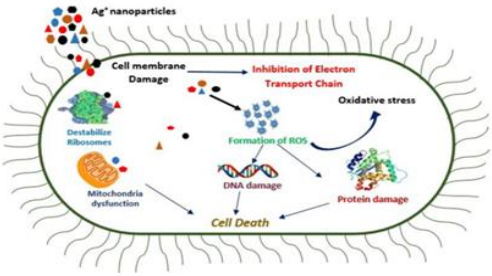

Figure 3. Antimicrobial effect of silver nanoparticles (Rahman et al., 2019).

Titanium Dioxide Nanomaterials and Mechanism of Action

Titanium dioxide nanomaterials (TiO_2) are shiny due to their high refractive index. In general, they exist in 3 different phases (anatase, rutile and brookite), each of which is different in size. Due to its small size and shine, it has a wide range of applications such as toothpaste, medicine, coating, paper, ink, plastic, food products, cosmetics and textiles. In addition, they are preferred in the preparation of cleaning cloths, car mirrors, window glasses due to their self-cleaning and anti-fogging feature. It has become a very popular nanoparticle due to its easy biosynthesis and cost-effectiveness. It has enormous industrial applications such as wastewater treatment, environmental applications, agriculture, aerospace applications, food industry (Waghmode et al., 2019). TiO_2 nanomaterials serve as photocatalysts for biological treatment of wastewater and removal of pharmaceuticals. Especially non-biodegradable water pollutants can be easily removed from wastewater by photocatalytic degradation (Esakkimuthu et al., 2014). In addition to all these, TiO_2 nanomaterials are used as packaging material for surface water treatment, pesticide removal from groundwater, dye and heavy metal removal from wastewater, and solid phase extraction (Waghmode et al., 2019).

The ecotoxicity of such widely used nanoparticles and their effects on living things are very worrying. The wide application area of TiO_2 nanomaterials increases the exposure rate. TiO_2 nanomaterials, which we frequently encounter in foods with the code E171, can be easily absorbed by intestinal cells. Exposure to nanoparticles can occur through inhalation, skin contact, ingestion, and injection. Studies have shown that exposure to nano TiO_2 in different ways causes damage to important organs (Chang et al., 2013). The effects of ingestion with food were investigated in in vivo experiments and its penetration into enterocytes of rats was confirmed (Jovanović, 2015). In a study conducted on mice, it was reported that orally ingested TiO_2 caused accumulation in liver, spleen, kidney and lung tissue (Wang et al. 2007). The cellular mechanism of action of TiO_2 nanomaterials for vertebrates is shown in Figure 4.

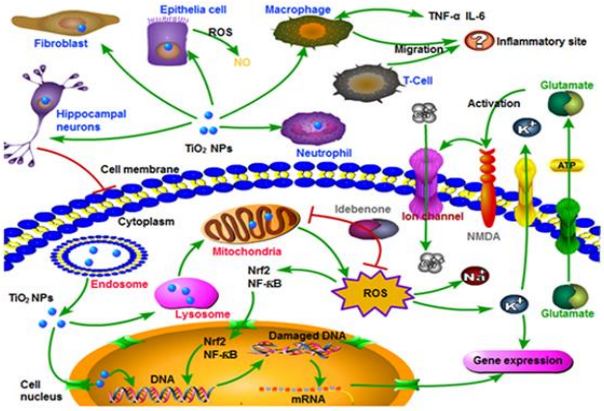

Figure 4. Mechanism of Nano TiO_2 in the cell (Hou et al., 2019)

Oxidative stress is one of the main mechanisms in TiO_2 genotoxicity. In mammals, oxidative stress damages lipids, carbohydrates, proteins, and DNA. Especially, peroxidation of lipids can cause changes in the cell membrane and impair vital functions. This causes the redox state of cells to deteriorate. Toxic effects may occur with the increase of peroxides and free radicals on cell components (Hou et al., 2019). According to the results of the studies, it can be said that TiO_2 toxicity is a public health problem. Due to environmental and occupational exposure from cosmetics, drugs, food and water, risk assessment should be performed and its use should be limited.

Conclusion

The use of nanomaterials, which offer effective solutions in solving environmental problems, is increasing rapidly. Day by day, many new products produced with nano technology are included in our lives. For this reason, nanomaterials will continue to be a popular topic that will keep researchers busy for a long time. The popularity of nanomaterials in water treatment, along with many other fields, has led to an increase in environmental exposure. The alarming consequences of this rapid rise have begun to emerge. Nanomaterials that are not seen as pollutants are transferred to the ecosystem by being released into the soil environment through water. As a result of their unlimited use, it has been revealed that they accumulate in the environments they are transported and turn into more polluting forms with new reactions. It is well known that nanoparticles generate oxidative stress in cells by generating reactive oxygen species and induce toxicity through inflammation. Therefore, their use should be limited by legal means. If this is not done, the emergence of new nano-pollutants that threaten public and environmental health seems inevitable.

Scientific Ethics Declaration

The author declares that the scientific ethical and legal responsibility of this article published in EPSTEM journal belongs to the author.

Acknowledgements or Notes

* This article was presented as an oral presentation at the International Conference on Technology, Engineering and Science (www.icontes.net) held in Antalya/Turkey on November 16-19, 2022.

References

Akbarzadeh, A., Mohammadhosseini, M., Najaf Abadi, A. J., Hasanzadeh, A., Abasi, E., Aberoumandi, S. M., & Panahi, Y. (2016). Nanomaterials toxin contamination in laboratories and potential harmful effects of their products: a review. *Toxin Reviews*, *35*(3-4), 180-186.

Cao, Y., & Luo, Y. (2019). Pharmacological and toxicological aspects of carbon nanotubes (CNTs) to vascular system: A review. *Toxicology and Applied Pharmacology*, *385*, 114801.

Chang, X., Zhang, Y., Tang, M., & Wang, B. (2013). Health effects of exposure to nano-TiO2: a meta-analysis of experimental studies. *Nanoscale Research Letters*, *8*(1), 1-10.

Costa, P.M., Bourgognon, M., Wang, J.T., & Al-Jamal, K.T., (2016). Functionalised carbon A nanotubes: From intracellular uptake and cell-related toxicity to systemic brain delivery. *J. Control. Release*, *241*, 200–219.

Esakkimuthu, T., Sivakumar, D., & Akila, S. (2014). Application of nanoparticles in wastewater treatment. *Pollut. Res*, *33*(03), 567-571.

Facciolà, A., Visalli, G., La Maestra, S., Ceccarelli, M., D'Aleo, F., Nunnari, G., & Di Pietro, A. (2019). Carbon nanotubes and central nervous system: Environmental risks, toxicological aspects and future perspectives. *Environmental Toxicology and Pharmacology*, *65*, 23-30.

Greulich, C., Braun, D., Peetsch, A., Diendorf, J., Siebers, B., Epple, M., & Köller, M. (2012). The toxic effect of silver ions and silver nanoparticles towards bacteria and human cells occurs in the same concentration range. *RSC advances*, *2*(17), 6981-6987.

Hou, J., Wang, L., Wang, C., Zhang, S., Liu, H., Li, S., & Wang, X. (2019). Toxicity and mechanisms of action of titanium dioxide nanoparticles in living organisms. *Journal of Environmental Sciences*, *75*, 40-53.

Hsiao, I. L., Hsieh, Y. K., Wang, C. F., Chen, I. C., & Huang, Y. J. (2015). Trojan-horse mechanism in the cellular uptake of silver nanoparticles verified by direct intra-and extracellular silver speciation analysis. *Environmental Science & Technology*, *49*(6), 3813-3821.

Hurt, R. H., Monthioux, M., & Kane, A. (2006). Toxicology of carbon nanomaterials: status, trends, and perspectives on the special issue. *Carbon*, *44*(6), 1028-1033.

Jangid, P., & Inbaraj, M. P. (2021). Applications of nanomaterials in wastewater treatment. *Materials Today: Proceedings*, *43*, 2877-2881.

Jovanović, B. (2015). Critical review of public health regulations of titanium dioxide, a human food additive. *Integrated Environmental Assessment and Management*, *11*(1), 10-20.

Kafa, H., Wang, J.T., Rubio, N., Klippstein, R., Costa, P.M., Hassan, H.A., Sosabowski, J.K., Bansal, S.S., Preston, J.E., Abbott, N.J., & Al-Jamal, K.T., (2016). Translocation of LRP1 targeted carbon nanotubes of different diameters across the blood-brain barrier in vitro and in vivo. *J. Control. Release, 225*, 217–229.

Lu, H., Wang, J., Stoller, M., Wang, T., Bao, Y., & Hao, H. (2016). An overview of nanomaterials for water and wastewater treatment. *Advances in Materials Science and Engineering*, Article ID 4964828 https://doi.org/10.1155/2016/4964828

Madenli, O., Deveci, E. U., & Gonen, C. (2021). Agir metal gideriminde grafen uygulamalari adsorpsiyon teknolojisi. *Firat Universitesi Muhendislik Bilimleri Dergisi, 33*(1), 151-159.

Martín-de-Lucía, I., Campos-Mañas, M. C., Aguera, A., Rodea-Palomares, I., Pulido-Reyes, G., Leganés, F., ... & Rosal, R. (2017). Reverse Trojan-horse effect decreased wastewater toxicity in the presence of inorganic nanoparticles. *Environmental Science: Nano, 4*(6), 1273-1282.

Mubarak, N. M., Sahu, J. N., Abdullah, E. C., & Jayakumar, N. S. (2014). Removal of heavy metals from wastewater using carbon nanotubes. *Separation & Purification Reviews, 43*(4), 311-338.

Ong, Y. T., Ahmad, A. L., Zein, S. H. S., & Tan, S. H. (2010). A review on carbon nanotubes in an environmental protection and green engineering perspective. *Brazilian Journal of Chemical Engineering*, *27*, 227-242.

Park, E. J., Yi, J., Kim, Y., Choi, K., & Park, K. (2010). Silver nanoparticles induce cytotoxicity by a Trojan-horse type mechanism. *Toxicology in Vitro, 24*(3), 872-878.

Rahman, S., Rahman, L., Khalil, A. T., Ali, N., Zia, D., Ali, M., & Shinwari, Z. K. (2019). Endophyte-mediated synthesis of silver nanoparticles and their biological applications. *Applied Microbiology and Biotechnology*, *103*(6), 2551-2569.

Rai, M., Gupta, I., Ingle, A. P., Biswas, J. K., & Sinitsyna, O. V. (2018). Nanomaterials: What are they, why they cause ecotoxicity, and how this can be dealt with?. In *Nanomaterials: Ecotoxicity, safety, and public perception* (pp. 3-18). *Springer, Cham*.

Sadegh, H., & Ali, G. A. (2021). Potential applications of nanomaterials in wastewater treatment: nanoadsorbents performance. In *Research anthology on synthesis, characterization, and applications of nanomaterials* (pp. 1230-1240). *IGI Global*.

Upadhyayula, V. K., Deng, S., Mitchell, M. C., & Smith, G. B. (2009). Application of carbon nanotube technology for removal of contaminants in drinking water: a review. *Science of the Total Environment, 408*(1), 1-13.

Waghmode, M. S., Gunjal, A. B., Mulla, J. A., Patil, N. N., & Nawani, N. N. (2019). Studies on the titanium dioxide nanoparticles: Biosynthesis, applications and remediation. *SN Applied Sciences*, *1*(4), 1-9.

Wang, J., Zhou, G., Chen, C., Yu, H., Wang, T., Ma, Y., ... & Chai, Z. (2007). Acute toxicity and biodistribution of different sized titanium dioxide particles in mice after oral administration. *Toxicology Letters*, *168*(2), 176-185.

Web 1. https://www.researchgate.net/publication/332524216_NANOTEKNOLOJIK_SU_ARITMA_METOTLARI_-_YUKSEK_LISANS_SEMINER_SUNUMU

Werkneh, A. A., & Rene, E. R. (2019). Applications of nanotechnology and biotechnology for sustainable water and wastewater treatment. In *Water and wastewater treatment technologies* (pp. 405-430). *Springer*.

Xu, P., Zeng, G. M., Huang, D. L., Feng, C. L., Hu, S., Zhao, M. H., ... & Liu, Z. F. (2012). Use of iron oxide nanomaterials in wastewater treatment: a review. *Science of the Total Environment*, *424*, 1-10.

Zhang, C., Hu, Z., Li, P., & Gajaraj, S. (2016). Governing factors affecting the impacts of silver nanoparticles on wastewater treatment. *Science of the Total Environment*, *572*, 852-873.

Author Information

Arzu Ozturk
Aksaray University
Bahcesehir mah. Aksaray, Turkey
Contact e-mail: *arz_ozturk@hotmail.com*

To cite this article:

Ozturk, A. (2022). Toxicology of nano-scale materials used in water treatment. *The Eurasia Proceedings of Science, Technology, Engineering & Mathematics (EPSTEM), 21*, 435-440.

The Eurasia Proceedings of Science, Technology, Engineering & Mathematics (EPSTEM)
ISSN: 2602-3199

The Eurasia Proceedings of Science, Technology, Engineering & Mathematics (EPSTEM), 2022

Volume 21, Pages 441-451

IConTES 2022: International Conference on Technology, Engineering and Science

Whale Optimization Algorithms for Multi-Objective Flowshop Scheduling Problems

Cecilia E. NUGRAHENI
Parahyangan Catholic University

Luciana ABEDNEGO
Parahyangan Catholic University

Craven S. SAPUTRA
Parahyangan Catholic University

Abstract: One of the most common scheduling classes in the industry is Flow Shop Scheduling Problem (FSP). Given a set of jobs that must be completed in a series of identical stages, each stage is performed by a single machine. The goal of the FSP is to find a series of jobs that meets specific optimization criteria. Multi-objective FSP (MOFSP) is an FSP with more than one optimization target. This study investigates the MOFSP solution using two variants of the Whale Optimization Algorithm technique, namely the basic Whale Optimization Algorithm (WOA) and an improved Whale Optimization Algorithm (I-WOA). The objective criteria are makespan and total flow time. This study aims to examine the performance of WOA and I-WOA and determine how the weight ratio of optimization criteria affects each method. Several experiments were conducted using the Taillard Benchmark, and it was concluded that in general, WOA outperforms I-WOA, and the best weight ratio is makespan:total flow time is 75:25.

Keywords: Scheduling, Flow shop, Multi-objective FSP, Whale optimization algorithm

Introduction

One class of scheduling problems commonly found in the industry is the Flow Shop Scheduling Problem (FSP). Given a set of jobs that must be processed in a series of stages with only one machine for processing the jobs at each stage, FSP aims to find a sequence of jobs that meets specific optimal criteria or objectives. FSP can therefore be viewed as an optimization problem. FSP with two or more objectives is called Multi-objective FSP (MOFSP) (Yenisey & Yagmahan, 2014).

The production process frequently uses a variety of optimization goals. Makespan and total flow time are two of them. Makespan is the total amount of time needed to complete all jobs, starting with the first job on the first machine and ending with the last job on the last machine. Flow time is the time needed to finish a job, i.e., the duration from a job is ready to be processed by the first machine and completed by the last machine. Total flow time is the sum of all the jobs' flow times. In this study, we are interested in solving MOFSP with the goal is to minimize the makespan and total flow time.

Scheduling problems, including production process scheduling problems in the manufacturing industry, are very challenging problems. Many techniques or approaches have been proposed to solve the production process scheduling problems. These approaches can be divided into two groups: the exact approach and the heuristic approach. Although the heuristic approach does not guarantee an optimal solution, it can provide a near-optimal solution in an acceptable time. Moreover, heuristic techniques are generally divided into two types, namely

constructive and improvement heuristics (Nugraheni & Abednego, 2016a). Some of the algorithms included in the constructive technique are dispatching rules such as FIFO, LIFO, SPT, LPT, and some popular algorithms such as NEH, CDS, Palmer, Gupta, and Pour. Improvement heuristics are called metaheuristics, such as genetic algorithm, simulated annealing, particle swarm optimization, firefly algorithm, bee colony algorithm, and whale optimization algorithm. Metaheuristics are widely used to solve production scheduling problems. Many studies have been conducted using metaheuristics to scheduling problems with multiple objectives (Demir & Gelen, 2021; Lu, Xiao, Li, & Gao, 2016; Singh, Oberoi & Singh, 2020; Schulz, Buscher & Shen, L., 2020; Yenisey & Yagmahan, 2014).

Whale optimization Algorithm (WOA) is a swarm intelligence optimization algorithm proposed by Seyedali Mirjalili and Andrew Lewis in 2016 (Alimoradi, 2021; Mirjalili & Lewis, 2016; Rana et al., 2020). WOA simulates mimics the hunting behavior of humpback whales called bubble-net feeding method (Mirjalili & Lewis, 2016), as shown in Figure 1. The whale will create distinctive bubbles along a circle or a spiral path once it finds its prey. WOA has been widely used to solve optimization problems, including production scheduling problems.

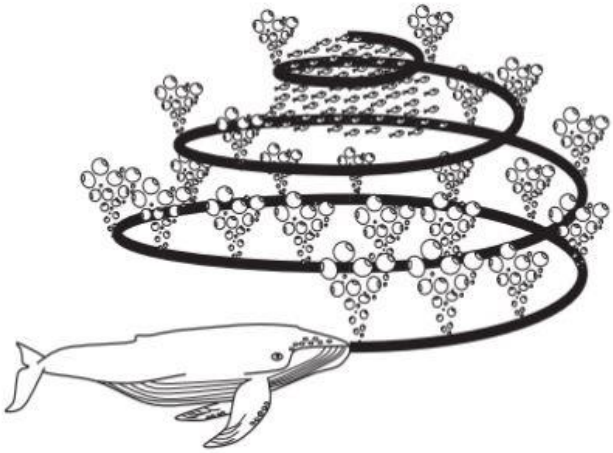

Figure 1. Bubble-net feeding behavior of humpback whales. (Mirjalili & Lewis, 2016)

There are many variations of the standard WOA from Mirjalili & Andrews proposed by the researchers, including *improved* WOA (Ning, & Cao, 2021; Wang, Deng, Zhu, & Hu, 2019), *boosted* WOA *enhanced* WOA (Cao, Xu, Yang, Dong, & Li, 2022; Chakraborty, Saha, Sharma, Mirjalili, & Chakraborty, 2020; Hassouneh et.al, 2021; Nadimi-Shahraki, Zamani, & Mirjalili, 2022), *augmented* WOA (Alnowibet, Shekhawat, Saxena, Sallam, & Mohamed, 2022), *modified* WOA (Liang, Xu, Siwen, Liu, & Sun, 2022) and *hybrid* WOA (Lin, Wu, Huang, & Li, 2018).

In this study, two types of Whale Optimization Algorithm, namely the basic (WOA) and the improved proposed by Wang et.al (I-WOA), will be used to solve FSP. Using a benchmark from Taillard, we conducted some experiments to compare the algorithms' performance. The rest of the paper is structured as follows. Section 2 describes the method, including WOA, I-WOA, and the implementation (computer program) of WOA and I-WOA developed in this study. Section 3 explains the computational experiments conducted in this study, including parameter setting and experiment results, as well as the analysis of the results. Section 4 summarizes this study's main findings and suggests future research directions.

Method

Basic Whale Optimization Algorithm (WOA)

The basic WOA consists of three main phases: prey encircling, exploitation phase through bubble-net and exploration phase, i.e., prey search. In this section, we will briefly describe the three parts.

1) Prey Encircling: Humpback whales choose their target prey through the capacity to find the location of prey. The best search agent is followed by other search agents to update their positions. This behavior is represented in Eq. 1 and Eq. 2:

$$D = |C \cdot X^*(t) - X(t)| \quad \text{Eq. 1}$$

$$X(t+1) = X^*(t) - A \cdot D \quad \text{Eq. 2}$$

where X^* denotes the position vector of the best-obtained solution, X is the position vector, t is the current iteration, |…| denotes the absolute value and · denotes the element-to-element multiplication. The coefficients A and C can be calculated as follows

$$A = 2a.r - a \quad \text{Eq. 3}$$

$$C = 2r \quad \text{Eq. 4}$$

where $r \in [0, 1]$ and a linearly decreases with every iteration from 2 to 0 as formulated as follows:

$$a = 2 - t.2/t_{max} \quad \text{Eq. 5}$$

where t_{max} is the total iteration number.

The present position of search agents was moved closer to the ideal position by modifying the values of the vectors A and C. This procedure of updating positions in the neighborhood direction also helps in n-dimensionally encircling the prey.

2) *Exploitation phase* - bubble net attack: There are two approaches to model the bubble-net behavior, i.e., shrinking encircling mechanism and spiral update position. The shrinking encircling mechanism is achieved by gradually decreasing the value of a in Eq. 5 from 2 to 0 throughout several iterations. By choosing a random value A from the range [−1, 1], we can define the new position of a search agent anywhere between the position of the current best agent and the initial position of the agent.

The spiral equation connecting the prey's position and the whale's position to mimic the humpback whales' helix-shaped movement can be stated as follows:

$$X(t+1) = D'.e^{bl}.\cos(2\pi l) + X^*(t) \quad \text{Eq. 6}$$

where b is the constant factor responsible for the shape of spirals, l randomly belongs to the interval [−1, 1] and D' shows the distance of the i-th whale to the prey (the best solution achieved until this moment) as stated in Eq 7.

$$D' = |X^*(t) - X(t)| \quad \text{Eq. 7}$$

There is a 50% chance of selecting either the spiral model or the shrinking encircling mechanism to model the two concurrent approaching behaviors during the bubble-net attacking strategy, as stated in Eq. 8.

$$X(t+1) = \begin{cases} X^*(t) - A \cdot D & \text{if } p < 0.5 \\ D'.e^{bl}.\cos(2\pi l) + X^*(t) & \text{if } p \geq 0.5 \end{cases} \quad \text{Eq. 8}$$

where p represents a random real number between [0, 1].

3) Exploration phase - search for prey: In searching for prey during the exploration stage, a whale should move away from a reference whale. The variation of the A vector can be used with random values less than -1 or greater than 1 to force search agents to move away from a reference whale. The mathematical model for the exploration phase is as follows:

$$D = |C \cdot X_{rand} - X| \quad \text{Eq. 9}$$

$$X(t+1) = X_{rand} - A \cdot D \quad \text{Eq. 10}$$

As opposed to the exploitation phase, in the exploration phase, the position of a search agent is updated according to a randomly selected search agent rather than the best search agent discovered thus far. The WOA algorithm can conduct a global search with the help of this mechanism and |A| > 1 emphasis on exploration.

Improved Whale Optimization Algorithm (I-WOA)

Wang et al. proposed an improvement of WOA (I-WOA). The improvement objectives are to increase exploration and exploitation potential and decrease the likelihood of entering the local optimum by introducing a nonlinearly modified convergence factor, incorporating a new inertia weight factor, and modifying the execution time of the present optimal individual (Wang, Deng, Zhu, & Hu, 2019).

The performance of basic WOA is improved in three aspects: nonlinear convergence factor, inertia weight factor, and random variation of best search agent. According to Wang et al. the linearly changed convergence factor *a* in Eq. 5 cannot reflect the real optimizing process of the algorithm and limits the exploration and exploitation ability. They proposed a nonlinearly changed convergence factor as follows:

$$a(t) = \frac{2(1-t/t_{\max})^2}{(1-\mu t/t_{\max})^3} \qquad \text{Eq.11}$$

where μ is the adjustment coefficient and the value is in the interval [15,35].

Inspired by the PSO algorithm, a new inertia weight factor is introduced to enhance exploration and exploitation ability and accelerate convergence speed. The position updated method with inertia weight factor is depicted in the following equation.

$$X(t+1) = \begin{cases} \omega X^*(t) - A.D & \text{if } p < 0.5, |A| < 1 \\ \omega X_{\text{rand}}(t) - A.D & \text{if } p < 0.5, |A| \geq 1 \\ D'.e^{bl}.\cos(2\pi l) + \omega X^*(t) & \text{if } p \geq 0.5 \end{cases} \qquad \text{Eq. 12}$$

where ω is inertia weight factor and is calculated as

$$\omega = \alpha \times rand() \qquad \text{Eq. 13}$$

where α is a number in the interval [0.5, 2.5].

In WOA, during the exploitation process, all search agents move toward the current best search agent. This situation could trap the algorithm in a local optimum if the present optimal solution is local. Wang et al. suggested a stochastic variation of the most effective search agent to lower the likelihood of a local optimum (Wang, Deng, Zhu, & Hu, 2019). Assuming that $X_i = (x_{i1}, x_{i2}, \ldots, x_{id})$ is the current best search agent, one element $x_k (k = 1, 2, \ldots, d)$ from X_i is chosen and is replaced with a random integer in $[l_i, u_i]$ where l_i and u_i is lower and upper bound of x_i, respectively.

WOA for MOFSP

WOA Flowchart

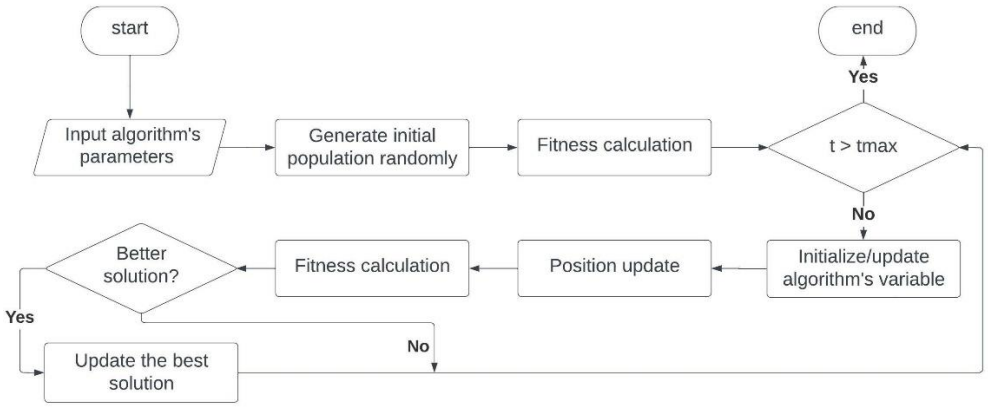

Figure 2. WOA flowchart

In general, WOA and I-WOA have the same framework. Figure 2 illustrates the workflow of the WOA and I-WOA algorithms. After determining the input parameters, the initial population is generated, namely a collection of whales representing candidate solutions to the problem. The whales with the best fitness are stored. Next, the fitness calculation of each whale is carried out. These whales will be subjected to several processes in several iterations. The algorithm variable is recalculated if the maximum iteration has not been reached. Changes in the value of these variables are used as a reference for changing the whales' positions. At this stage, each algorithm may use different formulas as explained in section 2. The fitness calculation is done again using the new whale position. The best candidate is replaced if a better solution is found. After reaching the maximum iteration, the algorithm stops and returns the best solution.

Whale Modeling

Every whale represents a candidate solution of MOFSP, which is a sequence of jobs whose length is the number of jobs. For example, W1 = ⟨1, 3, 2⟩ and W2 = ⟨2, 1, 3⟩ are two whales for a MOFSP with 3 jobs and can be depicted in Figure 3. The value of each whale's *i*-th element states the whale's position in the *i*-th dimension as well.

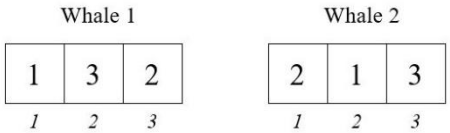

Figure 3. Two whales

Fitness

In this paper, the fitness value used is the objective of MOFSP, which is a combination of makespan and total flow time. For each whale, the formula for its fitness is defined as follows:

$$Fitness = w_m \,.\, C_{max} + w_{tft} \,.\, TFT \qquad \text{Eq. 14}$$

where $0 \leq w_m \leq 1$ and $0 \leq w_{tft} \leq 1$ are real values such that $w_m + w_{tft} = 1$. C_{max} and TFT represent the makespan and the total flow time of the corresponding whale, respectively. The smaller the fitness, the better the quality of a whale.

Distance between Two Whales

Since each whale represents its position, the distance between two whales, w_1 and w_2, can be calculated using the Euclidean Distance:

$$D(w_1,w_2)=\sqrt{\sum_{i=1}^{n}(w_1 - w_2)^2} \qquad \text{Eq. 15}$$

Position Updating

The position of each whale changes with each iteration based on the parameter values. This position update is carried out in the following manner:

1) Store the whale's initial location.
2) Update the vector's elements using Eq. 8, Eq. 10, or Eq. 12.
3) Sort the elements of the vector in ascending order.
4) Set the new location by referencing the element's index that shifted during sorting.

Figure 3 gives an example of position updating.

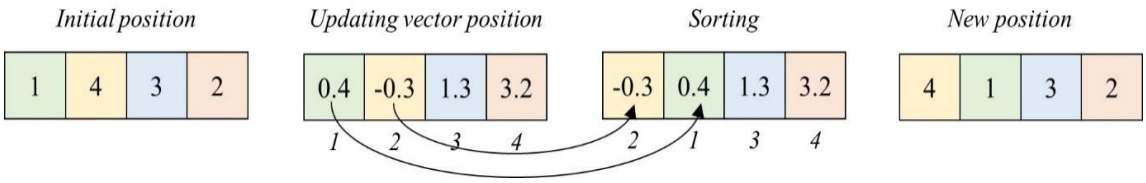

Figure 3. Position update

Computational Experiments

Experiment Setting

As stated previously, this research aims to compare the performance of the WOA and I-WOA algorithms in solving the MOFSP problem. These objectives are divided into two subgoals:

1) determines the effect of algorithm parameters on the performance of WOA and I-WOA.
2) compares the performance of the WOA and I-WOA algorithms.

The parameter to be measured is the combination of objective weights used to determine fitness, as shown in Eq. 14. There are three weight combinations, namely w_1, w_2, and w_3, are used. Table 1 describes the ratio of w_m: w_{tft} for each weight combination.

Table 1. Weight ratio setting

Ratio	w_m	w_{tft}
w_1	0.25	0.75
w_2	0.5	0.5
w_3	0.75	0.25

The other two algorithm parameters are N for the number of whales and t_{max} for the number of iterations. Both are set to 100. Taillard's benchmark was employed in this experiment. There are 12 groups of problem instances. The variation of each group is determined by the number of jobs and machines, as shown in Table 2. Each group contains ten instances. As a result, there are 120 problem instances in total.

Table 2. Problem size

Group	Number of jobs	Number of machines	Group	Number of jobs	Number of machines
c_1	20	5	c_7	100	5
c_2	20	10	c_8	100	10
c_3	20	20	c_9	100	20
c_4	50	5	c_{10}	200	10
c_5	50	10	c_{11}	200	20
c_6	50	20	c_{12}	500	20

For each problem instance, for each parameter combination, we perform 100 computations. So, for each problem and each parameter combination, 100 best solutions are obtained, namely the whales with the best fitness values. In addition, the makespan and total flow time of each of the best solutions are also stored.

From these values, the makespan, total time flow, and fitness values will be generated, which represent the solution of the problem instance. For this, we use two methods. The first way is to calculate the average of 100 fitness, makespan, and total flow time values. Whereas for the second approach, we take the median values instead of the average values. This approach is considered due to the randomness factor applied by each algorithm.

Results and Analysis

To determine the effect of weight ratio, for each solution of a problem, we determine whether the ratio produces the best makespan value, total flow time value, or a combination of the best makespan and total flow time values at once.

Table 3 shows the computation results generated by the WOA algorithm with the average value approach. The columns are grouped into four types. The first column informs the instances group. The second, third, and fourth groups inform the values related to makespan (MS), total flow time (TFT), and the combination of makespan and total flow time (MS-TFT). Each second, third, and fourth group consists of three columns.

Every column represents the weight ratio w_1, w_2, and w_3 as previously explained. Each table entry (except the one from the first column) represents how often the corresponding weight ratio yields the best results in its corresponding instance group. For example, the first-row states that for the c1 instance group, w_3 and w_1 are the best weight ratio relative to makespan and total time flow, respectively. However, no weight ratio simultaneously yields the best makespan and total time flow for this case.

The last row summarizes the results. The best ratio relative to makespan alone is w_3 and the best ratio relative to total flow time alone is w_1, whereas for both objectives, the w_3 is the best ratio. Figure 5 illustrates this summary. The same explanation applies to the other three tables: Table 4, Table 4, and Table 6. The computation results provided by the modified WOA algorithm with the average value technique are shown in Table 4 and the summary is illustrated in Figure 6. The best ratio relative to makespan alone is w_3 and the best ratio relative to total flow time alone is w_1, whereas for both objectives, the w_3 is the best ratio.

Table 3. WOA computation results using the average value approach

Group	MS			TFT			MS-TFT		
	w_1	w_2	w_3	w_1	w_2	w_3	w_1	w_2	w_3
c_1	0	0	10	8	2	0	0	0	0
c_2	0	0	10	6	4	0	0	0	0
c_3	0	0	10	6	3	1	0	0	1
c_4	0	3	7	3	3	4	0	1	2
c_5	0	2	8	2	2	6	0	1	6
c_6	1	2	7	2	4	4	0	2	3
c_7	0	5	5	4	3	3	0	2	2
c_8	1	1	8	3	4	3	0	1	2
c_9	3	2	5	7	3	0	3	1	0
c_{10}	0	3	7	4	2	4	0	1	3
c_{11}	1	2	7	4	3	3	1	1	3
c_{12}	4	4	2	2	7	1	0	3	0
Total	10	24	86	51	40	29	4	13	22

Table 4. I-WOA computation results using the average value approach

Group	MS			TFT			MS-TFT		
	w_1	w_2	w_3	w_1	w_2	w_3	w_1	w_2	w_3
c_1	0	0	10	6	3	1	0	0	1
c_2	0	0	10	5	4	1	0	0	1
c_3	0	0	10	6	4	0	0	0	0
c_4	0	1	9	5	3	2	0	0	2
c_5	0	1	9	4	5	1	0	0	1
c_6	0	2	8	4	3	3	0	1	2
c_7	2	1	7	3	2	5	0	0	2
c_8	1	1	8	2	2	6	1	0	4
c_9	1	2	7	3	2	5	2	1	4
c_{10}	4	3	3	2	4	4	1	2	2
c_{11}	5	2	3	2	3	5	2	1	2
c_{12}	3	3	4	4	1	5	6	1	3
Total	16	16	88	46	36	38	6	6	24

Table 5. WOA computation results using the median value approach

Group	MS			TFT			MS-TFT		
	w_1	w_2	w_3	w_1	w_2	w_3	w_1	w_2	w_3
c_1	0	1	10	5	3	2	0	1	2
c_2	0	0	10	6	3	1	0	0	1
c_3	0	0	10	7	1	2	0	0	2
c_4	1	3	6	3	5	2	1	1	0
c_5	3	2	5	4	3	3	0	0	1
c_6	0	3	7	2	5	3	0	2	3
c_7	0	4	6	5	1	4	0	1	3
c_8	0	2	8	2	2	6	0	1	5
c_9	2	1	7	5	3	2	1	1	2
c_{10}	1	3	6	5	2	3	1	1	2
c_{11}	1	1	8	2	5	3	1	1	3
c_{12}	4	6	0	3	6	1	2	4	0
Total	12	26	83	49	39	32	6	13	24

Table 6. I-WOA computation results using the median value approach

Group	MS			TFT			MS-TFT		
	w_1	w_2	w_3	w_1	w_2	w_3	w_1	w_2	w_3
c_1	0	0	10	4	4	2	0	0	2
c_2	0	0	10	3	6	1	0	0	1
c_3	0	0	10	7	3	1	0	0	1
c_4	0	0	10	5	3	2	0	0	2
c_5	0	1	9	4	4	2	0	0	2
c_6	0	3	7	2	6	2	0	2	1
c_7	1	4	5	1	1	8	0	0	3
c_8	2	4	4	1	5	4	0	1	0
c_9	2	4	4	2	3	5	1	2	3
c_{10}	5	2	3	0	1	9	0	0	3
c_{11}	4	5	2	4	2	4	1	2	1
c_{12}	4	1	5	2	1	7	1	0	4
Total	18	24	79	35	39	47	3	7	23

The computation results provided by the basic WOA with the median value technique is given in Table 5. Similarly, to the preceding cases, the best ratio for makespan with the median technique is w_1, for total flow time is w_3, and for both objectives is w_3. Figure 7 shows the summary of Table 5.

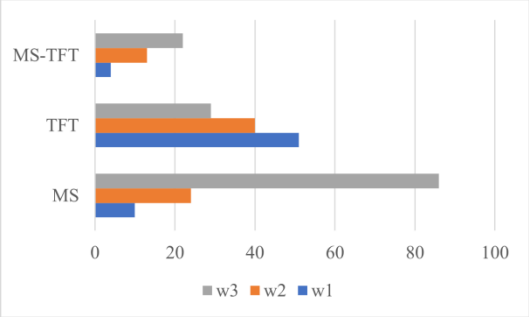

Figure 5. WOA weight ratio effect using average value approach.

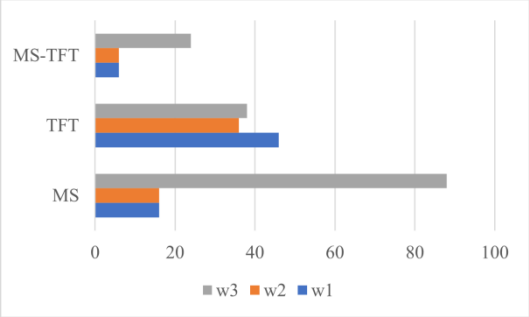

Figure 6. I-WOA weight ratio effect using average value approach.

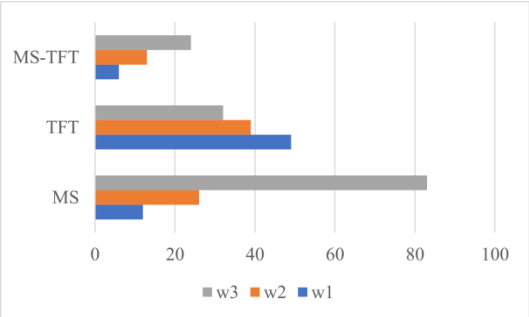

Figure 7. WOA weight ratio effect using median value approach.

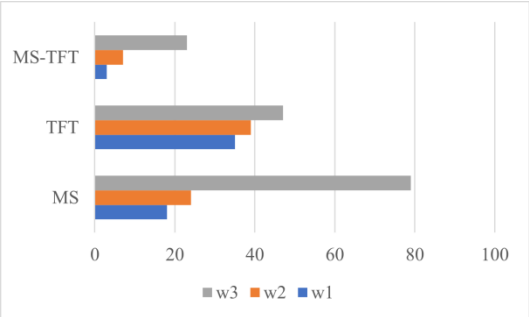

Figure 8. I-WOA weight ratio effect using median value approach.

Table 6 shows the computation results generated by the improved WOA using the median value technique. In contrast to the preceding three cases, the best ratio for time flow ratio is w_3. This condition is shown by the last column in Table 6 and furthermore illustrated in Figure 8. The four tables above show that the effect of the weight ratio varies depending on the group. Table 3, Table 4, and Table 5 all follow a similar pattern, while Table 6 is different, namely the effect on the total flow time.

Furthermore, to compare the performance of the basic and improved WOA algorithms, the results of the computations generated by WOA with the average value approach and the median value approach are juxtaposed with the corresponding results of improved WOA. The comparisons are given in Table 7 and Table 8. Each table entry represents the number of the values generated by the WOA algorithm that are better than the corresponding values generated by the I-WOA algorithm. For all columns, from 120 values, the WOA algorithm produces more than 60 better values (more than half). As a summary, Figure 9 presents the comparison between the performance of WOA and I-WOA in the percentage version. It can be concluded that basic WOA performs better than I-WOA.

Table 7. WOA results with the average value approach

Group	MS			TFT			Fitness		
	w_1	w_2	w_3	w_1	w_2	w_3	w_1	w_2	w_3
c_1	5	4	3	5	6	5	5	6	5
c_2	4	4	5	4	4	4	4	4	4
c_3	4	5	2	6	6	5	6	6	5
c_4	8	5	2	6	6	5	6	5	6
c_5	5	7	7	4	4	6	4	5	6
c_6	7	4	5	6	6	4	6	6	4
c_7	6	6	7	6	6	4	6	6	4
c_8	5	7	5	8	8	7	8	8	7
c_9	4	7	6	3	4	5	3	4	5
c_{10}	8	7	9	9	9	7	9	9	7
c_{11}	6	3	6	6	6	6	6	5	7
c_{12}	8	9	5	10	9	5	10	9	5
Total	70	68	67	73	73	64	73	73	65

Table 8. I-WOA results with the average value approach

Group	MS			TFT			MS-TFT		
	w_1	w_2	w_3	w_1	w_2	w_3	w_1	w_2	w_3
c_1	5	4	3	7	6	5	5	6	5
c_2	4	1	6	3	4	3	5	4	4
c_3	5	4	2	6	7	5	6	7	5
c_4	8	6	4	6	5	6	6	5	6
c_5	6	6	5	4	4	5	4	4	6
c_6	6	4	6	5	7	4	5	6	5
c_7	7	7	7	7	6	4	6	6	4
c_8	6	6	6	8	8	7	8	8	7
c_9	4	4	6	4	5	5	2	5	5
c_{10}	8	7	10	8	8	7	8	8	7
c_{11}	5	5	6	6	6	6	6	5	7
c_{12}	8	7	5	10	9	7	10	9	6
Total	72	61	66	74	75	64	71	73	67

Similarly, Table 8 shows the full comparison results for each group using the median value approach, and Figure 10 shows the summary. The same conclusion is obtained for the approach with the median value. Once again, WOA performs better than I-WOA in general.

Conclusion

In this paper, we have discussed how to solve the Multi-objective Flow Shop Scheduling Problem using the basic WOA algorithm and improved WOA with the objectives of minimizing makespan and total flow time. The performance of the two algorithms is compared by conducting several experiments. In addition, the effect of the objective weight ratio on the performance of each algorithm was also investigated. The conclusions obtained by this study are that the objective weight ratio affects the performance of WOA and I-WOA and the best objective ratio is MS:TFT = 75:25. The second conclusion is that WOA provides better performance than I-WOA.

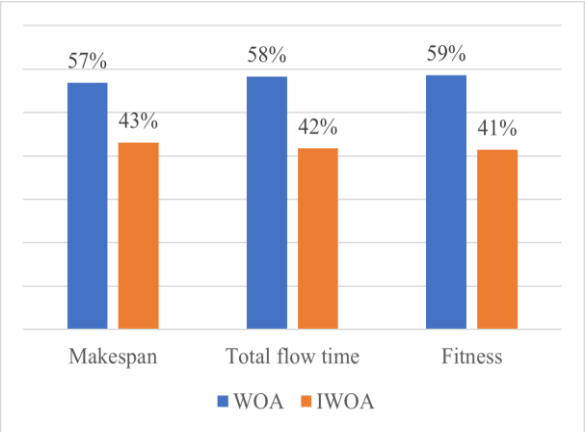

Figure 9. Performance comparison with the average value approach.

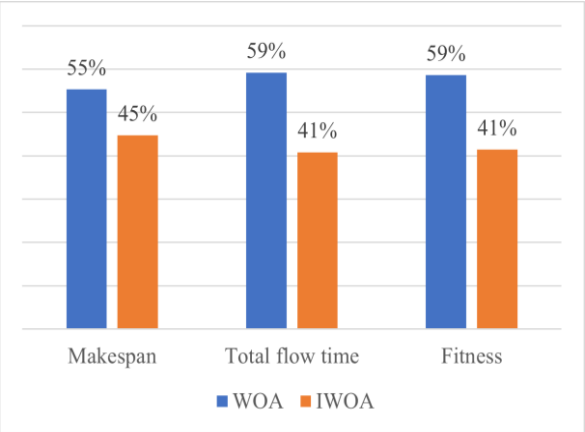

Figure 10. Performance comparison with the median value approach.

Only one variation of the basic WOA was investigated in this study. Many other variants of WOA have been proposed by researchers. There are numerous options for comparing the performance of various algorithms. The performance of WOA in comparison to other metaheuristics, such as the Bee Colony Algorithm lain (Halim & Nugraheni, 2021), is interesting. Hyper-heuristic techniques can also be used in scheduling solutions, such as (Nugraheni & Abednego, 2016b; Nugraheni & Abednego, 2017). The application of WOA with hyper-heuristics is also worth investigating. In addition, research into the applicability of WOA to other optimization issues is also challenging.

Scientific Ethics Declaration

The authors declare that the scientific ethical and legal responsibility of this article published in EPSTEM journal belongs to the authors.

Acknowledgements

* This article was presented as an oral presentation at the International Conference on Technology, Engineering and Science (www.icontes.net) held in Antalya/Turkey on November 16-19, 2022.

* This work is supported by Institution of Research and Community Services, Parahyangan Catholic University with Contract Nr. III/LPPM/2022-02/78-P.

References

Alimoradi, M. (2021). *A report on the whale optimization algorithm (WOA).* https://doi.org/10.13140/RG.2.2.30154.90563.

Alnowibet, K. A., Shekhawat, S., Saxena, A., Sallam, K. M., & Mohamed, A. W. (2022). Development and applications of augmented whale optimization algorithm. *Mathematics*, *10*(12), 2076.

Cao, D., Xu, Y., Yang, Z., Dong, H., & Li, X. (2022). An enhanced whale optimization algorithm with improved dynamic opposite learning and adaptive inertia weight strategy. *Complex & Intelligent Systems*. https://doi.org/10.1007/s40747-022-00827-1.

Chakraborty, S., Saha, A.K. Sharma, S., Mirjalili, S., & Chakraborty, R. (2020). A novel enhanced whale optimization algorithm for global optimization. *Computers & Industrial Engineering. 153*, 107086. https://doi.org/107086.10.1016/j.cie.2020.107086.

Demir, A., & Gelen, M. (2021). A new approach to solving multi-objective flowshop scheduling problems: A multi-MOORA based genetic algorithm. *Journal of Engineering Research. 9*(4A). 191-200. https://doi.org/10.36909/jer.8307.

Halim, Y., & Nugraheni, C. E. (2021). A bee colony algorithm based solver for flow shop scheduling problem. *JOIV: International Journal on Informatics Visualization*, *5*(2), 170-176. https://doi.org/10.30630/joiv.5.2.491.

Hassouneh, Y., Turabieh, H., Thaher, T., Tumar, I., Chantar, H., & Too, J. (2021). Boosted whale optimization algorithm with natural selection operators for software fault prediction. *IEEE Access*, *9*, 14239-14258.

Liang, X., Xu, S., Siwen, Liu, Y., & Sun, L. (2022). *A modified whale optimization algorithm and its application in seismic inversion problem. Mobile Information Systems. 2022*. https://doi.org/1-18. 10.1155/2022/9159130.

Lin, C.-C., Wu, Z.-X., Huang, K.-W., & Li, Y.-M. (2018). *A hybrid whale optimization algorithm for flow shop scheduling problems*. *Proceeding of the Fourth International Conference on Electronics and Software Science (ICESS2018*), Japan.

Lu, C., Xiao, S., Li, X., & Gao, L. (2016). An effective multi-objective discrete grey wolf optimizer for a real-world scheduling problem in welding production. *Advances in Engineering Software, 99*, 161-176. https://doi.org/10.1016/j.advengsoft.2016.06.004.

Mirjalili, S. & Lewis, A. (2016). The whale optimization algorithm. *Advances in Engineering Software, Volume 95*, 51-67, ISSN 0965-9978, https://doi.org/10.1016/j.advengsoft.2016.01.008.

Nadimi-Shahraki, M. H., Zamani, H., & Mirjalili, S. (2022). Enhanced whale optimization algorithm for medical feature selection: A COVID-19 case study. *Computers in Biology and Medicine, 148*, 105858. https://doi.org/10.1016/j.compbiomed.2022.105858.

Ning, G. Y., & Cao, D. Q. (2021). Improved whale optimization algorithm for solving constrained optimization problems. *Discrete Dynamics in Nature and Society*, 1-13. https://doi.org/10.1155/2021/8832251.

Nugraheni, C. E., & Abednego, L. (2016a). A comparison of heuristics for scheduling problems in textile industry. *Jurnal Teknologi, 78*, 99-104. https://doi.org/10.11113/jt.v78.9034

Nugraheni, C. E., & Abednego, L. (2016b). On the development of hyperheuristics-based framework for scheduling problems in textile industry. *International Journal of Modeling and Optimization, 6*, 272-276. https://doi.org/10.7763/IJMO.2016.V6.539.

Nugraheni, C. E., & Abednego, L. (2017). A tabu-search based constructive hyper-heuristics for scheduling problems in textile industry. *Journal of Industrial and Intelligent Information*, *5*(2). https://doi.org/ 10.18178/jiii.5.2.23-27.

Rana, N., Latiff, M. S. A., Abdulhamid, S. I. M., & Chiroma, H. (2020). Whale optimization algorithm: A systematic review of contemporary applications, modifications and developments. *Neural Computing and Applications*, *32*(20), 16245-16277. https://doi.org/10.1007/s00521-020-04849-z.

Robert, R.B. &, Rajkumar, R. (2019). A hybrid algorithm for multi-objective optimization of minimizing makespan and total flow time in permutation flow shop scheduling problems. *Information Technology and Control. 48*, 47-57. https://doi.org/10.5755/j01.itc.48.1.20909.

Schulz, S., Buscher, U., & Shen, L. (2020). Multi-objective hybrid flow shop scheduling with variable discrete production speed levels and time-of-use energy prices. *Journal of Business Economics*, *90*(9), 1315-1343. https://doi.org/10.1007/s11573-020-00971-5.

Singh, H., Oberoi, J. S., & Singh, D. (2021). Multi-objective permutation and non-permutation flow shop scheduling problems with no-wait: a systematic literature review. *RAIRO-Operations Research*, *55*(1), 27-50. https://doi.org/10.1051/ro/2020055.

Wang, Z., Deng, H., Zhu, X., & Hu, L. (2019). Application of improve whale optimization algorithm in muti-resource allocation. *Int. J. Innovative Comput*, *15*(3), 1049–1066.

Author Information

Cecilia Esti Nugraheni
Informatics Dept.
Parahyangan Catholic University
Jl. Ciumbuleuit 94, Bandung, 40141
Indonesia
Contact e-mail: *cheni@unpar.ac.id*

Craven Sachio Saputra
Informatics Dept.
Parahyangan Catholic University
Jl. Ciumbuleuit 94, Bandung, 40141
Indonesia

Luciana Abednego
Informatics Dept.
Parahyangan Catholic University
Jl. Ciumbuleuit 94, Bandung, 40141
Indonesia

To cite this article:

Nugraheni, C. E., Saputra, C. S., & Abednego, L. (2022). Whale optimization algorithms for multi-objective flowshop scheduling problems. *The Eurasia Proceedings of Science, Technology, Engineering & Mathematics (EPSTEM), 21,* 441-451.

The Eurasia Proceedings of Science, Technology, Engineering & Mathematics (EPSTEM)
ISSN: 2602-3199

The Eurasia Proceedings of Science, Technology, Engineering & Mathematics (EPSTEM), 2022

Volume 21, Pages 452-463

IConTES 2022: International Conference on Technology, Engineering and Science

Numerical Investigation of a Tubular Heat Exchanger Fitted with Triangular Ribs

Nabil BENAMARA
Djillali Liabes University of Sidi-Bel-Abbes

Djelloul LAHMER
Djillali Liabes University of Sidi-Bel-Abbes

Mohamed MERZOUG
Djillali Liabes University of Sidi-Bel-Abbes

Abdelkader LAHCENE
Djillali Liabes University of Sidi-Bel-Abbes

Abdelkader BOULENOUAR
Djillali Liabes University of Sidi-Bel-Abbes

Miloud AMINALLAH
Djillali Liabes University of Sidi-Bel-Abbes

Abstract: In the present work we numerically study the effect of the presence of triangular shaped promoters on the efficiency of a tubular heat exchanger. When we talk about efficiency, we are generally faced with problems of dynamic and thermal behavior within the latter. The main objective is to optimize the geometric parameters of the triangular-shaped promoters in order to collect the maximum energy at a minimum cost. Indeed, in the case of a two-dimensional simplified geometry, we considered the flow of an incompressible fluid (air) in a cylindrical heat exchanger tube equipped with baffles placed perpendicular to the direction of flow. Several baffle arrangements are considered according to the angle of inclination β, the space between the two successive baffles (space ratio PR: P/Dh) and the length of the baffle (blocking ratio BR: e/Dh) . The calculations are carried out by means of the fluent computer code using the k-ε turbulence model, RNG, with a Reynolds number Re varying from 3000 up to 13000. The results found indicated that the best thermal performance obtained corresponds to β=30°;BR=0.2; PR=1 and Re=4000.

Keywords: Turbulence ribs, Nusselt number Nu, Friction number Fr, Turbulence model K-ε RNG, Thermal-hydraulic factor

Introduction

The heat exchanger is one of the most important pieces of equipment in industry because it allows the recovery of energy, by convective transfer, between two or more fluids. In order to improve the heat transfer rate with minimal pressure drop, researchers have tried to develop several techniques. Two major classes of heat transfer enhancement techniques are used in heat exchangers: so-called active and passive techniques (Alam et al., 2018). In our study, we focus on passive methods (Sheikholeslami et al., 2015), as they do not require an external power supply and generally use modified surfaces by inserting vortex generators into the main flow. According to the published works in this field, the method which succeeded, successfully, in improving the heat

- Selection and peer-review under responsibility of the Organizing Committee of the Conference

exchange with a reduced cost and bulk with a low pressure drop of the fluid is the promoters of longitudinal turbulence (Kumar B et al., 2018). Indeed, several studies are carried out on this technique in order to give a better design of the turbulence generator inserted on the heat exchanger which can improve the heat transfer by the destruction of the thermal boundary layer (Nakhchi et al., 2019; Targui et al., 2008). In some experimental studies, Han et al. (1991) used ribs on two walls of a square channel with different angles of attack for pitch ratio (P/e = 10) and blocking ratio (e/D = 0.0625). They found that the angled "V" shaped ribs have a significant effect on the performance of the heat exchanger. According to Promvonge et al (2010) baffles with a 45° angle of attack increase the heat transfer coefficient from 150% to 850%. Torii et al (2002) concluded that installing "winglet" delta type baffles on a finned tube heat exchanger significantly improves heat transfer and reduces the friction factor. The effect of baffle angle of attack on heat transfer and fluid flow is investigated numerically by Kwankaomeng et al. (2010) for which they used baffles inclined at 30° with different values of the blocking ratio (BR). They found that baffles angled at 30° significantly increased the heat transfer coefficient in the channel because they generated vortices in the fluid flow. But this increase in heat transfer associated with a large pressure drop ranging from 1 to 17 times over the channel without baffles. Zhang et al, (2013) studied the effect of the arc belt inserted in the tube heat exchanger. They found that the arc belt can swirl the fluid pipe and plays the role of enhanced heat transfer, but also significantly increases fluid resistance, where the PEC is anything above 1.5. A numerical analysis of vortex generators (VG), placed on the tubes of an exchanger, was carried out by J. Jang et al. The results obtained showed that the optimal values of the angle of inclination (θ) and the transverse location (Ly), are respectively between: $30° < \theta < 60°$ and 2 mm < Ly < 20 mm. Omidi et al (2019) numerically investigated the effect of alumina nanofluid inside a three-lobe twisted ribbon tube on heat exchanger performance for various volume fractions of nanofluid from 0 .01, 0.02 and 0.03 with a Reynolds number between 5000 and 20,000; they noticed that increasing the nanoparticle concentration improves the heat transfer rates for these cases, while it does not increase the relative Nusselt number inside the twist tube with a Y-insert at a Reynolds number and high nanoparticle concentration. Shobahana et al (2018) concluded that the overall performance of the double fin and tube heat exchanger can be improved by 27-91% using 20 degree RWVGs for the studied Reynolds number range.

As part of the understanding and improvement of the convective transfer phenomenon in tubular heat exchangers with the presence of inclined baffles, the objective of this work is to numerically study the optimal geometry, the angle of attack, the ratio pitch (PR) and blocking ratio (BR), which provides the best efficiency of a heat exchanger.

Geometry Studied

The configuration of the rough circular duct proposed for the ram air stream is a simple two-dimensional (2D) rectangular channel with dimensions: H×L2= 0.05×1.3 m^2 and a hydraulic diameter D_h=50 mm, The dimensions of the heat exchanger tubular are given in the following table:

Table 1. Geometry dimensions.

Parameters	Range
Reynolds number (Re)	3000-13000 (7 valeurs)
Hydraulic diameter (Dh)	50 mm
Angle of inclination Ribs (β)	20°, 30°, 40°, 60°
Roughness height(e)	5 et 10 mm
Block report (BR: e/Dh)	0.1et 0.2
spacing roughness(P)	50, 100,150 et 200 mm
Space ratio(PR:P/Dh)	1, 2,3 et 4

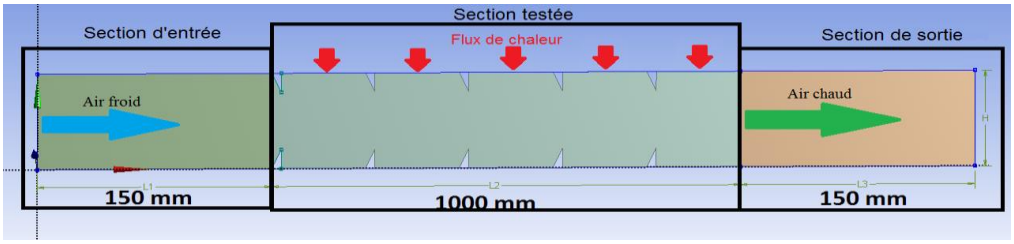

Figure 1. Geometry of an exchanger equipped with artificial roughness

In our studied tubular heat exchanger two other rectangles are placed, one before the test area of dimensions H×L1= 0.05×0.150 m^2 and the other after the test area of dimensions H×L3= 0.02×0.150 m^2. The objective of adding these two rectangles are to obtain a steady state before the air enters the test area, and on the other hand, to ensure a good mixture of air leaving the latter. The ribs of triangular geometric shape are arranged at a fixed spacing ratio, on the internal wall of the exchanger.

Boundary Conditions

In our numerical study, we take a uniform airflow velocity at the U_{inlet} inlet section with a fixed temperature of 300K corresponding to the Prandtl number (Pr) equal to 0.7. The tube wall temperature of the test section is set at 350K while the baffle walls and the inlet and outlet extension tube wall are considered adiabatic. The pressure of the fluid flow at the outlet is atmospheric (fig.1). The physical properties of air are given in the table below (Table 2).

Table 2. Thermo-physical properties

Properties	Tube (al)	Fluid (air)
Cp (J/kg k)	871	1006.43
ρ (kg/ m3)	2719	1.225
λ (w/m k)	202.4	0.0242
μ (N.s/ m2)	-	1.7894e-05

Governing Equations

In order to study the problem of heat transfer of an incompressible fluid in a two-dimensional turbulent regime of our heat exchanger design, one has to solve the equations of continuity, momentum and energy.

Continuity equation:

$$\frac{\partial u}{\partial x}+\frac{\partial V}{\partial y}=0 \qquad (1)$$

Momentum conservation equation:

$$\frac{\partial}{\partial x_i}\left(\rho u_i u_j\right)=-\frac{\partial p}{\partial x_i}+\frac{\partial}{\rho x_i}\left[\mu\left(\frac{\partial u_i}{\partial u_j}-\overline{\rho u_i' \rho u_j'}\right)\right] \qquad (2)$$

Energy conservation equation

$$\frac{\partial}{\partial x_i}\left(\rho u_i T\right)=\frac{\partial}{\rho x_i}\left[\left(r+r_t\right)\frac{\partial T}{\partial x_j}\right] \qquad (3)$$

Knowing that (r) is the thermal diffusion given by:

$$r=\frac{\mu}{Pr} \qquad (4)$$

In this study, the standard k-ε turbulence model is adopted over other turbulence models available in the ANSYS Fluent computer code, because it is robust and gives accurate results in the case of convective transfer of a flow fully turbulent in the test section of a heat exchanger equipped with turbulence promoters.

$\overline{-\rho u_i' u_j'}$: is called Reynolds constraints defined by the turbulence model ε.

μ_t : is the turbulence viscosity defined by:

$$\mu_t=\rho c_\mu \frac{k^2}{\varepsilon} \qquad (5)$$

For ANSYS-Fluent software the coefficient $c_\mu = 0.9$ and for the other empirical constants are defined as indicated below:

$$c_{1\varepsilon}=1.44\ ;\ c_{2\varepsilon}=1.92\ ;\ \sigma_k=1.0\ ;\ \sigma_\varepsilon=1.3\ .$$

To evaluate the heat transfer in each geometric configuration of our exchanger, we calculate the average Nusselt number given by:

$$Nu = \frac{hD_h}{\lambda} \quad (6)$$

h: is the heat transfer coefficient of the heated wall obtained from ANSYS fluent.

Where D_h: is the hydraulic diameter defined as follows:

$$D_h = \frac{4\times section}{perimeter} = D_{tube} \quad (7)$$

Reynolds number

$$Re = \frac{u_{in}D}{\mu} \quad (8)$$

The friction factor is calculated by the following equation:

$$f_r = \frac{2\,\Delta P}{\rho u_{in}^2 (\frac{L}{D_h})} \quad (9)$$

Where ΔP: is the pressure drop along the tube.

The best baffle arrangement in the heat exchanger is the one with the highest thermal enhancement factor value given by (Webb and Eckert., 1972) :

$$\eta = \frac{Nu/Nu_0}{(\frac{Fr}{Fr_0})^{\frac{1}{3}}} \quad (10)$$

Geometry Mesh

In this numerical work a block-structured, quadratic type mesh is used in order to control the size and the spacing of the first line of the mesh close to the heated wall and to minimize the iterative calculation error.

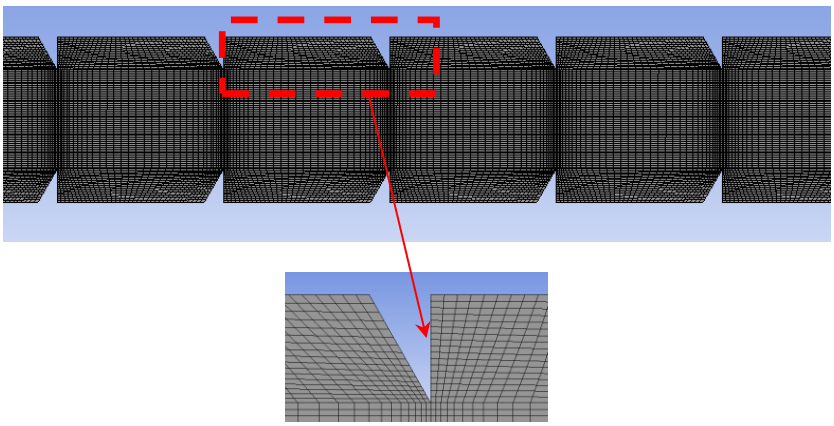

Figure 2. Mesh of the computational domain

Table 1. Mesh size sensitivity

N° of elements	Element size	Nu	Fr	% diff Nu	%diff Fr
46350	1	30,84557	0,278849	--	--
53766	0,9	30,35513	0,276743	0,49044	0,002106
59328	0,8	29,96112	0,274552	0,39401	0,002191
67671	0,7	29,73213	0,272688	0,22899	0,001864
77868	0,6	29,719913	0,271979	0,012217	0,000709

The strategy of using a more refined block-structured mesh close to the walls aims to minimize errors and calculation stability, particularly in regions where temperature and speed gradients are the greatest, as in the case of thermal boundary layers and hydraulics. The sensitivity of the mesh size on the variations of the Nusselt number and the coefficient of friction is represented in Table 3. It was found that at larger grid numbers the relative error of Nusselt and of the coefficient of friction is almost zero.

Results and Discussions

Validation of Results

In order to validate the results of our numerical study obtained, we compared the values of the number of Nusselt and coefficient of friction in the case of a smooth tube with the correlations of Dittus-Boelter (1930) and Gnielinski (1976) (see figures 3 and 4).

Dittus-Boelter Correlation:

$$Nu = 0.023\, Re^{0.8} Pr^{0.4}$$

Gnielinski Correlation:

$$Nu = \frac{\left(fr/8\right)RePr}{1+12.7\left(fr/8\right)^{\frac{1}{2}}\left(Pr^{2/3}-1\right)} \qquad \text{For} \quad 2300 \leq \text{Re} \leq 5.106$$

with:

$$Fr = (0.76 ln Re - 1.64)^{-2} \qquad \text{For } 2300 \leq \text{Re} \leq 5.106$$

Moody Correlation (1944):

$$Fr = 0.316 Re^{0.25} \qquad \text{For Re} \leq 2.104$$

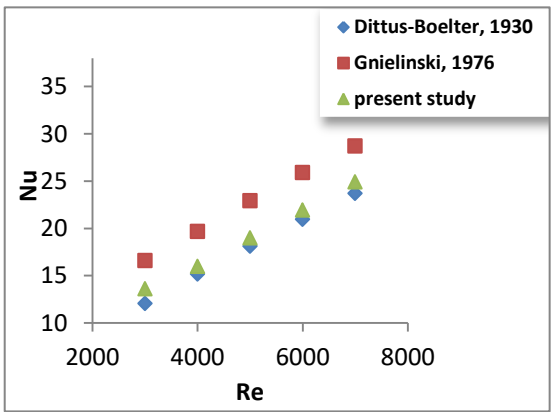

Figure 3. Comparison between the Nusselt Nu number of the present study and Gnielinski, Dittus-Boelter.

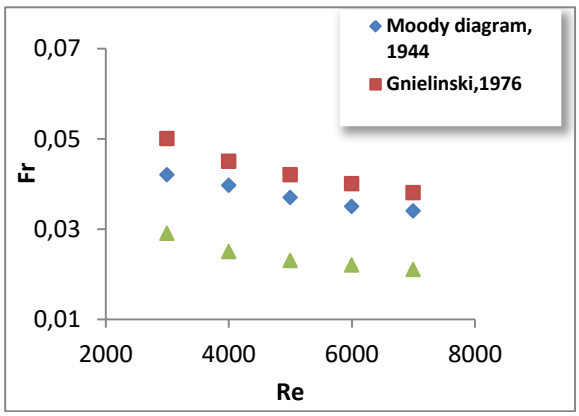

Figure 4. Comparaison between the friction facor Fr of the present study and Gnielinski, Moody diagram.

Effect of Reynolds Number on Nusselt Number

Figures 5 and 6 show the evolution of Nusselt numbers as a function of Reynolds numbers, for different parameters of deflector arrangements and inclinations: β (20°, 30°, 40° and 60°), PR (1, 2, 3 and 4) and for two fixed values of BR (0. 1 and 0. 2). The results obtained indicate that the Nusselt number increases with the increase in the Reynolds number for the different angles of inclination β. The best heat transfer recorded corresponds to the following geometric parameters (β, PR and BR) = (30°, 1 and 0.2) at a number of Re equal to 13000. This improvement in convective transfer is about 97% compared to the smooth tube due to the presence of the ribs which disturbs the main flow by creating zones of separation and reattachment of the turbulent

boundary layer, thus promoting heat transfer through the appearance of secondary flows. We also notice that the increases in the thickness of the ribs (BR=0.1 and 0.2), for fixed values of β, PR and Re, have a great influence on the improvement of the exchange coefficient of about 32% at fixed values of (β, PR and Re) = (30°, 1 and 13000) respectively.

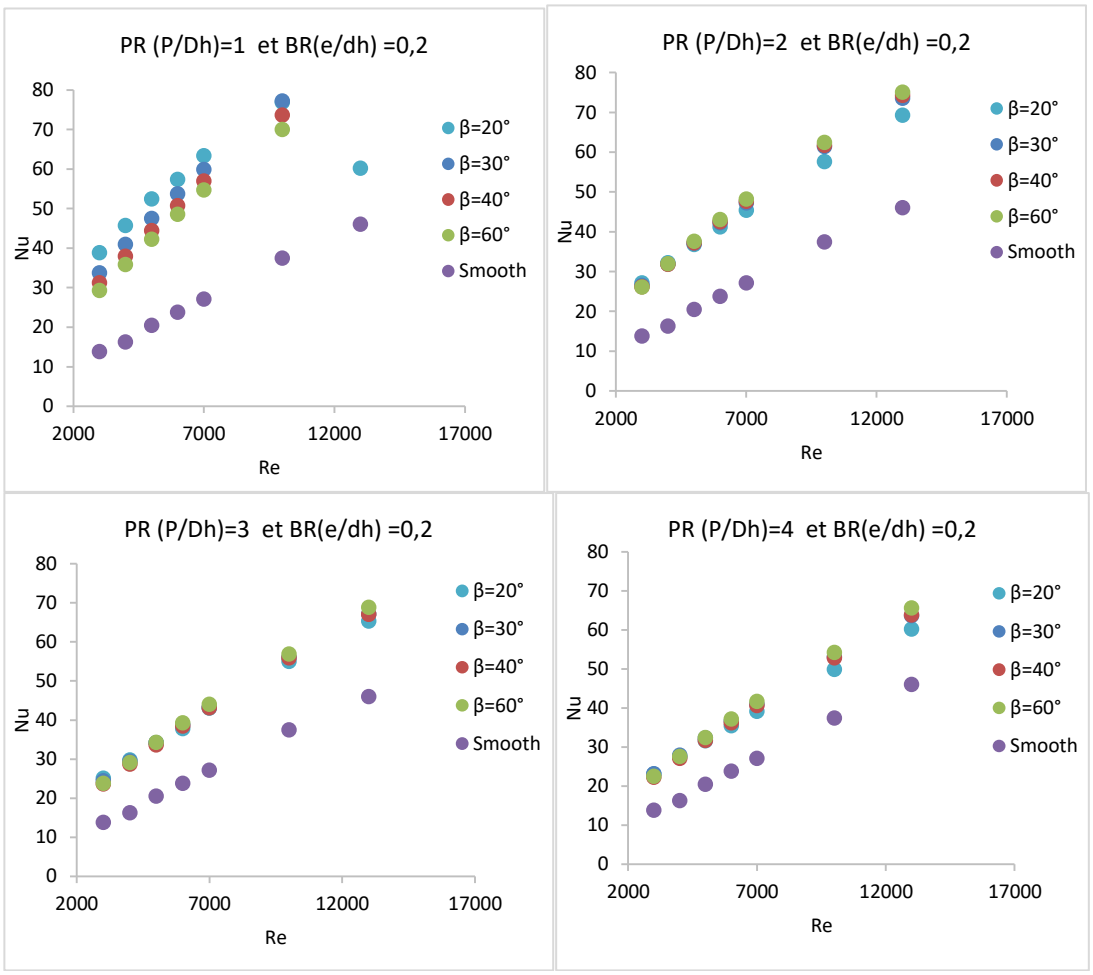

Figure 5. Effect of the Re number on the average Nu number for different inclination angles β (PR = 1, 2, 3.4 and BR = 0.2).

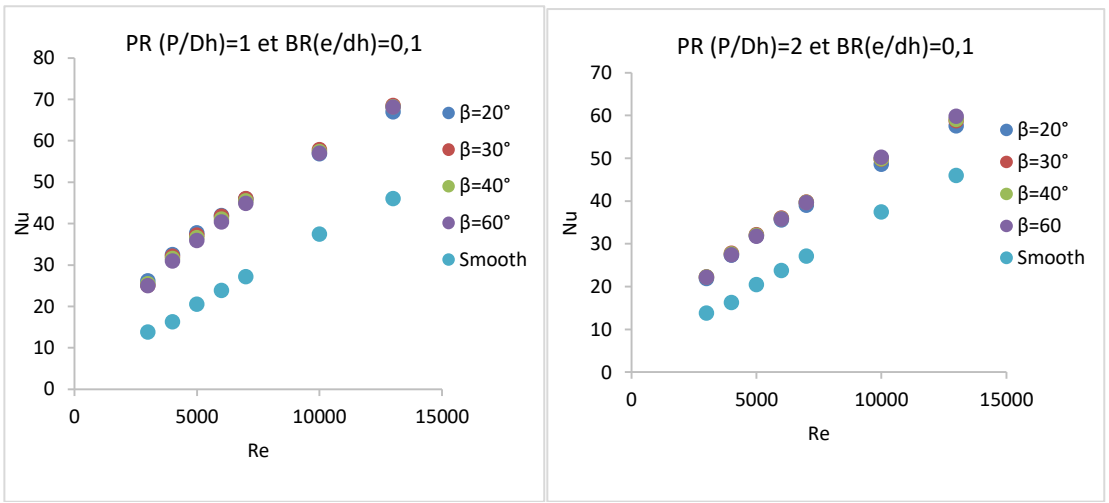

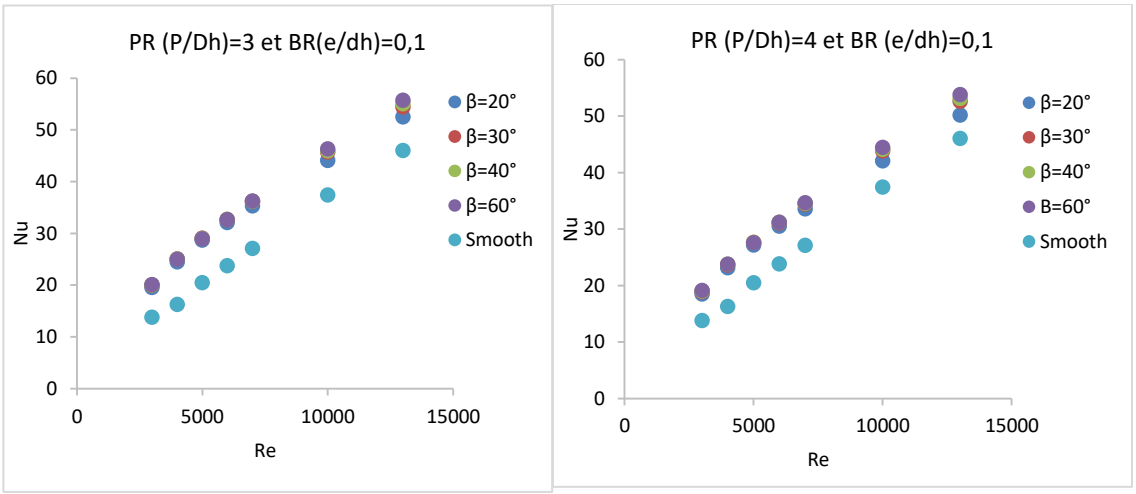

Figure 6. Effect of the number Re on the average number Nu for different angles of inclination β (PR =1, 2, 3.4 and BR=0.1).

Effect of the Reynolds Number on the Coefficient of Friction Fr

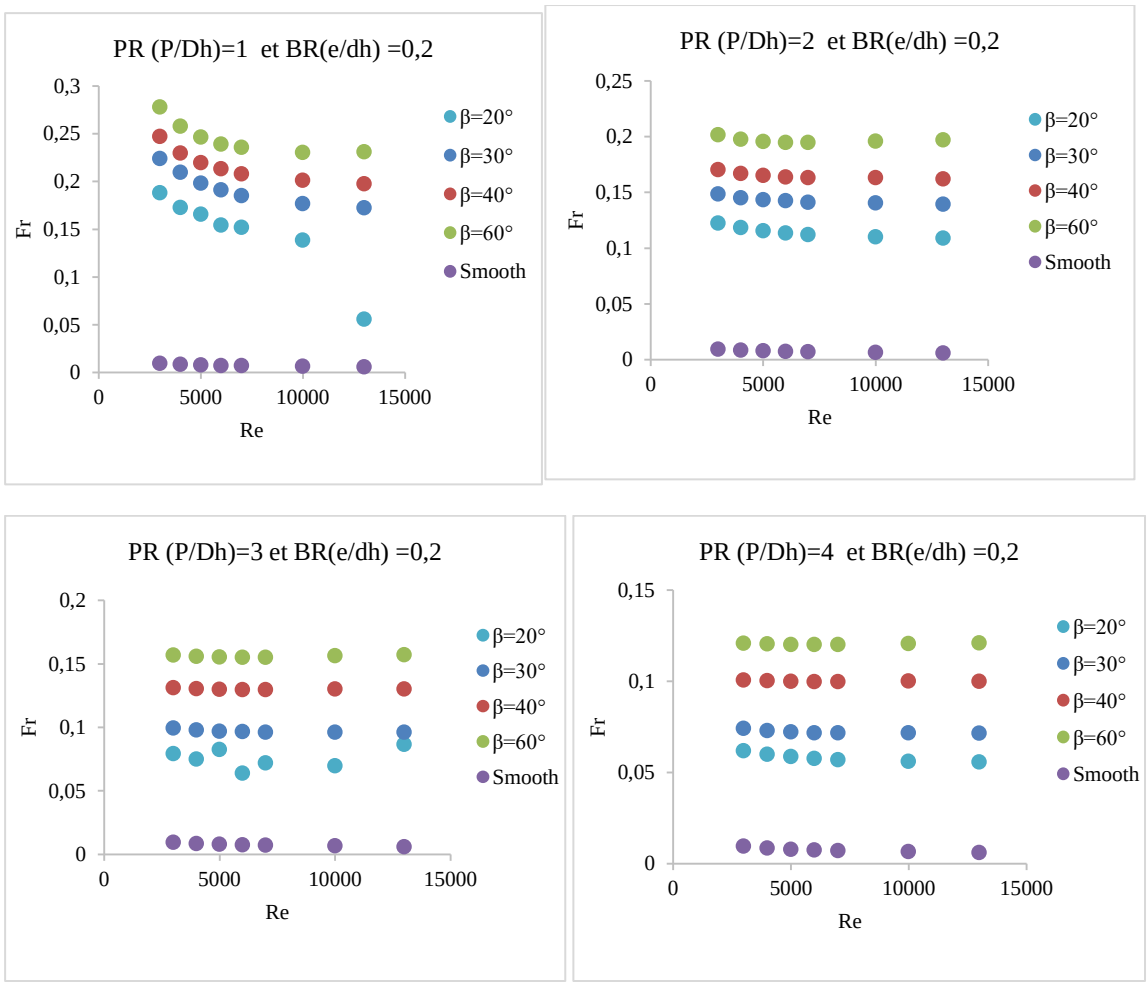

Figure 7. Effect of the number Re on the friction number Fr for different angles of inclination β (PR =1, 2, 3.4 and BR=0.2)

The turbulent flow generated by the baffles increases both the heat exchange coefficient and the friction factor, due to the development and increase in thickness of the turbulent dynamic boundary layer. Figures 7 and 8 shows that all the arrangements of the baffles examined at different values of (β, PR and BR) increase the

friction factor in comparison with the case of a smooth tube. A high friction factor value of around 0.27 is obtained at Re = 3000 and geometric values equal to (β = 60°; PR = 1; BR= 0.2). There is a great influence of the angle of inclination (β) on the increase in the friction factor which can reach 12% at β = 60° compared to an inclination of 40°. A significant increase in the coefficient of friction is recorded with the increase in the blocking ratio BR in comparison with the other parameters examined, which is quite logical since the duct becomes more and more obstructed.

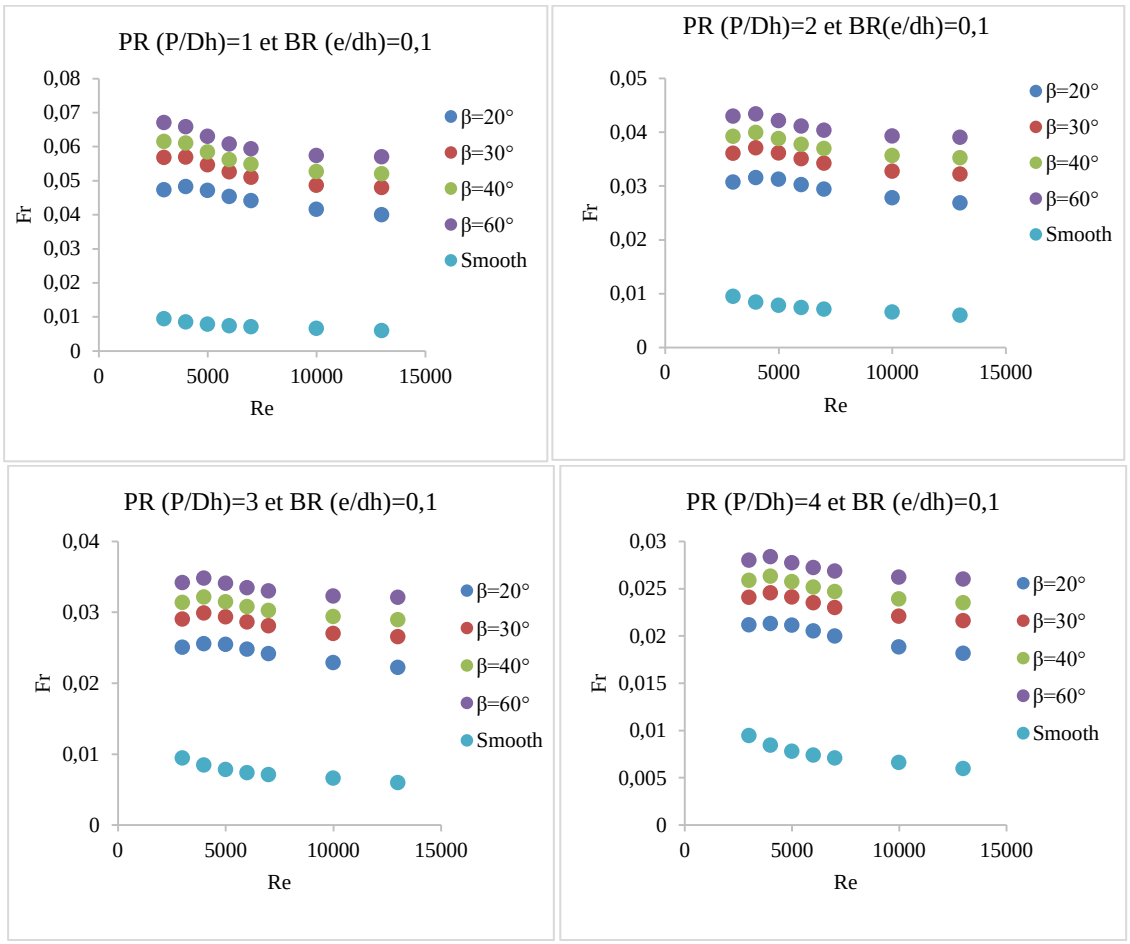

Figure 8. Effect of the number Re on the friction number Fr for different angles of inclination β (PR =1, 2, 3.4 and BR=0.1)

Effect of Reynolds Number on the Thermal-Hydraulic Performance (η)

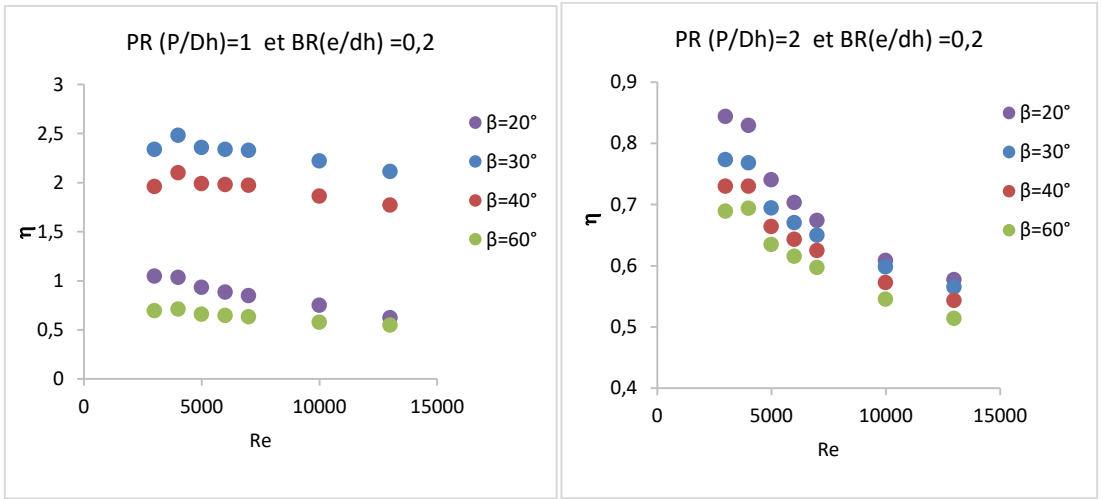

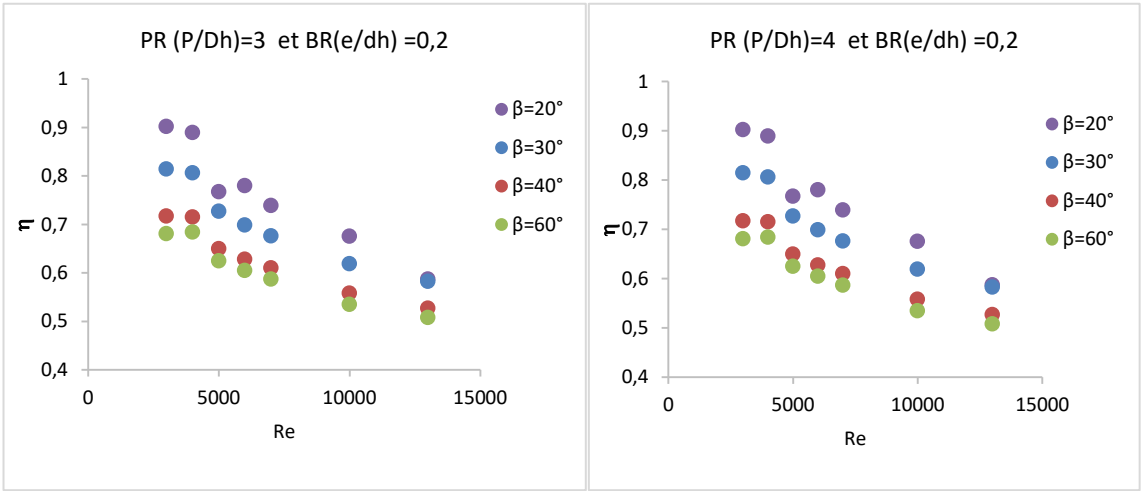

Figure 9. Effect of the number Re on the efficiency η for different angles of inclination β (PR =1, 2, 3.4 and BR=0.2).

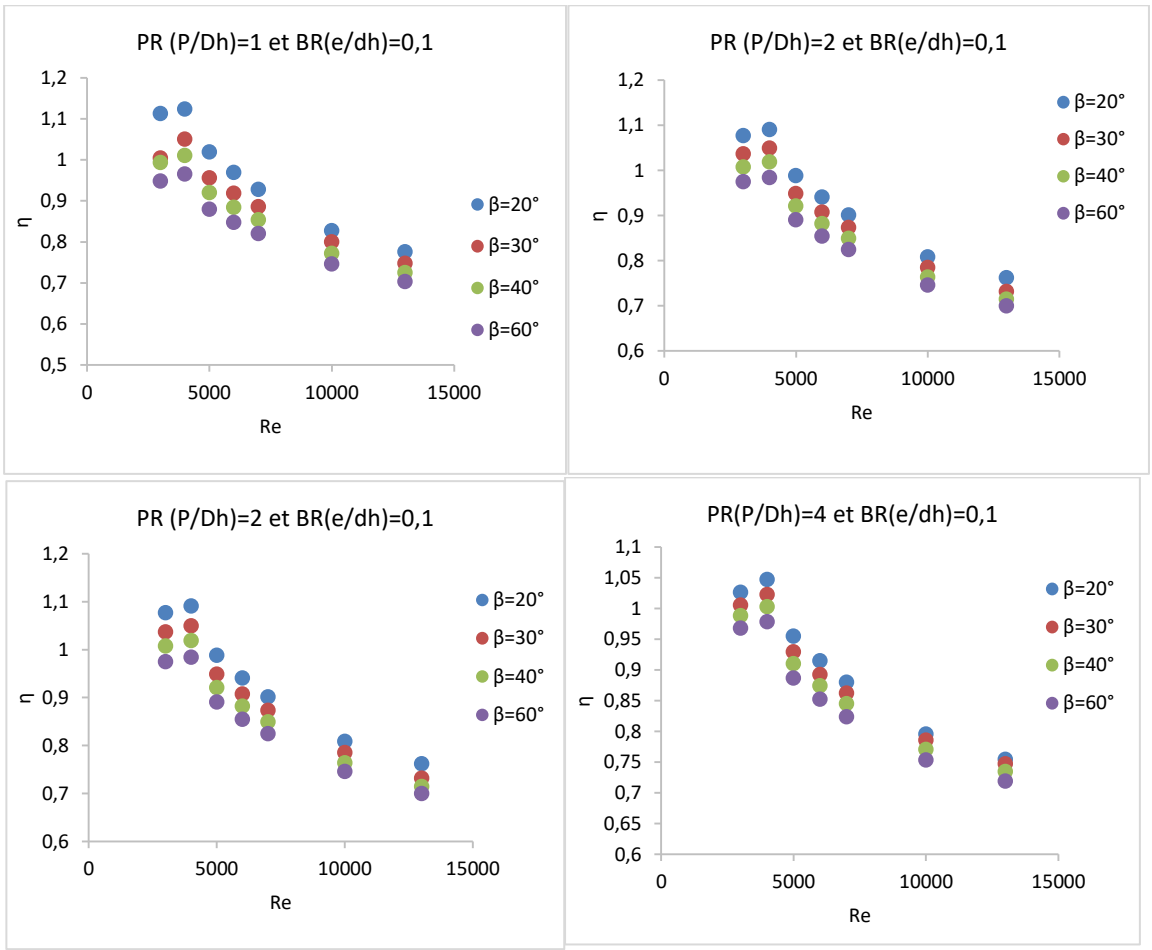

Figure 2. Effect of the number Re on the efficiency η for different angles of inclination β (PR =1, 2, 3.4 and BR=0.1).

In this part, we will analyze another important parameter called thermal-hydraulic performance factor (η) often used as an optimization parameter. This coefficient of performance therefore allows us to find a compromise between the increase in transfer and the pressure drop. From the results obtained, it is possible to define the optimal parameters for thermal improvements at a minimum cost.

Figures 9 and 10 represent the variation of the performance factor for different values of the pitch ratio (PR), of the blocking ratio (BR) and of the angle of inclination (β) as a function of the Reynolds number. It is clear that the performance factor decreases with the increase of β and BR. It can be seen that the best efficiency of 2.48 is obtained for β = 30°; PR=1; BR = 0.2 and a Reynolds number equals 4000. Also, the obstruction effect disappears at large Reynolds numbers.

The Case Where the Main Flow is Reversed

In this part, in order to improve the thermal-hydraulic performance factor as much as possible, we have tried to see the impact of reversing the conditions of entering and leaving our exchanger. Reversing the flow direction completely changes the geometric shape of the baffles. To do this and according to our subsequent results, we took the case which provided us with the best performance factor corresponding to the following geometric parameters: β=30, BR= 0.2 and PR=1 to 4000 Re (see Figure 9 : η depending on Re case P=50). On the whole, the reversal of the inlet and outlet conditions (case AA) gave an acceptable improvement in the performance of the exchanger, but it remains insignificant in comparison with the first case examined (case A) (see histogram figure 11).

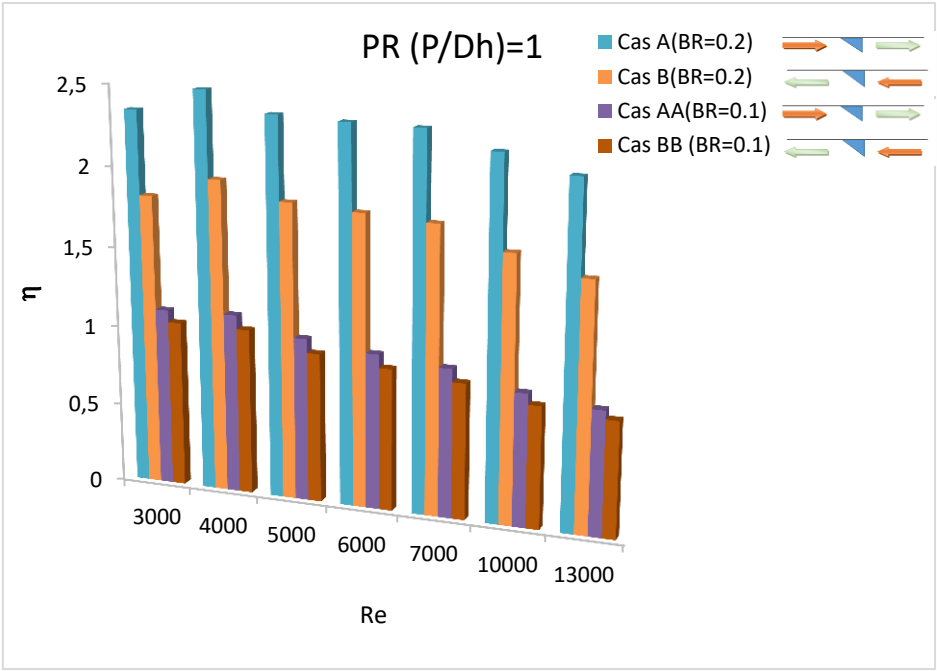

Figure 3. Comparison of efficiency between the case of a flow from left to right and the case of a reversed flow of the optimal values obtained under the conditions: (β=30, BR= 0.2 and PR=1) and (β=20, BR= 0.1 and PR=1).

Conclusion

In this work we have numerically studied the effect of the variation of the geometric parameters of the ribs (β; PR; BR) on the dynamic field of the flow of the fluid and the improvement of the convective transfer in a tubular exchanger. The results obtained showed that all the ribs arrangements examined increase both heat transfer due to vortex generation in the flow and the friction factor. This study also allowed us to show the effect of the layout of the ribsand their shapes on the thermo-hydraulic performance compared to a smooth wall:

• In comparison with the smooth case, the presence of roughness disturbs the flow and increases both the convective transfer and the pressure losses.

• The Nusselt number increases with increasing Reynolds number and decreasing inclination angle β due to the modification of the laminar sublayer of the fully developed turbulent flow in the near-wall region.

• Of all the parameters examined, the blocking ratio is the most influential on the thermal-hydraulic performance factor.

• The observations, from the results obtained, have shown that there are two optimal efficiency values that can be reached at a number of Re = 4000. The first corresponds to β=30°; PR=1; BR = 0.2 and the second at β = 20°; PR = 1 and BR = 0.1. Between these two baffle layout values, the first case is more interesting.

Scientific Ethics Declaration

The authors declare that the scientific ethical and legal responsibility of this article published in EPSTEM journal belongs to the authors.

Acknowledgements

* This article was presented as an oral presentation at the International Conference on Technology, Engineering and Science (www.icontes.net) held in Antalya/Turkey on November 16-19, 2022.

References

Alam T., & Kim M.-H. (2018). A comprehensive review on single phase heat transfer enhancement techniques in heat exchanger applications. *Renew. Sustain. Energy Rev. 81*, 813–839.

Dittus, F. W., & Boelter, L. M. K. (1985). Heat transfer in automobile radiators of the tubular type. *International Communications in Heat and Mass Transfer*, *12*(1), 3-22.

Fluent (2003). Fluent user's guide. *Fluent Inc.*, *2*(3).

Gilinsky, V., (1976). New equations for heat and mass transfer in turbulent pipe flow and channel flow. *Int. Chem. Eng, 16***,** 359–368.

Han, J.C., Zhang, Y.M., & Lee, C.P. (1991). Augmented heat transfer in square channels with parallel, crossed and V-shaped angled ribs. *ASME Journal of Heat Transfer, 113*, 590-596.

Jang, J. Y., Hsu, L. F., & Leu, J. S. (2013). Optimization of the span angle and location of vortex generators in a plate-fin and tube heat exchanger. *International Journal of Heat and Mass Transfer*, *67*, 432-444.

Karima A., (2018). CFD investigations of thermal and dynamic behaviors in a tubular heat exchanger with butterfly baffles. *Frontiers in Heat and Mass Transfer (FHMT), 10*, 27. http://dx.doi.org/10.5098/hmt.10.27

Kumar B., Srivastava G.P., Kumar M., & Patil A.K. (2018). A review of heat transfer and fluid flow mechanism in heat exchanger tube with inserts. *Chem. Eng. Process. – Process intensif. 123*, 126–137.

Kwankaomeng, S., Jedsadaratanachai, W., & Promvonge, P. (2010, June). Laminar periodic flow and heat transfer in square channel with 30° inclined baffles. In *Proceedings of the International Conference on Energy and Sustainable Development: Issues and Strategies (ESD 2010)* (pp. 1-7). IEEE.

Moody, L. F. (1944). Friction factors for pipe flow. *Transactions of the American Society of Mechanical Engineers*, *66*(8), 671-678.

Nakhchi, M. E., & Esfahani, J. A. (2019). Numerical investigation of rectangular-cut twisted tape insert on performance improvement of heat exchangers. *International Journal of Thermal Sciences*, *138*, 75-83.

Omidi, M., Rabienataj Darzi, A. A., & Farhadi, M. (2019). Turbulent heat transfer and fluid flow of alumina nanofluid inside three-lobed twisted tube. *Journal of Thermal Analysis and Calorimetry*, *137*(4), 1451-1462.

Targui N., & Kahalerras H. (2008). *Analyse du transfert de chaleur et de la chute de pression dans un échangeur de chaleur muni de chicanes poreuses*. Retrieved from https://www.sft.asso.fr/Local/sft/dir/user-3775/documents/actes/congres_2008/354.pdf

Promvonge, P., Sripattanapipat, S., & Kwankaomeng, S. (2010). Laminar periodic flow and heat transfer in square channel with 45° inline baffles on two opposite walls. *Int. J. Therm. Sci*, *49*, 963–975.

Sheikholeslami M., Gorji-Bandpy M., & Ganji D. D. (2015). Review of heat transfer enhancement methods: Focus on passive methods using swirl flow devices. *Renew. Sustain. Energy Rev. 49*, 444–469.

Singh, S., Sørensen, K., & Condra, T. (2018). Investigation of vortex generator enhanced double-fin and tube heat exchanger. *Journal of Heat Transfer, 141*(2), 021802. https://doi.org/10.1115/1.4042050.

Sun Z., Zhang K., & Li W. (2020). Investigations of the turbulent thermal-hydraulic performance in circular heat exchanger tubes with multiple rectangular winglet vortex generators. *Applied Thermal Engineering 168*, 114-838.

Torii, K., Kwak, K.M., & Nishino, K. (2002). Heat transfer enhancement accompanying pressure-loss reduction with winglet type vortex generators for fin tube heat exchangers. *Int. J. Heat Mas Transfer*, *45*, 3795–3801.

Webb, R. L., & Eckert, E. R. G. (1972). Application of rough surfaces to heat exchanger design. *International Journal of Heat and Mass Transfer*, *15*(9), 1647-1658.

Zhang, D. H., & Gao, J. (2013). Numerical study of circular tube inserted arc belt on fluid flow and heat transfer under laminar flow. In *Key Engineering Materials* (Vol. 561, pp. 460-465). Trans Tech Publications Ltd.

Zina, B., Filali, A., Laouedj, S., & Benamara, N. (2019). Numerical investigation of a solar air heater (SAH) with triangular artificial roughness having a curved top corner. *Journal of Applied Fluid Mechanics*, *12*(6), 1919-1928.

Nabil BENAMARA
Materials and Reactive Systems Laboratory,
Mechanical Engineering Department,
Djillali Liabes University of Sidi-Bel-Abbes (22000),
BP. 89, City Larbi Ben Mhidi, Algeria
benamarana@gmail.com

Abdelkader LAHCENE
Materials and Reactive Systems Laboratory,
Mechanical Engineering Department,
Djillali Liabes University of Sidi-Bel-Abbes (22000),
BP. 89, City Larbi Ben Mhidi, Algeria

Djelloul LAHMER
Materials and Reactive Systems Laboratory,
Mechanical Engineering Department,
Djillali Liabes University of Sidi-Bel-Abbes (22000),
BP. 89, City Larbi Ben Mhidi, Algeria

Abdelkader BOULENOUAR
Materials and Reactive Systems Laboratory,
Mechanical Engineering Department,
Djillali Liabes University of Sidi-Bel-Abbes (22000),
BP. 89, City Larbi Ben Mhidi, Algeria

Mohamed MERZOUG
Materials and Reactive Systems Laboratory,
Mechanical Engineering Department,
Djillali Liabes University of Sidi-Bel-Abbes (22000),
BP. 89, City Larbi Ben Mhidi, Algeria

Miloud AMINALLAH
Materials and Reactive Systems Laboratory,
Mechanical Engineering Department,
Djillali Liabes University of Sidi-Bel-Abbes (22000),
BP. 89, City Larbi Ben Mhidi, Algeria

To cite this article:

Benamara, N., Lahmer, D., Merzoug, M., Lahcene, A., Boulenouar. A., & Aminallah, M. (2022). Numerical investigation of a tubular heat exchanger fitted with triangular ribs. *The Eurasia Proceedings of Science, Technology, Engineering & Mathematics (EPSTEM), 21*, 452-463.

The Eurasia Proceedings of Science, Technology, Engineering & Mathematics (EPSTEM)
ISSN: 2602-3199

The Eurasia Proceedings of Science, Technology, Engineering & Mathematics (EPSTEM), 2022

Volume 21, Pages 464-468

IConTES 2022: International Conference on Technology, Engineering and Science

Effect of Neon Ion Implantation on the Electrical Propertie of CIGS Photovoltaic Cells

Mustapha DJABAR
Université Ferhat ABBAS Sétif 1

Abstract: The global energy demand is huge. Conventional fossil fuels such as oil, natural gas and coal are running out fast. These fossil fuels produce a huge amount of carbon dioxide, which is one of the greenhouse gases identified as the main cause of the global warming of the planet. More and more alternative sources of energy are being used: renewable and environmentally friendly. Solar energy is one of them. The photovoltaic sector converts solar radiation into electricity. This is done using photovoltaic cells. The highest conversion yields are obtained from mono-crystalline silicon cells. mono-crystalline silicon becomes relatively expensive, the ternary and quaternary chalcopyrite semiconductors are a viable economic alternative. Thin films chalcopyrite (CuInGaSe2) semiconductors have gained their place in solar energy harvesting. CIGS solar cells are increasingly efficient every year. It has been shown that the ion implantation affects the structure by changing or introducing defects. This in turn affects the electric properties of the material and may increase the efficiency of the solar cells. Thin films of Cu(InGa)Se2 deposited by low cost process were studied by simulating the ion implantation using SRIM software. Different energies and different doses of implantation were simulated in order to analyze the electrical properties of photovoltaic cells.

Keywords: Ion implantation, CIGS, Thin films, Solar cells, SRIM

Introduction

In a modern society, energy is vital for social and economic development. In today's world the comfort of modern computers, internet, and mobile phones lead to an increase in the energy demand. Providing the necessary energy without polluting our environment needs some sort of renewable energy resources. Green power represents those renewable energy resources and technologies that provide the greatest environmental benefit. It is defined as electricity produced from solar, wind, geothermal, biogas and hydroelectric sources. Solar energy is one of the most important sources among these renewable energy sources. Solar energy is sufficient enough to meet all of the Earth's energy demands. Generating electricity from solar energy is done using solar cells. Photovoltaic cells convert sunlight directly into electricity.

The the oldest cells called first generation solar cells are made of silicon and involve single and multicrystalline solar cells. Power conversion efficiencies of cells made from silicon exceeds 25%. Second generation solar cells are made from materials like copper indium diselenide (CIS), and copper indium gallium selenide , amorphus silicon (A-Si) thin films, and cadmium telluride (CdTe). Conversion efficiencies are a bit smaller than that of first generation solar cells, but the cells use small quantities of material and are compatible with flexible substrates. Perovskite solar cells, dye sensitized solar cells (DSSCs) and nanocrystal solar cells counte as third generation solar cells. Conversion efficiencies are even lower that that of second generation solar cells, but these cells are flexible, low-cost and easily fabricated (Dincer, 2018).

Manufacturers look for stability and efficiency when producing solar cells. Researchers take these two factors into account for improving solar cells. Some researchers are looking for new materials to achieve those goals,

- Selection and peer-review under responsibility of the Organizing Committee of the Conference

others are trying to improve existing materials by tuning the fabrication process or by adding dopents or impurities to affect the crystalline structure of the material. Ion implantation is one of these techniques.

Ion Implantation

During the ion implantation process, the strongly accelerated ions will collide with the substrate (target material). By entering the substrate, these ions will lose their energy following the collisions with the atoms of the substrate until the complete stop of these ions.

Certain atoms of the crystalline network of the material will be moved from their site (primary collisions) and can in turn move other atoms (secondary collisions). This phenomenon depends on their masses as well as the temperature and energy of the implanted ions. These relocations induce an appearance and an accumulation of vacant sites and interstitials (Frenkel effect) which can be dissociated or agglomerated, as well as more complex defects along the course of the implanted ion (Nastasi, 1969).

Ionic implantation is not without effects on the crystalline network of the substrate. Each incident ion has kinetic energy which decreases during its interactions with the atoms of the target material. This energy is thus transferred to the crystalline network in the forms of electronic stopping and nuclear shocks until the ion is immobilized. If by meeting the target atom, the ion has an energy greater than E_L (threshold energy which depends on the substrate), it will eject it from its substitutional site and give it energy between 0 and $E\text{-}E_L$ (Rouha, 2014). If this energy is sufficiently high, the atom thus moved will generate a cascade of collisions within the substrate. With each movement of an atom of the crystalline network, an interstitial-lacune pair called the pair of Frenkel, will be created called elementary defect. Part of these pairs can recombine during the very implantation process or during the receipt phase. The concentration of these defects depends on the conditions of implantation (dose, temperature, energy, etc.) (Ziegler, 2008).

Radiation damage has a large impact on the electrical properties of semiconductors. Often, low doses are enough to reduce the lifespan of minority carriers. The mobility of the carriers is considerably affected. There are two types of implantations according to the degree of damage to the crystalline network. When the density of punctual defects is greater than a critical density, an amorphous area is created to a depth determined by the conditions of implantation and the implantation is said to be amorphizing. The thickness of this amorphous layer is generally greater than the free RP route of the implanted ions and depends on their mass, their energy and the implanted dose. For lower concentrations of punctual defects, the substrate, while being damaged, retains its crystalline character and the implantation is said to be non-amorphizing. (Ryssel, 1986)

Some researchers chose sodium ions for implantation on polycrystalline $CuIn_{1-x}Ga_xSe2$ films. Energy and dose for the simulation were 100KeV and 10^{+15} cm^{-2} respectively. The mean range and straggling of implanted Na were 1469 Å and 895 Å. Na-implantation on CIGS films induced lattice displacement and lead to an enhancement in electrical properties of devices made with these films (Wu, 2012). Other researchers chose xenon implantation for their material. (Satour, 2012) showed a mean projected range Rp of 170 Å and a mean straggling range ΔRp of 78 Å. The implantation energy used was 40 keV. Atom displacement is limited to a small region very close to the surface.

Oxygen ion implantation into CuInSe2 crystals revealed some concentration changes of already existing defects and the creation of new defects. These defects influence the photoelectric properties of the material (Zegadi, 2015). The energy was 40 keV, ion doses were 10^{+15} cm^{-2} and 10^{+16} cm^{-2} the obtained mean projected range Rp was 744 Å, the mean straggling range ΔRp was 364 Å.

Neon ion implantation in silicon was used by Wegierek (2021) for generating intermediate levels in the band gap of the material in order to change the electrical properties of the silicon implanted with neon ions and thus improving the efficiency of photovoltaic cells. From our side we intend to study the neon ion implantation of CIGS photovoltaic cells. We primarily look at the effect of ion damage on the structure of the material and try to relate this to the electrical properties of the cells.

Simulations

In the present work we used the SRIM tools to simulate the effects of the irradiation of the ternary (or quaternary) semiconductor CuInGaSe2 by Neon ions. The simulations were carried out for a 40KeV

implantation energy and an angle of incidence perpendicular to the substrate. We choose a number of ions N=10000, in a crystalline structure of CuInSe2 with a mass density of 5.8g/cm3. The SRIM simulator, designed on the basis of the Ion-Matter interaction, makes it possible to predict the distribution of these defects (distribution of displaced atoms, interstitial sites, etc.). Figure 1 shows the neon accelerated ions inside CIS material. Ions diffuse inside the material in all direction due to cascade elastic collisions with angular deflexions. The maximum depth penetration is about 2000 Å.

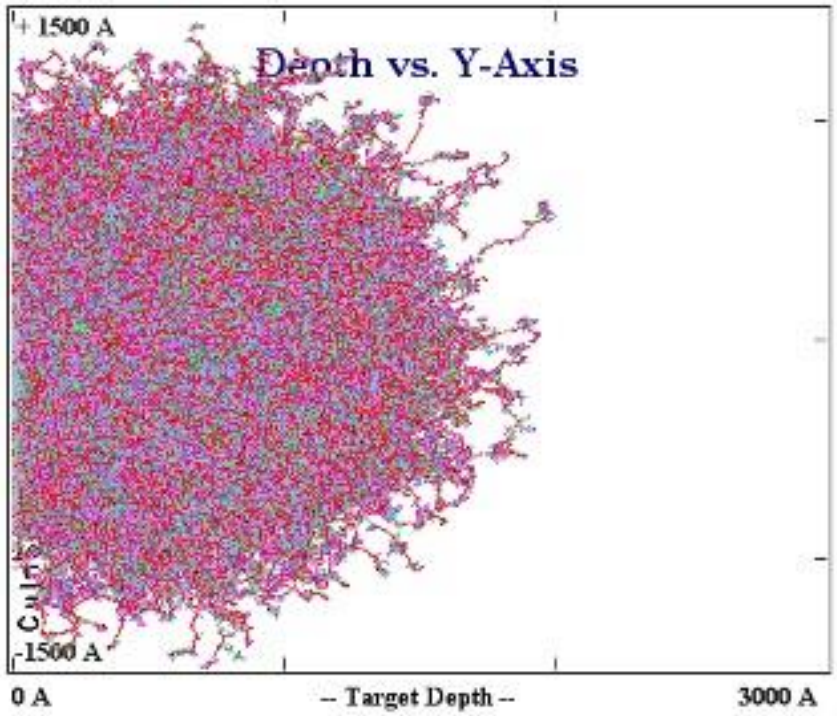

Figure 1. Neon diffusion inside CIS

The penetration profile is showed in Figure 2. The mean projected range Rp was 642 Å with a mean straggling range ΔRp of 340 Å.

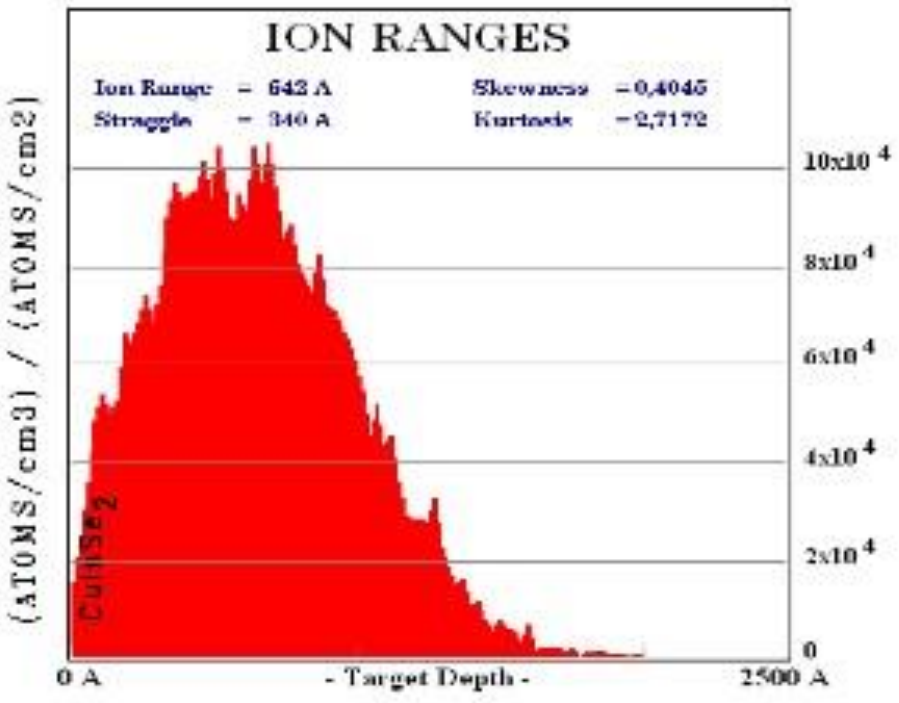

Figure 2. Ion range profile

A lot of other parameters can be extracted from SRIM simulation tools: energy losses due to the ionization process and phonons, the energy given to target electrons, energies absorbed by target atoms and so on, all of which tell us about the damage created in the target. There are some more simulations that need to be calculated in order to determine the defects introduced by ion implantation in the quaternary semiconductor films of CIGS. Electrical behavior of devices made from these films depend on those defect changes.

Conclusion

In this paper, we presented the need for efficient electrical solar energy converter devices, we reviewed few generations of these solar cells. In the way of improving electrical and physical properties of these cells, we recalled the physical phenomena of the implantation of ions in solids. We reviewed the works that have been conducted by other researchers with various ion sources. We mentioned the impact of accelerated ions on the crystalline structure of the photovoltaic material. Knowledge of the distribution and evolution of defects thus created in the structure is essential as to the use of this semiconductor. SRIM tools were used to simulate the neon ion implantation in the $CuInSe_2$ compound, various parameters were examined like the course of neon ions and their distribution in the semiconductor. There has been a modification of chemical defects close to the surface of the crystal. These changes include a variation in the concentration of existing defects and the creation of new faults. Those defects are supposed to influence the electric properties of the photovoltaic material.

Scientific Ethics Declaration

The authors declare that the scientific ethical and legal responsibility of this article published in EPSTEM journal belongs to the authors.

Acknowledgements

* This article was presented as an oral presentation at the International Conference on Technology, Engineering and Science (www.icontes.net) held in Antalya/Turkey on November 16-19, 2022.

* This work was done at the LCCNS laboratory, Ferhat Abbas University Sétif 1. I thank all the members of the laboratory for their help and support.

References

Dincer, I. (2018). *Comprehensive energy systems*, Elsevier inc.

Lazar, M. B. (2002). *Etude du dopage par implantation ionique d'aluminium dans le carbure de silicium pour la réalisation de composants de puissance*, (Doctoral dissertation), INSA de Lyon, France.

Nastasi, M., Mayer, J. W., & Hirvonen, J. K. (1969). *Ion-solid interactions: Fundamentals and applications*, Cambridge: Cambridge University Press.

Rouha, M. (2014). *Etude de l'effet de l'implantation ionique dans le $CuInSe_2$ et autres ternaires*, (Doctoral dissertation), Electronics Dept. Ferhat ABBAS University Sétif 1, Algeria.

Ryssel, H., & Ruge, I. (1986). *Ion implantation*, USA: John Wiley & Sons.

Satour, F. Z., & Zegadi, A. (2012). Xe irradiation-induced defects in CuInSe2 by phase resolved photoacoustic spectroscopy. *Materials Science and Engineering: B*, *177*(5), 436-440.

Węgierek, P., & Pastuszak, J. (2021). Application of neon ıon ımplantation to generate ıntermediate energy levels in the band gap of boron-doped silicon as a material for photovoltaic cells. *Materials*, *14*(22), 6950.

Wu, W. Y., Chen, C. H., Hsu, C. H., Wei, S. Y., Chen, C. H., Wu, Y. C., ... & Lai, C. H. (2012, June). The effect of Na ion implantation on the polycrystalline $CuIn_{1-x}Ga_xSe_2$. In *2012 38th IEEE Photovoltaic Specialists Conference* (pp. 000185-000187). IEEE.

Zegadi, A., Rouha, M., & Satour, F. Z. (2015). A study on the effect of oxygen implants in CuInSe2 by photoacoustic spectroscopy. *Crystal Research and Technology*, *50*(1), 49-54.

Ziegler, J. F., Biersack, J. P., & Ziegler, M. D. (2008). *The stopping and range of ions in matter*. Maryland: SRIM Co.

Author Information

Mustapha DJABAR
Université Ferhat ABBAS Sétif 1
Campus Maabouda, Sétif 19000 Algeria.
Contact e-mail: mustapha.djabar@*univ-setif.dz*

To cite this article:

Djabar, M. (2022). Effect of neon ion implantation on the electrical properties of CIGS photovoltaic cells. *The Eurasia Proceedings of Science, Technology, Engineering & Mathematics (EPSTEM), 21*, 464-468.

The Eurasia Proceedings of Science, Technology, Engineering & Mathematics (EPSTEM)
ISSN: 2602-3199

The Eurasia Proceedings of Science, Technology, Engineering & Mathematics (EPSTEM), 2022

Volume 21, Pages 469-476

IConTES 2022: International Conference on Technology, Engineering and Science

Comparative Study of Encryption Algorithms Applied to the IOT

Abdelkrim GHAZ
University Djillali Liabes, Algeria

Ali SEDDIKI
University Djillali Liabes, Algeria

Nadhir NOUIOUA
University Djillali Liabes, Algeria

Abstract: Cryptography has long been known as the mechanism for protecting secret data especially from being captured by dishonest people. Nowadays, with the rapid development of the expansion and use of digital data on the Internet and IOT applications, it has become important to develop cryptographic algorithms that guarantee the confidentiality of data, especially visual data such as digital images.In this work, we demonstrate in the comparative study between four cryptographic algorithms (DES, RSA, CR4 and SIT) for image encryption. We make an objective and visual analysis of the results to know which is the most appropriate algorithm for security data in the Internet of Things environment, which requires fast execution time, and less power consumption. We use certain measurement parameters such as PSNR, correlation, NPCR, UACI, encryption and decryption time and visual comparison of histograms before and after encryption to judge the performance between these different algorithms.

Keywords: Confidentiality, PSNR, NPCR, UACI.

Introduction

Today, the world is experiencing great development in all areas (cultural, social, and economic ...) especially the field of computing. This leads to the creation of many devices and programs to facilitate the exchange and processing of information and data in the form of images or words or signals. The majority of all digital documents manipulated and exchanged in internet networks are mainly in the form of images.

Indeed, the image affected several areas: weather, medicine, telecommunications, detection, video surveillance, etc. therefore the security of this information has become an essential necessity to preserve the authenticity and confidentiality of the messages transmitted and to avoid the intrusion of unauthorized persons, the technique ensuring this protection is called cryptography. Several encryption methods have been developed to solve the security problem (Nagesh & Thejaswini, 2017). They can be classified according to key types into two main families: symmetric and asymmetric cryptography.

The usual encryption and decryption algorithms (DES, RC4, RSA SIT) extend from powerful computers, enormous execution time and energy which present a problem in the case of the Internet of Things where one seeks to minimize time calculation and reduce energy consumption. The Internet of Things represents the network of physical objects “Things” that are integrated with sensors, software and other technologies for the purpose of exchanging data with other devices and systems on the Internet.

Literature Survey and Overview of Algorithms

During its development, cryptography has undergone a corresponding transformation In terms of problems encountered in all data security, hence the emergence of several terms in cryptography often used to characterize the secret process of sending data. Data encryption has also evolved over time from the beginning with symmetry in common Symmetric or asymmetric key for modern encryption key (Henriques &Vernekar, 2017).

Serving information from the Internet of Things (IoT) device to cloud server has several security issues, such as Intercept, modify and steal information. Communication between IoT devices and cloud servers should Protected by encryption methods. However, there are also a few Encryption technology options that fit your needs Lightweight Communication required by IoT devices.(Baiq Yuniar Yustiarini, 2022).

Due to these circumstances, a comparative study will be conducted to find the most suitable encryption algorithms for use in IoT. Therefore, we wanted to test and compare in this study The impact of cryptographic algorithms on the network The performance of IoT devices. Currently, most IoT uses Advanced Encryption Standard (AES) encryption algorithm to protect their communication lines. Therefore this study Check the effect of using DES, SIT and CR4.

The Secure Internet of Things (SIT)

The Secure Internet of Things (SIT) algorithm is a hybrid approach based on Feistel and Substitute Permutation (SP) networks. In this way, the properties of both methods are used to develop a lightweight algorithm that exhibits significant security in IoT environments while keeping the computational complexity at a moderate level. SIT is a symmetric key block cipher consisting of a 64-bit key and plaintext. In symmetric key algorithms, the encryption process consists of multiple rounds of encryption, each of which is based on a specific mathematical function to generate confusion and diffusion. Increasing the number of revolutions can provide better safety, but ultimately leads to an increase in restricted energy consumption (Chandramouli & Bapatla, 2006).

Cryptographic algorithms are usually designed to take an average of 10-20 rounds to keep the encryption process strong enough for system requirements. However, the simulation was limited to five laps to further improve energy efficiency, each encryption round includes mathematical operations that operate on 4 bits of data. Muhammad Usman and al "SIT: A Lightweight Encryption Algorithm for Secure Internet of Things,"

The Data Encryption Standard (DES)

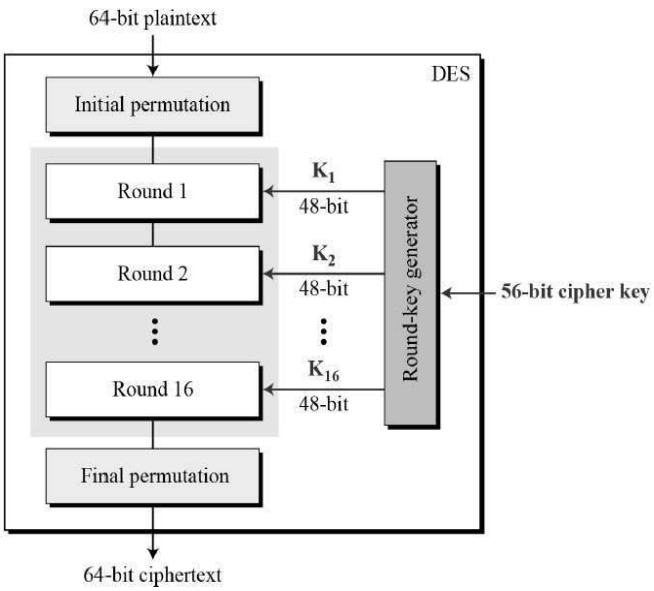

Figure 1. Structure of DES

The Data Encryption Standard (DES) is a symmetric-key block cipher published by the National Institute of Standards and Technology (NIST). DES is an implementation of a Feistel Cipher. It uses 16 round Feistel structure. The block size is 64-bit. Though, key length is 64-bit, DES has an effective key length of 56 bits, since 8 of the 64 bits of the key are not used by the encryption algorithm (function as check bits only). (Coppersmith,1994). General Structure of DES is depicted in the following illustration Figure 1.

Rivest Cipher 4 CR4

Rivest Cipher 4 (RC4) is a type of cryptography that belongs to the class of stream ciphers with a symmetric key (Shyul & Chen, 2008), where this key is used for encryption and decryption. The function of RC4 is to generate a keystream using a pseudo-random number generator. The resulting keystream is manipulated using XOR and plaintext logical operations that encrypt each bit. Then perform the RC4 decryption process in the same way, and the tip bit is used as the encryption operation, because the XOR operation is symmetrical

RSA Algorithm

In 1977, Ron Rivest, Adi Shamir, and Leonard Adleman developed a new algorithm called RSA. This algorithm is a type of asymmetric cryptography because it uses different keys for encryption and decryption. The RSA algorithm includes three main steps of encryption and decryption (Ray & Potnis, 2017). These steps are shown as a flowchart in Figure 2, explaining how the algorithm works. Key Generation: In this step, two keys will be generated.

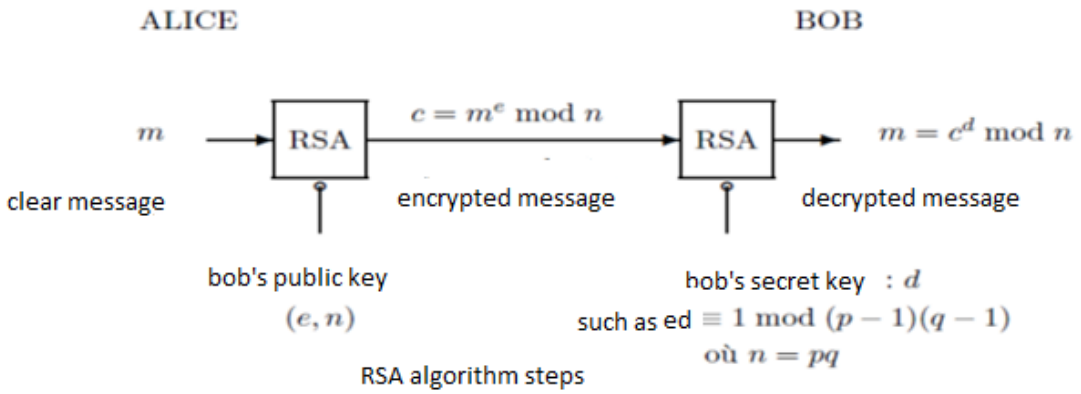

Figure 2. Principle of the RSA algorithm

Evaluation Metrics

For the sake of measuring high fidelity and robustness, some powerful metrics in the image-processing field were employed, in reason of making a fair judgment on the proposed work.

Peak Signal to Noise Ratio (PSNR)

Calculates the error among the original cover image and the encrypted image, mathematically is given by:

$$PSNR = 10\ log_{10}\ \frac{255^2}{MSE} \qquad (1)$$

Mean Square Error (MSE)

Determines mean error magnitude between two images.

Number of Pixels Change Rate (NPCR) and Unified Average Changing Intensity (UACI)

To ensure the security of the image encryption scheme for differential scanning, two quantification measures are used: NPCR (Number of Pixels Change Rate) and UACI (Unified Average Changing Intensity). NPCR measures the number of distinct pixels as a percentage of the total number of pixels between two images, whereas UACI measures the difference in mean intensity between two images.

$$NPCR = \frac{\sum_{i,j} D(i,j)}{M \times N} \times 100\% \qquad (2)$$

$$UACI = \frac{1}{M \times N}\left[\sum_{i,j} \frac{C_1(i,j) - C_2(i,j)}{255}\right] \times 100\% \qquad (3)$$

NPCR > 99.094 % and UACI > 33.4635 % ensure that an image encryption scheme is secure against differential attack. (Hasnat,& Barman, 2016).

Results and Discussion

Visual Comparison:

Comparison of Histograms

Knowing that a good encryption requires that the histogram of encrypted images must have a uniform distribution, we note that for the image lena and cameraman that the encryption algorithms SIT, DES and CR4 satisfied this condition of uniform distribution while the RSA has not this property which weakens the robustness of this algorithm, show figures 3, 4 and 5.

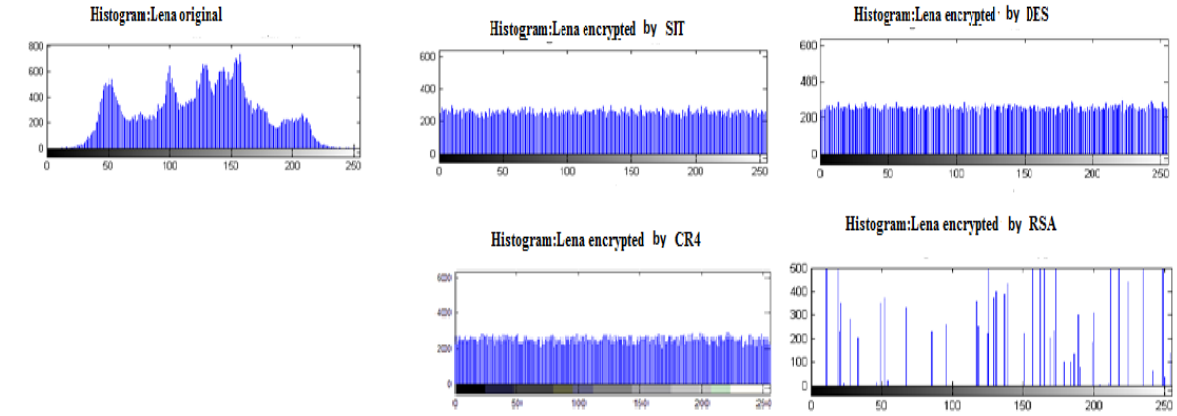

Figure 3. Histograms of the image Lena encrypted by the four algorithms

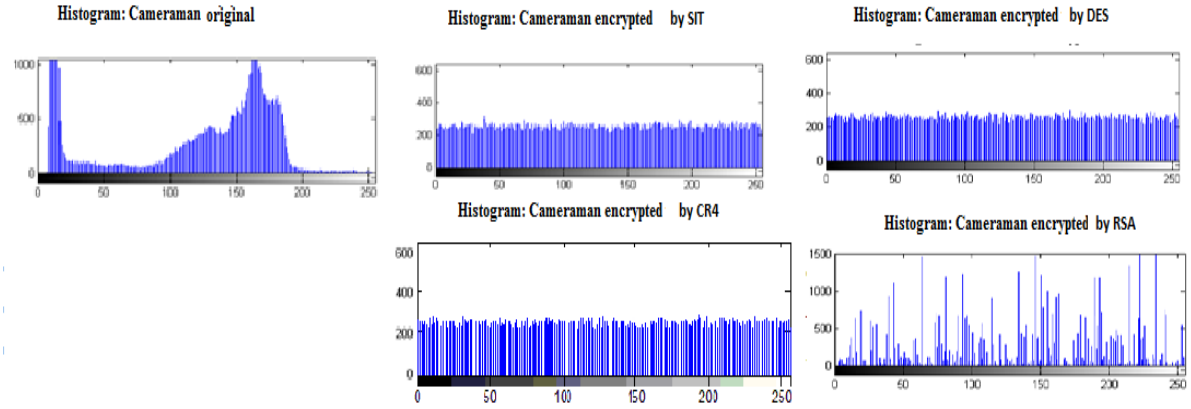

Figure 4. Histograms of the image Cameraman encrypted by the four algorithms

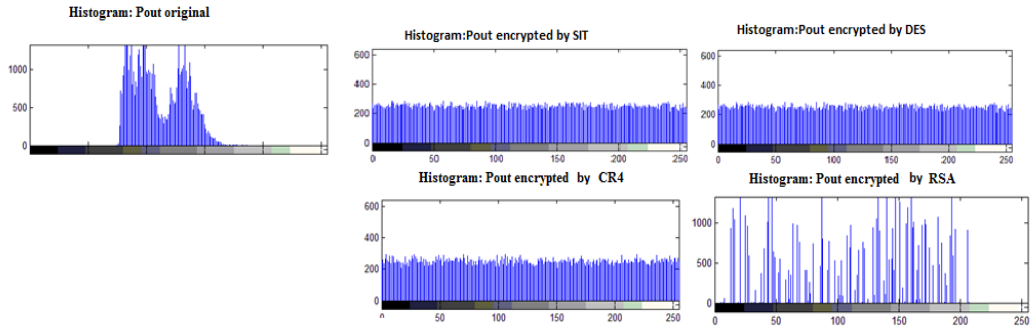

Figure 5. Histograms of the image Cameraman encrypted by the four algorithms

We have increased the size of the images (512) and have traced their histograms to see if there are changes, even figures 6. We always see that the RSA algorithm gives non -uniform histograms for all images, namely Lena, Cameraman while for the algorithms DES, SIT and RC4 the distribution remains uniform.

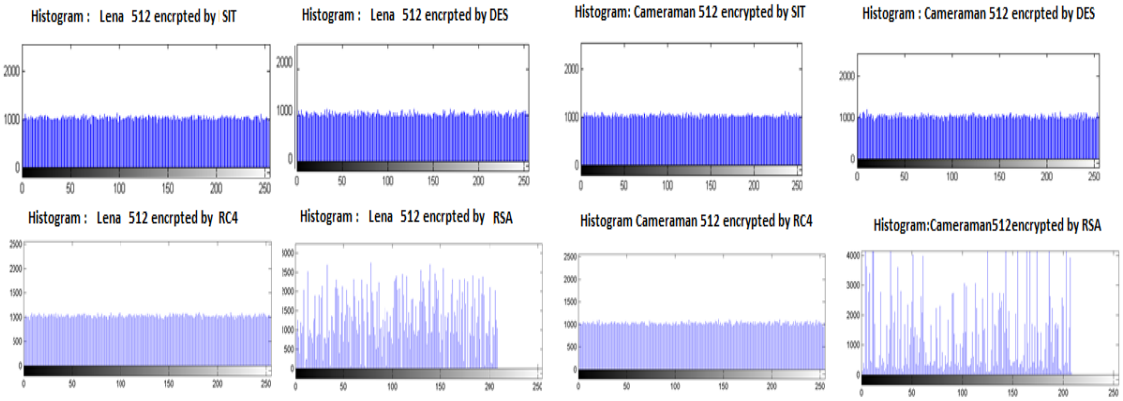

Figure 6. Histograms encrypted Lena and Cameraman

Visual Comparison of Encrypted Images

We found that the Lena image was absolutely well encrypted by 4 algorithms (especially DES, SIT, and CR4), and the RSA algorithm was slightly less robust, see Figure 7 (E). For 4 encryption algorithms, we were able to recover the decrypted image with a correlation coefficient of 1, see (C,F,I and L) above. The encryption defect of the RSA algorithm appears strongly by viewing the encrypted Pout image, where one can guess the shapes of the contours of this image which facilitates differential attacks, see Figure 8

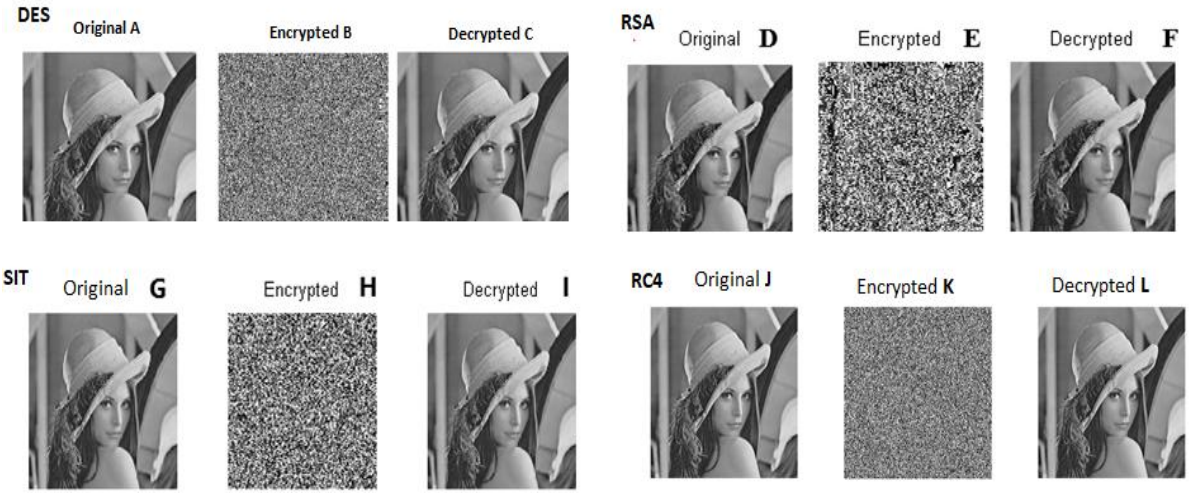

Figure 7. Encrypted and decrypted Lena and Cameraman

Figure 8. Encrypted and decrypted Pout by RSA (size: 256 and 512)

By increasing the size of the Pout image to 512 pixels, we still see that the contours of the encrypted image by the RSA remain visible, see figure 8.

Objective Comparison

Table 1 shows that the PSNR and correlation of DES, SIT and CR4 algorithms are close, we can take the Cameraman image as an example, the PSNR shows the following values (8.4156, 8.3970 and 83870) and the correlation (0.0049, 0.0037, -0.0062) while the RSA algorithm gives a lower PSNR than the previous algorithm (5.1252) we searched in the encrypted area, but a visual comparison of the images shows that the RSA encryption is less efficient. from a correlation point of view The values gives advantages to the SIT and RC4 algorithms.

Table 1. Psnr and correlation for different encryption algorithms

Images	PSNR				Correlation			
256 pixels	DES	RC4	RSA	SIT	DES	RC4	RSA	SIT
Lena	9.2190	9.2571	6.4392	9.2758	-0.0055	-0.0003	-0.0135	0.0036
Cameraman	8.4156	8.3798	5.1252	8.3970	0.0049	-0.0062	0.0430	0.0037
Pout	10.1442	10.1152	5.64	10.1554	-0.030	0.0026	0.0654	0.0052

According to the values of the measures table 2 (NPCR, UACI), larger values indicate that the encryption is strong and efficient So we can clearly see that RC4 and SIT algorithms return values close to DES in terms of NPCR compared to RSA. About UACI, we observe that the values obtained with the RSA algorithm are better, but visual comparisons show the opposite (detected contour shapes of the images encrypted by RSA).

Table 2. NPCR and UACI for different encryption algorithms

Images	NPCR				UACI			
256 pixels	DES	RC4	RSA	SIT	DES	RC4	RSA	SIT
Lena	99.5911	99.5895	99.9985	99.5972	15.0325	14.8831	45.0594	14.8598
Cameraman	99.5712	99.5895	98.8525	99.5712	17.2153	17.3143	42.8844	17.3551
Pout	99.6109	99.5895	98.2437	99.5438	16.6590	16.5358	46.6916	16.5503

Table 3 shows the advantages of the RC4 algorithm and SIT compared to DES in terms of encryption and decryption execution time, although RSA takes less time than CR4 and SIT, this can be explained by choosing p and q and public key value e below 100, i.e. if we increase p, q and e value to make encryption more efficient. We noticed a huge increase in execution time for RSA encryption (encryption time = 49.793459 seconds for Lena image, decryption time = 411.369710), almost 15 times.

Table 3. Calculation time for different Encryption and Decryption algorithms

Images	Encryption Time (Seconds)				Decryption Time (Seconds)			
256 pixels	DES	RC4	RSA	SIT	DES	RC4	RSA	SIT
Lena	525.4367	7.8586	0.000738	33.0943	524.582154	7.17554	0.098294	29.5721
Cameraman	563.35	7.5320	0.005759	33.3252	561.94	7.83811	0.051146	29.6903
Pout	558.1	6.76731	0.000979	33.1999	556.889	7.2989	0.033195	29.6782

We have found time and time again that the computation time of the RC4 algorithm is still better compared to DES, their time has greatly increased. The second is the SIT algorithm. Using RSA algorithm, by increasing the value of p, q and e to improve encryption, the time will be higher than using CR4 and SIT algorithm.

Table 4. Calculation time for different Encryption and Decryption algorithms (image 512)

Images	Encryption Time (Seconds)				Decryption Time (Seconds)			
512 pixels	DES	RC4	RSA	SIT	DES	RC4	RSA	SIT
Lena	2129.3767	42.8535	0.0037	130.0736	2132.6279	43.9544	0.5717	116.4549
Cameraman	2235.5715	43.8916	0.0023	143.4658	2239.9611	42.2810	0.3868	129.4439
Pout	2233.0038	44.3373	0.0055	133.8145	2229.2112	43.3176	0.1787	118.9075

Conclusion

From objective analysis (PSNR, correlation, NPCR, UACI, and computation time) and visual analysis (histogram, comparison of encrypted and decrypted images), it was concluded that the RC4 encryption algorithm and SIT gave better results in both encryption and decryption. Value calculation time and PSNR and correlation close to DES, the calculation time of DES is 15 times higher and requires high energy consumption, making CR4 and SIT algorithms suitable for adoption in IoT applications, with better robustness and efficiency DES and RSA are When used, the latter represents optically unsatisfactory encryption.

Scientific Ethics Declaration

The authors declare that the scientific ethical and legal responsibility of this article published in EPSTEM journal belongs to the authors.

Acknowledgements

* This article was presented as an oral presentation at the International Conference on Technology, Engineering and Science (www.icontes.net) held in Antalya/Turkey on November 16-19, 2022.

References

Chandramouli, R., Bapatla, S., Subbalakshmi, K. P., & Uma, R. N. (2006). Battery power-aware encryption. *ACM Transactions on Information and System Security (TISSEC)*, *9*(2), 162-180.

Coppersmith, D. (1994). The Data Encryption Standard (DES) and its strength against attacks. *IBM Journal of Research and Development*, *38*(3), 243-250.

Hasnat, A., Barman, D., & Mandal, S. N. (2016, October). A novel image encryption algorithm using pixel shuffling and pixel intensity reversal. In *2016 International Conference on Emerging Technological Trends (ICETT)* (pp. 1-6). IEEE.

Henriques, M. S., & Vernekar, N. K. (2017, May). Using symmetric and asymmetric cryptography to secure communication between devices in IoT. In *2017 International Conference on IoT and Application (ICIOT)* (pp. 1-4). IEEE.

Nagesh, H. R., & Thejaswini, L. (2017, March). Study on encryption methods to secure the privacy of the data and computation on encrypted data present at cloud. In *2017 International Conference on Big Data Analytics and Computational Intelligence (ICBDAC)* (pp. 383-386). IEEE.

Ray, A., Potnis, A., Dwivedy, P., Soofi, S., & Bhade, U. (2017, October). Comparative study of AES, RSA, genetic, affine transform with XOR operation, and watermarking for image encryption. In *2017 International Conference on Recent Innovations in Signal processing and Embedded Systems (RISE)* (pp. 274-278). IEEE.

Shyu, S. J., & Chen, Y. R. (2008, December). Threshold secret image sharing by Chinese remainder theorem. In *2008 IEEE Asia-Pacific Services Computing Conference* (pp. 1332-1337). IEEE.

Yustiarini, B. Y., Dewanta, F., & Nuha, H. H. (2022, July). A comparative method for securing ınternet of things (IoT) devices: AES vs Simon-Speck Encryptions. In *2022 1st International Conference on Information System & Information Technology (ICISIT)* (pp. 392-396). IEEE.

Author Information

Abdelkrim GHAZ
University Djillali Liabes**,** Algeria
Contact e-mail: *gabkarim@gmail.com*

Ali SEDDIKI
University Djillali Liabes**,** Algeria

Nadhir NOUIOUA
University Djillali Liabes**,** Algeria

To cite this article:

Ghaz, A., Seddıkı, A., & Nouıoua, N. (2022). Comparative study of encryption algorithms applied to the IOT. *The Eurasia Proceedings of Science, Technology, Engineering & Mathematics (EPSTEM), 21,* 469-476

The Eurasia Proceedings of Science, Technology, Engineering & Mathematics (EPSTEM)
ISSN: 2602-3199

The Eurasia Proceedings of Science, Technology, Engineering & Mathematics (EPSTEM), 2022

Volume 21, Pages 477-483

IConTES 2022: International Conference on Technology, Engineering and Science

Material Selection of Batch Type Supercritical Reactor for Biodiesel Production

Filiz ALSHANABLEH
Near East University

Mahmut A. SAVAS
Near East University

Abstract: Non-catalytic biodiesel production using supercritical alcohol may replace time and energy-consuming catalytic biodiesel production. Production of biodiesel with supercritical methanol requires extreme process conditions such as high temperature and pressure. To enable this process to take place a batch-type reactor has been designed and constructed. Materials for the construction of high-pressure vessels should satisfy strength requirements, temperature characteristics, and corrosion resistance. Besides, these factors also availability, cost, and ease of fabrication are other factors that must be considered during material selection. Among those factors, the mechanical strength of the chosen material for pressure vessels is the most important design factor for safety operation. Small pressure vessels should be designed in such a way that the operating pressure is still too low to cause any crack to propagate in the vessel (‘‘yield before break’’). For this study, a batch type of reactor was designed with a capacity of 600 mL, and operating temperature and pressure were taken as 240˚C (513 K) and 83 bars (8.3 MPa), respectively, which were just above the critical temperature and pressure of methanol. The most common and widely used construction materials for pressure vessels are stainless steels due to their high mechanical strength, corrosion resistance, ease of availability, and low costs such as Grade 304 and Grade 316 as compared to nickel-rich alloys (such as Inconel, Incoloy, Hastelloy). As a result, 316 stainless steel was found to be the best choice of material for the reactor planned to be designed for supercritical biodiesel production.

Keywords: Material selection, Supercritical reactor, Non-catalytic biodiesel

Introduction

The supercritical technique looks into an alternative to the traditional method of producing biodiesel in which usually catalyst is used. Due to the procedures involved in feedstock preprocessing, product separation, and purification, catalytic biodiesel production requires a lot of time and energy. Pre-processing and post-processing steps might be facilitated by non-catalytic biodiesel synthesis using supercritical fluid. A supercritical fluid is one of the alternatives recommended for addressing the fundamental issues in the development of catalytic biodiesel processing (Nematian et al., 2021). The working fluid is categorized as a supercritical fluid if the reaction conditions are higher than the critical temperature (T_c) and pressure (P_c) of the fluid. Compared to catalytic biodiesel production, the use of supercritical alcohol as a solvent for biodiesel manufacture is a simple method (Saka & Kusdiana, 2001; Demirbas, 2006). High pressures (>5 MPa) and high temperatures (>200 °C) can be used in the supercritical technique to produce a homogenous phase between the supercritical alcohol and the triglycerides (Al-Shanableh, 2017).

The supercritical reaction could occur without the use of a catalyst because no need for limitations in the feedstock used, such as free fatty acid and water content. Also, separating the biodiesel from the glycerol is easier because fewer discrete processes, such as catalyst purification, are needed (Sharma & Singh, 2009).

Diasakou et al. in 1998 developed non-catalytic transesterification using subcritical methanol at temperatures of 240°C, 220°C, and 235°C to overcome these drawbacks. In 2001, Saka and Kusdiana successfully produced the first biodiesel by supercritical methanol from rapeseed oil at 350°C and 45 MPa in a 5 mL-Inconel 625 batch type of reactor. Later, many other researchers investigated supercritical methanol for biodiesel production at various temperatures and pressures with various reactor sizes, and they also achieved high conversion in a short time (Pinnarat & Savage, 2010; Silva & Oliveria, 2014). In previous studies, the maximum operating pressure and temperature and reactor size were 45 MPa and 350°C (Saka & Kushidiana, 2001), the maximum reactor size was 200 mL (He et al., 2007), while the minimum values were 10 MPa, 270°C (Lee et al., 2012) and 5 mL (Saka & Kushidiana, 2001) respectively. In all these studies, the reactor with the largest volume has 200 mL, but this volume is often insufficient in terms of seeing the difficulties that may be experienced in the production of commercial biodiesel.

The aim of this study is the material selection for a bench-scale reactor that meets the operating conditions of supercritical methanol. The reactor could be scaled up to a larger size after it was designed and built on a bench scale. The investigation of problems encountered during the construction and operation of the bench-scale reactor will facilitate large-scale biodiesel production.

Supercritical Reactor for Biodiesel Production

The reactor design for supercritical processes can have a significant impact on productivity and resource consumption. The pilot plant or bench scale is preferred in many laboratory batch processes due to its low risk and ease of setup (Qadeer et al., 2021). Before designing a bench-scale-batch-type supercritical reactor, four parameters must be determined; operating pressure and temperature, reactor dimension, and materials of construction. The minimum operating pressure is 7.86 MPa (1140 psi), which is the methanol critical pressure, as shown in Figure 1, while the maximum operating pressure that could be applied was 45 MPa (Ebert, 2008). The design pressure should be 5–10% higher than the maximum operating pressure (Moss, 2004). Because design pressure is used to assign the most severe conditions, 47 MPa was chosen. The maximum operating pressure is the most important parameter in a reactor design because it is the basis for the majority of calculations, such as the nominal thickness of the reactor. The operating temperature could range from 240°C (the critical temperature of methanol) to 350°C. Temperature is an important design parameter; in particular, high temperatures are associated with thermal expansion and corrosion; therefore, material selection should be focused on the operating temperature. For evaluating the size of the reactor amount of biodiesel produced was questioned in the first place. The tests for quality evaluation required a minimum of 100 mL of the final product for each batch (Evcil et al., 2018; Al-Shanableh et al., 2019). The methanol used in biodiesel production by the supercritical method is very high, with a 1:40 oil-to-alcohol mole ratio (that corresponds to approximately 1:2 oil-to-alcohol volume ratio). To be able to produce 100 mL of biodiesel as the end product, the reactor size should be at least 600 mL which was going to hold 175 mL triglyceride and 325 mL methanol as raw materials. The last step was the material selection process and it is presented detailed in the methodology section.

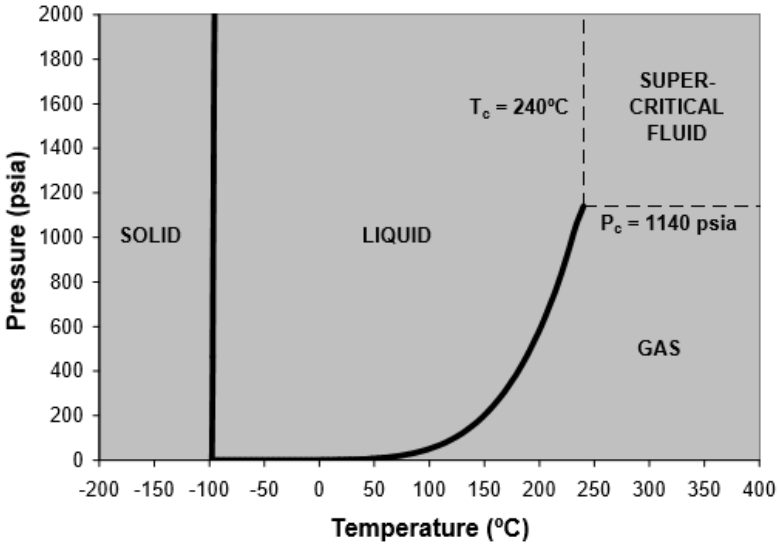

Figure 1. Phase diagram of methanol

Method

Material Selection for Supercritical Reactor

Choosing materials entails attempting to find the best match between design requirements and the properties of the materials that may be used to create the design. In the present study, Ashby's approach was followed for the material selection process that involves three steps; the definition of the problem statement, the translation that identifies material indices, and the last step is the screening and ranking, by which a full menu of materials is reduced to a shortlist (Ashby, 2011). The problem statement was to design a supercritical reactor that should be able to withstand a minimum stress of 47 MPa and a temperature of 400°C.

The most crucial design factor for a safe operation is the mechanical strength of the selected material for pressure vessels. Pressure vessels are typically built to yield at a pressure that is still too low to allow any cracks they may contain to spread ("yield before break"). To identify the stress-σ- in the wall of a spherical pressure vessel of radius R_i Equation 1 could be used;

$$\sigma = \frac{pR_i}{2t} \qquad \text{Eqn.1}$$

where t is the thickness of the vessel. According to the ASME Section VIII, Division 1, paragraph UG27, wall thickness of high pressure vessel should be $t > 0.5\ R_i$, then maximum σ will be 47 MPa and also minimum σ_f (yield stress) will be 47 MPa. Then wall thickness t,

$$t \geq \frac{pR_i}{2\sigma_f} \qquad \text{Eqn.2}$$

In a small pressure vessel if flaw is observed that should not have a diameter greater than a_c^*; then, the stress required for the crack propagate is given below;

$$\sigma = \frac{CK_{1C}}{\sqrt{\pi a_c^*}} \qquad \text{Eqn.3}$$

where C is a constant near unity, a_c^* is half of the flaw length and K_{1C} is the plane-strain fracture toughness of the material. Combination of Equations 2 and 3 gives Equation 4 that indicates the largest pressure is carried by the material with the greatest value of K_{1C}.

$$p \leq \frac{2t}{R}\frac{K_{1C}}{\sqrt{\pi a_c^*}} \qquad \text{Eqn.4}$$

A requirement that the crack is not spread even if the force surpasses the material's yield strength could increase safety. This condition is expressed by setting σ equal to the yield stress σ_y as shown in Equation 4.5,

$$\pi a_c \leq C^2\left[\frac{K_{1C}}{\sigma_f}\right]^2 \qquad \text{Eqn.5}$$

The tolerable crack size a_c, is maximized by selecting a material with the highest value of K_{1C}/σ_f, which is the criterion that meets the "yield before break". Figure 2 (Ashby, 2005) depicts the material selection criterion for safe design against fracture. Two material indices were developed;

i. $M_1 = \sigma_f > 47$ MPa
ii. The largest K_{1C}/σ_f; $M_2 = K_{1C}/\sigma_f$

Materials with equivalent performance are connected by a diagonal line with constant value $M_2 = K_{1C}/\sigma_f$; materials performing better are those above the line. Aluminum alloys are disqualified due to the first criterion however stainless steels, nickel alloys, copper, and copper alloys are all appropriate materials for the yield-before-break criteria. Other design factors such as maximum service temperature, corrosion resistance, and cost need to be considered in order to select the best material among these contenders. Out of these materials, only the steels (low alloy & stainless) and nickel alloys remain as an option, once the maximum service temperature was considered as 400°C (Ashby, 2011).

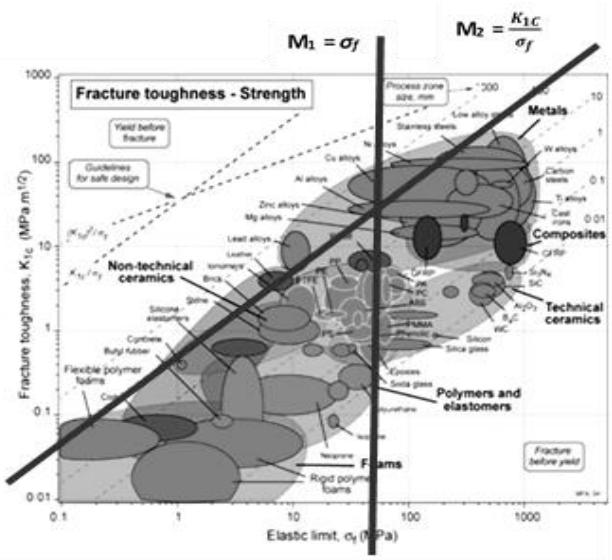

Figure 2. Material selection chart- fracture toughness, K_{1C} against strength, σ_f

Transesterification reaction involves alcohols and triglycerides that are a mixture of fatty acids so the corrosion resistance of some common metal alloys is shown in Table 1 (Peters and Timmerhaus, 2003). Stainless steel (Grade 304 and 316), nickel alloys, and copper alloys except for red brass seemed possible candidates.

Table 1. The corrosion resistance of candidate materials

Chemical	Iron and steel	Stainless steel		Nickel (Inconel™)	Copper (Monel™)	Red brass
		Grade 304	Grade 316			
Fatty acids	C	A	A	A	A	C
Methanol	A	A	A	A	A	A
Oleic acid	C	A	A	A	A	C
Glycerol	A	A	A	A	A	A
Methyl esters	C	A	A	A	A	C

A= acceptable, can be used successfully, C= caution, resistance varies widely depending on conditions

Both stainless steels and nickel alloys possessed the necessary qualities: non-magnetic, corrosion resistant, and can be worked into a cylindrical vessel from a single block. Figure 3 shows the average cost difference (30 $/kg for Ni alloys vs. 7 $/kg only for stainless steels) (Ashby, 2011)

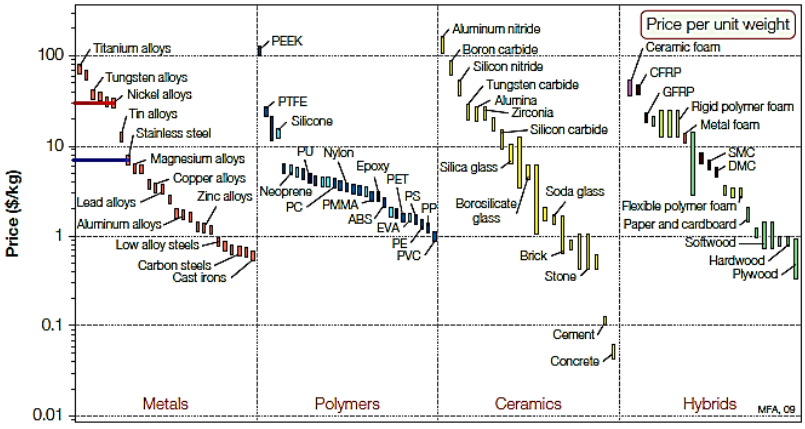

Figure 3. The approximate price/kg of materials

Results and Discussion

Materials used in the construction of high pressure vessels must meet strength, temperature, and corrosion resistance requirements, besides availability, cost, and ease of fabrication are other factors during material

selection. Stainless steels, such as Grade 304 and Grade 316, and metal alloys with higher chromium, nickel, and/or molybdenum content, such as Incoloy™, Inconel™, and Hastelloy™ are the most common and widely used construction materials for pressure vessels due to their high mechanical strength, excellent corrosion resistance and stiffness (Al-Shanableh, 2017).

In the present study, it was determined that the best material for the reactor that was intended to be built for the manufacture of supercritical biodiesel was 316 stainless steel. While Grade 304 is the standard "18/8" stainless steel with excellent welding and forming properties, Grade 316 is the standard molybdenum-bearing grade with better overall corrosion-resistant properties. Besides Grade 316, with higher nickel content is considered the "most non-magnetic" stainless steel. However, 316 stainless steel with an appropriate amount of welding may be sufficiently magnetic. Since the intent of the project was to fabricate the reactor from a single piece of material without welding, Grade 316 would be a suitable option. Although, nickel-rich alloys are suitable for high pressure vessels due to their excellent corrosion resistance and stiffness, stainless steels are preferred over due to their low cost and availability. Some material properties of 316 stainless steel are shown in Table 2 (from ASME Section VIII, Div. 2, Table AMG-1 and AMG-2).

Table 2.Material properties of stainless steel-Grade 316

Properties	
Chemical Composition	Fe; < 0.03 C; 16-18.5 Cr; 10-14 Ni; 2-3 Mo; < 2 Mn; < 1 Si; < 0.045 P; < 0.03 S
Young' Modulus	205 GPa
Elastic Limit (σ_f)	310 MPa
Poison's Ratio	0.275
Ductility	0.51
Tensile Strength	620 MPa
Maximum Allowable Working Stress (*S*)	117 MPa
Fracture Toughness	278 MPa.$m^{1/2}$
Maximum Service Temperature	1198 K
Minimum Specified Yield Strength (σ_y)	at 200°C: 160 MPa at 300°C: 136 MPa at 400°C: 123 MPa

Tümtes Company, Istanbul, Turkey, manufactured the reactor by drilling and grinding a single cylindrical block of 316 stainless steel to give it the desired shape (no welding). Figure 4 depicts the plain reactor that was built (without equipment or accessories). It was critical to assess the reactor's functionality and safety before beginning any experimental research. A hydrostatic test was conducted at 90°C and 120 bar for one hour. The hydrostatic test was successfully completed by the intended supercritical reactor without showing even a minor damage.

Figure 4. Fabricated vessel with hatch and clamps

Conclusion

In order to design and fabricate a reactor for biodiesel production under supercritical methanol conditions, the material selection of the reactor was investigated in the present study. The selected material should have specifications to fulfill the task expected for the design requirements. 316 stainless steel was found to be the best

choice of material for the reactor planned to be designed for supercritical biodiesel production. The reactor made up of Grade 316 stainless steel satisfies all requirements; withstands minimum stress of 47 MPa and a temperature of 400°C, offers vastly superior corrosion resistance, is not affected by the magnetic field, is relatively cost-effective, and is easy to shape into a cylindrical vessel without the need for welding. The reactor is manufactured from a single piece of cylindrical solid Grade 316 stainless steel and has passed all safety tests before it reaches the production stage.

Scientific Ethics Declaration

The authors declare that the scientific ethical and legal responsibility of this article published in EPSTEM journal belongs to the authors.

Acknowledgements

* This article was presented as an oral presentation at the International Conference on Technology, Engineering and Science (www.icontes.net) held in Antalya/Turkey on November 16-19, 2022.

* The authors would like to express their sincere thanks to Assoc. Prof. Dr. Ali Evcil for his contributions during the reactor design and biodiesel production phase.

* The authors would also like to acknowledge to Eng. Birgul Kaya, and Eng. Muzaffer Kaya for their endless financial and moral support during the manufacturing and testing of the reactor.

* This work was supported by the Near East University Research Fund under project no. YDU/2010-2-21.

References

Al-Shanableh, F. (2017). *Characterization of cold flow properties of biodiesel transesterified from waste frying oil.* Ph. D. Thesis in Mechanical Engineering. http://docs.neu.edu.tr/library/6533447758.pdf.

Al-Shanableh, F., Bilin, M., Evcil, A., & Savas, M.A. (2019): Estimation of cold flow properties of biodiesel using ANFIS-based models, *Energy Sources, Part A: Recovery, Utilization, and Environmental Effects*, 1-18. https://doi.org/10.1080/15567036.2019.1672832.

Ashby, M.F. (2011). *Material selection in mechanical design*. 4th ed. Oxford. Published by Elsevier Ltd.

Demirbas, A. (2006). Biodiesel production via non-catalytic SCF method and biodiesel fuel characteristics. *Energy Conversion Management*, *47*, 2271–82.

Diasakou, M., Louloudi, A., & Papayannakos, N. (1998). Kinetics of the non-catalytic transesterification of soybean oil. *Fuel*, *77*, 1297-1302.

Ebert, J. (2008). Supertical methanol for biodiesel production. *Biodiesel Magazine*, *April*, 80-85.

Evcil, A., Al-Shanableh, F., Savas, M.A.. (2018). Variation of solid fraction with cold flow properties of biodiesel produced from waste frying oil. *Fuel*, 215:522–27. https://doi.org/10.1016/j.fuel.2017.11.055.

He, H., Sun, S., & Wang, T. (2007). Transesterification kinetics of soybean oil for production of biodiesel in supercritical methanol. *The Journal of the American Oil Chemists' Society*, *84*, 399.

Lee, Y., Park, S.H., Lim, I.T., Han, K., & Lee, S.Y. (2000). Preparation of alkyl (R)-(2)-3hydroxybutyrate by acidic alcoholysis of poly-(R)-(2)-3-hydroxybutyrate. *Enzyme Microbial Technology*, *27*, 33–6.

Moss, D.R. (2004). *Pressure vessel design manual*. 3rd edition. Gulf Professional Publishing, Oxford, Elsevier.

Nematian, T., Fatehi, M., Hosseinpour, M., & Barati, M. (2021). One-pot conversion of sesame cake to low N-content biodiesel via nano-catalytic supercritical methanol. *Renewable Energy*, *170*, 964–973.

Peters, M.S., & Timmerhaus, K.D. (2003). *Plant design and economics for chemical engineers*. 5th ed. New York: McGraw Hill.

Pinnarat, T., & Savage, P.E. (2010). Noncatalytic esterification of oleic acid in ethanol. *The Journal of Supercritical Fluids*, *53* (1-3), 53-59.

Qadeer, M.U., Ayoub, M., Komiyama, M., Daulatzai, M. U. K., Mukhtar, A., Saqib, S. Ullah, S., Qyyum, M.A., Asif, A., & Bokhari, A. (2021). Review of biodiesel synthesis technologies, current trends, yield influencing factors and economical analysis of supercritical process. *Journal of Cleaner Production*, *309*, 127388.

Saka, S., & Kusdiana, D. (2001). Biodiesel fuel from rapeseed oil as prepared in supercritical methanol. *Fuel*, *80*, 225–31.

Sharma, Y.C., Singh, Y.C., & Upadhyay, S.N. (2007). Advancements in development and characterization of biodiesel: A review. *Fuel, 87,* 2355-2373.

Silva, C., & Oliveria, V. (2014). Biodiesel production through non-catalytic supercritical transesterification: current state and perspectives. *Brazilian Journal of Chemical Engineering*, *31*, 271–285.

Author Information

Filiz Al-Shanableh
Near East University
Nicosia, Mersin 10, Turkey
Contact e-mail: *filiz.shanableh@neu.edu.tr*

Mahmut A. Savas
Near East University
Nicosia, Mersin 10, Turkey

To cite this article:

Al-Shanableh, F. & Savas, M.A. (2022). Material selection of batch type supercritical reactor for biodiesel production. *The Eurasia Proceedings of Science, Technology, Engineering & Mathematics (EPSTEM), 21,* 477-483.

The Eurasia Proceedings of Science, Technology, Engineering & Mathematics (EPSTEM)
ISSN: 2602-3199

The Eurasia Proceedings of Science, Technology, Engineering & Mathematics (EPSTEM), 2022

Volume 21, Pages 484-499

IConTES 2022: International Conference on Technology, Engineering and Science

An Analysis of Flexural Bond Length and Anchorage Length of Prestressed Fiber Reinforced Polymer Reinforcement

Aidas JOKŪBAITIS
Vilnius Gediminas Technical University

Juozas VALIVONIS
Vilnius Gediminas Technical University

Abstract: The main aim of this paper is to provide a broader analysis of the flexural bond length and anchorage length of different types of prestressed Fiber Reinforced Polymer (FRP) reinforcement and to provide corrections to the existing theoretical models. Therefore, this paper presents a description of the main parameters that influence the flexural bond length and anchorage length of different types of FRP reinforcement based on experimental results found in the literature. The database of more than 70 specimens was compiled with the results of the transfer length, flexural bond length, and anchorage length of FRP reinforcement and the main influencing parameters. The analysis of a larger database of flexural bond length revealed that propositions of coefficients α_{fb} = 2.8 and α_{fb} = 1.0 found in the literature for Carbon Fiber Composite Cable (CFCC) strands and Carbon Fiber Reinforced Polymer (CFRP) bars, respectively, should be corrected. Therefore, corrected values of coefficient α_{fb} are proposed in this article for CFCC strands (α_{fb} = 3.0) and CFRP bars (α_{fb} = 0.9). Additionally, the new value of α_{fb} = 1.4 is proposed for flexural bond length of Aramid Fiber Reinforced Polymer (AFRP) bars. Moreover, the main existing theoretical models are presented, and the comparison of theoretical and experimental flexural bond length and anchorage length results is discussed. Additionally, the analysis of the flexural bond length and anchorage length and the proposed new values of the coefficient α_{fb} provides possibilities for adapting it to design codes for engineering applications and performing additional research that fills the missing gaps in the field.

Keywords: Prestress, Fiber reinforced polymer, Flexural bond length, Anchorage length, Bond

Introduction

The corrosive environment of such structures as marine structures, bridges, parking garages, and railway sleepers (Jokūbaitis et al., 2020b; Jokūbaitis, Marčiukaitis, et al., 2016; Jokūbaitis, Valivonis, et al., 2016) is the main concern with regard to steel corrosion (deicing salts, etc.). Therefore, there is increasing interest in the use of FRP materials, namely, CFRP, AFRP, GFRP, and relatively new BFRP (E. Atutis et al., 2018; M. Atutis et al., 2018) as replacements for steel reinforcement.

FRPs have important properties that make them particularly attractive for prestressed concrete applications: high strength, which is similar to or greater than that of steel, and low modulus of elasticity, which results in lower concrete prestress losses due to concrete creep and shrinkage as well as the relaxation of the prestressing element. The major difficulty in using FRP reinforcement for prestressing is that anchorage systems require greater attention than those for steel strands. Therefore, three types of anchorage systems are developed for FRP reinforcement: mechanical, bonded, and composite (Wang et al., 2018).

The use of FRP reinforcement in prestressed concrete structures is highly dependent on the reliability of the reinforcement anchorage zone. That is, the behavior of concrete members is mainly dependent on the bond between reinforcement and concrete (Jokūbaitis et al., 2017, 2018, 2020a). Combinations of several factors have been shown to contribute to the bond of pretensioned reinforcement to concrete. Depending on the circumstances, adhesion, Hoyer effect, and mechanical interlocking can act alone or in combination to resist slip of reinforcement in concrete. While adhesion is weak, mechanical interlock and friction create higher bond strength and are quite dependent on the surface characteristics of the reinforcement.

The pretension technique relies on the bond between the prestressing reinforcement and the surrounding concrete to transfer the stresses from the prestressing reinforcement to the concrete. Figure 1 provides a curve illustrating the variation in reinforcement stresses along the length of the flexural member starting from the free end of the strand. Transfer length (L_t) is defined as the length from the free end of the member to the point along the length of the beam where the effective prestress in the strand is fully transferred to the concrete during reinforcement release. The stress in the strand along the length of the transfer length is assumed to vary linearly from zero at the free end to an effective prestress after losses (f_{pe}) at the end of the transfer length. The flexural bond length (L_{fb}) is defined as the length of a fully bonded reinforcement beyond the transfer length required to fully develop the stress in the reinforcement to the maximum stress (f_{pu}) at the flexural bearing capacity, when load is applied to the member. Anchorage length (L_a) is the sum of the transfer length (L_t) and the flexural bond length (L_{fb}). Transfer length, flexural bond length, and development length are illustrated in Figure 1.

The transfer and development length of an FRP reinforcement is a function of the perimeter and surface condition of the FRP, the stress in the FRP, the method used to transfer the force of the FRP to the concrete and the strength and cover of the concrete. The mechanism of the bond differs between FRP and steel strands due to differences in shape, surface treatment, and modulus of elasticity. FRP reinforcement may be produced using unique manufacturing processes, which result in different properties and configurations of the reinforcement surface. The stronger the bond strength, the shorter the length required to transfer a certain amount of stress between the reinforcement and the concrete. Therefore, the strand length required to transfer the effective prestress and develop its ultimate strength should be predicted with careful consideration. At any point along the section, the loss of the bond between the reinforcement and concrete can lead to sudden failure: due to splitting failure or pull-out failure.

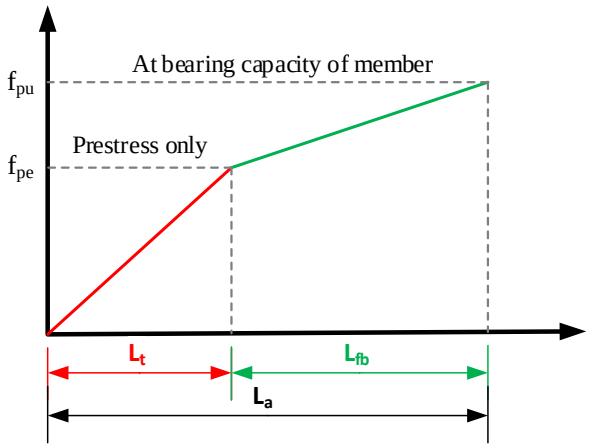

Figure 1. Anchorage zone of pretensioned reinforcement

In the last 30 years, numerous experimental researchers have investigated the transfer, flexural bond, and anchorage lengths of different prestressed FRP reinforcements. The large variation of different FRP types leads to the need for experimental research. Therefore, some studies were performed to investigate the transfer, flexural bond, and anchorage length of CFCC strands (Domenico, 1995; Domenico et al., 1998; Ehsani et al., 1997; Mahmoud, 1997; Mahmoud et al., 1999), CFRP bars (Dolan et al., 2001; Ehsani et al., 1997; Krem, 2013; Krem et al., 2018; Lu et al., 2000; Mahmoud, 1997; Mahmoud et al., 1999) and AFRP bars (Dolan et al., 2001; Ehsani et al., 1997; Lu et al., 2000; Nanni et al., 1992; Nanni & Tanigaki, 1992). However, the large variation in FRP bars in terms of shape, surface conditions, strength, and modulus of elasticity indicates that a deeper understanding of the transfer and flexural bond length of FRPs with different properties remains necessary. Therefore, this article presents a database of transfer, flexural bond, and anchorage length results for pretensioned FRP reinforcement and provides a comparative analysis of the anchorage zones of different types of FRP.

Theoretical Models

Table 1 presents a summary of the recommended expressions for the transfer and flexural bond lengths of the FRP reinforcement (Equations (1), (2), (6), (7), and (8)) and the steel strands (Equations (3), (4), (5), (9) and (10)). The nomenclature is presented in this table. The transfer length equations (Table 1) are discussed in detail in (Jokūbaitis et al., 2022).

Equations (4) and (9) provided in (ACI 318-11, 2011) evaluate the fewest different parameters (f_{pi}, f_{pe}, f_{pu}, and Ø) that influence the transfer length and flexural bond length. Additionally, with an empirical coefficient of 20.7 and 0.145, which are based on the large database of transfer and flexural bond length results, respectively, Equations (3), (4) and (9) were developed for steel strands. Lu et al. (Lu et al., 2000) modified Equation (8) provided in (ACI 318-11, 2011) for the flexural bond length of FRP reinforcement. However, the modified Equation 8 gives a conservative prediction of the experimental results. In addition, Mitchell et al. (Mitchell et al., 1993) suggested supplementing the ACI-318-11 (ACI 318-11, 2011) Equations (4) and (9) with the concrete compressive strength at the transfer and in service stages. As concrete strength enhances the bond of reinforcement, it becomes a good additional parameter to increase the accuracy of the transfer length and the prediction of the flexural bond length. However, Equations (4) and (9) are proposed for the steel strands. Compared with Equations (1) and (6), Equations (2) and (7) proposed by Domenico (Domenico, 1995) replace the reinforcement diameter (Ø) with a cross-sectional area (A_p) of the reinforcement and propose empirical coefficients $C_t = 80$ and $C_{fb} = 40$ for the transfer and flexural bond lengths of the CFCC strand, respectively. Additionally, it evaluates $f_{ci}^{1/2}$ and $f_c^{1/2}$ as also in Equations (5) and (10), respestively.

Table 1. Theoretical models of transfer and flexural bond length

References	Transfer length	Equation No	Flexural bond length	Equation No	Notes
(Mahmoud, 1997)	$L_t = \frac{f_{pi} \cdot \varnothing}{\alpha_t \cdot f_{ci}^{\frac{2}{3}}}$	(1)	$L_{fb} = \frac{(f_{pu} - f_{pe}) \cdot \varnothing}{\alpha_{fb} \cdot f_c^{\frac{2}{3}}}$	(6)	f_{pi} - is the initial prestress level, f_{pe} – effective prestressing stress in the CFCC strand, f_{pu} stress at first slip or at rupture of reinforcement, f_{ci} - is the concrete compressive strength at the time of transfer, f_c concrete compressive strength at the time of testing, Ø - is the reinforcement diameter, A_p – cross-sectional area of prestressed reinforcement, α_t and α_{fb} - is a material dependent coefficient, C_T – constant is equal to 80 for CFCC strands, C_{fb} constant is equal to 40 for CFCC strands.
(Domenico, 1995)	$L_t = \frac{f_{pe} \cdot A_p}{C_T \cdot \sqrt{f_{ci}}}$	(2)	$L_{fb} = \frac{(f_{pu} - f_{pe}) \cdot A_p}{C_{fb} \cdot \sqrt{f_c}}$	(7)	
(Lu et al., 2000)	$L_t = \frac{f_{pi} \cdot \varnothing}{20.7}$	(3)	$L_{fb} = 0.10875 \cdot (f_{pu} - f_{pe}) \cdot \varnothing$	(8)	
(ACI 318-11, 2011)	$L_t = \frac{f_{pi} \cdot \varnothing}{20.7}$	(4)	$L_{fb} = 0.145 \cdot (f_{pu} - f_{pe}) \cdot \varnothing$	(9)	
(Mitchell et al., 1993)	$L_t = \frac{f_{pi} \cdot \varnothing}{20.7} \cdot \sqrt{\frac{20.7}{f_{ci}}}$	(5)	$L_{fb} = 0.145 \cdot (f_{pu} - f_{pe}) \cdot \varnothing \cdot \sqrt{\frac{30}{f_c}}$	(10)	

Equations (1) and (6) were proposed by (Mahmoud, 1997; Mahmoud et al., 1999) for CFRP Leadline bars and CFCC strands and were adopted in several design codes (ACI 404.4R-04, 2004; CAN-CSA S806-12, 2012). It takes into account reinforcement diameter (Ø), stresses in reinforcement (f_{pi}, f_{pe}, f_{pu}), and concrete compressive strength (f_{ci}, f_c). The main difference from other theoretical models is that Equations (1) and (6) propose empirical coefficients α_t and α_{fb}, respectively, depending on the type of FRP reinforcement. Therefore, these coefficients can be calibrated for different types of FRP reinforcement (GFRP, CFCC, CFRP, AFRP, BFRP) with different surface conditions. Additionally, it presents the concrete strength as $f_c^{2/3}$ instead of $f_c^{1/2}$ (Equations (2), (5), (7), and (10)). The presentation of concrete strength as $f_c^{2/3}$ can be explained by the correlation of concrete compressive strength with concrete tensile strength $f_{ctm} = 0.3 \cdot f_c^{2/3}$ provided in (EN 1992-1-1, 2004; MC 1990, 1991; MC 2010, 2012).

Table 2 presents the values of coefficients α_t, α_{fb}, C_t, and C_{fb} provided in Equations (1), (6), (2), and (7), respectively, for different types of FRP reinforcement found in the literature. Domenico (Domenico, 1995) proposed empirical coefficients $C_t = 80$ and $C_{fb} = 40$ for the transfer and flexural bond lengths of the CFCC strand, respectively. The values proposed by (Mahmoud, 1997; Mahmoud et al., 1999) and adopted in (ACI 404.4R-04, 2004; CAN-CSA S806-12, 2012) are $\alpha_t = 1.9$, $\alpha_{fb} = 1.0$ and $\alpha_t = 4.8$, $\alpha_{fb} = 2.8$ for CFRP Leadline bars and CFCC strands, respectively. Additionally, (Krem, 2013; Krem et al., 2018) investigated specimens made of self-compacting concrete (SCC) and prestressed with CFRP bars and proposed $\alpha_t = 2.84f_{pi}/800$, $\alpha_{fb} = 0.37+(f_{pu}-f_{pe})/2500$.

Table 2. Theoretical models of transfer and flexural bond length

References	Reinforcement Type	Transfer length	Flexural bond length
(Mahmoud, 1997; Mahmoud et al., 1999)	CFRP Leadline bars	$\alpha_t = 1.9$	$\alpha_{fb} = 1.0$
	CFCC strands	$\alpha_t = 4.8$	$\alpha_{fb} = 2.8$
(Domenico, 1995; Domenico et al., 1998)	CFCC strands	$C_t = 80$	$C_t = 40$
(Krem, 2013; Krem et al., 2018)	CFRP bars (SCC concrete)	$\alpha_t = 2.84\text{-}f_{pi}/800$	$\alpha_{fb} = 0.37+(f_{pu}\text{-}f_{pi})/2500$
(Jokūbaitis & Valivonis, 2022)	AFRP smooth braided bars	$\alpha_t = 1.5$	–
	AFRP rough and sanded bars	$\alpha_t = 4.0$	–

Results

The Database of the Results

A literature review of the transfer length, flexural bond length, and anchorage length of concrete specimens pretensioned with different FRP reinforcement was performed. The results of 106 beams were collected (Annex A). The ranges of the initial parameters of the database are provided in Table 3. A literature review revealed that prestressed concrete flexural members tested for flexural bond and anchorage lengths showed flexural failure or reinforcement anchorage failure (Mahmoud, 1997; Mahmoud et al., 1999; Nanni & Tanigaki, 1992). The flexural member can be designed to fail either in the concrete compressive zone (Nanni & Tanigaki, 1992) or by reinforcement rupture (Mahmoud, 1997; Mahmoud et al., 1999). The flexural bond and anchorage lengths can be determined when the beam failure is between the flexural failure and the reinforcement anchorage failure. Therefore, for the analysis of the flexural bond and anchorage lengths, only the results of beams that failed between flexural failure and reinforcement anchorage failure were taken into account. Specifically, 16 of 36, 16 of 36, and 21 of 34 specimens prestressed with CFCC (Table A1), CFRP (Table A2), and AFRP (Table A3) reinforcement were used for the analysis, respectively. Tables A1-A3 (Annex A) provide original markings of specimens from the experimental research, type and surface conditions of FRP reinforcement, specimen type, concrete protective cover (c), reinforcement diameter (Ø), cross-sectional area of the bar (A_p), modulus of elasticity of reinforcement (E_p), concrete compressive strength at the time of testing (f_c), effective stresses in reinforcement taking into account losses of prestress (f_{pe}), stress at first slip or at rupture of reinforcement (f_{pu}), transfer length (L_t), flexural bond length (L_{fb}), anchorage length (L_a) and mode of failure of beam.

Table 3. Summary of initial parameters of the database

FRP Type	c, mm	Ø, mm	A_p, mm^2	E_p, GPa	f_{pu}, MPa	f_{pe}, MPa	f_c, MPa
CFCC	45–75	10.5–15.2	55.7–113.6	137–141	1734–2305	735–1306	31–64
CFRP	35–40.6	7.9–12.7	46.1–126.7	144–171	1360–3000	535–1400	37–70.9
AFRP	40.6–66	7.4–16	38.1–1802	45–127	1021–2448	258–1061	31–47.1

Derivation of Coefficient α_{fb}

The most widely used equation (Equation (6)) for the flexural bond length of the pretensioned FRP reinforcement is proposed by (Mahmoud, 1997; Mahmoud et al., 1999) and is adopted in design codes (ACI 404.4R-04, 2004; CAN-CSA S806-12, 2012). Additionally, it takes into account the reinforcement diameter (Ø), concrete compressive strength (f_c), stresses in reinforcement (f_{pe}, f_{pu}) and material dependent coefficient (α_{fb}), which are one of the main parameters that influence the flexural bond length of pretensioned FRP reinforcement. Therefore, for a better analysis of the results based on Equation (6), a graphical comparison of

the flexural bond length of different FRP reinforcements (CFCC, CFRP, and AFRP) and $\left(f_{pu}-f_{pe}\right)\cdot\varnothing/f_c^{2/3}$ is presented in Figure 2. Additionally, these graphs (Figure 2) represent a distribution of the results with the proposed mean values of the coefficient α_{fb}. For the CFCC strand database, the average value of the coefficient α_{fb} is 3.0 with a standard deviation (STD) of 0.62 and a coefficient of variation (COV) of 20.5% (Table 4) (for concrete strength 31–64 MPa, effective prestress 735–1306 MPa, stresses at failure 1734–2305 MPa and reinforcement diameter 10.5–15.2 mm).

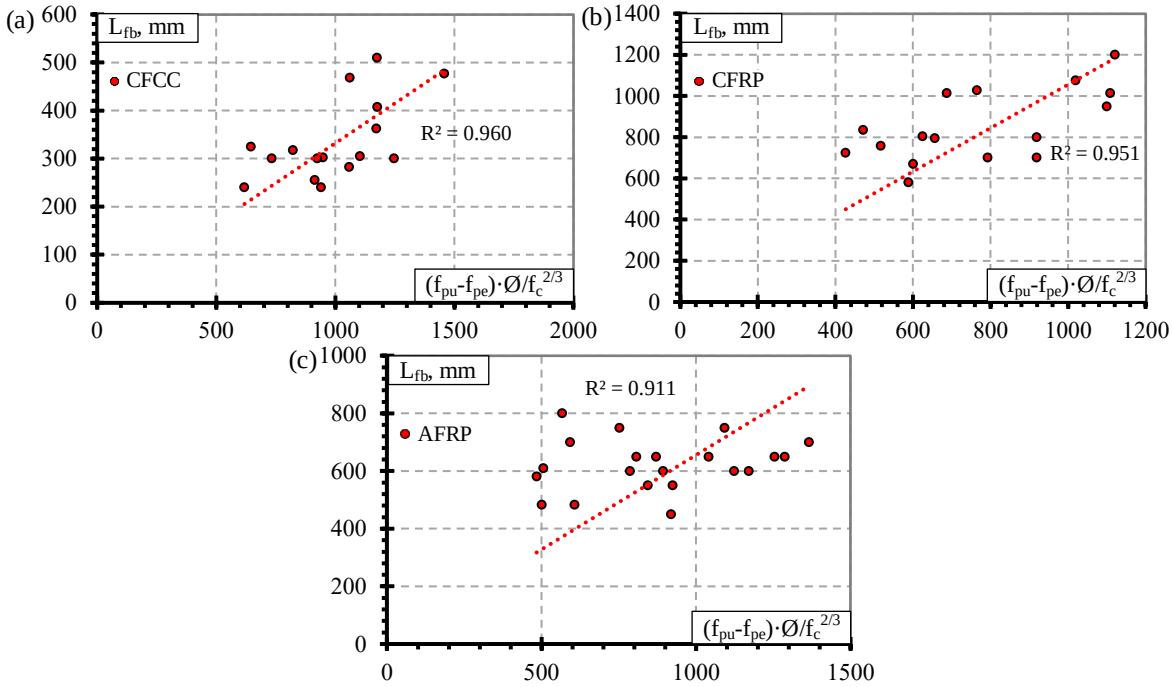

Figure 2. Relationship between flexural bond length and $\left(f_{pu}-f_{pe}\right)\cdot\varnothing/f_c^{2/3}$ of (a) CFCC strands, (b) CFRP bars, and (c) AFRP bars

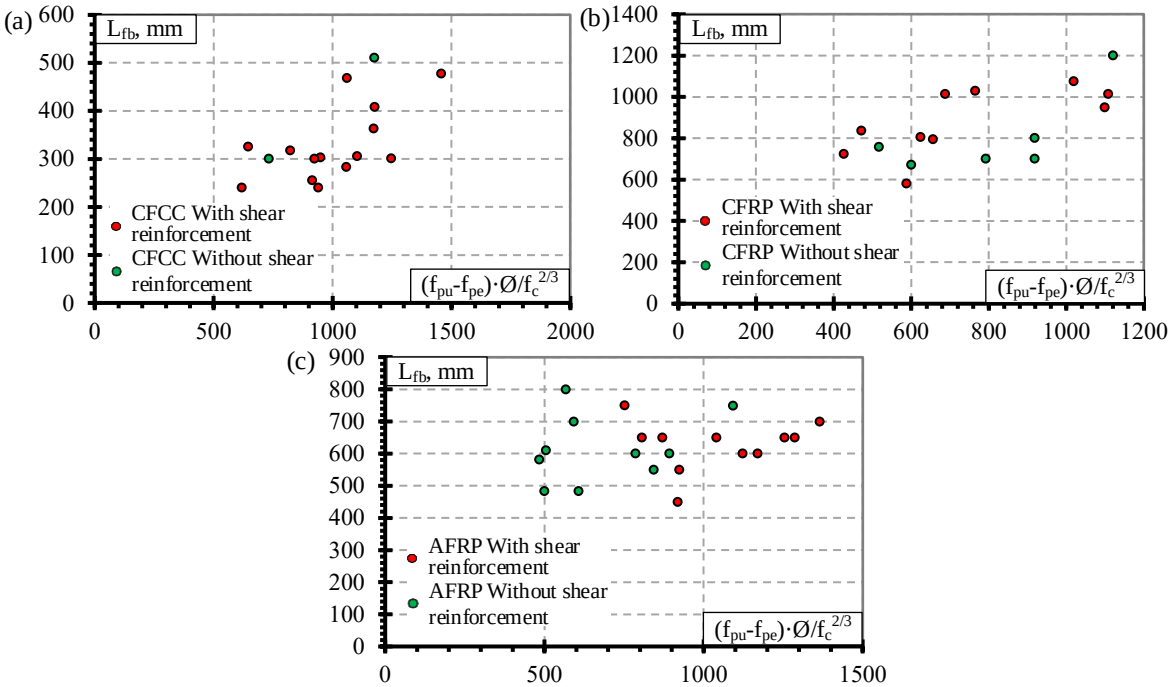

Figure 3. Relationship between flexural bond length and $\left(f_{pu}-f_{pe}\right)\cdot\varnothing/f_c^{2/3}$ of (a) CFCC strands, (b) CFRP bars, and (c) AFRP bars

The graphical representation is presented in Figure 2a with a very strong correlation coefficient $R^2 = 0.96$. Figure 2b presents the relationship between flexural bond length and $\left(f_{pu} - f_{pe}\right) \cdot \varnothing / f_c^{2/3}$ with an average $\alpha_{fb} = 0.9$ with STD = 0.22, COV = 24.0%, and $R^2 = 0.95$ (Table 4) (for concrete strength 37–71 MPa, effective prestress 535–1400 MPa, stress at failure 1360–3000 MPa, and reinforcement diameter 7.9–12.7 mm). Figure 2c presents the transfer length distribution of the AFRP bars with respect to $\left(f_{pu} - f_{pe}\right) \cdot \varnothing / f_c^{2/3}$ with an average $\alpha_{fb} = 1.4$ with STD = 0.42, COV = 29.8%, and $R^2 = 0.91$ (Table 4) (for concrete strength 31–47 MPa, effective prestress 258–1061 MPa, stress at failure 1021–2448 MPa, and reinforcement diameter 7.4–16 mm).

Table 4. Results of coefficient α_{fb}

α_{fb}	CFCC (Mahmoud, 1997)	Proposed	CFRP (Mahmoud, 1997)	Proposed	AFRP Proposed
Mean	2.8	3.0	1.0	0.9	1.4
Standard deviation	-	0.62	-	0.22	0.42
Coefficient of variation, %	-	20.5	-	24.0	29.8

In the database (Annex A) all CFCC strands had a helical plain surface, CFRP bars had a spirally indented (Leadline) or sanded surface, and AFRP bars had a smooth braided or rough surface. However, there were no clear influence of different reinforcement surface conditions on the flexural bond length of prestressed FRP reinforcement. Additionally, Figure 3 shows the influence of shear reinforcement on the relationship between flexural bond length and $\left(f_{pu} - f_{pe}\right) \cdot \varnothing / f_c^{2/3}$. It is clear that there is no clear influence of shear reinforcement on the flexural bond length of CFCC strands (Figure 3a), CFRP bars (Figure 3b), and AFRP bars (Figure 3c). However, Mahmoud (Mahmoud, 1997) determined that the absence of shear reinforcement resulted in an increase of the flexural bond length by 25% compared with specimens with shear reinforcement. This was explained by the helical shape of CFCC seven-wire strand which activates the confining of shear reinforcement due to higher radial stresses than that in the case of CFRP Leadline bar. Furthermore, concrete protective cover also plays an important role, in that the deeper the cover around the tendon, the less likely is the propagation of split (Nanni & Tanigaki, 1992).

Comparison of Experimental and Theoretical Results

In this section, the theoretical models for the calculation of transfer length, flexural bond length, and anchorage length (Table 1) are compared with experimental results from the literature (Tables A1–A3). The results presented in Figures 4 and 5 show the relationships between the experimental and theoretical results of the transfer, flexural bond, and anchorage lengths of different FRP reinforcements. In addition, they show the differences between different theoretical models for calculating transfer, flexural bond, and anchorage lengths. The theoretical model proposed by (Mahmoud, 1997; Mahmoud et al., 1999), is presented in Figures 4 and 5 with the coefficients α_t taken from (Jokūbaitis & Valivonis, 2022) and the coefficients α_{fb} proposed in this article (Table 4).

In Jokūbaitis & Valivonis (2022), a detailed comparison of the experimental and theoretical transfer length results (more than 300) is provided for different types of FRP reinforcement. Despite the lower number of transfer length results of CFCC, CFRP, and AFRP reinforcement analyzed in this article, it is evident that the tendency of comparison of the experimental and theoretical results is similar to that provided in Jokūbaitis & Valivonis (2022) (Figures 4a, 5a and 6d).

In the case of CFCC strands (Figure 4b), Equations (8), (9), and (10) give the most inappropriate results with a significant overestimation of the experimental flexural bond length results with $L_{fb,teor}/L_{fb.exp} = 4.2$, STD = 1.21, COV = 28.7%; $L_{fb,teor}/L_{fb.exp} = 5.6$, STD = 1.62, COV = 28.7%; and $L_{fb,teor}/L_{fb.exp} = 4.5$, STD = 1.0, COV = 21.9%, respectively (Figure 4b). A similar tendency is observed for the anchorage length of the CFCC strands (Figure 4c).

Equation (7) gives an overestimation of 8% of the experimental results of flexural bond length ($L_{fb,teor}/L_{fb.exp} = 0.92$, STD = 0.21, COV = 22.7%) (Figure 4b). However, the experimental results on anchorage length are more overestimated ($L_{a,teor}/L_{a.exp} = 0.83$, STD = 0.17, COV = 22.0%) (Figure 4c). This is due to the 25% higher experimental transfer length results (Equation 2) with respect to the theoretical results ($L_{t,teor}/L_{t.exp} = 0.75$, STD = 0.15, COV = 22.0%) (Figure 4a). Equations (2) and (7) were proposed for the CFCC

strands (Domenico, 1995; Domenico et al., 1998). However, the results of the larger database showed that its accuracy is not sufficient.

Equations (1) and (6) with the proposed values of coefficients α_t = 4.8 (Jokūbaitis et al., 2022; Mahmoud, 1997; Mahmoud et al., 1999) and α_{fb} = 3.0 gave the most accurate prediction of the transfer and flexural bond lengths (Figure 4a and 4b) ($L_{t,teor}/L_{t.exp}$ = 1.03, STD = 0.14, COV = 13.6% and $L_{fb,teor}/L_{fb.exp}$ = 1.0, STD = 0.20, COV = 19.7%), respectively. Therefore, the prediction of anchorage length was also very accurate ($L_{a,teor}/L_{a.exp}$ = 1.03, STD = 0.13, COV = 12.9%) (Figure 4c).

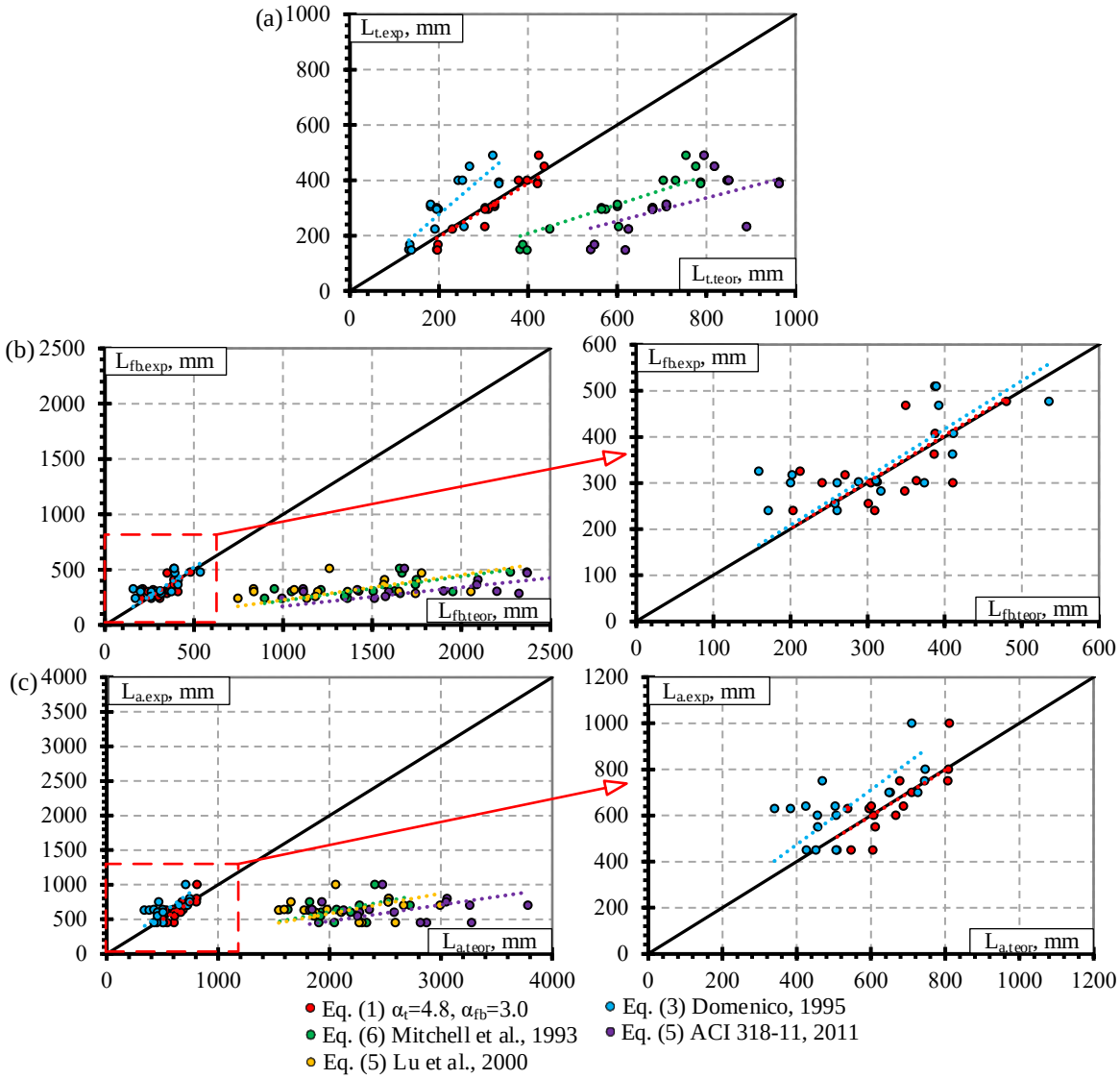

Figure 4. Relationship between the experimental and theoretical (a) transfer length, (b) flexural bond length and (c) anchorage length of CFCC strands

The prediction of the experimental results of the flexural bond and anchorage length of the CFRP bars is significantly underestimated according to Equation (7) with $L_{fb,teor}/L_{fb.exp}$ = 0.35, STD = 0.10, COV = 28.6% (Figure 5b) and $L_{a,teor}/L_{a.exp}$ = 0.37, STD = 0.11, COV = 28.9% (Figure 5c), respectively. The same tendency is observed in the case of the AFRP bars with $L_{fb,teor}/L_{fb.exp}$ = 0.30, STD = 0.09, COV = 29.0% (Figure 5e) and $L_{a,teor}/L_{a.exp}$ = 0.31, STD = 0.07, COV = 22.8% (Figure 5f).

The flexural bond (Figures 5b and 5e) and anchorage (Figures 5c and f) length results of prestressed CFRP bars determined according to the theoretical models of (Lu et al., 2000) and (Mitchell et al., 1993) are similar. However, it overestimates the experimental results of flexural bond length with $L_{fb,teor}/L_{fb.exp}$ = 1.38, STD = 0.32, COV = 22.9% and $L_{fb,teor}/L_{fb.exp}$ = 1.39, STD = 0.32, COV = 23.1%, respectively (Figure 5b) and the anchorage

length with $L_{a,teor}/L_{a.exp}$ = 1.28, STD = 0.25, COV = 19.4% and $L_{a,teor}/L_{a.exp}$ = 1.18, STD = 0.22, COV = 18.4%, respectively (Figure 5c). Even higher overestimation of experimental flexural bond and anchorage length results of prestressed AFRP bars determined according to the theoretical models of (Lu et al., 2000) and (Mitchell et al., 1993) can be seen in Figures 5e and f. Therefore, $L_{fb,teor}/L_{fb.exp}$ = 1.50, STD = 0.31, COV = 20.9% and $L_{fb,teor}/L_{fb.exp}$ = 1.62, STD = 0.36, COV = 22.2%, respectively (Figure 5e) and $L_{a,teor}/L_{a.exp}$ = 1.40, STD = 0.30, COV = 21.2% and $L_{a,teor}/L_{a.exp}$ = 1.39, STD = 0.33, COV = 23.9%, respectively (Figure 5f).

The highest difference between the experimental and theoretical flexural bond and anchorage length results of CFRP and AFRP bars was observed according to the theoretical model provided in (ACI 318-11, 2011). An overestimation of experimental flexural bond length results is up to 85% with STD = 0.42, COV = 22.9% and 100% with STD = 0.42, COV = 20.9% for CFRP and AFRP bars, respectively (Figure 5b and e). In addition, an overestimation of the experimental anchorage length results is up to 57% with STD = 0.33, COV = 21.3% and 71% with STD = 0.38, COV = 22.4% for CFRP and AFRP bars, respectively (Figure 5c and f).

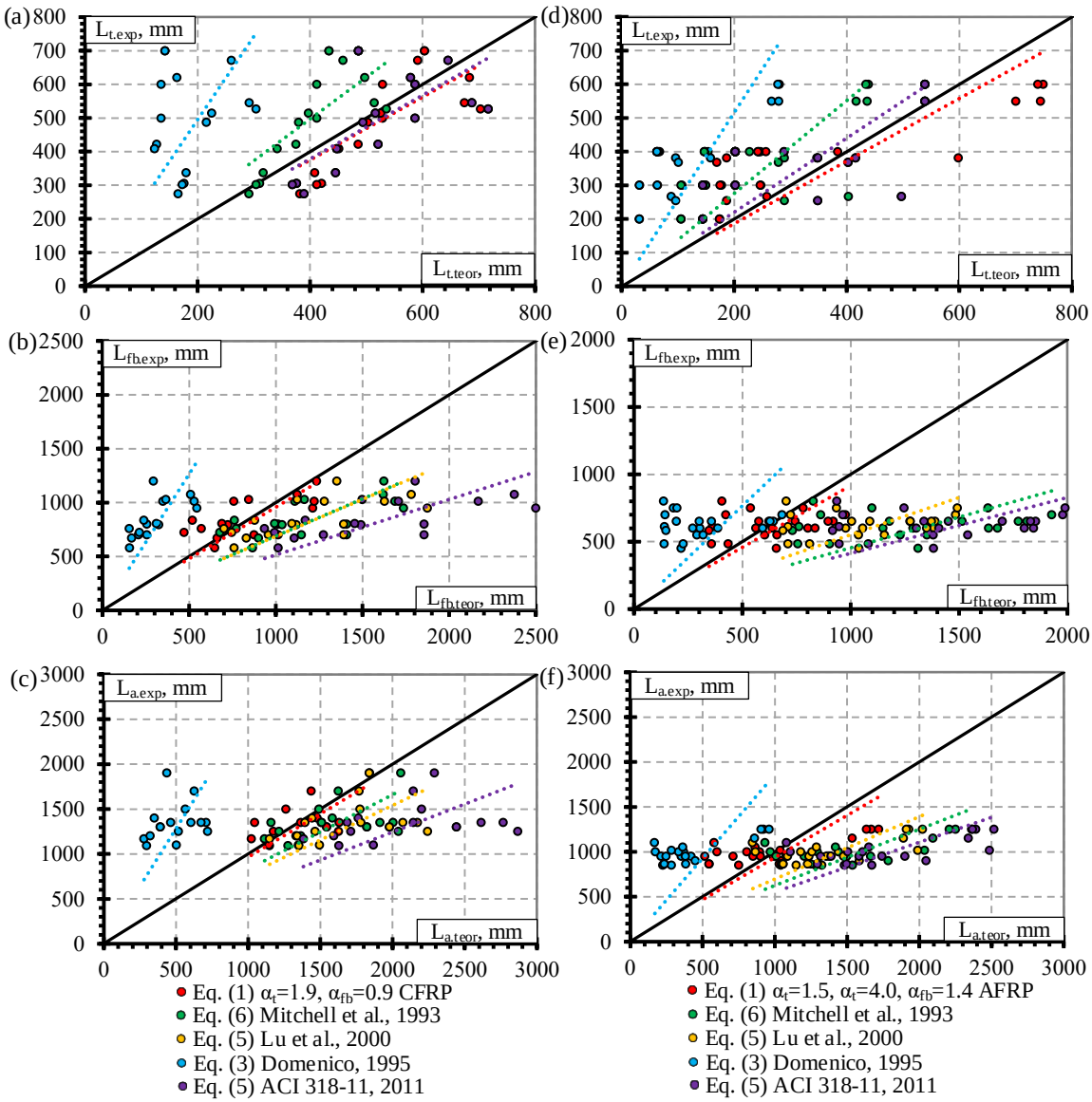

Figure 5. Relationship between experimental and theoretical (a) transfer, (b) flexural bond and (c) anchorage length of CFRP bars and (d) transfer, (e) flexural bond and (f) anchorage length of AFRP bars

The proposed coefficients α_{fb} = 0.9 and α_{fb} = 1.4 for the flexural bond lengths of the CFRP and AFRP bars, respectively, gave the most accurate prediction of the experimental results ($L_{fb,teor}/L_{fb.exp}$ = 1.0, STD = 0.24, COV = 24.0% (Figure 5b) and $L_{fb,teor}/L_{fb.exp}$ = 1.02, STD = 0.30, COV = 29.8% (Figure 5e), respectively) by applying the theoretical model proposed by (Mahmoud, 1997; Mahmoud et al., 1999). In addition, the

combination of the proposed coefficients $\alpha_t = 1.9$, $\alpha_t = 2.9$ (Jokūbaitis et al., 2022) and $\alpha_{fb} = 0.9$, $\alpha_{fb} = 1.4$ (Equations 1 and 6) gives the most accurate prediction of anchorage length of CFRP and AFRP bars, respectively with $L_{a,teor}/L_{a.exp} = 1.03$, STD = 0.15, COV = 14.1% (Figure 5c) and $L_{a,teor}/L_{a.exp} = 0.95$, STD = 0.27, COV = 28.7%, respectively (Figure 5f). Comparison of the ratio between theoretical and experimental results of the transfer length ($L_{t.teor}/L_{t.exp}$), flexural bond length ($L_{fb.teor}/L_{fb.exp}$) and anchorage length ($L_{a.teor}/L_{a.exp}$) of the CFCC strands, CFRP and AFRP bars with different values of coefficients α_t and α_{fb} is presented in Figures 6, 7 and 8, respectively. In Jokūbaitis & Valivonis (2022), it was confirmed that the coefficients $\alpha_t = 1.9$ and $\alpha_t = 4.8$ proposed by other authors are suitable for predicting the transfer length of the CFRP bars, and CFCC strands (only gradual type of release), respectively. Additionally, new values of coefficient α_t were proposed for smooth braided AFRP bars ($\alpha_t = 1.9$) and for sanded and rough AFRP bars $\alpha_t = 4.0$.

The coefficient α_t (used in Equation (1)) was proposed for CFCC strands and CFRP bars (Mahmoud, 1997; Mahmoud et al., 1999) (Table 2) and validated with a larger database of the transfer length results in (Jokūbaitis et al., 2022). Additionally, in Jokūbaitis et al. (2022), new values of coefficient α_t were proposed for the transfer length of smooth braided AFRP bars ($\alpha_t = 1.9$) and for sanded and rough AFRP bars ($\alpha_t = 4.0$). Therefore, these values are used for the comparison of theoretical and experimental transfer length results of the CFCC strands (Figure 6a), CFRP bars (Figure 7a), and AFRP bars (Figure 8a). The results showed sufficiently good agreement between theoretical and experimental transfer lengths with $L_{t.teor}/L_{t.exp} = 1.03$, STD = 0.14, COV = 13.6% for CFCC strands (Figure 6a), $L_{t.teor}/L_{t.exp} = 1.11$, STD = 0.18, COV = 16.4% for CFRP bars (Figure 7a) and $L_{t.teor}/L_{t.exp} = 0.86$, STD = 0.31, COV = 36.0% for AFRP bars (Figure 8a). The 14% underestimation of the experimental transfer length results of AFRP bars could be related to a lower number of specimens analyzed in this article (21 specimens) and the high variation of the transfer length results reported in Jokūbaitis et al., (2022).

Different values of the coefficient α_{fb} (used in Equation (6)) were proposed by other authors and determined in this article (Table 4). The proposed value of $\alpha_{fb} = 3.0$ for the flexural bond length of the CFCC strands is slightly higher compared to $\alpha_{fb} = 2.8$ (Mahmoud, 1997; Mahmoud et al., 1999). For the CFCC strand, the proposed value of $\alpha_{fb} = 3.0$ gives better agreement with the experimental results of flexural bond length ($L_{fb.teor}/L_{fb.exp} = 1.0$, STD = 0.19, COV = 19.7%) compared to the theoretical results higher by 8% ($L_{fb.teor}/L_{fb.exp} = 1.08$, STD = 0.22, COV = 20.5%) with $\alpha_{fb} = 2.8$ (Figure 6b). Additionally, the linear trend line presented in Figure 6b shows that the theoretical results with $\alpha_{fb} = 3.0$ are in closer agreement with the experimental flexural bond length. Furthermore, the combination of $\alpha_t = 4.8$ and $\alpha_{fb} = 3.0$ gives better agreement with the experimental anchorage length results of the CFCC strands ($L_{a.teor}/L_{a.exp} = 1.03$, STD = 0.13, COV = 12.9%) compared to the combination of $\alpha_t = 4.8$ and $\alpha_{fb} = 2.8$ ($L_{a.teor}/L_{a.exp} = 1.08$, STD = 0.15, COV = 13.5%) (Figure 6c).

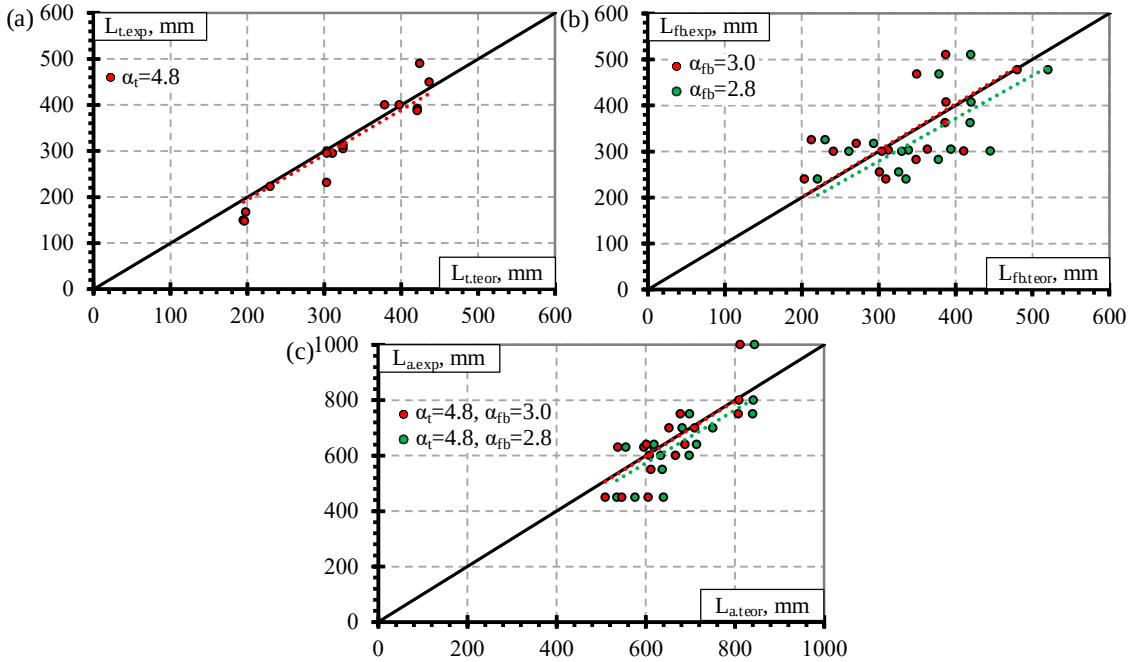

Figure 6. Comparison of experimental and theoretical (a) transfer, (b) flexural bond and (c) anchorage length results of prestressed CFCC strands

The proposed value of α_{fb} = 0.9 for the flexural bond length of CFRP bars agrees better with the experimental results ($L_{fb.teor}/L_{fb.exp}$ = 1.0, STD = 0.24, COV = 24.0%) compared to the theoretical results lower by 9% ($L_{fb.teor}/L_{fb.exp}$ = 0.91, STD = 0.22, COV = 24.0%) with α_{fb} = 1.0 (Mahmoud, 1997; Mahmoud et al., 1999) (Figure 7b). It shows that the theoretical results of the flexural bond length with α_{fb} = 0.9 are higher compared to the results with α_{fb} = 1.0 and therefore are on the safe side. Additionally, the combination of α_t = 1.9 and α_{fb} = 0.9 gives better agreement with the experimental anchorage length results of CFRP bars ($L_{a.teor}/L_{a.exp}$ = 1.03, STD = 0.14, COV = 14.1%) compared to the combination of α_t = 1.9 and α_{fb} = 1.0 ($L_{a.teor}/L_{a.exp}$ = 0.97, STD = 0.13, COV = 13.6%) (Figure 7c).

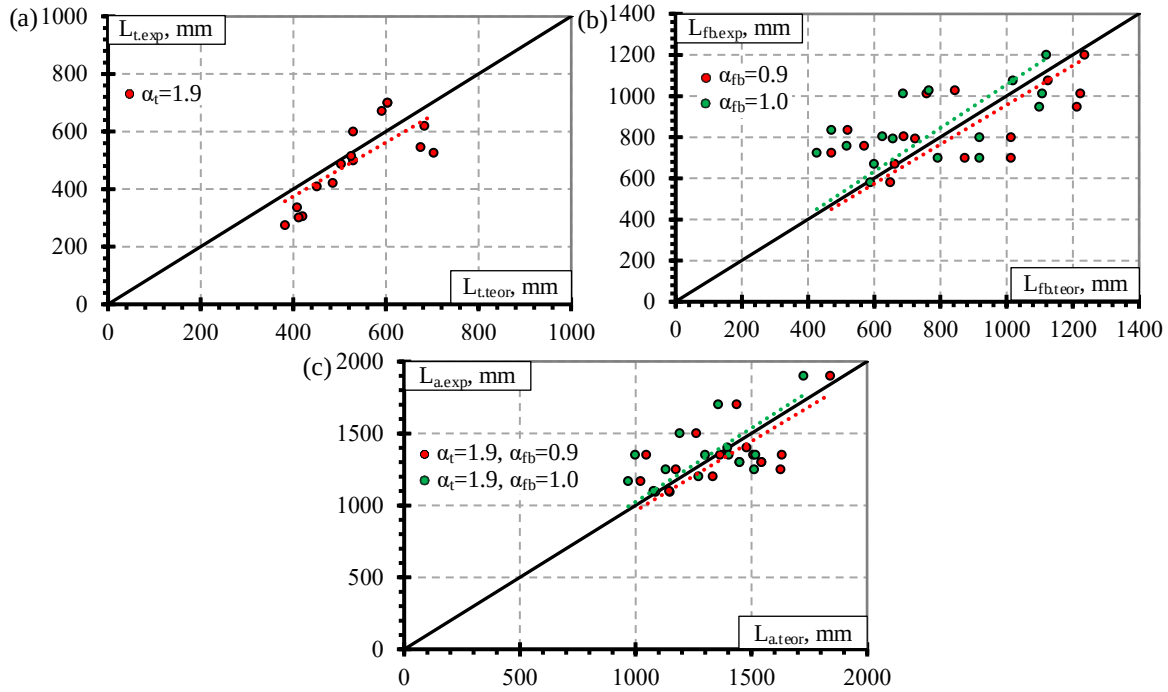

Figure 7. Comparison of experimental and theoretical (a) transfer, (b) flexural bond and (c) anchorage length results of prestressed CFRP bars

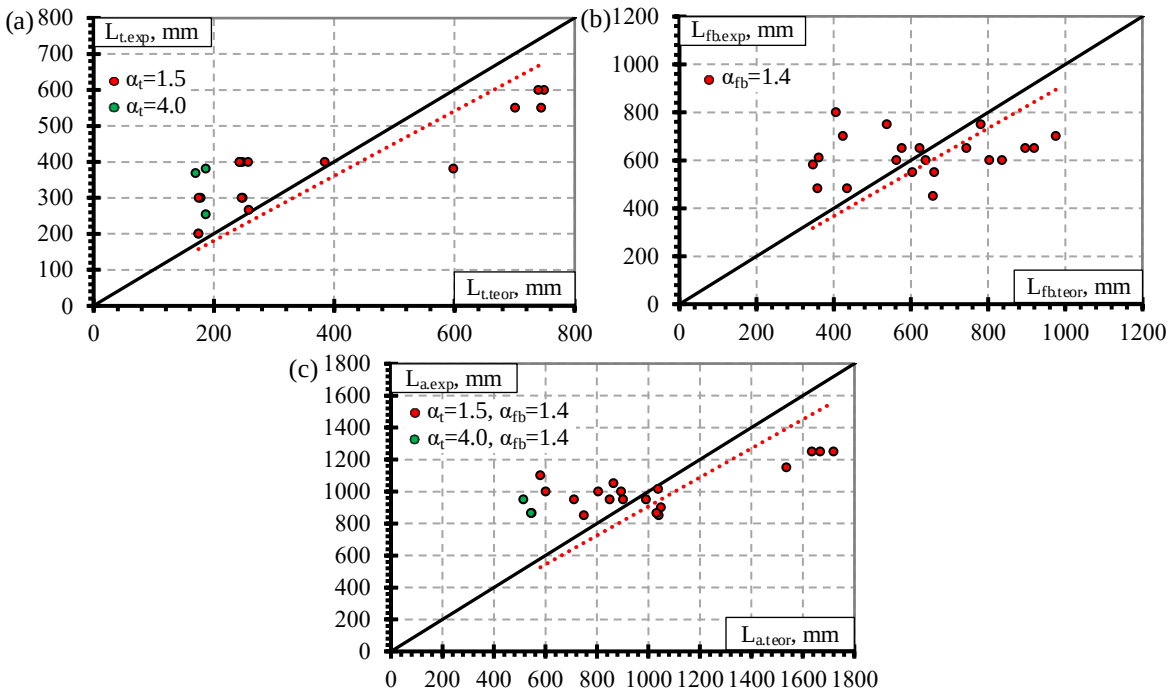

Figure 8. Comparison of experimental and theoretical (a) transfer, (b) flexural bond and (c) anchorage length results of prestressed AFRP bars

The literature review does not provide any proposition of α_{fb} for the flexural bond length of AFRP reinforcement. Therefore, in this article, the value of $\alpha_{fb} = 1.4$ is proposed (Table 4) for the flexural bond length of the AFRP bars with $L_{fb.teor}/L_{fb.exp} = 1.02$, STD = 0.30, COV = 29.8% (Figure 8b). In addition, a combination of $\alpha_t = 2.9$ and $\alpha_{fb} = 1.4$ gives good agreement with the experimental anchorage length results of the AFRP bars ($L_{a.teor}/L_{a.exp} = 0.95$, STD = 0.27, COV = 28.7%) (Figure 8c).

The variation of the flexural bond and anchorage length results is highest for AFRP bars compared to CFCC strands and CFRP bars. However, a combination of $\alpha_t = 1.5$ (for smooth braided AFRP bars), $\alpha_t = 4.0$ (for rough and sanded AFRP bars), and $\alpha_{fb} = 1.4$ gives a significantly lower variation of flexural bond and anchorage length compared to the transfer length of the AFRP bars presented in (Jokūbaitis & Valivonis, 2022).

Conclusions

A large database of the transfer, flexural bond and anchorage lengths of different FRP reinforcements was collected, and the analysis of experimental results, description of theoretical models, and comparison of experimental and theoretical results led to the following conclusions and proposals:

The database analysis revealed that the coefficients $\alpha_t = 4.8$, $\alpha_t = 1.9$, $\alpha_t = 1.5$, and $\alpha_t = 4.0$ proposed in the literature are suitable for predicting the transfer length of the CFCC strands, CFRP bars, AFRP bars with smooth braided surface and AFRP bars with rough and sanded surface, respectively. The analysis of the results of a larger database in this article shows that the coefficients $\alpha_{fb} = 2.8$ and $\alpha_{fb} = 1.0$ proposed by other authors for the flexural bond length of CFCC strands and CFRP bars, respectively, should be corrected. Therefore, the corrected values of $\alpha_{fb} = 3.0$ for CFCC strands (for concrete strength 31–64 MPa, stresses in reinforcement 735–1306 MPa, and reinforcement diameter 10.5–15.2 mm) and $\alpha_{fb} = 0.9$ for CFRP bars (for concrete strength 37–71 MPa, stresses in reinforcement 535–1400 MPa and reinforcement diameter 7.9–12.7 mm) are proposed, respectively. In addition, Equation (6) was determined to give the most accurate prediction of the flexural bond length by applying the proposed α_{fb} values for different types of FRP reinforcement.

The database is too small to clearly define the influence of different surface conditions of AFRP bars on the flexural bond length. Therefore, the new general value of the coefficient $\alpha_{fb} = 1.4$ was proposed for the prediction of the flexural bond length of the AFRP bars. The proposed value is valid for a concrete strength 31–47 MPa, stresses in reinforcement 258–1061 MPa, and reinforcement diameter 7.4–16 mm.

The combination of coefficients α_t proposed in the literature ($\alpha_t = 4.8$ for CFCC strands, $\alpha_t = 1.9$ for CFRP bars, $\alpha_t = 1.5$ for AFRP bars with smooth braided surface and $\alpha_t = 4.0$ for AFRP bars with rough and sanded surface) and coefficients α_{fb} proposed in this article ($\alpha_{fb} = 3.0$ for CFCC strands, $\alpha_{fb} = 0.9$ for CFRP bars and $\alpha_{fb} = 1.4$ for AFRP bars) for the prediction of the anchorage length of different FRP reinforcement according to Equations (1) and (6) gives the most accurate results.

The analysis of the flexural bond and anchorage length and the new values proposed for the coefficient α_{fb} provides possibilities for adapting it to design codes for engineering applications and performing additional research that fills the missing gaps in the field. In particular, additional research is needed on the effects of shear reinforcement of CFCC strands, CFRP and AFRP bars, and the surface conditions of the AFRP and CFRP bars. Furthermore, the prediction of flexural bond and anchorage length of BFRP reinforcement could be a subject of future research.

Scientific Ethics Declaration

The authors declare that the scientific, ethical, and legal responsibility of this article published in EPSTEM journal belongs to the authors.

Acknowledgements

* This article was presented as an oral presentation at the International Conference on Technology, Engineering and Science (www.icontes.net) held in Antalya/Turkey on November 16-19, 2022.

* This research was funded by the European Social Fund (project No 09.3.3-LMT-K-712-23-0161) under a grant agreement with the Research Council of Lithuania (LMTLT).

References

ACI 318-11, Committee 318, & American Concrete Institute. (2011). *ACI 318-11. Building code requirements for structural concrete (ACI 318-11) and commentary*. American Concrete Institute.

ACI 404.4R-04, Committee 440, & American Concrete Institute. (2004). *ACI 404.4R-04. Prestressing concrete structures with FRP tendons*. American Concrete Institute.

Atutis, E., Valivonis, J., & Atutis, M. (2018). Experimental study of concrete beams prestressed with basalt fiber reinforced polymers under cyclic load. *Composite Structures, 183*(1), 389–396. https://doi.org/10.1016/j.compstruct.2017.03.106

Atutis, M., Valivonis, J., & Atutis, E. (2018). Experimental study of concrete beams prestressed with basalt fiber reinforced polymers. Part I: Flexural behavior and serviceability. *Composite Structures, 183*(1), 114–123. https://doi.org/10.1016/j.compstruct.2017.01.081

CAN-CSA S806-12, & Canadian Standards Association. (2012). *CAN-CSA S806-12. Design and construction of building structures with fibre-reinforced polymers.* https://www.csagroup.org/store/product/S806-12/

Dolan, C. W., Hamilton, H. R. III., Bakis, C. E., & Nanni, A. (2001). Design recommendations for concrete structures prestressed with FRP tendons. FHWA Contract. DTFH61-96-C-00019. Final Report. http://wwweng.uwyo.edu/civil/research/papers/.

Domenico, N. G. (1995). Bond properties of CFCC prestressing strands in pretensioned concrete beams [Master Thesis]. University of Manitoba.

Domenico, N. G., Mahmoud, Z. I., & Rizkalla, S. H. (1998). Bond properties of carbon fiber composite prestressing strands. *ACI Structural Journal, 95*(3), 281–290.

Ehsani, M. R., Saadatmanesh, H., & Nelson, C. T. (1997). Transfer and flexural bond performance of aramid and carbon frp tendons. *PCI Journal, 42*(1), 76–86. https://doi.org/10.15554/pcij.01011997.76.86

EN 1992-1-1. (2004). *EN 1992-1-1 Eurocode 2. Design of concrete structures. Part 1-1: General rules and rules for buildings*. European Committee for Standardization. https://www.phd.eng.br/wp-content/uploads/2015/12/en.1992.1.1.2004.pdf

Jokūbaitis, A., Marčiukaitis, G., & Valivonis, J. (2016). Influence of technological and environmental factors on the behaviour of the reinforcement anchorage zone of prestressed concrete sleepers. *Construction and Building Materials, 121*, 507–518. https://doi.org/10.1016/j.conbuildmat.2016.06.025

Jokūbaitis, A., Marčiukaitis, G., & Valivonis, J. (2017). Analysis of reinforcement anchorage zone behavior of prestressed concrete elements under static and cyclic loads. *Procedia Engineering, 172*, 457–464. https://doi.org/10.1016/j.proeng.2017.02.028

Jokūbaitis, A., Marčiukaitis, G., & Valivonis, J. (2020a). Bond of bundled strands under static and cyclic load and freezing-thawing effect. *Engineering Structures, 208*, 1–11. https://doi.org/10.1016/j.engstruct.2019.109922

Jokūbaitis, A., Marčiukaitis, G., & Valivonis, J. (2020b). Experimental research on the behavior of the rail seat section of different types of prestressed concrete sleepers. *Materials, 13*(11), 1–22. https://doi.org/10.3390/ma13112432

Jokūbaitis, A., Marčiukaitis, G., Valivonis, J., & Strauss, A. (2018). Influence of cyclic loading and frost on the behavior of bond of three-wire strand. *Structural Concrete, 19*(5), 1363–1375. https://doi.org/10.1002/suco.201700245

Jokūbaitis, A., & Valivonis, J. (2022). An analysis of the transfer lengths of different types of prestressed fiber-reinforced polymer reinforcement. *Polymers, 14*(19), 3931. https://doi.org/10.3390/polym14193931

Jokūbaitis, A., Valivonis, J., & Marčiukaitis, G. (2016). Analysis of strain state and cracking of concrete sleepers. *Journal of Civil Engineering and Management, 22*(4), 564–572. https://doi.org/10.3846/13923730.2016.1147494

Krem, S. (2013). Bond and flexural behaviour of self consolidating concrete beams reinforced and prestressed with FRP Bars [PhD Thesis]. University of Waterloo.

Krem, S. S., & Soudki, K. A. (2018). Bond behaviour of CFRP bars prestressed in self-consolidating concrete beams. *ACI Symposium Paper, 327*, 1–20.

Lu, Z., Boothby, T. E., Bakis, C. E., & Nanni, A. (2000). Transfer and development lengths of FRP prestressing tendons. *PCI Journal, 45*(2), 84–95. https://doi.org/10.15554/pcij.03012000.84.95

Mahmoud, Z. I. (1997). Bond characteristics of fibre reinforced polymers prestressing reinforcement [PhD Thesis]. Alexandria University.

Mahmoud, Z. I., Rizkalla, S. H., & Zaghoul, E. E. R. (1999). Transfer and development lengths of carbon fiber reinforced polymers prestressing reinforcement. *ACI Structural Journal, 96*(4), 594–602.

MC 1990, & Comite Euro-International du Beton. (1991). *CEB-FIP Model Code 1990*. Thomas Telford.

MC 2010, & Internationa Federation of Structural Concrete. (2012). *fib Bulletin 65: Model Code 2010,* Final draft. Ernst & Sohn.

Mitchell, D., Cook, W. D., & Tham, T. (1993). Influence of high strength concrete on transfer and development length of pretensioning strand. *PCI Journal, 38*(3), 52–66. https://doi.org/10.15554/pcij.05011993.52.66

Nanni, A., & Tanigaki, M. (1992). Pretensioned prestressed concrete members with bonded fiber reinforced plastic tendons: Development and flexural bond lengths (Static). *ACI Structural Journal, 89*(4), 433–441.

Nanni, A., Utsunomiya, T., Yonekura, H., & Tanigaki, M. (1992). Transmission of prestressing force to concrete by bonded fiber reinforced plastic tendons. *ACI Structural Journal, 89*(3), 335–344.

Wang, L., Zhang, J., Xu, J., & Han, Q. (2018). Anchorage systems of CFRP cables in cable structures—A review. *Construction and Building Materials, 160*, 82–99. https://doi.org/10.1016/j.conbuildmat.2017.10.134

Author Information

Aidas Jokūbaitis
Department of Reinforced Concrete Structures and Geotechnics,
Faculty of Civil Engineering,
Vilnius Gediminas Technical University
Sauletekio av. 11, LT-10223 Vilnius, Lithuania
Contact e-mail: *aidas.jokubaitis@vilniustech.lt*

Juozas Valivonis
Department of Reinforced Concrete Structures and Geotechnics,
Faculty of Civil Engineering,
Vilnius Gediminas Technical University
Sauletekio av. 11, LT-10223 Vilnius, Lithuania

To cite this article:

Jokubaitis, A. & Valivonis, J. (2022). An analysis of flexural bond length and anchorage length of prestressed fiber reinforced polymer reinforcement. *The Eurasia Proceedings of Science, Technology, Engineering & Mathematics (EPSTEM), 21,* 484-499.

Appendix A

Table A1. Experimental data of prestressed CFCC strands

References	Specimen No	FRP Type	FRP Surface	Specimen Type	Shear Reinforcement	c, mm	Ø, mm	A_p, mm^2	E_p, GPa	f_c, MPa	f_{se}, MPa	f_{pu}, MPa	L_t, mm	L_{fb}, mm	L_a, mm	Mode of failure
(Domenico, 1995; Domenico et al., 1998)	B6	CFCC 7-wire Strand	Helical plain	T Beam	Yes	50	12.5	76	137	68.3	848	2632	126.5	573.5	700	Rupture
	B7			T Beam	Yes	50	12.5	76	137	68.3	875	2674	148.5	401.5	550	Rupture
	B8			T Beam	Yes	50	12.5	76	137	59	794	2305	149.5	300.5	450	Shear/bond slip
	D10			T Beam	Yes	75	12.5	76	137	59	837	2120	167.5	282.5	450	Shear/bond slip
	C9			T Beam	Yes	50	12.5	76	137	64	905	2120	147.5	302.5	450	Shear/bond slip
	BT7			Beam	Yes	50	12.5	76	137	37	1285	2120	400	240.0	640	Bond slip
	BT8			Beam	Yes	50	12.5	76	137	37	1244	2120	375	225.0	600	Bond slip
	A3			T Beam	Yes	50	15.2	113.6	137	57.8	734	2168	223	477.0	700	Bond slip
	D5			T Beam	Yes	75	15.2	113.6	137	57.8	809	2150	200.5	499.5	700	Rupture
	C4			T Beam	Yes	50	15.2	113.6	137	60.5	1074	2150	232	468.0	700	Shear/bond slip
(Mahmoud, 1997; Mahmoud et al., 1999)	BT11	CFCC 7-wire Strand	Helical plain	Beam	Yes	45	10.5	55.7	140	41	1203	1934	305	325.0	630	Rupture
	BT12			Beam	Yes	45	10.5	55.7	140	41	1200	1577	312.5	217.5	530	Bond slip
	BT13			Beam	Yes	45.0	10.5	55.7	140	41	1237	2168	312.5	317.5	630	Bond slip
	BT14			Beam	Yes	45.0	10.5	55.7	140	41	1237	1906	312.5	267.5	580	Bond slip
	BT7			Beam	Yes	50.0	12.5	76.0	141	37	1306	1855	400.0	240.0	640	Bond slip
	BT8			Beam	Yes	50.0	12.5	76.0	141	37	1300	1815	375.0	225.0	600	Bond slip
	BT9			Beam	Yes	50.0	12.5	76.0	141	37	1290	1700	360.0	190.0	550	Bond slip
	BT10			Beam	Yes	50.0	12.5	76.0	141	37	1310	1616	360.0	140.0	500	Bond slip
	BT15a			Beam	Yes	49.0	12.5	76.0	141	41	1000	1924	300.0	400.0	700	Rupture
	BT15b			Beam	Yes	50.0	12.5	76.0	141	41	1000	1879	300.0	300.0	600	Rupture
	BT16a			Beam	Yes	49.0	12.5	76.0	141	41	984	1853	295.0	255.0	550	Bond slip
	BT16b			Beam	Yes	50.0	12.5	76.0	141	41	984	2033	295.0	305.0	600	Rupture
	BT19			Beam	No	50.0	12.5	76.0	141	34	1215	2100	500.0	450.0	950	Rupture
	BT20			Beam	No	50.0	12.5	76.0	141	34	1215	1830	450.0	300.0	750	Rupture
	BT1			Beam	Yes	60.0	15.2	113.6	138	46	905	1814	365.0	435.0	800	Bond slip
	BT2			Beam	Yes	60.0	15.2	113.6	138	46	905	1916	355.0	445.0	800	Bond slip
	BT3			Beam	Yes	60.0	15.2	113.6	138	43	1200	2150	392.5	407.5	800	Rupture
	BT4			Beam	Yes	60.0	15.2	113.6	138	43	1223	2170	387.5	362.5	750	Slip/rupture
	BT5			Beam	Yes	60.0	15.2	113.6	138	43	1232	1756	400.0	200.0	600	Bond slip
	BT6			Beam	Yes	60.0	15.2	113.6	138	43	1223	1720	400.0	200.0	600	Bond slip
	BT17a			Beam	No	59.0	15.2	113.6	138	33	1165	1600	650.0	250.0	900	Bond slip
	BT17b			Beam	No	60.0	15.2	113.6	138	33	1165	1744	650.0	450.0	1100	Bond slip
	BT18			Beam	No	60.0	15.2	113.6	138	33	1170	1932	600.0	650.0	1250	Bond slip
	BT21			Beam	No	60.0	15.2	113.6	138	31	979	2260	510.0	840.0	1350	Rupture
	BT22a			Beam	No	59.0	15.2	113.6	138	31	971	1734	490.0	510.0	1000	Slip/rupture
	BT22b			Beam	No	60.0	15.2	113.6	138	31	971	1618	490.0	410.0	900	Bond slip

Table A2. Experimental data of prestressed CFRP bars

References	Specimen No	FRP Type	FRP Surface	Specimen Type	Shear Reinforcement	c, mm	O, mm	A_p, mm^2	E_p, GPa	f_c, MPa	f_{se}, MPa	f_{pu}, MPa	L_t, mm	L_{fb}, mm	L_a, mm	Mode of failure
(Lu et al., 2000)	CL	CFRP Leadline tendon	Spirally Indented	Beam	No	40.6	7.9	47.1	171	45.4	1241	2208	421.6	670.4	1092	
	CS			Beam	No	40.6	7.9	50.3	161	44.1	1006.6	1823	408.9	758.1	1167	
(Mahmoud, 1997; Mahmoud et al., 1999)	BL1	CFRP Leadline tendon	Spirally Indented	Beam	Yes	35.0	8.0	46.1	147	50	1068	1870	452.5	347.5	800	Bond slip
	BL2			Beam	Yes	35.0	8.0	46.1	147	50	1078	1850	462.5	337.5	800	Bond slip
	BL3			Beam	Yes	35.0	8.0	46.1	147	46	1082	1753	480	320	800	Bond slip
	BL4			Beam	Yes	35.0	8.0	46.1	147	46	1082	1764	480	320	800	Bond slip
	BL5			Beam	Yes	35.0	8.0	46.1	147	41	1255	2129	620	580	1200	Bond slip
	BL6			Beam	Yes	35.0	8.0	46.1	147	41	1227	1420	625	175	800	Bond slip
	BL7			Beam	Yes	35.0	8.0	46.1	147	41	1248	1820	610	390	1000	Bond slip
	BL8			Beam	Yes	35.0	8.0	46.1	147	41	1248	1700	625	375	1000	Bond slip
	BL9			Beam	No	36.0	8.0	46.1	147	37	1100	2655	700	1200	1900	Rupture
	BL10			Beam	No	36.0	8.0	46.1	147	37	1100	2200	700	700	1400	Bond slip
	BL11			Beam	No	36.0	8.0	46.1	147	52	1400	3000	600	700	1300	Slip/rupture
	BL12a			Beam	No	36.0	8.0	46.1	147	52	1365	2770	500	600	1100	Bond slip
	BL12b			Beam	No	36.0	8.0	46.1	147	52	1365	2965	500	800	1300	Rupture
	PL1			Prism	No	35.0	8.0	46.1	147	34	1123	1777	490	260	750	Bond slip
	PL2			Prism	No	35.0	8.0	46.1	147	34	1123	1247	480	270	750	Bond slip
	PL3			Prism	No	40.0	8.0	46.1	147	31	1340	2073	540	210	750	Bond slip
	PL4			Prism	No	40.0	8.0	46.1	147	31	1340	2311	525	225	750	Slip/rupture
(Ehsani et al., 1997)	CL-1 (J)	CFRP Leadline tendon	Spirally Indented	Beam	No	64.7	7.9	46.5	150	46	1013	1847	432	965	1397	Bond slip
(Krem, 2013; Krem et al., 2018)	I-SCC30-1	CFRP Bar	Sanded	Beam	Yes	38.1	12.7	126.7	144	62.1	549	1360	306	794	1100	Pullout
	I-SCC30-2			Beam	Yes	38.1	12.7	126.7	144	62.1	534	1892	302	948	1250	Rupture
	I-SCC30-3			Beam	Yes	38.1	12.7	126.7	144	49.6	626	1804	337	1013	1350	Pullout/Rupture
	I-SCC30-4			Beam	Yes	38.1	12.7	126.7	144	49.6	604	1187	320	1180	1500	Rupture
	II-SCC45-1			Beam	Yes	38.1	12.7	126.7	144	70.9	750	1332	534	566	1100	Pullout
	II-SCC45-2			Beam	Yes	38.1	12.7	126.7	144	70.9	794	1509	516	734	1250	Pullout
	II-SCC45-3			Beam	Yes	38.1	12.7	126.7	144	70.9	776	1412	515	835	1350	Pullout
	II-SCC45-4			Beam	Yes	38.1	12.7	126.7	144	70.9	741	1669	487	1013	1500	Rupture
	III-SCC60-1			Beam	Yes	38.1	12.7	126.7	144	62.1	932	1302	669	431	1100	Pullout
	III-SCC60-2			Beam	Yes	38.1	12.7	126.7	144	62.1	995	1473	733	617	1350	Pullout
	III-SCC60-3			Beam	Yes	38.1	12.7	126.7	144	49.6	920	1531	662	838	1500	Pullout
	III-SCC60-4			Beam	Yes	38.1	12.7	126.7	144	49.6	974	1787	672	1028	1700	Pullout/Rupture
	IV-N30-1			Beam	Yes	38.1	12.7	126.7	144	64.5	563	1854	275	1075	1350	Rupture
	IV-N60-2			Beam	Yes	38.1	12.7	126.7	144	64.5	1076	1616	527	723	1250	Pullout
	IV-N60-3			Beam	Yes	38.1	12.7	126.7	144	64.5	1026	1817	545	805	1350	Rupture
	IV-N60-4			Beam	Yes	38.1	12.7	126.7	144	64.5	1052	1859	534	966	1500	Rupture

Table A3. Experimental data of prestressed AFRP bars

References	Specimen No	FRP Type	FRP Surface	Specimen Type	Shear Reinforcement	ς, mm	$\emptyset$, mm	A_p, mm^2	E_p, GPa	f_c, MPa	f_{se}, MPa	f_{pu}, MPa	L_t, mm	L_{fb}, mm	L_d, mm	Mode of failure
(Ehsani et al., 1997)	AA-1 (D)	AFRP Arapee	Smooth	Beam	No	63.7	9.9	38.1	128	44.5	1061	2448	267	749	1016	
	AF-3 (J)	AFRP Fibra	Smooth-braided	Beam	No	63.4	10.4	83.2	48	43	717	1434	381	483	864	
	AT-3 (J)	AFRP Technora	Rough	Beam	No	64.9	7.4	43.2	69	46.4	841	1724	254	610	864	
	AT-3 (D)		Rough	Beam	No	64.9	7.4	43.2	69	47.1	841	1724	381	483	864	
(Lu et al., 2000)	AT	AFRP Technora	Rough	Beam	No	40.6	7.9	50.3	45	47.1	910	1710	368	582	950	
(Nanni et al., 1992; Nanni & Tanigaki, 1992)	A2-1	AFRP Tendon 2-K64	Braided (Smooth)	Beam	No	66	8	42	76	37.4	295	1133	300	650	950	Slip/split crack
	A2-2(J)			Beam	No	66	8	42	76	37.5	295	1126	300	700	1000	Slip/split crack
	A2-2(F)			Beam	No	66	8	42	76	38.4	288	1095	300	800	1100	Crushing/shear failure
	A2-S3(J)			Beam	Yes	66	8	42	76	38.6	288	1362	200	750	950	Crushing/shear failure
	A2-S3(F)			Beam	Yes	66	8	42	76	38.7	288	1442	200	650	850	Slip/split crack
	A2-S4(F)			Beam	Yes	66	8	42	76	33.1	650	1674	400	550	950	Concrete crush
	A2-S4(J)			Beam	Yes	66	8	42	76	33.4	650	1843	400	450	850	Concrete crush
	B1-1(F)	AFRP Tendon 1-K128		Beam	No	64	12	90	68	37.8	272	1163	400	650	1050	Crushing/shear failure
	B1-1(J)			Beam	No	64	12	90	68	37.9	272	1066	400	550	950	Slip/split crack
	B1-2(F)			Beam	No	64	12	90	68	35.8	272	1081	400	600	1000	Crushing/shear failure (slip/split crack)
	B1-2(J)			Beam	No	64	12	90	68	38.6	272	1021	400	600	1000	Crushing/shear failure
	B1-S3(J)			Beam	Yes	64	12	90	68	37.6	276	1271	300	800	1100	Concrete crush
	B1-S3(F)			Beam	Yes	64	12	90	68	37.8	276	1253	300	650	950	Concrete crush
	B1-S6(J)			Beam	Yes	64	12	90	68	38.0	276	1269	300	550	850	Bond slip
	B1-S6(F)			Beam	Yes	64	12	90	68	38.1	276	1336	300	600	900	Slip/split crack
	B1-S7(F)			Beam	Yes	64	12	90	68	33.7	607	1463	450	500	950	Bond slip
	B1-S7(J)			Beam	Yes	64	12	90	68	34.0	607	1525	450	550	1000	Slip/split crack
	B2-S1(J)	AFRP Tendon 2-K128		Beam	Yes	64	12	90	68	38.9	258	1092	400	650	1050	Crushing/shear failure
	B2-S1(F)			Beam	Yes	64	12	90	68	39.0	258	1144	400	550	950	Slip/split crack
	C1-S4(F)	AFRP Tendon 1-K256		Beam	Yes	62	16	180	63	34.3	593	1383	550	500	1050	Slip/split crack
	C1-S4(J)			Beam	Yes	62	16	180	63	34.6	593	1370	550	600	1150	Concrete crush (slip/split crack)
	C1-S6/1			Beam	Yes	62	16	180	63	31.3	607	1406	600	650	1250	Slip/split crack
	C1-S6/2			Beam	Yes	62	16	180	63	31.9	607	1396	600	650	1250	Concrete crush
	C1-S7/1			Beam	Yes	62	16	180	63	31.6	607	1460	550	700	1250	Concrete crush
	C1-S7/2			Beam	Yes	62	16	180	63	32.2	607	1284	550	480	1030	Concrete crush
	D1-1(J)	AFRP Tendon 1-K128S	Sanded	Beam	No	63	13.5	90	68	39.0	565	1347	250	800	1050	Crushing/shear failure
	D1-1(F)			Beam	No	63	13.5	90	68	39.1	565	1272	250	700	950	Crushing/shear failure
	D1-S3(J)			Beam	Yes	63	13.5	90	68	39.2	565	1814	200	650	850	Concrete crush
	D1-S3(F)			Beam	Yes	63	13.5	90	68	39.4	565	1876	200	500	700	Concrete crush

The Eurasia Proceedings of Science, Technology, Engineering & Mathematics (EPSTEM)
ISSN: 2602-3199

The Eurasia Proceedings of Science, Technology, Engineering & Mathematics (EPSTEM), 2022

Volume 21, Pages 500-505

IConTES 2022: International Conference on Technology, Engineering and Science

Design of a Reversible Full Adder Using Quantum Cellular Automata

Sourabh T
PES University

Wrileena SANYAL
PES University

Rashmi SEETHUR
PES University

Abstract: Contemporary times holds a substantial hurdle in the designing of chips and ICs due to the roadblocks in the nanotech scaling of transistors, which is an obvious reason for Moore's Law to be working at a slower pace. The CMOS, VLSI technology imposes serious challenges when it enters the nano-domain, leading to the need of an innovation in nanotech scale. Quantum Dot Cellular Automata (QDCA or QCA) is a novel emerging transistor-less revolution for computation in the nanotech order. Besides this, irreversibility is a major concern in digital computation due to the loss of information. Therefore, here a reversible methodology is followed to address the problem of power dissipation. The purpose of this paper is to present a novel reversible full adder (RFA) of complexity 123 cells, 1.5 delay and area of 0.11um2 is introduced using single layer cross over coplanar scheme, employing the demonstrated adder universal basic gates are implemented. On the basis of this adder we construct a 3-bit Comparator with a delay of 4.25 factors and cell count of 581.

Keywords: QCA, Reversible, gates, Reversible Full Adder(RFA), Power dissipation

Introduction

The notion of 'More Moore' talks about the persistent scaling of silicon-based CMOS transistors (Haron & Hamdioui , 2008). More and more a number of transistors can now be integrated on a single chip, but this has led to its own disadvantages, such as increase in leakage and tunneling current due to shrinking size (Haron & Hamdioui , 2008) and high-power dissipation. A reversible logic gate is one where there's no loss of energy. It has a uniform number of inputs and outputs. Following the bijective algorithm, it performs one to one mapping. The inputs or the outputs can easily be retrieved from one another and the main advantage is its almost zero power dissipation (Sen et al., 2014). The need to balance the number of inputs and outputs owing to Lindauer's principle (Sen et al., 2014) garbage outputs are utilized.

Reversible circuits are obtained from reversible gates. A reversible gate existing in nature is a NOT gate. Due to advancements in highly compact and dense nanoscale circuits, QCA technology is a viable alternative to Very Large-Scale Integration (VLSI) and Complementary Metal-Oxide Semiconductor (CMOS) technology. As a result, QCA technology operates at very low power and has a high switching speed in computational arithmetic and logical operations. (B.S et al ., 2021). Hence due to the above-mentioned reasons, reversible gates are often designed using QCA technology for the best results. The ensuing sections of this paper illustrates the fundamentals of QCA, discussion about some existing full adders in literature, presenting a reversible full adder designed using QCA technology on QCA Designer (ver 2.0.3), simulation and implementation of universal gates with the proposed RFA and a comparator has been designed using this reversible full adder as a building block.

Fundamentals of QCA

Cell

Four quantum dots and two extra electrons, which can represent binary data, make up a standard QCA cell (Hashemi et al., 2018). The dots are placed opposite to one another and represent two stable states of polarization, -1 for logic "0" and +1 for logic "1". Polarization of one cell depends on the polarization of the other (Figure 2.1a). QCA wire propagates the input to the output. (Figure 2.1b)

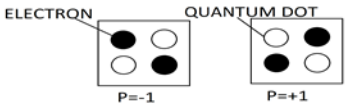

Fig 2.1a

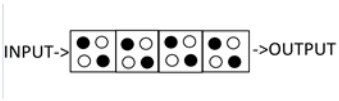

Fig 2.1b

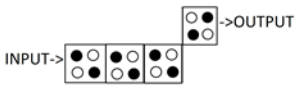

Fig 2.1c

Basic Gates in QCA

The operation of the five input majority gate(Figure 2.2a) is described by the formula: OUT=MAJ5(A, B, C, D , E) = ABC +ABD +ABE +ACD+ACE +ADE+BCD+BCE+BDE+CDE [4] and Maj=MAJ3(a,b,c) = ab+bc+ac, defines the functionality of 3-input majority gate (Abbasizadeh , & Mosleh , 2020) (Figure 2.2b). This gate behaves as an OR gate when the third output is changed to polarization state +1 and the same behaves as an AND gate if it is polarized to -1.

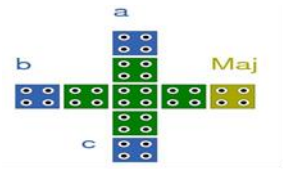

Figure 2.2a. MAJ3 gate

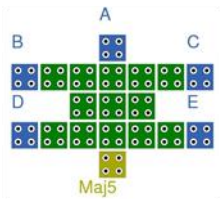

Figure 2.2b. MAJ5 gate

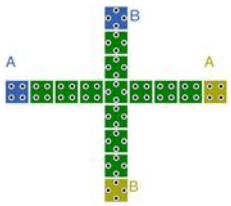

Figure 2.2c. Coplanar Crossover

Coplanar Crossover in QCA

Coplanar crossing occurs when two wires cross each other. The vertical cells need to be rotated by 45 degrees in order to propagate the correct information (Askari , & Taghizadeh , 2011) A is the input that goes to Y and B is the input that goes to X. In order for the input to be transmitted correctly, cells in the vertical plane should be rotated by 45 degrees.

Reversible Gates and Adders

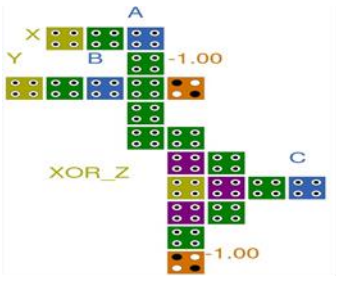

Figure 3. Toffoli gate

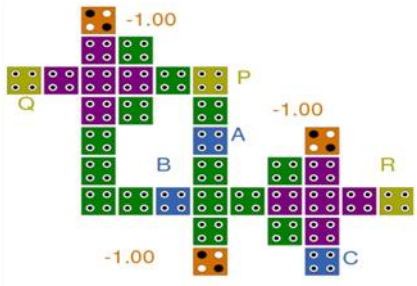

Figure 3b. Peres gate

The reason to work with reversible circuits is due to its minimum energy dissipation and relatively higher operating speed. Toffoli (Fig 3a), Peres (Fig 3b), Feyman, Double Feyman, Fredkin gate, CNOT are some of the standard reversible gates. The standard Toffoli and Peres gates are presented in (Patidar & Gupta , 2021 ; Bilal et al , 2017) respectively. In (Kianpour & Sabbaghi-Nadooshan , 2017 ; Taherkhani et al ., 2017) designed reversible gate is used to implement an 8-bit adder-subtractor. (Taherkhani et al ., 2017) has a lower garbage output and does require the rotation of cells in comparison with (Kianpour & Sabbaghi-Nadooshan , 2017). In

Thapliyal et al., (2013) and Islam & Islam (2005), an efficient reversible carry looks ahead adder is demonstrated as a vital unit in effective computing. Babu et al ., (2003), Islam & Islam (2003), Haghparast & Navi (2008), AnanthaLakshmi & Sudha (2013) are a few curated papers which investigate reversible gates. The table2 brings about the comparison between few existing reversible gates and the proposed RFA layout in terms of complexity, area and necessarily delay.

Proposed Full Adder

It so happens that preponderance of circuits performing addition and subtraction employs a full adder as a pre-dominant integrant. Its aptness to combine the binary digits along with a carry in to churn out a carry out and sum has earned its reputation as such. The proposed reversible full adder (Figure 4) comprises 3 important gates, namely MAJ3, MAJ5 and a XOR gate. As shown in fig 4a the RFA includes 2 garbage outputs (G1, G2) and the other two outputs are carried and sum. Besides the 3 evident inputs A, B, C the fourth is a constant input D=0 during which the circuit behaves as a full adder, and at D=1 the sum remains same but however the carry is inverted opposite to what happens in case of D=0. The functionality of the demonstrated adder is as follows:

- G1(garbage) = B
- G2(garbage) = C
- CARRY = Maj(A,B,C) ⊕ D = D(‗(MAJ(A,B,C))) + ‗D(MAJ(A,B,C))
- SUM = Maj(A,B,C, ‗(MAJ(A,B,C)), ‗(MAJ(A,B,C))) = ‗(MAJ(A,B,C))(A+B+C) + ABC

Table 1. Truth table of Adder

D	A	B	C	G1	G2	Carry	Sum
0	0	0	0	0	0	0	0
0	0	0	1	0	1	0	1
0	0	1	0	1	0	0	1
0	0	1	1	1	1	1	0
0	1	0	0	0	0	0	1
0	1	0	1	0	1	1	0
0	1	1	0	1	0	1	0
0	1	1	1	1	1	1	1

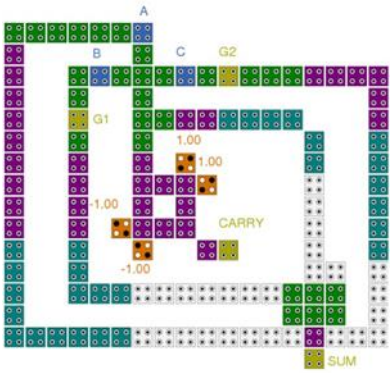

Figure 4. Proposed RFA

Implementation of the Proposed Full Adder as a Universal Gate

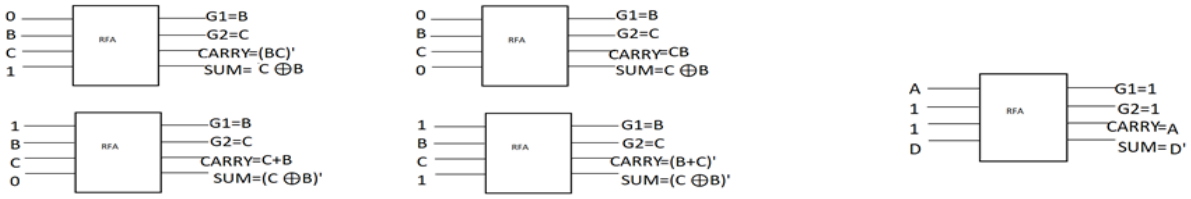

Figure 5a and Figure b. Implementation of the full adder as a universal gate

The proposed RFA is employed as different basic gates by changing the input combinations. The RFA performs all the universal operations: AND, NAND, OR, NOR, XOR, XNOR, Inverter. Figure 5a and Figure 5b shows the implementation of all the universal gates. Figure 5c shows the simulation of NAND and XOR gate.

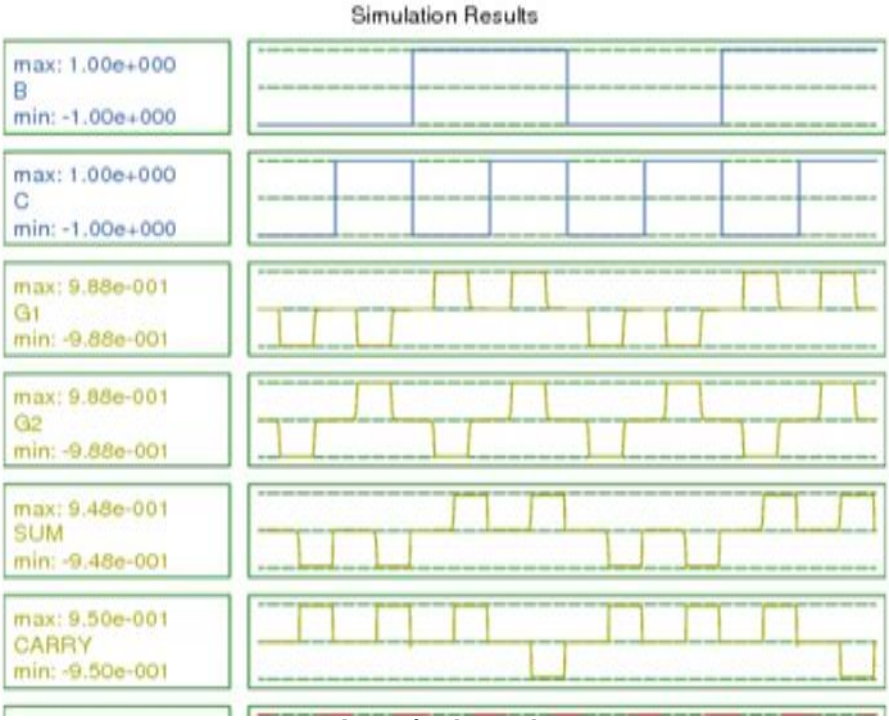

Figure 5c. Simulation for the combination 0 B C 1

Simulation and Comparison

Bi-stable approximation and coherence simulation engines are used to simulate and verify the proposed adder, signifying the adder's correctness. The RFA comprises 123 cells occupying an area of 0.11um2. The output SUM is delayed by a factor of 1.5, meanwhile the CARRY has a delay of about 0.5 following the negative edge of clock 1. The table (Table2) below demonstrates the performance of the few existing adders in the literature and the proposed one depending on the size, complexity (cell count), and latency. It is noticed that the proposed RFA is conducive with area, complexity, delay than the previous work (Hashemi et al ., 2018) although the functionality remains the same.

Table 2. Comparison of proposed RFA with existing

RFA	Area(um^2)	Cells	Delay
Kianpour & Sabbaghi- Nadooshan (2017	1.32	744	7.75
Taherkhani et al. (2017)	0.69	510	5
Thapliyal et al. (2013)	0.72	561	5
Babu et al. (2003)	0.47	305	3.2
Proposed RFA	0.11	123	1.5

Comparator

A comparator is an electronic circuit which compares the two applied inputs to generate a result indicating the relation between the inputs as greater, lesser or equal. A 3-bit comparator is designed using the proposed RFA. Comparators are used in applications in Analog to Digital converters and relaxation oscillations. The functionality of the comparator: X>Y is detected as the carry out of the third adder, X=Y is obtained by the AND operation of the sum obtained from 3 stages of the comparator, which is combined with X>Y through a nor gate to generate X<Y. The complexity (cell count) of the implemented comparator is 581with the area occupancy of 1.29 um2, and the delay factor of the comparator is 4.25

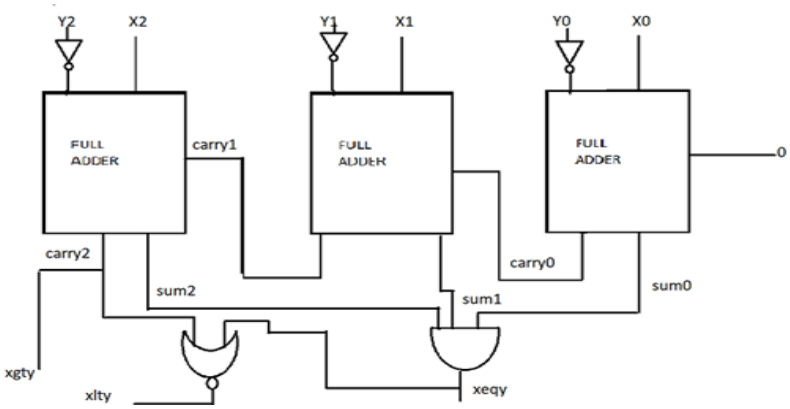

Fig.7a Comparator block diagram

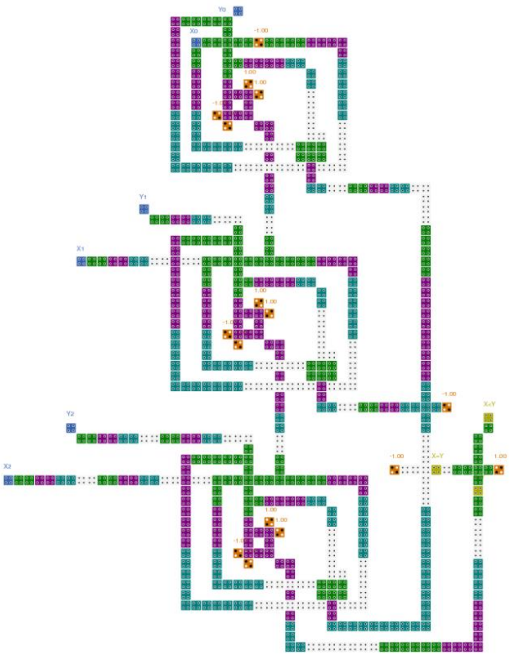

Fig.7b Comparator QCA implementation

Conclusion

This research work reports the design of a coplanar RFA for QCA applications. This design can easily be interfaced with other gates in larger designs. A comparator designed in this paper using the reversible full adder is found to have a delay at the cost complexity (cell count) 581. This can also be used as a universal gate as it is able to give results for every logical expression. The full adder design is more efficient than a lot of the existing designs as it occupies an area of 0.11um2 and a delay of only 1.5. This design has created the path to simplify creation of many other circuits accurately and has led to the advancement of QCA technology.

Scientific Ethics Declaration

The authors declare that the scientific ethical and legal responsibility of this article published in EPSTEM journal belongs to authors.

Acknowledgements or Notes

* This article was presented as an oral presentation at the International Conference on Technology, Engineering and Science (www.icontes.net) held in Antalya/Turkey on November 16-19, 2022.

References

Abbasizadeh, A., & Mosleh, M. (2020). Ultradense 2-to-4 decoder in quantum-dot cellular automata technology based on MV32 gate. *ETRI Journal, 42*(6), 912–921. https://doi.org/10.4218/etrij.2019-0068

AnanthaLakshmi, A. V., & Sudha, G. F. (2013). Design of a novel reversible full adder and reversible full subtractor. In *Advances in Computing and Information Technology* (pp. 623-632). Springer, Berlin, Heidelberg.

Askari, M., & Taghizadeh, M. (2011). Logic circuit design in nano-scale using quantum-dot cellular automata. *European Journal of Scientific Research, 48*(3), 516–526.

B.S., P., C., S., & B., S. (2021). Area and energy efficient QCA based decoder. *2021 6th International Conference on Communication and Electronics Systems (ICCES)*. https://doi.org/10.1109/icces51350.2021.9489011

Bilal, B., Ahmed, S., & Kakkar, V. (2017). Optimal realization of universality of peres gate using explicit interaction of cells in quantum dot cellular automata nanotechnology. *International Journal of Intelligent Systems and Applications, 9*(6), 75–84. https://doi.org/10.5815/ijisa.2017.06.08

Babu, H. M. H., Islam, M. R., Chowdhury, A. R., & Chowdhury, S. M. A. (2003). On the realization of reversible full-adder circuit. In *International Conference on Computer and Information Technology Vol. 2*, pp. 880-883.

Haghparast, M., & Navi, K. (2008). A novel reversible BCD Adder for nanotechnology based systems. *American Journal of Applied Sciences, 5*(3), 282–288. https://doi.org/10.3844/ajassp.2008.282.288

Haron, N. Z., & Hamdioui, S. (2008). Why is CMOS scaling coming to an END? *2008 3rd International Design and Test Workshop*. https://doi.org/10.1109/idt.2008.4802475

Hashemi, S., Rahimi Azghadi, M., & Navi, K. (2018). Design and analysis of efficient QCA reversible adders. *The Journal of Supercomputing, 75*(4), 2106–2125. https://doi.org/10.1007/s11227-018-2683-0

Islam, S., & Islam, M. R. (2005). Minimization of reversible adder circuits. *Asian Journal of Information Technology, 4*(12), 1146–1151. http://dro.deakin.edu.au/eserv/DU:30009225/islam-minimizationofreversible-2006.pdf

Kianpour, M., & Sabbaghi-Nadooshan, R. (2017). Novel 8-bit reversible full adder/subtractor using a QCA reversible gate. *Journal of Computational Electronics, 16*(2), 459–472. https://doi.org/10.1007/s10825-017-0963-1

Patidar,M., & Gupta, N., (2021). Optimal energy estimation of toffoli and peres gate design using quantum-dot cellular automata. *Res. Sq.*

Sen, B., Dutta, M., Some, S., & Sikdar, B. K. (2014). Realizing reversible computing in QCA framework resulting in efficient design of testable ALU. *ACM Journal on Emerging Technologies in Computing Systems, 11*(3), 1–22. https://doi.org/10.1145/2629538

Taherkhani, E., Moaiyeri, M. H., & Angizi, S. (2017). Design of an ultra-efficient reversible full Adder-subtractor in quantum-dot cellular automata. *Optik, 142*, 557–563. https://doi.org/10.1016/j.ijleo.2017.06.024

Thapliyal, H., Jayashree, H. V., Nagamani, A. N., & Arabnia, H. R. (2013). Progress in reversible processor design: A novel methodology for reversible carry look-ahead Adder. *Transactions on Computational Science XVII*, 73–97. https://doi.org/10.1007/978-3-642-35840-1_4

Author Information

Sourabh T
PES University
Karnataka, India
Contact e-mail:pes1ug20ec339@pesu.pes.edu

Wrileena Sanyal
PES University
Karnataka, India

Rashmi Seethur
PES University
Karnataka, India

To cite this article:

T, S., Sanyal, W., & Seethur, R., (2022). Design of a reversible full adder using quantum cellular automata. *The Eurasia Proceedings of Science, Technology, Engineering & Mathematics (EPSTEM), 21*, 500-505.

The Eurasia Proceedings of Science, Technology, Engineering & Mathematics (EPSTEM)
ISSN: 2602-3199

The Eurasia Proceedings of Science, Technology, Engineering & Mathematics (EPSTEM), 2022

Volume 21, Pages 506-516

IConTES 2022: International Conference on Technology, Engineering and Science

Water Remediation from Recalcitrant Pollution Using the Galvano-Fenton Process: A Modeling Approach of the Hydroxyl Radical Generation and the Energy Efficiency

Kaouther KERBOUA
Higher School of Industrial Technologies

Naoufel HADDOUR
Laboratoire Ampère, Ecole Centrale de Lyon

Intissar GASMI
Badji Mokhtar - Annaba University

Oualid HAMDAOUI
King Saud University

Abstract: The hydroxyl radical is the most powerful oxidant after fluorine, and is the key reactant of the advanced oxidation processes AOP. Monitoring the kinetics of formation and reaction of this short life species is one of the challenging tasks from an experimental point of view. Thus, modelling is suggested to be one efficient tool for a comprehensive and predictive study of AOPs, particularly the Galvano-Fenton process. In the present study, mathematical modelling is used to describe the kinetics of hydroxyl radical $HO^{\bullet}$ generation and organic substrate RO degradation within the Galvano-Fenton process, based on the spontaneous galvanic corrosion of iron waste and in situ ferrous ion catalyst generation. A range of typical absolute kinetic constants of 10^6 à 10^{10} $M^{-1}.s^{-1}$ is considered to characterize the attack of RO species by $HO^{\bullet}$. Phenol is presented as a model pollutant for a total mineralization model. The numerical simulations demonstration a quasi-linear evolution of hydroxyl radical production during the first stage of the Galvano-Fenton process. A comparison of the Galvano-Fenton process with the classic Fenton in terms of kinetics, and electro-Fenton in terms of energetic performance, revealed that the spontaneous galvanic generation of ferrous ions in the Galvano-Fenton process leads to a higher rate of the reaction a higher instantaneous concentration of ferric ions accompanying the release of hydroxyl radicals and hence a better oxidation efficiency, as well as a positive energy balance. A particular attention was given to the ratio of the degradation efficiency to the released energy.

Keywords: Advanced oxidation, Spontaneous corrosion, Kinetics, Chemical mechanism, Energy efficiency.

Introduction

The non-selective and highly reactive $^{\bullet}$OH radical (Haag 1992) is a chemical species of great interest in terms of degradation of organic pollutants and recalcitrant contaminants in aqueous solutions (Madhavan, Grieser, and Ashokkumar 2010; Pawar and Gawande 2015). Fenton mechanism though known since the thirties of the last century (Haber and Weiss 1932; Liochev and Fridovich 2002), remains an up to date technique still studied by several researchers (Shokri 2018; Xu, Chu, and Graham 2014). The Fenton reaction plays fundamental roles in in vivo and advanced oxidation processes (AOPs) (De Laat and Gallard 1999; De Laat and Le 2006; De Laat, Truong Le, and Legube 2004; Madhavan, Grieser, and Ashokkumar 2010), with both of its classic or modified forms included in the so-called “Fenton-based techniques”. The most challenging aspects of Fenton mechanism

concerns the resolution of one of the major limitations of classic Fenton process (Fe^{2+}/H_2O_2), which is the need to use stoichiometric amount of the catalyst, Fe(II) (Andreozzi, Apuzzo, and Marotta 2000). Indeed, the decomposition of hydrogen peroxide in the Fenton reaction is catalyzed by Fe(II). The Fe(II) oxidizes to Fe(III), while the hydroxyl radical is produced as illustrated in Figure 1a. Fe(III) is expected to regenerate Fe(II) through the reaction with hydrogen peroxide. However, this reaction is known to be very slow, owing to the formation of intermediate non-radical species such as $Fe(HO_2)^{2+}$. Hence, the classic Fenton process needs high amounts of Fenton's reagent to generate a high enough quantity of $HO^{\bullet}$, which implies economic and environmental issues. Moreover, the formation of Fe^{3+} ions and their slow transformation into Fenton's catalyst promote the occurrence of wasting reactions, directly impacting the overall efficiency of the process (Monteil et al. 2019).

Fenton based techniques such as photo-Fenton or electro-Fenton for the treatment of wastewater were studied by several scientists such as Martins et al. (Martins et al. 2006), Tarkwa et al. (Tarkwa et al. 2019), and more recently, Lu et al. (Lu et al. 2021). These techniques use additional energy and/or chemicals to generate highly oxidizing agents, mainly hydroxyl radicals. The required energy constitutes another techno-economic limitation of the Fenton based techniques.

The fundamental idea of Galvano Fenton process is rightly keeping on the advantage of in situ production of Fenton's reagents but without consuming energy, along with insuring continuity of the process. Galvano-Fenton process was designed by coupling classic Fenton to the principle of galvanic cell, with the objective of recovering solid iron waste in form of sacrificial anode and hence produce the ferrous iron catalyst in situ. In galvanic cell, the sacrificial anode is expected to corrode spontaneously under the effect of the higher standard potential of the cathode, selected among the more noble metals (Lower, 2012). In Galvano-Fenton process, this principle is harnessed by coupling iron to copper, the iron being of lower standard redox potential (Shreir, Jarman & Burstein 1994), its corrosion produces continuously and in situ ferrous ions, which are the catalyst of the Fenton mechanism. The Galvano-Fenton process clearly presents three major technical benefits. On one hand, it does not require external energy supply and it provides a catalyst for the targeted process, which is Fenton, preventing then the need of catalyst addition, on the other hand and especially at larger scale, it would serve as ecological solution for recovering solid iron wastes.

The present paper aims to numerically assess the performance of the Galvano-Fenton process based on the simultaneous immersion of electrodes in the electrolyte and the addition of hydrogen peroxide, with particular attention to an energetic parameter, namely, the ratios of hydroxyl radical production and degradation efficiency to the released energy. The Galvano-Fenton process is investigated in terms of the degradation of a model pollutant, namely phenol, until its total mineralization. It is studied based on the kinetics of formation and transformation of ferrous and ferric ions, the free radicals' generation, and the pollutant degradation. Furthermore, energetic insights are given, particularly for the comparison of the positive and negative energy balances presented by the electro-Fenton and the Galvano-Fenton processes, relating their respective performances in terms of the generation of hydroxyl radicals and phenol's degradation.

Method

Configuration of the Modelled Process

The Galvano-Fenton process is designed by immersing a galvanic cell of iron anode (sacrificial anode) and copper cathode within an acidified electrolyte, at the pH condition allowing the formation of ferrous ions according to the Pourbaix diagram. Hydrogen peroxide is added to the electrolyte while the spontaneous corrosion of iron occurs, provoking the Fenton reaction. The process is simulated considering a corrosion current of 300 µA, determined experimentally during the preliminary test described below. The current value is equivalent to a current density of 25 $\mu A/cm^2$ reported to the active surface of the anode of 12 cm^2. The Galvano-Fenton system is modeled by combining electrochemical reactions taking place at the anode and the cathode with chemical reactions related to the Fenton mechanism occurring in the bulk liquid volume. In the presence of phenol, a detailed oxidation mechanism is proposed in Table. 2, to describe the whole evolution of the reactions occring at the electrodes and in the electrolyte.

The Fenton based mechanism is validated experimentally using blank tests, i.e., in the absence of phenol. The test consists of immersing both electrodes in the acidified electrolyte at pH 3 using sulfuric acid (mother solution concentration 0.1 N, supplied from Sigma-Aldrich), and simultaneously adding hydrogen peroxide (mother solution concentration 30% v/v, purchased from Sigma-Aldrich) in initial concentration of 0.35 mM.

The electrolyte is stirred at 200 RPM to homogenize the mixture and promote displacement of ionic species between electrodes. The kinetics of Fe(III) is monitored over time using spectrophotometric measurements of absorbance at 303 nm ($\varepsilon = 2197\ \mathrm{L.mol^{-1}.cm^{-1}}$) (Merouani et al. 2010). Each preliminary blank test lasts 20 minutes with 1 min spaced regular sampling during the first 10 minutes, and 2 min spaced withdrawals during the rest of the time. The corrosion current is determined during the same test using A zero ammeter placed between both electrodes of the galvanic cell described in Table.1. The polarization curves have been also plotted using a galvanostat-potentiostat connected to the same cell, the corrosion current has been confirmed by this method as well, through the intersection of both Tafel's lines.

Table 1. Specifications of the Galvano-Fenton cell

Parameter	Specification
Electrodes form	rectangular smooth plates
Immersed electrodes surface	6 cm^2
Electrolyte volume	100 mL
Electrodes disposition	In parallel
Electrolyte nature	Acidified water (H_2SO_4)
pH	3
Electrical connection	External wire
Ionic displacement	Aided by a magnetic stirring
Initial concentration of hydrogen peroxide (In the presence of phenol)	0.186 mM
Initial concentration of hydrogen peroxide (blank test)	0.35 mM

Numerical Modelling

Iron constitutes the sacrificial electrode, Fe oxidizes to Fe^{2+} ($E^0 = -0.44$ V vs. SHE) according to Equation 1, in Table.2. At the cathode, the most probable reaction concerns the reduction of H^+ to form H_2 ($E^0 = 0$ V vs. SHE) according to Eq.2 in Table.2, owing to the acidity of the medium. This has been proven in a previous work conducted by our research group (Gasmi et al. 2020). The kinetics related to all of the electrochemical reactions are governed by Faraday's law (Z. Ahmad 2006), given in Equation (1), and describe the evolution of the C_k concentration of the species involved in the electrochemical reactions in a function of time.

$$\frac{dC_k}{dt} = \pm\frac{i_{corr}}{nFV} \tag{1}$$

n represents the valence number; it equals 2 for reaction 1 and 1 for reaction 2. *F* is Faraday's number, which equals 96,490 C/mol. i_{corr} represents the corrosion current, while *V* constitutes the volume of the electrolyte. Table 2. Electrochemical and chemical scheme of the possible reactions occurring at the electrodes and in the electrolyte by the Galvano Fenton-based processes in the presence of phenol; k_i is the absolute reaction constant of the i^{th} reaction. Adapted from (Bray 1931; Koprivanac and Lon, 2006; De Laat and Le 2006; Machulek Jr et al., 2009).

The chemical kinetic equations describing the evolution of the chemical mechanism occurring in the electrolyte are set based on the kinetics constant reported in previous table. Each reaction can be schematized according to Equation (2).

$$\sum_{k=1}^{K} v'_{ki} X_k \rightarrow \sum_{k=1}^{K} v''_{ki} X_k \tag{2}$$

v'_{ki} is the stoichiometric coefficient related to the kth species X_k within the ith chemical reaction. The kinetics rate related to the i^{th} reaction is expressed as reported in Equation (3).

$$r_i = k_i \prod_{k=1}^{K} [C_k]^{\vartheta'_{ki}} \tag{31}$$

k_i is the kinetic constant related to the i^{th} reaction occurring in the electrolyte in the presence of phenol among the 49 reported in Table 2 and is determined at the operating temperature of 25 °C in the present study.

	i	i^{th} Reaction	k_i	Unit of k_i
Anode	1	$Fe \rightarrow Fe^{2+} + 2e^-$	-	-
Cathode	2	$2\,H^+ + 2e^- \rightarrow H_2$	-	-
	3	$Fe^{2+} + H_2O_2 \rightarrow Fe^{3+} + OH^- + HO^\bullet$	6.3×10^{-2}	$mol^{-1}.m^3.s^{-1}$
	4	$Fe^{3+} + H_2O_2 \rightarrow Fe(HO_2)^{2+} + H^+$	3.1×10^{4}	$mol^{-1}.m^3.s^{-1}$
	5	$Fe(HO_2)^{2+} + H^+ \rightarrow Fe^{3+} + H_2O_2$	1.0×10^{7}	$mol^{-1}.m^3.s^{-1}$
	6	$Fe(HO_2)^{2+} \rightarrow Fe^{2+} + HO_2^\bullet$	2.3×10^{-3}	s^{-1}
	7	$H_2O_2 + HO^\bullet \rightarrow HO_2^\bullet + H_2O$	3.3×10^{4}	$mol^{-1}.m^3.s^{-1}$
	8	$HO_2^\bullet \rightarrow O_2^{\bullet-} + H^+$	1.58×10^{5}	s^{-1}
	9	$O_2^{\bullet-} + H^+ \rightarrow HO_2^\bullet$	1.0×10^{7}	$mol^{-1}.m^3.s^{-1}$
	10	$Fe^{2+} + HO^\bullet \rightarrow Fe^{3+} + OH^-$	3.2×10^{5}	$mol^{-1}.m^3.s^{-1}$
	11	$HO_2^\bullet + Fe^{2+} + H_2O \rightarrow Fe^{3+} + H_2O_2 + OH^-$	1.2×10^{3}	$mol^{-1}.m^3.s^{-1}$
	12	$HO_2^\bullet + Fe^{3+} \rightarrow Fe^{2+} + H^+ + O_2$	3.6×10^{2}	$mol^{-1}.m^3.s^{-1}$
	13	$O_2^{\bullet-} + Fe^{2+} + 2H_2O \rightarrow Fe^{3+} + H_2O_2 + 2\,OH^-$	1.0×10^{4}	$mol^{-1}.m^3.s^{-1}$
	14	$O_2^{\bullet-} + Fe^{3+} \rightarrow Fe^{2+} + O_2$	5.0×10^{4}	$mol^{-1}.m^3.s^{-1}$
	15	$HO^\bullet + HO^\bullet \rightarrow H_2O_2$	5.2×10^{6}	$mol^{-1}.m^3.s^{-1}$
	16	$HO_2^\bullet + HO_2^\bullet \rightarrow H_2O_2 + O_2$	8.3×10^{2}	$mol^{-1}.m^3.s^{-1}$
	17	$O_2^{\bullet-} + H^+ \rightarrow HO_2^\bullet$	1.0×10^{7}	$mol^{-1}.m^3.s^{-1}$
	18	$HO^\bullet + HO_2^\bullet \rightarrow O_2 + H_2O$	7.1×10^{6}	$mol^{-1}.m^3.s^{-1}$
	19	$HO^\bullet + O_2^{\bullet-} \rightarrow O_2 + OH^-$	1.01×10^{7}	$mol^{-1}.m^3.s^{-1}$
	20	$HO_2^\bullet + O_2^{\bullet-} + H_2O \rightarrow H_2O_2 + O_2 + OH^-$	9.7×10^{4}	$mol^{-1}.m^3.s^{-1}$
	21	$HO_2^\bullet + H_2O_2 \rightarrow O_2 + HO^\bullet + H_2O$	5.0×10^{-4}	$mol^{-1}.m^3.s^{-1}$
	22	$O_2^{\bullet-} + H_2O_2 \rightarrow O_2 + HO^\bullet + OH^-$	1.3×10^{-4}	$mol^{-1}.m^3.s^{-1}$
	23	$Fe^{2+} + {SO_4}^{2-} \rightarrow FeSO_4$	2.29×10^{8}	$mol^{-1}.m^3.s^{-1}$
	24	${SO_4}^{2-} + HO^\bullet \rightarrow {SO_4}^{\bullet-} + OH^-$	1.4×10^{4}	$mol^{-1}.m^3.s^{-1}$
	25	${HSO_4}^- + HO^\bullet \rightarrow {SO_4}^{\bullet-} + H_2O$	3.5×10^{2}	$mol^{-1}.m^3.s^{-1}$
	26	${SO_4}^{\bullet-} + H_2O \rightarrow H^+ + {SO_4}^{2-} + HO^\bullet$	3.0×10^{5}	s^{-1}
Electrolyte	27	${SO_4}^{\bullet-} + OH^- \rightarrow {SO_4}^{2-} + HO^\bullet$	1.4×10^{4}	$mol^{-1}.m^3.s^{-1}$
	28	${SO_4}^{\bullet-} + H_2O_2 \rightarrow {SO_4}^{2-} + H^+ + HO_2^\bullet$	1.2×10^{4}	$mol^{-1}.m^3.s^{-1}$
	29	${SO_4}^{\bullet-} + HO_2^\bullet \rightarrow {SO_4}^{2-} + H^+ + O_2$	3.5×10^{6}	$mol^{-1}.m^3.s^{-1}$
	30	${SO_4}^{\bullet-} + Fe^{2+} \rightarrow Fe^{3+} + {SO_4}^{2-}$	3.0×10^{5}	$mol^{-1}.m^3.s^{-1}$
	31	$FeSO_4 \rightarrow Fe^{2+} + {SO_4}^{2-}$	1.0×10^{10}	s^{-1}
	32	$Fe^{3+} + H_2O \rightarrow FeOH^{2+} + H^+$	2.9×10^{7}	s^{-1}
	33	$FeOH^{2+} + H^+ \rightarrow Fe^{3+} + H_2O$	1.0×10^{7}	$mol^{-1}.m^3.s^{-1}$
	34	$FeOH^{2+} + H_2O_2 \rightarrow Fe(OH){HO_2}^+ + H^+$	2.0×10^{3}	$mol^{-1}.m^3.s^{-1}$
	35	$Fe(OH){HO_2}^+ + H^+ \rightarrow FeOH^{2+} + H_2O_2$	1.0×10^{7}	$mol^{-1}.m^3.s^{-1}$
	36	$Fe(OH){HO_2}^+ \rightarrow Fe^{2+} + HO_2^\bullet + OH^-$	2.3×10^{-3}	s^{-1}
	37	$Ph + HO^\bullet \rightarrow DHCD^\bullet$	7.3×10^{6}	$mol^{-1}.m^3.s^{-1}$
	38	$DHCD^\bullet + H^+ \rightarrow Ph^\bullet + H_2O$	5.0×10^{5}	$mol^{-1}.m^3.s^{-1}$
	39	$DHCD^\bullet + O_2 \rightarrow CC + HO_2^\bullet$	1.5×10^{6}	$mol^{-1}.m^3.s^{-1}$
	40	$DHCD^\bullet + O_2 \rightarrow HQ + HO_2^\bullet$	5.0×10^{5}	$mol^{-1}.m^3.s^{-1}$
	41	$DHCD^\bullet + O_2 \rightarrow BQ + HO_2^\bullet$	5.0×10^{5}	$mol^{-1}.m^3.s^{-1}$
	42	$DHCD^\bullet + BQ \rightarrow Ph^\bullet + CC + HQ$	3.7×10^{6}	$mol^{-1}.m^3.s^{-1}$
	43	$2DHCD^\bullet \rightarrow Ph + CC$	5.0×10^{5}	$mol^{-1}.m^3.s^{-1}$
	44	$2DHCD^\bullet \rightarrow products$	5.0×10^{5}	$mol^{-1}.m^3.s^{-1}$
	45	$DHCD^\bullet + Ph^\bullet \rightarrow products$	5.0×10^{5}	$mol^{-1}.m^3.s^{-1}$
	46	$DHCD^\bullet + Ph^\bullet \rightarrow Ph + CC + HQ$	5.0×10^{5}	$mol^{-1}.m^3.s^{-1}$
	47	$Ph^\bullet + Ph^\bullet \rightarrow products$	1.0×10^{6}	$mol^{-1}.m^3.s^{-1}$
	48	$BQ + {O_2}^{\bullet-} \rightarrow HPH^\bullet + O_2$	1.0×10^{6}	$mol^{-1}.m^3.s^{-1}$
	49	$CC + HO^\bullet \rightarrow products$	1.1×10^{7}	$mol^{-1}.m^3.s^{-1}$
	50	$HQ + HO^\bullet \rightarrow products$	5.0×10^{6}	$mol^{-1}.m^3.s^{-1}$
	51	$BQ + HO^\bullet \rightarrow products$	1.2×10^{6}	$mol^{-1}.m^3.s^{-1}$

PH: phenol, C_6H_6O. DHCD•: dihydroxy cyclohexadienyl radical, $C_{12}H_{16}O_3$. PH•: phenyl radical, C_6H_5. HPH•: hydroxyphenyl radical, C_6H_4OH. CC: catechol, $C_6H_6O_2$. HQ: hydroquinone, $C_6H_6O_2$. BQ: benzoquinone $C_6H_4O_2$

The kinetics of apparition and the disappearance of a species X_k in the electrolyte is governed by Equation (4) for species involved in the electrochemical reactions:

$$\frac{d[X_k]}{dt} = \pm\frac{1}{nV}\frac{i_{corr}}{F} + \sum_{i=1}^{N}(v''_{ki} - v'_{ki})\, k_i \prod_{j=1}^{K}[X_j]^{\vartheta'_{ji}} \quad (4)$$

Equation (5) is applicable to species that are only implicated in the electrolytic reactions (Davis and Davis 2003).

$$\frac{d[X_k]}{dt} = \sum_{i=1}^{N}(v''_{ki} - v'_{ki})\, k_i \prod_{j=1}^{K}[X_j]^{\vartheta'_{ji}} \quad (5)$$

The system of non-linear differential equations derived from Equations (1) to (5) is resolved using the fourth-order Runge–Kutta algorithm on Matlab with a fixed step of 1 s. The simulation is performed over 1200 s.

Results and Discussion

Validation of the Simulation

The preliminary blank tests performed in the absence of phenol allowed the validation of the chemical mechanism combining the electrochemical reactions occurring at the electrodes and the chemical reactions related to Fenton mechanism, occurring in the electrolyte, without considering the presence of an organic substrate susceptible to be attacked by the hydroxyl radicals. The validation is based on the experimental quantification of Fe(III) species, and the comparison with the predicted trend retrieved numerically.

The kinetics of Fe(III) was assessed experimentally using the Fricke dosimetry principle. Fig.1 reports the experimental results for the evolution of the concentration of Fe(III) species, as well as the simulation results, returning the total concentration of species containing Fe at its +3 oxidation state, and the concentration of each one of these species. The concentrations of Fe(II) species obtained by simulation are reported as well. The simulation curve of Fe(III) concentration obtained based on no cathodic regeneration of Fe^{2+}, the reactivity of sulfate ions and emergence of ferric complexes within the electrolyte solution is well correlated with the experimental results and shows a correlation coefficient based on Bravais-Pearson formula (Artusi, Verderio, and Marubini 2002) of 93.5%. The numerical model is then validated.

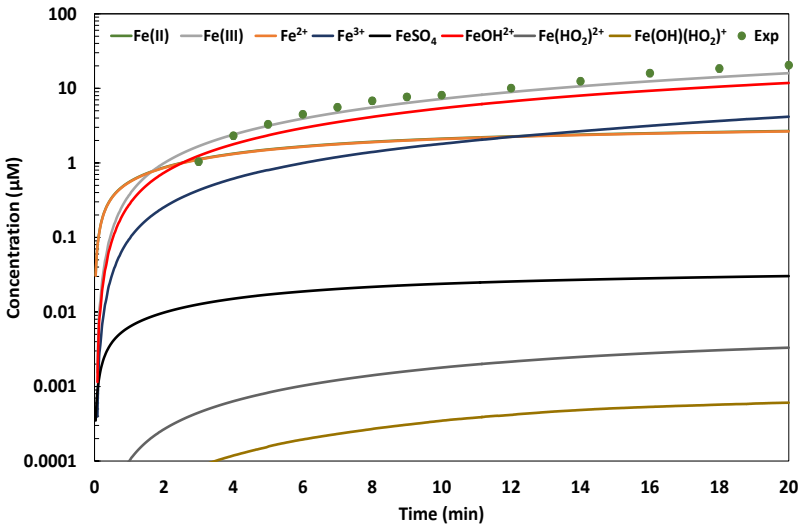

Figure 1. Evolution of Fe(III) concentration in experiment, and iron species concentrations obtained by simulation in function of time. Fe(II) and Fe^{2+} curves are superimposed because of the low $FeSO_4$ concentration. Concentration axis is in logarithmic scale

Hydroxyl Radical Production

Hydroxyl radical is characterized by the second highest redox potential after fluor, and has a non-selective character in terms of oxidized species. Advanced oxidation processes take advantage of both particularities of

hydroxyl radical to oxidize the organic molecules, notably the recalcitrant pollutant. In this part of the study, the validated numerical model is applied to simulate the evolution of the concentration of hydroxyl radical over 20 minutes of operation. The performance of the Galvano-Fenton degradation of pollutants, based on the generation of highly oxidative free radicals, principally $HO^{\bullet}$, is also compared to the performance of classic Fenton technique, considering a similar configuration and an initial concentration of added ferrous catalyst which is equivalent to the yield generated by galvanic corrosion over 20 min under the adopted conditions. Fig.2 reports these results in the presence of 2 µM of phenol.

This figure reveals that the kinetics of hydroxyl radical generation can be divided into two stages; the first stage would comprise the first 5 minutes starting from the beginning of the processes, while the second stage would correspond to the interval ranging from 5 to 20 min. During the first stage, the classic Fenton process results in a drastic increase of the concentration of $HO^{\bullet}$ in the electrolyte at the initial instant to the order of 10^{-8} mM. As soon as Fenton reagent and catalyst are added and put in contact, the rate of the H_2O_2 decomposition reaction strongly increases due to high concentrations of both reagent and catalyst. However, this scenario is only valid during the very beginning of the process, i.e., as long as the concentrations of H_2O_2 and Fe^{2+} are high. Once consumed, the concentration of H_2O_2 becomes limited, and the regeneration of Fe^{2+} becomes very slow, which inhibits the continuous release of $HO^{\bullet}$ during the second stage, and its concentration drops to less than 10^{-9} mM. Nevertheless, the high concentration of $HO^{\bullet}$ during the initial stage would strongly enhance the degradation process that would be decelerated afterward. In contrast, the Galvano-Fenton process is characterized by a quasi-linear increase of $HO^{\bullet}$ concentration during the first stage. At 5 min, it ends up at an order of magnitude of 10^{-9} mM. The concentration of $HO^{\bullet}$ continues its increase with the Galvano-Fenton process during the second stage and attains the highest concentration compared to the classic Feton process, with a value of 2.5×10^{-9} mM at 20 min.

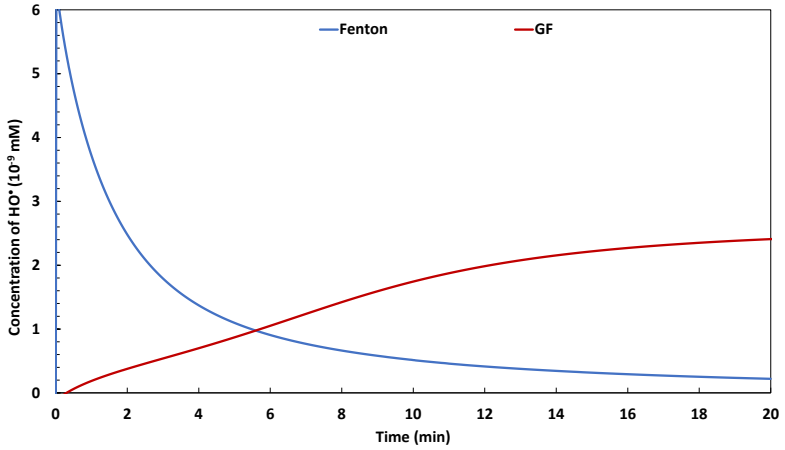

Figure 2. Evolutions of $HO^{\bullet}$ concentration in a function of time with classic Fenton and Galvano-Fenton processes in the presence of phenol at 2 µM.

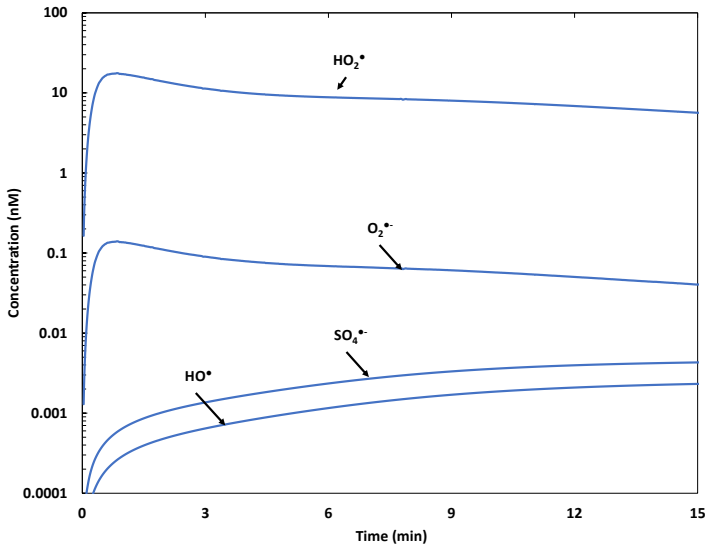

Figure 3. Analysis of the Galvano-Fenton technique in terms of the concentrations of free radicals.

We suggest inspecting the kinetics of the production of free radicals, namely, $HO^{\bullet}$, $HO_2^{\bullet}$, $SO_4^{\bullet-}$, and $O_2^{\bullet-}$, through the Galvano-Fenton process. Fig.3 reports the simulation results considering the addition of hydrogen peroxide at the initial time. The concentration of $HO^{\bullet}$ is quasi-null at t_0. The highest concentration among the four aforementioned free radicals is reached by $HO_2^{\bullet}$. At the initial instant, its concentration is about 0.2 nM at the addition of the hydrogen peroxide. In terms of molar yields, $HO_2^{\bullet}$ remains the free radical with the highest concentration within the electrolyte, followed by $O_2^{\bullet-}$, then $SO_4^{\bullet-}$ and finally $HO^{\bullet}$. This is due to the high reactivity of hydroxyl radical, making its lifetime within the electrolyte very short and its instantaneous concentration relatively low.

Degradation of Phenol

In the presence of an organic molecule, the hydroxyl radical produced by the Galvano-Fenton process is expected to provoke an oxidative attack initiating a decomposition process. With phenol, this mechanism is susceptible to lead to complete mineralization, as described in Table 2. In this part of the study, the evolution of phenol's concentration in function of time starting from an initial concentration of 2 µM is tracked and reported in Fig.4.

The Galvano-Fenton process shows a null initial degradation rate of phenol, revealed by the horizontal tangent of the curve of concentration of phenol vs. time. This observation is explained by the absence of the ferrous ion catalyst at t_0. However, this lasts a few seconds, then the phenol concentration starts decreasing linearly between 0.5 and 6 min. The phenol concentration reaches then 0.5 µM, which is equivalent to 75% degradation. The linear evolution of the phenol degradation through the Galvano-Fenton process occurs in parallel to the linear increase of the hydroxyl radical concentration, resulting from the gradual release of Fe^{2+} in the electrolyte through galvanic corrosion. The achievement of a degradation rate exceeding 96% requires almost 12 min. The initial latency, due to the absence of the Fenton catalyst when the process is started, is probably the reason for the delay observed in terms of the performance of the Galvano-Fenton process for the degradation of phenol.

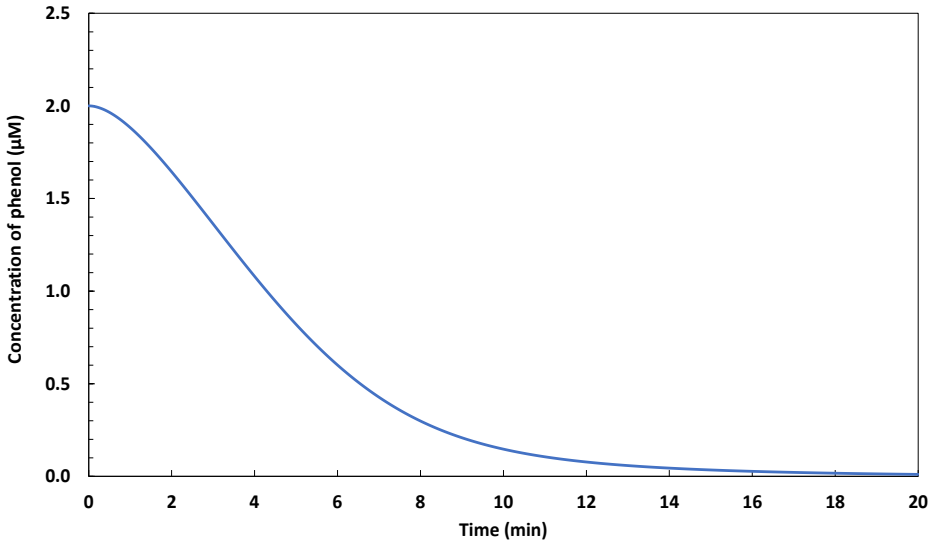

Figure 4. Evolution of the concentration of phenol in function of time with Galvano-Fenton process with an initial phenol concentration of 2 µM.

The mechanism of phenol degradation, which has been adopted in a previous work of our research group (Kerboua et al. 2021), is closely dependent on the release of free radicals in the electrolyte; hence, in Fig.5, we examine the evolution of the concentration of the intermediate species formed during phenol degradation using Galvano Fenton process, as described in Table 2. We notice that the concentration of the phenyl radical gradually increases in the case of the Galvano-Fenton process until it reaches a maximum value of 1.7 nM at 3 min. The same delay is observed in the evolution of the concentrations of the other intermediate species. For instance, the peak of the hydroxyphenyl radical concentration is observed at 3.6 min in the Galvano-Fenton process. Similarly, the maximum concentration of benzoquinone is reached at 5.5 min. The early apparition of the intermediate phenol degradation species reveals the most rapid degradation of phenol tending to its mineralization.

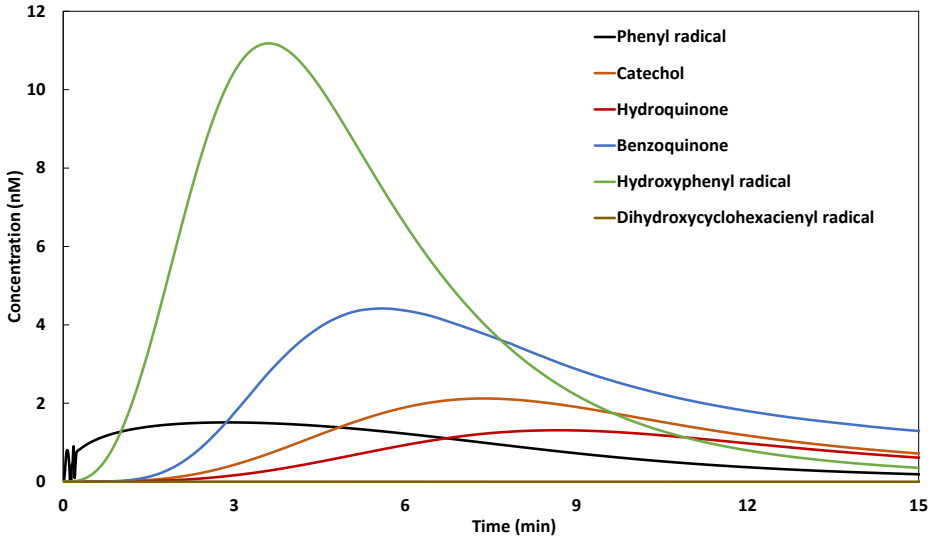

Figure 5. Kinetics of the formation of intermediate species from the degradation of phenol in the Galvano-Fenton process

Energetic Performance of the Technique

At present, we suggest relating the efficiency of the Galvano-Fenton to the energy release (Gasmi et al. 2021), compared to the efficiency of the electro-Fenton process to the energy consumption, considering similar conditions of spontaneous and forced electrochemical reactions. The polarization curves of the Fe-Cu galvanic cell within the Galvano-Fenton process with the configuration described earlier showed that the corrosion current is estimated at 298.75 µA for a corrosion potential of 0.277 V, which is equivalent to a maximum power of 82.75 mW. Considering an operating duration of 20 min, the total energy released by both configurations of the Galvano-Fenton process starting from the instant of the addition of H_2O_2would be to the order of 110.33 J.

In Fig.6, the ratios of the yield of hydroxyl radicals emerging over the process duration to the energy released by the Galvano-Fenton process is presented. In the same figure, we report the ratio of the yield of the produced hydroxyl radical in the electro-Fenton process, reported to the energy consumption using the same process. Conventionally, the energy release is expressed negatively. The figure demonstrates that with the Galvano-Fenton process, the ratio is estimated to be at 0.0311 nM per released Joule. On the opposite hand, an electro-Fenton process operating at the same conditions would produce 0.0059 nM per consumed Joule.

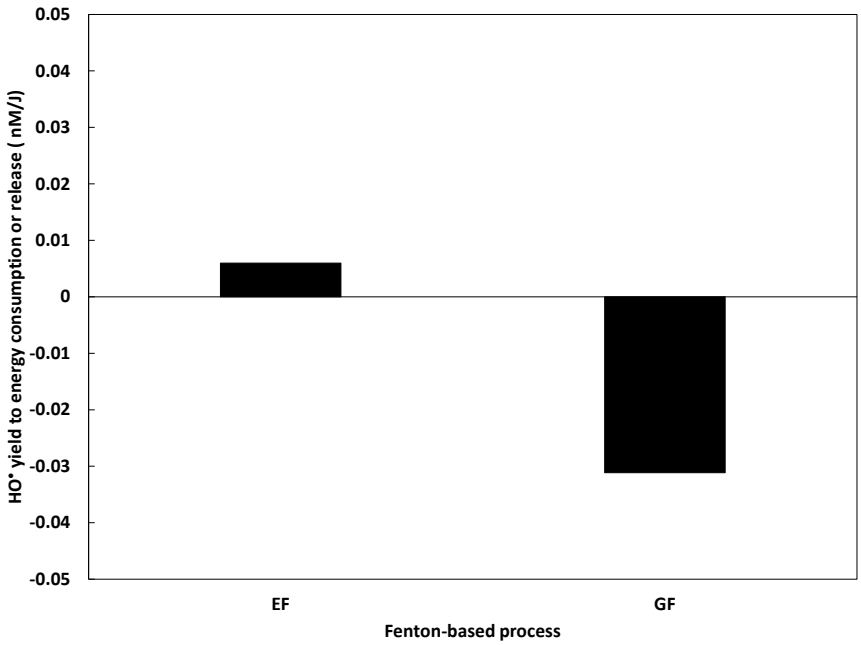

Figure 6. Ratios of the HO• yield to the consumed or released energy using Galvano-Fenton and Electro-Fenton processes.

In terms of phenol degradation efficiency, Fig.7 reports the ratio of the percentage of phenol degradation to the released or consumed energy when considering an initial phenol concentration of 2 µM. This figure shows that the Galvano-Fenton process can degrade 1.32% the initial phenol concentration by for each released Joule. The electro-Fenton process, however, would degrade 1.05% for each consumed joule. Overall, the Galvano-Fenton process, when treated as energetic systems, is characterized by a higher performance added to an energy release, in contrast, electro-Fenton process shows a lower performance and is associated with an energy consumption.

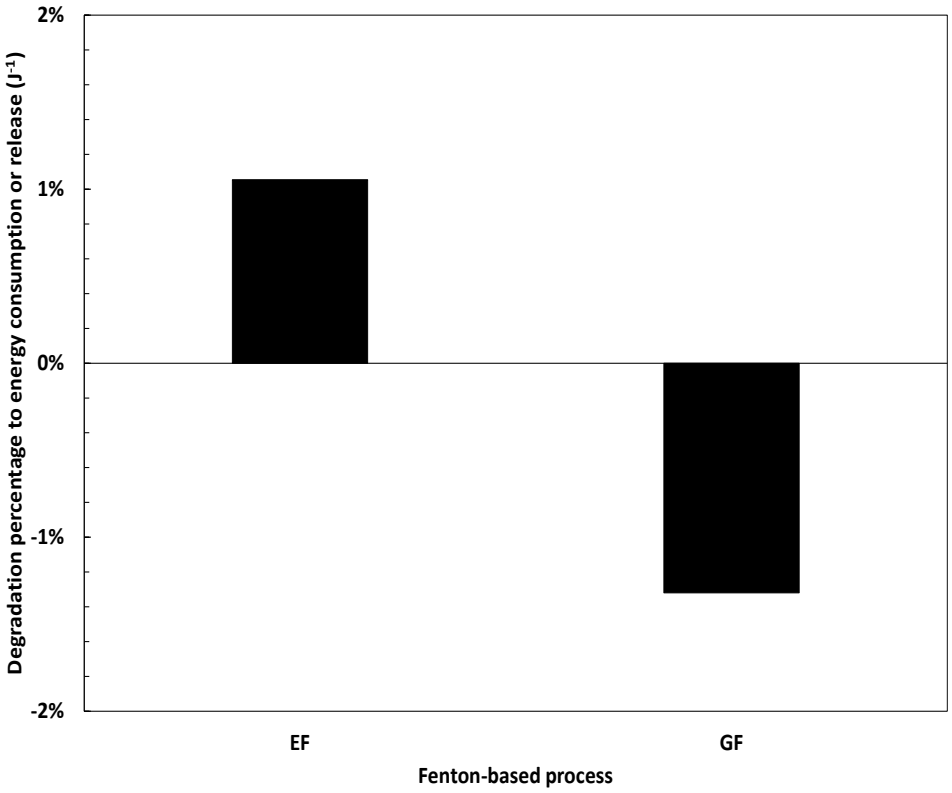

Figure 7. Ratios of phenol degradation percentage to the consumed or released energy using Galvano-Fenton and Electro-Fenton processes.

Conclusion

The mechanistic scenario considering no anodic regeneration of Fe2+ from Fe3+, and accounting for sulfate ions reactivity and iron complex formation showed a high correlation with experimental results of 93.5%. The concentration of HO$^{\bullet}$ continues its increase with the Galvano-Fenton process during the second stage and attains the highest concentration compared to Fenton, with a value of 2.5×10^{-9} mM at 20 min.

In terms of molar yields, $HO_2^{\bullet}$ remains the free radical with the highest concentration within the electrolyte, followed by $O_2^{\bullet-}$, then $SO_4^{\bullet-}$ and finally HO$^{\bullet}$. Hydroxyl radical shows the lowest concentration because of its high reactivity, making its lifetime within the electrolyte very short and its instantaneous concentration relatively low.

The achievement of a phenol degradation rate exceeding 96% requires almost 12 min. The initial latency, due to the absence of the Fenton catalyst when the process is started, is probably the reason for the delay observed in terms of the performance of the Galvano-Fenton process for the degradation of phenol. In terms of the mechanism concerns of phenol degradation, the early apparition of the intermediate species reveals the rapid degradation of phenol tending to its mineralization.

Overall, the Galvano-Fenton process, when treated as energetic systems, is characterized by a higher performance added to an energy release, in contrast, electro-Fenton process shows a lower performance and is associated with an energy consumption.

Scientific Ethics Declaration

The authors declare that the scientific ethical and legal responsibility of this article published in EPSTEM journal belongs to the authors.

Acknowledgements

* This article was presented as an oral presentation at the International Conference on Technology, Engineering and Science (www.icontes.net) held in Antalya/Turkey on November 16-19, 2022.

* This work was financially supported by the "Hubert Curien Program" through the PHC MAGHREB Project number 19MAG23/41382WC, the Deep Tech Innovation Incubator of Lyon and Saint-Etienne PULSALYS and the Deanship of Scientific Research at King Saud University through research group No. RG-1441-501.

References

Ahmad, Z. (2006). Corrosion kinetics. In Zaki B. T. (Ed.), *Principles of corrosion engineering and corrosion control*, (pp. 57–119) Oxford: Butterworth-Heinemann,). https://www.sciencedirect.com/science/article/pii/B9780750659246500040.

Andreozzi, R., Antonio D. A., & Raffaele M. (2000). A kinetic model for the degradation of benzothiazole by Fe3+ -photo-assisted fenton process in a completely mixed batch reactor. *Journal of Hazardous Materials*, *80*: 241–57.

Artusi, R., Verderio, P., & Marubini, E. (2002). Bravais-Pearson and Spearman correlation coefficients: Meaning, test of hypothesis and confidence ınterval. *International Journal of Biological Markers 17*(2): 148–51.

Bray, W. C. (1931). The mechanism of reactions in aqueous solution examples involving equilibria and steady states. *Chemical Reviews*, *X*(1): 161–77.

Davis, M. E. & Davis, M. E., & Robert J. D. (2003). The basics of reaction kinetics for chemical reaction engineering. In Davis, R. J. (Ed). *Fundamentals of chemical reaction engineering*, New York: McGraw Hill, 1–52. http://resolver.caltech.edu/CaltechBOOK:2003.001.

De Laat, J., & Gallard, H. (1999). Catalytic decomposition of hydrogen peroxide by fe(ıı) in homogeneous aqueous solution: Mechanism and kinetic modeling. *Environmental Science and Technology*, *33*(16): 2726–32.

Duesterberg, C. K., & Waite, T. D. (2006). Process optimization of fenton oxidation using kinetic modeling. *Environmental Science and Technology*, *40*(13): 4189–95.

Gasmi, I., Kerboua, K., Haddour, N., Hamdaoui, O., Alghyamah, A., & Buret, F. (2020). Kinetic pathways of ıron electrode transformations in Galvano-Fenton process: A mechanistic ınvestigation of in-situ catalyst formation and regeneration. *Journal of the Taiwan Institute of Chemical Engineers*, *116*, 81–91.

Gasmi, I., Haddour, N., Hamdaoui, O., Kerboua, K., Alghyamah, A., & Buret, F. (2021). A novel energy-from-waste approach for electrical energy production by galvano – Fenton Process. *Molecules*, 26(4013), 1–14.

Haag, W. R., & Yao, C. D. (1992). Rate constants for reaction of hydroxyl radicals with several drinking water contaminants. *Environmental Science and Technology*, *26*(5), 1005–13.

Haber, F., & Weiss, J. (1932) The catalytic decomposition of hydrogen peroxide by ıron salts. *Proceedings of the Royal Society of London. Series A, Mathematical and Physical Sciences*, *147*(861), 332–51.

Machulek Jr, A., Quina, F. H., Gozzi, F., Silva, V. O., Friedrich, L. C., & Moraes, J. E. (2012). Fundamental mechanistic studies of the photo-fenton reaction for the degradation of organic pollutants. In *Organic Pollutants Ten Years After the Stockholm Convention - Environmental and Analytical Update*, , 272–92.

Kerboua, K., Hamdaoui, O., Haddour, N., & Alghyamah, A. (2021). Simultaneous galvanic generation of Fe2+ catalyst and spontaneous energy release in the Galvano-Fenton Technique : A numerical ınvestigation of phenol's oxidation and energy production and saving. *Catalysts* 11(943).

Kušić, H., Koprivanac, N., Božić, A. L., & Selanec, I. (2006).Photo-assisted fenton type processes for the degradation of phenol : A kinetic study. *Journal of Hazardous Materials*, *136*, 632–44.

Liochev, S. I., & Fridovich, I. (2002). The Haber-Weiss cycle—70 years later: an alternative view. *Redox Report*, *7*(1), 55-57.

Lower, S. K. (2004). Chemical reactions at an electrode, galvanic and electrolytic cells. *Electrochemistry. Simon*

Fraser University, 35-38.
Lu, M., Wang, J., Wang, Y., & He, Z. (2021). Heterogeneous photo-fenton catalytic degradation of practical pharmaceutical wastewater by modified attapulgite supported multi-metal oxides. *Water*, *13*(2), 156.
Machulek, A., Moraes, J. E. F., Okano, L. T., Silvérioc, C. A., & Quina, F. H. (2009). Photolysis of ferric ions in the presence of sulfate or chloride ions: implications for the photo-Fenton process. *Photochemical & Photobiological Sciences*, *8*(7), 985-991.
Madhavan, J., Grieser, F., & Ashokkumar, M. (2010). Combined advanced oxidation processes for the synergistic degradation of ibuprofen in aqueous environments. *Journal of Hazardous Materials*, *178*(1-3), 202-208. http://dx.doi.org/10.1016/j.jhazmat.2010.01.064.
Martins, A. F., Wilde, M. L., Vasconcelos, T. G., & Henriques, D. M. (2006). Nonylphenol polyethoxylate degradation by means of electrocoagulation and electrochemical Fenton. *Separation and Purification Technology*, *50*(2), 249-255.
Merouani, S., Hamdaoui, O., Saoudi, F., & Chiha, M. (2010). Influence of experimental parameters on sonochemistry dosimetries: KI oxidation, Fricke reaction and H2O2 production. *Journal of Hazardous Materials*, *178*(1-3), 1007-1014.
Monteil, H., Pechaud, Y., Oturan, N., & Oturan, M. A. (2019). A review on efficiency and cost effectiveness of electro-and bio-electro-Fenton processes: Application to the treatment of pharmaceutical pollutants in water. *Chemical Engineering Journal*, *376*, 119577.. https://doi.org/10.1016/j.cej.2018.07.179.
Pawar, V. & Sagar G. (2015). An overview of the fenton process for ındustrial wastewater. *IOSR Journal of Mechanical and Civil Engineering (IOSR-JMCE)*: 127–36.
Shokri, A. (2018). Application of Sono–photo-Fenton process for degradation of phenol derivatives in petrochemical wastewater using full factorial design of experiment. *International Journal of Industrial Chemistry*, *9*(4), 295-303.
Shreir, L. L, Jarman R. A., & Burstein G. T. (1994). 2 Butterworth-Heinemann *Corrosion Control*.
Tarkwa, J. B., Oturan, N., Acayanka, E., Laminsi, S., & Oturan, M. A. (2019). Photo-Fenton oxidation of Orange G azo dye: process optimization and mineralization mechanism. *Environmental Chemistry Letters*, *17*(1), 473-479. https://doi.org/10.1007/s10311-018-0773-0.
Xu, L. J., Chu, W., & Graham, N. (2014). Degradation of di-n-butyl phthalate by a homogeneous sono–photo–Fenton process with in situ generated hydrogen peroxide. *Chemical Engineering Journal*, *240*, 541-547.
Zhang, M. H., Dong, H., Zhao, L., Wang, D. X., & Meng, D. (2019). A review on Fenton process for organic wastewater treatment based on optimization perspective. *Science of the Total Environment*, *670*, 110-121.Wastewater Treatment Based on Optimization Perspective." *Science of the Total Environment* 670: 110–21.

Author Information

Kaouther Kerboua
Department of Engineering, Higher School of Industrial Technologies
PO box 2018, 23000, Annaba, Algeria
Contact e-mail: *k.kerboua@esti-annaba.dz*

Naoufel Haddour
Laboratoire Ampère, Ecole Centrale de Lyon
36 Avenue Guy de Collongue, 69134, Ecully, France

Intissar Gasmi
Laboratory of Environmental Engineering, Process Engineering Department, Faculty of Engineering, Badji Mokhtar - Annaba University,
P.O. Box 12, 23000, Annaba, Algeria
Laboratoire Ampère, Ecole Centrale de Lyon
36 Avenue Guy de Collongue, 69134, Ecully, France

Oualid Hamdaoui
Chemical Engineering Department, College of Engineering, King Saud University
P.O. Box 800, 11421 Riyadh, Saudi Arabia

To cite this article:

Kerboua, K., Haddour, N., Gasmi, I. & Hamdaoui, O. (2022). Water remediation from recalcitrant pollution using the galvano-fenton process: a modeling approach of the hydroxyl radical generation and the energy efficiency. *The Eurasia Proceedings of Science, Technology, Engineering & Mathematics (EPSTEM), 21,* 506-516.

The Eurasia Proceedings of Science, Technology, Engineering & Mathematics (EPSTEM)
ISSN: 2602-3199

The Eurasia Proceedings of Science, Technology, Engineering & Mathematics (EPSTEM), 2022

Volume 21, Pages 517-524

IConTES 2022: International Conference on Technology, Engineering and Science

Numerical Study of a Shell and Tubes Heat Exchanger: Impact of the Geometrical Change of the Tube Section on the Overall Exchange Coefficient and the Pressure Drop

Sara SAHRANE
Higher School of Industrial Technologies

Slimane NIOU
Badji Mokhtar University

Abdassalam OTMANI
Higher School of Industrial Technologies

Salah-Eddine AZZOUZ
Higher School of Industrial Technologies

Abstract: Shell and tube heat exchanger is the most widely used type in industry because of its advantages: solid design, excellent reliability, compact, resistant to fouling fluids, having a very high exchange coefficient...etc. Several studies have highlighted the importance of this configuration. This study consists in the design and the thermo-fluid simulation by COMSOL software of a shell and tube exchanger with two different tubular geometries: i) circular, ii) square, iii) elliptical 90° using segmental baffles at 25% and two working fluids: water-air. The mass flow rates of the two fluids are varied and their influence on the energy performance of the heat exchanger is also examined. The results show that changing the geometry of the tube bundles affects the pressure drop especially on the shell side, the square geometry created a higher pressure drop than the circular tube geometry. A considerable improvement in the overall exchange coefficient was recorded for the exchanger with the circular tube bundle by increasing the fluid velocity.

Keywords: Shell and tube heat exchanger, Simulation, Thermo-fluid, Circular tubes, Square tubes , Elliptical 90°.

Introduction

Heat exchangers play a crucial roler in various industries and engineering field: chemical, petroleum, food processing, nuclear power plant, thermal power plant, electric power plant, ... etc., by the transmission and recovery of energy (Master, Chunangad, & Pushpanathan, 2003). The shell and tube heat exchanger are the most used type in the industry (35% - 40%) (El Maakoul et al., 2016)]due to its advantages: easy to maintain, efficient, compact and resistant. It consists of two main elements: i) tubes, ii) shell. The tubes ensure the transport of aggressive fluids (hot or cold), compressible and incompressible and especially at high pressure. The shell ensures the circulation of fluids at low pressure, it generally includes longitudinal and/or transverse baffles. The implementation of the baffles makes it possible to lengthen the path of the fluid in the shell, accelerate its turbulence and thus increase the exchanged flow. However, they have certain disadvantages, such as a high resistance to flow, vibrations induced by the flow, and dead flow areas on the side of the envelope (Ünverdi, 2022).

In order to improve the performance of the shell and tube type heat exchanger many researchers have conducted a lot of research work. Some of the recent researches are focused on the shell side more precisely the baffles: material type, number, shape, cutting angle.....etc. Juan Xiao et al. (2020) studied the effect of geometric variation of baffles on the performance of exchangers, they used baffles: segmental, helical and folded. Ali Akbar Abbasian Arania et al. (2019) examined the combination of disk baffles with other drawn baffles. Another part of the research is studied the tube side, The study of tube side is quite trouble-free with a smaller number of parameters.

The tube arrangement has an influence on the energy performance of tube and shell heat exchangers, Sachin Kallannavar et al. (2020) studied the effect of variation of four types of tube arrangement 30°, 90°,60°and 45°, for a tube and shell heat exchanger with circular tube. Arania & Moradi (2019) segmental baffles and combined segmental-disk baffle with two types of circular and triangular ribbed tube. Matos et al. (2014a, 2014b) compared 12 elliptical and circular tubes at Reynolds numbers between 300 and 800. Elliptical tubes increase the heat transfer with 20% compared to circular tubes. Tao et al (2007) numerically studied a tube and shell heat exchanger with elliptical tubes and found a 30% increase in heat transfer compared to circular tubes.

The objective of this manuscript is to study the effect of varying the different tube cross-sections (square, circular and elliptical tube with 900 attach angle) on the hydro-thermal performance of a tube and shell heat exchanger using numerical software for design, modeling and simulation. A coupling of heat transfer with fluid mechanics was performed based on the Navier - Stokes equations and the k-**ε** turbulence model.

Methodology

Feometric Model

The exchanger used in this study belongs to the family of multi-tube exchangers with a bundle of 37 tubes. It has 1 tube side pass and 1 shell side pass with counterflow. The shell has four vertical single segment baffles with a 25% cut. The geometry of this exchanger was drawn in 3D using COMSOL Multiphysics 5.5 software (Figure 1).

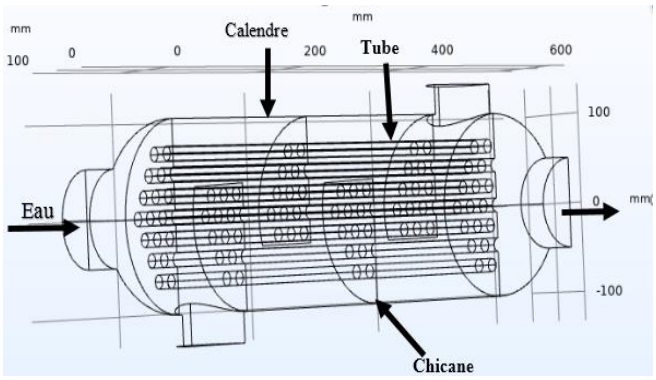

Figure 1 Numerical model of the shell and tube exchanger

The hot fluid (water) enters the shell at of 80°C while the cold fluid (air) enters the tubes with a temperature of 5°C. Table 1 shows the thermo-physical properties of the two fluids.

Table 1. Thermophysical properties of shell and tube heat exchanger

Properties	Fluid		
	water	air	unit
T_{inlet}	80	5	°C
Thermal conductivity	0.6562	0.02401	(W/m.K)
Density	971.8	1006	(kg/m^3)
Specifc heat capacity	4194	1006	(J/Kg K)
Dynamic viscosity	3.54×10^{-4}	1.75×10^{-5}	(Pa s)

The geometry of the exchanger was maintained in the three cases examined only the tubes bundles which was varied (Figure 2), the dimensional specifications of this heat exchangers are presented in the Table 2.

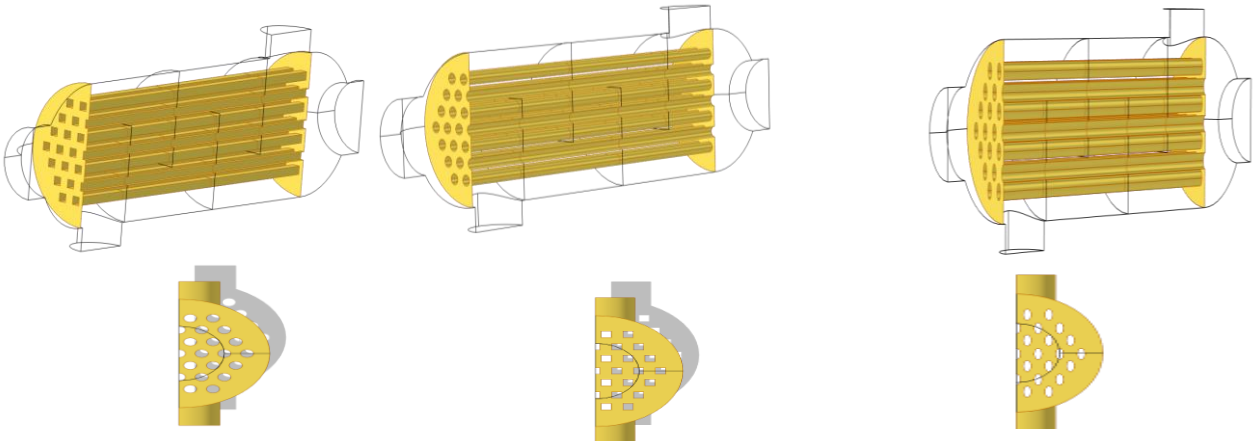

Circular cross section Square cross section Elliptical 90° cross section

Figure 2. Cross sectional models of the shell and tube exchanger

Table 2. Size of the heat exchanger

Propertie	Value	Unit
Shell diameter	200	mm
Tube diameter	15	mm
Length shell /tube	500	mm
Number of tubes	37	
Number of baffles	4	

Mathematical Model

Heat Transfer Coefficient

The overall heat transfer coefcient is calculated by the following equation (Allen & Gosselin, 2008; He et al., 2016):

$$U = \frac{1}{\frac{1}{hi} + \frac{diln(\frac{de}{di})}{2\lambda} + \frac{1}{he}} \quad (1)$$

hi : convective transfer coefficients for the tube side, he : convective transfer coefficients for the shell side, k : thermal conducivity of the tube, d_i : inner diameters of the tube, d_e: outer diameters of the tube.

Pressure Drop in Shell Side

The pressure drop in the shell side can be obtained using the following equation (2) (Allen & Gosselin, 2008; He et al., 2016)

$$\Delta P = f\frac{D_S}{D_e}(N_b + 1)\frac{1}{2}\rho V^2$$
$$f = \exp(0.576 - 0.19lnR_{es})$$
$$D_e = \frac{4\left(\frac{\sqrt{3}P_t^2}{4} - \frac{\pi d_0^2}{8}\right)}{\frac{\pi d_0}{2}}$$
$$Re_s = \frac{\rho u_m D_e}{\mu} \quad (2)$$

ΔP: pressure drop in shell side $\mathbf{Re_s}$: Reynold's number in shell, **f** = friction factor, $\mathbf{D_s}$: Sell diameter, $\mathbf{D_e}$: equivalent diameter for the triangular pitch,, $\mathbf{N_b}$: number of bafe, **ρ**= density of the fluid, **μ**= dynamic viscosity of the fuid, $\mathbf{u_m}$: velocity of the fuid,,**V** : mean fow velocity, $\mathbf{P_t}$: tube pith ,d_0: outer diameters of the tube.

Turbulent Fow k–ε Model

The turbulent flow model (k - ε) is widely used in the literature to the study the turbulent flows with very high Reynolds numbers. It is a model with two partial differential equations: i) turbulent kinetic energy (k) and ii) dissipation (ε). COMSOL uses the Navier - Stokes equations as the basic equations to solve the fluid flow models (3)

$$\rho(\mu.\nabla)\mu = \nabla.\left[-PI + (\mu+\mu_T)(\nabla\mu + (\nabla\mu)^T - \frac{2}{3}(\mu+\mu_T)(\nabla.\mu)I - \frac{2}{3}\rho kI\right] \quad (3)$$
$$\nabla.(\rho\mu) = 0$$

ρ : density (kg/m^3) ; μ : Dynamic viscosity (kg/m/s) ; P : fluid pressure (Pa)
k : Turbulent kinetic energy (m²/s²) et μ_T : turbulent viscosity (Pa.s).

The turbulent kinetic energy is defined as follows (4):

$$\rho(\mu.\nabla)k = \nabla.\left[\left(\mu + \frac{\mu_T}{\sigma_k}\right)\nabla k\right] + p_k - \rho\varepsilon \quad (4)$$

σ_k : the turbulent Prandtl number; ε : Turbulent dissipation(m²/s²)

Turbulent dissipation is the rate at which velocity fluctuations dissipate. It is defined by the equation (5)

$$\rho(u.\nabla)\varepsilon = \nabla.\left[\left(\mu + \frac{\mu_T}{\sigma_\varepsilon}\right)\nabla\varepsilon\right] + C_{e1}\frac{\varepsilon}{k}\,p_k - C_{e2}\rho\frac{\varepsilon^2}{k} \quad (5)$$

u : fuid flow velocity,.
For a turbulent flow, the viscosity is defined by the equation (6)

$$\mu_T = \rho C_\mu \frac{k^2}{\varepsilon} \quad (6)$$

La production d'énergie cinétique turbulente est peut-être exprimée par l'équation (7)

$$P_k = \mu_T\left[\nabla u:(\nabla u + (\nabla u)^T) - \frac{2}{3}(\nabla.u)^2\right] - \frac{2}{3}\rho k\nabla.u \quad (7)$$

The constants used in the equations for turbulent kinetic energy, turbulent dissipation and turbulent viscosity are: C_{e1}=1.44, C_{e2}=1.92, C_μ=0.99, σ_k = 1, σ_ε =1.3

Mesh Control

The computational grid was generated using the COMSOL software. The volume of the shell and tube assembly was discretized using a free unstructured tetrahedral mesh (figure 3). A sensitivity study of the mesh was performed to choose the number and size of the meshes and to minimize the computational cost

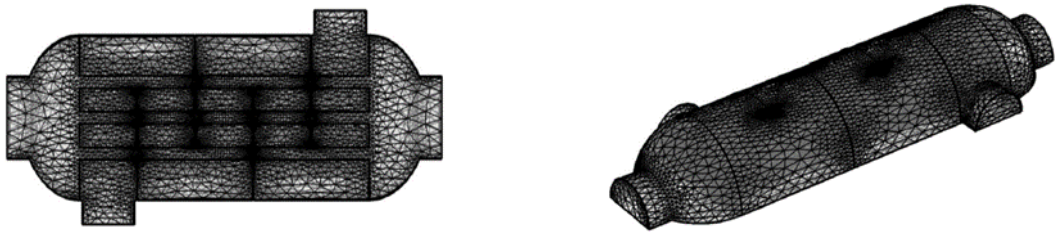

Figure 3. The meshed model used in the numerical calculations of the heat exchangers

Result and Discussion

Temperature Evolution

The 3D temperature contours in the heat exchanger for the three geometries are shown in Figure 4. The heat transfer in the shell and tube exchanger is performed by both modes of heat transfer: conduction and convection. The separating walls between the two fluids, namely the tube plate inside the exchanger and the shell wall as well as , the baffles ensure the conductive transfer. The convective transfer is carried out between the cold fluid (air) and the interior faces of the tubes as well as the hot fluid and the exterior faces of the tubes and the interior of the shell. The temperature evolution is uniform along the exchanger, the lowest temperature for the tube bundle corresponds to the outlet temperature of the cold fluid 324.35K, 328.44K and 328.22 corresponds to the 90° elliptical square section respectively. The heat transfer is higher for the exchanger with circular tubular section compared to the square and 90° elliptical geometry. The specification of the square geometry which disadvantages the convective transfer and decreases the heat exchange rate.

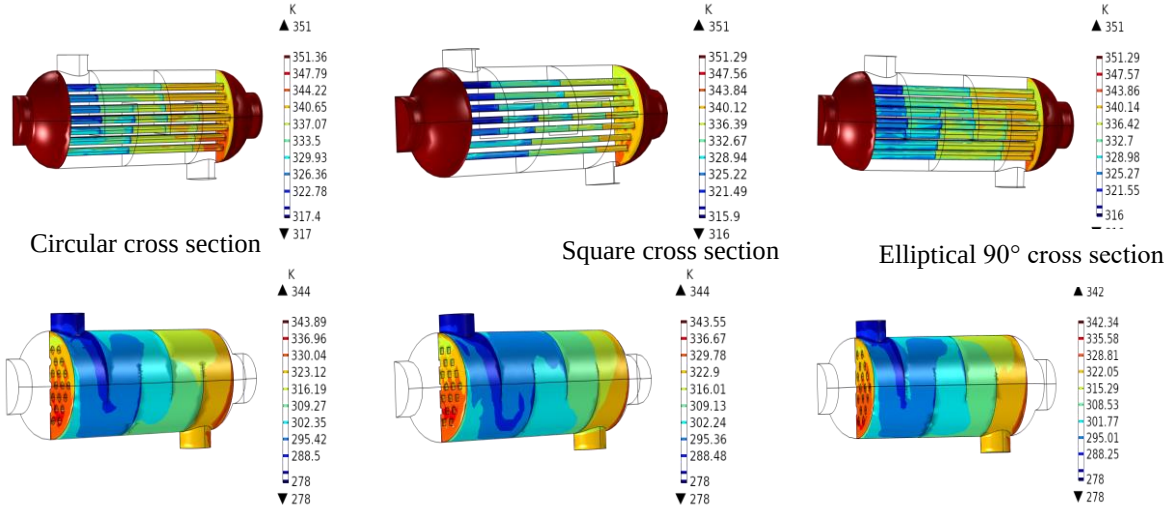

Figure 4. 3D temperature contours for both shell and tube exchanger geometries

Velocity Evolution

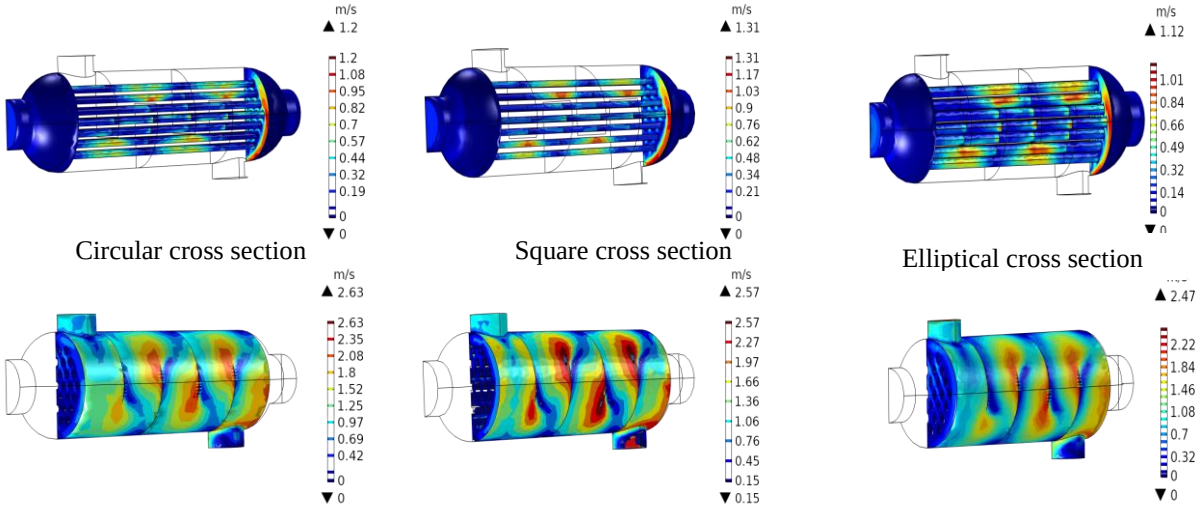

Figure 5. 3D velocity contours for three shell and tube exchanger geometries

The velocity contours across the cross section of the three geometries (square and circular section) are shown in figure 5. The maximum velocity value in the three exchanger geometries (1.31 m/s ,1.2m/sand 1.12 m/s for the square, circular and 90° elliptical section respectively) was in the baffle edge. The restriction of the flow area

between the shell and the baffle plates as well as the external shape of the tube bundle induces a flow acceleration on the shell side and has no influence on the tube side.

Pressure Evolution

The pressure drop is one of the fundamental criteria to be respected in the design of heat exchangers. This parameter has a very important impact on the thermal performance of shell and tube heat exchangers. Figure 6 presents the influence of the variation of the circular, square and elliptical 90° tube section on the pressure drop for a shell and tube heat exchanger. The results show an increase in pressure drop of 1.28% and 1.27% for the square and 90° elliptical tube sections respectively. 1.28% and 1.26% for the square and 90° elliptical geometry on the shell side compared to the circular heat exchanger. The change of cross section in the square configuration causes a sudden expansion and contraction of the fluid and increases the pressure drop (Arani & Uosofvand, 2021). The choc created between the fluid and the shell and the change of the cross section between the shell and the baffles induces a higher creation of the dead zones and increases the pressure drop.

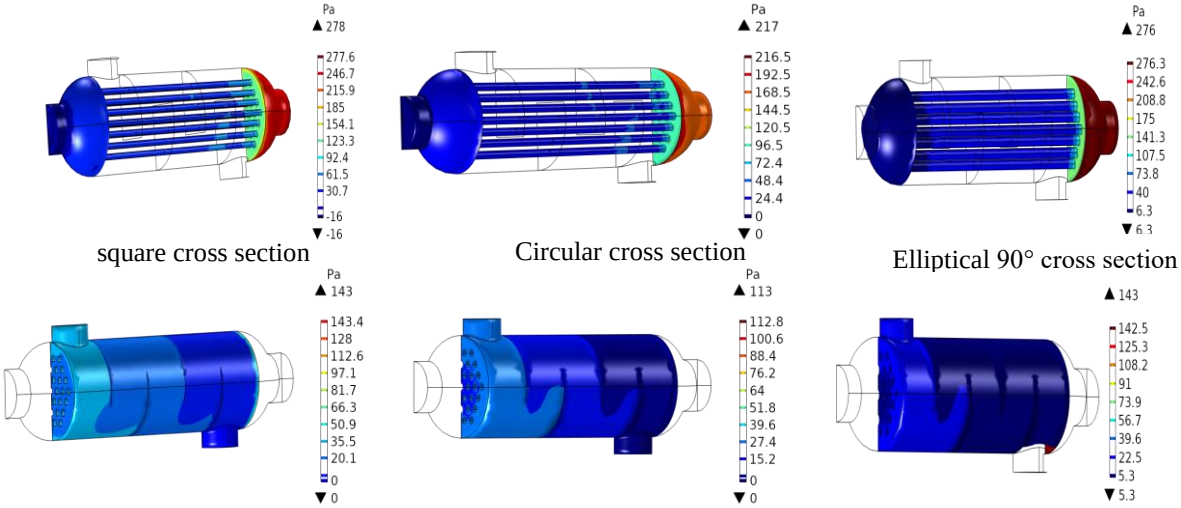

Figure 6. 3D Pressure contours for shell and tube exchanger geometries

Heat Transfer Coefficient

Figure 7, shows the variation of the global heat transfer coefficient as a function of the Reynolds number for the three geometries of heat exchangers circular, square and elliptical 90 ° The global exchange coefficient varies proportionally with the Reynolds number. The maximum value of Reynolds corresponds to the highest mass flow rate and the largest transfer coefficient. the heat exchangers with circular section presents the highest heat transfer 10. 458 (W/m^2.K) compared to the square (9.056 (W/m^2.K) and 90° elliptical (9.9552 W/m^2.K) geometries, due to the decrease of the higher flow section for the circular geometry in the shell side which causes an increase in the flow rate which in turn causes the heat transfer to penetrate the cold fluid at a higher rate.

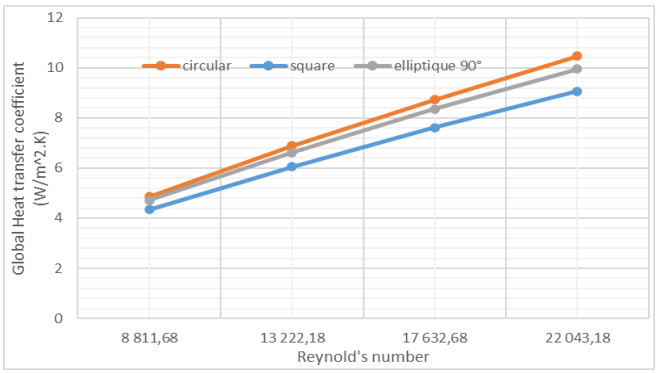

Figure 7. The overall heat transfer coeffcient in the three geometries

Pressure Drop ın Shell Side

According to the results presented in figure 8 which represents the variation of the pressure drop in the shell side as a function of the Reynolds number for the three different cross sections, the pressure drop varies proportionally with the Reynolds number. The maximum value of the pressure drop corresponds to shell and tube heat exchanger with the square cross-section, while the circular geometry shows the minimum pressure drop. The variation of the square and 90° elliptical geometry increases the creation of recirculation zone and the friction factor on the shell side then increases the pressure drop.

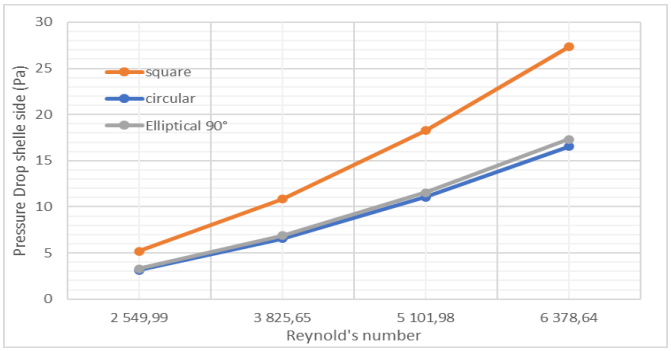

Figure 8. Pressure drop in shell side of three geometries heat exchangers

Conclusion

The overall heat transfer coefficient and the pressure drop are studied through three different types of tube bundles (circular, square and 90° elliptical) of a water/air shell and tube heat exchanger, in order to determine the influence of the tube geometry on the pressure drop and the heat transfer by varying the mass flow rate. The numerical study was performed with the modeling and simulation software CONSOL Multiphysics 5.5a. The heat exchanger with circular cross section has the highest heat transfer coefficient. The square section increases the pressure drop on the shell side compared to the circular section. Reynolds number varies proportionally with the fluid mass flow rate, the higher the Reynolds number the higher the flow rate. The variation in flow velocity influences the heat transfer in the tube and shell heat exchanger.

Scientific Ethics Declaration

The authors declare that the scientific ethical and legal responsibility of this article published in EPSTEM journal belongs to the authors.

Acknowledgements

* This article was presented as an oral presentation at the International Conference on Technology, Engineering and Science (www.icontes.net) held in Antalya/Turkey on November 16-19, 2022.

References

Allen, B., & Gosselin, L. (2008). Optimal geometry and flow arrangement for minimizing the cost of shell-and-tube condensers. *International Journal of Energy Research*, *32*(10), 958-969.

Arani, A. A. A., & Moradi, R. (2019). Shell and tube heat exchanger optimization using new baffle and tube configuration. *Applied Thermal Engineering*, *157*, 113736.

Arani, A. A. A., & Uosofvand, H. (2021). Double-pass shell-and-tube heat exchanger performance enhancement with new combined baffle and elliptical tube bundle arrangement. *International Journal of Thermal Sciences*, *167*, 106999.

El Maakoul, A., Laknizi, A., Saadeddine, S., El Metoui, M., Zaite, A., Meziane, M., & Abdellah, A. B. (2016). Numerical comparison of shell-side performance for shell and tube heat exchangers with trefoil-hole, helical and segmental baffles. *Applied Thermal Engineering, 109*, 175-185.

Harlow, H. F. (1983). Fundamentals for preparing psychology journal articles. *Journal of Comparative and Physiological Psychology, 55*, 893-896.

He, Z., Fang, X., Zhang, Z., & Gao, X. (2016). Numerical investigation on performance comparison of non-Newtonian fluid flow in vertical heat exchangers combined helical baffle with elliptic and circular tubes. *Applied Thermal Engineering, 100*, 84-97.

Kallannavar, S., Mashyal, S., & Rajangale, M. (2020). Effect of tube layout on the performance of shell and tube heat exchangers. *Materials Today: Proceedings, 27,* 263-267. (Doctoral dissertation). Retrieved from Name of database. (Accession or Order Number)

Master, B. I., Chunangad, K. S., & Pushpanathan, V. (2003). Fouling mitigation using helixchanger heat exchangers. *ECI Symposium Se*ries. https://dc.engconfintl.org/heatexchanger/43

Matos, R. S., Laursen, T. A., Vargas, J. V. C., & Bejan, A. (2004). Three-dimensional optimization of staggered finned circular and elliptic tubes in forced convection. *International Journal of Thermal Sciences*, *43*(5), 477-487..

Matos, R. S., Vargas, J. V. C., Laursen, T. A., & Bejan, A. (2004). Optimally staggered finned circular and elliptic tubes in forced convection. *International Journal of Heat and Mass Transfer*, *47*(6-7), 1347-1359.

Schultz, S. (2005, December 28). Calls made to strengthen state energy policies. *The Country Today*, pp. 1A, 2A.

Tao, Y. B., He, Y. L., Wu, Z. G., & Tao, W. Q. (2007). Three-dimensional numerical study and field synergy principle analysis of wavy fin heat exchangers with elliptic tubes. *International Journal of Heat and Fluid Flow*, *28*(6), 1531-1544.

Ünverdi, M. (2022). Prediction of heat transfer coefficient and friction factor of mini channel shell and tube heat exchanger using numerical analysis and experimental validation. *International Journal of Thermal Sciences*, *171*, 107182

Xiao, J., Wang, S., Ye, S., Wen, J., & Zhang, Z. (2020). Multiphysics field coupling simulation for shell-and-tube heat exchangers with different baffles. *Numerical Heat Transfer, Part A: Applications*, *77*(3), 266-283.

Author Information

Sara SAHRANE
"LTSE" Energy Systems Technology Laboratory, Higher School of Industrial Technologies
BP 218, 23012 ANNABA, ALGERIA
Contact e-mail: *s.sahrane@esti-annaba.dz*

Slimane NIOU
Mechanics of Materials and Plant Maintenance Research Laboratory (LR3MI), Mechanical Eng.Dept Faculty of Engineering, Badji Mokhtar University,
PO Box 12, 23052 Annaba, Algeria

Abdassalam OTMANI
Departmnte,Higher School of Industrial Technologies,,Annaba 23000, Algeria

Salah-Eddine AZZOUZ
Departmnte,Higher School of Industrial Technologies,,Annaba 23000, Algeria

To cite this article:

Sahrane, S., Niou, S., Otmani, A., & Azzouz, S. (2022). Numerical study of a shell and tubes heat exchanger: impact of the geometrical change of the tube section on the overall exchange coefficient and the pressure drop. *The Eurasia Proceedings of Science, Technology, Engineering & Mathematics (EPSTEM), 21,* 517-524.

The Eurasia Proceedings of Science, Technology, Engineering & Mathematics (EPSTEM)
ISSN: 2602-3199

The Eurasia Proceedings of Science, Technology, Engineering & Mathematics (EPSTEM), 2022

Volume 21, Pages 525-540

IConTES 2022: International Conference on Technology, Engineering and Science

Investigation on the RCCI Engine on Performance and Emission

Ahmad Fitri YUSOP
Universiti Malaysia Pahang

Mohamad Adzuan AZIZ
Universiti Malaysia Pahang

Mohd Adnin HAMIDI
Universiti Malaysia Pahang

Daing Mohamad Nafiz DAING IDRIS
Universiti Malaysia Pahang

Ummi Hafsah ZAIDI
Universiti Malaysia Pahang

Abstract: RCCI engine is among the most promising combustion technology for the upcoming generation of heavy-duty motors. In RCCI mode combustion, different combinations of low reactivity fuels (LRF) and high reactivity fuels (HRF) such as PRF-Diesel, can be used to achieve a chemical reaction or reactivity stratification in the engine combustion chamber. The high reactivity fuel (HRF) which is diesel will be injected in the direct fuel injection and the low reactivity fuel (LRF) which is Primary Reference Fuel (PRF) will be injected in port fuel injection. Combustion in the engine combustion chamber will convert the chemical energy of fuels to heat that can be used directly or further converted to mechanical energy. Internal combustion engine outputs mechanical power by extracting energy in fuels via combustion reaction in the cylinders. Fuels are burned in the combustion chambers to generate high temperature and high-pressure gas which delivers power to the piston. RCCI had a low performance at high engine speed due to its high tendency on knocking and high pressure rise rate. Therefore, this study investigates the effect of the fuel stratification on the RCCI combustion and it's extended to the interaction of high and low reactive fuels, PRF and diesel in the RCCI combustion system. Modified engine was tested for engine performance. The change in BSFC, Power and Torque are observed at all loads and speeds with different PRF percentages. For emissions, this RCCI engine was said to produces extremely low in nitrogen oxide. On a regular diesel engine, these kinds of pollutants cause problems. The cool burning, on the other hand, does not emit nitrogen oxide when using an RCCI engine. Aside from that, because the RCCI engine uses less diesel fuel, the diesel fuel has more time to mix in the cylinder.

Keywords: RCCI engine, Performance, Emission, Engine speed, Engine load

Introduction

Homogeneous-charge compression ignition (HCCI) engines are said to have higher thermal efficiency and lower pollutant emissions than conventional diesel and gasoline engines over the last two decades The reactivity-controlled compression ignition (RCCI) mode has been developed and extensively explored to achieve ultra-high efficiency and near-zero emissions in an internal combustion engine. The reactivity-controlled combustion ignition is achieved by producing reactivity stratification in the cylinder by using two fuels with different cetane numbers. The low reactivity (low cetane number) fuel is premixed with air before being charged into the

cylinder via the intake manifold; the high reactivity (high cetane number) fuel is then injected into the charged mixture via a direct injector. With that, the reactivity stratification is created (Reitz & Duraisamy, 2015). According to earlier research, the LRF should contribute as the majority of total injected fuel in order to create a highly efficient RCCI operation with minimal emissions, while the HRF is used to initiate the combustion process. Furthermore, HRF plays an important role in in-cylinder reactivity stratification because HRF injection settings are one of the most important parameters for the combustion process development. The RCCI concept has recently been demonstrated in a variety of engine platforms, including single-cylinder, multi-cylinder, heavy-duty, medium-duty, and light-duty diesel engines with low, medium, and high compression ratios (CR). These studies show that, under stationary circumstances, RCCI can produce lower NOx emissions, as well as ultra-low soot emissions. Despite this, RCCI has a number of issues, including excessive unburned HC and CO emissions during low engine load operation, as well as excessive maximum pressure rise rates (MPRR) and in-cylinder maximum pressure peaks (Pmax) at high loads. These two constraints limit the RCCI's operating range to medium loads, making it unsuitable for use in real engines situations. As a result, the large number of operating conditions within the RCCI range produced after the gear shifting optimization is predicted to result in a significant reduction in aftertreatment requirement (Benajes et al., 2018). Kokjohn et al., in particular, studied at the combustion characteristics of diesel low temperature combustion (LTC), ethanol-diesel RCCI, and E85-diesel RCCI combustion numerically. The consumption of high reactive diesel and low reactive E85 in E85-diesel RCCI combustion was found to be staged combustion, with E85 not being used until the gradual shift of diesel consumption to the second stage ignition (Benajes et al., 2018).

RCCI combustion is a dual-fuel technique that takes advantage of the benefits of employing different reactivity fuels. High-reactivity fuels, such as diesel, are injected directly into the chamber, whereas low-reactivity fuels, such as gasoline, are delivered through the intake ports. These engines feature more effective combustion phasing control and operate better at higher loads (Kahnooji & Yazdani, 2021). The overall combustion of RCCI cases occurs earlier and its mean heat release rate (HRR) is more evenly distributed over time than that of the corresponding SCCI cases in the low and intermediate-temperature regimes. This is due to the fact that within the negative temperature coefficient (NTC) zone, PRF number stratification, PRF', is governing and the different level of temperature, T', has a small effect on overall combustion. The difference between RCCI and SCCI combustion becomes negligible in the high-temperature regime, however, because the ignition of the PRF/air mixture is mainly sensitive to T' rather than PRF' and different level of equivalence ratio, phi'(Luong et al., 2017). Chemical kinetics, which is known to be heavily impacted by mixture pressure, influences the RCCI strategy. When diesel is introduced into a homogenous gasoline/air combination, the local PRF number in the cylinder is reduced, resulting in an increase in local reactivity (Han et al., 2018).

Studies on dual combustion of gasoline and hybrid powertrains have shown that lower maximum ICE outputs result in reduced NOx and soot emissions (García et al., 2020). The narrow angle direct injection technique was used in a study on homogenous charging compression ignition engine features powered by biofuels to create practically zero percentiles of nitrogen oxides and high output power particle emissions, torque at part load conditions (Saiteja & Ashok, 2021). Additionally, a strain gauge cell was used in a performance and operating cost study to compute the brake power of the dynamometer in the dual-mode RCCI diesel-natural gas and diesel combustion engines (Ansari et al., 2018). Further studies on the technique for injecting and changing a single-cylinder diesel engine's combustion chamber have shown that if engine injection properties are improved so that the new swirl bowls produce the same amount of power, NOx emissions may also be reduced (Sener et al., 2020). In order to keep CA10 constant, the SOI should be advanced by increasing load. The reason for this is that the local equivalence ratio will increase by enhancing load; therefore, injection should be start earlier to more homogenize the mixture. This dual stage HTHR qualifies for lower engine noise and higher engine torque operation due to increased fuel injection (Pan et al., 2020). Additionally, studies on natural gas diesel injection techniques with dual fuel compression premixed ignition combustion in low load conditions have demonstrated that great fuel economy and torque of diesel engines are accomplished (Park et al., 2019). In addition, a study on energy's dual-combustion exergy testing for oxygenated biofuels found that the essential elements in increasing an engine's torque output—which in turn enhanced brake power—were lessened pumping effort, lessened compression work, and improved expansion processes (Rangasamy et al., 2020). Additionally, according to research on combustion, performance, and emission characteristics, CI engines are more widely used in a variety of economic sectors, such as transportation, agriculture, and construction, because they offer better power/driving output, durability, and dependability due to their higher BTE braking efficiency (Singh et al., 2020). In the meantime, data from the study on air intake method for low HC and CO emissions in dual fuel premixed (Shim et al., 2018) shows that the engine's maximum torque is at 1400 rpm. Additionally, research on the combustion of dual fuel diesel and natural gas at low loads shows that, even with changes in NG quantity after other burning limitations are established (W. Li et al., 2016), the test setup parameter remains constant with engine speed and torque output. Furthermore, research into the emissions and performance of dual direct

injection hydrogen-diesel engines set their engine at a constant speed of 2000 rpm, which is the speed at which the production engine achieves its maximum torque output. Before more data is collected, research into comparisons between dual combustion of pure diesel and diesel methanol sets the engine torque parameters at 440N.m and 220N.m.

Exhaust Gas Temperature (EGT) and Brake Specific Fuel Consumption (BSFC) are lower in RCCI mode as compared to CDC (Charitha et al., 2019). The fuels with S=5 and S=8 exhibit a minor increase in BSFC values for dual mode with differing octane numbers seen under low load situations because of the early combustion start, which releases more energy during the compression stroke and reduces cycle efficiency (García et al., 2019). In addition, the performance of the RCCI with diesel demonstrates that the inclusion of biodiesels results in a higher fuel demand to provide a similar engine output due to the fuel's reduced heat content (Charitha et al., 2019). Additionally, a study of fuel on RCCI demonstrates the effects of RON of PI fuels and CN of DI fuels on the indicated fuel consumption (ISFC) under various premixed ratios and reveals that the ISFC of the majority of fuel combinations was higher than the DICI mode, primarily because of the insufficient combustion of port injection fuel and the delayed combustion phase. Additionally, research on methanol and the extra air/fuel ratio reveals that during lean burn conditions, the equivalent BSFC decreased (L. Wang et al., 2019).

According to a performance study of hydrogen diesel, the temperature of the exhaust gas as it travels through the turbocharger drops by roughly 45 K (Liu et al., 2021). Additionally, research on oxidation catalysts indicates that keeping the exhaust gas temperature below 150 °C helps to increase HC adsorption (Piqueras et al., 2019). Additionally, research on diesel-natural gas indicates that the highest EGT is 480 °C (Ansari et al., 2018). The exhaust temperatures of this dual-fuel strategy were greater, according to a research of dual fuel in full operational map (Raza et al., 2019). The hotter combustion processes also produced reduced CO and unburned HC emissions as well as greater exhaust gas temperatures, according to a research of ethanol/diesel (Pedrozo, May, Lanzanova, et al., 2016). Additionally, according to a study on the optimization of performance and operating costs for a dual mode diesel-natural gas RCCI and diesel combustion engine, Diesel-NG fuel blends are used more and more in RCCI internal combustion engines due to their high Brake Thermal Efficiency (BTE), low NOx and PM emissions, and relatively low Exhaust Gas Temperature (EGT). In this configuration, the EGT was predicted using data from the RCCI exhaust gas temperature after the turbine (Ansari et al., 2018). On the other hand, research on the impact of equivalence ratio on the combustion and emissions of a dual-fuel natural gas engine ignited with diesel claimed that the high equivalence ratio in dual-fuel ignition mode is responsible for the increased exhaust gas temperature and decreased combustion duration. Additionally, it is claimed that the high equivalence ratio combustion has a higher cylinder average temperature than the lean burn combustion, in which the temperature of the exhaust gas is elevated as a result of a reduction in air mass. It is further claimed that regardless of strategy variations such nozzle specifications, an increase in equivalent ratio can be used to obtain the highest heat release rate, an increase in exhaust gas temperature, and a shorter combustion time. Additionally, the findings showed that an increase in EGT causes CO emissions to rise noticeably when the equivalency ratio exceeds 0.95 (Salahi et al., 2017). The reactivity-controlled compression ignition (RCCI) mode has been developed and extensively explored to achieve ultra-high efficiency and near-zero emissions in an internal combustion engine. They determined that the fuel reactivity gradient was the main parameter in the RCCI mode combustion process and emission product control after examining the fuel mixing process.

Researchers have devoted a lot of time and attention into studying fuel injection parameters in order to improve efficiency and reduce emissions. Premixed fuel ratio, injection pressure, direct-injected fuel spray angle, and SOI (start of injection) timing, among other injection parameters, are all related to an engine's injection method (J. Li et al., 2018). According to the study, for moderate-to-high loads, a gasoline/diesel dual-fuel RCCI regime may achieve ultra-low NOx and soot emissions as well as high thermal efficiency, but diesel low temperature combustion (LTC) with single-shot fuel injection is more suitable for low-load operations (Y. Wang, Yao, et al., 2016). Pressure and temperature are reduced, and combustion phasing is delayed, when engine speed is increased at three different piston bowl profiles. Higher engine speeds not only allow for fewer chemical reactions, resulting in more incomplete combustion, but they also allow for less heat transmission, potentially leading to higher in-cylinder temperatures (Kakaee et al., 2016). It has been demonstrated that an optimised mid-speed RCCI engine with a compression rate of 15.2 may achieve gross indicated efficiencies of 52 percent while maintaining the benefits of a high blend rate (over 90 percent) and achieving NO_x, CH4, and CO emissions below the strict Stage V standard (Mikulski et al., 2019). The RCCI engine with a pre-chamber experiences a completely full combustion process during the fuel mixtures with a greater equivalence ratio, which resulting in high combustion efficiency, nearly to no UHC emission, and low CO emissions. However, at high load conditions, substantial levels of NO are produced due to high temperatures. While flame propagation does not occur adequately during the fuel mixtures with low equivalence ratios. The RCCI engine with a pre-

chamber encounters incomplete combustion, resulting in lower combustion efficiency and higher UHC and CO emissions (Salahi et al., 2017). In addition, study on performance of RCCI shows that the CO_2 emissions indicate an increase for RCCI at higher engine loads (Reitz & Duraisamy, 2015). With the introduction of COME, there was a simultaneous reduction in NOx and smoke emissions. Unburnt hydrocarbons (UHC) dropped at lower percentages of COME and increased at higher percentages of COME, while CO_2 emissions fell marginally (Charitha et al., 2019). The CO_2 content in the intake and exhaust was used to compute the EGR rate. Furthermore, as CA10 decreased, more combustion took place towards the top dead centre. Less fuel accumulates on the cylinder head in the case of 30% biodiesel in the first pulse. As a result, the rate of evaporative fuel consumption (EFC) is faster than the case with 70% in the first pulse. When it comes to the effect of fraction in the first pulse, the NO emissions decrease as the fraction in the first pulse increases. Fuel deposition in the squish zone is severe when more fuel is delivered through the first pulse (J. Li et al., 2018).

The RCCI combustion strategy's major purpose is to decrease emissions, particularly NO_x and soot, by managing in-cylinder reactions through low temperature and lean combustion (Kakoee et al., 2020). RCCI combustion can operate at a wide range of engine loads (4.6–14.6 bar) with near-zero NOx and soot levels (meet regulation standards), a low pressure rise rate and ringing intensity, and a high indicated efficiency (J. Li et al., 2017). Over a wide engine IMEP range of 4 bar to 14.5 bar using gasoline and diesel fuels, RCCI results revealed high thermal efficiency and also very low NO_x and soot emissions. NO_x emissions and combustion noise were reduced as low as possible by adopting Exhaust Gas Recirculation (EGR) during high load operating conditions. However, owing of the PPRR constraint and EGR rate requirements, extending to loads over 14.5 bar IMEP with gasoline/diesel has been challenging (Nazemi & Shahbakhti, 2016). A lower amount of NO_x and higher soot emissions can be obtained through the longer diffusion combustion resulted from shorter mixing interval. Higher injection pressure increased diesel atomisation and resulted in a more uniform charge, causing the SOC to be delayed. This resulted in a faster combustion process, increased PRR, and increased NO_x emissions (Pedrozo, May, Dalla Nora, et al., 2016). The use of E85 as the LRF allows the RCCI operating zone to be extended, resulting in a larger ultra-low NOx region but higher HC and CO levels in the RCCI zone. RCCI soot levels are lower with E85 than with gasoline (Benajes et al., 2018). In comparison to gasoline and natural gas, alcoholic fuels have a higher heat of vaporisation. This ability to absorb heat during evaporation might result in a cooling effect, lowering the temperature of the charged mixture. The reduction in temperature has the ability to lower NO_x production (J. Li et al., 2017).

Furthermore, as IMEP (load) increases, HC and CO emissions decrease dramatically for methanol combustion. With a higher IMEP (load), more turbulence and warmer in-cylinder temperatures can lessen the problem of unburned methanol, lowering HC emissions dramatically (Dong et al., 2020). According to experimental results of RCCI engine with variable percentages of Bio-Diesel (COME) ranging from 10% to 30% at various engine loads, the reduced percentages of COME result in lower HC emissions, with a maximum reduction of roughly 33% at 15% of COME. While, the higher percentages of COME result in higher HC emissions (Charitha et al., 2019). Another study found that when the 2-butanol/diesel is used in RCCI combustion mode, the HC emissions released are much higher compare to the Conventional Combustion Mode (CCM) under various engine loads. The decreased in combustion temperature, which results in poor combustion, and the 2-butanol trapped in crevices throughout the combustion process could be the main causes of this outcome (Pan et al., 2017). At moderate engine speeds, high thermal and combustion efficiency can be attained with relatively low CO and HC emissions and low fuel consumption. When compared to the cases where EGR was not used, less CO and HC emissions were released, implying that further fuel consumption improvements could be achieved. This is due to the adoption of EGR, which causes a longer ignition delay (Y. Wang, Zhu, et al., 2016).

Experimental Setup

Flowchart

Figure. 1 demonstrates the working process of the experiment. The experiment starts with Literature Review on related past researches journal of RCCI Engine. The best fuels are then determined to be used in this research. The different types of Primary Reference Fuel (PRF) used are PRF20, PRF40, and PRF60. PRF uses iso-octane and n-heptane for fuel blending. For PRF20, it means the fuel blending is 20% of iso-octane and n-heptane, while PRF40 means 40% iso-octane, 60% n-heptane and 40% iso-octane, 60% n-heptane for PRF60. Diesel was chosen in this experiment due to its high cetane number. The ease at which diesel fuel ignites, influences engine starting and combustion roughness. The higher the cetane rating, the shorter the lag time between the time the fuel enters the combustion chamber and the time it begins to burn. For each PRF value, various engine speed at 900, 1200, 1500, 1800, 2100 rpm and various engine loads at 0%, 20%, 40%, 60% by using PRF 20%, 40%,

60% are used to investigated the performance, and emission of RCCI Engine. The experiment continues step by step until the desired data are obtained. All results will be recorded and transfer into graphs.

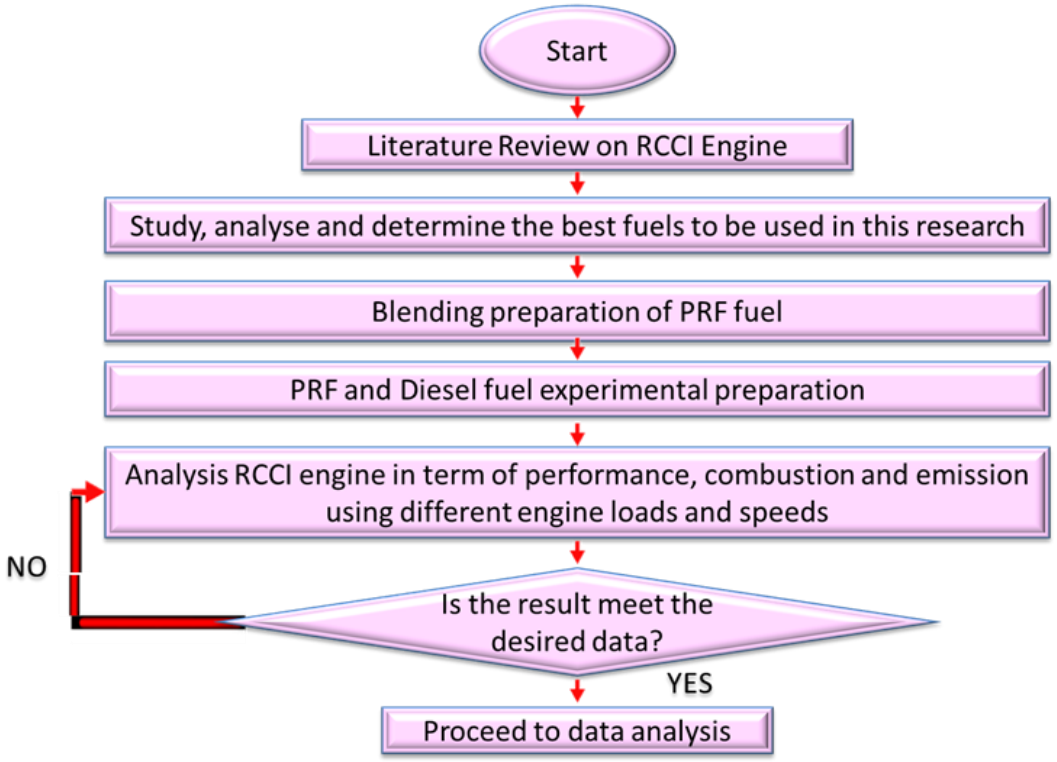

Figure 1. Project flowchart

Engine Modification

The diesel engine used to conduct the experiment and run the sample fuels is YANMAR Model TF120-M, a single cylinder diesel engine with 2400RPM and 12HP, water cooled, 4 cycle diesel engine with direct injection (DI) and natural aspirated engine. YANMAR TF120-M is manufactured by Yanmar Co.Ltd. The engine swept volume is 638cm3 with bore × stroke of 92 × 96 mm.

The experiment will be started by using diesel in normal engine mode at engine speed 900rpm, 1200rpm, 1500rpm, 1800rpm, and 2100rpm with various engine loads at 0%, 20%, 40% and 60%. The experiment then will be continued by using PRF20 in RCCI engine mode. Two beakers will be filled with PRF20 and diesel respectively. In this study, both beakers serve as fuel tanks. Low reactivity fuel (PRF) is used at the port injection system while pure diesel is used at direct injection system. The two fuel tanks will be placed on separate weighing scales to determine the weight losses, which corresponds to fuel consumption. The engine switch will be turned on to start the engine power. Measure the engine performance first if the engine has been running for 15 minutes or has reached an oil temperature of 600C in order to ensure the engine reaches an appropriate operating condition. The selected engine performances parameters to be measured are torque, exhaust gas temperature, and power. It is also necessary to ensure that all computers are turned on and that all software is connected to the computer for data collection. The experiment will be repeated with different PRF values of PRF40 and PRF60 at five different rpm which is 900, 1200, 1500, 1800, 2100 rpm with four different stages of load which is 0%, 20%, 40% and 60% at TPS 0% and 15%. All data is checked and recorded.

The engine was modified to run the engine in a dual fuel injection. The change is made to the injection system at the port and dynamometer. To establish the RCCI engine mode, the diesel engine must be transformed from single fuel injection to dual fuel injection, which includes direct injection and port injection. Low reactivity fuel, which is the variable PRF values in this research is used at the port injection while pure diesel is used at direct injection as high reactivity fuel. Further details of the engine specifications used in this research can be obtained from Table 1.

Table 1. Engine specifications

Model	Yanmar Model TF120M
Type	Horizontal single-cylinder 4-stroke diesel engine
Bore (mm)	92
Stroke (mm)	96
Displace volume (cm^3)	638
Compression ratio	17.7:1
Continuous rating output	10.5 HP @ 2400 rpm
Maximum rating output	12.0 HP @ 2400 rpm
Fuel injection type	Direct Injection
Injection timing	17^o BTDC
Max power	7.7 kW @ 2400 rpm
Max torque	161 Nm @ 4500 rpm
Cooling system	Water-radiation
Fuel tank capacity	11L

Experimental Software

KANE LIVE displays "real time" readings for HC, CO, CO2, NOx, and O2 emission. All data is viewable digitally in computer, allowing for easy tracking of parameters as they change over speeds and loads. The standard file for importing and exporting data, a.CSV file, can be used to save and keep all the live data in the computer. DynoMonV4 is used to measure the performance of the RCCI engine. The performance parameters measured by the engine speeds and loads in this experiment are torque, power, Brake Specific Fuel Consumption and Exhaust Gas Temperature. Standard factors like RPM, Coolant temperature, load, MAP, and MAF can be modified by TunerStudio MS Lite filtering data to fit your configuration or preferences. The calibration settings of the controller are being changed. You can use it to record runtime data and capture it. Offline tuning, loading and saving tune files, and basic data logging are among the functions offered. Picolog6 is used to measure the temperature of the engine such as intake temperature, engine oil temperature and exhaust temperature.

KANE AUTOplus Gas Analyser, which is handheld and portable, is used to measure combustion characteristics of CO, HC, CO2, O2, and NOx. It is connected to KANELIVE software and the software will display the results of gas emissions. A weighing balance is an instrument that is used to measure the weight of the fuel decrement for the combustion process in this experiment. The additional dynamometer connected to the diesel engine is employed for measuring force, torque, and power. The power produced by the engine, motor or other rotating prime mover can be calculated by simultaneously measuring torque and rotational speed (RPM). The dynamometer used in this experiment act as load in a real-world vehicle. It can be adjusted to increase or reduce the load during the experiment. The dynamometer is also connected to the diesel engine to measure the torque, power and force.

Fuel Preparation

The RCCI engine mode used two types of fuel which are Low Reactivity Fuel (LRF) and High Reactivity Fuel (HRF). In this experiment, pure diesel (B0) that was injected by direct injection was employed as the high reactivity fuel (HRF), while Primary Reference Fuel (PRF 20, 40, 60), which were injected using a port injection technique employed as the low reactivity fuel in this experiment. Additionally, as the pure diesel is supplied to the direct injection system, it requires no blending process. The volume of each n-heptane and iso-octane used in this experiment are tabulated in Table 2 below.

Heptane, commonly known as n-heptane, is an important component of gasoline and has the chemical formula of H3C(CH2)5CH3 or C7H16 (petrol). When used as a test fuel component in anti-knock test engines, a fuel that is 100% heptane corresponds to the zero point on the octane rating scale. The percentage of iso-octane in heptane, which is stated on gasoline (petrol) pumps around the world, is the octane number, which relates to the antiknock qualities of a comparative mixture of heptane and isooctane. Table 3 shows N-heptane properties. Isooctane is an alkane composed of pentane with two methyl substituents at position 2 and one methyl substituent at position 4 as illustrated in Table 4. It acts as a fuel additive, a nonpolar solvent, and a nephrotoxin. It is a volatile organic substance and an alkane.

Table 2. Fuel matrices

Fuel mixture (500ml each blend)		
Primary reference fuel	n-heptane	iso-octane
PRF20	80%	20%
PRF40	60%	40%
PRF60	40%	60%

Table 3. N-heptane properties

n-heptane properties	
Properties	Description
IUPAC Name	heptene@Dipropylmethane
Molecular formula	C7H16
Molecular Weight	100.2
Physical Description	-clear colourless liquid -petroleum-like odor -Flash point 25°F -Less dense than water - insoluble in water - Vapours heavier than air
Boiling Point	98.5 °C
Melting Point	-90.6
Autoignition Temperature	433 °F (285 °C)
Experimental Properties	It is a lighter component in gasoline, burns more explosively, causing engine pre-ignition (knocking) in its pure form, as opposed to octane isomers, which burn more slowly and give less knocking.

Table 4. Iso-octane properties

Iso-octane properties	
Properties	Description
IUPAC Name	2,2,4-trimethylpentane
Molecular formula	C8H18
Molecular Weight	114.23
Physical Description	-clear colourless liquid -petroleum-like odor -Less dense than water - insoluble in water - Vapours are heavier than air
Boiling Point	99.2 °C
Melting Point	-107.3
Autoignition Temperature	784 °F (418 °C)
Experimental Properties	Less than 32 Saybolt universal second Antiknock octane number 100; dipole moment: 0
Usage	2,2,4-Trimethylpentane is used in determining octane numbers of fuels, in spectrophotometric analysis, as a solvent and thinner, and in organic syntheses.

The process of blending the PRF20, PRF40 and PRF60 involved in this experiment is the mixing of two types of fuels in a beaker which are iso-octane and n-heptane. Pure isooctane (2, 2, 4-trimethylpentane) has been assigned an octane number of 100 because of its excellent antiknock properties and n-heptane is assigned an octane number of zero because of its propensity to auto-ignite easily. Therefore, a 80:20, 60:40 and 40:60 blending ratio of iso-octane and n-heptane respectively are used to prepare the PRF20, PRF40 and PRF60 in this experiment. The fuel blending requires stirring process for 15 minutes with 500rpm by using IKA RW20 Digital

Overhead Stirrer. After the fuel blending process is completed, the blended fuel will be kept for at least 2 hours before can be used for the experiment.

Result and Discussion

This experiment investigates the the effect of blending Diesel-PRF in RCCI engine mode on torque, power, exhaust gas temperature (EGT), and gas emissions. The experiment was conducted under the determined operational conditions. This chapter explains the engine results for the throttle positioning sensor (TPS) 0% and 15%.

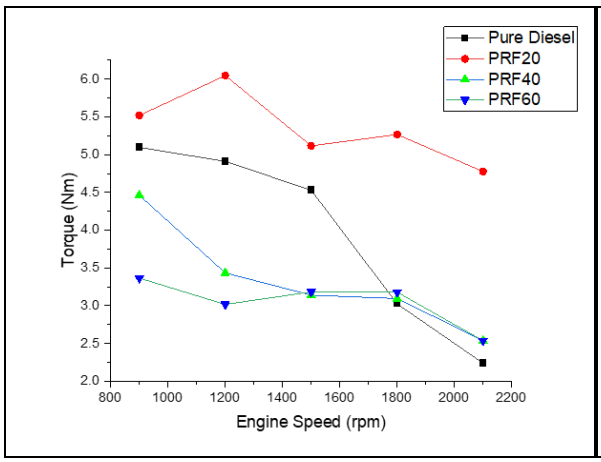

Figure 2. Torque at 0% Load

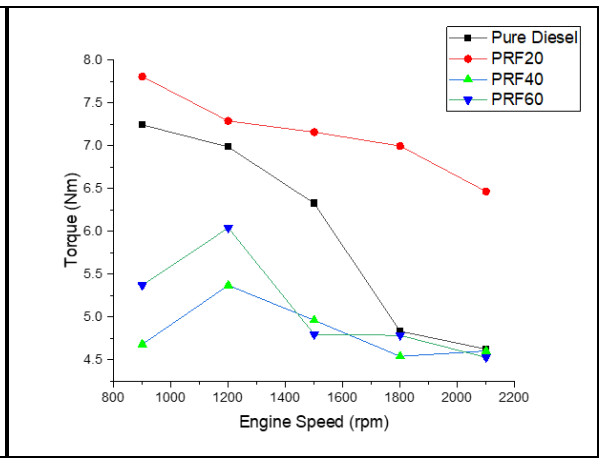

Figure 3. Torque at 20% Load

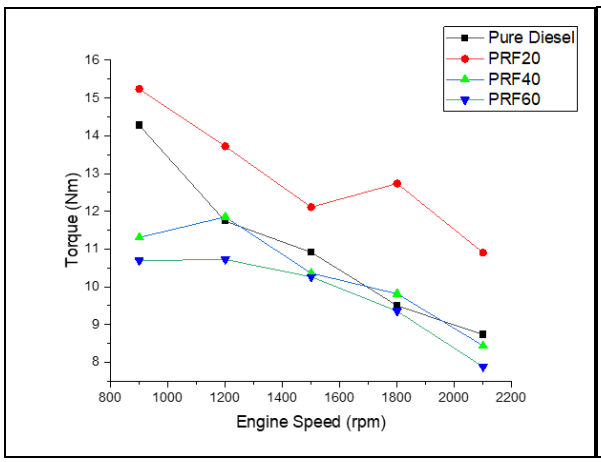

Figure 4. Torque at 40% Load

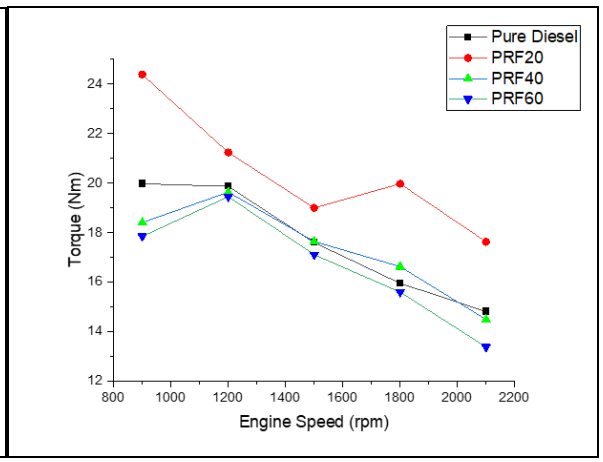

Figure 5. Torque at 60% Load

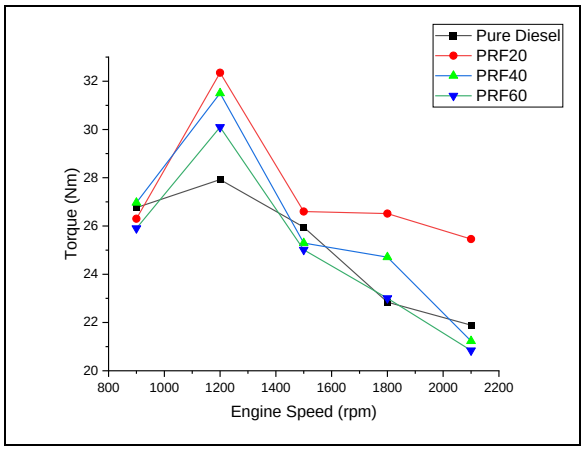

Figure 6. Torque at 80% Load

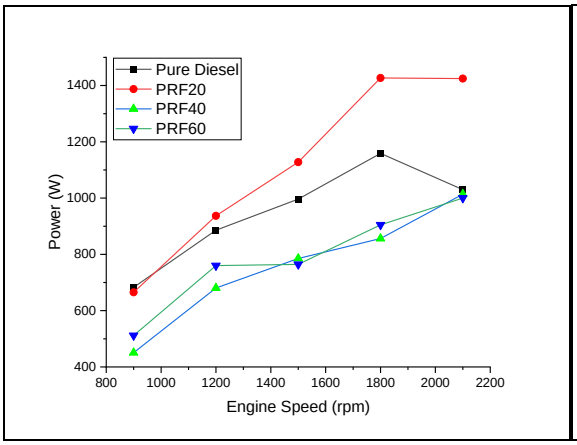

Figure 7. Power at 0% load

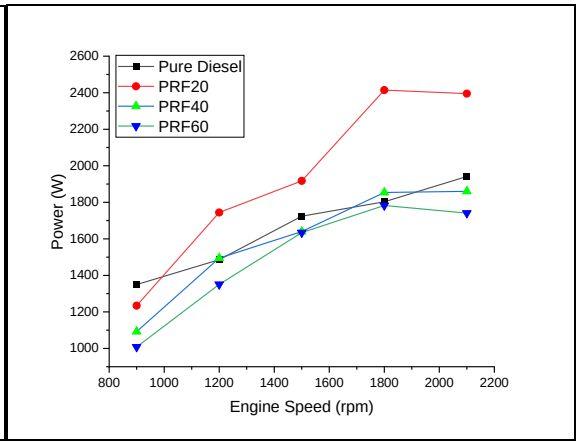

Figure 8. Power at 20% load

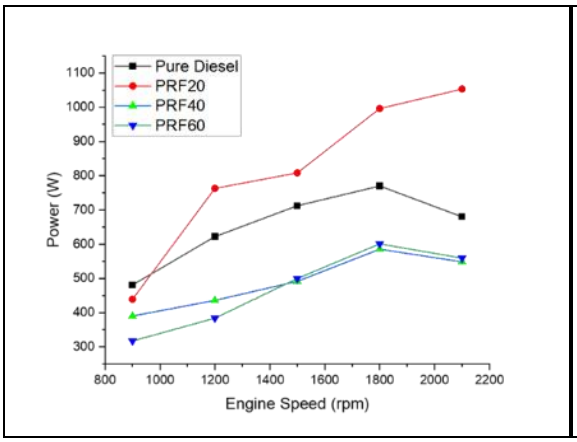

Figure 9. Power at 40% load

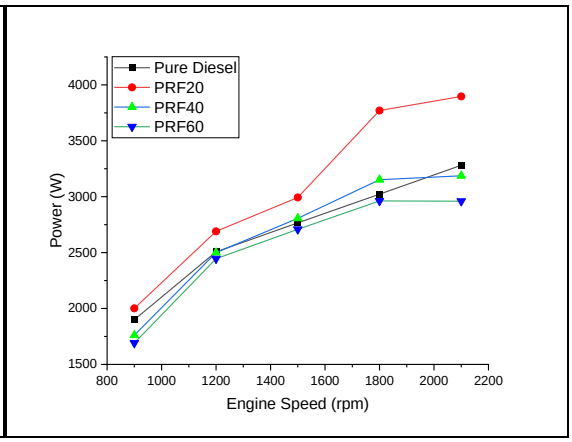

Figure 10. Power at 60% load

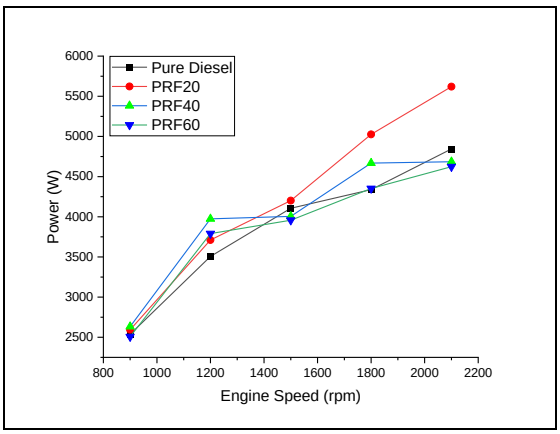

Figure 11. Power at 80% load

Figures 2-6 show the result of the torque output with five different loads for 0 % 15 throttle positioning sensors (TPS). Torque decreases with increased engine speed and load. The torque increases with increase load is because as the load increases, the engine will increase its speed resulting the torque to decrease. The torque graph shows increasing trend with increase the various of load test. Moreover, more air and diesel were injected for the engine to stay at each rpm which provide more chemical energy burnt is convert into kinetic energy which means the torque produces of the engine will also increase. Additionally, the torque illustrates a significant decrease trend with 15% throttle positioning sensor's opening. This is due to the fact that a lower temperature combustion process is the only way to fulfil the LTC's goal of improved emission efficiency. Because not all of the fuel is burned during LTC, a rich mixture is used to accomplish low temperature combustion, which results in a low temperature. The pressure in the cylinder is lower than other advanced combustion strategies because of the low temperature at which combustion is accomplished and the amount of unburned fuel that is still present in the cylinder, which results in reduced torque output from the engine.

When more PRF fuel is pumped into the RCCI engine mode, the mixture becomes richer. Rich mixture causes the fuel to remain unburned, which causes the mixture's temperature to slightly decrease. Therefore, the lower the temperature, the lower the torque output as the combustion's low temperature also causes a drop in cylinder pressure. When low reactivity fuel is not injected in the RCCI engine, the cylinder temperature is at its ideal level or is not low as the low reactivity fuel is injected. Because of this, under these conditions, the pressure and complete combustion produced by the temperature and the lack of a rich mixture, respectively, deliver the higher torque output.

Figures 7-11 show result of power output with five different loads with five different loads and five different loads for 0% and 15% throttle positioning sensors (TPS). Power increase as the engine speed and load increases. The power increase with increase load is because from the beginning torque is always increase with increasing load. Since power and torque are directly proportional, the power is also increase with increase in engine load. The power also increased with the increasing the amount of rpm. This is because more air and fuel caused more energy to be released, thus the engine provides more power to the vehicle. Additionally, as the quantity of the throttle positioning sensor is increased, the power value output decreases. This happens as a result of the injection of low reactivity fuel into the combustion chamber. The low temperature of the combustion techniques is utilised to minimise the potential value production of the emissions because the LTC's major goal is to reduce emissions. Since power and torque are directly inversely correlated, as the throttle positioning sensor that controls the amount of low reactivity fuel increases, power will also decrease. The lower temperature of the combustion caused low torque because there is still unburned fuel in the cylinder.

Highest engine speed combines with only high reactivity create much higher temperature and pressure thus there is no unburnt fuel left in the cylinder which create the most power value ouput. The higher load also makes the torque and power increase since the torque and power are directly proportional. This is because the low temperature combustion left the unburnt fuel in the cylinder hence not all the fuel is burn to make the temperature higher. Plus, with the low load and low rpm make the torque available at this point is not higher enough to make greater power output. Hence, the load, rpm and the amount of tps opening is directly proportional to the power output is produced.

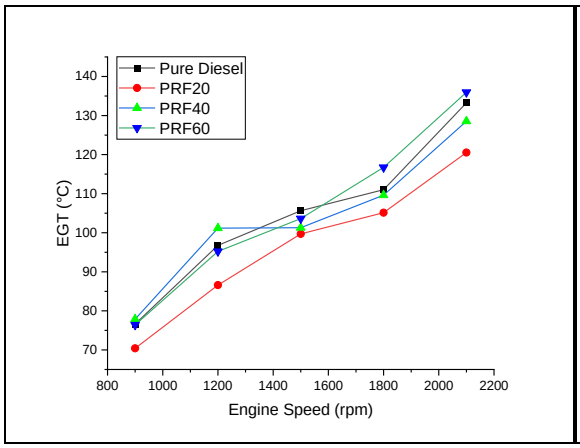

Figure 12. EGT at 0% Load

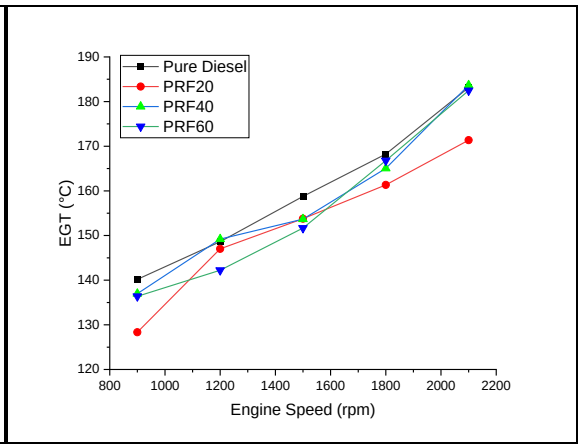

Figure 13. EGT at 20% Load

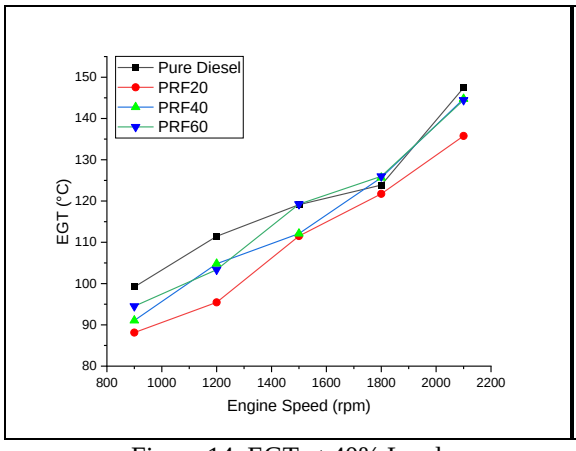

Figure 14. EGT at 40% Load

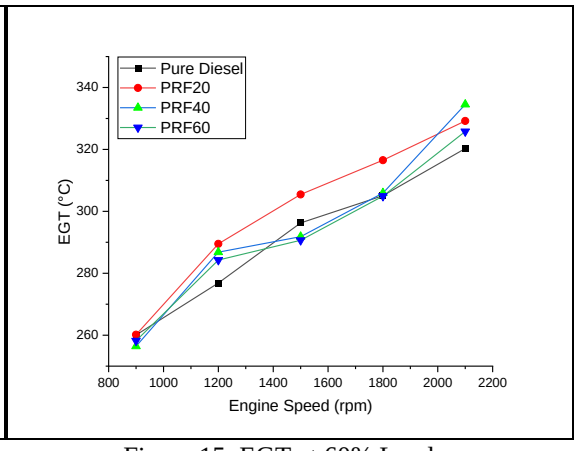

Figure 15. EGT at 60% Load

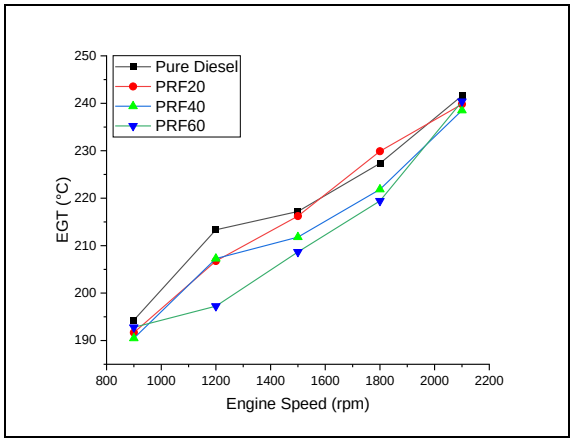

Figure 16. EGT at 60% Load

Figures 12-16 show the result of the Exhaust Gas Temperature with five different loads for various throttle positioning sensor (TPS). EGT is increase with increase engine speed and load. The EGT increase when the engine speed increase is because more air and fuel is injected in the combustion cylinder hence increase the combustion temperature thus make the EGT is also increase. EGT and engine is directly proportional. In addition, EGT is also increase with increase the engine load. This is because, the torque increase with load increase. Torque is increase due to engine speed is slow down hence pressure and temperature is increase too. Hence, the EGT will increase by the load. EGT and engine load is also directly proportional. Another than that, EGT will decrease with increase in Throttle Positioning Sensor (TPS). This is because a rich fuel mixture by opening a TPS will left the unburnt fuel in the cylinder. Hence, the combustion temperature is low because of the unburnt fuel thus lower the EGT value. The EGT and the TPS is inversely proportional.

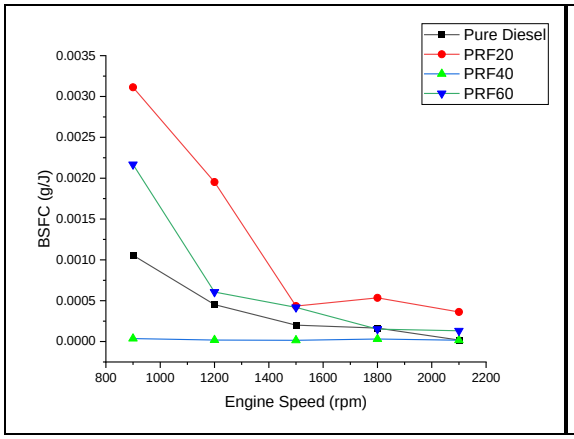

Figure 17. BSFC at 0% Load

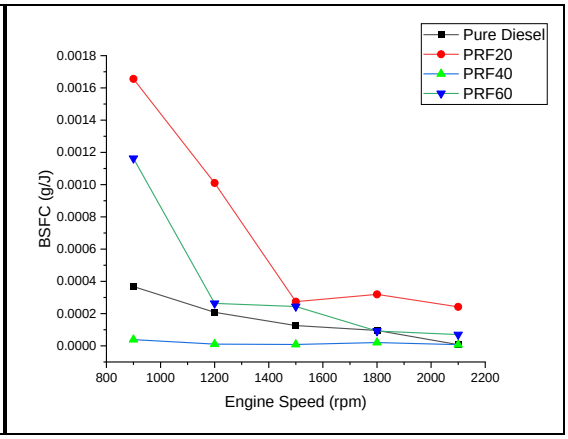

Figure 18. BSFC at 20% Load

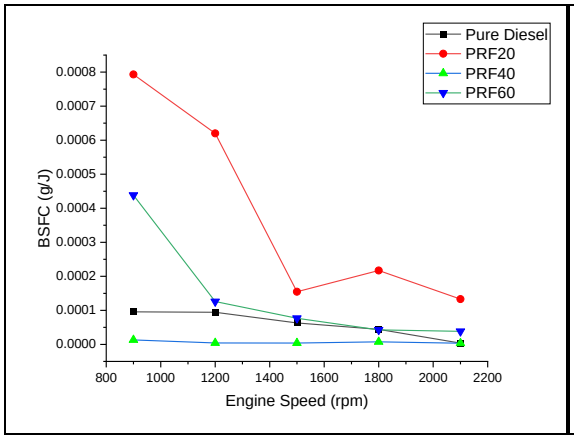

Figure 19. BSFC at 40% Load

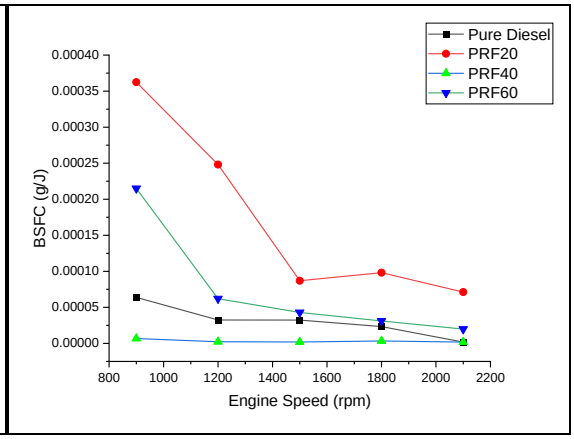

Figure 20. BSFC at 60% Load

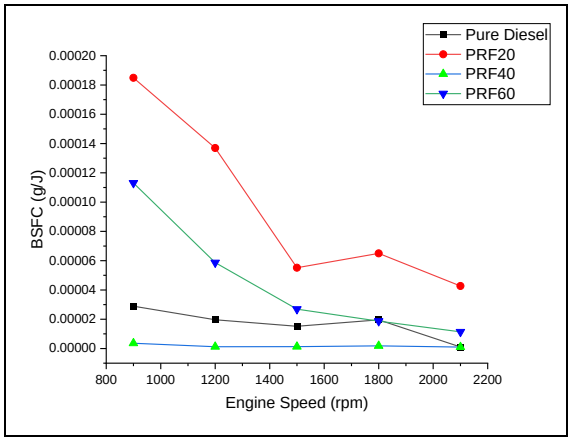

Figure 21. BSFC at 80% Load

Without the presence of the low reactivity fuel, the temperature of the combustion cylinder is higher since there is no unburnt fuel left. Moreover, the highest load is also contributed to the maximum EGT value output created. This is because, the higher the engine load, the higher the torque value to the engine. Pressure and temperature always directly proportional to the torque value. Hence, at the highest torque occur, the temperature is always the highest at the circumstances. Plus, the EGT output is also depends on the engine speed. This is because, the higher the engine speed, the higher the amount of air and fuel is injected in the cylinder create more pressure and temperature. But it is vice versa when the low reactivity fuel is start to inject because the combustion is richer hence the temperature will decrease. It only applicable at tps 0% or only high reactivity fuel is running.

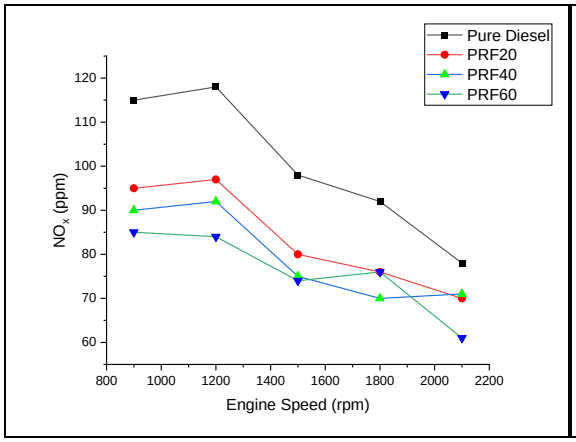

Figure 22. NOx at 0% Load

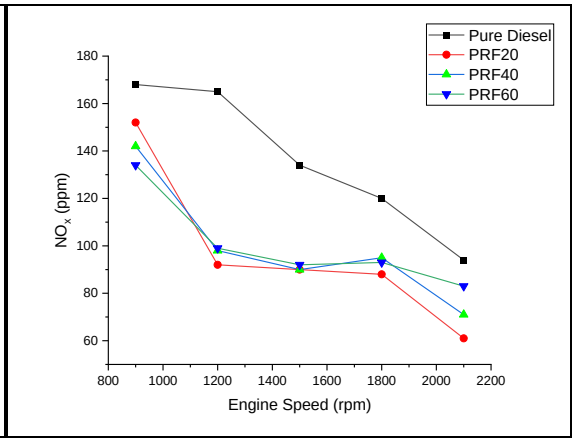

Figure 23. NOx at 20% Load

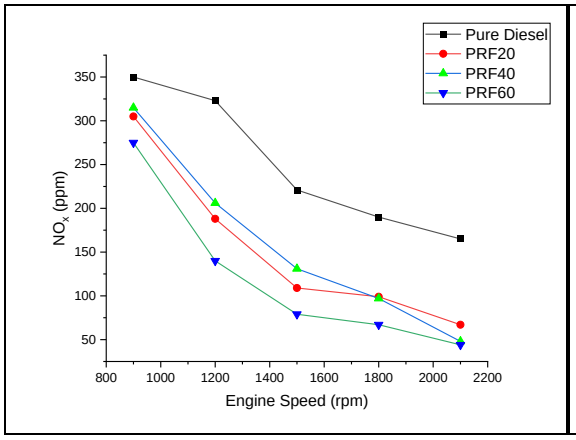

Figure 24. NOx at 40% Load

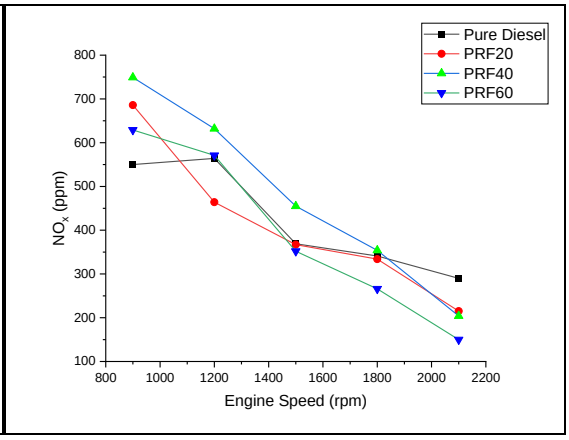

Figure 25. NOx at 60% Load

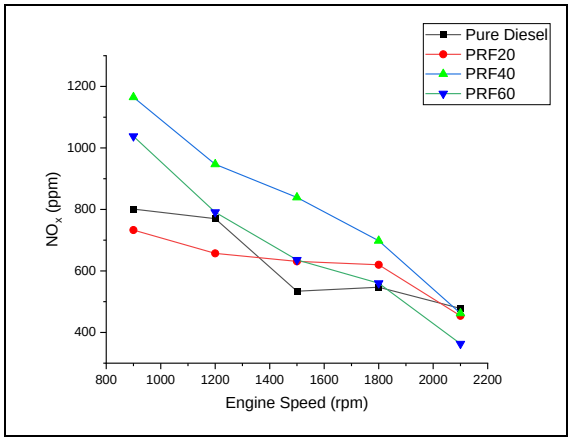

Figure 26. NOx at 80% Load

Figure 17-21 show BSFC result with five different loads for various throttle positioning sensor (TPS). The BSFC was found to decrease with increase in load and speeds for all tested fuels at 0% and 15% TPS. This is due to the higher percentage increase in brake power with load as compared to the increase in fuel consumption. The main reason for reduction in BSFC with load is the conversion efficiency of the fuel. At higher loads, the turbulence and in-cylinder temperature inside the combustion chamber will be high which helps in the atomization and proper mixing of fuel resulting in higher combustion efficiency. Other than that, the engine will be running with richer air fuel ratio at lower loads compared to full load condition. However, if a constant speed engine is used, then BSFC will be affected by the torque speed characteristics. Low BSFC values are obviously desirable.

Figures 22-26 show result of NOx emission with five different loads and five different loads for 0% and 15% throttle positioning sensors (TPS). NOx emission increase as the engine load increases and decreases as the engine speed increase. Another advantage of this engine is its emissions, which are extremely low in nitrogen oxide and particulate matter, such as soot. On a regular diesel engine, these kinds of pollutants cause problems. The cool burning, on the other hand, does not emit nitrogen oxide when using an RCCI engine. As the engine speed increases, the RCCI engine uses less diesel fuel, therefore it allows the diesel fuel to have more time to mix. The majority of diesel fuel is well blended and does not produce particulate matter. As a result, particulate matter and nitrogen oxide levels are extremely low in this engine, and it is super-efficient, up to 10-15% more efficient than a standard diesel engine. This is mainly as a result of having lower combustion temperature and because of the less heat transfer within the cylinder. Other possible assumption is it could be due to the higher latent heat of vaporization of PRF, which leads to reduction in the combustion gas temperature thereby reducing the NOx emissions.

Conclusion

This paper provides a brief summary of the project and a list of recommendations that can be used in future research. The application of the RCCI engine has been investigated to increase the capacity of the modified diesel engine to operate with port injection system. In order to investigate whether diesel engines can be made to burn more efficiently and perform better than other conventional engines, the application of the RCCI engine has also been investigated experimentally with the PRF20, PRF40 and PRF60. Regarding the consequences of the dual injection system or RCCI utilised in diesel engines in terms of performance and gas emissions, new information is created. This experiment involved creating a PRF20, PRF40 and PRF60 fuel by blending iso-octane by 20%, 40% and 60% and n-heptane by 80%, 60% and 40% in order to carry out the research.

Engine performance in terms of torque, power, BSFC and exhaust gas temperature are measured in this project. While the exhaust gas temperature was manually retrieved using PICOLOG software, the raw data for torque and power were collected from Focus Applied Technologies' software. According to the results, engine speed and load both enhance the power value. However, due to the LTC strategy implemented during the RCCI engine mode combustion, there is a considerable reduction in torque when operating in the RCCI mode as opposed to merely running pure diesel or tps0. The torque value kept decreasing from low to highest rpm but increasing as engine load increases. The lowest torque value is recorded at 2100rpm at tps 0% with load 0%. Due to the low temperature in the cylinder caused by the rich mixture in RCCI mode, the engine is unable to completely burn the mixture, which reduces the torque produced. The power value follows the same pattern. It is impacted by the

torque as well. The power is significantly reduced compared to simply when pure diesel is operating because of the LTC effect encouraged by RCCI. The EGT data demonstrates that when the RCCI mode is operating, the temperature was lower than when simply pure diesel was operating. NOx, was analyzed in this project. NOx emissions increased as the engine load increased but decreased as the engine speeds increased.

Recommendations

While the exhaust gas temperature is decreasing, the recommendation of this RCCI mode combustion strategy may be useful to reduce emissions. However, due to the low temperature combustion provided when running the RCCI mode, the performance in terms of torque and power is not really improved. To further enhance engine performance and reduced the gas emissions in this project, new strategies can be implemented.

Scientific Ethics Declaration

The authors declare that the scientific ethical and legal responsibility of this article published in EPSTEM journal belongs to the authors.

Acknowledgements or Notes

* This article was presented as an oral presentation at the International Conference on Technology, Engineering and Science (www.icontes.net) held in Antalya/Turkey on November 16-19, 2022.

*The authors would like to thank the Ministry of Higher Education for providing fi-nancial support under Research Acculturation of Early Career Researchers No. RACER/1/2019/TK03/UMP/1 and University Malaysia Pahang for laboratory facilities as well as additional financial support under Internal Research grant RDU192605.

References

Ansari, E., Shahbakhti, M., & Naber, J. (2018). Optimization of performance and operational cost for a dual mode diesel-natural gas RCCI and diesel combustion engine. *Applied Energy*, *231*(September), 549–561. https://doi.org/10.1016/j.apenergy.2018.09.040

Benajes, J., García, A., Monsalve-Serrano, J., & Lago Sari, R. (2018). Fuel consumption and engine-out emissions estimations of a light-duty engine running in dual-mode RCCI/CDC with different fuels and driving cycles. *Energy*, *157*, 19–30. https://doi.org/10.1016/j.energy.2018.05.144

Charitha, V., Thirumalini, S., Prasad, M., & Srihari, S. (2019). Investigation on performance and emissions of RCCI dual fuel combustion on diesel - bio diesel in a light duty engine. *Renewable Energy*, *134*(x), 1081–1088. https://doi.org/10.1016/j.renene.2018.09.048

Dong, Y., Kaario, O., Hassan, G., Ranta, O., Larmi, M., & Johansson, B. (2020). High-pressure direct injection of methanol and pilot diesel: A non-premixed dual-fuel engine concept. *Fuel*, *277*(April), 117932. https://doi.org/10.1016/j.fuel.2020.117932

García, A., Monsalve-Serrano, J., Martinez-Boggio, S., Gaillard, P., Poussin, O., & Amer, A. A. (2020). Dual fuel combustion and hybrid electric powertrains as potential solution to achieve 2025 emissions targets in medium duty trucks sector. *Energy Conversion and Management*, *224*(June), 113320. https://doi.org/10.1016/j.enconman.2020.113320

García, A., Monsalve-Serrano, J., Villalta, D., & Sari, R. (2019). Fuel sensitivity effects on dual-mode dual-fuel combustion operation for different octane numbers. *Energy Conversion and Management*, *201*(October). https://doi.org/10.1016/j.enconman.2019.112137

Han, W., Li, B., Pan, S., Lu, Y., & Li, X. (2018). Combined effect of inlet pressure, total cycle energy, and start of injection on low load reactivity controlled compression ignition combustion and emission characteristics in a multi-cylinder heavy-duty engine fueled with gasoline/diesel. *Energy*, *165*, 846–858. https://doi.org/10.1016/j.energy.2018.10.029

Kahnooji, M., & Yazdani, K. (2021). The effect of direct water injection on a diesel-gasoline reactivity controlled compression ignition engine. *Fuel*, *285*(September 2020). https://doi.org/10.1016/j.fuel.2020.119109

Kakaee, A. H., Nasiri-Toosi, A., Partovi, B., & Paykani, A. (2016). Effects of piston bowl geometry on combustion and emissions characteristics of a natural gas/diesel RCCI engine. *Applied Thermal Engineering*, *102*, 1462–1472. https://doi.org/10.1016/j.applthermaleng.2016.03.162

Kakoee, A., Bakhshan, Y., Barbier, A., Bares, P., & Guardiola, C. (2020). Modeling combustion timing in an RCCI engine by means of a control oriented model. *Control Engineering Practice*, *97*(February). https://doi.org/10.1016/j.conengprac.2020.104321

Li, J., Ling, X., Liu, D., Yang, W., & Zhou, D. (2018). Numerical study on double injection techniques in a gasoline and biodiesel fueled RCCI (reactivity controlled compression ignition) engine. *Applied Energy*, *211*(August 2017), 382–392. https://doi.org/10.1016/j.apenergy.2017.11.062

Li, J., Yang, W., & Zhou, D. (2017). Review on the management of RCCI engines. *Renewable and Sustainable Energy Reviews*, *69*(November 2016), 65–79. https://doi.org/10.1016/j.rser.2016.11.159

Li, W., Liu, Z., & Wang, Z. (2016). Experimental and theoretical analysis of the combustion process at low loads of a diesel natural gas dual-fuel engine. *Energy*, *94*, 728–741. https://doi.org/10.1016/j.energy.2015.11.052

Liu, X., Srna, A., Yip, H. L., Kook, S., Chan, Q. N., & Hawkes, E. R. (2021). Performance and emissions of hydrogen-diesel dual direct injection (H2DDI) in a single-cylinder compression-ignition engine. *International Journal of Hydrogen Energy*, *46*(1), 1302–1314. https://doi.org/10.1016/j.ijhydene.2020.10.006

Luong, M. B., Yu, G. H., Chung, S. H., & Yoo, C. S. (2017). Ignition of a lean PRF/air mixture under RCCI/SCCI conditions: A comparative DNS study. *Proceedings of the Combustion Institute*, *36*(3), 3623–3631. https://doi.org/10.1016/j.proci.2016.08.038

Mikulski, M., Ramesh, S., & Bekdemir, C. (2019). Reactivity Controlled Compression Ignition for clean and efficient ship propulsion. *Energy*, *182*, 1173–1192. https://doi.org/10.1016/j.energy.2019.06.091

Nazemi, M., & Shahbakhti, M. (2016). Modeling and analysis of fuel injection parameters for combustion and performance of an RCCI engine. *Applied Energy*, *165*, 135–150. https://doi.org/10.1016/j.apenergy.2015.11.093

Pan, S., Li, X., Han, W., & Huang, Y. (2017). An experimental investigation on multi-cylinder RCCI engine fueled with 2-butanol/diesel. *Energy Conversion and Management*, *154*(August), 92–101. https://doi.org/10.1016/j.enconman.2017.10.047

Pan, S., Liu, X., Cai, K., Li, X., Han, W., & Li, B. (2020). Experimental study on combustion and emission characteristics of iso-butanol/diesel and gasoline/diesel RCCI in a heavy-duty engine under low loads. *Fuel*, *261*(August 2019). https://doi.org/10.1016/j.fuel.2019.116434

Park, H., Shim, E., & Bae, C. (2019). Injection strategy in natural gas–diesel dual-fuel premixed charge compression ıgnition combustion under low load conditions. *Engineering*, *5*(3), 548–557. https://doi.org/10.1016/j.eng.2019.03.005

Pedrozo, V. B., May, I., Dalla Nora, M., Cairns, A., & Zhao, H. (2016). Experimental analysis of ethanol dual-fuel combustion in a heavy-duty diesel engine: An optimisation at low load. *Applied Energy*, *165*, 166–182. https://doi.org/10.1016/j.apenergy.2015.12.052

Pedrozo, V. B., May, I., Lanzanova, T. D. M., & Zhao, H. (2016). Potential of internal EGR and throttled operation for low load extension of ethanol-diesel dual-fuel reactivity controlled compression ignition combustion on a heavy-duty engine. *Fuel*, *179*, 391–405. https://doi.org/10.1016/j.fuel.2016.03.090

Piqueras, P., García, A., Monsalve-Serrano, J., & Ruiz, M. J. (2019). Performance of a diesel oxidation catalyst under diesel-gasoline reactivity controlled compression ignition combustion conditions. *Energy Conversion and Management*, *196*(May), 18–31. https://doi.org/10.1016/j.enconman.2019.05.111

Rangasamy, M., Duraisamy, G., & Govindan, N. (2020). A comprehensive parametric, energy and exergy analysis for oxygenated biofuels based dual-fuel combustion in an automotive light duty diesel engine. *Fuel*, *277*(November 2019), 118167. https://doi.org/10.1016/j.fuel.2020.118167

Raza, M., Wang, H., & Yao, M. (2019). Numerical investigation of reactivity controlled compression ignition (RCCI) using different multi-component surrogate combinations of diesel and gasoline. *Applied Energy*, *242*(March), 462–479. https://doi.org/10.1016/j.apenergy.2019.03.115

Reitz, R. D., & Duraisamy, G. (2015). Review of high efficiency and clean reactivity controlled compression ignition (RCCI) combustion in internal combustion engines. *Progress in Energy and Combustion Science*, *46*, 12–71. https://doi.org/10.1016/j.pecs.2014.05.003

Saiteja, P., & Ashok, B. (2021). A critical insight review on homogeneous charge compression ignition engine characteristics powered by biofuels. *Fuel*, *285*(September 2020), 119202. https://doi.org/10.1016/j.fuel.2020.119202

Salahi, M. M., Esfahanian, V., Gharehghani, A., & Mirsalim, M. (2017). Investigating the reactivity controlled compression ignition (RCCI) combustion strategy in a natural gas/diesel fueled engine with a pre-chamber. *Energy Conversion and Management*, *132*, 40–53. https://doi.org/10.1016/j.enconman.2016.11.019

Sener, R., Yangaz, M. U., & Gul, M. Z. (2020). Effects of injection strategy and combustion chamber modification on a single-cylinder diesel engine. *Fuel*, *266*(January), 117122. https://doi.org/10.1016/j.fuel.2020.117122

Shim, E., Park, H., & Bae, C. (2018). Intake air strategy for low HC and CO emissions in dual-fuel (CNG-diesel) premixed charge compression ignition engine. *Applied Energy*, *225*(May), 1068–1077. https://doi.org/10.1016/j.apenergy.2018.05.060

Singh, A. P., Kumar, V., & Agarwal, A. K. (2020). Evaluation of comparative engine combustion, performance and emission characteristics of low temperature combustion (PCCI and RCCI) modes. *Applied Energy*, *278*(July). https://doi.org/10.1016/j.apenergy.2020.115644

Wang, L., Chen, Z., Zhang, T., & Zeng, K. (2019). Effect of excess air/fuel ratio and methanol addition on the performance, emissions, and combustion characteristics of a natural gas/methanol dual-fuel engine. *Fuel*, *255*(May), 115799. https://doi.org/10.1016/j.fuel.2019.115799

Wang, Y., Yao, M., Li, T., Zhang, W., & Zheng, Z. (2016). A parametric study for enabling reactivity controlled compression ignition (RCCI) operation in diesel engines at various engine loads. *Applied Energy*, *175*, 389–402. https://doi.org/10.1016/j.apenergy.2016.04.095

Wang, Y., Zhu, Z. W., Yao, M., Li, T., Zhang, W., & Zheng, Z. (2016). An investigation into the RCCI engine operation under low load and its achievable operational range at different engine speeds. *Energy Conversion and Management*, *124*, 399–413. https://doi.org/10.1016/j.enconman.2016.07.026

Author Information

Ahmad Fitri Yusop
Universiti Malaysia Pahang,
26600, Pekan, Pahang, Malaysia
Contact e-mail: *fitriy@ump.edu.my*

Mohamad Adzuan Aziz
Universiti Malaysia Pahang,
26600, Pekan, Pahang, Malaysia

Mohd Adnin Hamidi
Universiti Malaysia Pahang,
26600, Pekan, Pahang, Malaysia

Daing Mohamad Nafiz Daing Idris
Universiti Malaysia Pahang,
26600, Pekan, Pahang, Malaysia

Ummi Hafsah Zaidi
Universiti Malaysia Pahang,
26600, Pekan, Pahang, Malaysia

To cite this article:

Yusop, A.F., Aziz, M.A., Hamidi, M.A., Daing Idris, D.M.N., & Zaidi, U.H. (2022). Investigation on the RCCI engine on performance and emission. *The Eurasia Proceedings of Science, Technology, Engineering & Mathematics (EPSTEM), 21*, 525-540.